MASARYK UNIVERSITY

FACULTY OF SCIENCE

Strategies of Parasitism in Early Branching Apicomplexa

Habilitation Thesis

Andrea Bardůnek Valigurová

Department of Botany and Zoology

Brno 2019

Abstrakt

Tato habilitační práce, jejíž součástí je 16 vědeckých publikací, se věnuje hostitelsko-parazitickým interakcím a pohybu u bazálních linií výtrusovců (Apicomplexa), kteří představují jednu z nejúspěšnějších skupin eukaryotických jednobuněčných parazitů. Zaměřuji se na bazální výtrusovce, jako jsou protokokcidie, agamokokcidie, blastogregariny a gregariny omezené na bezobratlé hostitele a kryptosporidie parazitující obratlovce včetně člověka. Organizace jejich buněčného kortexu a cytoskeletu koreluje s různými způsoby motility a je výsledkem strukturálních změn invazivního stadia během proměny na trofozoita u parazitů s různými strategiemi parazitismu (epicelulární, extracelulární a intracelulární lokalizace), vedoucím k významným modifikacím nebo dokonce ztrátě mechanismů buněčné motility. Výsledky této studie odhalily obrovskou rozmanitost v subcelulární organizaci u bazálních výtrusovců související s jejich různými strategiemi parazitismu, což potvrzuje důležitost dalšího výzkumu, který by měl poskytnout hlubší pochopení biologie a evolučních cest u Apicomplexa obecně.

Abstract

This habilitation thesis, supplemented by 16 research papers, deals with host-parasite interactions and motility in early branching lineages of Apicomplexa, one of the most successful groups of eukaryotic unicellular parasites. I focus on basal apicomplexans such as protococcidia, agamococcidia, blastogregarines and gregarines restricted to invertebrate hosts and cryptosporidia parasitising vertebrates, including humans. The organisation of their cell cortex and cytoskeleton correlates with their diverse modes of motility and results from modifications to the zoite structure during transformation to the trophozoite stage in parasites with different parasitism strategies (epicellular, extracellular and intracellular localisation), leading to significant changes or even loss of cell motility mechanisms. The results of this study revealed enormous diversity in the subcellular organisation of deep-branching apicomplexans related to their different parasitism strategies, thereby confirming the importance of further research, which should provide a deeper understanding of the biology and evolutionary pathways of Apicomplexa in general.

Acknowledgement

I would like to thank all colleagues and friends who helped with the research presented in this thesis.

In particular, Timur G. Simdyanov, Gita G. Paskerova and Joseph Schrével contributed greatly to the papers dealing with marine apicomplexans from invertebrate hosts. I am also grateful to Isabelle Florent for her help with the research on cryptosporidia motility. Great thanks go to Naděžda Vaškovicová, who led me into the mysteries of freeze etching and taught me to read the replicas. My special thanks go to my students Magdaléna Kováčiková, Andrei Diakin, Janka Melicherová, Veronika Mazourová, Jana Ilgová and Lenka Tůmová, whose enthusiasm and friendly attitude gave me the energy to continue my research under all circumstances. I am deeply grateful to Milan Gelnar for the possibility to perform my research at the Department of Botany and Zoology of Masaryk University in Brno. I am also greatly indebted to the Laboratory of Electron Microscopy, Biology Centre of the Czech Academy of Sciences in České Budějovice, where the majority of my ultrastructural investigations were performed.

Finally, I would like to thank my family, in particular my parents for their endless support and my husband Petr, who was very patient with me during the thesis completion and took great care of our little son.

Content

7.1 Valigurová A. (2012). Sophisticated adaptations of *Gregarina cuneata* (Apicomplexa) feeding stages for epicellular parasitism. PLoS One 7(8), e42606.

7.2 Valigurová A., Vaškovicová V., Musilová N., Schrével J. (2013). The enigma of eugregarine epicytic folds: where gliding motility originates? Frontiers in Zoology 10, 57.

7.3 Melicherová J., Ilgová J., Kváč M., Sak B., Koudela B., Valigurová A. (2014). Life cycle of *Cryptosporidium muris* in two rodents with different responses to parasitization. Parasitology 141(2), 287-303.

7.4 Valigurová A., Paskerova G.G., Diakin A., Kováčiková M., Simdyanov T.G. (2015). Protococcidian *Eleutheroschizon duboscqi*, an unusual apicomplexan interconnecting gregarines and cryptosporidia. PLoS One 10(4), e0125063.

7.5 Melicherová J., Mazourová V., Valigurová A. (2016). In vitro excystation of *Cryptosporidium muris* oocysts and viability of released sporozoites in different incubation media. Parasitology Research 115(3), 1113-1121.

7.6 Diakin A., Paskerova G.G., Simdyanov T.G., Aleoshin V.V., Valigurová A. (2016). Morphology and molecular phylogeny of coelomic gregarines (Apicomplexa) with different types of motility: *Urospora ovalis* and *U. travisiae* from the polychaete *Travisia forbesi*. Protist 167(3), 279-301.

7.7 Schrével J., Valigurová A., Prensier G., Chambouvet A., Florent I., Guillou L. (2016). Ultrastructure of *Selenidium pendula*, the type species of archigregarines, and phylogenetic relations to other marine Apicomplexa. Protist 167(4), 339-368.

7.8   Chambouvet A., Valigurová A., Pinheiro L.M., Richards T.A., Jirků M. (2016). *Nematopsis temporariae* (Gregarinasina, Apicomplexa, Alveolata) is an intracellular infectious agent of tadpole livers. Environmental Microbiology Reports 8(5), 675-679.

7.9   Diakin A., Wakeman K.C., Valigurová A. (2017). Description of *Ganymedes yurii* sp. n. (Ganymedidae), a new gregarine species from the Antarctic amphipod *Gondogeneia* sp. (Crustacea). Journal of Eukaryotic Microbiology 64(1), 56-66.

7.10   Kováčiková M., Simdyanov T.G., Diakin A., Valigurová A. (2017). Structures related to attachment and motility in the marine eugregarine *Cephaloidophora* cf. *communis* (Apicomplexa). European Journal of Protistology 59, 1-13.

7.11   Valigurová A., Vaškovicová N., Diakin A., Paskerova G.G., Simdyanov T.G., Kováčiková M. (2017). Motility in blastogregarines (Apicomplexa): Native and drug-induced organisation of *Siedleckia nematoides* cytoskeletal elements. PLoS One 12(6), e0179709.

7.12   Melicherová J., Hofmannová L., Valigurová A. (2018). Response of cell lines to actual and simulated inoculation with *Cryptosporidium proliferans*. European Journal of Protistology 62, 101-121.

7.13   Valigurová A., Pecková R., Doležal K., Sak B., Květoňová D., Kváč M., Nurcahyo W., Foitová I. (2018). Limitations in the screening of potentially anti-cryptosporidial agents using laboratory rodents with gastric cryptosporidiosis. Folia Parasitologica 65, 010.

7.14   Kováčiková M., Vaškovicová N., Nebesářová J., Valigurová A. (2018). Effect of jasplakinolide and cytochalasin D on cortical elements involved in the gliding motility of the eugregarine *Gregarina garnhami* (Apicomplexa). European Journal of Protistology 66, 97-114.

7.15   Simdyanov T.G., Paskerova G.G., Valigurová A., Diakin A., Kováčiková M., Schrével J., Guillou L., Dobrovolskij A.A., Aleoshin V.V. (2018). First ultrastructural and molecular phylogenetic evidence from the blastogregarines, an early branching lineage of plesiomorphic Apicomplexa. Protist 169(5), 697-726.

7.16   Paskerova G.G., Miroliubova T.S., Diakin A., Kováčiková M., Valigurová A., Guillou L., Aleoshin V.V., Simdyanov T.G. (2018). Fine structure and molecular phylogenetic position of two marine gregarines, *Selenidium pygospionis* sp. n. and *S. pherusae* sp. n., with notes on the phylogeny of Archigregarinida (Apicomplexa). Protist 169(6), 826-852.

8   Other publications related to the habilitation thesis

1 Introduction

Apicomplexa consist entirely of parasitic genera occurring in a wide spectrum of invertebrates and vertebrates, including humans. Their representatives have evolved unique adaptations for invading and surviving within hosts. It is assumed that ancestral apicomplexans parasitised marine annelids and that their adaptation to a parasitic lifestyle and further radiation took place before the era of vertebrates, spreading first to other marine invertebrates (crustaceans, turbellarians, echinoderms, etc.), then freshwater and terrestrial invertebrates, and finally vertebrates. In contrast to apicomplexan etiologic agents of globally significant human and animal diseases (e.g. malaria, toxoplasmosis, cryptosporidiosis), which have been well studied, the enormously diversified basal apicomplexan lineages restricted to invertebrate hosts remain poorly understood, despite being important from an evolutionary perspective due to their basal phylogenetic position. New findings on biodiversity and other biological aspects, such as cell motility, invasion strategies and host-parasite interactions, in representatives of early branching lineages will facilitate our understanding of evolutionary pathways in Apicomplexa.

From the beginning of my research activity in the Department of Botany and Zoology, I have directed my studies on basal Apicomplexa to cryptosporidia and gregarines, which are thought to be deep-branching apicomplexans. Direct comparison of host-parasite interactions in both parasite groups revealed that they exhibit specific morphological and developmental similarities, indicating that cryptosporidia may represent a missing link between the gregarines and coccidia. This thesis, summarising observations on apicomplexan representatives of diverse basal lineages published in the enclosed papers, offers a novel perspective on parasitism strategies in Apicomplexa, and highlights the importance of deeper investigations into parasites that have not been attributed as having any economic or medical significance.

2 Early branching lineages of Apicomplexa

2.1 Recent views on apicomplexan taxonomy and evolution

Apicomplexa Levine, 1970, emend. Adl et al., 2012, which inhabits almost all known phyla of multicellular organisms, is one of the most monitored groups of unicellular eukaryotic parasites. Based largely on phenotypic characteristics, Apicomplexa were traditionally considered to contain four clearly defined groups: gregarines, coccidia, haemosporidia and piroplasmids. These groups were originally designed to be utilitarian rather than phylogenetic (Morrison, 2009). Recently, phylogenetic evidence provided by molecular data has led to this traditional taxonomic scheme being questioned. Subsequently, numerous works dealing with phylogeny and systematic arrangements within the Apicomplexa have been published (e.g. Adl et al., 2012; Cavalier-Smith, 2014; Cavalier-Smith and Chao, 2004; Perkins, 2000).
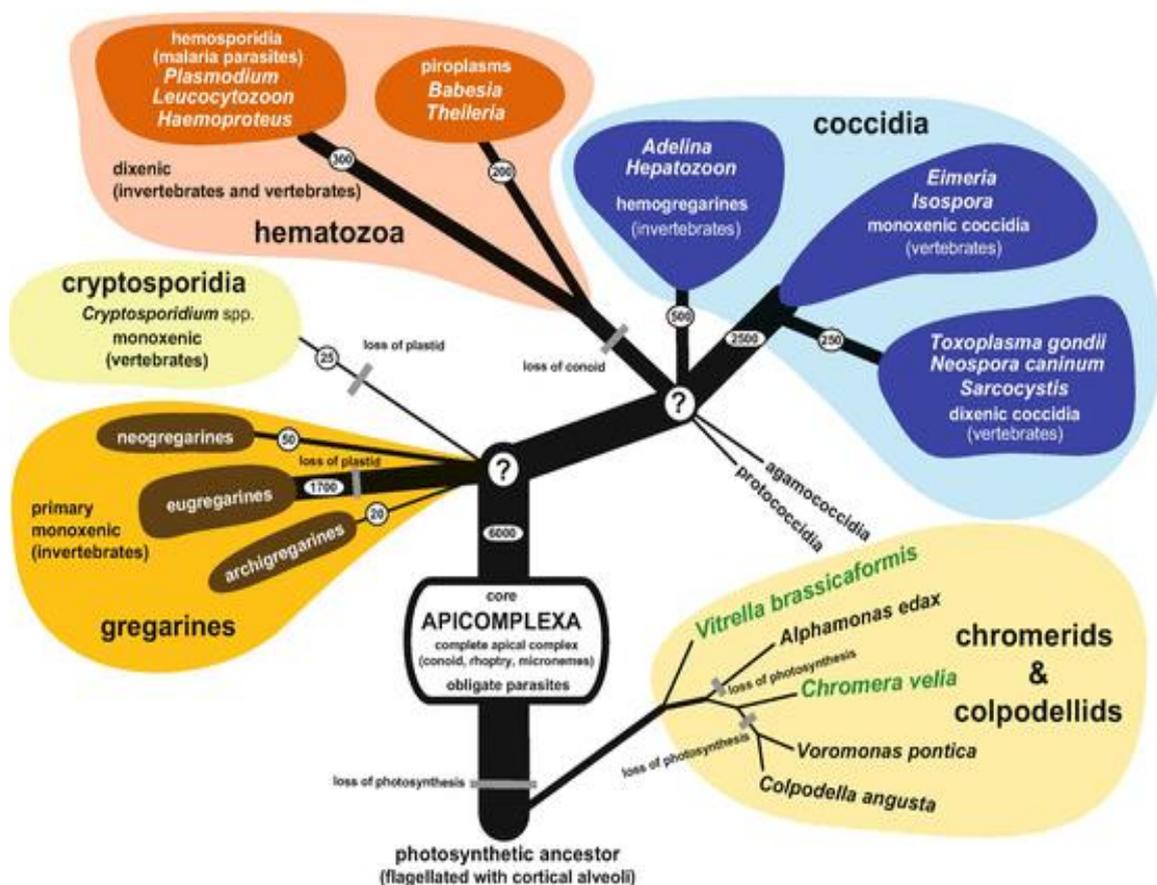

Fig. 1. Hypothetical tree of life for the Apicomplexa (taken from Votýpka et al, 2017).

Parasite taxonomy in this thesis follows the non-rank classification of eukaryotes published by Adl et al. (2012), in which the Apicomplexa, along with protalveolates, dinoflagellates and ciliates, form the higher order group Alveolata. However, phylogenetic relationships and the evolutionary history of organisms within the Apicomplexa remain an open question (Simdyanov et al., 2018). It is generally accepted that ancestral apicomplexans parasitised marine annelids and that their adaptation to a parasitic lifestyle took place before the vertebrate period (Cox, 1994; Théodoridès, 1984). Several early-dispersed apicomplexan branches are hypothesised, e.g. blastogregarines, archigregarines, eugregarines and neogregarines, agamococcidia, protococcidia and cryptosporidia. These exhibit an enormous diversity in both dimension and cell architecture, depending on their surrounding environment and parasitism strategy, and appear to be perfect examples of coevolution between parasites and their hosts. It is thought most likely that an archigregarine stem group gave rise to cryptosporidia, and a lineage uniting (eu)coccidia with piroplasmids (Leander et al., 2006).

2.2 Introduction to model parasites

Gregarines (Conoidasida Levine, 1988, Gregarinasina Dufour, 1828) are deep-branching apicomplexan parasites of invertebrates. Based on differences in their life history, gregarines are traditionally classified into three subgroups: archigregarines (Archigregarinorida Grassé, 1953; prevailing extracellular development with merogony), eugregarines (Eugregarinorida Léger, 1900; merogony absent, predominant extracellular development) and neogregarines (Neogregarinorida Grassé, 1953; merogony present, intracellular or extracellular development) (Adl et al., 2012; Perkins, 2000). Studies on the following archigregarines and eugregarines are included in this thesis: *Selenidium pendula* Giard, 1884 from the intestine of the marine polychaete *Scolelepis squamata* (Müller, 1806); *S. pygospionis* Paskerova, Miroliubova, Diakin, Kováčiková, Valigurová, Guillou, Aleoshin and Simdyanov, 2018 from the intestine of the marine polychaete *Pygospio elegans* Claparède, 1863; *S. pherusae* Paskerova, Miroliubova, Diakin, Kováčiková, Valigurová, Guillou, Aleoshin and Simdyanov, 2018 from the intestine of the marine polychaete *Pherusa plumosa* (Müller, 1776); *Cephaloidophora* cf. *communis* Mawrodiadi, 1908 from the intestine of the barnacle *Balanus balanus* Linnaeus, 1758; *Ganymedes yurii* Diakin, Wakeman

and Valigurová, 2016 from the intestine of the marine amphipod *Gondogeneia* sp.; *Urospora ovalis* Dogiel, 1910 and *U. travisiae* Dogiel, 1910 from the body cavity of the marine polychaete *Travisia forbesii* Johnston, 1840; *Gregarina cuneata* Stein, 1848, *G. polymorpha* (Hammerschmidt, 1838) and *G. steini* Berndt, 1902 from the intestine of larval mealworm beetle *Tenebrio molitor* Linnaeus, 1758; *G. garnhami* Canning, 1956 from the intestine of the desert locust *Schistocerca gregaria* (Forskål, 1775); and the first gregarine reported from a vertebrate host, *Nematopsis temporariae* Nöller, 1920 from the liver of tadpoles (Diakin et al., 2014, 2016, 2017; Chambouvet et al., 2016; Kováčiková et al., 2017a, 2017b, 2018; Paskerova et al., 2018; Schrével et al., 2016; Valigurová, 2012; Valigurová et al., 2013).

Until recently, **blastogregarines** (Blastogregarinea Chatton and Villeneuve, 1936, emend), apicomplexan parasites of marine polychaetes with uncertain taxonomic affiliation and comprising four known species, were poorly studied. Previous studies considered them to be highly modified gregarines, an intermediate lineage between gregarines and coccidia or even an isolated group of eukaryotes. Superficially, they resemble gregarines but lack syzygy and gametocyst stages in their life cycle, and are characterised by permanent multinuclearity and gametogenesis by means of budding, which distinguishes them considerably from other apicomplexans (Caullery and Mesnil, 1898). The studied blastogregarines, the type species *Siedleckia nematoides* Caullery and Mesnil, 1898 from the intestine of *Scoloplos armiger* (Müller, 1776) and *Chattonaria mesnili* (Chatton and Dehorne, 1929) from the intestine of *Orbinia latreillii* (Audouin and Milne Edwards, 1833), possess both gregarine (folded or smooth pellicle, persisting mucron and apical complex during the larger part of lifecycle, oocysts with free sporozoites) and coccidian (gametes associated with two kinetosomes, absence of gametocyst, pronounced difference in size between male and female gametes, microgametes with two flagella) features. Phylogenetic analysis indicates that blastogregarines are an independent, early diverging lineage of Apicomplexa. The traits shared with archigregarines, i.e. distinctive tegument structure and myzocytotic feeding via a well-developed apical complex, probably represent the ancestral states of the corresponding cell structures for Apicomplexa (Simdyanov et al., 2018; Valigurová et al., 2017).

Cryptosporidia (Conoidasida Levine, 1988, *Cryptosporidium* Tyzzer, 1907)

comprise causative agents of zoonotic diseases of the gastrointestinal and respiratory tract of vertebrates, including humans. The genus *Cryptosporidium* was conceived for a peculiar parasite found in the stomach of laboratory mice, whose endogenous stages develop attached to the host epithelium with development including both asexual and sexual developmental stages (Tyzzer, 1907). Based on Perkins (2000), the family Cryptosporidiidae Léger, 1911, with a single genus *Cryptosporidium*, was previously placed within the class Conoidasida Levine, 1988 (subclass Coccidiasina Leuckart, 1879; order Eucoccidiorida Léger and Duboscq, 1910; suborder Eimeriorina Léger, 1911). The first doubts regarding the taxonomic position of cryptosporidia came following the publication of a work reporting cross-reactivity of an anti-*Cryptosporidium* monoclonal antibody with a monocystid gregarine (Bull et al., 1998), leading to speculation that cryptosporidia represent a missing link between the gregarines and coccidia. Later studies revealed that *Cryptosporidium* has closer phylogenetic affinity to gregarines than coccidia *sensu stricto* and that it represents an early emerging branch of Apicomplexa (Barta and Thompson, 2006; Carreno et al., 1999; Leander et al., 2006). Recent systematic work has placed cryptosporidia within Conoidasida Levine, 1988, comprising Coccidia Leuckart, 1879, Gregarinasina Dufour, 1828 and the genus *Cryptosporidium* (Adl et al., 2012). Publications included in this thesis deal with the gastric species *Cryptosporidium proliferans* Kváč, Havrdová, Hlásková, Daňková, Kanděra, Ježková, Vítovec, Sak, Ortega, Xiao, Modrý, Chelladurai, Prantlová and McEvoy, 2016 (previously known as strain TS03 of *C. muris* Tyzzer, 1907) originating from a naturally infected East African mole rat *Tachyoryctes splendens* (Rüppell, 1835) and passaged in laboratory BALB/c mice and southern multimammate mice *Mastomys coucha* (Smith, 1834) (Melicherová et al., 2014, 2016, 2018; Valigurová et al., 2018).

One of the most poorly explored basal apicomplexans are the **protococcidia** (Incertae sedis Apicomplexa: Protococcidiorida Kheisin, 1956), with uncertain subdivisions and comprising eight genera: *Angeiocystis*, *Coelotropha*, *Grellia*, *Eleutheroschizon*, *Mackinnonia*, *Myriosporides, Myriospora* and *Sawayella*. These are expected to lack merogony, with gamogony and sporogony occurring extracellularly (Adl et al., 2012; Perkins, 2000). The genus *Eleutheroschizon* Brasil, 1906 contains two known intestinal species from marine polychaetes, the type species *E. duboscqi* Brasil, 1906 from *S. armiger* (investigated in this study) and *E. murmanicum*

Awerinzew, 1908 from *Ophelia limacina* (Rathke, 1843). In these species, endogenous stages exhibit epicellular development and share the features of coccidia and gregarines; i.e. cell polarity in advanced developmental stages (trophozoites, gamonts) characteristic for gregarines, localisation within the parasitophorous sac similar to that of cryptosporidia and a life cycle lacking merogony and syzygy stages, despite showing a coccidian type of gametogony (Brasil, 1906; Chatton and Villeneuve, 1936; Valigurová et al., 2015). Gamonts detach from the host intestinal epithelium and disperse into the environment, where gametogenesis and sporogenesis take place.

Agamococcidia (Incertae sedis Apicomplexa: Agamococcidiorida Levine, 1979) are another small and poorly investigated group of Apicomplexa (comprising two genera, *Gemmocystis* and *Rhytidocystis*) from marine polychaetes, each displaying an unusual life cycle lacking gametogony and merogony (Adl et al., 2012). Included here is an unpublished study dealing with a new species of *Rhytidocystis* Henneguy, 1907, an intracellular parasite from the intestine of the marine polychaete *T. forbesii* (Diakin and Valigurová, 2014).

3 Host-parasite interactions in early branching Apicomplexa

3.1 Attachment strategies of epicellular parasites

Apicomplexans exhibit highly specific adaptations for invading and surviving within their hosts. These have evolved under distinct evolutionary pressures, resulting in diverse host-parasite interactions. Host cell invasion by apicomplexan zoites is a rapid process depending on a sequence of tightly controlled events (Dubremetz et al., 1998). First, they have to orient on the surface of the target host tissue/cell and find an appropriate site for invading. The next steps include attaching and/or penetrating the host tissue/cell, often accompanied by a parasite-induced modification of the target cells. These critical steps are facilitated by differentiation of the parasite into a highly specialised, motile invasive stage, the zoite, equipped with a set of sophisticated organelles and a cytoskeleton dedicated to reaching and invading the host cell. The zoite exhibits high cell polarity by having an anterior pole equipped with a unique invasion apparatus, the apical complex, consisting of

specialised secretory organelles (rhoptries, micronemes), polar ring(s) and a conoid. This apparatus, traditionally used as the best-defined feature for Apicomplexa, can also be found in other Myzozoa, a group comprising apicomplexans, dinoflagellates and several lineages of free-living predatory or parasitic flagellates that employ a myzocytosis-based mode of feeding, i.e. the process by which the predator/parasite attaches to the prey/target cell and sucks out or feeds permanently on its cytoplasm via specialised organelles (Cavalier-Smith and Chao, 2004). It is probable that the evolution of Apicomplexa progressed from myzocytotic predation to myzocytotic extracellular parasitism, as exhibited by some gregarines and cryptosporidia, and finally to intracellular parasitism, typical for coccidia. The Apicomplexa demonstrate two main determinative evolutionary trends: i) the origination of epicellular parasitism, observed mostly in gregarines, with subsequent modification of the attachment apparatus and motility mode in the vegetative stage (trophozoite); and ii) origination of intracellular parasitism in typical coccidia and Aconoidasida, accompanied by a rejection of trophozoite polarity and motility (Valigurová et al., 2015).

The attachment apparatus of deep-branching apicomplexans evolved at the apical end of the sporozoite (the first, invasive stage in the apicomplexan life cycle) and demonstrates an enormous diversity in architecture. Gregarines and blastogregarines, for example, exhibit diverse strategies for attachment to the host tissue, including (i) intratissular or intracellular localisation with or without a reduced area of attachment in neogregarines; (ii) a mucron in blastogregarines, archigregarines, monocystid eugregarines and some neogregarines; (iii) a more advanced mucron-like structure in aseptate eugregarines, losing the apical complex and strengthening its attachment function, (iv) a simple (Fig. 2) or (v) complicated epimerite, equipped with various structures (e.g. hooks or spines, digitations, hairs) in eugregarines (Fig. 3); and (vi) a sucker-like protomerite or modified protomerite with rhizoids in septate eugregarines (Fig. 4) (Cook et al., 2001; Desportes and Schrével, 2013; Kováčiková et al., 2017b; Lucarotti, 2000; MacMillan, 1973b; Paskerova et al., 2018; Schrével et al., 2016; Schrével and Vivier, 1966; Simdyanov and Kuvardina, 2007; Simdyanov et al., 2018; Tronchin and Schrével, 1977; Valigurová, 2012; Valigurová et al., 2007, 2009; Valigurová and Koudela, 2005, 2006, 2008).
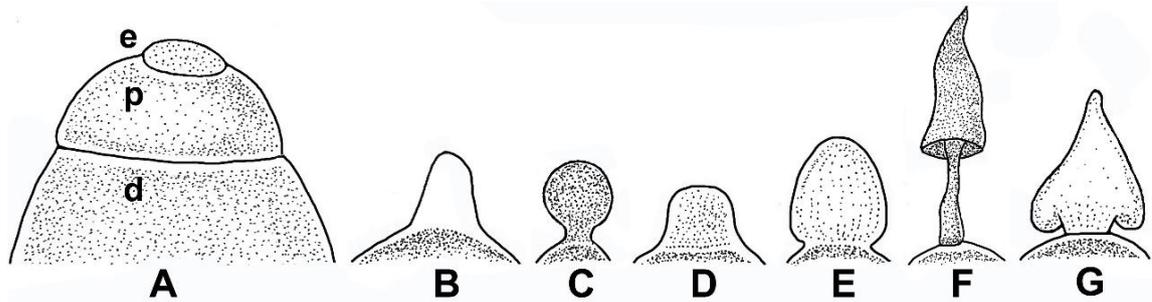
Fig. 2. Schematic diagram of the differing forms of simple epimerite (taken and modified from Valigurová, 2001). A. Rudimentary. B. Conical papilla. C. Spherical. D. Button-shaped E. Ovoid. F. Lance-shaped. G. Reverse heart-shaped. e – epimerite, p – protomerite, d – deutomerite.
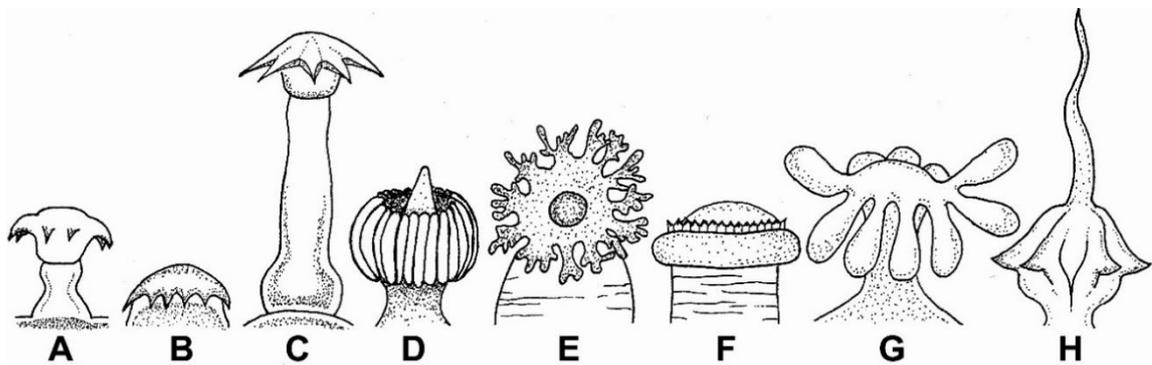

Fig. 3. Schematic diagram of the differing forms of complicated epimerite (taken and modified from Valigurová, 2001). A-C. Various forms with hooks. D. Segmented disc with a pivot. E. Sucker-shaped with branched papillae. F. Papilla with peripheral teeth, basally bound by a pillow. G. Spherical with club-shaped protrusions. H. Spherical with peripheral hooks and a central spike.
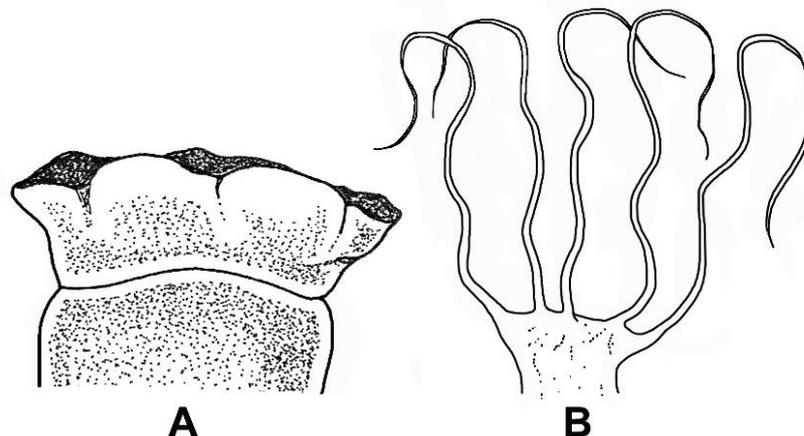

Fig. 4. Schematic diagram of modified protomerite. A. Sucker-like protomerite. B. Protomerite with rhizoids (taken and modified from Valigurová, 2001).

Blastogregarines embed their mucron into the enterocyte's brush border, which bears the microcilia and microvilli. The mucronal complex of *S. nematoides* is

equipped with apical organelles, the conoid, internal and external polar rings, numerous rhoptries and putative micronemes, and a mucronal vacuole (Simdyanov et al., 2018; Valigurová et al., 2017). The mucron is covered with a trimembrane pellicle typical of Apicomplexa, except for the region against the conoid where the mucronal vacuole has a wide inlet opening, considered a cytostome-cytopharyngeal complex performing myzocytosis (Fig. 5). The cytostome opens into a tiny gap between the parasite and host cell plasma membranes with the appearance of a septate cell junction. No significant modifications of the host cell are present, except for increased electron density of the host plasma membrane directly facing the cytostome, which bears uniformly spaced dense structures on its external surface, most likely a perforated or modified host cell coat. The strongly modified mucron of *C. mesnili* lacks the conoid and rhoptries, and anchors to the host cell via peripheral bulges formed by large alveoli between the cytomembranes of the inner membrane complex (IMC). A gap of varying width is present between the *C. mesnili* pellicle and the host cell membrane, with no evidence of a septate cell junction.
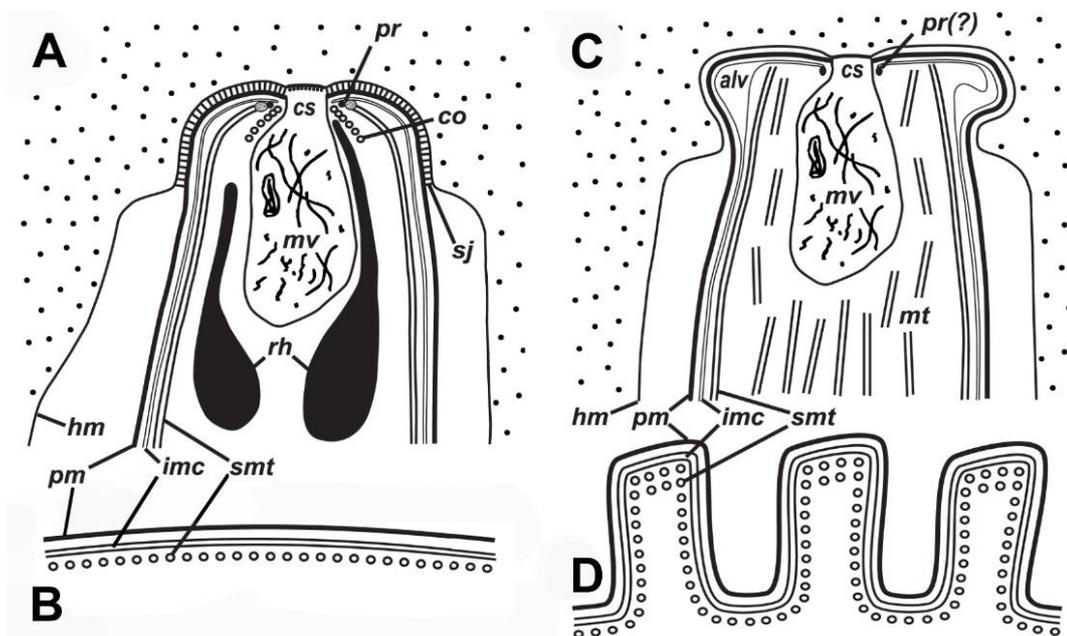
Fig. 5. Schematic diagram of the mucronal complex in blastogregarines (taken and modified from Simdyanov et al., 2018). A-B. *Siedleckia nematoides*, C-D. *Chattonaria mesnili*: the schemes of the longitudinal and cross sections of the mucron and pellicle, respectively. alv – alveoles between the cytomembranes of the inner membrane complex, co – conoid, cs – cytostome, hm – host cell plasma membrane, imc – inner membrane complex, mt – microtubules, mv – mucronal vacuole, pm – parasite plasma membrane, pr – polar ring (giving rise to the subpellicular microtubules in *Siedleckia*); rh – rhoptries, sj – septate cell junction between the parasite and host cell, smt – subpellicular microtubules.

The apical phagotrophy in alveolate free-living predators with open conoid and rhoptries may be at the origin of the anchoring apparatus of archigregarines. The mucron of *S. pendula* appears as a regular mammiliform area and a series of shortened microvilli are visible at the periphery of the mucron when embedded in epithelial cells. A tropism for host cells rich in granules can be seen in intestinal epithelium parasitised by *S. pendula*. After trophozoite detachment, the trace left by the mucron in the host tissue is regular, sometimes with a small hole in a subcentral position (Schrével et al., 2016). The mucronal complex comprises the conoid, mucronal vacuoles, numerous rhoptries and micronemes (Fig. 6).
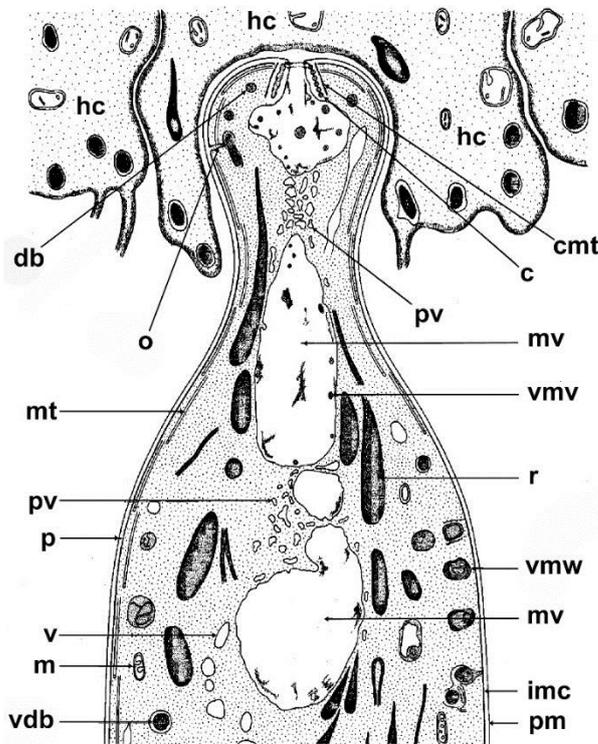

Fig. 6. Schematic diagram of the anterior region of the *Selenidium* trophozoite (taken and modified from Schrével, 1968). Mucronal vacuoles form at the level of the conoid and, after detachment, these migrate posteriorly. Numerous pinocytotic vesicles are present at the periphery of the mucronal vacuoles. c – conoid, cmt – microfibrillar curtain that covers the microtubular network forming the conoid, db – dense body, hc – host cell, imc – inner membrane complex, m – mitochondrion, mv – mucronal vacuole, o – opening in the pellicle, p – pellicle, pm – parasite plasma membrane, pv – pinocytotic vesicles, r – rhoptry, v – empty vesicles, vdb – vesicles containing dense bodies, vmv – vesicles in the mucronal vacuole, vmw – vesicles with multi-membrane whorls.

As *S. pendula* is the archigregarine type species and an early branching apicomplexan, its conoid represents a good model for studying the transition between Apicomplexa with a closed conoid and free-living alveolate ancestors with an open conoid, as found in the early branching dinoflagellates (Okamoto and Keeling, 2014; Schrével et al., 2016). The conoids of *S. pendula*, *S. hollandei* and *S. orientale* appear similar to those in eugregarine sporozoites and *Toxoplasma gondii*, but lack the apical polar ring (Desportes, 1969; Sheffield et al., 1971; Schrével, 1968; Schrével et al., 2016; Simdyanov and Kuvardina, 2007). In contrast, the polar ring,

adjacently located to the IMC at the apical conoid end and giving rise to subpellicular microtubules, has been documented in *S. pherusae* (Paskerova et al., 2018).

The eugregarine sporozoite develops into a large extracellular vegetative stage, the trophozoite, equipped with an apical region specialised for attachment to the host cell (Valigurová, 2012). The epimerites of eugregarines from herbivorous hosts are usually simple and button-shaped, while they are complicated and equipped with strong hooks, spines or numerous filaments in carnivorous hosts (Schrével and Philippe, 1993). The attachment process of septate eugregarines (Fig. 7) from the intestines of terrestrial hosts has been well studied. After sporozoite attachment to the host cell, an epimeritic bud arises over the opened apical region and gradually develops into an epimerite overlain by an electron-translucent cortical vesicle (Desportes, 1969; Tronchin and Schrével, 1977; Valigurová, 2012; Valigurová et al., 2007, 2009; Valigurová and Koudela, 2005, 2008). Most likely, this develops from fused flat vesicles (distributed at the epimerite periphery and originating from the parasite's endoplasmic reticulum) that turn into a single large vesicle packed with microfilaments. Formation of the cortical vesicle appears to be related to the presence of a flask-shaped organelle in the youngest stages (suggestive of a rhoptry), which empties its contents during the transformation of the sporozoite into a trophozoite (Sheffield et al., 1971; Tronchin and Schrével, 1977; Valigurová et al., 2007; Valigurová and Koudela, 2005). Interestingly, the cortical vesicle in *Didymophyes gigantea* has been interpreted as a periparasitic space between the host and parasite, functioning as a parasitophorous vacuole (Hildebrand, 1976). The cortical vesicle does indeed resemble the internal space of the parasitophorous vacuole due to its translucent appearance with traces of an opaque or filamentous material. In addition, fine tubules passing through the cortical vesicle and attaching to the epimerite-host cell interface have been documented in *G. garnhami* (Valigurová and Koudela, 2008). Hence, it could be speculated that the cortical vesicle is in fact an incomplete parasitophorous envelope restricted to the embedded apical region (epimerite) of gregarines (Valigurová et al., 2015). This idea is supported by the fact that the cortical vesicle appears subsiding and irregular during the course of epimerite gradual regression before trophozoite detachment from the host tissue (Valigurová et al., 2009). The epimerite is only covered by a plasma membrane, while the rest of the eugregarine is covered by a pellicle consisting of the

plasma membrane underlain by two cortical cytomembranes of the IMC. Along with the formation of the epimerite, a membrane fusion site (i.e. osmiophilic ring) forms connecting the host plasma membrane, the membrane-like structure beneath the cortical vesicle and the epimerite plasma membrane. The IMC extends only as far as the top of the protomerite and ends at the membrane fusion site. The trophozoite remains epicellular and the only part in close contact with the host cell is the epimerite plasma membrane. The growing epimerite gradually implants into the host cell, causing a deep invagination of the host cell plasma membrane, but does not penetrate it (Valigurová 2012; Valigurová et al., 2007, 2009). The trilaminate interface between the host cell and the epimerite is formed by the epimerite and host plasma membranes, separated by a dense layer. The accumulation of actin at the base of the epimerite suggests that the osmiophilic ring is contractile (Ghazali et al., 1989; Schrével and Vivier, 1966; Tronchin and Schrével, 1977). Phalloidin labelling has confirmed the presence of filamentous form of actin (F-actin) at the position of the osmiophilic ring (Valigurová, 2012; Valigurová et al., 2009). A continuous or discontinuous fibrillar septum separates the epimerite from the protomerite in a few species, supported by a ring rich in α-tubulin in one documented case (Kováčiková et al., 2017b; Valigurová and Koudela, 2008).

Two contradictory hypotheses describe trophozoite detachment from host tissue at the end of development. One describes detachment via epimerite retraction, self-regulated by the vegetative stage (Lucarotti, 2000; Valigurová and Koudela, 2008; Valigurová et al., 2009), while the other is based on gradual epimerite constriction facilitated by the contractility of the osmiophilic ring surrounding the base of the epimerite, acting as a sphincter during the separation of the epimerite from the rest of the gregarine (Desportes and Schrével, 2013; Ghazali et al., 1989; Ghazali and Schrével, 1993; Schrével and Philippe, 1993; Tronchin et al., 1986; Tronchin and Schrével, 1977). Insofar as the vegetative phase of the eugregarine life cycle usually lasts longer than four days (Harry, 1970; Valigurová and Koudela, 2005), trophozoites must be adapted either to keeping the host cell alive during their development or for eventual reattachment to a younger cell in better physiological condition after abandoning the senescing cell. The latter could be facilitated by a retractable epimerite and progressive gliding motility in eugregarines (Lucarotti, 2000; Valigurová, 2012). This is especially true in gregarines with a permanent

epimerite, with its architecture reminiscent of a modified protomerite and persisting in gamonts (Kováčiková et al., 2017b). In this case, the feeding stages of *G. cuneata*, which exhibit spectacular adaptations to epicellular parasitism, provide further support for the epimerite retraction hypothesis. Though the parasite becomes firmly anchored to the brush border of the epithelium via numerous epimerite digitations deeply invaginating the host plasma membrane, trophozoites are able to detach and retain an intact epimerite (Valigurová, 2012). After epimerite retraction in mature trophozoites, early syzygies (syzygy = pairing up of gamonts before the formation of a gametocyst) of *G. cuneata* are often found to be attached to the host tissue via a modified protomerite of the primite (the anterior, female member of the syzygy), the apex of which exhibits an undulating pattern. Accumulation of actin in *Gregarina* protomerite indicates that attachment via a modified protomerite could be facilitated by increased flexibility in this region (Heintzelman, 2004; Valigurová, 2012; Valigurová et al., 2009, 2013). Likewise, actinocephalid gamonts lose their simple globular epimerite and attach by a sucker-like protomerite. The interspace between the epicytic folds of the attached protomerite and the intestinal epithelium is packed with host microvilli embedded in a dense adhesive material, likely produced by exocytic vesicles in the protomerite apical cytoplasm (Cook et al., 2001; Valigurová, 2012).

3.2 Attachment strategies of epicellular parasites enveloped by a parasitophorous sac

The peculiar niche of cryptosporidia at the brush border of the gastrointestinal epithelium has been the subject of extensive debate for decades. While some refer to cryptosporidia as intracellular though extracytoplasmic parasites, others prefer the term epicellular to describe the unique localisation of cryptosporidian developmental stages within a parasitophorous sac of host cell origin (Barta and Thompson, 2006; Borowski et al., 2010; Cavalier-Smith, 2014; Clode et al., 2015; Ryan et al., 2016; Valigurová et al., 2008). The parasitophorous sac, introduced for the first time by Paperna and Vilenkin (1996), is the preferable term for the host-derived structure enveloping cryptosporidian endogenous stages. The parasitophorous sac is an epicellular niche enveloping the entire parasite composed of two continuous host plasma membranes on the outer and inner sides and

enclosing a thin layer of host cell cytoplasm (Valigurová et al., 2008). In contrast, the term 'parasitophorous vacuole' previously applied for *Cryptosporidium* is misleading as it refers solely to a vacuolar space bordered by a membrane (Scholtyseck, 1979). Long-term observations of several cryptosporidian species developing *in vivo* and *in vitro* support the term epicellular to reflect their localisation within host tissue as the invasive stages do not penetrate under the host cell plasma membrane and do not come into close contact with the host cytoplasm (Jirků et al., 2008; Melicherová et al., 2014, 2018; Valigurová et al., 2007, 2008; Valigurová, personal observation). The invading zoite induces modulation of the host plasma membrane, which loses its microvillous nature and forms a circular membrane fold, tightly encircling the apical end of the zoite and gradually rising up along the zoite (Fig. 7). This membrane protrusion and encapsulation of the parasite is actin-dependent (Nelson et al., 2006). Parasite-induced reorganisation and accumulation of host cell actin at the attachment site leads to the formation of a dense band supported by the actin plaque, which is intimately involved in parasite anchoring (Forney et al., 1999; O'Hara et al., 2008). This dense band in the host cytoplasm, located just beneath the parasite attachment site and separating the unmodified and modified parts of the host cell, consists of electron-dense microfibrils interwoven perpendicularly with an adjacent filamentous network of polymerised actin (Beyer et al., 2000; Landsberg and Paperna, 1986; O'Hara et al., 2008; Valigurová et al., 2008, 2015). Observations on tubular structures in oblique sections of the dense band have led to the hypothesis that it serves as a barrier against deeper penetration of the parasite into the host cell cytoplasm (Beyer et al., 2000). Vacuolation of the parasite apical cytoplasm during invasion appears to be the first sign of the incoming anterior vacuole, which is considered a precursor of the feeder organelle. The anterior vacuole membrane folds to form the lamellae of the feeder organelle. Later, both the parasite plasma membrane and the anterior vacuole membrane fuse with the inner membrane of the parasitophorous sac to form the Y-shaped membrane junction (= annular ring). The parasite remains attached to the host cell surface, only enveloped by the host membrane folds. Pore-like structures are occasionally seen on the surface of the sac (Valigurová et al., 2007, 2008). The parasitophorous sac serves as a protective coat against the hostile conditions of the vertebrate gastrointestinal tract and reinforces attachment of the parasite to host epithelium. Simulated parasitisation of cell lines

with polystyrene microspheres has revealed that, in addition to intact or even empty cryptosporidian oocysts, polybeads coated with a parasite antigen 'cocktail' (obtained from oocysts with sporozoites) are able to induce the same plasma membrane modification in affected cultured cells. Contact with oocysts or parasite antigen-coated polybeads induces actin reorganisation in cultured cells, resulting in the formation of an F-actin network surrounding the foreign object. Encapsulation of cryptosporidian oocysts by cultured cells is induced by parasite antigens and occurs independently of any active invasion by motile stages (Melicherová et al., 2018). It is likely that oocyst adherence to host cell is aided by molecules containing N-acetyl-galactosamine on their surface. Lectin-enhanced attachment of oocysts to host tissue/cell lines increases infection efficiency by bringing sporozoites into close proximity with host cells (Stein et al., 2006). In addition to their adhesive function, oocyst surface antigens may also represent a passive means of host cell manipulation at the oocyst stage (Yao et al., 2007).

Cryptosporidia share striking similarities with epicellular gregarines, especially in their attachment strategy, i.e. the eugregarine epimerite resembles the feeder organelle and the entire attachment site in cryptosporidia (Fig. 7). The dense line at the base of the feeder organelle, serving as a primary barrier between the parasite and host cell cytoplasm, is homologous to the interface between the epimerite and the host cell (Jirků et al., 2008; Melicherová et al., 2014, 2018; Valigurová et al., 2007, 2008, 2015). Similarly, the protococcidian *E. duboscqi* exhibits an extraordinary attachment strategy, sharing features with cryptosporidia and gregarines, i.e. the parasite itself conspicuously resembles an epicellular gregarine, while the parasitophorous sac develops in a similar manner to that in cryptosporidia (Tronchin and Schrével, 1977; Valigurová et al., 2007, 2008, 2015). In *E. duboscqi* mature stages, a thick glycocalyx layer covers the external surface of their plasma membrane, which probably hinders potential fusion of the parasitophorous sac with the parasite surface. In contrast to cryptosporidian parasitophorous sacs, which have low amounts of F-actin (Bonnin et al., 1999), actin filaments accumulate in the *E. duboscqi* parasitophorous sac and are more stable than those in the surrounding host tissue. Accumulation of host F-actin at the base of the parasitophorous sac appears to be induced by the parasite, similarly to cryptosporidia; however, the dense band in *E. duboscqi* is thinner and closely apposed to the sac's inner

21

membrane. Restriction of polymerised α-tubulin to the parasitophorous sac wall indicates involvement of host microcilia in the formation of the *E. duboscqi* epicellular niche. Re-evaluation of epicellular development in other apicomplexans and direct comparison of their niche with that of *E. duboscqi* (Fig. 7; Valigurová et al., 2015) has revealed similarities with certain eimeriid coccidia from fish and reptiles (*Eimeria* formerly known as *Epieimeria*, some *Goussia*, *Acroeimeria*, *Choleoeimeria*) (e.g. Dyková and Lom, 1981; Lukeš, 1992; Molnar and Baska, 1986). The most distinctive feature common to eugregarines, cryptosporidia, protococcidia and eimeriids from poikilotherms is that they develop a specialised epicellular host-parasite interface, reflecting analogous modes of adaptation for development in similar environments (Melicherová et al., 2018, 2014; Valigurová et al., 2007, 2008, 2015). Extracellular but attached parasites are usually of a heteropolar nature, while intracellular parasites are generally non-polar. Gregarines, cryptosporidia and *E. duboscqi* are heteropolar cells, i.e. they exhibit a high degree of cell polarity in that their anterior and posterior ends differ in shape, structure and function. They attach by apical processes, i.e. epimerite in eugregarines, feeder organelle in cryptosporidia and the apparatus formed by circularly arranged lobes, crowned by a ring of filamentous fascicles in *E. duboscqi.* Epicellular eimeriids, on the other hand, appear to be non-polar, as they have no attachment organelles (Benajiba et al., 1994). They do, however, create projections of the parasitophorous sac equipped with pores that enlarge the contact zone with the host cell, resembling the *E. duboscqi* attachment lobes and fascicles. Presumably, the epicellular localisation leads to the occurrence of cell polarity. All these parasites stimulate additional growth and fusion of host cell microvilli along with modifications to the host plasma membrane, leading to parasitophorous sac formation; in this way they develop in the cavity of a host-derived envelope that separates them from the host internal environment. The parasitophorous sac of cryptosporidia is not complete as they connect directly to the host cell via a feeder organelle, while the inner membrane of the parasitophorous sac contains the entire parasite in *E. duboscqi* and eimeriids. In contrast to intracellular coccidia, evolutionary selection has presumably favoured an epicellular niche for these parasites, allowing them to more effectively evade the host immune response, though the parasite thereby becomes dependent upon its connection with the host cell for nutrient acquisition (Valigurová et al., 2015).
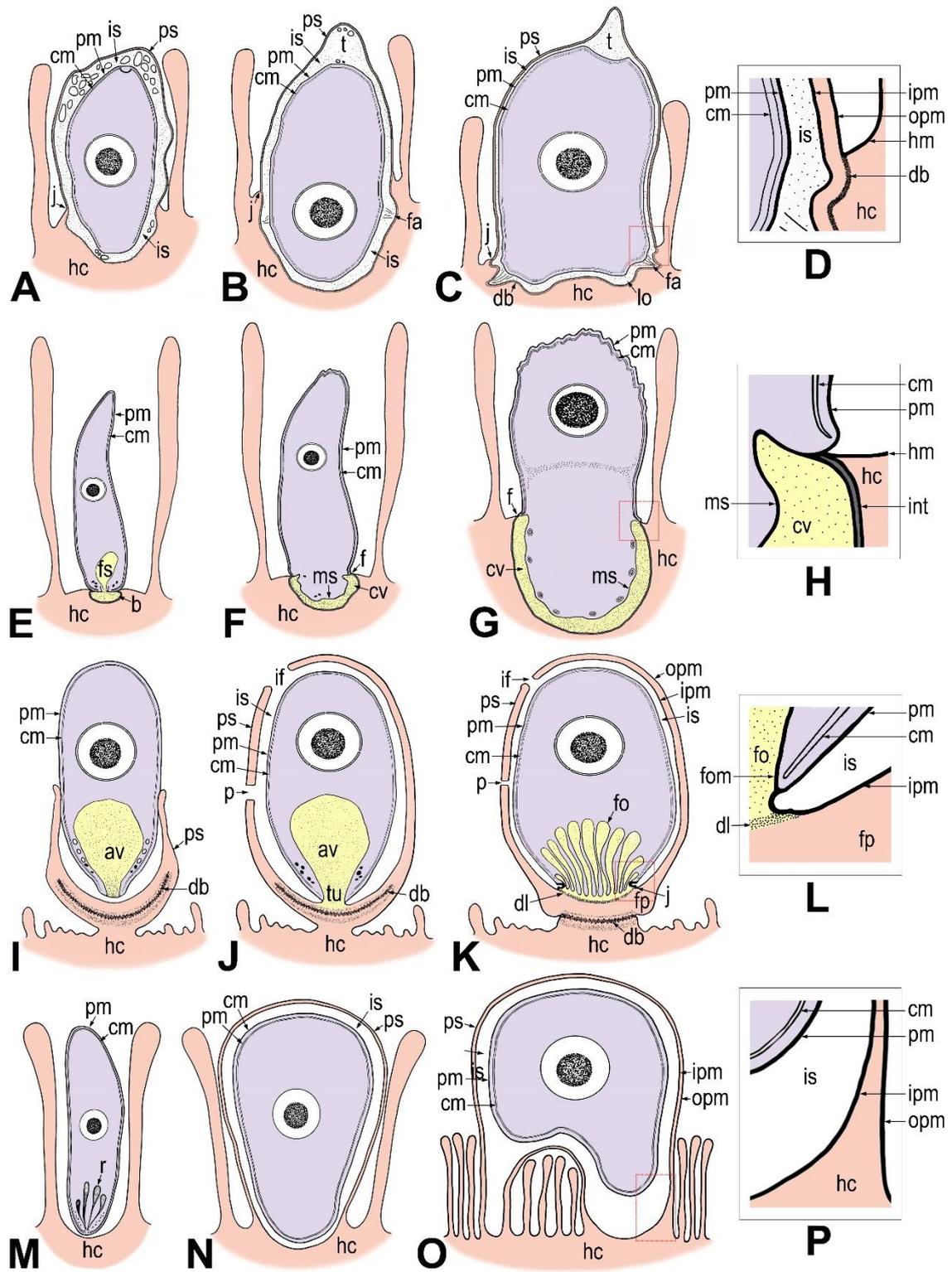
Fig. 7. Schematic diagram of host-parasite interactions in *Eleutheroschizon duboscqi*, eugregarines, cryptosporidia and epicellular eimeriids (taken from Valigurová et al., 2015). Three colours are used to distinguish between the parasite (in purple); the host cell, including parts modified due to parasitisation (in pink) and the contact zone between the host and the parasite (in yellow), where the interrelationships of the two organisms become more intimate. In *E. duboscqi* and epicellular eimeriids, the internal space between the parasite and parasitophorous sac (PS) remained

23

colourless, even though the authors do not exclude the possibility that this region may serve as a transitional zone for intensive interactions between the host and parasite. A-D. *Eleuteroschizon duboscqi*. A. Attached zoite transforming into a trophozoite, completely enveloped by a PS. B. Maturing trophozoite with a forming ring of fascicles at the attachment site. C. Mature trophozoite with well-developed attachment fascicles and lobes. D. Detail of the annular joint point (the cut-out is marked by a red square in C). E-H. Eugregarines. E. Sporozoite freshly attached to the host epithelial cell. F. Sporozoite transforming into a trophozoite. G. Early trophozoite with a well-developed epimerite. H. Detail of the membrane fusion site (the cut-out is marked by red square in G). The two cytomembranes end at the point of membrane fusion (= osmiophilic ring). I-L. Cryptosporidia. I. Attached zoite transforming into a trophozoite, partially enveloped by a PS. J. Young trophozoite almost completely enveloped by a PS. The tunnel connection between the interior of the anterior vacuole and the host cell cytoplasm develops as a result of the Y-shaped membrane junction. K. Mature stage with a filamentous projection at the base of the PS and fully developed feeder organelle, the lamellae of which form from the anterior vacuole membrane. L. Detailed view of the Y-shaped membrane junction (the cut-out is marked by a red square in K). M-P. Epicellular eimeriids. M. Invading zoite. N. Trophozoite/meront stage enveloped by a PS with a single attachment area (monopodial form). O. Extension of the gamont stage above the host microvillous region leading to establishment of a new contact with the host cell apart from the primary attachment zone by penetration of the PS membrane to the base of fused host cell microvilli (spider-like form). P. Detailed view of the attachment area (the cut-out is marked by a red square in O). av – anterior vacuole, b – epimeritic bud, cm – parasite cytomembranes, cv – epimeritic cortical vesicle, db – dense band (in cryptosporidia usually consisting of several layers), f – membrane fusion site, dl – dense line separating the feeder organelle from the filamentous projection of the PS, fa – attachment fascicle of filaments, fo – feeder organelle with membranous lamellae, fom – membrane limiting the lamellae of feeder organelle, fp – filamentous projection of the PS, fs – flask-shaped structure, hc – host cell, hm - host cell plasma membrane, if – incomplete fusion of PS, int – interface between the host cell and epimerite, ipm – inner membrane of the PS, is – internal space between the parasite and PS, j – annular joint point (Y-shaped membrane junction in cryptosporidia), lo – attachment lobe, ms – membrane-like structure limiting the cortical vesicle from the epimerite cytoplasm, opm – outer membrane of the PS, p – pore on the PS, pm – parasite plasma membrane, ps – parasitophorous sac, r – rhoptries, t – tail of the PS, tu – tunnel connection.

Aside from *Ditrypanocystis* archigregarine, which develops within a multimembranous envelope originating from fused enterocyte cilia, gregarines are usually not surrounded by a host-derived sac (Butaeva et al., 2006). Host cilia, clustering around *Ditrypanocystis*, lose their microtubular content and fuse to form the membrane of a parasitophorous sac (Fig. 8), the contact area of which is considerably enlarged. The ciliary membranes fold heavily beneath the parasite attachment site to form a network of channels, opening in the immediate proximity

of the enterocyte apical surface and contacting directly with the contents of the enterocyte transport vacuoles that cross the host cell plasma membrane. In contrast to cryptosporidia, neither parasite membrane folds (feeder organelle) nor fusion with the host cell membrane are formed. The trophozoite pellicle and subpellicular microtubules remain preserved in the contact region. These host-parasite interactions, which differ from other Selenidiidae, may result from parasitism of polychaetes that are not primarily marine (e.g. *Enchytraeus albidus*).
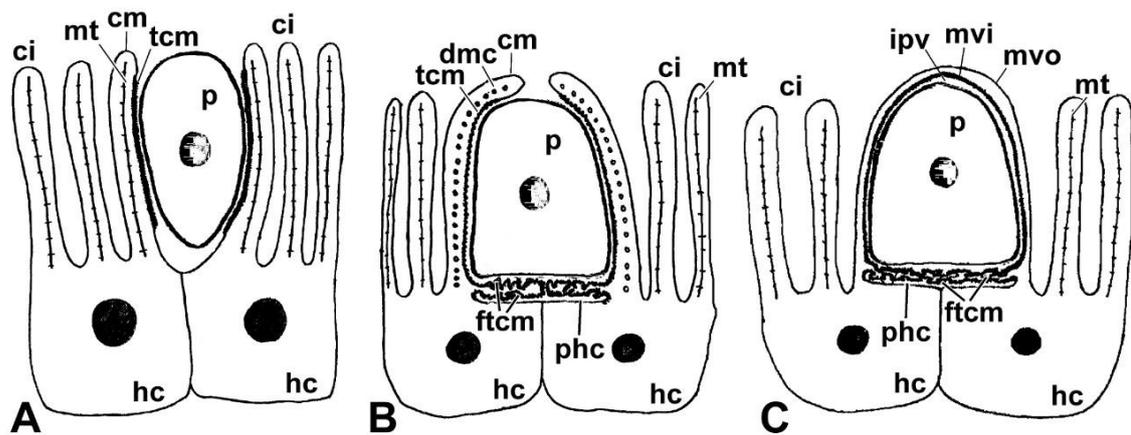

Fig. 8. Hypothetical scheme of host-parasite interface formation in archigregarine *Ditrypanocystis* sp. (taken and modified from Butaeva et al., 2006). A. Parasite contacting cilia of the host enterocytes. B. Enterocyte cilia transform and cluster around the parasite, with ciliary plasma membranes forming branched folds in the host-parasite contact region. C. Plasma membrane of clustered cilia fuse to form a parasitophorous sac (PS) with a heavily folded contact area. ci – enterocyte cilia, cm – membrane of cilia, dmc – degraded microtubules of cilia, ftcm – folds of transformed ciliary membrane, ipv – inner space of PS, mt – microtubules, mvi – inner membrane of PS, mvo – outer membrane of PS, p – parasite, phc – host cell plasma membrane, tcm – transformed ciliary membrane.

3.3 Niches of intracellular parasites

Eugregarines do not usually exhibit intracellular development. However, intracellular stages are documented in some archigregarines, in which the sporozoites, released into the lumen of host intestine, move through the intestinal epithelium and reach the basal lamina to transform into trophozoites and undergo merogony. In polychaetes highly parasitised by *S. hollandei*, for example, intraepithelial cysts located near the basal lamina contain several dozen well-developed merozoites (Schrével and Desportes, 2016). In *S. pygospionis*, small trophozoites with cellular organisation identical to that of well-developed

25

trophozoites locate intracellularly within a parasitophorous vacuole (Paskerova et al., 2018). The internal space of this parasitophorous vacuole contains filamentous material and electron-dense granules, accumulation of which increases towards the periphery. In enterocytes, a host cytoplasm rich in dense fibrillar material, mitochondria, endoplasmic reticulum and vesicles surrounds the parasitophorous vacuole, whereas the rest of the host cell cytoplasm is electron-lucent with rare organelles. Similarly, reduced vegetative stages of neogregarines, which mostly invade insect fat bodies, the haemocoel, the Malpighian ducts and intestines, are usually intracellular or lie within tissues, with no or a reduced attachment region (Schrével and Desportes, 2016). Some of these are reported to be enclosed within a parasitophorous vacuole (Larsson, 1991; Vávra and McLaughlin, 1970; Žižka, 2005). Of special interest is the occurrence of the enigmatic protist *N. temporariae* in tadpoles, observed for the first time in 1920 (Nöller, 1920) and putatively assigned to gregarines. A recent study, using both microscopy and ribosomal DNA sequencing of *N. temporariae* oocysts from three different frog species (*Rana temporaria*, *R. dalmatina* and *Hyla arborea*), has confirmed that this parasite belongs to the Gregarinasina (Chambouvet et al., 2016). This is the only known case of a gregarine found in a vertebrate. The oocysts of *N. temporariae*, including empty ones, are regularly present in macrophages located in tadpole liver sinusoids and contained within a parasitophorous vacuole (Valigurová, personal observation). All tadpoles investigated were *Nematopsis* positive, while only empty oocysts were found in organisms 4–6 weeks after metamorphosis. Oocysts are the only gregarine developmental stage found in dissected tadpoles, making it unclear whether the tadpoles serve as definitive or intermediate hosts (Chambouvet et al., 2016).

The poorly investigated life cycle of agamococcidian *Rhytidocystis* spp. in polychaetes is expected to be streamlined and involving sporozoites that penetrate the host intestine and then persist in the connective tissue, gonads and coelom, developing into trophozoites (Rueckert and Leander, 2009b). Trophozoites later form numerous sporoblasts by budding from their surface (Perkins, 2000). In a new species of *Rhytidocystis*, several intracellular developmental stages covered by a trimembrane pellicle (all of them lacking the parasitophorous vacuole), distributed along the middle third of the host intestine (Diakin and Valigurová, 2014). Presumably, sporozoites penetrate the enterocytes and, during trophozoite

maturation, move to the base of the host cell. These, unlike *R. polygordiae* trophozoites reported as residing within the extracellular matrix between the epithelial cells (Leander and Ramey, 2006), induce formation of a syncytium around themselves from several of the surrounding epithelial cells. The apical part of the syncytium exhibits a typical morphology, though the basal region is free of organelles and cytoplasmic inclusions. Two or more mature stages can occur in one syncytium. Numerous giant mitochondria with tubular cristae accumulate at the trophozoite periphery, closely adjacent to the pellicle. The developmental stages differ in the density of cytoplasm and morphology of some organelles (mitochondria, nucleus). Some forms possess rhizoid-like appendages (Diakin and Valigurová, 2014). Neither a mucron nor an apical complex is present in species investigated so far (Diakin and Valigurová, 2014; Leander and Ramey, 2006; Rueckert and Leander, 2009b).

3.4 Feeding strategies

While the nutrition of gregarines has been the subject of extensive debate, their mechanism of nutrition acquisition remains poorly understood. The gregarine feeding mode depends on the long-term environmental conditions forming their niche. Correlations between trophozoite characteristics and the environment occupied within the host are discussed elsewhere (Leander et al., 2006). Archigregarines, the earliest diverging apicomplexan lineage, have retained myzocytosis as their principal feeding mode and myzocytosis is also expected to occur in blastogregarines (Simdyanov et al., 2018). Unlike blastogregarines, where the mucronal complex remains active (myzocytosis) during the trophozoite lifespan, archigregarines have non-feeding gamonts, though their conoid and rhoptries persist until at least progamic mitoses starts (Desportes and Schrével, 2013; Simdyanov and Kuvardina, 2007; Simdyanov et al., 2018). Myzocytosis is clearly illustrated in *S. pendula*, with mucronal (digestive) vacuoles inserted into the conoid and surrounded by numerous rhoptries and micronemes (Schrével et al., 2016). The myzocytosis process starts at the top of the conoid, with continuity of the mucronal vacuole membrane up to its contact with the host epithelial cell indicating that evagination through the apex of the conoid allows the parasite to suck out nutriments from the host cell (Fig. 9). The initial mucronal vacuole then fragments into numerous vacuoles (Schrével et al., 2016; Simdyanov and Kuvardina, 2007). An

axial streak of optically distinct cytoplasm reported in some species, extending from the anterior to the posterior end and forming an expansion around the nucleus, may represent a nutrient distribution system (Fowell, 1936; Paskerova et al., 2018). The presumed digestive vacuoles observed in the axial row, most likely originating in the mucron during myzocytosis, transport nutrients posteriorly along the cell axis. Accordingly, numerous vacuoles surround the nucleus in *S. pendula* (Schrével, 1971).
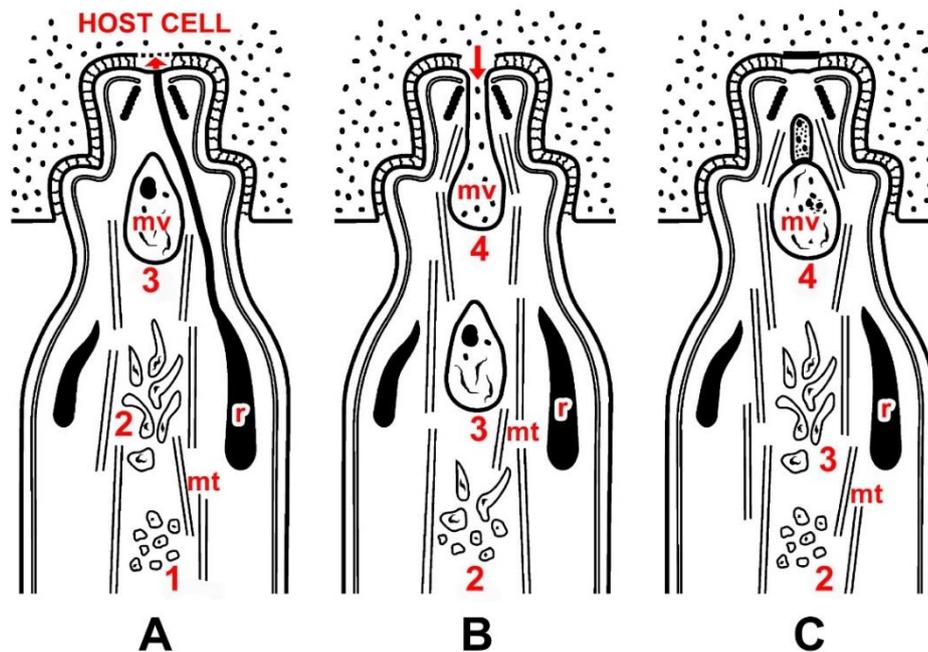

Fig. 9. Putative feeding scheme of *Selenidium* archigregarines (taken and modified from Simdyanov and Kuvardina, 2007). A. Local lysis of the host cell plasma membrane by rhoptry (r) secretion (red arrow). B. The process of myzocytosis: swallowing of the host cytoplasm through the temporary cytostome–cytopharyngeal complex (red arrow) and formation of the nascent mucronal vacuole (mv). C. Cytopharynx closure, the nascent mucronal vacuole (mv) is fully formed; the previous vacuole is divided into smaller vacuoles that are transported via a microtubular network (mt) into the trophozoite. The disrupted site of the host cell plasma membrane is restored. Numbers 1–3 indicate the positions of vacuoles formed during the preceding myzocytosis events (the current event is No. 4).

On the other hand, many eugregarines seem not to feed through the myzocytosis, except, perhaps, at the youngest developmental stage (Hildebrand, 1976; Valigurová et al., 2015). The apical complex of eugregarine trophozoites is reduced and instead a complicated attachment apparatus forms. Some authors attribute the feeding function in eugregarines to these attachment organelles (Schrével and Philippe, 1993). The concentration of host cell mitochondria and the endoplasmic reticulum surrounding the epimerite, along with the presence of parasite mitochondria located

just beneath the epimeritic cortical vesicle, indicate both the existence of active interaction between the eugregarine epimerite and the host cell (Hildebrand, 1976; Lucarotti, 2000) and that the epimerite is a metabolically active organelle (Baudoin, 1969; Ormieres, 1977). The abundant endoplasmic reticulum observed in the expanding epimerite of young trophozoites indicates activation of metabolic pathways (Valigurová, 2012). As host cells affected by attached eugregarines usually do not show any obvious pathological changes, the epimerite cortical vesicle and vacuoles most likely absorb nutrients via a mechanism based on membrane permeability, while numerous mitochondria underlying the cortical vesicle could provide the energy necessary for absorption (Schrével and Philippe, 1993; Tronchin and Schrével, 1977; Valigurová and Koudela, 2008; Valigurová et al., 2009). A reduction in the size of cortical vesicle in some species appears to be related to the convoluted character of their epimerites, significantly increasing the absorptive surface (Hildebrand, 1976; Valigurová, 2012). In the monocystid eugregarine *Nematocystis*, the trilaminar junction between its mucron and host cell forms extensive folds that increase the contact zone between apposing cell membranes (MacMillan, 1973b). Using radioisotopes, this study demonstrated that metabolites pass directly from host cell to the trophozoite by crossing the attachment site. However, feeding strategies differ between distant eugregarine taxa (Valigurová, 2012). An example can be found in the lecudinids, whose supposed lytic effect on host tissue is an indicator for the nutritional function of the mucron via extracellular secretion of enzymes and absorption of digested host tissue (Schrével and Philippe, 1993). The high concentration of actin-like proteins in the mucron of *Lecudina pellucida*, corresponding to the numerous 7-nm filaments in this region, concurs with its supposed sucker function. The protomerites, modified for attachment like those described in *G. cuneata* and actinocephalid gregarines, act as feeding organelles in eugregarines lacking an epimerite (Cook et al., 2001; Valigurová, 2012). Numerous pores and ducts interrupting the pellicle of *G. cuneata* at the protomerite apex, along with abundant dense bodies, vesicles and the Golgi apparatus in the protomerite cytoplasm, are most likely involved in gamont nutrition and/or attachment. A further nutrition possibility may be suggested, especially for gregarines growing in coelomic fluid with no attachment to the host tissue, and considering the fact that gregarines generally continue to grow after detaching from the host tissue (Schrével

and Philippe, 1993; Valigurová, 2012). The extensive folding of the pellicle covering the surface of large trophozoites in marine eugregarines appears to optimise surface-mediated nutrition (pinocytosis via micropores), and could explain the loss of myzocytosis and apical complex in eugregarines accompanied by development of a bulky attachment apparatus (Leander, 2008). Questions arise as to whether, and under what circumstances, the epimerite serves as a feeding organelle, and whether the gregarine micropores are points implicated in pinocytosis (Vivier et al., 1970) or serve for mucus extrusion (Schrével, 1972; Valigurová et al., 2013; Warner, 1968). The role of micropores in feeding appears to be especially true in eugregarines, the sporozoite of which is equipped by a single micropore located in its anterior third (Desportes, 1969; Sheffield et al., 1971), while advanced stages possess numerous micropores located in the grooves between the epicytic folds and smaller pores randomly distributed on the fold's base or lateral side (Diakin et al., 2016; Kováčiková et al., 2017b, 2018; Lucarotti, 2000; Schrével et al., 1983; Valigurová et al., 2013; Walker et al., 1984). While no typical micropores are present in the blastogregarines (Simdyanov et al., 2018; Valigurová et al., 2017), there is evidence for pinocytosis in *Selenidium* archigregarines based on rows of micropores with associated pinocytotic whorled vesicles interrupting the pellicle in the grooves between the longitudinal bulges (Kováčiková et al., 2017a; Leander, 2007; Paskerova et al., 2018; Schrével et al., 2016).

While *Cryptosporidium* exhibits unique features that characterise its biochemistry and metabolism (Thompson et al., 2016), its mechanism of nutrient acquisition remains unresolved. Presumably, the parasitophorous sac has a protective role, while the feeder organelle, directly separating the host cell and the parasite cytoplasm, provides an entry point for nutrients from the host (Tzipori and Griffiths, 1998; Valigurová et al., 2007). The feeder organelle, consisting of numerous folds that markedly enlarge the contact area between host and parasite, may be the site of nutrient and drug transport regulation into the parasite (Perkins et al., 1999). The feeder organelle lamellae are fringed by structures suggestive of endocytic vesicles (Landsberg and Paperna, 1986). Freeze fracture replicas show that the membrane folds of the feeder organelle close at the attachment site, but connect with cytoplasmic vesicles on the opposite side (Yoshikawa and Iseki, 1992). The parasite-induced cytoskeletal rearrangement in the host cell probably results in the formation

30

of a network for vesicle trafficking, facilitating the movement of nutrients between the host cell and the parasitophorous sac (Forney et al., 1999). The majority of studies suggest that cryptosporidia rely solely on the host for nutrient acquisition and encode for a number of transporters that likely serve this purpose (O'Hara and Chen, 2011). The presence of ABC-cassette binding proteins at the parasite-host interface provides further support for this hypothesis (Perkins et al., 1999). Based on their similarity to gregarines, the question arises as to whether the feeder organelle obtains nutrients from the host cell in an analogous manner to myzocytosis. Considering the debatable existence of *Cryptosporidium* extracellular stages reported from *in vitro* systems, it is unclear how this parasite, which lacks key *de novo* synthesis of amino acids, fatty acids, and nucleosides, acquires nutrients directly from an extracellular niche. As the feeder organelle has been observed in extracellular stages from biofilms, cryptosporidia may be able to acquire nutrients in a cell-free environment (Koh et al., 2014; Thompson et al., 2016).

It has already been emphasised that the general picture of metabolic interaction between host and parasite in cryptosporidia resembles that documented in *Eimeria* spp. (Beyer et al., 1995). However, epicellular eimeriids, though sharing features with cryptosporidia, are likely to differ in the mode of nutrient uptake, which probably occurs through the parasitophorous sac membrane which is considerably enlarged by projections equipped with pores, thereby increasing the area of the contact with the host cell (Benajiba et al., 1994; Beyer et al., 2002; Valigurová et al., 2015). Feeding via myzocytosis would also appear to be atypical for *E. duboscqi*, as its endogenous stages lack the apical complex. Further, there is no organelle similar to the flask-shaped structure nor a mucronal vacuole in freshly attached *E. duboscqi* parasites. Whether the complicated attachment apparatus of *E. duboscqi* is involved in the nutrient acquisition remains unclear. Numerous pores distributed along the entire parasite pellicle and the attachment site could be involved in feeding, with the second option appearing more likely as some pores appear to be associated with parasite vesicles and mitochondria (Valigurová et al., 2015).

3.5 Pathogenicity to the host

As a rule, eugregarines are considered non-pathogenic to their hosts (Henry, 1981); however, their actual impact on host fitness and viability has been poorly

investigated. Considering that the parasite load in eugregarines depends entirely on the number of oocysts ingested, they are relatively benign. Theoretically, heavy gregarine infestation in the mesenteron could affect the host's nutritional state. Some species could occlude the host gut, thereby preventing food passage (Lucarotti, 2000); however, this disagrees with a study on water striders *Gerris buenoi*, which showed eugregarines to be rather harmless commensals as there was no reduction in final host size or prolonged development time, despite heavy infections almost blocking the gut passage (Klingenberg et al., 1997). Similarly, eugregarines from *T. molitor* larvae kept in laboratory colonies did not appear to harm their host; instead, they seemed to be mutualistic as their presence had a positive impact on host development, fitness and longevity, despite heavy infection (Sumner, 1933; Valigurová, 2012). Some substances (e.g. vitamins or enzymes) secreted by these gregarines may be essential for larval growth. Pathogenicity is mostly attributed to the trophozoites as they could theoretically cause some degree of damage to parasitised tissue, depending on the dimensions and shape of their attachment structures (Lipa, 1967). Epicellular trophozoites mostly affect the microvillous site of epithelial cells. Microvilli are essential for efficient absorption and excretion, hence their destruction might limit host digestion and lead to malnutrition, resulting in weakening or even death (Valigurová, 2012). However, although the intestinal epithelium of parasitised mealworms shows some changes that could be associated with gregarine infection (i.e. vacuolation of individual parasitised cells), eugregarines have no negative impact on host health (Valigurová, 2012). Likewise, there is no evidence of direct damage to neighbouring epithelial cells caused by trophozoites attached to intestinal tissue, even at their high densities. Presumably, the continual regeneration of epithelial cells accounts for the apparent harmless effect of the parasite. Even if the trophozoites destroy individual cells, therefore, the overall damage to the epithelium is negligible and easily repaired. Even robust epimerite with rigid hooks in *Ancyrophora* does not appear to induce drastic damage to host cells (Baudoin, 1969). Species occurring in intestinal caeca appear more pathogenic as they cause hypertrophy of parasitised cells, or even rupture of the caecal wall, leading to secondary bacterial infection (Tanada and Kaya, 1993). The gregarine *N. temporariae* from tadpoles also appears not to cause disease or fitness impairment in the host, though livers of some tadpoles appear slightly enlarged and

light coloured; indeed, no mortalities of tadpoles or metamorphs have been recorded in the field (Chambouvet et al., 2016).

In contrast, neogregarines undergo multiple division (merogony), hence the level of parasitisation is not necessarily related to the number of oocysts ingested by the host. Further, autoinfection occurring in some neogregarines (Naville, 1930; Valigurová and Koudela, 2006; Weiser, 1954) appears to contribute to a rapid spread of infection. Consequently, neogregarines cause significant pathological changes to their insect hosts and are frequent causes of host morbidity and mortality due to cell lysis and destruction of tissue invaded by the merogony stages (Schrével and Desportes, 2016; Tanada and Kaya, 1993; Valigurová and Koudela, 2006). As hosts often do not survive heavy neogregarine infection, they are considered potential candidates for biological control of insect pests (Žižka, 1977). Neogregarine nutritional requirements are very high and, at the end of parasite development, the destroyed host tissue is replaced with neogregarine oocysts (Weiser, 1954). For example, the fat body cells of *Ephestia kuehniella* larvae parasitised by *Mattesia dispora* become vacuolated and degenerate (Valigurová and Koudela, 2006). Though *M. dispora* parasitises the host cell with no obvious response, its meronts decrease fat excretion and deposition within the parasitised cell (Weiser, 1954). Consequently, the fat body becomes overgrown with plasma-rich cells lacking lipid vacuoles. With progressing infection, the affected cells appear hypertrophied with the nucleus pushed back. During the micronuclear merogony of *M. dispora*, a moderate reduction in host activity and food intake can be observed, while larvae exhibit lethargy and cease moving during the course of macronuclear merogony. Thereafter, their bodies become pale and the larvae cease feeding, following which the infection spreads to the entire larval body. During the final stage, the haemocoel of the insect is packed with numerous oocysts, while the tissue is destroyed. Massively infected larvae turn an intense pink colour before death (Valigurová and Koudela, 2006). On the other hand, in *Farinocystis triboli*, which does not induce formation of parasitophorous vacuole, presence of host mitochondria surrounding the meronts is the only response to infection (Žižka, 1977). It is likely that the formation of parasitophorous vacuole results from an interaction between parasite invasion and host defence, as documented in *Galleria mellonella* parasitised by *M. dispora* (Žižka, 2005).

It has been suggested that epicellular development might be considered as a more primitive form of host-parasite association (Paperna and Landsberg, 1989). There is evidence, however, that epicellular parasites have a lower negative effect on the host epithelium than intracellular parasites (Eli et al., 2012). The attachment strategy of epicellular parasites may be more progressive as, generally speaking, it is more advantageous for the parasite to maintain acceptable fitness in their hosts. As with the flat holes left in the epithelium (devoid of microvilli) by detached gregarine trophozoites, detached stages of cryptosporidia and *E. duboscqi* leave only shallow craters, with the parasitophorous sac remaining at the epithelial surface (Jirků et al., 2008; Valigurová et al., 2008, 2009, 2015). In addition, cryptosporidia and *E. duboscqi* regularly detach from the unmodified part of the host cell with their sacs; while the detachment of cryptosporidia takes place in the area of the dense band, *E. duboscqi* parasites expose their naked basis when tearing away from parasitophorous sacs, leaving the intact inner sac membrane at the place of attachment. In contrast to cryptosporidia, *E. duboscqi* appears to induce only moderate alterations in the host cell. Cytoskeletal remodelling of epithelial cells induced by cryptosporidia leads to microvillous hypertrophy, i.e. elongation and protrusion of host cell microvilli surrounding the parasite (Forney et al., 1999). The long microvilli clustered at the attachment site of cryptosporidia suggest an active manipulation of the host membrane structure by the parasite. The microvilli associated with the cryptosporidian parasitophorous sac are thick and packed with dense bundles of F-actin. Despite having a similar attachment strategy to cryptosporidia, *E. duboscqi* has a lower pathological effect on host tissue as no pathological changes or significant extension of adjacent microvilli occurs in parasitised tissue (Valigurová et al., 2015).

In immunocompetent hosts, cryptosporidiosis is usually an acute, self-limiting gastrointestinal disease, characterised by watery diarrhoea, abdominal cramps, vomiting, low-grade fever and appetite loss. The intensity of pathological alteration depends on parasite species and load, as well as host age and immunological status. Increased morbidity and mortality has been reported in patients with severe immunodeficiency and in malnourished children. Other pathogens, such as *Helicobacter*, *Escherichia coli* and rotavirus, may escalate the impacts of cryptosporidiosis on host tissue, possibly leading to death (Santin, 2013; Tatar et al.,

1995). The overall effect of parasitism on host health is closely related to the parasite's preference for particular target tissues or cells. Presumably, cryptosporidia prefer a specific type of cells for attachment as direct observations on cultures have shown that, while numerous sporozoites inspect potential host cells with their prolonged apical ends, they often leave without invasion (Melicherová et al., 2018). Indeed, the developmental stages of *C. proliferans* and *C. parvum* frequently occur near dividing or newly formed round cells (Melicherová et al., 2018; Tůmová, 2019). Particularly interesting is that cryptosporidia appear to interact with and regulate host-cell gene expression as they can inhibit (trophozoites) or promote (sporozoites, merozoites) host cell apoptosis, depending on their developmental stage (Chen et al., 1998; Mele et al., 2004). A loss of absorptive surface area is frequently associated with intestinal cryptosporidiosis (Leitch and He, 2012). For example, the major histopathological changes induced by *C. parvum* infecting enterocytes of the distal small intestine, caecum and colon comprise villous atrophy, shortening of microvilli and sloughing of enterocytes (Santin, 2013). Gastric cryptosporidiosis in animals tends to cause mild histopathological changes with no obvious alterations to host health status, and no, or only insignificant, inflammatory responses in *lamina propria*. Cryptosporidia affect gastric tissues irregularly, in an island-like manner (Melicherová et al., 2014; Val-Bernal et al., 2013; Valigurová et al., 2018). For example, *C. muris*, a gastric species from rodents, induces less significant pathological changes than *C. proliferans* (Kváč et al., 2016), where pathological changes in mouse gastric tissues escalate during chronic phases of cryptosporidiosis, including marked deformation of the gastric glandular epithelium surface and a cauliflower-like appearance in gastric mucosa (Valigurová et al., 2018). The heavily parasitised epithelium proliferates into the luminal space, resulting in extensive folding of the stomach. Subsequently, expansion of the *lamina propria* leads to an increase in the distance between gastric glands, twisting, and deformation of the longitudinal folds, and diffuse mucosal hypertrophy occurs, typified by the presence of giant gastric folds and intensive epithelial hyperplasia. The gastric glands, packed with parasites and necrotic material, become markedly dilated and hypertrophied and lose their normal architecture, while the atrophic epithelial cells exhibit cuboidal or squamous metaplasia. A thickening of the *muscularis mucosae* is typical of advanced gastric cryptosporidiosis. The tissue

exhibits oedema and infiltration of the *lamina propria* and submucosa with neutrophils. Though stomach weight and epithelial height increase considerably, neither clinical signs of cryptosporidiosis nor weight lost have been documented in laboratory rodents parasitised by *C. proliferans* (Kváč et al., 2016; Melicherová et al., 2014; Valigurová et al., 2018).

4   Motility in early branching Apicomplexa

4.1   Apicomplexan motility and cytoskeleton

Zoites, the highly motile stages of Apicomplexa, exhibit considerable variation in movement, such as the progressive circular or helical gliding and non-progressive twirling of *T. gondii* and *Plasmodium* zoites. Reported gliding rates in Apicomplexa are usually in the range of 1–10 μm/s, with maximum rates reported from gregarines, e.g. 22.86 μm/s in *G. polymorpha* and up to 60 μm/s in *Porospora gigantea* (King and Sleep, 2005; King, 1988; Valigurová et al., 2013). Apicomplexans are generally characterised by a complicated cell cortex consisting of a continuous plasma membrane, underlined by cortical alveoli forming the IMC. The IMC connects with cytoskeletal elements, such as the actomyosin complex, microtubules and the network of intermediate filamentous proteins, and may be interrupted by micropores (Morrissette and Sibley, 2002; Valigurová et al., 2013). Remarkably, apicomplexan subpellicular microtubules are unusually stable and withstand high pressure, cold and detergents, while actin filaments are transient. Actin is mostly present in its globular form and microfilaments are usually detected only after treatment with F-actin stabilising drugs such as jasplakinolide. Previous studies (focusing predominantly on *T. gondii* and *Plasmodium*) concur with the so-called glideosome concept applied for apicomplexan zoites, describing a substrate-dependent gliding motility facilitated by a conserved form of actomyosin motor and subpellicular microtubules. This actomyosin motor is thought to be localised between the plasma membrane and IMC, with zoite gliding based on the locomotion of myosin fixed to the IMC along actin filaments, together with translocation of apically released adhesins to the parasite's posterior end, resulting in a forward movement (Daher and Soldati-Favre, 2009; Frenal et al., 2010; Tardieux and Baum, 2016). This unique machinery (which requires a stable subpellicular network of

microtubules to provide structural stability and maintain polarity) is based on, and limited by, the formation of transient actin filaments and their fixation to the IMC.

Basal apicomplexans differ from other Apicomplexa in that (i) their trophozoites and gamonts are often motile, at least to some degree; (ii) locomotion usually differs from substrate-dependent gliding based on glideosome, and (iii) they use several cell motility mechanisms that correlate with various modifications of their cell cortex (epicyte). The differing motility modes exhibited by basal Apicomplexa, comprising bending, rolling, coiling and nematode-like motility, gliding, metaboly or peristalsis, most likely represent specific adaptations to parasitism in different environments within their hosts (Valigurová et al., 2013, 2017).

4.2 Motility and cytoskeleton in archigregarines and blastogregarines

The spindle-shaped trophozoites and gamonts of *Selenidium* archigregarines display bending, coiling, rolling and pendular non-progressive movements, along with cell shape contraction (Fowell, 1936; Kováčiková et al., 2017a; Leander, 2007; Schrével et al., 2016). The pendular motility of *S. pendula* exhibits a regular periodicity of about 2–3 seconds, with propagation waves generated in the parasite's anterior region (Desportes and Schrével, 2013). The trimembrane pellicle of most *Selenidium* spp. is organised in broad longitudinal bulges separated by grooves; though additional cortex modifications occur in species that contract their body. For example, the motility of *S. vivax* trophozoites, which actively and irregularly change their conformation by twisting, folding, shrinking and expanding cell volume, is somewhat peristaltic (Desportes and Schrével, 2013; Leander, 2006). The folded pellicle of contracted and semi-relaxed parasites exhibits transverse striations, which vary in depth and number while they disappear and reappear (Rueckert and Leander, 2009a). In general, the pellicle is underlain by longitudinally oriented subpellicular microtubules, which tend to be arranged in a single layer, the continuity of which is interrupted under the grooves with micropores, and deeper located groups of irregularly arranged microtubules (Kováčiková et al., 2017a; Paskerova et al., 2018; Schrével et al., 2016). The pellicle may act as a stiff skeletal component, while the regular sets of subpellicular microtubules have a motility function (Macgregor and Thomasson, 1965). It has been proposed that this represents a unicellular analogue to the musculocuticular system of nematodes, in

which longitudinal muscles function antagonistically against the elastic cuticle (Leander, 2007; Stebbings et al., 1974). Archigregarines lacking subpellicular microtubules are non-motile, though their longitudinal bulges are supported by arrays of fibrils reminiscent of circular myonemes (Wakeman et al., 2014). The intracellular axial streak with laterally branching radial fibrils reported in some *Selenidium* archigregarines may be involved in motility as an additional skeletal element helping to reverse movements and maintain cell shape in bends, as suggested by the statomotor system concept (Fowell, 1936; Paskerova et al., 2018).

The elongated, flattened trophozoites and gamonts of *S. nematoides* exhibit highly active movements, with motility of both attached and detached parasites in a liquid environment resembling a sequence of undulation, pendular, twisting and, occasionally, spasmodic movements (Valigurová et al., 2017). In attached parasites with typically wavy movements, the waves develop in their proximal region, just behind the attachment area, and proceed distally, the last third of the cell being more rigid with limited mobility. The bending movements of detached individuals also initiate from the apical region. The blastogregarines beat at a rate of 0.51 beats per second on average, with a beat-to-beat interval of 2.18 seconds. In *S. nematoides*, the surface of the trimembrane pellicle in endogenous stages (from early trophozoites up to gamonts) is smooth, lacking grooves or folds. A distinct glycocalyx layer, thickening towards the apical region, covers the entire parasite and, in mature stages, numerous pores interrupt the pedicle, mostly organised in four lateral rows running parallel to the longitudinal cell axis. The helical arrangement of microtubules in *S. nematoides* follows its serpentine body shape, similar to those of apicomplexan zoites. The regularly arranged subpellicular microtubules exhibit a characteristic longitudinal organisation and are nucleated from the apical polar ring, a microtubule-organising centre unique to the Apicomplexa. In contrast to glideosome, the majority of *S. nematoides* actin is present in a polymerised form and appears to be located beneath the IMC. The subpellicular microtubules are associated with filamentous structures (cross-linking protein complexes), presumably of an actin-like nature (Valigurová et al., 2017). In contrast to the active movement of S*. nematoides*, *C. mesnili* blastogregarines show only weak motility, typified by slow and intermittent bending movements. These differences in motility can be attributed to specific cortex modifications. The pellicle of *C. mesnili*, covered

by a trimembrane pellicle organised in longitudinal folds with flattened tops, is underlined by numerous longitudinal and regularly distributed subpellicular microtubules which are arranged in two layers at the tops of the folds and as a single layer between the folds and on their lateral sides. These microtubules arise from the fibrillar matter lying beneath the pellicle in the frontal region of the mucron. The putative polar ring of this species is not subdivided, as observed in *S. nematoides*, and does not contact with the microtubules, even though they are abundant within the mucron (Simdyanov et al., 2018).

Due to similarities in their external morphology and movement patterns, *Siedleckia* has been associated with *Selenidium* archigregarines. Despite bearing a striking resemblance with overgrown apicomplexan zoites, the trophozoites and gamonts of both genera move independently on solid substrates with no signs of gliding motility. The motility mechanisms of *S. nematoides* and *Selenidium* archigregarines differ from the glideosome, despite the presence of key glideosome components such as a pellicle comprising a plasma membrane and IMC, subpellicular microtubules, actin, myosin, micronemes and a glycocalyx layer. The subpellicular microtubules organised in several layers appear to be the leading motor structures in blastogregarine and *Selenidium* spp. motility. In both taxa, the individual microtubules are localised within lucent areas (the so-called chambers) that most likely act in microtubule sliding. Experimental assays have shown that polymerised forms of actin and tubulin play an essential role in their movement (Kováčiková et al., 2017a; Valigurová et al., 2017). Nevertheless, while treatment with membrane-permeable drugs influencing polymerisation of actin, jasplakinolide and cytochalasin D, affects motility and actin organisation in *S. pygospionis*, no significant changes occur in the position of the subpellicular microtubules, contrary to observations on *S. nematoides*. The cross-linking protein complexes in *S. nematoides*, which presumably anchor the subpellicular microtubules to the cytoplasmic face of IMC, may correspond to microtubule-associated proteins (MAPs) (Valigurová et al., 2017). MAPs are expected to control the spacing of microtubules within the cell by interconnecting them with other cytoskeletal elements or with the plasma membrane. It is likely that the heavy decoration of subpellicular microtubules in Apicomplexa may account for their unusual stability. The fact that tubulin-specific antibodies commonly do not label the full length of microtubules in apicomplexan

zoites may be due to occlusion of tubulin epitopes by MAPs (Tran et al., 2012). The MAPs, such as dyneins or kinesins, are responsible for sliding between adjacent microtubules. As with the ciliary axoneme, a mechanism with microtubules sliding against one another could account for the undulating motility of blastogregarines and archigregarines. A MAP-based mechanism has been proposed to explain the undulating and bending movements in *Selenidium* spp. (Leander, 2006; Mellor and Stebbings, 1980; Schrével, 1971; Stebbings et al., 1974). Numerous peripheral mitochondria in *Selenidium* spp. and *S. nematoides* probably play an important role in the rapid and continuous generation of ATP, which is essential for the support of highly dynamic cell plasticity and may provide the chemical energy necessary for MAP activity. Actively moving *Selenidium* spp. exhibit more ectoplasmic mitochondria and subpellicular microtubules than less active species (Leander, 2006, 2007; Paskerova et al., 2018; Schrével, 1971; Valigurová et al., 2017). If axoneme-like sliding of microtubules is applicable to *S. nematoides*, the putative actin cytoskeleton associates with the subpellicular microtubules lengthwise in order to position them within the cytoplasm just beneath the pellicle; otherwise, the actin filaments could force synchronised bending of the microtubules in some cell regions, thereby generating typical undulating motility (Valigurová et al., 2017).

4.3   Motility and cytoskeleton in eugregarines

Eugregarine sporozoites display a typical apicomplexan zoite organisation. The sporozoites are covered by a trimembrane pellicle underlain by subpellicular microtubules and their apical region is equipped with a conoid, polar rings, rhoptries and numerous micronemes (Desportes, 1967; 1969; Diakin et al., 2014; Sheffield et al., 1971). While a sinuous movement without gliding activity is reported for *Pyxinia crystalligera* sporozoites (Collins, 1972), sporozoites of *N. temporariae* glide and keep their banana shape, with only the apical end appearing fully flexible (Chambouvet et al., 2016). Sporozoites of *G. rigida* contacting the host epithelium form a small conical protuberance devoid of endoplasm, elongating into a slender neck as long as the sporozoite itself (Kamm, 1920). Later stages of eugregarines (comprising trophozoites and gamonts) exhibit diverse modes of locomotion and appear to use several motility mechanisms, depending on their physiological and environmental conditions. Their complicated cell cortex, the epicyte, forms a range

of superficial structures. The majority of eugregarines, for example, have a cortex consisting of a dense array of longitudinal epicytic folds, while some species exhibit further epicyte modifications such as superfolds, fusion of the plasma membrane at the apex or a lateral site of several folds, numerous cytopilia or microvilli covering the surface, or rows of small knobs. All these modifications lead to an increase in gregarine surface in contact with the host environment. Bacteria found in the canals between partially fused folds may induce their fusion (Desportes and Schrével, 2013; Desportes et al., 1977; Diakin et al., 2017). A glycocalyx layer covering the pellicle has been documented in a number of species (Kováčiková et al., 2017b; Philippe et al., 1979). Most eugregarines exhibit progressive gliding motility, which is described as an irregular, erratic process, usually corresponding to a unidirectional movement with respect to the antero-posterior cell axis, without changes in cell shape (Desportes and Schrével, 2013; Diakin et al., 2016, 2017; King and Sleep, 2005). As trophozoites and gamonts in the species analysed lack subpellicular microtubules, they must use a gliding mechanism differing from glideosome (Kováčiková et al., 2017b, 2018; Valigurová et al., 2013). Further, eugregarines are able to free-float in liquid, lacking any contact with the substrate, but they move at a significantly higher rate than shown during regular gliding (Valigurová et al., 2013). Undulations of the epicytic folds can be seen in floating individuals (Desportes and Schrével, 2013). Eugregarine trophozoites attached to the host tissue usually show no obvious motility, though near-surface currents of host liquids, most likely produced by the parasite's undulating folds, can be noticed around them (Diakin et al., 2016).

Gliding on a solid surface is accompanied by the shedding of a mucous trail behind the gregarine. Though the material in the trail is generally designated as mucus, its exact composition is unknown. The origin of this mucosal substance could be related to an abundant Golgi apparatus present in the cytoplasm of eugregarines. It has previously been suggested that the secreted mucus pushes the gregarine forward passively (Desportes and Schrével, 2013). However, the translocation of concanavalin-A beads posteriorly along the parasite surface at rates similar to the forward gliding movement, and the fact that large beads comparable in mass to the gregarine itself can be actively translocated, indicates that eugregarines generate substantial locomotory forces (King, 1981). Hence, it is more likely that the mucus acts as a lubricant. The increased load of mucus in eugregarine cytoplasm is

correlated with gliding rate, in contrast to the general architecture and supramolecular organisation of the pellicle (Valigurová et al., 2013). More recently, it was suggested that the eugregarine gliding mechanism involves a mechanico-chemical system related to lateral undulations of the epicytic folds, frequently documented with undulated and straight folds alternating (Desportes and Schrével, 2013). Generally, the epicytic folds have identical ectoplasmic structures and are built up from the plasma membrane with IMC, 12-nm filaments with properties of intermediate filaments, rippled dense structures and basal lamina (Schrével et al., 1983; Valigurová and Koudela, 2008; Valigurová et al., 2013; Vávra and Small, 1969; Walker et al., 1984). The number of 12-nm filaments does not influence gliding speed but appears to control the direction of movement. Gregarines equipped with epicytic folds bearing a lower number of 12-nm filaments glide at a relatively high speed, though their gliding path tends to be widely semi-circular rather than linear. The rippled dense structures, located at the external cytomembrane, presumably serve as supporting elements interconnecting 12-nm filaments and the plasma membrane. The half-moon-shaped dense structure often seen to underline the 12-nm filaments could function as a skeleton reinforcing the tips of folds directly contacting the substrate during gliding (Kováčiková et al., 2017b; Valigurová et al., 2013).

Though involvement of actin and myosin (associated with the eugregarine pellicle) in eugregarine motility has been reported, the actual gliding motor remains unknown (Baines and King, 1989; Ghazali et al., 1989; Ghazali and Schrével, 1993; Heintzelman, 2004; Heintzelman and Mateer, 2008; Kováčiková et al., 2017b; Valigurová et al., 2013). Positive phalloidin labelling suggests that the majority of actin in eugregarines is present in a filamentous form and could play a role in gliding (Kováčiková et al., 2017b, 2018; Valigurová et al., 2009, 2013). The actin accumulates in two layers of eugregarine cell cortex: the longitudinal epicytic folds and a deeper layer of rib-like myonemes running perpendicularly to the cell axis (Heintzelman, 2004; Heintzelman and Mateer, 2008; Kováčiková et al., 2018). The myonemes, localised at the border between the ectoplasm and endoplasm, correspond to the concentric bundles of F-actin (Fig. 10). A further element most likely involved in motility is the anastomosing ectoplasmic network of intermediate filamentous proteins localised immediately beneath the epicytic folds (Beams et al., 1959; Kováčiková et al., 2018; Valigurová et al., 2013). Of the three myosin genes

characterised in *G. polymorpha*, myosins A (93 kDa) and B (96 kDa) belong to class XIV, restricted to the Apicomplexa, and myosin F (222 kDa) to class XII. Myosin A localises on the longitudinal epicytic folds and subjacent rib-like myonemes, while myosin B is restricted to the folds and myosin F to the myonemes (Heintzelman and Mateer, 2008). If some form of actomyosin motor is present, it could be localised at the links observed between the plasma membrane and the external cytomembrane of the IMC, which are supposed to be related to the lateral undulations of the folds (Desportes and Schrével, 2013; Valigurová et al., 2013). However, an experimental study on *G. garnhami*, using actin-targeting drugs, contradicts the expectation that lateral undulation of the epicytic folds provides the force behind gregarine gliding as the wavy pattern did not change in drug-treated parasites where motility was completely blocked (Kováčiková et al., 2018). Observations on drug-treated gamonts demonstrate that the organisation and density of the subpellicular structures, ectoplasmic network and myonemes, change in accordance with gliding activity. Degradation of myonemes accompanies the blocking of gliding motility in cytochalasin D-treated gamonts due to the depolymerisation of existing actin filaments, while jasplakinolide-induced changes lead to further stabilisation of already present F-actin and do not significantly affect gliding. These data suggest that the dynamic process of actin polymerisation and rapid depolymerisation described in glideosome is not essential for gliding in eugregarines, where polymerised actin alone appears to be the main motor structure responsible for gliding.
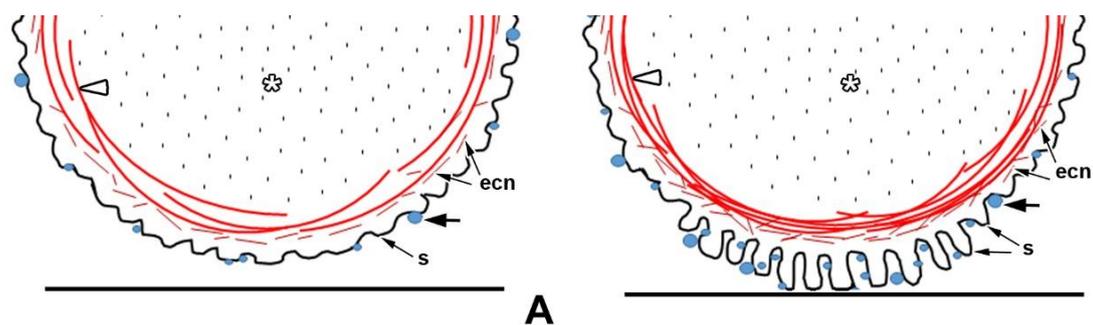

Fig. 10. Schematic diagram illustrating a possible function of cortical filaments (myonemes, ectoplasmic network) facilitating gliding motility in *Gregarina garnhami* gamonts (taken from Kováčiková et al., 2018). A. Gamont in non-gliding phase. The myonemes and the ectoplasmic network are evenly distributed around the ectoplasm. B. Gamont during gliding on a solid substrate. Note the presence of protruding superfolds that group together, resulting from contraction of myonemes, along with more a compact ectoplasmic network and denser accumulation of mucus in this region. black arrow – mucus drops, ecn – ectoplasmic network, s – superfolds, white arrowhead – myonemes, white asterisk – cytoplasm.

Besides gliding, some species exhibit intense bending, curving or shortening of the longitudinal axis, especially in their protomerite region. For example, the trophozoites and gamonts of *C.* cf. *communis* enrich their gliding by jumping and rotational movements, with rapid changes in gliding direction and cell flexions (Kováčiková et al., 2017b). While it is generally believed that the eugregarine cortex became rigid over the course of environmental adaptation, resulting in a loss of wriggling ability (typical for archigregarines), these active movements indicate a relatively high cellular plasticity. The rib-like myonemes girding the cell cortex and the ectoplasmic network are thought to be involved in the bending motions of eugregarines (Beams et al., 1959; Valigurová et al., 2013).

Coelomic eugregarines, which evolved as free-floating parasites within the host tissue, move by pulsations of the body wall (corresponding to non-progressive peristaltic or metabolic motility) accompanied by periodic changes in body shape (Diakin et al., 2016; Landers, 2001; Leander et al., 2006; MacMillan, 1973a; Miles, 1966, 1968). These peristaltic waves, which occur about every two seconds, move backward and forward, the gregarines being driven in spiral-like movements during wave propagation (Desportes and Schrével, 2013). The annular myonemes are considered responsible for these peristaltic movements. Abundant mitochondria distributed uniformly in the cell cytoplasm of *U. ovalis* may be correlated with active metaboly, which can be accompanied by transient modifications of the cell cortex, such as formation of superfolds in the contracted regions (Diakin et al., 2016; MacMillan, 1973a). The cellular deformations demonstrated by urosporid gamonts pulsating freely within host fluids may be necessary to provoke an exchange of host liquid around them, thereby improving the effectiveness of nutrient acquisition (Leander, 2008). Active movements could also provide an effective protection against adhesion of host coelomocytes to their surfaces (Diakin et al., 2016).

Urosporid eugregarines represent a perfect example of Apicomplexa exhibiting enormous morphological and behavioural plasticity according to their localisation within the host. Phylogenetically related species that occupy different ecological niches in the host to decrease the intensity of species competition, often demonstrate diverse parasitism strategies (Diakin et al., 2016; Wakeman et al., 2014). The diversity of urosporids demonstrates an intermediate character state related to the evolutionary transformation of trophozoites following colonisation of coelomic

environments. As an example, two closely related coelomic *Urospora* species parasitising the polychaete *T. forbesii* exhibit different modes of motility. The trophozoites of *U. ovalis*, located free in the host coelom, show metaboly, while the V-shaped *U. travisiae* trophozoites, which are able to attach to the host tissue, demonstrate gliding (Diakin et al., 2016). The gliding motility of *U. travisiae* presumably allows the parasite to move along the inner coelomic wall and other host tissues, as shown in other urosporids (Leander, 2008).

4.4 Motility and cytoskeleton in protococcidia and agamococcidia

In the protococcidian *E. duboscqi*, subpellicular microtubules, connected with posterior polar ring, are only present during its early development (Valigurová et al., 2015). Accordingly, in native preparations, the drop-shaped invading zoites and earliest developmental stages, with their pointed end attached to the host epithelium, exhibit oscillating movements, while helmet-shaped early trophozoites show only weak movement. Despite the absence of microtubules in maturing trophozoites and later stages of *E. duboscqi*, positive α-tubulin labelling of the parasite surface and cytoplasm suggests either preservation of tubulin in a non-polymerised form or its presence in other tubulin-rich structures. The second option is more likely, considering the disappearance of labelling from the parasite periphery after treatment with oryzalin, resulting in dispersion of putatively unpolymerised α-tubulin throughout the cytoplasm. Instead of microtubules, subpellicular bands of longitudinally oriented actin-rich filaments form beneath the IMC during trophozoite maturation, these presumably functioning as the parasite's cytoskeleton. Aside from the frequent detachment of parasites along with their parasitophorous sacs from host tissue observed in native preparations, neither attached nor detached mature *E. duboscqi* stages exhibit obvious movement. In squash preparations, some attached advanced stages exhibit slight signs of movements and cytoplasmic streaming resembling metaboly; however, due to the intense waving and beating motion of host enterocyte cilia it is not possible to determine with certainty whether this is actual movement of the parasite inside the sac (Valigurová et al., 2015; Valigurová, personal observation).

After being picked out mechanically from the host tissue, agamococcidian *Rhytidocystis* spp. transform into oval or round immotile cells. The trophozoites are

covered by a trimembrane pellicle forming short folds, with numerous micropores located between and on top of the folds (Diakin and Valigurová, 2014; Rueckert and Leander, 2009b). All observed intracellular stages lack the subpellicular microtubules, though a single microtubule located deeper within the cytoplasm can occasionally be seen in ultrathin sections (Valigurová and Diakin, personal observation).

4.5   Motility and cytoskeleton in cryptosporidia

While motility of apicomplexan zoites is considered the essential mechanism for host cell invasion, motility of *C. proliferans* sporozoites freshly excysted from oocysts is rather limited and featureless in a range of excystation media (Melicherová et al., 2016). In cell cultures, however, released sporozoites can be seen probing the plasma membrane of potential host cells with their prolonged apical end and attempting to invade the cultured cells (Melicherová et al., 2018). This thin and prolonged apical end is only typical for sporozoites contacting the host cell, as sporozoites isolated from the supernatant do not exhibit apical prolongation (Borowski et al., 2010; Melicherová et al., 2018). This behaviour appears to be important for invasion success as cryptosporidian sporozoites are only equipped with a single rhoptry and, therefore, have only a single attempt for successful attachment to suitable host cell (O'Hara et al., 2005). The sporozoite of *C. parvum* shows a uniform distribution of actin throughout the cell and its gliding motility depends upon an intact actomyosin motor (Forney et al., 1998). Using the anti-actin antibody raised against *Dictyostelium*, which recognises the actin in *T. gondii* and *Plasmodium*, Western Blot analysis of *C. proliferans* sporozoites has confirmed the presence of actin (42 kDa) at very low concentrations, despite negative immunofluorescent labelling. Immunofluorescence has also detected homogeneously distributed myosin (Mazourová, 2013, 2015; Valigurová et al., 2014). The subpellicular microtubules of cryptosporidian sporozoites originate at the region of the dense collar with associated apical rings and appear to spiral around the apical region (O'Hara et al., 2005). In *C. proliferans*, Western Blot analysis has revealed the presence of high consternations of α-tubulin (50 kDa), while immunofluorescent labelling has confirmed presence of subpellicular microtubules extending from the apical pole for up to two thirds of the sporozoite body, as shown

in other apicomplexan zoites (Mazourová, 2013, 2015; Morrissette and Sibley, 2002). In merozoites, the subpellicular microtubules are present in *C. muris* and *C. proliferans* (Melicherová et al., 2014; Uni et al., 1987), while studies focusing on *C. parvum* and *C. wrairi* failed to detected them (Current and Reese, 1986; Vetterling et al., 1971). The trails of gliding *C. parvum* sporozoites are threadlike and relatively short (typically 1-2 times the sporozoite length), with a straight to slightly curved pattern extending from the posterior end of the parasite. The sporozoites of *C. prolifera*ns excysted *in vitro* in various incubation media exhibit an oscillating movement (short forward/backward shifts), appearing to move progressively forward without obvious changes in cell shape (Melicherová et al., 2016). Motility of sporozoites is lower in pure RPMI 1640 and RPMI 1640 enriched by 1 % BSA compared to media with higher concentrations of BSA (5% and 10 %). In the medium with 5 % BSA, sporozoites remain motile for a long period (tested over 240 minutes), while in 10 % BSA the activity of excysted sporozoites decreases slightly. Sporozoites in BSA free medium are most active during the first 30 minutes after excystation, though motility rapidly declines thereafter. The motility of unexcysted sporozoites appears to create 'dancing' oocysts prior to their final excystation and the liberation of sporozoites (Melicherová et al., 2016). Frequently observed is the positioning of unexcysted oocysts with their sutures orientated towards the cultured cell's surface, presumably resulting from sporozoite movement inside the oocyst. Such behaviour may help to shorten the distance between free sporozoites and the host cells (Melicherová et al., 2018). The enclosure of oocysts by cultured cells, as observed in HCT-8 and HT-29 cell lines, is induced by parasite antigens (Melicherová et al., 2018). This encapsulation occurs independently of any active invasion by motile stages and concurs with Forney et al. (1998), who stated that, in contrast to other apicomplexan zoites, invasion of cryptosporidian zoites is a passive process that does not require actomyosin motility machinery as the effect of treatment with actin and myosin inhibitors on infectivity was insignificant. In contrast, antimicrotubular drugs block cryptosporidian infectivity for host cells (Wiest et al., 1993). Irrespective of their structural similarities, it is evident that cryptosporidia have evolved strategies for host cell invasion that differ significantly from those described in phylogenetically related apicomplexan parasites.

5 Conclusions

Apicomplexans cause human and animal diseases that represent a major world health problem and have a considerable impact on the global economy. Attempts to control these pathogens are usually hampered by their localisation and strategies to evade host immune responses and chemotherapeutics. Whilst the nature of the diseases caused by Apicomplexa differs significantly, their common origin led them to share specific metabolic pathways unique to this group, and these may constitute potential targets for intervention. In contrast to well-studied vertebrate pathogens, Apicomplexa restricted to invertebrates are considered of no economic or medical significance and they remain poorly understood, despite their enormous diversity.

In summarising the publications produced for this thesis, as well as those closely related to the topic, I have tried to highlight the diversity of apicomplexan survival and parasitism strategies occurring in different environments. Two main aspects are discussed in detail, i.e. host-parasite interactions and parasite motility, as these represent a potential target for chemotherapeutic intervention. The study has attempted to determine which structures and mechanisms are responsible for the various modes of motility, attachment to host cell/tissue and nutrient acquisition in basal lineages and how these are modified in comparison to other Apicomplexa. Detailed observations indicate that even seemingly insignificant modifications in apicomplexan subcellular structures may result in different parasitism strategies. The presented data, especially those obtained on type species such as the protococcidian *E. duboscqi*, blastogregarine *S. nematoides* and archigregarine *S. pendula*, indicate the importance of further research on deep-branched apicomplexans, which exhibit enormous diversity in subcellular organisation and highly specialised adaptations to the parasitic life style. Such research will provide a deeper understanding of the biology and evolutionary pathways of the Apicomplexa in general. The results presented herein support the hypothesis of Apicomplexa evolution progressing from myzocytotic predation to myzocytotic extracellular parasitism, accompanied by the origination of epicellular parasitism and significant modifications to the attachment apparatus and motility mode at the trophozoite stage, and finally intracellular parasitism along with a rejection of trophozoite polarity and motility.

6 References

Adl S.M., Simpson A.G., Lane C.E., Lukeš J., Bass D., Bowser S.S., Brown M.W., Burki F., Dunthorn M., Hampl V., Heiss A., Hoppenrath M., Lara E., Le Gall L., Lynn D.H., McManus H., Mitchell E.A., Mozley-Stanridge S.E., Parfrey L.W., Pawlowski J., Rueckert S., Shadwick R.S., Schoch C.L., Smirnov A., Spiegel F.W. (2012). The revised classification of eukaryotes. J. Eukaryot. Microbiol. 59, 429-493.

Baines I., King C.A. (1989). Demonstration of actin in the protozoan *Gregarina*. Cell. Biol. Int. Rep. 13, 679-686.

Barta J.R., Thompson R.C.A. (2006). What is *Cryptosporidium*? Reappraising its biology and phylogenetic affinities. Trends Parasitol. 22, 463-468.

Baudoin J. (1969). Sur l'ultrastructure de la région antérieure de la grégarine *Ancyrophora puytoraci*. Protistologica 5, 431-439.

Beams H.W., Tahmisian T.N., Devine R.L., Anderson E. (1959). Studies on the fine structure of a gregarine parasitic in the gut of the grasshopper, *Melanoplus differentialis*. J. Protozool. 6, 136-146.

Benajiba M.H., Marques A., Lom J., Bouix G. (1994). Ultrastructure and sporogony of *Eimeria* (syn. *Epieimeria*) *anguillae* (Apicomplexa) in the eel (*Anguilla anguilla*). J. Eukaryot. Microbiol. 41, 215-222.

Beyer T.V., Sidorenko N.V., Svezhova N.V. (1995). Cell interaction with intracellular parasitism of cryptosporidia. I. The influence of *Cryptosporidium parvum* (Coccidia, Sporozoa) on phosphatase activity in the small intestine of experimentally infected new-born rats. Cytology 37, 829-837.

Beyer T.V., Svezhova N.V., Radchenko A.I., Sidorenko N.V. (2002). Parasitophorous vacuole: morphofunctional diversity in different coccidian genera (a short insight into the problem). Cell Biol. Int. 26, 861-871.

Beyer T.V., Svezhova N.V., Sidorenko N.V., Khokhlov S.E. (2000). *Cryptosporidium parvum* (Coccidia, Apicomplexa): Some new ultrastructural observations on its endogenous development. Eur. J. Protistol. 36, 151-159.

Bonnin A., Lapillonne A., Petrella T., Lopez J., Chaponnier C., Gabbiani G., Robine S., Dubremetz J.F. (1999). Immunodetection of the microvillous cytoskeleton molecules villin and ezrin in the parasitophorous vacuole wall of *Cryptosporidium parvum* (Protozoa: Apicomplexa). Eur. J. Cell. Biol. 78, 794-801.

Borowski H., Thompson R.C., Armstrong T., Clode P.L. (2010). Morphological characterization of *Cryptosporidium parvum* life-cycle stages in an in vitro model system. Parasitology 137, 13-26.

Brasil L. (1906). *Eleutheroschizon duboscqi*, sporozoaire nouveau parasite de *Scoloplos armiger* O.F. Müller. Arch. Zool. Exp. Gen. 4, 17-22.

Bull S., Chalmers R., Sturdee A.P., Curry A., Kennaugh J. (1998). Cross-reaction of an anti-*Cryptosporidium* monoclonal antibody with sporocysts of *Monocystis* species. Vet. Parasitol. 77, 195-197.

Butaeva F., Paskerova G., Entzeroth R. (2006). *Ditrypanocystis* sp. (Apicomplexa, Gregarinia, Selenidiidae): the mode of survival in the gut of *Enchytraeus albidus* (Annelida, Oligochaeta, Enchytraeidae) is close to that of the coccidian genus *Cryptosporidium*. Tsitologiia 48, 695-704.

Carreno R.A., Martin D.S., Barta J.R. (1999). *Cryptosporidium* is more closely related to the gregarines than to coccidia as shown by phylogenetic analysis of apicomplexan parasites inferred using small-subunit ribosomal RNA gene sequences. Parasitol. Res. 85, 899-904.

Caullery M., Mesnil F. (1898). Sur un Sporozoaire aberrant (*Siedleckia* n. g.). C. R. Soc. Biol. 5, 1093-1095.

Cavalier-Smith T. (2014). Gregarine site-heterogeneous 18S rDNA trees, revision of gregarine higher classification, and the evolutionary diversification of Sporozoa. Eur. J. Protistol. 50, 472-495.

Cavalier-Smith T., Chao E.E. (2004). Protalveolate phylogeny and systematics and the origins of Sporozoa and dinoflagellates (phylum Myzozoa nom. nov.). Eur. J. Protistol. 40, 185-212.

Chambouvet A., Valigurová A., Pinheiro L.M., Richards T.A., Jirků M. (2016). *Nematopsis temporariae* (Gregarinasina, Apicomplexa, Alveolata) is an intracellular infectious agent of tadpole livers. Environ. Microbiol. Rep. 8, 675-679.

Chatton E., Villeneuve F. (1936). Le cycle évolutif del'*Eleutheroschizon duboscqui* Brasil. Preuve expérimentale de l'absence de schizogonie chez cette forme et chez la *Siedleckia caulleryi* Ch. et Vill. C.R. Acad. Sci. 203, 833-836.

Chen X.M., Levine S.A., Tietz P., Krueger E., McNiven M.A., Jefferson D.M., Mahle M., LaRusso N.F. (1998). *Cryptosporidium parvum* is cytopathic for cultured human biliary epithelia via an apoptotic mechanism. Hepatology 28, 906-913.

Clode P.L., Koh W.H., Thompson R.C.A. (2015). Life without a host cell: What is *Cryptosporidium*? Trends Parasitol. 31, 614-624.

Collins R.L. (1972). In vitro maintenance of the trophonts and sporozoites of *Pyxinia crystalligera*. J. Protozool. 19, 355-362.

Cook T.J.P., Janovy J., Clopton R.E. (2001). Epimerite-host epithelium relationships among eugregarines parasitizing the damselflies *Enallagma civile* and *Ischnura verticalis*. J. Parasitol. 87, 988-996.

Cox F.E.G. (1994). The evolutionary expansion of the Sporozoa. Int. J. Parasitol. 24, 1301-1316.

Current W.L., Reese N.C. (1986). A comparison of endogenous development of three isolates of *Cryptosporidium* in suckling mice. J. Protozool. 33, 98-108.

Daher W., Soldati-Favre D. (2009). Mechanisms controlling glideosome function in apicomplexans. Curr. Opin. Microbiol. 12, 408-414.

Desportes I. (1967). Ultrastructure et évolution du sporozoite de *Stylocephalus africanus* Théodorids, Desportes et Jolivet, eugrégarine, Stylocephalidae. C.R. Acad. Sci. 265, 423-426.

Desportes I. (1969). Ultrastructure et développement des grégarines du genre *Stylocephalus*. Ann. Sci. Nat. Zool. 12, 31-96.

Desportes I., Schrével J. (2013). Treatise on zoology - Anatomy, taxonomy, biology. The gregarines (2 vols): The early branching Apicomplexa. Brill, Leiden, 796 pp.

Desportes I., Théodoridès J., Vivarès C. (1977). Association entre la grégarine *Porospora portunidarum* (Frenzel) et des bactéries intestinales de son hôte: *Carcinus mediterraneus* Czer. (Crustacé Décapode). Protistologica 13, 611-619.

Diakin A., Kováčiková M., Valigurová A. (2014). Oocysts and gametocyst morphology of extraordinary coelomic gregarine *Urospora travisiae* from marine polychaete. In: A variety of interactions in the marine environment. Abstracts volume from 49th European Marine Biology Symposium, Zoological Institute Russian Academy of Sciences, St. Petersburg, Russia, pp. 59-60.

Diakin A., Paskerova G.G., Simdyanov T.G., Aleoshin V.V., Valigurová A. (2016). Morphology and molecular phylogeny of coelomic gregarines (Apicomplexa) with different types of motility: *Urospora ovalis* and *U. travisiae* from the polychaete

Travisia forbesii. Protist 167, 279-301.

Diakin A., Valigurová A. (2014). Development of new agamococcidia *Rhytidocystis* sp. from *Travisia forbesii*. In: A variety of interactions in the marine environment. Abstracts volume from 49th European Marine Biology Symposium, Zoological Institute Russian Academy of Sciences, St. Petersburg, Russia, pp. 83-84.

Diakin A., Wakeman K.C., Valigurová A. (2017). Description of *Ganymedes yurii* sp n. (Ganymedidae), a new gregarine species from the Antarctic amphipod *Gondogeneia* sp. (Crustacea). J. Eukaryot. Microbiol. 64, 56-66.

Dubremetz J.F., Garcia-Reguet N., Conseil V., Fourmaux M.N. (1998). Apical organelles and host-cell invasion by Apicomplexa. Int. J. Parasitol. 28, 1007-1013.

Dyková I., Lom J. (1981). Fish coccidia: critical notes on life cycles, classification and pathogenicity. J. Fish Dis. 4, 487-505.

Eli A., Briyai O.F., Abowei J.F.N. (2012). A review of some parasite diseases of African fish gut lumen protozoa, coccidioses, *Cryptosporidium* infections, haemoprotozoa, haemosporidia. Res. J. Appl. Sci. Eng. Tech. 4, 1438-1447.

Forney J.R., DeWald D.B., Yang S.G., Speer C.A., Healey M.C. (1999). A role for host phosphoinositide 3-kinase and cytoskeletal remodeling during *Cryptosporidium parvum* infection. Infect. Immun. 67, 844-852.

Forney J.R., Vaughan D.K., Yang S.G., Healey M.C. (1998). Actin-dependent motility in *Cryptosporidium parvum* sporozoites. J. Parasitol. 84, 908-913.

Fowell R.R. (1936). The fibrillar structures of protozoa, with special reference to schizogregarines of the genus *Selenidium*. J. R. Microsc. Soc. 56, 12-28.

Frenal K., Polonais V., Marq J.B., Stratmann R., Limenitakis J., Soldati-Favre D. (2010). Functional dissection of the apicomplexan glideosome molecular architecture. Cell Host Microbe 8, 343-357.

Ghazali M., Philippe M., Deguercy A., Gounon P., Gallo J.M., Schrével J. (1989). Actin and spectrin-like (Mr=260-240 000) proteins in gregarines. Biol. Cell 67, 173-184.

Ghazali, M., Schrével, J. (1993). Myosin-like protein (M(r)175,000) in *Gregarina blaberae*. J. Eukaryot. Microbiol. 40, 345-354.

Harry O.G. (1970). Gregarines: their effect on the growth of the desert locust (*Schistocerca gregaria*). Nature 225, 964-966.

Heintzelman M.B. (2004). Actin and myosin in *Gregarina polymorpha*. Cell Motil. Cytoskeleton 58, 83-95.

Heintzelman M.B., Mateer M.J. (2008). GpMyoF, a WD40 repeat-containing myosin associated with the myonemes of *Gregarina polymorpha*. J. Parasitol. 94, 158-168.

Henry J.E., (1981). Natural and applied control of insects by protozoa. Annu. Rev. Entomol. 26, 49-73.

Hildebrand H.F. (1976). Elektronenmikroskopische Untersuchungen an den Entwicklungsstadien des Trophozoiten von *Didymophyes gigantea* (Sporozoa, Gregarinida). I. Die Feinstruktur des Proto- und Epimeriten und die Beziehung zwischen Wirt und Parasit. Z. Parasitenkd. 49, 193-215.

Jirků M., Valigurová A., Koudela B., Křížek J., Modrý D., Šlapeta J. (2008). New species of *Cryptosporidium* Tyzzer, 1907 (Apicomplexa) from amphibian host: morphology, biology and phylogeny. Folia Parasitol. 55, 81-94.

Kamm M.W. (1920). The development of gregarines and their relation to the host tissues: (III) in *Gregarina rigida* (Hall) Ellis. J. Parasitol. 7, 23-28.

King C., Sleep J. (2005). Modelling the mechanism of gregarine gliding using bead translocation. J. Eukaryot. Microbiol. 52, 7S-27S.

King C.A. (1981). Cell-surface interaction of the protozoan *Gregarina* with

concanavalin-a beads - implications for models of gregarine gliding. Cell Biol. Int. Rep. 5, 297-305.

King C.A. (1988). Cell motility of sporozoan protozoa. Parasitol. Today 4, 315-319.

Klingenberg C.P., Leigh R.H.B., Keddie B.A., Spence J.R. (1997). Influence of gut parasites on growth performance in the water strider *Gerris buenoi* (Hemiptera: Gerridae). Ecography 20, 29-36.

Koh W., Thompson A., Edwards H., Monis P., Clode P.L. (2014). Extracellular excystation and development of *Cryptosporidium*: tracing the fate of oocysts within *Pseudomonas aquatic* biofilm systems. BMC Microbiol. 14, 281.

Kováčiková M., Paskerova G.G., Diakin A., Valigurová A. (2017a). Cytoskeletal elements and motility in the archigregarine *Selenidium* sp.: observations on native and drug-treated parasites. In: 15th International Congress of Protistology: Book of Abstracts, Prague, Czech Republic, p. 113.

Kováčiková M., Simdyanov T.G., Diakin A., Valigurová A. (2017b). Structures related to attachment and motility in the marine eugregarine *Cephaloidophora* cf. *communis* (Apicomplexa). Eur. J. Protistol. 59, 1-13.

Kováčiková M., Vaškovicová N., Nebesářová J., Valigurová A. (2018). Effect of jasplakinolide and cytochalasin D on cortical elements involved in the gliding motility of the eugregarine *Gregarina garnhami* (Apicomplexa). Eur. J. Protistol. 66, 97-114.

Kváč M., Havrdová N., Hlásková L., Daňková T., Kanděra J., Ježková J., Vítovec J., Sak B., Ortega Y., Xiao L., Modrý D., Chelladurai J.R., Prantlová V., McEvoy J. (2016). *Cryptosporidium proliferans* n. sp. (Apicomplexa: Cryptosporidiidae): Molecular and biological evidence of cryptic species within gastric *Cryptosporidium* of mammals. PLoS One 11(1), e0147090.

Landers S.C. (2001). *Pterospora floridiensis*, a new species of acephaline gregarine (Apicomplexa) from the maldanid polychaete *Axiothella mucosa* in St. Andrew Bay, Florida. Syst. Parasitol. 48, 55-59.

Landsberg J.H., Paperna I. (1986). Ultrastructural study of the coccidian *Cryptosporidium* sp. from stomachs of juvenile cichlid fish. Dis. Aquat. Organ. 2, 13-20.

Larsson J.I.R. (1991). On the cytology and fine structure of the neogregarine *Syncystis aeshnae* Tuzet and Manier, 1953 (Apicomplexa, Syncystidae). J. Protozool. 38, 383-392.

Leander B.S. (2006). Ultrastructure of the archigregarine *Selenidium vivax* (Apicomplexa) - A dynamic parasite of sipunculid worms (host: *Phascolosoma agassizii*). Mar. Biol. Res. 2, 178-190.

Leander B.S. (2007). Molecular phylogeny and ultrastructure of *Selenidium serpulae* (Apicomplexa, Archigregarinia) from the calcareous tubeworm *Serpula vermicularis* (Annelida, Polychaeta, Sabellida). Zool. Scr. 36, 213-227.

Leander B.S. (2008). Marine gregarines: evolutionary prelude to the apicomplexan radiation? Trends Parasitol. 24, 60-67.

Leander B.S., Lloyd S.A.J., Marshall W., Landers S.C. (2006). Phylogeny of marine gregarines (Apicomplexa) - *Pterospora*, *Lithocystis* and *Lankesteria* - and the origin(s) of coelomic parasitism. Protist 157, 45-60.

Leander B.S., Ramey P.A. (2006). Cellular identity of a novel small subunit rDNA sequence clade of apicomplexans: Description of the marine parasite *Rhytidocystis polygordiae* n. sp. (Host: *Polygordius* sp., Polychaeta). J. Eukaryot. Microbiol. 53, 280-291.

Leitch G.J., He Q. (2012). Cryptosporidiosis - an overview. J. Biomed. Res. 25, 1-16.

Lipa J.J. (1967). Studies on gregarines (Gregarinomorpha) of arthropods in Poland. Acta Protozool. 5, 97-179.

Lucarotti C.J. (2000). Cytology of *Leidyana canadensis* (Apicomplexa: Eugregarinida) in *Lambdina fiscellaria fiscellaria* larvae (Lepidoptera: Geometridae). J. Invertebr. Pathol. 75, 117-125.

Lukeš J. (1992). Life cycle of *Goussia pannonica* (Molnar, 1989) (Apicomplexa, Eimeriorina), an extracytoplasmic coccidium from the white bream *Blicca bjoerkna*. J. Protozool. 39, 484-494.

Macgregor H.C., Thomasson P.A. (1965). The fine structure of two archigregarines, *Selenidium fallax* and *Ditrypanocystis cirratuli*. J. Protozool. 12, 438-443.

MacMillan W.G. (1973a). Conformational changes in the cortical region during peristaltic movements of a gregarine trophozoite. J. Protozool. 20, 267-274.

MacMillan W.G. (1973b). Gregarine attachment organelles - structure and permeability of an interspecific cell junction. Parasitology 66, 207-214.

Mazourová V. (2013). Cell motility in cryptosporidia (Apicomplexa). Bachelor's thesis (In Czech). Masaryk University, Brno.

Mazourová V. (2015). Cell motility and invasion in cryptosporidia (Apicomplexa). Master's thesis (In Czech). Masaryk University, Brno.

Mele R., Morales M.A.G., Tosini F., Pozio E. (2004). *Cryptosporidium parvum* at different developmental stages modulates host cell apoptosis in vitro. Infect. Immun. 72, 6061-6067.

Melicherová J., Hofmannová L., Valigurová A. (2018). Response of cell lines to actual and simulated inoculation with *Cryptosporidium proliferans*. Eur. J. Protistol. 62, 101-121.

Melicherová J., Ilgová J., Kváč M., Sak B., Koudela B., Valigurová A. (2014). Life cycle of *Cryptosporidium muris* in two rodents with different responses to parasitization. Parasitology 141, 287-303.

Melicherová J., Mazourová V., Valigurová A. (2016). In vitro excystation of *Cryptosporidium muris* oocysts and viability of released sporozoites in different incubation media. Parasitol. Res. 115, 1113-1121.

Mellor J.S., Stebbings H. (1980). Microtubules and the propagation of bending waves by the archigregarine, *Selenidium fallax*. J. Exp. Biol. 87, 149-161.

Miles H.B. (1966). The contractile system of the acephaline gregarine *Nematocystis magna*: Observations by electron microscope. Rev. Iber. Parasitol. 26, 361-368.

Miles H.B. (1968). The fine structure of the epicyte of the acephaline gregarines *Monocystis lumbriciolidi*, and *Nematocystis magna*: Observations by electron microscope. Rev. Iber. Parasitol. 28, 455-465.

Molnar K., Baska F. (1986). Light and electron microscopic studies on *Epieimeria anguillae* (Léger and Hollande, 1922), a coccidium parasitizing the European eel, *Anguilla anguilla* L. J. Fish Dis. 9, 99-110.

Morrison D.A. (2009). Evolution of the Apicomplexa: Where are we now? Trends Parasitol. 25, 375-382.

Morrissette N.S., Sibley L.D. (2002). Cytoskeleton of apicomplexan parasites. Microbiol. Mol. Biol. Rev. 66, 21-38.

Naville A. (1930). Recherches cytologiques sur les schizogrégarines. Z. Zellforsch. Mikrosk. Anat. 11, 375-396.

Nelson J.B., O'Hara S.P., Small A.J., Tietz P.S., Choudhury A.K., Pagano R.E., Chen X.M., LaRusso N.F. (2006). *Cryptosporidium parvum* infects human cholangiocytes via

sphingolipid-enriched membrane microdomains. Cell. Microbiol. 8, 1932-1945.

Nöller W. (1920). Kleine Beobachtungen an parasitischen Protozoen. Arch. Protistenkunde 41, 169-189.

O'Hara S.P., Huang B.Q., Chen X.M., Nelson J., LaRusso N.F. (2005). Distribution of *Cryptosporidium parvum* sporozoite apical organelles during attachment to and internalization by cultured biliary epithelial cells. J. Parasitol. 91, 995-999.

O'Hara S.P., Chen X.M. (2011). The cell biology of *Cryptosporidium* infection. Microbes Infect. 13, 721-730.

O'Hara S.P., Small A.J., Chen X.M., LaRusso N.F. (2008). Host cell actin remodeling in response to *Cryptosporidium*. Subcell. Biochem. 47, 92-100.

Okamoto N., Keeling P.J. (2014). The 3D structure of the apical complex and association with the flagellar apparatus revealed by serial TEM tomography in *Psammosa pacifica*, a distant relative of the Apicomplexa. PLoS One 9(1), e84653.

Ormieres R. (1977). *Pyxinia firmus* (Léger, 1892), Eugrégarine parasite du Coléoptère *Dermestes frischi* Kugel. Étude ultrastructurale. Z. Parasitenk. 53, 13-22.

Paperna I., Landsberg J.H. (1989). Description and taxonomic discussion of eimerian coccidia from African and Levantine geckoes. S. Afr. J. Zool. 24, 345-355.

Paperna I., Vilenkin M. (1996). Cryptosporidiosis in the gourami *Trichogaster leeri*: description of a new species and a proposal for a new genus, *Piscicryptosporidium*, for species infecting fish. Dis. Aquat. Organ. 27, 95-101.

Paskerova G.G., Miroliubova T.S., Diakin A., Kováčiková M., Valigurová A., Guillou L., Aleoshin V.V., Simdyanov T.G. (2018). Fine structure and molecular phylogenetic position of two marine gregarines, *Selenidium pygospionis* sp. n. and *S. pherusae* sp. n., with notes on the phylogeny of Archigregarinida (Apicomplexa). Protist 169, 826-852

Perkins F.O., Barta J.R., Clopton R.E., Peirce M.A., Upton S.J. (2000). Phylum Apicomplexa Levine, 1970, In: Lee J.J., Leedale G.F., Bradbury P. (Eds.) An illustrated guide to the Protozoa. Society of Protozoologists, Lawrence, Kansas, pp. 190-369.

Perkins M.E., Riojas Y.A., Wu T.W., Le Blancq S.M. (1999). CpABC, a *Cryptosporidium parvum* ATP-binding cassette protein at the host-parasite boundary in intracellular stages. Proc. Natl. Acad. Sci. USA 96, 5734-5739.

Philippe M., Fournet B., Caigneaux E., Schrével J. (1979). Les polysaccharides associés à la surface cellulaire d'une grégarine (protozoaire parasite). II. Caractérisation cytochimique et anal-yses biochimiques des ghosts. Biol. Cell. 35, 165-174.

Rueckert S., Leander B.S. (2009a). Molecular phylogeny and surface morphology of marine archigregarines (Apicomplexa), *Selenidium* spp., *Filipodium phascolosomae* n. sp., and *Platyproteum* n. g. and comb. from North-Eastern Pacific peanut worms (Sipuncula). J. Eukaryot. Microbiol. 56, 428-439.

Rueckert S., Leander B.S. (2009b). Phylogenetic position and description of *Rhytidocystis cyamus* sp. n. (Apicomplexa, Rhytidocystidae): a novel intestinal parasite of the north-eastern Pacific 'stink worm' (Polychaeta, Opheliidae, *Travisia pupa*). Mar. Biodivers. 39, 227.

Ryan U., Paparini A., Monis P., Hijjawi N. (2016). It's official - *Cryptosporidium* is a gregarine: What are the implications for the water industry? Water Res. 105, 305-313.

Santin M. (2013). Clinical and subclinical infections with *Cryptosporidium* in animals. N. Z. Vet. J. 61, 1-10.

Sheffield H.G., Garnham P.C., Shiroishi T. (1971). The fine structure of the sporozoite of *Lankesteria culicis*. J. Protozool. 18, 98-105.

Scholtyseck E. (1979). Fine structure of parasitic protozoa: an atlas of micrographs, drawings and diagrams. Springer-Verlag, Berlin-Heidelberg-New York, 206 pp.

Schrével J. (1968). L'ultrastructure de la région antérieure de la grégarine *Selenidium* et son intérêt pour l'étude de la nutrition chez les sporozoaires. J. Microscopy 7, 391-410.

Schrével J. (1971). Contribution a l'étude des Selenidiidae parasites d'annélides polychètes. II. Ultrastructure de quelques trophozoïtes. Protistologica 7, 101-130.

Schrével J. (1972). Polysaccharides of cell-surface of gregarines (Protozoa Parasites). 1. Ultrastructure and cytochemistry. J. Microscopy 15, 21-40.

Schrével J., Caigneaux E., Gros D., Philippe M. (1983). The three cortical membranes of the gregarines. I. Ultrastructural organization of *Gregarina blaberae*. J. Cell Sci. 61, 151-174.

Schrével J., Desportes I. (2016). Gregarines, In: Mehlhorn H. (Ed.) Encyclopedia of parasitology. Springer, Berlin, Heidelberg, pp. 1142-1188.

Schrével J., Philippe M. (1993). The gregarines, In: Kreier, J.P. (Ed.) Parasitic Protozoa. Academic Press, San Diego, pp. 133-245.

Schrével J., Valigurová A., Prensier G., Chambouvet A., Florent I., Guillou L. (2016). Ultrastructure of *Selenidium pendula*, the type species of archigregarines, and phylogenetic relations to other marine Apicomplexa. Protist 167, 339-368.

Schrével J., Vivier E. (1966). Etude au microscope électronique de la région antérieure des grégarines: le mucron de *Lecudina pellucida* (Koll.) Mingazzini et l'épimérite de *Sycia inopinata* Léger. Protistologica 2, 17-28.

Simdyanov T.G., Kuvardina O.N. (2007). Fine structure and putative feeding mechanism of the archigregarine *Selenidium orientale* (Apicomplexa: Gregarinomorpha). Eur. J. Protistol. 43, 17-25.

Simdyanov T.G., Paskerova G.G., Valigurová A., Diakin A., Kováčiková M., Schrével J., Guillou L., Dobrovolskij A.A., Aleoshin V.V. (2018). First ultrastructural and molecular phylogenetic evidence from the blastogregarines, an early branching lineage of plesiomorphic Apicomplexa. Protist 169, 697-726.

Stebbings H., Boe G.S., Garlick P.R. (1974). Microtubules and movement in the archigregarine, *Selenidium fallax*. Cell Tissue Res. 148, 331-345.

Stein B., Stover L., Gillem A., Winters K., Leet J.H., Chauret C. (2006). The effect of lectins on *Cryptosporidium parvum* oocyst in vitro attachment to host cells. J. Parasitol. 92, 1-9.

Sumner R. (1933). Influence of gregarines on growth in the mealworm. Science 78, 125.

Tanada Y., Kaya H.K. (1993). Insect pathology. Academic Press, San Diego, 666 pp.

Tardieux I., Baum J. (2016). Reassessing the mechanics of parasite motility and host-cell invasion. J. Cell. Biol. 214, 507-515.

Tatar G., Haziroglu R., Hascelik G. (1995). *Helicobacter felis* as a cofactor alone or together with stress in cryptosporidial activation in mice. J. Int. Med. Res. 23, 473-479.

Théodoridès J. (1984). The phylogeny of the Gregarinia (Sporozoa). Orig. Life Evol. Biospheres 13, 339-342.

Thompson R.C.A., Koh W.H., Clode P.L. (2016). *Cryptosporidium* - What is it? Food Waterborne Parasitol. 4, 54-61.

Tran J.Q., Li C., Chyan A., Chung L., Morrissette N.S. (2012). SPM1 Stabilizes

subpellicular microtubules in *Toxoplasma gondii*. Eukaryot. Cell 11, 206-216.

Tronchin G., Philippe M., Mocquard J.P., Schrével J. (1986). Cycle biologique de *Gregarina blaberae*: description, chronologie, étude de la croissance, influence du cycle de l'hôte, *Blaberus craniifer*. Protistologica 22, 127-142.

Tronchin G., Schrével J. (1977). Chronologie des modifications ultrastructurales au cours de la croissance de *Gregarina blaberae*. J. Protozool. 24, 67-82.

Tůmová L. (2019). Cultivation of cryptosporidia in cell and cell-free cultures. Master's thesis (In Czech). Masaryk University, Brno.

Tyzzer E.E. (1907). A sporozoan found in the peptic glands of the common mouse. Proc. Soc. Exp. Biol. Med. 5, 12-13.

Tzipori S., Griffiths J.K. (1998). Natural history and biology of *Cryptosporidium parvum*, Adv. Parasitol. 40, 5-36.

Uni S., Iseki M., Maekawa T., Moriya K., Takada S. (1987). Ultrastructure of *Cryptosporidium muris* (strain RN 66) parasitizing the murine stomach. Parasitol. Res. 74, 123-132.

Val-Bernal J.F., Mayorga M., Azueta A., Cabezas J., Lozano J.L., Fernández F. (2013). AIDS-related gastric cryptosporidiosis simulating malignancy. Rev. Esp. Patol. 46, 247-251.

Valigurová A. (2001). Eugregariny (Gregarina, Apicomplexa) niektorých bezchordátov Slovenska. Master's thesis (In Slovak). Comenius University, Bratislava.

Valigurová A. (2012). Sophisticated adaptations of *Gregarina cuneata* (Apicomplexa) feeding stages for epicellular parasitism. PLoS One 7(8), e42606.

Valigurová A., Florent I., Mazourová V., Melicherová J. (2014). Cell motility in sporozoites of *Cryptosporidium muris*. In: 5th International *Giardia* and *Cryptosporidium* Conference, Uppsala, Sweden, p. 186.

Valigurová A., Hofmannová L., Koudela B., Vávra J. (2007). An ultrastructural comparison of the attachment sites between *Gregarina steini* and *Cryptosporidium muris*. J. Eukaryot. Microbiol. 54, 495-510.

Valigurová A., Jirků M., Koudela B., Gelnar M., Modrý D., Šlapeta J. (2008). Cryptosporidia: Epicellular parasites embraced by the host cell membrane. Int. J. Parasitol. 38, 913-922.

Valigurová A., Koudela B. (2005). Fine structure of trophozoites of the gregarine *Leidyana ephestiae* (Apicomplexa: Eugregarinida) parasitic in *Ephestia kuehniella* larvae (Lepidoptera). Eur. J. Protistol. 41, 209-218.

Valigurová A., Koudela B. (2006). Ultrastructural study of developmental stages of *Mattesia dispora* (Neogregarinorida: Lipotrophidae), a parasite of the flour moth *Ephestia kuehniella* (Lepidoptera). Eur. J. Protistol. 42, 313-323.

Valigurová A., Koudela B. (2008). Morphological analysis of the cellular, interactions between the eugregarine *Gregarina garnhami* (Apicomplexa) and the epithelium of its host, the desert locust *Schistocerca gregaria*. Eur. J. Protistol. 44, 197-207.

Valigurová A., Michalková V., Koudela B. (2009). Eugregarine trophozoite detachment from the host epithelium via epimerite retraction: Fiction or fact? Int. J. Parasitol. 39, 1235-1242.

Valigurová A., Paskerova G.G., Diakin A., Kováčiková M., Simdyanov T.G. (2015). Protococcidian *Eleutheroschizon duboscqi*, an unusual apicomplexan interconnecting gregarines and cryptosporidia. PLoS One 10(4), e0125063.

Valigurová A., Pecková R., Doležal K., Sak B., Květoňová D., Kváč M., Nurcahyo W., Foitová I. (2018). Limitations in the screening of potentially anti-cryptosporidial

agents using laboratory rodents with gastric cryptosporidiosis. Folia Parasitol. 65, 010.

Valigurová A., Vaškovicová N., Diakin A., Paskerova G.G., Simdyanov T.G., Kováčiková M. (2017). Motility in blastogregarines (Apicomplexa): Native and drug-induced organisation of *Siedleckia nematoides* cytoskeletal elements. PLoS One 12(6), e0179709.

Valigurová A., Vaškovicová N., Musilová N., Schrével J. (2013). The enigma of eugregarine epicytic folds: where gliding motility originates? Front. Zool. 10, 57.

Vávra J., McLaughlin R.E. (1970). Fine Structure of some developmental stages of *Mattesia grandis* Mclaughlin (Sporozoa, Neogregarinida), a parasite of boll weevil *Anthonomus grandis* Boheman. J. Protozool. 17, 483-496.

Vávra J., Small E.B. (1969). Scanning electron microscopy of gregarines (Protozoa, Sporozoa) and its contribution to the theory of gregarine movement. J. Protozool. 16, 745-757.

Vetterling J.M., Takeuchi A., Madden P.A. (1971). Ultrastructure *of Cryptosporidium wrairi* from the guinea pig. J. Protozool. 18, 248-260.

Vivier E., Devauchelle G., Petitprez A., Porchet-Hennere E., Prensier G., Schrével J., Vinckier D. (1970). Observations on comparative cytology in sporozoans. 1. The sperficial structures in vegetative forms. Protistologica 6, 127-150.

Votýpka J., Modrý D., Oborník M., Šlapeta J., Lukeš J. (2017). Apicomplexa, In: Archibald J.M., Simpson A.G.B., Slamovits C.H. (Eds.) Handbook of the Protists. Springer International Publishing, Cham, pp. 567-624.

Wakeman K.C., Heintzelman M.B., Leander B.S. (2014). Comparative ultrastructure and molecular phylogeny of *Selenidium melongena* n. sp. and *S. terebellae* Ray 1930 demonstrate niche partitioning in marine gregarine parasites (Apicomplexa). Protist 165, 493-511.

Walker M.H., Lane N.J., Lee W.M. (1984). Freeze-fracture studies on the pellicle of the eugregarine, *Gregarina garnhami* (Eugregarinida, Protozoa). J. Ultrastr. Res. 88, 66-76.

Warner F.D. (1968). The fine structure of *Rhynchocystis pilosa* (Sporozoa, Eugregarinida). J. Protozool. 15, 59-73.

Weiser J. (1954). Schizogregariny z hmyzu škodícího zásobám mouky II. *Mattesia dispora* Naville 1930 a *Coelogregarina ephestiae* Gheleovitch 1947. Věstník československé zoologické společnosti 17, 73-90.

Wiest P.M., Johnson J.H., Flanigan T.P. (1993). Microtubule inhibitors block *Cryptosporidium parvum* infection of a human enterocyte cell line. Infect. Immun. 61, 4888-4890.

Yao L., Yin J., Zhang X., Liu Q., Li J., Chen L., Zhao Y., Gong P., Liu C. (2007). *Cryptosporidium parvum*: Identification of a new surface adhesion protein on sporozoite and oocyst by screening of a phage-display cDNA library. Exp. Parasitol. 115, 333-338.

Yoshikawa H., Iseki M. (1992). Freeze-fracture study of the site of attachment of *Cryptosporidium muris* in gastric glands. J. Protozool. 39, 539-544.

Žižka Z. (1977). Fine structure of the neogregarine *Farinocystis tribolii* Weiser, 1953. Developmental stages in sporogony and parasite-host relations. Z. Parasitenkd. 54, 217-228.

Žižka Z. (2005). Formation of a parasitophorous vacuole in a nonadequate experimental host: Electron microscopical and X-ray microanalytical study. Folia Microbiol. 50, 5-12.

7 List of publications included in the thesis

7.1 Valigurová A. (2012). Sophisticated adaptations of *Gregarina cuneata* (Apicomplexa) feeding stages for epicellular parasitism. PLoS One 7(8), e42606.

7.2 Valigurová A., Vaškovicová V., Musilová N., Schrével J. (2013). The enigma of eugregarine epicytic folds: where gliding motility originates? Frontiers in Zoology 10, 57.

7.3 Melicherová J., Ilgová J., Kváč M., Sak B., Koudela B., Valigurová A. (2014). Life cycle of *Cryptosporidium muris* in two rodents with different responses to parasitization. Parasitology 141(2), 287-303.

7.4 Valigurová A., Paskerova G.G., Diakin A., Kováčiková M., Simdyanov T.G. (2015). Protococcidian *Eleutheroschizon duboscqi*, an unusual apicomplexan interconnecting gregarines and cryptosporidia. PLoS One 10(4), e0125063.

7.5 Melicherová J., Mazourová V., Valigurová A. (2016). In vitro excystation of *Cryptosporidium muris* oocysts and viability of released sporozoites in different incubation media. Parasitology Research 115(3), 1113-1121.

7.6 Diakin A., Paskerova G.G., Simdyanov T.G., Aleoshin V.V., Valigurová A. (2016). Morphology and molecular phylogeny of coelomic gregarines (Apicomplexa) with different types of motility: *Urospora ovalis* and *U. travisiae* from the polychaete *Travisia forbesii*. Protist 167(3), 279-301.

7.7 Schrével J., Valigurová A., Prensier G., Chambouvet A., Florent I., Guillou L. (2016). Ultrastructure of *Selenidium pendula*, the type species of archigregarines, and phylogenetic relations to other marine Apicomplexa. Protist 167(4), 339-368.

7.8 Chambouvet A., Valigurová A., Pinheiro L.M., Richards T.A., Jirků M. (2016). *Nematopsis temporariae* (Gregarinasina, Apicomplexa, Alveolata) is an intracellular infectious agent of tadpole livers. Environmental Microbiology Reports 8(5), 675-679.

7.9 Diakin A., Wakeman K.C., Valigurová A. (2017). Description of *Ganymedes yurii* sp. n. (Ganymedidae), a new gregarine species from the Antarctic amphipod *Gondogeneia* sp. (Crustacea). Journal of Eukaryotic Microbiology 64(1), 56-66.

7.10 Kováčiková M., Simdyanov T.G., Diakin A., Valigurová A. (2017). Structures related to attachment and motility in the marine eugregarine *Cephaloidophora* cf. *communis* (Apicomplexa). European Journal of Protistology 59, 1-13.

7.11 Valigurová A., Vaškovicová N., Diakin A., Paskerova G.G., Simdyanov T.G., Kováčiková M. (2017). Motility in blastogregarines (Apicomplexa): Native and drug-induced organisation of *Siedleckia nematoides* cytoskeletal elements. PLoS One 12(6), e0179709.

7.12 Melicherová J., Hofmannová L., Valigurová A. (2018). Response of cell lines to actual and simulated inoculation with *Cryptosporidium proliferans*. European Journal of Protistology 62, 101-121.

7.13 Valigurová A., Pecková R., Doležal K., Sak B., Květoňová D., Kváč M., Nurcahyo W., Foitová I. (2018). Limitations in the screening of potentially anti-cryptosporidial agents using laboratory rodents with gastric cryptosporidiosis. Folia Parasitologica 65, 010.

7.14 Kováčiková M., Vaškovicová N., Nebesářová J., Valigurová A. (2018). Effect of jasplakinolide and cytochalasin D on cortical elements involved in the gliding motility of the eugregarine *Gregarina garnhami* (Apicomplexa). European Journal of Protistology 66, 97-114.

7.15 Simdyanov T.G., Paskerova G.G., Valigurová A., Diakin A., Kováčiková M., Schrével J., Guillou L., Dobrovolskij A.A., Aleoshin V.V. (2018). First ultrastructural and molecular phylogenetic evidence from the blastogregarines, an early branching lineage of plesiomorphic Apicomplexa. Protist 169(5), 697-726.

7.16 Paskerova G.G., Miroliubova T.S., Diakin A., Kováčiková M., Valigurová A., Guillou L., Aleoshin V.V., Simdyanov T.G. (2018). Fine structure and molecular phylogenetic position of two marine gregarines, *Selenidium pygospionis* sp. n. and *S. pherusae* sp. n., with notes on the phylogeny of Archigregarinida (Apicomplexa). Protist 169(6), 826-852.

8 Other publications related to the habilitation thesis

This list includes conference abstracts with results that are part of habilitation thesis, but have not yet been published in the form of research papers.

Diakin A., Valigurová A. (2014). Development of new species of agamococcidian *Rhytidocystis* sp. from *Travisia forbesii*. In: A variety of interactions in the marine environment. Abstracts volume from 49th European Marine Biology Symposium, Zoological Institute Russian Academy of Sciences, St. Petersburg, Russia, pp. 83-84.

Diakin A., Kováčiková, M., Valigurová A. (2014). Morphology of gametocyst, oocyst and sporozoites of extraordinary coelomic gregarine *Urospora travisiae* from marine polychaete. In: A variety of interactions in the marine environment. Abstracts volume from 49th European Marine Biology Symposium, Zoological Institute Russian Academy of Sciences, St. Petersburg, Russia, pp. 59-60.

Valigurová A., Florent I., Mazourová V., Melicherová J. (2014). Cell motility in sporozoites of *Cryptosporidium muris*. In: 5th International *Giardia* and *Cryptosporidium* Conference, Uppsala, Sweden, p. 186.

Kováčiková M., Paskerova G.G., Diakin A., Valigurová A. (2017). Cytoskeletal elements and motility in the archigregarine *Selenidium* sp.: observations on native and drug-treated parasites. In: 15th International Congress of Protistology: Book of Abstracts, Prague, Czech Republic, p. 113.

Valigurová A.

2012

Sophisticated adaptations of *Gregarina cuneata* (Apicomplexa) feeding stages for epicellular parasitism

PLoS One 7(8), e42606

PLOS ONE

Sophisticated Adaptations of *Gregarina cuneata* (Apicomplexa) Feeding Stages for Epicellular Parasitism

Andrea Valigurová*

Department of Botany and Zoology, Faculty of Science, Masaryk University, Brno, Czech Republic

Abstract

Background: Gregarines represent a very diverse group of early emerging apicomplexans, parasitising numerous invertebrates and urochordates, and are considered of little practical significance. Recently, they have gained more attention since some analyses showed that cryptosporidia are more closely related to the gregarines than to coccidia.

Methodology/Principal Findings: Using a combined microscopic approach, this study points out the spectacular strategy of *Gregarina cuneata* for attachment to host tissue and nutrient acquisition while parasitising the intestine of yellow mealworm larvae, and reveals the unusual dynamics of cellular interactions between the host epithelium and parasite feeding stages. Trophozoites of *G. cuneata* develop epicellularly, attached to the luminal side of the host epithelial cell by an epimerite exhibiting a high degree of morphological variability. The presence of contractile elements in the apical region of feeding stages indicates that trophozoite detachment from host tissue is an active process self-regulated by the parasite. A detailed discussion is provided on the possibility of reversible retraction and protraction of the eugregarine apical end, facilitating eventual reattachment to another host cell in better physiological conditions. The gamonts, found in contact with host tissue via a modified protomerite top, indicate further adaptation of parasite for nutrient acquisition via epicellular parasitism while keeping their host healthy. The presence of eugregarines in mealworm larvae even seems to increase the host growth rate and to reduce the death rate despite often heavy parasitisation.

Conclusions/Significance: Improved knowledge about the formation of host-parasite interactions in deep-branching apicomplexans, including gregarines, would offer significant insights into the fascinating biology and evolutionary strategy of Apicomplexa. Gregarines exhibit an enormous diversity in cell architecture and dimensions, depending on their parasitic strategy and the surrounding environment. They seem to be a perfect example of a coevolution between a group of parasites and their hosts.

Introduction

The alveolates (Alveolata), a major line of protists, include three extremely diverse groups of unicellular eukaryotes: ciliates, dinoflagellates and apicomplexans. Gregarines belong to the phylum Apicomplexa Levine, 1970, a large group characterised by the presence of a unique organelle called an apical complex, and which consists entirely of parasitic genera that infect a wide spectrum of invertebrates and vertebrates. Many of these are intensively studied etiologic agents of globally significant human disease, including malaria, toxoplasmosis and cryptosporidiosis. In contrast, gregarines are restricted to the internal organs and coelom of invertebrates and urochordates, and recently have been classified into three orders: Archigregarinorida Grassé, 1953; Eugregarinorida Léger, 1900; and Neogregarinorida Grassé, 1953 [1]. They are considered of no economic or medical significance and thus, despite their enormous diversity, the general biology of gregarines remains poorly understood. Recent phylogenetic

analyses, however, have pointed out their close affinity with *Cryptosporidium*, and have drawn attention to this enigmatic group [2,3].

Apicomplexans exhibit very specific adaptations for invading and surviving within their hosts, which have evolved under distinct evolutionary pressures, resulting in diverse attachment strategies and host-parasite interactions. In general, gregarines exhibit several known strategies for attachment to the host tissue: (i) intracellular or intratissular localisation with or without a reduced area of attachment in neogregarines; (ii) a mucron in archigregarines, monocystid eugregarines and some neogregarines; (iii) a simple epimerite in eugregarines and a few neogregarines; (iv) a complicated epimerite equipped with various structures, e.g. digitations, hooks or spines, hairs in eugregarines; (v) a sucker-like protomerite or modified protomerite with rhizoids in eugregarines. Eugregarines, similarly to cryptosporidia, are specific with their unique epicellular localisation [4,5,6,7,8]. Their sporozoites usually invade epithelial cells; however, some species

are able to invade even the intercellular space. As the majority of eugregarines do not exhibit intracellular development, sporozoites generally develop into large extracellular vegetative stages, called trophozoites, exhibiting a high degree of cell polarity in that they possess an anterior part specialised for attachment to the host cell in general [9]. In intestinal species, the development of the trophozoite starts after sporozoite interaction with the microvillus border of the host epithelium, when apical organelles disappear and an epimeritic bud derived from the conoid forms at the apical end [4,10]. The epimeritic bud gradually transforms into a specialised structure called the epimerite, which serves to anchor the parasite firmly to the host cell [4,8,10]. It is already known that epimerites of eugregarines parasitising herbivore hosts are usually simple button-shaped; however, they are much more complicated in carnivorous hosts, equipped with strong hooks, spines or numerous filaments [9].

The mechanism of nutrition acquisition in gregarines, however, is still poorly understood. Some authors attribute feeding function to the attachment organelles, such as the epimerite or mucron [9]. The higher concentration of host cell mitochondria and endoplasmic reticulum surrounding the epimerite, and the presence of mitochondria under the epimeritic cortical vesicle, indicate the existence of an active interaction between the gregarine epimerite and the host cell [11,12]. Furthermore, the presence of organelles associated with nutritive function suggests that the epimerite is a metabolically active organelle [13,14,15]. Some eugregarine species are equipped with additional structures located in the grooves between the epicytic folds covering the gregarine body, resembling the micropores (diminished cell mouth) reported in other apicomplexans [11,16,17]. Thus, questions arise as to whether and under what circumstances the epimerite serves as a feeding organelle, and whether the micropore-like structures in gregarines are points implicated in pinocytosis [18] or are exclusively dedicated to mucus extrusion [19]. Similarly, the exact mechanisms responsible for trophozoite attachment to the host cell and for abandoning the host tissue at the end of development still remain enigmatic. There are two contradictory hypotheses on gregarine detachment from host tissue at the end of the trophozoite stage. One of them describes trophozoite detachment via epimerite retraction, self-regulated by the vegetative stage [8], while the other is based on gradual epimerite constriction facilitated by the supposed contractility of an osmiophilic ring surrounding the base of the epimerite and acting as a sphincter during the separation of the epimerite from the rest of the gregarine body [9,10,20,21,22]. All of these questions raised by conflicting data must be satisfactorily answered to clarify the parasitic strategies of gregarines and to better understand the evolutionary history of the phylum Apicomplexa.

This study endeavours to address the questions set out above and aims provide a new insight into the dynamics and architecture of the attachment site of *G. cuneata*. Unique relationships with the host epithelium, not only in trophozoites but also in more advanced developmental stages including gamonts, are described herein. Though there are few published works dealing with the life cycle and host specificity of *G. cuneata* [23,24,25], complete data on its early development and host-parasite interactions at the cellular level are still lacking. Based on personal observations of four eugregarine species (*Gregarina cuneata*, *G. polymorpha*, *G. steini* and *G. niphandrodes*) parasitising the yellow mealworm beetle *Tenebrio molitor*, in many aspects, *G. cuneata* appears to be the most spectacular of them all. Conclusions are supported by identification and detailed descriptions of structures involved in the formation of host-parasite interactions using a combined microscopic approach.

Materials and Methods

Larvae of the yellow mealworm, *Tenebrio molitor* Linnaeus, 1758 (Coleoptera, Tenebrionidae) with eugregarine infection were obtained from colonies maintained in our laboratory. Gametocysts of *Gregarina cuneata* were collected from the faeces of infected larvae and placed in moist chambers at 25°C for maturation and dehiscence. Larvae sterilised of eugregarines were allowed to feed for 24 h on flour contaminated with the oocysts of *G. cuneata*, and were subsequently maintained on a sterile substrate. Insects were anesthetised with cold and dissected at different time points after feeding with eugregarine oocysts. Squash and/or wet smear preparations were investigated with the use of an Olympus BX51 light microscope.

For observations on living gregarines, different solutions, including phosphate buffered saline, Insect Ringer's solution or Minimum Essential Medium [3% bovine foetal serum with penicillin, streptomycin, amphotericin B and L-glutamine], were used to prepare squash preparations.

Transmission electron microscopy

Parasitised intestines were fixed overnight at 4°C in freshly prepared 2.78% glutaraldehyde in 0.2 M phosphate buffer for transmission electron microscopy. The specimens were then washed for 1 h in phosphate buffer (pH 7.0), post-fixed in 1% osmium tetroxide in the same buffer for 3 h and dehydrated in an alcohol series, before embedding in Epon (Polybed 812). Sections were cut with glass knives and stained with uranyl acetate and lead citrate. Procedures for freeze etching follow Schrevel et al. [26] using the BAL-TEC BAF 060 freeze-etching system. Observations were made using a JEOL 1010 TEM.

Scanning electron microscopy

Specimens were fixed overnight at 4°C in freshly prepared 3% glutaraldehyde in 0.2 M cacodylate buffer (pH 7.4), washed 3×15 min in cacodylate buffer, post-fixed in 2% osmium tetroxide in cacodylate buffer (pH 7.4) for 2 h at room temperature and finally washed 3×15 min in the same buffer. After dehydration in a graded series of acetone, specimens were critical point-dried using CO_2, coated with gold and examined using a JEOL JSM-7401F field emission scanning microscope.

Fluorescence microscopy

The *G. cuneata* cell suspension was washed in 0.2 M phosphate buffered saline (PBS), fixed for 15 min at room temperature in 4% paraformaldehyde in 0.2 M PBS, washed again, and permeabilised for 10 min in 0.1% Triton X-100 (Sigma-Aldrich). For direct fluorescence, samples were washed for 2 h in the antibody diluent (0.1% bovine serum albumin, 0.5% Triton X-100 and 0.1% sodium azide in 0.1 M PBS), incubated for 2 h at room temperature with fluorescein isothiocyanate (FITC)-phalloidin (Sigma-Aldrich) and then washed again in antibody diluent. Preparations were mounted in anti-fade mounting medium based on 2.5% DABCO (Sigma-Aldrich) mixed with glycerol and 0.1 M PBS. For indirect immunofluorescence, samples were incubated for 2 h at room temperature in rabbit anti-myosin antibody (smooth and skeletal, whole antiserum from Sigma-Aldrich; dilution 1:5) or in mouse monoclonal IgG anti-actin antibody raised against *Dictyostelium* actin that recognises *Toxoplasma* and *Plasmodium* actin (provided by Prof. Dominique Soldati-Favre) diluted in PBS with 0.1% BSA (dilution 1:500), washed three times in PBS for 10 min and incubated with FITC-conjugated anti-rabbit IgG (dilution 1:40) or anti-mouse polyvalent immunoglobulins (1:125) in PBS with 1% BSA at 37°C for 1 h. After washing

in PBS, preparations were counterstained with Evans blue (1:5000) and mounted. Controls were labelled with FITC-conjugated secondary antibody alone without the primary antibody. Preparations were observed and documented using an Olympus BX60 fluorescence microscope fitted with a WB filter cube, a fully motorized inverse epi-fluorescence microscope Olympus IX 81 equipped with Cell^R imaging station or an Olympus IX80 microscope equipped with a laser-scanning FluoView 500 confocal unit (Olympus FluoView 4.3 software).

Results

Feeding stages of Gregarina cuneata under light microscopy

All vegetative stages of *Gregarina cuneata* exhibited epicellular development, i.e. sporozoites and trophozoites developed attached to microvillous sites of host epithelial cells; no developmental stage was observed penetrating under the host cell plasma membrane. When observed under the light microscope, it was difficult or even impossible to detect the earliest stages, such as sporozoites transforming into the trophozoites, and very young two-segmented trophozoites. These stages were small and inconspicuous (Figure 1A), and seemingly it was quite impossible to detach them from the host tissue without any damage. The only observed earliest trophozoite stages exhibited an irregular triangular shape, tapering towards their apical part with a polymorphous epimerite (Figure 1A - upper micrographs). The irregular shape of epimerites, as shown in these micrographs, seemed to be the consequence of mechanical damage due to the forced separation of the gregarine from the host epithelium during the processing of squash preparations. Three-segmented stages were irregularly shaped, with a cylindrical deutomerite widest at its posterior rounded end (Figure 1A - lower micrographs). Only few maturing detached trophozoites, with an apparently non-damaged epimerite still located on a relatively short protomerite and typical cylindrical deutomerite, were observed in squash preparations (Figure 1B). Their epimerites were usually conical to lance-shaped or prolonged of irregular shape. More often, however, were trophozoites released from the host epithelium and still bearing the affected host cell on their epimerites (Figure 1C) or trophozoites with ruptured epimerites (Figure 1D). The most frequently observed stages were small-sized hyaline gamont-like individuals (in size comparable to trophozoites) typical by a cylindrical protomerite, which was constricted at the septum and widely rounded at its apical top, and a prolonged cylindrical deutomerite widest at the posterior end (Figure 1E). These stages lacked an obvious epimerite. Gamonts of *G. cuneata* formed so-called early syzygies and thus only few non-associated gamonts could be found. This means that mature individuals transforming into gamonts (satellites) joined to individuals still attached to the host cell (future primites). Living (non-fixed) gamonts, either single or associated in syzygies, exhibited a prolonged cylindrical protomerite with a widely rounded top and cylindrical deutomerite (Figures 1F - left micrograph, 1G). The protomerite of paraformaldehyde fixed primites or single gamonts, however, showed a lance-shape hyaline apical top (Figures 1F - right micrograph, 1H). Light microscopic observations confirmed that the number of amylopectin granules increased with the age of the trophozoites and the cytoplasm of mature gamonts was fully packed with amylopectin, except in the region of the lance-shaped protomerite top in gamonts (Figures 1A–H).

Localisation of actin and myosin

The homogenous distribution of the fluorescence signal throughout the surface of FITC-phalloidin labelled trophozoites and gamonts (Figure 1I) corresponded to the localisation of filamentous actin (F-actin) associated with the typical apicomplexan cell cortex. Labelling also confirmed the presence of F-actin in the peripheral region of growing epimerites. In all individuals, the fluorescence signal was more evident in the area of fibrillar septum separating the protomerite from the deutomerite. In addition, a large circular area in the deutomerite, suggestive of a nucleus, exhibited a more intense signal. In maturing single gamonts, the cytoplasm of protomerite exhibited more evident labelling of F-actin than that of deutomerite (Figure 1I), and it corresponded to the dot-like pattern of actin labelling restricted to the protomerite cytoplasm in individuals stained with the specific anti-actin antibody (proved to recognize the actin in *Toxoplasma* and *Plasmodium*) (Figure 1J). In comparison with the phalloidin-stained specimens, however, the gregarine cell cortex and septum exhibited only slight labelling of actin when stained with this antibody (Figure 1J).

Indirect immunofluorescence using rabbit anti-myosin antibody revealed the presence of myosin restricted to the epimerite region in trophozoites (Figure 1K) as well as to the gregarine cell cortex in trophozoites and gamonts (Figures 1K–L, 1N). In contrast to F-actin, no specific labelling of myosin corresponding to the septum was observed (Figures 1K–N). The intense fluorescence signal observed in the area of the obviously uneven protomerite top of some individuals lacking the epimerite most likely corresponded to a labelling of myosin in host tissue remnants covering the protomerite surface (Figures 1L–N). In addition, the intensely labelled apical end of the protomerite in some individuals seemed to be protracted or slightly retracted with an attached fragment of the host epithelium (Figure 1M). These data suggest that, in *G. cuneata*, more advanced stages than trophozoites remained in close contact with the host epithelium and detailed electron microscopic observations described below confirmed this assumption. In addition, some of the primites exhibited distinct circumscribed circular accumulation of myosin restricted to the periphery at the base of their lance-shaped protomerite top (Figure 1N). This structure might be related to the gamont feeding and/or attachment, however, its exact functions remains unclear as no comparable structure was observed under transmission electron microscope.

Fine structure of feeding stages and their interactions with the host epithelium

After entering the host intestine, invasive stages (sporozoites) excysted from the oocyst and invaded the host epithelium. During the invasion process, a slender sporozoite, tapering towards its posterior end, attached to the host cell plasma membrane via its apical part (Figure 2A) and, subsequently, the development of electron-lucent epimeritic bud started (Figures 2B–E, 2G). The apical cytoplasm of the invading parasite was packed with numerous electron-dense micronemes (Figures 2E–F) and a more or less translucent rhoptry-like organelle, passing through a conoid, that seemed to empty its contents at this stage (Figures 2D–E, 2G). In the course of transformation into a trophozoite, the sporozoite enlarged and attained a more round shape, and the epimeritic bud developed into an epimerite, gradually implanting into the host epithelial cell (Figures 2H–K).

The early trophozoite was attached to the host cell via an irregularly shaped epimerite, with its protodeutomerite hanging free into the intestinal lumen, and developed surrounded by host cell microvilli (Figures 2H–K). The irregularly shaped epimerite
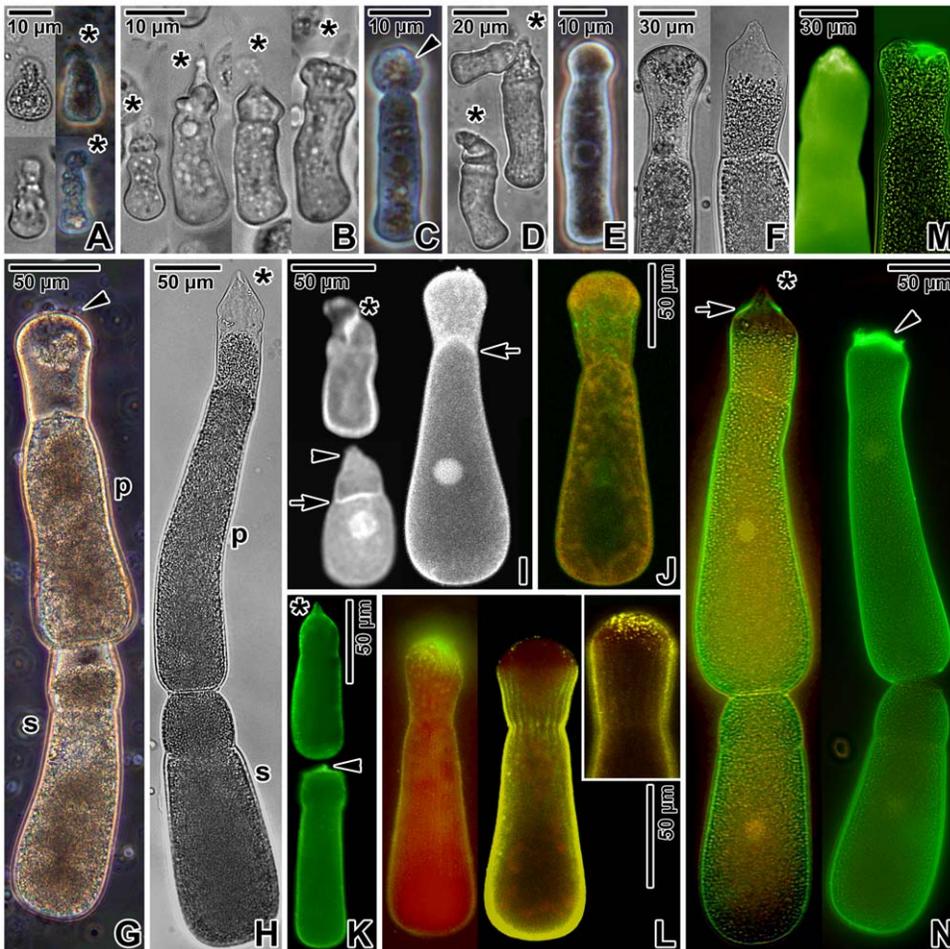
Figure 1. Early development of *Gregarina cuneata* observed using a light microscope. A. Earliest stages of trophozoites with developed epimerites (asterisks) under transmission light (left) and in phase contrast (right). **B.** Early trophozoites with polymorphous epimerites (asterisks). Transmission light. **C.** Detached maturing trophozoite with an epimerite surrounded by the host cell (arrowhead). Phase contrast. **D.** Three maturing trophozoites exhibiting obvious injury to their epimerites (asterisks) after forced separation from the host tissue by specimen processing. Transmission light. **E.** Maturing two-segmented individual exhibiting a well-developed protomerite and a cylindrical deutomerite. Note the rounded top of the protomerite lacking an epimerite. Phase contrast. **F.** Detailed view of the rounded protomerite top of a living gamont (left) and of the lance-shaped protomerite top of a chemically fixed gamont (right). Transmission light. **G.** Living gamonts associated in syzygy; primite (p), satellite (s). Note the rounded top of the primite protomerite with some remnants of the host tissue (arrowhead). Phase contrast. **H.** Chemically fixed gamonts associated in syzygy; lance-shaped top of the primite protomerite (asterisk), primite (p), satellite (s). **I.** Localisation of F-actin in early trophozoites (left) and maturing gamont (right); epimerite (asterisk), ruptured epimerite (arrowhead), septum (arrows) separating the protomerite from the deutomerite. Note that the septum (arrow) in the gamont is bulging into the protomerite. Direct fluorescence. **J.** Localisation of actin in maturing gamont. Note the patchy accumulation of actin with a very intense signal (green) in the protomerite cytoplasm. Immunofluorescence, counterstained with Evans blue. **K.** Localisation of myosin in trophozoites; epimerite (asterisk), ruptured epimerite (arrowhead). Immunofluorescence. **L.** Localisation of myosin in maturing individuals. The top of the protomerite exhibits more (left) or less (right) intense labelling, suggesting the presence of host tissue fragments. The *inset* shows the protomerite of more advanced stage of maturing gamont. Immunofluorescence, counterstained with Evans blue. **M.** Localisation of myosin in single maturing gamonts after detachment from host epithelium. The protracted (left) and retracted (right) protomerite tops exhibit strong labelling, suggesting the presence of host tissue fragments. Immunofluorescence; fluorescence and combination of fluorescence with transmission light. **N.** Localisation of myosin in mature gamonts associated in syzygies. Note the primite (left) with a lance-shaped top of the protomerite (asterisk) exhibiting distinct labelling in the peripheral area at its base (arrow) as well as the primite (right) with fragments of the host tissue covering its protomerite top (arrowhead). Immunofluorescence; combination of fluorescence with transmission light.
doi:10.1371/journal.pone.0042606.g001

was still increasing in its size and was overlain by an indistinct cortical vesicle. The membrane-like structure, limiting the cortical vesicle on its cytoplasmic face, was discontinuous and often not apparent (Figures 2H–K). A few mitochondria were observed in the cytoplasm just beneath the epimeritic cortical vesicle (Figure 2H). The interface between the epimerite and the host cell was trilaminate, consisting of the epimerite and host plasma membranes with an intercellular space in between them. In some individuals, the epimerite plasma membrane covering the cortical

vesicle formed numerous digitations and rhizoids (Figure 2I). The gradually expanding epimerite in the young trophozoite was very rich in endoplasmic reticulum connected to the nuclear envelope and often seen to be associated with the cortical vesicle covering the epimerite (Figures 2J–K). In addition, an apically located structure of unknown origin and function could be found close to (or in contact with) the cortical vesicle in some maturing trophozoites (Figure 2K). Considering its appearance and apical localisation, this structure could correspond to the residuum of the
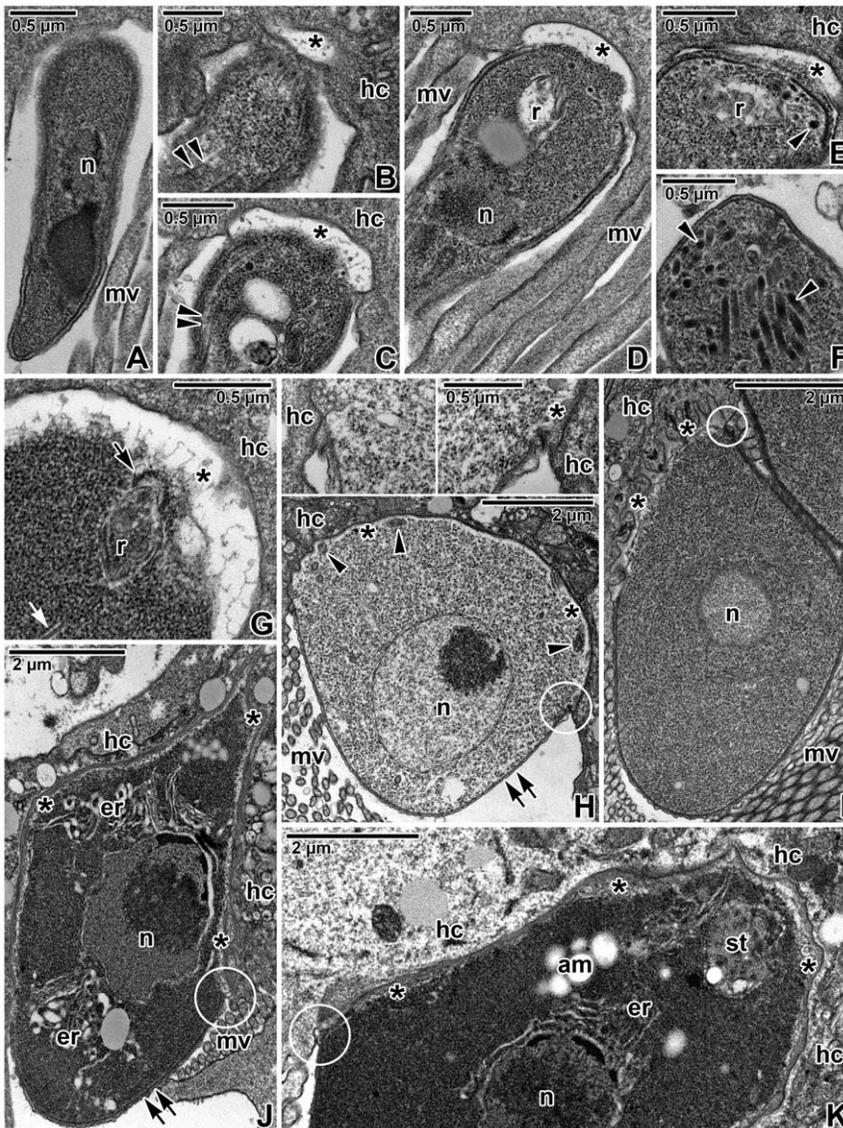
Figure 2. Early development of *Gregarina cuneata* observed using a transmission electron microscope. A. Invading sporozoite; host cell microvilli (mv), sporozoite nucleus (n). **B–G.** Sporozoite transforming into the trophozoite stage; conoid (arrow), developing epimeritic bud (asterisks), host cell (hc), host cell microvilli (mv), micronemes (arrowheads), microtubule (white arrow), nucleus (n), rhoptry-like organelle (r), subpellicular microtubules (double arrowheads). **H.** Early trophozoite stage. Note the anterior part of the gregarine, covered by a developing cortical vesicle (asterisks), causing an invagination of the host cell (hc) plasma membrane; host cell microvilli (mv), membrane fusion site (in circle), mitochondria (arrowheads), nucleus (n), pellicle (double arrow). Insets show details of the membrane fusion sites. **I.** Early trophozoite. Note the folded plasma membrane covering the cortical vesicle (asterisks) and forming numerous digitations; host cell (hc), host cell microvilli (mv), membrane fusion site (in circle), nucleus (n). **J.** Developing trophozoite; cortical vesicle (asterisks), endoplasmic reticulum (er), host cell (hc), host cell microvilli (mv), membrane fusion site (in circle), nucleus (n), pellicle with raising epicytic folds (double arrow). **K.** The apical end of another maturing trophozoite; amylopectin granules (am), cortical vesicle (asterisks), endoplasmic reticulum (er), host cell (hc), membrane fusion site (in circle), nucleus (n), unknown structure (st).

doi:10.1371/journal.pone.0042606.g002

rhoptry-like organelle described above in the invading stages. The trophozoite was covered by a classical apicomplexan pellicle, consisting of a plasma membrane and an inner membrane complex, organised in raising longitudinal epicytic folds (Figures 2I–J). This three-layered pellicle, however, extended only to the protomerite top, at which point the inner membrane complex ceased and only the plasma membrane covered the embedded epimerite. The membrane fusion site between the epimerite plasma membrane, host cell plasma membrane and the

membrane-like structure limiting the cortical vesicle was inconspicuous (Figures 2H–K).

During trophozoite maturation, a thin septum developed and separated the protomerite from the deutomerite, retaining the large nucleus (Figure 3A). The epimerite appeared as an apical extension of the protomerite, growing through the host cell and interwoven with its plasma membrane, and overlain by an indistinct cortical vesicle (Figures 3A–B). The cytoplasm of the protomerite possessed numerous inclusions, including amylopectin granules. The cytoplasmic area interconnecting the epimerite and

protomerite contained numerous membrane cisternae and vesicles (Figure 3B). In the course of trophozoite maturation, the epimerite seemed to decrease and the host cell and epimerite plasma membranes previously forming the trilaminate interface became indistinguishable from each other (Figures 3C–E). At this stage of gregarine epicellular development, the affected host cell exhibited some degree of vacuolation and in some sections cellular disorganisation (Figures 3C–E, 3I). The epimerite was irregularly embedded into the host cell (or in close contact with it), and formed numerous rhizoids or digitations of variable size and shape. The cytoplasm of these epimerite digitations appeared translucent, filled with numerous fine filamentous structures and mitochondria-like organelles underlying the cortical vesicle. The membrane fusion site, though not so prominent as in other eugregarines parasitising mealworms, was still visible (Figures 3C–E, 3I) and the freeze-etching technique revealed further details of its typical architecture (Figures 3F–H). According to the results of ultrathin sectioning, the border between the epimeritic cortical vesicle and the host cell was formed by the epimerite plasma membrane and the invaginated host plasma membrane, the second one of which was continuous with the plasma membrane covering surrounding microvilli. The parasite plasma membrane covering the epimerite was continuous with plasma membrane of the protomerite (Figure 3G). Similarly to the observations of ultrathin sections of mature trophozoites, epimerite and host cell plasma membranes were difficult to be distinguished from each other. The so-called 'membrane-like structure' limiting the cortical vesicle on its cytoplasmic face appeared as a membrane that was discontinuous in some areas, but often better visible than in ultrathin sections (Figures 3F–G). Nevertheless, it still remains unclear whether this membranous structure beneath the cortical vesicle was directly linked to the membrane fusion site or not (Figures 3G–H). Longitudinally oriented epicytic folds were a feature of both the trophozoite (Figure 3A) and gamont (e.g. Figure 4A) stages. In the course of trophozoite development, the decrease of epimerite proceeded and its detachment from host epithelium initiated. The protomerite top of individuals transforming from a trophozoite into a gamont exhibited an uneven surface with short rhizoid-like structures irregularly attached to the host tissue (Figure 3I) and thus resembling a retracted epimerite. The contact with the intestinal epithelium, however, was partially discontinuous, at least when observed in ultrathin sections.

Older stages, considered to be single maturing gamonts or primites, exhibited protomerites with broad lance-shaped apical ends (Figures 4A–D), similar to the light microscopic observations on chemically fixed parasites (Figures 1F, 1H, 1N), and usually in contact with host tissue. Less often, the protomerite top, contacting host microvilli, appeared widely rounded (Figures 4G–H). The apical end of the protomerite, regardless of its shape, was covered by a trilaminate pellicle lacking the typical organisation into longitudinal epicytic folds (Figures 4A–I). Under the scanning electron microscope, the cylindrical protomerite reached its maximum width at the interface between the apical part covered by a smooth pellicle and the posterior part with a pellicle organised into longitudinal epicytic folds (Figure 4H). The outer surface of the widely rounded protomerite top was wrinkled, bearing numerous non-specified globules of different size (Figures 4E–F). The localization and size of these globules corresponded to the myosin labelling of host tissue remnants still attached to the protomerite surface (as shown in Figure 1L). Many of the gamonts processed for scanning electron microscopy exhibited serious injury on the apical part of the protomerite (Figure 4E), often bearing scraps of host tissue (Figures 4H–I).

Detailed ultrastructural analysis of protomerite top found in close contact with host tissue revealed its unusual organisation, most likely dedicated to parasite food intake (Figures 5A–H). The contact of the gamont protomerite with host tissue was uneven, lacking any continuous intimate connection between the host cell and parasite plasma membranes (Figures 5B–E); more often, the protomerite top touched the host microvilli (Figure 5A). The apical end of the protomerite was covered by a smooth trilaminate pellicle, not organised in epicytic folds, with irregularly distributed pore-like structures (Figures 5C–E, 5H). In some sections, the protomerite top even showed a more undulated pattern (Figure 5G). Using higher magnification, a dense layer with non-membranous character, resembling the internal lamina usually underlining eugregarine epicytic folds, could be seen underlying the inner membrane complex at its cytoplasmic face (Figures 5D–E, 5H). The pore-like structures interrupting the inner membrane complex were more concentrated in some areas. In addition, structures similar to dense bodies, in some sections already half-emptied, could be seen in connection with them (Figures 5C–D). Unusual duct-like structures of unknown function could be found in the protomerite apical cytoplasm; usually, they were linked to the dense layer and in some sections their connection to abovementioned pore-like structures could be seen (Figure 5C). When observed under higher magnification, these structures appeared as elongated dense sacs passing through the inner membrane complex and plasma membrane and opening outwards (Figures 5E, 5H). The protomerite cytoplasm was packed with dense bodies, various vesicles and an abundant Golgi apparatus (Figure 5F).

Although the ultrastructural analysis revealed localized, mild pathological changes of the parasitised epithelium (usually limited to the affected cell), they seemed to be of minimal or no clinical significance. Despite often heavy infestation by *G. cuneata* in the host mid-gut, the experimentally infected larvae exhibited no obvious signs of sickness that could be considered to correlate with the progress of parasitisation. Parasitised larvae did not show any behavioural changes, weight loss or decreased food intake. In fact, the presence of eugregarines (regardless of eugregarine species) in experimentally as well as naturally infected mealworm larvae even seemed to increase the host growth rate and to reduce the death rate, and these larvae appeared to be more aggressive and agile in comparison to the gregarine-free individuals.

Discussion

The observations on early development of *Gregarina cuneata* generally support previously published data on another eugregarines [4,6,7,8]. Although *G. cuneata* trophozoites possess epimerite that slightly differs from those reported in other eugregarines parasitising mealworms, they also develop epicellularly and exhibit the same stages during their life cycle. Nevertheless, the later developmental stages exhibit more advanced adaptations to the epicellular parasitism and to the nutrient acquisition in intestinal environment, and details of these will be discussed below.

Eugregarine attachment to host tissue

It has been determined that mesenteric epithelial cells are short-lived, living only four days in *T. molitor* [27]. The destiny of trophozoites with their epimerites still embedded in degenerating epithelial cells, often observed in insect hosts, is still unknown. Harry [28] described trophozoite detachment from the host tissue as a random and passive process at any stage of its development, depending on the degeneration of epithelial cells and their extrusion under the pressure of replacement cells. He referred to
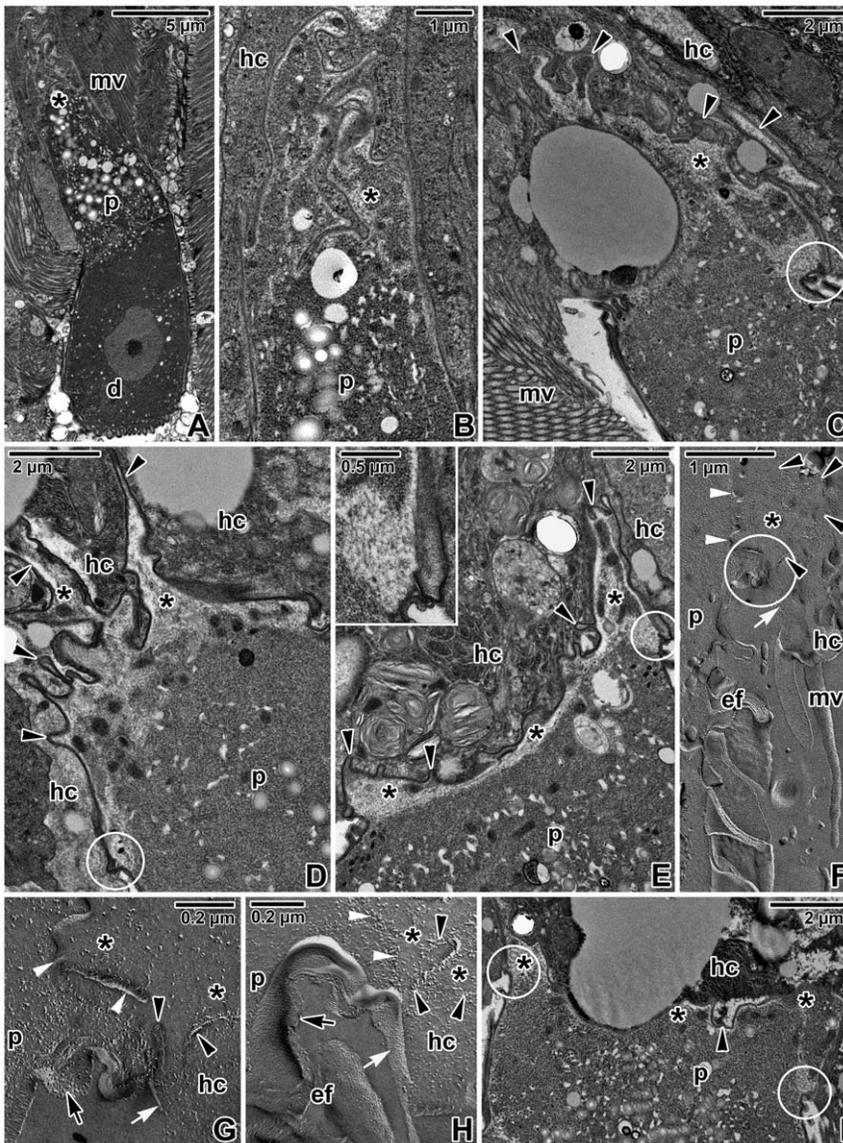
Figure 3. Trophozoites of *Gregarina cuneata* observed using a transmission electron microscope. A. Trophozoite with a well-developed epimerite (asterisk); deutomerite (d) with a nucleus, host cell microvilli (mv), protomerite (p). **B.** A more detailed view of the epimerite (asterisk) shown in Fig. 3A; host cell (hc), protomerite (p) cytoplasm packed with numerous inclusions. **C–E.** Decreasing epimerite (asterisks) forming numerous rhizoids and digitations (arrowheads) in more advanced stages of trophozoites as observed in different planes of sectioning; host cell (hc), host cell microvilli (mv), membrane fusion site (in circle), protomerite (p). The *inset* in Fig. 3E shows the membrane fusion site in detail. **F–H.** Host cell-epimerite interactions visualised by a freeze-etching technique. Fig. 3G shows a more detailed view of the membrane fusion site (in circle) from Fig. 3F. Note the border (arrowheads) between the epimerite and host cell (hc); cortical vesicle (asterisks), epicytic folds (ef) of the protomerite region (p), host cell microvilli (mv), host cell plasma membrane (white arrow), membrane-like structure limiting the cortical vesicle on its cytoplasmic face (white arrowheads), parasite plasma membrane (arrow). **I.** Trophozoite exhibiting a quite completely decreased epimerite (asterisks) with numerous mitochondria and gradual detachment (arrowhead) from host cell (hc), membrane fusion sites (in circles), protomerite (p).
doi:10.1371/journal.pone.0042606.g003

detached trophozoites still possessing epimerites observed in histological sections. On the contrary, recently published data [8,11] revealed that epimerite detachment is an active process, and thus trophozoites most likely detach and search for a new host cell in better physiological conditions. Insofar as the vegetative phase of the eugregarine life cycle usually lasts longer than four days [6,29], trophozoites must be adapted either to keeping the host cell alive during their development or for eventual reattachment to another cell. Therefore, Lucarotti [11] speculated about hypothetical reattachment of *Leidyana* trophozoites to younger cells after abandoning senescing cells, facilitated by a retractable epimerite

and eugregarine gliding motility. The presence of contractile elements in the area of the epimerite [20,21] and protomerite top [30,31] serves as a more convincing argument in favour of the structural dynamics of these cell regions and epimerite retraction theory [8,11]. Similarly, actin-like filaments demonstrated in the mucron of lecudinid eugregarine are considered to facilitate its adhesion to the host cell [20,32]. As the parasite's fixation to host tissue might be of a temporary nature, the contact between the host cell and parasite attachment organelle must be very loose. Studies on attachment strategies of several eugregarines [4,6,7,8,10,24] support this hypothesis in that they showed that,
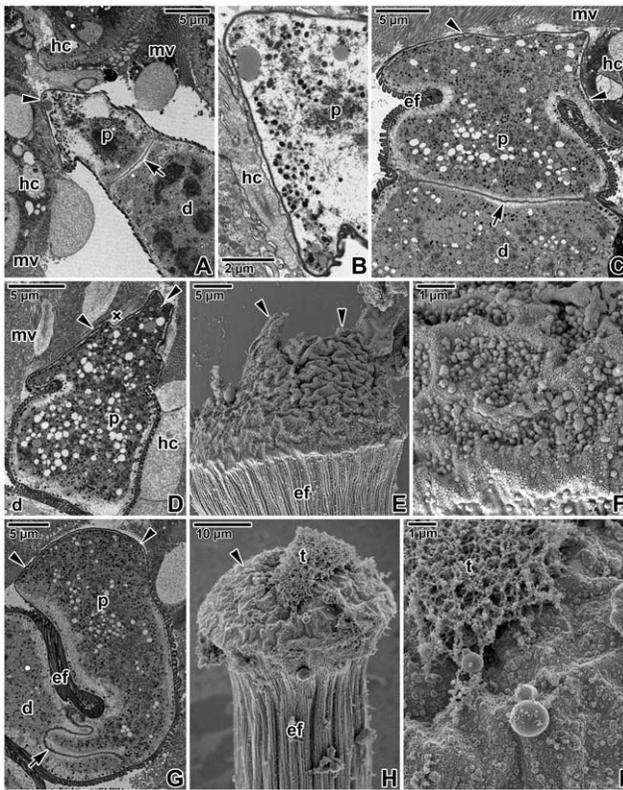
Figure 4. Gamonts of *Gregarina cuneata* observed using an electron microscope. A. Individual exhibiting a lance-shaped top (arrowhead) of the protomerite (p) in contact with a host cell (hc); deutomerite (d), microvilli (mv), septum (arrow). **B.** Higher magnification of the protomerite top shown in Fig. 4A. Note the close contact of protomerite (p) with the host cell (hc) in some areas. **C.** Longitudinal section of the protomerite (p) separated from the deutomerite (d) by a septum (arrow). Note that the tapered protomerite top, which is in contact (arrowheads) with host cell microvilli (mv), lacks the epicytic folds (ef) covering the rest of the gregarine body. **D.** A view of the protomerite (p) top (arrowheads) in close contact with the microvillous surface (mv) of host epithelial cells (hc); amorphous material (×), deutomerite (d). **E.** Scanning electron micrograph showing the protomerite top covered by a wrinkled plasma membrane; protomerite epicytic folds (ef). The apical end of the protomerite is obviously damaged (arrowheads), probably due to mechanical separation of the gregarine from the host tissue during specimen processing. **F.** A more detailed view of the protomerite top exhibiting small remnants of host tissue still attached to its plasma membrane. **G.** A general view of the protomerite (p) separated from the deutomerite (d) by a distinct septum (arrow); epicytic folds (ef). Arrowheads indicate the rounded protomerite top in contact with host cell microvilli. **H.** Scanning electron micrograph showing the rounded protomerite top (arrowhead) with a scrap of host tissue (t) attached; epicytic folds (ef) covering the rest of protomerite. **I.** A more detailed view of the plasma membrane covering the protomerite top shown in Fig. 4H; scrap of host tissue (t).

doi:10.1371/journal.pone.0042606.g004

Figure 5. Host-parasite interactions in *Gregarina cuneata* as observed by transmission electron microscopy. A, B. A more detailed view of the protomerite top (p) in close contact with host microvilli (mv) or epithelial cells (hc); amorphous material (×). **C–E.** A detail of the protomerite (p) apical region covered by a three-layered pellicle underlined by a dense layer; Golgi apparatus (g), host cells (hc), microvilli (mv). Note the ducts (arrows) passing to the exterior, numerous dense bodies (asterisks), semi-empty (Fig. 5C) and filled (Fig. 5D) dense structures (in circle) directly linked to the pore-like structures (arrowheads) interrupting the inner membrane complex. **F.** Higher magnification of the Golgi apparatus frequently observed in the protomerite cytoplasm. **G.** A view of the protomerite top (p) exhibiting a more undulating pattern (arrowheads) in the area adjacent to the host epithelium (hc) with microvilli (mv); epicytic folds (ef), numerous dense bodies (asterisks). **H.** A higher magnification showing the protomerite (p) apical region with unusual duct-like structures (arrows). This region is obviously covered by a typical three-layered pellicle consisting of a plasma membrane and inner membrane complex underlined by a dense layer, but it lacks epicytic folds. Note that the inner membrane complex is discontinuous in a periodic pattern (interrupted by pore-like structures); amorphous material (×), dense bodies (asterisks), host cells (hc).

doi:10.1371/journal.pone.0042606.g005

in the course of early trophozoite development, the gradually enlarging epimerite causes a deep invagination of the host plasma membrane, thus allowing the parasite to anchor to the surface of the host cell and to develop in an epicellular position. The interface between the epimerite and the host cell consists of epimerite and host plasma membranes, and a dense layer of unknown nature and origin in between them [4,6,7,8,10,33]. The contact between the epimerite and the host plasma membrane is reported to be of the membrane-to-membrane type; lecudinid

eugregarines establish an intimate contact with the host cell without an interspecific cell junction [34]. In fact, numerous detached trophozoites retaining intact epimerites, commonly observed in native or fixed squash preparations, are the evidence that no real fusion develops between the epimerite and host plasma membranes along the trilaminar interface. It seems that, simultaneously with trophozoite maturation, the host and epimerite membranes start to lose adhesion to one another and the epimerite gradually detaches from the epithelium. I repeatedly observed attached mature trophozoites of various species, in which the epimerite membrane was already separated from the host plasma membrane [7].

The feeding stages of *G. cuneata* exhibit an even more spectacular adaptation to epicellular parasitism. The atypical epimerite of *G. cuneata* develops from the epimeritic bud in accordance with other eugregarines, and later in development forms numerous digitations, deeply invaginating the plasma

membrane on the luminal side of the affected host cell. Despite this parasite's firm anchoring to the brush border of the host cell, especially in mature stages when the host and epimerite membranes become almost indistinguishable from each other, *G. cuneata* trophozoites are able to detach while retaining an intact epimerite. Nevertheless, in contrast to other gregarines from mealworms, detached trophozoites of *G. cuneata* more often were found to have ruptured epimerites. Although the trophozoite development is more or less identical in all eugregarines from *T. molitor*, the destiny of *G. cuneata* mature trophozoites significantly differs in that they form so-called early syzygies, often found to be still attached to the host tissue. Surprisingly, the attachment site of attached primites significantly differs from the epimerite in younger stages, despite their resemblance at the light microscopic level. The 'real' epimerite disappears (retracts) and the top of the protomerite with a more or less undulating pattern remains in contact with the epithelium. The attachment by means of a modified protomerite could be facilitated by an increased flexibility of this region, as suggested by the dot-like accumulation of actin in the protomerite of *G. cuneata* as well as *G. polymorpha* [30]. Comparable attachment strategy has been reported from actinocephalid eugregarines [35] and it could be expected that protomerites modified for attachment act as feeding organelles in eugregarines lacking an epimerite. Similarly to *G. cuneata*, gamonts of some actinocephalids lose their small globular epimerites and subsequently attach by a modified, sucker-like protomerite [35]. The space between the epicytic folds of the attached protomerite and the host epithelium is filled by the microvilli embedded in a dense material interpreted to be adhesive. The authors speculate that this material could be produced by small dense (exocytic) vesicles in the protomerite apical cytoplasm. The space between the host microvilli and the *G. cuneata* protomerite top was also filled with an amorphous ropey material of unknown origin, probably serving as an adhesive. These observations are supported by the frequent presence of host tissue remnants attached to the *G. cuneata* protomerite, which was confirmed by the fluorescence labelling of myosin and not reported in other gregarines from mealworms.

Nutrient acquisition in eugregarines

Nutrition of gregarines has been the subject of extensive debate for decades. There is evidence that feeding mode in gregarines depends on the long-term environmental conditions forming their niche. Correlations between trophozoite characteristics and the environment occupied within the host are discussed elsewhere [36]. The earliest diverging apicomplexans, archigregarines parasitising marine invertebrates, have retained myzocytosis as their principal mode of feeding [36]. The extensive folding of the pellicle covering the surface of large trophozoites of marine eugregarines seems to optimise surface-mediated nutrition (pinocytosis via micropores), and thus could explain the loss of an apical complex and myzocytosis in eugregarines along with the development of a bulky attachment apparatus, such as an epimerite or mucron [37].

The feeding strategy might even differ between distant eugregarine taxa. For instance, the supposed lytic effect of lecudinids on host cells indicates the nutritional function of the mucron via extracellular secretion of enzymes and absorption of digested host tissue [9]. In general, the epimerite cytoplasm contains many organelles usually associated with nutritive function [14]. Ghazali et al. [20] concluded that epimerites do not have a direct sucker function because of the absence of actin in the *G. blaberae* epimerite. On the contrary, our data confirmed the presence of F-actin in the epimerite region of eugregarines from mealworms [8,this study]. As host cells affected by attachment of

Gregarina spp. vegetative stages usually do not show obvious pathological changes, the cortical vesicle and epimerite vacuoles most likely absorb nutrients via a mechanism based on membrane permeability [9]. Numerous mitochondria underlying the cortical vesicle, regularly observed in various eugregarine species [7,8,10], could provide the energy necessary for this putative absorption mechanism. The abundant endoplasmic reticulum repeatedly observed in the area of the expanding epimerite in young trophozoites of *G. cuneata* indicates the activation of metabolic pathways, probably involved in the synthesis and secretion of proteins and membrane manufacturing. The significant reduction in size of *G. cuneata* cortical vesicle might be related to the convoluted character of the epimerite, significantly increasing its absorptive surface, as reported in *Didymophyes* [12]. Similarly, the trilaminar junction between the mucron of the monocystid eugregarine *Nematocystis* and the host epithelial cell forms extensive folds to increase the surface contact between their apposing cell membranes [33]. Using radioisotopes, the study demonstrated that metabolites pass directly from the host cell to the trophozoites by crossing the attachment site of *Nematocystis*.

In gamonts of *G. cuneata* with their modified protomerites contacting the host epithelium, the pore- and duct-like structures were associated with the pellicle covering the protomerite top. Although the function of these structures remains uncertain, they are most likely involved in gamont nutrition and/or attachment. The apical localisation of numerous dense bodies, various vesicles and abundant Golgi apparatus in the protomerite cytoplasm of *G. cuneata* gamonts similarly indicates the involvement of protomerite top in the feeding.

The basic mechanisms of nutrient acquisition in gregarines, however, are still to be resolved. Despite all these studies attributing the major nutritional role to the attachment organelles, another possibility must be sketched, especially when considering the existence of gregarines growing in the coelomic fluid without an attachment to the host tissue. In addition, eugregarines usually continue to grow after detaching from the host tissue [9]. There are often speculations on the functionality of the micropore-like structures that are often observed in the spaces between epicytic folds [11,16,17,18]; nevertheless, more elaborate analyses are needed to determine their involvement in gregarine nutrition and/or movement.

Pathogenicity to insect hosts

Eugregarines are probably the most frequently encountered protists in insects and probably the most innocuous. As a rule, they are considered to be non-pathogenic to their hosts [38]; however, the real impact of eugregarine infection on host fitness and viability is still poorly understood. Misinterpretation of regular cellular processes in host tissue might significantly contribute to the controversy surrounding the pathogenicity of eugregarines. In addition, gregarines usually parasitise digestive epithelia that are the first to undergo autolysis after dissection, and this could hinder the correct determination of pathological changes induced by gregarines and distinguishing them from the post-mortem autolytic changes to the tissue. Some authors attributed pathogenicity mostly to trophozoites, which theoretically might cause some degree of damage to host tissue depending on the size and shape of their embedded epimerites [39]. The robust epimerite of *Ancyrophora* equipped with rigid hooks, however, does not appear to induce drastic damage to the host cell [14]. In fact, although eugregarines infecting the intestinal epithelium might cause certain damage to affected cells, continual regeneration of these cells accounts for the apparent harmless effect of the parasite. Usually, even if the eugregarine trophozoites destroy individual cells, the

overall damage to epithelial tissue is negligible and easily repaired. Nevertheless, some species appear to reduce the host's fitness by occluding its gut and thus preventing the passage of food [11]. In addition, heavy infestations of gregarines in the mesenteron can have a significant impact on the host's nutritional state. As microvilli are important structures for efficient absorption and excretion, their destruction might limit the host digestive process and lead to its malnutrition with consequent weakening or even death. Gregarines parasitising intestinal caeca are even much more pathogenic, as they may cause the hypertrophy of parasitised cells or even rupture the caecal wall, leading to a secondary bacterial infection [40].

The eugregarines from mealworms were previously considered to be parasitic because of their negative impact on the development of larvae grown on a suboptimal diet [41]. Eugregarines occurring in larval *T. molitor* from our colonies, however, not only do not appear to harm their host, but could actually be considered to be mutualistic from a certain point of view. My personal long-term observations on *T. molitor* confirmed that despite heavy infection completely filling the larval mid-gut, the presence of eugregarines seems to have a positive impact on host development, fitness and longevity. Identical observations were made on naturally infected mealworm larvae from our laboratory colonies, usually parasitised by multiple eugregarine species (*G. cuneata*, *G. polymorpha* and *G. steini*) simultaneously. Similarly, Sumner [42] considered gregarines from mealworms to be symbiotic, and necessary for the normal growth and longevity of the host. This author even suggested that gregarines probably secrete essential substances such as vitamins or enzymes essential for larval growth. This study confirms that, though the affected epithelium shows some changes, parasitisation by *G. cuneata* seems to have no negative impact on host health that is essential for the gregarine survival. Despite high densities of vegetative stages attached to the host intestinal tissue, there is no evidence of direct damage to neighbouring epithelial cells. Vacuolation and eventual subsequent death of individual affected epithelial cells represented the most marked changes that could be considered to be associated with gregarine infection.

Morphological changes of *Gregarina cuneata* in different environmental conditions

In the course of development, the epimerite of *G. cuneata* undergoes dramatic changes and some of these have been shown to be reversible depending on actual environmental conditions. Various stimuli from the trophozoite environment, such as changes in the chemical composition of the dissection buffer/host tissue, pH or temperature, seem to induce significant morphological changes of the epimerite and the protomerite top. Significant differences in the protomerite shape, evident especially in the primites, were noticed in this study prior to and after chemical fixation with different cross-linking fixatives - paraformaldehyde and glutaraldehyde. Non-fixed living gamonts exhibited a rounded protomerite top; however, those fixed with a paraformaldehyde solution often exhibited a lance-shaped protomerite top. These individuals are assumed to have been mechanically detached from the host tissue during specimen processing and simultaneously chemically fixed, thus maintaining the real shape of the protomerite when in close contact with the epithelium. Corresponding stages fixed with glutaraldehyde, however, did not exhibit such an obvious extension and tapering of their apical

ends, although the protomerite top of gamonts was often slightly raised and covered by host tissue fragments. Only individuals found in contact with the host tissue after fixation preserved the lance-shaped protomerite top. Formaldehyde-based solutions fix the tissue by cross-linking proteins; its effects are reversible by excess water and the benefits include good tissue penetration. As glutaraldehyde is a larger molecule, the weakness of this fixative includes a slower rate of diffusion across membranes, resulting in poor tissue penetration and the changes caused by fixation are irreversible [43]. As the fixatives are known to induce remarkable changes in cell shape, rapid fixation by paraformaldehyde is thought to be the source of differences in the protomerite morphology in this study. This unexpected outcome of different fixations revealed morphological adaptations of *G. cuneata* to epicellular parasitism that are not commonly observed in living specimens. The facts discussed herein suggest that this gregarine is able not only retract but even repeatedly protract its apical end (epimerite or protomerite top dedicated to attachment) depending on environmental conditions and the need to reattach to another part of the host tissue.

Conclusions

Gregarines are important from an evolutionary perspective because of their suspected deep-branching position within the phylum Apicomplexa. Although some ancestral features found in gregarines have given them a reputation of being a 'primitive' lineage of the Apicomplexa, the majority of them exhibit unique and novel adaptations to their environment [37]. A wide variety of morphological and functional adaptations that can be found in all gregarine taxa, along with the fact that only few invertebrate groups escaped infection with gregarines, indicates that they must be regarded as very successful and highly specialized parasites. The fascinating biology of these apicomplexans is derived from the basic cellular organization of the so-called zoite, an infectious developmental stage devoted to the invasion of host tissue. The detachment of vegetative stage from host tissue and its eventual reattachment, self-regulated by the parasite, might represent a higher degree of gregarine adaptation to epicellular development in hosts exhibiting a rapid epithelial replacement (e.g. insects). The modified protomerite of *G. cuneata* gamonts, serving for attachment to the host tissue and parasite feeding, indicates further adaptation of eugregarines for nutrient acquisition in older developmental stages that were previously considered to be non-vegetative. Such modifications for epicellular parasitism do not seem to be primitive ancestral characteristics, but rather advanced features occurring in some eugregarines in the course of their coevolution with the host.

Author Contributions

Conceived and designed the experiments: AV. Performed the experiments: AV. Analyzed the data: AV. Contributed reagents/materials/analysis tools: AV. Wrote the paper: AV.

References

1. Perkins FO, Barta JR, Clopton RE, Peirce MA, Upton SJ (2000) Phylum Apicomplexa Levine, 1970. In: Lee JJ, Leedale GF, Bradbury P, editor. An Illustrated Guide to the Protozoa. Second Edition, Vol. 1, Society of Protozoologists, Lawrence, Kansas, USA, pp. 190–369.

2. Carreno RA, Martin DS, Barta JR (1999) *Cryptosporidium* is more closely related to the gregarines than to coccidia as shown by phylogenetic analysis of apicomplexan parasites inferred using small-subunit ribosomal RNA gene sequences. Parasitology Research 85: 899–904.

3. Templeton TJ, Enomoto S, Chen WJ, Huang CG, Lancto CA, et al. (2010) A genome-sequence survey for *Ascogregarina taiwanensis* supports evolutionary affiliation but metabolic diversity between a gregarine and *Cryptosporidium*. Molecular Biology and Evolution 27: 235–248.

4. Valigurova A, Hofmannova L, Koudela B, Vavra J (2007) An ultrastructural comparison of the attachment sites between *Gregarina steini* and *Cryptosporidium muris*. Journal of Eukaryotic Microbiology 54: 495–510.

5. Valigurova A, Jirku M, Koudela B, Gelnar M, Modry D, et al. (2008) Cryptosporidia: Epicellular parasites embraced by the host cell membrane. International Journal for Parasitology 38: 913–922.

6. Valigurova A, Koudela B (2005) Fine structure of trophozoites of the gregarine *Leidyana ephestiae* (Apicomplexa : Eugregarinida) parasitic in *Ephestia kuehniella* larvae (Lepidoptera). European Journal of Protistology 41: 209–218.

7. Valigurova A, Koudela B (2008) Morphological analysis of the cellular interactions between the eugregarine *Gregarina garnhami* (Apicomplexa) and the epithelium of its host, the desert locust *Schistocerca gregaria*. European Journal of Protistology 44 : 197–207.

8. Valigurova A, Michalkova V, Koudela B (2009) Eugregarine trophozoite detachment from the host epithelium via epimerite retraction: Fiction or fact? International Journal for Parasitology 39: 1235–1242.

9. Schrevel J, Philippe M (1993) The gregarines. In: Kreier JP, editor. Parasitic Protozoa Second edition, Vol. 4, Academic Press, pp. 133–245.

10. Tronchin G, Schrevel J (1977) Chronology of ultrastructural changes during growth of *Gregarina blaberae*. Journal of Protozoology 24: 67–82.

11. Lucarotti CJ (2000) Cytology of *Leidyana canadensis* (Apicomplexa : Eugregarinida) in *Lambdina fiscellaria fiscellaria* larvae (Lepidoptera : Geometridae). Journal of Invertebrate Pathology 75: 117–125.

12. Hildebrand HF (1976) Electron-microscopic investigation on evolution stages of trophozoite of *Didymophyes gigantea* (Sporozoa, Gregarinida). 1. Fine structure of protomerite and epimerite and relationship between host and parasite. Zeitschrift Fur Parasitenkunde-Parasitology Research 49: 193–215.

13. Ormieres R (1977) *Pyxinia firmus* (Leger, 1892), eugregarine parasite of Coleoptera *Dermestes frischi* Kugel - Ultrastructural study. Zeitschrift fur Parasitenkunde-Parasitology Research 53: 13–22.

14. Baudoin J (1969) Sur l'ultrastructure de la région antérieure de la grégarine *Ancyrophora puytoraci*. Protistologica 5: 431–439.

15. Schrevel J, Vivier E (1966) Étude de l'ultrastructure et du role de la région antérieure (mucron et épimérite) de grégaries parasites d'annélides polychètes. Protistologica 2: 17–28.

16. Talluri MV, Dallai R (1983) Freeze-fracture study of the gregarine trophozoite: II. Evidence of "rosette" organization on cytomembranes in relation with micropore structure. Bolletino di zoologia 50: 247–256.

17. Dyakin AY, Simdyanov TG (2005) The cortical zone of skittle-like cells of *Urospora chiridotae*, a gregarine from an apode holothuria *Chiridota laevis*. Protistology 4: 97–105.

18. Vivier E, Devauchelle G, Petitprez A, Porchet-Hennere E, Prensier G, et al. (1970) Observations on comparative cytology in sporozoans. Part 1. The sperficial structures in vegetative forms. Protistologica 6: 127–150.

19. Schrevel J (1972) Polysaccharides of cell-surface of gregarines (Protozoa Parasites). 1. Ultrastructure and cytochemistry. Journal of Microscopy-Oxford 15: 21–40.

20. Ghazali M, Philippe M, Deguercy A, Gounon P, Gallo JM, et al. (1989) Actin and spectrin-like (Mr = 260–240 000) proteins in gregarines. Biology of the Cell 67: 173–184.

21. Ghazali M, Schrevel J (1993) Myosin-like protein (M(r)175,000) in *Gregarina blaberae*. Journal of Eukaryotic Microbiology 40: 345–354.

22. Tronchin G, Philippe M, Mocquard JP, Schrevel J (1986) Life cycle of *Gregarina blaberae* - Description, chronology, study of the growth, influence of the cycle of the host *Blaberus craniifer*. Protistologica 22: 127–142.

23. Ruhnke TR, Janovy J (1990) Life history differences between 2 species of *Gregarina* in *Tenebrio molitor* larvae. Journal of Parasitology 76: 519–522.

24. Devauchelle G (1968) Étude ultrastructurale du développement des grégaries du *Tenebrio molitor* L. Protistologica 4: 313–332.

25. Ruhnke TR, Janovy J (1989) The site specificity of 2 species of *Gregarina* in *Tenebrio molitor* larvae. Journal of Protozoology 36: 428–430.

26. Schrevel J, Caigneaux E, Gros D, Philippe M (1983) The 3 cortical membranes of the gregarines. 1. Ultrastructural organization of *Gregarina blaberae*. Journal of Cell Science 61: 151–174.

27. Thomas D, Gouranto J (1973) Durée de formation des cristaux protéiques intranucléaires de l'intestin moyen de *Tenebrio molitor*. Journal of Insect Physiology 19: 515–522.

28. Harry OG (1965) Studies on early development of eugregarine *Gregarina garnhami*. Journal of Protozoology 12: 296–305.

29. Harry OG (1970) Gregarines: their effect on the growth of the desert locust (*Schistocerca gregaria*). Nature 225: 964–966.

30. Heintzelman MB (2004) Actin and myosin in *Gregarina polymorpha*. Cell Motility and the Cytoskeleton 58: 83–95.

31. Heintzelman MB, Mateer MJ (2008) GpMyoF, a WD40 repeat-containing myosin associated with the myonemes of *Gregarina polymorph*a. Journal of Parasitology 94: 158–168.

32. Schrevel J, Vivier E (1966) Etude au microscope électronique de la région antérieure des Grégaries: le mucron de *Lecudina pellucida* (Koll.) Mingazzini et l'épimérite de *Sycia inopinata* Léger. Protistologica 2: 17–28.

33. MacMillan WG (1973) Gregarine attachment organelles - structure and permeability of an interspecific cell junction. Parasitology 66: 207–214.

34. Desportes I, Theodorides J (1986) *Cygnicollum lankesteri* n.sp., grégarine (Apicomplexa, Lecudinidae) parasite des annélides polychètes *Laetmonice hystrix* et *L. producta*; particularités cytologiques de l'appareil de fixation et implications taxonomiques. Protistologica 22: 47–60.

35. Cook TJP, Janovy J, Clopton RE (2001) Epimerite-host epithelium relationships among eugregarines parasitizing the damselflies *Enallagma civile* and *Ischnura verticalis*. Journal of Parasitology 87: 988–996.

36. Leander BS, Lloyd SAJ, Marshall W, Landers SC (2006) Phylogeny of marine gregarines (Apicomplexa) - *Pterospora*, *Lithopystis* and *Lankesteria* - and the origin(s) of coelomic parasitism. Protist 157: 45–60.

37. Leander BS (2008) Marine gregarines: evolutionary prelude to the apicomplexan radiation? Trends in Parasitology 24: 60–67.

38. Henry JE (1981) Natural and applied control of insects by protozoa. Annual Review of Entomology 26: 49–73.

39. Lipa JJ (1967) Studies on gregarines (Gregarinomorpha) of arthropods in Poland. Acta Protozoologica 5: 97–179.

40. Tanada Y, Kaya HK (1993) Insect pathology. Academic Press, San Diego, CA, USA.

41. Harry OG (1967) The effect of a eugregarine *Gregarina polymorpha* (Hammersch-midt) on the mealworm larva of *Tenebrio molitor* (L.). Journal of Eukaryotic Microbiology 14: 539–547.

42. Sumner R (1932) Influence of gregarines on growth in the mealworm. Science 78: 1.

43. Dykstra MJ (1993) A manual of applied techniques for biological electron microscopy. Plenum Press, New York, N.Y, USA.

7.2

Valigurová A., Vaškovicová V., Musilová N., Schrével J.

2013

The enigma of eugregarine epicytic folds:
where gliding motility originates?

Frontiers in Zoology 10, 57
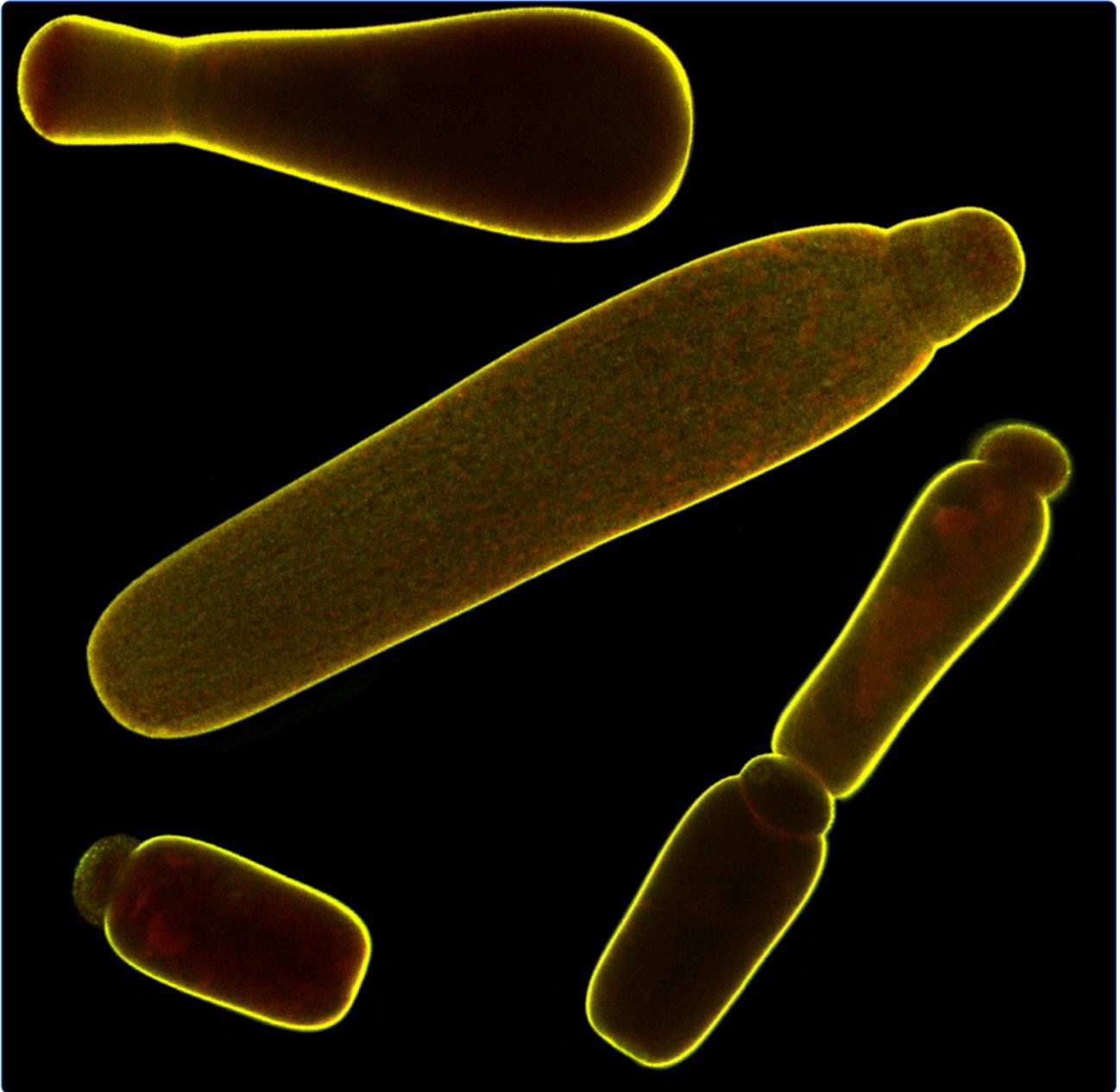
The enigma of eugregarine epicytic folds: where gliding motility originates?

Valigurová *et al.*

FRONTIERS IN ZOOLOGY

The enigma of eugregarine epicytic folds: where gliding motility originates?

Andrea Valigurová[1*], Naděžda Vaškovicová[2], Naďa Musilová[1] and Joseph Schrével[3]

Abstract

Background: In the past decades, many studies focused on the cell motility of apicomplexan invasive stages as they represent a potential target for chemotherapeutic intervention. Gregarines (Conoidasida, Gregarinasina) are a heterogeneous group that parasitize invertebrates and urochordates, and are thought to be an early branching lineage of Apicomplexa. As characteristic of apicomplexan zoites, gregarines are covered by a complicated pellicle, consisting of the plasma membrane and the closely apposed inner membrane complex, which is associated with a number of cytoskeletal elements. The cell cortex of eugregarines, the epicyte, is more complicated than that of other apicomplexans, as it forms various superficial structures.

Results: The epicyte of the eugregarines, *Gregarina cuneata*, *G. polymorpha* and *G. steini*, analysed in the present study is organised in longitudinal folds covering the entire cell. In mature trophozoites and gamonts, each epicytic fold exhibits similar ectoplasmic structures and is built up from the plasma membrane, inner membrane complex, 12-nm filaments, rippled dense structures and basal lamina. In addition, rib-like myonemes and an ectoplasmic network are frequently observed. Under experimental conditions, eugregarines showed varied speeds and paths of simple linear gliding. In all three species, actin and myosin were associated with the pellicle, and this actomyosin complex appeared to be restricted to the lateral parts of the epicytic folds. Treatment of living gamonts with jasplakinolide and cytochalasin D confirmed that actin actively participates in gregarine gliding. Contributions to gliding of specific subcellular components are discussed.

Conclusions: Cell motility in gregarines and other apicomplexans share features in common, i.e. a three-layered pellicle, an actomyosin complex, and the polymerisation of actin during gliding. Although the general architecture and supramolecular organisation of the pellicle is not correlated with gliding rates of eugregarines, an increase in cytoplasmic mucus concentration is correlated. Furthermore, our data suggest that gregarines utilize several mechanisms of cell motility and that this is influenced by environmental conditions.

Keywords: Actin, Cytochalasin D, Epicyte, Epicytic folds, Eugregarine, Glideosome, Gliding motility, Jasplakinolide, Mucus, Myosin, Pellicle

Introduction

Apicomplexans are one of the most successful and diverse groups of eukaryotic unicellular parasites that exhibit unique adaptations to life in a wide spectrum of vertebrate and invertebrate hosts. Many cause major human diseases, i.e. malaria, toxoplasmosis, coccidiosis and cryptosporidiosis. Because apicomplexan diseases are still problematic, therapeutic research focuses either on parasitic structures or metabolic pathways which might serve

as drug targets. The cytoskeleton of these parasites has become a focus for drug development because it plays an important role in various life processes, e.g., locomotion, division, invasion and formation of parasite cell polarity [1]. This is especially true of invasive stages of *Toxoplasma gondii* and *Plasmodium falciparum* [2,3].

Infective stages of Apicomplexa are characterised by an apical complex of organelles as well as a complicated cell cortex consisting of cortical alveoli, i.e., flattened vesicles limited by a membrane and packed into a continuous layer (inner membrane complex), underlying the plasma membrane. The inner membrane complex (IMC) has micropores and connects numerous cytoskeletal elements

* Correspondence: andreav@sci.muni.cz
[1]Department of Botany and Zoology, Faculty of Science, Masaryk University, Kotlářská 2, 611 37 Brno, Czech Republic
Full list of author information is available at the end of the article

that include an actomyosin complex, microtubules and a network of intermediate filamentous proteins. The invasive zoites of Apicomplexa are motile and use actin-based gliding for host invasion and tissue traversal. This gliding mechanism called 'glideosome' was first described for *Toxoplasma* [4] and has been extended as a concept to sporozoites of *Plasmodium* [5] and other apicomplexans [6]. In *Toxoplasma* and *Plasmodium*, myosin A is linked to the IMC and probably interacts with subpellicular microtubules. The head of myosin A moves along the actin filament, which is connected to a cell adhesion molecule (TRAP in *Plasmodium* spp. or TgMIC2 in *T. gondii*) via a tetrameric aldolase [6].

As deep-branching apicomplexan parasites of invertebrates and urochordates, gregarines (Gregarinasina) are generally thought to be of no economic importance. Recent analyses, however, indicate a close affinity of gregarines with species of *Cryptosporidium* [7,8] that parasitize humans. Most eugregarine gamonts are covered by a pellicle folded in numerous longitudinal epicytic folds (e.g., *Gregarina*, *Lecudina*) [9-11] and exhibit gliding motility [12-14]. Using a laser trap and bead translocation, King and Sleep [15] have described gliding as an irregular, erratic process. Some marine gregarines (e.g. archigregarines) possess regular sets of subpellicular microtubules under the pellicle [16,17] and typically display a pendular or rolling movement. In contrast, urosporidians that evolved as free-floating parasites within the host tissue move by pulsation of their body wall corresponding to the so-called peristaltic motility. The possible function of epicytic folds has been often discussed, and it is generally thought that they increase the surface area for nutrient acquisition and facilitate actomyosin-based gliding motility. The involvement of actin- and myosin-like proteins in gregarine cell motility has been previously reported [18-20]. Several electron microscopic studies have revealed the typical organisation of epicytic folds in eugregarines [10,11,21-23]. These suggest that there are undulating epicytic folds located between those that do not move [24-26], but the exact mechanism of motility remains unclear. Therefore, it is imperative that structural observations be integrated with biochemical and molecular data for the actin and myosins of *Gregarina* species [20,27]. Of the three myosin genes so far characterised in *Gregarina polymorpha*, myosins A (93 kDa) and B (96 kDa) belong to the class of myosin (XIV) that is restricted to the phylum Apicomplexa [28] and myosin F (222 kDa) to the class XII [27,29]. King and Sleep [15] estimated that the number of myosin heads at the site of interaction in *Gregarina* gamonts to be in excess of 200 and showed that the gliding rate in a giant eugregarine *Porospora gigantea* is four times higher (up to 60 μm/s) than the speed of myosin movement along the actin filaments of a muscle sarcomere. In spite of a few

freeze-etching studies that focus on the supramolecular cell organisation of some *Gregarina* species [11,22,30], the precise location of the actomyosin complex is as yet unknown. However, the TRAP or TgMIC2 molecules that are in contact with the substrate suggest that the concept of a glideosome might help shed light on the role of the mucus [12] in the gliding mechanism of gregarines [31-33].

Laboratory-reared colony of the mealworm *Tenebrio molitor* parasitized by three species of *Gregarina* has permitted the comparison of gliding by *G. cuneata*, *G. polymorpha* and *G. steini* under identical environmental conditions. This study was performed so that the respective roles of the apical and lateral parts of the epicytic folds in apicomplexan zoite gliding could be discerned. Our intent was to evaluate the presumptive involvement of specific subcellular components such as the 12-nm filaments, rippled dense structures [11], and mucus in eugregarine gliding motility [32,33] using both the experimental and morphological approaches.

Results

Light microscopic observations on gregarine movement behaviour and gliding motility

The pellicle (epicyte) appeared as a thick but transparent layer of even width covering the entire gregarine (Figures 1A, 2A and 3A). Longitudinal striations that were easily recognisable in the pellicle corresponded to the epicytic folds. During gliding, the shape of the cell varied by species. In *G. cuneata* and *G. polymorpha*, the changes of direction during gliding seemed to be controlled by protomerite activity. In *G. polymorpha* the protomerite and deutomerite were very flexible. The bending of the protomerite may take place in any plane, but in *G. polymorpha* it was sometimes so extensive that the axis of the protomerite (or even with the one-third of the deutomerite) came to form a right or even acute angle with that of the deutomerite. This behaviour was especially noted when gamonts encountered barriers in their gliding path. In *G. polymorpha*, a partial pulling of the protomerite into the deutomerite, so that the corresponding pellicle became pleated, could be observed. A slight bending of the protomerite could be detected also in *G. cuneata*, but the angle between the planes of protomerite and deutomerite was only obtuse. In contrast, the protomerite of *G. steini* did not show any changes during gliding; only a slight bending of the gamont deutomerite, usually in its posterior half, was observable when turning to the side. In syzygies of all species, the satellite seemed to be passive and just followed the path given by the obviously active primite, and this path corresponded to a forward unidirectional gliding. In all three species, the gliding locomotion of single and associated gamonts was usually discontinuous with multiple stops and frequent changes of direction, and

often occurred with discernible changes in speed. The gregarines glided in an almost linear pattern. The gliding movement, however, was not constant and varied among species as well as every gliding individual. The maximum speed of gliding gamonts achieved during our observations was 5.66 μm/s in single gamonts and 8.49 μm/s in syzygies of *G. cuneata*, 22.86 μm/s in single gamonts and 16.18 μm/s in syzygies of *G. polymorpha*, and 9.42 μm/s in single gamonts and 9.25 μm/s in syzygies of *G. steini* (Table 1). Based on contact stimuli, gregarines were able to quite rapidly change the direction of their otherwise straightforward gliding to avoid a barrier in their gliding path. When a gliding gamont encountered a barrier, it usually endeavoured to bore or wriggle its way through. Obviously, gamonts of *G. steini* exhibited the most continuous and constant gliding with a linear or widely semicircular track. The gliding of *G. cuneata* gamonts was characterised by multiple and prolonged stops, and thus many individuals did not exhibit gliding during the recording. In contrast, gamonts of *G. polymorpha* covered the greatest distance per unit of time in one continuous track.

Treatment of gregarine gamonts with jasplakinolide and cytochalasin D

Various concentrations of both drugs were used to treat gregarine gamonts. Concentrations of jasplakinolide (JAS), a strong actin stabilizer, lower than 5 μM had no effect. Thus, in order to obtain reliable results on active and vital gregarines, they were treated with 5, 10, 20 and 30 μM concentrations of JAS in Ringer's solution. Gregarines not only survived in these very high doses of JAS, but even actively moved for the next 90–150 min, depending on the drug concentration and gregarine species (Table 2). Experiments revealed that JAS treatment led to an increased speed of gliding movement beyond 5 minutes after drug application, followed by subsequent decrease to normal in all three species. Afterwards, individual reactions rates to JAS differed by species with the most rapid occurring in *G. steini* whose gamonts moved up to 90 minutes. The most delayed reaction to the drug (inhibition of gliding motility) exhibited syzygies of *G. cuneata*, which moved in large numbers up to 150 minutes after JAS application. After a uniform period of 1 hour, independently on above mentioned

concentrations of JAS, all three species exhibited obvious cellular changes including shrivelling and some degree of cytoplasmic disorganisation. In all species, cell shape restoration took place immediately after returning gamonts to the Ringer's solution. Nevertheless, the time needed for full recovery of gregarines along with the restoration of their motility varied by species (or even individuals) and applied JAS concentrations. The most rapid recovery has been observed in *G. cuneata*. In contrast, gamonts of *G. steini* needed much longer time, and on top of that, some of them did not survive the experiment. In all control preparations, the gamonts continued to move until the end of the experiment. Interestingly, during the first 30 minutes, in contrast to *G. polymorpha* and *G. steini*, gamonts of *G. cuneata* moved more rapidly in a drop of Ringer's solution than was observed on microbiological agar only slightly moistened with Ringer's solution. Although their movement in this period resembled regular gliding in contact with the substrate, detailed observations revealed that they were rather free-floating in a liquid. After 30 minutes, gamonts of all three species sank to the surface of the microscopic slide and started to glide in a regular way, exhibiting the same speed of movement as observed during the motility experiments performed on moistened agar or in the Bürker counting chamber described above (Table 1).

Treatments with cytochalasin D (10, 20 and 30 μM in Ringer's solution), an inhibitor of actin polymerisation, completely inhibited gregarine motility in a species- and concentration dependent manner; i.e. at 10-30 minutes in *G. steini*, 30-75 minutes in *G. polymorpha* and 75-120 minutes in *G. cuneata*. The cellular changes, observed in all assays after a uniform period of 30 minutes, were less obvious than those induced by JAS. In all species, cell shape restoration took place immediately after returning to the Ringer's solution. The time needed for full recovery and restoration of gregarine motility varied by species and drug concentrations (Table 3).

Confocal microscopic analysis of actomyosin motor

In all three species, the homogenous distribution of the fluorescence signal throughout the surface of phalloidin- and antibody-labelled gamonts corresponded to the localisation of an actomyosin motor associated with the apicomplexan cell cortex. Phalloidin labelling confirmed the

Table 1 The speed in observed gliding gregarines

Species	Gliding speed in single gamonts (μm/s)					Gliding speed in syzygies (μm/s)				
	Minimum - maximum	Mean	Standard deviation	N. of gamonts	N. of records	Minimum - maximum	Mean	Standard deviation	N. of syzygies	N. of records
G. cuneata	0.38 - 5.66	2.20	1.51	18	24	1.15 - 8.49	3.96	2.47	8	8
G. polymorpha	3.46 - 22.86	9.91	5.15	12	16	1.05 - 16.18	6.73	4.08	14	17
G. steini	1.32 - 9.42	5.02	2.19	33	39	2.51 - 9.25	5.33	1.62	23	23

Table 2 The treatment of living gregarines with jasplakinolide

Species/JAS concentration	Gregarina cuneata				Gregarina polymorpha				Gregarina steini			
	5 µM JAS	10 µM JAS	20 µM JAS	30 µM JAS	5 µM JAS	10 µM JAS	20 µM JAS	30 µM JAS	5 µM JAS	10 µM JAS	20 µM JAS	30 µM JAS
Changes/time left after drug application (in minutes)												
Initial increase of gliding speed	≥ 5 min+	≥ 5 min+	≥ 5 min++	≥ 5 min++	≥ 5 min+	≥ 5 min+	≥ 5 min++	≥ 5 min++	≥ 5 min+	≥ 5 min+	≥ 5 min++	≥ 5 min++
Decrease of gliding speed to the normal rate	≥ 90 min+	≥ 20 min++	≥ 20 min++	≥ 20 min++	≥ 90 min+	≥ 20 min++	≥ 20 min++	≥ 20 min++	≥ 90 min+	≥ 20 min++	≥ 20 min++	≥ 20 min++
Further decrease of gliding speed	≥ 100 min+	≥ 30 min++	≥ 30 min++	≥ 30 min++	≥ 100 min+	≥ 30 min++	≥ 30 min++	≥ 30 min++	≥ 100 min+	≥ 30 min+	≥ 30 min++	≥ 30 min++
Cellular changes (shrivelling)	≥ 60 min	≥ 60 min	≥ 60 min	≥ 60 min	≥ 60 min	≥ 60 min	≥ 60 min	≥ 60 min	≥ 60 min	≥ 60 min	≥ 60 min	≥ 60 min
Complete stoppage of gliding motility	≤ 150 min	≤ 140 min	≤ 100 min	≤ 100 min	≤ 150 min	≤ 140 min	≤ 100 min	≤ 100 min	≤ 130 min	≤ 120 min	≤ 90 min	≤ 90 min
Recovery of cell shape after washing in Ringer's solution	≤ 1 min	≤ 1 min	≤ 1 min	≤ 1 min	≤ 1 min	≤ 1 min	≤ 1 min	≤ 1 min	≤ 1 min	≤ 1 min	≤ 1 min	≤ 1 min
Full recovery of motility after washing in Ringer's solution	≥ 5 min	≥ 5 min	≥ 5 min	≥ 5 min	≤ 10 min	≥ 10 min	≥ 10 min	≥ 10 min	≤ 30 min	≥ 30 min	≥ 30 min	≥ 30 min

The symbol + indicates an intensity of observed change ranging from + to +++ when compared among gregarine species and JAS concentrations. Applied only if the listed phenomenon showed significant differences in its intensity.

**Table 3 The treatment of living gregarines with cytochalasin D**

Species/Cytochalasin D concentration	*Gregarina cuneata*			*Gregarina polymorpha*			*Gregarina steini*		
	10 µM CytD	20 µM CytD	30 µM CytD	10 µM CytD	20 µM CytD	30 µM CytD	10 µM CytD	20 µM CytD	30 µM CytD
Changes/time left after drug application (in minutes)									
Initial decrease of gliding speed	≥ 5 min+	≥ 5 min++	≥ 5 min+++	≥ 5 min+	≥ 5 min++	≥ 5 min+++	≥ 5 min+	≥ 5 min++	≥ 5 min+++
Further decrease of gliding speed	≥ 20 min+	≥ 10 min++	≥ 10 min+++	≥ 15 min+	≥ 10 min++	≥ 10 min+++	≥ 10 min+	≥ 10 min++	≥ 10 min+++
Cellular changes (shrivelling)	≥ 30 min	≥ 30 min	≥ 30 min	≥ 30 min	≥ 30 min	≥ 30 min	≥ 30 min	≥ 30 min	≥ 30 min
Complete stoppage of gliding motility	≤ 120 min	≤ 90 min	≤ 75 min	≤ 75 min	≤ 60 min	≤ 30 min	≤ 30 min	≤ 20 min	≤ 10 min
Recovery after washing in Ringer's solution	≤ 1 min	≤ 1 min	≤ 1 min	≤ 1 min	≤ 1 min	≤ 1 min	≤ 1 min	≤ 1 min	≤ 1 min
Full recovery after washing in Ringer's solution	≥ 5 min	≤ 10 min	≤ 10 min	≥ 5 min	≤ 10 min	≤ 10 min	≥ 5 min	≥ 10 min	≥ 10 min

The symbol + indicates an intensity of observed change ranging from + to +++ when compared between gregarine species and concentrations of cytochalasin D. Applied only if the listed phenomenon showed significant differences in its intensity.
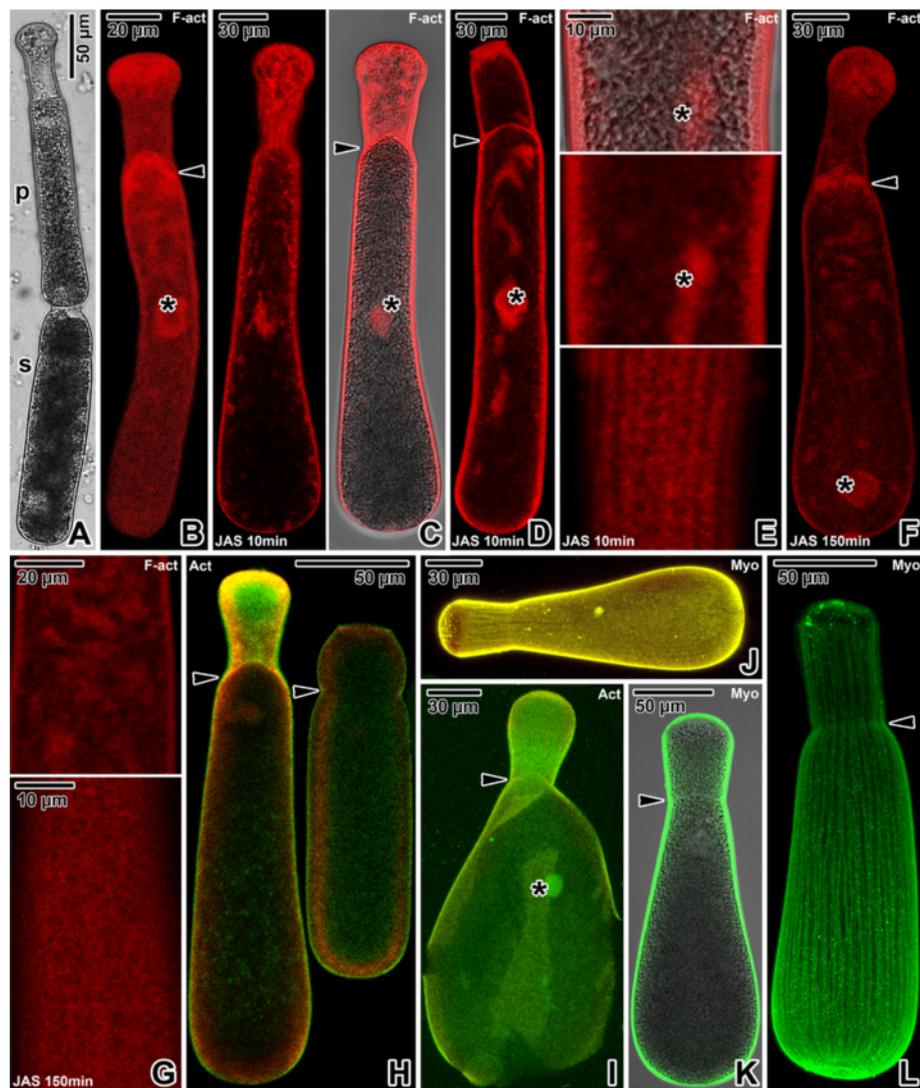
Figure 1 Actin and myosin in *Gregarina cuneata* gamonts. A. Gamonts in syzygy; primite (p), satellite (s). LM, transmitted light. **B**. Localisation of F-actin in a gamont; nucleus (asterisk), septum (arrowhead) between protomerite and deutomerite. CLSM, phalloidin-TRITC. **C-D**. Localisation of F-actin in gamonts (previously associated in syzygy) treated for 10 minutes with 10 μM JAS. Intense labelling is restricted to the cortex and cytoplasmic F-actin aggregations; septum (arrowhead), nucleus (asterisk). Figure **C** shows a primite. CLSM (left) and merged CLSM/transmitted light (right), phalloidin-TRITC. Figure **D** shows a satellite. CLSM, phalloidin-TRITC. **E**. The deutomerite of a gamont treated for 10 minutes with 10 μM JAS. F-actin localisation corresponds to the cortex and nucleus (asterisk). Upper two figures show the gamont middle plane; lower figure shows the cortex in the area of epicytic folds. Merged CLSM/transmitted light (upper) and CLSM, phalloidin-TRITC. **F**. F-actin localisation in a gamont treated for 150 minutes with 10 μM JAS. Note the decreased labelling of cell cortex and septum (arrowhead), and formation of numerous cytoplasmic aggregations of F-actin; nucleus (asterisk). CLSM, phalloidin-TRITC. **G**. The deutomerite of a gamont treated for 150 minutes with 10 μM JAS. F-actin labelling is restricted to the cortex in the area of epicytic folds (lower); cytoplasmic F-actin aggregations (upper). CLSM, phalloidin-TRITC. **H**. Actin localisation in previously associated gamonts; septum (arrowheads). CLSM, IFA. **I**. Actin localisation in a gamont ghost; nucleus (asterisk), septum (arrowhead). CLSM, IFA. **J**. Myosin labelling in a maturing gamont. CLSM, IFA. **K**. Myosin labelling in a mature gamont is restricted to the cortex, but not to the septum (arrowhead). Merged CLSM/transmitted light, IFA. **L**. Labelling of myosin in a gamont cortex shows a pattern of longitudinal rows; septum (arrowhead). CLSM, IFA. Figures **H**, **I** and **J** show merged FITC (antibody) and rhodamine (counterstaining with Evans blue) fluorescence channels.

presence of filamentous actin (F-actin) in the gregarine cell cortex, the fibrillar septum separating the protomerite from the deutomerite and the area of the nucleus (Figures 1B, 2B and 3B). After treatment with 10 μM JAS for 10 minutes, when gregarines glided with increased speed, the F-actin staining became more bright and confined to the cell cortex, the septum and the perinuclear space (Figures 1C-E, 2C-E and 3C-D). Higher magnification revealed numerous transverse and oblique actin filaments in the area of epicytic folds (Figures 1E, 2E and 3D). In addition, several aggregations of F-actin were observed in the cytoplasm of *G. cuneata* protomerite and deutomerite (Figure 1C-D). This
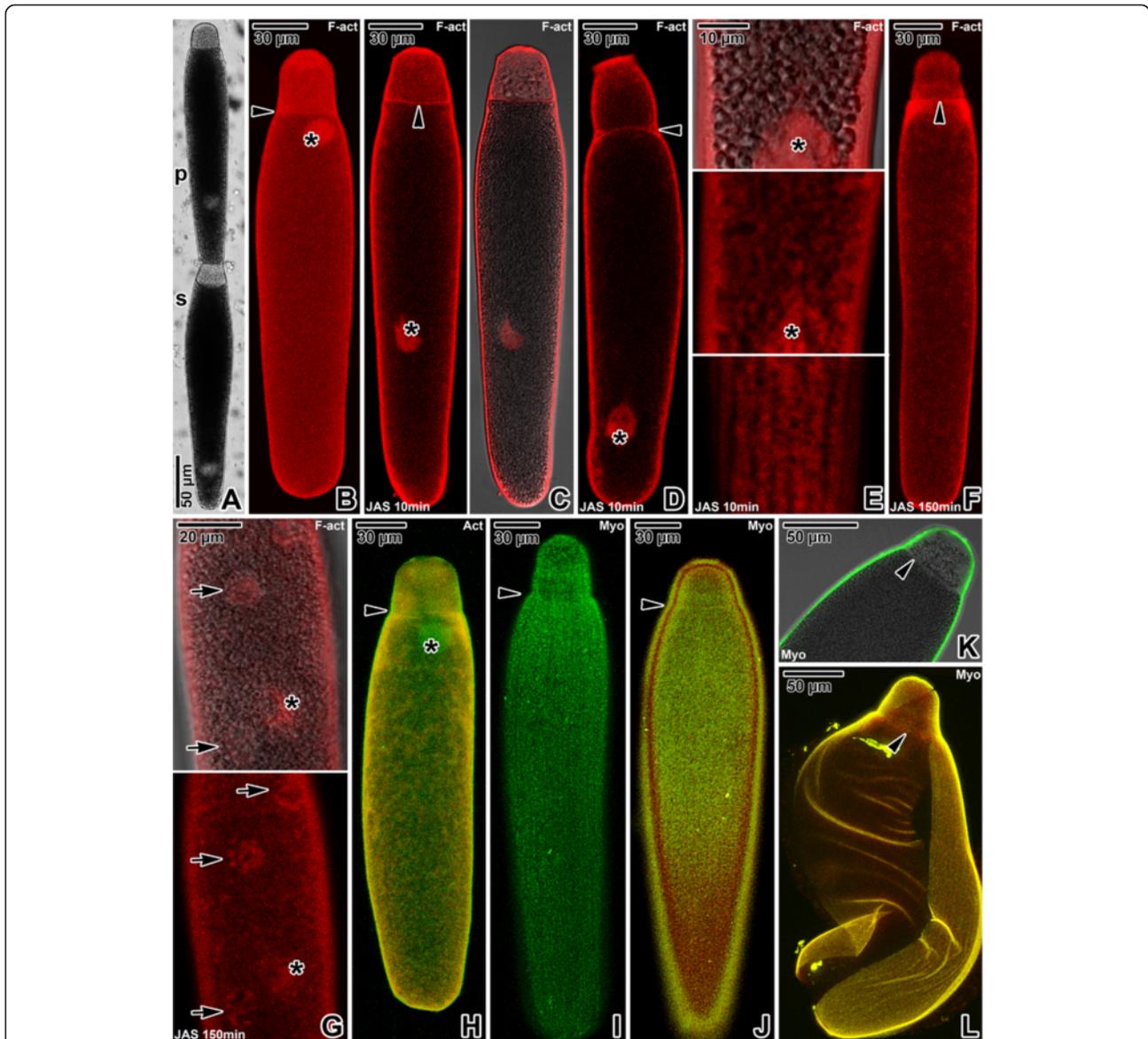
Figure 2 Actin and myosin in *Gregarina polymorpha* gamonts. A. Gamonts in syzygy; primite (p), satellite (s). LM, transmitted light. **B**. F-actin localisation in a gamont; nucleus (asterisk), septum (arrowhead). CLSM, phalloidin-TRITC. **C-D**. F-actin localisation in gamonts (previously associated in syzygy) treated for 10 minutes with 10 μM JAS. The more intense labelling is restricted to the cortex; septum (arrowhead), nucleus (asterisk). Figure **C** shows a primite. CLSM (left) and merged CLSM/transmitted light (right), phalloidin-TRITC. Figure **D** shows a satellite. CLSM, phalloidin-TRITC. **E**. The deutomerite of a gamont treated for 10 minutes with 10 μM JAS. F-actin localisation corresponds to the cortex; nucleus (asterisk). Upper two figures show the gamont middle plane; lower figure shows the cortex in the area of epicytic folds. Merged CLSM/transmitted light (upper) and CLSM, phalloidin-TRITC. **F**. F-actin localisation in a gamont treated for 150 minutes with 10 μM JAS, showing decreased labelling of cortex and septum (arrowhead). Numerous cytoplasmic F-actin aggregations give the labelling homogenous appearance. CLSM, phalloidin-TRITC. **G**. The deutomerite of a gamont treated for 150 minutes with 10 μM JAS; rosette-like aggregations of F-actin (arrows), nucleus (asterisk). Merged CLSM/transmitted light (upper) and CLSM (lower), phalloidin-TRITC. **H**. Actin localisation in a gamont; nucleus (asterisk), septum (arrowhead). The indistinct labelling (green) is more evident in the cortex covering the anterior part of cell. CLSM, IFA. **I–J**. Myosin localisation in a gamont. The labelling is restricted to the cortex, with a pattern of longitudinal rows; septum (arrowhead). CLSM, IFA. **K**. The anterior part of the gamont shown in J. Myosin localisation is restricted to the cortex, but not to the septum (arrowhead). Merged CLSM/transmitted light, IFA. **L**. Myosin localisation in a gamont ghost; septum (arrowhead). CLSM, IFA. Figures **H**, **J** and **L** show merged FITC (antibody) and rhodamine (counterstaining with Evans blue) fluorescence channels.

was accompanied by an obvious decrease of diffuse F-actin in all analysed gregarines. The localisation of F-actin did not significantly change even after 150 minutes incubation in 10 μM JAS, when gregarines completely stopped their movement and showed obvious cellular changes, but the intensity of cell cortex labelling significantly decreased and numerous small aggregations of F-actin appeared in the cell cytoplasm (Figures 1F-G, 2F-G and 3E). The transverse
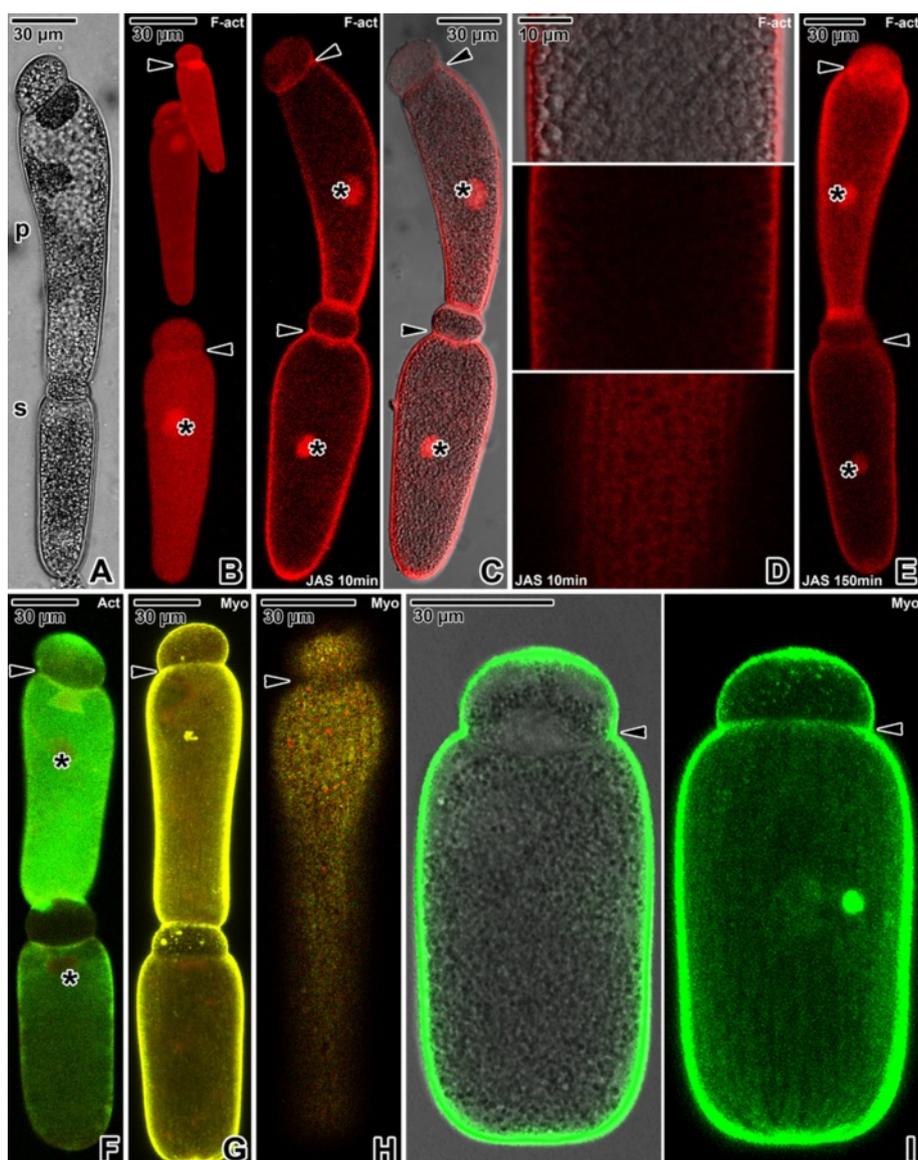
Figure 3 Actin and myosin in *Gregarina steini* gamonts. A. Gamonts associated in syzygy; primite (p), satellite (s). LM, transmitted light.
B. Localisation of F-actin in three single gamonts; nucleus (asterisk), septum (arrowheads). CLSM, phalloidin-TRITC. **C**. Localisation of F-actin in gamonts associated in syzygy treated for 10 minutes with 10 μM JAS. The intense labelling is restricted to the cortex, septum (arrowheads) and nucleus (asterisks). CLSM (left) and merged CLSM/transmitted light (right), phalloidin-TRITC. **D**. The deutomerite of a gamont treated for 10 minutes with 10 μM JAS. The localisation of F-actin corresponds to the cortex. Upper two figures show the gamont middle plane; lower figure is a view of the cortex in the area of epicytic folds. Merged CLSM/transmitted light (upper) and CLSM, phalloidin-TRITC. **E**. Localisation of F-actin in gamonts associated in syzygy treated for 150 minutes with 10 μM JAS. Note the decreased labelling of cell cortex and septum (arrowheads); nucleus (asterisks). Numerous indistinct, small cytoplasmic aggregations of F-actin give the labelling a more homogenous appearance. CLSM, phalloidin-TRITC. **F**. Actin localisation in gamonts associated in syzygy; nucleus (asterisks). The septum (arrowhead) exhibits an intense labelling. CLSM, IFA. **G**. Myosin labelling in gamonts associated in syzygy; septum (arrowhead). CLSM, IFA. **H**. An optical plane of the gamont cortex showing the distribution of myosin corresponding to the epicytic folds; septum area (arrowhead). CLSM, IFA. **I**. Myosin localisation in a single gamont. The labelling is restricted to the cortex and exhibits a pattern of longitudinal rows. A slight labelling in the septum area is shown (arrowhead). Merged CLSM/transmitted light (left) and CLSM (right), IFA. Figures **F**, **G** and **H** show merged FITC (antibody) and rhodamine (counterstaining with Evans blue) fluorescence channels.

actin filaments in epicytic folds appeared to fuse into a homogeneous layer. In *G. polymorpha*, rosette-like aggregations of F-actin were situated in the cell periphery (Figure 2G).

Gamonts stained with the specific anti-actin antibody (known to recognise the actin in *Toxoplasma* and *Plasmodium*) exhibited a similar actin localisation, however, in comparison with the phalloidin-stained specimens, only slight labelling of actin was associated with the cell cortex and the septum in *G. cuneata* (Figure 1H–I) and *G. polymorpha* (Figure 2H). Gamonts of *G. steini*

exhibited a higher intensity of actin labelling with this antibody, and gamonts associated in syzygy labelled with a different intensity in that a higher concentration of actin was observed in the primite (Figure 3F).

Similarly to actin, the myosin was restricted to the cell cortex (Figures 1J–L, 2I–L and 3G–I), but no specific labelling corresponding to the septum was observed. When focussing on the gregarine surface, the organisation of myosin exhibited a pattern of longitudinal rows corresponding to the epicytic folds (Figures 1L, 2I–J and 3H-I). The primites and satellites in syzygies (Figure 3G) exhibited more or less identical intensity of labelling.

The results of immunofluorescent labelling using an anti-α-tubulin antibody were negative (data not shown) in agreement with the absence of subpellicular microtubules.

Mucus shedding

Only phase contrast microscopy was able to show mucus shedding and trail formation of gamonts gliding on agar (Figure 4A–F). The most evident mucous trails were that of associated (Figure 4C) or single (Figure 4D) gamonts of *G. polymorpha* due to the distance travelled by them, which left long and regular mucous paths. In contrast, *G. cuneata* (Figure 4A) and *G. steini* (Figure 4E) gliding gamonts exhibited irregular and short paths containing greater accumulations of mucus, especially when these species were avoiding barriers or altering direction (Figure 4B and F).

The mucous substances were visualized by Alcian blue staining within the gamont cytoplasm (Figure 4G–I). The most intense labelling occurred in the deutomerite cytoplasm of *G. polymorpha* (Figure 4H). In contrast to *G. cuneata* (Figure 4G) and *G. steini* (Figure 4I), this gregarine showed an increased volume of mucus in the protomerite cytoplasm, which might be correlated with the increased motility of the *G. polymorpha* protomerite.

Ultrastructural features of the pellicle

The pellicle in all the species was organised in numerous longitudinal narrow folds, which were more raised in the deutomerite region than in the protomerite. The epicytic folds of the deutomerite were more or less undulated, depending on the species. Similarly, the number of epicytic folds per square micrometer varied among species, and their number did not significantly changed in the course of gamont growth (Table 4). The gamonts *G. cuneata* were covered by almost linear folds and numerous mucus-like drops were often present in the grooves separating them (Figure 5A–F). Occasionally, rings of undulated folds could be observed, especially in the posterior half of the gamont deutomerite (Figure 5E). The pellicle appeared to be slightly helically coiled along the gregarine longitudinal axis, resulting in a helical course of epicytic folds (Figure 5A, the syzygy on the right). The pellicle

of *G. polymorpha* gamonts exhibited zones of almost linear folds alternating with zones of much undulated folds; however, surprisingly when considering the results of the Alcian blue staining, only a few mucus drops could be detected (Figure 6A–E). The epicytic folds of *G. steini* were undulated in a more regular pattern than in *G. polymorpha*, and numerous mucus-like drops covered the entire surface of the gamonts (Figure 7A–G). Depending on the species, more or less evident constriction could be found at the interface between the protomerite and deutomerite; however, no interruption of folds, running from the gamont apical to its posterior end, was present in this area (Figures 5A, 6A and 7A). Syzygies were caudo-frontal, i.e. the posterior end of the primite deutomerite was joined with the apical part of the satellite protomerite (Figures 5A, 6A and 7A). The connection area appeared as a collar-like junction composed of modified epicytic folds of the primite deutomerite meshing in a gear-like manner with the folds of the sucker-like apical region of the satellite (Figures 5B–C, 6B–C and 7B–D). In *G. cuneata*, two or more satellites were often found to be associated with one primite (Figure 5A and E). In some cases, a large primite was associated with several tiny satellites (up to four satellites associated with one primite were observed). Occasionally, three individuals of *G. cuneata* were seen to be associated in a row, the last one of which was the smallest.

The folded pellicle was three-layered, composed of the superficial plasma membrane covering the entire gregarine and a middle lucent region, underlined by two distinct and tightly apposed membranes, i.e., external and internal cytomembrane, forming the inner membrane complex (IMC). Epicytic folds emerged from the peripheral ectoplasm bounding the endoplasm. Three types of associated structures were constantly present in each fold: an internal lamina, 12-nm filaments and rippled dense structures. The internal lamina, running under the IMC, not only linked the bases of epicytic folds but also bifurcated just beneath each fold, and its thinner part extended to the individual folds (Figures 5G, 6G and 7I). The localisation along with the organisation of internal lamina suggest its function in the stabilisation of individual folds as well their interconnection. The thickness of the internal lamina varied by species; i.e., 50–75 nm in *G. polymorpha* (Figure 6F–G), 17–30 nm in *G. cuneata* (Figure 5G–H) and 8–11 nm in *G. steini* (Figure 7H–I). The compact organisation of the internal lamina usually disappeared when reaching the region of 12-nm filaments. In fact, the 12-nm filaments seemed to be embedded in the widened area of the internal lamina (Figures 5G, 6G and 7I). The 12-nm filaments, exhibiting the properties of intermediate filaments, ran under the IMC along the longitudinal axis of each fold. Their numbers varied by species and developmental stage, i.e., in gamonts of
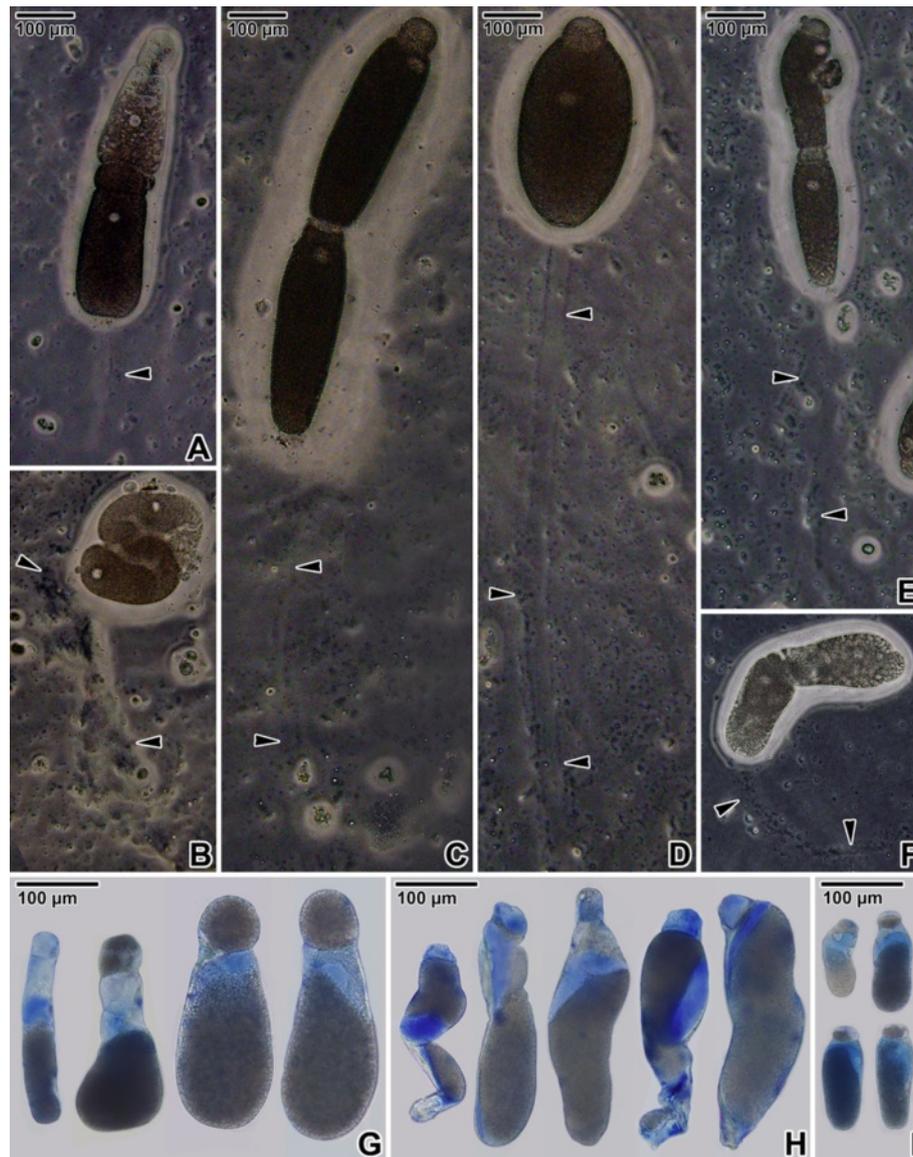
Figure 4 Gliding motility and mucus. A–F. Mucous trail (arrowheads) left behind gliding gregarines; syzygy of *Gregarina cuneata* **(A, B)**, syzygy **(C)** and single gamont **(D)** of *Gregarina polymorpha*, syzygy of *Gregarina steini* **(E, F)**. Note the increased mucus shedding by the syzygy of *G. cuneata* exhibiting rotary movement **(B)**. **G–I.** Light micrographs showing the volume of mucus in gamonts of *G. cuneata* **(G)**, *G. polymorpha* **(H)** and *G. steini* **(I)** revealed with Alcian blue staining at low pH.

Table 4 The number of epicytic folds in deutomerite of gamonts

Species	G. cuneata		G. polymorpha		G. steini	
Gamont N.	Number of folds/µm^2	Deutomerite perimeter (µm)	Number of folds/µm^2	Deutomerite perimeter (µm)	Number of folds/µm^2	Deutomerite perimeter (µm)
1	4.5	53.4	4.3	94.3	5.6	31.4
2	4.4	98.1	4.2	103.7	6.3	34.6
3	3.9	113.1	4.9	106.8	6.3	37.7
4	3.6	114.0	4.3	110.0	5.9	58.0
5	3.2	150.9	4.5	132.0	5.0	66.0
6	3.3	163.4	3.6	144.5	4.0	113.1
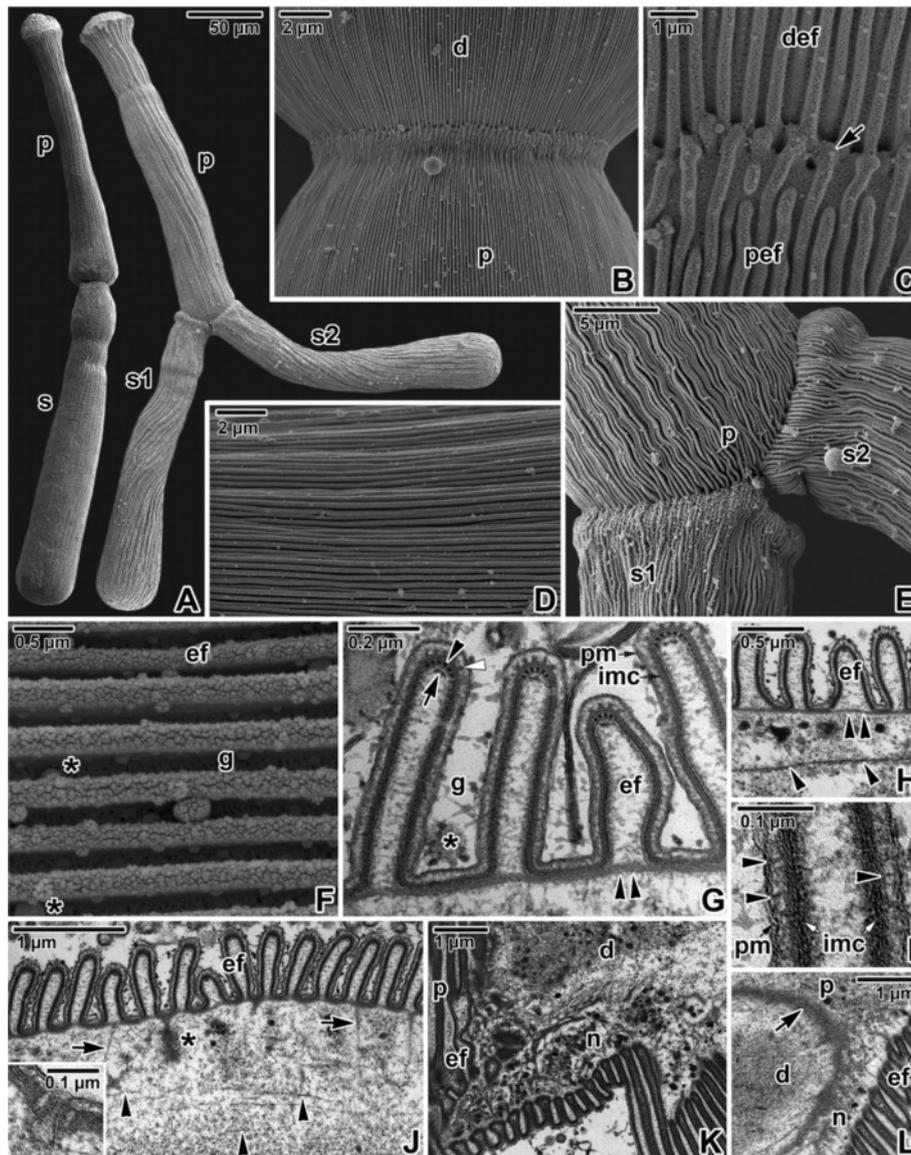
Figure 5 Pellicle architecture in *Gregarina cuneata* gamonts. A. Gamonts associated in syzygy; primite (p), satellite (s). SEM. The syzygy on the right is composed of one primite (p) and two satellites (s1, s2). **B**. Higher magnification of the junction between the posterior end of the primite deutomerite (d) and the apical part of the satellite protomerite (p). SEM. **C**. A detail of the junction (arrow) between folded pellicles covering the primite deutomerite (def) and satellite protomerite (pef). SEM. **D**. Organisation of linear epicytic folds covering the deutomerite. SEM. **E**. Higher magnification of the junction between the primite (p) and two satellites (s1, s2) shown in panel A. SEM. **F**. A higher magnification of deutomerite epicytic folds (ef); grooves (g) between folds, mucus drops (*). SEM. **G**. Cross section of deutomerite epicytic folds; grooves (g) with mucus (*) between folds (ef), 12-nm filaments (arrowhead), inner membrane complex (imc), internal lamina (double arrowhead), plasma membrane (pm), rippled dense structures (white arrowhead), unknown dense structure (arrow). TEM. **H**. Cross section of deutomerite epicytic folds (ef); internal lamina (double arrowhead), rib-like myonemes (arrowheads). TEM. **I**. Detailed view of an epicytic fold in cross section revealing filamentous connections (arrowheads) localised between the plasma membrane (pm) and inner membrane complex (imc). TEM. **J**. Cross section showing the organisation of the deutomerite pellicle; ectoplasmic network (arrows), epicytic folds (ef), duct (*), rib-like myonemes (arrowheads). The insect shows the micropore located in the groove between two epicytic folds. TEM. **K**. Organisation of the pellicle and ectoplasmic network (n) during gregarine movement; epicytic folds (ef), deutomerite (d), protomerite (p). TEM. **L**. Higher magnification of a septum (arrow) separating the protomerite (p) from the deutomerite (d); epicytic folds (ef). Note the ectoplasmic network (n) connected to the septum. TEM.

G. cuneata up to 7 (Figure 5G) and in *G. polymorpha* up to 10 filaments were observed (Figure 6G), while in *G. steini* only 2–4 filaments could be seen (Figure 7I). Their number increased with fold maturation, i.e., new rising folds contained fewer filaments than the older and evidently higher epicytic folds. Rippled dense structures, located between the plasma membrane and IMC, appeared as electron-dense, triangle-shaped structures
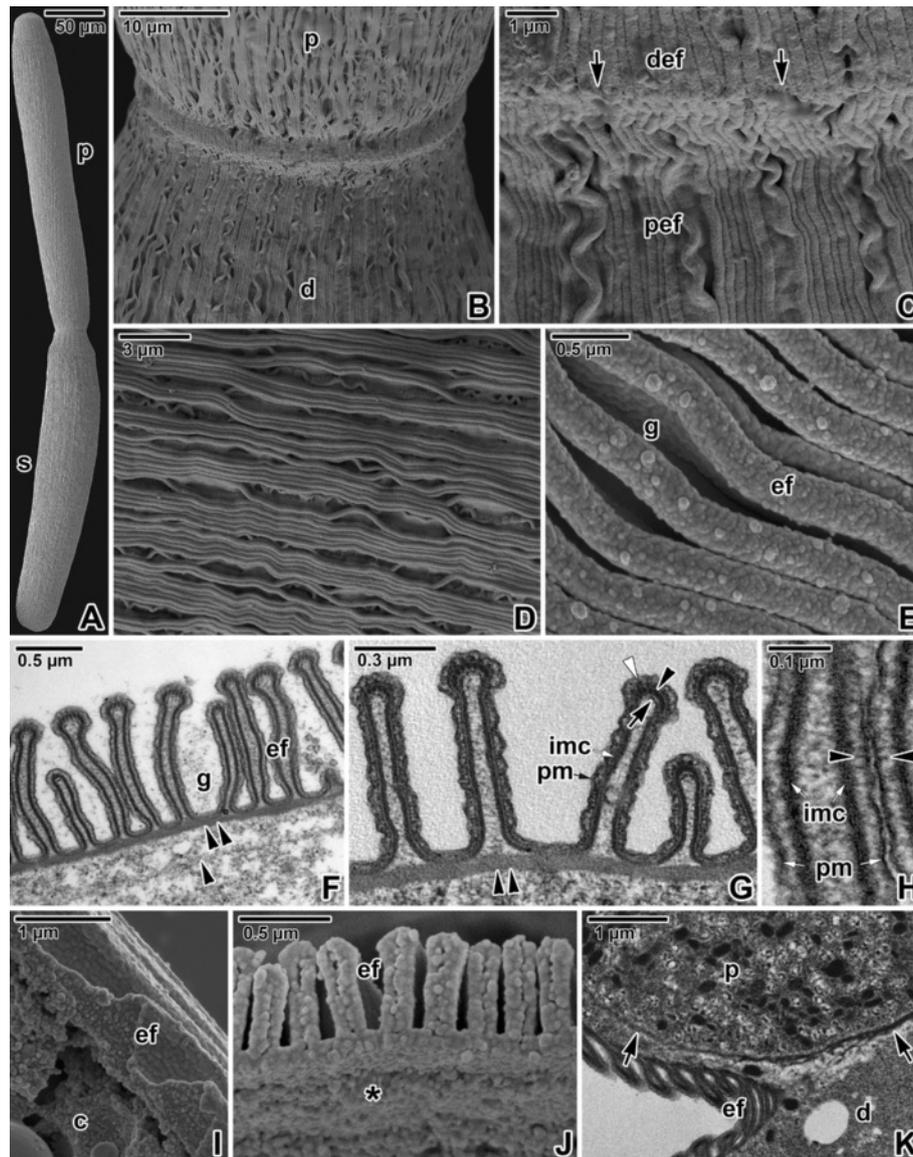
Figure 6 Pellicle architecture in *Gregarina polymorpha* gamonts. A. Gamonts associated in syzygy; primite (p), satellite (s). SEM. **B**. Higher magnification of the junction between the posterior end of the primite deutomerite (d) and apical part of the satellite protomerite (p). SEM. **C**. Detailed view of the junction (arrows) between folded pellicles covering the primite deutomerite (def) and the satellite protomerite (pef). SEM. **D**. Organisation of undulated epicytic folds covering the deutomerite. SEM. **E**. Higher magnification of deutomerite epicytic folds (ef); grooves (g) between folds. SEM. **F**. Cross section of the deutomerite pellicle; epicytic folds (ef), grooves (g), internal lamina (double arrowhead), rib-like myonemes (arrowhead). TEM. **G**. Cross section of deutomerite epicytic folds; 12-nm filaments (arrowhead), inner membrane complex (imc), internal lamina (double arrowhead), plasma membrane (pm), rippled dense structures (white arrowhead), unknown dense structure (arrow). TEM. **H**. Detailed view of epicytic folds in cross section revealing filamentous connections (arrowheads) localised between the plasma membrane (pm) and inner membrane complex (imc). TEM. **I**. Pellicle organisation revealed in a mechanically ruptured gamont; cytoplasm (c) with ectoplasmic network, epicytic folds (ef). SEM. **J**. The view of an ectoplasmic face (*) of a pellicle separated from the gamont cytoplasm; epicytic folds (ef). SEM. **K**. The septum (arrow) separating the protomerite (p) from the deutomerite (d); epicytic folds (ef). TEM.

with base lying on the external cytomembrane and median running in between two adjacent 12-nm filaments. Their number varied by species and developmental stages, in correlation with the number of 12-nm filaments (Figures 5G, 6G and 7I). Unknown dense and usually half-moon-shaped structures underlined the 12-nm

filaments at their cytoplasmic face in all gregarines. This structure achieved its maximum length in *G. polymorpha*, in which its ends were in obvious contact with the internal lamina extending to the top of the fold (Figure 6G). In *G. cuneata*, this structure was evidently shorter and thicker (Figure 5G), and in *G. steini* it was shortest and in
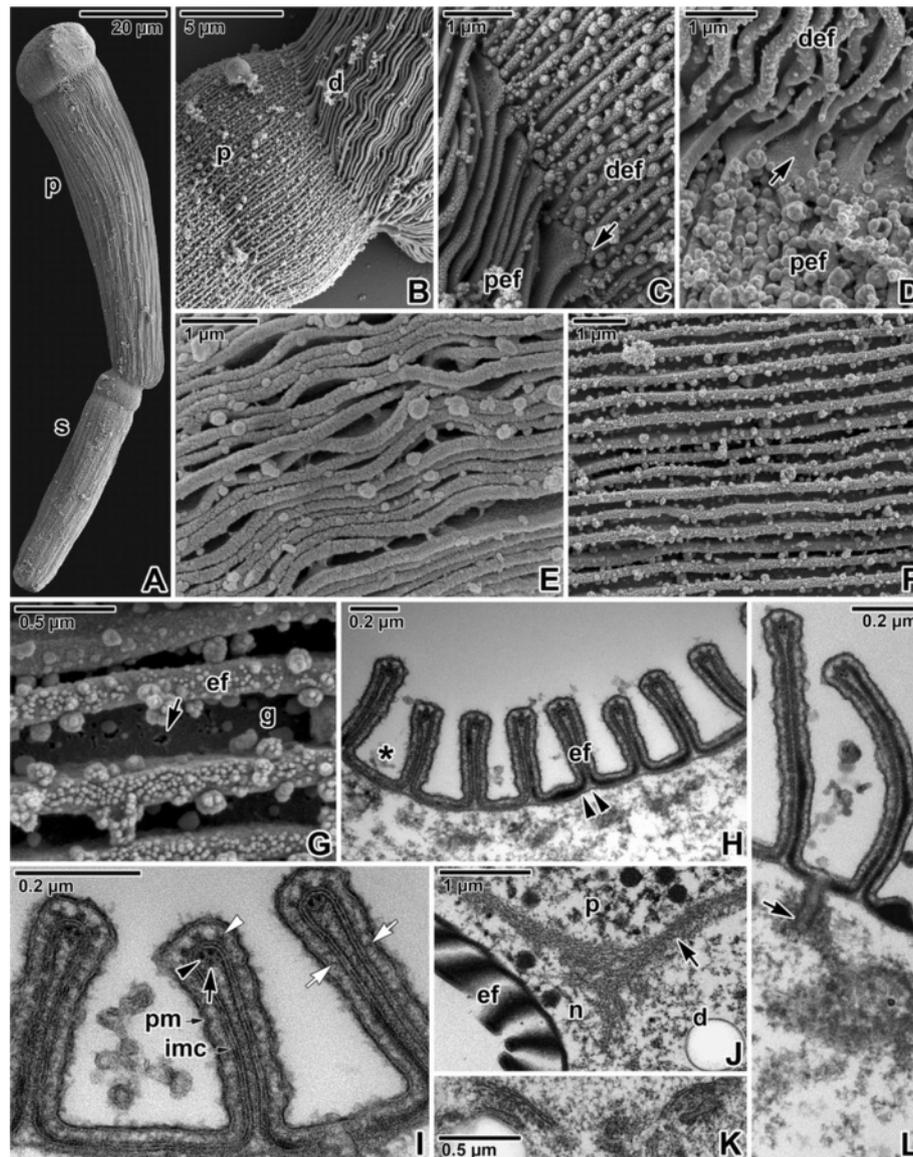
Figure 7 Pellicle architecture in *Gregarina steini* gamonts. A. Gamonts associated in syzygy; primite (p), satellite (s). SEM. **B**. Higher magnification of the junction between the posterior end of the primite deutomerite (d) and apical part of the satellite protomerite (p). SEM. **C**, **D**. Detailed views of the junction (arrow) between folded pellicles covering the primite deutomerite (def) and satellite protomerite (pef). SEM. **E**, **F**. Organisation of more and less undulated epicytic folds covering the deutomerite. SEM. **G**. Higher magnification of deutomerite epicytic folds (ef); grooves (g) between folds, pore-like structure (arrow). SEM. **H**. Organisation of the deutomerite pellicle in cross section; epicytic folds (ef), grooves with mucus (*), internal lamina (double arrowhead). TEM. **I**. Cross section of deutomerite epicytic folds. Note the filamentous connections (white arrows) localised between the plasma membrane (pm) and inner membrane complex (imc); 12-nm filaments (arrowhead), rippled dense structures (white arrowhead), unknown dense structure (arrow). TEM. **J**. The septum (arrow) and ectoplasmic network (n); deutomerite (d), epicytic folds (ef), protomerite (p). TEM. **K**. Golgi apparatus in deutomerite cytoplasm. TEM. **L**. The duct (arrow) opening outwards to the groove between epicytic folds. TEM.

some sections it was even reversed with its ends facing the apical top of the fold (Figure 7I). As the internal lamina lacked its typical compact look in this area, it is possible that the mentioned half-mooned structures represent its component. Careful analysis of the pellicle covering the lateral part of epicytic folds revealed novel thin filamentous connections interconnecting the IMC and the plasma membrane (Figures 5I, 6H and 7I).

In addition to structures restricted to the epicytic folds, an ectoplasmic network and rib-like myonemes, present to some degree in the deutomerite ectoplasm of all studied species, could be observed in some ultrathin

sections. The ectoplasmic network contacting the bases of the epicytic folds was most prominent in fully matured gamonts of *G. cuneata* (Figure 5J–L), especially at the septum periphery or in areas with an obviously pleated pellicle (Figure 5K). This local pleating of the pellicle seemed to be the result of gregarine movement. The rib-like myonemes, running perpendicularly to the longitudinal axis of the gregarine and located beneath the deutomerite ectoplasm, were very distinct in gamonts of *G. cuneata* (Figure 5H and J) and *G. polymorpha* (Figure 6F), but were hard to detect and often absent in *G. steini*. The septum separating the protomerite from the deutomerite was well developed in all three species (Figures 5L, 6K and 7J). The micropores, interrupting the IMC, were sometimes seen in the grooves between the folds of *G. cuneata* (Figure 5J). In addition, ducts, appearing as elongated dense sacs passing through the pellicle and opening outwards, were often present in the ectoplasm of *G. cuneata* and *G. steini* gamonts (Figures 5J and 7L).

Membranes as exposed by freeze etching

The freeze-etching technique confirmed the presence of three fracture planes in the pellicle of all analysed gregarines, corresponding to the three membranes, i.e., two cytomembranes (IMC) underlying the plasma membrane. The general aspects of the epicytic folds in freeze-fracture are shown in Figures 8, 9 and 10, and their architecture corresponded to the TEM observations. At the tip of each fold, double linear rows of tightly aligned intramembranous particles (IMP) were observed in both fractures of the external and internal cytomembranes. These rows seemed to correspond to the apical site of the 12-nm filaments and to the base of the triangle-shaped, rippled dense structures. The number of these lines roughly coincided with the number of 12-nm filaments. The freeze-etching approach proved to be a strong tool for visualisation of structures that are hardly documented on TEM micrographs including round micropores (110–130 nm in diameter) at the base of the grooves between the folds (Figures 8A, 8G, 9E, 9G and 10E) or smaller pores (35–50 nm in diameter) randomly distributed on the base or on the lateral side of the folds (Figures 8A–D, 8F-G, 9A–E, 9G, 10A, 10C and 10E–F), ducts and cisternae often connected these pores or to the pellicle (Figures 8B, 8E, 8H, 9F–G and 10A), as well as mucus drops often present in the grooves between the folds of *G. cuneata* (Figure 8B) and *G. steini* (Figure 10A–D and F).

The densities of the IMP for the fracture faces of the plasma membrane and both cytomembranes are summarised in Table 5. The density of the IMP in membranes differed in analysed gregarines; in general, the values in *G. polymorpha* were significantly lower in comparison to *G. cuneata* and *G. steini*. In *G. cuneata* and *G. polymorpha*, the IMP density in the IMC was lower than in the plasma membrane. In *G. steini*, however, the IMP density in the plasma membrane was lower than those in the IMC. The IMP in all three membranes showed a high variability in their size distribution (see histograms in Figures 11, 12 and 13); nevertheless, only particles in a range of 6–14 nm were included in statistical calculations to obtain data comparable with those previously published on other apicomplexans. Membranes forming the pellicle in *G. cuneata*, especially the plasma membrane, were the most extraordinary given the wide range of the IMP size along with its distribution (Figure 11).

Discussion

Gliding movement is a feature observed in a wide range of unicellular organisms including diatoms, flagellates, apicomplexan zoites, and gregarines. The speed of these organisms varies along with the special locomotive structures and is affected mostly by their physiological status and surrounding environmental conditions. The reported motility rates in Apicomplexa are usually in the range of 1–10 μm/s, and the maximal rate was observed in gregarines [34]. To minimise a potential effect of different environmental conditions on gregarine motility in this study, we took advantage of a naturally mixed infection with three *Gregarina* species occurring in the intestine of larval mealworms kept under laboratory conditions. In addition, the experimental part of this work, including the light microscopic observations on gliding and treatment of living gamonts with JAS and cytochalasin D, has been performed on suspensions consisting of all three species (often from a single host). Göhre [35] states that gregarines parasitising the intestine of larval *T. molitor* are distributed based on intestinal pH, i.e., *G. cuneata* inhabits a part of the intestine with pH 4.5–5.5, and *G. steini* (pH 5.5–8.2) inhabits a part of the intestine together with *G. polymorpha* (pH 6.4–7.5). Therefore, it could be expected that the mixed suspensions of gamonts are not preferable for motility assays, nevertheless, pH-restricted localisation of gregarines in mealworms applies only to attached trophozoites [36] not to gamonts that are usually found in luminal part of the mesenteron. During our observations, eugregarines isolated from one host were gliding at speeds ranging from 0.38 to 22.86 μm/s, while the highest speed was reached by gamonts of *G. polymorpha* and the lowest by *G. cuneata*. To explain these evident differences study focussed on structures that were generally considered to be responsible for gregarine gliding - epicytic folds and mucus. Longitudinal folds formed by the pellicle represent the most conspicuous feature differentiating eugregarine trophozoites and gamonts from the other apicomplexans. The presence of the swellings along
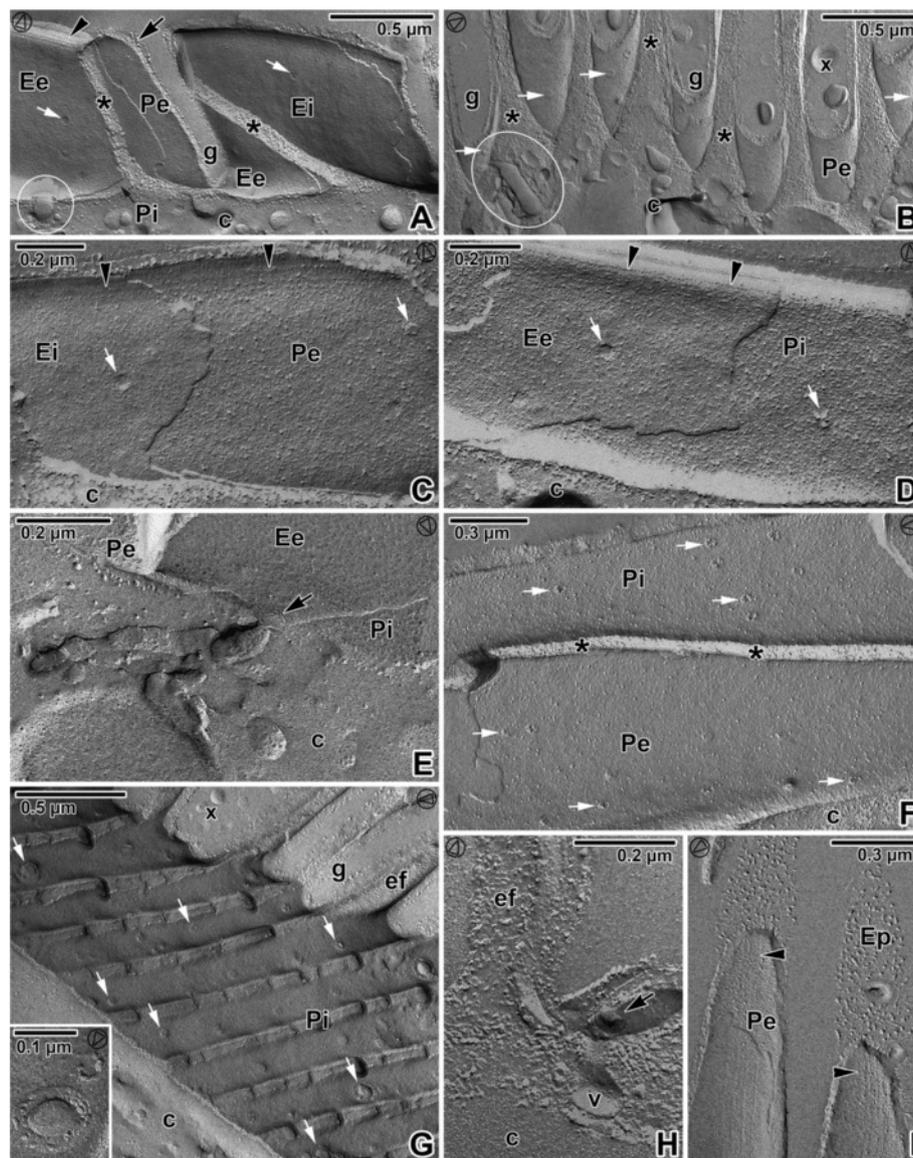
Figure 8 Pellicle organisation in *Gregarina cuneata* gamonts as revealed by the freeze-etching. A. The general view of fractured epicytic folds; cytoplasm (c), micropore (encircled), cytoplasm of folds (*), groove (g), EF face of external cytomembrane (Ee), EF face of internal cytomembrane (Ei), IMP alignments (arrowhead), PF face of external cytomembrane (Pe), PF face of internal cytomembrane (Pi), plasma membrane (arrow), pores (white arrows). **B**. The base of the epicytic folds; cytoplasm of folds (*), deutomerite cytoplasm (c), duct (encircled), grooves (g), mucus (x), PF face of the external cytomembrane (Pe), pores (white arrows). **C, D**. The fracture of the epicytic fold; cytoplasm (c), EF of the external cytomembrane (Ee), EF face of the internal cytomembrane (Ei), PF face of the external cytomembrane (Pe), PF face of the internal cytomembrane (Pi), pores (white arrows), IMP alignments (arrowheads). **E**. The base of the fold with a duct opening outwards (arrow) to the groove; deutomerite cytoplasm (c), EF of the external cytomembrane (Ee), PF face of the external cytomembrane (Pe), PF face of the internal cytomembrane (Pi). **F**. The longitudinal fracture of the fold; cytoplasm (c), cytoplasm of fold (*), PF face of the external cytomembrane (Pe), PF face of the internal cytomembrane (Pi), pores (white arrows). **G**. The grooves (g) between the folds (ef); cytoplasm (c), mucus (x), numerous pores (some of them are shown by white arrows), PF face of the external cytomembrane (Pi). The inset shows a micropore and a pore of smaller size. **H**. A detail of the grove between folds (ef) showing the part of micropore (arrow) with vesicle (v); deutomerite cytoplasm (c). **I**. The top of the fold; EF face of the plasma membrane (Ep), IPM alignments (arrowheads), PF face of the external cytomembrane (Pe). The arrowhead in the circle shows the direction of shadowing.

the longitudinal epicytic folds of gliding gregarines suggests that these structures, pushed against the substrate, may provide the force for gliding [33], and the mucus seems to enhance the efficiency of their interaction with

the substrate to produce gregarine forward movement. It is important, however, to mention that gregarine gamonts in performed experiments were able to move without any contact with the substrate when put in a drop of Ringer's
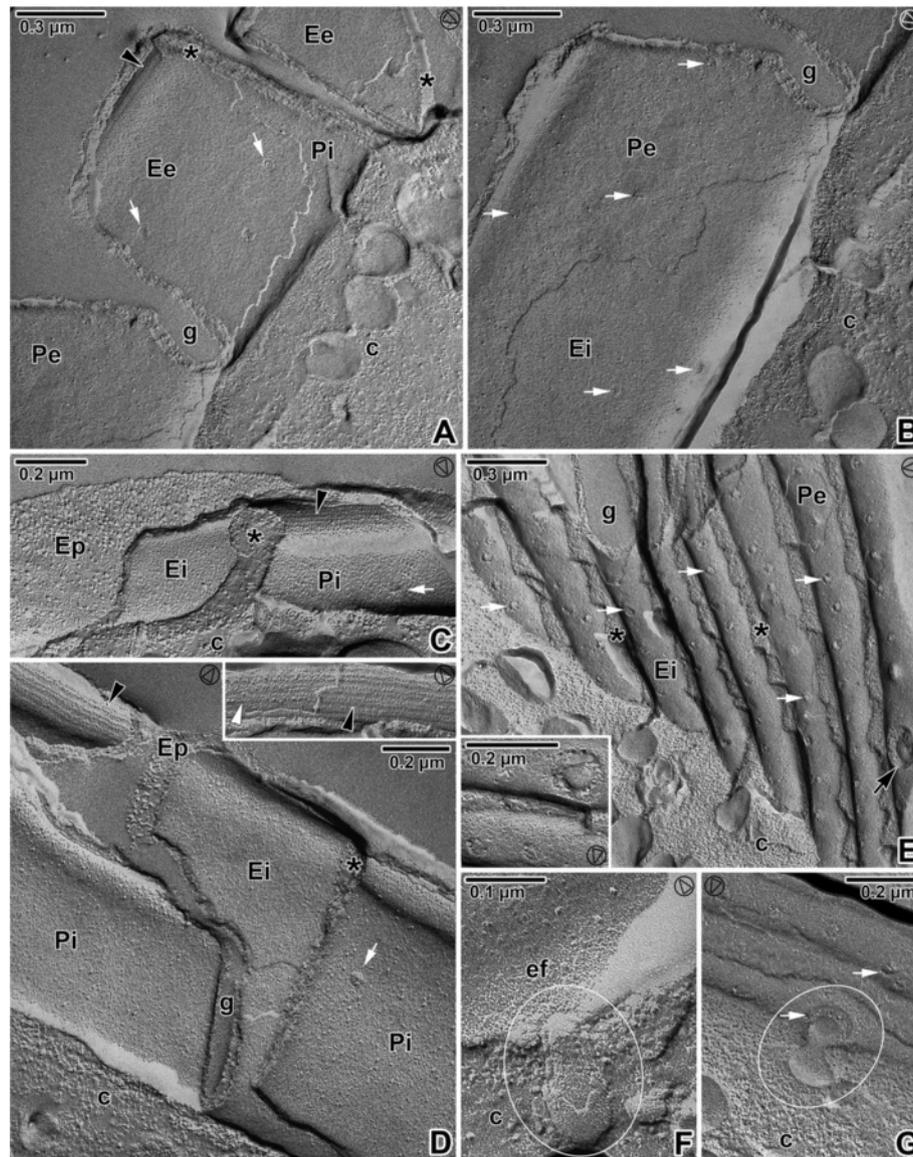
Figure 9 Pellicle organisation in *Gregarina polymorpha* gamonts as revealed by the freeze-etching. A. The general view of fractured epicytic folds; cytoplasm of folds (*), deutomerite cytoplasm (c), EF face of external cytomembrane (Ee), IMP alignments (arrowhead), groove (g), PF face of external cytomembrane (Pe), PF face of internal cytomembrane (Pi), pores (white arrows). **B**. The fractured epicytic fold; deutomerite cytoplasm (c), EF face of the internal cytomembrane (Ei), groove (g), PF face of the external cytomembrane (Pe), pores (white arrows). **C**. The fracture of the lower epicytic fold; cytoplasm of folds (*), deutomerite cytoplasm (c), EF face of the internal cytomembrane (Ei), EF face of the plasma membrane (Ep), IMP alignments (arrowhead), PF face of the internal cytomembrane (Pi), pore (white arrow). **D**. The fracture of higher epicytic folds; cytoplasm of folds (*), deutomerite cytoplasm (c), EF of the internal cytomembrane (Ei), EF of the plasma membrane (Ep), groove (g), IMP alignments (arrowhead), PF face of the internal cytomembrane (Pi), pore (white arrow). The inset shows the IMP alignments located on the EF face of the external cytomembrane (white arrowhead) and on the PF of the internal cytomembrane (arrowhead) at the top of the epicytic fold. **E**. The grooves (g) between epicytic folds with numerous pores (some of them shown by white arrows); cytoplasm of folds (*), deutomerite cytoplasm (c), EF face of the internal cytomembrane (Ei), PF face of the external cytomembrane (Pe). Note the large opened micropore (arrow). The inset shows a micropore and three pores of different sizes. **F**. The base of the epicytic fold (ef) with a duct (encircled); cytoplasm (c). **G**. The base of the epicytic folds showing the micropore connected to a vesicle (encircled); cytoplasm (c), pores (white arrows). The arrowhead in the circle shows the direction of shadowing.

solution, i.e., for approximately 30 min, they were floating in a liquid until sinking to the surface of microscopic slide. These observations conflict with the supposed need of their contact with some solid matter [37]. Although some correlations can be found between speed and the number of epicytic folds, i.e., gamonts of *G. cuneata* are quipped by fewer folds (3.2–4.5) per square micrometer than small gamonts of *G. steini* (4.0–6.3) or similarly-sized gamonts
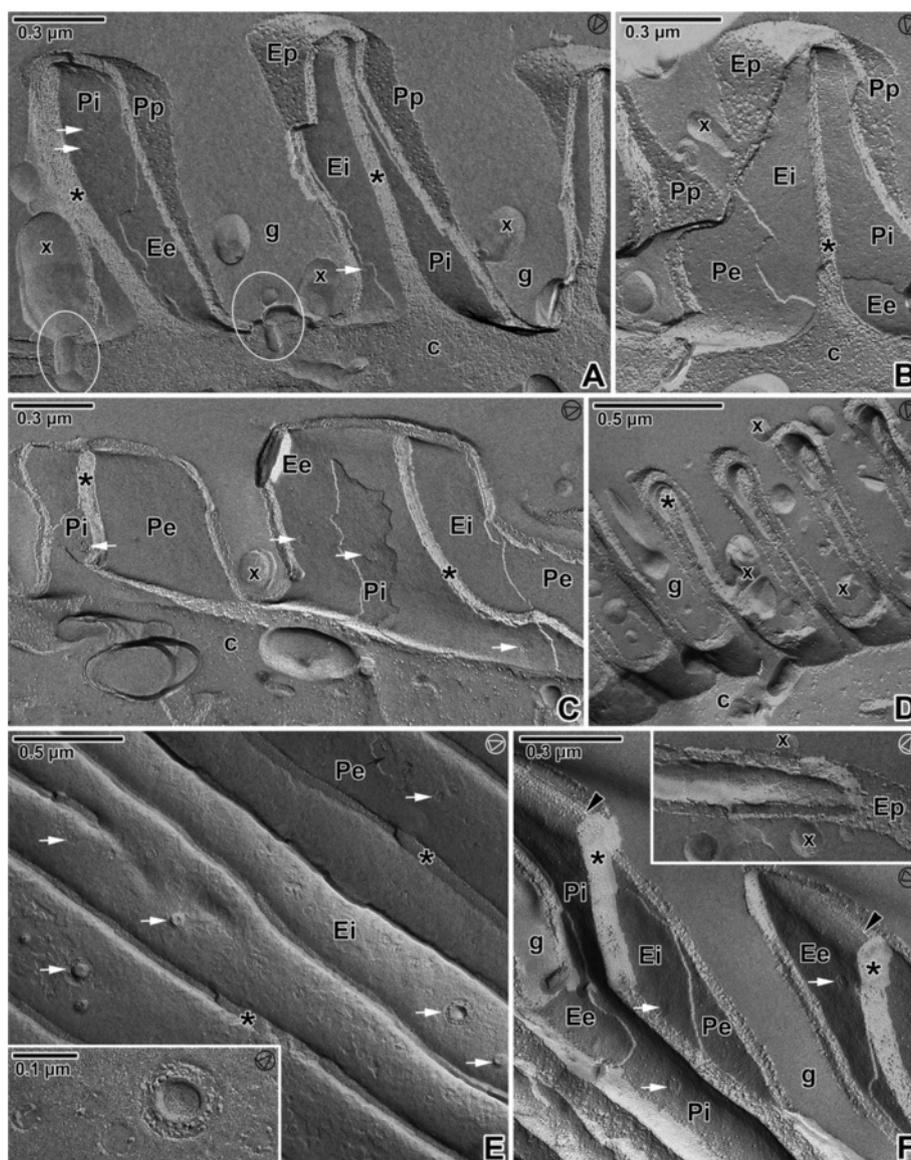
Figure 10 Pellicle organisation in *Gregarina steini* gamonts as revealed by the freeze-etching. A–C. Fractured epicytic folds; cytoplasm of epicytic folds (*), deutomerite cytoplasm (c), ducts (encircled), EF face of the external cytomembrane (Ee), EF face of the internal cytomembrane (Ei), EF face of the plasma membrane (Ep), groove (g), mucus (x), PF face of the external cytomembrane (Pe), PF face of the internal cytomembrane (Pi), PF face of the plasma membrane (Pp), pores (white arrows). **D**. General view of the epicytic folds showing the grooves (g) with mucus drops (x); cytoplasm of epicytic folds (*), deutomerite cytoplasm (c). **E**. The cytoplasmic face of the grooves between epicytic folds with micropores and numerous pores (some of them shown by white arrows); cytoplasm of epicytic folds (*), EF face of the internal cytomembrane (Ei), PF face of the external cytomembrane (Pe). The inset shows the detailed view of micropore and four pores of different sizes. **F**. Fractured epicytic folds showing their IMP alignments (arrowheads) located on the PF of the internal cytomembrane (Pi) and on the EF face of the external cytomembrane (Ee); cytoplasm of epicytic folds (*), EF face of internal cytomembrane (Ei), grooves (g), PF face of external cytomembrane (Pe), pores (white arrows). The inset shows EF of the plasma membrane (Ep) with mucus drops (x). The arrowhead in the circle shows the direction of shadowing.

of *G. polymorpha* (3.6–4.9), these differences were only slight and we do not consider them to significantly influence the gliding rate. More important, however, seem to be undulations of folds documented by SEM. In accordance with Vávra and Small [24], the folds of glutaraldehyde-fixed *G. cuneata* were almost linear, forming occasional rings of undulated folds, while the pellicle of *G. polymorpha* formed zones of undulated as well as almost linear folds, and the folds in *G. steini* were undulated in quite a regular pattern. Microscopic observations indicate that the lateral undulations of folds arise during gliding. Nevertheless, the question of whether epicytic folds might be responsible for

Table 5 A protein particle density in the fracture faces of the membranes of studied gregarines

Species		*Gregarina cuneata*		*Gregarina polymorpha*		*Gregarina steini*	
Membrane	Face	Density = number of particles/μm^2 (± SE)	Kp	Density = number of particles/μm^2 (± SE)	Kp	Density = number of particles/μm^2 (± SE)	Kp
Plasma membrane	PF	2244 ± 283	0.81	1446 ± 158	0.59	2265 ± 154	1.27
	EF	2770 ± 96		2473 ± 147		1783 ± 233	
External cytomembrane	PF	1420 ± 190	1.13	602 ± 265	0.70	2588 ± 189	0.68
	EF	1260 ± 211		863 ± 202		3820 ± 211	
Internal cytomembrane	PF	1993 ± 253	1.33	1276 ± 200	1.57	2339 ± 132	1.24
	EF	1502 ± 273		814 ± 246		1886 ± 274	

The size of IMP is in range 6-14 nm.
Kp partition coefficient defined as the ratio of number of particles per μm^2 in the PF face/number of particles per μm^2 in the EF face.
SE standard error.

gliding in gregarines can be satisfactorily answered only after careful analysis of all subcellular components forming the complicated pellicle in gregarines.

The 'glideosome' concept and eugregarine gliding
First, it must be highlighted that no similar structures resembling epicytic folds can be found on the surface of the zoite stage (e.g., sporozoites in gregarines or *Plasmodium*, tachyzoites of *Toxoplasma*), which are used to illustrate the mechanism of gliding motility in apicomplexans. The concept of the 'glideosome' [4] describes apicomplexan zoites as actively entering host cells and moving by a substrate-dependent gliding motility, which requires coordinated interactions between parasite surface adhesins and its cytoskeleton. This machinery is considered an unusual form of eukaryotic locomotion. The so-called actomyosin motor, which is generally assumed to be embedded between the plasma membrane and the IMC, consists of immobilised unconventional myosins, short actin stubs, and TRAP-family invasins. This motor is expected to be oriented by subpellicular microtubules [38]. Micronemal proteins, inserted into the plasma membrane, are carried along the IMC by the motor and interact with the parasite substrate, or associate with a GPI-anchored protein interacting with the substrate, resulting in gliding [38].

Considering the possible application of this concept for eugregarine gliding, the first striking inconsistency is the fact that in the eugregarines analysed here, there are no subpellicular microtubules in the epicytic folds (confirmed also by negative results of immunolabelling). Thus, a question arises concerning the real motor in their motility. It could be expected that enigmatic 12-nm filaments, running under the IMC and exhibiting the properties of intermediate filaments [34,39], could support the actomyosin motor in a similar way. Longitudinal arrays of IMP found in the area of the 12-nm filaments and the rippled dense structures [11,22,30,40] are comparable to the lines of higher particle density overlaying the subpellicular microtubules in *Eimeria* or *Plasmodium*

sporozoites [41,42]. Our data show, however, that the number of 12-nm filaments does not influence the speed of gregarine gliding (up to 7 filaments in *G. cuneata* vs. 10 filaments in *G. polymorpha* and maximally 4 filaments in *G. steini*), but rather seem to control the direction of movement. Indeed, despite folds equipped by a low number of 12-nm filaments, gamonts of *G. steini* glided with relatively high speed, but their gliding path was rather widely semi-circular than linear. The question remains whether apical rippled dense structures, with their base located at the external cytomembrane, serve as supporting elements interconnecting 12-nm filaments and the plasma membrane. Such speculation is supported by the existence of filamentous interconnections occasionally observed between their tips and the plasma membrane in ultrathin sections [39]. The half-moon-shaped dense structure underlining the 12-nm filaments could play the role of a 'skeleton' reinforcing the tips of folds, which contact the substrate during gliding.

The apicomplexan gliding motility relies on the dynamic turnover of actin, the polymerisation of which is controlled by a number of regulators. A general model for the organisation of the apicomplexan actomyosin motor depicts actin filaments lying in the space between the parasite IMC and plasma membrane, parallel to the plasma membrane [43]. In gregarines, actin is generally expected to be localised in the epicytic folds [20,27]. Using a specific anti-actin antibody known to recognise the actin in *Toxoplasma* and *Plasmodium*, actin in all three gregarine species was localised. The unusual nature of apicomplexan actin, where its unpolymerised form seems to have an increased potential to form filaments relative to vertebrate actin, is discussed elsewhere [44]. In contrast to other eukaryotic cells, which maintain comparable amounts of globular and F-actin, in *Toxoplasma* more than 97% of actin is found in its globular form and in *Plasmodium*, where more F-actin may be recovered, the filamentous fraction appears to represent a collection of short polymers [27]. The apparent lack of visible, stable filaments in apicomplexans, however, does not fit eugregarines, in

Figure 11 Histograms illustrating the IMP size distribution in *Gregarina cuneata*; protoplasmic (PF) and exoplasmic fracture (EF) faces of the plasma membrane (PM), external cytomembrane (EC), internal cytomembrane (IC). The mean diameter (nm) of IMP, with its standard error, is given for each. Ordinate - number of particles; abscissa - particle diameter in nm.
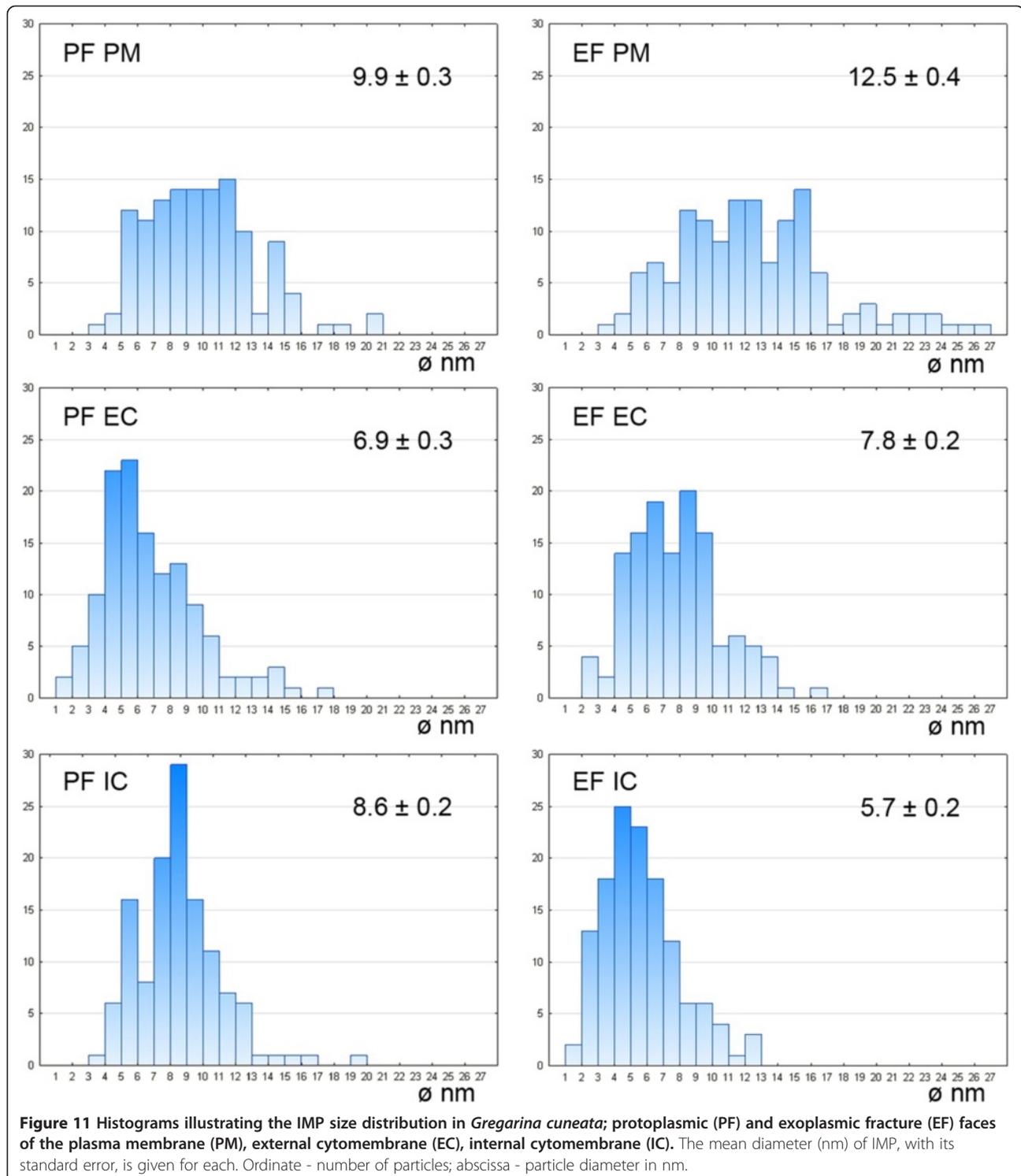
which the phalloidin labelling revealed that the presence of F-actin does not require filament-stabilising drugs [45,46]. Still, the results of JAS (a toxin that stabilizes actin filaments and induces actin polymerisation) and cytochalasin D (disrupts actin filaments and inhibits actin polymerisation) treatments are the clear evidence of an essential role of actin in eugregarine gliding. Both probes are membrane-permeable probes and thus suitable for examining actin dynamics in living cells, and are known to disrupt *Toxoplasma* motility and invasion [1]. The treatment of *Toxoplasma* tachyzoites with 1–2 μM JAS inhibited their gliding and cell invasion, but once the drug

Figure 12 Histograms illustrating the IMP size distribution in *Gregarina polymorpha*; protoplasmic (PF) and exoplasmic fracture (EF) faces of the plasma membrane (PM), external cytomembrane (EC), internal cytomembrane (IC). The mean diameter (nm) of IMP, with its standard error, is given for each. Ordinate - number of particles; abscissa - particle diameter in nm.
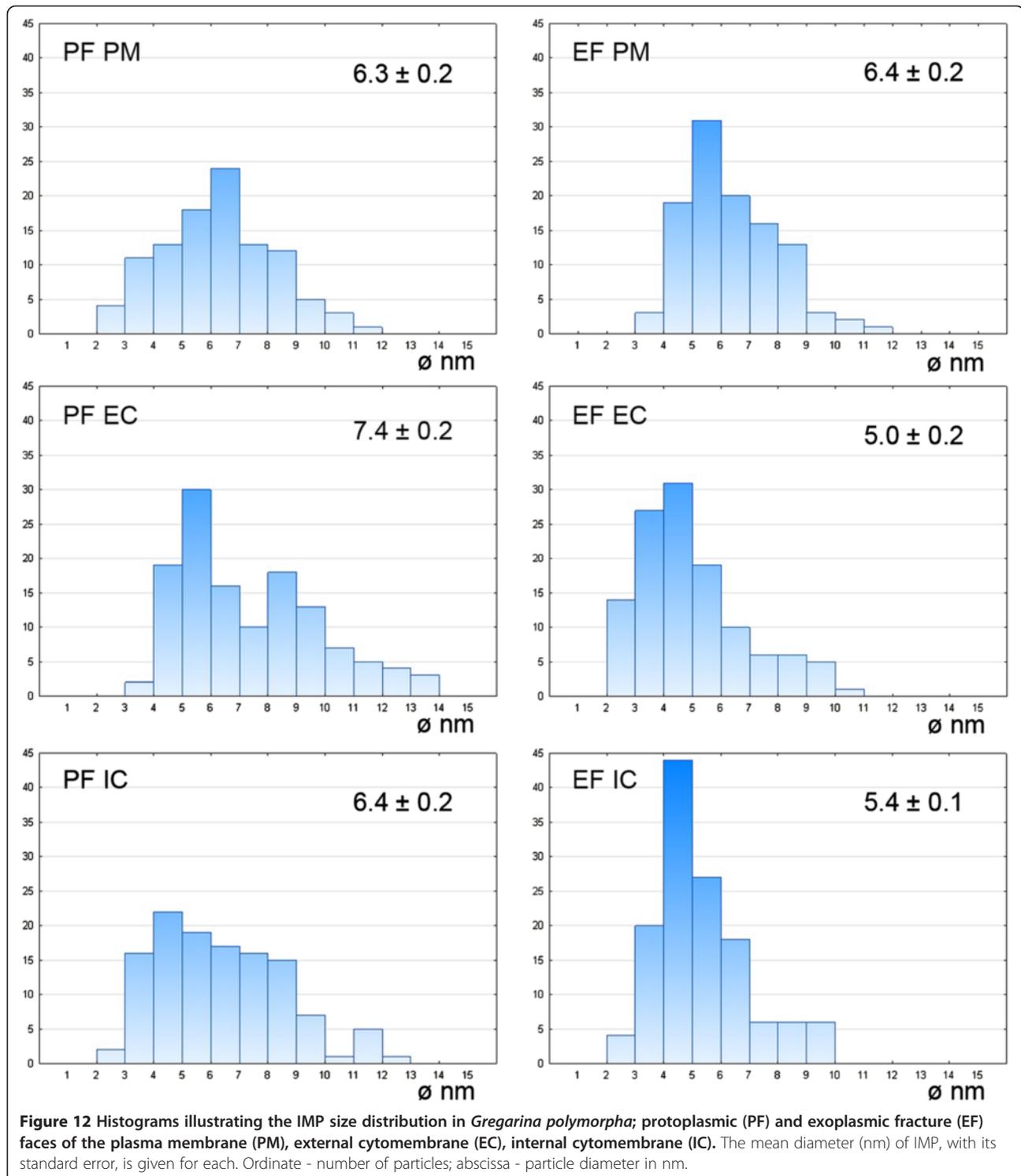
was removed the parasites were able to invade host cells [43]. Furthermore, JAS treatment increased the rate of *Toxoplasma* gliding [43], indicating that filaments are rate-limiting for motility and also caused frequent reversals of direction [3]. In *Eimeria* sporozoites, the inhibitor of actin polymerisation, cytochalasin B, reversibly

inhibited the gliding; nevertheless, the bending was only slightly less [47]. In agreement with these studies, the treatment of living gregarines with JAS and cytochalasin D suspended their gliding motility, and they were able to recover after returning to normal physiological conditions in insect saline. In spite of high doses of both probes used

Figure 13 Histograms illustrating the IMP size distribution in *Gregarina steini*; protoplasmic (PF) and exoplasmic fracture (EF) faces of the plasma membrane (PM), external cytomembrane (EC), internal cytomembrane (IC). The mean diameter (nm) of IMP, with the standard error, is given for each. Ordinate - number of particles; abscissa - particle diameter in nm.
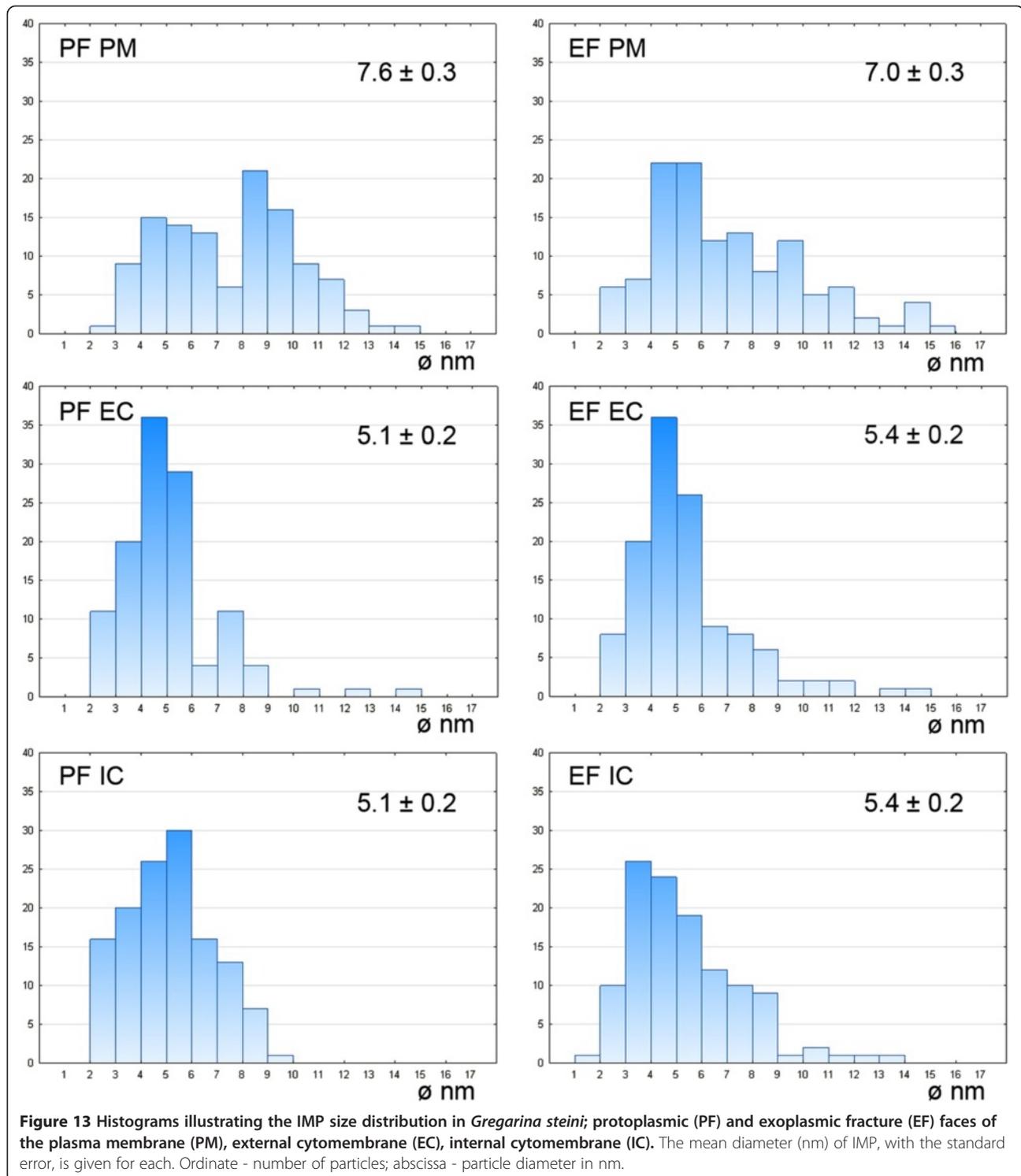
in this study, prolonged incubations were necessary to inhibit gregarine gliding completely. Similar to *Toxoplasma* tachyzoites [43], JAS application led to an initial increased gliding activity, which gradually decreased until complete blocking. In contrast, reversals or changes of gliding direction and apical protrusion were not observed

in gregarine gamonts. Interestingly, an enhanced deposition of actin, resembling an apical protrusion, occurred on the apical end of the migrating trophozoites of eugregarine *Ascogregarina* [48].

High concentrations of JAS can increase the density of actin filaments adjacent the plasma membrane [49].

Despite studies reporting competitive binding of JAS and phalloidin with F-actin [50], this work also revealed an increase in F-actin labelling in the cell cortex after a short treatment of living gamonts with JAS (corresponding to the period of their increased motility). These observations are supported by another study reporting that washing of cells before fixation and staining with phalloidin-TRITC to remove JAS revealed brighter staining of F-actin [51]. Prolonged treatment with JAS (until complete inhibition of gliding), however, resulted in an obvious decrease in F-actin labelling. These data concur with studies reporting that treatment of living cells with JAS causes a redistribution of their actin cytoskeleton, formation of F-actin aggregates and cell shape change, and can result in a patchy appearance of cortical actin [52]. Observations on gregarines during cytochalasin D treatment are supported by another study in which gliding was inhibited by cytochalasin B [53]. With regards to the Ca++ activation of the actomyosin system, it is interesting that the anti-psychotic drug trifluoperazine can inhibit gregarine gliding. This observation suggests that the calcium-binding protein calmodulin might affect motility even though extracellular Ca++ is not required [53].

Although the localisation of actin seems to be more diffuse in gregarines, myosin seems to be organised in longitudinal rows corresponding to epicytic folds similar to observations in *G. blaberae* [54]. The micrographs obtained with the anti-myosin antibody (smooth and skeletal, the whole antiserum from Sigma-Aldrich, Czech Republic) showed similar localization of myosin as obtained by Heintzelman with specific antibodies directed against the myosins A, B and F [20,27]. Nevertheless, the commercial antibody used in this study is developed for immunofluorescence and in the absence of conclusive results from Western Blotting this point needs further investigation. The presence of previously unreported tiny filamentous connections observed in some ultrathin sections between the plasma membrane and the IMC suggests that the actomyosin complex could be restricted to the lateral parts of the epicytic folds and, thus, this could be the source of the lateral undulations described above.

Subcortical filamentous structures

In the course of environmental adaptations, the cortex of eugregarines became very rigid and, hence, they lost the wriggling ability of archigregarines. Nonetheless, when considering active movements of the protomerite, the cellular plasticity must be relatively high. Indeed, additional but very prominent forms of motility, such as bending, curving or shortening of the longitudinal axis and intense movements of the protomerite, commonly observed in eugregarines, were attributed to the presence of contractile elements entitled 'myocyte' as early as one hundred

years ago [37]. A network of intermediate filamentous proteins can be often found associated with the gregarine cortex. Early studies reporting the filamentous character of eugregarine 'myonemes' suggest that they may consist of actin microfilaments [55], and recent studies confirmed them to be actin-rich [20]. An additional robust population of actin filaments, forming a series of annular (rib-like) myonemes girding the cell cortex, was reported from *G. polymorpha* but not seen in other apicomplexans [20,27]. Actin and myosin A were detected in both the epicytic folds and rib-like myonemes, while myosin B was exclusively restricted to folds [20]. Later on, a WD40 repeat-containing myosin designed myosin F, unique to the Apicomplexa and associated with rib-like myonemes, was reported in *G. polymorpha* [27]. Interestingly, the bending of the protomerite that is expected to be related to the ectoplasmic network and rib-like myonemes occurred in *G. polymorpha* and *G. cuneata* gamonts, which are indeed proven to possess these structures, while the stiff gamonts of *G. steini* missing the rib-like myonemes on ultrathin sections showed no shape changes during their rapid gliding. Despite the work reporting myosin- and actin-like proteins restricted to the vegetative stages of *G. blaberae* [54], the presence of these proteins was documented in both the gamonts as well as the trophozoites of *Gregarina* representatives [45,46]. Nevertheless, we do not exclude that there may exist some correlation between the abundance or form of actin and gregarine developmental stage.

Shedding of mucous material

The next point that is worth noting with regard to the glideosome is the lack of micronemes in gregarine gamonts. Eugregarine gliding resembles the gliding motility in sporozoites of *Plasmodium* [56]. The trail left behind gliding ookinetes of *Plasmodium* was shown to correspond to the release of the Pbs25 and the circumsporozoite thrombospondin-related protein (CTRP) [57]. The material observed in the trail left after gliding eugregarines is generally designated as mucus, but more detailed biochemical analyses are needed to determine the exact composition. It could be expected the origin of this mucous material is related to numerous Golgi apparatuses present in the cytoplasm of gregarines [46,58,59]. The longest mucous trail was left behind gamonts of *G. polymorpha*. Similarly, Alcian blue staining at low pH, which proved to be very helpful to visualise mucous substances (i.e., glycosaminoglycans) [59,60], showed the highest amount of mucous material in the cytoplasm of *G. polymorpha* and lowest in *G. cuneata*. The results of this staining, however, conflict with the seemingly mucus-free surface of *G. polymorpha* and the abundant mucus-like drops covering the surface of *G. cuneata*, supported by the observations on the secretion of a mucus-like material in the grooves between

G. cuneata folds [24]. Accepting the possibility that the increased production of mucus allows gregarines to glide with higher speeds, the differences in its viscosity could be the reason for mentioned observations on mucus secretion. Nevertheless, the origin of these drops remains unclear as no reliable conclusions about the chemical composition could be drawn from electron microscopic observations. Furthermore, the way of mucus secretion is not clear. It could be expected that openings or pore-like structures observed in the grooves between the folds might be related to mucus. Freeze-etching data further supported these speculations by the demonstration of numerous micropores in the pellicle lined by a collar and often in connections with some cisternae, vesicles or ducts, similar to those observed in *G. garnhami* [22]. Generally, the micropore is defined as an organelle formed by the apicomplexan pellicle, which is composed of two concentric rings (in transverse section), the inner of which corresponds with an invagination of the outer pellicle membrane. Micropores are assumed to have a feeding function but their real function is still poorly understood. A typical micropore was documented in ultrathin sections of the pellicle of *G. cuneata* (Figure 5J), and we assume that this structure corresponds to the pores revealed by the freeze-etching. Similar structures were observed in the pellicle of trophozoites of another *Gregarina* species [22,61] or in the pellicle of *Plasmodium* ookinete [62]. In addition, numerous tiny pore-like structures, located at the base and lateral side of epicytic folds, were found on the fractured faces of membranes, especially on the protoplasmic faces of IMC. The typical organisation of the proteins forming these structures proved them as pores.

Intramembranous particles

We did not find any correlation between IMP density in membranes forming the pellicle and the gregarine gliding rate. Although the density of IMP, as well as the Kp, in studied gregarines differs, the overall values are highest in *G. steni* and lowest in *G. polymorpha*, both of which glide at high speed. Only IMP with their size ranging from 6 to 14 nm were used for statistical evaluation of their densities in order to get data comparable with those already published on other apicomplexans (Table 6). Most conspicuous differences in IMP densities can be seen between the values reported for IMC of *G. garnhami* [11] and our data, especially when considering that both studies focused on representatives of the same genus. It must be highlighted, however, that the statistical values differ considerably when including all visible IMP. A magnification of 56,000X used for statistics in this study allows visualisation of tiny IMP of 1 nm in diameter. That is why we included histograms illustrating the IMP size distribution in all analysed membranes to show their size variability among species as well as the frequency of particles with their sizes beyond this range. Considering the frequency of particles beyond the size range of 6–14 nm, especially in *G. cuneata*, it is questionable if this range set in previous studies really offers reliable data on IMP densities. An example is the differences in Kp for membranes when considering all detectable IMP in contrast to statistical values calculated for a size range 6–14 nm shown in Table 5; i.e., the Kp for the *G. cuneata* plasma membrane is 0.91 (in contrast to 0.81 for a set range of 6–14 nm), for the external cytomembrane is 0.93 (1.13) and for the internal cytomembrane is 1.49 (1.33); Kp for the *G. polymorpha* plasma membrane is 1.69 (0.59), for the external cytomembrane is 0.38 (0.70) and for the internal cytomembrane is 1.41 (1.57); and the Kp for the *G. steini* plasma membrane is 1.02 (1.27), for the external cytomembrane is 0.93 (0.68) and for the internal cytomembrane is 0.90 (1.24).

Conclusions

Neither the general architectural features of the pellicle, including the number of epicytic folds or its subcellular components, nor the supramolecular organisation of the plasma membrane and IMC (density of IMP and their Kp) correlate with a gliding rate in eugregarines. Phalloidin and

Table 6 Densities of IMP (particles/μm^2) in different apicomplexans

Species	Plasma membrane		External cytomembrane		Internal cytomembrane	
	EF	PF	PF	EF	EF	PF
Gregarina cuneata	2770 ± 96	2244 ± 283	1420 ± 190	1260 ± 211	1502 ± 273	1993 ± 253
Gregarina polymorpha	2473 ± 147	1446 ± 158	602 ± 265	863 ± 202	814 ± 246	1276 ± 200
Gregarina steini	1783 ± 233	2265 ± 154	2588 ± 189	3820 ± 211	1886 ± 274	2339 ± 132
Gregarina blaberae[1]	977 ± 235	1469 ± 233	285 ± 39	133 ± 34	158 ± 72	297 ± 33
Eimeria nieschulzi[2]	218 ± 21	648 ± 73	2360 ± 133	29 ± 7	146 ± 31	1780 ± 97
Plasmodium knowlesi[3]	185 ± 25	2198 ± 528	17511 ± 228	38 ± 15	48 ± 28	574 ± 200

The size of IMP is in range 6-14 nm.
[1]Values taken from Schrével et al. [11].
[2]Values taken from Dubremetz and Topier [41].
[3]Values taken from McLaren et al. [63].

antibody labelling repeatedly confirmed the presence of actin and myosin restricted to the cell cortex. Moreover, the reaction of gregarines to the application of JAS and cytochalasin D serves as indirect proof of the importance of actin dynamic polymerisation during gregarine gliding. The location of the actomyosin complex seems to be restricted to the lateral parts of the epicytic folds rather than to their tips, as the number of 12-nm filaments and rippled dense structures running along their length does not influence the speed of gliding. The results of Alcian blue staining along with the mucous trail left behind gliding gamonts are the proof that the increased load of mucus in the cytoplasm correlates with gliding rate, as shown in *G. polymorpha* vs. *G. cuneata*, however, the viscosity of the mucus of the seemingly mucus-free surface of *G. polymorpha* needs further investigation. It is also worthy to highlight that despite the basic concept describing a substrate-dependent gliding in gregarines [31], for some period subsequent to drugs application to the cell suspension, gamonts were free-floating in a liquid lacking any contact with the substrate but with a significantly higher rate than exhibited during regular gliding.

Gregarines retained some ancestral features and are considered to be deep-branching apicomplexans. They evolved an enormous morphological and ecological diversity, and exhibit unique and novel adaptations to surrounding environment. Various gregarines parasitizing terrestrial and marine invertebrates not only exhibit diverse modes of locomotion (e.g., gliding in eugregarines with well-developed epicytic folds vs. bending, rolling or coiling known from marine archigregarines that probably evolved from hypertrophic zoite and retained subpellicular microtubules [9,17], and finally peristalsis-like movements observed in urosporidians), but even might use several mechanisms of cell motility depending on their actual physiological and environmental conditions. An understanding of the mechanism of gregarine motility and host cell invasion would offer significant insights into the parasitic strategy of apicomplexan parasites and evolution of obligate intracellular parasitism from free-living photosynthetic ancestors.

Materials and methods
Material collection
Larvae of the yellow mealworm, *Tenebrio molitor* Linnaeus, 1758 (Coleoptera, Tenebrionidae) infected with gregarines were obtained from colonies maintained in our laboratory. Gamonts of *Gregarina cuneata*, *G. polymorpha* and *G. steini* were collected from the intestinal lumen of naturally infected larvae. As all three eugregarine species can be simultaneously present in the larvae of *T. molitor*, experimental infections of larvae previously sterilised of gregarines were performed using infective oocysts in order to obtain a model infected with a single species for electron microscopic analyses.

Protocols concerning experimental infection and following dissection of infected larvae are described elsewhere [8,45].

Light microscopic observations on gliding motility
Single gamonts and gamonts associated in syzygy were removed from the host and placed on glass slides in Minimum Essential Medium [enriched with 3% bovine foetal serum with penicillin, streptomycin, amphotericin B and L-glutamine] (Sigma-Aldrich, Czech Republic). Incubation in this medium increased the viability of gregarines after isolation from host intestine. Light microscopic (LM) observations of gliding movement, orientation, and conformational changes were made. Results were confirmed by observations on gregarines incubated in Ringer's insect physiological solution (pH 7.2) [64]. For speed calculations, short video records were taken using Bürker counting chamber. Individual cell speeds (in micrometers per second) were calculated from individual gregarine tracks by measurements of distances between initial and final positions covered over the time interval. The interval between selected recorded positions was normalised to 1 second using the ImageJ2x software developed at the National Institutes of Health.

For observations on mucus shedding, living gamonts were put on microscopic slides covered by a thin layer of microbiological agar, slightly moistened with Ringer's solution and observed using phase contrast microscopy.

For treatment of gregarines with jasplakinolide (JAS; Invitrogen, Czech Republic) and cytochalasin D (Invitrogen, Czech Republic), living gamonts of *G. cuneata*, *G. steini* and *G. polymorpha* (a mixture of suspensions obtained from the guts of several hosts) were put on single cavity microscope glass slides with a drop of JAS or cytochalasin D in Ringer's insect physiological solution (pH 7.2). The JAS was reconstituted in dimethyl sulfoxide (DMSO) to prepare a 1 mM stock solution and diluted in Ringer's solution to prepare final working concentrations (5, 10, 20 and 30 μM JAS). Similarly, the 1 mM stock solution of cytochalasin D in DMSO was diluted in Ringer's solution to obtain working concentrations (10, 20 and 30 μM cytochalasin D). Control assays of living gregarines were performed in pure Ringer's solution as well as corresponding concentrations of DMSO in Ringer's solution.

Cell suspensions, squash and/or wet smear preparations were investigated with the use of a motorised Olympus microscope BX61 equipped with Olympus DP71 digital camera and software (Olympus Stream Motion version 1.5.1).

Mucus staining with alcian blue
Living gamonts were centrifuged at 10 000 × g for 30 minutes and subsequently fixed in freshly prepared

4% paraformaldehyde in phosphate buffered saline (PBS). After washing in 0.2 M PBS, cell suspensions were stained with Alcian blue (pH 1.3) for 1 hour, rinsed with 0.1 M hydrochloric acid and washed again in PBS [59]. For light microscopic analyses, the drops of stained cell suspension in PBS were dropped onto microscopic slides and covered by a cover slip.

Electron microscopy

Cell suspensions were fixed overnight at 4°C in freshly prepared 2.5–3% glutaraldehyde in 0.2 M cacodylate buffer (pH 7.4). Procedures for sample processing for transmission (TEM) and scanning electron microscopy (SEM) follow Valigurová et al. [8,45]. Observations were made using a JEOL 1010 TEM and JEOL JSM-7401 F - Field emission scanning microscope.

Freeze etching

Cell suspensions were fixed overnight at 4°C in freshly prepared 3% glutaraldehyde in 0.2 M cacodylate buffer (pH 7.4) followed by cryoprotection with 20% glycerol (w) treatment, concentrated on glass slides by using tweezers and put on the gold carrier. Specimens were then frozen in melting liquid nitrogen (-210°C), and for one cycle three carriers were mounted on a gold stand (subcooled in liquid nitrogen). Using the manipulator, the gold stand was transported into the working chamber (Freeze-etching system device, BAF 060 BAL-TEC) cooled to a temperature of -100°C at a pressure of 10^{-5} Pa. Subsequently, the specimens were cut and fractured with a microtome knife, etched (ice sublimation) for 2 minutes, and replicas were prepared by vacuum-deposition of platinum (the angle of evaporation was 45°, the thickness of layer 2.4 nm) and carbon (90° angle of evaporation, 22.2-nm thick layer) onto the frozen, fractured surface. The replicas were cleaned with 7% sodium hypochlorite and chromo-sulphuric acid to remove all the biological material, and washed in distilled water. The pieces of replica were mounted on copper grids and examined under a transmission electron microscope (Morgagni 268 D, FEI). Statistical evaluation of intramembranous particles (IMP) per a unit area (1 μm^2) and histograms illustrating the IMP size distribution were done in ACC (Adaptive Contrast Control) developed by the Institute of Mathematics, Faculty of Mechanical Engineering, University of Technology, Brno. The nomenclature follows that proposed in Branton et al. [65] and used in Schrével et al. [11].

Confocal laser scanning microscopy

Cell suspensions were washed in 0.2 M PBS, fixed for 15 minutes at room temperature in freshly prepared 4% paraformaldehyde in 0.2 M PBS, washed, and permeabilised for 15 minutes in 0.1-0.5% Triton X-100 (Sigma-Aldrich, Czech Republic). Protocols for direct staining of filamentous actin with phalloidin–tetramethylrhodamine B isothiocyanate (phalloidin-TRITC; Sigma-Aldrich, Czech Republic), as well as indirect immunofluorescent antibody (IFA) staining using the rabbit anti-myosin antibody (smooth and skeletal, the whole antiserum, Sigma-Aldrich, Czech Republic), the mouse monoclonal IgG anti-actin antibody that was raised against *Dictyostelium* actin (provided by Prof. Dominique Soldati-Favre) and mouse monoclonal anti-α-tubulin antibody (Clone B-5-1-2, Sigma-Aldrich, Czech Republic) follow Valigurová et al. [45,46]. Similarly, living gamonts treated for 10 and 150 minutes with 10 μM JAS were briefly washed in 0.2 M PBS and fixed for subsequent phalloidin labelling. Preparations were observed and documented using an Olympus IX80 microscope equipped with a laser-scanning FluoView 500 confocal unit (Olympus FluoView 4.3 software).

Author details

[1]Department of Botany and Zoology, Faculty of Science, Masaryk University, Kotlářská 2, 611 37 Brno, Czech Republic. [2]Department of Biophysics, Faculty of Medicine, Masaryk University, Kamenice 3, 625 00 Brno, Czech Republic. [3]Muséum National d'Histoire Naturelle, UMR 7245 CNRS/MNHN, CP 52, 61 rue Buffon, 75231 Paris Cedex 05, France.

References

1. Morrissette NS, Sibley LD: Cytoskeleton of apicomplexan parasites. *Microbiol Mol Biol Rev* 2002, **66**:21–38.
2. Kappe SHI, Buscaglia CA, Bergman LW, Coppens I, Nussenzweig V: Apicomplexan gliding motility and host cell invasion: overhauling the motor model. *Trends Parasitol* 2004, **20**:13–16.
3. Wetzel DM, Hakansson S, Hu K, Roos D, Sibley LD: Actin filament polymerization regulates gliding motility by apicomplexan parasites. *Mol Biol Cell* 2003, **14**:396–406.
4. Opitz C, Soldati D: 'The glideosome': a dynamic complex powering gliding motion and host cell invasion by *Toxoplasma gondii*. *Mol Microbiol* 2002, **45**:597–604.
5. Kappe SHI, Buscaglia CA, Nussenzweig V: *Plasmodium* sporozoite molecular cell biology. *Annu Rev Cell Dev Biol* 2004, **20**:29–59.
6. Santos JM, Lebrun M, Daher W, Soldati D, Dubremetz JF: Apicomplexan cytoskeleton and motors: key regulators in morphogenesis, cell division, transport and motility. *Int J Parasitol* 2009, **39**:153–162.
7. Barta JR, Thompson RCA: What is *Cryptosporidium*? Reappraising its biology and phylogenetic affinities. *Trends Parasitol* 2006, **22**:463–468.
8. Valigurová A, Hofmannová L, Koudela B, Vávra J: An ultrastructural comparison of the attachment sites between *Gregarina steini* and *Cryptosporidium muris*. *J Eukaryotic Microbiol* 2007, **54**:495–510.
9. Schrével J, Goldstein S, Kuriyama R, Prensier G, Vávra J: Biology of gregarines and their host-parasite interactions. In *The gregarines: the early branching Apicomplexa*. Volume 1st edition. Edited by Desportes I, Schrével J. Leiden, Netherlands: BRILL; 2013:26–196.
10. Vivier E, Devauchelle G, Petitprez A, Porchet-Hennere E, Prensier G, Schrével J, Vinckier D: Observations on comparative cytology in sporozoans. Part 1. The sperficial structures in vegetative forms. *Protistologica* 1970, **6**:127–150.
11. Schrével J, Caigneaux E, Gros D, Philippe M: The 3 cortical membranes of the gregarines. 1. Ultrastructural organization of *Gregarina blaberae*. *J Cell Sci* 1983, **61**:151–174.
12. Schewiakoff W: Über die Ürsache der fortschreitenden Bewegung der Gregarinen. *Z wiss Zool* 1894, **58**:340–354.
13. Mühl D: Beitrag zur Kenntnis der Morphologie und Physiologie der Mehlwurm-Gregarinen. *Arch Protistenkd* 1921, **43**:361–414.
14. Richter IE: Bewegungsphysiologische Untersuchungen an polycystiden Gregarinen unter Anwendung des Mikrozeitrafferfilmes. *Protoplasma* 1959, **51**:197–241.
15. King C, Sleep J: Modelling the mechanism of gregarine gliding using bead translocation. *J Eukaryot Microbiol* 2005, **52**:7S–27S.
16. Vivier E, Schrével J: Etude au microscope electronique dune gregarine du genre *Selenidium* parasite de *Sabellaria alveolata* L. *J De Microscopie* 1964, **3**:651–670.
17. Schrével J: Biological and ultrastructural observations on Selenidiidae and their relation to systematics of gregarines. *J Protozool* 1971, **18**:448–470.
18. Baines I, King CA: Demonstration of actin in the protozoan *Gregarina*. *Cell Biol Int Reports* 1989, **13**:679–686.
19. Ghazali M, Philippe M, Deguercy A, Gounon P, Gallo JM, Schrével J: Actin and spectrin-like (Mr = 260-240 000) proteins in gregarines. *Biol Cell* 1989, **67**:173–184.
20. Heintzelman MB: Actin and myosin in *Gregarina polymorpha*. *Cell Motil Cytoskeleton* 2004, **58**:83–95.
21. Reger JF: The fine structure of the gregarine *Pyxinoides balani* parasitic in the barnacle *Balanus tintinnabulum*. *J Protozool* 1967, **14**:488–497.
22. Walker MH, Lane NJ, Lee WM: Freeze-fracture studies on the pellicle of the eugregarine, *Gregarina garnhami* (Eugregarinida, Protozoa). *J Ultrastruct Res* 1984, **88**:66–76.
23. Korn H, Ruhl H: Comparative study of ultrastructure of *Gregarina polymorpha* and *Gregarina cuneata* (Sporozoa, Gregarinida). *Z Parasitenkd - Parasitol Res* 1972, **39**:285–301.
24. Vávra J, Small EB: Scanning electron microscopy of gregarines (Protozoa, Sporozoa) and its contribution to the theory of gregarine movement. *J Protozool* 1969, **16**:745–757.
25. Valigurová A, Koudela B: Morphological analysis of the cellular, interactions between the eugregarine *Gregarina garnhami* (Apicomplexa) and the epithelium of its host, the desert locust *Schistocerca gregaria*. *Eur J Protistol* 2008, **44**:197–207.
26. Vivier E: L' organisation ultrastructurale corticale de la grégarine *Lecudina pellucida*; ses rapports avec l' alimentation et la locomotion. *J Protozool* 1968, **15**:230–246.
27. Heintzelman MB, Mateer MJ: GpMyoF, a WD40 repeat-containing myosin associated with the myonemes of *Gregarina polymorpha*. *J Parasitol* 2008, **94**:158–168.
28. Heintzelman MB, Schwartzman JD: Characterization of myosin-A and myosin-C: two class XIV unconventional myosins from *Toxoplasma gondii*. *Cell Motil Cytoskeleton* 1999, **44**:58–67.
29. Foth BJ, Goedecke MC, Soldati D: New insights into myosin evolution and classification. *Proc Nat Acad Sci U S A* 2006, **103**:3681–3686.
30. Dallai R, Talluri MV: Freeze-fracture study of the gregarine trophozoite: I the top of the epicyte folds. *Boll Zool* 1983, **50**:235–244.
31. King CA: Cell-surface interaction of the protozoan gregarina with concanavalin-a beads - implications for models of gregarine gliding. *Cell Biol Int Rep* 1981, **5**:297–305.
32. Walker MH, Mackenzie C, Bainbridge SP, Orme C: Study of the structure and gliding movement of *Gregarina garnhami*. *J Protozool* 1979, **26**:566–574.
33. Mackenzie C, Walker MH: Substrate contact, mucus, and eugregarine gliding. *J Protozool* 1983, **30**:3–8.
34. King CA: Cell motility of sporozoan protozoa. *Parasitol Today* 1988, **4**:315–319.
35. Göhre E: Untersuchungen über den plasmatischen Feinbau der Gregarinen, mit besonderer Berücksichtigung der Sexualitätsverhältnisse. *Arch Protistenkd* 1943, **96**:295–324.
36. Weiser J: *Nemoci hmyzu*. Praha: Nakladatelství Československé akademie věd; 1966.
37. Crawley H: The Movements of gregarines. *Proc Acad Nat Sci Philadelphia* 1905, **57**:89–99.
38. Dubremetz JF, Garcia-Reguet N, Conseil V, Fourmaux MN: Apical organelles and host-cell invasion by Apicomplexa. *Int J Parasitol* 1998, **28**:1007–1013.
39. Schrével J, Philippe M: The gregarines. In *Parasitic Protozoa second edition*. Vol. 4th edition. Edited by Kreier JP. San Diego, United States: Academic Press, Inc. edition; 1993:133–245.
40. Dallai R, Talluri MV: Evidence for septate junctions in the syzygy of the protozoan *Gregarina plymorpha* (Protozoa, Apicomplexa). *J Cell Sci* 1988, **89**:217–224.
41. Dubremetz JF, Torpier G: Freeze fracture study of the pellicle of an eimerian sporozoite (Protozoa, Coccidia). *J Ultrastruct Res* 1978, **62**:94–109.
42. Dubremetz JF, Torpier G, Maurois P, Prensier G, Sinden R: Structure de la pellicule du sporozoite de *Plasmodium yoelii*: étude par cryofracture. *C R Acad Sci Paris* 1979, **Ser. D**:623–626.
43. Shaw MK, Tilney LG: Induction of an acrosomal process in *Toxoplasma gondii*: visualization of actin filaments in a protozoan parasite. *Proc Nat Acad Sci U S A* 1999, **96**:9095–9099.
44. Olshina MA, Wong W, Baum J: Holding back the microfilamentu - structural insights into actin and the actin-monomer-binding proteins of apicomplexan parasites. *Iubmb Life* 2012, **64**:370–377.
45. Valigurová A, Michalková V, Koudela B: Eugregarine trophozoite detachment from the host epithelium via epimerite retraction: fiction or fact? *Int J Parasitol* 2009, **39**:1235–1242.
46. Valigurová A: Sophisticated adaptations of *Gregarina cuneata* (Apicomplexa) feeding stages for epicellular parasitism. *PLoS ONE* 2012, **7**:e42606.
47. Russell DG, Sinden RE: The role of the cytoskeleton in the motility of coccidian sporozoites. *J Cell Sci* 1981, **50**:345–359.
48. Chen WJ, Fan-Chiang MH: Directed migration of *Ascogregarina taiwanensis* (Apicomplexa: Lecudinidae) in its natural host *Aedes albopictus* (Diptera: Culicidae). *J Eukaryot Microbiol* 2001, **48**:537–541.
49. Bubb MR, Spector I, Beyer BB, Fosen KM: Effects of jasplakinolide on the kinetics of actin polymerization. An explanation for certain *in vivo* observations. *J Biol Chem* 2000, **275**:5163–5170.
50. Bubb MR, Senderowicz AM, Sausville EA, Duncan KL, Korn ED: Jasplakinolide, a cytotoxic natural product, induces actin polymerization and competitively inhibits the binding of phalloidin to F-actin. *J Biol Chem* 1994, **269**:14869–14871.
51. Ayscough KR: Endocytosis and the development of cell polarity in yeast require a dynamic F-actin cytoskeleton. *Curr Biol* 2000, **10**:1587–1590.
52. Posey SC, Bierer BE: Actin stabilization by jasplakinolide enhances apoptosis induced by cytokine deprivation. *J Biol Chem* 1999, **274**:4259–4265.
53. King CA, Lee K: Effect of trifluoperazine and calcium ions on gregarine gliding. *Experientia* 1982, **38**:1051–1052.
54. Ghazali M, Schrével J: Myosin-like protein (M(r)175,000) in *Gregarina blaberae*. *J Eukaryotic Microbiol* 1993, **40**:345–354.
55. Hildebrand HF: Electron-microscopic investigation on evolution stages of trophozoite of *Didymophyes gigantea* (Sporozoa, Gregarinida). 3.

The fine structure of the epicyte with emphasis on the contractile elements. *Z Parasitenkd* 1980, **64**:29–46.

56. Vanderberg JP: **Studies on the motility of** *Plasmodium* **sporozoites.** *J Protozool* 1974, **21**:527–537.

57. Lecona AN, Rodriguez MH, Argotte RS, Alvarado A, Rodriguez MC: *Plasmodium* **berghei ookinetes glide and release Pbs25 and circumsporozoite thrombospondin-related protein on solid surface substrata.** *J Parasitol* 2010, **96**:216–218.

58. Desportes I: **Ultrastructure et développement des grégarines du genre** *Stylocephalus*. *Ann Sci Nat Zool Paris* 1969, **12**:31–96.

59. Schrével J: **Polysaccharides of cell-surface of gregarines (Protozoa Parasites). 1. Ultrastructure and cytochemistry.** *J Microscopy-Oxford* 1972, **15**:21–40.

60. Schrével J, Gros D, Monsigny M: **Cytochemistry of cell glycoconjugates.** *Prog Histochem Cytochem* 1981, **14**:1–269.

61. Talluri MV, Dallai R: **Freeze-fracture study of the gregarine trophozoite: II. Evidence of "rosette" organization on cytomembranes in relation with micropore structure.** *Boll Zool* 1983, **50**:247–256.

62. Raibaud A, Lupetti P, Paul RE, Mercati D, Brey PT, Sinden RE, Heuser JE, Dallai R: **Cryofracture electron microscopy of the ookinete pellicle of** *Plasmodium gallinaceum* **reveals the existence of novel pores in the alveolar membranes.** *J Struct Biol* 2001, **135**:47–57.

63. McLaren DJ, Bannister LH, Trigg PI, Butcher GA: **Freeze fracture studies on the interaction between the malaria parasite and the host erythrocyte in** *Plasmodium knowlesi* **infections.** *Parasitology* 1979, **79**:125–139.

64. Belton P, Grundfest H: **Potassium activation and K spikes in muscle fibers of the mealworm larva (***Tenebrio molitor***).** *Am J Physiol* 1962, **203**:588–594.

65. Branton D, Bullivant S, Gilula NB, Karnovsky MJ, Moor H, Muhlethaler K, Northcote DH, Packer K, Satir B, Satir P, *et al*: **Freeze etching nomenclature.** *Science* 1975, **190**:54–56.

7.3

Melicherová J., Ilgová J., Kváč M., Sak B., Koudela B., **Valigurová A.**

2014

Life cycle of *Cryptosporidium muris* in two rodents
with different responses to parasitization

Life cycle of *Cryptosporidium muris* in two rodents with different responses to parasitization

JANKA MELICHEROVÁ[1]†, JANA ILGOVÁ[1]†, MARTIN KVÁČ[2], BOHUMIL SAK[2], BŘETISLAV KOUDELA[3] *and* ANDREA VALIGUROVÁ[1]*

[1] *Department of Botany and Zoology, Faculty of Science, Masaryk University, Kotlářská 2, 611 37 Brno, Czech Republic*
[2] *Institute of Parasitology, Biology Centre of the Czech Academy of Sciences, Branišovská 31, 370 05 České Budějovice, Czech Republic*
[3] *Department of Pathological Morphology and Parasitology, University of Veterinary and Pharmaceutical Sciences, Palackého 1/3, 612 42 Brno, Czech Republic*

SUMMARY

This study focuses on mapping the life cycle of *Cryptosporidium muris* in two laboratory rodents; BALB/c mice and the southern multimammate rat *Mastomys coucha*, differing in their prepatent and patent periods. Both rodents were simultaneously experimentally inoculated with viable oocysts of *C. muris* (strain TS03). Animals were dissected and screened for the presence of the parasite using a combined morphological approach and nested PCR (SSU rRNA) at different times after inoculation. The occurrence of first developmental stages of *C. muris* in stomach was detected at 2·5 days post-infection (dpi). The presence of Type II merogony, appearing 36 h later than Type I merogony, was confirmed in both rodents. Oocysts exhibiting different size and thickness of their wall were observed from 5 dpi onwards in stomachs of both host models. The early phase of parasitization in BALB/c mice progressed rapidly, with a prepatent period of 7·5–10 days; whereas in *M. coucha*, the developmental stages of *C. muris* were first observed 12 h later in comparison with BALB/c mice and prepatent period was longer (18–21 days). Similarly, the patent periods of BALB/c mice and *M. coucha* differed considerably, i.e. 10–15 days *vs* chronic infection throughout the life of the host, respectively.

Key words: cryptosporidia, development, gastric, oocyst, pathology, Type II merogony.

INTRODUCTION

The phylum Apicomplexa includes significant and widespread unicellular pathogens of humans and animals and one of these is the genus *Cryptosporidium* that is the causative agent of zoonotic disease of the gastrointestinal and respiratory tract, called cryptosporidiosis. In general, the progress of infection in immunocompetent individuals is mild, without fatal consequences, and usually self-curing or self-limiting (Chappell *et al.* 1999). The gastric species *Cryptosporidium muris* parasitizes epithelial cells in the glandular part of the gastric mucosa and was first described in mice by Tyzzer (1907) as a *Cryptosporidium* species. Uni *et al.* (1987) extended his work and provided new morphometrical data of its developmental stages. Although *C. muris* is considered to be a predominantly rodent species, occasionally it can be transmitted from its natural host to other animals (Aydin and Ozkul, 1996; Hůrková *et al.* 2003; Pavlásek and Ryan, 2007; Lupo *et al.* 2008) and possibly humans (Katsumata *et al.* 2000; Guyot *et al.* 2001; Gatei *et al.* 2002; Tiangtip and Jongwutiwes, 2002; Palmer *et al.* 2003).

The general life cycle, which is well documented for *Cryptosporidium parvum* parasitizing the intestine (Current and Reese, 1986), includes four phases of development: excystation, merogony, gametogony and sporogony. Each phase occurs in a particular chronological period and depends on both the species of *Cryptosporidium* as well as the host. Diversity in patent and prepatent periods has been reported from various animals (Tarazona *et al.* 1998; Hijjawi *et al.* 2001; Fayer and Santin, 2009). The infective oocysts are transmitted by the fecal–oral route. The invasive sporozoites, being released from oocysts inside the host, evolve to trophozoites and multiply in the asexual phase involving two types of merogony. Type II merogony produces four merozoites and has been recorded in *C. parvum* and *Cryptosporidium wrairi* but not confirmed in *C. muris*. The sexual part of the life cycle, gametogony, is typified by the occurrence of numerous macrogamonts and microgamonts that produce 16 non-flagellated microgametes. After macrogamont fertilization, the zygote is enveloped by a wall and matures into the oocyst, which sporulates inside the host. A few studies report the existence of two types of oocysts, i.e. thick- and thin-walled (Current and Reese, 1986; Uni *et al.* 1987).

* Corresponding author: Department of Botany and Zoology, Faculty of Science, Masaryk University, Kotlářská 2, 611 37 Brno, Czech Republic. E-mail: andreav@sci.muni.cz
† These authors contributed equally to this work.

Due to lack of efficient treatment of cryptosporidiosis, further knowledge on cryptosporidia biology and host–parasite interactions, depending on the host immunological status, is still required. Our aim was to map the complete life cycle of *C. muris* in two laboratory rodents, BALB/c mice and the southern multimammate rat *Mastomys coucha*, and to verify the presence of Type II merogony and thin-walled oocysts during the life cycle of *C. muris*, using a combined microscopic approach, i.e. electron microscopy as well as observations on native and stained preparations using light microscopy (LM), and supplemented with molecular detection. We also attempted to record and re-evaluate the stage-dependent characteristics depicted in the detailed drawings of Tyzzer ([1910]) and for this reason, we have followed the techniques used in his study. Since the endogenous developmental stages of *C. muris* attack the stomach tissue, we expected to find some differences in its life cycle when compared with the findings for *C. parvum*.

MATERIALS AND METHODS

Laboratory animal models

The southern multimammate rat (*M. coucha*; the Institute of Parasitology Biology Centre, ASCR, v.v.i. in České Budějovice) and BALB/c mice (Anlab s.r.o, Czech Republic) were used for the purposes of this study. Animals were housed in plastic cages (5 animals per cage) with sterile wood-chip bedding and supplied with sterilized food and water *ad libitum*. The rearing of animals is regulated by Czech legislation (Act No 246/1992 Coll., on protection of animals against cruelty). These documents are consistent with the legislation of the European Commission. All housing, feeding and experimental procedures were conducted under protocols approved by the Institute of Parasitology, Biology Centre of the Academy of Sciences of the Czech Republic and Central Commission for Animal Welfare, Czech Republic (Protocol # 066/2010). The minimum number of animals has been involved to produce statistically reproducible results.

Parasite

Cryptosporidium muris strain TS03 originating from an East African mole rat (*Tachyoryctes splendens*) previously characterized by Kváč *et al*. ([2008], [2011]) was used for all experiments in this study. Over 10 years the *C. muris* TS03 has been passaged through susceptible laboratory hosts, *M. coucha* and SCID mice, in the Institute of Parasitology Biology Centre, ASCR, v.v.i. in České Budějovice. Fresh rat feces were collected regularly every morning. The presence of oocysts in feces was verified using the staining method according to Miláček and Vítovec ([1985]). Oocysts were purified using Sheather's sugar flotation

method (Arrowood and Sterling, [1987]) and modified caesium chloride gradient centrifugation (Kilani and Sekla, [1987]). Obtained oocysts of *C. muris* were either immediately used for experimental inoculations of laboratory animals or mixed with aqueous potassium dichromate (2·5% w/v, final concentration) and stored at 4 °C. Oocysts less than 1 week old were exclusively used for the experiment in this study. Before their use, the residue of aqueous potassium dichromate was removed by centrifugation at 1000 *g* for 10 min, the supernatant was aspirated, and the pelleted oocysts were resuspended in distilled water. This procedure was repeated three times.

Experimental inoculations and parasitological dissection of laboratory rodents

Rodents, 8–10 weeks old, were inoculated *per os* using the oesophagus gavage with a dose of 10^6 viable oocysts of *C. muris* that had previously been checked for their viability via propidium iodide staining (Sauch *et al*. [1991]). Inoculations of both rodent models were performed simultaneously. Animals (one per host model), were euthanased by cervical dislocation at 0·5, 1, 6 and 12 h post infection (hpi) and then consecutively every 12 h until 11 dpi, and onwards at 12, 13, 14, 18, 21 and 28 dpi. In *M. coucha*, additional parasitological examination was performed, of animals kept for 4, 8 and 18 months, and 2 years after inoculation. The negative controls of both models, BALB/c mice and *M. coucha*, were prepared to evaluate pathological alterations in gastric tissue induced by cryptosporidiosis. A total of 33 individuals of BALB/c mice and 37 individuals of *M. coucha* were examined. In subsequent repetition of the experiment, performed to detect cryptosporidia during the early phase of parasitization, the infective doses were increased to 10^8 oocysts of *C. muris* per animal. Animals were dissected at selected time points after inoculation (a total of 8 individuals of BALB/c mice and 17 individuals of *M. coucha*).

Excision of the stomach, consisting of both the glandular and non-glandular part was performed. As endogenous developmental stages of *C. muris* are known to be restricted to the glandular part, this area of the gastric tissue was divided lengthways through the *curvatura major* and then transversely. The resulting four sections were processed using the various approaches described in the following subchapters. Differences between the course of parasitization in groups of BALB/c mice and *M. coucha* were tested by the non-parametric Mann–Whitney *U* test. Testing was performed using the software Statistica® 10.0 (StatSoft CR, Prague, Czech Republic).

Native and stained preparations

As the first step, the blood serum of both BALB/c and *M. coucha* was obtained from non-infected

controls. A total of $10\,\mu L$ (BALB/c) or $30\,\mu L$ (*M. coucha*) of adequate sera were subsequently added to the processed gastric tissue in order to release the *C. muris* developmental stages. Native preparations, prepared from suspensions obtained from scrapings of the gastric luminal epithelium, were evaluated immediately via LM and checked for the presence of cryptosporidia. Preparations with gastric scrapings were also stained with Lugol's iodine. The protocols according to Giemsa and Wright staining procedures (Tyzzer, 1910) were used to visualize the characteristic morphological features of individual *C. muris* developmental stages. For this purpose, specimens were fixed with a vapour of 2% osmium tetroxide (v/v). Slightly modified staining procedures followed Tyzzer (1910). Preparations were viewed and documented using the light motorized microscope Olympus BX61 equipped with phase contrast optics and Olympus BX51 with Nomarski interference-contrast microscopy (DIC).

Electron microscopy

Samples of gastric tissue were fixed in freshly prepared 3% glutaraldehyde (v/v) in cacodylate buffer and further processed for transmission (transmission electron microscopy (TEM)) and scanning electron microscopy (SEM) as described elsewhere (Valigurová *et al*. 2007, 2008). The grids for TEM were coated with Formvar film at a thickness of 15–25 nm. Ultrathin sections transferred to the Formvar coated copper grids were evaluated using a JEOL 1010 transmission electron microscope. Micrographs from SEM were performed by JEOL JSM-7401F. In the case of negative results obtained during the early phase of infection, samples of gastric tissue already viewed under SEM were broken into smaller pieces to expose the interior of the closed gastric pits, were re-coated with gold and re-evaluated.

Histology

Gastric tissue was fixed in AFA (alcohol – formalin – acetic acid) solution and processed as described previously (Valigurová *et al*. 2008). The blocks in Histoplast II were cut using a Zeiss Hyrax M 300 rotary microtome. The $7\,\mu m$ thick sections were stained with haematoxylin–eosin (H&E). Preparations were viewed and documented using the light motorized microscope Olympus BX61.

Molecular method; nested PCR

This method was chosen to verify the presence (or absence) of specific DNA of developmental stages of *C. muris* in the stomachs of both animal models during the early phase of parasitization (up to 3 dpi).

In addition, this approach was essential to disprove the localization of *C. muris* developmental stages in other organs such as the gall bladder, pancreas, oesophagus, spleen, liver, Peyer's patches, duodenum, jejunum, ileum, colon, lung and kidney.

Total DNA was extracted from tissue by bead disruption for 60 s at $5\cdot5\,\mathrm{m\,s}^{-1}$ using $0\cdot5\,\mathrm{mm}$ glass beads in a FastPrep®–24 Instrument (MP Biomedicals, CA, USA), followed by isolation/purification using a commercially available kit according to the manufacturer's instructions (DNeasy Blood and Tissue Kit, Qiagen, Hilden, Germany). Purified DNA was stored at $-20\,^{\circ}\mathrm{C}$ prior to being used for PCR. The presence of *C. muris* was confirmed by sequence analysis of the SSU gene using previously described methods (Jiang *et al*. 2005). The positive (sample containing DNA of *C. hominis*) and negative control were included in each PCR. Secondary PCR products were detected by agarose gel electrophoresis (2·0%) and visualized by ethidium bromide staining ($0\cdot2\,\mu\mathrm{g\,mL}^{-1}$).

RESULTS

The effect of parasitization by C. muris on laboratory rodents

Laboratory rodents exhibited significantly different responses to parasitization and chronology of pathological changes of gastric tissue induced by the parasite, in contrast to the negative control of gastric tissue (Figs 1A–C and 2A, B); nevertheless, the sequence of individual changes during the acute phase of parasitization corresponded in both models. At the beginning of parasitization, the gastric tissue of both host models was irregularly affected by endogenous developmental stages of *C. muris* in an island-like manner and individual parasitized gastric pits were surrounded by areas of healthy tissue (Figs 1D, F and 2D, F). This specific feature of *C. muris* hampered the localization of parasites in host stomachs and made the detection of its earliest developmental stages almost impossible in both rodent models. Therefore, a variety of different microscopic approaches along with nested PCR were necessary to confirm the presence or absence of *C. muris* developmental stages during the early phase of infection.

The BALB/c mice showed a significantly shorter prepatent period ($P < 0\cdot05$), in contrast to that of *M. coucha*, and the first oocysts in their feces were detected at 7·5 dpi with range of 7·5–10 dpi. The patent period in BALB/c mice lasted 10–15 dpi. The first obvious alterations of its gastric surface were noticeable after 3 dpi (Figs 1D–F). Some gastric pits were slightly open and thus enlarged (Fig. 1E). At 8 dpi, the majority of the gastric glandular part was obviously affected (Fig. 1G–I), whereas the
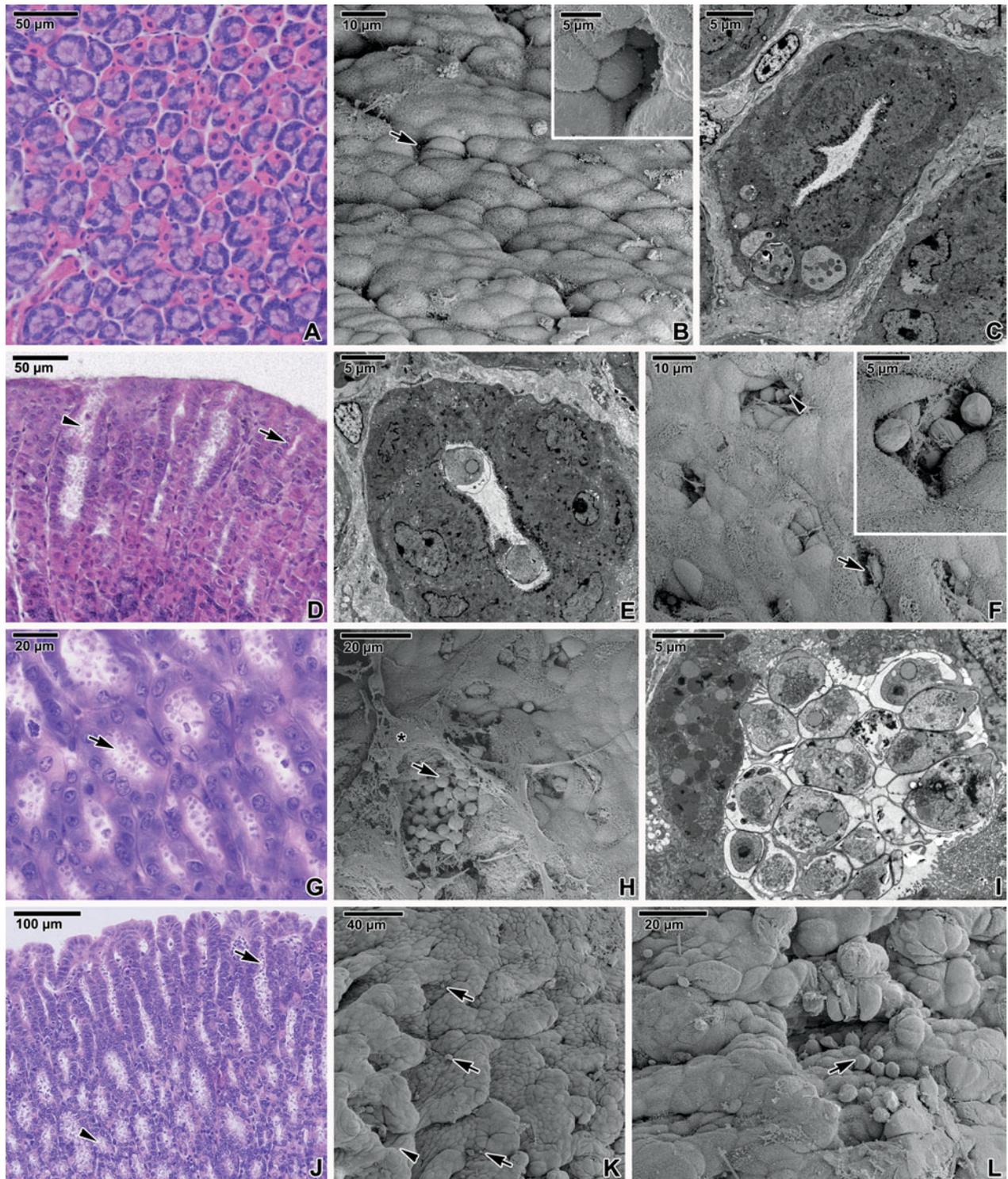
Fig. 1. Pathology of gastric cryptosporidiosis in BALB/c mice. (A) Cross-section of gastric glands; negative control. LM (Histology, H&E). (B) The surface of the gastric epithelium showing empty gastric pits (arrow). Inset shows a detailed view inside an empty gastric pit; negative control. SEM. (C) Cross-section of a gastric gland; negative control. TEM. (D) Longitudinal section of gastric epithelium; gastric pits (arrow) parasitized by *C. muris* (arrowhead) at 5·5 dpi. LM (Histology, H&E). (E) Cross-section of a gastric gland with *C. muris* individuals at 3 dpi. TEM. (F) Surface of the gastric epithelium showing gastric pits filled with *C. muris* (arrowhead) at 7 dpi; an apparently empty gastric pit (arrow). Inset shows a detailed view inside the gastric pit filled by *C. muris* developmental stages. SEM. (G) Cross-section of enlarged gastric glands after 8·5 dpi (arrow). LM (Histology, H&E). (H) Gastric pits completely filled by *C. muris* (arrow) at 8·5 dpi; the surface is covered by a mucus layer (asterisk). SEM. (I) Cross-section of a gastric gland completely filled with various developmental stages of *C. muris* at 8 dpi. TEM. (J) Longitudinal section of a stomach showing parasitized gastric pits (arrow) and glands (arrowhead) at 13 dpi. LM (Histology, H&E). (K) The folds of the enlarged gastric epithelium (arrowhead); *C. muris* developing at the surface of epithelium (arrows) at 13 dpi. SEM. (L) Hypertrophy and hyperplasia of the gastric tissue; numerous developmental stages of *C. muris* (arrow) at 13 dpi. SEM.
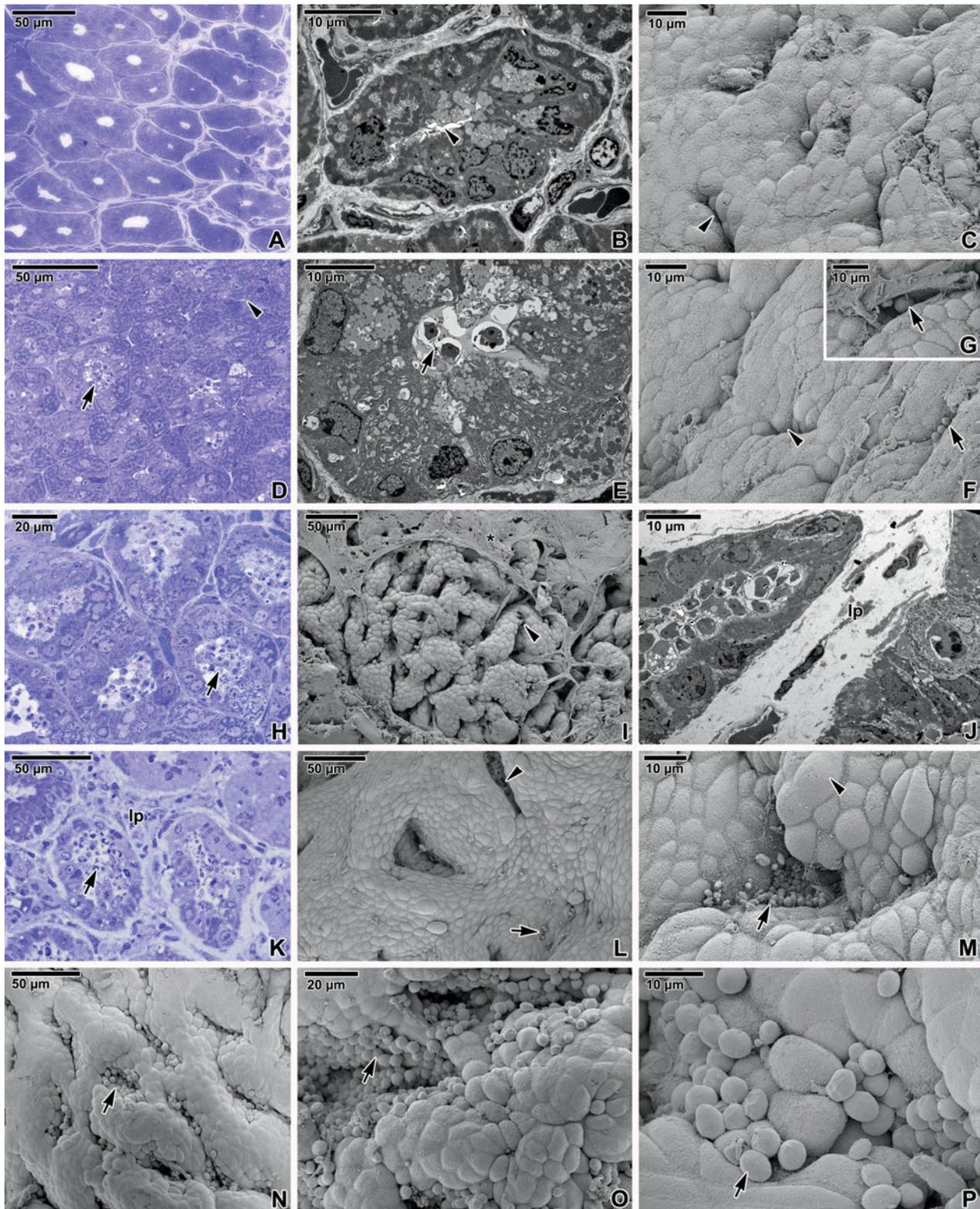
Fig. 2. Pathology of gastric cryptosporidiosis in *Mastomys coucha*. (A) Cross-section of gastric glands; negative control. LM (Histology, toluidine blue). (B) Cross-section of the gastric gland; negative control. TEM. (C) Surface of the gastric epithelium at 1 dpi; gastric pits (arrowhead). SEM. (D) Cross-section of the parasitized gastric gland (arrow) surrounded by non-parasitized glands (arrowhead) at 5 dpi. LM (Histology, toluidine blue). (E) Cross-section of the gastric gland filled with *C. muris* (arrow) at 5 dpi. TEM. (F) Surface of the gastric epithelium exhibiting seemingly empty and closed gastric pits (arrowhead) and parasitized gastric pits (arrow) at 5 dpi. SEM. (G) A detailed view inside the gastric pit with stages of *C. muris* (arrow) at 5·5 dpi. SEM. (H) Cross-section showing an acute phase of parasitization; obvious dilatation of the gastric glands filled with various stages of *C. muris* (arrow) at 10·5 dpi. LM (Histology, toluidine blue). (I) Surface of the gastric epithelium exhibiting enlarged gastric folds (arrow) covered by mucus (asterisk) at 21 dpi. SEM; (J) Oblique section showing hyperplasia of the gastric gland filled with *C. muris* at 8 months PI; a massive

non-glandular part exhibited no changes. The most obvious changes were observed at the peak of parasitization around 13 dpi. Pathological modifications of the host tissue induced by the parasite included an intensive epithelial hyperplasia (Fig. 1K) and a mucosal hypertrophy without inflammatory exudates. The gastric surface of the glandular part was markedly deformed due to intense pathological changes, including extension of gastric longitudinal folds, and numerous cryptosporidia were seen to be attached to superficial gastric epithelium outside pits (Fig. 1J–L). The most significant feature that distinguished the progress of parasitization in both host models was the host self-recovery of all BALB/c mice from cryptosporidiosis that occurred after 21 dpi. Similarly, the pathological modifications of gastric tissue in BALB/c mice gradually retreated from 21 dpi onwards. At 28 dpi, the necrotic cells were almost completely replaced by new ones and the gastric tissues appeared to be completely regenerated.

In *M. coucha*, the prepatent period was significantly longer ($P < 0.05$) and the first oocysts in the feces were detected at 18 dpi. In the early phase of parasitization, the gastric tissue showed no observable changes and no parasites were detected in closed pits evaluated under SEM (Fig. 2C). In the course of parasitization, individual gastric pits were progressively invaded by parasites and thus became slightly dilated at 5 dpi (Fig. 2D–G). Subsequently, the dilatation of gastric glands and pits became increasingly noticeable. At the peak of parasitization at 10–14 dpi, almost all pits and glands were filled by *C. muris* (Fig. 2H). The further progress of parasitization caused a distinctive diffuse mucosal hypertrophy characterized by the formation of enlarged or giant gastric folds (Fig. 2I, L and N), without inflammatory exudates, and subsequently an intensive epithelial hyperplasia occurred (Fig. 2M). The massive increase in the volume of the *lamina propria*, located beneath the epithelium, caused an enlarged distance between individual affected gastric glands (Fig. 2J–K) and longitudinal folds were twisted and deformed. When the infection entered a chronic phase, all the above-described pathological alterations of parasitized gastric tissue became much more obvious (Fig. 2N–P) and the feces of *M. coucha* remained positive on the presence of *C. muris* oocysts.

The life cycle of C. muris

The life cycle of *C. muris* was studied and documented in detail at set time intervals after inoculation of both host models; BALB/c mice and *M. coucha*. Oocysts released active sporozoites (Figs 3A and 7O, P), which rapidly penetrated deep into the bottom of the pits of the gastric glands to avoid the adverse conditions in the host stomach. The first documented attached developmental stages of *C. muris* in both hosts (for chronology and dimensions see Table 1) were oval to ovoid young trophozoites observed at 2·5 dpi in BALB/c mice and at 3 dpi in *M. coucha* (Figs 3B and 4A–F). In preparations stained with Giemsa and Wright, the apical part of the attachment site of the parasitophorous sac (PS) enveloping the trophozoite stained intensively pink, thereby confirming its host cell origin, and the cytoplasmic region packed with lamellae of the feeder organelle appeared transparent (Fig. 3B–D). The alteration of the gastric microvillous surface and the gradual formation of a PS from the host cell plasma membrane were observed (Fig. 4A–C). The formation of lamellae of the feeder organelle from the membrane of an anterior vacuole was observed exclusively in the earliest trophozoites (Fig. 4B and C). The apical part of the mature trophozoites enveloped by the PS, which were mechanically detached from the host tissue, exhibited strong adhesive properties, causing the clustering of trophozoites and subsequent formation of rosettes (Fig. 3C). A slight elongation of host cell microvilli surrounding some of the attached parasites was observed. Further observations on early development of *C. muris* were described in detail previously (Valigurová *et al.* 2007, 2008) and hence not reported again.

The progress of the asexual phase into Type I merogony was characterized by clusters of chromatin localized in the peripheral cytoplasm of the parasite (Fig. 3E). Daughter nuclei formed inside a Type I meront undergoing a nuclear division (Fig. 5B–D). The asynchrony of nuclear division often resulted in an odd number of chromatin clusters. By the process of multiple budding from the residuum still attached to the host cell (ectomerogony), motile and invasive merozoites differentiated (Figs 3F–G and 5A, E–O). Almost the entire cytoplasm of the mother meront appeared to be used up for merozoite

increase in the volume of the *lamina propria* (lp). TEM. (K) Cross-section showing hyperplasia of the parasitized gastric glands filled with numerous *C. muris* individuals (arrow) at 8 months PI. LM (Histology, toluidine blue). (L) Hypertrophy of the gastric glandular part at 8 months PI; enlarged gastric pits (arrowhead), parasite expanding from the pits to the luminal gastric epithelium (arrow). SEM. (M) View inside the dilated gastric pit filled by *C. muris* (arrow) at 8 months PI; hyperplasia of gastric cells (arrowhead). SEM. (N–P) Heavily modified gastric epithelium covered by numerous *C. muris* parasites (arrow) during the course of chronic infection after 2 years PI. SEM.
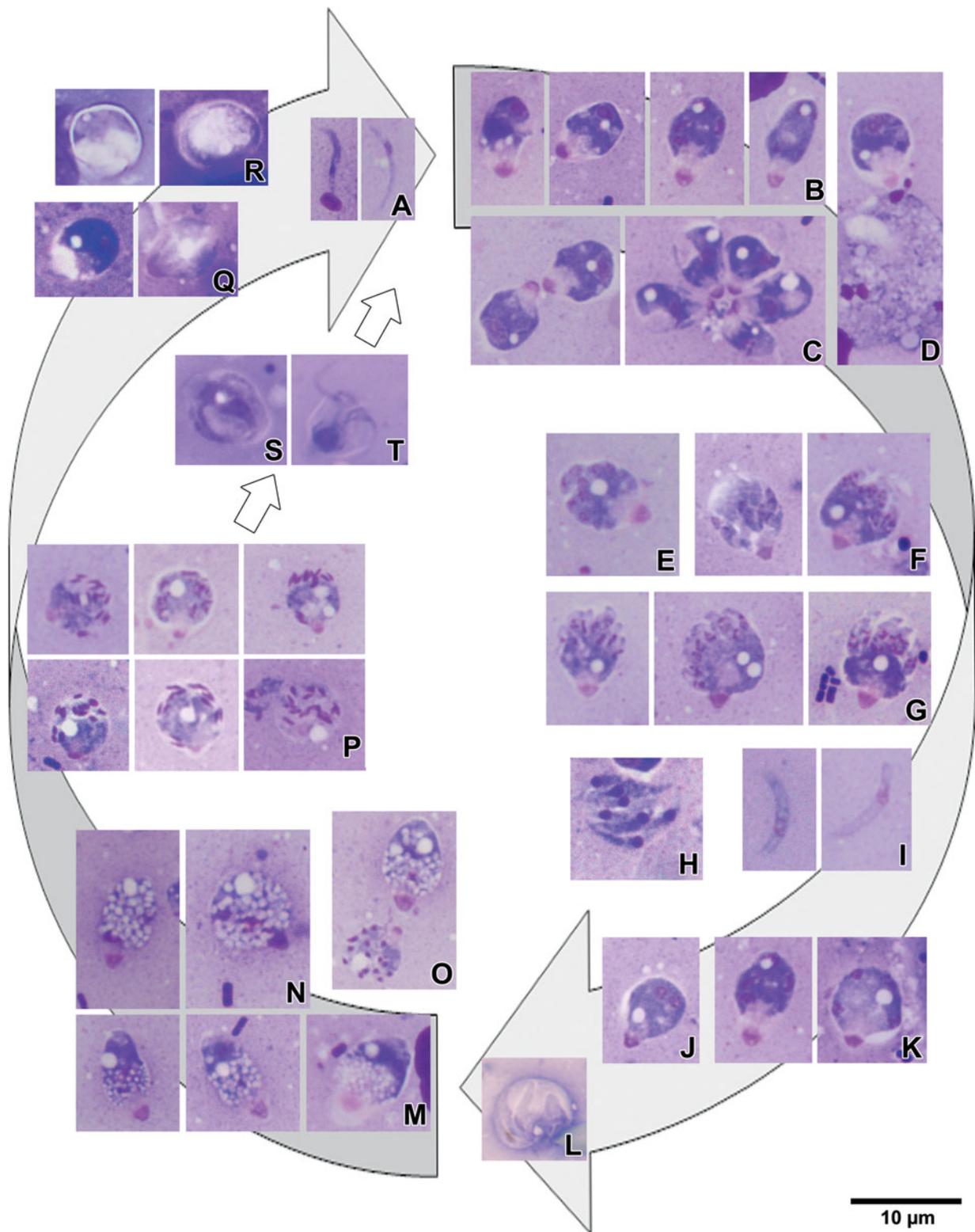
Fig. 3. The life cycle of *Cryptosporidium muris* as observed in smear preparations stained with Wright. (A) Free, infective sporozoites. (B–D) Trophozoite stage; gradually maturing trophozoites (B), clustering of trophozoites (C), trophozoite attached to a host cell (D). (E–G) Type I merogony; clusters of chromatin in the cytoplasm at the periphery of parasite (E), budding of merozoites from the meront cytoplasm (F, G). (H–I) Free, motile Type I merozoites. (J–K) Type II merogony; first mitotic division (J), four daughter nuclei formed following the second mitotic division (K). (L) Type II merozoites inside the parasitophorous sac. (M–N) Macrogamont stage; maturing macrogamonts (M) transforming into mature ones (N) typified by an increased number of amylopectin granules, giving their cytoplasm (purple) a foam-like appearance; (O) Mature macrogamont and microgamont exhibiting multiple divisions of nuclei. (P) Microgamont stage; small compact nuclei localized at the cytoplasm periphery or at the distal end of the microgamont. (Q–R) Thick-walled oocysts; zygote (left) transforming into an oocyst (right) still enveloped by the parasitophorous sac (Q), more advanced stages of oocyst sporulation following release from the sac (R). (S–T) Thin-walled oocysts enveloped by parasitophorous sacs, one of them releasing four sporozoites (T).

Table 1. *The occurrence of specific developmental stages of* C. muris

Developmental stages of C. muris	Size (µm)	First detection in the stomach of BALB/c mice	First detection in the stomach of M. coucha
Trophozoites	7·85 × 4·89	2·5 dpi	3·0 dpi
Type I Meront	9·51 × 7·25	2·5 dpi	3·0 dpi
Type II Meront	9·36 × 7·39	4·0 dpi	4·5 dpi
Free merozoites	9·64 × 1·52	4·0 dpi	4·5 dpi
Macrogamont	8·04 × 6·49	5·0 dpi	5·0 dpi
Microgamont	6·18 × 5·54	5·5 dpi	6·0 dpi
Thick-walled oocysts	7·48 × 5·86	5·0 dpi	5·0 dpi
Thin-walled oocysts	8·03 × 6·69	5·0 dpi	14·0 dpi
Sporozoites in stomach	11·72 × 0·98	6·0 dpi	14·0 dpi
Oocysts in feces	7·48 × 5·86	7·5 dpi	18·0 dpi

dpi = days post-infection; hpi = hours post-infection.

formation. Type I merogony usually resulted in the formation of 6–8 merozoites, most likely depending on the number of nuclear divisions (Figs 3H, I and 5K, L). Occasionally, five merozoites still attached to the residual body were observed (Fig. 5O). Type I merozoites (9·64 × 1·52 µm), which were released from the PS, either recycled to form another generation of Type I meronts, or transformed into the Type II meront stage and produced four merozoites. Observation on Type II merogony is well documented by scanning electron micrographs showing the ruptured PS releasing four merozoites and further confirmed by native/stained smear preparations (Figs 3J–L and 5P–S). The Type I meronts (9·51 × 7·25 µm) were observed in both hosts at the same time as the trophozoites; however, Type II meronts (9·36 × 7·39 µm) were first observed at 4 dpi in BALB/c mice and at 4·5 dpi in *M. coucha*.

Merozoites exhibited a typical subcellular organization (Fig. 5M and T), including presence of subpellicular microtubules, however no mitochondria were observed. In both host models, the Type I merozoites were usually present simultaneously with Type II merozoites, the latter being slightly shorter and broader. Merozoites seemed to possess several rhoptries (Fig. 5J and T).

Released merozoites (it is generally assumed that Type II merozoites) initiated sexual multiplication, called gametogony, via differentiating into either female (Fig. 3M–O) or male microgamonts (Fig. 3O and P). Macrogamonts (8·04 × 6·49 µm) were detected in both hosts at 5 dpi and microgamonts (6·18 × 5·54 µm) were successfully documented slightly later, i.e. at 5·5 dpi in BALB/c mice and at 6 dpi in *M. coucha*. The mature macrogamonts were easily recognized, as their cytoplasm was packed with

numerous oval-shaped amylopectin granules, the quantity of which was directly proportional to the maturation stage (Figs 3M–O and 6A–F, I). Their cytoplasm possessed typical wall-forming bodies localized just beneath the pellicle (Fig. 6D, E).

Non-mature microgamonts in stained smears resembled the meront stage but contained smaller and more compact nuclei (Fig. 3O). The nucleus of the microgamonts divided four times and gave rise to the 16 clusters of chromatin usually localized at the distal end or periphery of microgamonts (Fig. 3P). After nuclear division, daughter nuclei migrated out of the microgamont cytoplasm into the space of the PS and subsequently developing microgametes budding from the surface of the microgamont were observed (Figs 3P and 6G–K). The beginning of microgamete budding was accompanied by an obvious evagination of the microgamont pellicle (Fig. 6J and K). The formation of microgametes appeared to be asynchronous (Fig. 6J and K) and resulted in the formation of up to 16 microgametes. After separation of the mature microgametes, a large residual body remained attached to the host cell via feeder organelles (Fig. 6K). The mature non-flagellated, bullet-shaped microgametes exhibited a slightly flattened, expanded anterior region and possessed an elongated, condensed nucleus (Fig. 6L–P). Microgametes were covered by a relatively thick plasma membrane and an additional single membrane was observed beneath this in the anterior half of the body. This single membrane formed an invagination beneath the apical cap and appeared to join the anterior conical structure (Fig. 6O). Originating at the anterior conical structure localized just beneath the apical cap, numerous (at least 10) parallel-arranged microtubules extended posteriorly surrounding the nucleus (Fig. 6M–P). The microtubule forming a loop was observed (Fig. 6P) behind the posterior end of nucleus and it might play a role in pushing out the nucleus from the microgamete towards the macrogamont nuclear envelope during the fertilization process.

After macrogamonts became fertilized by microgametes (Fig. 6Q–R) their wall appeared thicker. Through a transient stage of the diploid zygote (Figs 3Q and 7A, C), they rapidly developed into oocysts (Figs 3R and 7A–M). The oocyst stage occurred within the same time period as macrogamonts, i.e. after 5 dpi in both hosts. In the course of sporulation, oocysts formed four sporozoites that were coiled around a large residual body (Fig. 7F–I). Based on TEM observations, oocysts appeared to sporulate *in situ* whilst being enveloped by the intact PS, as they exhibited already well-differentiated sporozoites (Fig. 7F, H and I). Both types of oocysts were observed: the typical thick-walled ones and a second type resembling the so-called 'thin-walled' oocysts (Figs 3R–T, 7H and I). Nevertheless, variability in oocyst wall thickness was very high.
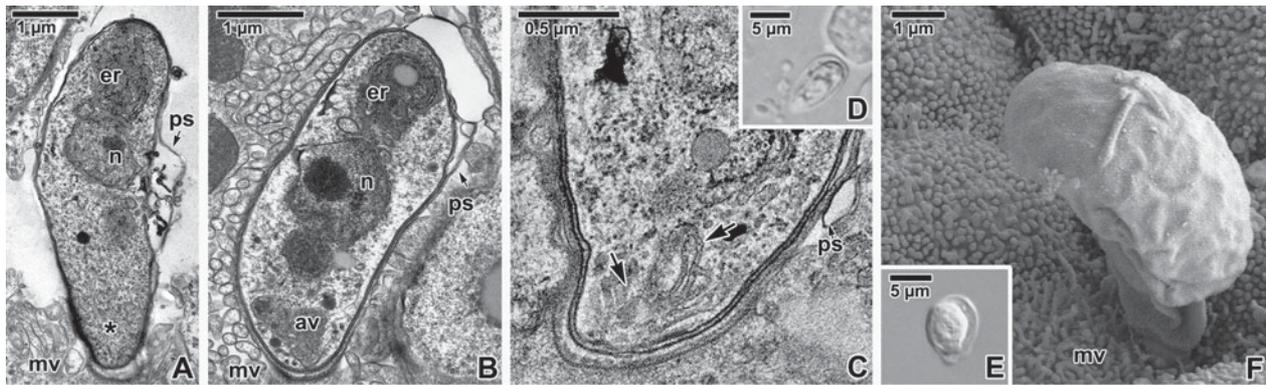
Fig. 4. Trophozoite stage. (A) Longitudinal section of an attached zoite gradually becoming enveloped by the parasitophorous sac (ps); endoplasmic reticulum (er), microvilli (mv), parasite nucleus (n). TEM. (B) Section of an early trophozoite enveloped by the parasitophorous sac (ps); anterior vacuole (av), endoplasmic reticulum (er), microvilli (mv), parasite nucleus (n). TEM. (C) Detailed view of an anterior part of a young trophozoite. Note the folded membrane of the anterior vacuole and its gradual transformation into the lamellae of the feeder organelle (arrows); parasitophorous sac (ps). TEM. (D) Young trophozoite. LM (native preparation). (E) Trophozoite enveloped by the parasitophorous sac. LM (native preparation); (F) View of a maturing trophozoite completely enveloped by the parasitophorous sac; elongated host cell microvilli (mv). SEM.

The suture present on the surface of a well-developed oocyst marks the place where sporozoites were released (Fig. 7D, J–L and N). As the 'thin-walled' oocysts found in BALB/c mice at 5 dpi appeared to open inside the host stomach, they are presumed to be responsible for the presence of free sporozoites ($11{\cdot}72 \times 0{\cdot}98\,\mu$m) observed in scrapings of gastric mucosa at 6 dpi (Fig. 7P) onwards and they appeared to result in autoinfection (Fig. 7O). In *M. coucha*, no 'thin-walled' oocysts were detected in the initial phase of parasitization, but they were observed from 14 dpi onwards, and the free sporozoites occurred simultaneously with them. In BALB/c mice, thick-walled oocysts ($7{\cdot}48 \times 5{\cdot}86\,\mu$m) that were shed into the environment in host feces were detected at 7·5 dpi, whereas this did not occur in feces of *M. coucha* until 18 dpi.

To detect early infection by *C. muris*, the experiment was repeated using a higher infective dose of 10^8 oocysts per host. Subsequently, additional microscopic and molecular analyses were performed. Based on PCR results, *C. muris* DNA was detected in the stomach of BALB/c mice at 1, 6, 12, 36, 48 and 72 hpi. Using the combined approach of SEM and PCR, other organs from BALB/c mice including pancreas, oesophagus, spleen, liver, Payer's patches, kidneys, lungs, duodenum, jejunum, ileum, gall bladder and feces were examined for the presence of *C. muris* developmental stages and specific *Cryptosporidium* DNA but none was found. The parasitization of the stomach in *M. coucha* was confirmed at 6, 48 and 72 hpi. The same organs as in BALB/c mice (except for the gall bladder) were analysed and showed positive results in the duodenum at 48 hpi and in the jejunum at 72 hpi. Using molecular tools, *C. muris* developmental stages were also found in the feces of *M. coucha* at 36 and 72 hpi.

DISCUSSION

Understanding the life cycle of parasitic organisms is fundamental to explain their pathogenicity. Parasitic strategies, such as the ability to enter into the host and avoid the host defence mechanisms, must be closely analysed. The essential factors influencing infectivity are morphological structure and the physiological processes occurring inside the parasite and host. The sensitivity of hosts to *C. muris* depends on its specific isolate or strain (Xiao *et al*. 1999; Kváč *et al*. 2008; Kodádková *et al*. 2010). Our observations on the life cycle of *C. muris* (strain TS03) in different rodent models showed a dissimilar chronology with respect to the occurrence of individual developmental stages. As the physiology and immune response to parasitization of both host models varies in many aspects, the host anatomy and tissue morphology together with enzymatic secretion appear to be important in the understanding and evaluation of differences in parasitization of both hosts with *C. muris*.

Localization

The gastric pathogen *C. muris* clearly prefers the acid environment of the stomach and the common use of hydrochloric acid to accelerate the *in vitro* excystation of its oocysts also serves as proof of this. The pH values in the gastrointestinal tract of a rat or mouse are about 5·5–6 in the mouth and intestinal parts, whereas those in the stomach rapidly decrease to 2–4 (Ward and Coates, 1987; McConnell *et al*. 2008). The stomach is comprised of a non-glandular and a glandular part. As the mucosa of the non-glandular stomach is lined by keratinized, stratified squamous epithelium without secretory activity, its surface is unsuitable for parasite attachment and development.
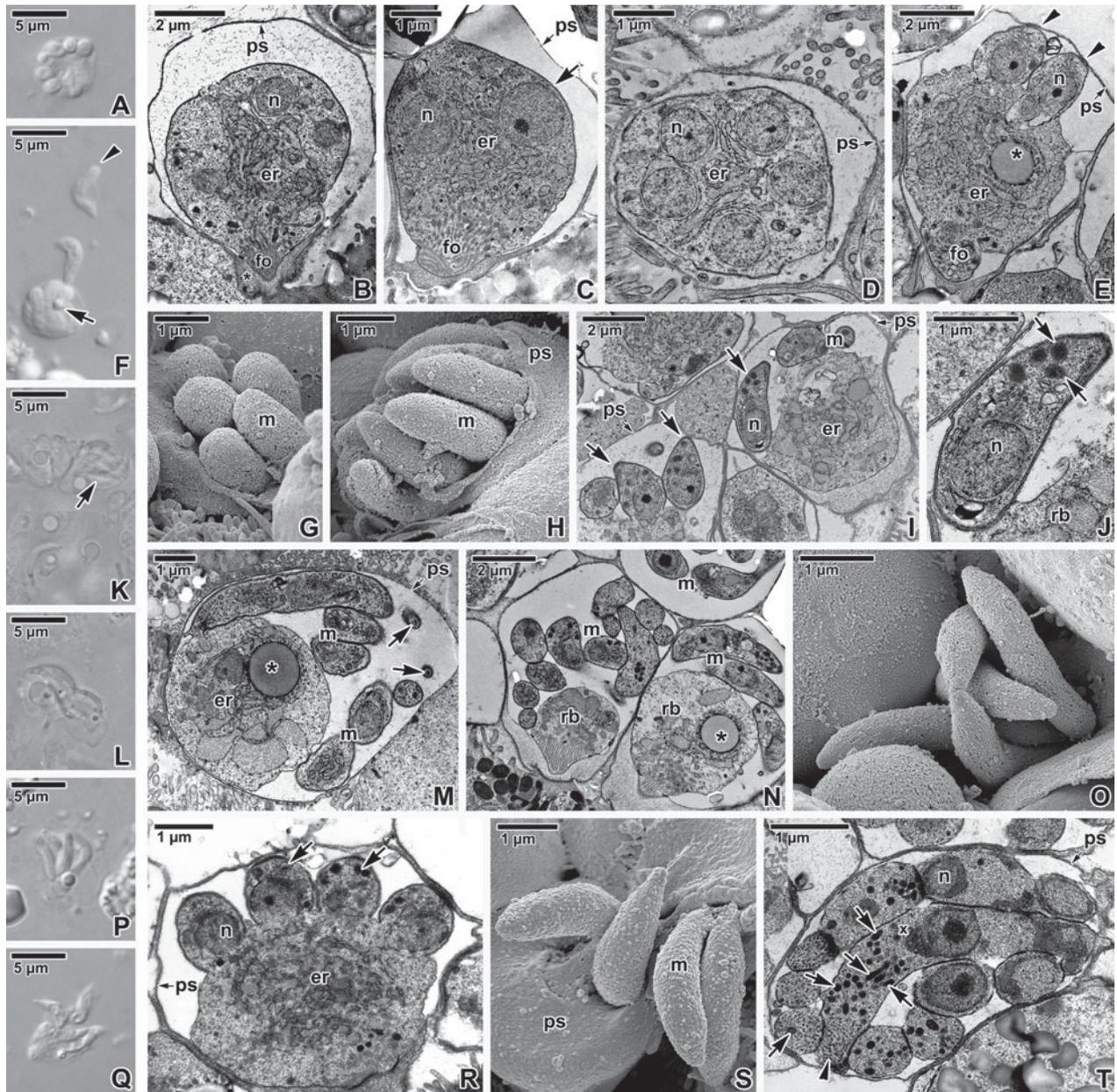
Fig. 5. Merogony. (A) Meront with six merozoites. LM (native preparation). (B–D) Asynchronous mitotic division of nuclei in a meront; cytoplasm with abundant endoplasmic reticulum (er), filamentous cytoplasm (asterisk), lamellae of feeder organelle (fo), nucleoli of future merozoites (n), parasitophorous sac (ps), pellicle of meront (arrow). TEM. Fig. D shows a meront with five daughter nuclei in cross section. TEM. (E) Meront with prominent endoplasmic reticulum (er), feeder organelle (fo) and lipid inclusion (asterisk). Note the formation of merozoites from the cytoplasm of the mother meront (arrowhead) still enveloped by an intact parasitophorous sac (ps). TEM. (F) Merozoite still attached to residual body with lipid inclusion (arrow); released merozoite (arrowhead). LM (native preparation). (G) Type I meront with budding merozoites (m). SEM. (H) Ruptured parasitophorous sac (ps) revealing more advanced stages of budding merozoites (m). SEM. (I) Daughter merozoites budding from a Type I meront still enveloped by a parasitophorous sac (ps); apical ends of merozoites (arrows), endoplasmic reticulum (er), nuclei (n). TEM. (J) Detailed view of budding merozoite from Fig. 5I; residual body of meront, nucleus (n), rhoptries (arrows). TEM. (K) Two parasitophorous sacs filled with Type I merozoites (arrow) inside and one free merozoite. LM (native preparation). (L) Merozoites being released from the parasitophorous sac. LM (native preparation). (M–N) Formation of merozoites (m) from the cytoplasm of a meront; ducts of merozoite rhoptries (arrows), large residual body (rb) with endoplasmic reticulum (er) and lipid inclusion (asterisk), parasitophorous sac (ps). TEM. (O) Odd numbers (5) of mature Type I merozoites attached to the residual body. SEM. (P–Q) Type II merogony producing four shorter merozoites. LM (native preparation). (R) Cross-section of a Type II meront; four merozoites with nucleus (n) and rhoptries (arrows). TEM. (S) Ruptured parasitophorous sac (ps) releasing four Type II merozoites (m). SEM. (T) Mature merozoites in a parasitophorous sac in longitudinal section; dense granules (×), micronemes (arrowhead), rhoptries (arrows).
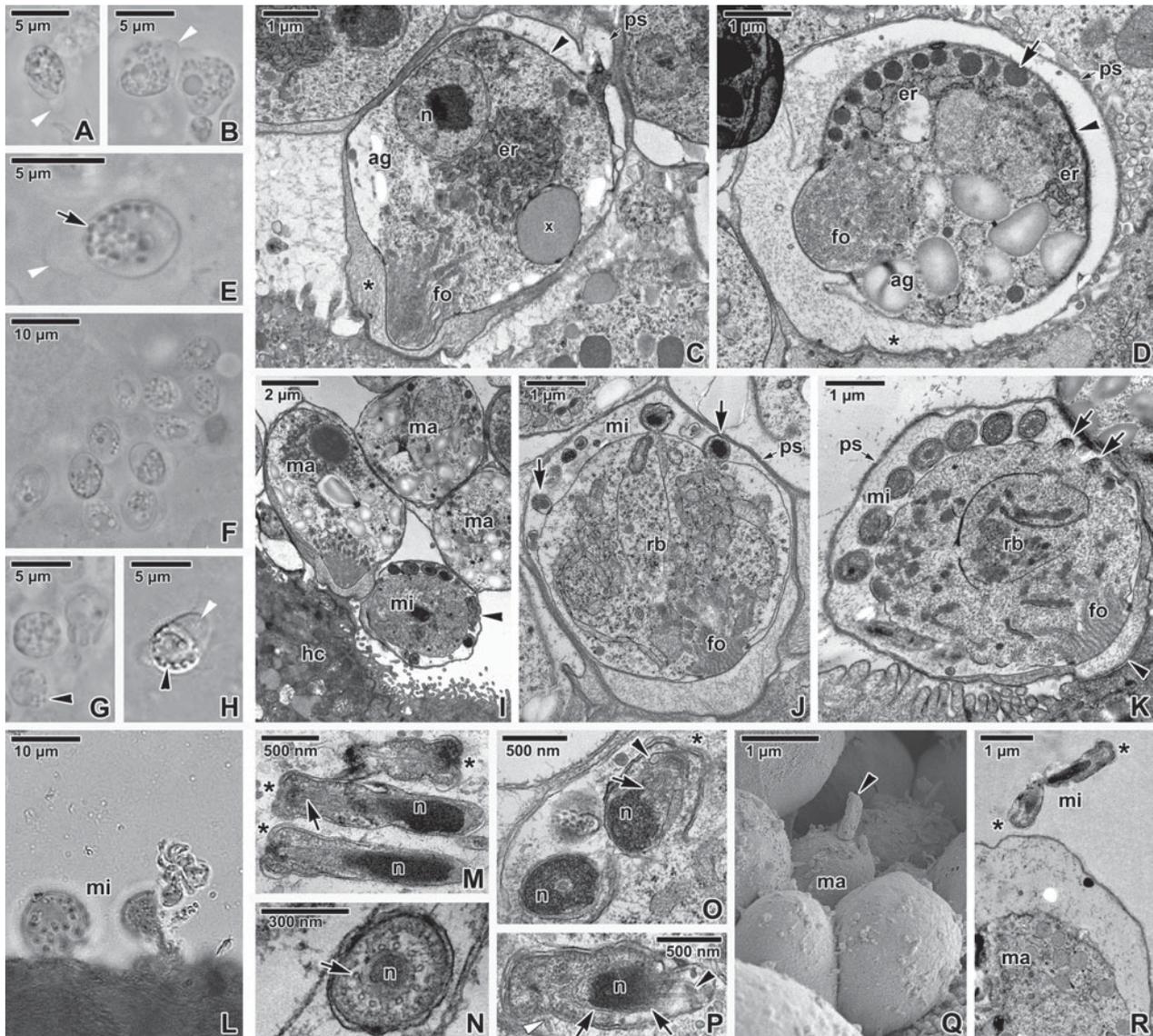
Fig. 6. Sexual multiplication. (A–B) Macrogamonts packed with numerous amylopectin granules giving them a foam-like appearance, feeder organelle (white arrowhead). LM (native preparation). (C) Maturing macrogamont with a few amylopectin granules (ag), prominent endoplasmic reticulum (er) situated in the centre, feeder organelle (fo), filamentous projection (asterisk), lipid inclusion (x), nucleus (n), pellicle of macrogamont (arrowhead). TEM. (D) Macrogamont with wall-forming bodies (arrow) localized just beneath its pellicle (arrowhead); the lamellae of the feeder organelle (fo), cytoplasm with prominent amylopectin granules (ag), endoplasmic reticulum (er), parasitophorous sac (ps). TEM. (E) Macrogamont with numerous wall-forming bodies (arrow), feeder organelle (white arrowhead). LM (native preparation). (F) Numerous macrogamonts at different stages of development. LM (native preparation). (G,H) Microgamonts with budding microgametes localized at their distal ends or periphery (arrowhead), feeder organelle (white arrowhead). LM (native preparation). (I) Various stages of mature macrogamonts (ma) and one microgamont (mi) with microgametes (arrowhead); host cell (hc). TEM. (J) Microgamont showing an asynchronous budding (arrows) of microgametes (mi); feeder organelle (fo), parasitophorous sac (ps), residual body (rb).TEM. (K) Microgamont exhibiting a formation of microgametes (mi) inside a parasitophorous sac (ps); dense band (arrowhead), feeder organelle (fo), residual body (rb). TEM. (L) Two microgamonts (mi) at different developmental stages stained with Lugol's iodine; free bullet-shaped microgametes (right). LM. (M) Higher magnification of three microgametes in longitudinal section. Note the apical cap (asterisks) and the elongated nucleus (n) surrounded by microtubules (arrow). TEM. (N) Higher magnification of a microgamete in cross-section; microtubules (arrow) surrounding the nucleus (n). TEM. (O) Microgamete in tangential section; apical cap (asterisk) showing the invagination of the inner single membrane (arrowhead) attached to an anterior conical structure; microtubules (arrow), nucleus (n). TEM. (P) Further microgamete in longitudinal section; concentric lamellae located posteriorly to the apical cap (white arrow), microtubules (arrows), microtubule forming a loop (arrowhead) around posterior end of nucleus (n). TEM. (Q) The microgamete (arrowhead) penetrating the parasitophorous sac most likely enveloping a macrogamont (ma). SEM. (R) Free microgametes (mi) close to the macrogamont (ma), apical caps of microgametes (asterisks). TEM.
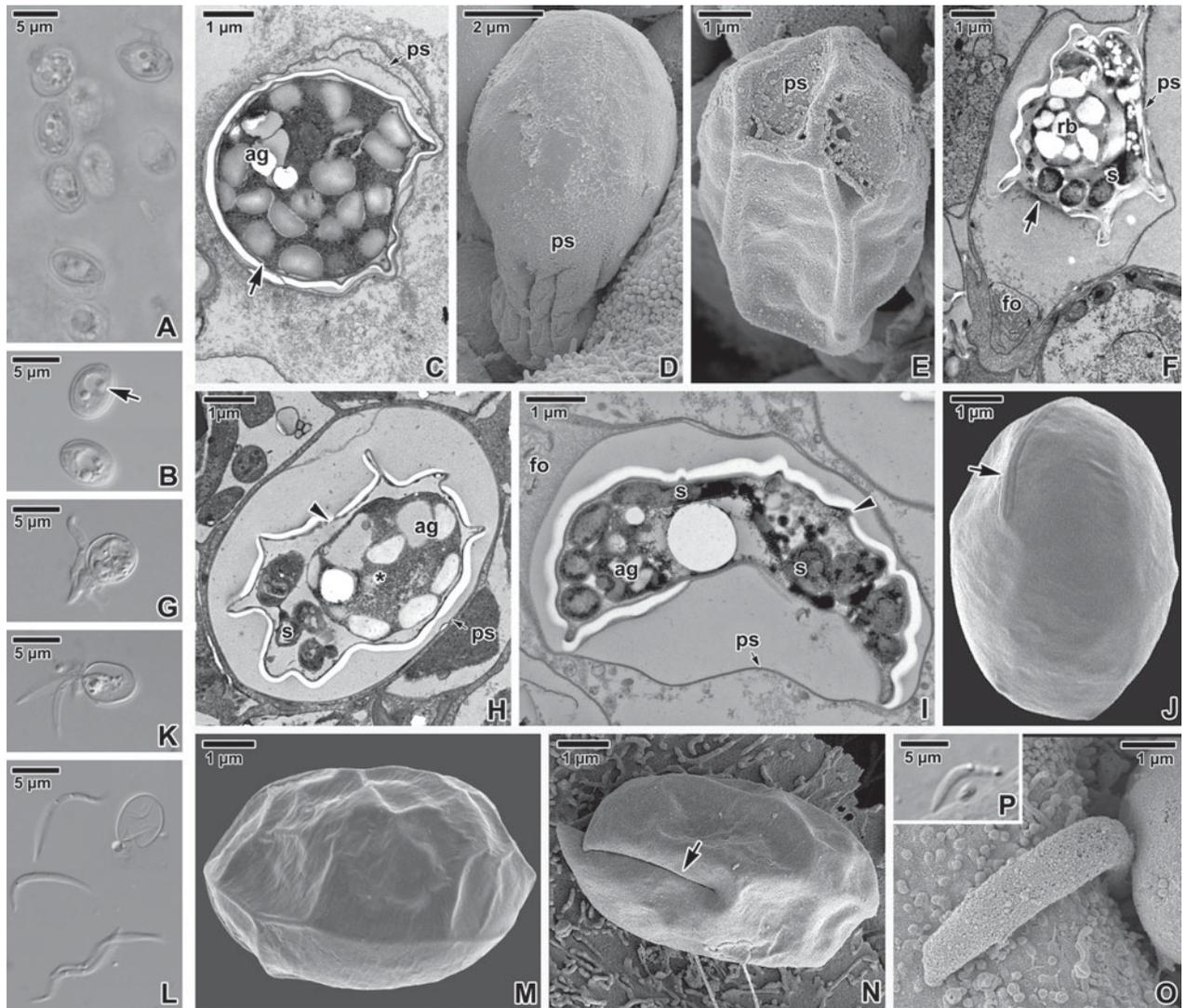
Fig. 7. Oocyst sporulation and excystation. (A) Various developmental stages from zygotes to oocysts. LM (native preparation). (B) Non-sporulated oocysts possessing a large residual body (arrow). LM (native preparation). (C) Zygote with numerous amylopectin granules (ag) after fertilization; developing oocyst wall (arrow), parasitophorous sac (ps). TEM. (D) Mature oocyst inside parasitophorous sac. SEM. (E) Oocyst in retreating parasitophorous sac (ps). SEM. (F) Longitudinal section of an oocyst in parasitophorous sac (ps); feeder organelle (fo), large residual body (rb), formed sporozoites (s), oocyst wall (arrow). TEM. (G) Excystation of sporozoites from the oocyst. LM (native preparation). (H) Thin-walled oocyst with sporozoites (s) inside a complete parasitophorous sac (ps); residual body (asterisk) with amylopectin granules (ag), wall of oocyst (arrowhead). TEM. (I) Thick-walled oocyst inside an intact parasitophorous sac (ps), amylopectin granules (ag), sporozoites (s). TEM. (J) Oocyst equipped with a typical suture (arrow). SEM. (K) The excystation of sporozoites from the oocyst. LM (native preparation). (L) Empty oocyst and free sporozoites. LM (native preparation). (M) Oocyst with an even surface considered to be thin-walled. SEM. (N) The ruptured empty oocyst. SEM. (O) Free sporozoite invading the gastric epithelium. SEM. (P) Invading sporozoite. LM (native preparation).

In contrast, the glandular part forms gastric pits lined by a simple columnar epithelium. Simple tubular gastric glands, found on the bottom of the gastric pit, are dedicated to the production of acids to maintain the low pH level of the stomach juice and proteases, as well as mucous substances. The wall of the glandular part of the stomach is thicker and creates longitudinal folds (Ward and Coates, 1987; Ghoshal and Bal, 1989). Considering all these morphological features, despite its extremely acid environment providing less hospitable conditions for parasites than the intestine,

the gastric glandular part appears to be more suitable for *Cryptosporidium* development when compared with the non-glandular part. Hence, the question arises how the invasive stages of these minute parasites avoid the effects of gastric juices containing strong acids. Matsubayashi *et al*. (2011) showed that the viability of sporozoites from oocysts excysted in medium at pH 7·0 is approximately 90% in the gastric species, *Cryptosporidium andersoni*, in contrast to 56% viable sporozoites for the intestinal species *C. parvum*. At a lower pH, however, the viability of

gastric sporozoites gradually declined to 61% after 3 h incubation at pH 2. Consequently, in comparison with intestinal cryptosporidia, the better adaptation of gastric species to an acidic environment enables them to survive for longer in the stomach (Matsubayashi *et al.* 2010).

In general, cryptosporidia have evolved efficient strategies to avoid the potential harmful effects of the gastrointestinal tract, e.g. direct exposure to digestive enzymes, possible mechanical damage or their peeling off from the host tissue. Probably one of the most important of these strategies is enveloping by the PS of host cell origin (Valigurová *et al.* 2007, 2008). Another is invading a proper shelter (e.g. gland or pits) and becoming covered by a mucus layer, especially in gastric species. To prevent too-rapid erosion of the gastric mucosa due to a hostile stomach environment, the surface cells and cells of the gland necks produce mucous secretions that form a relatively thick protective layer, which often hampers the ability to view inside the gastric gland using SEM. Even very careful washing of gastric tissue is often not sufficient to clear the entire surface from mucus, which forms a compact and non-transparent layer after chemical fixation. As even this protection is not perfect, the shedding of dead cells from the gastric pits into the lumen is often observed and might also be one of the reasons for the occasional detachment of PS filled with cryptosporidia and their subsequent presence in the host intestine or feces.

Another curiosity is the progress and mode of parasitization by *C. muris* as well as its dispersal throughout the gastric tissue in an irregular, island-like pattern. Obviously, invasive stages preferred regions that were already occupied by *C. muris*. This evidently non-competitive behaviour could be understood as exploiting the colonization of epithelial tissue (cell) already modified by the parasite. Stained smear preparations, showing parasites oriented by their apical ends to each other, confirmed this speculation.

Pathological changes

Both host models displayed the same pathological manifestations, but significantly differed in the chronology of parasitization. Taylor *et al.* (1999) observed the correlation between increased infective dose and subsequent shortening of the prepatent period of mice as well as the increased shedding of oocysts. In this study, increased infective doses used for inoculation did not influence the success of parasite detection in the host stomach in the early course of parasitization, even if all mentioned detection methods including molecular tools were used.

The pathological alterations induced by the multiplication of cryptosporidia in BALB/c mice, were compared with other studies (Ozkul and Aydin, 1994; Aydin and Ozkul, 1996; Taylor *et al.* 1999; Kváč *et al.* 2008). Our observations correspond with previous reports on the self-curing process in BALB/c mice infected with different strains of *C. muris* linked with migration and proliferation of T-cells in the site of infection (Jalovecká *et al.* 2010; Kváč *et al.* 2011).

In *M. coucha*, the immune system obviously failed and modifications of gastric tissue persisted during the entire chronic phase of infection. The parasite continued to expand from affected gastric pits to the surrounding healthy gastric epithelium and these observations are in concordance with previous study (Valigurová *et al.* 2008). Kváč *et al.* (2008) and Kváč and Vítovec (2003) observed the dispersal of parasitization in the abomasum of domestic ruminants from the region of the *curvature major*. Pathological alterations in this study concur with their histological observations. In contrast to Taylor *et al.* (1999), the infiltration of the *lamina propria* was not observed and these findings correspond with the study of Kváč *et al.* (2008).

Life cycle

In general, excystation is a very rapid process (Lumb *et al.* 1988). As it was almost impossible to record invading stages and the first observed stages were usually trophozoites, more sensitive molecular tools were used to detect *C. muris* DNA. Considering the irregular manner of parasitization, negative results of PCR for the presence of *C. muris* in stomachs of *M. coucha* could be the consequence of tissue excision from the non-parasitized part. Although molecular methods specifically proved the presence of *C. muris* DNA in the feces or stomach, they did not provide information concerning the presence of its concrete developmental stages, i.e. residual oocysts passing through the body *vs* real infection. For example, after unsuccessful attachment of zoites to the epithelium or due to the mechanical detachment of the PS in the area of the dense band reported previously (Valigurová *et al.* 2008), various stages apart from oocysts might be present in host feces. This could also explain positive testing of *M. coucha* duodenum and jejunum. Miller and Schaefer (2007) claim that intact or excysted oocysts in the first hours following inoculation were neither detected in the host (stomach, caecum and colon) nor in its feces. They suggested that oocysts were destroyed during normal transit through the gut to the feces. Considering the persistence of sporulating oocysts released from the stomach and passing through the intestine to the feces, it is questionable whether well-developed and resistant oocysts used for inoculation could be destroyed by digestion if not excysted. Acknowledging such a possibility, sporulating oocysts leaving the host should also be destroyed.

Several studies highlight extraordinary epicellular development of cryptosporidia and their phylogenetic affinity with gregarines (e.g. Barta and Thompson, 2006; Valigurová *et al.* 2007; Valigurová *et al.* 2008). Despite few studies reporting a complete development of cryptosporidia in cell-free cultures (Hijjawi *et al.* 2001, 2010; Borowski *et al.* 2010), we did not noticed any extracellular stages resembling those of gregarines and developing without host cells. This study did not focus on the formation of the attachment site and the epicellular localization of *C. muris* as newly obtained data confirmed our previous published findings (Valigurová *et al.* 2007, 2008). Because of the unique niche of *C. muris* developing within the PS, this parasite requires a more sophisticated defence strategy against the unfriendly host environment when compared with typical intracellular coccidians. The PS is a product of the host cell extensions enveloped by the plasma membrane, modified by products of the parasite (Robert *et al.* 1994; Bonnin *et al.* 1995; McDonald *et al.* 1995; O'Hara *et al.* 2004; Valigurová *et al.* 2007, 2008) and thus perfectly masks the parasite from host immune mechanisms (McDonald *et al.* 1992, 1996). Although we noticed the formation of several layers of PS in early stage of trophozoites, we did not observe the pre-parasitophorous vacuole described by Huang *et al.* (2004).

Generally, the occurrence of two generations of merogony is described for cryptosporidia (Vetterling *et al.* 1971; Current and Reese, 1986) and even merogony including three generations has been observed for *C. baileyi* (Current *et al.* 1986). Only one published report on Type II merogony in *C. muris* exists to date (Aydin, 1999), but because this is exclusively based on TEM, it cannot be considered reliable. This observation might be influenced by the plane of sectioning and only serial sectioning or a complete view of the entire parasite (as obtained by LM or SEM) would avoid any possible misinterpretations. This study, however, succeeds to reliably document the presence of both the Type I and Type II merogony. Considering three cycles of mitotic divisions in Type I meronts, it might be possible that Type II merogony comprises only two generations of nuclei, resulting in the formation of four merozoites. In addition, an anomaly in the final number of Type I merozoites often occurred. In accordance with a previous TEM study on *C. muris* (Uni *et al.* 1987), we observed subpellicular microtubules in merozoites. The failure of studies on *C. parvum* (Current and Reese, 1986) and *C. wrairi* (Veterling *et al.* 1971) to document subpellicular microtubules, might be due to the known instability of these structures and to their frequent damage due to improper fixation. In addition, as the basic mechanism of apicomplexan motility is expected to be based on the orientation of the actomyosin motor by subpellicular microtubules (Dubremetz *et al.*

1998), it is not likely that motile merozoites lack these structures.

Concerning the sexual phase of the life cycle, the most easily recognized stages were macrogamonts. Microgamonts are often found in close proximity to macrogamonts, probably to facilitate macrogamont fertilization, considering that microgametes are non-flagellated. The ratio of their occurrence in comparison to that of macrogamonts, however, was much lower. This might be the consequence of a large number of microgametes (up to 16) produced by a single microgamont, that are sufficient to fertilize the surrounding macrogamonts. The presence of minute microgamonts in low numbers might be the reason for our failure to detect them in the early phase of parasitization (they were detected later than oocysts). Fertilization as described previously (Current and Reese, 1986; Aydin and Ozkul, 1996), was not observed using TEM, but we observed migrating microgametes towards the macrogamont surface and found similar coupled individuals in smears stained with Lugol's iodine as well as in SEM preparations.

Endogenous stages of thick-walled oocysts were detected in the stomachs of both hosts. In the same time period, oocysts enveloped by an obviously thinner wall were noticed in BALB/c mice, whereas similar 'thin-walled' oocysts in *M. coucha* were absent. We speculate that sporulated oocysts might also have been present during earlier phases of infection in *M. coucha*, but stomach dimensions and anatomical features probably did not allow their detection. Since the first microscopic detection of sporulated oocysts of *C. muris* in host feces was possible only after several hours or even days, the destiny of oocysts found inside the host stomach and identified as thick-walled oocysts remains enigmatic. In the course of early parasitization, we repeatedly observed structures resembling empty oocysts in mucosal scrapings or fecal smears, and often, the wall of these structures appeared to be very thin. We consider them to be oocysts, but since the identification of developmental stages based exclusively on native (unstained) preparations is problematic and usually not reliable, we cannot conclude this with absolute certainty. Current and Reese (1986) claimed to show endogenous thick-walled oocysts releasing sporozoites (Fig. 23 in their study), but this stage more resembles an earlier stage of merogony than an oocyst. Numerous released sporozoites found in mucosal scrapings 6 dpi in BALB/c mice and 14 dpi in *M. coucha* support the existence of oocysts that release sporozoites in an early phase of infection. Considering the variability of wall thickness in mature oocysts observed in ultrathin sections during this study, several conflicts arose. Firstly, it appears almost impossible to strictly identify oocysts as thick- or thin-walled, even via electron microscopy. Furthermore, the size of the oocyst wall in cryptosporidia is not uniform and varies significantly

during oocyst maturation. The study that reported the existence of so-called 'thin-walled' oocysts (Current and Reese, 1986; Aydin, 1999), described them as structures comprising a single unit membrane, in contrast to that of thick-walled oocysts that contain both the inner and outer membrane. Despite the high-quality micrographs showing the wall in maturing oocysts in detail, the magnification in micrographs showing sporulated oocysts in the mentioned study is not sufficient to evaluate the true number of oocysts in membranes. Moreover, we often observed detached PS containing oocysts in various stages of sporulation and the outer layer reported to be the outer membrane of the oocyst wall in Fig. 45 in Current and Reese (1986) actually more resembles the PS shown in micrographs showing attached stages. Whether the variability in the thickness of the oocyst wall found in the stomach is the consequence of oocyst structural disorder, their malfunction or simply misinterpretation of observations caused by the oblique plane of ultrathin sectioning, remains open. The 'thin-walled' oocysts are believed to be responsible for autoinfection. Nevertheless, oocysts release only four sporozoites equipped with a single rhoptry and thus having only a single attempt for successful attachment to the suitable host cell (Tetley *et al*. 1998; Petry and Harris, 1999; Blackman and Bannister, 2001; Petry, 2004; O'Hara *et al*. 2005). In contrast, merogony produces six to eight merozoites, which seem to possess several rhoptries and numerous micronemes (Figs 5J and 5T in this study), providing them more chances for successful attachment (Current and Bick, 1989; Tetley *et al*. 1998; Jirků *et al*. 2008). Since the cyclic multiplication of parasites during Type I merogony (asexual division resulting in identical daughter cells) is undoubtedly more than sufficient for the infestation of the host tissue by *C. muris* and the zygote is the only heterozygous diploid stage in the life cycle of cryptosporidia (McLauchlin and Nichols, 2002), the multiplication via autoinfective oocysts (sexual stage) appears to be of benefit to increase the genetic variability of the parasite and thereby its fitness and probably infectivity.

CONCLUSIONS

A combined approach used in this study was crucial to achieve reliable and complex data on the life cycle of *C. muris* in two host models. The most problematic issue proved to be the detection of parasite developmental stages in gastric pits during the early phase of parasitization. Light micrographs helped to record the presence of individual developmental stages of *C. muris* in host stomachs and to visualize their typical morphological features in staining preparations, and these are in accordance with Tyzzer's detailed depictions shown in his work (Tyzzer, 1910). The Wright staining procedure has been evaluated to be the most suitable method, since it allows a reliable and relatively rapid identification of all developmental stages found in scrapings from host stomach.

REFERENCES

Arrowood, M. J. and Sterling, C. R. (1987). Isolation of *Cryptosporidium* oocysts and sporozoites using discontinuous sucrose and isopycnic Percoll gradients. *Journal of Parasitology* **73**, 314–319.

Aydin, Y. (1999). The ultrastructure of the parasite and the mucus cell relationship and endogenous stages of *Cryptosporidium muris* in the stomach of laboratory mice. *Turkish Journal of Veterinary and Animal Sciences* **23**, 117–125.

Aydin, Y. and Ozkul, I. A. (1996). Infectivity of *Cryptosporidium muris* directly isolated from the murine stomach for various laboratory animals. *Veterinary Parasitology* **66**, 257–262.

Barta, J. R. and Thompson, R. C. (2006). What is *Cryptosporidium*? Reappraising its biology and phylogenetic affinities. *Trends in Parasitology* **22**, 463–468.

Blackman, M. J. and Bannister, L. H. (2001). Apical organelles of Apicomplexa: biology and isolation by subcellular fractionation. *Molecular and Biochemical Parasitology* **117**, 11–25. doi: 10.1016/S0166-6851(01)00328-0.

Bonnin, A., Gut, J., Dubremetz, J. F., Nelson, R. G. and Camerlynck, P. (1995). Monoclonal antibodies identify a subset of dense granules in *Cryptosporidium parvum* zoites and gamonts. *Journal of Eukaryotic Microbiology* **42**, 395–401.

Borowski, H., Thompson, R. C., Armstrong, T. and Clode, P. L. (2010). Morphological characterization of *Cryptosporidium parvum* life-cycle stages in an *in vitro* model system. *Parasitology* **137**, 13–26. doi: 10.1017/s0031182009990837.

Chappell, C. L., Okhuysen, P. C., Sterling, C. R., Wang, C., Jakubowski, W. and Dupont, H. L. (1999). Infectivity of *Cryptosporidium parvum* in healthy adults with pre-existing anti-*C. parvum* serum immunoglobulin G. *American Journal of Tropical Medicine and Hygiene* **60**, 157–164.

Current, W. L. and Bick, P. H. (1989). Immunobiology of *Cryptosporidium* spp. *Pathology and Immunopathology Research* **8**, 141–160.

Current, W. L. and Reese, N. C. (1986). A comparison of endogenous development of three isolates of *Cryptosporidium* in suckling mice. *Journal of Protozoology* **33**, 98–108.

Current, W. L., Upton, S. J. and Haynes, T. B. (1986). The life cycle of *Cryptosporidium baileyi* n. sp. (Apicomplexa, Cryptosporidiidae) infecting chickens. *Journal of Protozoology* **33**, 289–296.

Dubremetz, J. F., Garcia-Reguet, N., Conseil, V. and Fourmaux, M. N. (1998). Apical organelles and host-cell invasion by Apicomplexa. *International Journal for Parasitology* **28**, 1007–1013. doi: 10.1016/s0020-7519(98)00076-9.

Fayer, R. and Santin, M. (2009). *Cryptosporidium xiaoi* n. sp. (Apicomplexa: Cryptosporidiidae) in sheep (*Ovis aries*). *Veterinary Parasitology* **164**, 192–200.

Gatei, W., Ashford, R. W., Beeching, N. J., Kamwati, S. K., Greensill, J. and Hart, C. A. (2002). *Cryptosporidium muris* infection in an HIV-infected adult, Kenya. *Emerging Infectious Diseases* **8**, 204–206.

Ghoshal, N. G. and Bal, H. S. (1989). Comparative morphology of the stomach of some laboratory mammals. *Laboratory Animals* **23**, 21–29.

Guyot, K., Follet-Dumoulin, A., Lelievre, E., Sarfati, C., Rabodonirina, M., Nevez, G., Cailliez, J. C., Camus, D. and Dei-Cas, E. (2001). Molecular characterization of *Cryptosporidium* isolates obtained from humans in France. *Journal of Clinical Microbiology* **39**, 3472–3480.

Hijjawi, N. S., Meloni, B. P., Morgan, U. M. and Thompson, R. C. (2001). Complete development and long-term maintenance of *Cryptosporidium parvum* human and cattle genotypes in cell culture. *International Journal for Parasitology* **31**, 1048–1055.

Hijjawi, N., Estcourt, A., Yang, R., Monis, P. and Ryan, U. (2010). Complete development and multiplication of *Cryptosporidium hominis* in cell-free culture. *Veterinary Parasitology* **169**, 29–36.

Huang, B. Q., Chen, X. M. and LaRusso, N. F. (2004). *Cryptosporidium parvum* attachment to and internalization by human biliary epithelia *in vitro*: a morphologic study. *Journal of Parasitology* **90**, 212–221.

Hůrková, L., Hajdúšek, O. and Modrý, D. (2003). Natural infection of *Cryptosporidium muris* (Apicomplexa: Cryptosporiidae) in Siberian chipmunks. *Journal of Wildlife Diseases* **39**, 441–444.

Jalovecká, M., Sak, B., Kváč, M., Květoňová, D., Kučerová, Z. and Salát, J. (2010). Activation of protective cell-mediated immune response in gastric mucosa during *Cryptosporidium muris* infection and re-infection in immunocompetent mice. *Parasitology Research* **106**, 1159–1166.

Jiang, J., Alderisio, K. A. and Xiao, L. (2005). Distribution of *Cryptosporidium* genotypes in storm event water samples from three watersheds in New York. *Applied and Environmental Microbiology* **71**, 4446–4454.

Jirků, M., Valigurová, A., Koudela, B., Křížek, J., Modrý, D. and Šlapeta, J. (2008). New species of *Cryptosporidium* Tyzzer, 1907 (Apicomplexa) from amphibian host: morphology, biology and phylogeny. *Folia Parasitologica* **55**, 81–94.

Katsumata, T., Hosea, D., Ranuh, I. G., Uga, S., Yanagi, T. and Kohno, S. (2000). Short report: possible *Cryptosporidium muris* infection in humans. *American Journal of Tropical Medicine and Hygiene* **62**, 70–72.

Kilani, R. T. and Sekla, L. (1987). Purification of *Cryptosporidium* oocysts and sporozoites by cesium chloride and Percoll gradients. *American Journal of Tropical Medicine and Hygiene* **36**, 505–508.

Kodádková, A., Kváč, M., Ditrich, O., Sak, B. and Xiao, L. (2010). *Cryptosporidium muris* in a reticulated giraffe (*Giraffa camelopardalis reticulata*). *Journal of Parasitology* **96**, 211–212.

Kváč, M. and Vítovec, J. (2003). Prevalence and pathogenicity of *Cryptosporidium andersoni* in one herd of beef cattle. *Journal of Medicine Series B–Infection Diseases and Veterinary Public Health* **50**, 451–457.

Kváč, M., Sak, B., Květoňová, D., Ditrich, O., Hofmannová, L., Modrý, D., Vítovec, J. and Xiao, L. (2008). Infectivity, pathogenicity, and genetic characteristics of mammalian gastric *Cryptosporidium* spp. in domestic ruminants. *Veterinary Parasitology* **153**, 363–367.

Kváč, M., Kodádková, A., Sak, B., Květoňová, D., Jalovecká, M., Rost, M. and Salát, J. (2011). Activated CD8+ T cells contribute to clearance of gastric *Cryptosporidium muris* infections. *Parasite Immunology* **33**, 210–216.

Lumb, R., Smith, K., O'Donoghue, P. J. and Lanser, J. A. (1988). Ultrastructure of the attachment of *Cryptosporidium* sporozoites to tissue culture cells. *Parasitology Research* **74**, 531–536.

Lupo, P. J., Langer-Curry, R. C., Robinson, M., Okhuysen, P. C. and Chappell, C. L. (2008). *Cryptosporidium muris* in a Texas canine population. *American Journal of Tropical Medicine and Hygiene* **78**, 917–921.

Matsubayashi, M., Ando, H., Kimata, I., Nakagawa, H., Furuya, M., Tani, H. and Sasai, K. (2010). Morphological changes and viability of *Cryptosporidium parvum* sporozoites after excystation in cell-free culture media. *Parasitology* **137**, 1861–1866.

Matsubayashi, M., Ando, H., Kimata, I., Takase, H., Nakagawa, H., Furuya, M., Tani, H. and Sasai, K. (2011). Effect of low pH on the morphology and viability of *Cryptosporidium andersoni* sporozoites and histopathology in the stomachs of infected mice. *International Journal for Parasitology* **41**, 287–292. doi: 10.1016/j.ijpara.2010.09.009.

McConnell, E. L., Basit, A. W. and Murdan, S. (2008). Measurements of rat and mouse gastrointestinal pH, fluid and lymphoid tissue, and implications for in-vivo experiments. *Journal of Pharmacy and Pharmacology* **60**, 63–70.

McDonald, V., Deer, R., Uni, S., Iseki, M. and Bancroft, G. J. (1992). Immune responses to *Cryptosporidium muris* and *Cryptosporidium parvum* in adult immunocompetent or immunocompromised (nude and SCID) mice. *Infection and Immunity* **60**, 3325–3331.

McDonald, V., McCrossan, M. V. and Petry, F. (1995). Localization of parasite antigens in *Cryptosporidium parvum*-infected epithelial cells using monoclonal antibodies. *Parasitology* **110**, 259–268.

McDonald, V., Robinson, H. A., Kelly, J. P. and Bancroft, G. J. (1996). Immunity to *Cryptosporidium muris* infection in mice is expressed through gut CD4+ intraepithelial lymphocytes. *Infection and Immunity* **64**, 2556–2562.

McLauchlin, J. and Nichols, G. (2002). Microbiology and the investigation of waterborne outbreaks. In *Drinking Water and Infectious Disease* (ed. McLauchlin, J. and Nichols, G.), pp. 87–96. CRC Press, Boca Raton, FL, USA.

Miláček, P. and Vítovec, J. (1985). Differential staining of cryptosporidia by aniline-carbol-methyl violet and tartrazine in smears from feces and scrapings of intestinal mucosa. *Folia Parasitologica* **32**, 50.

Miller, T. A. and Schaefer, F. W., III (2007). Characterization of a *Cryptosporidium muris* infection and reinfection in CF-1 mice. *Veterinary Parasitology* **144**, 208–221.

O'Hara, S. P., Yu, J. R. and Lin, J. J. (2004). A novel *Cryptosporidium parvum* antigen, CP2, preferentially associates with membranous structures. *Parasitology Research* **92**, 317–327.

O'Hara, S. P., Huang, B. Q., Chen, X. M., Nelson, J. and LaRusso, N. F. (2005). Distribution of *Cryptosporidium parvum* sporozoite apical organelles during attachment to and internalization by cultured biliary epithelial cells. *Journal of Parasitology* **91**, 995–999.

Ozkul, I. A. and Aydin, Y. (1994). Natural *Cryptosporidium muris* infection of the stomach in laboratory mice. *Veterinary Parasitology* **55**, 129–132.

Palmer, C. J., Xiao, L., Terashima, A., Guerra, H., Gotuzzo, E., Saldias, G., Bonilla, J. A., Zhou, L., Lindquist, A. and Upton, S. J. (2003). *Cryptosporidium muris*, a rodent pathogen, recovered from a human in Peru. *Emerging Infectious Diseases* **9**, 1174–1176.

Pavlásek, I. and Ryan, U. (2007). The first finding of a natural infection of *Cryptosporidium muris* in a cat. *Veterinary Parasitology* **144**, 349–352.

Petry, F. (2004). Structural analysis of *Cryptosporidium parvum*. *Microscopy and Microanalysis* **10**, 586–601.

Petry, F. and Harris, J. R. (1999). Ultrastructure, fractionation and biochemical analysis of *Cryptosporidium parvum* sporozoites. *International Journal for Parasitology* **29**, 1249–1260.

Robert, B., Antoine, H., Dreze, F., Coppe, P. and Collard, A. (1994). Characterization of a high molecular weight antigen of *Cryptosporidium parvum* micronemes possessing epitopes that are cross-reactive with all parasitic life cycle stages. *Veterinary Research* **25**, 384–398.

Sauch, J. F., Flanigan, D., Galvin, M. L., Berman, D. and Jakubowski, W. (1991). Propidium iodide as an indicator of *Giardia* cyst viability. *Applied and Environmental Microbiology* **57**, 3243–3247.

Tarazona, R., Blewett, D. A. and Carmona, M. D. (1998). *Cryptosporidium parvum* infection in experimentally infected mice: infection dynamics and effect of immunosuppression. *Folia Parasitologica* **45**, 101–107.

Taylor, M. A., Marshall, R. N., Green, J. A. and Catchpole, J. (1999). The pathogenesis of experimental infections of *Cryptosporidium muris* (strain RN 66) in outbred nude mice. *Veterinary Parasitology* **86**, 41–48.

Tetley, L., Brown, S. M., McDonald, V. and Coombs, G. H. (1998). Ultrastructural analysis of the sporozoite of *Cryptosporidium parvum*. *Microbiology* **144**, 3249–3255.

Tiangtip, R. and Jongwutiwes, S. (2002). Molecular analysis of *Cryptosporidium* species isolated from HIV-infected patients in Thailand. *Tropical Medicine & International Health* **7**, 357–364.

Tyzzer, E. E. (1907). A sporozoan found in the peptic glands of the common mouse. *Proceedings of the Society for Experimental Biology and Medicine* **5**, 12–13. doi: 10.3181/00379727-5-5

Tyzzer, E. E. (1910). An extracellular Coccidium, *Cryptosporidium muris* (Gen. Et Sp. Nov.), of the gastric glands of the common mouse. *Journal of Medical Research* **23**, 487–510.

Uni, S., Iseki, M., Maekawa, T., Moriya, K. and Takada, S. (1987). Ultrastructure of *Cryptosporidium muris* (strain RN 66) parasitizing the murine stomach. *Parasitology Research* **74**, 123–132.

Valigurová, A., Hofmannová, L., Koudela, B. and Vávra, J. (2007). An ultrastructural comparison of the attachment sites between *Gregarina steini* and *Cryptosporidium muris*. *Journal of Eukaryotic Microbiology* **54**, 495–510. doi: 10.1111/j.1550-7408.2007.00291.x.

Valigurová, A., Jirků, M., Koudela, B., Gelnar, M., Modrý, D. and Šlapeta, J. (2008). Cryptosporidia: epicellular parasites embraced by the host cell membrane. *International Journal for Parasitology* **38**, 913–922. doi: 10.1016/j.ijpara.2007.11.003.

Vetterling, J. M., Takeuchi, A. and Madden, P. A. (1971). Ultrastructure of *Cryptosporidium wrairi* from the guinea pig. *Journal of Protozoology* **18**, 248–260.

Ward, F. W. and Coates, M. E. (1987). Gastrointestinal pH measurement in rats: influence of the microbial flora, diet and fasting. *Laboratory Animals* **21**, 216–222.

Xiao, L., Escalante, L., Yang, C., Sulaiman, I., Escalante, A. A., Montali, R. J., Fayer, R. and Lal, A. A. (1999). Phylogenetic analysis of *Cryptosporidium* parasites based on the small-subunit rRNA gene locus. *Applied and Environmental Microbiology* **65**, 1578–1583.

7.4

Valigurová A., Paskerova G.G., Diakin A., Kováčiková M.,

Simdyanov T.G.

2015

Protococcidian *Eleutheroschizon duboscqi*, an unusual apicomplexan interconnecting gregarines and cryptosporidia

Protococcidian *Eleutheroschizon duboscqi*, an Unusual Apicomplexan Interconnecting Gregarines and Cryptosporidia

Andrea Valigurová[1] *****, **Gita G. Paskerova**[2], **Andrei Diakin**[1], **Magdaléna Kováčiková**[1], **Timur G. Simdyanov**[3]

1 Department of Botany and Zoology, Faculty of Science, Masaryk University, Kotlářská 2, 611 37, Brno, Czech Republic, 2 Department of Invertebrate Zoology, Faculty of Biology, Saint-Petersburg State University, Universitetskaya emb. 7/9, St. Petersburg, 199034, Russian Federation, 3 Department of Invertebrate Zoology, Faculty of Biology, Lomonosov Moscow State University, Leninskiye Gory 1–12, Moscow, 119234, Russian Federation

***** andreav@sci.muni.cz

Abstract

This study focused on the attachment strategy, cell structure and the host-parasite interactions of the protococcidian *Eleutheroschizon duboscqi*, parasitising the polychaete *Scoloplos armiger*. The attached trophozoites and gamonts of *E. duboscqi* were detected at different development stages. The parasite develops epicellularly, covered by a host cell-derived, two-membrane parasitophorous sac forming a caudal tipped appendage. Staining with Evans blue suggests that this tail is protein-rich, supported by the presence of a fibrous substance in this area. Despite the ultrastructural evidence for long filaments in the tail, it stained only weakly for F-actin, while spectrin seemed to accumulate in this area. The attachment apparatus consists of lobes arranged in one (trophozoites) or two (gamonts) circles, crowned by a ring of filamentous fascicles. During trophozoite maturation, the internal space between the parasitophorous sac and parasite turns translucent, the parasite trilaminar pellicle seems to reorganise and is covered by a dense fibrous glycocalyx. The parasite surface is organised in broad folds with grooves in between. Micropores are situated at the bottom of the grooves. A layer of filaments organised in bands, underlying the folds and ending above the attachment fascicles, was detected just beneath the pellicle. Confocal microscopy, along with the application of cytoskeletal drugs (jasplakinolide, cytochalasin D, oryzalin) confirmed the presence of actin and tubulin polymerised forms in both the parasitophorous sac and the parasite, while myosin labelling was restricted to the sac. Despite positive tubulin labelling, no microtubules were detected in mature stages. The attachment strategy of *E. duboscqi* shares features with that of cryptosporidia and gregarines, i.e. the parasite itself conspicuously resembles an epicellularly located gregarine, while the parasitophorous sac develops in a similar manner to that in cryptosporidia. This study provides a re-evaluation of epicellular development in other apicomplexans and directly compares their niche with that of *E. duboscqi*.

Introduction

Phylum Apicomplexa Levine 1980, emend. Adl et al. 2012 [1] represents one of the most successful groups of eukaryotic unicellular organisms, consisting entirely of parasitic genera that infect a broad range of vertebrates and invertebrates. In contrast to the apicomplexan etiologic agents of globally significant human and animal diseases (e.g. malaria, toxoplasmosis, cryptosporidiosis), the enormously diversified basal groups of Apicomplexa, that are restricted to invertebrate hosts, remain poorly understood. Nevertheless, they appear to be very important in the comprehension of evolutionary pathways and phylogenetic relations within the phylum Apicomplexa.

Apicomplexans evolved various adaptations for invading and surviving within their hosts. It is assumed that ancestral apicomplexans parasitised marine annelids, and their radiation and adaptation to the parasitic life style took place before the era of vertebrates. First, they spread to other marine invertebrates (turbellaria, crustaceans, echinoderms, etc.), then to freshwater and terrestrial invertebrates, and finally to vertebrates [2]. The apicomplexan zoite is characterised by a high degree of cell polarity in that it has an apical pole equipped with a so-called apical complex, usually comprising specialised secretory organelles (rhoptries, micronemes), polar rings, and a conoid. This unique invasion apparatus, traditionally used as the best defining feature for the phylum Apicomplexa, is initially linked with a myzocytosis-based mode of feeding as it is in colpodellids and archigregarines [3,4]. Most likely, apicomplexan evolution progressed from myzocytotic predation to myzocytotic extracellular parasitism, a characteristic of lower gregarines and cryptosporidia, and finally to intracellular parasitism which is typical for coccidia. This means apicomplexans demonstrate two main determinative evolutionary trends: i) the origination of intracellular parasitism in typical coccidia and Aconoidasida, accompanied by a rejection of trophozoite polarity and motility; and ii) the origination of epicellular parasitism, observed mostly in gregarines, with subsequent modifications of attachment apparatus along with the motility mode/mechanism in the trophozoite stage. Recent studies have pointed out the unique epicellular localisation of cryptosporidia within the host cell-derived parasitophorous sac (PS), and the similarities in their attachment and feeding strategy with gregarines. Thus, these parasites reflect analogous modes of adaptation to a similar environment within the host [5,6]. Based on phylogenetic analyses reporting the close affinity of gregarines and cryptosporidia [7,8], speculation that cryptosporidia represent a 'missing link' between the gregarines and coccidia is frequently discussed.

One of the poorly explored basal apicomplexan lineages is the order Protococcidiorida Kheisin, 1956 (subclass Coccidiasina Leuckart, 1879; class Conoidasida Levine, 1988) comprising four families: Eleutheroschizonidae Chatton & Villeneuve, 1936; Myriosporidae Grassé, 1953; Angeiocystidae Léger, 1911 and Grelliidae Levine, 1973 [9]. Protococcidia are expected to lack merogony, and their gamogony and sporogony occurs extracellularly [9]. Genus *Eleutheroschizon* Brasil, 1906 was placed in the family Eleutheroschizonidae, representatives of which are characterised by epicellular development [9,10,11]. Their gamonts detach from the host tissue and disperse into the environment where gametogenesis and sporogenesis take place. Oocysts contain fan-shaped clusters of sporozoites, with one end of each sporozoite attached to the residuum [9]. There are reported only two species of the genus *Eleutheroschizon*, the type species *E. duboscqi* Brasil, 1906 from *Scoloplos armiger* and *E. murmanicum* Awerinzew, 1908 from *Ophelia limacina* (Rathke) [11,12]. Apart from the original description [11] and one study focusing on the life cycle of *E. duboscqi* [10], no further studies dealing with this parasite have been published. The aim of this study was to provide a morphological analysis of the attachment strategy, cell cortex and cytoskeleton of trophozoites and gamonts *of*

Eleutheroschizon duboscqi, a representative of marine apicomplexans, which shares features of both the gregarines and coccidia.

Materials and Methods

Material collection

The polychaetes *Scoloplos armiger* (Müller, 1776) were collected from 2006 to 2014 at the sand-silt littoral zone close to the White Sea Biological Station of M. V. Lomonosov Moscow State University (66°33.200' N, 33°6.283' E) and the Marine Biological Station of St. Petersburg State University (66°18.770' N; 33°37.715' E). Both stations are situated in the Kandalaksha Bay of the White Sea. The dissection of polychaetes and extraction of parasites were performed using a MBS-10 stereomicroscope. Squash preparations with living parasites and semi-thin sections stained with toluidine blue were investigated with the use of a Leica DM 2000 microscope connected to a DFC 420 digital camera, a Zeiss Axio Imager.A1 connected to an AxioCam MRc5 digital camera or with an Olympus microscope BX61 equipped with DP71 digital camera.

Electron microscopy

Specimens were fixed in an ice bath in 2.5–5% (v/v) glutaraldehyde, in different concentrations of cacodylate buffer (0.05–0.15 M; pH 7.4; osmolarity was reached up to 720 mOsm by adding NaCl), for over two hours. For transmission electron microscopy (TEM), the specimens were then washed in buffer used for fixation or in filtered (0.22 μm Millipore) sea water and post-fixed in 1–2% (w/v) OsO_4 in the same buffer for 1–3 h at room temperature. Some specimens were fixed with 3% glutaraldehyde-ruthenium red [0.15% (w/v) stock water solution] in 0.2 M cacodylate buffer (pH 7.4) and postfixed with 1% OsO_4-ruthenium red in the same buffer. The subsequent procedure follows published protocols [6,13,14]. Observations were made using microscopes JEM-1010 (JEOL) and LEO 910 (Zeiss). For scanning electron microscopy (SEM), the specimens were washed in buffer used for fixation or in filtered (0.22 μm Millipore) sea water, processed according to Valigurová et al. [13,15] and examined using microscopes JSM-7401F —FE SEM (JEOL), LEO 420 (Zeiss) or GEMINI Supra 40V (Zeiss).

Confocal laser scanning microscopy

Fragments of parasitised intestines were washed in 0.1 M phosphate buffered saline (PBS), fixed for 30 minutes at room temperature in freshly prepared 4% paraformaldehyde in 0.1 M PBS (PFA) or in ice-cold methanol, washed, and permeabilised for 15–30 minutes in 0.5% Triton X-100. Some of the PFA fixed samples were stained with Evans blue. Protocols for direct staining of filamentous actin (F-actin) with phalloidin—tetramethylrhodamine B isothiocyanate (phalloidin-TRITC; Sigma-Aldrich, Czech Republic), as well as indirect immunofluorescent antibody (IFA) staining using a rabbit anti-myosin antibody (smooth and skeletal, the whole antiserum), a rabbit anti-chicken spectrin antibody (the whole antiserum), a mouse monoclonal anti-α-tubulin antibody (Sigma-Aldrich, Czech Republic) and a mouse monoclonal IgG anti-actin antibody that was raised against *Dictyostelium* actin (provided by Prof. Dominique Soldati-Favre), follow Valigurová et al. [13,15]. For double labelling, specimens were incubated in phalloidin-TRITC after washing off the secondary antibody. Some preparations were counterstained with DAPI. Confocal laser scanning microscopic (CLSM) observations were made with an inverted Olympus IX81 microscope equipped with a laser-scanning FluoView 500 confocal unit (FluoView 4.3 software); using the rhodamine (Evans blue), tetramethylrhodamine isothiocyanate (TRITC—phalloidin, anti-myosin), fluorescein isothiocyanate (FITC—anti-actin, anti-α-tubulin, anti-spectrin) and/or UV (DAPI) filter sets. Some

micrographs were processed using the software Fiji (an image processing package based on ImageJ developed at the National Institutes of Health). For better interpretation of fluorescent data, a set of 6 linguistic variables, such as No fluorescence (-), Very weak (-/+), Weak (+), Medium (++), Strong (+++) and Very strong (++++), were used (symbols are only illustrative and not used in the text). Quantification of fluorescence intensity was made using the visual assessment of CLSM micrographs (using the raw images), comparison was made to those obtained from two sets of control samples: negative (omitting the primary antibody or phalloidin) and positive controls (labelled, but not treated with cytoskeletal drugs).

Experimental part

As a control for potential false positive results from the fluorescent labelling of F-actin and microtubules, specimens were treated with probes that influence the polymerisation of actin and tubulin: jasplakinolide (JAS, Invitrogen; a toxin that stabilises actin filaments and induces actin polymerisation), cytochalasin D (Invitrogen, Czech Republic; a drug disrupting actin filaments and inhibiting actin polymerisation), and oryzalin (Sigma-Aldrich, Czech Republic; a dinitroaniline herbicide acting through the disruption/depolymerisation of microtubules). Drugs were reconstituted in dimethyl sulfoxide to prepare a 1 mM stock solution. The final concentration of these membrane-permeable probes lower than 5 µM had no obvious effect. To obtain reliable results on vital cells, final solutions of 10 and 30 µM JAS, cytochalasin D and oryzalin prepared in filtered (0.22 µm Millipore) sea water were applied. Controls were performed in pure filtered sea water as well as corresponding concentrations of dimethyl sulfoxide in filtered sea water.

Results

Light microscopic observations

We observed several development stages of *E. duboscqi* in squash preparations with living parasites. The earliest developmental stages, presumably zoites during the invasion process, were drop-shaped cells, 1 µm in length, with their pointed end attached to the host tissue (Fig 1A). At the light microscope (LM) level, it was not possible to identify the presence or absence of any membrane structure enclosing these parasites. The next stage was represented by helmet-shaped trophozoites, 2–10 µm in length, with a wide basal part attached to the host cell, and a large nucleus located near the base. They were enveloped by a parasitophorous sac (PS) of host membrane origin (Fig 1B–1E). The caudal part of the sac, in all attached parasites, was usually prolonged in a prominent translucent, tail-like appendage (Fig 1B–1I). The length of this tail varied. Gamonts corresponded to the helmet-shaped cells, about 20 µm in length, with a granular cytoplasm containing numerous light-refracting amylopectin granules (Fig 1F–1N). Two morphs of *E. duboscqi* gamonts were observed, i.e. macro- and microgamonts, agreeing with the life cycle description by Chatton and Villeneuve [10]. Macrogamonts possessed one large nucleus with a dense nucleolus (Fig 1K), while microgamonts had numerous small nuclei with fragmented nucleoli (Fig 1M and 1N). During light microscopic observations, parasites along with their PS frequently detached from host tissue (Fig 1J).

Ultrastructural analysis

With the exception of putative zoite stages (Fig 1A), trophozoites and gamonts of various developmental stages, corresponding to our light microscopy data (Fig 1B–1N), were observed under the electron microscope. All these attached stages were covered by a PS.
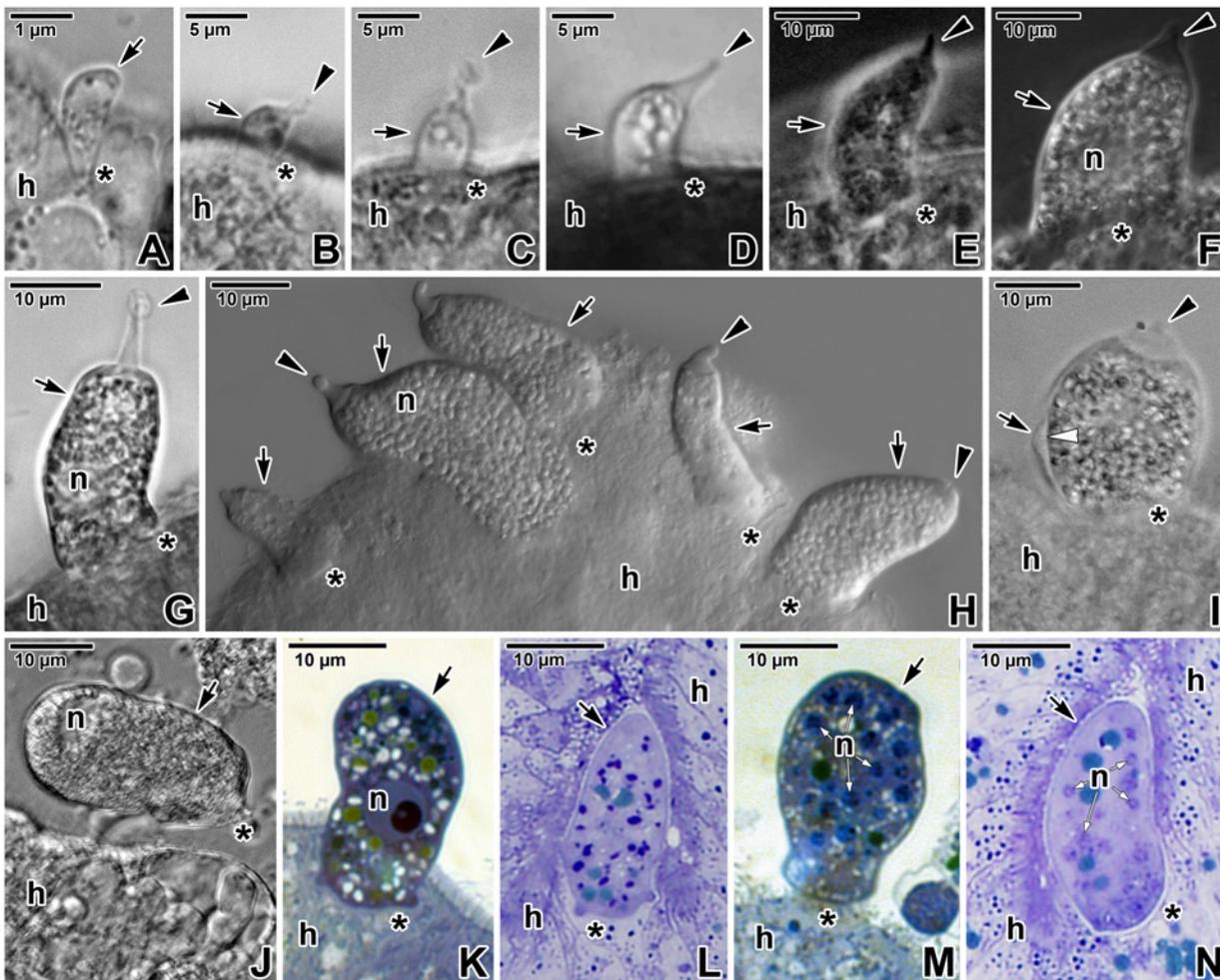
Fig 1. Light microscopic observations on attached stages of *Eleutheroschizon duboscqi*. A. Putative zoite of *E. duboscqi* invading the host intestinal epithelium. LM, bright field. **B-C.** Early trophozoites within an already formed PS. Note the caudal prolongation of the sac into a tail. LM, bright field. **D.** Maturing trophozoite. LM, bright field. **E.** Mature trophozoite. LM, phase contrast. **F.** A gamont stage. LM, phase contrast. **G.** Gamont exhibiting a prolonged tail at the PS. LM, bright field. **H.** Various stages of trophozoites and gamonts attached to the host intestinal epithelium. LM, differential interference contrast. **I.** A macrogamont after fixation in PFA. Note the separation of PS from the parasite cortex. LM, bright field. **J.** Detached macrogamont still enveloped by a PS. LM, bright field. **K-N.** Macrogamonts (K-L) and microgamonts (M-N) in semi-thin sections. LM, bright field, Toluidine blue. *arrow*—parasite, *arrowhead*—tail of the PS, *asterisk*—parasite attachment site, *h*—host tissue, *n*—parasite nucleus/nuclei.

doi:10.1371/journal.pone.0125063.g001

The earliest trophozoites, about 2 μm in length, that obviously transformed from attached zoites a short time before fixation, were already enveloped by a loose but complete PS ([Fig 2A]). Early trophozoites were barrel-shaped ([Fig 2B]). The space between the parasite and PS was filled by numerous vesicles of various sizes. The fine structure of the pellicle was not discernible in all observed early stages (Fig [2A] and [2B]). The attachment site at the base of PS was mostly indistinct ([Fig 2B]). Ultrathin sections revealed a dense, equally thick and continuous, double layer which separated the unmodified part of the host cell from its apical region bearing an attached parasite. Early trophozoites were equipped with subpellicular microtubules (21–23 nm in outer diameter) connecting to a ring-like structure, presumably a posterior ring ([Fig 2B]). No organelles of the apical complex were detected (Fig [2A] and [2B]).

During progressive maturation, the trophozoites underwent changes in their shape and size (Figs [2B]–[2L] and [3A]–[3J]). Gradually they took the shape of a helmet and reached up to 10 μm in
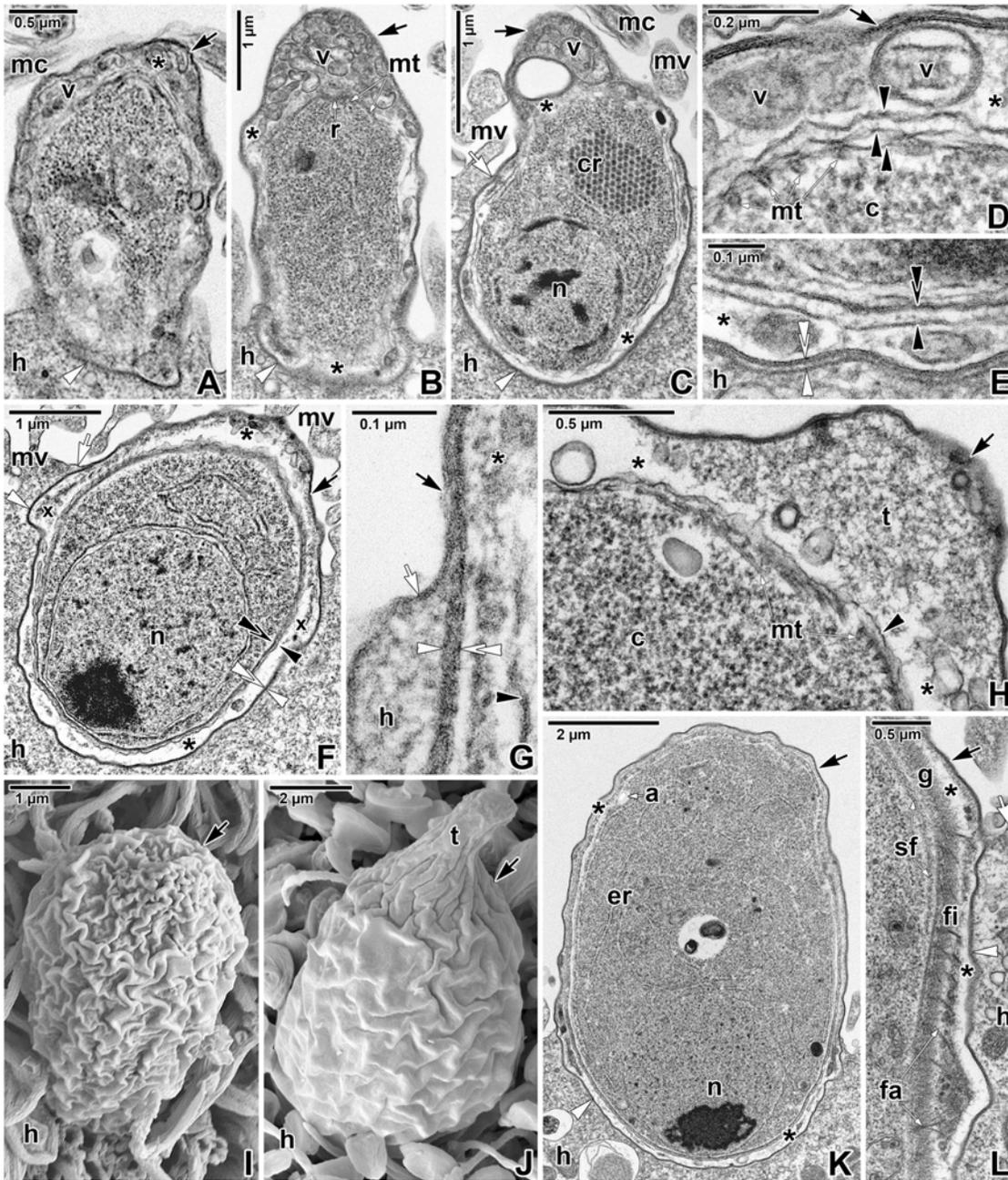
Fig 2. Ultrastructural features of *Eleutheroschizon duboscqi* early development. A. Early trophozoite in the process of transformation from an attached zoite, already enveloped by a host-derived PS. TEM. **B.** Early trophozoite. Note the numerous vesicles in the space between parasite and PS, especially in caudal region. TEM. **C-E.** Young trophozoite. D shows the space between the parasite caudal region and PS; E shows the host parasite interface at the attachment site. TEM. **F-H.** Maturing trophozoite. G shows an annular joint point of two host membranes; H focuses on the parasite caudal region and PS. TEM. **I.** Early trophozoite. SEM. **J.** Young trophozoite. SEM. **K.** Mature trophozoite. TEM. **L.** Detailed view of the attachment site of the trophozoite shown in K, focusing on the developing fascicles of filaments and the annular joint point. TEM. *a*—parasite amylopectin, *asterisk*—space between the parasite and PS, *black arrow*—PS, *black arrowhead*—parasite plasma membrane, *black double/paired arrowheads*—parasite cytomembranes, *c*—parasite cytoplasm, *cr*—crystalloid body, *er*—parasite endoplasmic reticulum, *fa*—attachment fascicles, *fi*—short attachment filaments, *g*—glycocalyx, *h*—host cell, *mc*—host microcilia, *mt*—parasite subpellicular microtubules, *mv*—host microvilli, *n*—parasite nucleus, *r*—parasite posterior ring, *sf*—parasite subpellicular filaments, *t*—tail of the PS, *v*—vesicles, *white arrow*—host cell plasma membrane, *white arrowhead*—dense band, *white double arrowhead*—base of the PS (membrane of host cell origin), *x*—forming attachment fascicles.

doi:10.1371/journal.pone.0125063.g002
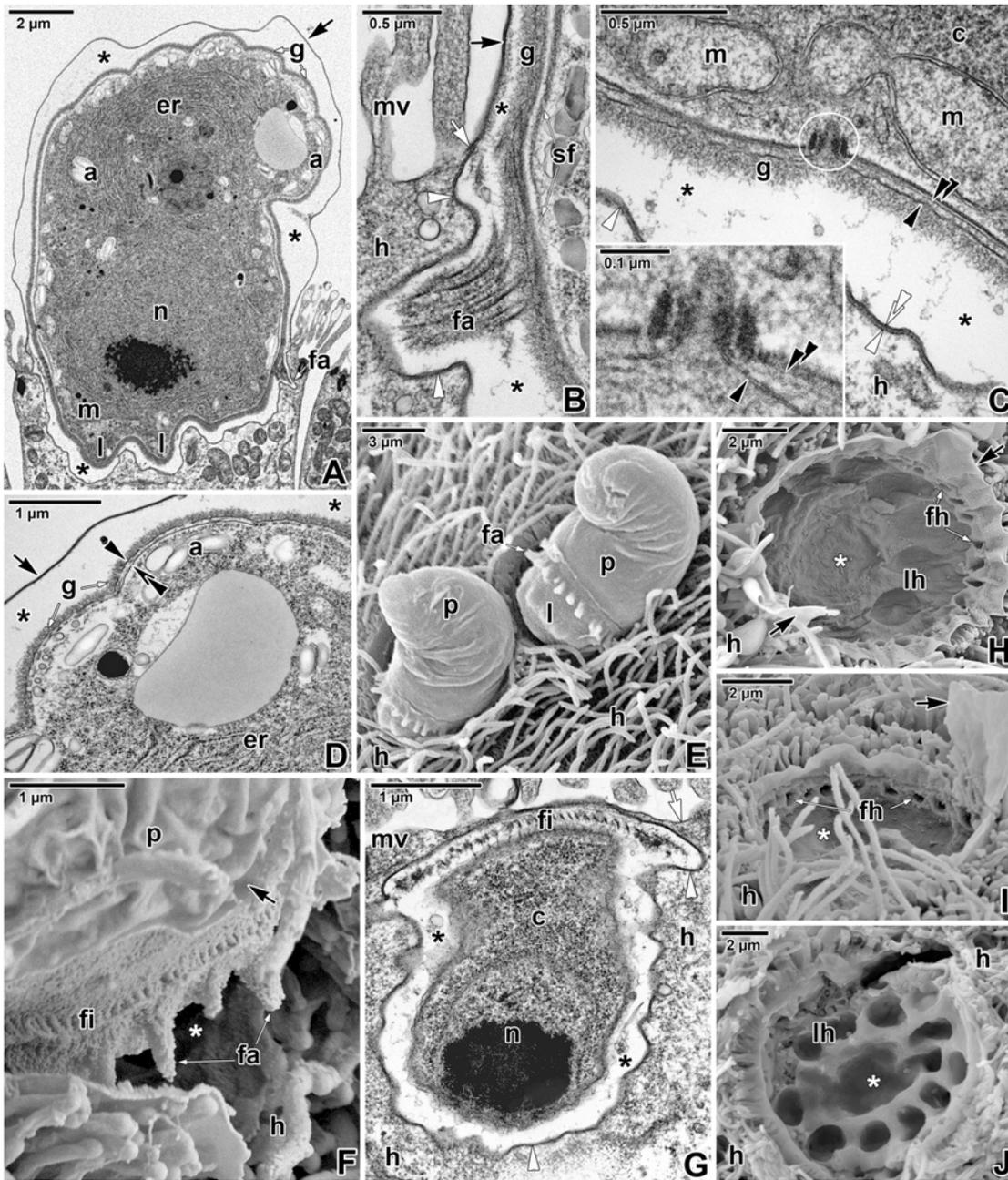
Fig 3. Fine structure of *Eleutheroschizon duboscqi* mature trophozoites. A. Mature trophozoite transforming into a gamont stage. TEM. **B.** Detailed view of the annular joint point and a well-developed fascicle of filaments. TEM. **C.** The view of mitochondria and a micropore (white circle) at the attachment site. The inset shows the micropore in detail. TEM. **D.** Higher magnification of the caudal region. TEM **E.** Two partially detached, mature trophozoites. SEM. **F.** The attachment site of a partially detached, mature trophozoite with well-developed fascicles and short filaments. SEM. **G.** Diagonal section of the apical part of a mature trophozoite. TEM. **H-I.** Craters left after detachment of mature trophozoites with well-developed attachment fascicles. Flat holes organised in one circle correspond to the developing lobes. SEM. **J.** A crater left after a trophozoite of more advanced stage as indicated by the presence of one circle of deep holes corresponding to well-developed lobes and one extra lobe starting the formation of a second circle. SEM. *a*—parasite amylopectin, *black arrow*—PS, *black arrowhead*—parasite plasma membrane, *black asterisk*—space between the parasite and PS, *black double/paired arrowheads*—parasite cytomembranes, *c*—parasite cytoplasm, *er*—parasite endoplasmic reticulum, *fa*—attachment fascicles, *fh*—holes in the host tissue left after the fascicles of the detached parasite, *fi*—short attachment filaments, *g*—glycocalyx, *h*—host cell, *l*—attachment lobe, *lh*—holes in the host tissue left after the lobes of the detached parasite, *m*—parasite mitochondria, *mv*—host microvilli, *n*—parasite nucleus, *p*—parasite, *sf*—parasite subpellicular filaments, *white arrow*—host cell plasma membrane, *white arrowhead*—dense band, *white asterisk*—empty attachment site, *white double arrowhead*—base of the PS.

doi:10.1371/journal.pone.0125063.g003

length. The developmental stage, defined as a young trophozoite (3–5 µm in length), was iden-
tifiable due to a large nucleus in the apical position, a crystalloid body of unknown nature, sub-
pellicular microtubules, and a cytoplasm rich in rough endoplasmic reticulum (Fig 2C–2E).
The pellicle membranes appeared to be folded, loose and still discontinuous in some regions
(Fig 2C–2E). In contrast to the earliest stages, the interface between the unmodified and modi-
fied part of the host cell at the base of the PS appeared clearly delineated, comprising of a mem-
brane of host cell origin (about 7–9 nm in thickness, corresponding to the plasma membrane
covering adjacent microvilli) underlain by a 4–7 nm thick dense band (Fig 2E). In maturing
trophozoites, the next developmental stage, the pellicle seemed to be more distinct and com-
pact along the entire surface, and its membranes became more evident than in parasites of pre-
vious developmental stages (Fig 2F). The internal space between the parasite and surrounding
PS continued to clarify so that it appeared translucent with several vesicles. The border between
the parasite PS and the neighbouring microvilli area formed a so called annular joint point.
That is where the host cell plasma membrane, forming the base of PS, comes closer to the plas-
ma membrane covering the neighbouring microvilli. Both membranes continuously proceed
into the rising PS, forming its inner and outer membranes, respectively (Fig 2G). The 4–7 nm
thick dense band underlying the inner PS membrane in the attachment site ended in this area
and did not continue into the PS. No structures obviously belonging to the parasite and con-
nected directly to the host-derived membranes of the PS were seen. In the attachment area of
parasites, one ring of filaments began to form just below the annular joint point (Fig 2F). Ma-
turing trophozoites still exhibited subpellicular microtubules (Fig 2H). In the course of tropho-
zoite development, the caudal part of the PS gradually formed a prolongation being
characteristic for E. duboscqi, the tail (Fig 2C and 2H). This is easily seen when comparing an
early trophozoite without a tail (Fig 2I) with a young trophozoite with a developing tail on the
PS (Fig 2J). In mature trophozoites, the next developmental stage, a cell coat (glycocalyx) ap-
peared as a thick layer of fibrous material (Figs 2K, 2L and 3A–3D). The pellicle was distinct; it
was comprised of a plasma membrane, two adjacent cytomembranes (i.e. the inner membrane
complex, IMC) and a thin dense layer underlining the inner cytomembrane (Fig 3C and 3D).
Under the pellicle, a thick layer of subpellicular filaments emerged (Figs 2L and 3B). The cyto-
plasm was filled with a large nucleus in the apical position, and an increasing rough endoplas-
mic reticulum. The crystalloid body observed in young trophozoites disappeared, while
peripheral amylopectin granules appeared and increased in number (Figs 2K, 3A and 3D).
Large mitochondria underlying the parasite pellicle appeared, especially at the attachment site
(Fig 3C). With increasing age, typical apicomplexan micropores (154 nm in outer diameter
and 132 nm deep when measured from the plane of cytomembranes to the bottom of the mi-
cropore) formed on the parasite surface (Fig 3C). The internal space of the PS enveloping the
mature trophozoites became completely translucent (Fig 3A–3D). At the attachment site of
parasite, the above-mentioned ring of filaments continued to develop: fascicles of long fila-
ments alternating with short filaments appeared (Figs 2K, 2L, 3A, 3B and 3E–3G). The para-
sites formed thick outgrowths, i.e. lobes, which were organised in a single circle at the
attachment site, just below the ring of filaments (Fig 3A and 3E). Correspondingly, craters in
the host tissue, left after detached trophozoites, confirmed the circular organisation of the fasci-
cles of filaments and lobes at the attachment site (Fig 3H–3J). These were seen as a peripheral
circle of narrow but very deep holes, left after the well-developed fascicles of filaments, and
larger flat holes, organised in one central circle and corresponding to the developing lobes (Fig
3H and 3I). In trophozoites transforming into gamonts, the attachment lobes became more
and more prominent, as also documented by the deeper holes left after detached individuals
(Fig 3J). In addition, the second circle of lobes started to develop in the centre of the attachment
site (Fig 3A). Accordingly, detached parasites left one peripheral circle of holes corresponding

to the well-developed lobes and one central, extra hole indicating the start of the formation of a second circle of lobes (Fig 3J).

The oldest developmental stages observed during our study were gamonts reaching about 20 μm in length (Figs 4A–4K, 5A–5E, 6A–6K, and 7A–7K). All gamonts were contained within a well-developed PS, with a prominent tail (Fig 4A and 4D–4G). A few individuals bearing two or three tails were observed (Fig 4K). The surface of gamonts exhibited about 12 (10–13, n = 20) shallow grooves showing through the PS under the SEM (Figs 4A, 4H, 4I, and 7A). Macrogamonts were characterised by a centrically located, large, roundish nucleus with one nucleolus, abundant amylopectin granules, large lipid droplets, and prominent dense bodies varying in shape and size (Fig 4B and 4D). In contrast, microgamonts possessed several nuclei (up to 20 in a longitudinal section) with fragmented nucleoli and cell inclusions (amylopectin granules, lipid droplets) of a smaller size (Fig 4C). Pores were often observed at the caudal region of the PS (Fig 4E and 4F). Dense substances staining intensively with ruthenium red (RR), most likely mucosubstances secreted by the parasite, were detected on the PS surface close to these pores (Fig 4E). The internal space between the PS and parasite was mostly translucent, while the internal space of the PS tail was packed with thin filaments running longitudinally (Fig 4E and 4G). The parasite surface (Fig 4G and 4J) bore a dense layer of fibrous glycocalyx (80–85 nm in thickness). Gamonts were often observed with a ruptured PS revealing their surface (Fig 4H and 4I). In such cases, the parasite pellicle in the caudal region was covered by a fibrous material (Fig 4H) that might correspond to the filaments observed in the PS tail under TEM. Small piles of unknown material organised in circles were observed to be present on the caudal part of the parasite surface (Fig 4I). The dense glycocalyx was visible under SEM as a woolly coat covering the surface (Fig 4I). Completely detached parasites, but still enveloped by a PS and located far away from the host tissue, were rarely detected in ultrathin sections.

Observations on mechanically detached gamonts under SEM revealed their complicated attachment sites, comprising of two circles of massive lobes crowned by a ring of fascicles of long filaments, alternating with short filaments (Fig 5A–5D). Detached individuals were covered by a PS, except for their attachment sites that seemed to be covered by a parasite pellicle only. The naked attachment lobes appeared as smooth protuberant, hemispheric structures. Detached gamonts left characteristic craters on the host intestinal tissue, indicating that they were fully matured, with well-developed attachment fascicles and two circles of lobes (Fig 5E–5G). The basal part of the PS was comprised of the host membrane (i.e. the inner membrane of PS) underlined by a dense band and was still present after parasite detachment (Fig 5H), corresponding to the observations of detached parasites with naked attachment sites.

Ultrathin sections of attached gamonts confirmed the SEM observations on the attachment site, and showed that lobes represent structures belonging to the parasite, as they are covered by a parasite pellicle and are filled with its cytoplasm packed with large mitochondria, various vesicles and the endoplasmic reticulum (Fig 6A, 6B, 6G and 6H). The pellicle membranes covering the lobes were usually well-preserved (Fig 6G). In contrast to lobes, attachment fascicles were located in the translucent space between the parasite and PS, and were not covered by the parasite pellicle (Fig 6A, 6B, 6D, 6E, 6J and 6K). Although the membranes of the parasite pellicle were not clearly distinguishable in this area, the short filaments (15–35 nm thick) and fascicles of longer filaments (about 60 nm thick) that seemed to arise from the pellicle and evidently extended through the glycocalyx, were deeply anchored into the IMC (Fig 6C–6E, 6J and 6K). Some sections clearly showed the hook-shaped short filaments that were anchored into the outer cytomembrane of IMC (Fig 6C). The subpellicular layer of filaments, localised just beneath the IMC, ended above the ring of the filaments and fascicles (Fig 6D and 6E). The organisation of structures at the annular joint point corresponded with the observations on younger stages (Fig 6F). The dense band (4–8.5 nm thick) underlying the inner PS membrane at the
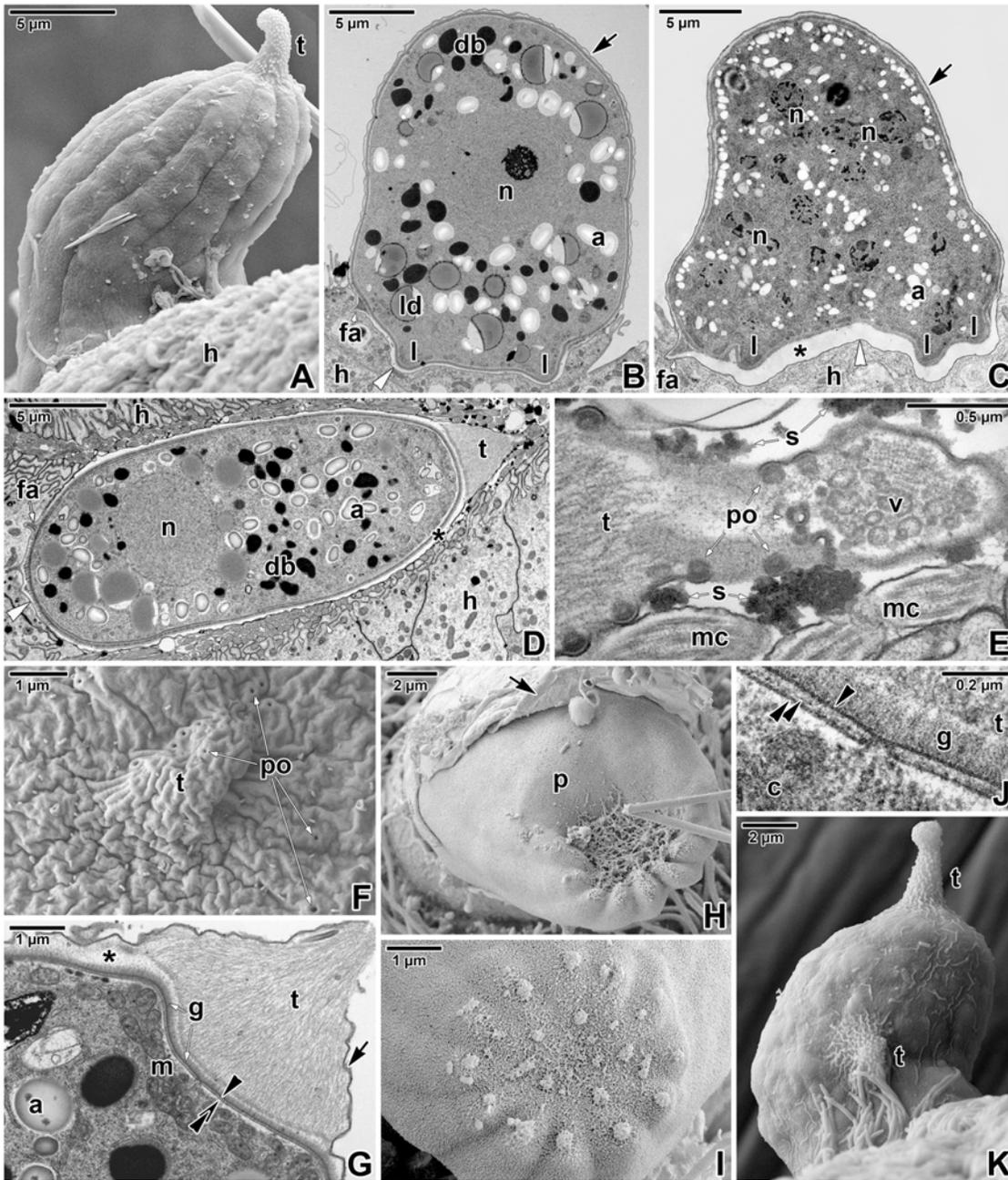
Fig 4. Morphology of *Eleutheroschizon duboscqi* gamonts. A. Attached gamont. SEM. **B.** Macrogamont with a large central nucleus. TEM. **C.** Microgamont with several nuclei. TEM. **D.** Macrogamont enclosed by host tissue. TEM, RR. **E.** The PS tail of the macrogamont shown in D. Note the pores and the mucosubstances present in their surroundings. TEM, RR. **F.** High magnification of the caudal PS part with the tail showing numerous pores. SEM. **G.** Detailed view of the tail and gamont caudal part. TEM, RR. **H.** Upper view of an individual with a ruptured PS. SEM. **I.** The caudal region of a naked individual. SEM. **J.** High magnification of the interface between the parasite and PS in the area of the tail. TEM, RR. **K.** Gamont with two tails at the PS. SEM. *a*—parasite amylopectin, *arrow*—PS, *asterisk*—space between the parasite and the PS, *black arrowhead*—parasite plasma membrane, *black double/paired arrowheads*—parasite cytomembranes, *c*—parasite cytoplasm, *db*—parasite dense bodies, *fa*—attachment fascicles, *g*—glycocalyx, *h*—host cell, *l*—attachment lobe, *ld*—parasite lipid droplets, *m*—parasite mitochondria, *mc*—host microcilia, *n*—parasite nucleus, *p*—parasite, *po*—pore, *s*—mucosubstances, *t*—tail of the PS, *v*—vesicles, *white arrowhead*—base of the PS.

doi:10.1371/journal.pone.0125063.g004
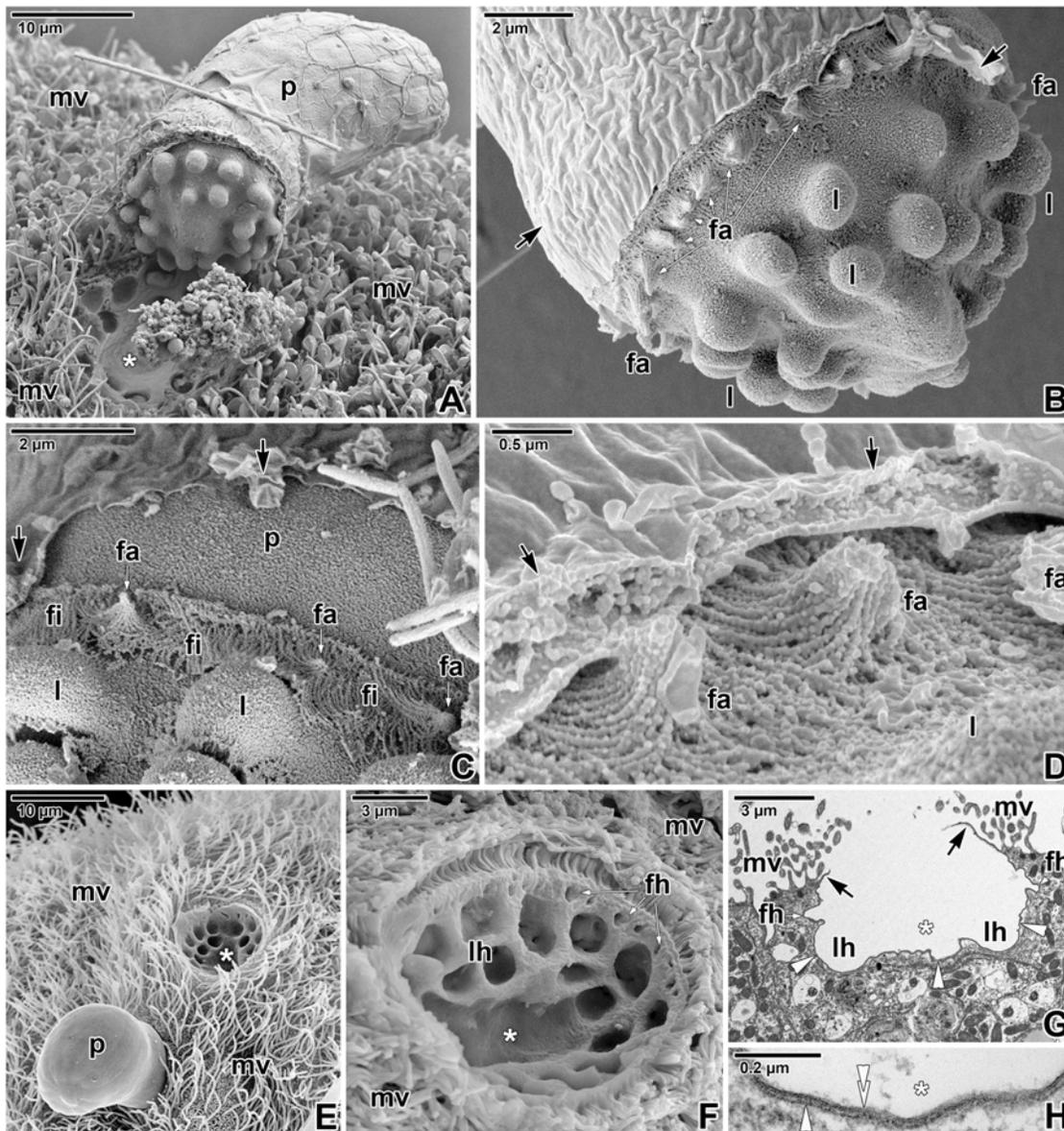
Fig 5. Architecture of attachment site of *Eleutheroschizon duboscqi* gamonts. A. Host intestinal tissue with a detached gamont revealing its attachment site at the base of PS. SEM. **B.** Detail of the gamont attachment site. SEM. **C.** Detailed view of the fascicles of long filaments alternating with short filaments, organised in ring. SEM. **D.** A detail of attachment fascicles. SEM. **E.** Host intestinal tissue with an attached parasite and a crater left after detached ones. SEM. **F.** A detail of crater left after gamont with well-developed attachment fascicles and two circles of lobes. SEM. **G.** Host epithelium showing the crater left after the parasite detached. TEM. **H.** A detail of the PS membrane remains covering the crater. TEM. *arrow*—PS, *fa*—attachment fascicle of filaments, *fh*—holes in the host tissue left after the fascicles of the detached parasite, *fi*—short attachment filaments, *l*—attachment lobe, *lh*—holes in the host tissue left after the lobes of the detached parasite, *mv*—microvilli and cilia of the host enterocyte, *p*—parasite, *white arrowhead*—dense band, *white asterisk*—empty attachment site, *white double arrowhead*—base of the PS.

doi:10.1371/journal.pone.0125063.g005

attachment site ended in this area. Numerous typical micropores (130–155 nm in outer diameter, 40–50 in inner diameter, the distance between the lumen of the duct and collar periphery is about 50–58 nm) were distributed at the attachment site of the parasite, especially in between individual lobes (Fig 6G–6I). Vesicles were rarely seen to be connected with micropores located at the attachment site of the parasite (Fig 6H). At the basal part of PS, an accumulation of
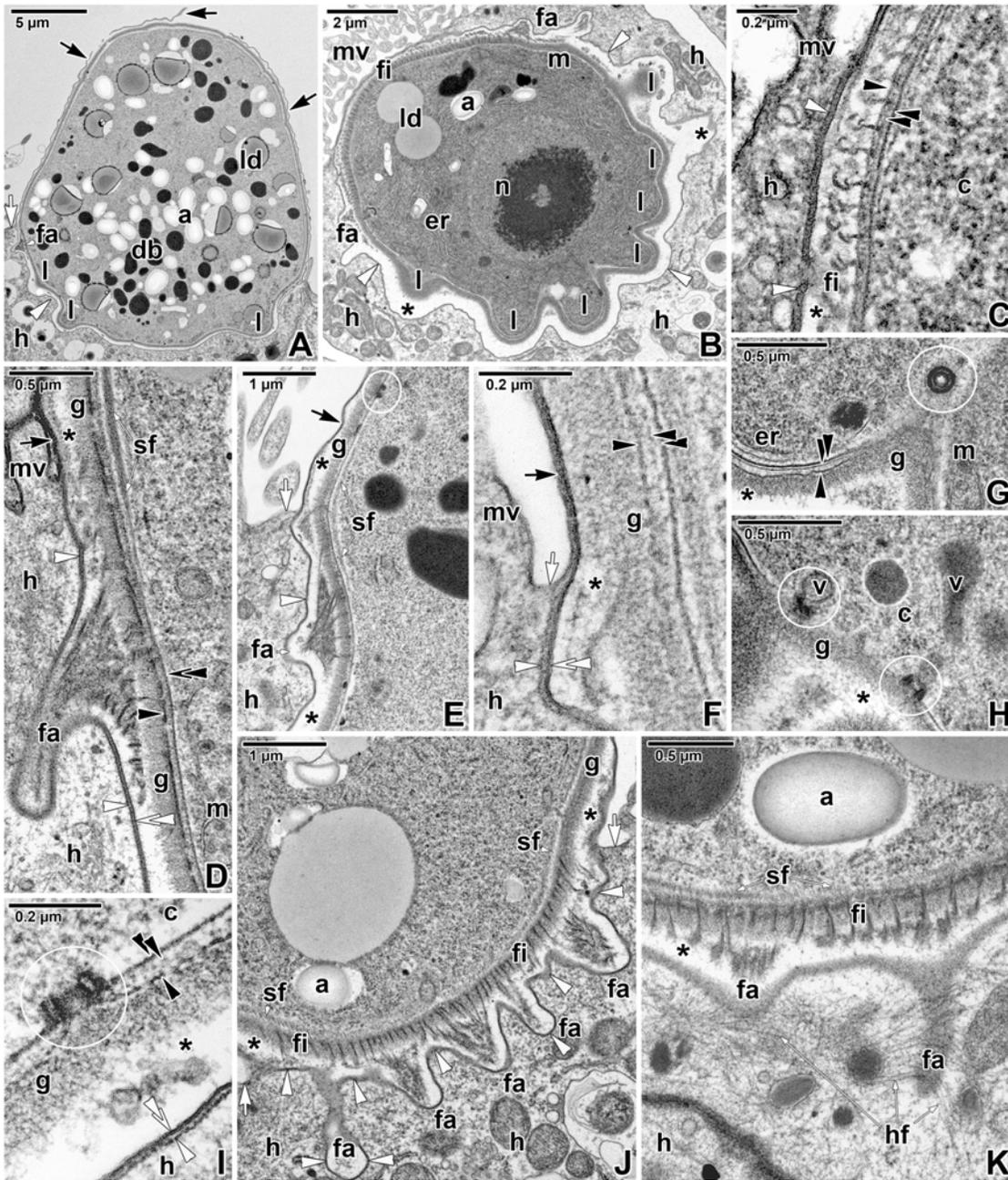
Fig 6. Fine structure of the attachment site of *Eleutheroschizon duboscqi* gamonts. A. Macrogamont with a ruptured PS. TEM. **B.** Oblique section of the attachment site. TEM. **C.** A detail showing the hook-shaped short filaments anchored into the parasite outer cytomembrane. TEM. **D-E.** The attachment fascicles in a longitudinal section. The subpellicular layer of filaments is localised just beneath the parasite IMC and ends above the fascicles. TEM; D is stained with RR. **F.** The annular joint point of two host membranes. TEM. **G.** A detail of the attachment lobe packed with endoplasmic reticulum and mitochondria. Note the cross-sectioned micropore. TEM. **H.** Detailed view of vesicles connected with the micropores located in the area of attachment lobes. TEM. **I.** Longitudinal section of a micropore localised at the parasite attachment site. TEM. **J.** Detailed view of the attachment fascicles of long filaments alternating with short filaments. TEM. **K.** The basal part of PS showing an accumulation of fine filaments in the host cell cytoplasm surrounding the PS invaginations with attachment fascicles. TEM, RR. *a*—parasite amylopectin, *asterisk*—space between the parasite and PS, *black arrow*—PS, *black arrowhead*—parasite plasma membrane, *black double/paired arrowheads*—parasite cytomembranes, *c*—parasite cytoplasm, *db*—parasite dense bodies, *er*—parasite endoplasmic reticulum, *fa*—attachment fascicle of filaments, *fi*—short attachment filaments, *g*—glycocalyx, *h*—host cell, *hf*—filaments in host cell cytoplasm, *l*—attachment lobe, *ld*—parasite lipid droplets, *m*—parasite mitochondria, *mv*—microvilli and cilia of the host enterocyte, *n*—parasite nucleus, *sf*—parasite subpellicular filaments, *v*—parasite vesicle, *white arrow*—host cell plasma membrane, *white arrowhead*—dense band, *white double arrowhead*—base of the PS. Micropores are indicated by white circles.

doi:10.1371/journal.pone.0125063.g006

filaments 7–10 nm thick (most likely of F-actin nature) was documented in the host cell cytoplasm surrounding the invaginations of PS with attachment fascicles (Fig 6K).

The cross-sections of mature gamonts confirmed that the surface was organised in weakly expressed broad folds with shallow grooves between them (Fig 7B). Each fold was underlain by a broad band of subpellicular filaments (apparently, it corresponds to the thick layer of subpellicular filaments observed in maturing trophozoites). Various planes of sectioning confirmed that 5–9 nm thick subpellicular filaments were oriented longitudinally (Fig 7C–7H) and formed 22–59 nm thick bands. Micropores were located at the bottom of the grooves, i.e. between these bands. Sectioning also revealed a regular arrangement of interruptions of subpellicular filaments, corresponding to the distribution of micropores (Fig 7B–7H). A lot of mitochondria could be observed in the cortical zone of the gamonts, and some were located so closely to micropores that they seemed to be connected to them (Fig 7F). In contrast to the individuals with the plasma membrane underlined by two well-preserved cytomembranes (Fig 7I), several gamonts clearly possessed discontinuous cytomembranes or a disorganised pellicle. Vesicles present in the area of subpellicular filaments can be evidence that cytomembranes underwent re-building due to pellicle reorganisation (completion or renewal) in a growing parasite (Fig 7J and 7K).

Fluorescent visualisation of cytoskeletal elements

For the unspecific visualisation of proteins in *E. duboscqi*, Evans blue staining viewed with a rhodamine filter set was used (Fig 8A–8E). Besides typical staining of cytoplasmic contents, it revealed a relatively high concentration of unspecified proteins in the PS tail and in the area of the parasite attachment site.

The strong phalloidin labelling revealed a high accumulation of filamentous actin (F-actin) in the layer corresponding to the host-derived PS as well as in the brush border of the host epithelium (Fig 8F–8P). The parasite surface and cytoplasm exhibited a fluorescent signal of medium intensity, similar to the cytoplasm of surrounding host cells. The PS tail exhibited F-actin staining of weak to medium intensity (Fig 8H and 8I). In agreement with the electron microscopic observations, the basal part of the PS enveloping the trophozoites and young gamonts showed numerous lobes organised in one circle (Fig 8F–8I), while lobes in mature gamonts formed two circles (Fig 8J–8P). The attachment site often exhibited brighter fluorescence than the rest of the parasite enclosed within the PS. After incubation in 10 μM JAS for 9 hours, the F-actin staining became very strong in the area of the PS but only slightly increased on the parasite surface (Fig 8Q). Treatment for 7 hours, with the concentration of JAS increased to 30 μM, induced even more advanced stabilisation of actin filaments, resulting in further amplification of the fluorescent signal (Fig 8R). Interestingly, the treatment with 10 μM cytochalasin D for 9 hours first caused depolymerisation of F-actin in the host tissue and parasites, while the F-actin restricted to the PS remained intact (Fig 8S) as it stained with the same intensity as non-treated controls. After incubation in 30 μM cytochalasin D for 7 hours, the fluorescence signal was very weak in all the host tissue, host-derived PS and parasites (Fig 8T).

Parasites labelled with the specific anti-actin antibody (known to recognise the actin in *Toxoplasma* and *Plasmodium*) exhibited fluorescence signal of medium intensity (Fig 9A and 9B). The immunolocalisation of actin differed from F-actin labelling in that the antibody did not label the PS, but labelled the host tissue with the same intensity as the parasite enclosed within the sac (Fig 9B). A slightly increased labelling was noticed at the base of the PS (Fig 9A), especially when viewing individual optical sections. A weak staining of the PS tail was observed in all individuals. The treatment with 30 μM JAS for 7 hours resulted in increased labelling of
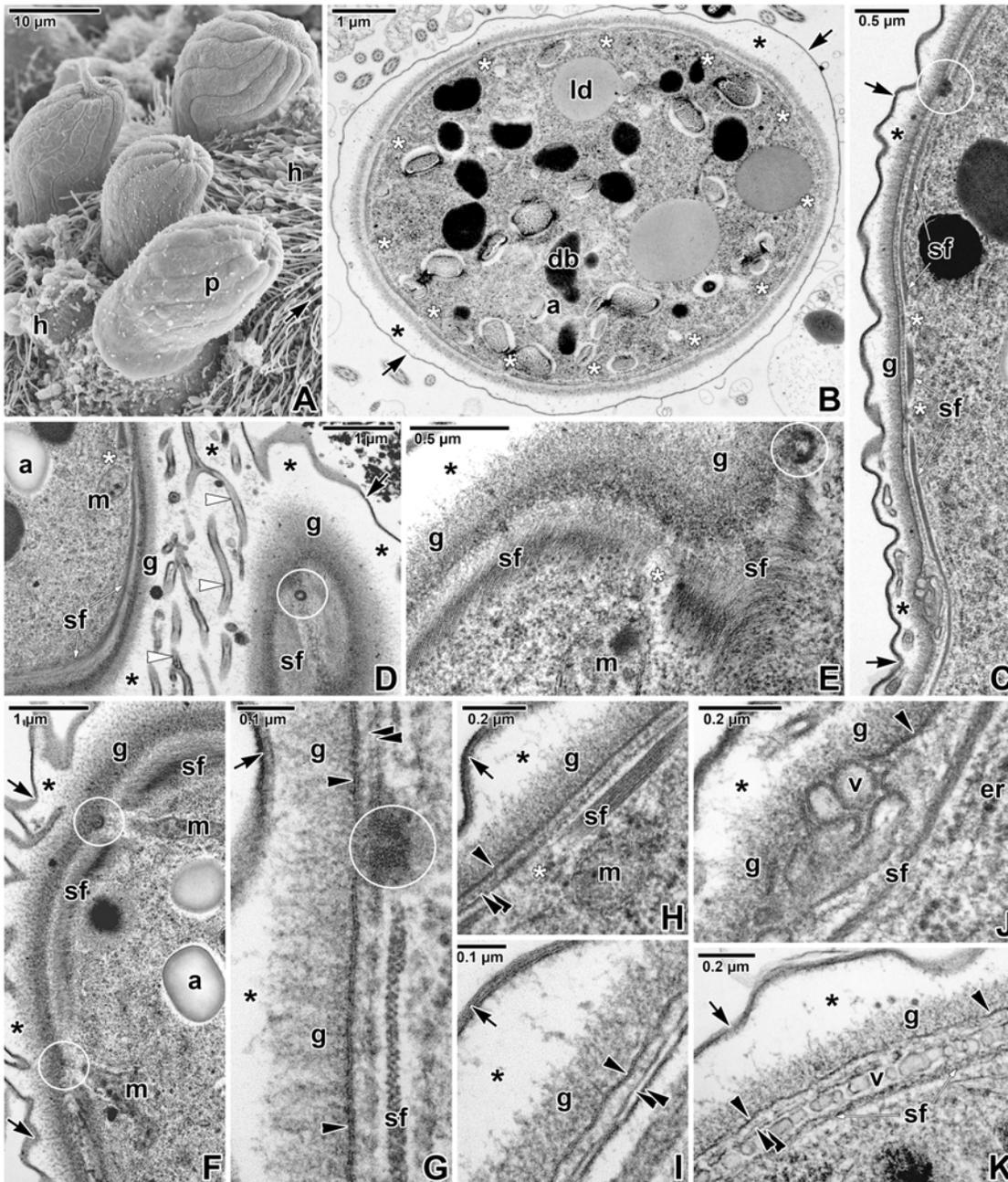
Fig 7. Fine structure of a parasitophorous sac and pellicle in *Eleutheroschizon duboscqi* gamonts. A. Attached gamonts. SEM. **B.** Cross-sectioned gamont showing its surface organised in 12 broad folds and shallow grooves corresponding to the regularly arranged interruptions of subpellicular filaments. TEM. **C.** Longitudinal section showing the organisation of PS, gamont pellicle and the subpellicular layer of filaments that is repeatedly interrupted in areas corresponding to the localisation of micropores. TEM, RR. **D.** Superficial section of the PS and the gamont pellicle. The channel-like structures located in the space between the PS and parasite correspond to the folding of the PS observed under SEM. TEM, RR. **E.** Tangential section of the gamont surface underlined with subpellicular layer of filaments. TEM, RR. **F.** Diagonal section of the gamont surface revealing mitochondria connected with micropores. TEM, RR. **G.** Cross-section of pellicle showing the subpellicular filaments interrupted in the micropore area. TEM, RR. **H.** Almost longitudinal section of pellicle with interrupted subpellicular filaments. TEM, RR. **I.** Pellicle with continuous cytomembranes. TEM. **J-K.** Re-building of the parasite IMC indicated by the discontinuous cytomembranes and numerous vesicles located between the parasite plasma membrane and the subpellicular layer of the filaments. TEM, RR. *a*—parasite amylopectin, *arrow*—PS, *asterisk*—space between the parasite and PS, *black arrowhead*—parasite plasma membrane, *black double/paired arrowheads*—parasite cytomembranes, *db*—parasite dense bodies, *er*—parasite endoplasmic reticulum, *g*—glycocalyx, *h*—host tissue, *ld*—parasite lipid droplet, *m*—parasite mitochondria, *p*—parasite, *sf*—parasite subpellicular filaments, *v*—vesicles, *white arrowheads*—channel-like structures. Micropores are indicated by white circles, interruptions of subpellicular filaments—by white asterisks.
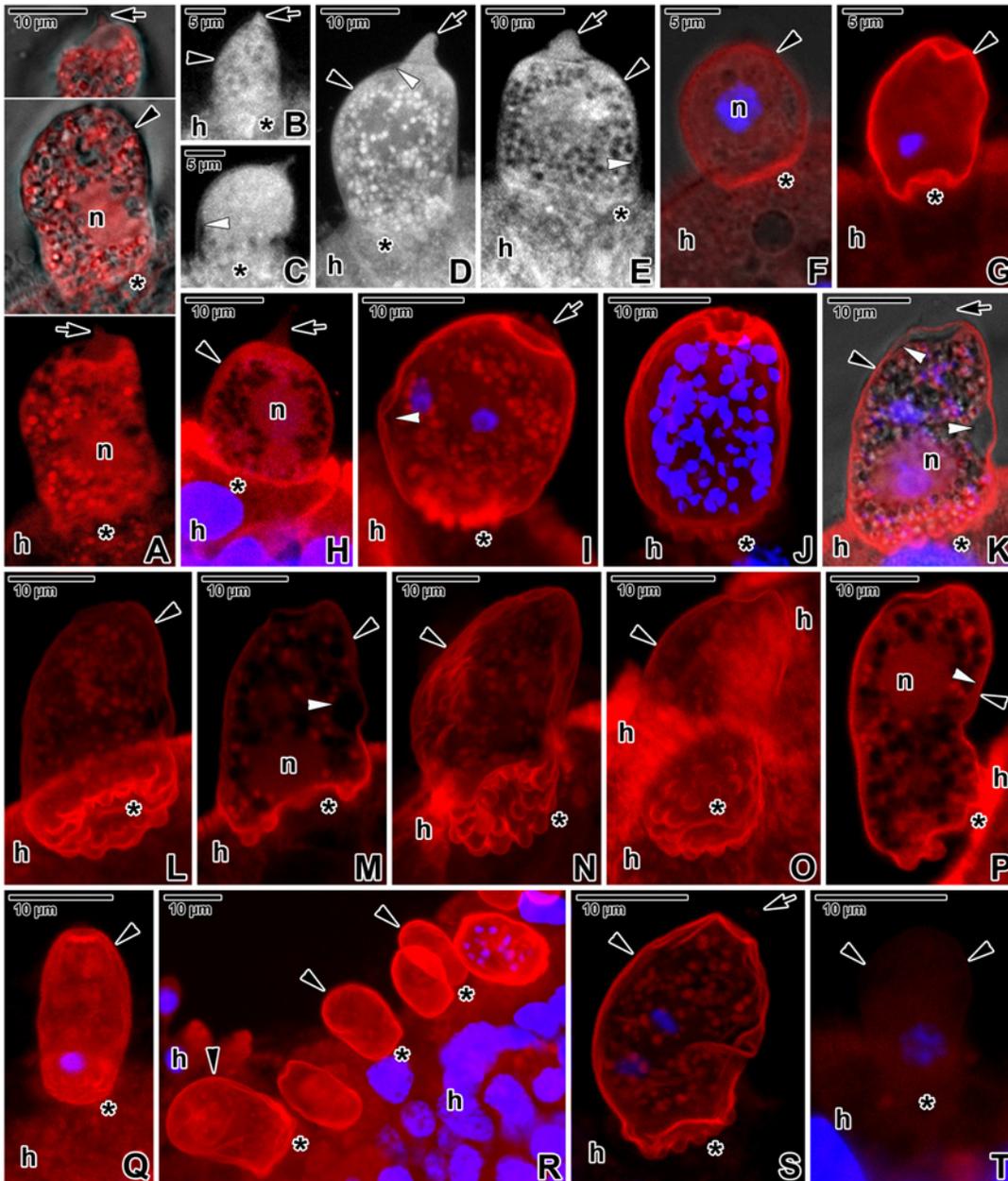
Fig 8. Fluorescent visualisation of an *Eleutheroschizon duboscqi* parasitophorous sac. A. Macrogamont stained with Evans blue. CLSM (lower) and CLSM in a combination with transmission LM (upper two). **B-E.** Trophozoites (B-D) and a gamont (E) stained with Evans blue. CLSM, output image not coloured. **F-H.** Localisation of F-actin in trophozoites. One circle of lobes is visible in the attachment site of the trophozoite shown in G. CLSM in a combination with transmission LM (F) and CLSM (G, H), phalloidin-TRITC/DAPI. **I.** F-actin labelling of a putative young microgamont with two primary nuclei. CLSM, phalloidin-TRITC/DAPI. **J.** F-actin in a microgamont with numerous nuclei. CLSM, phalloidin-TRITC/DAPI. **K-M.** F-actin in a putative macrogamont. CLSM in a combination with transmission LM (K) and CLSM (L, M), phalloidin-TRITC/DAPI. **N-P.** F-actin in a macrogamont equipped with attachment lobes organised in two circles. CLSM, phalloidin-TRITC. The intensity of signal for F-actin shown in F-P was strong for PS and medium for parasites. **Q.** Labelling of F-actin in an individual treated for 9 hours with 10 μM JAS showing the very strong labelling of PS. Individual optical sections also revealed a slightly increased F-actin labelling of the parasite. CLSM, phalloidin-TRITC/DAPI. **R.** Treatment with 30 μM JAS for 7 hours resulted in further increase of F-actin labelling in the PS, parasite and host tissue. The individual with several nuclei corresponds to the microgamont stage. CLSM, phalloidin-TRITC/DAPI. **S.** Visualisation of F-actin in an individual (putative young microgamont with two primary nuclei) treated for 9 hours with 10 μM cytochalasin D. Note the strong labelling of PS in contrast to the parasite and host tissue exhibiting only very weak signal. CLSM, phalloidin-TRITC/DAPI. **T.** Very weak F-actin labelling in a specimen treated for 7 hours with 30 μM cytochalasin D. CLSM, phalloidin-TRITC/DAPI. A-L, N-O, Q-T are composite views created by flattening a series of optical sections, while M and P represent single median optical sections. All samples were fixed in PFA. *arrow*—tail of the PS, *asterisk*—parasite attachment site, *black arrowhead*—PS, *h*—host tissue, *n*—parasite nucleus, *white arrowhead*—parasite pellicle.

doi:10.1371/journal.pone.0125063.g008
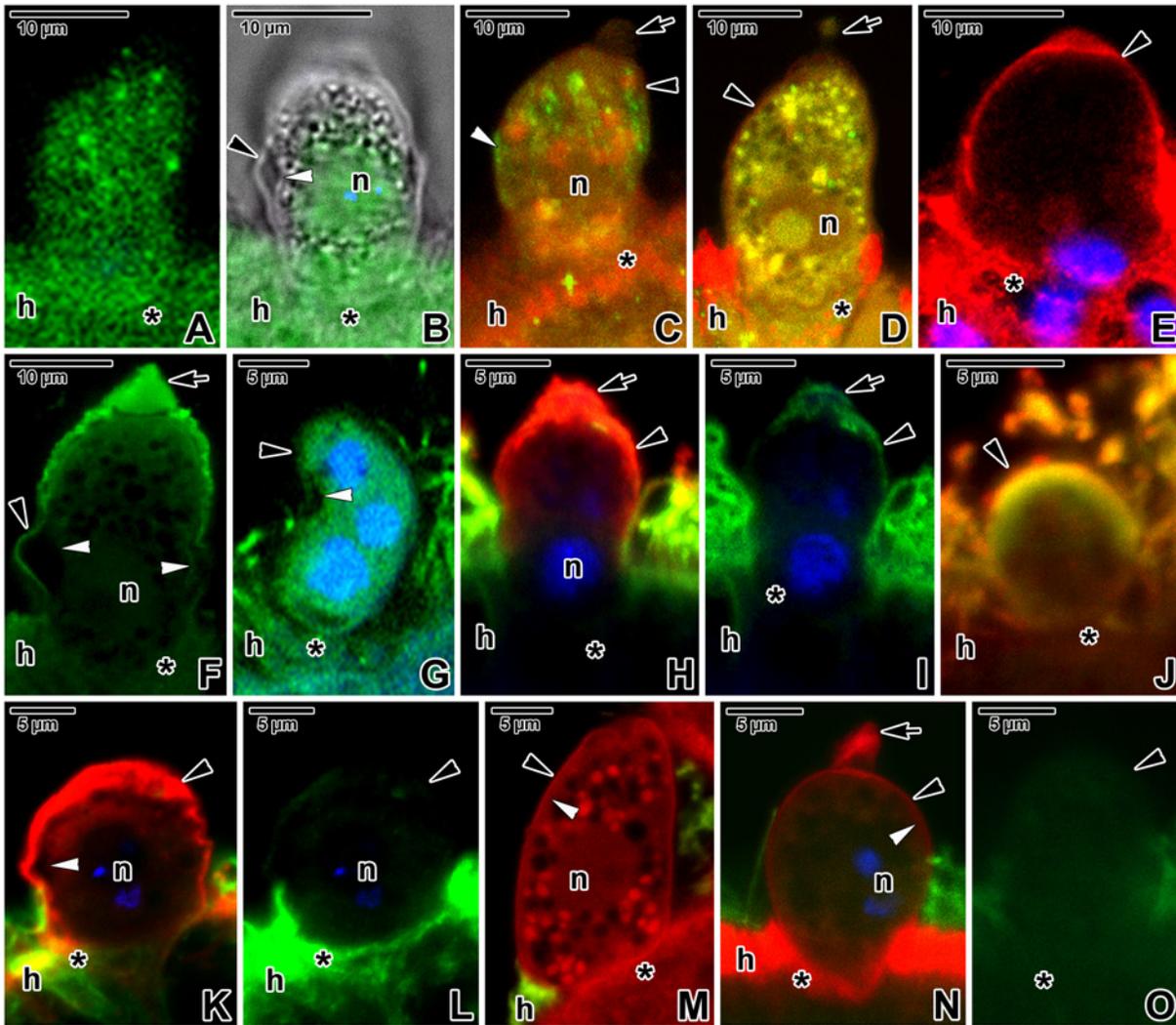
Fig 9. Immunolocalisation of *Eleutheroschizon duboscqi* cytoskeletal proteins. A-B. Actin labelling with a medium intensity in a trophozoite (PFA fixation). CLSM, IFA (A) and CLSM in a combination with transmission LM, IFA/DAPI (B). B represents a single median optical section. **C.** Actin labelling in a macrogamont treated with 30 μM JAS for 7 hours (PFA fixation). Note the increased accumulation of parasite actin (FITC) organised in longitudinal bands exhibiting strong fluorescence and strong F-actin (TRITC) labelling with a diffuse character. CLSM, IFA/phalloidin-TRITC. **D.** A gamont exhibiting a more diffuse actin (FITC) labelling of medium intensity after treatment with 10 μM cytochalasin D for 9 hours (PFA fixation). The F-actin (TRITC) labelling of the parasite did not change significantly. CLSM, IFA/phalloidin-TRITC. **E.** Very strong myosin (TRITC) labelling restricted to the PS and host tissue (PFA fixation). CLSM, IFA/DAPI. **F.** Strong spectrin (FITC) labelling of the PS in a macrogamont (PFA fixation). CLSM, IFA/DAPI. Single median optical section. **G.** Labelling of α-tubulin (FITC) of strong intensity in a young microgamont (PFA fixation). CLSM, IFA/DAPI. **H-I.** A trophozoite (fixed in ice-cold methanol) exhibiting a labelling of medium intensity for α-tubulin (FITC) and very strong intensity for myosin (TRITC). CLSM, IFA/DAPI. **J.** Labelling of α-tubulin (FITC) and myosin (TRITC) in an early trophozoite treated for 7 hours with 10 μM oryzalin (fixed in ice-cold methanol). The fluorescence signals for both antibodies did not change significantly. CLSM, IFA. **K-L.** Localisation of α-tubulin (FITC) and myosin (TRITC) in an individual (probably a young microgamont) treated with 30 μM oryzalin for 3 hours (fixed in ice-cold methanol). The fluorescence signal for tubulin became very weak, while it remained very strong for myosin. CLSM, IFA/DAPI. **M.** Co-localisation of α-tubulin (FITC) and F-actin (TRITC) in a macrogamont treated for 7 hours with 10 μM oryzalin (PFA fixation). CLSM, IFA/phalloidin-TRITC. **N-O.** Labelling of α-tubulin (FITC) and F-actin (TRITC) in a maturing trophozoite treated for 3 hours with 30 μM oryzalin (PFA fixation). CLSM, IFA/phalloidin-TRITC/DAPI. In both the preparations (M-O), there was almost no fluorescence signal for α-tubulin, while the F-actin labelled with a strong intensity. *arrow*—tail of the PS, *asterisk*—parasite attachment site, *black arrowhead*—PS, *h*—host tissue, *n*—parasite nucleus, *white arrowhead*—parasite pellicle.

doi:10.1371/journal.pone.0125063.g009

actin with a strong fluorescence signal, revealing its higher accumulation in longitudinal bands corresponding to the localisation of subpellicular filaments (Fig 9C). Nevertheless, the counter-staining with phalloidin did not show increased actin polymerisation in this area; the strong F-actin labelling of the parasite had diffuse character. The treatment with 10 μM cytochalasin D for 9 hours caused more homogenous labelling of actin with a medium intensity dispersed within the parasite cytoplasm, but only slightly decreased staining of F-actin (Fig 9D). The very strong labelling of myosin was restricted to the PS and host tissue (Fig 9E and 9H). Spectrin appeared to be dispersed in low concentrations in the parasite cytoplasm and surrounding host tissue (medium signal), while the PS, especially in the tail region, stained with a strong intensity (Fig 9F). Immunolabelling with an anti-α-tubulin antibody, used for visualisation of subpellicular microtubules and related structures, was repeatedly very strongly positive for the brush border of the host intestinal epithelium densely covered by microcilia. Both the parasite and the PS unexpectedly (formaldehyde is known to not satisfactory preserve microtubules) exhibited medium to strong labelling in PFA-fixed samples that were processed immediately after fixation (Fig 9G), while only weak to medium labelling was observed in those fixed in methanol (Fig 9H and 9I). Though more diffuse, the labelling of the same intensity was still noticeable at the parasite periphery after treatment with 10 μM oryzalin for 7 hours (Fig 9J). After incubation in 30 μM oryzalin for 3 hours, the peripheral labelling became weak to very weak in methanol-fixed samples, and putatively unpolymerised α-tubulin seemed to be more dispersed throughout the cytoplasm (Fig 9K and 9L). The very strong labelling of myosin in methanol-fixed samples was restricted to the periphery of PS and independent of oryzalin treatment (Fig 9H, 9J and 9K). High doses of oryzalin induced more frequent detachment of *E. duboscqi*, along with its sac, from the host tissue. To confirm that the modified microtubules were the reason for parasite detachment but not the redistribution of F-actin, the correct fixation for phalloidin staining was essential to retain the quaternary protein structure of F-actin (methanol destroys its native conformation and is not suitable for F-actin staining with phalloidin). Hence, control PFA fixation was performed for the co-localisation F-actin and α-tubulin. Parasites treated either with 10 μM or 30 μM oryzalin and subsequently fixed in PFA exhibited no changes in the F-actin distribution (Fig 9M and 9N), except for, when compared to the rest of PS, stronger labelling of the tail (Fig 9N). In contrast to methanol-fixed samples, the labelling with anti-α-tubulin antibody was almost undetectable in parasites and less conspicuous in the host brush border (Fig 9M–9O).

Discussion

This study confirmed the epicellular localisation of the protococcidian *Eleutheroschizon duboscqi* on the gut epithelium of the polychaete *Scoloplos armiger*, as described in the original studies [10,11]. We use the term 'parasitophorous sac' to underline the peculiar localisation of the developmental stages of *E. duboscqi* in the host-derived two-membrane structure. Parasitophorous sac is the preferable term introduced for the first time by Paperna and Vilenkin [16] for the host-derived structure enveloping cryptosporidia. We believe that the term 'parasitophorous vacuole' to describe the location of epicellular organisms like *Cryptosporidium* and *Eleutheroschizon* is misleading, because it refers solely to a vacuolar space bordered by a membrane [5,17]. The parasitophorous sac (PS) is an epicellular structure (niche) enveloping the entire parasite composed of two continuous host plasma membranes on the outer and inner sides, enclosing a thin layer of host cell cytoplasm. In addition, a dense band of microfilaments separates the unmodified and modified parts of the host cell ([5], this manuscript).
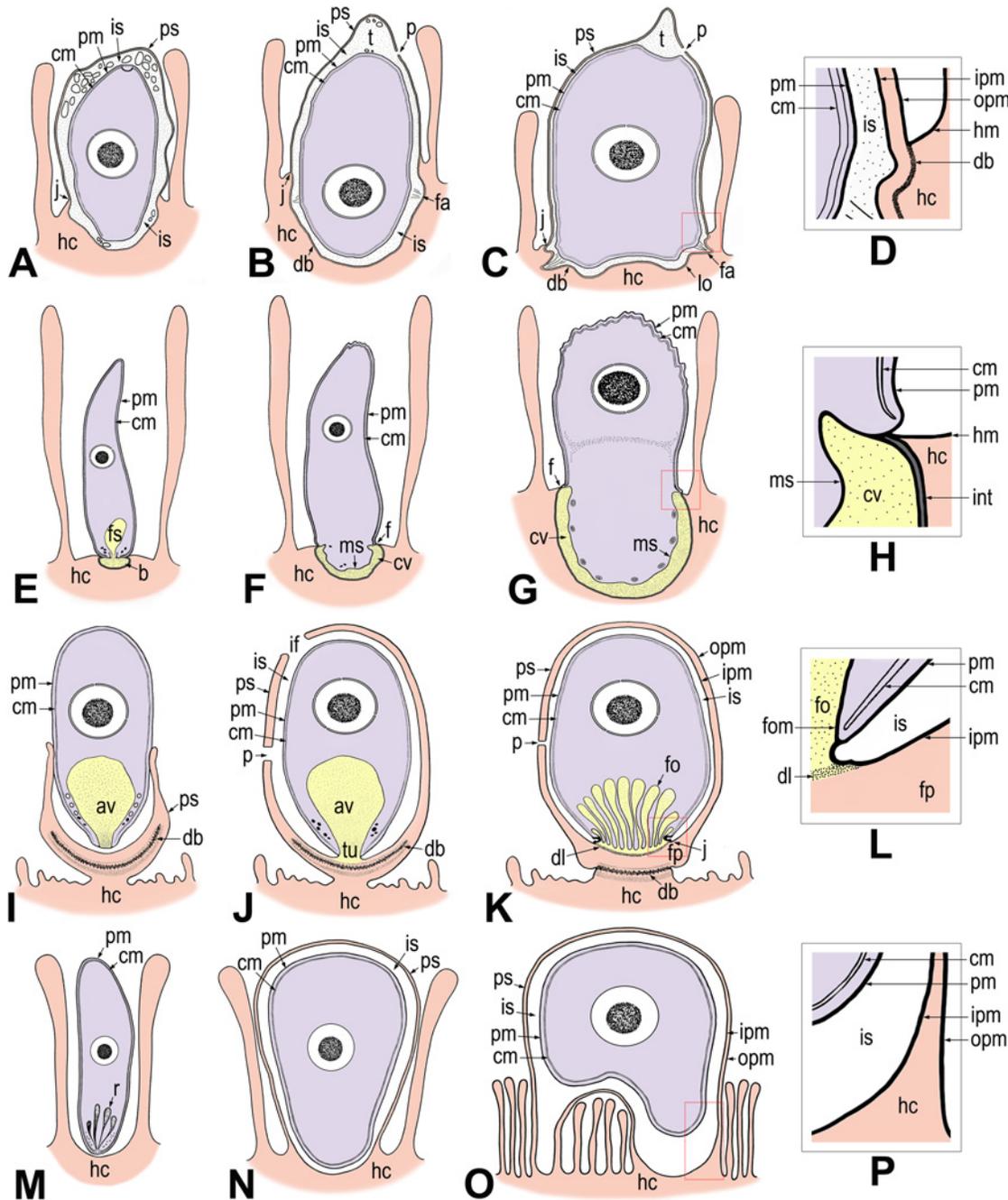
Fig 10. Schematic diagram of host-parasite interactions in *Eleutheroschizon duboscqi*, eugregarines, cryptosporidia, and epicellular eimeriids. The diagrams of *E. duboscqi*, gregarines and cryptosporidia are based on our personal observations enriched by published data. The diagram of eimeriids represents our interpretation and summary of published micrographs, where only maturing or mature stages were clearly shown [36–38,40,42– 44,64,65]. In this scheme, we refer to the host-derived envelope (described as a parasitophorous vacuole throughout literature) of eimeriids in epicellular location as a parasitophorous sac (PS) due to its organisation similar to that in cryptosporidia and *E. duboscqi*. Three colours are used to distinguish between the parasite (in purple), the host cell including its parts modified due to parasitisation (in pink) and the contact zone between the host and the parasite (in yellow) where the interrelationships of the two organisms become more intimate. In the case of host-parasite cellular interactions in *E. duboscqi* and epicellular eimeriids, the internal space between the parasite and PS remained colourless, even though we do not exclude the possibility that this region may serve as a transitional zone for intensive interactions between the host and its parasite. **A-D.** *Eleutheroschizon duboscqi*. **A.** Attached zoite transforming into a trophozoite stage, already completely enveloped by a PS. **B.** Maturing trophozoite with a forming ring of fascicles at the attachment site. The tail forms at the caudal part of the PS. **C.** Mature trophozoite with a prominent tail. Note the presence of attachment fascicles and lobes. **D.** Detailed view of the annular joint point (the cut-out is marked by a red square in C). **E-H. Eugregarines. E.** Sporozoite immediately after attachment to the host epithelial cell. **F.** Transformation of the sporozoite into a trophozoite stage. **G.** Early trophozoite with a well-developed epimerite. **H.** Detailed view of the membrane fusion site (the cut-out is marked by red

square in G). The two cytomembranes end at the point of membrane fusion, where the osmiophilic ring is formed. **I-L. Cryptosporidia. I.** Attached zoite transforming into a trophozoite stage, partially enveloped by an incomplete PS. **J.** Young trophozoite almost completely enveloped by a PS. Note the tunnel connection between the interior of the anterior vacuole and the host cell cytoplasm that developed as the result of the Y-shaped membrane junction. **K.** Mature stage with a prominent filamentous projection at the base of the PS and with a fully developed feeder organelle, the lamellae of which formed from the anterior vacuole membrane. **L.** Detailed view of the Y-shaped membrane junction (the cut-out is marked by a red square in K). **M-P. Epicellular eimeriids. M.** Invading zoite. **N.** Trophozoite/meront stage enveloped by a PS with a single attachment area (monopodial form). **O.** Extension of the gamont stage above the microvillous region leading to an establishment of a new contact with the host cell apart from the primary attachment zone by penetration of the PS membrane to the base of fused microvilli (spider-like form). **P.** Detailed view of the attachment area (the cut-out is marked by a red square in O). *av*—anterior vacuole, *b*—epimeritic bud, *cm*—parasite cytomembranes, *cv*—epimeritic cortical vesicle, *db*—dense band (in cryptosporidia usually consisting of several layers), *f*—membrane fusion site, *dl*—dense line separating the feeder organelle from the filamentous projection of the PS, *fa*—attachment fascicle of filaments, *fo*—feeder organelle with membranous lamellae, *fom*—membrane limiting the lamellae of feeder organelle, *fp*—filamentous projection of the PS, *fs*—flask-shaped structure, *hc*—host cell, *hm*—host cell plasma membrane, *if*—incomplete fusion of PS, *int*—interface between the host cell and eugregarine epimerite, consisting of host cell plasma membrane, epimerite plasma membrane and a dense layer in between, *ipm*—inner membrane of the PS, *is*—internal space between the parasite and PS, *j*—annular joint point (Y-shaped membrane junction in cryptosporidia), *lo*—attachment lobe, *ms*—membrane-like structure limiting the cortical vesicle from the epimerite cytoplasm, *opm*—outer membrane of the PS, *p*—pore on the PS, *pm*—parasite plasma membrane, *ps*—parasitophorous sac, *r*—rhoptries, *t*—tail of the PS, *tu*—tunnel connection.

doi:10.1371/journal.pone.0125063.g010

Attachment strategy and host-parasite interactions in *E. duboscqi* compared to other epicellular apicomplexans

According to our analysis, *E. duboscqi* develops within the host-derived PS, resembling cryptosporidia [5,6,18,19,20]. Moreover, the parasite attaches to the host cell with the help of the complicated attachment site, by analogy with an invading gregarine [6,13,15,21–24] (Fig 10A–10L).

Gregarines are mostly intestinal epicellular parasites, equipped with a specialised attachment apparatus that might also serve as a feeding organelle (epimerite, mucron, modified protomerite) [13,15,21,22,25–29]. Archigregarines suck out the host cell cytoplasm using organelles of the apical complex [3,30,31]. Such a mechanism of feeding is called myzocytosis. On the contrary, many eugregarines seem to not feed through myzocytosis, except, probably, at their youngest developmental stages [32]. Their apical complex of organelles is reduced, and a new, more complicated, attachment apparatus forms (Fig 10G). This apparatus does not penetrate the host cell, but simply causes the invagination of the host plasmalemma (Fig 10E–10H) [6,15,22]. Cryptosporidia have a typical feeder organelle that attaches to the host cell and remains separated from the host cytoplasm by a dense line (Fig 10K and 10L) [5,6]. Similar to gregarines and cryptosporidia, *E. duboscqi* has a complicated attachment apparatus (fascicles and lobes in circles) (Fig 10C); and it remains unclear whether this apparatus is involved in the parasite feeding. Numerous pores are distributed along the entire pellicle of *E. duboscqi*, including the attachment site and some of them seem to be connected with vesicles and mitochondria. These pores may participate in parasite feeding. The apical complex of organelles is absent in *E. duboscqi* during the endogenous phase of its life cycle; and, apparently, feeding through myzocytosis is not typical for this parasite. Neither organelle similar to the flask-shaped structure described in the early stages of the eugregarines [6,13,22,23,32] nor the mucronal vacuole, characteristic of the archigregarine *Selenidium* [3,30], was detected in freshly attached *E. duboscqi* individuals. The flask-shaped structure observed in gregarines with an opening towards the apical pole (Fig 10E) initially appears electron-dense, but, with the formation of the cortical vesicle, it turns electron-lucent [6], suggesting that it might be a rhoptry emptying its enzymes. As rhoptry proteins are generally expected to be involved in the transformation of the host cell membrane into a parasitophorous vacuole (PV) [33], we cannot exclude the possibility that a similar structure may be present in *E. duboscqi* at a stage younger than the early trophozoite already enveloped by a PS.

Epicellular gregarines are usually not surrounded by any sac of host cell origin (Fig 10E–10H), except for the archigregarine *Ditrypanocystis* sp., which is enveloped by a multimembranous structure, originated from fused cilia of the host cell [24]. Cryptosporidia are enveloped

by the PS, the inner membrane of which came from the plasmalemma presented on the host cell microvilli (Fig 10I–10L). In gregarines, as well as in cryptosporidia, the membrane fusion site is formed at the contact area between the parasite and host cell. In contrast, there is no connection between the host and *E. duboscqi* plasma membranes at the annular joint point. The internal space between the *E. duboscqi* plasmalemma and the inner membrane of the PS does not seem to be a part of the parasite. It rather resembles the space between the PV and intracellular coccidia located inside the host cell. As all early stages of *E. duboscqi* were seen to be completely contained within a PS, this host cell-derived envelope must develop much more rapidly than that documented in cryptosporidia, in which, during the invasion process, a tight-fitting membrane fold of the invaded host cell gradually rises up along the zoite, resulting in the formation of the PS [5,20]. The presence of a crystalloid body, a typical feature of sporozoites [26,34], in the stages attached and completely enveloped by the PS, confirms that the earliest observed stages were only slightly modified sporozoites, after their attachment to the host cell. Interestingly, the cortical vesicle in eugregarine *Didymophyes gigantea* was interpreted as a periparasitic space between the host and parasite, functioning as a PV [35]. At first glance, the gregarine cortical vesicle indeed resembles the internal space of the PV due to its translucent appearance with traces of an opaque or filamentous material [6,13,22,23]. In *Gregarina garnhami*, fine tubular structures pass through the cortical vesicle and attach to the epimerite-host cell interface [21]. We could speculate that the cortical vesicle is in fact an incomplete PV, restricted to the embedded apical region (epimerite) of the gregarine. It most likely develops from fused flat vesicles distributed in the epimerite periphery, originating from the parasite endoplasmic reticulum, and turns into a single large vesicle filled with microfilaments [23]. This vesicle is limited on its cytoplasmic face by a membranous structure, often discontinuous or multi-layered [6,15,21]. It retracts along with the epimerite during detachment of mature trophozoite from the host cell [15].

Epicellular localisation within the host tissue has also been described for certain eimeriid coccidia from fish (some *Eimeria* or former *Epieimeria*, some *Goussia*) [36–41] and reptiles (*Choleoeimeria, Acroeimeria*) [42,43]. According to multiple studies, they are localised at the enterocyte apical site among microvilli and covered by a double membrane envelope (the enterocyte and PV membranes), but a single PV membrane in contact areas (Fig 10M–10P). The arrangement of the PV membrane in contact zones is species specific based on various projections and undulations. No direct contact between the parasite and parasitised cell was observed [37,38,40,42–44]. During intracellular development of *Eimeria anguillae* merozoites, the PV with a parasite inside is expelled into the apical region of the parasitised cell, hereby taking an epicellular position [37]. In *Goussia pannonica* and *G. janae*, the parasites either attach to the host cell at a single contact area resulting from multiple fusions of microvilli ('monopodial' form) or are located above the microvillar zone, connected with the epithelium (occasionally to more than one enterocyte) through multiple thin projections in a spider-like arrangement [40,44]. The PV membrane of the spider-like projections have been described to be closely apposed to the enterocyte plasmalemma and to penetrate to the base of the villus where it contacts the host cytoplasm. The referenced micrographs, though not provided in satisfactory magnification, however, do not show any PV membrane penetrating into the host cytoplasm, which would indicate an intracellular (epicytoplasmic) position of the parasite. It rather suggests a deep invagination of the enterocyte membrane, at the connection with PV projections, i.e. epicellular localisation. Representatives of *Acroeimeria* are also considered to be epicellular parasites developing within a PV bulging above the epithelium surface [43]. From there, despite intracellular or epicellular initial stages of the development, some eimeriid coccidia of poikilothermic animals localise at the host cell apical part and are surrounded by the host-derived two-membrane PV.

Cryptosporidia, *E. duboscqi* and gregarines represent heteropolar cells; i.e. they exhibit a high degree of cell polarity in that their anterior and posterior ends differ in shape, structure and function. Extracellular but attached parasites are usually of a heteropolar nature, while the intracellular ones are generally non-polar. Epicellular eimeriids seem to be non-polar as they do not have any attachment organelles and seem to take up nutrients exclusively via the PV [37]. Nevertheless, they create projections of the PV [37,38] equipped with pores; these projections enlarge the contact area with the host cell and resemble the *E. duboscqi* attachment lobes and fascicles. Similarly, the complicated attachment organelles in many eugregarines seem to significantly increase the absorptive surface [13,29,35]. Apparently, the epicellular localisation, independent of its origin (whether initial stages of the parasite development are extracellular or intracellular), leads to the occurrence of cell polarity. All the above-mentioned apicomplexans form a specialised host-parasite interface, reflecting analogous modes of adaptation for survival and development in a similar host environment (i.e. the gastrointestinal epithelial brush border) [45] (Fig 10A–10P). It seems that, once attached to a proper host cell, all these parasites stimulate additional growth and subsequent fusion of host microvilli as well as further modifications to the host plasmalemma, leading to PS/PV formation. They tend to create a host-derived envelope around themselves and develop in its cavity so as to be separated from the host cytoplasm/environment. In cryptosporidia, the PS is not complete as they are directly connected to the host cell via a feeder organelle (i.e. they form the so-called Y-shaped junction between the host and parasite membranes), while in eimeriids and *E. duboscqi*, the inner membrane of this envelope contains the entire parasite. The mode of connection with the host cell remains inconclusive in the earliest developmental stages of *E. duboscqi*. Most likely it never invades the host cytoplasm, but attaches to the apical site of the host cell for a short time (until the formation of the PS).

It has been suggested that eimeriid epicellular development might be considered as a more primitive form of host-parasite association [42]. Some studies showed, however, that parasites developing epicellularly seem to have a less negative effect on the host epithelium than intracellular ones [46]. In general, it is more advantageous for the parasite to maintain its host in acceptable fitness; from this perspective, the evolution of this attachment strategy could be more progressive. While the most serious pathological changes in *E. anguillae* are induced by intracellular stages and vary depending on the intensity of parasitisation, the epicellular development causes alterations to the host epithelium, such as local swellings or a reduction in the number of microvilli [37]. Similar changes are reported in cryptosporidiosis, where the destiny of the host depends on its health status and immunocompetence [47,48]. In *E. anguillae*, the host epithelium, discharged from parasites, has lesions on the intestinal surface resembling circular holes [37]. Cryptosporidia and *E. duboscqi* leave only shallow craters with PS remains at the epithelial surface after their detachment [5]. Similarly, detached gregarine trophozoites leave flat holes in the epithelium lacking microvilli [15]. Microvilli are essential for digestion and nutrient absorption and their destruction might lead to host malnutrition with consequent weakening or even death. Although epicellular parasites destroy individual cells, the overall damage to epithelium in mild infections is negligible and often easily repaired thanks to its continual regeneration.

Host actin distribution and architecture of *E. duboscqi* parasitophorous sac in comparison to cryptosporidia

Phalloidin staining, along with the application of drugs that influence the polymerisation of actin, confirmed the presence of actin filaments in host tissue and their increased accumulation in the PS surrounding *E. duboscqi*. Moreover, the higher doses of cytochalasin D, required for destroying actin filaments in the PS wall, suggest that the polymerised form of actin is more

stable in the host-derived PS than in surrounding host tissue. This accumulation of host actin filaments might be induced by invading *E. duboscqi*, similarly to cryptosporidia, which induce the rearrangement and accumulation of actin and actin-binding proteins to their attachment site during invasion [49,50–52]. Cryptosporidia, however, show a low amount of F-actin in their PS [53]. Furthermore, the wall of the *E. duboscqi* PS exhibited a high accumulation of myosin. In cryptosporidia, the motor activity of host myosin seems to play an important role, putatively in association with microvilli extensions, in the formation of a parasite niche [49,52]. This theory is supported by a model for the protrusion of membranous structures, illustrating the significant involvement of myosin in the movement of actin filaments toward the apical surface of membrane extensions [54]. The involvement of host microcilia in the formation of the *E. duboscqi* PS is indicated by the presence of α-tubulin restricted to the PS wall, especially in the caudal region with the tail. The tubulin seemed to be in polymerised form, as incubation in oryzalin resulted in the vanishing of fluorescence as well as frequent detachment of parasites with their sacs from epithelium observed *in vitro*.

In contrast to intracellular coccidia, evolutionary selection presumably favoured the unique epicellular niche for cryptosporidia to more effectively evade the host immune response, though as a consequence, the attached parasite became dependent upon its connection with the host cell for nutrient acquisition. In *E. duboscqi*, the strategy could be similar. Host actin polymerisation and subsequent membrane protrusion are considered to be important for the establishment of a productive infection site in cryptosporidia [52], in which induced membrane extensions encapsulate the parasite and form the PS, with a dense band in the host cytoplasm located just beneath the attachment zone [5,6,20]. This band consists of electron-dense microfibrils interwoven perpendicularly [55], with an adjacent filamentous network of polymerised actin [52]. The dense band underlining the base of *E. duboscqi* is much thinner and closely apposed to the PS inner membrane. CLSM confirmed an increased accumulation of F-actin at the attachment site. In cryptosporidia, the actin reorganisation and formation of dense bands supported by the actin plaque were shown to be intimately involved in parasite anchoring and retention at the host cell apical surface [5,49,56]. An explanation for such a cytoskeletal rearrangement in parasitised cells is that this process results in the formation of a network for vesicle trafficking, facilitating the movement of nutrients between the host cell and the PS [49]. This hypothesis is in agreement with our observations on the accumulation of tiny filaments located within host cytoplasm surrounding the invaginations of PS membrane in the area of *E. duboscqi* attachment fascicles. These fascicles develop during *E. duboscqi* trophozoite maturation and seem to anchor the growing PS with the parasite to the host cell, while host filaments overlapping them could strengthen this fixation and prevent mechanical detachment.

Both parasites, cryptosporidia and *E. duboscqi*, regularly detach (most likely due to damage) along with their sacs from the unmodified part of the host cell. While the detachment of cryptosporidia takes place in the area of a dense band [5], individuals of *E. duboscqi* tear away from their sacs at the base, thereby exposing their naked basal region (i.e. covered by the parasite pellicle only) and leaving the intact inner membrane of the PS at the place of previous attachment. It seems that *E. duboscqi* induces only moderate alterations of the host cell in contrast to cryptosporidia, in which, along with actin remodelling, remarkable alteration of host membrane organisation has been documented [57]. Cytoskeletal remodelling of the host cell induced by cryptosporidia can be noted as microvillous hypertrophy, i.e. elongation and protrusion of host cell microvilli surrounding the parasite [49]. The persistence of long microvilli clustered at the attachment site suggests an active manipulation of the host membrane structure by the parasite. The microvilli associated with the cryptosporidian PS were particularly thick and contained dense bundles of F-actin. In *E. duboscqi*, we did not observe any significant extension of the adjacent host cell microvilli; only a few microcilia were occasionally attached to the PS

surface (Fig 4A and 4K) and no obvious pathological changes were seen in the parasitised area. Despite a similar strategy of PS formation and architecture with cryptosporidia, epicellular stages of *E. duboscqi* seem to have less of a pathological effect on host tissue.

The function of the tail of the *E. duboscqi* PS remains unknown. Staining with Evans blue showed that the tail is protein-rich, confirmed by the SEM observations of the presence of a fibrous substance at the caudal region of parasites with a ruptured PS. Numerous pores along with a dense matrix, intensively stained by RR, in their vicinity indicate the role of the tail in the transportation of mucus and/or other parasite metabolites outside. Despite the presence of long filaments, the F-actin labelling in the tail turned out to be less distinct than the rest of the PS, but surprisingly, the incubation with oryzalin resulted in much stronger F-actin labelling in the tail in contrast to the proximal part of the PS. Tails of different sizes in maturing trophozoites may be a result of extra growth of the PS. Spectrin accumulation seemed to increase towards the PS caudal area with a tail, suggesting that plasma membrane proteins are accumulated in this zone. So, hypothetically, the fibrous substance could be a stock of membrane material needed for the PS development during the parasite maturation and growth. It remains unclear as to whether the ruptured PS observed in our preparations is a consequence of damage due to material processing or it represents a natural process in the life cycle allowing *E. duboscqi* gamonts to leave the host cell. It could be also a result of incomplete fusion of the PS during early parasite development.

Cell cortex and cytoskeleton of *E. duboscqi*

In the course of transformation of *E. duboscqi* trophozoites into gamonts, a thick glycocalyx layer appears on the external surface of the parasite plasmalemma. Similar fibrillar coat, most likely of glycocalyx nature, has been documented covering the entire parasite in *Acroeimeria pintoi* [43]. In *E. duboscqi*, it forms earlier than the subpellicular filaments and seems to be essential for the attached stages. The most important role of glycocalyx might be a mechanical defence against potential fusion of the PS with the parasite surface. Importantly, the short and long attachment filaments that arise from the pellicle are anchored in the IMC and extend through the glycocalyx. They evidently represent a modified form of the glycocalyx.

The pellicle of *E. duboscqi* also appears unique in that it seems to re-build or reorganise during the parasite development. Vesicles observed under the plasma membrane in the area of discontinuous or absent cytomembranes of some gamonts indicate a process of membrane insertion into the cortex, most likely needed for pellicle completion during parasite growth. The barely distinguishable pellicle of early trophozoites provides further support for the hypothesis of its repetitive reorganisation. It is not clear how the parasite undergoes fertilisation and if its life cycle comprises additional free stages, but *in vitro* we often observed detachment of *E. duboscqi* along with PS, and documented detached parasites enveloped by the PS under electron microscope. All this suggests the participation of the PS in parasite protection from the surrounding environment even after detachment from the host tissue, probably as a consequence of pellicle reorganisation during *E. duboscqi* development.

The cytoskeleton of this parasite comprises subpellicular microtubules, but only during early development. While the posterior ring of *Toxoplasma gondii* does not connect with subpellicular microtubules [58], in *E. duboscqi* it does, similar to the 'posterior polar ring' in tachyzoites of *Besnoitia besnoiti* [59] or the so-called 'proximal polar ring' in *Plasmodium* sporozoites [60]. Usually, these structures are only recognised as pellicular (IMC) thickening. Although the microtubules disappeared during *E. duboscqi* trophozoite maturation and were not present in gamonts, we obtained positive α-tubulin labelling of the parasite surface and cytoplasm, suggesting the preservation of tubulin either in its non-polymerised form or its

presence in other tubulin-rich structures. The second speculation seems to be more likely, because incubation in oryzalin resulted in the disappearance of labelling from the parasite periphery, and the putatively unpolymerised α-tubulin seemed to be more dispersed throughout the cytoplasm. Apicomplexan microtubules are selectively susceptible to drug-induced disruption; after prolonged treatment in 2.5 μM oryzalin all tubulin is usually unpolymerised and dispersed [61]. Oryzalin prevents the formation of microtubules in *T. gondii* daughter cells, but has a more moderate effect on existing microtubules in the mother cell [62,63]. This is in agreement with our results on *E. duboscqi*, where high drug doses must be applied for prolonged period to observe a dispersed character of tubulin staining. Of special interest are also the subpellicular bands of longitudinally oriented filaments, located beneath the parasite IMC, that form during the trophozoite maturation. Positive labelling of the parasite surface for actin/F-actin and the effect of cytoskeletal drugs on its staining suggest that these filaments are actin-rich. Considering the lack of subpellicular microtubules in mature stages, these bands could play the role of the parasite cytoskeleton.

Conclusions

The endogenous stages of *Eleutheroschizon duboscqi* life cycle exclusively comprise trophozoites and gamonts. They develop in the intestine of *Scoloplos armiger* being attached to the host cell in an epicellular position and covered by a host-derived parasitophorous sac. Attached parasites share features of cryptosporidia and gregarines, i.e. they conspicuously resemble a maturing trophozoite of epicellular eugregarines with morphologically pronounced attachment apparatus, but are contained within a PS similar to that in cryptosporidia. However, *E. duboscqi* parasites have no intimate contact with the enterocyte membrane. The parasite pellicle seems to reorganise repeatedly during development. Detached parasites are enveloped by a PS covering their distal area above the attachment site, hereby suggesting that after detachment from the host tissue they preserve this envelope of host origin, providing them ongoing protection in a potentially unfriendly surrounding environment.

Acknowledgments

Author Contributions

Conceived and designed the experiments: AV. Performed the experiments: AV. Analyzed the data: AV GGP AD MK TGS. Contributed reagents/materials/analysis tools: AV GGP AD MK TGS. Wrote the paper: AV. Discovered *Eleutheroschizon duboscqi* in *Scoloplos armiger* from the White Sea and shared her findings with other authors for further collaboration, and

contributed considerably to manuscript writing: GGP. Performed field sampling: AV GGP AD TGS. Contributed to the study design: GGP AD TGS. Performed light and electron microscopic analyses: AV GGP AD MK TGS. Performed CLSM analyses: AV. Assisted in sample processing for CLSM: MK. Reviewed and edited the manuscript, and approved its final version: AV GGP AD MK TGS.

References

1. Adl SM, Simpson AG, Lane CE, Lukes J, Bass D, Bowser SS, et al. The revised classification of eukaryotes. J Eukaryot Microbiol. 2012; 59: 429–493. doi: 10.1111/j.1550-7408.2012.00644.x PMID: 23020233

2. Cox FEG. The evolutionary expansion of the Sporozoa. Int J Parasitol. 1994; 24: 1301–1316. PMID: 7729983

3. Simdyanov TG, Kuvardina ON. Fine structure and putative feeding mechanism of the archigregarine *Selenidium orientale* (Apicomplexa: Gregarinomorpha). Eur J Protistol. 2007; 43: 17–25. PMID: 17126539

4. Leander BS. Marine gregarines: evolutionary prelude to the apicomplexan radiation? Trends Parasitol. 2008; 24: 60–67. doi: 10.1016/j.pt.2007.11.005 PMID: 18226585

5. Valigurova A, Jirku M, Koudela B, Gelnar M, Modry D, Slapeta J. Cryptosporidia: Epicellular parasites embraced by the host cell membrane. Int J Parasitol. 2008; 38: 913–922. PMID: 18158154

6. Valigurova A, Hofmannova L, Koudela B, Vavra J. An ultrastructural comparison of the attachment sites between *Gregarina steini* and *Cryptosporidium muris*. J Eukaryot Microbiol. 2007; 54: 495–510. PMID: 18070327

7. Barta JR, Thompson RCA. What is *Cryptosporidium*? Reappraising its biology and phylogenetic affinities. Trends Parasitol. 2006; 22: 463–468. PMID: 16904941

8. Carreno RA, Martin DS, Barta JR. *Cryptosporidium* is more closely related to the gregarines than to coccidia as shown by phylogenetic analysis of apicomplexan parasites inferred using small-subunit ribosomal RNA gene sequences. Parasitol Res. 1999; 85: 899–904. PMID: 10540950

9. Perkins FO, Barta JR, Clopton RE, Peirce MA, Upton SJ. Phylum Apicomplexa Levine, 1970. In: Lee JJ, Leedale GF, Bradbury P, editors. An illustrated guide to the Protozoa. 2nd ed. Society of Protozoologists, Lawrence, Kansas, USA; 2000. pp. 190–369.

10. Chatton E, Villeneuve F. Le cycle évolutif del'*Eleutheroschizon duboscqui* Brasil. Preuve expérimentale de l'absence de schizogonie chez cette forme et chez la *Siedleckia caulleryi* Ch. et Vill. CR Acad Sci. 1936; 203: 833–836.

11. Brasil L. *Eleutheroschizon duboscqi*, sporozoaire nouveau parasite de *Scoloplos armiger* O.F. Müller. Arch zool exp gen. 1906; 4: 17–22.

12. Awerinzew S. Izsledovaniya nad' paraziticheskimi prosteishimi I-VII. [Studies on parasitic protozoa I-VII. In Russian, German summary]. Trudy Imp S Petersburg Obsch Estestvoisp Vypusk 2: Otd Zool i Fiziol. 1908; 38: 1–139.

13. Valigurova A. Sophisticated adaptations of *Gregarina cuneata* (Apicomplexa) feeding stages for epicellular parasitism. PLoS ONE. 2012; 7: e42606. doi: 10.1371/journal.pone.0042606 PMID: 22900033

14. Sokolova YY, Paskerova GG, Rotari YM, Nassonova ES, Smirnov AV. Description of *Metchnikovella spiralis* sp. n. (Microsporidia: Metchnikovellidae), with notes on the ultrastructure of metchnikovellids. Parasitology. 2014; 141: 1108–1122. doi: 10.1017/S0031182014000420 PMID: 24813231

15. Valigurova A, Michalkova V, Koudela B. Eugregarine trophozoite detachment from the host epithelium via epimerite retraction: Fiction or fact? Int J Parasitol. 2009; 39: 1235–1242. doi: 10.1016/j.ijpara.2009.04.009 PMID: 19460380

16. Paperna I, Vilenkin M. Cryptosporidiosis in the gourami *Trichogaster leeri*: description of a new species and a proposal for a new genus, *Piscicryptosporidium*, for species infecting fish. Dis Aquat Organ. 1996; 27: 95–101.

17. Scholtyseck E. Fine structure of parasitic protozoa: an atlas of micrographs, drawings and diagrams. Berlin: Springer-Verlag; 1979.

18. Huang BQ, Chen XM, LaRusso NF. *Cryptosporidium parvum* attachment to and internalization by human biliary epithelia in vitro: A morphologic study. J Parasitol. 2004; 90: 212–221. PMID: 15165040

19. Umemiya R, Fukuda M, Fujisaki K, Matsui T. Electron microscopic observation of the invasion process of *Cryptosporidium parvum* in severe combined immunodeficiency mice. J Parasitol. 2005; 91: 1034–1039. PMID: 16419745

20. Lumb R, Smith K, Odonoghue PJ, Lanser JA. Ultrastructure of the attachment of *Cryptosporidium* sporozoites to tissue-culture cells. Parasitol Res. 1988; 74: 531–536. PMID: 3194366

21. Valigurova A, Koudela B. Morphological analysis of the cellular, interactions between the eugregarine *Gregarina garnhami* (Apicomplexa) and the epithelium of its host, the desert locust *Schistocerca gregaria*. Eur J Protistol. 2008; 44: 197–207. doi: 10.1016/j.ejop.2007.11.006 PMID: 18304787

22. Valigurova A, Koudela B. Fine structure of trophozoites of the gregarine *Leidyana ephestiae* (Apicomplexa: Eugregarinida) parasitic in *Ephestia kuehniella* larvae (Lepidoptera). Eur J Protistol. 2005; 41: 209–218.

23. Tronchin G, Schrevel J. Chronologie des modifications ultrastructurales au cours de la croissance de *Gregarina blaberae*. J Protozool. 1977; 24: 67–82. PMID: 405485

24. Butaeva F, Paskerova G, Entzeroth R. *Ditrypanocystis* sp. (Apicomplexa, Gregarinia, Selenidiidae): the mode of survival in the gut of *Enchytraeus albidus* (Annelida, Oligochaeta, Enchytraeidae) is close to that of the coccidian genus *Cryptosporidium*. Tsitologiia. 2006; 48: 695–704. PMID: 17147263

25. Schrevel J, Vivier E. Étude de l'ultrastructure et du role de la région antérieure (mucron et épimérite) de grégarines parasites d'annélides polychètes. Protistologica. 1966; 2: 17–28.

26. Desportes I. Ultrastructure et développement des grégarines du genre *Stylocephalus*. Ann Sci Nat Zool Paris. 1969; 12: 31–96.

27. Schrevel J, Goldstein S, Kuriyama R, Prensier G, Vavra J. Biology of gregarines and their host-parasite interactions. In: Desportes I, Schrevel J, editors. The gregarines: the early branching Apicomplexa: BRILL, NL; 2013. pp. 26–196.

28. Baudoin J. The ultrastructure of the anterior region in the gregarine *Ancyrophora puytoraci* Protistologica. 1969; 5: 431–439.

29. MacMillan WG. Gregarine attachment organelles—structure and permeability of an interspecific cell junction. Parasitology. 1973; 66: 207–214.

30. Schrevel J. L'ultrastructure de la région antérieure de la grégarine *Selenidium* et son intérêt pour l'étude de la nutrition chez les sporozoaires. J Microsc. 1968; 7: 391–410.

31. Schrevel J. Observations biologiques et ultrastructurales sur les Selenidiidae et leurs consequences sur la systematique des Gregarinomorphes. J Protozool 1971; 18: 448–470.

32. Sheffield HG, Garnham PC, Shiroishi T. The fine structure of the sporozoite of *Lankesteria culicis*. J Protozool. 1971; 18: 98–105. PMID: 4993836

33. Dubremetz JF, Garcia-Reguet N, Conseil V, Fourmaux MN. Apical organelles and host-cell invasion by Apicomplexa. Int J Parasitol. 1998; 28: 1007–1013. PMID: 9724870

34. Roberts WL, Mahrt JL, Hammond DM. The fine structure of the sporozoites of *Isospora canis*. Z Parasitenkd. 1972; 40: 183–194. PMID: 4346237

35. Hildebrand HF. Electron-microscopic investigation on evolution stages of trophozoite of *Didymophyes gigantea* (Sporozoa, Gregarinida). 1. Fine structure of protomerite and epimerite and relationship between host and parasite. Z Parasitenkd. 1976; 49: 193–215. PMID: 824879

36. Lukes J. A coccidian (Apicomplexa: Eimeriidae) with extracytoplasmally located stages in the kidney tubules of golden carp (*Carassius auratus gibelio* L.) (Cyprinidae). Folia Parasitol. 1993; 40: 1–7. PMID: 8325562

37. Benajiba MH, Marques A, Lom J, Bouix G. Ultrastructure and sporogony of *Eimeria* (syn. *Epieimeria*) *anguillae* (Apicomplexa) in the eel (*Anguilla anguilla*). J Eukaryot Microbiol. 1994; 41: 215–222.

38. Molnar K, Baska F. Light and electron microscopic studies on *Epieimeria anguillae* (Léger & Hollande, 1922), a coccidium parasitizing the European eel, *Anguilla anguilla* L. J Fish Dis. 1986; 9: 99–110.

39. Dyková I, Lom J. Fish coccidia: critical notes on life cycles, classification and pathogenicity. J Fish Dis. 1981; 4: 487–505.

40. Lukes J. Life cycle of *Goussia pannonica* (Molnar, 1989) (Apicomplexa, Eimeriorina), an extracytoplasmic coccidium from the white bream *Blicca bjoerkna*. J Protozool. 1992; 39: 484–494.

41. Jirku M, Modry D, Slapeta JR, Koudela B, Lukes J. The phylogeny of *Goussia* and *Choleoeimeria* (Apicomplexa; Eimeriorina) and the evolution of excystation structures in coccidia. Protist. 2002; 153: 379–390. PMID: 12627867

42. Paperna I, Landsberg JH. Description and taxonomic discussion of eimerian coccidia from African and Levantine geckoes. S A J Zool. 1989; 24: 345–355.

43. Paperna L, Lainson R. Fine structure of the epicytoplasmic eimerid coccidium *Acroeimeria pintoi* Lainson & Paperna, 1999, a gut parasite of the lizard *Ameiva ameiva* in north Brazil. Parasite. 1999; 6: 359–364. PMID: 10633508

44. Lukes J, Stary V. Ultrastructure of the life-cycle stages of *Goussia janae* (Apicomplexa, Eimeriidae), with X-ray microanalysis of accompanying precipitates. Can J Zool. 1992; 70: 2382–2397.

45. Ortega-Pierres G, Caccio S, Fayer R, Mank TG, Smith HV, Thompson RCA. *Giardia* and *Cryptosporidium*: From molecules to disease. CABI Publishing; 2009.

46. Eli A, Briyai OF, Abowei JFN. A Review of some parasite diseases of African fish gut lumen Protozoa, Coccidioses, *Cryptosporidium* infections, Haemoprotozoa, Haemosporidia. Res J Appl Sci Eng Technol. 2012; 4: 1438–1447.

47. Melicherova J, Ilgova J, Kvac M, Sak B, Koudela B, Valigurova A. Life cycle of *Cryptosporidium muris* in two rodents with different responses to parasitization. Parasitology. 2014; 141: 287–303. doi: 10.1017/S0031182013001637 PMID: 24128742

48. Bouzid M, Hunter PR, Chalmers RM, Tyler KM. *Cryptosporidium* pathogenicity and virulence. Clin Microbiol Rev. 2013; 26: 115–134. doi: 10.1128/CMR.00076-12 PMID: 23297262

49. Forney JR, DeWald DB, Yang SG, Speer CA, Healey MC. A role for host phosphoinositide 3-kinase and cytoskeletal remodeling during *Cryptosporidium parvum* infection. Infect Immun. 1999; 67: 844–852. PMID: 9916099

50. Elliott DA, Coleman DJ, Lane MA, May RC, Machesky LM, Clark DP. *Cryptosporidium parvum* infection requires host cell actin polymerization. Infect Immun. 2001; 69: 5940–5942. PMID: 11500478

51. Hashim A, Mulcahy G, Bourke B, Clyne M. Interaction of *Cryptosporidium hominis* and *Cryptosporidium parvum* with primary human and bovine intestinal cells. Infect Immun. 2006; 74: 99–107. PMID: 16368962

52. O'Hara SP, Small AJ, Chen XM, LaRusso NF. Host cell actin remodeling in response to *Cryptosporidium*. Subcell Biochem. 2008; 47: 92–100. PMID: 18512344

53. Bonnin A, Lapillonne A, Petrella T, Lopez J, Chaponnier C, Gabbiani G, et al. Immunodetection of the microvillous cytoskeleton molecules villin and ezrin in the parasitophorous vacuole wall of *Cryptosporidium parvum* (Protozoa: Apicomplexa). Eur J Cell Biol. 1999; 78: 794–801. PMID: 10604656

54. Mitchison TJ, Cramer LP. Actin-based cell motility and cell locomotion. Cell. 1996; 84: 371–379. PMID: 8608590

55. Landsberg JH, Paperna I. Ultrastructural study of the coccidian *Cryptosporidium* sp. from stomachs of juvenile cichlid fish. Dis Aquat Organ. 1986; 2: 13–20.

56. Elliott DA, Clark DP. *Cryptosporidium parvum* induces host cell actin accumulation at the host-parasite interface. Infect Immun. 2000; 68: 2315–2322. PMID: 10722635

57. Yoshikawa H, Iseki M. Freeze-fracture study of the site of attachment of *Cryptosporidium muris* in gastric glands. J Protozool. 1992; 39: 539–544. PMID: 1387896

58. Ferguson DJ, Sahoo N, Pinches RA, Bumstead JM, Tomley FM, Gubbels MJ. MORN1 has a conserved role in asexual and sexual development across the Apicomplexa. Eukaryot Cell. 2008; 7: 698–711. doi: 10.1128/EC.00021-08 PMID: 18310354

59. Reis Y, Cortes H, Viseu Melo L, Fazendeiro I, Leitao A, Soares H. Microtubule cytoskeleton behavior in the initial steps of host cell invasion by *Besnoitia besnoiti*. FEBS Letters. 2006; 580: 4673–4682. PMID: 16876796

60. Kudryashev M, Lepper S, Stanway R, Bohn S, Baumeister W, Cyrklaff M, et al. Positioning of large organelles by a membrane-associated cytoskeleton in *Plasmodium* sporozoites. Cell Microbiol. 2010; 12: 362–371. doi: 10.1111/j.1462-5822.2009.01399.x PMID: 19863555

61. Beck JR, Rodriguez-Fernandez IA, de Leon JC, Huynh MH, Carruthers VB, Morrissette NS, et al. A novel family of *Toxoplasma* IMC proteins displays a hierarchical organization and functions in coordinating parasite division. PLoS Pathog. 2010; 6: e1001094. doi: 10.1371/journal.ppat.1001094 PMID: 20844581

62. Morrissette NS, Mitra A, Sept D, Sibley LD. Dinitroanilines bind alpha-tubulin to disrupt microtubules. Mol Biol Cell. 2004; 15: 1960–1968. PMID: 14742718

63. Morrissette NS, Sibley LD. Disruption of microtubules uncouples budding and nuclear division in *Toxoplasma gondii*. J Cell Sci. 2002; 115: 1017–1025. PMID: 11870220

64. Kim SH, Paperna I. Fine structure of epicytoplasmic stages of *Eimeria vanasi* from the gut of cichlid fish. Dis Aquat Organ. 1992; 12:191–197.

65. Paperna I, Landsberg JH. Tubular formations extending from parasitophorous vacuoles in gut epithelial cells of cichlid fish infected by *Eimeria* (s. l.) *vanasi*. Dis Aquat Organ. 1987; 2: 239–242.

7.5

Melicherová J., Mazourová V., **Valigurová A.**

2016

In vitro excystation of *Cryptosporidium muris* oocysts and viability of released sporozoites in different incubation media

Parasitology Research 115(3), 1113-1121

CrossMark

ORIGINAL PAPER

In vitro excystation of *Cryptosporidium muris* oocysts and viability of released sporozoites in different incubation media

Janka Melicherová[1] · **Veronika Mazourová**[1] · **Andrea Valigurová**[1]

Abstract This study aimed to evaluate and document the excystation process of *Cryptosporidium muris* oocysts in various incubation media, and to monitor the behaviour of excysting and freshly excysted sporozoites. A test of oocyst viability, using fluorescent double staining with fluorescein diacetate and propidium iodide, was performed prior to each experimental assay. Light microscope observations confirmed that relatively often only three sporozoites were released; the fourth one either left the oocyst later together with a residual body or remained trapped within the oocyst wall. These results suggest that successful oocyst excystation is not limited by the viability of all four sporozoites. Darkening of oocysts to opaque and their specific movement (the so-called "oocyst dancing") preceded the final excystation and liberation of sporozoites, while the dormant oocysts appeared refractive. The process of excystation in *C. muris* is not gradual as generally described in cryptosporidia but very rapid in an eruptive manner. Experiments were performed using oocysts stored at 4 °C for various time periods, as well as oocysts freshly shed from host rodents (*Mastomys coucha*) of different ages. The most suitable medium supporting high excystation rate (76 %) and prolonged motility of sporozoites was RPMI 1640, enriched with 5 % bovine serum albumin (BSA). Our results emphasize that to reliably evaluate the success of in vitro excystation of cryptosporidia, not only the number of released sporozoites in a set time period should be taken into consideration but also their subsequent activity (motility), as it is expected to be essential for the invasion of host cells.

✉ Janka Melicherová
jankam@sci.muni.cz

[1] Department of Botany and Zoology, Faculty of Science, Masaryk University, Kotlářská 2, 611 37 Brno, Czech Republic

Abbreviations
BSA bovine serum albumin
FDA fluorescein diacetate
LM   light microscopy
PBS phosphate-buffered saline
PI   propidium iodide

Introduction

The genus *Cryptosporidium*, belonging to the phylum Apicomplexa, was previously placed to the subclass Coccidiasina, Leuckart, 1879. Based on more recent phylogenetic and comparative morphologic analyses, *Cryptosporidium* spp. are considered to be close relatives of gregarines (Barta and Thompson 2006; Carreno et al. 1999; Kváč et al. 2008; Valigurová et al. 2007, 2008). Cryptosporidia differ significantly from representatives of order Eucoccidiorida due to (i) the putative lack of sporocysts; (ii) the presence of microgamonts producing 16 non-flagellated, bullet-shaped microgametes; and finally (iii) their unique epicellular localization within a host-derived parasitophorous sac (Current and Reese 1986; Valigurová et al. 2008). The host specificity of cryptosporidia varies according to species and genotype (Feng et al. 2011; Kar et al. 2011).

Two main branches are recognized within gastrointestinal cryptosporidia, i.e. species/genotypes infecting either the intestine or the stomach (Pavlasek and Ryan 2007). The process of excystation initiates when oocysts reach the gastrointestinal tract. In a proper host environment, oocysts excyst and release four infectious sporozoites, capable of actively invading the

host epithelial cells. Excystation of oocysts under in vitro conditions has been studied predominately with intestinal species, where various protocols have been tested (Kato et al. 2001; Robertson et al. 1993; Smith et al. 2005). Whereas excystation of cryptosporidian intestinal species can be stimulated with acidic components or bile salts, gastric species seem to require raised temperature only (Gold et al. 2001; Widmer et al. 2007). Hence, different protocols for in vitro experiments must be applied for successful excystation of *Cryptosporidium muris* oocysts resulting in the release of viable sporozoites.

In this study, we focused on the gastric parasite *C. muris* strain TS03. Although *C. muris* is specific for rodent hosts, it can be occasionally found in other mammals (FitzGerald et al. 2011; Kodádková et al. 2010), including humans (Gatei et al. 2002; Palmer et al. 2003). The main aim of this study was to compare the viability of *C. muris* oocysts collected from host rodents at different time points of the patent period and stored for different periods of time. Moreover, a detailed investigation of the entire excystation process could reveal the behaviour of freshly excysted sporozoites prior to the active invasion of appropriate host cells. This study underlines that the success rate of in vitro excystation should consider not only the number of released sporozoites in a set time period but also the activity (motility) of freshly excysted sporozoites, which is essential for the invasion process of host cells.

Materials and methods

C. muris

Faeces from multimammate rats, *Mastomys coucha*, experimentally inoculated with *C. muris* (strain TS03) oocysts (dose of 1×10^6 oocysts suspended in 200 μl of distilled water), were collected daily and stored in an aqueous solution of 2.5 % potassium dichromate ($K_2Cr_2O_7$) at 4 °C. The TS03 strain of *C. muris* was characterized in detail by Kváč et al. (2008), with descriptions of differences in its genetic characteristics, infectivity and pathogenicity from other isolates of gastric *Cryptosporidium* spp. Collected oocysts were purified using the Sheather's sugar flotation method (Arrowood and Sterling 1987) and a modified caesium chloride gradient centrifugation (Kilani and Sekla 1987). The purified oocyst suspension was stored in 0.1 M phosphate-buffered saline (PBS), pH 7.2, at 4 °C.

Animals were housed in plastic cages (five animals per cage) with sterile wood chip bedding and supplied with sterilized food and water ad libitum. The rearing of animals is regulated by Czech legislation (Act No 246/1992 Coll., on protection of animals against cruelty). These documents are consistent with the legislation of the European Commission. All housing, feeding and experimental procedures were conducted under protocols approved by University of Veterinary

and Pharmaceutical Sciences Brno and Central Commission for Animal Welfare, Czech Republic (protocol # 066/2010). The minimum number of animals has been involved to produce statistically reproducible results.

Oocyst viability test

Double staining with fluorescein diacetate (FDA) and propidium iodide (PI) was performed to verify the viability of oocysts prior to all experimental assays. Some samples were stained only with PI. Since PI, a red fluorescent nuclear and chromosome counterstain is not live cell permeable, it is commonly used to detect the dead cells in a population, using an excitation maximum at 535 nm and fluorescence emission maximum at 617 nm (Jones and Senft 1985). The principle of the FDA test is the ability of living cells to metabolize the esterase substrate to a derivative that can be subsequently detected or quantified by measuring the fluorescence, using an excitation maximum at 450–490 nm, and fluorescence emission maximum at 520 nm. Non-fluorescent FDA is a non-polar compound that easily penetrates the plasma membrane of viable cells, where it converts into a fluorescent metabolite (fluorescein). Fluorescein cannot penetrate cell membranes and can be detected by a fluorescence microscope at an appropriate pH, when accumulated in some concentrations. Hence, a green fluorescent signal as well as no or a weak fluorescence signal (due to a low concentration of accumulated metabolite) indicates a viable oocyst with living sporozoites. Stock solutions were prepared by dissolving FDA in acetone (5 mg/1 ml) and PI in deionized water (1 mg/1 ml). Oocysts were suspended in 300 μl of RPMI in an Eppendorf microtube, and subsequently 100 μl of FDA (4 μl/ml in PBS, pH 7.2) and 30 μl of PI (1 mg/ml in distilled water) working solutions were added. Specimens were incubated for 10 min in the dark at room temperature (RT). Microscopic slides with stained oocyst suspensions were viewed with a fluorescence microscope, Olympus BX60.

In vitro excystation of oocysts

In order to investigate the effect of various factors on the excystation rate, in vitro incubations of oocysts in various media were performed and the process of oocyst excystation was evaluated. Simultaneously, the effect of a specific medium on the motility rate of sporozoites was monitored. Oocysts of *C. muris* were not chemically pre-treated (e.g. with sodium hypochlorite routinely used for oocysts disinfection) to avoid any alternations of the oocyst wall, potentially causing the death of enclosed sporozoites. To obtain the maximum possible excystation rate, various excystation media were applied, including distilled water with 0.6 % HCl (0.1 N HCl, Sigma-Aldrich, Czech Republic), 0.1 M phosphate-buffered saline (PBS) enriched by 10 % trypsin or 5 % bovine serum albumin

(BSA) (Sigma-Aldrich, Czech Republic), Ringer's solution (containing 154.00 mM NaCl, 5.64 mM KCl, 2.16 mM CaCl$_2$, 11.10 mM dextrose and 2.38 mM NaHCO$_3$ in 1 L H$_2$O) and finally RPMI 1640 (Sigma-Aldrich, Czech Republic) with 5 % BSA or without BSA. Volumes of 4×10^6 *C. muris* oocysts were diluted in 1000 µl of a selected medium and divided into 200-µl aliquots in Eppendorf microtubes to achieve a final concentration of 8×10^5 oocysts. The incubation temperature was set at 37 °C.

The second set of experimental assays was performed using the most effective medium, RPMI 1640, enriched with BSA at the following concentrations: 1, 5, 10, 20 and 50 %. Oocyst excystation counts were performed in a Bürker chamber (with at least 100 oocysts counted) where ten squares were used for counting released sporozoites and excysted and unexcysted oocysts. Excystation percentage was calculated as [*number of excysted oocysts / a total number of counted oocyst*] × 100. Excystation rate was monitored at set time intervals of 5, 15, 30, 60, 90, 120, 180 and 240 min. Statistical evaluation of the excystation rate in all tested media was performed using the non-parametric methods of the Kruskal–Wallis test. Furthermore, motility of released sporozoites was recorded. The result of excystation was evaluated and documented (imaging, video) using a motorized light microscope Olympus BX61 at phase contrast, equipped with a digital camera Olympus DP71 and the software Olympus Stream Motion v. 1.5.1.

Results

Excystation of oocysts in various media

Oocysts used in the first set of experiments were collected from the faeces of *M. coucha* at the beginning of the last part of the chronic infection period (8 months post-inoculation). These relatively old oocysts (4 months old) were incubated for 1–3 hours at 37 °C in different incubation media (mammalian Ringer's solution, PBS with 10 % trypsin, PBS with 5 % BSA, PBS with 0.6 % HCl and finally RPMI 1640 with or without 5 % BSA), to check their viability after prolonged storage (data not shown). The highest ratio (50 %) of excystation, a process where viable sporozoites are released from the oocyst, was observed in RPMI 1640 containing 5 % BSA, where the motility of excysted sporozoites was the most evident. A pure RPMI 1640 without any supplements also increased the rate of oocyst excystation, but the difference in motility of sporozoites was negligible when compared to a medium enriched with BSA. Excystation of these oocysts in Ringer's solution reached 45 % after 2 hours at 37 °C, but the motility of freshly excysted sporozoites was very low. Reduction of medium pH, achieved by adding 0.6 % HCl, was shown not to significantly increase the excystation rate. PBS that contained 10 % trypsin

or 5 % BSA supported the motility of sporozoites, but its positive effect on the excystation process was not confirmed; i.e. less than 30 % oocysts excysted successfully. As the obtained results seemed to correlate with the length of oocyst storage (at 4 °C), and most likely also with the age of the host rodent, further experiments with younger oocysts were designed to test the influence of various concentrations of BSA diluted in RPMI 1640 on the excystation rate and sporozoite motility.

Viability of *C. muris* oocysts

Viability of *C. muris* oocysts stored for different time periods was compared to freshly collected oocysts, 2-week- and 4-month-old oocysts stored in PBS at 4 °C. The percentage of viable oocysts was determined for each age group individually by subtracting the percentage of dead oocysts from the percentage of total oocysts. The viability of oocysts was evaluated using double PI/FDA staining or simple PI staining for fluorescence analysis. If the oocysts with sporozoites stained red, they were considered non-viable because PI had penetrated through their damaged membrane regions. FDA causes live cells to fluoresce green under blue light excitation. The viability of oocysts correlated negatively with the length of their storage after collection from host faeces. The highest percentage of viability (99 %) was documented in fresh oocyst samples (Fig. 1a, b), whereas after 2 weeks, the viability of oocysts decreased to 95 %. The oocysts were often stained with both dyes; i.e. a more or less intense PI staining of sporozoites was observed in an oocyst emitting green fluorescence (Fig. 1c). The 4-month-old oocysts showed 20 % viability (Fig. 1d). The viability of oocysts also depended on the phase of the host patent period. At the end of the patent period, *M. coucha* excreted *C. muris* oocysts that were about 50 % less viable than oocysts excreted at the beginning of the patent period. The fluorescent test of oocyst viability was used also prior to each experimental assay.

Excystation rate and sporozoite motility in various concentrations of BSA

After primary evaluation of the viability of *C. muris* oocysts stored for different time periods, an experimental group of 2-week-old oocysts from a rodent host of reproductive age was chosen as the most appropriate material for further research. Evaluation of the oocyst excystation ratio and the motility of released sporozoites was performed in various concentrations of BSA (1, 5, 10 and 50 %) diluted in RPMI 1640, as well as in RPMI 1640 without BSA (Table 1). In view of the fact that the condition of dispersion was not achieved in our data (tested by statistical Bartlett's test), statistical comparison of the excystation rate in different media at selected time periods was tested using the non-parametric Kruskal–Wallis test (Fig. 3).

Fig. 1 Viability test of *C. muris* oocysts using PI or double PI/ FDA staining. **a, b** Fresh oocysts stained with PI. Non-viable, red-stained oocysts are shown by *arrows*. Fluorescence combined with transmission LM (**a**) and fluorescence (**b**). **c** Fluorescent visualization of 2-week-old oocysts double stained with PI/ FDA. Note the viable, green-stained oocyst and the green oocysts with red spots (*white arrowheads*). **d** Fluorescent detection of dead oocysts and oocyst with dying sporozoites (*white arrowhead*) from a 4-month-old sample. Stained with PI/FDA. *Inset* shows the released dead sporozoites and two sporozoites still attached to the residual body (*white arrowhead*). Stained with PI (Colour figure online)
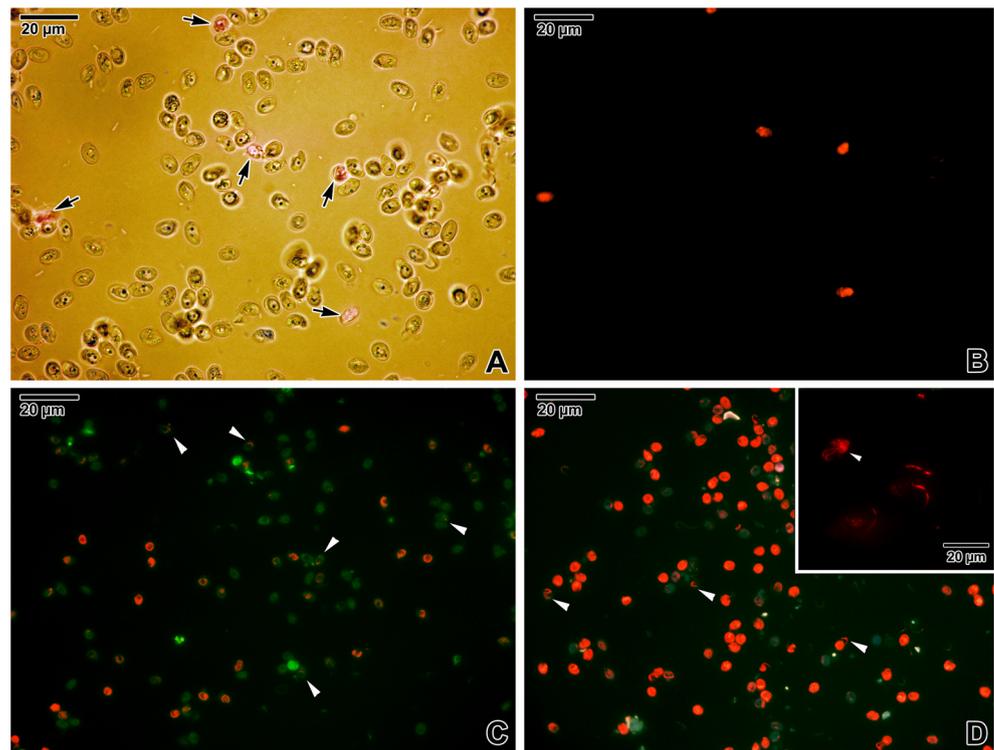
Detailed observations on oocyst excystation revealed that a typical darkening of oocysts predicted that activated sporozoites are ready to be released from the oocyst (Fig. 2a). A vibrating movement of these dark and opaque oocysts, resembling a dance (oocyst dancing), was observed preceding the excystation and indicated the activation of oocysts. Repeated observations showed that the final release of sporozoites from the oocyst is not gradual, but unexpectedly very rapid and ejection-like. The dormant oocysts appeared refractive when observed in the medium by light microscopy.

Excystation with the highest concentration of BSA (50 %) was affected negatively and seemed to block the oocyst suture opening, as the oocysts remained refractive with light micros-copy and did not excyst till the end of experiment (Fig. 3 (yellow line) and Fig. 2d). The process of excystation was successfully initiated in pure RPMI 1640 as well as RPMI

1640 with 1–10 % BSA, almost at the same rate. The first obvious differences in the excystation rate appeared after the first 15 min of oocyst incubation ($p < 0.001$, for RPMI 1640 with 0–5, 1–5 and 5–10 % BSA). In the course of the entire experiment, numerous "dancing oocysts" were observed. The significant peak period of excystation was noticed after 30 min ($p < 0.001$, for RPMI 1640 with 0–5, 1–5 and 5–10 % BSA), when an obvious variation in the excystation rate occurred in individual media. The highest excystation rate was observed in a medium with 5 % BSA. The second peak period of excystation was documented after 1 hours ($p < 0.018$, for RPMI 1640 with 0–5 % BSA), when the percentage of excystation reached over 50 % in all tested media (except media with 50 % BSA). The third peak period of excystation occurred after 3 hours ($p < 0.001$, for RPMI 1640 with 0–5 % and 0–10 % BSA), when the percentage of excystation in

Table 1 The percentage of oocyst excystation in RPMI with or without BSA

Percentage of excystation

	0 min	5 min	15 min	30 min	60 min	90 min	120 min	180 min	240 min
RPMI	0	18,9 ± 4.2	25 ± 1.7	28,7 ± 2.7	48,5 ± 0.8	56,1 ± 0.9	60,5 ± 0.7	65 ± 0.9	67 ± 1.8
1 % BSA	0	23,3 ± 2.2	27 ± 0.9	32,5 ± 1.7	50,6 ± 0.6	57,2 ± 0.5	61,3 ± 0.5	67,2 ± 1.4	68,4 ± 0.9
5 % BSA	0	29,6 ± 1.6	46,5 ± 1.5	50 ± 1.4	54,5 ± 1.0	59,7 ± 1.7	68,4 ± 0.3	72,9 ± 2.2	76 ± 1.8
10 % BSA	0	25 ± 1.1	32 ± 0.8	36,7 ± 0.9	51,7 ± 1.7	58,5 ± 1.8	63,5 ± 0.7	68,9 ± 1.6	74 ± 2.5
50 % BSA	0	0	0	0	0	0	0	0	0

Mean % ± SD, $n = 3$

BSA bovine serum albumin

Fig. 2 Excystation of *C. muris* oocysts in different incubation media. Phase contrast LM. **a** RPMI 1640 medium. **b** RPMI 1640 enriched by 5 % BSA. **c** RPMI 1640 with 10 % BSA. Note the contact of sporozoites with their apical ends (*black asterisk*). **d** RPMI 1640 with 50 % BSA. Darkened oocysts ready for excystation (*black arrowhead*), released viable sporozoites (*black arrows*), non-viable sporozoites (*white arrows*) and sporozoites remaining inside the oocyst (*black double arrowheads*), unexcysted oocysts (*white arrowheads*) and empty oocysts (*white asterisk*) (Colour figure online)
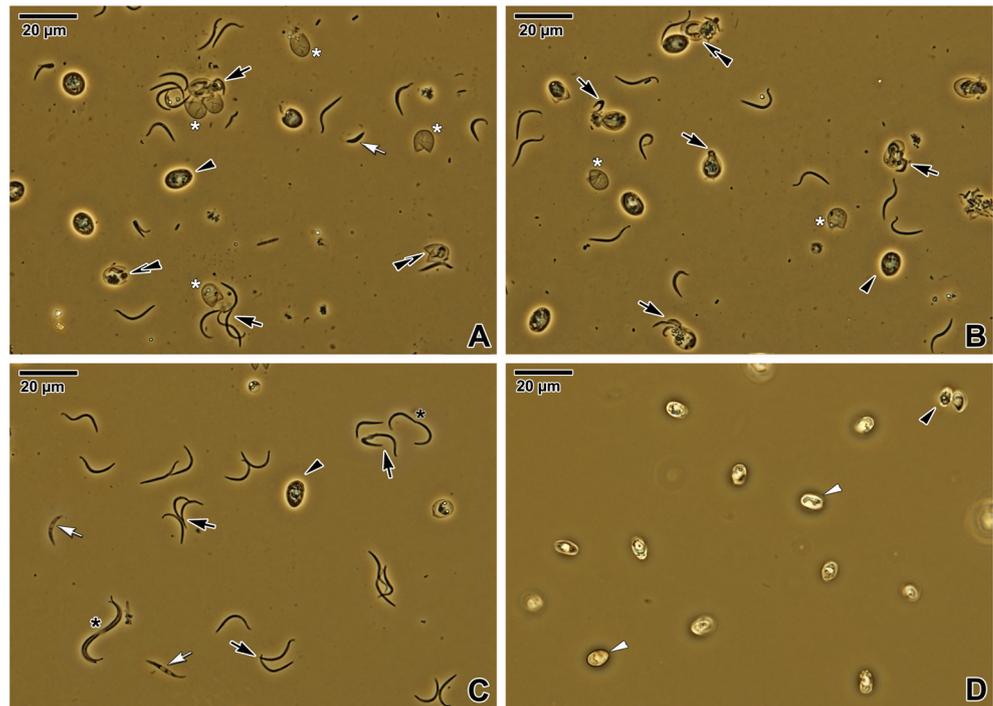
media without BSA or with 1 % of BSA reached almost maximum. The blue and black lines (RPMI 1640 without BSA and RPMI 1640 with 1 % BSA) in the graph started to be constant or only increased slightly, while the red and green lines demonstrating the excystation in media with 5 and 10 % BSA continued to gradually increase (Fig. 3). Furthermore, in pure medium and 1 % BSA, more dormant oocysts were observed. All experimental assays were stopped after 4 hours ($p < 0.001$, for RPMI 1640 with 0–5 % and 1–5 % BSA) because of a natural decrease in the viability of excysted sporozoites, correlating with the length of their in vitro incubation.

Although the percentage of excystation in a pure RPMI 1640 medium was comparable with the percentage of excystation in this medium supplemented with BSA, the motility of excysted sporozoites was significantly lower in the former one. Focusing exclusively on the excystation process, the best results (76 % excystation at 37 °C) were obtained in RPMI 1640 enriched by 5 % BSA (Fig. 3, red line). In this medium, the activity of sporozoites was obviously higher and their motility did not significantly change (decrease) with time (the majority were motile till the end of the experiment), in contrast to those incubated in medium without BSA. In the

Fig. 3 Curves showing the percentage of oocysts' excystation, depending on tested medium and time of incubation. *Black line* represents the pure RPMI medium, *blue line* the RPMI medium enriched with 1 % BSA, *red line* the medium with 5 % BSA and *green line* the medium with 10 % BSA. Statistical Kruskal–Wallis test assessed significant differences for each time period of incubation between tested media. The *p* value was smaller than 0.01 and statistically significant differences between all tested media are marked with *asterisk* (colour figure online)
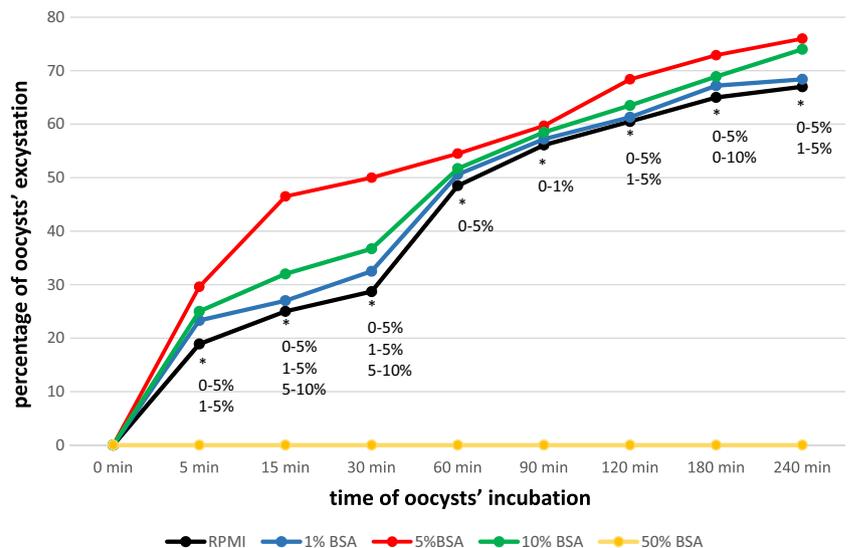
RPMI 1640 medium with 10 % BSA, the excystation ratio achieved almost 74 % (Fig. 3, green line). The motility of released sporozoites was comparable with their motility in the medium with 5 % BSA. Nevertheless, in the medium with 10 % BSA, the sporozoites seemed to be active for a shorter time, i.e. their motility decreased more rapidly, and by the end of experiment, more of them appeared less active.

The elongated, slender sporozoites exhibited an oscillating movement (short forwards/backwards shifts) appearing to move progressively forward and without obvious changes in cell shape (Fig. 2c). This movement was observed, at least to some degree, in all tested media (except for 50 % BSA), but the activity of excysted sporozoites decreased with lower concentrations of BSA. In the medium enriched with 1 % BSA, oocysts reached an excystation rate of 68.5 % after 4 hours at 37 °C (Fig. 3, blue line). The lowest motility of sporozoites was recorded in the medium without BSA, where a 67 % excystation ratio was observed (Fig. 3, black line). These sporozoites were most active during the first 30 min after excystation, but thereafter, motility rapidly declined.

Discussion

Viability of *C. muris* oocysts

Viability testing of *C. muris* oocysts using fluorescent double PI/FDA staining is generally considered standard procedure prior to experimental work (Jones and Senft 1985). However, it is important to mention that Boyd et al. (2008) investigated the membrane integrity and cell viability using the FDA/PI staining and claimed that the staining of viability is dependent upon a number of other factors (the effect of FDA diluent or the time elapsed from the staining procedure). Likewise, Smith and Smith (1989) observed that some cysts could not be stained with either FDA or PI. While some studies claim that the viability of *Cryptosporidium parvum* oocysts can be maintained in appropriate conditions for 6 months (Fayer et al. 1998a, b), others recommend working with oocysts younger than 3 months (Kar et al. 2011). Likewise, Jenkins et al. (2003) recorded a 50 % decrease in excystation success after 3 months of oocyst storage, while 9-month-old oocysts were non-viable. Furthermore, other studies concerning the viability of cryptosporidian oocysts found them to be affected by biotic and abiotic factors, such as age of oocysts, temperature, purification procedure, storage period or chemical composition of media (Fayer et al. 1998a, b; Jenkins et al. 2003; Reduker et al. 1985; Reinoso et al. 2008; Robertson et al. 1992). Based on our empirical knowledge, prolonged storage is not acceptable for successful in vitro experiments with *C. muris* (strain TS03). Oocysts of *C. muris* used in our studies preserve their infectivity only for a short period of storage; i.e. after 4 months, the viability of oocysts stored in PBS

decreased to 20 %. Of special interest is a study claiming that it is almost impossible to reduce the viability of all oocysts in a sample to zero (Robertson et al. 1992). This hypothesis was supported by an experiment showing that even putatively non-viable oocysts of *C. parvum* (not excysted during in vitro excystation experiments) could infect host laboratory models (Neumann et al. 2000). In a study reporting the lowest infective dose of nine oocysts in total for *C. parvum* for humans (Okhuysen et al. 1999), a possible explanation could be that the viability test is not sensitive enough to detect sporadic viable oocysts. On the other hand, our in vitro experiments also provided support for such a controversial hypothesis, as despite almost negative viability tests (PI/FDA), an excystation rate of up to 50 % was achieved in 4-month-old oocysts incubated in RPMI 1640 with 5 % BSA.

The influence of incubation medium on excystation rate

In the current study, the excystation process of *C. muris* oocysts collected from faeces of *M. coucha* was evaluated in various excystation media. The majority of published studies focus on the intestinal pathogen *C. parvum*, which is more widespread. Our research deals with a gastric parasite, originally obtained from *Tachyoryctes splendens* and described as *C. muris* by Kváč et al. (2008), and subsequently maintained in laboratory rodent hosts. During its monoxenous life cycle, the oocysts of *C. muris* are ingested into the stomach, a suture present on the oocyst surface opens provided the environmental chemistry and physical factors are favourable. For study purposes, the entire process of *C. muris* oocyst excystation, normally taking place in vivo within the host stomach, was performed in vitro in a series of experiments. These ran under modified conditions in order to examine the possible effect of individual media components on the excystation process. The composition of these media as well as the incubation times (usually from 15 min up to 4 hours) varied in individual experimental sets. Basic physiological solution and a saline solution, though applicable in some experimental studies and also tested in this study, do not represent media suitable for long-term in vitro cultivation. Based on personal long-term experience, RPMI 1640 was chosen as a proper medium for our study because of its wide applicability for in vitro cultivation of various cell cultures and unicellular parasites. This medium was first supplemented with trypsin and HCl because these have been recorded as having a reversible stimulatory effect on sporozoite motility (Smith et al. 2005; Widmer et al. 2007). However, no similar impact was observed in *C. muris* during this study. Hence, BSA was used to enrich the excystation medium because of its known positive effect on the motility of some organisms (Galvani et al. 2007; Harrison et al. 1982).

Although the excystation rate was not significantly affected by BSA supplementation, the motility of sporozoites was lower in pure RPMI 1640, and that enriched by 1 % BSA, when

compared to the media with higher concentrations of BSA (5 % and 10 %). The most suitable medium for further studies is the one supplemented with 5 % BSA, in which sporozoites remained motile during the entire experiment (the activity of excysted sporozoites slightly decreased in 10 % BSA). Excystation in medium with 50 % BSA failed. We assume that a medium with such a high concentration of BSA represents a very dense and viscous environment that could seal the oocyst, thereby preventing it from excysting.

Previous studies indicate that cryptosporidian oocysts generally only require the temperature to reach 37 °C for successful excystation, but the excystation rate can accelerate as pH decreases, e.g. by adding HCl or NaOCl (Fayer and Leek 1984; Forney et al. 1996; Smith et al. 2005; Gold et al. 2001; Reduker et al. 1985) . Pre-treatment of oocysts with bleaching agents seems unnecessary (Arrowood 2002; Robertson et al. 1993), but various chemical factors such as trypsin, taurocholic acid or hypochloric acid can be added to the incubation medium as stimuli for excystation. These acidic chemical substances are not essential for gastric cryptosporidia excystation, but they slightly accelerate the excystation process (Widmer et al. 2007).

Our data showing that the age of *C. muris* oocysts (i.e. length of their storage) and the age of the host organism represent further important factors are inconsistent with a study of Widmer et al. (2007), in which no significant influence of these factors was recorded. The patent period of *M. coucha* progresses continuously into a chronic infection and results in the death of the host (usually about 1–1.5 years after experimental inoculation) or, in rare cases, the infection with *C. muris* spontaneously disappears (personal unpublished data). The amount of oocysts in faeces decreases with increasing age of the host. Hence, the best period for parasite collection from host faeces seems to be up to 4 months from the beginning of the patent period.

Behavioural activity of sporozoites during the excystation process

Surprisingly, our observations showed that the release of sporozoites from oocysts is an extremely rapid process, resembling the shooting out of sporozoites through the suture in the oocyst wall. It is known that the most significant excystation factors, appropriate pH and temperature, modify permeability of the oocyst wall (Matsubayashi et al. 2011; Jenkins et al. 2003; Robertson et al. 1993). Hence, we expect that some factors might increase the pressure inside the oocyst by absorbing liquids through the permeable oocyst wall (most likely through the suture) into the enlarging residual body. Subsequently, the hypothetical excessive pressure within an oocyst results in shot-like releasing of sporozoites to the surrounding environment.

Other chemicals usually added to the incubation media can also influence the behaviour of oocysts or sporozoites.

Although trypsin or BSA do not increase the excystation success rate, they can cause translucency in oocysts and increase the motility of excysted, as well as still unexcysted sporozoites (Smith et al. 2005; Galvani et al. 2007; Harrison et al. 1982). The motility of unexcysted sporozoites seems to be a source of dancing oocysts, observed at the start of the excystation process in this study. Enlarging the load of amylopectin in the residual body just before excystation can serve as an energy source for sporozoite activation (Fayer et al. 1998b; Harris et al. 2004). Similar to gregarines (Steele et al. 2012), the activation of *C. muris* sporozoites was obvious due to the darkening of individual sporozoites within the enclosed oocyst until both became opaque. Furthermore, our data concur with that of Kar et al. (2011), where usually only three sporozoites were released from oocysts while the fourth one remained within the oocyst walls, eventually being liberated along with the residual body. This could be a strategy to preserve one viable sporozoite by protecting it within the oocyst wall in case of potential failure of those already excysted. However, it is more likely that the remaining sporozoite is already dead. This corresponds to the red spots observed in some green oocysts stained with FDA/PI. If the second variant applies, the dying of sporozoites within the oocyst must be gradual, and the oocyst excystation is induced by the other three, still viable sporozoites.

It still remains unknown whether the percentage of successfully excysted oocysts correlates with the infectivity of released sporozoites. Previous studies, as well as results from experiments using BSA herein, indicate that excysted sporozoites require binding of specific lectins to their surface to become invasive.

Conclusions

This study demonstrated that at the beginning of excystation assays, the excystation process was only slightly accelerated by adding the suitable concentration (5–10 %) of BSA to the incubation medium, while the motility of sporozoites increased significantly. Hence, although not for oocyst excystation as such, the choice of an appropriate excystation medium is undoubtedly essential for activation and prolonged motility of excysted sporozoites, as well as for further successful in vitro cultivations. Data presented herein also revealed that requirements for successful oocyst excystation in gastric species *C. muris* differ from those in intestinal species *C. parvum*.

References

Arrowood MJ (2002) In vitro cultivation of *Cryptosporidium* species. Clin Microbiol Rev 15(3):390–400. doi:10.1128/CMR.15.3.390-400.2002

Arrowood MJ, Sterling CR (1987) Isolation of *Cryptosporidium* oocysts and sporozoites using discontinuous sucrose and isopycnic Percoll gradients. J Parasitol 73(2):314–319

Barta JR, Thompson RC (2006) What is *Cryptosporidium*? Reappraising its biology and phylogenetic affinities. Trends Parasitol 22(10):463–8. doi:10.1016/j.pt.2006.08.001

Boyd V, Cholewa OM, Papas KK (2008) Limitations in the use of fluorescein diacetate/propidium iodide (FDA/PI) and cell permeable nucleic acid stains for viability measurements of isolated islets of Langerhans. Curr Trends Biotechnol Pharm 2(2):66–84

Carreno RA, Martin DS, Barta JR (1999) *Cryptosporidium* is more closely related to the gregarines than to coccidia as shown by phylogenetic analysis of apicomplexan parasites inferred using small-subunit ribosomal RNA gene sequences. Parasitol Res 85(11):899–904

Current WL, Reese NC (1986) A comparison of endogenous development of three isolates of *Cryptosporidium* in suckling mice. J Protozool 33(1):98–108

Fayer R, Leek RG (1984) The effects of reducing conditions, medium, pH, temperature, and time on in vitro excystation of *Cryptosporidium*. J Protozool 31(4):567–9

Fayer R, Graczyk TK, Lewis EJ, Trout JM, Farley CA (1998a) Survival of infectious *Cryptosporidium parvum* oocysts in seawater and eastern oysters (*Crassostrea virginica*) in the Chesapeake Bay. Appl Environ Microbiol 64(3):1070–4

Fayer R, Trout JM, Jenkins MC (1998b) Infectivity of *Cryptosporidium parvum* oocysts stored in water at environmental temperatures. J Parasitol 84(6):1165–9

Feng Y, Yang W, Ryan U, Zhang L, Kváč M, Koudela B, Modrý D, Li N, Fayer R, Xiao L (2011) Development of a multilocus sequence tool for typing *Cryptosporidium muris* and *Cryptosporidium andersoni*. J Clin Microbiol 49(1):34–41. doi:10.1128/JCM.01329-10

FitzGerald L, Bennett M, Ng J, Nicholls P, James F, Elliot A, Slaven M, Ryan U (2011) Morphological and molecular characterisation of a mixed *Cryptosporidium muris*/*Cryptosporidium felis* infection in a cat. Vet Parasitol 175(1–2):160–4. doi:10.1016/j.vetpar.2010.10.003

Forney JR, Yang S, Healey MC (1996) Protease activity associated with excystation of *Cryptosporidium parvum* oocysts. J Parasitol 82(6):889–92

Galvani CD, Li Y, Burr TJ, Hoch HC (2007) Twitching motility among pathogenic *Xylella fastidiosa* isolates and the influence of bovine serum albumin on twitching-dependent colony fringe morphology. FEMS Microbiol Lett 268(2):202–8. doi:10.1111/j.1574-6968.2007.00601.x202–208

Gatei W, Ashford RW, Beeching NJ, Kamwati SK, Greensill J, Hart CA (2002) *Cryptosporidium muris* infection in an HIV-infected adult, Kenya. Emerg Infect Dis 8(2):204–6. doi:10.3201/eid0802.010256

Gold D, Stein B, Tzipori S (2001) The utilization of sodium taurocholate in excystation of *Cryptosporidium parvum* and infection of tissue culture. J Parasitol 87(5):997–1000. doi:10.1645/0022-3395(2001)087[0997:TUOSTI]2.0.CO;2

Harris JR, Adrian M, Petry F (2004) Amylopectin: a major component of the residual body in *Cryptosporidium parvum* oocysts. Parasitology 128(Pt 3):269–82

Harrison RAP, Dott HM, Foster GC (1982) Bovine serum albumin, sperm motility, and the "dilution effect". J Exp Zool 222(1):81–88. doi:10.1002/jez.1402220111

Jenkins M, Trout JM, Higgins J, Dorsch M, Veal D, Fayer R (2003) Comparison of tests for viable and infectious *Cryptosporidium parvum* oocysts. Parasitol Res 89(1):1–5. doi:10.1007/s00436-002-0720-6

Jones KH, Senft JA (1985) An improved method to determine cell viability by simultaneous staining with fluorescein diacetate-propidium iodide. J Histochem Cytochem 33(1):77–9

Kar S, Daugschies A, Cakmak A, Yilmazer N, Dittmar K, Bangoura B (2011) *Cryptosporidium parvum* oocyst viability and behaviour of the residual body during the excystation process. Parasitol Res 109(6):1719–23. doi:10.1007/s00436-011-2442-0

Kato S, Jenkins MB, Ghiorse WC, Bowman DD (2001) Chemical and physical factors affecting the excystation of *Cryptosporidium parvum* oocysts. J Parasitol 87(3):575–81. doi:10.1645/0022-3395(2001)087[0575:CAPFAT]2.0.CO;2

Kilani RT, Sekla L (1987) Purification of *Cryptosporidium* oocysts and sporozoites by cesium chloride and Percoll gradients. Am J Trop Med Hyg 36(3):505–8

Kodádková A, Kváč M, Ditrich O, Sak B, Xiao L (2010) *Cryptosporidium muris* in a reticulated giraffe (*Giraffa camelopardalis reticulata*). J Parasitol 96(1):211–2. doi:10.1645/GE-2212.1

Kváč M, Sak B, Květoňová D, Ditrich O, Hofmannová L, Modrý D, Vítovec J, Xiao L (2008) Infectivity, pathogenicity, and genetic characteristics of mammalian gastric *Cryptosporidium* spp. in domestic ruminants. Vet Parasitol 153(3–4):363–7. doi:10.1016/j.vetpar.2008.01.033

Matsubayashi M, Ando H, Kimata I, Takase H, Nakagawa H, Furuya M, Tani H, Sasai K (2011) Effect of low pH on the morphology and viability of *Cryptosporidium andersoni* sporozoites and histopathology in the stomachs of infected mice. Int J Parasitol 41(3–4):287–292. doi:10.1016/j.ijpara.2010.09.009

Neumann NF, Gyurek LL, Finch GR, Belosevic M (2000) Intact *Cryptosporidium parvum* oocysts isolated after in vitro excystation are infectious to neonatal mice. FEMS Microbiol Lett 183(2):331–6. doi:10.1111/j.1574-6968.2000.tb08980.x331–336

Okhuysen PC, Chappell CL, Crabb JH, Sterling CR, DuPont HL (1999) Virulence of three distinct *Cryptosporidium parvum* isolates for healthy adults. J Infect Dis 180(4):1275–81

Palmer CJ, Xiao L, Terashima A, Guerra H, Gotuzzo E, Saldías G, Bonilla JA, Zhou L, Lindquist A, Upton SJ (2003) *Cryptosporidium muris*, a rodent pathogen, recovered from a human in Peru. Emerg Infect Dis 9(9):1174–6. doi:10.3201/eid0909.030047

Pavlasek I, Ryan U (2007) The first finding of a natural infection of *Cryptosporidium muris* in a cat. Vet Parasitol 144(3–4):349–52. doi:10.1016/j.vetpar.2006.10.005

Reduker DW, Speer CA, Blixt JA (1985) Ultrastructure of *Cryptosporidium parvum* oocysts and excysting sporozoites as revealed by high resolution scanning electron microscopy. J Protozool 32(4):708–11

Reinoso R, Becares E, Smith HV (2008) Effect of various environmental factors on the viability of *Cryptosporidium parvum* oocysts. J Appl Microbiol 104(4):980–6. doi:10.1111/j.1365-2672.2007.03620.x

Robertson LJ, Campbell AT, Smith HV (1992) Survival of *Cryptosporidium parvum* oocysts under various environmental pressures. Appl Environ Microbiol 58(11):3494–500

Robertson LJ, Campbell AT, Smith HV (1993) In vitro excystation of *Cryptosporidium parvum*. Parasitology 106(Pt 1):13–9

Smith AL, Smith HV (1989) A comparison of fluorescein diacetate and propidium iodide staining and in vitro excystation for determining *Giardia intestinalis* cyst viability. Parasitology 3:329–31

Smith HV, Nichols RA, Grimason AM (2005) *Cryptosporidium* excystation and invasion: getting to the guts of the matter. Trends Parasitol 21(3):133–42. doi:10.1016/j.pt.2005.01.007

Steele SM, Clopton DT, Clopton RE (2012) Excystation signals do not isolate gregarine gene pools: experimental excystation of *Blabericola migrator* among 11 species of cockroaches. J Parasitol 98(5):946–50. doi:10.1645/GE-3122.1

Valigurová A, Hofmannová L, Koudela B, Vávra J (2007) An ultrastructural comparison of the attachment sites between *Gregarina steini* and *Cryptosporidium muris*. J Eukaryot Microbiol 54(6):495–510. doi:10.1111/j.1550-7408.2007.00291.x

Valigurová A, Jirků M, Koudela B, Gelnar M, Modrý D, Šlapeta J (2008) Cryptosporidia: Epicellular parasites embraced by the host cell membrane. Int J Parasitol 38(8–9):913–922. doi:10.1016/j.ijpara.2007.11.003

Widmer G, Klein P, Bonilla R (2007) Adaptation of *Cryptosporidium* oocysts to different excystation conditions. Parasitology 134(Pt 11):1583–8. doi:10.1017/S0031182007002922

Diakin A., Paskerova G.G., Simdyanov T.G., Aleoshin V.V., **Valigurová A.**

2016

Morphology and molecular phylogeny of coelomic gregarines (Apicomplexa) with different types of motility: *Urospora ovalis* and *U. travisiae* from the polychaete *Travisia forbesii*

Protist

ORIGINAL PAPER

Morphology and Molecular Phylogeny of Coelomic Gregarines (Apicomplexa) with Different Types of Motility: *Urospora ovalis* and *U. travisiae* from the Polychaete *Travisia forbesii*

CrossMark

Andrei Diakin[a,1], Gita G. Paskerova[b,1], Timur G. Simdyanov[c],
Vladimir V. Aleoshin[d], and Andrea Valigurová[a]

[a]Department of Botany and Zoology, Faculty of Science, Masaryk University, Kotlářská 2,
 611 37, Brno, Czech Republic
[b]Department of Invertebrate Zoology, Faculty of Biology, St. Petersburg State University,
 Universitetskaya emb. 7/9, Saint-Petersburg, 199 034, Russian Federation
[c]Department of Invertebrate Zoology, Faculty of Biology, Lomonosov Moscow State
 University, Leninskie Gory, Moscow 119 234, Russian Federation
[d]Belozersky Institute for Physico-Chemical Biology, Lomonosov Moscow State University,
 Leninskie Gory, Moscow 119 234, Russian Federation

Urosporids (Apicomplexa: Urosporidae) are eugregarines that parasitise marine invertebrates, such as annelids, molluscs, nemerteans and echinoderms, inhabiting their coelom and intestine. Urosporids exhibit considerable morphological plasticity, which correlates with their different modes of motility and variations in structure of their cortical zone, according to the localisation within the host. The gregarines *Urospora ovalis* and *U. travisiae* from the marine polychaete *Travisia forbesii* were investigated with an emphasis on their general morphology and phylogenetic position. Solitary ovoid trophozoites and syzygies of *U. ovalis* were located free in the host coelom and showed metabolic activity, a non-progressive movement with periodic changes of the cell shape. Solitary trophozoites of *U. travisiae*, attached to the host tissue or free floating in the coelom, were V-shaped. Detached trophozoites demonstrated gliding motility, a progressive movement without observable cell body changes. In both gregarines, the cortex formed numerous epicytic folds, but superfolds appeared exclusively on

[1]Corresponding authors;
 e-mail diakin@sci.muni.cz (A. Diakin), gitapasker@yahoo.com (G.G. Paskerova).

the surface of *U. ovalis* during metabolic activity. SSU rDNA sequences obtained from *U. ovalis* and *U. travisiae* revealed that they belong to the Lecudinoidea clade; however, they are not affiliated with other coelomic urosporids (*Pterospora* spp. and *Lithocystis* spp.), but surprisingly with intestinal lecudinids (*Difficilina* spp.) parasitising nemerteans.

Introduction

Apicomplexa Levine 1980, emend. Adl et al. 2012 (Adl et al. 2012) consist entirely of unicellular organisms parasitising various animals. Some of them cause important human and domestic animal diseases (e.g. malaria, toxoplasmosis, and cryptosporidiosis); therefore, these species have been intensively studied in different aspects of biology, medicine and phylogeny. However, basal apicomplexans (e.g. gregarines, agamococcidia, blastogregarines, and protococcidia), inhabiting exclusively invertebrate hosts, are crucial for our understanding of the evolutionary pathways of Apicomplexa, yet they still remain poorly investigated. Gregarines parasitise a broad range of terrestrial and aquatic invertebrates (annelids, turbellarians, arthropods, echinoderms, and urochordates), and inhabit different sites within the host organism, e.g. the gut and its derivatives (the Malpighian tubules, respiratory trees), the body cavity, and the reproductive system.

According to their morphological features, life cycles, and host range, gregarines are usually subdivided into three groups: Archigregarinorida Grassé, 1953, Eugregarinorida Léger 1900, and Neogregarinorida Grassé, 1953 (Adl et al. 2012; Desportes and Schrével 2013; Grassé 1953; Perkins et al. 2000). In contrast to coccidia, developmental stages of gregarines are predominantly extracellular and of large dimensions. The feeding stages (trophozoites) of gregarines are usually motile and heteropolar, with opposite ends differing in their structure and function. Usually gregarines undergo their vegetative phase of development when attached to the host tissue; the majority of them lack the form of asexual reproduction called merogony (=schizogony). Another important characteristic of the gregarine life cycle is the presence of a pre-sexual association, the so-called syzygy, usually consisting of two partners. There are several types of syzygies: caudo-frontal (head-to-tail), frontal (head-to-head), caudal (tail-to-tail), and lateral (partners are in contact at their lateral

surfaces). In the majority of eugregarines and archigregarines, the partners in the syzygies retain the motility characteristic of solitary trophozoites. In the course of time, the partners become hemispherical in shape, form a common envelope (a gametocyst wall), and undergo gametogenesis, followed by sporogenesis (Desportes and Schrével 2013; Grassé 1953; Perkins et al. 2000).

Gregarines show a great variety of cell shapes and different modes of motility that seem to correlate with trophozoite localisation within the host. Gregarines from the intestine are generally vermiform (archigregarines) and demonstrate pendular (rolling) motility, or elongated (most eugregarines) and show gliding motility. Parasites from the body cavity, tissues, or the reproductive system are usually oval or roundish (some of the urosporids and monocystids), or dendritic (*Pterospora* spp.). As a rule, such gregarines possess metabolic or peristaltic motility (*Nematopsis magna*, *Lithocystis schneideri*, *Urospora neapolitana*); some of them are non-motile (*Gonospora varia*, *Lythocystis foliaceae*, *Urospora chiridotae*) (Coulon and Jangoux 1987; Desportes and Schrével 2013; Dyakin and Paskerova 2004; Dyakin and Simdyanov 2005; Frolov 1991; Landers and Gunderson 1986; Levine 1977; MacMillan 1973; Miles 1968; Perkins et al. 2000; Schrével 1964, 1971a, b, and others). While gliding is a progressive movement, both pendular (rolling) and metaboly are non-progressive. In addition, metaboly is accompanied with periodic changes of the cell body shape.

The exact mechanism of gregarine motility remains unknown. Gliding motility seems to be facilitated by the complex organisation of the parasite's cortical zone. The pellicle forms longitudinal epicytic folds with special sets of filamentous structures in their apex (the so-called rippled dense structures [RDS and 12-nm apical filaments) and an internal lamina, which underlays the inner membrane complex (IMC) (Schrével et al. 1983; Vivier 1968). The polymerised form of actin and cytoplasmic mucus, excreted outside the cell, both actively participate in gregarine gliding (Valigurová et al.

2013). Peristaltic or metabolic motility is accompanied by the forming of one or several contracted regions running from one end to the other along the longitudinal axis of the cell. It was assumed that this type of motility can be facilitated by the presence of a subpellicular cytoskeletal network; however, its nature, whether it is composed of fibrils or microtubules, remains unknown (MacMillan 1973; Warner 1968).

The family Urosporidae, established by L. Léger (Léger 1892), combining the monocystid gregarines with heteropolar oocysts, nowadays comprises several genera of parasites inhabiting various marine and freshwater invertebrates (mainly echinoderms and polychaetes, as well as oligochaetes, sipunculids, molluscs, nemerteans) (Desportes and Schrével 2013; Dogiel 1906, 1909, 1910; Grassé 1953, Levine 1977; Perkins et al. 2000; Pixell-Goodrich 1915, 1950). To date, most investigations concerning urosporids are either faunistic studies or morphological descriptions of various developmental stages (mostly trophozoites and oocysts), performed at light microscopic level. Only a few members have been studied from an ultrastructural viewpoint (Corbel et al. 1979; Dyakin and Simdyanov 2005; Landers and Leander 2005; Pomory and Lares 1998), and even fewer have been investigated at the molecular biological level (Leander et al. 2006).

The type genus *Urospora* Schneider, 1895 unites monocystid gregarines from the body cavity or tissues of hosts, with lateral or frontal syzygies, and with heteropolar oocysts possessing a thin appendage at one end and a conical transparent funnel at the other (Desportes and Schrével 2013; Grassé 1953; Levine 1977). In the present study, we investigated the morphology and molecular phylogeny of gregarines of two closely related urosporid species *Urospora ovalis* Dogiel, 1910 and *U. travisiae* Dogiel, 1910, parasites of the body cavity of the marine polychaete *Travisia forbesii* Johnston, 1840, noting, in addition, the biodiversity and adaptations of gregarines from coelomic habitats.

Results

All dissected hosts (approx. 400 individuals) were infected with *Urospora ovalis* and *Urospora travisiae* (Fig. 1A). The parasites inhabited the host body cavity. In addition, spherical gametocysts with typical urosporid oocysts were found. The oval-shaped oocysts were heteropolar, with a funnel and a tail at opposite ends, and about 20 μm (n = 40) in length, 7 μm (n = 40) in width (Fig. 1A, inset).

The intensity of parasitisation by both gregarine species varied during the summer season. In the case of *U. ovalis*, it reached up to 50 parasites per host in June/July, while no more than 5 in August/early September. In the case of *U. travisiae*, it also reached up to 50 parasites per host (in rare cases, no more than 5) during the entire summer season. For *U. ovalis*, both solitary trophozoites (June/August) and syzygies (August/early September) were found, while for *U. travisiae*, mostly solitary trophozoites were observed, and syzygies were found in a few cases only.

The main species characteristics of *U. ovalis* and *U. travisiae* are summarised in Table 1.

General Morphology and Ultrastructure of *Urospora ovalis*

The solitary trophozoites of *U. ovalis*, occurring freely in the host body cavity, were ovoid with rounded ends and showed no signs of heteropolarity under the light microscope (LM) (Fig. 1A-D). The cell size varied widely: 19.6 - 294.0 μm (av. 179 μm, mode 252 μm, n = 36) in length and 12.6 - 187.6 μm (av. 114 μm, mode 134 μm, n = 36) in width. We did not observe any young stages of *U. ovalis*.

Some parasites were glued to the host peritoneal epithelium by means of a mucous substance surrounding them. (Fig. 1B-C). Living parasites which had fallen out of the host during dissection showed characteristic metabolic (peristaltic) activity, during which cells alternately contracted at their ends causing the migration of the cytoplasm from one end to the other (Fig. 1D, Supplementary Material Video 1). Several superficial, longitudinal ridges formed in the contracted regions during gregarine movement. These ridges were visible even in histological sections (Fig. 1B-C).

Under SEM, these ridges corresponded to the so-called superfolds that run along the surface of the contracted region (Fig. 2A, C). However, during processing for electron microscopy (EM), solitary motile cells of *U. ovalis* completely contracted in most cases, and superfolds identical to those observed in contracted regions appeared on the entire gregarine surface (Fig. 2B, E). In transversal sections, both narrow (0.4-0.5 μm wide at the base) and wide (2.5-3.5 μm wide at the base) superfolds of uniform height (1 μm on average) were present at the surface of contracted cells (Fig. 3A-C).

The cells of *U. ovalis* were covered with a typical three-layered pellicle consisting of the plasma
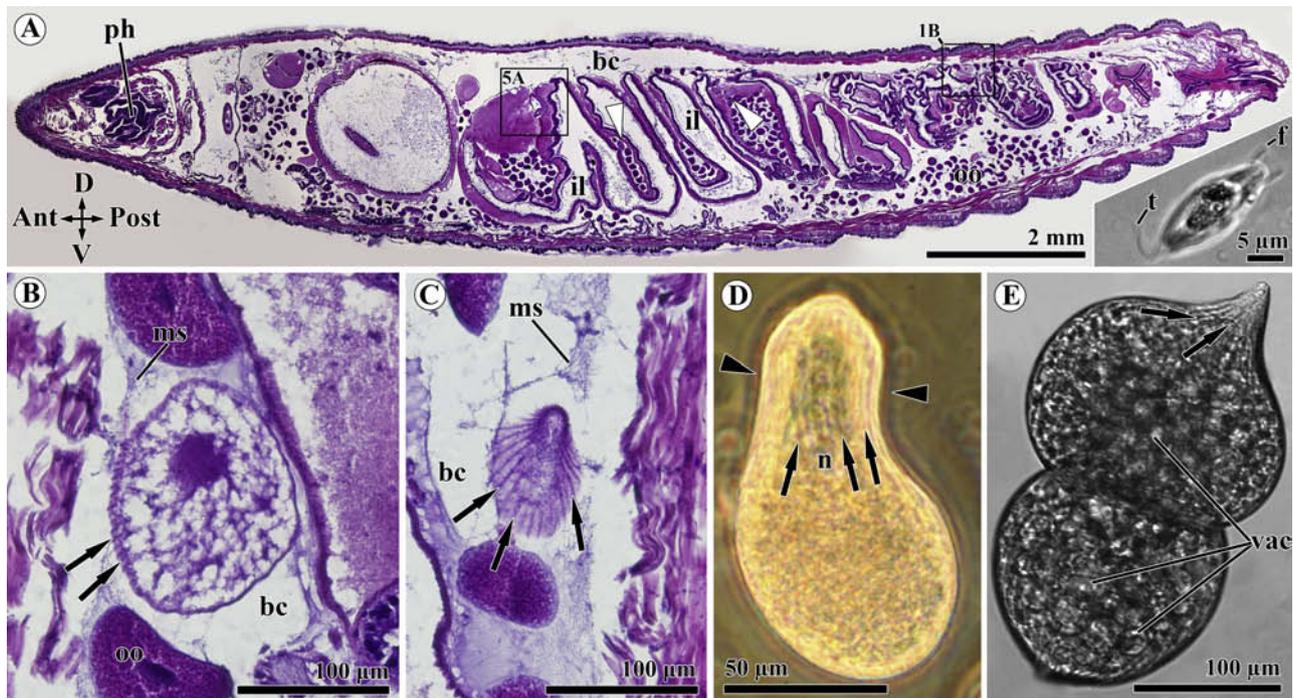
Figure 1. Localisation of *Urospora ovalis* and *U. travisiae* in the polychaete *Travisia forbesii* and light microscopic observations of *U. ovalis* **A**. Sagittal section of the host infected with *U. ovalis* and *U. travisiae* (white arrowheads) located in the body cavity (bc). The black rectangles mark the parasites presented in Figure 1B (*U. ovalis*) and Figure 5A (*U. travisiae*) at high magnification. Ant – anterior end of the host, D – dorsal side of the host; il – intestinal lumen of the host, ph – pharynx; oo – oocytes of the host, Post – posterior end of the host, V – ventral side of the host. LM, H&E. The inset shows an oocyst with a funnel (f) and a tail (t) at opposite ends. LM. **B** – **C**. Histological sections of trophozoites of *U. ovalis* located in the host body cavity (bc), in different planes. Note mucous substance (ms) surrounded parasites and ridges (black arrows) at the parasite surface. oo – oocytes of the host. LM, H&E. **D**. Micrograph of the solitary *U. ovalis* trophozoite during cell metaboly. Note contracted region (black arrowheads) of the cell with ridges at the surface (black arrows). n – nucleus. PC. **E**. Syzygy of *U. ovalis.* Note ridges (black arrows) at free ends of gamonts. vac – vacuoles. BF.

membrane and the inner membrane complex (IMC). The pellicle formed numerous thin and waved epicytic folds (Fig. 2D). Their width was usually about 90 nm, while their height cyclically varied within the range from 0.5 to 1.4 μm. (Fig. 3B-C, E). The number of epicytic folds in 1 μm of the surface varied from 3 to 7, in dependence of the degree of cell contraction. The rippled dense structures and 12-nm apical filaments were not distinguishable; however, there was a single electron-dense rod located just beneath the IMC in the apical part of each epicytic fold (Fig. 3D-E). The 19-24 nm thick internal lamina underlay the IMC and formed curved bridges in the basal part of each fold, thereby separating the cytoplasm of folds from the rest of the gregarine cytoplasm (Fig. 3D-E). Under SEM the folds in non-contracted, as well as contracted regions were undulating or waving (Fig. 2D-E). Each superfold bore 10-20 epicytic folds (Fig. 3B-C).

Numerous cortical microtubules were arranged in transversal bundles located just beneath the pellicle. They did not form a continuous ring in the cell periphery, and some of the microtubules extended into the superfolds (Fig. 3B-D).

Typical apicomplexan micropores, appearing as short cylindrical invaginations of the plasma membrane terminated by a vesicle (about 55 nm in diameter), could occasionally be observed (Fig. 3F). The cylindrical part was enforced by an electron-dense collar (ca. 130 nm in diameter), formed by the IMC and the internal lamina. In addition, numerous structures resembling micropores (micropore-like structures) were located in the gregarine cortex between the epicytic folds (Fig. 3E, G-H). In these structures, the IMC and internal lamina formed an electron-dense cone-shaped collar situated beneath the intact plasma membrane (Fig. 3E, G). Numerous cytoplasmic vesicles (about 0.2 μm in diameter) filled with an electron-dense,

Table 1. Main species characters of *Urospora ovalis* and *U. travisiae*.

	Urospora ovalis	*Urospora travisiae*
Host		*Travisia forbesii*
Localisation in the host		coelom
Attachment to the host tissues	non-attached	attached
Cell shape	ovoid	V-like
Number of cell axis	1	2
Cell dimension (average, μm) of mature trophozoites	179 × 114	395 × 380 per branch
Cell motility	metaboly or peristalsis (non-progressive movement)	gliding (progressive movement)
Cell polarity	-	+
Attachment site	-	+
Cortex		
Epicytic folds		typical for gliding eugregarines
Superfolds	+	-
Cytoplasm differentiation into ectoplasm and endoplasm	-	+
Oocysts		spindle-shaped, heteropolar, with a funnel and the hairy-tail at opposite ends
Distribution		Barents Sea (Murmansk coast), White Sea (Karelian coast)
References		Dogiel 1910; present study

homogeneous material were usually situated in the vicinity of micropore-like structures as well as deeper within the parasite cytoplasm (Fig. 3B). Some of them were in contact with the collar. Except for a few cases, there was no fusion between these vesicles and the plasma membrane (Fig. 3G-H). The electron-dense droplets occasionally observed between the epicytic folds could be secreted by these vesicles (Fig. 3E).

There was no obvious division of cell cytoplasm into two zones, ectoplasm and endoplasm, as is typical for eugregarines. Many amylopectin granules were irregularly distributed in the cytoplasm, and several mitochondria could be observed at the cell periphery (Fig. 3A-C). The dictyosomes of Golgi apparatus, surrounded by numerous small and round vesicles, were mainly localised in the central zone of the cell (Fig. 3A).

The cytoplasm was packed with numerous and different structures, exhibiting a lower quantity at the cell periphery in comparison to the central cell region (Fig. 3A). Electron-dense, homogeneous inclusions of uncertain shape (di) accumulated predominantly around the nucleus. Some of them were in group of 2-3 and were usually accompanied by small transparent vesicles (Fig. 3A, I). Another type of inclusions was represented by large and

round electron-transparent vacuoles (ov) with a loose filamentous content (Fig. 3A, J). In addition, electron-dense, roundish vacuoles (dv) with a heterogeneous granular content were found in the cytoplasm (Fig. 3A, K).

The eccentrically located nucleus possessed one large and several small nucleoli. The large nucleolus lay close to the nuclear envelope; the rest of the nucleoplasm was homogenous with a fine-grained content (Fig. 3A). This nucleolus consisted of two parts: the larger one was dense, homogeneous and directed towards the centre of the nucleus, while the smaller one was heterogeneous and faced the rough and two-layered nuclear envelope. There were several inclusions of nucleoplasm in both parts of the nucleolus (Fig. 3A).

Mature trophozoites (gamonts) in syzygies were connected to each other by their ends. The free ends of partners in syzygies were rounded (in rare cases) or bulb-shaped (in most cases). In the first case, syzygies showed active metabolic motility comparable with that of solitary parasites. In the second case, they moved much more slowly. In all cases, both partners demonstrated ridges on their surface in contracted regions (Fig. 1E), similar to those observed in moving solitary trophozoites (Fig. 1D). The gamonts in all of the observed
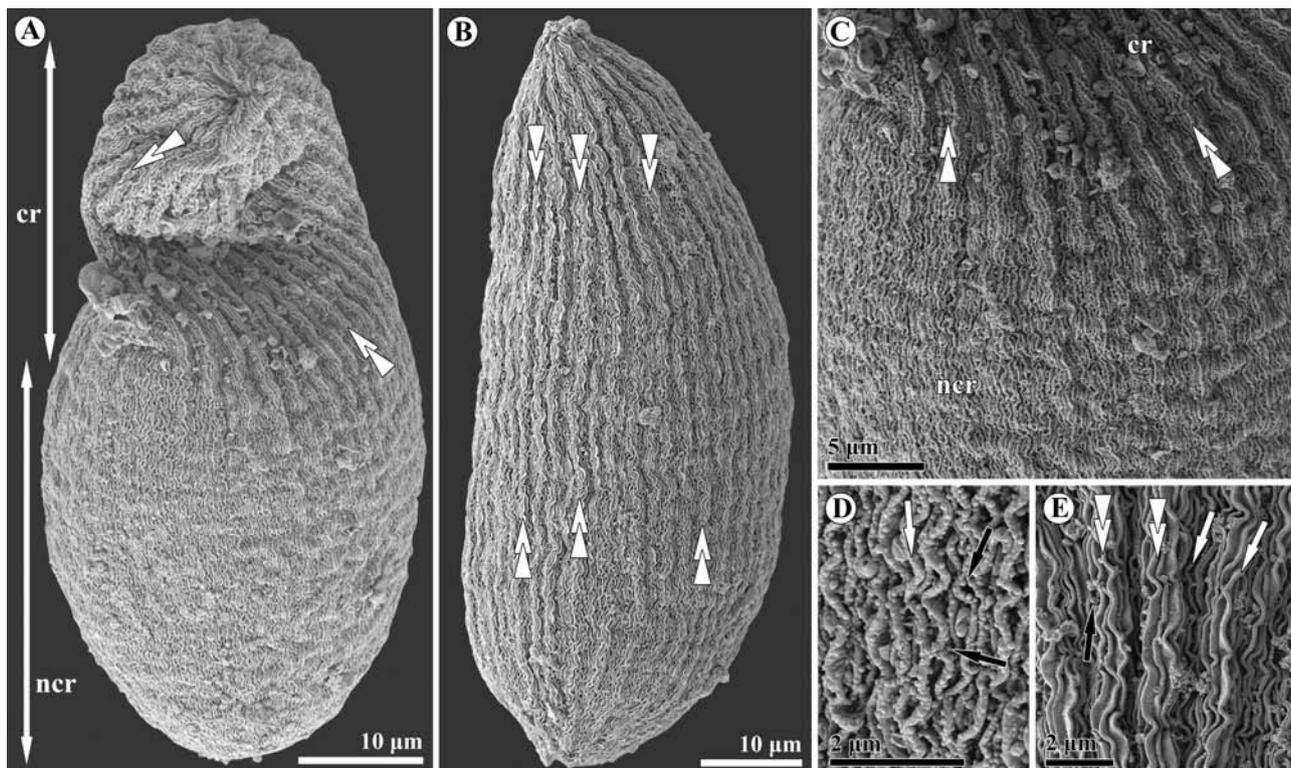
Figure 2. General morphology and surface ultrastructure of solitary *Urospora ovalis* trophozoites. **A**. General view of a trophozoite fixed during its movement. Contracted (cr) and non-contracted (ncr) regions are visible in the cell. White double arrowheads indicate superfolds. SEM. **B**. General view of a completely contracted trophozoite with superfolds (white double arrowheads) that ran over the entire cell surface. SEM. **C.** Detailed view of Figure 2A showing a transition between the contracted (cr) and non-contracted (ncr) regions of the cell. White double arrowheads mark superfolds in the contracted region. SEM. **D.** Details of epicytic folds (white arrow) covering the non-contracted region. Note electron-dense droplets (black arrow) located between the epicytic folds. SEM. **E.** Details of superfolds (white double arrowheads) and epicytic folds (white arrow) of a contracted cell. Black arrow points to an electron-dense droplet between epicytic folds. SEM.

syzygies were larger than solitary trophozoites, and their cytoplasm was completely filled with large transparent vacuoles (Fig. 1E).

During processing for EM, gamonts in syzygies changed their shape by rounding their free ends (Figs 1E vs. 4A). In contrast to solitary trophozoites, fixed gamonts had no superfolds on their surface (Figs 2A-C vs. 4A-C, Figs 3A-C vs. 4E). The height of epicytic folds in syzygies cyclically varied within the range from 0.7 to 2 μm, so that longitudinal sets of high epicytic folds alternating with lower ones were good visible on the syzygies surfaces (Fig. 4A-E). The number of epicytic folds in 1 μm of the surface varied from 3 to 5. There were droplets of mucus between these folds (Fig. 4C). Neither micropores, nor similar structures interrupting the cortex were found in all examined ultrathin sections (Fig. 4E).

The contact zone between two syzygy partners appeared simple, lacking an additional collar or other pellicle modifications (Fig. 4D). Usually, the sets of high epicytic folds of both partners coincided with each other (Fig. 4A, D). The free ends of gamonts in syzygy exhibited almost identical superficial morphology: they were slightly bulged-in (Fig. 4F-G).

The cytoplasm of syzygy partners was filled with a huge amount of electron- transparent vacuoles with loose filamentous content (Fig. 4E), similar to those found in solitary trophozoites (Fig. 3J, ov), but extremely enlarged in volume. Among them, there were many other inclusions such as lipid droplets and amylopectin granules. Electron-dense vacuoles and inclusions resembling the "di" and "dv" found in solitary trophozoites (Fig. 3I, K) were also observed (Fig. 4E).
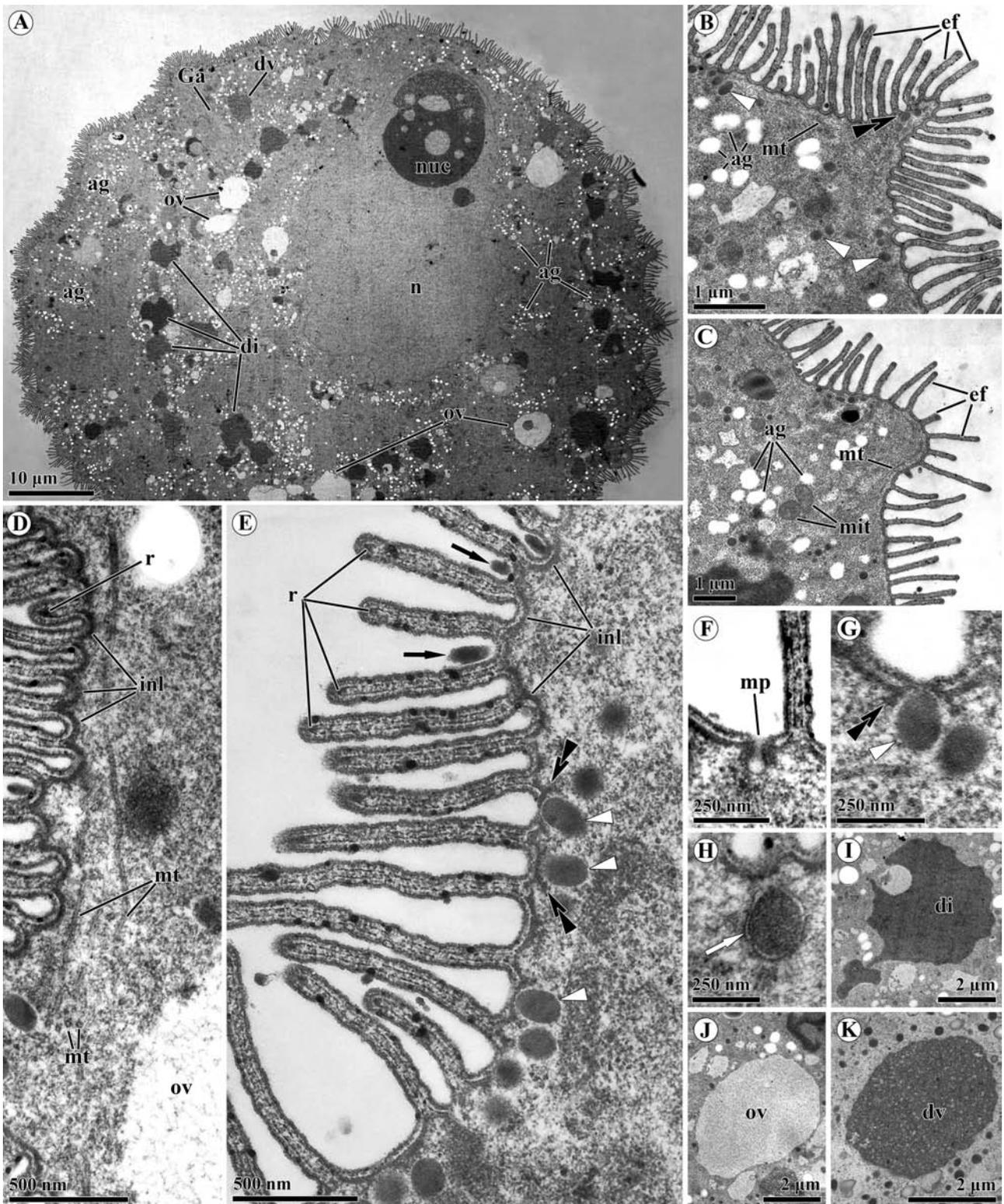
Figure 3. Fine structure of solitary *Urospora ovalis* trophozoites. **A.** Transversal section of a solitary trophozoite contracted during fixation. The nucleus (n) with the nucleolus (nuc) inside is located eccentrically in the cell. The cytoplasm is enriched by numerous and different inclusions: ag – amylopectin granules, di - electron-dense homogeneous inclusions of uncertain shape, dv – electron-dense vacuole with granular content,

General Morphology and Ultrastructure of *Urospora travisiae*

Solitary trophozoites were found in the host body cavity (Fig. 1A). Some gregarines were attached to the intestine wall (Fig. 5A) and occasionally to the blood vessels, but they easily detached during host dissection or sample manipulation. The young trophozoites and syzygies of *U. travisiae* were observed rarely during this study (Fig. 5B-C). Young trophozoites were elongated, and drop-like in shape, with up to three transverse constrictions at the tapering end. The length of them varied from 100 to 130 μm (n = 2) (Fig. 5B). The nucleus was located in the widest part of the cell. Detached young trophozoites exhibited a gliding motility, with a wide, rounded leading end.

Mature trophozoites of *U. travisiae* were V-shaped. They possessed two narrowing branches and attached to the host tissue with the tip where the branches converged, the so-called attachment tip. In syzygies, the V-shaped partners were in contact with each other by means of this attachment tip (Fig. 5C); however, the contact was not strong, and partners easily disassociated.

Each branch had 5-15 transverse permanent constrictions; thus, branches appeared as a string of pearls with differently sized beads (Fig. 5D-G). The angle between the branches in a cell varied in the range from 10° to 180°, generally from 90° to 130° (n = 25) (Figs 5D-G, 6A). Commonly, one of the branches was longer than the other: 195-660 μm (av. 392 μm; standard deviation (SD) = 99.4; n = 25) vs. 165-580 μm (av. 352 μm; SD = 96.8; n = 25). A single oval nucleus with 2-3 nucleoli was usually situated in the longest branch close to the attachment tip (Fig. 5D-G).

Detached V-shaped trophozoites demonstrated the typical gliding motility. Cells with an angle of about 10° - 100° between their branches usually moved with the attachment tip forward. The gliding path was straight or curved, as if the cell branches possessed equal or different motion forces, respectively (Supplementary Material Video 2). In cases where the angle was about 180°, cells glided with one of the branches forward.

The attachment tip appeared like a plateau, usually surrounded by a circular, wide furrow (Fig. 6B). Some traces of the epicytic folds were visible on the surface of the plateau, while the well-developed longitudinal folds extended radially from the circular furrow. Most of these aforementioned folds ran parallel till the distal end of each branch (Fig. 6A-E). On the lateral surface of the cell, the folds, passing from opposite branches, converged and merged with each other, while on the inner side of the V-shaped cell, the epicytic folds passed continuously from one branch to another (Fig. 6F). There were no evident changes in the form or structure of these folds in the region close to the attachment tip and at the constrictions between individual beads (Fig. 6E-G). Some of the folds ended at constriction regions, while others continued to the next beads. Additional epicytic folds that passed only on the surface of the beads also appeared (Fig. 6D-E).

The parasites were covered by a typical three-layered pellicle consisting of plasma membrane underlain by the closely adjacent membranes of IMC. The cortex of *U. travisiae* did not exhibit any secondary superfolds. Epicytic folds reached 0.5 μm in height and 0.1 μm in width, and were regularly distributed with a distance of about of 0.1 μm between them, 3-4 folds per 1 μm (Figs 6C, G, 7A-D). As in the epicytic folds of *U. ovalis*, the rippled dense structures and 12-nm apical filaments were indistinguishable in the apex of the epicytic fold; however, a dense fibrillar rod was observed just beneath the IMC. The pellicle was underlain

ov – electron-transparent vacuole with loose filamentous content. Ga – dictyosome of the Golgi apparatus. TEM. **B** – **C.** Details of the narrow (**B**) and wide (**C**) superfolds bearing the epicytic folds (ef). Note a micropore-like structure (black double arrowhead) and electron-dense vesicles (white arrowhead). ag – amylopectin granules, mit – mitochondria, mt – microtubules. TEM. **D.** Details of the trophozoite cortex showing peripheral transversal microtubules (mt). A single electron-dense rod (r) located just beneath the IMC is visible at the apex of one completely visible epicytic fold. inl – internal lamina, ov – electron-transparent vacuole with loose filamentous content. TEM. **E.** Transversal section of the gregarine cortex showing micropore-like structures (black double arrowhead) accompanied by electron-dense vesicles (white arrowhead). Electron-dense rods (r) are visible in the epicytic folds. Note electron-dense droplets (black arrow) between the epicytic folds. inl – internal lamina. TEM. **F.** Details of a typical micropore (mp). TEM. **G.** Details of a micropore-like structure (black double arrowhead) in contact with an electron-dense vesicle (white arrowhead). TEM. **H.** Details of an electron-dense vesicle beneath the trophozoite cortex; note the membrane (white arrow) limiting the vesicle. TEM. **I.** Higher magnification of a dense inclusion (di) of uncertain shape. TEM. **J.** Higher magnification of an electron-transparent vacuole (ov) with loose filamentous material. TEM. **K.** Higher magnification of an electron-dense vacuole (dv) with granular content. TEM.
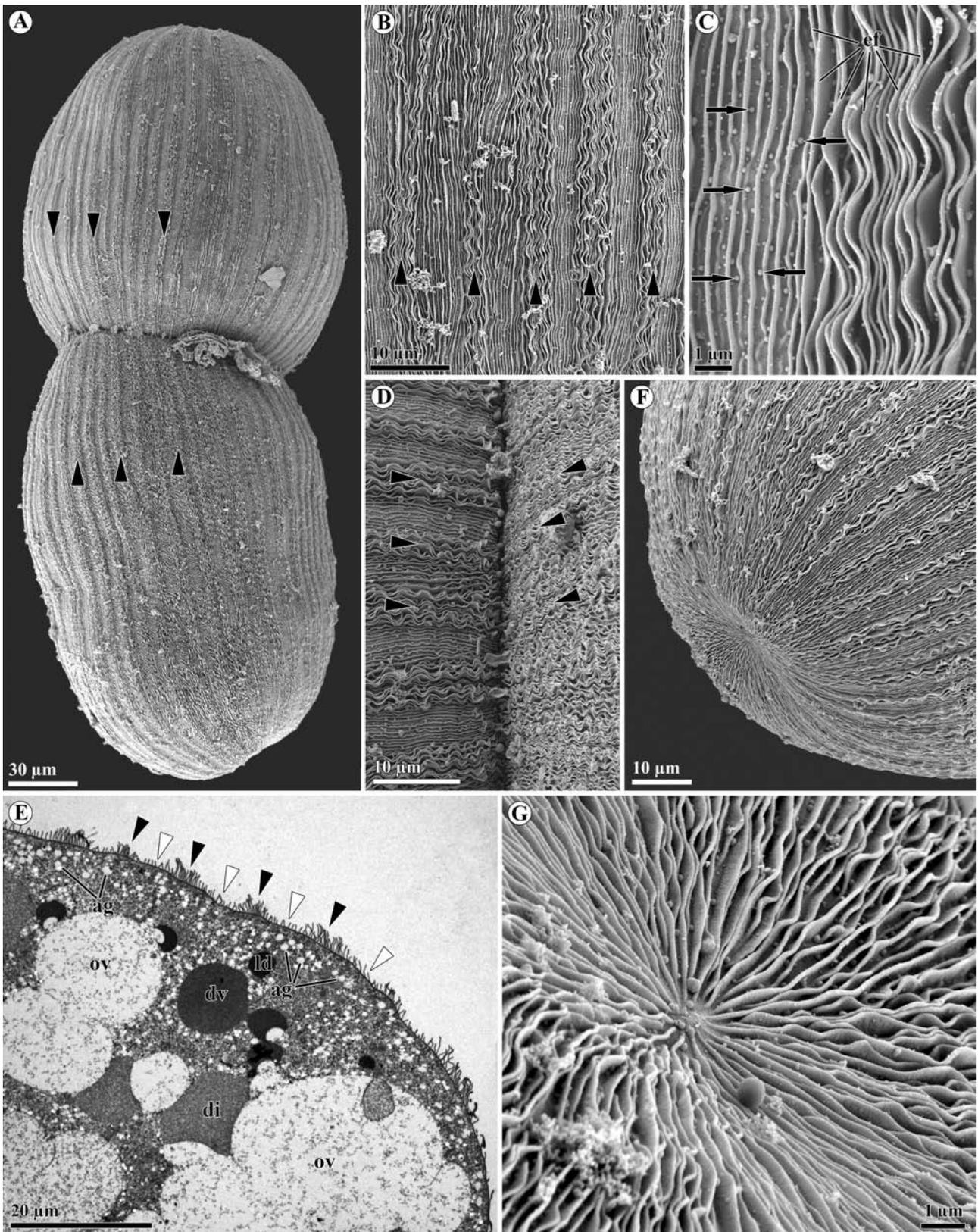
by an internal lamina, which did not form links at the base of individual epicytic folds (Fig. 7A). Typical micropores were situated between the folds (Fig. 7A). Several micropore-like structures, similar to those in *U. ovalis*, were seen between the epicytic folds. They appeared as a cone-shaped collar, formed by an IMC and internal lamina, and electron-dense vesicles were associated with them (Fig. 7B). The same vesicles were also found deeper within the parasite cytoplasm (Fig. 7D). Electron-dense inclusions, oval in profile and apparently located between the pellicle membranes, were seen at the base or at the lateral sides of most folds (Fig. 7B, D). Transversal subpellicular microtubules underlay the bases of epicytic folds, as observed in *U. ovalis* (Figs 6G, 7A).

In cross-sections of a branch near the attachment tip, the cell was almost round, and the cytoplasm was subdivided into an ectoplasm and endoplasm (Fig. 7C-E). The endoplasm was packed with electron-transparent inclusions of irregular shape, vacuoles with homogeneous translucent content, electron-dense vesicles, numerous lipid droplets, and dictyosomes of the Golgi apparatus. The ectoplasm mostly comprised mitochondria and electron-dense vesicles (Fig. 7C-E).

Molecular Phylogenetic Analysis

The new SSU sequences of *U. ovalis* (1623 bp) and *U. travisiae* (1604 bp) were obtained by direct sequencing of PCR products. There are 3.5% differences between them (46 substitutions and 3 indels) across the distance of their pairwise alignment, where they completely overlapped (1604 sites), and distinctive nucleotides did not show any polymorphism (Supplementary Material Fig. S1). Like other lecudinid and urosporid SSU rDNA sequences, the novel sequences were considerably shorter in comparison with other eukaryotes (*U. ovalis*: 1604 bp vs 1731 bp in *Bigelowiella natans* across the same interval of the alignment; *U. travisiae*: 1623 bp vs

1742 bp in *B. natans*; the full length of SSU rDNA of *B. natans* and the large majority of other eukaryotes is about 1800 bp) and contained motifs specific to other lecudinid and urosporid gregarines.

The constructed Bayesian (Fig. 8) and maximum-likelihood (ML) trees of SSU rDNA of 99 OTUs showed similar topology with two exceptions: (i) the flipped positions of two eugregarine clades: Gregarinoidea + Cephaloidophoroidea and Stylocephalids; and (ii) the branching order of archigregarines (data not shown). However, both of these variable branching patterns were weakly supported by both methods (Fig. 8).

The Bayesian tree of SSU rDNA sequences (Fig. 8) fitted recent opinions on alveolate phylogeny: the main robust clades are ciliates, dinoflagellates and apicomplexans. The backbone of the apicomplexans was weakly supported; nevertheless, the sequences clustered into several major well-supported clades: (1) coccidia and hematozoa (not supported by BP in ML analyses); (2) cryptosporidia; (3) Actinocephaloidea (Cavalier-Smith 2014) consisting of neogregarines and some terrestrial eugregarines, e.g., *Monocystis* spp. and representatives of family Actinocephalidae (not supported by BP (91%); (4) Gregarinoidea (Clopton 2009); (5) Cephaloidophoroidea (Rueckert et al. 2011a); (6) the clade of *Polyplicarium* spp. and related environmental sequences (not supported by BP (74%)); and (7) Lecudinoidea (= Urosporoidea in Cavalier-Smith 2014), a clade consisting of the marine aseptate gregarine families Lecudinidae and Urosporidae, and the unusual gregarine *Veloxidium leptosynaptae*. The SSU rDNA sequences from archigregarines did not form a common clade. All gregarine and cryptosporidia subclades formed a monophyletic clade – however, with low supports (PP = 0.81, BP = 43%), and these subclades were shuffled inside this common clade, i.e. their branching order was unresolved because of low support both in Bayesian and ML analyses. The new SSU rDNA sequences of *U. ovalis* and *U. travisiae* belonged to the Lecudinoidea clade

---

Figure 4. General morphology and fine structure of *Urospora ovalis* syzygies. **A**. General view of a syzygy. Black arrowheads mark sets of high epicytic folds. SEM. **B**. Detailed view of the surface showing the sets of high epicytic folds (black arrowheads). SEM. **C**. Higher magnification of the gregarine surface with low and high epicytic folds (ef). Note the droplets of mucous substance (black arrows) between folds. SEM. **D**. Detailed view of the contact between two syzygy partners. Black arrowheads indicate sets of high epicytic folds at the surface of both gamonts. SEM. **E**. Transversal section of a gamont showing the alternating sets of high (black arrowheads) and low epicytic folds (white arrowheads). Inclusions of the cytoplasm are similar to that in cytoplasm of solitary trophozoites: ag – amylopectin granules, di – electron-dense homogeneous inclusions of uncertain shape, dv – electron-dense vacuole with granular content, ld – lipid droplets, ov – electron-opaque vacuole with loose filamentous material. TEM. **F-G**. Semi-axial view (**F**) and higher magnification (**G**) of the free ends of gamonts. Note that the apex of the free ends is slightly bulged-in. SEM.
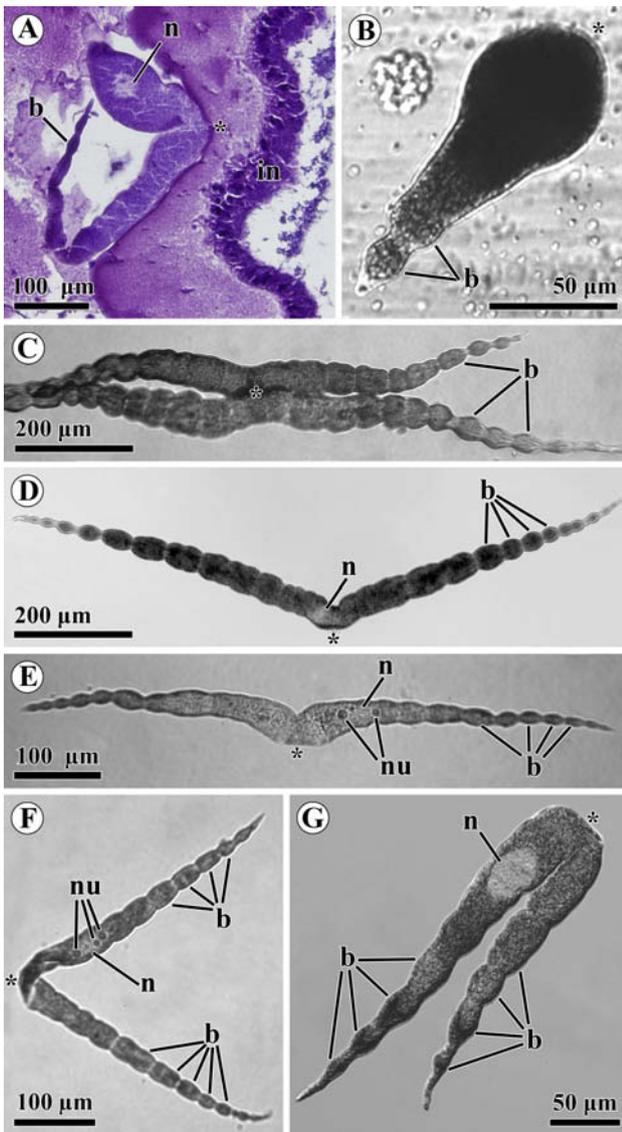
Figure 5. Light microscopic observations of *Urospora travisiae* gregarines. **A.** Histological section of the trophozoite clamped between the folds of the host intestine (in). Asterisk indicates the attachment tip, n – nucleus, b – bead of the branch in the cell. LM, H&E. **B.** Young trophozoite with a single tapering branch bearing two transverse constriction near the end. Asterisk marks the attachment tip, b – beads of the branch in the cell. BF. **C.** Syzygy of two V-shaped partners attached to each other by their attachment tips (asterisk). b – beads of the branches. BF. **D – G.** Micrographs of trophozoites with different angles between their branches: **D** – approx. 140°; **E** – 180°; **F** – 70°; **G** – 10°. Note the different number of the beads (b) in their branches and the oval nucleus (n) with 2-3 nucleoli (nu) situated in the longest branch close to the attachment tip (asterisk) of each individual.

(Fig. 8). Within this clade, however, they closely affiliated with lecudinids (*Difficilina* species), but not with other urosporids (*Pterospora* spp. and *Lithocystis* spp.).

Despite the fact that the new sequences were fully supported by both the BI and ML analyses in the 99 OTUs tree, topological tests were performed using the resulting phylogeny of 23 selected lecudinid and urosporid sequences (Fig. 9A-I, Table 2). The topology of the main clades in this tree (Fig. 9A) remained the same as the topology of those in the 99 OTUs tree. Further, 8 trees with alternative topologies were constructed (Fig. 9B-I), in which the clade *U. ovalis* + *U. travisiae* sequentially changed their position. We tested all of these topologies using a set of the most common tests. The majority of topologies were discarded with the exception of three permissible ones: the Bayesian tree, the alternative topology F (but not the BP test), and the alternative topology I (Fig. 9A, F, I, Table 2). All these trees contained the clade *Difficilina* spp. + *Urospora* spp. in contrast to the discarded topologies, where this combination was absent.

Discussion

The morphology of the gregarines investigated in this study completely corresponds to the original description of *Urospora ovalis* and *U. travisiae* trophozoites presented by V. A. Dogiel (1910). According to the original descriptions, oocysts of *U. ovalis* and *U. travisiae* were heteropolar (with a funnel and a tail at opposite ends), very similar, but differ in size; oocysts of *U. travisiae* were larger than those of *U. ovalis* (Dogiel 1910). All oocysts observed in the present study were of the same size and typical of representatives of the genus *Urospora*. Although, species affiliation of the observed oocysts was not identified in this study, they obviously belong to one of the investigated species.

The investigated gregarines differ in cell shape and morphology (Table 1). In *U. ovalis*, the solitary trophozoites do not demonstrate any signs of cell heteropolarity. This phenomenon was also described for gamonts of *Gonospora ormieri* (Porchet 1978). Young and mature trophozoites of *U. travisiae* are heteropolar. The young individuals of *U. travisiae* can attach to the substrate with the wider end, which is most likely the anterior end. We assume that during gregarine growth, a second branch of the cell starts to develop, so that the cell gradually transforms from a monoaxial to a V-like biaxial form. The anterior end of the

Table 2. Results of alternative topology tree tests (alignment of 23 OTUs, 1676 bp).

Tree topology	– ln L	BP[a]	ELW[b]	KH[c]	SH[d]	WSH[e]	AU[f]
Bayesian consensus tree (Fig. 9, A)	**13536.74**	**0.84736**	**0.84736**	**1.0**	**1.0**	**1.0**	**0.9023058**
Alternative topologies							
B	13686.58	0	0	0	0	0	0
C	13747.51	0	0	0	0	0	0
D	13813.34	0	0	0	0	0	0
E	13813.32	0	0	0	0	0	0
F	**13541.49**	0.04601	**0.07659232**	**0.11657**	**0.64057**	**0.37045**	**0.1236613**
G	13698.65	0	0	0	0	0	0
H	13747.51	0	0	0	0	0	0
I	**13541.15**	0.10663	0.1215358	0.13904	0.65436	0.41608	0.1578981

[a]Bootstrap Probability (Felsenstein 1985);
[b]Expected-Likelihood Weights (Strimmer and Rambaut 2002);
[c]P-value of the Kishino-Hasegawa test (Kishino and Hasegawa 1989);
[d]P-value of the Shimodaira-Hasegawa test (Shimodaira and Hasegawa 1999);
[e]P-value of the Weighted Shimodaira-Hasegawa Test (Shimodaira and Hasegawa 1999);
[f]P-value of the Approximately Unbiased test (Shimodaira 2002). P-values <0.05 discard the suggested topology. Permissible topologies are bolded.

young cell remains as the attachment site of V-like shaped cell. The older (or primary) branch is usually longer and contains the nucleus. It is important to note that trophozoites of *Pterospora* spp. can be characterised as biaxial as well (Dogiel 1910; Landers 1991, 2001; Landers and Gunderson 1986; Leander 2008).

Most eugregarines possess a cortex with a complicated structure (Schrével et al. 1983; Vivier 1968; Vivier et al. 1970). Investigated gregarines from *Travisia forbesii* also possessed a well-developed cortex with numerous longitudinal epicytic folds. In both species, rippled dense structures (RDS) and 12-nm apical filaments were not well preserved and were poorly detectable only in a few folds, despite the application of different fixation protocols. Electron-dense rods, observed in both species, were located in the apex of the longitudinal folds, under the IMC, and appear to be similar to those described in *Gonospora beloneides, Lankesteria* spp., *Gregarina* spp., *Difficilina cerebratuli*, *Thiriotia pisae*, *Ganymedes vibiliae*, and *Porospora portunidarum* (Corbel et al. 1979; Desportes et al. 1977; Simdyanov 1995a, 2009; Valigurová et al. 2013). It was assumed that it has the role of reinforcing the fold tips (Valigurová et al. 2013).

Micropores, appearing as invaginations of the plasma membrane encircled by a collar formed from the IMC, are typical for apicomplexans. The exact function of these structures, although often discussed, remains unclear. Micropores could

function as organelles for the acquisition of nutrients (Chobotar and Scholtyseck 1982; Scholtyseck 1973; Scholtyseck and Mehlhorn 1970; Vivier et al. 1970) or as extrusomes for mucus secretion (Desportes and Schrével, 2013; Philippe and Schrével 1982; Valigurová et al. 2013; Vegni Talluri and Dallai 1983). We observed typical micropores and micropore-like structures (MLS) in *U. ovalis* and *U. travisiae*. We assume that typical micropores play a role in the gregarine's acquisition of nutrients, while the second structures serve to secrete mucus onto the parasite surface in between the folds. Under SEM and TEM, the excreted mucus appears as droplets (Fig. 3E, 4B), as was also demonstrated in other gregarines (Simdyanov 1995a, 2009; Valigurová et al. 2013; Walker et al. 1984). In addition, the pore-like structures interrupting the IMC (and the plasma membrane, in some cases), but lacking the collar, were documented in the attachment site at the top of the protomerite of *Gregarina cuneata* gamonts (Valigurová 2012). These structures could also play a role in the secretion of adhesive material, which is often present between the attached gregarine and adjacent host tissue. Mucous material was also observed on the sucker-like protomerite of some actinocephalid eugregarines (Cook et al. 2001).

In a series of transverse sections of the studied gregarines, we observed the non-uniform accumulation of presumably mucus-secretory vesicles under the pellicle. It allows us to speculate that mucus excretion occurs with different intensities

in various zones of the parasite surface at the same moment. Therefore, an eruptive (or impulsive) nature of the mucus excretion could take place in the investigated gregarines. We can assume that the release of the mucus by gregarine into the environment may serve as a protective mechanism against attack by host coelomocytes. It is expected that the gliding motility of eugregarines is facilitated by the specific structure of the epicytic folds; therefore, mucus secretion may also help to decrease frictional forces during forward movement. This was previously proposed for *Gregarina* spp., in which the mucus load in the gregarine cytoplasm was positively correlated with gliding speed (King 1981, 1988; Mackenzie and Walker 1983; Valigurová et al., 2013; Vávra and Small 1969).

Gliding motility is characteristic of the majority of eugregarines. This motility can easily be observed in free (non-attached) eugregarines contacting with a substrate, when they move forward, usually without any obvious changes in their cell shape (unlike metaboly or rolling). However, when attached to the host tissue, eugregarines do not usually demonstrate any signs of motility, although near-surface currents in the internal environment of the host can be noticed around parasites. Obviously, parasites produce these currents by themselves. It is important to note that contact between a gregarine and solid matter might not be necessary for gregarine motion, as *Gregarina* spp. gamonts are able to free-float in a liquid lacking any contact with the substrate and with a significantly higher rate than exhibited during regular gliding (Valigurová et al. 2013).

Metaboly is another type of motility, which is accompanied by significant changes in cell shape. Gregarines demonstrating metabolic (or peristaltic) motility, or even immobility, as a rule, possess an epicyte of unusual organisation. Various modifications of the epicyte typical for eugregarines along with the loss of gliding motility have been reported in representatives of the families Monocystidae and Urosporidae, parasitising the coelom, respiratory trees, and seminal vesicles of various invertebrates (Dyakin and Simdyanov 2005; Frolov 1991; Landers 1991, 2001; Landers and Gunderson 1986; Landers and Leander 2005; MacMillan 1973; Miles 1968; Vinckier 1969; Vinckier and Vivier 1968). *Urospora ovalis* and *U. travisiae* both possess a typical epicyte; nevertheless, the trophozoites and young syzygies of *U. ovalis* demonstrate metabolic motility, during which the cell cortex in the contracted regions generates several superfolds. Similar superfolds have been documented in trophozoites of *Nematocystis magna*, a monocystid

eugregarine demonstrating peristaltic-like motility (MacMillan 1973; Miles 1968). Mitochondria observed in *U. ovalis* are similar to those reported in *Pterospora floridensis* (Landers 2002). We assume that the relatively great number of mitochondria distributed uniformly in the cell cytoplasm appears to be correlated with the active metaboly of *U. ovalis.*

The motility of gregarines seems to be an adaptation to their localisation in a certain niche in the host body. Gregarines inhabiting the host digestive tract usually possess pendular or gliding motility types (e.g. *Selenidium* spp., *Lecudina* spp.). They develop clamped in narrow spaces between the intestinal folds or between the intestine and food. We assume that motility in intestinal gregarines might be necessary to provoke an exchange of host internal environmental liquids around them in order to improve the effectiveness of their nutrient acquisition and/or reduce frictional forces to retain the attachment to host tissues, as also suggested by Leander (2008). This also applies to *U. travisiae*, which attaches to the outer wall of the intestine. Metaboly seems to be characteristic of detached parasites (numerous representatives of the families Urosporidae and Monocystidae) inhabiting the host body cavities. Presumably, monocystids have acquired this type of motility as an adaptation to their life style, being detached and motile within the gametes agglomeration of oligochaete hosts. Moreover, some urosporids could have evolved their motility as an adaptation for living in the liquid environments of host cavities without any attachment to host tissue. In addition, motility in gregarines could provide an effective protection against the adhesion of host coelomocytes to their surfaces, as shown for other coelomic parasites (De Ridder and Jangoux 1984; Coulon and Jangoux 1988, 1991; Siedlecki 1903).

Both gregarines investigated in this study showed signs of active metabolism, represented by the presence of various vacuoles and inclusions. We assume that, along with an increase in amylopectin load, the maturation of trophozoites of both species is accompanied by an increase in the quantity and size of these inclusions and vacuoles, which occupy almost the entire cell volume. Their function remains unclear; however, we can suggest that their contents may be used for further gametocyst and oocyst wall formation, similar to wall-forming bodies in coccidia (Long 1982).

The frontal and lateral syzygies are characteristic of urosporids (Levine 1977). In the present study, we documented end-to-end syzygy in *U. ovalis* and frontal syzygy in *U. travisiae*. We cannot identify the exact type of syzygy present in *U. ovalis* gregarines:
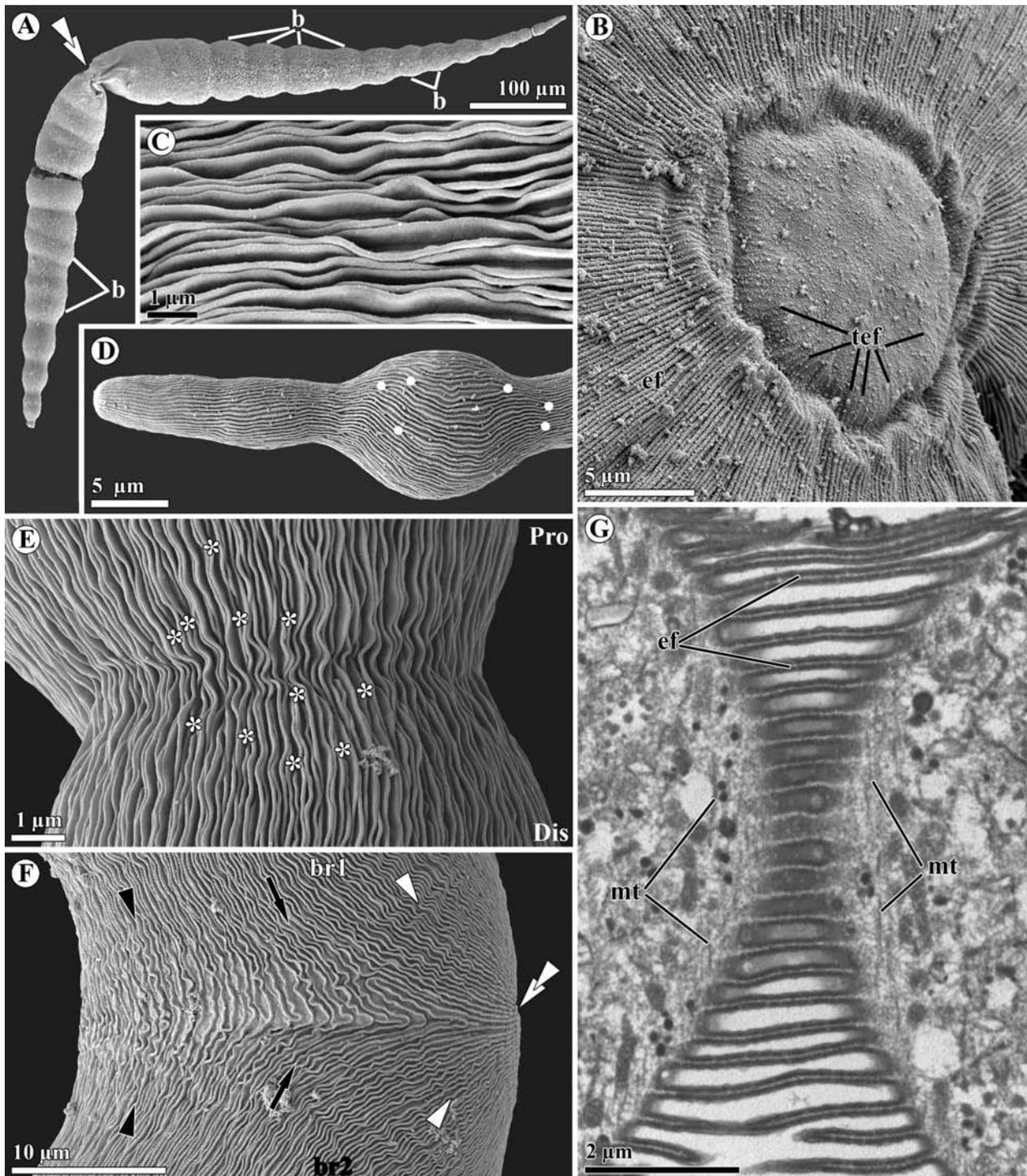
Figure 6. General morphology and fine structure of *Urospora travisiae* trophozoites. **A.** General view of a trophozoite. White double arrowhead points to the attachment site placement, b - beads of the branches. SEM. **B.** Detailed view of the attachment tip; traces of the epicytic folds on the surface of the plateau (tef) and well-developed epicytic folds (ef) extended from the furrow are well visible. SEM. **C.** Higher magnification of the gregarine surface demonstrating epicytic folds. SEM. **D.** Higher magnification of the distal part of the branch with one bead. White dots mark the beginning/end of additional epicytic folds on the bead surface. SEM. **E.** Higher magnification of the constricted region between two individual beads. Asterisks mark the epicytic folds terminating near the region of constriction. Dis – distal end of the branch, Pro – proximal end of the branch.

caudo-frontal, frontal, or caudal. The syzygy of *U. travisiae* is obviously frontal, as partners are in contact by their attachment tips. Syzygies of *U. travisiae* are comparable with those of *Pterospora* spp., in which partners are of V-like shape, with two piriform branches possessing posterior dendritic trunks (Landers 1991, 2001; Landers and Gunderson 1986; Landers and Leander 2005).

Molecular phylogenetic analyses confirmed the morphological data: both species belong to the clade Lecudinoidea comprising representatives of the families Lecudinidae and Urosporidae. Previously, it was shown that, within the Lecudinoidea clade, some species have small interspecific differences (Mita et al. 2012; Rueckert et al. 2015). Alternatively, some of them have high intraspecific differences in SSU rDNA (Rueckert et al. 2011b), even in the species with negligible morphological interspecific differences (Rueckert et al. 2010). In a pair of studied species *U. ovalis* and *U. travisiae* a set of distinctive sites in the sequences was identified by direct sequencing of PCR products from genomic DNA obtained from 10-20 individuals of each species, and distinctive nucleotides were neither polymorphic nor ambiguous (Supplementary Material Fig. S1). Consequently, there is a genetic hiatus conforming to considerable morphological differences between gregarines of these species. Further investigations including single-cell sequencing and analysing of other genetic markers, such as ITS2, LSU rDNA and the whole ribosomal operon sequences, are desirable for revealing of distinctions, undiscovered by cell-pool sequencing, between *U. ovalis* and *U. travisiae*.

In our study, the representatives of the families Lecudinidae and Urosporidae were partially mixed with each other (clades corresponding to these families were not well-supported). At the same time, representatives of the family Urosporidae exhibited a clear diagnostic feature, probably a synapomorphy: the characteristic morphology of oocysts, with a funnel at one of the poles and one or more projections of the oocyst wall, sometimes quite long, at the opposite pole (Dogiel 1906, 1909, 1910; Léger 1892). Therefore, we assume that SSU rDNA phylogeny cannot resolve the real branching order in the clade Lecudinoidea, either because of the insufficient sensitivity of the method or because of the limited number of taxon samples. Furthermore, removing the *Veloxidium leptosynaptae* sequence (see below) from the analysis led to the uniform shuffling of all lecudinids and urosporids within the clade (data not shown). The high sensibility of gregarine SSU rDNA phylogeny to taxonomic sample size was noted earlier (Simdyanov et al. 2015). On the other hand, SSU rDNA phylogeny confirms the close relations between lecudinids and urosporids, which were included in the 'aseptate' eugregarines, parasites of marine invertebrates, according to Grassé's concept of host-parasite coevolution (Grassé 1953).

In this study, *Veloxidium leptosynaptae*, an unusual gregarine from the intestine of the sea cucumber *Leptosynapta clarcki*, was closely affiliated with the clade Lecudinoidea (Figs 8, 9). In addition, the SSU rDNA sequence of *V. leptosynaptae* possessed motifs that were unique to this clade. However, on the basis of the bending motility and surface morphological characteristics of the gregarine, the authors of the original description of *V. leptosynaptae* (Wakeman and Leander 2012) suggested that this species belongs to the order Archigregarinorida. Nevertheless, they noticed that the 'Veloxidium clade' branched as the nearest sister lineage to the clade of marine lecudinids and urosporids. We have several objections to such a classification of *V. leptosynaptae*: 1) the syzygy of *V. leptosynaptae* appears frontal (typical for lecudinids) rather than caudal (typical for archigregarines); and 2) some eugregarines are also capable of bending their body, sometimes quite dramatically (Hildebrand 1981; Simdyanov, 1995b; Valigurová et al. 2013). Therefore, further TEM studies of the cortex are necessary to establish the taxonomic position of *V. leptosynaptae* more reliably.

It was suggested that coelomic gregarines evolved more than once from different marine intestinal eugregarines (Leander et al. 2006). One of the possible ways for the transition from intestinal to coelomic parasitism was demonstrated in some marine eugregarines from polychaetes when, during host reproductive metamorphosis, intestinal gregarines located in the host body cavity for a short time (Durchon and Vivier 1961). Such temporary location of gregarines in the host coelom

---

SEM. **F**. Higher magnification showing converging and merging epicytic folds (black arrows) that cover the lateral side, black arrowheads mark folds passing from one branch (br1) to another (br2) on the inner surface of the cell near the attachment tip, and folds (white arrowheads) arising from the attachment tip (white double arrowheads). SEM. **G**. Tangential section of the constricted region between adjoining beads. ef – epicytic folds; mt – microtubules. TEM.
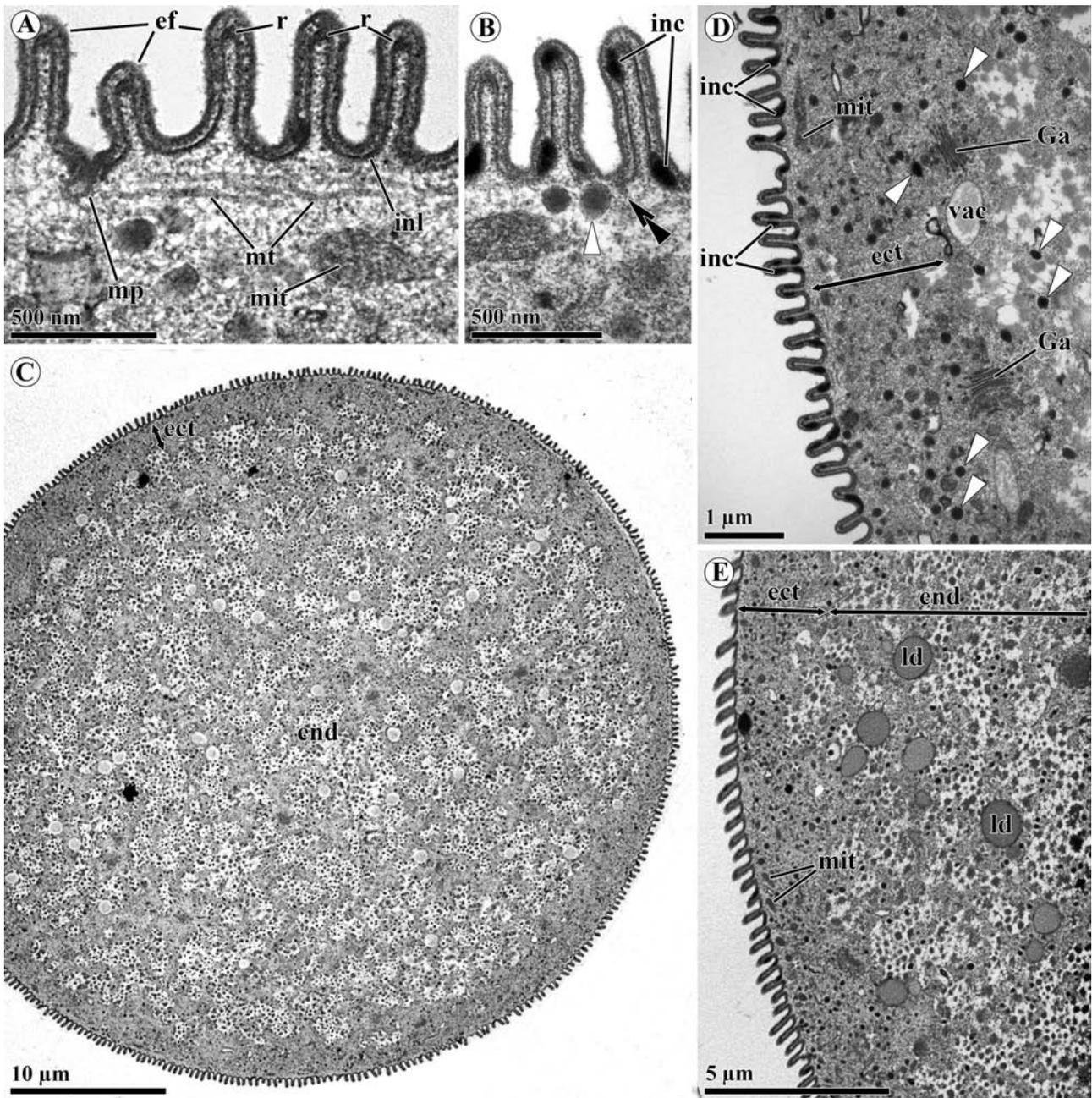
Figure 7. Fine structure of the cortex and cytoplasm of *Urospora travisiae* trophozoites. **A**. Transversal section of a trophozoite demonstrating the cell cortex in detail. Note a typical micropore (mp) between epicytic folds (ef) and an electron-dense rod (r) in the apex of each fold. inl – internal lamina, mit – mitochondrion, mt – microtubules. TEM. **B**. Transversal section of the gregarine cortex showing a micropore-like structure (black double arrowhead) with a closely located electron-dense vesicle (white arrowhead), and an electron-dense inclusion between cortex cytomembranes (inc). TEM. **C**. Transversal section of one of the branches near the attachment tip. The cytoplasm is subdivided into ectoplasm (ect) and endoplasm (end). TEM. **D.** Transversal section of a trophozoite demonstrating the cell cortex and ectoplasm (ect) in detail. Ga – Golgi apparatus, inc – electron-dense inclusion; mit – mitochondrion, vac – electron-transparent vacuoles. TEM. **E**. Detailed view of the cell ecto- (ect) and endoplasm (end) in transversal section; ld – lipid droplets; mit – mitochondrion. TEM.
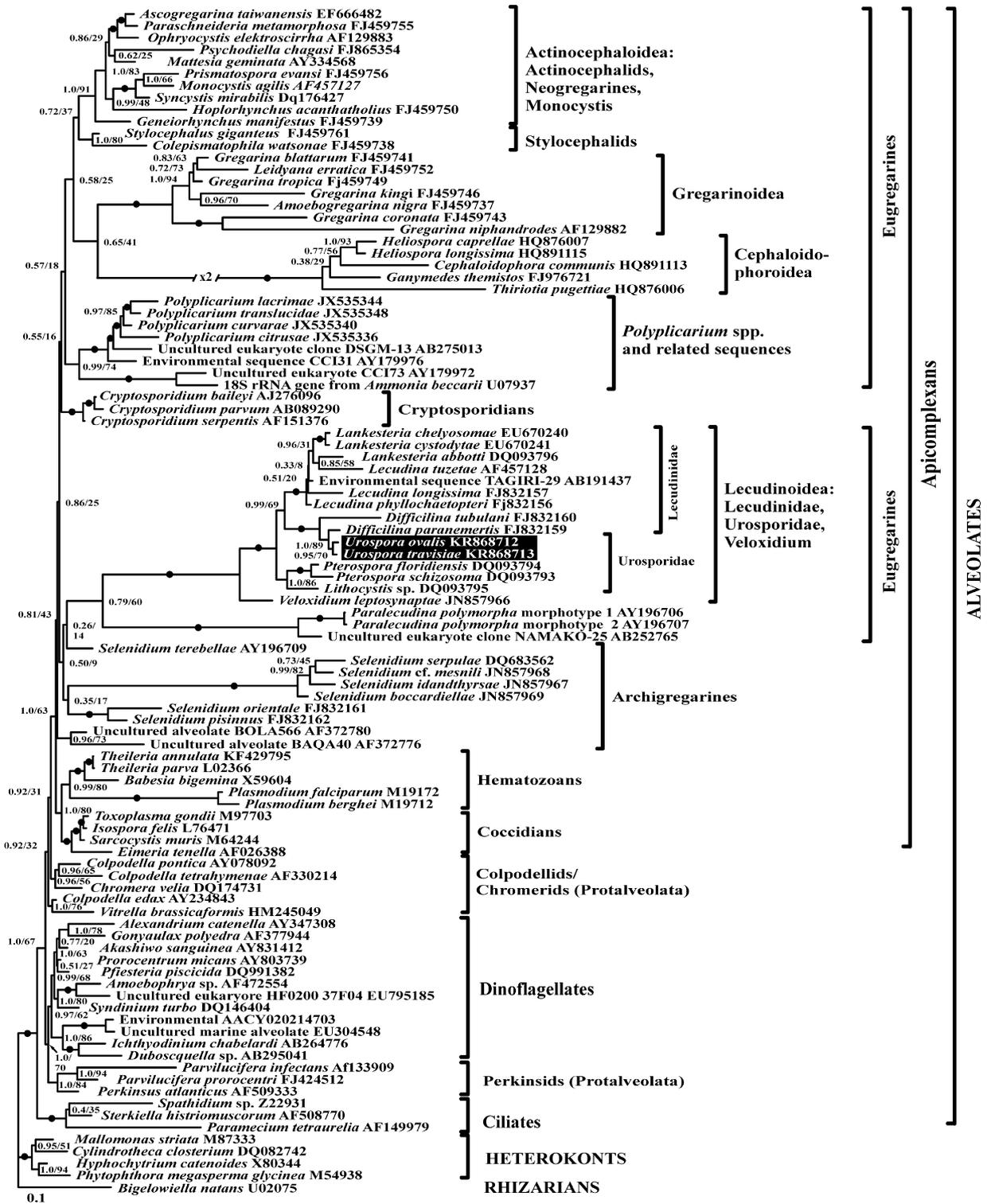
Figure 8. SSU rDNA Bayesian tree of alveolates (99 OTUs, alignment of 1557 bp) constructed using the GTR+Γ+I model. Numbers at the nodes denote Bayesian posterior probabilities (numerator) and ML bootstrap percentage (denominator). Black disks on the branches indicate the Bayesian posterior probabilities and the bootstrap percentages equal to or more than 0.95 and 95%, respectively. A black box highlights the sequences from *Urospora ovalis* and *U. travisiae*.
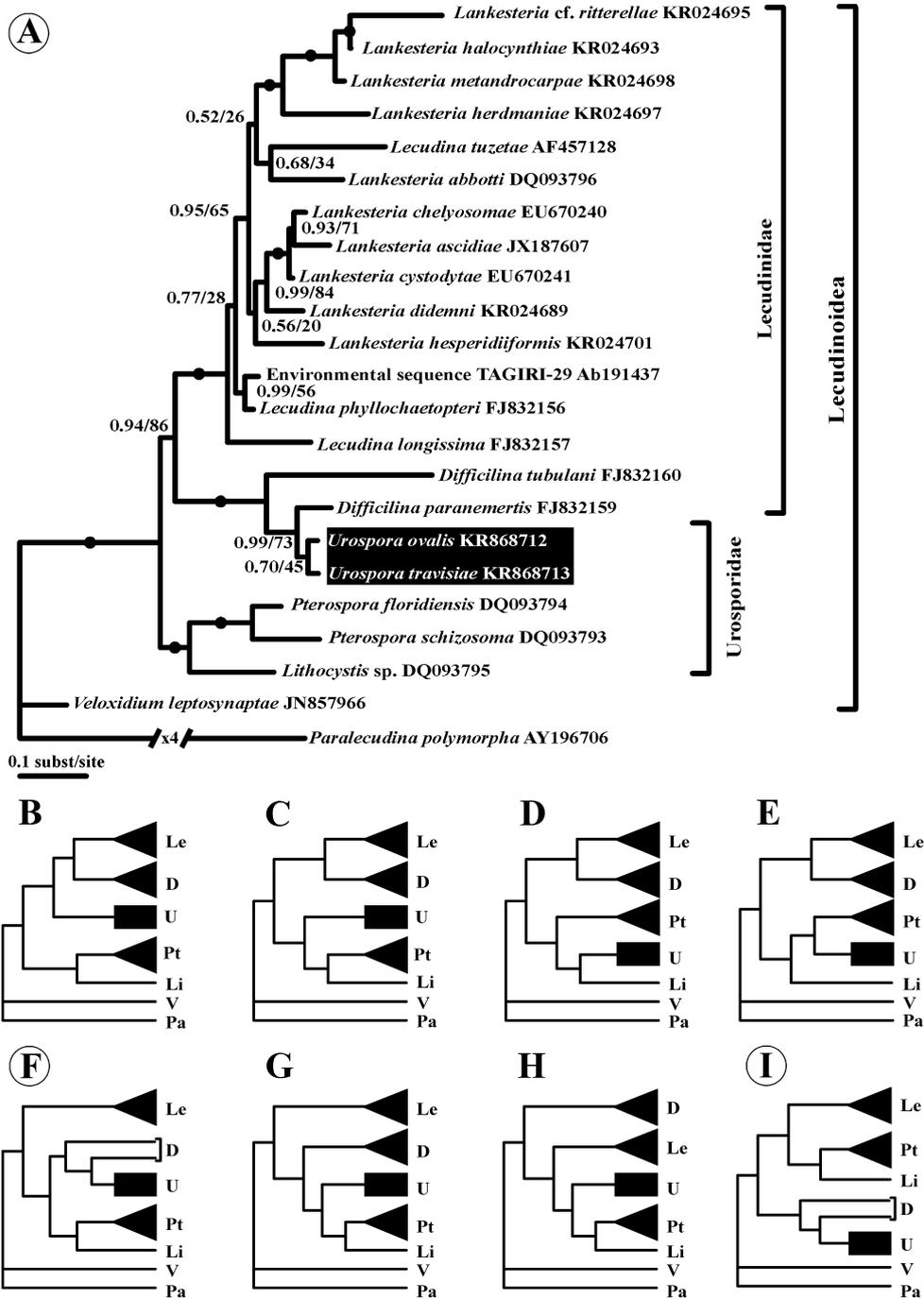
Figure 9. Results of topology tests of 23 selected lecudinid and urosporid sequences. **A**. SSU rDNA Bayesian tree of selected OTUs (alignment of 1676 bp) constructed using the GTR+Γ+I model (8 categories). Numbers at the nodes denote Bayesian posterior probabilities (numerator) and ML bootstrap percentage (denominator). A black box highlights the sequences from *Urospora ovalis* and *U. travisiae*; black disks on the branches indicate the Bayesian posterior probabilities and the bootstrap percentages equal to or more than 0.95 and 95%, respectively. **B** – **I**. alternative topologies which were tested together with tree A; there are just three permissible topologies: **A**, **F**, and **I,** marked by circles. Abbreviations: D = *Difficilina* spp., Le = *Lecudina* spp. + *Lankesteria* spp., Li = *Lithocystis* sp., Pa = *Paralecudina polymorpha*, Pt = *Pterospora* spp., U = *Urospora* spp., V = *Veloxidium leptosynaptae*.

could be fixed in their life cycle. It is an argument that supports the hypothesis that haemocoelic gregarines originated from intestinal ones in insects (Léger 1892). The explanation for such a transition is that phylogenetically related parasites, occupying different ecological niches in the host, decrease the intensity of species competition, and demonstrate diverse adaptations to parasitism (Wakeman et al. 2014).

Conclusions

This study revealed that the closely related eugregarines *Urospora ovalis* and *U. travisiae*, inhabiting the coelom of the polychaete *Travisia forbesii*, demonstrate different strategies of parasitism. The V-shaped cells of *U. travisiae* attach to the host and retain gliding motility when detached. In contrast, the cells of *U. ovalis* are oval-shaped, non-attached, and exhibit peristaltic activity. Both gregarines possess a typical organised cortex with epicytic folds of similar structure. In metabolic *U. ovalis*, the cell cortex generates superfolds in the contracted regions.

Methods

The cells of both gregarine species (*Urospora ovalis* and *Urospora travisiae*) were isolated from the coelom of the marine polychaete *Travisia forbesii* Johnston, 1840. The hosts were collected from June to July each year from 2004 to 2006 and in the second half of August each year from 2011 to 2013 at upper sublittoral of two sites: in the vicinity of the Marine Biological Station of Saint-Petersburg State University (inlet Yakovleva, Chupa Inlet, Kandalaksha Bay, White Sea, 66°18′99″N, 33°49′95″E) and the White Sea Biological Station of Moscow State University (Rugozerskaya Inlet, Kandalaksha Bay, White Sea, 66°33′12″N, 33°06′17″E).

The dissection of hosts and subsequent manipulation with parasites was performed under MBS-10 stereomicroscopes (LOMO, Russia). Light micrographs were provided using an MBR-1 microscope (LOMO, Russia) equipped with phase contrast and connected to a Canon EOS 300D digital camera. The gregarines of both species were isolated separately with thin glass pipettes, washed in Millipore filtered sea water (SW) (Millex-GC 0.22 μm) and subsequently prepared for light, electron microscopy and DNA extraction.

Histological procedure: Several entire worms were anesthetised and fixed in AFA (Alcohol–Formalin–Acetic Acid) fixative solution. The material was dehydrated through a graded alcohol series, cleared in xylene, infiltrated in a graded series of xylene/Histoplast II (3:1, 1:1, 1:3) and finally embedded in Histoplast II (Sigma-Aldrich, Czech Republic). Serial sections (transversal, sagittal, and coronal) of the fixed worms were prepared on a Microm HM 360 rotary microtome and stained with haematoxylin-eosin. Micrographs were obtained using an Olympus BX61 microscope equipped with an Olympus DP 71 digital camera.

Electron microscopy: The hosts were dissected and the parasites were collected separately from the host body cavity using thin glass pipettes. The trophozoites were fixed in 2% or 2.5% glutaraldehyde in 0.1 M cacodylate buffer (CB), 0.1 M PBS, or SW. For transmission electron microscopy the gregarines were then post-fixed with 1% OsO_4 (Os) in 0.2 M CB, 0.1 M PBS or SW, dehydrated in an ethanol series, and embedded into Epon blocks. The ultra-thin sections were stained according to standard protocols (Reynolds 1963) and observed with LEO-910 and JEOL-1010 transmission electron microscopes. For scanning electron microscopy, fixed trophozoites were critical point dried in liquid CO_2 and then coated with gold. The samples were observed with a JEOL JSM-7401F scanning electron microscope.

DNA isolation, PCR and sequencing: Individual trophozoites of each species, about 10 and 20 trophozoites of *Urospora ovalis* and *Urospora travisiae*, respectively, were isolated from dissected hosts, washed three times in Millipore filtered SW, and deposited into 0.5 ml microcentrifuge tubes. All samples were fixed and stored in RNA-later reagent (Life Technologies, USA). DNA extraction was performed with the Diatom DNA Prep 200 kit (Isogen, Russia).

The new partial SSU rDNA sequences (1623 bp for *U. travisiae* and 1603 bp for *U. ovalis*) were amplified with Encyclo PCR kit (Evrogen, Russia) using a T3000 Thermocycler (Biometra, Germany) according to the following protocol: initial denaturation at 95 °C for 3 min; 40 cycles of 95 °C for 30 sec, 45 °C for 30 sec, and 72 °C for 1.5 min; and a final extension at 72 °C for 10 min with primers 5′-GTAGTCATAYGCTTGTCTYGC-3′ (forward) and 5′- GATCCTTCTGCAGGTTCACCTAC -3′ (reverse). Only weak bands of an expected size were obtained by electrophoresis in agarose gel; therefore, small pieces of the gel were sampled from those bands (using pipette tips under a transilluminator) and re-amplification PCR with ColoredTaq DNA polymerase kit (Silex, Russia) using the DNA Engine Dyad thermocycler (Bio-Rad) and the same primers was performed.

PCR products of the expected size were gel isolated using a Cytokine DNA isolation kit (Cytokine, Russia) and sequenced using an ABI PRISM BigDye Terminator v. 3.1 reagent kit on an Applied Biosystems 3730 DNA Analyzer automatic sequencer. The newly obtained SSU rDNA sequences (GenBank Accession numbers: *Urospora ovalis* KR868712 and *Urospora travisiae* KR868713) were preliminarily identified by BLAST analysis including the built-in NJ-tree tool.

Molecular phylogenetic analysis: The two novel SSU rDNA sequences were aligned with 97 other SSU rDNA sequences, representing the major lineages of apicomplexans, as well as dinoflagellates, ciliates, heterokonts and rhizarians as outgroups, using the MUSCLE 3.6 programme (Edgar 2004) and manual tuning with the BioEdit 7.0.9.0 programme (Hall 1999). After removing hypervariable regions, the length of the alignment of the final 99 operational taxonomic units (OTUs) was 1557 sites. Bayesian analysis of this alignment was conducted using the MrBayes 3.2.1 programme (Ronquist and Huelsenbeck 2003). The programme was set to operate using the following parameters: nst = 6, ngammacat = 8, rates = invgamma, covarion = yes; parameters of Metropolis Coupling Markov Chains Monte Carlo (mcmc): nchains = 4, nruns = 4, temp=0.2, ngen = 7 000 000, samplefreq = 1 000, burninfrac = 0.5 (the first 50% of 7 000 sampled trees, i.e. the first 3500, were discarded in each run). An average standard deviation of split frequencies of 0.013232 was achieved at the end of calculations. Maximum-likelihood analysis of the 99 OTU alignment and calculations of Bayesian tree bootstrap support were performed with the RAxML 7.2.8 programme (Stamatakis 2006) under the GTR+Γ+I model with 4 categories of discrete gamma

distribution. The procedure included bootstrap analysis with 1000 replicates and 100 independent runs of ML analysis. All of these computations were performed using the University of Oslo Bioportal free service (www.bioportal.uio.no).

For the testing of alternative topologies, another alignment of 23 selected OTUs including lecudinids and urosporids (all available sequences from GenBank) was created. The sequences of *Veloxidium leptosynaptae* and *Paralecudina polymorpha* were used as outgroups for this analysis. This gave us the opportunity to include 119 additional nucleotides from hypervariable regions in the analyses, so that the final length of the alignment increased to 1676 bp. Topology tests for the 23 OTUs Bayesian tree were performed using the TREEFINDER programme under the same model as in the Bayesian analyses (GTR+Γ+I, 8 categories) (Jobb 2011; Jobb et al. 2004).

List of Abbreviations

BF – Bright Field light microscopy; CB – Cacodylate Buffer; DIC – Differential Interference Contrast microscopy; IMC – Inner Membrane Complex; H&E – Haematoxylin & Eosin staining; LM – Light Microscopy; ML – Maximum-likelihood analyses; MLS – Micropore-like structures; OTU – Operational Taxonomic Unit; PBS – Phosphate Buffered Saline; PC – Phase Contrast light microscopy; RDS – Rippled Dense Structure; SEM – Scanning Electron Microscopy; SW – Sea Water; TEM – Transmission Electron Microscopy

Author Contributions

AD and GGP conceived and designed the study, performed field sampling, carried out the research, performed the light and electron microscopic analyses, and wrote the manuscript. AD and TGS designed and performed the molecular-biology experiments and phylogenetic analyses. VVA provided the laboratory equipment, necessary reagents, and materials, and gave consultations. AV contributed to material collection and processing (2011-2013), to the light microscopic observations, and to the interpretation of microscopic data. All authors contributed to the writing of the manuscript, and read and approved the final manuscript.

Acknowledgements

Appendix A. Supplementary data

Supplementary data associated with this article can be found, in the online version, at http://dx.doi.org/10.1016/j.protis.2016.05.001.

References

Adl SM, Simpson AG, Lane CE, Lukes J, Bass D, et al. (2012) The revised classification of eukaryotes. J Eukaryot Microbiol **59**:429–493

Cavalier-Smith T (2014) Gregarine site-heterogeneous 18S rDNA trees, revision of gregarine higher classification, and

the evolutionary diversification of Sporozoa. Eur J Protistol **50**:472–495

Chobotar B, Scholtyseck E (1982) Ultrastructure. In Long PL (ed) The Biology of the Coccidia. University Park Press, BaltimoreUniversity Park Press, Baltimore, pp 101–165

Clopton RE (2009) Phylogenetic relationships, evolution, and systematic revision of the septate gregarines (Apicomplexa: Eugregarinorida: Septatorina). Comp Parasitol **76**:167–190

Cook TJP, Janovy J, Clopton RE (2001) Epimerite-host epithelium relationships among eugregarines parasitizing the damselflies *Enallagma civile* and *Ischnura verticalis*. J Parasitol **87**:988–996

Coulon P, Jangoux M (1987) Gregarine species (Apicomplexa) parasitic in the burrowing echinoid *Echinocardium cordatum*: occurrence and host reaction. Dis Aquat Org **2**:135–145

Coulon P, Jangoux M (1988) Coelomocyte Reaction Against *Lithocystis schneideri* (Apicomplexa: Sporozoea), a Gregarine Parasite of the Spatangoid Echinoid *Echinocardium cordatum*. In Burke RD, Mladenov PV, Lambert P, Parsley RL (eds) Echinoderm Biology. Rotterdam, Balkerna, pp 769–773

Coulon P, Jangoux M (1991) Cyclic occurrence of gregarine trophozoites (Apicomplexa) in the burrowing echinoid *Echinocardium cordatum* (Echinodermata, Spatangoidea). Dis Aquat Org **12**:71–73

Corbel JC, Desportes I, Théodoridès J (1979) Étude de *Gonospora beloneides* (Ming.) (=*Lobianchella beloneides* Ming.) (grégarine Urosporidae), parasite coelomique d'une Alciopidae (Polychaeta) et remarques sur d'autres grégarines d'Alciopidae. Protistologica **15**:55–65

Desportes I, Schrével J (eds) The Gregarines. The Early Branching Apicomplexa. Treatise on Zoology - Anatomy, Taxonomy, Biology. Brill, Leiden, Boston, pp 781

Desportes I, Vivarès C, Théodoridès J (1977) Intérêt taxonomique de l'ultrastructure épicytaire chez *Ganymedes* Huxley, *Porospora* Schneider et *Thiriotia* n. g., grégarines parasites de crustacés. Ann Sci Nat Zool **19**:261–277

De Ridder C, Jangoux M (1984) Intracoelomic parasitic Sporozoa in the burrowing spatangoid, *Echinocardium cordatum*: coelomocyte reaction and formation of brown bodies. Helgoländer Meeresunters **37**:225–231

Dogiel V (1906) Beiträge zur Kenntnis der Gregarinen. I. *Cystobia chiridotae* nov. sp. II. *Hyalosphaera gregarinicola* nov. gen. nova spec. Arch Protistenkd **7**:106–130

Dogiel V (1909) Beiträge zur Kenntnis der Gregarinen. III. Über die Sporocysten der Cölom-Monocystideae. Arch Protistenkd **16**:194–208

Dogiel V (1910) Beiträge zur Kenntnis der Gregarinen. IV. *Callynthrochlamys phronimae* Frenz. u. a. m. Arch Protistenkd **20**:60–78

Durchon M, Vivier E (1961) Déterminisme de la gamogonie chez une Grégarine parasite de *P. cultrifera* G. (Annelide Polychète). C R Acad Sci Paris **253**:318–320

Dyakin AY, Paskerova GG (2004) *Urospora chiridotae* (Sporozoa: Gregarinomorpha: Eugregarinida) – a neogamic parasite of sea cucumber *Chiridota laevis* (Echinodermata:

Holothuroidea: Apoda). Parazitologiya **38**:225–238 (in Russian with English summary)

Dyakin AY, Simdyanov TG (2005) The cortical zone of skittle-like cells of *Urospora chiridotae*, a gregarine from an apode holothuria *Chiridota laevis*. Protistology **4**: 97–105

Edgar RC (2004) MUSCLE: multiple sequence alignment with high accuracy and high throughput. Nucleic Acids Res **35**:1792–1797

Felsenstein J (1985) Confidence limits on phylogenies: an approach using the bootstrap. Evolution **39**:783–791

Frolov AO (1991) World fauna of gregarines. Family Monocystidae. Zool Inst Acad Sci USSR, Leningrad (in Russian with English summary)

Grassé PP (1953) Classe des Grégarinomorphes. In Grassé P-P (ed) Traité de Zoologie. Masson, Paris, pp 550–690

Hall TA (1999) BioEdit: a user-friendly biological sequence alignment editor and analysis program for Windows 95/98/NT. Nucleic Acids Symp Ser **41**:95–98

Hildebrand HF (1981) Elektronenmikroskopische Untersuchungen an den Entwicklungsstadien des Trophozoiten von *Didymophyes gigantea* (Sporozoa, Gregarinida). 3. Die Feinstruktur des Epizyten mit besonderer Berücksichtigung der kontraktilen Elemente. Z Parasitenkd **64**:29–46

Jobb G (2011) TREEFINDER version of March 2011. 2011. Munich, Germany. Distributed by the author at www.treefinder.de

Jobb G, von Haeseler A, Strimmer K (2004) TREEFINDER: A powerful graphical analysis environment for molecular phylogenetics. BMC Evol Biol **4**:18, http://dx.doi.org/10.1186/1471-2148-4-18

King CA (1981) Cell surface interaction of the protozoa Gregarina with concanavalin A beads. Implications for models for gregarine gliding. Cell Biol Int Rep **5**:297–305

King CA (1988) Cell motility of sporozoan protozoa. Parasitol Today **4**:297–305

Kishino H, Hasegawa M (1989) Evaluation of the maximum likelihood estimate of the evolutionary tree topologies from DNA sequence data, and the branching order in hominoidea. J Mol Evol **29**:170–179

Landers SC (1991) *Pterospora demodendrion* sp. nov. and *Pterospora clymenellae*, acephaline eugregarines from coastal North Carolina. Eur J Protistol **27**:55–59

Landers SC (2001) *Pterospora floridiensis*, a new species of acephaline gregarine (Apicomplexa) from the maldanid polychaete *Axiothella mucosain* St. Andrew Bay, Florida. Syst Parasitol **48**:55–59

Landers SC (2002) The fine Structure of the Gamont of *Pterospora floridiensis* (Apicomplexa: Eugregarinida). J Eukaryot Microbiol **49**:220–226

Landers SC, Gunderson J (1986) *Pterospora schizosoma*, a new species of aseptate gregarine from the coelom of *Axiothella rubrocincta* (Polychaeta, Maldanidae). J Protozool **33**:297–300

Landers SC, Leander BS (2005) Comparative surface morphology of marine coelomic gregarines (Apicomplexa,

Urosporidae): *Pterospora floridiensis* and *Pterospora schizosoma*. J Eukaryot Microbiol **52**:23–30

Leander BS (2008) Marine gregarines: evolutionary prelude to the apicomplexan radiation? Trends Parasitol **24**:60–67

Leander BS, Lloyd SAJ, Marshall W, Landers SC (2006) Phylogeny of marine gregarines (Apicomplexa) — *Pterospora*, *Lithocystis* and *Lankesteria* — and the origin(s) of coelomic parasitism. Protist **157**:45–60

Levine ND (1977) Checklist of the species of the aseptate gregarine family Urosporidae. Int J Parasitol **7**:101–108

Léger L (1892) Recherches sur les Grégarines. Tablettes Zoologiques **3**:1–182

Long PL (ed) The Biology of the Coccidia. Edward Arnold Press, London, pp 502

Mackenzie C, Walker MH (1983) Substrate contact, mucus, and eugregarines gliding. J Protozool **30**:3–8

MacMillan WG (1973) Conformation changes in the cortical region during peristaltic movements of a gregarine trophozoite. J Protozool **20**:267–274

Miles HB (1968) The fine structure of the epicyte of the acephaline gregarines *Monocystis lumbrici-olidi*, and *Nematocystis magna*: observations by electron microscope. Rev Iber Parasitol **28**:455–465

Mita K, Kawai N, Rueckert S, Sasakura Y (2012) Large-scale infection of the ascidian *Ciona intestinalis* by the gregarine *Lankesteria ascidiae* in an inland culture system. Dis Aquat Org **101**:185–195

Perkins FO, Barta JR, Clopton RE, Peirce MA, Upton SJ (2000) Phylum Apicomplexa Levine, 1970. In Lee JJ, Leedale GF, Bradbury P (eds) An Illustrated Guide to the Protozoa **Vol 1**, 2nd edn Society of Protozoologists, Lawrence, Kansas, USA, pp 190–369

Philippe M, Schrével J (1982) The three cortical membranes of the gregarines (parasitic protozoa). Characterization of the membrane proteins of *Gregarina blaberae*. Biochem J **201**:455–464

Pixell-Goodrich H (1915) On the life-history of the sporozoa of spatangoids, with observations on some allied forms. Quart J Microsc Sci **61**:84–106

Pixell-Goodrich H (1950) Sporozoa of *Sipunculus*. Quart J Microsc Sci **91**:469–476

Pomory CM, Lares MT (1998) *Gonospora holoflora* - a new species of gregarine protozoan parasite (Apicomplexa) in *Holothuria floridana* (Echinodermata, Holothuroidea) from the Florida-Keys. Bull Marine Sci **62**:213–218

Porchet E (1978) Etude de cinq sporozoaires parasitant un meme hote: l'annelide polychaete *Notomastus latericeus*. Protistologica **14**:59–76

Reynolds ES (1963) The use of lead citrate at high pH as an electron opaque stain in electron microscopy. J Cell Biol **17**:208–212

Ronquist F, Huelsenbeck JP (2003) MrBayes 3: Bayesian phylogenetic inference under mixed models. Bioinformatics **19**:1572–1574

Rueckert S, Chantangsi C, Leander BS (2010) Molecular systematics of marine gregarines (Apicomplexa) from Northeastern Pacific polychaetes and nemerteans, with descriptions of three novel species: *Lecudina phyllochaetopteri* sp. nov., *Difficilina tubulani* sp. nov. and *Difficilina paranemertis* sp. nov. Int J Syst Evol Microbiol **60**:2681–2690

Rueckert S, Villette PM, Leander BS (2011b) Species boundaries in gregarine apicomplexan parasites: a case study-comparison of morphometric and molecular variability in Lecudina cf. tuzetae (Eugregarinorida, Lecudinidae). J Eukaryot Microbiol **58**:275–283

Rueckert S, Simdyanov TG, Aleoshin VV, Leander BS (2011a) Identification of a divergent environmental DNA sequence clade using the phylogeny of gregarine parasites (Apicomplexa) from crustacean hosts. PLoS ONE **6**:e18163, http://dx.doi.org/10.1371/journal.pone.0018163

Rueckert S, Wakeman KS, Holger Jenke-Kodama H, Leander BS (2015) Molecular systematics of marine gregarine apicomplexans from Pacific tunicates, with descriptions of five novel species of *Lankesteria*. Int J Syst Evol Microbiol **65**:2598–2614

Scholtyseck E (1973) Ultrastructure. In Hammond DM, Long PL (eds) The Coccidia: *Eimeria, Isospora, Toxoplasma*, and Related Genera. University Park Press, Baltimore, MD, pp 81–144

Scholtyseck E, Mehlhorn H (1970) Ultrastructural study of characteristic organelles (paired organelles, micronemes, micropores) of Sporozoa and related organisms. Z Parasitenkd **34**:97–127

Schrével J (1964) Contribution à l'étude de trois Grégarines parasites d'Annélides Polychètes: *Lecudina elongata* Mingazzini, 1891; *Lecudina tuzetae* Schrével, 1963; *Gonospora varia* Léger, 1892. Arch Zool exp gén **104**:125–142

Schrével J (1971a) Contribution à l'étude à l'étude des selenidiidae parasites d'annélides Polychètes: II. ultrastructure de quelques trophozoites. Protistologica **7**:101–130

Schrével J (1971b) Observations biologiques et ultrastructurales sur les Selenidiidae et leurs consequences sur la systematique des Gregarinomorphes. J Protozool **18**:448–470

Schrével J, Caigneaux E, Gros D, Philippe M (1983) The three cortical membranes of the gregarines. I. Ultrastructural organization of *Gregarina blaberae*. J Cell Sci **61**:151–174

Shimodaira H (2002) An approximately unbiased test of phylogenetic tree selection. Syst Biol **51**:492–508

Shimodaira H, Hasegawa M (1999) Multiple comparisons of log-likelihoods with applications to phylogenetic inference. Mol Biol Evol **16**:1114–1116

Siedlecki M (1903) Quelques observations sur les rôles des amibocytes dans le coelome d'une Annélide. Ann Inst Pasteur **17**:449–462

Simdyanov TG (1995a) An ultrastructure of two species of gregarines of the genus *Lankesteria* (Eugregarinida: Lecudinidae). Parazitologiya **29**:424–432 (in Russian with English summary)

Simdyanov TG (1995b) Two new species of gregarines with the aberrant structure of epicyte from the White Sea. Parazitologiya **29**:305–315 (in Russian with English summary)

Simdyanov TG (2009) *Difficilina cerebratuli* gen. et sp. n. (Eugregarinida: Lecudinidae) - a new gregarine species from the nemertean *Cerebratulus barentsi* (Nemertini: Cerebratulidae). Parazitologiya **43**:273–287 (In Russian with English summary)

Simdyanov TG, Diakin AY, Aleoshin VV (2015) Ultrastructure and 28S rDNA phylogeny of two gregarines: *Cephaloidophora* cf. *communis* and *Heliospora* cf. *longissima* with remarks on gregarine morphology and phylogenetic analysis. Acta Protozool **54**:241–263

Stamatakis A (2006) RAxML-VI-HPC: maximum likelihood-based phylogenetic analyses with thousands of taxa and mixed models. Bioinformatics **22**:2688–2690

Strimmer K, Rambaut A (2002) Inferring confidence sets of possibly mis-specified gene trees. Proc R Soc Lond B **269**:137–142

Valigurová A (2012) Sophisticated adaptations of *Gregarina cuneata* (Apicomplexa) feeding stages for epicellular parasitism. PLoS ONE **7**:e42606, http://dx.doi.org/10.1371/journal.pone.0042606

Valigurová A, Vaškovicová N, Musilová N, Schrével J (2013) The enigma of eugregarine epicytic folds: where gliding motility originates? Front Zool **10**:57, http://dx.doi.org/10.1186/1742-9994-10-57

Vávra J, Small EB (1969) Scanning electron microscopy of gregarines (Protozoa, Sporozoa) and its contribution to the theory of gregarine movement. J Protozool **16**:745–757

Vegni Talluri M, Dallai R (1983) Freeze-fracture study of the gregarine trophozoite: II. Evidence of "rosette" organization on cytomembranes in relation with micropore structure. Boll Zool **50**:245–255

Vinckier D (1969) Organisation ultrastructurale corticale de quelques Monocystidées parasites du ver Oligochète *Lumbricus terrestris* L. Protistologica **5**:505–517

Vinckier D, Vivier E (1968) Organisation ultrastructurale corticale de la Grégarine *Monocystis herculea*. C R Acad Sci D **266**:1737–1739

Vivier E (1968) L'organisation ultrastructurale corticale de la Grégarine *Lecudina pellucida*; ses rapports avec l'alimentation et la locomotion. J Protozool **5**:230–246

Vivier E, Devauchelle G, Petitprez A, Porchet-Henneré E, Prensier G, Schrével J, Vinckier D (1970) Observations de cytologie comparée chez les Sporozoaires. I.- Les structures superficielles chez les formes végétatives. Protistologica **6**:127–150

Wakeman KC, Leander BS (2012) Molecular phylogeny of pacific archigregarines (Apicomplexa), including descriptions of *Veloxidium leptosynaptae* n. gen., n. sp., from the sea cucumber *Leptosynapta clarki* (Echinodermata), and two new species of *Selenidium*. J Eukaryot Microbiol **59**:232–245

Wakeman KC, Reimer JD, Jenke-Kodama H, Leander BS (2014) Molecular phylogeny and ultrastructure of *Caliculium glossobalani* n. gen. et sp. (Apicomplexa) from a Pacific *Glossobalanus minutus* (Hemichordata) confounds the relationships between marine and terrestrial gregarines. J Eukaryot Microbiol **61**:343–353, http://dx.doi.org/10.1111/jeu.12114

Walker MH, Lane NJ, Lee WM (1984) Freeze-fracture studies on the pellicle of the eugregarine, *Gregarina garnhami* (Eugregarinida, Protozoa). J Ultrastruct Res **88**:66–76

Warner FD (1968) The fine structure of *Rhynchocystis pilosa* (Sporozoa, Eugregarinida). J Protozool **15**:59–73

7.7

Schrével J., **Valigurová A.**, Prensier G., Chambouvet A.,

Florent I., Guillou L.

2016

**Ultrastructure of *Selenidium pendula*,
the type species of archigregarines, and phylogenetic relations
to other marine Apicomplexa**

Protist

ORIGINAL PAPER

Ultrastructure of *Selenidium pendula*, the Type Species of Archigregarines, and Phylogenetic Relations to Other Marine Apicomplexa

Joseph Schrével[a,1], Andrea Valigurová[b], Gérard Prensier[c,2], Aurélie Chambouvet[d], Isabelle Florent[a], and Laure Guillou[e]

[a]Unité Molécules de Communication et Adaptation des Microorganismes, (MCAM, UMR 7245), Muséum National Histoire Naturelle, Sorbonne Universités, CNRS, CP 52, 57 Rue Cuvier, 75005 Paris, France
[b]Department of Botany and Zoology, Faculty of Science, Masaryk University, Kotlářská 2, 611 37 Brno, Czech Republic
[c]Cell Biology and Electron Microscopy Laboratory, François Rabelais University, 10 Boulevard Tonnellé, BP 3223, 37032 Tours Cedex, France
[d]Laboratoire des Sciences de l'Environnement Marin (LEMAR), UMR6539 UBO/CNRS/IRD/IFREMER, Institut Universitaire Européen de la Mer (IUEM), Technopole Brest Iroise, 29280 Plouzané, France
[e]Sorbonne Universités, Université Pierre et Marie Curie - Paris 6, CNRS, UMR 7144, Station Biologique de Roscoff, Place Georges Teissier, CS90074, 29688 Roscoff cedex, France

Archigregarines, an early branching lineage within Apicomplexa, are a poorly-known group of invertebrate parasites. By their phylogenetic position, archigregarines are an important lineage to understand the functional transition that occurred between free-living flagellated predators to obligatory parasites in Apicomplexa. In this study, we provide new ultrastructural data and phylogenies based on SSU rDNA sequences using the type species of archigregarines, the Selenidiidae *Selenidium pendula* Giard, 1884. We describe for the first time the syzygy and early gamogony at the ultrastructural level, revealing a characteristic nuclear multiplication with centrocones, cryptomitosis, filamentous network of chromatin, a cyst wall secretion and a 9+0 flagellar axoneme of the male gamete. *S. pendula* belongs to a monophyletic lineage that includes several other related species, all infecting Sedentaria Polychaeta (Spionidae, Sabellariidae, Sabellidae and Cirratulidae). All of these *Selenidium* species exhibit similar biological characters: a cell cortex with the plasma membrane - inner membrane complex - subpellicular microtubule sets, an apical complex with the conoid, numerous rhoptries and

[1]Corresponding author; fax +33 1 40 79 34 99
[2]This work is dedicated to the memory of Brigitte Arbeille-Brassart.
e-mail schrevel@mnhn.fr (J. Schrével).

micronemes, a myzocytosis with large food vacuoles, a nuclear multiplication during syzygy and young gamonts. Two other distantly related *Selenidium*-like lineages infect Terebellidae and Sipunculida, underlying the ability of archigregarines to parasite a wide range of marine hosts.

Key words: Archigregarines; Apicomplexa; *Selenidium pendula*; ultrastructure; phylogeny; sporozoite.

Introduction

Apicomplexa, a large subgroup of the Alveolata, are unicellular parasites infecting a wide range of invertebrate and vertebrate hosts. Most known Apicomplexa belong to Coccidia and Haemosporidia and are involved in human and veterinary diseases (malaria, toxoplasmosis, coccidiosis, babesiosis, piroplasmosis). However, a very large group of the early branching Apicomplexa, the gregarines, is comparatively poorly known. Most of the gregarines infect invertebrate hosts and usually do not have deleterious effects on their hosts (Desportes and Schrével 2013). The number of Apicomplexa species is estimated to be ~2,000-6,000, however the ability of gregarines to infect a wide range of insects could significally enhance this estimation to several thousand or more than one million (e.g., the Coleoptera (beetles) class corresponds to about 40% of the insect biodiversity with an expected species number around 1 to 2 million) (Schrével and Desportes 2013).

All apicomplexan species are characterized by an infective life stage, the so-called zoite, a polarized cell with an original apical complex. This apical complex is an assembly of specific organelles including club-shaped rhoptries, filament-like micronemes, dense granules and apical polar rings. In Apicomplexa, the presence of a conoid in the apex of the zoite, observed in coccidia and gregarines, defines the Conoidasida Levine, 1988. In contrast, no conoid is observed in Haemosporidia and Piroplasmida designated Aconoidasida Mehlhorn et al., 1980. Except gregarines and some other taxa developing in epicellular localization, such as cryptosporidia, most Apicomplexa have an intracellular development in their host cells and there, the apical organelles as well as the conoid, play an essential role in cell invasion processes through sophisticated cascades of molecular interactions (Boothroyd and Dubremetz 2008; Bradley et al. 2005; Santos et al. 2009). In Apicomplexa displaying an intracellular life style, the cycle usually occurs in two hosts, the sexual phase being performed in the definitive host while asexual phases occur in one or several host

intermediate hosts. Gametogenesis, as observed in Coccidia or Haemosporidia, exhibits a clear anisogamy with production of small flagellated male gametes (microgametes) and large non-flagellated female gametes (macrogametes). After fertilization, the sporogony produces sporozoites in the definitive hosts while asexual schizogny or merogony, producing merozoites, is realized in intermediate hosts. In contrast, most gregarines exhibit an extracellular development and their entire life cycle usually occurs within a single host. Their zoites transform into large vegetative cells, the trophozoites, with an extraordinary diversity in their morphologies and behaviours. In addition to this extracellular development, gregarines share a unique sexual phase. The sexual association between two gamonts, named syzygy, produces a cyst where the gametogenesis differentiates a large and equal number of male and female gametes; at this stage, this cyst is called a gametocyst. Then, fertilization and sporogenesis take place within the cyst yielding the final stages with the sporocysts usually containing each 8 sporozoites. These sporocysts can survive for a long period generally waiting for their ingestion by their specific hosts. Gregarine biochemistry and physiology are still poorly documented. Studies of their zoite apical apparatus as well as of the variation of their cytoskeleton and microtubule organizing centers (MTOCs), with unique organization as the 6+0 or 3+0 flagellar axonemes described for some male gametes (Prensier et al. 1980; Schrével and Besse 1975), contributed, however, to a more general understanding of many biological aspects of Apicomplexa including pathogenic species.

Among Apicomplexa, there is a consensus on the stem group of archigregarines commonly found in Polychaeta, Sipunculida and some Hemichordata. These marine gregarines represent the earliest diverging lineage of Apicomplexa (Leander 2007a; Schrével 1971b). The type species of archigregarines is *Selenidium pendula* Giard 1884 and its life cycle was established during the second part of the 20th century (Schrével 1966, 1970). Beside this type species, a long series

of contributions have been performed on other *Selenidium* and related species at the cytological (Brasil 1907, Caullery and Mesnil 1899, 1900, Ray 1930, Reed 1933) and ultrastructural (Leander 2006, 2007b; Macgregor and Thomasson 1965; Schrével 1968, 1970, 1971a; Simdyanov and Kuvardina 2007, Vivier and Schrével 1964, 1966) levels and more recently also at the molecular level through the analysis of SSU rDNA sequences (Leander et al. 2003a; Leander 2006, 2007b; Rueckert and Leander 2009; Wakeman and Leander 2012, 2013; Wakeman et al. 2014). Most of these studies focused on the trophozoite stages with few descriptions on nutrition modalities (Schrével 1968; Simdyanov and Kuvardina 2007). Additionally, these studies highlighted several incongruities among Selenidiidae at the molecular level that could not be elucidated in absence of the type species of the family. Here, we report on the cell organization of the *Selenidium pendula* trophozoite with a special attention to the conoid, the abundance of rhoptries and micronemes, and we provide the first ultrastructural description of the syzygy (pairing stage), the early gamogony with the cryptomitosis and the secretion of the cyst walls. We also provide the first phylogenetic analysis of the SSU rDNA gene sequences encompassing the type species of archigregarines *S. pendula*. Molecular phylogenetic analyses revealed three lineages within archigregarines, *S. pendula* belonging to the Selenidiidae that includes parasites of Spionidae, Sabellidae, and Sabellariidae, all polychaete annelids, as well as two Selenidiidae–like lineages, parasites of hosts belonging to Terebellidae and Sipunculida, respectively.

Results

The Trophozoite of *Selenidium pendula*

The mature *S. pendula* trophozoite is a crescent-shaped cell of about 150 μm in length with a circular cross section of about 35 μm in diameter. The cell surface exhibits about 30 striations in phase contrast light microscopy as well as in scanning electron microscopy (SEM), appearing as a series of longitudinal bulges of about 2.5-3 μm in width separated by grooves (Fig. 1A). The trophozoite is inserted into the intestinal epithelium of the *Scolelepis squamata* polychaete worm by a special apical apparatus called the mucron (Figs 1B, 2A-C). In transmission electron microscopy (TEM), a tropism for host cells rich in granules can be observed (Fig. 1B). The mucron of *S. pendula* corresponds to the attachment apparatus anchoring the parasite to the host epithelial cell. In SEM, the mucron appears as a regular mammiliform area without bulges and grooves (Fig. 2A). After detachment of the trophozoite, the trace of the mucron in the host cell is very regular with sometimes a small hole in a subcentral position (Fig. 2B).

A series of short microvilli is seen at the periphery of the epithelial cells (Fig. 2B). All around the trophozoite attachment, numerous long ciliary structures of the host epithelium are observed (Figs 1A, 2B).

Asexual schizogony in *S. pendula* could be an explanation to the exceptional clotting of trophozoites, with thousands and thousands of cells that obstruct the intestinal lumen of some *Scolelepis squamata* hosts. In vivo, trophozoites are dispersed along the host intestine, except for the first thirty segments. The distinction between these two intestinal regions is facilitated by the yellow color of the first segments versus the green color of the posterior region. Motility of the *S. pendula* trophozoites is clearly of pendular type, as proposed by Giard (1884) for the species diagnosis, and the stroboscopic records show regular pendular beats with a period of about 0.2 second (Golstein and Schrével 1982).

In TEM cross sections, the bulges of *S. pendula* exhibit a characteristic ultrastructure described for the first time in *Selenidium hollandei* (Vivier and Schrével 1964). The plasma membrane is underlain by a regular flat vesicle designated as the inner membrane complex (imc) while a very slight cell coat covers the cell surface. Under these three cortical membranes, a regular set of longitudinal subpellicular microtubules and some other dispersed microtubules within the cortical cytoplasm are seen below the bulges but not in the area of the grooves (Fig. 3B-C). In TEM cross sections, each subpellicular microtubule of *S. pendula* is surrounded by an electron-lucent sheath (Fig. 3C) as observed in *S. hollandei* (Vivier and Schrével 1964), *Platyproteum (Selenidium) vivax* (Leander 2006), *Selenidium serpulae* (Leander 2007b) and *Selenidium terebellae* (Wakeman et al. 2013). Abundant mitochondria are present under the subpellicular network of the bulges.

Different ectoplasmic structures along the grooves are observed with lamellar elements, dense material structures that crossed the imc and are in contact with the plasma membrane (Fig. 3B, D-F). Under SEM, series of holes are observed in the grooves with an irregular distribution and distances ranging from 0.3-0.4 μm to 0.8-0.9 μm
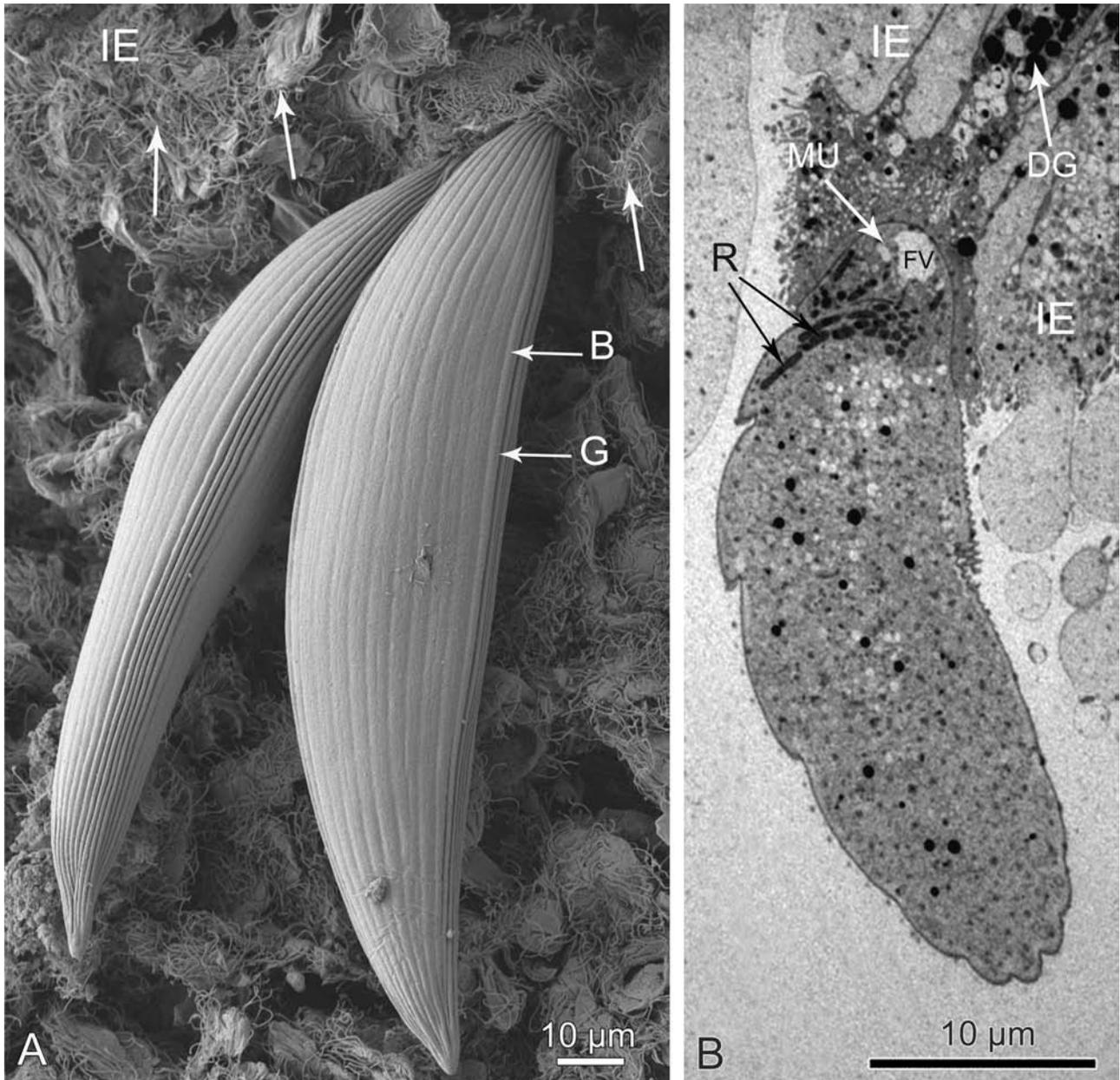
Figure 1. Scanning and transmission electron microscopy of *Selenidium pendula* trophozoites fixed to the intestine of the polychaete worm *Scolelepis squamata* (**A-B**). Abbreviations: bulge (B), dense granule (DG), food vacuole (FV), groove (G), intestinal epithelium (IE), mucron (MU), rhoptry (R). **A.** SEM micrograph of trophozoites with their apical region inserted into the intestinal epithelium, exhibiting on this face about 18 longitudinal bulges separated by grooves. The long filamentous structures covering the intestinal epithelium correspond to ciliary structures (arrows). **B.** Longitudinal TEM section of a trophozoite with the apical end designated as mucron containing a food vacuole and numerous rhoptries. In the intestinal epithelium, the trophozoite preferentially anchors to the host cells enriched in dense granules having mucous secretions.

(Fig. 3A). Such a distribution seems to correspond to the opening sites of the above-mentioned ectoplasmic structures and their density might indicate a role that was previously underestimated.

Interestingly, the longitudinal microtubular bundles, abundantly distributed beneath the cortex in the trophozoite apical part corresponding to the mucron, could represent the biogenesis site of the
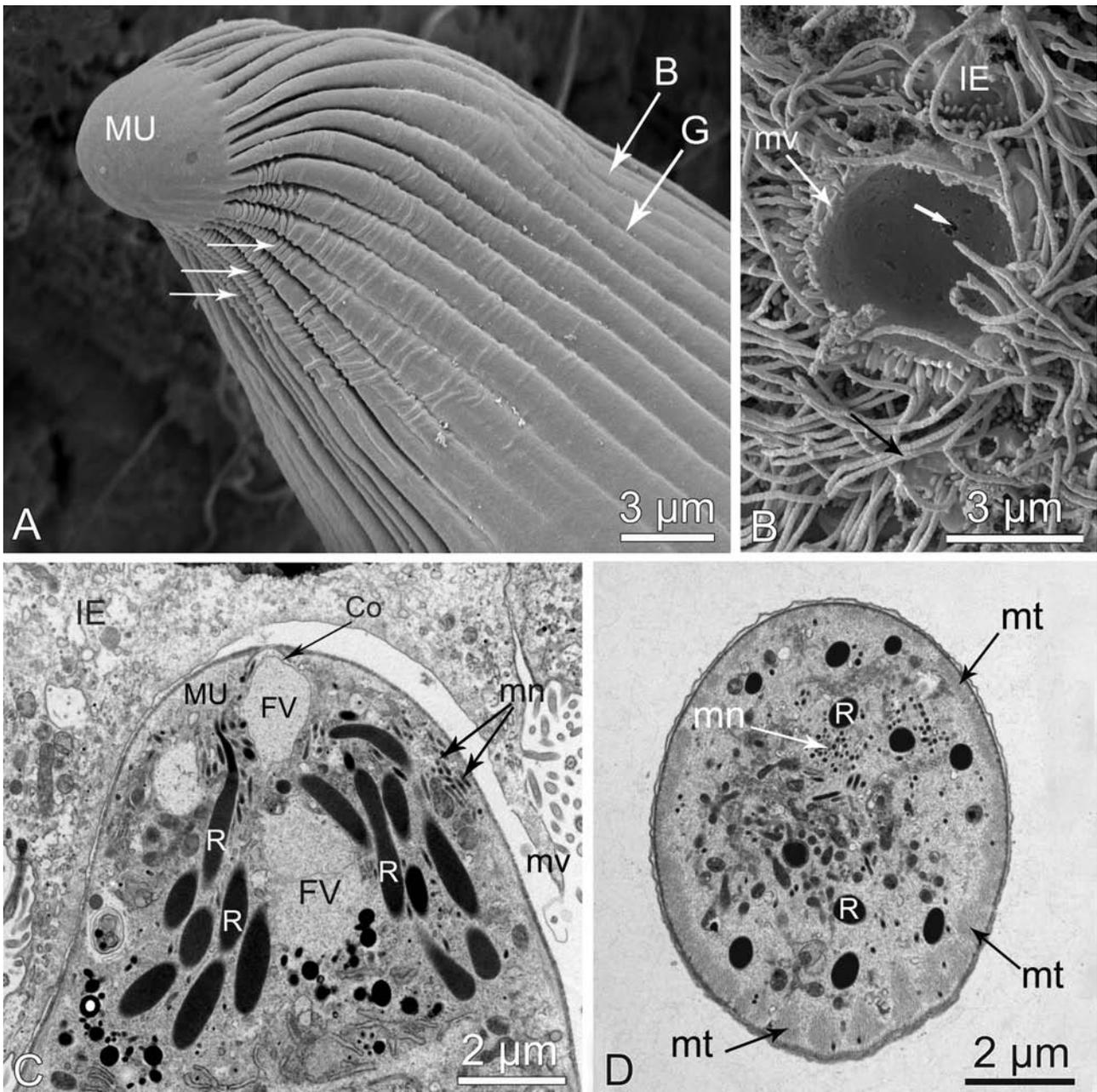
Figure 2. Apex of the *Selenidium pendula* trophozoite (**A-D**). Abbreviations: bulge (B), conoid (Co), food vacuole (FV), groove (G), intestinal epithelium (IE), microneme (mn), microtubules (mt), microvilli (mv), mucron (MU), rhoptry (R). **A.** SEM micrograph of the apex surface showing that bulges and grooves of the epicyte start from a regular mammiliform area corresponding to the external surface of the mucron. Small folds (arrows) are observed on the bulges located on the internal curvature of the cell **B.** SEM micrograph of intestinal epithelium after the detachment of a mucron, with small microvilli on the periphery, a small hole in the subcentral position (white arrow) and the long ciliary structures (black arrow). **C.** TEM micrograph of a median longitudinal section of the apex with several food vacuoles that enter via the conoid and are surrounded by an accumulation of rhoptries and micronemes. **D.** TEM longitudinal section of the apical region (= trophozoite apex with numerous micronemes and rhoptries) revealing that the subpellicular microtubule bundles start before the differentiation of the epicytic bulges of the cell surface.
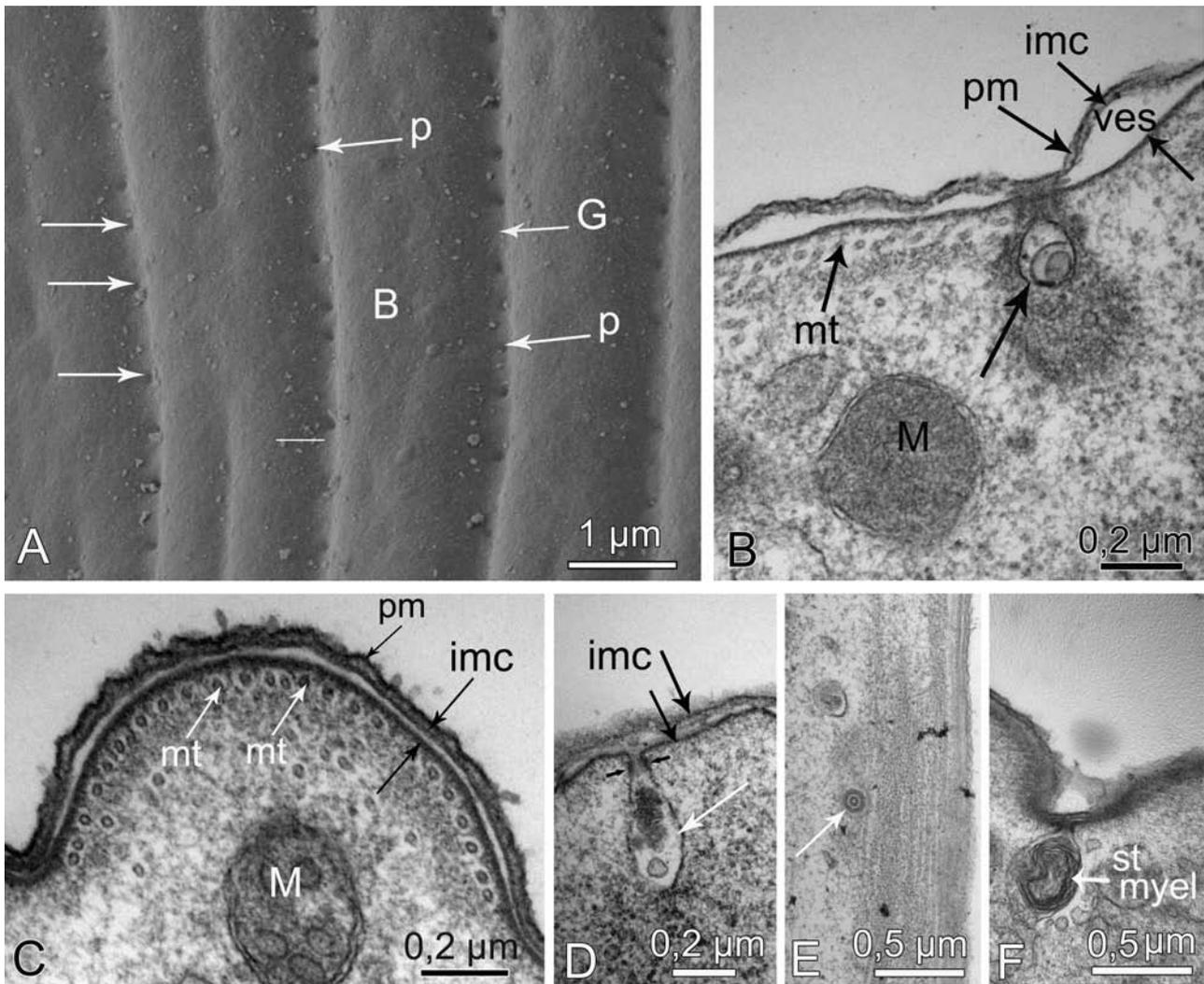
Figure 3. Cell surface and cortex of *Selenidium pendula* trophozoite **(A-F).** Abbreviations: bulge (B), groove (G), inner membrane complex (imc), microneme (mn), microtubules (mt), mitochondrion (M), myelin-like structure (st myel), plasma membrane (pm), pore (p), rhoptry (R), vesicle (ves). **A.** SEM view of the cell surface with the apertures of pores along the grooves (arrows). **B-F.** TEM cross sections of the cortex with the plasma membrane, the dilated inner membrane complex and the subpellicular microtubules under the epicytic bulges (C). In cross section, each microtubule is surrounded by a white hexagonal area. Ectoplasmic organelles in the grooves, connected to the cortical membranes via the imc, contain lamellar structures (arrow in B) or dense material (white arrow in D). These organelles form an annular ring in cross section parallel to the cell surface (white arrow in E) corresponding to the cross section of a micropore or myelin-like structures (F).

longitudinal networks of the subpellicular microtubules (Fig. 2D).

Conoid and Myzocytosis

The conoid of *S. pendula* is a truncated cone of about 225 nm height, with apical and distal diameters about 260 nm and 1 μm respectively (Fig. 4A-C). In TEM cross sections, the diameter of filaments is about 23-32 nm; 9 sections are well identified in one side of the conoid, while only an opaque layer can be observed on the other side due to their spiral organization (Fig. 4B-C). This structure is quite similar to the well-described conoid of *Toxoplasma gondii* (Hu et al. 2002, 2006) but the apical polar ring is not present in the distal part of *S. pendula* mucron and the preconoidal rings are not clearly identified in its apical part but a dilatation of the imc and the ends of the subpellicular microtubules are unambiguously demonstrated (Fig. 4A,
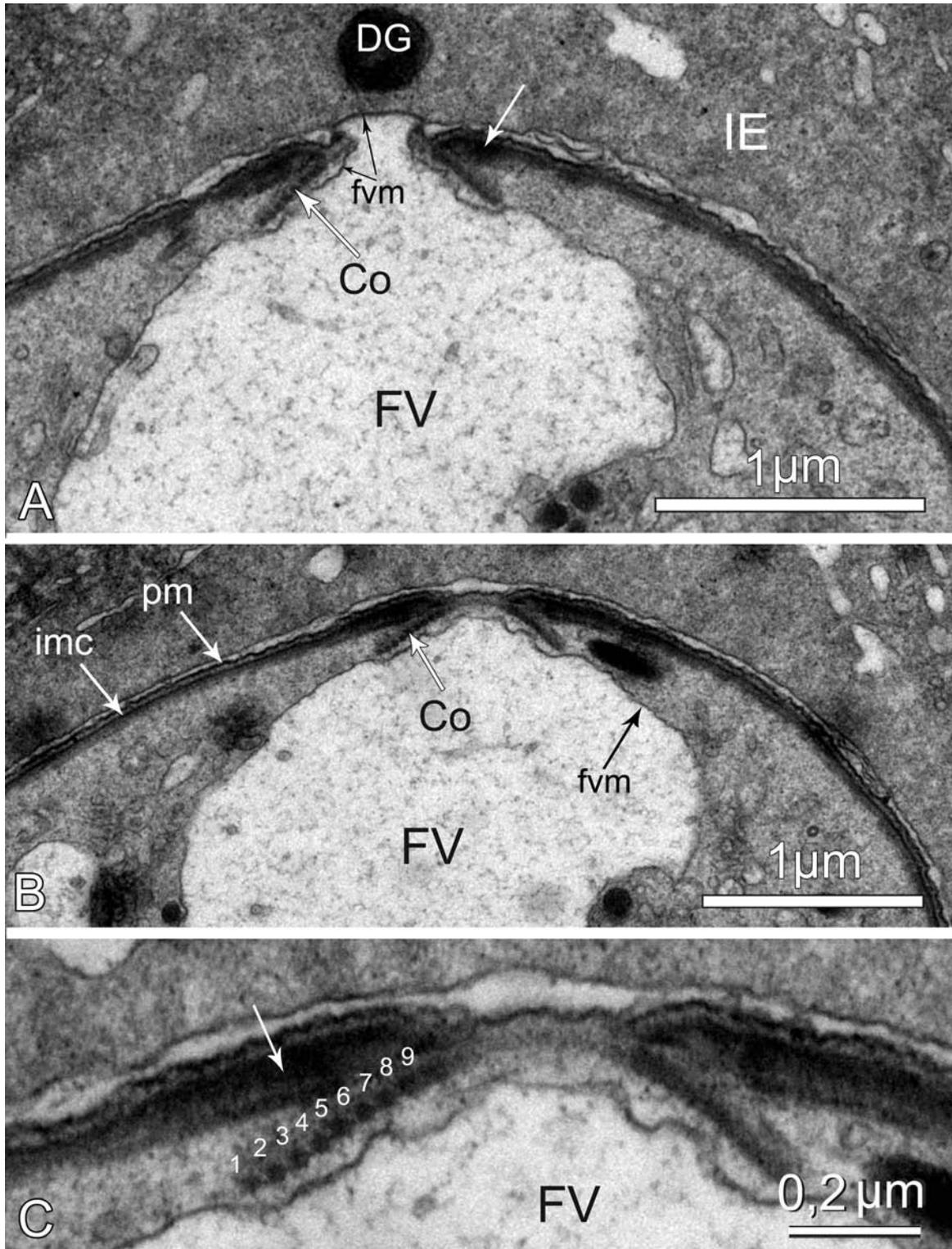
Figure 4. Conoid in the *Selenidium pendula* mucron **(A-C).** Abbreviations: dense granule (DG), conoid (Co), food vacuole (FV), food vacuole membrane (fvm), inner membrane complex (imc), host intestinal epithelium (IE), parasite plasma membrane (pm). **A-B.** Two longitudinal sections of the *S. pendula* mucron, showing the conoid structure and the opening, allowing a contact between the fvm and the host cell, visible in **A. C.** High magnification showing the 9 cross sections of the microtubular network forming the conoid.

C, white arrows). This imc dilatation could correspond to a site of a Microtubule Organizing Center (MTOC) able to generate the subpellicular microtubules since abundant bundles are found in the anterior area of the trophozoite (Fig. 2D). In few TEM cross sections, dense structures corresponding to the neck of the rhoptries are observed inside the conoid (Fig. 2C).

Myzocytosis, the predatory mode of nutrition characteristic of archigregarines, is clearly illustrated in *S. pendula* with food vacuoles inserted inside the conoid (Figs 2C, 4A-B). In the axis of the mucron, one or several clear food vacuoles, likely formed via the conoid, are present (Fig. 2C). These food vacuoles are surrounded by many rhoptries and micronemes, two apical organelles characteristic of zoites (Figs 1B, 2C). As shown by the continuity of the food vacuole membrane up to its contact with the host epithelial cell, an evagination process through the apex of the conoid has occurred, allowing the parasite to suck out the nutriments from the host. This myzocytosis process starts at the top of the conoid (Fig. 4A). The food vacuoles are large, reaching sometimes up to 7 μm, and several additional food vacuoles of about 2 or 3 μm are observed in the axis of the trophozoite (Figs 2C, 5A-B). The lumen of the food vacuoles has a low electron-dense aspect with some vesicles and the membrane of the food vacuole exhibits a very irregular border with numerous digitations.

Vital staining with low concentrations of neutral red (1 $^0/_{00}$) allowed to visualize large vacuoles of about 4x2 μm located in the apex of the *S. pendula* trophozoite with several small vesicles (data not shown). This observation is in agreement with a fragmentation of the initial food vacuole into numerous vacuoles present in the anterior part of the trophozoite (Fig. 5A).

Rhoptries, Micronemes, and Intrareticular Granules in Trophozoites

In addition to the conoid, the apical end of *S. pendula* trophozoites exhibits about 8-10 rhoptries corresponding to the long, electron-dense club-shaped, tubular or saccular organelles. They appear in the trophozoite as cylindrical organelles reaching up to 6 μm in length, with a diameter of 0.3-0.4 μm in the basal bulbous. At the apex, a rhoptry neck could be observed. The rhoptry orientation usually follows the direction of the conoid. In some cases, the rhoptry neck penetrates the conoid (Fig. 2C).

The rough endoplasmic reticulum (RER) and the Golgi apparatus of *S. pendula* show an original association between the swollen cisternae containing numerous intrareticular granules of about 0.5-1 μm and the first saccule of the cis-region of the Golgi apparatus (Fig. 6D). Similar associations are observed in *S. hollandei* (Vivier and Schrével 1966) but not in Selenidiidae species parasitizing Cirratulidae (Schrével 1971a), Serpulidae (Leander 2006), Terebellidae (Wakeman et al. 2014) or Sipunculida (Simdyanov and Kuvardina 2007, Leander 2006). Some micrographs show an accumulation of numerous micronemes close to the nuclear envelope (Fig. 7D) or to the Golgi apparatus (Fig. 6C) with annular sections likely corresponding to the neck of micronemes (Fig. 6B). The relation of these RER-Golgi apparatus to the biogenesis of the rhoptries and/or the micronemes is not clear, since numerous micronemes are mixed with large rhoptries (Fig. 6A).

Nucleus and the Perinuclear Cytoplasm

The ovoid nucleus of the *S. pendula* trophozoite is characterized by the presence of a large spherical nucleolus of about 4-5 μm in diameter (Fig. 7A). No accumulation of chromatin is observed in the nucleoplasm and the nuclear envelope lacks the nuclear lamina as observed in *S. hollandei* (Schrével 1971a; Vivier 1967). The nuclear envelope, typically comprising two membranes, is rich in nuclear pores (about 5 per μm) regularly distributed all over the entire nuclear surface (Fig. 7C). In tangential sections, the pores appear as rings of about 100-110 nm in their largest diameter with the presence of a central particle of about 10 nm in diameter (Fig. 7C).

The periphery of the nucleus exhibits a special cytoplasmic area comprising a regular, 0.5 μm thick fibrillar zone, lacking any organelle, and surrounding the nucleus in a distance of 1.5-2 μm from the nuclear envelope (Fig. 7A-B, E). This fibrillar zone corresponds to the axial ducts described in living cells (Schrével 1970).

Apicoplast-like Organelles

In the trophozoite of *S. pendula*, organelles with four membranes are frequently observed (Fig. 5C) and they appear morphologically similar to the apicoplast of *Toxoplasma* and *Plasmodium* (Lim and McFadden 2010) with some dense structures (Fig. 5D) or in contact with multilamellar organelle (Fig. 5E).
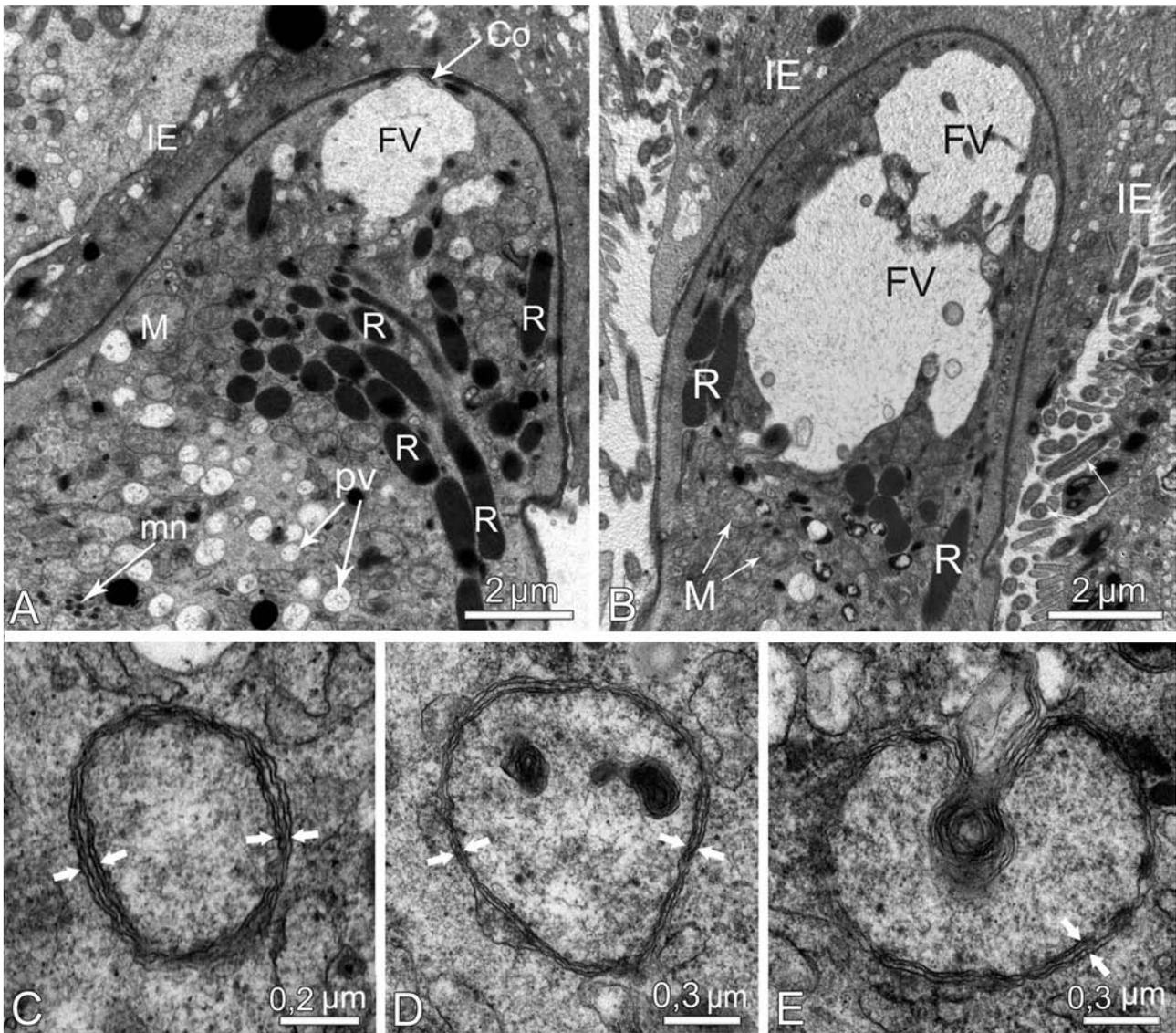
Figure 5. Food vacuoles and rhoptries in the apex of the *S. pendula* trophozoite (**A-B**), and apicoplast-like organelles (**C, D, E**). Abbreviations: conoid (Co), food vacuole (FV), host intestinal epithelium (IE), microneme (mn), mitochondrion (M), fragmented food vacuoles similar to pinocytotic vesicles (pv), rhoptry (R). **A.** TEM cross section with the initial food vacuole passing through the conoid and the fragmented food vacuoles similar to the pinocytotic vesicles (pv) observed in *S. hollandei* (Schrével 1968). Numerous rhoptries are accumulated around these food vacuoles. **B.** Another cross section showing the irregular shapes of the initial food vacuole and the intravacuolar vesicles. **(C-E).** Apicoplast-like organelles, characterized by the presence of four membranes morphologically similar to the apicoplast of *Toxoplasma* and *Plasmodium*.

Nuclear Multiplication During the Syzygy and Young Gamonts

The sexual phase of the *S. pendula* life cycle starts with the syzygy, characterized by the pairing of two haploid trophozoites, now called gamonts: one male and one female. During the young syzygy stage of *S. pendula*, the two gamonts are linked by their posterior parts, while their pendular motility continues with waves starting from the apex to the posterior end (Schrével 1970).

In TEM, each gamont exhibits a similar intracellular organization with a nucleus of about 20 μm in diameter containing a spherical nucleolus of about 5 μm in diameter (Supplementary Material 1). In each nucleolus, several clear areas are observed with sizes varying from 0.3 to 1 μm in diameter (Supplementary Material 1, arrows). The cell
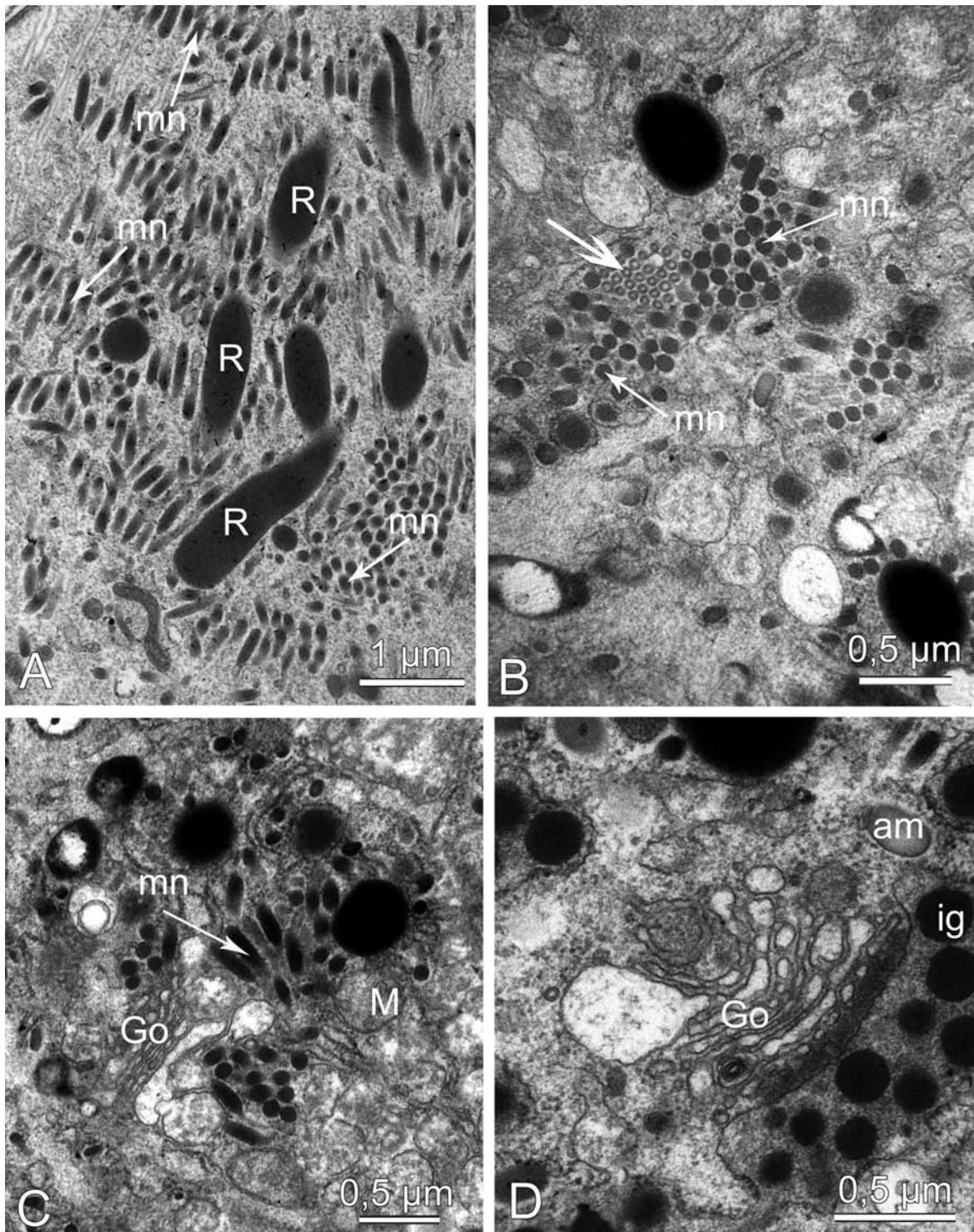
Figure 6. Rhoptries, micronemes and Golgi apparatus **(A-D).** Abbreviations: amylopectin granule (am), Golgi apparatus (Go), intrareticular granule (ig), microneme (mn), mitochondrion (M), rhoptry (R). **A-B.** TEM cross sections of an accumulation of rhoptries and micronemes within the cytoplasm. The micronemes appear as long-necked bottles, the necks appear as dense rings in cross sections (white thick arrow in B). **C-D.** Golgi apparatus and mitochondrion occur close to the micronemes; the *cis*-region of the Golgi apparatus usually contains numerous intrareticular granules (D).
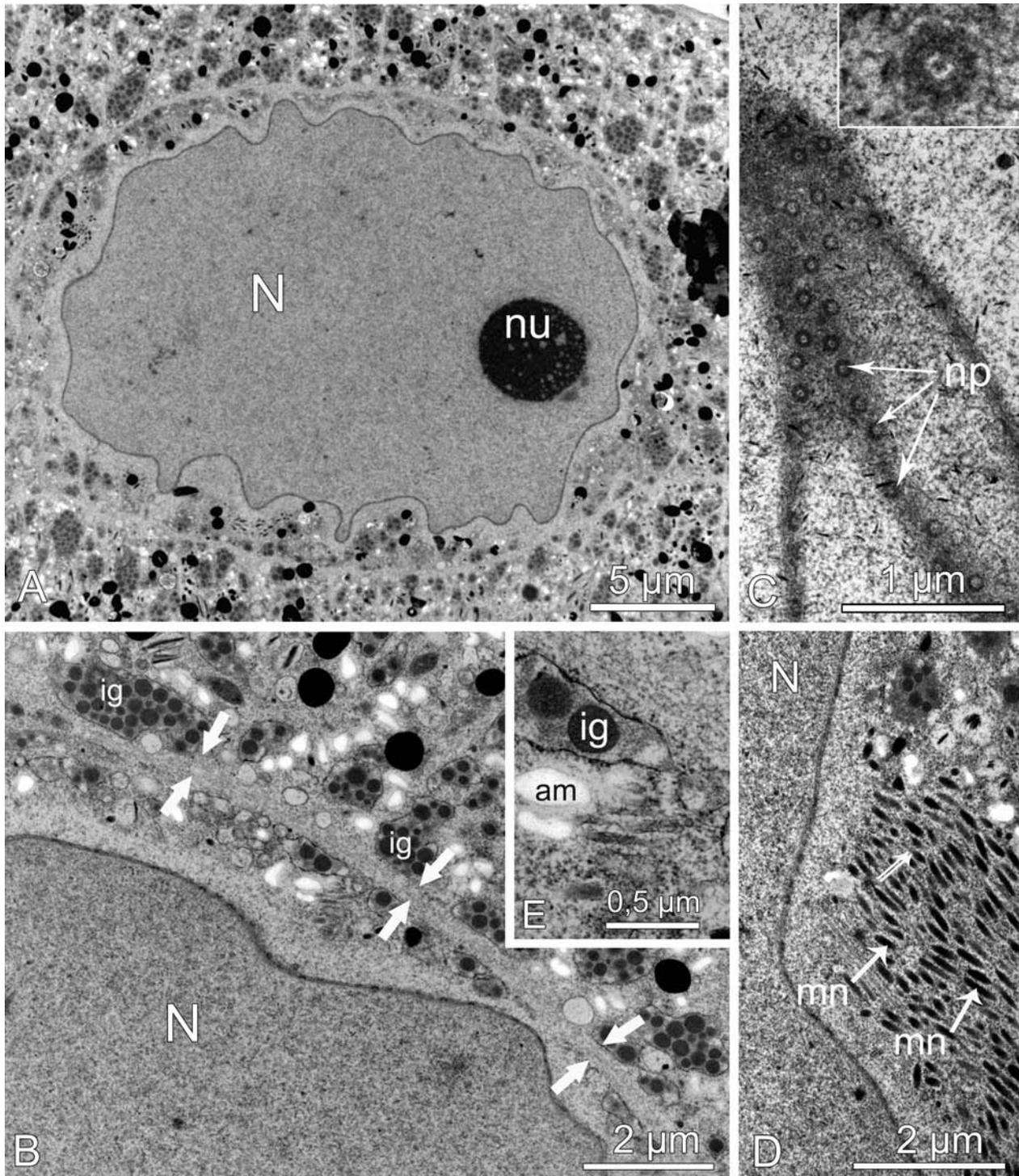
Figure 7. Nuclear area of *Selenidium pendula* trophozoite **(A-E).** Abbreviations: amylopectin granule (am), intrareticular granule (ig), microneme (mn), nuclear pores (np), nucleus (N), nucleolus (nu). **A-B.** TEM cross sections of the nucleus containing a spherical nucleolus (A) and surrounded by the regular fibrillar zone without organelles (white arrows in B). This fibrillar area is delimited by large vesicles of the rough endoplasmic reticular containing numerous granules and amylopectin granules. **C.** Tangential section of the nuclear envelope exhibits numerous pores. **D.** Occasional accumulation of micronemes can be observed near the nucleus. **E.** Higher magnification of the micronemes and intrareticular granules.

surface and the cytoplasm of the two gamonts also exhibit a similar organization (Supplementary Material 1).

A clear characteristic of archigregarines belonging to the family Selenidiidae is the early nuclear multiplication within the two gamonts at the site corresponding to the initial trophozoite nucleus that occurs before the encystment of the gamonts. The localization of the nuclei at the initial site of the trophozoite nucleus is clearly shown by the DAPI staining highlighting the DNA-containing structures (Fig. 8A-B). Bright spots are observed inside spherical structures, each of them corresponding to a nucleus. In about two hours, the pendular motility of each gamont is progressively reduced and cyst formation occurs with a widening of the nuclear zone in the gamont's median plane (Fig. 8A-B). In TEM, the concentration of the nuclei at this stage is not easy to observe due to the relatively high rate of this process. In favourable cross sections, the nuclei are observed in the central area of the gamont and before the secretion of the cyst wall. Each spherical nucleus is about 5 μm in diameter (Fig. 8C). From this central site, the nuclei migrate to the periphery of each gamont while the cyst wall is forming (Fig. 8D). In many nuclei of the gamonts, centrocones and other stages of cryptomitosis were detected.

Centrocones and Cryptomitosis in Gamonts

The mitosis in *S. pendula* gamonts is a closed-mitosis, also called cryptomitosis, with the persistence of the nuclear envelope as observed in all Apicomplexa (Francia and Striepen 2014). All the nuclei of the *S. pendula* gamonts are spherical with a diameter of about 5 μm and many are associated to a cupule with microtubules radiating from the Microtubule Organizing Center (MTOC) in order to form half-spindles (Fig. 9A-B). The chromatin is localized all around the internal face of the nuclear envelope as shown in TEM images (Fig. 9A-B). This chromatin forms an electron dense filamentous network with spotty dark nodes and in some cases, an important dense accumulation is observed inside the nucleoplasm (Fig. 9A). This dense accumulation of at least 1 μm could correspond to the bright spots visualized by the DAPI-staining (Fig. 8B). The distribution of chromatin in *S. pendula* nucleus appears as a continuous filamentous network quite similar to the model of Apicomplexa cryptomitosis proposed by Francia and Striepen (2014).

In *S. pendula* gamonts, many nuclei exhibit a centrocone resulting probably from the high rate

of nuclear divisions since the chronology from the syzygy to the encystment of the gamonts represents only 2-3 hours (Schrével 1970). The centrocone depends upon the MTOC that appears as an electron dense annular structure of about 200 nm in diameter. From the MTOC, microtubules radiate and form a half-spindle that pushes the nuclear envelope without penetration in the nucleus (Fig. 9A). The resulting cupule exhibits an outer diameter of about 1.6-1.9 μm and the distance from the MTOC to the inner border of the cupule is about 1.4-1.6 μm. This typical centrocone can duplicate and the second centrocone migrates to the opposite direction of the initial cupule (Fig. 9B). Micrographs with two centrocones are rather rare and an intranuclear spindle was not observed most likely due to the high rate of the progamic nuclear division in *S. pendula.*

As the progamic nuclei migrate from the central part of the gamont to the periphery, the cryptomitosis continues after this migration, since the duplication of the centrocones is observed in the border of the cyst where the wall is secreted.

Modifications of the Gamont Cell Surface and Secretion of the Gametocyst Wall

When the gametocyst wall is forming, the cortical membranes of each gamont are strongly modified (Fig. 10A-C). The plasma membrane is always present but the imc is disorganized with a series of folds and clear dissociation from the plasma membrane (Fig. 10B-C). In TEM, the gametocyst wall exhibits two major layers, a homogeneous internal layer of about 500-700 nm in thickness and a fuzzy external layer with long filaments reaching about 300 nm. The total thickness of the gametocyst wall at the beginning of gamogony is about 1 μm. The secretion of this wall is the result of two types of vesicles, one with rather electron dense components (vesicle 1) and the second with a network of very spotty filaments (Fig. 10A). The mechanism of discharge of these two types of vesicles was not clearly observed. As the gametocyst wall formation occurs only two hours after the early syzygy step, the secretion is probably the result of accumulations of numerous intrareticular granules in the cisterns of the rough reticulum endoplasm that represent storage material for this process (Fig. 6D). However, a potential dual function of the RER-Golgi apparatus for both the formation of rhoptries and micronemes and the storage of material for gametocyst formation needs further investigations (Fig. 6A).
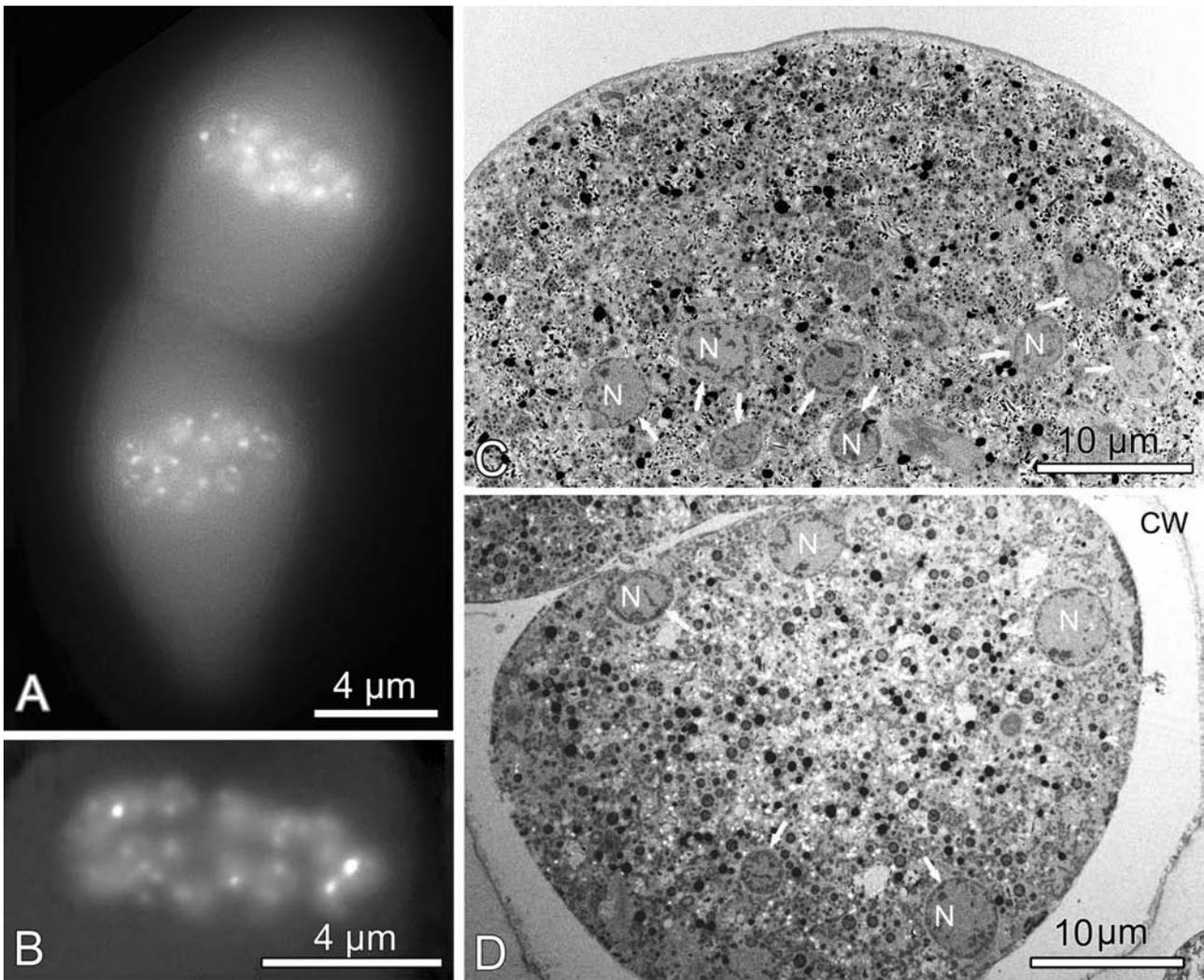
Figure 8. Nuclear development during the syzygy of *Selenidium pendula* **(A-D).** Abbreviations: nucleus (N), cyst wall (CW). **A-B.** Fluorescence staining with DAPI showing nuclei in the median plane of each gamont corresponding to the initial position of the nucleus at the beginning of the syzygy stage. Their numbers are quite similar in the two gamonts and some bright spots are observed in some nuclei (B). **C-D.** TEM cross sections in an early cyst where the nuclei are accumulating in the central position of the gamont while the cell wall is not secreted (C) and later after the secretion of the cyst wall where the nuclei migrate to the gamont periphery (D).

The Gametocyst and the Sporocyst Walls

The gametogenesis is a fast process in *S. pendula*, lasting about one hour (Schrével 1970). After the series of progamic nuclear divisions yielding syncytium nuclei in the same gametocyst, cellularization occurs, producing flagellated male gametes and female gametes without flagellum. In TEM, the gametocyst wall is more compact with dense layers (Fig. 11A-B). The fuzzy coat observed at the beginning of the gamogony is now very irregular in width and the internal homogenous layers are more electron dense (Fig. 11A). In some cases the internal

layers show a regular opaque layer of 0.3 µm and an irregular homogenous layer with a lower electron density (Fig. 11A).

In cross sections, the flagellar axoneme of the male gamete of *S. pendula* exhibits a 9+0 pattern (Fig. 11B). After fecundation, the life cycle moves into the sporogony phase with the formation of sporocysts corresponding to the evolution of the zygotes toward the sporozoite formation inside each sporocyst. A new secretion process occurs around this sporocyst (Fig. 11C). The thickness of the sporocyst wall is about 0.1 µm with small thin spine-like digitations of about 0.2 µm (Fig. 11C).
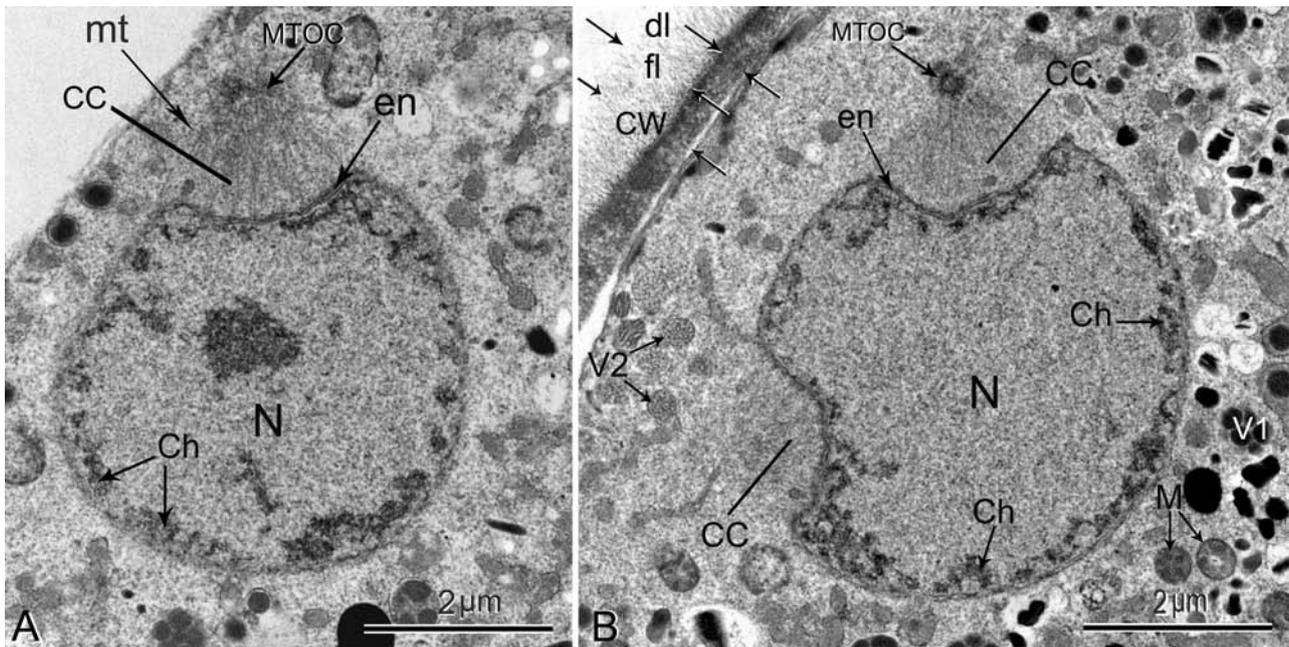
Figure 9. Centrocones and mitosis stages during the gametogenesis of *Selenidium pendula* **(A-B).** Abbreviations: centrocone (CC), chromatin (Ch), cyst wall (CW), dense layer (dl), filamentous layer (fl), nuclear envelope (en), mitochondrion (M), microtubule-organizing center (MTOC), microtubule (mt), nucleus (N), vesicle type 1 (V1) and type 2 (V2). **A.** Early gametogenesis stage before the secretion of the gametocyst wall exhibiting centrocone where the microtubules radiate from the MTOC to the cupule of the nuclear envelope forming a truncated cone. The chromatin covers the inner face of the nuclear envelope and a dense accumulation is observed in the nucleus. **B.** A second centrocone migrating on the other side of the nucleus. No intranuclear spindle is observed, the chromatin is attached to the persistent nuclear envelope. Two types of vesicles are observed one with dense granules (V1) and a second one with filamentous material (V2). The gametocyst wall exhibits an external filamentous layer and an internal dense layer.

Molecular Phylogenetic Analyses of the SSU rDNA Sequence

Type species are important to build solid bridges between molecular phylogenies and taxonomy. A phylogenetic tree was constructed using 115 sequences including nine novel small subunit (SSU) rDNA sequences (two sequences from *S. pendula*, the type species for Selenidiidae, one from *S. hollandei*, one from *Lecudina pellucida*, the type species for Lecudinidae, and 5 from *L. tuzetae*, all specimen isolated from host organisms collected in the Roscoff area, France) and 106 previously published ones available from public databases, taking into account all available data for archigregarine species (Table 1). Sequences known to produce extreme long branches in SSU rDNA-based phylogenies, such as those of the gregarines *Trichotokara* spp. *and Pyxinia robusta*, were excluded from this analysis. Globally, the Maximum Likelihood and the Bayesian tree topologies were congruent (Fig. 12) and in good agreement

with recently published phylogenies (Wakeman and Leander 2013; Wakeman et al. 2014). The two early lineages emerging among Apicomplexa were from marine gregarines with archigregarines and eugregarines. Interestingly the phylogenetic position of the type species *Lecudina pellucida* (Fig. 12) fell within the Lecudinidae, with a good support with lecudinids of tunicates represented by the *Lankesteria* genus. In the terrestrial gregarines, the *Gregarina* lineage belongs to rather old insects such as Coleoptera, Blattaria, and Orthoptera, in contrast to the *Ascogregarina* lineage that infects more recent insects according to the most recent knowledge on insect evolution (Misof et al. 2014).

An analysis of the SSU rDNA sequences clearly demonstrated the paraphyly of Selenidiidae, which are split into three major groups (Fig. 13, Supplementary Material 2-4). The type species *Selenidium pendula* is closely related to *Selenidium boccardiella* (Wakeman and Leander 2013). These two gregarines infect members of the Spionidae family of Polychaeta. Similarly,
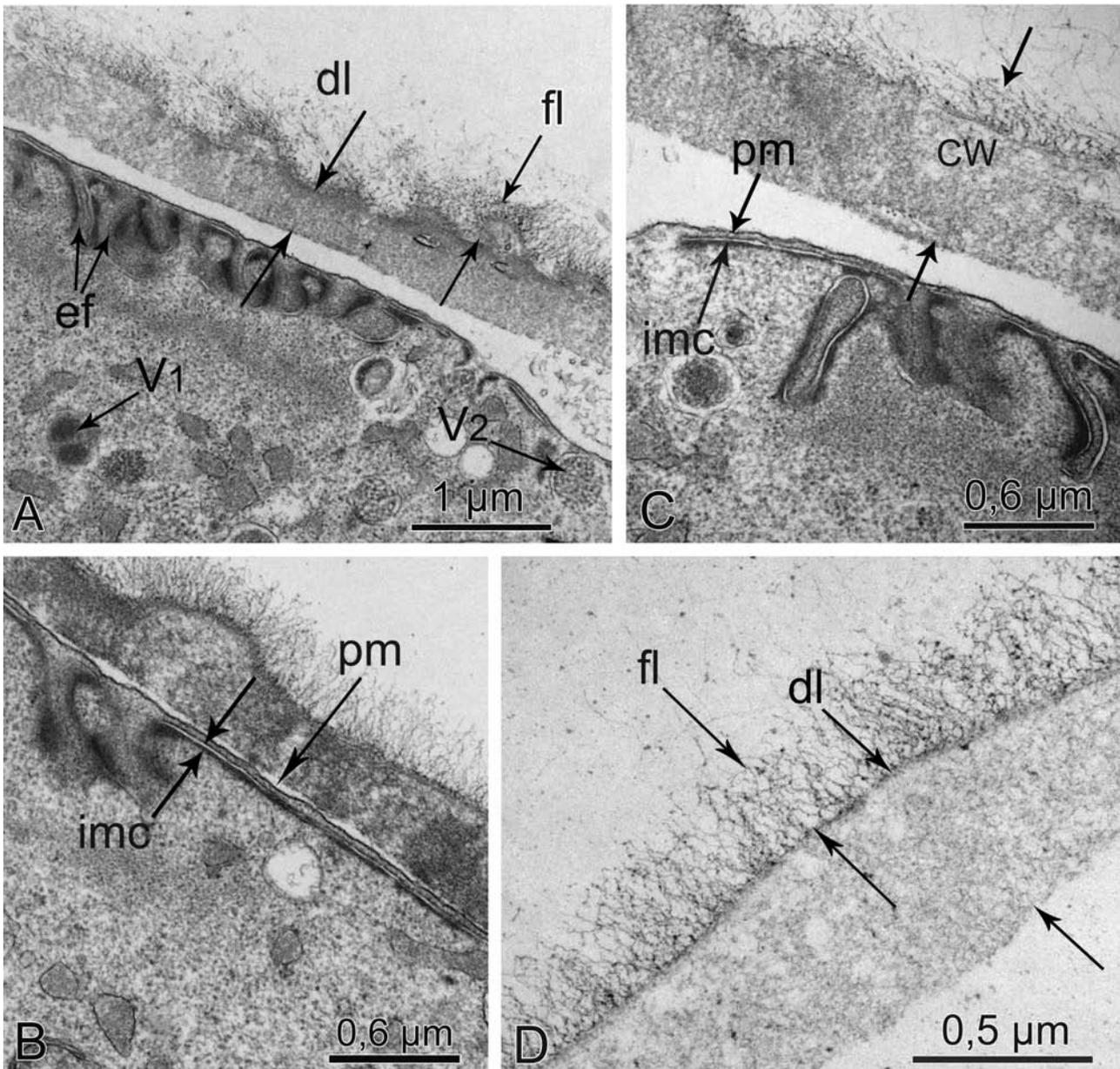
Figure 10. Reorganisation of the cortical membranes in *Selenidium pendula* gamonts and ultrastructure of the gametocyst wall during the gametogenesis stage **(A-D).** Abbreviations: gametocyst wall (CW), dense layer (dl), epicytic folds (ef), filamentous layer (fl), inner membrane complex (imc), plasma membrane (pm), vesicle type 1 (V1) and type 2 (V2). **A-C.** TEM cross sections of the gamont's periphery where the epicytic folds are disorganized with dissociation of the inner member complex under the plasma membrane. The wall of the gametocyst exhibits a filamentous external layer and a more homogenous internal layer; the vesicles of type 2 are probably involved in the cyst wall construction. **D.** Higher magnification of the cyst wall with large amount of filaments attached to the surface of the internal homogenous layer.

S. hollandei is closely related to *S. neosabellariae* and *S. identhyrsae* (Wakeman and Leander 2013), these three species being parasites of hosts belonging to Sabellariidae. Parasites infecting Spionidae and Sabellariidae diverged from 3.4 to

13.7% from each other (sequence identity, Supplementary Material 2, 3).

Selenidium parasites of Terebellidae group form a second divergent lineage with a wider global divergence with true Selenidiidae of 25.8-28.2%,
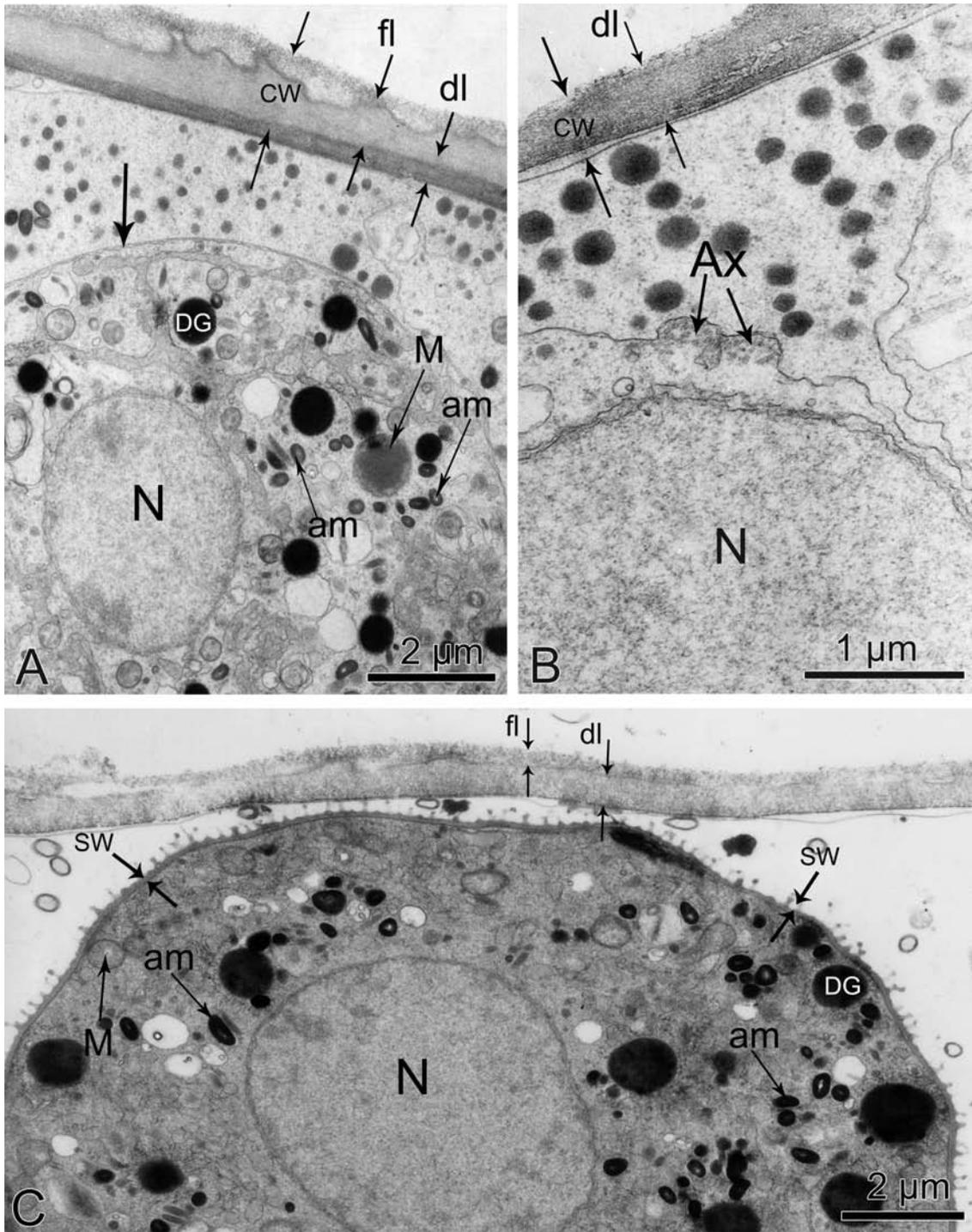
Figure 11. Gamonts with gametes and young sporocysts after the fertilization **(A-C).** Abbreviations: amylopectin granule (am), axoneme (Ax), gametocyst wall (CW), dense granule (DG), dense layer (dl), filamentous layer (fl), mitochondrion (M), nucleus (N), sporocyst wall (SW). **A.** Gametocyst wall after the formation of the gametes exhibits a third layer with more dense material under the two layers observed in more early gamont stages (Figure 12). Residual amylopectin and dense granules are observed between the gametes and the gametocyst wall. **B.** Cross sections of flagellar axonemes indicate a male gamete (B) and two serial sections are of a 9+0 pattern. **C.** After the fertilization process the young sporocysts are surrounded by a thin wall covered by very small spines.

(Supplementary Material 2, 3). Finally, all Selenidiidae described in *Phascolosoma* formed a third group which is the most divergent (26.3 - 28.8% of divergence with the two precedent groups, Supplementary Material 2, 3).

Discussion

Selenidium spp. and archigregarines

Since 2003, the morphology of some trophozoites of Selenidiidae and related archigregarines was investigated using SEM and more than 25 SSU rDNA sequences were deposited in the GenBank/EMBL/DDBJ databases (Leander 2006, 2007b; Leander et al. 2003a; Rueckert and Leander 2009; Wakeman and Leander 2012, 2013; Wakeman et al. 2014). However, data on sexual stages (gamogony and sporogony) were missing. By combining electron microscopic descriptions with phylogenies using SSU rDNA sequence data, new *Selenidium* species have been proposed such as *S. pisinnus* Rueckert and Leander, 2009, *S. boccardiella* Wakeman and Leander, 2012, *S. idanthyrsae* Wakeman and Leander, 2012, *S. neosabellariae* Wakeman and Leander, 2013, *S. sensimae* Wakeman and Leander, 2013 and *S. melongena* Wakeman et al., 2014. A new genus *Platyproteum* (Rueckert and Leander 2009) was erected to replace the former species *Selenidium vivax* Gunderson and Small 1986. A new enigmatic genus related to archigregarines was also proposed as *Veloxidium* (Wakeman and Leander 2013). In their discussion, Leander and co-workers produced a comparative table with morphological data of all Selenidiidae described in the last century (Ray 1930; Schrével 1970, 1971b). Few mistakes within Selenidiidae were reported in this table (Table 2 in Wakeman and Leander 2012) as for example the mention of *S. spionis*, presented as a parasite of *Polyrabdina spionis*. *Polyrhabdina spionis* is in fact a lecudinid gregarine and the host of *S. spionis* is the polychaete *Scolelepis fuliginosa* Claparède, 1870 now called *Malacoceros fuliginosus* (Claparède, 1870) Schrével and Desportes, 2013. However, the SSU rDNA sequences analysis of *S. spionis* revealed lineages inside archigregarines and Leander and co-workers underlined the importance of future work on additional *Selenidium*-like gregarines especially the type species *S. pendula* (Wakeman et al. 2014). This current work on the type species *S. pendula* Giard, 1884 and on *S. hollandei* Vivier and Schrével, 1966 therefore enlighten with less

ambiguities parts of the evolutionary history of archigregarines.

The SSU rDNA sequence phylogeny trees with the different SSU rDNA sequences of archigregarines (Table 1), show three clearly delimited lineages among Selenidiidae (Figs 12-13, Supplementary Material 3, 4). A major group corresponds to the true-*Selenidium* lineage, for which sexual stages (syzygy to sporocyst) have been described. Its members are parasites of Sedentaria polychaetes, such as *S. pendula* that infects the Spionidae family, *S. hollandei* infecting Sabellariidae and *Selenidium* cf. *meslini* infecting Sabellidae. These true-*Selenidium* share common important features, such as a nuclear multiplication during the syzygy, the gamogony and the sporocysts with usually four sporozoites. Many archigregarines have developed atypical variations in their cell morphology and their motility from pendular to rolling type, with subpellicular microtubule sets under the inner membrane complex (imc), but without the gliding type observed in eugregarines. Trophozoites of true-*Selenidium* exhibit a three-membrane cortex where the imc forms a complete envelope underlying the plasma membrane, with sets of longitudinal subpellicular microtubules running under the large folds designated as bulges (Schrével 1970a, 1971a; Schrével et al. 2013; Vivier and Schrével 1964). The grooves correspond to the striations well described this last century by light microscopic (Brasil 1907; Ray 1930; Schrével 1970). The cytoplasm beneath the grooves is devoid of microtubules but exhibits micropores and residual membranous organelles in connection with the imc (Schrével et al. 2013; Vivier and Schrével 1964). These parasites feed by myzocytosis using the conoid located at the apex of the trophozoite (Schrével 1968; Simdyanov and Kuvardina 2007; this work).

In this true-*Selenidium* lineage, the sexual stage starts by the syzygy where the formation of progametic nuclei is observed inside the gamont nucleus before encystment. This observation in the type species *S. pendula* (Fig. 8) is the confirmation of histological previous descriptions by Caullery and Mesnil (1900), Ray (1930), Reed (1933), Tuzet and Ormières (1958) and in vivo observations by Schrével (1970). This gamogony is quite different from all other eugregarines where the first gamogony division starts inside the cyst and is followed by successive series of nuclear divisions called progamic mitoses without cytokinesis such as in *Lecudina tuzetae* (Kuriyama et al. 2005). So, the *Lecudina* type gamogony produces a syncytium until the cellularization process yielding the
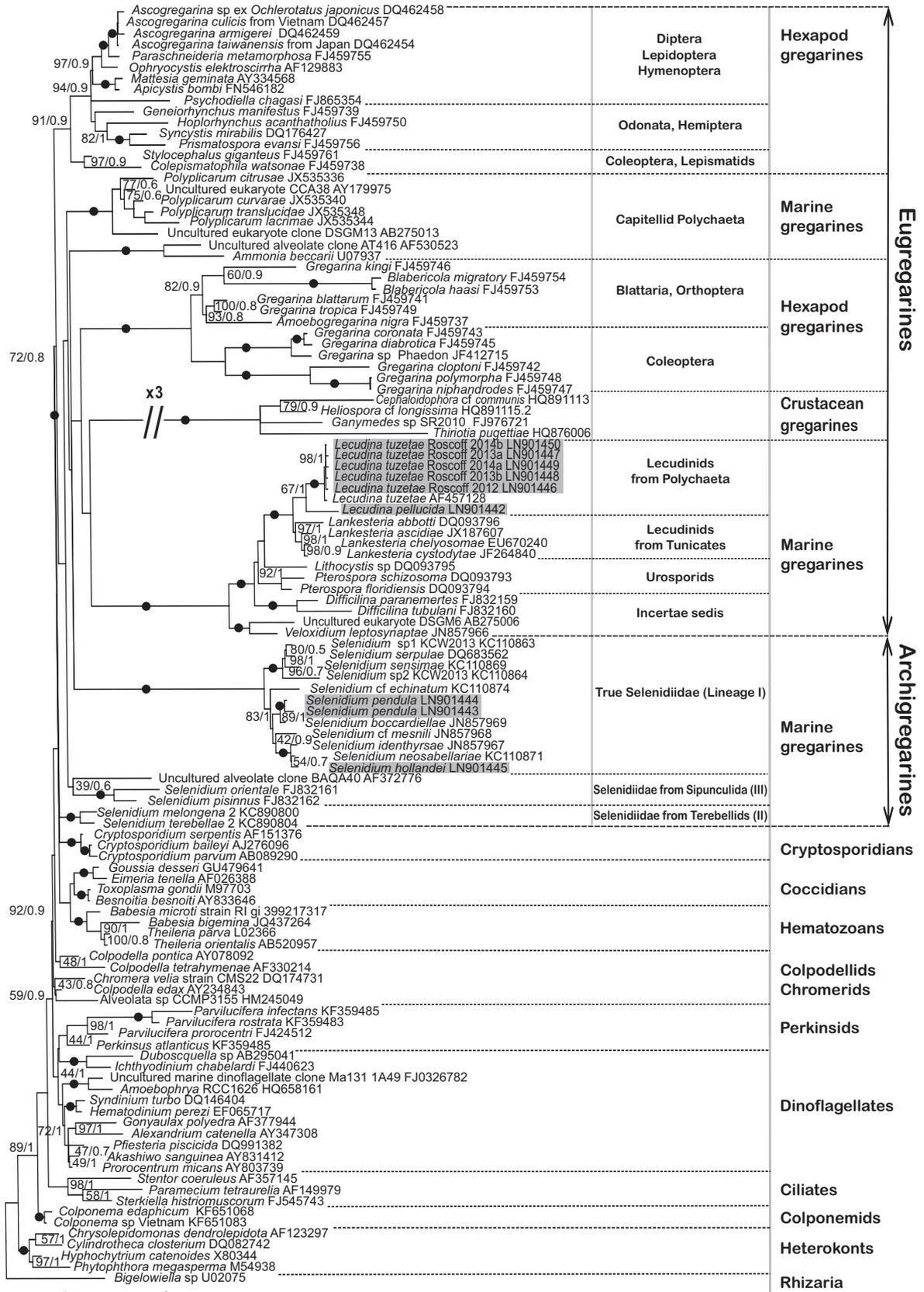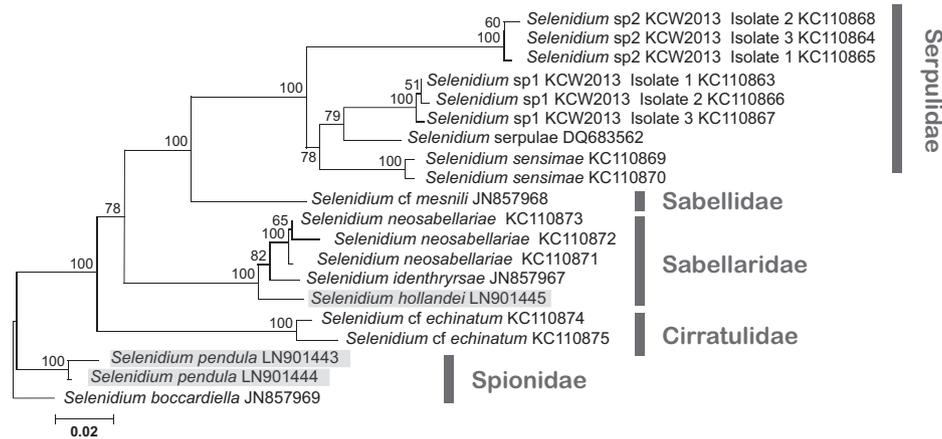
Phylogenetic tree

Figure 13. Molecular phylogenetic analysis by Maximum Likelihood method of Selenidiidae lineage retrieved from polychaete annelids (host families in bold black).
The evolutionary history was inferred by using the Maximum Likelihood method based on the General Time Reversible model (Nei and Kumar 2000). The tree with the highest log likelihood (-5446.5092) is shown. A discrete Gamma distribution was used to model evolutionary rate differences among sites (5 categories with gamma parameter = 0.2711). The rate variation model allowed for some sites to be evolutionarily invariable (+I), 39.8364% sites). The tree is drawn to scale, with branch lengths measured in the number of substitutions per site. Novel sequences are highlighted in grey boxes.

gametes. Another clear difference concerns the degree of condensation of the chromatin with a continuous filamentous network attached to the nuclear envelope all around the nucleus in *S. pendula* cryptomitosis. Chromosome condensation does not seem to occur in *S. pendula* in contrast to cryptomitosis of *L. tuzetae* (Kuriyama et al. 2005) and *Grebnickiella gracilis* (Moblon-Noblot 1980). Sporogony then leads to spherical sporocysts that differentiate usually into four sporozoites per sporocyst (Ray 1930; Schrével 1970).

Other *Selenidium*-like species infecting sipunculids and Terebellidae are only known through their trophozoites and their localization within hosts (Leander 2006; Wakeman et al. 2014). The intestinal trophozoite of *S. terebellae* Ray 1930 exhibits large bulges but differences with the true-*Selenidium* have been observed. As an example, a regular layer of about 30-33 nm in thickness

(Supplementary Material 5 and Wakeman et al. 2014) similar to the internal lamina of eugregarines (Schrével et al. 1983) or to some euglenoid cortex (Mignot 1966) is attached to the imc. Numerous sets of longitudinal subpellicular microtubules are immediately under this regular dense layer and many residual membranous organelles are highly concentrated under the imc of the grooves (Supplementary Material 5). *S. melongena* trophozoites were described in the same host as *S. terebellae*, but inside the coelom, an unusual localization for archigregarines (Wakeman et al. 2014). The cortex of *S. melongena* Exhibits 30-40 epicytic folds helically arranged along the axis of the cell. Surprisingly, although the subpellicular sets of microtubules were not observed in TEM, a strong fluorescent labelling of alpha-tubulin was detected below the helical folds. *S. melongena* are non-motile without pendular or rolling motility nor gliding.

Figure 12. Maximum Likelihood (ML) tree inferred on an alignment of 115 small subunit (SSU) rDNA sequences corresponding to 9 *Selenidium* and *Lecudina* species from this current study (highlighted in grey boxes) and 106 sequences from diverse eukaryotes corresponding mostly to representatives of Alveolata with one Rhizaria as outgroup. The Maximum Likelihood method is based on the General Time Reversible +G +I model (Nei and Kumar 2000). The tree is drawn to scale, with branch lengths measured in the number of substitutions per site. A branch was shortened by a multiple (3) of the length of substitutions/site scale bar. There were a total of 1153 positions in the final dataset. ML evolutionary analyses were conducted in MEGA6 (Tamura et al. 2013). Numbers at the branches denote ML bootstrap percentage (first value). Bayesian posterior probabilities are also indicated (second value). Black dots on branches denote bootstrap percentages above 99% and Bayesian posterior probabilities superior to 0.97.

Table 1. List of the SSU rDNA sequence numbers of archigregarines and *Veloxidium* initially included in this group and the references: 1. This work; 2. Leander et al. 2003; 3. Leander et al. 2007; 4. Rueckert and Leander 2009; 5. Wakeman and Leander 2012; 6. Wakeman and Leander 2013; 7. Wakeman et al. 2014.

Archigregarines	SSU rDNA sequences	Ref.	Host	Infraclass	Order	Family
Selenidium pendula LG	LN901443	1	*Scolelepis squamata*	Canalipalpata	Spionida	Spionidae
Selenidium pendula IF	LN901444	1	*Scolelepis squamata*	Canalipalpata	Spionida	Spionidae
Selenidium boccardiella	JN857969	5	*Boccardiella ligerica*	Canalipalpata	Spionida	Spionidae
Selenidium mesnili	JN857968	5	*Myxicola infundibulum*	Canalipalpata	Sabellida	Sabellidae
Selenidium hollandei	LN901445	1	*Sabellaria alveolata*	Canalipalpata	Sabellida	Sabellariidae
Selenidium neosabellariae	KC110871 KC110872 KC110873	6	*Neosabellaria cementarium*	Canalipalpata	Sabellida	Sabellariidae
Selenidium identhyrsae	JN857967	6	*Idanthyrsus saxicavus*	Canalipalpata	Sabellida	Sabellariidae
Selenidium serpulae	DQ683562	3	*Serpula vermicularis*	Canalipalpata	Sabellida	Serpulidae
Selenidium sensimae	KC110869 KC110870	6	*Spirobranchus giganteus*	Canalipalpata	Sabellida	Serpulidae
Selenidium Sp1	KC110863 KC110866 KC110867	6	*Spirobranchus giganteus*	Canalipalpata	Sabellida	Serpulidae
Selenidium Sp2	KC110864 KC110865 KC110868	6	*Spirobranchus giganteus*	Canalipalpata	Sabellida	Serpulidae
Selenidium terebellae	AY196709	2	*Thelepus* sp,	Canalipalpata	Terebellida	Theleponidae
Selenidium terebellae	KC890803 KC890804 KC890805 KC890806	7	*Thelepus japonica*	Canalipalpata	Terebellida	Theleponidae
Selenidium melongena	KC890799 KC890800 KC890801 KC890802	7	*Thelepus japonica*	Canalipalpata	Terebellida	Terebellinae
Selenidium cf echinatum	KC110874 KC110875	6	*Dodecaceria concarum*	Canalipalpata	Terebellida	Cirratulidae
Selenidium vivax	AF236097	2	*Phascolosoma agassizii*	Sipunculida	Phascolosimida	Phascolosomatidae
Platyproteum vivax	AY196708	4	*Phascolosoma agassizii*	Sipunculida	Phascolosimida	Phascolosomatidae
Filipodium phascolosoma	FJ832163	4	*Phascolosoma agassizii*	Sipunculida	Phascolosimida	Phascolosomatidae
Selenidium pisinnus	FJ832162	4	*Phascolosoma agassizii*	Sipunculida	Phascolosimida	Phascolosomatidae
Selenidium orientale	FJ832131	4	*Themiste pyroidea*	Sipunculida	Golfingiida	*Veloxidium leptosynaptae*
Veloxidium leptosynaptae	JN857966	5	*Leptosynapta clarki*	Echinodermata	Apodida	Synaptidae

According to Wakeman et al. (2014), such atypical cell organization of *S. melongena* trophozoites seems to be closer to lecudinids than to Selenidiidae. These original observations as well as the lack of description of syzygy and sporocysts require future work, especially to explain the way by which *S. melongena* can infect its host.

The third *Selenidium*-like lineage described here corresponds to a group of intestinal parasites of Sipunculida. These parasites are mainly known from SEM and TEM observations on *Selenidium vivax* trophozoites (Leander 2006). Renaming of *S. vivax* as *Platyproteum vivax* was supported by archigregarine flat shape when observed under TEM with important sets of longitudinal subpellicular microtubules and numerous mitochondria probably in relation to the very active plasticity of *S. vivax* (Rueckert and Leander 2009). This cellular organization appears similar to that of *S. hollandei* (Schrével 1970). Here also, descriptions of the syzygy with their characteristic progametic nuclei as well as the sporocysts require clarifications. This point is also important for *Filipodium* trophozoites where numerous microvilli from 1.6-10 µm long and about 0.15 µm in diameter were clearly described in TEM (Hoshide and Todd 1996).

All archigregarines are intestinal parasites of Annelida belonging to the clade Sedentaria except one *Selenidium metchnikovi* reported in Hemichordata (Léger and Duboscq 1917). In contrast, many lecudinids are intestinal parasites of the clade Errantia from Annelida (Schrével and Desportes 2013). This separation between archigregarines and marine lecudinid eugregarines is probably related to the different modes of living of their hosts. For instance, lecudinids are adapted to the errant and predatory life of Errantia while archigregarines are adapted to sedentary life of Sedentaria with microphage species living below stones, or as tube builders or ingesting sediment as the representatives of the family Spionidae or surface deposit feeders with head appendages (Sabellidae, Sabellariidae). Evolutionary history of Annelida is still poorly understood as the classic morphological cladistic analysis with a monophyletic Polychaeta (Rouse and Fauchald 1997) was challenged in the light of the recent molecular evidences. Today, Polychaeta are inferred to be paraphyletic with the inclusion of the Clitella (earthworms) and the non-segmented taxa Echiura and Sipunculida (Struck et al. 2011). Complexity of the phylogeny of *Selenidium* species may reflect the one of their hosts. The true-*Selenidium* lineage within the Selenidiidae family likely forms the core of archigregarines while the two other distant lineages infecting respectively the Sipunculids and Terebellids orders, could be considered as related *Selenidium*-like lineages. These results, deduced from molecular phylogeny analyses need to be confirmed at the biological and cellular levels but are crucial since they open new trends in evolutionary history among Apicomplexa.

The enigmatic *Veloxidium leptosynaptae*, initially placed within archigregarines after phylogenetic analyses (Wakeman and Leander 2012) was later included within lecudinids and urosporids (Wakeman et al. 2014). In our phylogenetic studies, it also groups with lecudinids and urosporids with strong supports (Fig. 12).

Apicoplasts, Conoid, MTOC and Rhoptries are Major Cell Structures in the Evolution of Apicomplexa

Gregarines represent interesting models to investigate the evolution from free-living flagellated alveolates status, likely photosynthetic, to obligatory parasites among Apicomplexa.

In archigregarines, the presence of an apicoplast remains an open question. Presence of a functional plastid is reported in *Chromera*, a free-living photosynthetic relative to Apicomplexa (Lim and McFadden 2010). The apicoplast, a non-photosynthetic plastid of red algae origin, is well documented in some Apicomplexa species such as *Plasmodium*, *Toxoplasma*, *Eimeria*, *Babesia*, *Theileria*. This relict plastid is limited by four membranes indicating its secondary endosymbiont origin. In the eugregarine *Gregarina niphandrodes*, the apicoplast seems to be absent (Toso and Omoto 2007). Here in *S. pendula*, apicoplast-like organelles are regularly observed in trophozoites at the ultrastructural level. Interestingly Ray (1930) reported the visualization of a dark spot stained with Heidenhain's haematoxylin, associated to each merozoite nucleus in *S. mesnili* parasitizing the polychaete *Myxicola infundibulum*. Such an observation at the light microscopy level was also observed by TEM, revealing the presence of an organelle with four membranes close to the anterior part of each *S. hollandei* merozoite (Schrével 1971b).

The apical phagotrophy in the free-living predators of alveolates, with open conoid and rhoptries, may be at the origin of the anchoring device of archigregarines like *Selenidium*, characterized by their mucron and the myzocytosis function. The conoid of *S. pendula*, similar to that of *S. hollandei* (Schrével 1968) and *S. orientale* (Simdyanov and Kuvardina 2007), is conserved in large trophozoites and appears similar to the conoid of sporozoites

from eugregarines *Stylocephalus africanus* (Desportes 1969) and *Ascogregarina (Lankesteria) culicis* (Sheffield et al. 1971). Among Conoidasida, the conoid of *T. gondii* is the most investigated at the structural and molecular levels, with the construction of unique coma-shaped tubulin sheets to form a spiral cone-shaped structure (Hu et al. 2002, 2006). As *S. pendula* is the archigregarine type species and an early branching Apicomplexa, its conoid appears a good model to study the transition between Apicomplexa with closed conoid and free-living alveolate ancestors with open conoid, as found in the early branching dinoflagellates as *Colpodella* (Brugerolle 2002; Leander et al. 2003b) or *Psammosa pacifica* (Okamoto and Keeling 2014).

Recently, the hypothesis of molecular links between Apicomplexa and algal ancestors was suggested with the demonstration of similar components in the apical complex of Myzozoa and the flagellar apparatus of protists. This hypothesis was mainly supported by the localization of striated fiber assemblies (Francia et al. 2012) and SAS-6 proteins (de Leon et al. 2013). *T. gondii* striated fiber assemblins (TgSFA2 and TgSFA3) proteins whose orthologs are found in the rootlet associated with the basal bodies from green algae, polymerize into a dynamic fiber that emerges from the centrosomes immediately after their duplication (Francia et al. 2012). Genetic experiments showed that the two proteins TgSFA2 and 3 play an essential role in the cell division of the *T. gondii* since cytokinesis is blocked in their absence. This Tg SFA fiber thus provides a robust spatial and temporal organizer for the parasite cell division. Also, Francia et al. (2012) indicated that other comparable SFA fibers were observed in previous ultrastructural studies on *Eimeria* (Dubremetz 1973, 1975) and *Plasmodium* (Schrével et al. 2008).

The SAS-6 protein is well known in the centriolar biogenesis of eukaryotes from protists to vertebrates (Leidel et al. 2005; van Breugel et al. 2011). This protein was described in the centrocone during *T. gondii* cryptomitosis (de Leon et al. 2013). In addition a novel SAS-6 like (SAS-6L) protein family that shares an N-terminal domain with SAS-6 but without the coiled-coil tails was localized above the *T. gondii* conoid (de Leon et al. 2013). Genomic analyses showed that SAS-6L is an ancient protein found in diverse eukaryotic lineages: *Trypanosoma, Leishmania*, ciliates and Apicomplexa (Hodges et al. 2010; de Leon et al. 2013). In *Trypanosoma brucei* trypomastigotes, the Tb SAS-6L was observed near the basis of the flagellum, consistent with the basal body location.

In *T. gondii*, the Tb SAS-6L antibody labelled the apex of tachyzoites, and after conoid extrusion triggered by ionomycin treatment, it labelled the tip of the "true" conoid. The SAS-6L and SAS-6 antibodies did not colocalize in *T. gondii*, the former one labelling the centriole and the latter one labelling the conoid tip (de Leon et al. 2013).

Complex connections between the "pseudoconoid" or "incomplete conoid" and the flagellar apparatus were also shown, by conventional TEM and 3D reconstruction, in the apical complex of *Psammosa pacifica*, a predator relative of apicomplexans and early dinoflagellates (Okamoto and Keeling 2014).

The MTOC of the centrocones of *S. pendula* appears as a disc similar to that observed in other eugregarines such as *L. tuzetae* where 9 singlets could be detected in favourable TEM sections (Kuriyama et al. 2005). From these MTOC discs, microtubules radiated to form a cone involved in the cup-shaped invaginations of the nuclear envelope. The continuity of these MTOC during the life cycle could be in agreement with a centriolar-like structure since a 9+0 axonemal pattern is observed in *S. pendula* male gamete (Fig. 11B). The question of the subpellicular microtubule biogenesis is not clear. The conoid is not, by itself, the MTOC since it is absent in the zoites of Hematosporida and Piroplasmida. The two polar rings, observed at the apex of the *Eimeria* or *Plasmodium* zoites were proposed as the MTOC sites generating the subpellicular microtubules (Russel and Burns 1984), but these two polar rings were not observed in *S. pendula*. The imc dilatation at the border of the proximal opening of the conoid could fulfil this function (Fig. 4). The exceptional accumulation of microtubule bundles in the anterior part of the mucron, before the regular subpellicular microtubule sets of the epicytic bulges (Fig. 2D), is in agreement with the strong labelling of *S. melongena* apex with fluorescent anti-alpha tubulin (Wakeman et al. 2014). Biogenesis of these abundant microtubule bundles needs further analysis.

Rhoptries are characteristic of the apicomplexan zoites and also of the Selenidiidae trophozoites (Schrével et al. 2013 for a review). Interestingly, presence of numerous intracytoplasmic thread-like bodies described by Ray (1930) in the apex of different *Selenidium* trophozoites was visualized after iron haematoxylin staining (Heidenhain's haematoxylin). By their sizes reaching 8-12 μm depending on the *Selenidium* species and their localization, these thread-like structures could correspond to the rhoptries described from TEM such as in *S. pendula* (Fig. 5A), *S. hollandei* (Schrével 1968)

and *S. orientale* (Symdyanov and Kurvidina 2007). Ray (1930) considered these thread-like structures as one of the morphological characters of each *Selenidium* species, however the abundance of rhoptries detected in TEM is in fact a general character for archigregarines (Schrével et al. 2013, for review). Biological functions of many apicomplexan rhoptry proteins remain largely unknown. In *Plasmodium* and *Toxoplasma*, the most investigated apicomplexans at the molecular level, there is growing evidence to suggest that the rhoptry neck proteins are predominantly involved in host-cell adhesion with some sharing evolutionary origins among apicomplexans. In contrast, the rhoptry bulb proteins appear mainly genus specific, suggesting that they evolved secondarily to become highly specific to their host cells (Counihan et al. 2013). In *S. pendula*, food vacuole membranes may have arisen from numerous rhoptries localized within the apex. A strong membrane trafficking is expected to produce the large and abundant food vacuoles observed during myzocytosis (Fig. 4A). Therefore *Selenidium* rhoptry proteins could play a role in producing intracellular food vacuole in contrast to Apicomplexa with an intracellular development, where the rhoptry proteins seem involved in the parasitophorous vacuole elaboration such as in *Plasmodium* and *Toxoplasma.*

Archigregarines and Eugregarines: Two Early Branching Lineages Among Apicomplexa

The transition from the free-living alveolates to apicomplexan parasites was supported by comparative ultrastructural studies and molecular phylogeny analyses of basal lineages, such as dinoflagellates (together with perkinsids) and apicomplexans (including colpodellids) (Leander and Keeling 2003). The myzocytosis is the most plesiomorphic features of apicomplexans with archigregarines having a closed conoid (Schrével 1968, 1971b), and colpodellids the sister lineage of Apicomplexa with an open conoid (Kuvardina et al. 2002). In perkinsids, representing the earliest diverging sister lineage of dinoflagellates (Saldarriaga et al. 2003), an open conoid is also observed (Perkins 1996). These three types of parasites also share rhoptry-like organelles and, together with their phylogenetic positions, they confidently infer that a common ancestor of apicomplexans and dinoflagellates had an apical complex involved in the acquisition of nutrients from the cytoplasm of prey cells (Leander and Keeling 2003).

Among the high diversity of gregarines in invertebrates, Polychaeta, an animal class known to be present at the Cambrian biodiversity explosion and to represent one of the earliest Bilateria organisms (De Rosa et al. 2005; Schrével and Desportes 2013), is well infected by gregarines. This situation supports the evolutionary prelude of marine gregarines to the apicomplexan radiation (Leander 2007). The initial archigregarine radiation is supported by the "hypersporozoite" cell organization of the trophozoite, the myzocytosis and the pendular or rolling motility (Schrével 1971b; Schrével and Desportes 2015). The subsequent eugregarine radiation, with an adaptation to the intestinal biome and an extracellular development, could have emerged from intestinal lecudinid gregarines. Here, their cell cortex is quite different from archigregarines by the presence of numerous epicytic folds, without the regular sets of subpellicular microtubules but with a sophisticated distribution of 12-nm filaments, apical rippled dense structures at the top of the folds (Schrével et al. 1983;Vivier 1968). Their gliding motility depends upon an actin-myosin system but the molecular mechanochemical properties are far from being understood (Heintzelman 2004; Valigurová et al. 2013). The myzocytosis, similar to the archigregarine model, is not observed in these marine eugregarines: their nutrition process is realized through a bulbous attachment apparatus usually designated by mucron.

The gregarine colonization of the coelom in invertebrate hosts by transmigration of the sporozoites through the intestinal epithelium and a coelomic development reveal additional adaptations of eugregarines to their host environment. These adaptations are a significant evolutionary step of marine gregarines as suggested by Leander (2007a), and represent an antithesis to any notion of "primitiveness". One of the best evidence is the unique adaptation of the coelomic eugregarine *Diplauxis hatti* to its host *Perinereis cultrifera* where a strict synchronization is observed between the maturation of the polychaete gametes and the sexual phases (gamogony and sporogony) of the parasite (Prensier et al. 2008). This example illustrates how gregarines are well adapted to their host environment. For instance, *D. hatti* is adapted to *P. cultrifera* but cannot invade other Nereidae host as *Hedistes (Nereis) diversicolor* nor *Nereis pelagica*. The extreme adaptation of some gregarines to their host environments could explain some unexpected situations such as the reduction observed from the canonical 9+2 flagellar pattern, in the male gametes, with a 9+0 pattern in *S. pendula* (this

study), 6+0 in *L. tuzetae* (Schrével and Besse 1975) and 3+0 in *D. hatti* (Prensier et al. 1980). The 9+0 pattern of *Selenidium*, close to the 9+2 normality, may be correlated to a fertilization phase lasting about 1 hour in a 1-day sexual phase (gamogony and sporogony), the 6+0 pattern of *L. tuzetae*, may result from a fertilization realized in few hours within a cyst, during a 3 days sexual phase of the *Lecudina* life cycle (Schrével 1969). More impressively, the 3+0 pattern in *D. hatti* could have been selected over evolution because of the fertilization step lasting only few hours in a highly extended complete life cycle, lasting 2.5 years (Prensier et al. 2008). Such evolutionary proposal, suggesting that each gregarine develops its own programme according to its environment is in agreement with the notion of regressive evolution in microorganisms proposed by Lwoff (1944). This type of regressive evolution could probably continue with other coelomic gregarines with the disappearance of the flagellum in male gametes of *Gonospora* species as suggested from histology studies (Schrével 1963; Trégouboff 1918). Expression of the own program of each coelomic eugregarines is also observed with the variations in their epicytic cell surface transformations with digits, surface swelling in *Pterospora*, microvillosities in *Diplauxis* or the development of peristaltic motility instead of gliding, sometimes a pendular motility is observed in young trophozoite and peristaltic motility during the fast growing period of the same trophozoite as observed in *D. hatti* (see Schrével et al. 2013 for a review).

Conclusion

Molecular phylogenetic analyses of archigregarines demonstrate that *S. pendula*, the type species of archigregarines, belongs to a lineage with a large number of *Selenidium* parasites of Spionidae, Sabellariidae, Sabellidae, Cirratulidae families of the Sedentaria Polychaeta. All these *Selenidium* exhibit similar biological characters such as the cell cortex with a plasma membrane, imc (inner-membrane-complex) and subpellicular microtubules, the apical complex with a conoid, the myzocytosis with large food vacuoles and abundance of large rhoptry organelles, the nuclear multiplication during the syzygy and the early gamonts. Two other *Selenidium*-like lineages are observed in the Terebellidae and Sipunculida where the sexual characters are not available at this time. Such a status underlines an adaptation of the family Selenidiidae to their host families and this first early evolutive lineage could correspond

to the transition step between the free-living flagellated alveolates and the Apicomplexa, before the diversification of the marine eugregarines without the typical myzocytosis realized through the conoid but with a gliding motility.

Methods

Preparation of annelids and gregarines: Isolates of the gregarine *Selenidium pendula* Giard, 1884 type species, were collected from the intestine of the polychaete worm *Scolelepis squamata* (O. F. Müller, 1806) (previously named *Nerine cirratulus*, Delle Chiaje, 1831) on the French coast of the English Channel at the "Station Biologique de Roscoff", in 2007 then again in 2012. Isolates of the gregarines *Selenidium hollandei* Vivier and Schrével, 1966, *Lecudina pellucida* (Mingazzini, 1891) type species and different isolates of *L. tuzetae* Schrével, 1963 were also collected from the intestines of polychaete worms from the same area, in 2007, 2012, 2013 and 2014 (Table 2).

After washing in seawater, each collected worm was kept, at the laboratory temperature, in a separate Petri dish. The medium (seawater) was changed daily. For long-term conservation, the collected worms were rinsed with 0.22 μm filtered seawater and stored at 4 °C. In order to collect *Selenidium pendula* Giard, 1884, the anterior part of the *Scololelepis squamata* worms, with a yellow color, was discarded since the parasites were always absent, then the worms were cut transversally in series of segments of about 1 to 1.5 cm of length. To collect *S. hollandei*, *L. pellucida* and *L. tuzetae*, a similar type of microdissection was performed from their corresponding hosts, under a classic binocular microscope, in order to expose the intestinal epithelial surface to the seawater. In addition, and only in the case of *L. tuzetae*, cysts excreted with feces were collected from the Petri dishes of individually kept *Neanthes (Nereis) diversicolor* (O. F. Müller, 1776). Trophozoites of *S. pendula*, attached to the intestine, were easily detected, in spite of their rather small sizes (usually 150 -180 μm x 30-35 μm), by their white color - contrasting to the characteristic green color of the intestinal epithelium of the worm - and by their active pendular movements. In highly infected *Scolelepis squamata*, trophozoites and sexual stages of *S. pendula* (syzygies and young cysts) were also collected in Petri dishes, among the gametes released from hosts during the dissection. *S. hollandei* trophozoites were easily observed in host epithelium by their very active rolling movements, immediately after sectioning the post abdominal segment of their hosts, *Sabellaria alveolata* Linnaeus, 1767.

Electron microscopy: For transmission electron microscopy (TEM), intestinal epithelial tissues of *Scolelepis squamata* highly infected with trophozoites of *S. pendula* were collected and fixed in 5% (v/v) glutaraldehyde in 100-150 mM phosphate or 0.2 M cacodylate buffer (pH 7.3), at 4 °C, for 6 to 12 hours. The syzygy and gametocytes of *S. pendula*, not attached to the epithelium, were collected directly in the seawater from the Petri dishes and fixed in the same conditions. After washing either in the same buffer or in buffer containing 0.3 M sucrose, the samples were post-fixed with 1% (w/v) OsO$_4$ in the same buffer for 1 hr, then processed through standard dehydration, infiltration, and embedding procedures, in Epon or Araldite mixtures, with the corresponding solvents (i.e. propylene oxide or acetone respectively), at room temperature. The blocks were thin sectioned, collected on grids

Table 2. Summary of biological, geographical and molecular data, for original isolates in this study. The number of corresponding stages used for DNA preparations is indicated; T, trophozoite; C, cyst. Gene Accession numbers of the new sequences are available from the EMBL database.

Gregarine	Host	Location	Isolate names	Stage	Gene Access number (18S)
Selenidium pendula Giard 1884	*Scolelepis squamata* (O. F. Müller 1806)	English Channel, Roscoff, Aber, Lat:48°43′35.25″N, Long:3°59′22.54″W.	*Selenidium pendula* LG	50-70 T	LN901443
Selenidium pendula Giard 1884	*Scolelepis squamata* (O. F. Müller 1806)	English Channel, Roscoff-Aber 2012, Lat:48°43′35.25″N, Long:3°59′22.54″W.	*Selenidium pendula* IF	50-70 T	LN901444
Selenidium hollandei Vivier & Schrével 1966	*Sabellaria alveolata* (Linnaeus 1767)	English Channel, Saint-Efflam-Ile Rouge Lat:48°40′57.96″N, Long:3°35′32.52″W.	*Selenidium hollandei* LG	50-70 T	LN901445
Lecudina pellucida (Mingazzini 1891)	*Perinereis cultrifera* (Grübe 1840)	English Channel, Roscoff-Ile de la Souris, Lat:48°43′41.73″N, Long:3°59′22.10″W.	*Lecudina pellucida* LG	50-70 T	LN901442
Lecudina tuzetae Schrével 1963	*Neanthes (Nereis) diversicolor* (O. F. Müller 1776)	English Channel, Roscoff-Penzé 2012, Lat:48°37′40.07″N, Long:3°57′13.40″W.	*Lecudina tuzetae Roscoff 2012* IF132	7 C	LN901446
Lecudina tuzetae Schrével 1963	*Neanthes (Nereis) diversicolor* (O. F. Müller 1776)	English Channel, Roscoff-Penzé 2013, Lat:48°37′40,07″N, Long:3°57′13.40″W.	*Lecudina tuzetae Roscoff 2013a* IF181	30 C	LN901447
Lecudina tuzetae Schrével 1963	*Neanthes (Nereis) diversicolor* (O. F. Müller 1776)	English Channel, Roscoff-Penzé 2013, Lat:48°37′40.07″N, Long:3°57′13.40″W.	*Lecudina tuzetae Roscoff 2013b* IF462	2 C	LN901448
Lecudina tuzetae Schrével 1963	*Neanthes (Nereis) diversicolor* (O. F. Müller 1776)	English Channel, Roscoff-Penzé 2014, Lat:48°37′40,07″N, Long:3°57′13.40″W.	*Lecudina tuzetae Roscoff 2014a* IF171	50 C	LN901449
Lecudina tuzetae Schrével 1963	*Neanthes (Nereis) diversicolor* (O. F. Müller 1776)	English Channel, Roscoff-Penzé 2014, Lat:48°37′40,07″N, Long:3°57′13.40″W.	*Lecudina tuzetae Roscoff 2014b* IF172	50 C	LN901450

and stained with saturated uranyl acetate in 50% (v/v) ethanol for 1-3 min then in lead citrate. Sections were observed with a Hitachi HU 11 E electron microscopy (Hitachi Ltd, Japan) or a JEOL 1010 TEM.

For SEM, the intestines were open along the axis of the polychaete, and the body parts highly infected by *S. pendula* were carefully washed in 0.22 μm-filtered seawater before fixation in glutaraldehyde as done above for TEM. After the post fixation in 1% OsO_4 in 0.2 M cacodylate buffer, specimens were dehydrated in a graded series of acetone, critical point-dried in liquid CO_2 and coated with gold. The samples were examined in a JEOL JSM-7401F FE SEM.

DNA isolation and sequencing: For the LG isolates (*S. pendula* LG, *S. hollandei* LG, *L. pellucida* LG Table 1), groups of ~50-70 isolated trophozoites were washed at least three times in 0.22 μm-filtered seawater and DNA was extracted from individual parasites using a modified GITC (Guanidinium isothiocyanate) protocol (Chomczynski and Sacchi 2006). Individuals were placed in 50 μl of the GITC extraction buffer and crushed using an adjusted micro-pilon (Kimble Chase®). Tubes were incubated at 72 °C for 20 min. Next, one volume of cold isopropanol was added at −20 °C overnight for DNA precipitation. The following day, samples were centrifuged (20,000 *g*, 15 min at 4 °C) and supernatants removed. The DNA pellet was cleaned using 70% ethanol (100 μl), followed by a last centrifugation (20,000 *g*, 10 min). Supernatant was removed and the DNA pellet was hydrated into 20 μl of sterile distilled water and stored at −20 °C. For *S. pendula* IF, a group of ~50-70 isolated trophozoites were washed at least three times in 0.22 μm filtered seawater and genomic DNA was isolated by using a phenol-chloroform extraction procedure as previously described for *Plasmodium falciparum* (Florent et al. 2000), and the purified DNA pellet was rehydrated into 20 μl of sterile distilled water and stored at -20 °C.

For *L. tuzetae* Roscoff 2012 IF462, DNA was isolated by using the phenol-chloroform extraction procedure described above, from 2 cysts, collected from the feces of a single *Neanthes (Nereis) diversicolor* (O. F. Müller, 1776) host individually kept in a Petri dish. The purified DNA pellet was rehydrated into 20 μl of sterile distilled water and was stored at -20 °C. Finally, for the 4 remaining *L. tuzetae* Roscoff, DNA extractions were performed using MasterPure™ Complete DNA and RNA Purification kit (Epicentre, Illumina Inc. USA) following supplier's recommendations for Cell Samples manipulations, with minor modifications, from respectively 7 cysts (IF131), 50 cysts (IF171 and IF172) and 30 cysts (IF181). Briefly, each group of cysts was isolated from the feces of a single *N. diversicolor* host individually kept in a Petri dish, from which each cyst was then extensively washed, one by one, in three successive drops of 0.22 μm filtered seawater supplemented with antibiotics penicillin (100 U/mL), streptomycin (100 μg/mL) and gentamycin (50 μg/mL) (Gibco, Life Technologies, USA) then pooled again. Then, isolated and washed cysts were submerged in 300 μL Tissue-and-Cell lysis solution, submitted to five series of freezing (liquid nitrogen) and thawing (37 °C) before addition of Proteinase K then RNAse A and, after sample processing as recommended, isolated DNA pellets were rehydrated in 35 μl TE (10 mM Tris-pH 7.5 and 1 mM EDTA) prior to subsequent storage at -20 °C.

These DNA extraction products were then used as templates in various series of PCR amplifications, in order to amplify the SSU rRNA gene of these gregarines, then sequenced using the Sanger sequencing methodology.

LG samples. The PCR mix (15 μl final volume) contained 1–6 μl of the DNA extract, 330 μM of each deoxynucleoside triphosphate (dNTP), 2.5 mM of $MgCl_2$, 1.25 U of GoTaq® DNA polymerase (Promega Corporation), 0.17 μM of both primers, 1× of buffer (Promega Corporation). The PCR cycle, run in an automated thermocycler (GeneAmp®PCR System 9700, Applied Biosystem, USA), was programmed to give an initial denaturating step at 95 °C for 5 min, 35 cycles of denaturating at 95 °C for 1 min, annealing at 55 °C for 45 s and extension at 72 °C for 1 min 15 s, and a final extension step at 72 °C for 7 min. PCR products were cloned into a TOPO TA cloning kit (Invitrogen®), following manufacturer's recommendations. Inserts inside white colonies were screened by PCR (same procedure as before). Positive PCR products were purified (ExoSAP-IT® For PCR Product Clean-Up, USB®) and sequenced using the Big Dye Terminator Cycle Sequencing Kit version 3.0 (PE Biosystems®) and an ABI PRISM model 377 (version 3.3) automated sequencer with specific internal primers.

The list of primers used for both PCR amplifications and Sanger sequencing is provided in the table of the Supplementary data 6.

IF samples. PCR amplifications were done using Hot firepol DNA polymerase as recommended (Solis BioDyne, Estonia), in a 50 μl final volume supplemented with 2 mM $MgCl_2$, 200 μM each dNTPs and 200 nM forward (P4+T or WL1) and reverse (EukP3) primers (Supplementary Material 6) and 1 μl of isolated gregarine DNAs. PCR cycles, run in an automated thermocycler (GeneAmp®PCR System 9700, Applied Biosystem, USA), were programmed to give an initial denaturation step at 95 °C for 4 min, 30 cycles of denaturation at 95 °C for 30 s, annealing at 51 °Cfor 30 s and extension at 72 °C for 2 min, and a final extension step at 72 °C for 7 min. PCR products were purified using Illustra™ GFX™ PCR DNA and Gel Band Purification kit (GE Healthcare, France) and were cloned into pGEM®-T Easy vector (Promega, Madison WI, USA) using supplier's recommendations. DNA sequences were obtained from positive clones selected by PCR using T7 and Sp6 universal primers flanking the pGEM®-T Easy vector cloning site, using T7, Sp6 and internal primers such as LWA1, LWA3, PIF3F and PIF3R (Table 6), by the Sanger method (Beckman Coulter Genomics, Takeley, UK). Raw were edited using the BioEdit 7.1.3.0 program (Hall 1999) and assembled by using MEGA6 (Tamura et al. 2013).

Phylogenetic analyses: SSU rDNA sequences from nine *Selenium* and *Lecudina* species were aligned to 106 rDNA sequences from diverse eukaryotes, mostly corresponding to representatives of Alveolata with one Rhizaria as outgroup. Sequences were aligned using the online version of MAFFT version 7 (http://mafft.cbrc.jp/alignment/server/ Katosh and Toh 2010), using the secondary structure of RNA (Q-INS-I option) and further refined manually taking as a reference the secondary structure of *T. gondii* small subunit rRNA (Gagnon et al. 1996). Ambiguously aligned positions were manually removed which yielded a confident alignment of 1350 positions. A GTR substitution model with gamma-distributed rate variation across sites was suggested as the best-fit model by JModeltest V2.1.3 (Darriba et al. 2012). Accordingly, a Bayesian phylogenetic tree was constructed with MrBayes v.3.2.3 (Ronquist et al. 2012) using lset nst=6 rates=Invgamma Ngammacat=4 parameters. Four simultaneous Monte Carlo Markov chains were run from random trees for a total of 13,000,000 generations in two parallel runs. A tree was sampled every 1000 generation and 25% of the trees were discarded as "burn-in". A consensus tree was constructed from the post-burn-in trees and posterior probabilities were calculated in MrBayes. Maximum Likelihood analyses were performed with MEGA 6.06 (Tamura et al. 2013) using the GTR+G+I model. Bootstraps were estimated from 1,000 replicates.

The phylogenetic tree for the Selenidiidae lineage from polychate annelids (Fig. 13) was contructed using the same alignment but for a subset of 20 sequences; all position containing gaps and missing data were eliminated; there were a total of 1,416 positions in the final dataset. Maximum Likelihood analyses were performed with MEGA 6.06 (Tamura et al. 2013) using the GTR+G+I model. Bootstraps were estimated from 1,000 replicates.

Estimate of evolutionary divergence between sequences: Evolutionary divergence between sequences was computed by using the MEGA 6.06 (Tamura et al. 2013) using a subset of sequences extracted from the main phylogenetic alignment. For the analysis of the Selenidiidae lineage (Supplementary Material 4) the analysis involved 33 nucleotide sequences for 16 distinct species, there were a total of 2088 positions in the final dataset and all positions containing gaps and missing data were eliminated.

Acknowledgements

Appendix A. Supplementary Data

Supplementary data associated with this article can be found, in the online version, at http://dx.doi.org/10.1016/j.protis.2016.06.001.

References

Boothroyd JC, Dubremetz JF (2008) Kiss and split: the dual roles of *Toxoplasma* rhoptries. Nat Rev Microbiol **6**:79–88

Bradley PJ, Ward C, Cheng SJ, Alexander DL, Coller S, Coombs GH, Dunn JD, Ferguson DJ, Sanderson SJ, Wastling JM, Boothroyd JC (2005) Proteomic analysis of rhoptry organelles reveals many novel constituents for host-parasite interactions in *Toxoplasma gondii*. J Biol Chem **280**:34245–34258

Brasil L (1907) Recherches sur le cycle évolutif des Selenidiidae, Grégarines parasites d'Annélides polychètes. I. La schizogonie et la croissance des gamétocytes chez *Selenidium caulleryi* n. sp. Arch Protistenkd **16**:370–397

Brugerolle G (2002) *Colpodella vorax*: ultrastructure, predation, life-cycle, mitosis, and phylogenetic relationships. Eur J Protistol **38**:113–125

Caullery M, Mesnil F (1899) Sur quelques parasites internes des Annélides. I. Grégarines nématoides des annélides. Trav Stat Zool Wimereux **7**:80–99

Caullery M, Mesnil F (1900) Sur un mode particulier de division nucléaire chez les Grégarines. Arch Anat Microsc **3**:146–167

Chomczynski P, Sacchi N (2006) The single-step method of RNA isolation by acid guanidinium thiocyanate-phenol-chloroform extraction: twenty-something years on. Nat Protoc **1**:581–585

Counihan NA, Kalanon M, Coppel RL, de Koning-Ward TF (2013) *Plasmodium* rhoptry proteins: why order is important. Trends Parasitol **29**:228–236

Darriba D, Taboada GL, Doallo R, Posada D (2012) jModeltest 2: more models, new heuristics and parallel computing. Nat Methods **9**:772

de Leon JC, Scheumann N, Beatty W, Beck JR, Tran JQ, Yau C, Bradley PJ, Gull K, Wickstead B, Morisette NS (2013) A SAS-6-like protein suggests that the *Trypanosoma* conoid complex evolved from flagellar components. Eukaryot Cell **12**:1009–1015

De Rosa R, Prud'homme B, Balavoine G (2005) Caudal and even-skipped in the annelid *Platynereis dumerilii* and the ancestry of the posterior growth. Evol Dev **7**:574–587

Desportes I (1969) Ultrastructure et développement des Grégarines du genre *Stylocephalus*. Ann Sci Nat Zool **11**:31–96

Desportes I, Schrével J (2013) The Gregarines: The Early Branching Apicomplexa. Brill, Leiden. 781p

Dubremetz JF (1973) Etude ultrastructurale de la mitose schizogonique chez la Coccidie *Eimeria necatrix* (Johnson, 1930). J Ultrastruct Res **42**:354–376

Dubremetz JF (1975) Genesis of merozoites in the coccidia, *Eimeria necatrix*: Ultrastructural study. J Protozool **22**:71–84

Florent I, Mouray E, Dali Ali F, Drobecq H, Girault S, Schrével J, Sergheraert C, Grellier P (2000) Cloning of *Plasmodium falciparum* protein disulfide isomerase homologue by affinity purification using the antiplasmodial inhibitor inhibitor 1,4-bis{3-[N-(cyclohexyl methyl)amino] propyl}piperazine. FEBS Lett **484**:246–252

Francia ME, Jordan CN, Patel JD, Sheiner L, Demerly JL, Fellows JD, de Leon JC, Morrissette NS, Dubremetz JF, Striepen B (2012) Cell division in apicomplexan parasites is organized by a homolog of the striated rootlet fiber of algal flagella. PLoS Biol **10**:e1001444

Francia ME, Striepen B (2014) Cell division in apicomplexan parasites. Nat Rev Microbiol **12**:125–136

Gagnon S, Bourbeau D, Levesque RC (1996) Secondary structures and features of the 18S, 5. 8S and 26S ribosomal RNAs from the apicomplexan parasite *Toxoplasma gondii*. Gene **173**:129–135

Giard A (1884) Note sur un nouveau groupe de protozoaires parasites de annélides polychétes et sur quelques points de l'histoire des grégarines (*Selenidium pendula*). CR Ass Fr Avanc Sci Congrés de Blois :192p

Goldstein SF, Schrével J (1982) Microtubules and cell motility. SFRS, France, CERIMES, www.cerimes.education.fr.

Gunderson J, Small EB (1986) *Selenidium fallax* n. sp. (Protozoa, Apicomplexa) from the sipunculid *Phascolosoma agassizii* Kerferstein 1867. J Parasitol **72**:107–110

Hall TA (1999) BioEdit: a user-friendly biological sequence alignment editor and analysis program for Windows 96/98NT. Nucleic Acids Symp Ser **41**:95–98

Heintzelman MB (2004) Actin and myosin in *Gregarina polymorpha*. Cell Motil Cytoskeleton **58**:83–95

Hodges ME, Scheumann N, Wickstead B, Langdale JA, Gull K (2010) Reconstructing the evolutionary history of the centriole from protein components. J Cell Biol **123**:1407–1413

Hoshide H, Todd KS (1996) The fine structure of cell surface and hair-like projections of *Filipodium ozakii* Hukui. Acta Protozool **35**:309–315

Hu K, Roos DS, Murray JM (2002) A novel polymer of tubulin forms the conoid of *Toxoplasma gondii*. J Cell Biol **156**:1039–1050

Hu K, Johnson J, Fraunholz M, Surajajjala S, DiLullo C, Yates J, Rossn DS, Murray JM (2006) Cytoskeletal Components of an Invasion Machine-The Apical Complex of *Toxoplasma gondii*. PLoS Pathogens **2(2)**, e13: 121-138

Katoh K, Toh H (2010) Parallelization of the MAFFT multiple sequence alignment program. Bioinformatics **26**:1899–1900

Kuriyama R, Besse C, Geze M, Omoto CK, Schrével J (2005) Dynamic organization of microtubules and microtubule-organizing centers during the sexual phase of a parasitic protozoan, *Lecudina tuzetae* (Gregarine, Apicomplexa). Cell Motil Cytoskeleton **62**:195–209

Kuvardina ON, Leander BS, Aleshin VV, Myl'nikov AP, Keeling PJ, Simdyanov TG (2002) The phylogeny of colpodellids (Alveolata) using small subunit rRNA genes sequences suggests there are the free-living group to apicomplexans. J Eukaryot Microbiol **49**:498–504

Leander BS (2006) Ultrastructure of the archigregarine *Selenidium vivax* (Apicomplexa)-A dynamic parasite of sipunculid worms (host: *Phascolosoma agassizii*). Mar Biol Res **2**:178–190

Leander BS (2007a) Marine gregarines: evolutionary prelude to the apicomplexan radiation? Trends Parasitol **24**:60–67

Leander BS (2007b) Molecular phylogeny and ultrastructure of *Selenidium serpulae* (Apicomplexa, Archigregarinia) from the calcareous tubeworm *Serpula vermicularis* (Annelida, Polychaeta, Sabellida). Zool Scripta **36**:213–222

Leander BS, Keeling PJ (2003) Morphostasis in alveolate evolution. Trends Ecol Evol **18**:395–404

Leander BS, Harper JT, Keeling PJ (2003a) Molecular phylogeny and surface morphology of marine aseptate gregarines (Apicomplexa): *Selenidium* spp. and *Lecudina* spp. J Parasitol **89**:1191–1205

Leander BS, Kuvardina ON, Aleshin VV, Mylnikov AP, Keeling PJ (2003b) Molecular phylogeny and surface morphology of *Colpodella edax* (Alveolata): insights into the phagotrophic ancestry of apicomplexans. J Eukaryot Microbiol **50**:334–340

Léger L, Duboscq O (1917) Sporozoaires de *Glossobalanus minutus* Kow. *Eimeria epidermica* n. sp.; *Eimeria beauchampi* n. sp.; *Selenidium metchnikowi* n. sp. Ann Inst Pasteur **31**:60–74

Leidel S, Delattre M, Cerutti L, Baumer K, Gonczi P (2005) SAS-6 defines a protein family required for centrosome duplication in *C. elegans* and human cells. Nat Cell Biol **7**:115–125

Lim L, McFadden GI (2010) The evolution, metabolism anf functions of the apicoplast. Philos Trans Royal Soc B **365**:749–763

Lwoff A (1944) L'évolution physiologique. Etude des pertes de fonction chez les microorganismes. Hermann Publ, Paris. 308p

Macgregor HC, Thomasson PA (1965) The fine structure of two archigregarines, *Selenidium fallax* and *Ditrypanocystis cirratuli*. J Protozool **12**:438–443

Mignot JP (1966) Ultrastructure des Eugléniens. Etude de la cuticule chez différentes espèces. Protistologica **2**:51–117

Misof B, Liu S, Meusemann K, et al. (2014) Phylogenomics resolves the timing and pattern of insect evolution. Science **346**:763–767

Molon-Noblot S, Desportes I (1980) Etude ultrastructurale des mitoses gamogoniques de la Grégarine *Grebnickiella gracilis* Gr. parasite de la scolopendre *Scolopendra cingulata* L. Considérations sur les mitoses schizogoniques des Sporozoaires (Apicomplexa). Protistologica **16**:395–411

Nei M, Kumar S (2000) Molecular Evolution and Phylogenetics. Oxford University Press, New York. 333p

Okamoto N, Keeling PJ (2014) The 3D structure of the apical complex and association with the flagellar apparatus revealed by serial TEM tomography in *Psammosa pacifica*, a distant relative of the Apicomplexa. PLoS ONE **9(1)**:e84653

Perkins FO (1996) The structure of *Perkinsus marinus* (Mackin, Owen and Collier, 1950) Levine, 1978 with comments on the taxonomy and phylogeny of *Perkinsus* spp. J Shellfish Res **15**:67–87

Prensier G, Dubremetz JF, Schrével J (2008) The unique adaptation of the life cycle of the coelomic gregarine *Diplauxis hatti* to its host *Perinereis cultrifera* (Annelida, Polychaeta): an experimental and ultrastructural study. J Eukaryot Microbiol **55**:541–553

Prensier G, Vivier E, Goldstein S, Schrével J (1980) Motile flagellum with a "3 + 0" ultrastructure. Science **207**:1493–1494

Ray HN (1930) Studies on some sporozoa in polychaete worms. I. Gregarines of the genus *Selenidium*. Parasitology **22**:370–398

Reed N (1933) Sporogony in *Selenidium mesnili* Brasil, a sporozoan parasite of *Myxicola infundibulum* Mont. Parasitology **25**:402–409

Ronquist F, Teslenko M, van der Mark P, Ayres DL, Darling A, Höhna S, Larget B, Liu L, Suchard MA, Huelsenbeck JP (2012) MrBayes 3. 2: efficient Bayesian phylogenetic inference and model choice across a large model space. Syst Biol **61**:539–542

Rouse GW, Fauchald K (1997) Cladistics and Polychaetes. Zool Scripta **26**:139–204

Rueckert S, Leander BS (2009) Molecular phylogeny and surface morphology of marine archigregarines (Apicomplexa), *Selenidium* spp. , *Filipodium phascolosomae* n. sp., and *Platyproteum* n. g. and comb. from North-Eastern pacific peanut worms (Sipuncula). J Eukaryot Microbiol **56**:428–439

Russell DG, Burns RG (1984) The polar ring of coccidian sporozoite: a unique microtubule-organizing centre. J Cell Sci **65**:197–207

Saldarriaga JF, McEwan ML, Fast NM, Taylor FJ, Keeling PJ (2003) Multiple protein phylogenies show that *Oxyrrhis marina* and *Perkinsus marinus* are early branches of dinoflagellate lineage. Int J Syst Evol Microbiol **53**:355–365

Santos JM, Lebrun M, Daher W, Soldati D, Dubremetz JF (2009) Apicomplexa cytoskeleton and motors: key regulators in morphogenesis, cell division, transport and motility. Int J Parasitol **39**:153–162

Schrével J (1963) Contribution à l'étude de trois Grégarines parasites d'Annélides Polychètes: *Lecudina elongata* Mingazzini1891; *Lecudina tuzetae* Schrével 1963; *Gonospora varia* Léger 1892. Arch Zool Exp Gén **104**:125–142

Schrével J (1966) Cycle de *Selenidium pendula* Giard 1884, Grégarine parasite de *Nerine cirratulus* Delle Chiaje (Annélide Polychète). Protistologica **2**:31–34

Schrével J (1968) L'ultrastructure de la région antérieure de la grégarine *Selenidium* et son intérêt pour l'étude de la nutrition chez les Sporozoaires. J Microsc Paris **7**:391–410

Schrével J (1969) Recherches sur le cycle des Lecudinidae grégarines parasites d'Annélides Polychètes. Protistologica **5**:561–588

Schrével J (1970) Contribution à l'étude à l'étude des Selenidiidae parasites d'Annélides Polychètes: I. Cycles biologiques. Protistologica **6**:389–426

Schrével J (1971a) Contribution à l'étude à l'étude des Selenidiidae parasites d'Annélides Polychètes:II. Ultrastructure de quelques trophozoites. Protistologica **7**:101–130

Schrével J (1971b) Observations biologiques et ultrastructurales sur les Selenidiidae et leurs conséquences sur la systématique des Grégarinomorphes. J Protozool **18**:448–470

Schrével J, Besse C (1975) Un type flagellaire fonctionel de base 6+0. J Cell Biol **66**:492–507

Schrével J, Desportes I (2013) Introduction: Gregarines among Apicomplexa. Chapter 1, 7-24. In Desportes I, Schrével J (eds) The Gregarines. The Early Branching Apicomplexa. Brill, Leiden, pp 7–24

Schrével J, Desportes I (2015) Gregarines. In Mehlhorn H (ed) Encyclopedia of Parasitology. 4 th edn Springer, Berlin, Heidelberg, pp 1–47

Schrével J, Caigneaux E, Gros D, Philippe M (1983) The three cortical membranes of the gregarines. I. Ultrastructural organization of *Gregarina blaberae*. J Cell Sci **61**:151–174

Schrével J, Desportes I, Goldstein S, Kuriyama R, Prensier G, Vávra J (2013) Biology of Gregarines and their Host-parasite Interactions. Chapter 2, 25-195. In Desportes I, Schrével J (eds) The Gregarines. The Early Branching Apicomplexa. Brill, Leiden, pp 25–195

Schrével J, Asfaux-Foucher G, Hopkins JM, Vincent R, Bourgouin C, Prensier G, Bannister LH (2008) Vesicle trafficking during sporozoite development in *Plasmodium berghei*: ultrastructural evidence for a novel trafficking mechanism. Parasitology **135**:1–12

Sheffield HG, Garnham PCC, Shiroishi T (1971) The fine structure of the sporozoite of *Lankesteria culicis*. J. Protozool **18**:98–105

Simdyanov TG, Kuvardina ON (2007) Fine structure and putative feeding mechanism of the archigregarine *Selenidium orientale* (Apicomplexa:Gregarinomorpha). Eur J Protistol **43**:17–25

Struck TH, Paul C, Hill N, Hartman S, Hösel C, Kube M, Lieb B, Meyer A, Tiedemann R, Purschke G, Bleidorn C (2011) Phylogenomic analyses unravel annelid evolution. Nature **471**:95–98

Tamura K, Stecher G, Peterson D, Filipski A, Kumar S (2013) MEGA6: Molecular Evolutionary Genetics Analysis Version 6.0. Mol Biol Evol **30**:2725–2729

Toso MA, Omoto CK (2007) *Gregarina niphandrodes* may lack both a plastid genome and organelle. J Eukaryot Microbiol **54**:66–72

Trégouboff G (1918) Etude monographique de *Gonospora testiculi* Treg. , grégarine parasite du testicule de *Cerithium vulgatum* Brug. Arch Zool Exp Gén **57**:471–509

Tuzet O, Ormières R (1958) *Selenidium flabelligerae* n. sp. parasite de *Flabelligera diplochaitos* Otto (Annélide sédentaire). Ann Sci Nat Zool **13**:71–76

Valigurová A, Vaškovicová N, Musilová N, Schrével J (2013) The enigma of eugregarine epicytic folds: where the gliding motility originates? Frontiers Zool **10**:57

van Breugel M, Hirono M, Andreeva A, Yanagisawa HA, Yamaguchi S, Nakazawa Y, Morgner N, Petrovitch M, Ebong IO, Robinson CV, Johnson M, Veprintsev D, Zuber B (2011) Structures of SAS-6 suggest its organization in centrioles. Science **331**:1196–1199

Vivier E (1967) Observations ultrastructurales sur l'enveloppe nucléaire et ses "pores" chez les Sporozoaires. J Microsc Paris **6**:371–390

Vivier E (1968) L'organisation ultrastructurale corticale de la grégarine *Lecudina pellucida*; ses rapports avec l'alimentation et la locomotion. J Protozool **15**:230–246

Vivier E, Schrével J (1964) Etude au microscope électronique d'une Grégarine du genre *Selenidium* parasite de *Sabellaria alveolata* L. J Microsc Paris **3**:651–670

Vivier E, Schrével J (1966) Les ultrastructures cytoplasmiques de *Selenidium hollandei*, n. sp., Grégarine parasite de *Sabellaria alveolata* L. J Microsc Paris **5**:213–228

Wakeman KC, Leander BS (2012) Molecular phylogeny of Pacific Archigregarines (Apicomplexa), including descriptions of *Veloxidium leptosynaptae* n. gen., n. sp., from the sea cucumber *Leptosynapta clarki* (Echinodermata), and two new species of *Selenidium*. J Eukaryot Microbiol **59**:1–14

Wakeman KC, Leander BS (2013) Molecular phylogeny of marine gregarine parasites (Apicomplexa) from tube-forming polychaetes (Sabellariidae, Cirratulidae and Serpulidae) including descriptions of two new species of *Selenidium*. J Eukaryot Microbiol **60**:514–525

Wakeman KC, Heintzelman MB, Leander BS (2014) Comparative ultrastructure and molecular phylogeny of *Selenidium melongena* n. sp. and *S. terebellae* Ray 1930 demonstrate niche partitioning in marine gregarine parasites (Apicomplexa). Protist **165**:493–511

Supplementary data 1. General view of a young syzygy of *Selenidium pendula* in TEM. Since the size of each gamont was too large for a single TEM micrograph, in this composite view we indicated the missing area between the two paired gamonts by a white band. Abbreviations: nucleus (N), nucleolus (nu). The sexual stages of gregarines start with the pairing of two gamonts. In one syzygy the gamont's cytoplasm as well the nuclei exhibit a similar organization. The spherical nucleoli of paired gamonts are of similar sizes and both contain several clear areas (Arrows).

Supplementary data 2. Estimates of evolutionary divergence between sequences. The numbers of base differences per site from between sequences are shown. The analysis involved 33 nucleotide sequences. All ambiguous positions were removed for each sequence pair. There were a total of 2088 positions in the final dataset. Evolutionary analyses were conducted in MEGA6 (Tamura et al. 2013).

|	1	2	3	4	5	6	7	8	9	10	11	12	13	14	15	16	17	18	19	20	21	22	23	24	25	26	27	28	29	30	31	32	33
1. Filipodium phascolosomae FJ832163.1																																	
2. Plathyproteum vivax AY196708.1	0.282																																
3. Selenidium pisinnus FJ832162.1	0.271	0.275																															
4. Selenidium orientale FJ832161.1	0.277	0.286	0.152																														
5. Selenidium melongena 1 KC890799.1	0.266	0.260	0.181	0.195																													
6. Selenidium melongena 2 KC890800.1	0.266	0.260	0.181	0.195	0.001																												
7. Selenidium melongena 3 KC890801.1	0.268	0.263	0.183	0.197	0.004	0.003																											
8. Selenidium melongena 4 KC890802.1	0.265	0.260	0.182	0.196	0.003	0.003	0.006																										
9. Selenidium terebellae AY196709.1	0.261	0.256	0.178	0.205	0.125	0.125	0.128	0.127																									
10. Selenidium terebellae KC890803.1	0.259	0.258	0.176	0.204	0.127	0.127	0.130	0.129	0.002																								
11. Selenidium terebellae 2 KC890804.1	0.258	0.257	0.176	0.203	0.126	0.126	0.129	0.128	0.001	0.002																							
12. Selenidium terebellae 3 KC890805.1	0.260	0.256	0.177	0.205	0.126	0.126	0.129	0.128	0.001	0.003	0.002																						
13. Selenidium terebellae 4 KC890806.1	0.260	0.256	0.177	0.206	0.127	0.127	0.130	0.129	0.002	0.004	0.003	0.001																					
14. Selenidium sp2 KCW2013 Isolate 1 KC110865.1	0.314	0.314	0.277	0.289	0.277	0.276	0.277	0.277	0.272	0.269	0.268	0.272	0.271																				
15. Selenidium sp2 KCW2013 Isolate 2 KC110868.1	0.319	0.318	0.281	0.291	0.280	0.279	0.281	0.280	0.276	0.273	0.273	0.276	0.275	0.008																			
16. Selenidium sp2 KCW2013 Isolate 3 KC110864.1	0.312	0.312	0.274	0.285	0.275	0.274	0.276	0.275	0.270	0.266	0.266	0.270	0.269	0.003	0.006																		
17. Selenidium sensimae KC110869.1	0.310	0.302	0.271	0.281	0.278	0.277	0.279	0.278	0.268	0.265	0.264	0.268	0.268	0.084	0.088	0.082																	
18. Selenidium sensimae KC110870.1	0.309	0.305	0.271	0.282	0.279	0.277	0.279	0.278	0.269	0.265	0.264	0.269	0.268	0.082	0.087	0.080	0.006																
19. Selenidium sp1 KCW2013 Isolate 1 KC110863.1	0.308	0.305	0.272	0.272	0.274	0.273	0.274	0.274	0.266	0.262	0.262	0.266	0.265	0.086	0.091	0.085	0.056	0.055															
20. Selenidium sp1 KCW2013 Isolate 2 KC110866.1	0.308	0.305	0.273	0.273	0.274	0.273	0.274	0.274	0.266	0.262	0.262	0.266	0.265	0.089	0.094	0.087	0.059	0.058	0.003														
21. Selenidium sp1 KCW2013 Isolate 3 KC110867.1	0.310	0.306	0.274	0.272	0.274	0.273	0.275	0.275	0.267	0.263	0.262	0.267	0.266	0.087	0.092	0.085	0.056	0.056	0.002	0.005													
22. Selenidium serpulae DQ683562.1	0.310	0.305	0.274	0.276	0.274	0.272	0.274	0.274	0.269	0.266	0.266	0.269	0.268	0.083	0.089	0.082	0.057	0.057	0.045	0.048	0.046												
23. Selenidium cf.mesnil JN857968.1	0.309	0.302	0.276	0.281	0.278	0.278	0.279	0.278	0.272	0.269	0.269	0.272	0.273	0.113	0.118	0.112	0.099	0.100	0.091	0.094	0.093	0.088											
24. Selenidium neosabellariae KC110871.1	0.310	0.301	0.265	0.273	0.271	0.271	0.273	0.271	0.270	0.268	0.268	0.269	0.270	0.127	0.131	0.125	0.111	0.111	0.106	0.108	0.108	0.099	0.089										
25. Selenidium neosabellariae KC110872.1	0.321	0.307	0.276	0.284	0.278	0.278	0.280	0.278	0.275	0.276	0.276	0.276	0.276	0.131	0.134	0.130	0.114	0.114	0.110	0.113	0.112	0.106	0.098	0.010									
26. Selenidium neosabellariae KC110873.1	0.315	0.301	0.269	0.277	0.271	0.271	0.273	0.271	0.270	0.271	0.270	0.270	0.270	0.125	0.128	0.124	0.110	0.109	0.105	0.107	0.107	0.101	0.091	0.003	0.008								
27. Selenidium hollandei thiswork	0.321	0.310	0.284	0.288	0.280	0.280	0.282	0.281	0.275	0.277	0.276	0.276	0.277	0.134	0.137	0.133	0.121	0.121	0.114	0.116	0.115	0.110	0.098	0.030	0.037	0.030							
28. Selenidium identhyrsae JN857967.1	0.312	0.307	0.269	0.277	0.275	0.275	0.277	0.276	0.273	0.270	0.270	0.273	0.273	0.126	0.129	0.124	0.114	0.114	0.106	0.108	0.108	0.101	0.093	0.022	0.030	0.023	0.034						
29. Selenidium cf. echinatum KC110874.1	0.313	0.309	0.269	0.285	0.269	0.269	0.271	0.270	0.266	0.262	0.261	0.266	0.266	0.133	0.138	0.132	0.124	0.124	0.111	0.113	0.113	0.118	0.108	0.104	0.110	0.103	0.114	0.101					
30. Selenidium cf echinatum KC110875.1	0.319	0.312	0.275	0.290	0.276	0.276	0.278	0.277	0.274	0.271	0.271	0.274	0.274	0.138	0.141	0.136	0.126	0.127	0.116	0.119	0.116	0.121	0.113	0.113	0.118	0.111	0.121	0.110	0.021				
31. Selenidium boccardiellae JN857969.1	0.299	0.292	0.263	0.272	0.259	0.259	0.260	0.259	0.263	0.260	0.259	0.263	0.263	0.122	0.125	0.119	0.103	0.103	0.101	0.104	0.103	0.095	0.085	0.083	0.092	0.084	0.089	0.089	0.086	0.093			
32. Selenidium pendula LG thiswork	0.305	0.305	0.268	0.285	0.270	0.270	0.272	0.271	0.269	0.267	0.266	0.269	0.269	0.134	0.138	0.133	0.113	0.113	0.111	0.114	0.112	0.109	0.095	0.093	0.102	0.094	0.100	0.100	0.098	0.107	0.042		
33. Selenidium pendula IF thiswork	0.309	0.300	0.263	0.285	0.259	0.259	0.261	0.260	0.259	0.258	0.258	0.260	0.261	0.118	0.122	0.117	0.101	0.100	0.104	0.107	0.106	0.102	0.087	0.081	0.089	0.082	0.088	0.085	0.088	0.097	0.034	0.012	

Supplementary data 3. Estimates of evolutionary divergence between sequences of Selenidiidae family.

The number of base differences per site between sequences of two given species is indicated as %. The analysis involved 33 nucleotide sequences for 16 distinct species. Indeed, for some species, up to 5 distinct sequences were taken into account in the calculations (this sequence number is indicated for each species in the first column, no indication corresponding to a unique sequence). Evolutionary analyses were conducted in MEGA6 (Tamura et al. 2013). There were a total of 2088 positions in the final dataset. For the pairwise analysis, all ambiguous positions were removed for each sequence pair.

	S. pendula (Lineage I)	*S. hollandei* (Lineage I)	*S. terebellae* (Lineage II)	*S. orientale* (Lineage III)	
S. pendula (2seq)	1.2%	8.5 - 9.5 %	25.8 - 26.9 %	28.5 %	Lineage I
S. boccardiella	3.4 - 4.2 %	8.9 %	25.9 - 26.3 %	27.2 %	Lineage I
S. neosabellariae (3seq)	8.1 - 10.2 %	3.0 - 3.7 %	26.8 - 27.6 %	27.3 - 28.4 %	Lineage I
S. hollandei	8.5 - 9.5 %	-	27.5 - 27.7 %	28.8 %	Lineage I
S. identhyrsae	8.5 - 10 %	3.4%	27.0 - 27.3 %	27.7%	Lineage I
S. cf mesnilli	8.7 - 9.5 %	9.8 %	26.9 - 27.3 %	28.1 %	Lineage I
S. echinatum (2seq)	8.8 - 10.7%	11.4 %	26.1 - 26.6 %	28.5%	Lineage I
S. sensimae (2seq)	10 - 11.3 %	12.1 %	26.4 - 26.8 %	28.1 - 28.2 %	Lineage I
S. serpulae	10.2 - 10.9 %	11 %	26.6 - 26.9 %	27.6 %	Lineage I
S. sp1 (3seq)	10.4 - 11.4 %	11.4 - 11.6 %	26.2 - 26.7 %	27.2 - 27.3 %	Lineage I
S. sp2 (3seq)	11.7 - 13.4 %	13.3 - 13.7 %	26.8 - 27.5 %	28.5 - 29.1 %	Lineage I
S. terebellae (5seq)	25.8 - 26.9 %	27.5 - 27.7 %	0.1 - 0.4 %	20.3 - 20.6 %	Lineage II
S. melongena (4seq)	25.9 - 27.2 %	28 - 28.2 %	12.5 - 13 %	19.5 - 19.7 %	Lineage II
S. pisinnus	26.3 - 26.8 %	28.4 %	17.6 - 17.8 %	15.2 %	Lineage III
S. orientale	28.5 %	28.8 %	20.3 - 20.6 %	-	Lineage III
Plathyproteum vivax	30 - 30.5 %	31 %	25.6 - 25.8 %	28.6	Lineage III
Filipodium phascolosomae	30.9 %	32.1 %	25.8 - 26.1 %	27.7 %	Lineage III

Supplementary data 4. Molecular phylogenetic analysis by Maximum Likelihood method of the Selenidiidae lineage parasites of polychaete annelids and the Selenidiidae-like lineage parasites of the Terebellidae family.

The evolutionary history was inferred by using the Maximum Likelihood method based on the General Time Reversible model (Nei and Kumar 2000). The tree with the highest log likelihood (-9626.0015) is shown. A discrete Gamma distribution was used to model evolutionary rate differences among sites (5 categories (+*G*, parameter = 0.5500). The rate variation model allowed for some sites to be evolutionarily invariable (+I), 16.4799% sites). The tree is drawn to scale, with branch lengths measured in the number of substitutions per site. The analysis involved 33 nucleotide sequences. All positions containing gaps and missing data were eliminated. There were a total of 1374 positions in the final dataset. Evolutionary analyses were conducted in MEGA6 (Tamura et al. 2013).
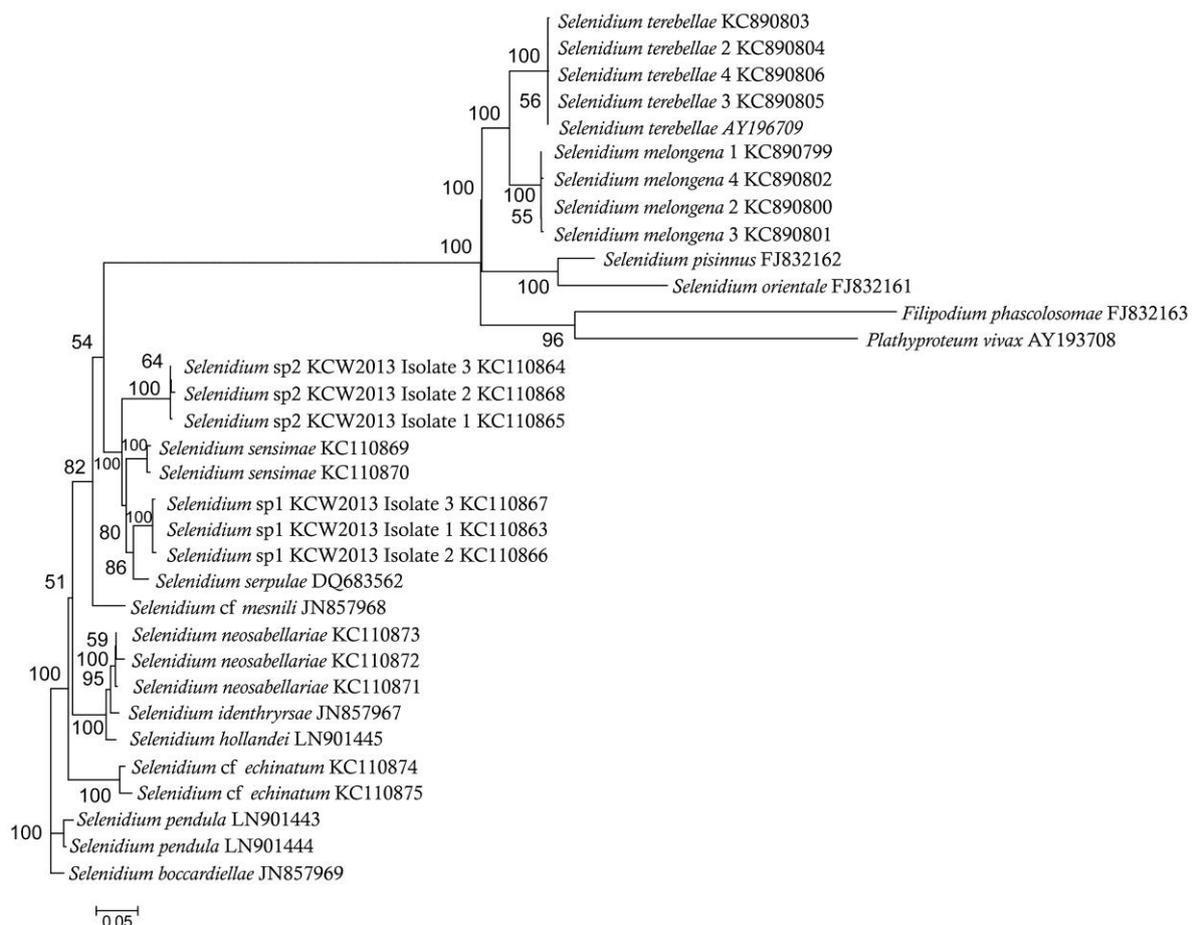
Supplementary data 5. Cross sections of *Selenidium terebellae* Ray 1930 intestinal parasite of the polychaete *Terebella lapidaria* Linnaeus 1776 from Roscoff **(A-D).** Abbreviations: amylopectin granule (am), bulge (B), dense layer (dl), groove (G), inner membrane complex (imc), mitochondria (M), microtubule (mt), nucleus (N). A. General view of a trophozoite with large bulges separated by grooves. **B.** Cross section of the cortex with a dense layer between the imc and the subpellicular microtubules. **C.** Cross section along a groove with accumulation of membranous residual organelles in the cytoplasm under the groove. **D.** Detail of the dense layer and the cross section of the microtubules (original data).
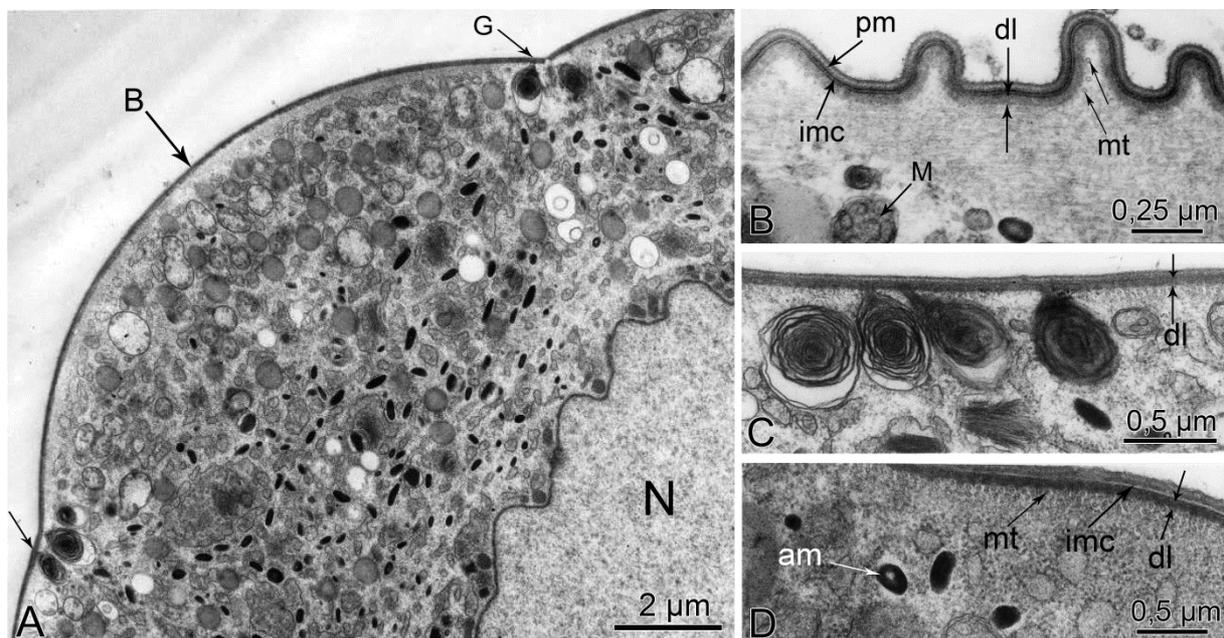
Supplementary data 6. Lists of primers used for SSU rDNA gene amplifications and sequencing by Sanger methodology.

Study	Primers name and sequence	Usage
LG	18S 328F: 5' ACCTGGTTGATCCTGCCAG 3'	PCR in forward
	18S 329R: 5' TGATCCTTCYGCAGGTTCAC 3'	PCR in reverse
	18S 528F 5' CCGCGGTAATTCCAGCTC 3'	Sequencing
	18S 690R 5' ATCCAAGAATTTCACCTCTGAC 3'	Sequencing
	18S 1055F 5' GGTGGTGCATGGCCGTTCTT 3'	Sequencing
	18S 1055R 5' ACGGCCATGCACCACCACCCAT 3'	Sequencing
IF	P4+T : 5' CTGGTTGATCCTGCCAG 3'	PCR in forward
	WL1(1) : 5' GCGCTACCTGGTTGATCCTGCC 3'	PCR in forward
	EukP3 (2) : 5' GACGGGCGGTGTGTAC 3'	PCR in reverse
	LWA1 : 5' GGAAGGCAGCAGGCGCGC 3'	Sequencing
	LWA3 : 5' AAACTTAAAGGAATTGACGG 3'	Sequencing
	PIF3F : 5' ATGCCTTGAACGATTTACC 3'	Sequencing
	PIF3R : 5' CTTGGCAGATGCTTTCGC 3'	Sequencing

(1): Leander BS Harper JT Keeling PJ 2003 J Parasitol. 89 1191-1205.

(2): Lara E Berney C Ekelund F Harms H Chatzinotas A 2007 Soil Biology and Biochemistry 39(1), 139-148

Chambouvet A., **Valigurová A.**, Pinheiro L.M.,

Richards T.A., Jirků M.

2016

Nematopsis temporariae (Gregarinasina, Apicomplexa, Alveolata) is an intracellular infectious agent of tadpole livers

Nematopsis temporariae (Gregarinasina, Apicomplexa, Alveolata) is an intracellular infectious agent of tadpole livers

Aurélie Chambouvet,[1]* Andrea Valigurová,[2]
Lara M. Pinheiro,[3] Thomas A. Richards[1,4] and
Miloslav Jirků[5]*

[1]*Biosciences, University of Exeter, Geoffrey Pope Building, Exeter, EX4 4QD, UK.*
[2]*Department of Botany and Zoology, Faculty of Science, Masaryk University, Kotlářská 2, Brno, 611 37, Czech Republic.*
[3]*National Council for Technological and Scientific Development (CNPq), Brazil.*
[4]*Integrated Microbial Biodiversity Program, Canadian Institute for Advanced Research (CIFAR), Toronto, Canada.*
[5]*Biology Centre, Czech Academy of Sciences, Institute of Parasitology, Branišovská 31, České Budějovice, 370 05, Czech Republic.*

Summary

Amphibians are in decline as a result of habitat destruction, climate change and infectious diseases. Tadpoles are thought susceptible to infections because they are dependent on only an innate immune system (e.g. macrophages). This is because the frog adaptive immune system does not function until later stages of their life cycle. In 1920, Nöller described a putative infectious agent of tadpoles named *Nematopsis temporariae*, which he putatively assigned to gregarine protists (Apicomplexa). Here, we identify a gregarine infection of tadpoles using both microscopy and ribosomal DNA sequencing of three different frog species (*Rana temporaria*, *R. dalmatina*, and *Hyla arborea*). We show that this protist lineage belongs to the subclass Gregarinasina Dufour 1828 and is regularly present in macrophages located in liver sinusoids of tadpoles, confirming the only known case of a gregarine infection of a vertebrate.

Introduction

Amphibian populations are in crisis with 48% of populations reported as declining (Stuart *et al.*, 2004). The emergence of infectious diseases is thought to be a major factor (Daszak *et al.*, 2003; Martel *et al.*, 2013). Amphibian physiology varies considerably during the life cycle. Tadpoles have a weak adaptive immunity with fewer antibody classes, poorer B and T lymphocyte function, no consistent expression of the major histocompability complex (MHC) class I protein and a poor switch from IgM to IgY (Du Pasquier *et al.*, 1989). Tadpoles, therefore, rely on an innate immune system that provides rapid and nonspecific protection. As such tadpoles host a diversity of different microbial organisms, acting as either definitive or intermediate hosts. Specifically, investigation of tadpole livers have identified a diversity of alveolate protists (Jirků *et al.*, 2002; 2009; Davis *et al.*, 2007; Chambouvet *et al.*, 2015) for which their role as putative parasites is unclear.

One enigmatic group of alveolates are the gregarines. Phylogenetic analyses show gregarines branch within the subphylum Apicomplexa Levine, 1980, emend. Adl *et al.* 2012 (Leander *et al.*, 2003; Adl *et al.*, 2012), which also includes parasites of mammals, e.g. *Plasmodium* spp. All described gregarines are parasites (Leander *et al.*, 2003) and are known to infect many groups of invertebrates, particularly annelids and insects (Leander, 2008). In 1920, Nöller described a gregarine named *Nematopsis temporariae* infecting the liver tissue of the frog *Rana temporaria* (Nöller, 1920). Here, we report the identification of an infectious microbe fitting this description from three species of frog tadpoles sampled in the Czech Republic using molecular and microscopy data.

Results and discussion

During an amphibian population survey in the Czech Republic we identified a gregarine-like intracellular infection of liver cells from tadpoles of *R. temporaria*, *R. dalmatina* and *H. arborea*. These tadpoles showed no signs of disease or impairment of fitness/function, although livers of some tadpoles appeared slightly enlarged and light coloured, they were not yellowish as previously reported for Perkinsea (Alveolata) infections (Davis *et al.*, 2007). No mortalities of tadpoles or metamorphs were recorded in the
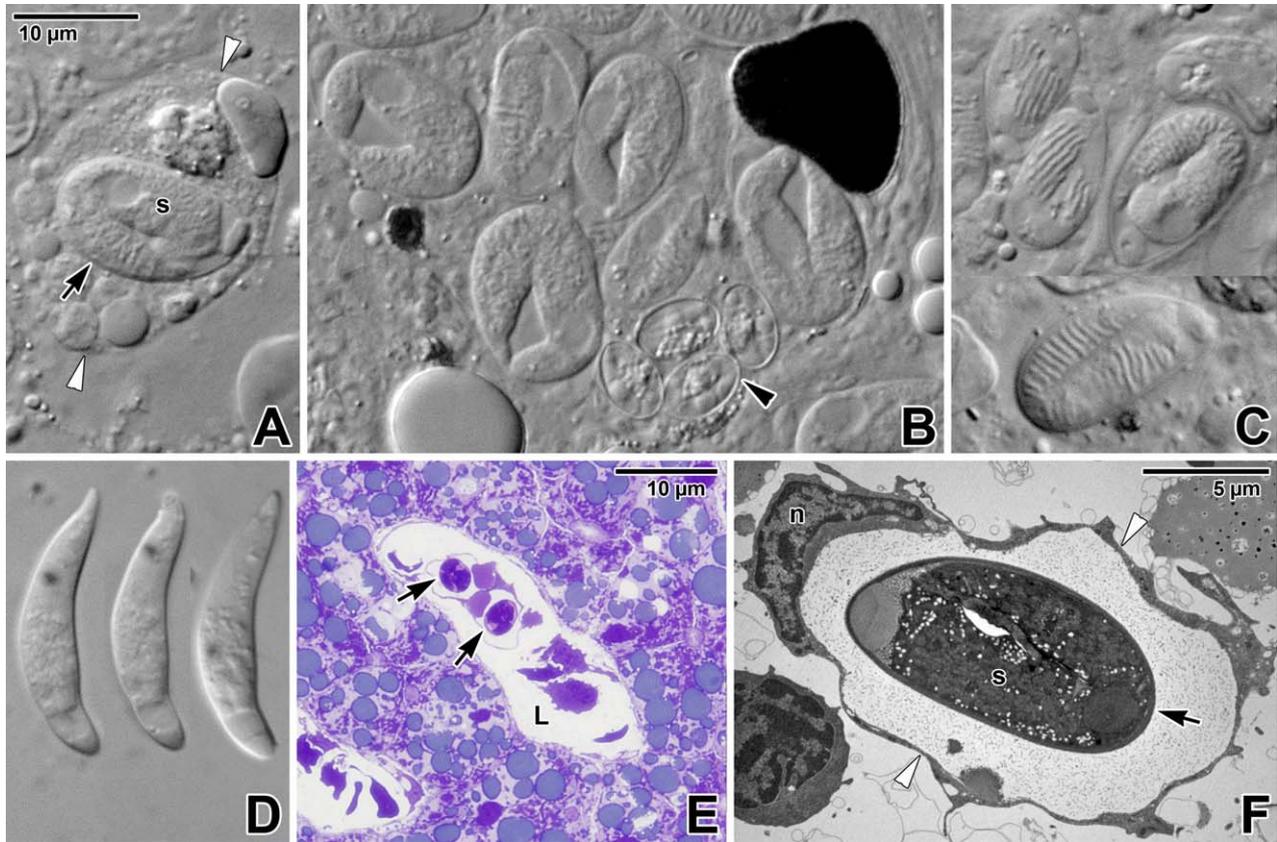
Fig. 1. Oocysts and free sporozoite of *Nematopsis temporariae* of *Rana dalmatina* tadpoles using microscopic analysis; fresh mount NIC (A–D), histological section stained with Toluidine-Blue (E), transmission electron microscopy (TEM) (F).
A. Intracellular oocyst (arrow) with single sporozoite (s) in a macrophage (white arrowheads).
B. Macrophage containing oocysts of both *N. temporariae* and *G. noelleri* (arrowhead); the macrophage as well as *G. noelleri* oocyst are ruptured by pressure during the squash preparation; *N. temporariae* oocysts are mechanically flattened, making the sporozoites more dispersed than normal; see the pigment granules upper right.
C. Composite micrograph of oocysts containing sporozoites showing distinct transverse striation.
D. Composite micrograph of a free sporozoite in gliding motion.
E. Macrophage containing two oocysts of *N. temporariae* (arrows) in lumen (L) of liver sinusoid.
F. Macrophage (white arrowheads) containing oocyst of *N. temporariae* (arrow); n – macrophage nucleus, s – sporozoite. A, B, C, D in the same scale.

field. Dissections of the tadpoles were carried out using standard procedures identifying the protist infection in multiple samples (*n* = 20 *R. damatina*, 20 *R. temporaria* and 15 *H. arborea*) from Zaječí potok, Brno, Czech Republic (49.23765N, 16.60637E) and Raduň, Czech Republic (49.88997N, 17.94375E). All specimens were in Gosner stage 26 or higher (Supporting Information Table S1 – and see below for discussion of sampling for *N. temporariae* beyond metamorphosis). The observed morphological characteristics are consistent with the original description of *N. temporariae*, specifically the protists observed possess monozoic oocysts and are morphologically and morphometrically consistent with the original description of *N. temporariae* (see description below), we therefore assign the gregarine-like oocysts to this species.

Standard light microscopy squash examination of liver, gall bladder, skin, heart, intestine and tail muscle of all examined tadpoles from the two localities revealed the presence of *N. temporariae* oocysts exclusively in host livers, demonstrating the intracellular microbial infection was not present in other host tissues examined. Samples of all examined tissues from each tadpole were fixed in 10% buffered formalin and glutaraldehyde, processed routinely, stained either with haematoxylin and eosin or Toluidine-Blue and examined by light or transmission electron microscopy. Each oocyst is ovoid, asymmetrical with one side usually flattened measuring 15.5 (14.0–17.0) × 6.5 (5.0–7.5) μm (Fig. 1A and B). Using light microscopy, sporozoites appeared transversely striated that corresponds to micronemes organized in parallel layers (Fig. 1C). On a few occasions, we observed a free sporozoite, keeping its' overall banana shape during gliding movement, with only apical end appearing fully flexible (Fig. 1D). Oocysts were the only developmental stage of *N. temporariae* consistently sampled, making unclear if the tadpoles serve as definitive or intermediate host of *N. temporariae*.

In most preparations ($n = 40$), both *N. temporariae* oocysts and *Goussia* oocysts (i.e. protists cell with a fine elastic oocyst wall and four dizoic sporocysts measuring 7.5 (7.0–8.0) × 4.7 (4.0–5.0) ($n = 50$) – Eimeriorina Léger, 1911, Apicomplexa) were observed to occupy the same cells (Fig. 1B) (Jirků *et al.*, 2009). However, in the *H. arborea* samples inspected ($n = 15$), this co-infection was not identified. In tadpole liver histological sections stained with Toluidine-Blue, oocysts were readily identified due to their characteristic morphology (Fig. 1E). Similarly as in fresh preparations, some oocysts were empty, sometimes containing residual granules. Interestingly, histological and transmission electron microscopy (TEM) examinations revealed presence of oocysts exclusively in phagocytic cells in liver sinusoids (Fig. 1E). Both non-pigmented (c.f. Kupffer cells) and pigmented (containing melanosomes) cell types were identified (Fig. 1A, B, E and F). The oocysts-containing cells belong to a macrophage lineage as reflected by their amoeboid nature with a notable variability in size and shape, typical filopodia, irregularly shaped nucleus, the presence of various quantities of lysosomes and phagosomes, poorly developed rough endoplasmic reticulum, Golgi bodies, a well-developed cortical microvacuolar system, small mitochondria and eventually melanosomes (e.g. Guida *et al.*, 1998) (Fig. 1F).

To investigate progression of the *Nematopsis* infection, an additional 45 tadpoles of *Rana dalmatina* (Gosner stages 33–42) were collected at Zaječí potok on the first of July 2004. Twenty-five tadpoles were euthanized by pithing and examined as described above for a presence of *Nematopsis* demonstrating presence of the infection in liver tissue. Additionally, tadpoles of *R. dalmatina* were kept in captivity beyond metamorphosis to assess the fate of *Nematopsis* oocysts in metamorphosed animals. A subset of 20 juvenile (and later subadult) frogs in total were dissected at intervals of 2 weeks for the first 2 months, then every one month for the third and fourth months, and every 3 months for the rest of the experiment up to the 15th month postmetamorphosis. In both fresh and histological preparations of livers from hosts examined, all tadpoles investigated were *Nematopsis* positive, while for organisms 4–6 weeks after metamorphosis, only empty oocysts were found.

In parallel to the histology analysis, we selected two liver samples from two different species: *R. temporaria* and *H. arborea* (four in total) and isolated 10–15 cells by mouth pipetting for DNA extraction. Using the eukaryotic forward primer (Euk1F) with the general -non-metazoan-reverse primer (Supporting Information Table S2), we PCR amplified and double strand sequenced (∼1000 bp of SSU gene) 10 clones per liver sample. All sequences recovered showed ≥ 97% identity. A conserved portion of the alignment was selected to design a 'Nematopsis' specific forward primer. This primer NEM-1F was used in association with the primer 28S-R1 targeting the 5′ of the LSU rRNA gene from *R. temporaria* (three samples), *H. arborea* (three samples) and *R. dalmatina* (two samples – Supporting Information Table S2). For each liver sample, three independent PCR amplifications were mixed and cloned. Three clones per sample were double strand sequenced (see SMM and Supporting Information Table S2).

Currently, there is only one sequence of the complete ribosomal RNA encoding gene belonging to the Gregarinasina Dufour, 1928 available in the Genbank nr database (*Gregarina* sp. JF412715, March 2016). To allow for comprehensive taxon sampling, phylogenetic analysis was, therefore, based on an alignment of the SSU gene that encompassed the V4 and V9 loops. The sequence alignment included 65 publically available sequences previously used for phylogenetic analysis (Rueckert *et al.*, 2011; Wakeman *et al.*, 2014) and 24 clone sequences recovered here. The ML and Bayesian phylogenies recovered a weakly supported backbone as previously described in phylogenies of the gregarines (Rueckert *et al.*, 2011; Wakeman *et al.*, 2014) (Fig. 2A). However, the SSU rDNA gene sequences recovered from the tadpole tissue form a highly supported clade (1/100/100) and branch with moderate bootstrap values (1/77/100) with the terrestrial gregarine clade 1 sequences (Rueckert *et al.*, 2011; Wakeman *et al.*, 2014) (Fig. 2A). Many alveolate genomes are highly AT rich (Gardner *et al.*, 2002; Kopecna *et al.*, 2006). We conducted Log-Det distance bootstrap analysis to account for differential base composition as a source of artifact (Foster and Hickey, 1999). This phylogenetic method provides strong support for phylogenetic association of *Nematopsis* with the terrestrial gregarines. This clade encompasses gregarine pathogens of a wide range of invertebrates, e.g. damselflies, earthworms, dragonflies, green darners, mosquitoes and sandflies (Fig. 2A). The phylogenetic results show that *N. temporariae* belongs to gregarines and confirms that this is the first example of a member of the subclass Gregarinasina, Dufour 1828, infecting a vertebrate.

Eukaryotic ribosomal RNA gene clusters (rRNA genes) are typically present in multiple copies within a nuclear genome (Long and Dawid, 1980). The internal transcribed spacers (ITS1 and ITS2) that separate the SSU, 5.8S and LSU genes have a high rate of sequence variation. We generated 24 independent clone sequences from eight liver samples (three clones per sample). These sequences showed between 96% and 99% sequence identities across the SSU-ITS1-5S-ITS2 ribosomal sequences (Fig. 2B and C, and Supporting Information Table S3). Considering only single nucleotide polymorphisms that occurred in at least two independent
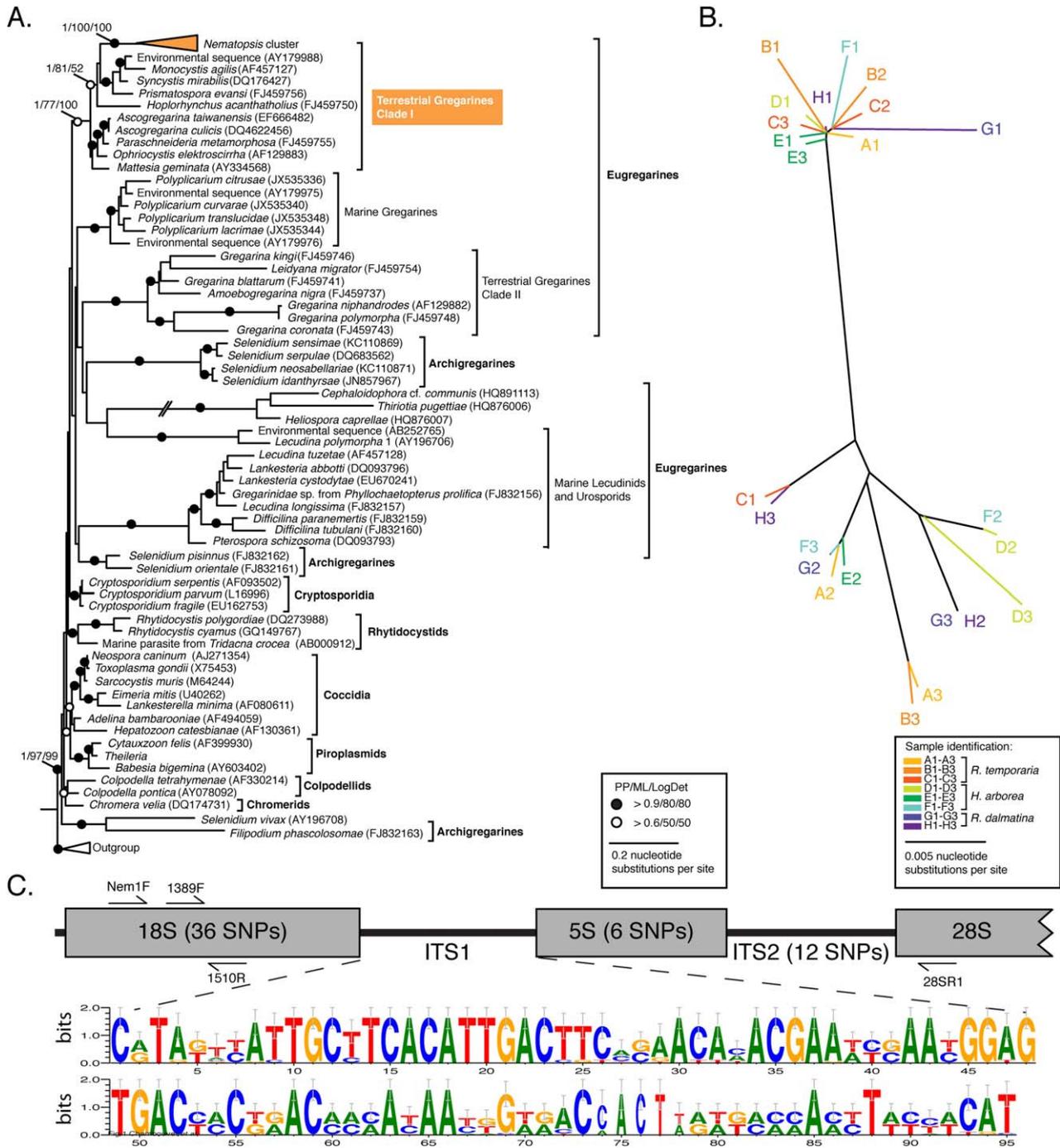
Fig. 2. A. RAxML tree investigating the phylogenetic placement of *N. temporariae*. The phylogeny is calculated from 89 sequences and 1276 alignment positions. Bayesian posterior probability, ML and Log-Det bootstrap values were notated using the following convention: support values are summarized by black circles when ≥ 0.9/80%/80% and white circles when this is not the case but all values are ≥ 0.6/50%/50%, actual values are shown for key branching relationships. The double-slashed line represents branches shortened by $1/2$. The identification of the different clades was reported as described in (Rueckert *et al.*, 2011; Wakeman *et al.*, 2014). B. Unrooted maximum likelihood phylogenetic tree of the ribosomal RNA gene cluster sequences. The colours of the clone's names identified the tadpole liver tissue samples and the host taxonomy (see key). C. Representation of the ribosomal gene cluster and the relative position of the different primer used in this study (not to scale). For each region of the rRNA gene cluster the number of SNPs were indicated in brackets if the mutation is retrieved in at least two independent clones. The ITS1 region where at least two separate nucleotide motifs have been detected is represented using http://weblogo.berkeley.edu.

clone sequences, we identified SNPs that identify variation specific for distinct rDNA-types. The main region of polymorphism was located within the ITS1 region identifying a minimum of two major rDNA-types (Fig. 2C), representing either inter or intraindividual genetic diversity.

This study represents the first molecular and microscopic description of the association between a gregarine and a vertebrate, and importantly shows that the *N. temporariae* oocysts form intracellular infections of tadpole cells. It is unclear whether tadpoles serve as definitive or intermediate hosts. These results provide the molecular tools for studying this infectious agent with regard to wider environmental ecology and specifically distribution in amphibian populations.

Acknowledgements

References

Adl, S.M., Simpson, A.G., Lane, C.E., Lukes, J., Bass, D., Bowser, S.S., *et al*, (2012) The revised classification of eukaryotes. *J Eukaryot Microbiol* **59**: 429–493.

Chambouvet, A., Gower, D.J., Jirků, M., Yabsley, M.J., Davis, A.K., Leonard, G., *et al*, (2015) Cryptic infection of a broad taxonomic and geographic diversity of tadpoles by Perkinsea protists. *Proc Natl Acad Sci USA* **112**: E4743–E4751.

Daszak, P., Cunningham, A.A., and Hyatt, A.D. (2003) Infectious disease and amphibian population declines. *Divers Distrib* **9**: 141–150.

Davis, A.K., Yabsley, M.J., Keel, M.K, and Maerz, J.C. (2007) Discovery of a novel alveolate pathogen affecting southern leopard frogs in georgia: description of the disease and host effects. *Ecohealth* **4**: 310–317.

Du Pasquier, L., Schwager, J., and Flajnik, M.F. (1989) The immune system of *Xenopus. Annu Rev Immunol* **7**: 251–275.

Foster, P.G., and Hickey, D.A. (1999) Compositional bias may affect both DNA-based and protein-based phylogenetic reconstructions. *J Mol Evol* **48**: 284–290.

Gardner, M.J., Hall, N., Fung, E., White, O., Berriman, M., Hyman, R.W., *et al*. (2002) Genome sequence of the human malaria parasite *Plasmodium falciparum*. *Nature* **419**: 498–511.

Guida, G., Maida, I., Gallone, A., Boffoli, D., and Cicero, R. (1998) Ultrastructural and functional study of the liver pigment cells from *Rana esculenta* L. *In Vitro Cell Dev Biol Anim* **34**: 393–400.

Jirků, M., Modrý, D., Šlapeta, J.R., Koudela, B., and Lukeš, J. (2002) The phylogeny of Goussia and Choleoeimeria (Apicomplexa; Eimeriorina) and the evolution of excystation structures in coccidia. *Protist* **153**: 379–390.

Jirků, M., Jirků, M., Oborník, M., Lukeš, J., and Modrý, D. (2009) *Goussia* Labbé, 1986 (Apicomplexa, Eimeriorina) in Amphibia: diveristy, biology, molecular phylogeny and comments on the status of the genus. *Protist* **160**: 123–136.

Kopecna, J., Jirku, M., Obornik, M., Tokarev, Y.S., Lukes, J., and Modry, D. (2006) Phylogenetic analysis of coccidian parasites from invertebrates: search for missing links. *Protist* **157**: 173–183.

Leander, B.S. (2008) Marine gregarines: evolutionary prelude to the apicomplexan radiation? *Trends Parasitol* **24**: 60–67.

Leander, B.S., Clopton, R.E., and Keeling, P.J. (2003) Phylogeny of gregarines (Apicomplexa) as inferred from small-subunit rDNA and beta-tubulin. *Int J Syst Evol Microbiol* **53**: 345–354.

Long, E.O., and Dawid, I.B. (1980) Repeated genes in eukaryotes. *Ann Rev Biochem* **49**: 727–764.

Martel, A., Spitzen-van der Sluijs, A., Blooi, M., Bert, W., Ducatelle, R., Fisher, M.C., *et al.* (2013) *Batrachochytrium salamandrivorans* sp. nov. causes lethal chytridiomycosis in amphibians. *Proc Natl Acad Sci USA* **110**: 15325–15329.

Nöller, W. (1920) Kleine beobachtungen an parasitischen protozoen. *Archiv Protistenkunde* **41**: 169–189.

Rueckert, S., Simdyanov, T.G., Aleoshin, V.V., and Leander, B.S. (2011) Identification of a divergent environmental DNA sequence clade using the phylogeny of gregarine parasites (Apicomplexa) from crustacean hosts. *PLoS One* **6**: e18163.

Stuart, S.N., Chanson, J.S., Cox, N.A., Young, B.E., Rodrigues, A.S.L., Fischman, D.L., and Waller, R.W. (2004) Status and trends of amphibian declines and extinctions worldwide. *Science* **306**: 1783–1786.

Wakeman, K.C., Heintzelman, M.B., and Leander, B.S. (2014) Comparative ultrastructure and molecular phylogeny of *Selenidium melongena* n. sp. and *S. terebellae* Ray 1930 demonstrate niche partitioning in marine gregarine parasites (apicomplexa). *Protist* **165**: 493–511.

Supporting information

Additional Supporting Information may be found in the online version of this article at the publisher's web-site:

Table S1. Detail of the tadpoles sampled, providence and the corresponding *Nematopsis* clone library sequences recovered.
Table S2. Primers used in this study.
Table S3. Identity percentage between the ribosomal operons sequences of *Nematopsis temporariae* from the different clone sequences. Data were calculated using the SIAS website (Available at http://imed.med.ucm.es/Tools/sias.html).

Diakin A., Wakeman K.C., **Valigurová A.**

2017

Description of *Ganymedes yurii* sp. n. (Ganymedidae), a new gregarine species from the Antarctic amphipod *Gondogeneia* sp. (Crustacea)

ORIGINAL ARTICLE

Description of *Ganymedes yurii* sp. n. (Ganymedidae), a New Gregarine Species from the Antarctic Amphipod *Gondogeneia* sp. (Crustacea)

Andrei Diakin[a], Kevin C. Wakeman[b] & Andrea Valigurová[a]

a Department of Botany and Zoology, Faculty of Science, Masaryk University, Kotlářská 2, Brno 611 37, Czech Republic
b Center for Global Communication Strategies, The University of Tokyo Meguro-ku, Komaba Campus, Tokyo 153-8902, Japan

ABSTRACT

A novel species of aseptate eugregarine, *Ganymedes yurii* sp. n., is described using microscopic and molecular approaches. It inhabits the intestine of *Gondogeneia* sp., a benthic amphipod found along the shore of James Ross Island, Weddell Sea, Antarctica. The prevalence of the infection was very low and only a few caudo-frontal syzygies were found. Morphologically, the new species is close to a previously described amphipod gregarine, *Ganymedes themistos*, albeit with several dissimilarities in the structure of the contact zone between syzygy partners, as well as other characteristics. Phylogenetic analysis of the 18S rDNA from *G. yurii* supported a close relationship between these species. These two species were grouped with other gregarines isolated from crustaceans hosts (Cephaloidophoroidea); however, statistical support throughout the clade of Cephaloidophoroidea gregarines was minimal using the available dataset.

THE Antarctic is an exceptional continent, with extreme climates and environmental conditions above and below the water surface. While not many species are thought to survive in these high latitudes, the diversity of marine fauna in this part of the world is enormously rich, especially in the plankton, nekton, and benthos. A number of reviews are dedicated to the climatology, geology, palaeontology, and fauna of vertebrates (fish, birds, and mammals) from the Antarctic region (Barbosa and Palacios 2009; Eastman 2005). Similarly, many investigations were devoted to apicomplexans parasitising fish, birds, and krill (Avdeev 1985, 1987; Barber and Mills Westermann 1988; Golemansky 2011; Takahashi et al. 2003, 2004, 2008, 2009). To date, only one study has been devoted to crustacean gregarines occurring in littoral/sublittoral invertebrates (Lipa and Rakusa-Suszczewski 1980).

Apicomplexans are a diverse group of unicellular parasites, inhabiting almost all known phyla of multicellular organisms. Some Apicomplexa such as *Toxoplasma*, *Plasmodium*, *Eimeria,* and *Cryptosporidium* are well known, as these parasites cause harmful diseases in humans and domestic animals. The invasive stages (zoites) in this group are characterised by the presence of an 'apical complex', comprising a set of subcellular organelles (conoid, rhopries, and miconemes), specialised for invading and subsequently modifying the host cells (Chobotar and Scholtyseck 1982; Scholtyseck 1973; Scholtyseck and Mehlhorn 1970).

Gregarines, in contrast to coccidia, largely exist as extracellular parasites of a broad range of invertebrate groups, for example, terrestrial insects, aquatic annelids, and crustaceans. Most gregarines inhabit the host intestinal lumen, are elongated and heteropolar, cylindrical, or vermiform in shape. Feeding stages (=trophozoites) generally develop attached to the host cell via their modified anterior end. Usually, the trophozoites are subdivided into three parts: epimerite (attachment function), and protomerite followed by a deutomerite containing a large nucleus. The last two regions are separated by a fibrillar septum. Gregarines with such organisation are classified as being "tricystid" or "septate" gregarines. On the other hand, gregarines that are not subdivided represent the "monocystid" form, and are known as aseptate gregarines. It should also be mentioned that, generally, trophozoites, as well as subsequent sexual stages (=gamonts), exhibit gliding motility and possess a unique organisation of the cell cortex. The

pellicle of eugregarines forms longitudinal epicytic folds equipped with special sets filamentous structures in their apex, represented by rippled-dense structure and 12-nm filaments. Before gametogenesis, the gamonts join into a sexual association called syzygy. Later on, the paired gregarines form a common envelope (gametocyst), under which further processes, including gametogenesis, fertilisation and formation of invasive stages (sporogenesis), take place (Desportes and Schrével 2013; Frolov 1991; Grassé 1953; Long 1982; Perkins et al. 2000; Simdyanov 2007).

Many septate and aseptate eugregarines have been described from different crustacean hosts from different marine and terrestrial aquatic localities, and have traditionally been distinguished based on their general morphology using light microscopy. These gregarines have been separated into different families including the Cephaloidophoridae, Porosporidae, Uradiophoridae, Ganymedidae, and others. However, this system of families and nomenclature at the level of genus and species remains unsettled (Desportes and Schrével 2013; Grassé 1953; Levine 1977a,b; Perkins et al. 2000; Simdyanov 2007). Furthermore, the data collected from each group are not uniform, for example, only some of these groups have been investigated using electron microscopic approaches and/or molecular techniques (Desportes and Théodoridès 1969, 1985; Rueckert et al. 2011; Simdyanov et al. 2015; Takahashi et al. 2009; Théodoridès and Desportes 1975). Recent phylogenetic analyses of SSU rDNA sequences showed that gregarines from different crustacean hosts clustered in a single clade, together with a number of environmental sequences (Rueckert et al. 2011). This finding was confirmed by phylogenetic analyses of LSU rDNA and whole ribosomal operon (SSU + 5.8S + LSU) (accession numbers HQ891113.2 – HQ891115.2) (Simdyanov et al. 2015).

The family Ganymedidae was established by Huxley (1910) and comprises intestinal aseptate gregarines possessing ball-like and cup-like structures at the anterior and posterior ends of the cell, respectively. He described the type species, *Ganymedes anaspidis*, from a mountain shrimp, *Anaspides tasmaniae* Thomson, 1892 (Huxley 1910). Later many aseptate gregarines were described from different freshwater and marine crustacean hosts (Cirripedia, Amphipoda, Decapoda etc.) (Jones 1968, 1969; Jones et al. 1994; Prokopowicz et al. 2010; Théodoridès and Desportes 1972, 1975). Subsequently, Levine (1977a, b) made a taxonomical revision of this genus; he placed all species lacking the above-mentioned ball-like and cup-like structures into a new genus, *Paraophioidina*, and only one species was retained in the genus *Ganymedes*, namely *G. anaspidis*. Perkins et al. (2000) and Simdyanov (2007) followed this opinion. In the latest revision of gregarine species, this point of view was rejected and many species were returned and assigned to the genus *Ganymedes* (Desportes and Schrével 2013).

In this study, we describe the general morphology and molecular phylogeny, based on SSU sequence data, of a new Antarctic gregarine, *Ganymedes yurii* sp. n. For this, we used a combined approach of transmission and scanning electron microscopy, and molecular phylogenetic analyses.

MATERIALS AND METHODS

Gondogeneia sp. Barnard, 1972, an amphipod, was collected in January and February 2013 in the littoral and upper sublittoral zone of Cape Lachman (63°47′32″S, 57°46′86″W), James Ross Island, Weddell Sea, Antarctica. The amphipods were transported to the laboratory and kept in cold conditions. About 400 crustaceans were dissected under a stereomicroscope (MST 131, Poland). Parasites released from the host intestine were collected using a thin glass pipette. Light microscopic observations of living parasites were performed using an Olympus CX41 Microscope (Olympus Corp., Tokyo, Japan) equipped with phase contrast and connected to an Olympus Camedia C-7070 Digital Camera (Olympus Corp.).

For electron microscopy, parasites were fixed in 2.5% glutaraldehyde in Millipore-filtered sea water (SW) (Millex-GC 0.22 μm). For transmission electron microscopy (TEM), gregarines were then postfixed with 1% OsO_4 (Os) in 0.2 M cacodylate buffer, dehydrated in an ethanol series and embedded in Epon blocks. Ultra-thin sections were made using Reichert Ultracut E and Leica UTC ultramicrotomes, stained according to a standard protocol (Reynolds 1963), and observed under a JEOL-1010 transmission electron microscope (JEOL Ltd., Peabody, MA, USA). For scanning electron microscopy (SEM), fixed trophozoites were postfixed for 2 h in 2% osmium tetroxide in 0.2 M cacodylate buffer, dehydrated, dried with CO_2 using Emitech K850, and then coated with gold using Emitech K550 sputter coaters. The samples were observed under a JEOL JSM-7401F field emission scanning microscope (JEOL Ltd.).

For molecular analysis, gamonts in syzygy were fixed in 100% ethanol and stored at room temperature. Genomic DNA was later extracted with the standard protocol provided in the MasterPure Complete DNA & RNA Purification Kit (Epicentre Biotechnologies, Madison, WI). However, the final elution step was lowered to 4 μl. Outside primers, PF1 5′–GCGCTACCTGGTTGATCCTGCC–3′ and SSUR4 5′–GATCCTTCTGCAGGTTCACCTAC–3′ (Leander et al. 2003), were used in a 25 μl PCR with EconoTaq 2X Master Mix (Lucigen Corp., Middleton, WI). The following programme was used on a thermocycler for the initial amplification: Initial denaturation at 94 °C for 2 min; 35 cycles of denature at 94 °C for 30 s, anneal at 52 °C for 30 s, extension at 72 °C for 1 min 50 s, final extension 72 °C 5 min. Subsequently, internal primers F2 5′–GCYTG AAAAGGTGACDATCTG–3′ and R2 5′–CATATCTGCTAAG GTTCTG–3′ were paired with outside primers in a nested PCR using the following programme on a thermocycler: Initial denaturation for 94 °C for 2 min; 25 cycles of denature at 94 °C for 30 s, anneal at 52 °C for 30 s, extension at 72 °C for 1 min 30 s; final extension at 72 °C for 7 min.

The newly obtained DNA sequence from *Ganymedes yurii* was initially identified by BLAST (http://

blast.ncbi.nlm.nih.gov). This sequence was then aligned with 89 additional alveolate sequences selected from NCBI/GenBank (to cover the diversity of apicomplexans, including some dinoflagellates as an outgroup), using MUSCLE 3.8.31 (Edgar 2004). The alignment of 90 OTUs was subsequently edited and fine-tuned using MacClade 4.08 (Maddison and Maddison 2005). Garli0.951-GUI (www.bio.utexas.edu/faculty/antisense/garli/Garli.html) was used to analyse the 90-sequence alignment (1,170 unambiguously aligned positions; gaps excluded) with maximum-likelihood (ML). Jmodeltest 0.1.1 selected a general-time reversible (GTR) model of nucleotide substitutions (Posada and Crandall 1998) that incorporated invariable sites and a discrete gamma distribution (eight categories) (GTR + Γ + I model: $\alpha = 0.6430$ and fraction of invariable sites = 0.2160) under Akaike Information Criterion (AIC) and AIC with correction (AICc.). ML bootstrap analyses were performed on 500 pseudo-replicates, with one heuristic search per pseudo-replicate (Zwickl 2006), using the same programme set to the GTR model + Γ + I. Bayesian analysis of the 90 OTU-dataset was performed using the programme MrBayes 3.1.2 (Huelsenbeck and Ronquist 2001). The programme was set to operate with GTR, a gamma-distribution, and four Monte Carlo Markov Chains (MCMC; default temperature = 0.2). A total of 10,000,000 generations were calculated with trees sampled every 100 generations and with a prior burn-in of 1,000,000 generations (10,000 sampled trees were discarded; burn-in was checked manually). When the average split fell below 0.01, the programme would terminate. All other parameters were left at the default. A majority rule consensus tree was constructed from 90,000 postburn-in trees. Posterior probabilities correspond to the frequency at which a given node was found in the postburn-in trees.

RESULTS

The prevalence and abundance of gregarines within the host were low; approximately 10% of crustacean hosts were parasitised with no more than 2–5 syzygies per host. Mostly, head-to-tail syzygies with two partners were found, while no solitary trophozoites, gametocysts or other stages were observed. Both partners in syzygy were of monocystid form, with the nucleus situated in the middle of the cell. Primites (anterior syzygy partner) were usually slightly curved, longer and more slender than the satellite (posterior syzygy partner) (190–160 µm vs. 140–150 µm, respectively) (Fig. 1A, B, 2A). The cytoplasm of both partners was packed with a granular content, corresponding to the grains of amylopectin. The thin transparent cortical layer was seen on the lateral sides of the cells; however, on the side of anterior ends of the primite and satellite, and posterior end of the satellite this zone was thicker (Fig. 1A, B). In contrast to the satellite, the anterior end of the primite possessed a transparent vacuolar zone (Fig. 1A–C). The nuclei of both partners were ovoid in shape and each contained one round nucleolus (Fig. 1D). The contact between the
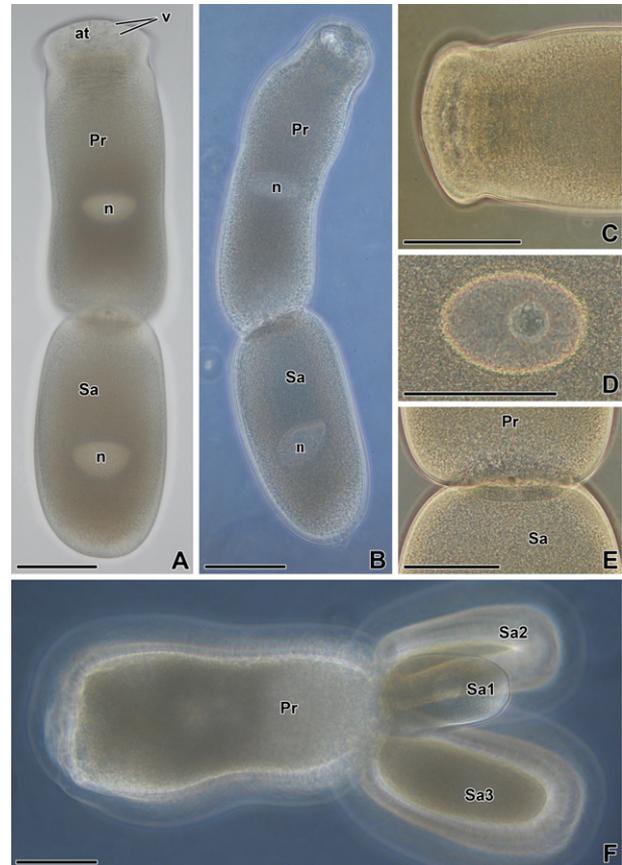
Figure 1 Bright field light microscopic observations of *Ganymedes yurii*. **A.** A general view of syzygy in the coronal plane, showing the attachment point (at) with transparent vacuoles (v), nuclei (n), primite (Pr) and satellite (Sa). **B.** A general view of syzygy with nuclei (n) in sagittal plane. **C.** Anterior end of the primite. (**D.**) Ovoid nucleus with one nucleolus. **E.** Contact between the primite (Pr) and satellite (Sa). **F.** Multiple association of a primite (Pr) with three attached satellites (Sa1-3). Scale bars: 50 µm.

primite and satellite was simple, without any visible interdigitations at LM level (Fig. 1E). Only once we observed a multiple association, when three differently sized satellites attached to the posterior end of the primite (Fig. 1F). All syzygies exhibited unidirectional gliding motility.

Under transmission electron microscopy, the cells were round in cross-section. The bulk of cytoplasm (=endoplasm) was packed with amylopectin granules and the zone of ectoplasm was very thin (Fig. 2B, C). The nucleus possessed granular karyoplasm and an uneven nuclear envelope (Fig. 2D, E). The parasites were covered with numerous epicytic folds (about 1 µm in length and 0.1 µm in width), which ran along the surface of the both partners (Fig. 2A, C, F, 3A, D, E), and most of these folds were wavy (Fig. 2F, 3H). The gregarine surface exhibited specific areas where some folds formed a loop; i.e. these folds went towards one of the ends, but reversed in the
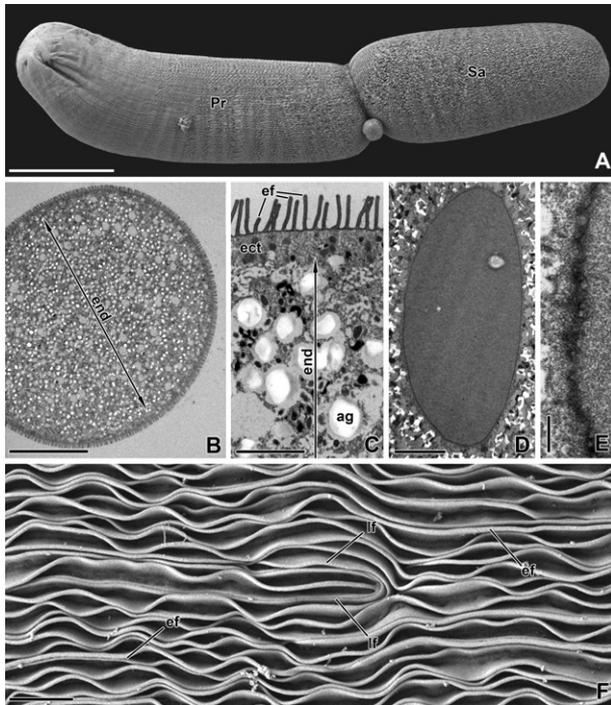
Figure 2 General morphology of *Ganymedes yurii*. **A.** General SEM view of syzygy with a primite (Pr) and satellite (Sa). **B.** Transverse section of a gamont, the bulk of the cell corresponds to endoplasm (end); TEM. **C.** Higher magnification view showing the gamont's cell cortex with epicytic folds (ef), ectoplasm (ect) and endoplasm (end) filled with amylopectin granules (ag); TEM. **D.** Tangential section of the nucleus; TEM. **E.** Higher magnification view of the nuclear envelope; TEM. **F.** Higher magnification view of the gamont surface covered by longitudinal epicytic folds (ef) and looped epicytic folds (lf); SEM. Scale bars: A = 50 μm; B = 20 μm; C, F = 2 μm; D = 5 μm; E = 500 nm.

opposite direction (Fig. 2F). Such patterns were found in all observed cells.

The three-layered pellicle was of typical apicomplexan organisation, having a plasma membrane, underlain by two closely adjacent membranes of the inner membrane complex (imc) (Fig. 3A, B). The base of the folds was underlain with a thick internal lamina, which formed bridges with dense triangular rods (Fig. 3A, I). The internal lamina, located underneath the pellicle, continued into the folds, where it became thinner and more dense (Fig. 3A, B). At the top of each epicytic fold, four to five rippled-dense structures could be observed, situated between the plasma membrane and imc. An electron-dense rod was also seen in the apex of epicytic folds, underlying the imc (Fig. 3A, B). Typical micropores were rarely found between the epicytic folds, they appeared as cylindrical invaginations of the plasma membrane (approximately 40 nm in diameter, and 50 nm in length) ending with a vesicle (approximately 50 nm in diameter). The cylindrical part of micropore was enforced by the internal lamina; however, no typical collar formed by imc was observed (Fig. 3C).
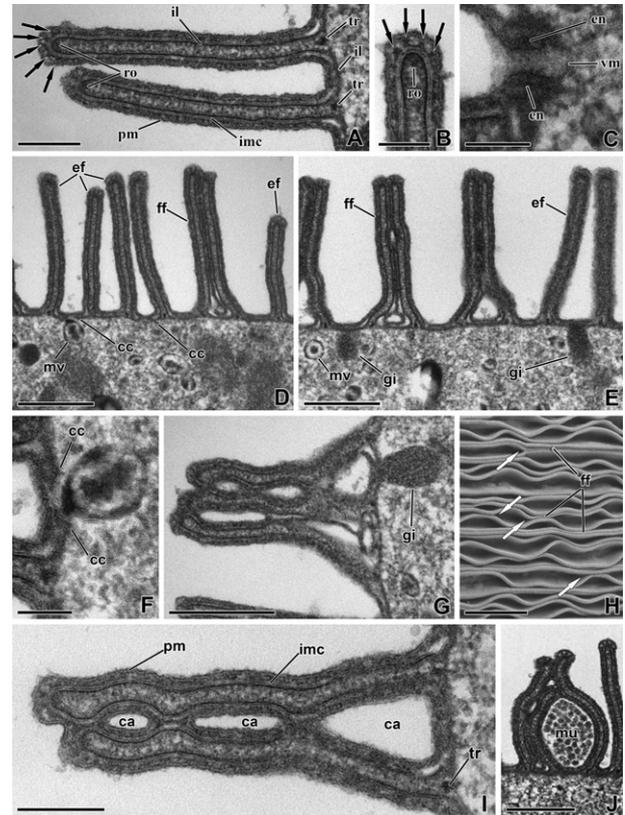
Figure 3 Organisation of cell cortex in *Ganymedes yurii*. **A.** General view of epicytic folds formed by plasma membrane (pm), inner membrane complex (imc) and internal lamina (il). Rippled-dense structures (black arrows) were situated between pm and imc. Electron-dense rod (ro) was found under imc in the fold apex. The internal lamina formed triangular rod (tr) at the base of the folds; TEM. **B.** Higher magnification of the top of epicytic fold, showing rippled-dense structures (black arrows) and electron-dense rod (ro); TEM. **C.** Typical micropore, showing the vacuole of micropore (vm) and cylindrical enforcement (en). **D.** and **E.** General view of the cortex with nonfused (ef) and fused (ff) epicytic folds, membranous vesicles (mv) with cone-shaped collar (cc), and teardrop granular inclusions (gi); TEM. **F.** Details of membranous vesicles with cone-shaped collar (cc); TEM. **G.** High magnification of teardrop granular inclusions (gi); TEM. **H.** Scanning electron micrograph showing fussed epicytic folds (ff) and starts/ends of the fusion (white arrows); SEM. **I.** Cross-section of fussed folds, showing the plasma membrane (pm) with inner membrane complex (imc) and triangle rod (tr) at their base. Note the canals (ca) formed between the fussed folds; TEM. **J.** Transversally sectioned fussed folds with mucous (mu) material inside the canal; TEM. Scale bars: A, I = 200 nm; B and C, F = 100 nm; D and E, G, J = 500 nm; H = 2 μm.

In addition to the aforementioned typical micropores, two different structures were observed in contact with the pellicle of the gregarine (Fig. 3D–G). The first was membranous vesicles. These were round. These were round in shape, with a central, and electron-dense inclusions. At the point of contact with the pellicle, the plasma membrane did not form an invagination, but the imc formed a cone-shaped, electron-dense collar, instead of

cylindrical collar present in typical micropores (Fig. 3D, F). The same membranous structures were also found in the ectoplasm (Fig. 3E). The second structures (gi) that came in a contact with the pellicle contained granular content and were round or teardrop in shape; no membrane surrounded these structures. No invaginations of the plasma membrane or the imc collar were observed in this region (Fig. 3E, G).

Fused epicytic folds were observed in cross-sections of the cells. Commonly two or three folds fused along their lateral surfaces (Fig. 3D, E, G–J). The fusion of the fold was discontinuous throughout the length of the cell; some folds were fused across a longer distance, while others were only fused across a short distance (Fig. 2F, 3H). At the point of fusion, only the imc membranes of two adjacent folds were present. Usually, a triangular canal was seen at the base of fused folds, while one or two narrow canals in the middle were observed (Fig. 3D, E, G, I). Occasionally, a mucus-like substance could be observed in the space between fused folds (Fig. 3J).

During preparation of samples for SEM, some cells previously associated in syzygy disassociated, so it was possible to compare the surface morphology of anterior and posterior ends of both the primite and satellite (Fig. 4A, B). The anterior end of primite was convex and had an oval-shaped attachment area with a wrinkled surface (Fig. 4A, C). The epicytic folds near this attachment tip were straight (Fig. 4C). Many small pores were visible on the surface of attachment area (Fig. 4D). In longitudinal sections through the anterior part of primite, the cytoplasm was subdivided into several zones along the longitudinal cell axis (Fig. 4E). The most anterior area (zone 1) was packed with heterogeneous electron-dense roundish inclusions; this was presumed to be condensed mitochondria. It was followed by a concaved zone (zone 2) filled with various opaque and transparent round inclusions (Fig. 4F). These two zones were generally located eccentrically to the longitudinal axis of the cell. The next zone was thicker and packed with various vacuolar and granular inclusions, while the rest of the cell was filled with numerous amylopectin granules (Fig. 4E–G). The apical part of the primite was covered with a typical three-membrane pellicle, underlain by a dense, thick internal lamina. The internal lamina and imc were interrupted at some points (Fig. 4F, inset), which corresponded to the pores observed under SEM (Fig. 4D). At the free posterior end of the satellite, wavy epicytic folds converged in the centre, where a light depression was usually observed (Fig. 4H–I). At the posterior end of the satellite, a lentil-shaped granular zone was situated without amylopectin granules (Fig. 4J).

While under light microscopy the contact site between the primite and satellite appeared simple (Fig. 1E), electron microscopic observations revealed its complex organisation (Fig. 5, 6). Two collars were observed at the posterior end of the primite. The innermost collar had an uneven edge, and tightly adhered to the anterior most part of the satellite. The outermost collar did not adhere to the innermost one, and the epicytic folds running along the surface of the primite merged to this collar (Fig. 5A, B,
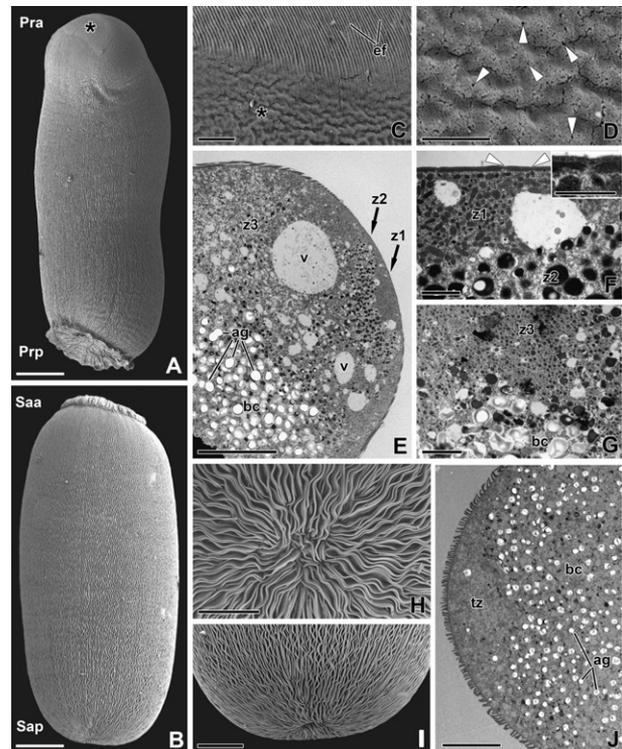

Figure 4 Morphology of the primite's anterior and satellite's posterior ends. **A.** General view of the primite with attachment tip (asterisk) at the anterior end (Pra), and free posterior end (Prp); SEM. **B.** General view of satellite disassociated from the primite during sample processing. Anterior end (Saa) has a cap-like appearance, while the posterior (Sap) is rounded; SEM. **C.** Details of the transition between the surface of attachment tip (asterisk) and the rest surface covered with epicytic folds (ef); SEM. **D.** High magnification view of the attachment tip with pores (white arrowheads) on the surface; SEM. **E.** Cross-section of the anterior part of the primite showing three zones (z1, z2, z3) containing vacuoles; the bulk of the cytoplasm (bc) is packed with amylopectin granules (ag); TEM. **F.** High magnification view of the transition between the zones 1 (z1) and 2 (z2), white arrowheads mark the pores; (insertion) – high magnification of pellicle showing one pore; TEM. **G.** High magnification of the transition between the zone 3 (z3) and the main bulk of the cytoplasm; TEM. Axial **H.** and lateral **I.** views of the posterior end of the satellite; SEM. **J.** Longitudinal section of the satellite's posterior end, showing a transparent zone (tz); the bulk of cytoplasm (bc) is filled with amylopectin granules (ag); TEM. Scale bars: A, B = 20 μm; C, G = 2 μm; D = 1 μm; E, I, J = 10 μm; F = 1 μm (insertion = 100 nm); H = 5 μm.

6A, B). The junction site of the partners from the side of the primite was crateriform, and was surrounded by the aforementioned collars. The radial ridges were observed on the surface of this area (Fig. 6A). The anterior end of the satellite, which contacted the primite, was cap-like and not surrounded by any collar (Fig. 6C, D). Usually, in the centre, it had a light depression from which many narrow grooves radiated. Small round and shallow caverns were found on the surfaces between these grooves (Fig. 6D).

60

Journal of Eukaryotic Microbiology 2017, **64**, 56–66
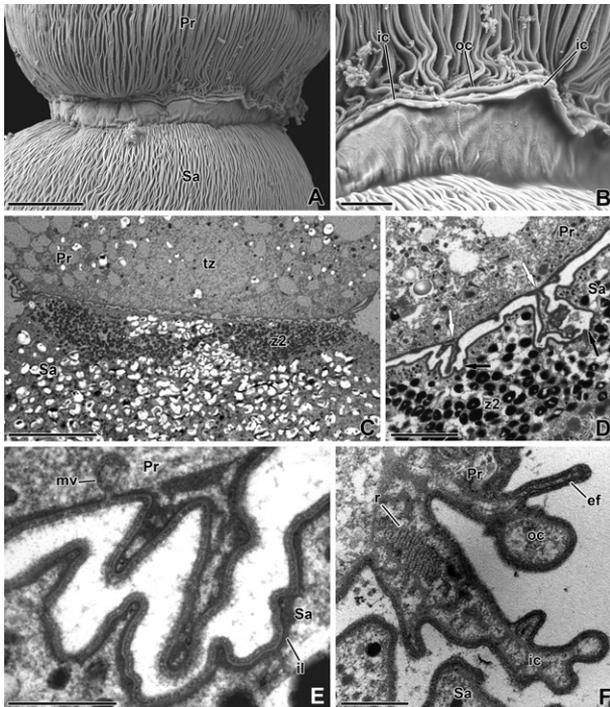
Figure 5 Morphology of junction between the primite and satellite. **A.** General view of the contact between the primite (Pr) and satellite (Sa); SEM. **B.** High magnification view of the junction area, showing the outer (oc) and inner (ic) collar; SEM. **C.** Cross-sectioned contact zone showing the transparent zone (tz) of the primite's posterior end (Pr) and zone 2 (z2) of the satellite's anterior end (Sa); TEM. **D.** Detail of the junction; white arrows mark ridges of the primite's posterior end (Pr), black arrows mark grooves in the satellite's anterior end (Sa); TEM. **E.** High magnification view of the primite's (Pr) ridges and satellite's (Sa) grooves coinciding to each other. Membranous vesicles (mv) is present in the primite. Thick internal lamina (il) underlies the pellicle of both the primite and satellite; TEM. **F.** Cross-section of the periphery of the junction site between the primite (Pr) and satellite (Sa), showing the outer collar (oc) bearing epicytic folds (ef) and the inner collar (ic) with rod of fibrillar material. Scale bars: A, C = 10 μm; B, D = 2 μm; E, F = 500 nm.

The junction site of both syzygy partners was covered with three-membrane pellicle, underlain with a thick internal lamina. Occasionally, membranous structures resembling "mv" (aforementioned) were found in the contact with the pellicle of the junction area (Fig. 5E). The profile of the ridges of the primite crateriform posterior end and the grooves at the satellite anterior end corresponded to each other (Fig. 5D, E). The cytoplasm of both ends, in general, had the same organisation as what was described previously. The posterior end of the primite exhibited the same granular zone without any amylopectin granules, as seen in the free posterior end of the satellite. However, in the satellite, there was only a zone of dense granules (zone 2), immediately followed by a cytoplasm filled with amylopectin granules (Fig. 5C, D). As described previously, the innermost collar tightly adjoined to the satellite and possessed the rod consisting of fibrillar-like material.
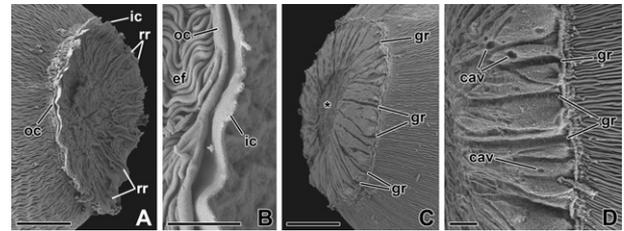
Figure 6 Surface morphology of the primite and satellite junction ends after disassociation; SEM. **A.** General view of the crateriform posterior end of the primite disassociated from satellite, showing prominent outer collar (oc), inner collar (ic) and radial ridges (rr). **B.** High magnification view of inner collar (ic), outer collar (oc) with epicytic folds (ef). **C.** General view of the anterior end of a satellite detached from the primite, showing a central depression (asterisk) and grooves (gr) radiating from this depression. **D.** High magnification view of the peripheral region of the anterior end of the satellite, showing caverns (cav) and radial grooves (gr). Scale bars: A, C = 10 μm; B, D = 2 μm.

In contrast, the outermost collar did not possess a rod, but some epicytic folds merged with it (Fig. 5B, F, 6D).

The new SSU rDNA sequence generated from *Ganymedes yurii* sp. n. had a 77% similarity to a closely related species, *Ganymedes themistos*; 354 sites were mismatched across their pairwise alignment of 1,553 bp.

Maximum-likelihood and Bayesian analysis (Fig. 7) generally agreed with previous work in this field. Clades comprising Cephaloidophoroidea (Rueckert et al. 2011), Lecudinoidea (Simdyanov and Diakin 2013) (=Urosporoidea in Cavalier-Smith 2014), Gregarinoidea (Clopton 2009) and Actinocephaloidea (Cavalier-Smith 2014) were recovered. Other selected gregarines including archigregarines, as well as eugregarines from sipunculids and polychaetes, were dispersed between these main clades. Additional alveolate sequences were also grouped into the main clades, namely cryptosporidia, rhytidocystids, coccidia, and piroplasmids. The relationships between these clades were unresolved with this current dataset.

The novel SSU rDNA sequence obtained from *G. yurii* sp. n. was strongly affiliate with the SSU rDNA sequence from a previously investigated species, namely *Ganymedes themistos*. Both of these sequences were grouped with robust support in the family Ganymedidae, which is incorporated into the clade Cephaloidophoroidea, comprising gregarines from crustaceans, as well as phylogenetically related environmental sequences. The sequences of two *Ganymedes* spp. branched early within the entire clade Cephaloidophoroidea, albeit, with low posterior probability and bootstrap support (Fig. 7).

TAXONOMIC SUMMARY

Family Ganymedidae Huxley 1910
Genus *Ganymedes* Huxley 1910
*Ganymedes yurii* sp. n. (Fig. 1A, B, 2A)
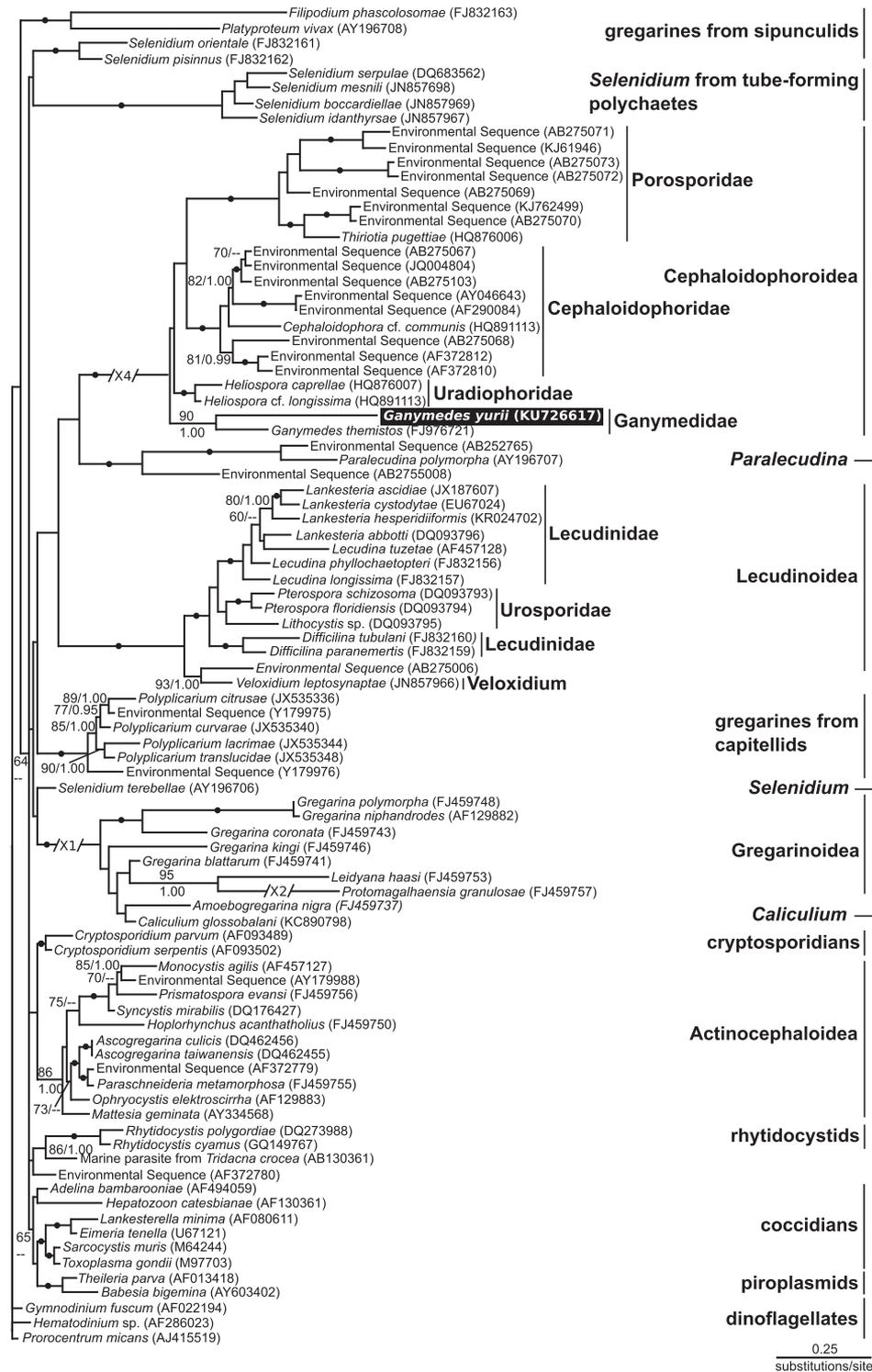
Figure 7 Combined maximum-likelihood (ML) and Bayesian interference tree derived from phylogenetic analyses of the 90 OTUs dataset. 1.170 unambiguously aligned sites) of small subunit (SSU) rDNA sequences. This tree was inferred using the GTR + Γ + I substitution model ($-\ln$ L = 16,7382.83829, gamma shape = 0.62738, proportion of invariable sites = 0.2381). Numbers at the nodes denote the ML bootstrap percentage (numerator) and Bayesian posterior probabilities (denominator). Bootstrap support values are listed above Bayesian posterior probabilities. Black dots on branches denote the bootstrap support values and Bayesian posterior probabilities of 95/0.95 or higher, respectively. Bootstrap and Bayesian values less than 55 and 0.95, respectively, were not added to this tree, the Bayesian values lower than 0.9 marked /"−". The novel sequence generated in this study is highlighted in a black box. Some branches were shortened by multiples of the length of the substitutions/site scale bar.

Diagnosis. Syzygy caudo-frontal, the primite being slightly curved and longer than satellite. Vacuolar region present at the anterior end of the primite. Nucleus situated in the centre of the cell. Dimensions of the primite varied between 190–160 μm and satellite between 140–150 μm (Fig. 1, 2A). The posterior end of the primite is crateriform (cup-like), with two peripheral collars at the point of satellite attachment (Fig. 4A, 5A, B, 6A). Satellites possess cap-like anterior end (Fig. 4B, 6C). GenBank accession number KU726617 of small subunit rDNA distinguishes *G. yurii* from other investigated species.

Type host. *Gondogeneia* sp. Barnard 1972 (Arthropoda, Crustacea, Malacostraca, Amphipoda, Caliopioidea, Pontogeneiidae).

Type host habitat. Cape Lachman, James Ross Island, Weddell Sea, Antarctica (63°47′32″S, 57°46′86″W). Littoral and upper sublittoral zone.

Type material deposition. Parasites on gold sputter-coated SEM stubs have been deposited at the Dept. of Botany and Zoology, Faculty of Science, Masaryk University, Brno, Czech Republic (Fig. 2A, 4A, B, 5A, B, 6A, C).

Etymology. The name of this species refers to a Russian name Yury (in the honour of first author's father name).

Localisation in host. Intestinal lumen.

Gene sequence. Sequence of SSU RNA GenBank accession number KU726617.

DISCUSSION

The genus *Ganymedes* contains several species of aseptate eugregarines infecting various groups of crustacea. All known gregarine species within the genus *Ganymedes* are aseptate and form caudo-frontal syzygy. On the anterior end of the primite, they have a transparent zone (ball-like structure), and most have a cup-like structure at the posterior end, as it is described in this study. However, some possess cup-like anterior ends of the satellite, as it was described for *G. themistos*. Under light microscopy, *G. yurii* differs from previous described species by its form and size of the cells/partners in syzygy. Most of the described species possess elongated and flexible cells (Huxley 1910; Jones 1968, 1969; Prokopowicz et al. 2010; Théodoridès and Desportes 1972, 1975), in case of species studied in this work, the syzygy partners are shortened and are more or less rigid.

Surface morphology of *G. themistos* and *G. yurii* is similar; both gregarines are covered by longitudinal epicytic folds that run from one end of the cell to the other (as is the case with most of eugregarines). However, *G. yurii* possesses unique "looped folds" on the surface, the function of which remains unclear. The ultrastructure of epicytic folds was studied in several eugregarines from crustacean hosts, namely *Porospora portunidarum*, *Thiriotia pisae*, *G. vibiliae*, *G. eucopiae*, *Uradiophora maetzi*, *Cephaloidophora* cf. *communis*, and *Heliospora* cf. *longissima* (Desportes and Théodoridès 1985; Desportes et al. 1977; Simdyanov et al. 2015). All of them show similar morphology among folds, which appear club-shaped in cross-section. At the top of each fold, there are several rippled-dense structures (3–6), and in some species, the 12-nm filaments were observed. Many of the aforementioned species, except *C.* cf. *communis* and *H.* cf. *longissima*, have electron-dense rods in the apical part of the fold; this has also been found in *G. yurii*. Similar structures were also found in other eugregarines, for example, in *Gregarina steini*, *G. polymorpha* and *G. cuneata*, parasites of mealworm larvae (Valigurová et al. 2013), urosporids *Gonospora beloneides* (Corbel et al. 1979), *Urospora ovalis* and *U. travisiae* (Diakin et al. 2016). Therefore, it can be assumed that this structure appeared (or was lost) in different lineages of eugregarines independently. The function of this dense rod is unknown; however, Valigurová et al. (2013) suggested that in mentioned *Gregarina* spp. the half-moon-shaped rod underlying the 12-nm filaments could serve as a 'skeleton' reinforcing the apex of the folds, which is in contact with the substrate while the gregarine is gliding.

In *G. yurii,* we observed micropores typical for apicomplexans, and in addition, two types of structures that differed in their morphology making contact with the cortex of the cell. However, there is no consensus regarding the function of these structures (typical micropores and two additional structures described in this study). Some authors assume that micropores could take part in the process of nutrient acquisition (Chobotar and Scholtyseck 1982; Scholtyseck 1973; Scholtyseck and Mehlhorn 1970; Vivier et al. 1970), while others suppose that they are in fact extrusomes, and function more in the process of secreting mucus (Desportes and Schrével 2013; Philippe and Schrével 1982; Valigurová et al. 2013; Vegni Talluri and Dallai 1983). In the light of these studies, and our recent observations, the following could be taken into consideration: (i) typical micropores could serve in the process of nutrient acquisition, and (ii) different structures observed to be in contact with the pellicle correspond to phases of mucous excretion. Previously, structures similar to teardrop granular inclusions (gi) were described in several species (*Gregarina* spp. and *Urospora* spp.). It is possible that at different stages of the life cycle or during the excretion process, these structures could look like vesicles or ducts in transverse sections of the cells (Diakin et al. 2016; Valigurová et al. 2013). However, it is important to mention that we did not observe any droplets of mucus on the surface of the cell; nonetheless, mucus-like substances between the laterally fused folds were detected.

Lateral fusions of epicytic folds are not unique to *G. yurii*. In *Porospora portunidarum*, for example, some folds are fused as well; however, it could be caused by the presence of bacteria disposed between the folds (Desportes et al. 1977). This phenomenon was also reported in the septate gregarine *Leidyana tinei* (Leidyaniidae) (Vivier et al. 1970); in which 2–3 folds were fussed (similar to *G. yurii*). Similar fusion has been reported in *Monocystis agilis* and *M. herculea*, (Monocystidae), aseptate eugregarines found in the seminal vesicles of Oligochaetes. In the case of *M. herculea*, 2–7 folds are fused at their tips; in *M. agilis* folds are fused at their tips, and 2–3 lateral points (Vinckier 1969; Vinckier and Vivier 1968). In all

mentioned cases, the canals between the folds were formed. It was proposed that for monocystids the fusion of the folds serves to reduce the friction force during metabolic movement of the parasite between seminal cells (Frolov 1991). In the case of intestinal gregarines, the functionality of the fused folds remains unknown.

Pores localised on the surface of the gregarine attachment site were described in several species: *C.* cf. *communis*, *Gregarina cuneata* and *G. yurii* (Rueckert et al. 2011; Simdyanov et al. 2015; Valigurová 2012; present study). In all cases, these pores exhibit similar morphology; e.g. imc and the internal lamina are interrupted in this region, while no obvious interruption or invagination of plasma membrane is observable. Interestingly, only *C.* cf. *communis* and *G. yurii* has heterogeneous inclusions situated under the pellicle. Simdyanov et al. (2015) considered these inclusions to be microneme-like structures, due to their elongated shape. In contrast, the inclusions from *G. yurii* were round. We assume that this could be condensed mitochondria. Another possible explanation is that these structures could represent vesicles varying in shape and containing mucus-like substances or adhesive material, which can be extruded outside the cell, facilitating the parasites adhesion to the host, as it was shown in *C.* cf. *communis*, *G. cuneata,* and some actinocephalid eugregarines (Cook et al. 2001; Simdyanov et al. 2015; Valigurová 2012).

The ball-like structure described in all representatives of the genus *Ganymedes* obviously corresponds to the vacuolar zone found in *G. yurii* (most likely zone 3) (Fig. 4E). The fine structure of anterior end of primite of *G. yurii* appears simple in comparison to the previously described gregarines from crustaceans, despite all of them being septate. As it was described in this study, the cytoplasm in the anterior end is subdivided into three zones differing in structure, which are not separated from each other by any fibrillar material (septum). The apical end in septate species is also subdivided into three zones; however, these zones are separated by a septum. The number of septae varies in different species: e.g. one septum separates the protomerite and deutomerite in *Heliospora* cf. *longissima*, *Callynthrochlamys phronimae*; while two septae divide the cell of *Cephaloidophora* cf. *communis* into the epimerite, protomerite, and deutomerite (Desportes and Théodoridès 1969; Simdyanov et al. 2015).

The fine structure of the contact site between the primite and satellite of *G. yurii* is comparable to the previously described syzygy contact zone in *Callynthrochlamys phronima* (Desportes and Théodoridès 1969). Both of these species possess collars formed by the posterior end of primite at the periphery of the contact site: two collars are present in *G. yurii*, whereas *C. phronima* has a single collar. The surface of the junction zone in the primite and satellite are covered with a three-membrane pellicle lacking epicytic folds; however, in *G. yurii*, radial ridges (on the primite) and grooves (on the satellite) were documented. In contrast to this, the anterior end of satellite in *G. themistos* forms the collar, and only a small area lacks epicytic folds, whereas the rest of the pellicle covering the junction site is folded (Prokopowicz et al. 2010). In *Cephaloidophora phrosinae*, only one of the partners (primite) possesses modified epicytic folds in the contact zone (with bifurcated or flattened tops), while the anterior end of satellite has a smooth surface. It is assumed that the role of these modifications is to increase the surface of the contact area (Desportes et al. 1977).

Phylogenetic analyses of the novel sequence generated from *G. yurii* supported a close relationship with *G. themistos*, a previously described gregarine that was also isolated from an amphipod. Both of these sequences formed a basal clade within the large clade (Cephaloidophoroidea), comprising other eugregarines from crustaceans and some environmental sequences. As in previous studies, this clade was long-branching, relative to other clades of gregarines and apicomplexans (Prokopowicz et al. 2010; Rueckert et al. 2011). It is generally assumed that all gregarines so far described from crustaceans are phylogenetically closely related to each other, despite the wide range and global distribution of the hosts. Nonetheless, the phylogenetic analyses of 18s rDNA were unable to resolve the relationships along the backbone and among many of gregarines isolated from crustaceans hosts (Simdyanov et al. 2015).

In conclusion, the new species described in this study, *G. yurii*, shares common features with *G. themistos* and with other investigated gregarine species from crustaceans. But, there exists specific regions throughout the sequence that clearly distinguish each species among members of the genus *Ganymedes*, and gregarines from other crustaceans, in general. While all crustacean gregarines share two common features: (i) all of them are intestinal parasites of crustaceans, and (ii) phylogenetic analyses group these isolates in a single clade – Cephaloidophoroidea. Despite this, it is difficult to resolve the phylogenetic backbone and morphological trends within this group. To solve this problem, further investigations focusing on molecular phylogeny in connection with ultrastructural studies are needed.

ACKNOWLEDGMENTS

CONFLICT OF INTEREST

The authors declare no conflict of interest.

LITERATURE CITED

Avdeev, V. V. 1985. New species of gregarines of genus *Cephaloidophora*: parasites of *Euphausia superba*. *Parasitologiya*, 19:72–75 (in Russian).

Avdeev, V. V. 1987. Certain specific characteristics of the development of gregarina *Cephaloidophora pacifica*, a parasite of *Euphausia superba*. *Parasitologiya*, 21:580–582 (in Russian).

Barber, D. L. & Mills Westermann, J. E. 1988. *Haemogregarina georgianae* n. sp., a new haemogregarine parasite from the Antarctic teleost *Parachaenichthys georgianus*. *Syst. Parasitol.*, 11:65–71.

Barbosa, A. & Palacios, M. J. 2009. Health of Antarctic birds: a review of their parasites, pathogens and diseases. *Polar Biol.*, 32:1095–1115.

Cavalier-Smith, T. 2014. Gregarine site-heterogeneous 18S rDNA trees, revision of gregarine higher classification, and the evolutionary diversification of Sporozoa. *Eur. J. Protistol.*, 50:472–495.

Chobotar, B. & Scholtyseck, E. 1982. Ultrastructure. *In:* Long, P. L. (ed.), The Biology of the Coccidia. University Park Press, Baltimore, MD. p. 101–165.

Clopton, R. E. 2009. Phylogenetic relationships, evolution, and systematic revision of the septate gregarines (Apicomplexa: Eugregarinorida: Septatorina). *Comp. Parasitol.*, 76:167–190.

Cook, T. J. P., Janovy, J. & Clopton, R. E. 2001. Epimerite-host epithelium relationships among eugregarines parasitizing the damselflies *Enallagma civile* and *Ischnura verticalis*. *J. Parasitol.*, 87:988–996.

Corbel, J.-C., Desportes, I. & Théodoridès, J. 1979. Étude de *Gonospora beloneides* (Ming.) (=*Lobianchella beloneides* Ming.) (grégarine Urosporidea), parasite coelomique d'une Alciopidae (Polychaeta) et remarques sur d'autres grégarines d'Alciopidae. *Protistologica*, 15:55–65.

Desportes, I. & Schrével, J. 2013. The gregarines, (2 Vols). *In:* Desportes, I. & Schrével, J. (ed.), Treatise on Zoology, Anatomy, Taxonomy, Biology. Brill, The Leiden, Boston, MA. p. 1–781.

Desportes, I. & Théodoridès, J. 1969. Ultrastructure de la Grégarine *Callynthrochlamys phronimae* Frenzel; étude comparée de son noyau avec celui de *Thalicola salpae* (Frenzel. (Eugregarina). *J. Protozool.*, 16:449–460.

Desportes, I. & Théodoridès, J. 1985. Particularités cytologiques d'*Uradiophora maetzi* Théod. Desp. (Eugregarine, *Uradiophoridae*) parasite du Mysidacé bathypelagique *Gnathophausia zoea* ws. *Ann. Sci. Nat. Zool.*, 7:119–123.

Desportes, I., Théodoridès, J. & Vivarès, C. 1977. Association entre la grégarine *Porospora portunidarum* (Frenzel) et des bactéries intestinales de son hôte: *Carcinus mediterraneus* Czer. (Crustacé Décapode). *Protistologica*, 13:611–619.

Diakin, A., Paskerova, G. G., Simdyanov, T. G., Aleoshin, V. V. & Valigurová, A. 2016. Morphology and molecular phylogeny of coelomic gregarines (Apicomplexa) with different types of motility: *Urospora ovalis* and *U. travisiae* from the polychaete *Travisia forbesii*. *Protist*, 167:279–301. doi:10.1016/j.protis.2016.05.001.

Eastman, J. T. 2005. The nature of the diversity of Antarctic fishes. *Polar Biol.*, 28:98–103.

Edgar, R. C. 2004. MUSCLE: multiple sequence alignment with high accuracy and high throughput. *Nucleic Acids Res.*, 35:1792–1797.

Frolov, A. O. 1991. The world fauna of gregarines. Family Monocystidae. *Proc. Zool. Inst. Acad. Sci. USSR*, 229:3–126 (in Russian).

Golemansky, V. 2011. Coccidian parasites (Apicomplexa. of penguins (*Pygoscelis* ssp.) from Livingston Island and King George Island, the Antarctic. *Pol. Polar Res.*, 32:263–268.

Grassé, P.-P. 1953. Classe des Grégarinomorphes. *In:* Grassé, P.-P. (ed.), Traité de Zoologie. Masson, Paris, France. p. 550–690.

Huelsenbeck, J. P. & Ronquist, F. 2001. MRBAYES: Bayesian inference of phylogenetic trees. *Bioinformatics*, 17:754–755.

Huxley, J. S. 1910. On *Ganymedes anaspidis* (nov. gen., nov. sp.), a gregarine from the digestive tract of *Anaspides tasmaniae* (Thompson). *Q. J. Microsc. Sci.*, 55:155–175.

Jones, I. 1968. The life cycle of *Ganymedes oaklandi* n. sp., an acephaline gregarine of *Gammarus fasciatus* (Say). *J. Protozool.*, 15:414–418.

Jones, I. 1969. Further observations on ganymedidae gregarines of Caribbean amphipods. *J. Protozool.*, 16:25.

Jones, T. C., Overstreet, R. M., Lotz, J. M. & Frelier, P. F. 1994. *Paraophioidina scolecoides* n. sp., a new aseptate gregarine from cultured Pacific white shrimp *Penaeus vannamei*. *Dis. Aquat. Org.*, 19:67–75.

Leander, B. S., Clopton, R. E. & Keeling, P. J. 2003. Phylogeny of gregarines (Apicomplexa) as inferred from small subunit rDNA and beta-tubulin. *Int. J. Syst. Evol. Microbiol.*, 53:345–354.

Levine, N. D. 1977a. Checklist of the species of the aseptate gregarine families Aikinetocystidae, Diplocystidae, Allantocystidae, Schaudinellidae, Ganymedidae and Enterocystidae. *J. Invert. Pathol.*, 29:175–181.

Levine, N. D. 1977b. Revision and checklist of the species (other than *Lecudina*. of the aseptate gregarine family Lecudinidae). *J. Protozool.*, 24:41–52.

Lipa, J. J. & Rakusa-Suszczewski, S. 1980. An amphipod *Paramoera walkerii* Stebbing (Crustacea, Amphipoda) as a new host of eugregarine *Rotundula gammari* (Diesing). *Pol. Arch. Hydrobiol.*, 27:313–315.

Long, P. L. 1982. The biology of the Coccidia. Edward Arnold Press, London, U.K. p. 502.

Maddison, D. R. & Maddison, W. P. 2005. MacClade 4.08. Sinauer Associates, Sunderland, MA.

Perkins, F. O., Barta, J. R., Clopton, R. E., Peirce, M. A. & Upton, S. J. 2000. Phylum Apicomplexa Levine, 1970. *In:* Lee, J. J., Leedale, G. F. & Bradbury, P. (ed.), An Illustrated Guide to the Protozoa, 2nd ed., Vol. 1. Society of Protozoologists, Lawrence, KS. p. 190–369.

Philippe, M. & Schrével, J. 1982. The three cortical membranes of the gregarines (parasitic protozoa). Characterization of the membrane proteins of *Gregarina blaberae*. *Biochem. J.*, 201:455–464.

Posada, D. & Crandall, K. A. 1998. MODELTEST: testing the model of DNA substitution. *Bioinformatics*, 14:817–818. doi:10.1093/bioinformatics/14.9.817.

Prokopowicz, A. J., Rueckert, S., Leander, B. S., Michaud, J. & Fortier, L. 2010. Parasitic infection of the hyperiid amphipod *Themisto libellula* in the Canadian Beaufort Sea (Arctic Ocean), with a description of *Ganymedes themistos* sp. n. (Apicomplexa, Eugregarinorida). *Polar Biol.*, 33:1339–1350.

Reynolds, E. S. 1963. The use of lead citrate at high pH as an electron opaque stain in electron microscopy. *J. Cell Biol.*, 17:208–212.

Rueckert, S., Simdyanov, T. G., Aleoshin, V. V. & Leander, B. S. 2011. Identification of a divergent environmental DNA sequence clade using the phylogeny of gregarine parasites (Apicomplexa) from crustacean hosts. *PLoS ONE*, 6:e18163. doi:10.1371/journal.pone.0018163.

Scholtyseck, E. 1973. Ultrastructure. *In:* Hammond, D. M. & Long, P. L. (ed.), The Coccidia: *Eimeria, Isospora, Toxoplasma*, and related genera. University Park Press, Baltimore, Md. p. 81–144.

Scholtyseck, E. & Mehlhorn, H. 1970. Ultrastructural study of characteristic organelles (paired organelles, micronemes, micropores) of Sporozoa and related organisms. *Z. Parasitenk.*, 34:97–127.

Simdyanov, T. G. 2007. The class Gregarinea Dufour, 1828. *In:* Krylov, M. V., Pugachev, O. N., Seravin, L. N. & Starobogatov, Y. I. (ed.), Protista: Handbook on Zoology, Vol. 2. Nauka, St-Petersburg, p. 20–148 (in Russian).

Simdyanov, T. G. & Diakin, A. Y. 2013. Remarks to taxonomy of Eugregarinida (Apicomplexa) as inferred from 18S rDNA phylogenetic analysis. ICOP XIV. Book of Abstract, 134.

Simdyanov, T. G., Diakin, A. Y. & Aleoshin, V. V. 2015. Ultrastructure and 28S rDNA phylogeny of two gregarines: *Cephaloidophora* cf. *communis* and *Heliospora* cf. *longissima* with remarks on gregarine morphology and phylogenetic analysis. *Acta Protozool.*, 54:241–263.

Takahashi, K. T., Kawaguchi, S., Kobayashi, M. & Toda, T. 2003. Parasitic eugregarines change their spatial distribution within the host digestive tract of Antarctic krill, *Euphausia superba*. *Polar Biol.*, 26:468–473.

Takahashi, K. T., Kawaguchi, S., Kobayashi, M. & Toda, T. 2004. The variability in abundance of eugregarines living in the Antarctic krill. *Polar Biosci.*, 17:16–25.

Takahashi, K. T., Kawaguchi, S. & Toda, T. 2009. Observation by electron microscopy of a gregarine parasite of Antarctic krill: its histological aspects and ecological explanations. *Polar Biol.*, 32:637–644.

Takahashi, K. T., Kobayashi, M., Kawaguchi, S., Saigusa, J., Tanimura, A., Fukuchi, M., Naganobu, M. & Toda, T. 2008. Circumpolar occurrence of eugregarinid protozoan *Cephaloidophora pacifica* associated with Antarctic krill, *Euphausia superba*. *Ant. Sci.*, 20:437–440.

Théodoridès, M. J. & Desportes, I. 1972. Mise en evidence de nouveaux representants de la famille des Ganymedidae Huxley, gregarines parasites de crustaces. *CR Acad. Sci. Paris*, 274:3251–3253.

Théodoridès, M. J. & Desportes, I. 1975. Sporozoaires d'invertebres pelagiques de Villefranche-sur-Mer (etude descriptive et faunistique). *Protistologica*, 11:205–220.

Valigurová, A. 2012. Sophisticated adaptations of Gregarina cuneata (Apicomplexa) feeding stages for epicellular parasitism. *PLoS ONE*, 7:e42606. doi:10.1371/journal.pone.0042606.

Valigurová, A., Vaskovicová, N., Musilová, N. & Schrével, J. 2013. The enigma of eugregarine epicytic folds: where gliding motility originates? *Front. Zool.*, 10:57.

Vegni Talluri, M. & Dallai, R. 1983. Freeze-fracture study of the Gregarine trophozoite: II. Evidence of "rosette" organization on cytomembranes in relation with micropore structure. *Boll. Zool.*, 50:245–255.

Vinckier, D. 1969. Organisation ultrastructurale corticale de quelques Monocystidées parasites du ver Oligochète *Lumbricus terrestris* L. *Protistologica*, 5:505–517.

Vinckier, D. & Vivier, E. 1968. Organisation ultrastructurale corticale de la grégarine *Monocystis herculea*. *C. R. Acad. Sci. Paris*, 266:1737–1739.

Vivier, E., Devauchelle, G., Petitprez, A., Porchet-Henneré, E., Prensier, G., Schrével, J. & Vinckier, D. 1970. Observations de cytologie comparée chez les Sporozoaires. I.- Les structures superficielles chez les formes végétatives. *Protistologica*, 6:127–150.

Zwickl, D. 2006. Genetic algorithm approaches for the phylogenetic analsysis of large biological sequence datasets under the maximum likelihood criterion. PhD thesis, University of Texas at Austin.

Kováčiková M., Simdyanov T.G., Diakin A., **Valigurová A.**

2017

Structures related to attachment and motility in the marine eugregarine *Cephaloidophora* cf. *communis* (Apicomplexa)

European Journal of Protistology 59, 1-13

Structures related to attachment and motility in the marine eugregarine *Cephaloidophora* cf. *communis* (Apicomplexa)

Magdaléna Kováčiková[a],[*], Timur G. Simdyanov[b], Andrei Diakin[a], Andrea Valigurová[a]

[a]*Department of Botany and Zoology, Faculty of Science, Masaryk University, Kotlářská 2, 611 37 Brno, Czech Republic*
[b]*Department of Invertebrate Zoology, Faculty of Biology, Lomonosov Moscow State University, Leninskiye Gory 1-12, Moscow 119234, Russian Federation*

Abstract

Gregarines represent a highly diversified group of ancestral apicomplexans, with various modes of locomotion and host-parasite interactions. The eugregarine parasite of the barnacle *Balanus balanus, Cephaloidophora* cf. *communis,* exhibits interesting organisation of its attachment apparatus along with unique motility modes. The pellicle covered gregarine is arranged into longitudinal epicytic folds. The epimerite is separated from the protomerite by a septum consisting of tubulin-rich filamentous structures and both are packed with microneme-like structures suggestive of their function in the production of adhesives important for attachment and secreted through the abundant epimerite pores. Detached trophozoites and gamonts are capable of gliding motility, enriched by jumping and rotational movements with rapid changes in gliding direction and cell flexions. Actin in its polymerised form (F-actin) is distributed throughout the entire gregarine, while myosin, detected in the cortical region of the cell, follows the pattern of the epicytic folds. Various motility modes exhibited by individuals of *C.* cf. *communis*, together with significant changes in their cell shape during locomotion, are not concordant with the gliding mechanisms generally described in apicomplexan zoites and indicate that additional structures must be involved (e.g. two 12-nm filaments; the specific dentate appearance of internal lamina inside the epicytic folds).

Introduction

Apicomplexans (Apicomplexa Levine 1980, emend. Adl et al. 2012) are one of the most investigated group of protists, comprising exclusively parasites of vertebrates as well as invertebrates. Besides important pathogens of human and agricultural animals (*Toxoplasma gondii*, *Plasmodium* spp.*, Cryptosporidium* spp., and *Eimeria* spp.), this group comprises highly diversified basal lineages, including gregarines. Gregarines are obligate parasites that inhabit a wide range of

terrestrial, freshwater, and marine invertebrates and urochordates (Desportes and Schrével 2013). In particular, gregarines occurring in marine environments have retained specific characteristics inferred to be ancestral and are considered to be deep-branching apicomplexans. Molecular phylogenetic evidence is concordant with this interpretation (Leander 2008). In general, the development of gregarines takes places in the digestive tract, reproductive organs and body cavities of their hosts, hereby explaining their varied shapes and motility modes. Gregarine trophozoites are attached to host tissue by a specialised apical part forming a mucron or an epimerite (Schrével and Desportes 2015). After the vegetative phase of their life cycle, trophozoites detach and transform into sexual stages, called gamonts, which are usually motile (Schrével and Desportes 2015).

The invasive stages (zoites) of apicomplexans are characterised by a unique set of organelles called the apical complex. Their pellicle consists of a plasma membrane which is underlain by a closely apposed inner membrane complex (IMC). The pellicle is associated with numerous cytoskeletal elements such as microtubules, a network of intermediate filament-like proteins, actin, and myosin (Morrissette and Sibley 2002). While motile apicomplexan zoites are reported to employ a unique mechanism of substrate-dependent gliding facilitated by a conserved form of the actomyosin motor (the so called glideosome concept) first proposed for *Toxoplasma gondii* and *Plasmodium* spp. (Kappe et al. 2004; Keeley and Soldati 2004; Opitz and Soldati 2002), the precise machinery involved in the motility of apicomplexan ancestral groups remains unclear. Indeed, in gregarine trophozoites and gamonts, several types of motility have been described. For example, the pendular or rolling movement in archigregarines of the family Selenidiidae Brasil, 1907 seems to be facilitated by regular sets of subpellicular microtubules (Schrével et al. 1974; Stebbings et al. 1974). Meanwhile, the motility mode mostly displayed by intestinal eugregarines is a form of progressive linear gliding usually without obvious changes in cell shape (King 1981, 1988) and accompanied by the secretion of mucus leaving a trail behind (Mackenzie and Walker 1983; Valigurová et al. 2013; Walker et al. 1979). The pellicle of most eugregarines forms numerous longitudinal epicytic folds. Electron microscopic analyses showed these folds to form lateral undulations, which were suggested to provide the force behind the gregarine gliding (Schrével and Philippe 1993; Vávra and Small 1969; Vivier 1968). Actin and myosin restricted to the cell cortex were identified in eugregarines of the genus *Gregarina* Dufour, 1828, and their involvement in gliding motility was proposed (Ghazali et al. 1989; Heintzelman 2004; Valigurová et al. 2013). As subpellicular microtubules were not observed in the investigated species of eugregarines, the mechanism of their gliding motility must differ from that described by the glideosome concept (Valigurová et al. 2013). Another type of motility, exhibited by coelomic (Urosporidae Léger, 1892 and Monocystidae Bütschli, 1882) and some intestinal eugregarines (e.g. *Didymophyes gigantea*), is the so-called peristaltic or metabolic

movement (Desportes and Schrével 2013; Diakin et al. 2016; Hildebrand and Vinckier 1975; Landers and Leander 2005; Leander et al. 2006; MacMillan 1973). These diverse modes of gregarine motility represent specific adaptations to parasitism in different environments (Valigurová et al. 2013).

The present study focuses on the eugregarine *Cephaloidophora* cf. *communis* (Cephaloidophoridae Kamm, 1922) parasitising the barnacle *Balanus balanus* Linnaeus, 1758 (Crustacea: Cirripedia). We performed ultrastructural and immunological analyses of structures, which are expected to be related to the attachment to host tissue and to the unique motility mode displayed by the trophozoites and gamonts of this eugregarine.

Material and Methods

The gregarine *Cephaloidophora* cf. *communis* was isolated from the intestine of its marine crustacean host *Balanus balanus*. Hosts were collected between 2013 and 2015 from the White Sea environment close to the White Sea Biological Station of Lomonosov Moscow State University (66°33.190′N, 33°06.550′E). Parasites were separated from host's intestine in filtered seawater using entomological needles and then transferred to embryo dishes with a 30 mm cavity for careful washing in filtered seawater and subsequent fixation procedures. The dissection and manipulation of parasites were performed using a stereomicroscope MBS-1 (LOMO, Russia). For native preparations, individual gregarines were put on microscope glass slides with filtered seawater and their motility was monitored using a Leica DM 2000 light microscope connected to a DFC 420 digital camera (Leica Microsystems, Germany).

For transmission electron microscopy (TEM), specimens were fixed in an ice bath in 2.5–3% (v/v) glutaraldehyde in filtered seawater or in 0.15 M cacodylate buffer (pH 7.4). Some specimens were fixed with 3% glutaraldehyde–ruthenium red [0.15% (w/v) stock solution in Milli-Q water] in cacodylate buffer or with 2.5% glutaraldehyde–alcian blue [1% (w/v) stock solution in Milli-Q water] in filtered seawater. Fixed samples were rinsed 3× for 20 min and post-fixed in 2% (w/v) OsO₄ for 2 h in the same buffer as used for fixation. After rinsing 3× for 20 min in the same fixation buffer and after dehydration in an acetone series, specimens were embedded in Epon (Polybed 812). Ultrathin sections were obtained with diamond knives using a Leica EM UC6 ultramicrotome (Leica Microsystems, Germany) and stained with uranyl acetate and lead citrate. Sections were examined under a JEM-1010 (Jeol, Japan).

For scanning electron microscopy (SEM), specimens were fixed in 2.5–5% (v/v) glutaraldehyde in 0.2 M cacodylate buffer (pH 7.4), washed 3× for 15 min in cacodylate buffer, post-fixed in 2% (w/v) OsO₄ for 2 h in the same buffer, and finally washed 3× for 15 min in cacodylate buffer. After dehydration in an acetone series, parasites were critical

point-dried with CO_2, coated with gold, and observed using a JEOL JSM-7401F (Jeol, Japan).

For confocal laser scanning microscopy (CLSM), specimens were fixed in 4% paraformaldehyde (PFA) in 0.1 M phosphate buffered saline (PBS) at room temperature for 45 min and then washed 3× for 15 min before further processing. Afterwards, the parasites were permeabilised in 0.3% Triton X-100 (Sigma-Aldrich, Czech Republic) for 20 min. For the direct fluorescent staining of F-actin, samples were incubated overnight at room temperature with phalloidin-tetramethylrhodamine B isothiocyanate (phalloidin-TRITC; Sigma-Aldrich, Czech Republic) and then washed 3× for 10 min in 0.1 M PBS. For indirect immunofluorescence, the samples were incubated overnight at 4 °C with the following primary antibodies: mouse monoclonal IgG anti-actin raised against *Dictyostelium* actin (provided by Prof. Dominique Soldati-Favre), rabbit anti-myosin (smooth and skeletal, the whole antiserum, dilution 1:5; Sigma-Aldrich, Czech Republic) and mouse monoclonal anti-α-tubulin (Clone B-5-1-2, dilution 1:1000; Sigma-Aldrich, Czech Republic), all in PBS with 0.1% BSA. After washing 3× for 10 min in 0.1 M PBS, the specimens were incubated at 37 °C for 4 h with the following secondary antibodies: FITC-conjugated anti-mouse (polyvalent immunoglobulins, dilution 1:125; Sigma-Aldrich, Czech Republic) and TRITC-conjugated anti-rabbit IgG (whole molecule, dilution 1:200; Sigma-Aldrich, Czech Republic), both in PBS with 1% BSA. They were then washed again. Controls were incubated with a mixture of secondary antibodies alone, i.e. without primary antibodies. Preparations were mounted in VECTASHIELD Hard Set Mounting Medium (Vector laboratories, USA). Samples were examined under an Olympus IX80 microscope equipped with a laser-scanning Fluo View 500 confocal unit (Fluo View 3.4 software; Olympus, Japan). Fluorescence was visualised using the TRITC (phalloidin, anti-myosin/544 nm) and FITC (anti-actin, anti-α-tubulin/457–515 nm) lasers sets. Some micrographs obtained under CLSM were processed using Fiji software (an image processing package based on ImageJ developed at the National Institutes of Health).

Results

Light microscopic observations of gregarine motility. The detached trophozoites and gamonts isolated from host intestine exhibited a very active gliding movement (Video S1, Supplementary material). When compared to gliding motility in other eugregarines, the behaviour of *C.* cf. *communis* during gliding differed in several aspects. In addition to progressive and rapid gliding, these gregarines displayed jumping or jerky movements, during which gliding was discontinuous and combined with abrupt stopping (Video S2, Supplementary material). Moreover, rotations around the longitudinal cell axis, rapid changes in direction (Video S3, Supplementary material), and flexion in the area of the septum separating the protomerite from the deutomerite and in

the first third of the deutomerite were observed during gliding (Video S4, Supplementary material). In some cases, the protomerite partially retracted into the deutomerite (Video S4). In addition, the parasites were capable of gliding motility even when contacting the microscopic slide via their apical or posterior regions only (Video S5, Supplementary material). Reverse movement was also observed (Video S6, Supplementary material).

Electron microscopic analyses. Trophozoites of *C.* cf. *communis* exhibited tricystid morphology; i.e. the cell was dived into three morphologically distinct regions: the epimerite, protomerite, and deutomerite (Fig. 1A–C). The lenticular epimerite, situated in the middle of the protomerite apical end, appeared as a thickened hyaline region when observed under the light microscope (Fig. 1A). Detailed SEM observations of the epimerite surface revealed a wrinkled plasma membrane with numerous pores, lacking epicytic folds. The epimerite of one specimen bore a long tiny protrusion in its central part (Fig. 2A–C). The epimerite was separated from the protomerite by a septum (Figs 1 A, 2 D–G). The tubular structures (20 ± 1 nm in diameter) forming the septum were difficult to detect (Fig. 2G). Another distinct septum separated the protomerite from the deutomerite, inside which a prominent nucleus was situated (Figs 1 A, C, 2 D, 3 G). A superficial constriction was evident at the interface between the protomerite and deutomerite in the area of the septum (Figs 1 B, 2 A, 3 A, F). The cytoplasm of the protomerite and deutomerite was divided into an inner granular endoplasm packed with various cytoplasmic organelles and inclusions, and an outer thinner hyaline ectoplasm lying under the pellicle and free of amylopectin grains (Figs 1 A, C, 4 A, B).

Both the epimerite and protomerite comprised abundant electron lucent vesicles of unknown origin and function surrounding the septum, giving this area a foam-like appearance (Fig. 2D–F), and microneme-like organelles (Figs 2 E, F, 3 D, E). One SEM specimen with a mechanically ruptured cortex revealed obvious differences between epimerite and protomerite organisation. While the epimerite contained only cylindrical organelles corresponding to the microneme-like structures shown by TEM, numerous filamentous structures were visible under the pellicle of the protomerite (Fig. 2H).

The typical gregarine pellicle of *C.* cf. *communis*, consisting of a plasma membrane and an inner membrane complex (IMC) (Fig. 3C), formed numerous longitudinally arranged epicytic folds (Figs 1 B, 2 A). The folds of the protomerite were lower in the gregarine apical end but their height increased posteriorly (Fig. 3A, B, D). In contrast, the folds of the deutomerite part were higher and their height was equal along the entire deutomerite (Fig. 4A–C, E, F). The epicytic folds exhibited an undulating appearance and new emerging folds between the already existed ones were observed (Figs 1 B, 2 B, C, 3 A, B, F, 4 E–G, 5 A–F). A thick internal lamina situated under the IMC linked the base of the folds, while a thin layer of the lamina separated and extended to each fold (Fig. 4C, D, F, G). A sparse network of filamentous structures
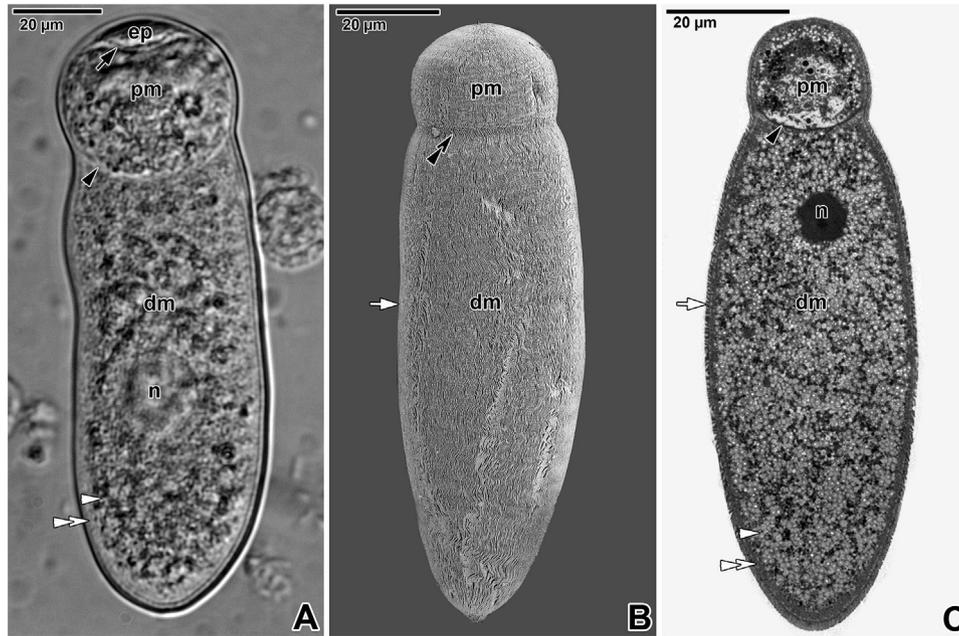
Fig. 1. General morphology of *Cephaloidophora* cf. *communis* trophozoites. **A.** A trophozoite exhibiting tricystid morphology. LM, bright field. **B.** General view of a trophozoite. SEM. **C.** A longitudinal section of a trophozoite. TEM.

black arrow—septum separating the epimerite from the protomerite, *black arrowhead*—septum separating the protomerite from the deutomerite, *dm*—deutomerite, *double black arrowhead*—constriction of the cell in the area of septum separating the protomerite from the deutomerite, *double white arrowhead*—ectoplasm, *ep*—epimerite, *n*—nucleus, *pm*—protomerite, *white arrow*—epicytic folds, *white arrowhead*—endoplasm.

(8 ± 1 nm thick) was detected inside the ectoplasm underlying the internal lamina (Fig. 4D). The nature of this network remains unknown, as, in some sections, these putative filaments seemed to demarcate vesicle-like structures. Each epicytic fold possessed in the apical part three rippled dense structures with their bases located at the external cytomembrane, and two poorly visible 12-nm filaments located under the IMC (Fig. 4F, inset). The thin layer of internal lamina extending into the folds and underlying the IMC had a specific dentate appearance (5 ± 1 nm in diameter) (Fig. 4G, H). In tangential sections, these dentations had a filamentous appearance and were revealed to be organised angle-wise to the epicytic fold longitudinal axis (Fig. 4H).

Typical apicomplexan micropores were present in the grooves between the epicytic folds, distributed at irregular distances from each other. Their duct (35–40 nm in diameter), interrupting the IMC, was lined by a cone-shaped, electron-dense collar (120–130 nm in diameter). These micropores were ending with a vesicle (Figs 3 B, 5 E–H). Staining with alcian blue and ruthenium red confirmed the presence of a glycocalyx layer forming a network along with an intense secretion of mucus accumulating between the epicytic folds (Fig. 5B, C). Further, amylopectin granules were clearly visible in the cytoplasm of stained gregarines (Figs 4 B, 5 A, C). Similarly, SEM observations showed mucus-like drops to be situated at the folds' apex and in the grooves between them (Figs 4 E, 5 D, E). In the ectoplasm, just beneath the

pellicle, numerous cisternae containing mucous substances were observed (Fig. 5C).

Confocal laser scanning microscopic analysis. The staining of α-tubulin showed a distinct ring structure located in the area of the epimerite-protomerite septum (Fig. 6B–D, compare with Fig. 6A). In addition, after α-tubulin labelling, a strong fluorescent signal was visible in some parasites in a form of a funnel-like structure extending from the epimerite centre and ending at the septum (Fig. 6C–F). In other specimens, the labelling of α-tubulin within the epimerite had the appearance of concentric rings (Fig. 6H, I). Also, clusters of putatively unpolymerised α-tubulin were dispersed in the cytoplasm of some individuals (Fig. 6C, D, H, I).

Filamentous actin occurred in the entire cell, with a slightly increasing intensity around both septa and in the area of the nucleus (Figs 6 F–I, 7 A, B). In addition, specific antibody labelling confirmed the localisation of actin in the gregarine cytoplasm in the form of abundant clusters occurring especially in the epimerite-protomerite region (Fig. 7B, C, E, F). A few actin clusters were visible in the deutomerite cytoplasm of some individuals, but their occurrence was mostly occasional (Fig. 7A–C, E). Myosin was restricted exclusively to the gregarine cortex (Figs 6 B, C, 7 C–F). Superficial optical sections showed that the organisation of myosin followed the pattern of longitudinally-organised epicytic folds (Fig. 7C, D).
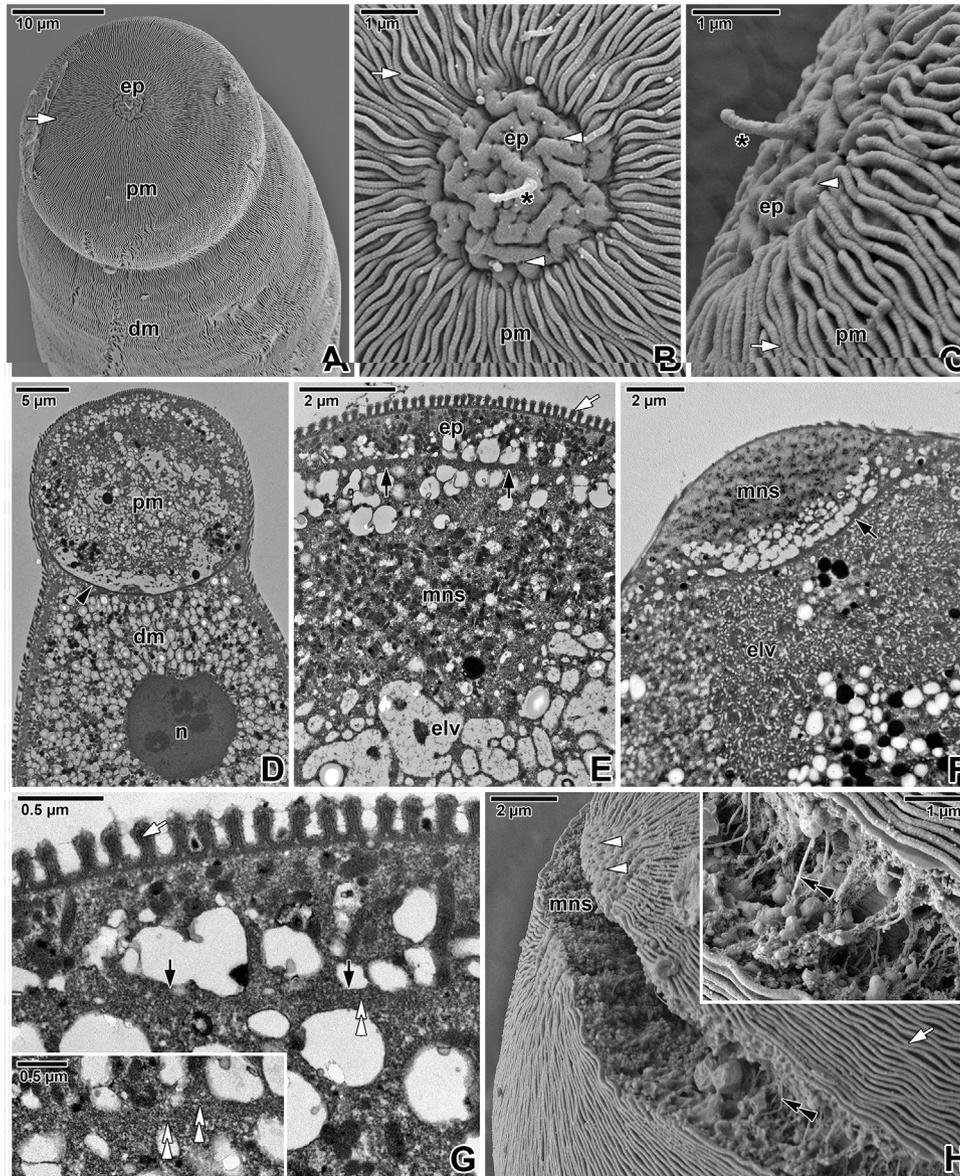
Fig. 2. Attachment region of *Cephaloidophora* cf. *communis* trophozoites. A. A front view of the cell showing the protomerite with centrally located epimerite. SEM. **B, C.** Frontal (B) and lateral (C) views showing the epimerite covered by a wrinkled plasma membrane with numerous pores and a central protrusion. SEM. **D.** Longitudinal section of the protomerite and anterior part of the deutomerite. TEM. **E, F.** Higher magnification of the epimerite separated from the protomerite by a septum comprising electron lucent vesicles and microneme-like structures. TEM. **G.** The area of the septum separating the epimerite from the protomerite. The inset shows a different view of the filaments in the septum. TEM. **H.** A mechanically ruptured cell revealing differences in organisation between the epimerite and the protomerite. The inset shows a detail of filamentous structures under the pellicle. SEM.

black arrow—septum separating the epimerite from the protomerite, *black arrowhead*—septum separating the protomerite from the deutomerite, *black asterisk*—epimerite protrusion, *dm*— deutomerite, *double black arrowhead*—filamentous structures in the protomerite, *double white arrowhead*—filaments in septum, *elv*—electron lucent vesicles, *ep*—epimerite, *mns*—microneme-like structures, *n*—nucleus, *pm*—protomerite, *white arrow*—epicytic folds, *white arrowhead*—epimerite pores.

Discussion

In our study on *C.* cf. *communis*, only trophozoites and gamonts were collected after dissection of the host intestine, but previous studies reported also intracellular stages occurring in the hyaline vacuoles of the enterocytes (Lacombe et al. 2002). The parasites exhibited tricystid morphology, with the attachment apparatus – the epimerite – in the apical part of the cell. The epimerite was defined as a rudimental and rounded or lenticular structure with evenly distributed superficial pores (Rueckert et al. 2011; this study). In addition, a long thin protrusion rising from the central part of the epimerite was observed in one individual, probably facilitating more stable attachment to the host gut tissue. So far, it
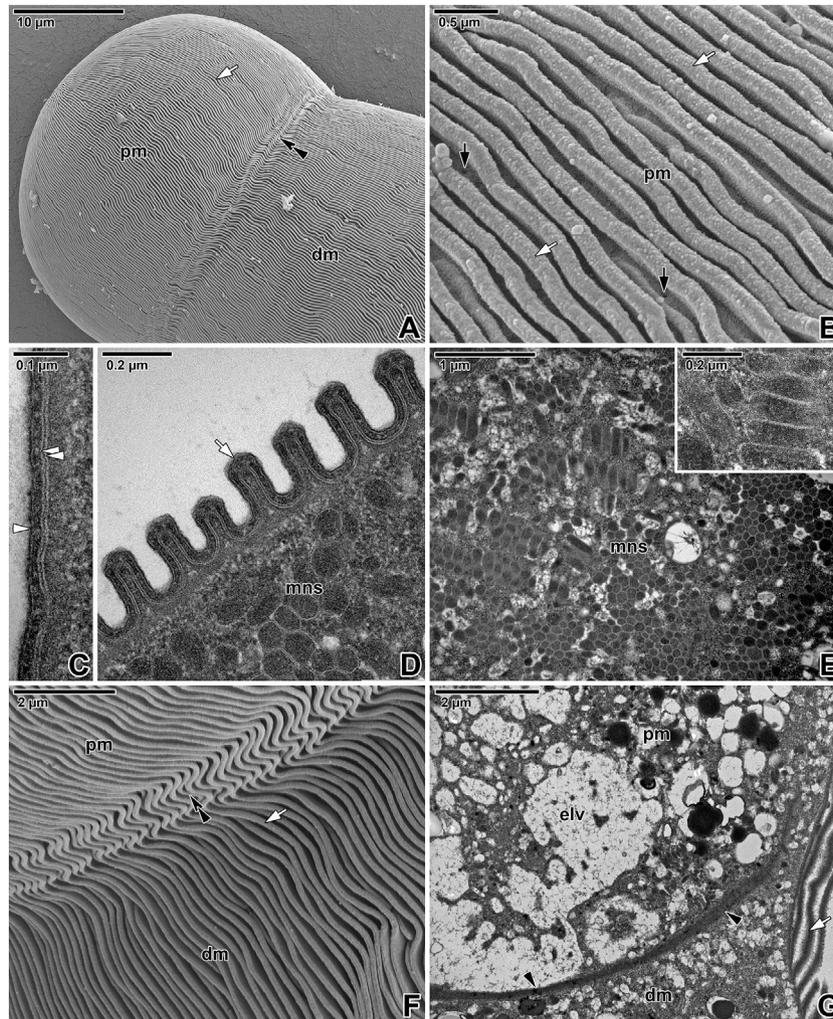
Fig. 3. Protomerite architecture in *Cephaloidophora* cf. *communis*. A. Protomerite and the apical part of deutomerite covered by dense arrays of longitudinal epicytic folds. SEM. **B.** Higher magnification of epicytic folds covering the protomerite. SEM. **C.** The three-layered pellicle. TEM. **D**. Higher magnification of protomerite epicytic folds in cross section. TEM. **E.** Detail of protomerite apical region showing microneme-like structures. The inset shows microneme-like structures in detail. TEM. **F.** The constriction at the protomerite-deutomerite septum. SEM. **G.** Septum separating the protomerite from the deutomerite. TEM.

black arrow—micropores, *black arrowhead*—septum separating the protomerite from the deutomerite, *dm*—deutomerite, *double black arrowhead*—constriction of the cell in the area of septum separating the protomerite from the deutomerite, *double white arrowhead*—IMC, *elv*—electron lucent vesicles, *mns*—microneme-like structures, *pm*—protomerite, *white arrow*—epicytic folds, *white arrowhead*—plasma membrane.

cannot be disproven that the protrusion is only an artefact. On the other hand, with regard to its thickness, this structure seems extremely fragile; thus, it could be broken off during the fixation procedure. Another possibility is that the protrusion is retracted before fixation. Inside the apical parts of the epimerite and the protomerite, numbers of electron dense vesicles similar to micronemes were detected. These structures are supposed to release a glutinous secretion through the pores situated on the epimerite and therefore to be responsible for parasite attachment (Simdyanov et al. 2015). The phenomenon of gluing was noted during our observation of *C.* cf. *communis*, where gregarines were capable of attaching to the surface of cover slides. This adhesive ability is also known in other eugregarines, where a dense adhesive

material likely produced by exocytic vesicles (Cook et al. 2001) is released through pore-like structures located at the top of the protomerite or the attachment site and which is thought to have the function of sticking to the host tissue (Diakin et al. 2017; Valigurová 2012). Alternatively, these pores might play a role in gamont nutrition (Valigurová 2012). The space inside the epimerite and protomerite is packed with translucent vesicular structures of unknown origin and function. These electron-lucent vesicular structures of foam-like appearance are supposed to be formed by a highly developed endoplasmic reticulum (Simdyanov et al. 2015).

In comparison with other eugregarines (Devauchelle 1968; Devauchelle and Oger 1968; Tronchin and Schrével 1977; Valigurová and Koudela 2005; Valigurová et al. 2009;
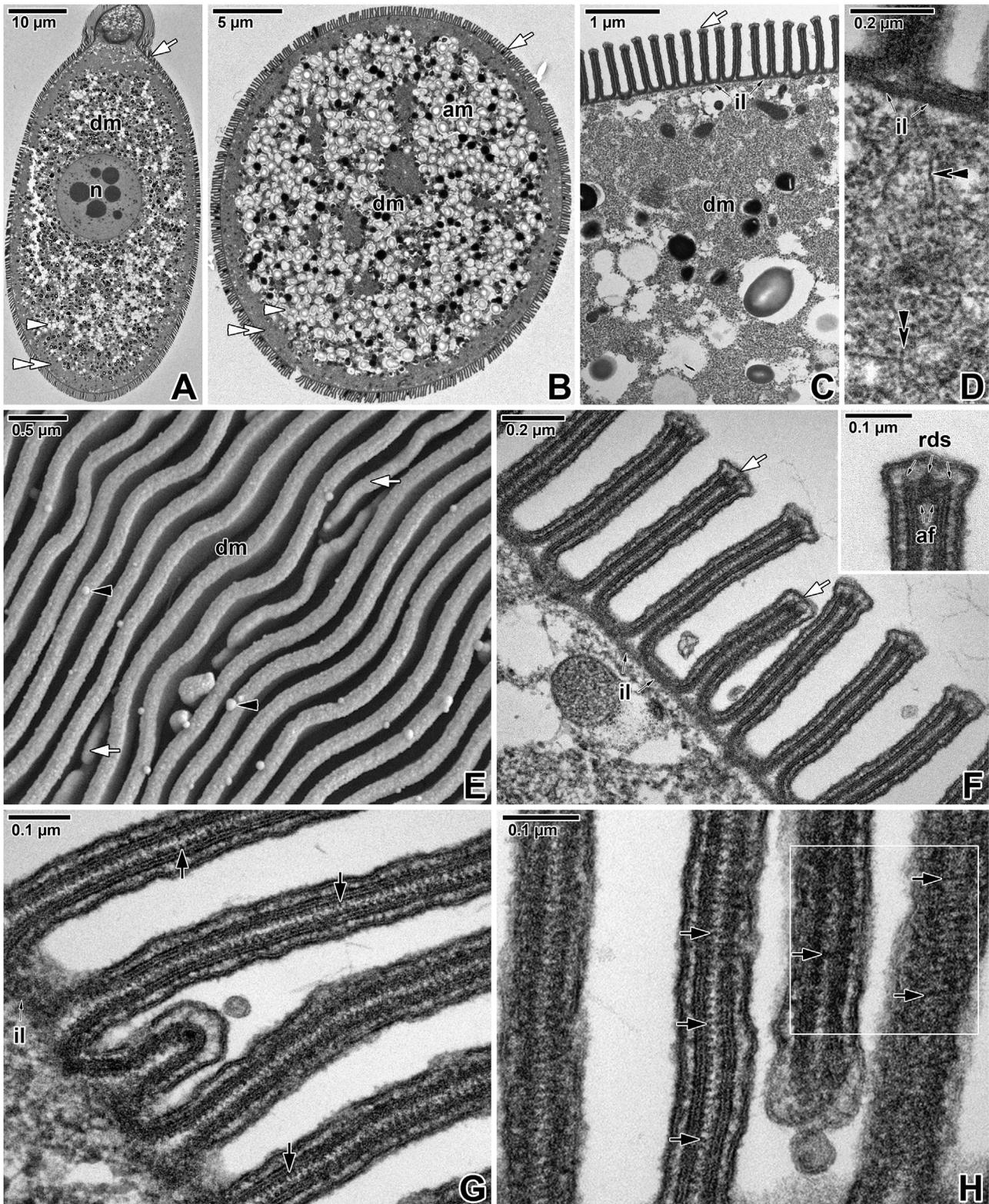
Fig. 4. Deutomerite architecture in *Cephaloidophora* cf. *communis*. A. Deutomerite and a part of protomerite in longitudinal section. TEM. **B.** Deutomerite in transversal section. AB, TEM. **C, D.** Detail of cortex and ectoplasm organisation. TEM. **E.** Detail of deutomerite epicytic folds. Note new folds appearing between the already existing ones. SEM. **F.** Higher magnification of deutomerite epicytic folds. Inset shows a detail of the folds' tip comprising three rippled dense structures and two 12-nm apical filaments. TEM. **G, H.** The dentation of internal lamina inside the epicytic folds. *White rectangle* demarcates the superficial section of epicytic folds. TEM.

af—12-nm apical filaments, *black arrow*—dentation of internal lamina, *black arrowhead*—mucus drop, *dm*—deutomerite, *double black arrowhead*—filamentous structures in ectoplasm , *double white arrowhead*—ectoplasm, *il*—internal lamina, *n*—nucleus, *rds*—ripple dense structures, *white arrow*—epicytic folds, *white arrowhead*—endoplasm.
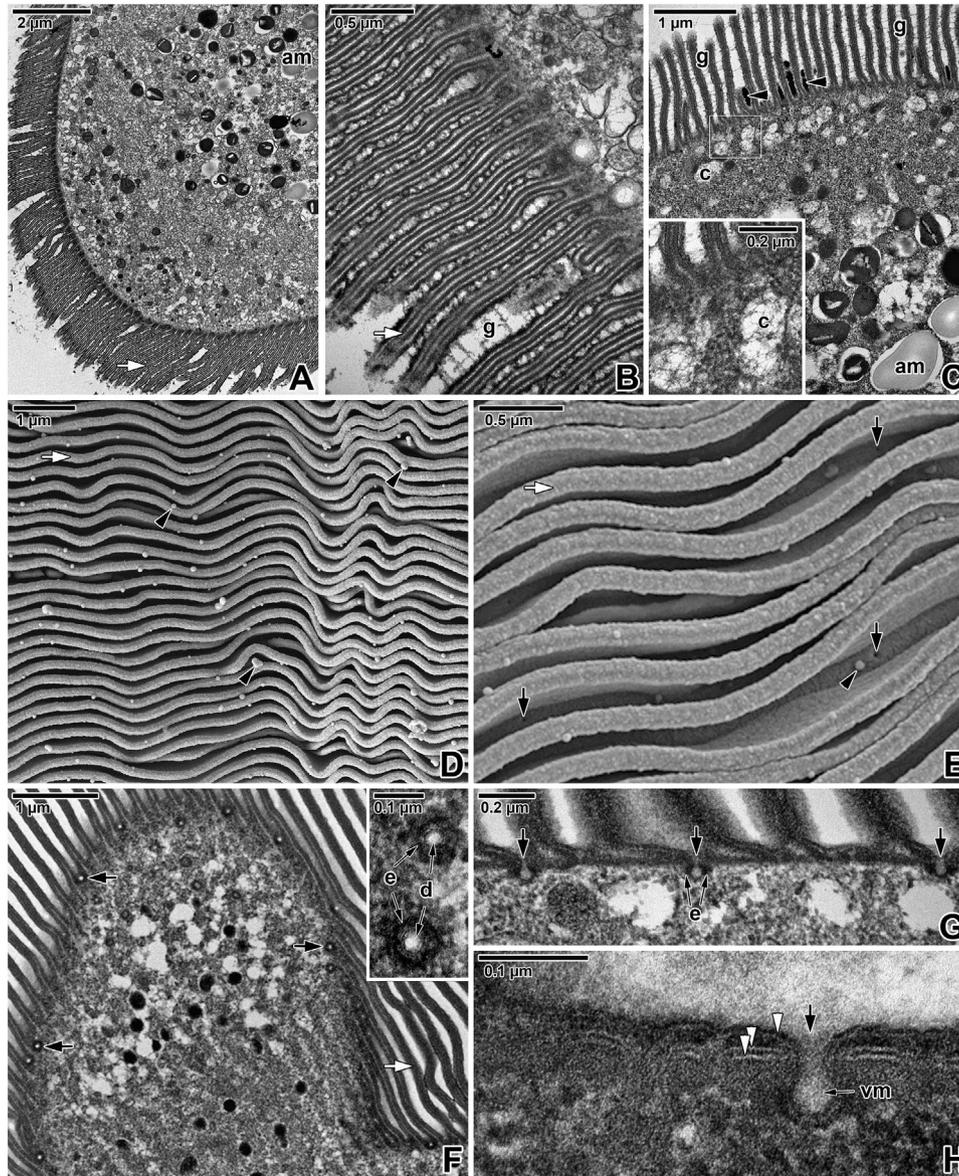
Fig. 5. Micropores, mucus secretion and glycocalyx in *Cephaloidophora* cf. *communis*. A. General view of posterior region showing cytoplasm with inclusions and amylopectin granules and epicytic folds. RR, TEM. **B.** Glycocalyx layer forming a network between the epicytic folds. RR, TEM. **C.** A view of the glycocalyx network and mucus accumulation between the folds and cisternae with mucous material located under the pellicle. The inset shows cisternae demarcated by a white rectangle in more detail. AB, TEM. **D, E.** A view of mucus-like drops situated at the folds' apex and in the grooves between them along with the micropores. SEM. **F.** Superficial cross section showing the cytoplasm and micropores. Inset shows the duct and electron-dense collar of micropores. TEM. **G, H.** Longitudinal sections of micropores. TEM.

am—amylopectin*, black arrow*—micropores, *black arrowhead*—mucus, *c*—cisternae, *d*—duct, *double white arrowhead*—IMC, *e*—electron-dense collar, *g*—glycocalyx, *vm*—vesicle of micropore, *white arrow*—epicytic folds, *white arrowhead*—plasma membrane.

Valigurová 2012), the epimerite of *C.* cf. *communis* is not retracted/discarded after trophozoite detachment. In *Cephaloidophora* spp. the epimerite is also present during the intracellular phase of trophozoites development (Poisson 1924) and is covered by a pellicle (Simdyanov et al. 2015), not only by a plasma membrane as in other species. Hence, the question arises of whether this structure represents an epimerite or is the modified apical end of the protomerite dedicated to attachment or eventually to feeding,

as described in eugregarines from mealworms (Devauchelle 1968; Valigurová 2012). The remaining epimerite could serve for the hypothetical reattachment of trophozoites to younger host cells after the abandonment of senescing cells, as suggested in some other eugregarines (Lucarotti 2000; Valigurová et al. 2009; Valigurová 2012).

In addition, labelling with α-tubulin antibody detected a ring structure located in the area of the septum separating the epimerite from the protomerite. In TEM sections, this
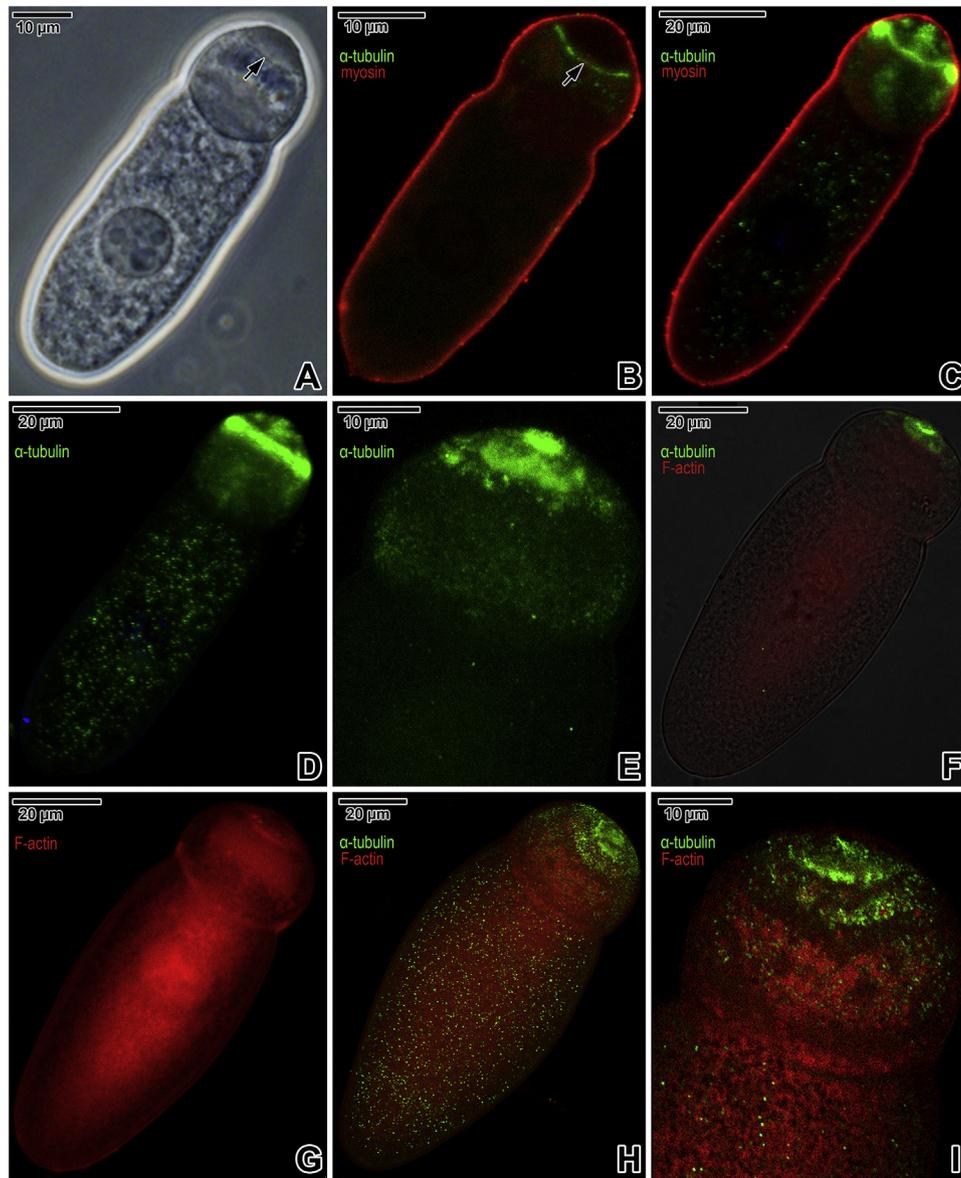
Fig. 6. Distribution of α-tubulin, myosin and F-actin in *Cephaloidophora* cf. *communis* trophozoites. A. General view of a PFA-fixed trophozoite. LM. **B, C.** Distribution of α-tubulin (FITC) forming a ring structure in the region of the epimerite-protomerite septum and the localisation of myosin (TRITC). CLSM, IFA. **D, E.** Localisation of α-tubulin (FITC). CLSM, IFA. **F.** Double labelling of α-tubulin (FITC) and F-actin (TRITC). CLSM, IFA/phalloidin-TRITC. **G.** Localisation of F-actin (TRITC). CLSM, phalloidin-TRITC. **H, I.** Double labelling of α-tubulin (FITC) and F-actin (TRITC). CLSM, IFA/phalloidin-TRITC. F: CLSM in combination with transmission LM.
black arrow—septum separating the epimerite from the protomerite.

structure was composed of tubular elements (20 ± 1 nm in diameter). The above mentioned α-tubulin-rich filamentous structures could be responsible for the epimerite controlling the attachment to and detachment from host tissue in accordance with the theory of epimerite retraction (Devauchelle 1968; Valigurová and Koudela 2008; Valigurová et al. 2009; Valigurová 2012). The presence of α-tubulin in clusters localised in gregarine cytoplasm, indicates the unpolymerised form of tubulin. In contrast, neither positive α-tubulin labelling nor tubular structures on ultrathin sections were detected in the septum separating the protomerite from the deutomerite.

Micropores are suggested to have a role in cell surface nutrition after the detachment of trophozoites from the host tissue (Warner 1968). In addition, their connection with cisternae or ducts was demonstrated by freeze-etching analysis, indicating that they might be related to mucus secretion (Valigurová et al. 2013). Superficial observations under SEM confirm the presence of mucus drops in between and on the top of epicytic folds. In addition, a strongly stained network was detected between the epicytic folds after the application of fixatives binding to mucopolysaccharides, thereby indicating the presence of a glycocalyx layer covering the gregarine surface. The presence of glycocalyx layer (glycoconjugates)
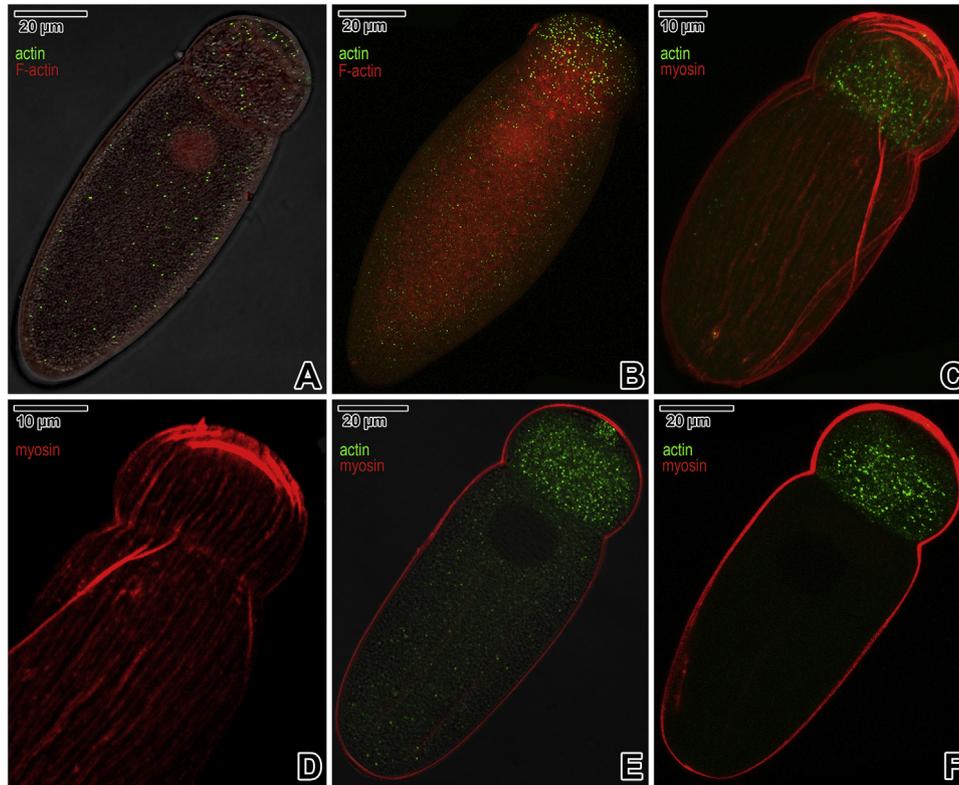
Fig. 7. Distribution of actin and myosin in *Cephaloidophora* cf. *communis* trophozoites. A, B. Co-localisation of actin (FITC) and F-actin (TRITC) in a single optical section (A) and composite picture (B). CLSM, IFA/phalloidin-TRITC. **C.** Composite picture of actin (FITC) clusters accumulated within epimerite and protomerite cytoplasm and myosin (TRITC) restricted to the cell cortex. CLSM, IFA. **D.** Higher magnification showing myosin (TRITC). CLSM, IFA. **E, F.** Localisation of actin (FITC) clusters and myosin (TRITC) in single optical sections. CLSM, IFA. A, E: CLSM in combination with transmission LM.

was documented from the surface of different gregarine species (Philippe et al. 1979; Simdyanov and Kuvardina 2007). Glycocalyx allows the parasite to interact with and respond to its external environment and represents an important protective barrier against hostile forces (Guha-Niyogi et al. 2001).

The epicytic folds covering the *C.* cf. *communis* surface exhibit an undulating arrangement and typical architecture as described in other eugregarine species (Desportes and Schrével 2013; Reger 1967; Schrével et al. 1983; Simdyanov et al. 2015; Vávra and Small 1969; Valigurová et al. 2013; Walker et al. 1984). It was proposed that polymerisation of the 12-nm filaments located in the tip of the epicytic fold under the IMC plays a significant role in the gliding motility and cell morphogenesis of eugregarine trophozoites with longitudinal folds, whose lateral undulation could be mediated by an actomyosin system (Schrével and Philippe 1993; Vávra and Small 1969; Vivier 1968). A more recent study on trophozoites of *Gregarina* spp. showed that the number of 12-nm filaments does not influence the speed of gregarine gliding, but seems to control the direction of movement (Valigurová et al. 2013). According to observations on *C.* cf. *communis* possessing only two 12-nm apical filaments in each epicytic fold (Simdyanov et al. 2015; this study), it was also demonstrated that the gliding path of species equipped with a low number of

12-nm filaments was rather semi-circular than linear and the individuals glided with a relatively high speed. Interestingly, each epicytic fold exhibited structures oriented angle-wise to the longitudinal axis of the fold, which appeared in cross section as dentations of the internal lamina, and have not so far been described in other eugregarines. These structures formed by internal lamina might possibly participate as a scaffold strengthening the epicytic folds involved in gliding motility.

In general, the glideosome, described in apicomplexan invasive stages (zoites) (first announced for *Toxoplasma gondii* and later for *Plasmodium* spp.), powers the gliding motility essential for their migration to the appropriate location in the host organism and for host cell invasion (Opitz and Soldati 2002). In this model, an actomyosin motor is expected to be embedded between the parasite plasma membrane and the IMC, and to require a stable subpellicular network of microtubules (Dubremetz et al. 1998; Kappe et al. 2004; Keeley and Soldati 2004; Matuschewski and Schüler 2007). Nowadays, the glideosome concept continues to be redefined as new components are discovered, but the principal mechanism still appears largely to be valid (Heintzelman 2015). Despite this, it has emerged that this mechanism cannot be applied to basal apicomplexans such as gregarines (Valigurová et al. 2013).

Eugregarines are usually capable of gliding motility, but the exact mechanism behind their movement must differ significantly from the generally accepted glideosome concept, as the presence of subpellicular microtubules and micronemes was, in the investigated species, disproven (Valigurová et al. 2013). In contrast to the substrate-dependent gliding of apicomplexan zoites, eugregarines from the genus *Gregarina* were able to move for a certain time without any contact with the substrate (Valigurová et al. 2013). In our study, the gliding movement of *C*. cf. *communis* also exhibited unusual characteristics (e.g. additional jumping and rotational movements, rapid changes in direction, and cell flexions) and, similarly to other eugregarines, subpellicular microtubules were not observed in the cortex.

The localisation of actin and myosin, which are considered to constitute the main motility motor in apicomplexan zoites, were studied within eugregarines mostly from the genus *Gregarina* from terrestrial insect hosts and the genus *Lecudina* Mingazzini, 1891 from marine polychaete hosts (Baines and King 1989; Ghazali et al. 1989; Ghazali and Schrével 1993; Heintzelman 2004; Valigurová et al. 2013). The presence of filamentous actin fluorescently tagged with phalloidin was studied only in gregarines parasitising mealworms. It localised in their cortex, in the septum separating the protomerite and deutomerite, and in the area of the nucleus (Valigurová et al. 2009; Valigurová 2012; Valigurová et al. 2013). In *C*. cf. *communis*, F-actin was distributed homogenously throughout the entire gregarine, but particularly in the area of both septa and in the position surrounding the nucleus; however, the intensity of the fluorescence signal was low. A different situation was described for other apicomplexans, where F-actin was considered to be highly unstable, forming short filaments (Matuschewski and Schüler 2007). For example, in *T. gondii*, actin filaments were not detected without treatment by F-actin stabilising drugs (e.g. jasplakinolide) and actin existed primarily in its globular form (Dobrowolski et al. 1997). In *Gregarina* spp., positive phalloidin labelling gave an indication that the majority of actin was present in filamentous form (Valigurová et al. 2013). On the other hand, actin fluorescently localised with a monoclonal antibody known specifically to recognise actin in *T. gondii* and *Plasmodium* spp. showed only clusters of actin predominantly distributed in the area of epimerite and protomerite cytoplasm. This situation is similar to that described in *Gregarina cuneata*, where a dot-like pattern of actin staining was demonstrated in the protomerite region of mature gamonts, suggesting that this actin could be responsible for the increased flexibility of this region (Valigurová 2012). In the present study, some individuals showed similar dot-like actin staining with a less intensive signal in the deutomerite region. The occurrence of actin clusters in the deutomerite, however, was irregular and occurred mostly in smaller individuals. This difference could be the result of features being specific to particular developmental stages (younger parasites) or eventually to particular gamont types (primite vs. satellite), and could indicate the diverse intensity of their

motility. In previous studies (Heintzelman 2004; Valigurová 2012; Valigurová et al. 2013), the localisation of actin in the eugregarine cortex was described with two distinct orientations (parallel and perpendicular) within the parasite. In spite of this, however, in our study the antibody used for actin labelling in apicomplexans failed to detect cortical actin. On the other hand, positive phalloidin labelling suggested that the polymerised form of actin could play a role in *C*. cf. *communis* gliding, as proposed for *Gregarina* spp. (Valigurová et al. 2013). The presence of the XIV subclass of unconventional myosins is characteristic of all so far investigated Apicomplexa groups (Foth et al. 2006; Frénal et al. 2008), and structural homologies exist between the myosins of gregarines and other apicomplexans (Heintzelman 2004). Similarly to previous studies (Ghazali and Schrével 1993; Heintzelman 2004; Valigurová et al. 2013), the myosin in *C*. cf. *communis* was localised in the cell cortex, following a pattern of longitudinal epicytic folds. The actomyosin complex in eugregarines was assumed to be localised in the lateral parts of epicytic folds (Valigurová et al. 2013).

Conclusion

The structural organisation of the attachment apparatus, the epimerite, in the marine eugregarine *C*. cf. *communis* exhibited a very specific pattern including numerous irregularly distributed pores in the plasma membrane. These pores are thought to release adhesives, most likely produced by the microneme-like structures localised in the parasite apical end and facilitating its adhesion to the host tissue. More stable anchoring to the host is likely to be secured by the tiny long protrusion rising from the epimerite centre, although its presence and function in the eugregarine is ambiguous. Accordingly, it may be the case that the attachment strategy combines both mechanical and chemical means.

Despite the fact that the presence of the basic motor proteins, actin and myosin, was demonstrated in this study, the motility mode in *C*. cf. *communis* obviously differs from the substrate-dependent gliding described for apicomplexan zoites. This outcome is also supported by the absence of subpellicular microtubules, which are essential components in apicomplexan motor machinery. Actin, predominantly occurring in polymerised form, was dispersed throughout the entire cell, while myosin was localised to the gregarine cortex. Nevertheless, the exact position of actin microfilaments as well as the role of the putative actomyosin motor in eugregarines remain to be elucidated. The unusually active and variable mode of gliding motility in this gregarine is facilitated by the architecture of its epicytic folds. Each fold comprises two 12-nm filaments responsible for the gregarine's variable gliding path, as previously proposed for *Gregarina* spp. (Valigurová et al. 2013), and internal lamina which exhibits an extraordinary dentate appearance. Furthermore, gliding is supported by the intensive secretion of mucopolysaccharides densely coating the entire gregarine surface.

Acknowledgements

Appendix A. Supplementary data

Supplementary data associated with this article can be found, in the online version, at http://dx.doi.org/10.1016/j.ejop.2017.02.006.

References

Adl, S.M., Simpson, A.G., Lane, C.E., Lukeš, J., Bass, D., Bowser, S.S., Brown, M.V., et al., 2012. The revised classification of eukaryotes. J. Eukaryot. Microbiol. 59 (5), 429–493, http://dx.doi.org/10.1111/j.1550-7408.2012.00644.x.

Baines, I., King, C.A., 1989. Demonstration of actin in the protozoon—Gregarina. Cell Biol. Int. Rep. 13 (8), 679–686.

Cook, T.J.P., Janovy, J., Clopton, R.E., 2001. Epimerite-host epithelium relationships among eugregarines parasitizing the damselflies Enallagma civile and Ischnura verticalis. J. Parasitol. 87, 988–996, http://dx.doi.org/10.1645/0022-3395(2001)087[0988:EHERAE2.0.CO;2].

Desportes, I., Schrével, J., 2013. The gregarines, the early branching Apicomplexa (2 vols.). Treatise on Zoology—Anatomy, Taxonomy, Biology. BRILL, Leiden, The Netherlands, 781 pp.

Devauchelle, G., 1968. Étude ultrastructurale du développement des grégarines du Tenebrio molitor L. Protistologica 4 (3), 313–332.

Devauchelle, G., Oger, C., 1968. Biometrical analysis of gregarines in Tenebrio molitor. Protistologica 4 (1), 37–52.

Diakin, A., Paskerova, G.G., Simdyanov, T.G., Aleoshin, V.V., Valigurová, A., 2016. Morphology and molecular phylogeny of coelomic gregarines (Apicomplexa) with different types of motility: Urospora ovalis and U. travisiae from the polychaete Travisia forbesii. Protist 167, 279–301, http://dx.doi.org/10.1016/j.protis.2016.05.001.

Diakin, A., Wakeman, K., Valigurová, A., 2017. Description of Ganymedes yurii sp. n. (Ganymedidae), a new gregarine species from the antarctic amphipod Gondogeneia sp. (Crustacea). J. Eukaryot. Microbiol. 64 (1), 56–66, http://dx.doi.org/10.1111/jeu.12336, PMID: 272881198.

Dobrowolski, J.M., Niesman, I.N., Sibley, L.D., 1997. Actin in the parasite Toxoplasma gondii is encoded by a single copy gene, ACT1 and exists primarily in a globular form. Cell Motil. Cytoskeleton 37 (3), 253–262, http://dx.doi.org/10.1002/(SICI)1097-0169(1997)37:3<253:AID-CM7>3.0.CO;2-7.

Dubremetz, J.F., Garcia-Reguet, N., Conseil, V., Fourmaux, M.N., 1998. Apical organelles and host–cell invasion by Apicomplexa. Int. J. Parasitol. 28 (7), 1007–1013.

Foth, B.J., Goedecke, M.C., Soldati, D., 2006. New insights into myosin evolution and classification. Proc. Natl. Acad. Sci. U. S. A. 103 (10), 3681–3686, http://dx.doi.org/10.1073/pnas.0506307103.

Frénal, K., Foth, B.J., Soldati, D., 2008. Myosins: A Superfamily of Molecular Motors Myosin Class XIV and Other Myosins in Protists. Proteins and Cell Regulation. Springer, Dordrecht, Netherlands, pp. 421–440.

Ghazali, M., Philippe, M., Deguercy, A., Gounon, P., Gallo, J.M., Schrével, J., 1989. Actin and spectrin-like (Mr = 260–240 000) proteins in gregarines. Biol. Cell 67 (2), 173–184, http://dx.doi.org/10.1111/j.1768-322X.1989.tb00860.x.

Ghazali, M., Schrével, J., 1993. Myosin-like protein (Mr 175,000) in Gregarina blaberae. J. Eukaryot. Microbiol. 40, 345–354, http://dx.doi.org/10.1111/j.1550-7408.1993.tb04927.x.

Guha-Niyogi, A., Sullivan, D.R., Turco, S.J., 2001. Glycoconjugate structures of parasitic protozoa. Glycobiology 11 (4), 45–59.

Heintzelman, M.B., 2004. Actin and myosin in Gregarina polymorpha. Cell Motil. Cytoskeleton 58, 83–95, http://dx.doi.org/10.1002/cm.10178.

Heintzelman, M.B., 2015. Gliding motility in apicomplexan parasites. Semin. Cell Dev. Biol. 46, 135–142, http://dx.doi.org/10.1016/j.semcdb.2015.09.020.

Hildebrand, H.F., Vinckier, D., 1975. Nouvelles observations sur la Grégarine Didymophyes gigantea Stein. J. Protozool. 22, 200–213.

Kappe, S.H., Buscaglia, C.A., Bergman, L.W., Coppens, I., Nussenzweig, V., 2004. Apicomplexan gliding motility and host cell invasion: overhauling the motor model. Trends Parasitol. 20 (1), 13–16, http://dx.doi.org/10.1016/j.pt.2003.10.011.

Keeley, A., Soldati, D., 2004. The glideosome: a molecular machine powering motility and host–cell invasion by apicomplexa. Trends Cell Biol. 14, 528–532, http://dx.doi.org/10.1016/j.tcb.2004.08.002.

King, C.A., 1981. Cell surface interaction of the protozoan gregarina with concanavalin A beads—implications for models of gregarine gliding. Cell Biol. Int. Rep. 5 (3), 297–305.

King, C.A., 1988. Cell motility of sporozoan protozoa. Parasitol. Today 4 (11), 315–319, http://dx.doi.org/10.1016/0169-4758(88)90113-5.

Lacombe, D., Jakowska, S., Silva, E., 2002. Gregarine Cephaloidophora communis Mawrodiadi, 1908 in the barnacle Euraphia rhyzophorae, Oliveira, 1940 from Brazil. Mem. Inst. Oswaldo Cruz 97 (7), 1057–1061.

Landers, S.C., Leander, B.S., 2005. Comparative surface morphology of marine coelomic gregarines (Apicomplexa, Urosporidae): Pterospora floridiensis and Pterospora schizosoma. J. Eukaryot. Microbiol. 52 (1), 23–30, http://dx.doi.org/10.1111/j.1550-7408.2005.3277rrr.x.

Leander, B.S., 2008. Marine gregarines: evolutionary prelude to the apicomplexan radiation? Trends Parasitol. 24 (2), 60–67, http://dx.doi.org/10.1016/j.pt.2007.11.005.

Leander, B.S., Lloyd, S.A., Marshall, W., Landers, S.C., 2006. Phylogeny of marine gregarines (Apicomplexa) –

Pterospora, *Lithocystis* and *Lankesteria* – and the origin(s) of coelomic parasitism. Protist 157 (1), 45–60, http://dx.doi.org/10.1016/j.protis.2005.10.002.

Lucarotti, C.J., 2000. Cytology of *Leidyana canadensis* (Apicomplexa: Eugregarinida) in *Lambdina fiscellaria fiscellaria* larvae (Lepidoptera: Geometridae). J. Invertebr. Pathol. 75, 117–125, http://dx.doi.org/10.1006/jipa.1999.4911.

Mackenzie, C., Walker, M.H., 1983. Substrate contact mucus and eugregarine gliding. J. Protozool. 30, 3–8.

MacMillan, W.G., 1973. Conformational changes in the cortical region during peristaltic movements of a gregarine trophozoite. J. Protozool. 20, 267–274.

Matuschewski, K., Schüler, H., 2007. Actin/myosin-based gliding motility in apicomplexan parasites. Molecular Mechanisms of Parasite Invasion, vol. 47. Subcell. Biochem., pp. 110–120, http://dx.doi.org/10.1007/978-0-387-78267-6_9.

Morrissette, N.S., Sibley, D.L., 2002. Cytoskeleton of apicomplexan parasites. Microbiol. Mol. Biol. Rev. 66 (1), 21–38, http://dx.doi.org/10.1128/MMBR.66.1.21.

Opitz, C., Soldati, D., 2002. 'The glideosome': a dynamic complex powering gliding motion and host cell invasion by *Toxoplasma gondii*. Mol. Microbiol. 45 (3), 597–604, http://dx.doi.org/10.1046/j.1365-2958.2002.03056.x.

Philippe, M., Fournet, B., Caigneaux, E., Schrével, J., 1979. Les polysaccharides associés à la surface cellulaire d'une Grégarine (protozoaire parasite). II. Caractérisation cytochimique et analyses biochimiques des ghosts. Biol. Cell 35, 165–174.

Poisson, R., 1924. Sur quelques grégarines parasites de crustacés, observées à Luc–sur–mer (Calvados). Bull. Soc. Zool. France 49, 238–248.

Reger, J.F., 1967. The fine structure of the gregarine *Pyxinoides balani* parasitic in the barnacle *Balanus tintinnabulum*. J. Protozool. 14, 488–497.

Rueckert, S., Simdyanov, T.G., Aleoshin, V.V., Leander, B.S., 2011. Identification of a divergent environmental DNA sequence clade using the phylogeny of gregarine parasites (Apicomplexa) from crustacean hosts. PLoS One 6 (3), e18163, http://dx.doi.org/10.1371/journal.pone.0018163.

Schrével, J., Buissonnets, S., Metais, M., 1974. Action de l'urée sur la motilité et les microtubules sous pelliculaires du protozoaire *Selenidium hollandei*. C. R. Acad. Sci. Paris 278, 2201–2204.

Schrével, J., Caigneaux, E., Gros, D., Philippe, M., 1983. The three cortical membranes of the gregarines. I. Ultrastructural organization of *Gregarina blaberae*. J. Cell Sci. 61, 151–174.

Schrével, J., Desportes, I., 2015. Gregarines. In: Mehlhorn, H. (Ed.), Encyclopedia of Parasitology. Springer-Verlag, Berlin, Heidelberg, http://dx.doi.org/10.1007/978-3-642-27769-6, 47 pp.

Schrével, J., Philippe, M., 1993. The Gregarines. In: Kreier, J.P., Baker, J.R. (Eds.), Parasitic Protozoa, vol. 4, 2nd edition. Academic Press, pp. 133–245.

Simdyanov, T.G., Diakin, A., Aleoshin, V.V., 2015. Ultrastructure and 28S rDNA phylogeny of two gregarines:

Cephaloidophora cf. *communis* and *Heliospora* cf. *longissima* with remarks on gregarine morphology and phylogenetic analysis. Acta Protozool. 54 (3), 241–262, http://dx.doi.org/10.4467/16890027AP.15.020.3217.

Simdyanov, T.G., Kuvardina, O.N., 2007. Fine structure and putative feeding mechanism of the archigregarine *Selenidium orientale* (Apicomplexa: Gregarinomorpha). Eur. J. Protistol. 43 (1), 17–25, http://dx.doi.org/10.1016/j.ejop.2006.09.003.

Stebbings, H., Boe, G.S., Garlick, P.R., 1974. Microtubules and movement in the archigregarine, *Selenidium fallax*. Cell Tissue Res. 345, 331–345.

Tronchin, G., Schrével, J., 1977. Chronologie des modifications ultrastructurales au cours de la croissance de *Gregarina blaberae*. J. Protozool. 24, 67–82.

Valigurová, A., 2012. Sophisticated adaptations of *Gregarina cuneata* (Apicomplexa) feeding stages for epicellular parasitism. PLoS One 7 (8), e42606, http://dx.doi.org/10.1371/journal.pone.0042606.

Valigurová, A., Koudela, B., 2005. Fine structure of trophozoites of the gregarine *Leidyana ephestiae* (Apicomplexa: Eugregarinida) parasitic in *Ephestia kuehniella* larvae (Lepidoptera). Eur. J. Protistol. 41 (3), 209–218, http://dx.doi.org/10.1016/j.ejop.2005.05.005.

Valigurová, A., Koudela, B., 2008. Morphological analysis of the cellular interactions between the eugregarine *Gregarina garnhami* (Apicomplexa) and the epithelium of its host, the desert locust *Schistocerca gregaria*. Eur. J. Protistol. 44 (3), 197–207, http://dx.doi.org/10.1016/j.ejop.2007.11.006.

Valigurová, A., Michalková, V., Koudela, B., 2009. Eugregarine trophozoite detachment from the host epithelium via epimerite retraction: Fiction or fact? Int. J. Parasitol. 39 (11), 1235–1242, http://dx.doi.org/10.1016/j.ijpara.2009.04.009.

Valigurová, A., Vaškovicová, N., Musilová, N., Schrével, J., 2013. The enigma of eugregarine epicytic folds: where gliding motility originates? Front. Zool. 10 (1), 57, http://dx.doi.org/10.1186/1742-9994-10-57.

Vávra, J., Small, B.E., 1969. Scanning electron microscopy of gregarines (Protozoa, Sporozoa) and its contribution to the theory of gregarine movement. J. Protozool. 42 (5), 1041–1057.

Vivier, E., 1968. L'organisation ultrastructurale corticale de la gregarine *Lecudina pellucida*; ses rapports avec l'alimentation et la locomotion. J. Protozool. 15, 230–246.

Walker, M.H., Mackenzie, C., Bainbridge, S.P., Orme, C., 1979. A study of the structure and gliding movement of *Gregarina garnhami*. J. Protozool. 26 (4), 566–574.

Walker, M.H., Lane, N.J., Lee, W.M., 1984. Freeze-fracture studies on the pellicle of the eugregarine, *Gregarina garnhami* (Eugregarinida, Protozoa). J. Ultrastruct. Res. 88, 66–76.

Warner, F.D., 1968. The fine structure of *Rhynchocystis pilosa* (Sporozoa, Eugregarinidae). J. Protozool. 15, 59–73.

7.11

Valigurová A., Vaškovicová N., Diakin A., Paskerova G.G., Simdyanov
T.G., Kováčiková M.

2017

Motility in blastogregarines (Apicomplexa):
Native and drug-induced organisation of *Siedleckia nematoides*
cytoskeletal elements

Motility in blastogregarines (Apicomplexa): Native and drug-induced organisation of *Siedleckia nematoides* cytoskeletal elements

Andrea Valigurová[1]*, Naděžda Vaškovicová[2], Andrei Diakin[1], Gita G. Paskerova[3], Timur G. Simdyanov[4], Magdaléna Kováčiková[1]

1 Department of Botany and Zoology, Faculty of Science, Masaryk University, Kotlářská 2, Brno, Czech Republic, 2 Institute of Scientific Instruments of the CAS, v. v. i., Královopolská 147, Brno, Czech Republic, 3 Department of Invertebrate Zoology, Faculty of Biology, Saint-Petersburg State University, Universitetskaya emb. 7/9, St. Petersburg, Russian Federation, 4 Department of Invertebrate Zoology, Faculty of Biology, Lomonosov Moscow State University, Leninskiye Gory 1–12, Moscow, Russian Federation

* andreav@sci.muni.cz

Abstract

Recent studies on motility of Apicomplexa concur with the so-called glideosome concept applied for apicomplexan zoites, describing a unique mechanism of substrate-dependent gliding motility facilitated by a conserved form of actomyosin motor and subpellicular microtubules. In contrast, the gregarines and blastogregarines exhibit different modes and mechanisms of motility, correlating with diverse modifications of their cortex. This study focuses on the motility and cytoskeleton of the blastogregarine *Siedleckia nematoides* Caullery et Mesnil, 1898 parasitising the polychaete *Scoloplos* cf. *armiger* (Müller, 1776). The blastogregarine moves independently on a solid substrate without any signs of gliding motility; the motility in a liquid environment (in both the attached and detached forms) rather resembles a sequence of pendular, twisting, undulation, and sometimes spasmodic movements. Despite the presence of key glideosome components such as pellicle consisting of the plasma membrane and the inner membrane complex, actin, myosin, subpellicular microtubules, micronemes and glycocalyx layer, the motility mechanism of *S. nematoides* differs from the glideosome machinery. Nevertheless, experimental assays using cytoskeletal probes proved that the polymerised forms of actin and tubulin play an essential role in the *S. nematoides* movement. Similar to *Selenidium* archigregarines, the subpellicular microtubules organised in several layers seem to be the leading motor structures in blastogregarine motility. The majority of the detected actin was stabilised in a polymerised form and appeared to be located beneath the inner membrane complex. The experimental data suggest the subpellicular microtubules to be associated with filamentous structures (= cross-linking protein complexes), presumably of actin nature.

Competing interests: The authors have declared that no competing interests exist.

Abbreviations: CLSM, confocal laser scanning microscopy; EF, exoplasmic fracture face; FE, freeze-etching; FITC, fluorescein isothiocyanate; IFA, indirect immunofluorescent assay; IMC, inner membrane complex; IMP(s), intramembranous particle(s); JAS, jasplakinolide; Kp, partition coefficient; LM, light microscopy; LP, large pore; MP, medium pore; PF, protoplasmic fracture face; PFA, 4% paraformaldehyde in 0.1 M phosphate buffered saline; RR, ruthenium red; SD, standard deviation; SE, standard error; SP, small pore; SEM, scanning electron microscopy; TEM, transmission electron microscopy; TRITC, tetramethylrhodamineisothiocyanate.

Introduction

Apicomplexans (Apicomplexa Levine 1980, emend. Adl et al. 2012 [1]) belong to the most monitored group of unicellular parasites. As many of them cause major human and animal diseases, recent research has focused on the motility of apicomplexan invasive stages (zoites) representing a potential target for chemotherapeutic intervention. Apicomplexan zoites are characterised by a typical apical complex of organelles and a complicated cell cortex consisting of a continuous plasma membrane underlined by cortical alveoli (inner membrane complex = IMC). The IMC can be interrupted by micropores and connected with numerous cytoskeletal elements such as actomyosin complex, microtubules and a network of intermediate filamentous proteins [2, 3].

Although apicomplexans share a number of cytoskeletal structures with other eukaryotic organisms, a number of remarkable differences makes them unique. First of all, apicomplexan subpellicular microtubules are unusually stable and withstand high pressure, cold, and detergents that are often used for their isolation, while actin filaments (F-actin) are extraordinarily transient [2] and actin is present mostly in its globular form [4]. Except for the study demonstrating the presence of long actin filaments in *Theileria* [5], apicomplexan microfilaments can be usually observed only after treatment with F-actin stabilising drugs such as jasplakinolide [2]. So far published studies, focusing mostly on *Toxoplasma gondii* and *Plasmodium* spp., concur with the so-called glideosome concept applied for motile zoites, describing their unique mechanism of substrate-dependent gliding motility facilitated by a conserved form of actomyosin motor [6–10]. This motor is expected to be localised between the parasite plasma membrane and IMC, and the gliding is based on the locomotion of myosin along actin filaments together with the translocation of apically released adhesins to the parasite's posterior end [11]. The above-mentioned differences in the apicomplexan cytoskeleton correspond to this machinery, which is based on and limited by the formation of transient actin filaments and their fixation to the IMC, and requires a stabile subpellicular network of microtubules.

In contrast to vertebrate pathogens, the motility mechanism in early emerging groups of Apicomplexa, such as lower coccidia and gregarines parasitising invertebrates and urochordates, still remains unclear. The basal apicomplexans studied to date are covered by a typical three-layered pellicle and use several mechanisms of motility, correlating with diverse modifications of their cortex. Among these organisms, only a few model archigregarines and eugregarines were investigated for specific aspects in their motility behaviour and related structures [3, 4, 12–43]. These studies showed that gregarine locomotion differs from the substrate-dependent gliding observed in apicomplexan zoites.

The present study focuses on the blastogregarine, *Siedleckia nematoides* Caullery et Mesnil, 1898 (Apicomplexa: Siedleckiidae), parasitising the polychaete *Scoloplos* cf. *armiger* from the family Orbiniidae. Blastogregarines are characterised by a permanent multinuclearity and complicated life cycle: gametogenesis goes through a budding of mononuclear or multinuclear spherical bodies at the posterior end of parasites and their further transformation into macrogametes and microgametes correspondingly [44]. Here, using a combined microscopic approach, for the first time we present an experimental study on the motility of the apicomplexan restricted to the marine invertebrate host.

Materials and methods

Material collection

The polychaetes *Scoloplos* cf. *armiger* (Müller, 1776), parasitised with *Siedleckia nematoides*, were collected at the sand-silt littoral zone at the White Sea Biological Station of M. V.

Lomonosov Moscow State University (66˚33.190′ N, 33˚06.550′ E) and the Marine Biological Station of Saint-Petersburg State University (66˚18.770′ N, 33˚37.715' E), both situated in the Kandalaksha Bay of the White Sea. The polychaetes were collected within the framework of regular scientific work at White Sea Biological Station of M. V. Lomonosov Moscow State University (WSBS), which is situated in the buffer zone of Kandalaksha State nature reserve. According agreement between WSBS and the reserve, the biological station can collect animals for the scientific work on its own territory and other sites situated in the buffer zone of the reserve. The field sampling locality at the Marine Biological Station of Saint-Petersburg State University is not part of any national park or private territory, so no special permission for their collection was required. The polychaetes *S. armiger* are not an endangered or protected species in those regions. Animal capturing, handling and dissecting was designed to avoid distress and unnecessary suffering. Parasitological dissection of polychaetes and manipulation with parasites were performed using MBS-1 stereomicroscope (LOMO, Russia).

Experimental motility assays and light microscopy

Parasites were treated with commercial membrane-permeable probes influencing the polymerisation of actin—jasplakinolide (JAS, Invitrogen, Czech Republic) and cytochalasin D (Invitrogen, Czech Republic), and microtubule-disrupting/antimitotic agents such as oryzalin (Sigma-Aldrich, Czech Republic) and colchicine (Sigma-Aldrich, Czech Republic). As a concentration of these probes lower than 5 μM has no obvious effect on gregarines [3], final concentrations of 10 and 30 μM for JAS, cytochalasin D and oryzalin, and 10 and 100 mM for colchicine in filtered (0.22 μm Millipore) seawater were applied to obtain reliable results on vital parasites. Cytochalasin D, JAS and oryzalin were reconstituted in dimethyl sulfoxide (DMSO) to prepare a 1 mM stock solution and diluted in filtered seawater to prepare final working concentrations, while colchicine was reconstituted directly in filtered seawater. Experimental assays that were processed for further microscopic analyses were performed in embryo dishes with a 30 mm diameter cavity. For continuous light microscopic observations of changes occurring during each assay, small pieces of host intestine with attached blastogregarines were put on single cavity microscope glass slides with a drop of drug diluted in filtered seawater. Controls were performed in filtered natural seawater and corresponding concentrations of DMSO in filtered seawater. Embryo dishes with parasites were kept in refrigerator with a temperature set point of 10˚C. Behavioural and morphological changes of parasites induced by drugs' application were monitored using a light microscope Leica DM 2000 connected to a DFC 420 digital camera. To assess the parasites' beat frequency, the motility of *S. nematoides* trophozoites and gamonts attached to the host epithelium was monitored at set time intervals. The number of beats performed over period of 30 seconds was counted by taking a sample of six (at least) randomly selected individuals. Average time for each beat was calculated for the anterior-most region of the cell, where waves develop.

Three repetitions of each experiment were performed in the course of three years. Each year, for controls and every drug treatment, twelve fragments of intestines, with not less than twenty parasites attached at the experiment beginning, were investigated. During each experiment a fragment with attached parasites was periodically selected for video recording of the parasite motility under the light microscope. At the end of each experiment, these fragments were equally divided into three portions and fixed for microscopic analyses (scanning and transmission electron microscopy, confocal laser scanning microscopy).

Electron microscopy

Specimens were fixed in an ice bath in freshly prepared 2.5–5% (v/v) glutaraldehyde either in cacodylate buffer (0.05–0.15 M; pH 7.4) or in filtered seawater. For transmission electron microscopy (TEM), the specimens were then washed 3×20 min in the same buffer as used for fixation, and post-fixed in 1–2% osmium tetroxide (OsO_4) in the same buffer for 1–3 h. Alternatively, specimens were fixed with 3% glutaraldehyde-ruthenium red [0.15% (w/v) stock water solution] in 0.2 M cacodylate buffer (pH 7.4) and post-fixed with 1% OsO_4-ruthenium red in the same buffer [45]. The following procedure was based on previously published protocols [46]. Observations were made using a JEM-1010 (JEOL). For scanning electron microscopy (SEM), the specimens were washed 3×15 min in the same buffer as used for fixation, processed according to Valigurová et al. [46, 47] and examined using a JSM-7401F –FE SEM (JEOL), GEMINI Zeiss Supra 40VP and REM LEO 420 (Zeiss).

Freeze-etching

Parasitised pieces of the intestine of freshly collected polychaetes, fixed at 4˚C in freshly prepared 5% (v/v) glutaraldehyde in 0.15 M cacodylate buffer (pH 7.4) or 2.5% (v/v) glutaraldehyde in 0.1 M phosphate buffered saline, were washed in the same buffer and processed according to Valigurová et al. [3] using the freeze-etching system device BAF 060 (BAL-TEC). The replicas were cleaned with 5% sodium hypochlorite, 70% sulphuric acid and 50% chromo-sulphuric acid, washed in distilled water and mounted on copper grids for examinations using a transmission electron microscope Morgagni 268 D (FEI). Evaluation of intramembranous particles (IMP) per a unit area (1 μm^2) and the size of IMP were performed in ImageJ software. The nomenclature follows that proposed in Branton et al. [48] and used in Schrével et al. [17].

Confocal laser scanning microscopy

Fragments of parasitised intestines were fixed for 45 min at room temperature in freshly prepared 4% paraformaldehyde in 0.1 M phosphate buffered saline (PFA) or in ice-cold methanol. Samples were carefully washed before further processing and permeabilised for 15–40 min in 0.3–0.5% Triton X-100 (Sigma-Aldrich, Czech Republic). Protocols used for the direct staining of filamentous actin with phalloidin–tetramethylrhodamine B isothiocyanate (phalloidin-TRITC; Sigma-Aldrich, Czech Republic) and indirect immunofluorescent antibody (IFA) staining using the mouse monoclonal IgG anti-actin antibody that was raised against *Dictyostelium* actin and recognises the actin in *Toxoplasma* and *Plasmodium* (provided by Prof. Dominique Soldati-Favre), mouse monoclonal anti-α-tubulin antibody (Cat. No. T5168, Sigma-Aldrich, Czech Republic), and rabbit anti-myosin antibody (Cat. No. M7648, Sigma-Aldrich, Czech Republic) follow Valigurová et al. [46, 47]. All preparations were counterstained for localisation of the cell nuclei with Hoechst 33342 (Molecular Probes, Czech Republic) and analysed using an Olympus IX80 microscope equipped with a laser-scanning FluoView 500 confocal unit (FluoView 4.3 software). Fluorescence was visualised using the TRITC (phalloidin, anti-myosin), FITC (anti-actin, anti-α-tubulin) and/or UV (Hoechst) filter sets. All specimen from one experimental assay (= particular staining and controls) were processed using the same protocol, and micrographs from confocal laser scanning microscopy (CLSM) were obtained under identical image capture conditions (filters, the laser intensity). Some micrographs were processed using the Fiji software (an image processing package based on ImageJ developed at the National Institutes of Health).

Results

Observations of the motility of *Siedleckia nematoides* trophozoites and gamonts

Parasites developed being attached between microvilli of the host intestinal epithelium. The earliest observed stages of *S. nematoides* were the lancet-shaped early trophozoites (Fig 1A and 1B) exhibiting only barely visible pendular movement. The pendular movement of more advanced stage, young trophozoites (Fig 1C), was more evident. The elongated and flattened maturing trophozoites and gamonts (Fig 1D–1G) of *S. nematoides* exhibited very active types of movement. In addition to the pendular and twisting motility of attached parasites, their movement was typically wavy, with waves developing in the proximal region of the cell (just behind the attachment area) and proceeding to its distal end, while the last third of the cell appeared more rigid with limited mobility (S1 Video). Detached individuals either showed the same kind of movement, or simply bent from side to side with movement initiated by the proximal region (Fig 1H and 1I; S2 Video). A spasmodic movement was often observed in physiologically stressed parasites (during experiments or prolonged observations under the light microscope).

Ultrastructural analysis of the cortex organisation

Parasites attached to the enterocyte via the mucron; the cytoplasm in their anterior region contained numerous rhoptries and micronemes (Fig 2A–2C). The surface of all observed *S. nematoides* individuals, comprising developmental stages from early trophozoites up to gamonts, appeared smooth, lacking any grooves or folds (Figs 1B–1F, 1I, 2C and 2D).

Ruthenium red staining revealed the presence of distinct glycocalyx layer covering the entire parasite. This cell coat was evidently thicker in the parasite apical region (Fig 2A and 2C) than in its middle to distal part (Fig 2G) (apical part 85 ± 4 nm vs. distal part 26 ± 2 nm). The parasite was covered by a typical apicomplexan pellicle consisting of a plasma membrane and IMC (Fig 2E and 2F). The IMC consisted of external and internal cortical cytomembranes, from which the former was usually poorly preserved. Only a few ultrathin sections showed well preserved and closely apposed membranes of IMC (Fig 2E). More often, these two cortical cytomembranes were separated from each other, thereby forming a translucent and optically empty space between them (Fig 2F). Freeze-etching revealed that the cytomembranes were unusually undulated, while the plasma membrane was almost smooth (Fig 2H and 2I).

Analysis of the supramolecular organisation of the plasma membrane showed that intra-membranous particles (IMP) are evenly distributed and arranged in a regular pattern (Fig 2H). The size of IMPs in *S. nematoides* pellicle membranes varied in the range from 0.5 to 21.3 nm, dependent on the membrane and its fractured face (Table 1). To compare our statistical data with known data on other apicomplexans [17, 49, 50], we additionally analysed density of IMP ranging from 6 to 14 nm (Table 2). The partition coefficient (Kp) was used as a tabulated factor for specimen comparison.

Numerous pores, mostly organised in four lateral rows (two per each flattened side) running parallel to the longitudinal cell axis, were observed (Fig 1D–1E). The distance between two lateral rows was 2.77 ± 0.05 μm (= width of the cell per flattened side) and the distance between individual pores in a row was in the range from 0.5 to 1.9 μm (0.94 ± 0.06 μm). While the rows of pores were conspicuous in some specimens (Figs 1D and 3A), in others they were less distinct (Fig 1E), or even not detected (Fig 1F and 1I). Young trophozoites did not exhibit any pores at their surface under SEM (Fig 1B and 1C), but because of their sporadic presence in our samples, it remains unclear whether the presence of pores is exclusively restricted to the
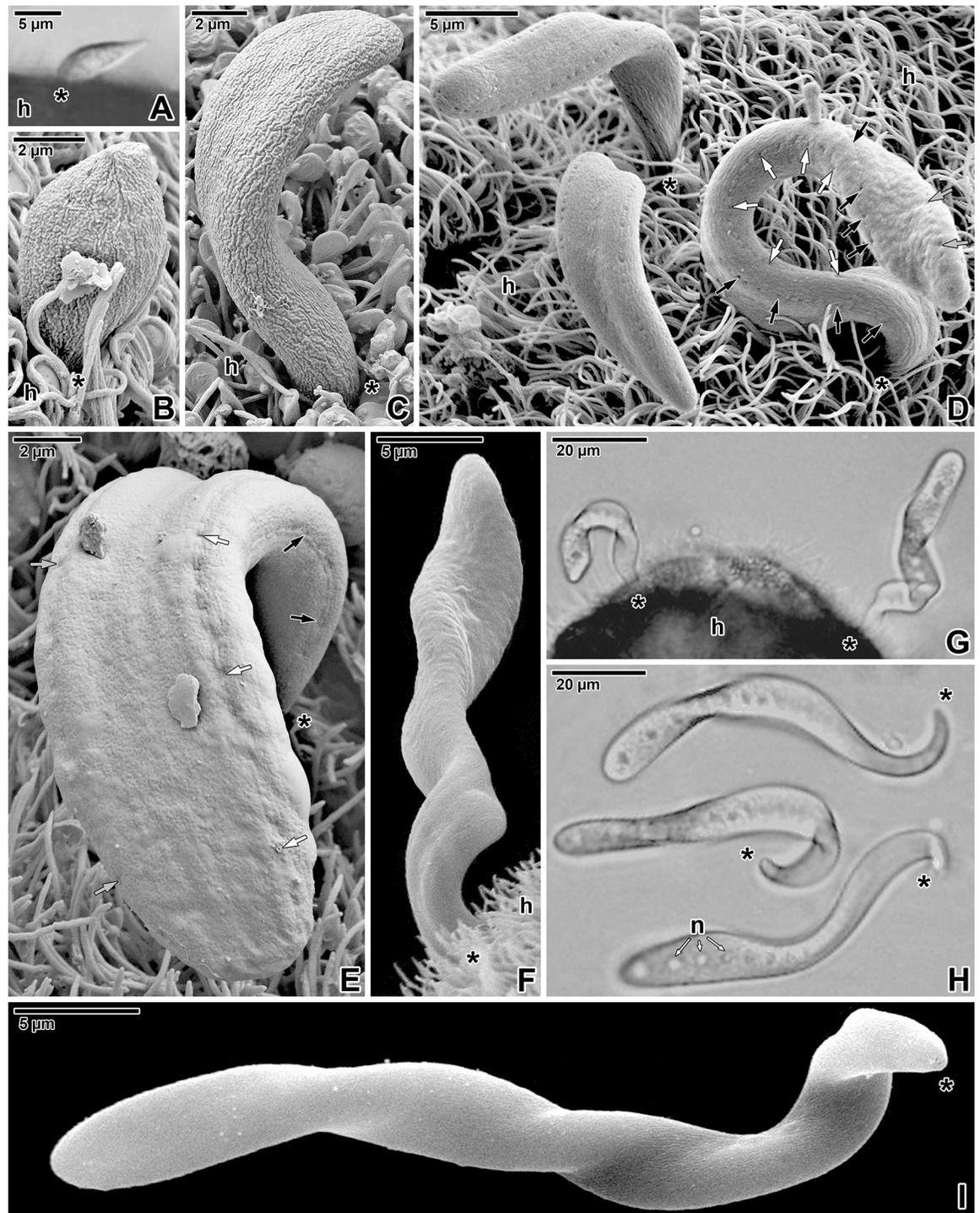
Fig 1. General view of *Siedleckia nematoides* trophozoites and gamonts. A-B. An early trophozoite. **C.** A young trophozoite. **D.** Composite micrograph of trophozoites attached to the host intestinal epithelium between microvilli and cilia. Note the pores organised in longitudinal rows, two per each flattened side. **E.** Attached trophozoite with a smooth surface showing the pores organised in rows. **F.** Attached gamont lacking the pores. **G.** Two parasites attached to the brush border of the host intestinal epithelium. **H.** Composite micrograph showing the sequence of movement of a single detached parasite. **I.** Detached parasite. A, G-H: LM, bright field; B-F, I: SEM. *black asterisk*–parasite apical end, *h*–host tissue, *n*–nucleus, *white/ grey/black arrows*–row of pores.
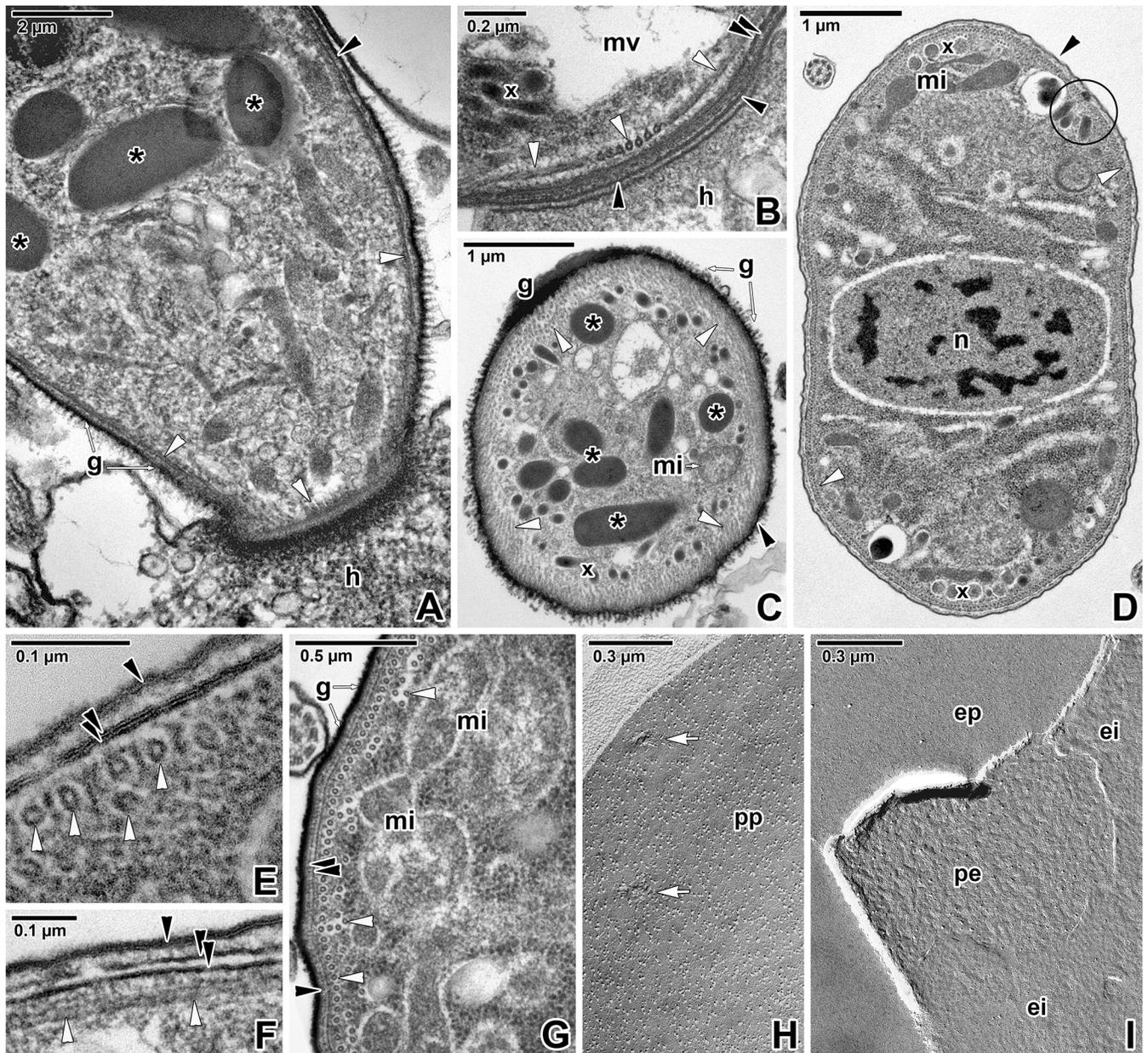
Fig 2. Cortex organisation in *Siedleckia nematoides*. A. Apical end of a parasite attached to the host enterocyte. Note the well-developed layer of glycocalyx. **B.** A detail of parasite apical end focusing on organisation of subpellicular microtubules. **C.** General view of parasite cross-sectioned in the anterior region. **D.** General view of a parasite cross-sectioned in the middle region. **E.** The cross-sectioned pellicle with well-preserved and adjacent cortical cytomembranes. **F.** Longitudinally-sectioned pellicle with obviously separated cortical cytomembranes. **G.** Cortex of parasite cross-sectioned in the middle region. **H.** Protoplasmic fracture face of the plasma membrane with pores. **I.** Fractured plasma membrane and cortical cytomembranes. A, C, G: RR TEM; B, D-F: TEM; H-I: FE TEM. *black arrowhead*–plasma membrane, *black asterisk*–rhoptry, *black circle*–pore, *double/paired black arrowhead*–IMC, *ei*–EF of the internal cytomembrane, *ep*–EF of the plasma membrane, *g*–glycocalyx, *h*–host tissue, *mi*–mitochondria, *mv*–mucronal vacuole, *n*–nucleus, *pe*–PF of the external cytomembrane, *pp*–PF of the plasma membrane, *white arrowhead*–subpellicular microtubule, *white arrows*–pores, *x*—micronemes.

older stages. At least three types of different sized pores were documented: small (16.6 ± 0.9 nm), medium (48.7 ± 3.2 nm), and large (123.0 ± 4.6 nm). The small and medium pores occurred only in the fracture plane of both the cortical cytomembranes, but were never

Table 1. The sizes and density of IMP in individual fracture faces of pellicle membranes in *Siedleckia nematoides*.

Membrane	Face	Size of IMP (nm)						Density of IMP (particles/μm^2)
		Mean	Median	SD	SE	Min	Max	Mean ± SE
Plasma membrane	PF	7.3	7.0	2.9	0.1	0.5	21.3	3109 ± 90
	EF	4.9	4.3	2.7	0.1	0.5	19.1	314 ± 56
External cytomembrane	PF	6.8	6.6	3.1	0.1	0.5	19.1	2877 ± 213
	EF	5.7	5.2	2.4	0.1	1.0	14.1	5758 ± 357
Internal cytomembrane	PF	6.1	6.1	2.4	0.1	0.5	13.3	4352 ± 279
	EF	4.9	4.6	1.9	0.1	0.5	12.1	3411 ± 260

A total number of all sizes of IMP in membrane fracture was used for density calculation. SD–standard deviation; SE–standard error.

https://doi.org/10.1371/journal.pone.0179709.t001

detected in the plasma membrane. All three types of pores were present in each lateral row (Fig 3C–3H). Their arrangement within rows was not regular, but the large pores usually alternated with several medium- and small-sized pores (Fig 3D–3H). In the anterior parasite region, the pores within a lateral row were organised in a single line (Fig 3F-top), while posteriorly, the small- and medium-sized pores started to form double lines (Fig 3E, 3F-bottom and 3G and 3H). The large pores were usually connected to a vesicle, containing a coiled lamellar structure or dense material and with a duct opening towards the IMC (Fig 3B and 3C). These vesicles were seen below the subpellicular microtubules, while the duct was situated in the plane of microtubule outermost layer (Fig 3B). The simple dense circle, visible in superficial ultrathin sections showing the outermost layer of subpellicular microtubules, seems to correspond to the vesicle duct, while the rosette-like organisation of dense particles could be a protein bridge connecting the vesicle duct with the pore at the IMC (Fig 3D). In replicas revealing the fractured IMC, the large pores appeared widely opened (Fig 3E). Interestingly, even in areas of lateral rows, the signs of pores were only rarely observed in fracture faces of the plasma membrane (Figs 2H and 3E). Besides the pores organised in four lateral rows, additional rows and randomly distributed pores were observed (Fig 3E–3H).

The subpellicular microtubules arose from the apical pole (Fig 2A and 2B) and run to the parasite posterior end. Their arrangement appeared to be slightly helically twisted along the longitudinal cell axis (Fig 4A). Cross-sections showed the organisation of microtubules in

Table 2. Density of IMP (particles/μm^2) in different apicomplexans.

Species	Plasma membrane			External cytomembrane			Internal cytomembrane		
	EF	PF	Kp	PF	EF	Kp	EF	PF	Kp
Gregarina blaberae[1]	977 ± 235	1469 ± 233	1.5	285 ± 39	133 ± 34	2.1	158 ± 72	297 ± 33	1.9
Gregarina cuneata	2770 ± 96	2244 ± 283	0.8	1420 ± 190	1260 ± 211	1.1	1502 ± 273	1993 ± 253	1.3
Gregarina polymorpha	2473 ± 147	1446 ± 158	0.6	602 ± 265	863 ± 202	0.7	814 ± 246	1276 ± 200	1.6
Gregarina steini	1783 ± 233	2265 ± 154	1.3	2588 ± 189	3820 ± 211	0.7	1886 ± 274	2339 ± 132	1.2
Eimeria nieschulzi[2]	218 ± 21	648 ± 73	3.0	2360 ± 133	29 ± 7	81.4	146 ± 31	1780 ± 97	12.2
Plasmodium knowlesi[3]	185 ± 25	2198 ± 528	11.9	1751 ± 228	38 ± 15	46.1	48 ± 28	574 ± 200	12.0
Siedleckia nematoides	183 ± 8	2926 ± 135	16.0	2745 ± 220	458 ± 15	6.0	797 ± 60	3342 ± 128	4.2

The size of IMP is in range 6–14 nm. Kp—partition coefficient defined as the ratio of number of particles per μm^2 in the PF face/number of particles per μm^2 in the EF face.
[1]Values taken from [17]
[2]Values taken from [49]
[3]Values taken from [50].

https://doi.org/10.1371/journal.pone.0179709.t002
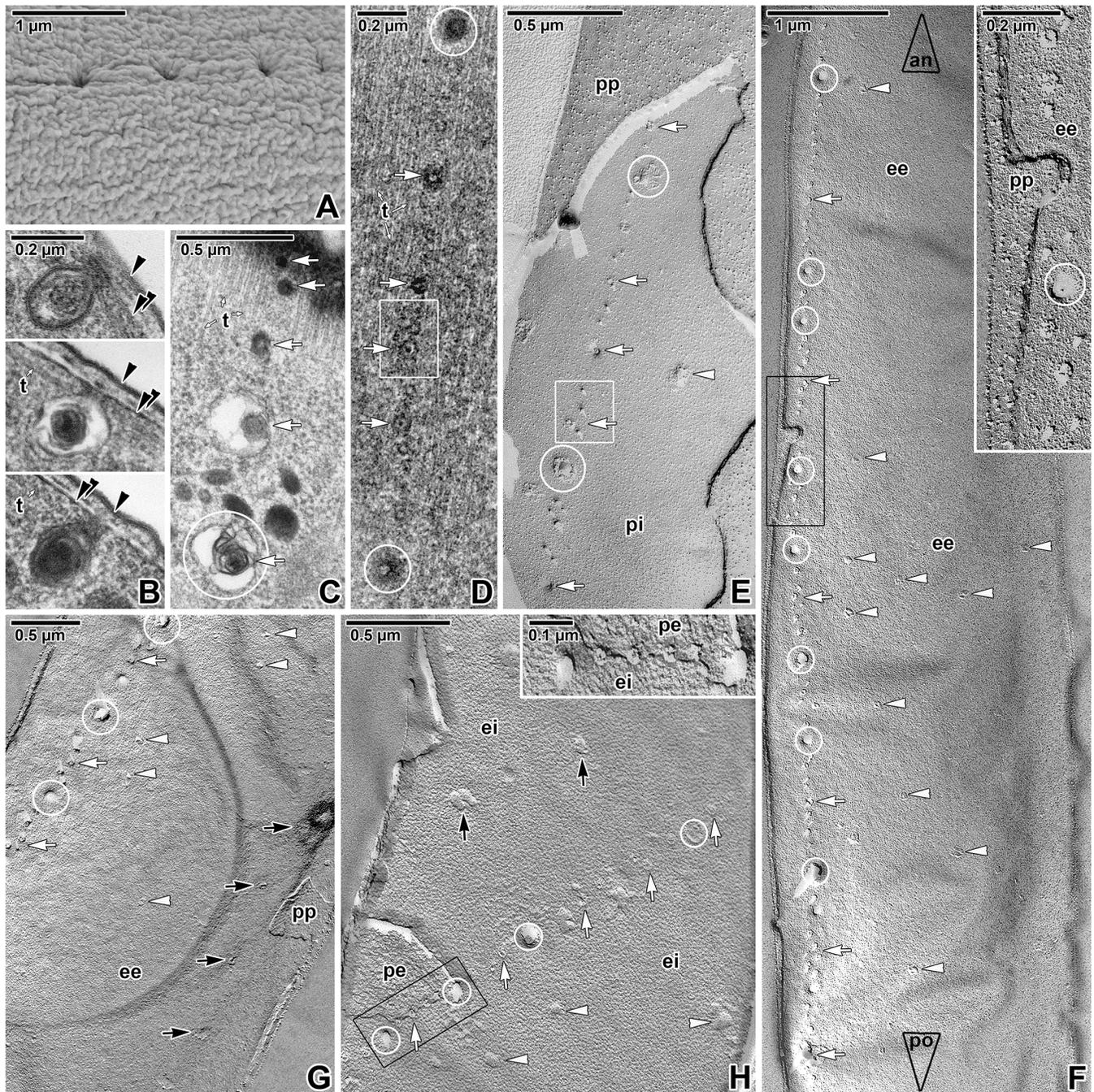
Fig 3. Distribution of the pores on the *Siedleckia nematoides* surface. A. Detail of pellicle surface with a well visible row of pores. **B.** Different longitudinally-sectioned vesicular structures connected to the pellicle and corresponding to the pores observed by SEM. **C.** An almost superficial section of a parasite revealing the pores and vesicles organised in row. **D.** Superficially-sectioned cortex showing the layer of subpellicular microtubules and a row of pores of various size. **E.** Fractured pellicle revealing the row of differently sized pores located on the PF of the internal cytomembrane, but not visible at the plasma membrane. **F.** A general view of the longitudinally fractured pellicle revealing the external cytomembrane with a lateral row of pores and few randomly distributed pores. The large empty arrowheads with labels show the direction towards anterior (an) and posterior (po) parasite ends. The inset shows the fractured pellicle and pores demarcated by black rectangle in more detail. **G.** Fractured pellicle showing pores organised in rows; few pores are distributed randomly. **H.** A fragment of fractured pellicle where several rows of variously sized pores are visible. Inset shows a more detailed view of area demarcated by black rectangle, with alternating small and large pores organised in row. A: SEM; B, D: TEM; C: RR TEM; E-H: FE TEM. *black arrowhead*–plasma membrane, *black arrows*–additional row of pores, *double/paired black arrowhead*–IMC, *ee*–EF of the external cytomembrane, *ei*–EF of the internal cytomembrane, *pe*–PF of the external cytomembrane, *pi*–PF of the internal cytomembrane, *pp*–PF of the plasma

membrane, *t*–subpellicular microtubules, *white arrows*–lateral row of pores, *white arrowheads*–randomly distributed pores, *white circles* indicate some of the large pores, *white rectangle* demarcates the doubled row of pores.

several layers; one of them was continual and located just beneath the IMC, while the other intermittent layers were to be found deeper in the cytoplasm (Figs 2G and 4E–4H). The number of microtubule layers significantly increased towards the parasite anterior region (Fig 2C). In ultrathin sections, the outer diameter of the microtubules was 22.9 ± 0.3 nm and the inner diameter was 9.8 ± 0.5 nm, while in replicas, the outer diameter was 31.8 ± 0.5 nm and inner 14 ± 1 nm. In cross-fractured replicas, the microtubules appeared as rosettes (Fig 4F and 4H), and the diameter of the putative microtubule subunits corresponded to 5.8 ± 0.2 nm. Ultrathin sections showed individual microtubules to be localised within more lucent areas (in contrast to the surrounding cytoplasm), the so-called 'chambers', with a diameter of 35 ± 2 nm (Figs 2E, 2G, 4E and 4G). The distance between the IMC and microtubules forming the outer layer was about 23.5 ± 0.7 nm.

In longitudinal sections of the microtubule layer, tiny filamentous structures were detected between individual microtubules (Fig 4B). These structures, running parallel to the microtubules, seemed to interact periodically with them via short oblique filamentous connections (Fig 4B). More superficial sections revealed these connections as filamentous structures being wound around each microtubule (Fig 4C). Ultrathin cross-sections as well as freeze-etching data revealed a complex of two large and one small particles around each microtubule (Fig 4D–4H and 4J). The small particle (8.9 ± 0.6 nm in ultrathin sections, 8.8 ± 0.5 nm in replicas) was embedded in the IMC and most likely serves as an anchor for an underlying microtubule (Fig 4D–4G and 4J). One of the large particles (19.4 ± 1.2 nm in ultrathin sections, 15±1 nm in replicas) interconnected the small particle and microtubules, and was localised within the electron-lucent microtubule chamber. The second large particle was located diagonally to the first one, below the microtubule (Fig 4D–4H and 4J). All these observations suggest that these electron-dense particles may play role of cross-linking protein complexes that anchor the subpellicular microtubules to the cytoplasmic face of the internal cortical cytomembrane, thereby forming a series of microtubule-membrane bridges along entire length of each microtubule.

Filamentous structures, 3.2 ± 0.2 nm (max = 9.65 nm) thick in ultrathin sections and 5.6 ± 0.2 nm (max = 9.7 nm) thick in replicas, were seen connecting the plasma membrane with the IMC (Fig 4G and 4I). Analysis of the cross-fractured pellicle confirmed the presence of large particles between the plasma membrane and the external cortical cytomembrane (Fig 4L). In oblique fractured specimens, these appeared as short filaments situated in the supra-alveolar space (Fig 4K). In replicas, the glycocalyx was seen as an agglomeration of large particles located on the external surface of the plasma membrane (Fig 4K and 4L).

Parasites' motility and cortex organisation after treatment with cytoskeletal drugs

To monitor the role of individual elements of the putative motility motor in *S. nematoides*, the living parasites were treated with commercial probes influencing the de-/polymerisation of cytoskeletal proteins. To investigate the involvement of subpellicular microtubules in parasite motility, incubation of living parasites with oryzalin or colchicine (toxins causing the disruption of the microtubules) was performed. To verify the essential role of actin microfilaments, drugs with a contradictory effect, i.e. jasplakinolide (stabilises actin filaments and induces actin polymerisation) and cytochalasin D (disrupts actin filaments and inhibits actin polymerisation) were applied to living parasites. All experimental assays were performed on parasites
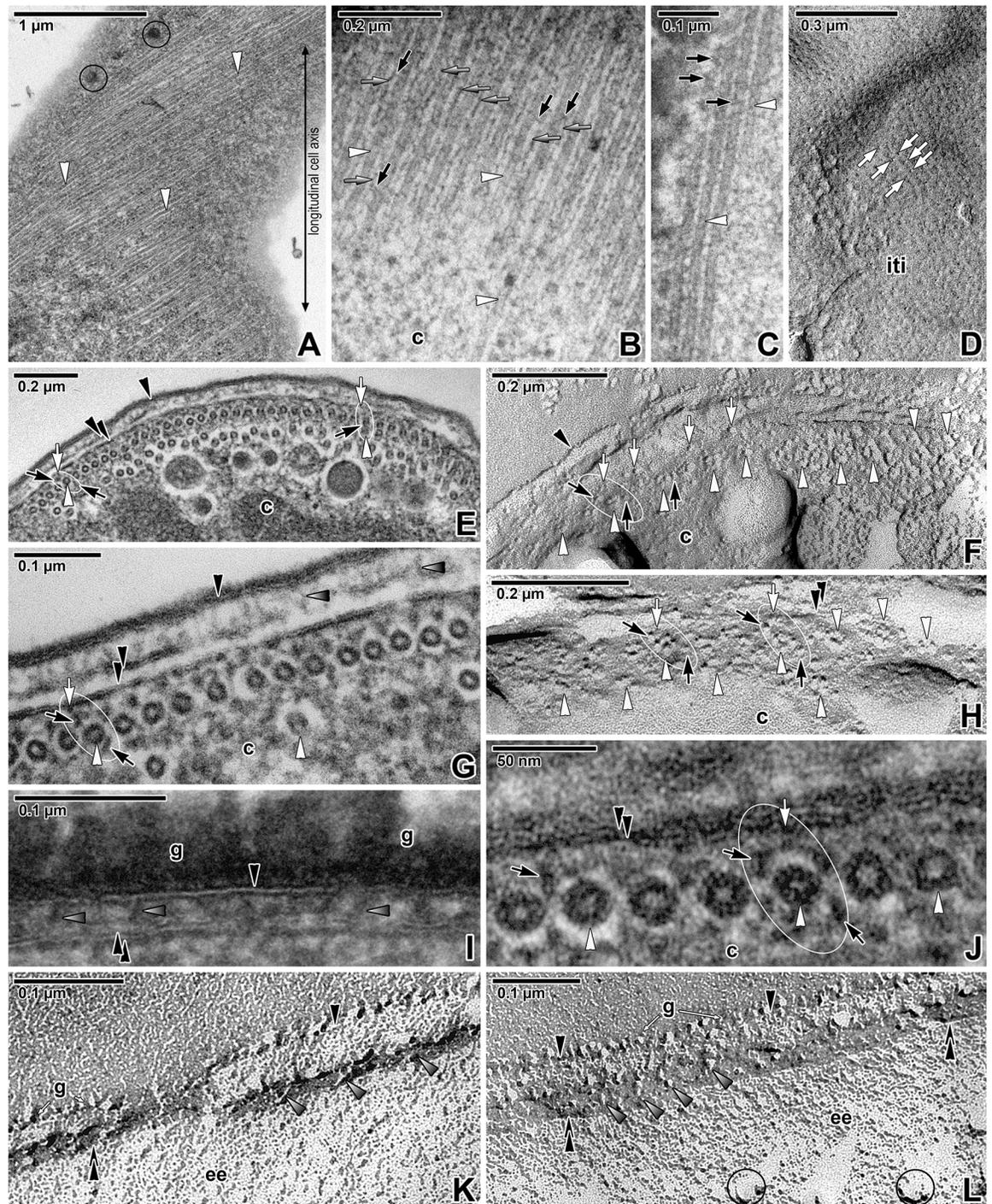
Fig 4. Organisation of the subpellicular microtubules in *Siedleckia nematoides*. A. A superficial section of a cortex revealing the pores and subpellicular microtubules being helically twisted along the longitudinal cell axis. **B-C.** Higher magnification of the longitudinally-sectioned subpellicular microtubules. Note the rows of filamentous structures running parallel to the adjacent microtubules (grey arrows) and filamentous connections with the microtubules (black arrows). **D.** Cytoplasmic face of the internal cytomembrane with IMP alignments (white arrows) that correspond to the localisation of subpellicular microtubules. **E.** The pellicle covering the anterior part of parasite, underlain by one continuous and several intermittent layers of subpellicular microtubules sectioned in cross (left) and tangential (right) plane. **F.** The view (similar to E) of fractured pellicle underlain with several layers of subpellicular microtubules. **G.** The cross-sectioned cortex in the middle region of parasite, showing the organisation of subpellicular microtubules with cross-linking protein complexes. **H.** Fractured subpellicular microtubules with cross-linking protein complexes. **I.** The detail of pellicle covered by a thick glycocalyx layer. **J.**

The high magnification of cross-sectioned microtubules partially revealing the organisation of tubulin protofilaments. **K-L.** Various views of fractured pellicle revealing the cross-linking protein complexes. A, E, G, J: TEM; B-C, I: RR TEM; D, F, H, K-L: FE TEM. *black arrow*–filamentous structures around subpellicular microtubules, *black arrowhead*–plasma membrane, *c*–cytoplasm, *double/paired black arrowhead*–IMC, *g*–glycocalyx, *grey arrow*–filamentous structures located between individual microtubules, *grey arrowhead*–protein complexes localised between the plasma membrane and IMC, *iti*–inner surface of the true (= not fractured) internal cytomembrane, *white arrow*–protein complex embedded in the IMC, *white arrowhead*–subpellicular microtubule. *Black circles* mark some of the large pores. *White ellipse* encircles the cross-linking protein complexes anchoring the subpellicular microtubules to the internal cytomembrane.

attached to the host tissue and those that detached spontaneously in the course of each experiment. Treated individuals survived in extremely high doses of all of the used cytoskeletal probes and showed signs of motility for the next couple of hours (2 h in 10 mM colchicine, up to 1 h in 100 mM colchicine, 8 h in 10 μM oryzalin, 5–7 h in 30 μM oryzalin, 8 h in 10 μM JAS, 6 h in 30 μM JAS, 8 h in 30 μM cytochalasin D and more than 9 h in 10 μM cytochalasin D) (Table 3).

Despite extremely high concentrations of all of the applied cytoskeletal drugs, the surface of parasites appeared undamaged (Figs 5A–5I and 6A–6H) as also seen in control parasites incubated in seawater or proportionate concentrations (10 and 30 μM) of DMSO (data not shown). Furthermore, after careful rinsing and returning of the treated parasites to pure seawater, the majority recovered to normal motility in the period from 10 to 120 min (Table 3).

The treatment of parasites with antimicrotubule agents (colchicine and oryzalin) confirmed the gradual disruption of microtubules, correlating with the increasing drug concentrations and prolongation of the incubation period (Fig 5A–5I), and resulted in the complete blocking of parasite motility. During the initial acceleration in parasite movement occurring in the first 10–20 min after drugs' application, some of the parasites showed an oscillating movement (S3 Video). Afterwards, parasites gradually decreased their movement until they completely stopped (Table 3). Drug-treated parasites exhibited irregular, spasmodic movement (mostly turning over from side to side) and the majority of them laid on the surface of the host tissue. In contrast to the very wavy movement of controls, attached parasites treated with antimicrotubule probes exhibited less pendular and twisting movements; their bodies appeared to be more rigid with obvious limitations in motility. The drug-induced cell rigidity first appeared in the posterior half of the parasite which bended in the anterior-most region (S4 Video), and afterwards the motility gradually ceased (S5 Video). During experiments with high doses of oryzalin, the frequent detachment of parasites from host tissue has been observed. The drug-treated parasites, especially those with larger dimensions (i.e. more mature), were more frequently found to be spirally curled (Fig 5C), but no signs of cell damage or collapse were seen. Ultrathin sections revealed that lower concentrations, i.e. 10 mM colchicine and 10 μM oryzalin, induced a gradual depolymerisation of subpellicular microtubules: in oryzalin treated parasites they appeared less distinct (Fig 5G), while in colchicine a few microtubules were completely lacking, as easily seen in the otherwise continuous outermost microtubule layer (Fig 5B). The majority of parasites treated with 10 μM oryzalin stopped moving after 8 h, while this effect was seen after 2 h in 10 mM colchicine. Higher doses, 100 mM colchicine and 30 μM oryzalin, obviously disrupted microtubules more rapidly, as proved by a rapid decrease of parasite motility within a considerably shorter time (20–60 min in 100 mM colchicine, 5–7 h in 30 μM oryzalin) and empty regions interrupting their outermost layer of subpellicular microtubules (Fig 5D, 5E and 5I). In comparison to oryzalin, colchicine seemed to be more efficient as it unambiguously caused the disruption of more than half of the microtubules (viewed in cross-section) in a considerably shorter time period (1 h). At the end of experiment, the number of subpellicular microtubules was 28.3 ± 1.9 per 1 μm of pellicle length in non-

Table 3. The treatment of living individuals of *Siedleckia nematoides* with cytoskeletal drugs.

Changes / Time left after drug application	Drug / Concentration							
	Colchicine		Oryzalin		Jasplakinolide		Cytochalasin D	
	10 mM	100 mM	10 µM	30 µM	10 µM	30 µM	10 µM	30 µM
Initial increase of movement speed ([0]compared to control)	≤ 10 min	≤ 10 min	≤ 20 min	≤ 20 min	≥ 5 min	≥ 5 min	≥ 30 min	≥ 20 min
	*0.55 ± 0.03 beats/s **1.86 ± 0.11 s	*0.56 ± 0.01 beats/s **1.78 ± 0.04 s	*0.57 ± 0.03 beats/s **1.77 ± 0.10 s	*0.59 ± 0.09 beats/s **1.85 ± 0.33 s	*0.59 ± 0.04 beats/s **1.70 ± 0.09 s	*0.54 ± 0.04 beats/s **1.99 ± 0.12 s	*0.61 ± 0.05 beats/s **1.68 ± 0.11 s	*0.59 ± 0.05 beats/s **1.79 ± 0.13 s
Oscillating movement	+ ≥ 10 min	+ ≥ 10 min	+ ≥ 20 min	+ ≥ 20 min	-	-	-	-
First documented decrease of movement speed	≤ 20 min	≤ 15 min	≥ 60 min	≥ 45 min	≥ 60 min	≥ 30 min	≥ 60 min	≥ 120 min
	Δ	Δ	*0.40 ± 0.05 beats/s **2.53 ± 0.32 s	*0.39 ± 0.04 beats/s **2.64 ± 0.28 s	*0.41 ± 0.02 beats/s **2.51 ± 0.12 s	*0.49 ± 0.06 beats/s **2.42 ± 0.24 s	*0.43 ± 0.03 beats/s **2.42 ± 0.20 s	*0.47 ± 0.04 beats/s **2.33 ± 0.23 s
Progressive decrease of movement speed	≥ 30 min	≥ 20 min	≥ 120 min	≥ 60 min	≥ 120 min	≥ 60 min	≥ 300 min	≥ 240 min
	*0.23 ± 0.03 beats/s **4.88 ± 0.65 s	*0.21 ± 0.02 beats/s **5.15 ± 0.46 s	*0.18 ± 0.02 beats/s **5.92 ± 0.60 s	*0.22 ± 0.04 beats/s **5.29 ± 0.69 s	*0.35 ± 0.04 beats/s **3.51 ± 0.72 s	*0.35 ± 0.04 beats/s **3.38 ± 0.61 s	*0.27 ± 0.05 beats/s **5.19 ± 0.82 s	*0.22 ± 0.01 beats/s **4.75 ± 0.27 s
Spasmodic movement (bending)	-	-	+	+ Restricted to anterior region	+	+ Prevailing from side to side	+	+ Prevailing to one side
Obvious cell rigidity (especially in posterior half)	+	+	+	+	-	-	-	-
Complete stoppage of motility	≤ 120 min	≤ 60 min	≤ 480 min	≤ 420 min	≤ 480 min	≤ 360 min	≥ 540 min	≤ 480 min
Recovery of motility in majority of blastogregarines after washing in seawater	≤ 120 min	≤ 90 min	≥ 60 min	≥ 60 min	≥ 60 min	≥ 60 min	≥ 60 min	≥ 60 min

The symbol + indicates some observed change in the character of motility;—no obvious changes; ≥ changes appeared after the noted time period; ≤ changes appeared only during the noted time period

* beat frequency (beats/s = in Hz equivalent to 1 beat cycle per second, average ± standard error of the mean)

** beat to beat interval (an average time between the two beats ± standard error of the mean)

Δ beat frequency not measurable due to high sample variability.

[0] Control individuals continued beating for more than 9 h (entire experiment duration); they beat at a rate of 0.51 ± 0.02 beats/s with beat to beat interval of 2.18 ± 0.13 s.

treated control parasites, 22.02 ± 1.9 in parasites treated in 10 mM colchicine, 11.6 ± 1.4 in 100 mM colchicine, 25.8 ± 1.3 in 10 µM oryzalin, and 20.6 ± 0.9 in 30 µM oryzalin.

When incubating with probes influencing actin polymerisation, the speed of parasite movement increased during the first 5–40 min in 10 µM JAS and 5–15 min in 30 µM JAS (S6 Video), followed by a gradual decrease of the motility intensity to zero (in 10 µM JAS after 8 h and in 30 µM JAS after 6 h) (Table 3). The movement of individuals treated with JAS appeared spasmodic and irregular, with parasites bending from side to side (S7 Video). Blocked parasites were twisted and completely non-motile. In cytochalasin D, after an initial increase of speed (30–40 min in 10 µM cytochalasin D and 20–60 min in 30 µM cytochalasin D) (S8 Video), the intensity of parasite movement gradually ceased (S9 Video) until it completely stopped in
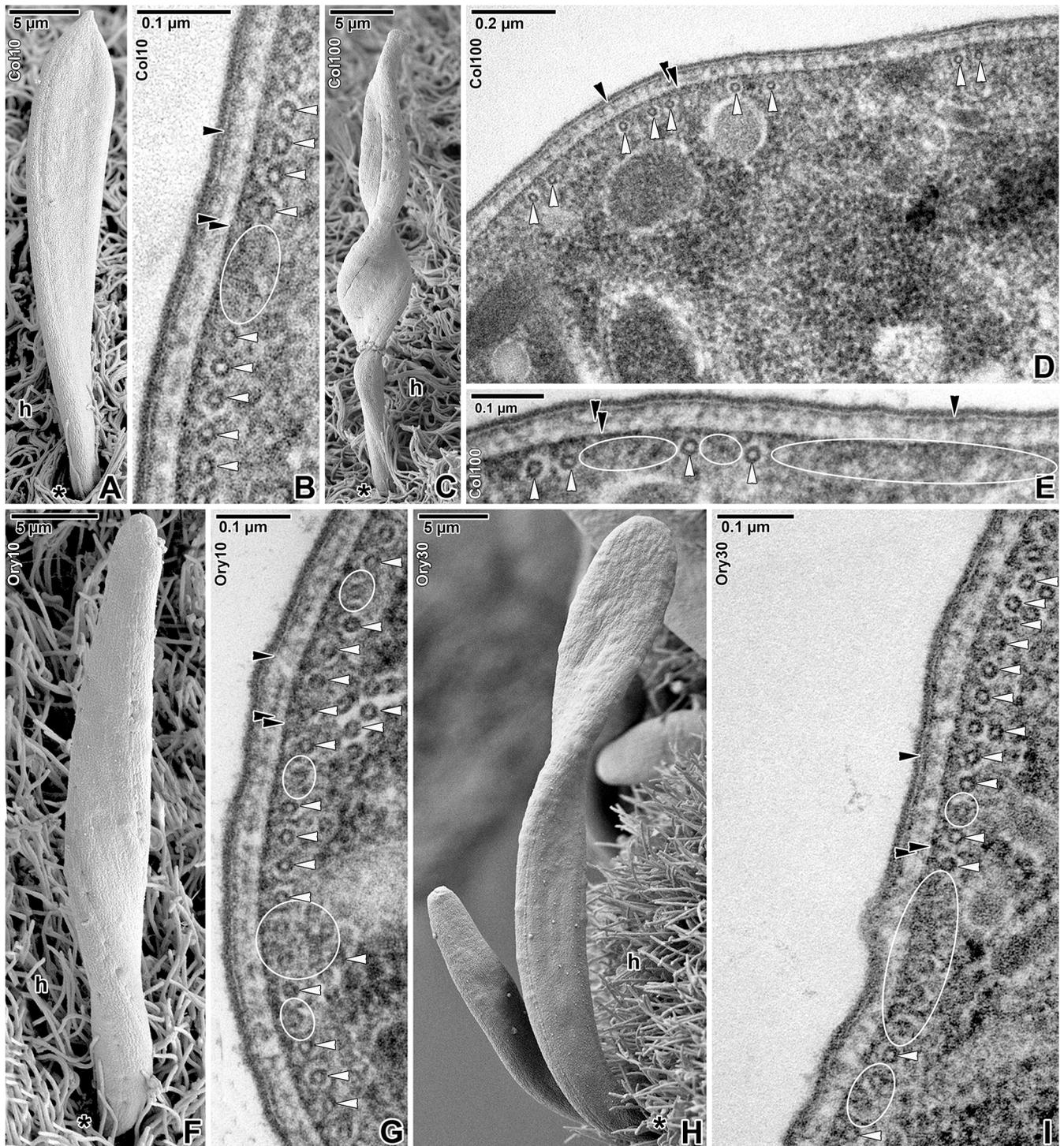
Fig 5. Organisation of the subpellicular microtubules in _Siedleckia nematoides_ after treatment with cytoskeletal drugs. A-B. Treatment with 10 mM colchicine for 2 h: **A.** Attached gamont. **B.** Cross-sectioned cortex with subpellicular microtubules. **C-E.** Treatment with 100 mM colchicine for 1 h: **C.** Attached gamont. **D-E.** General view (D) and higher magnification (E) of the cross-sectioned cortex with subpellicular microtubules. **F-G.** Treatment with 10 µM oryzalin for 8 h: **F.** Attached gamont. **G.** Cross-sectioned cortex with subpellicular microtubules. **H-I.** Treatment with 30 µM oryzalin for 7 h: **H.** Attached trophozoite and gamont. **I.** Cross-sectioned cortex with subpellicular microtubules. A, C, F, H: SEM; B, D-E, G, I: TEM. _black asterisk_–parasite apical end, _black arrowhead_–plasma membrane, _double/paired black arrowhead_–IMC, _h_–host tissue, _white arrowhead_–subpellicular microtubule. _White ellipses_ demarcate the regions with disrupted microtubules.
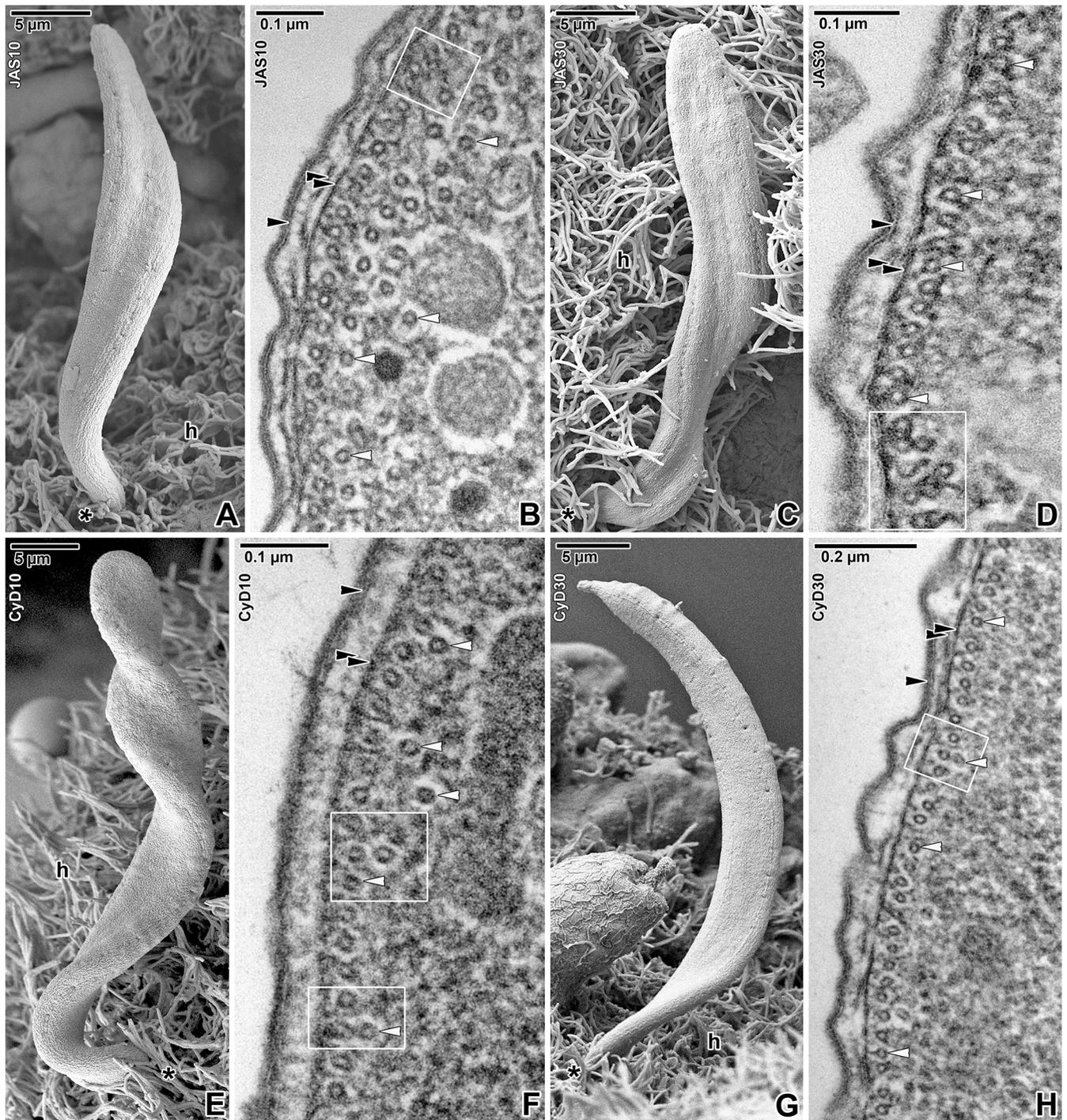
Fig 6. Organisation of the cortex in *Siedleckia nematoides* after treatment with cytoskeletal drugs. A-B. Treatment with 10 µM JAS for 8 h: A. Attached gamont. **B.** Cross-sectioned cortex with subpellicular microtubules. **C-D. Treatment with 30 µM JAS for 6 h: C.** Attached gamont. **D.** Cross-sectioned cortex with subpellicular microtubules. **E-F. Treatment with 10 µM cytochalasin D for 9 h: E.** Attached gamont. **F.** Cross-sectioned cortex with subpellicular microtubules. **G-H. Treatment with 30 µM cytochalasin D for 8 h: G.** Attached gamont. **H.** Cross-sectioned cortex with subpellicular microtubules. A, C, E, G: SEM; B, D, F, H: TEM. *black asterisk*–parasite apical end, *black arrowhead*–plasma membrane, *double/paired black arrowhead*–IMC, *h*–host tissue, *white arrowhead*–subpellicular microtubule. *White rectangles* highlight the reduced spacing between microtubule layers.

most individuals after 8 h when incubated with 30 μM cytochalasin D. Nevertheless, in 10 μM cytochalasin D, although significantly suppressed and spasmodic, the majority of parasites continued to move until the end of each experiment (more than 9 h). The ultrastructural observations in parasites after the application of actin de-/polymerising agents did not allow us to provide unequivocal interpretations (Fig 6A–6H). Ultrastructural analysis of parasites treated with JAS indicated only moderate changes in contraction and condensation of filamentous structures around the subpellicular microtubules (Fig 6B and 6D). Localisation of these structures corresponds to the cross-linking protein complexes, consisting of proteins embedded in the IMC and the network around subpellicular microtubules, which apparently anchor the microtubules to the internal cytomembrane. With an increasing concentration of JAS (10 and 30 μM), these complexes seemed to contract, thereby changing the usually regular distribution of subpellicular microtubules (Fig 6B and 6D). The most notable was the reducing or vanishing of spacing between the outer continuous and inner discontinuous microtubule layers (Fig 6B and 6D) (35.4 ± 0.4 nm in 10 μM JAS and 32.5 ± 0.2 nm in 30 μM JAS when compared to 44.8 ± 0.8 nm in controls; calculated from two adjacent microtubule layers). In individuals treated either with 10 or 30 μM cytochalasin D, density of all above-mentioned structures did not significantly differ from the normal status (Fig 6F and 6H). However, similarly to JAS, the spacing between the individual microtubule layers was reduced to 38.1 ± 1.3 nm in 10 μM cytochalasin D and 34.3 ± 1.1 nm in 30 μM cytochalasin D (Fig 6F and 6H). No conspicuous changes have been documented in the density of protein complexes localised between the plasma membrane and IMC in JAS or cytochalasin D-treated individuals (Fig 6B, 6D, 6F and 6H). The distance between the internal cytomembrane of the IMC and the outer continuous microtubule layer, however, was significantly reduced (36.3 ± 0.2 nm in controls vs. 22.5 ± 0.3 nm in 10 μM JAS, 23.7 ± 0.2 nm in 30 μM JAS, 23.0 ± 0.5 nm in 10 μM cytochalasin D, and 25.3 ± 0.3 nm in 30 μM cytochalasin D).

Confocal laser scanning microscopic analysis of cytoskeletal structures before and after treatment with cytoskeletal drugs

Fluorescence labelling was used to visualise the arrangement of cytoskeletal structures before and after treatment of *S. nematoides* with cytoskeletal drugs. The myosin accumulated at the parasite periphery (Fig 7A and 7C). Similar localisation was documented in α-tubulin immunolabelling used for visualisation of the subpellicular microtubules (Fig 7B–7G). The labelling with an anti-α-tubulin antibody was also strongly positive for brush border of host intestinal epithelium. Co-localisation of myosin and α-tubulin showed both proteins continuously distributed in the cell periphery of young and mature parasites, with increasing labelling intensity towards the parasite posterior region, and overlapped to some degree (Fig 7C). The superficial optical section in the area of the parasite cortex showed patchy organisation of α-tubulin, just beneath the parasite pellicle, organised in barely visible, tiny longitudinal lines corresponding to the subpellicular microtubules (Fig 7D and 7G). Though, methanol-fixed individuals showed more intense labelling of myosin and α-tubulin (Fig 7A–7D), the less intense fluorescence signal in PFA-fixed samples allowed the pattern of cytoskeletal elements staining to be more precisely identified (Fig 7E–7G). The labelling also revealed patchy distribution of α-tubulin in the posterior half of parasites (Fig 7E). Younger parasites exhibited obviously stronger labelling of α-tubulin.

Incubation with microtubule destroying agents resulted in an overall decrease of the fluorescent signal for α-tubulin labelling (Fig 7H–7M). PFA-fixed samples were investigated for the distribution of F-actin and α-tubulin to verify that the influenced microtubules were the reason for the changes in parasite motility after the application of high doses of oryzalin or colchicine, but not potential F-actin redistribution (= treated parasites exhibited no changes in F-
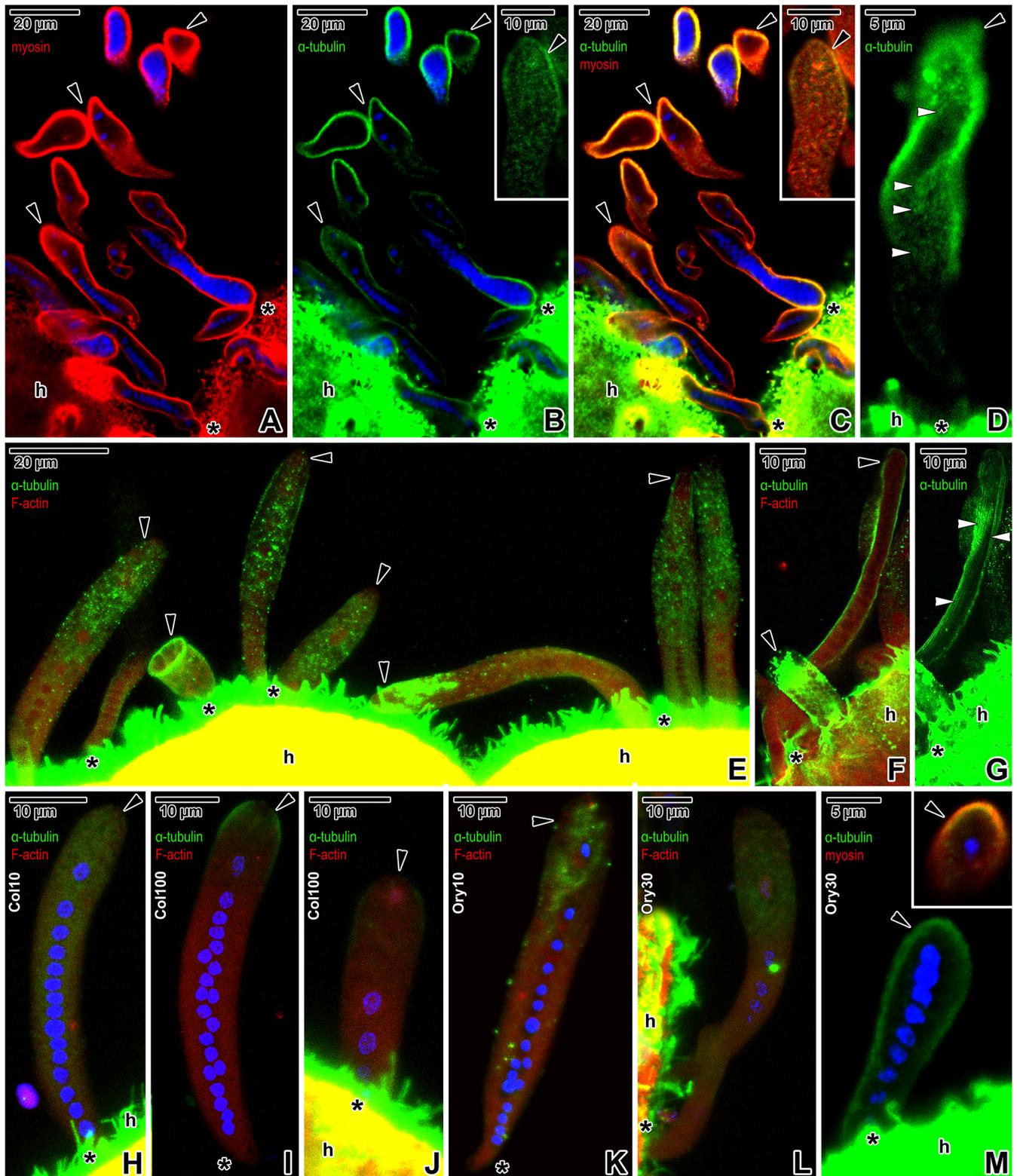
Fig 7. Distribution of myosin (TRITC), α-tubulin (FITC) and F-actin (TRITC) in *Siedleckia nematoides* before and after application of cytoskeletal drugs. A–G. Non-treated parasites. A-B. Single optical section revealing the localisation of myosin (A) and α-tubulin (B). The inset in B shows a localisation of α-tubulin in a caudal part of an individual from another optical section. **C.** Composite view showing the co-localisation of myosin and α-tubulin in a single optical section of parasites shown in A-B. The inset shows a co-localisation of myosin and α-tubulin in a caudal part

of an individual from another optical section. **D.** The localisation of α-tubulin in the superficial region of a gamont. **E.** Co-localisation of α-tubulin and F-actin in parasites of various developmental stages. **F.** Composite view revealing the co-localisation of α-tubulin and F-actin in a macrogamont and microgamont in a single optical section. **G.** More superficial optical section revealing the localisation of α-tubulin in macrogamont shown in F. **H-J. Co-localisation of α-tubulin and F-actin in parasites treated with colchicine: H.** 10 mM colchicine (2 h). **I-J.** 100 mM colchicine (1 h). **K-M. Co-localisation of α-tubulin and F-actin in parasites treated with oryzalin: K.** 10 μM oryzalin (8 h). **L.** 30 μM oryzalin (7 h). **M.** Labelling of α-tubulin in a trophozoite treated with 30 μM oryzalin (5 h). The inset shows a co-localisation of α-tubulin and myosin in the trophozoite caudal region. Note the patchy distribution of α-tubulin underlying the pellicle, corresponding to the localisation of subpellicular microtubules. A-C, M: CLSM, IFA/Hoechst, methanol fixation; D: CLSM, IFA, methanol fixation; E-F: CLSM, IFA/phalloidin-TRITC, PFA fixation; G: CLSM, IFA, PFA fixation; H-L: CLSM, IFA/phalloidin-TRITC/Hoechst, PFA fixation. *black arrowhead*–parasite caudal end, *black asterisk*–parasite apical end, *h*–host tissue, *white arrowheads*–tiny longitudinal lines corresponding to the subpellicular microtubules.

actin distribution; Fig 7E–7G vs. 7H–7M). Incubation with 10 mM colchicine for 2 h resulted in a more diffuse pattern of α-tubulin labelling, which was especially apparent in the caudal region of attached parasites (Fig 7H). Individuals treated for 1 h with 100 mM colchicine showed a further decrease in tubulin labelling, the localisation of which remained restricted to the caudal region only (Fig 7I and 7J). Similarly, parasites treated with 10 μM oryzalin for 8 h (Fig 7K) showed less intensive staining of α-tubulin in contrast to non-treated ones. The intensity of α-tubulin labelling in parasites treated with 30 μM oryzalin for 7 or 5 h respectively was further decreased (Fig 7L and 7M). The patchy distribution of α-tubulin organised in a line underlying the pellicle corresponded to the localisation of subpellicular microtubules (Fig 7M-inset).

The phalloidin labelling confirmed the presence of F-actin in the blastogregarine cortex and cytoplasm (Fig 8A–8D), with a slightly increased staining in the anterior half of the cell. The pattern of staining in the caudal end exhibited a more spotted and fibrous pattern. The brush border of the host epithelium also stained intensively with phalloidin. Parasites labelled with the specific anti-actin antibody exhibited a patchy accumulation of actin (Fig 8C and 8D). Actin was distributed almost homogenously in younger stages (Fig 8C), while in mature gamonts (Fig 8D), it mostly accumulated in their middle part. The immunolocalisation of actin differed from direct F-actin labelling with phalloidin in that the antibody did not bind to the cell periphery corresponding to the cortex, and labelled the host tissue with intensity comparable to the labelling of parasites. The treatment with 10 μM JAS for 8 h resulted in the overall stronger immunolabelling of actin, with a spotted character being obvious, especially in the caudal regions of parasites (Fig 8E). The phalloidin staining of F-actin in parasites showed no or only a slight increase in fluorescence signal when compared to the control samples. The incubation with 30 μM JAS for 6 h induced a more advanced stabilisation of actin filaments, resulting in amplification of the fluorescence signal for phalloidin labelling (Fig 8F). These parasites also exhibited a strong immunolabelling of actin, distributed within entire cell and often more accumulated in parasite apical region. Parasites treated with 10 μM (9 h) or 30 μM (8 h) cytochalasin D exhibited low or almost no F-actin labelling (Fig 8G and 8H), nevertheless the signal for antibody labelling of actin did not change significantly.

Discussion

Blastogregarines, comprising a single genus *Siedleckia*, represent rather a problematic group of unclear taxonomic position within Apicomplexa. Besides a unique life cycle [44, 51, 52], these enigmatic organisms also exhibit unusually active motility, composed of pendular and twisting movements.

The motility in gregarines vs. the concept of glideosome in apicomplexan zoites

Typical movement generally described for apicomplexan zoites is a substrate-dependent gliding, relying on dynamic turnover of actin, the unpolymerised form of which seems to have an
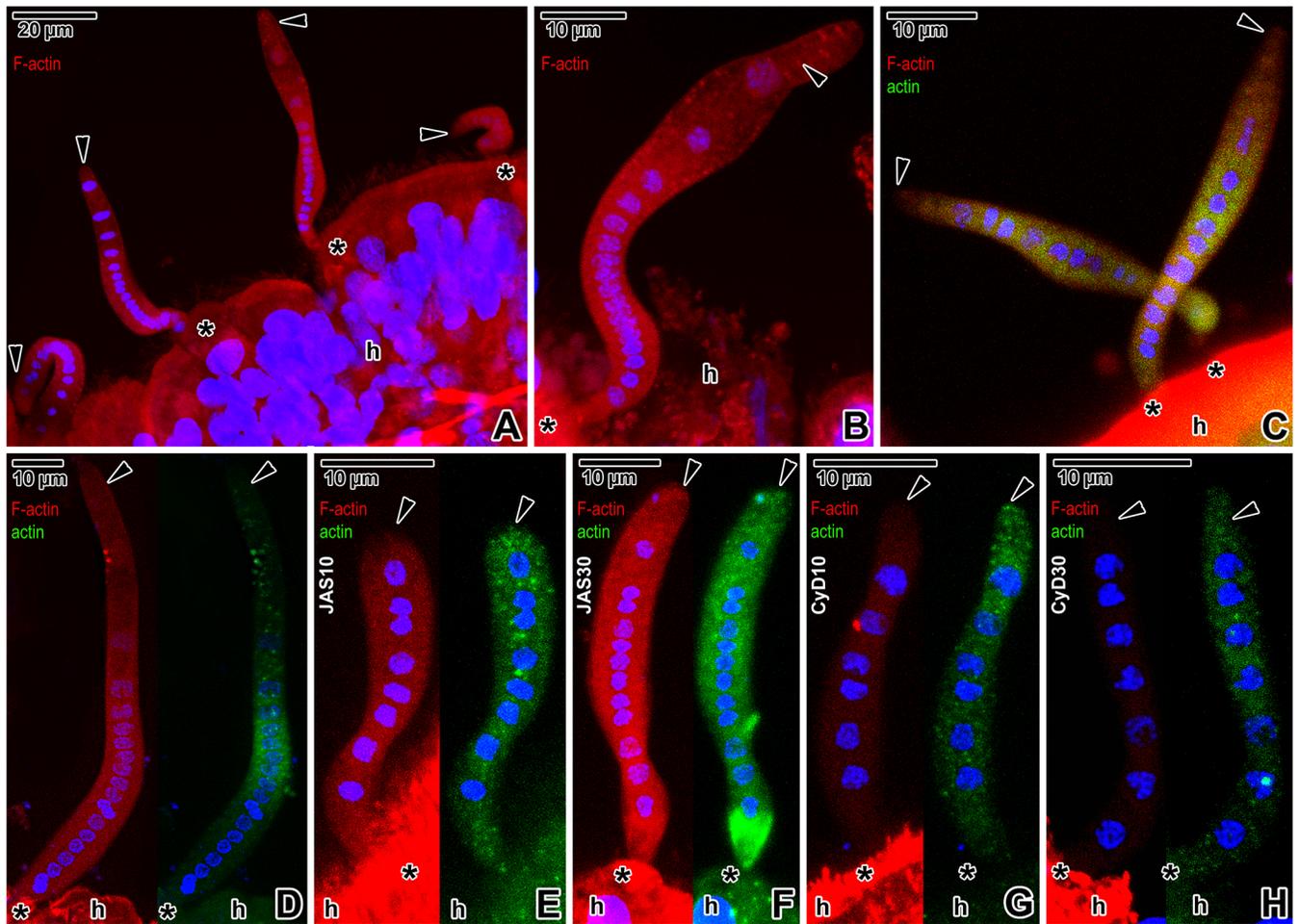
Fig 8. Phalloidin (TRITC) and antibody (FITC) staining of actin in *Siedleckia nematoides* before and after application of cytoskeletal drugs. A-D. Non-treated parasites: A-B. Localisation of F-actin with phalloidin in parasites attached to the host tissue. **C.** Double labelling with phalloidin and specific anti-actin antibody. **D.** Double labelling with phalloidin (left) and anti-actin antibody (right), image split into two separate channels. **E-F. Double labelling with phalloidin (left) and anti-actin antibody (right) in parasites treated with JAS, images split into two separate channels: E.** 10 μM JAS (8 h). **F.** 30 μM JAS (6 h). **G-H. Double labelling with phalloidin (left) and anti-actin antibody (right) in parasites treated with cytochalasin D, images split into two separate channels: G.** 10 μM cytochalasin D (9 h). **H.** 30 μM cytochalasin D (8 h). A-B, D-H left: CLSM, phalloidin-TRITC/Hoechst; C: CLSM, IFA/phalloidin-TRITC/Hoechst; D-H right: CLSM, IFA/Hoechst; A-H: PFA fixation. *black arrowhead*–parasite caudal end, *black asterisk*–parasite apical end, *h*–host tissue.

https://doi.org/10.1371/journal.pone.0179709.g008

increased potential to form filaments relative to vertebrate actin [53]. This so-called glideosome concept, so far described for zoites of *Toxoplasma* and few other apicomplexans [6–10], requires coordinated interactions between surface adhesins and the cytoskeleton of the parasite. The actomyosin motor is described as being embedded between the plasma membrane and the IMC, and oriented by subpellicular microtubules [11]. The myosin A is linked to the IMC against the subpellicular microtubules and its head moves along the actin filament connected to a cell adhesion molecule (TgMIC2, TRAP, MIC2) [9, 10]. The complex of adhesins and actin filaments is transported towards the posterior end of the cell. As a result, the actomyosin motor generates cell gliding by transposing transmembrane adhesins through the plasma membrane by bearing against the IMC [54]. The structure and function of the glideosome require re-evaluation, as recent results have shown that numerous glideosome components (including actin and myosin) can be knocked out without complete blocking of motility [55–57].

Moreover glideosome apparently cannot be applied to all apicomplexans; e.g., gregarines exhibit diverse modes of locomotion and seem to use several mechanisms of cell motility. Different modes of gregarine motility could represent specific adaptations to a parasitism in different environments within hosts. Most eugregarines, covered by a cortex consisting of a dense array of longitudinal epicytic folds and exhibiting progressive linear gliding, were shown to use a modified machinery to move forwards on a solid surface, as they lack both the subpellicular microtubules and micronemes [3]. In contrast, coelomic eugregarines move by pulsation of their body corresponding to the peristaltic or metabolic motility accompanied with periodic changes of the body shape [24, 26–33]. The spindle shaped trophozoites and gamonts of archigregarines (*Selenidium* spp.), possessing regular sets of subpellicular microtubules, display a bending, coiling, and rolling or pendular movements along with contracting their cell shape [34–43, 58]. These movements could be also described as nematode-like [43, 58]. Both the pendular and peristaltic movement are non-progressive.

Due to similarities in external morphology and movement patterns, genus *Siedleckia* has been associated with *Selenidium* archigregarines [59]. Besides the pendular movement similar to that in *Selenidium* [34, 36, 37], additional motility modes, such as twisting, undulation, spasmodic and thrashing movements, could be observed depending on the stage and physiological status of *S. nematoides*. Apicomplexan zoites also show variability in their movement; e.g. circular/helical gliding (progressive) and twirling (non-progressive) of *Toxoplasma* and *Plasmodium* zoites, but their motility relies on contact with a substrate [60]. Trophozoites and gamonts of *S. nematoides*, however, despite bearing a striking resemblance with overgrown apicomplexan zoites, showed no signs of gliding motility. Though the pendular/twisting movements of *S. nematoides* might be considered to be reminiscent of twirling in *Toxoplasma* tachyzoites (occurring when the parasite rights itself vertically, remaining attached to the substrate by its posterior end and spinning clockwise) [60], the individuals of *S. nematoides* continued to bend/twist also after detachment from the host tissue. In this view, the movements of *S. nematoides* are most comparable to the attached waving of *Plasmodium* sporozoites that attach at their apical ends and then exhibit waving or flexing, or may swivel or rotate [61].

Actin filaments

The apparent lack of visible, stable filaments does not fit for all apicomplexans, as in *S. nematoides*, some eugregarines and protococcidian *Eleutheroschizon duboscqi*, the phalloidin labelling revealed the presence of F-actin, even without the application of filament-stabilising probes [3, 46, 47, 62]. The research on involvement of actin- and myosin-like proteins in gregarine cell motility has been restricted to representatives of the genus *Gregarina* [3, 4, 12, 15, 16, 21]. The gregarine movement is often attributed to the F-actin cytoskeleton that is assumed to exist in the form of a myocyte (= outer layer of longitudinal and inner layer of circular myonemes) underlying the pellicle [12, 24, 25, 30, 32, 34] and to the ectoplasmic network [63], e.g. the peristalsis is accompanied by the contraction of circular myonemes [24, 25].

In *S. nematoides*, the F-actin is distributed throughout the parasite cytoplasm and cell cortex. Using a specific antibody recognising the *Toxoplasma* and *Plasmodium* actin, previous studies successfully localised the actin within both the pellicle and cytoplasm of several gregarine species [3, 46]. In *S. nematoides*, however, the actin immunolabelling was of patchy character and restricted to the cytoplasm only. Under TEM, only short filamentous structures with a maximal thickness of 9.7 nm were seen oriented perpendicularly between the plasma membrane and IMC. These structures did not react to the JAS or cytochalasin D treatment indicating that they are not of actin origin, and fluorescently-localised F-actin might be located deeper, i.e. beneath the IMC. Irregular distribution of microtubules observed in JAS-treated

parasites (reduced spacing of individual microtubule layers occurred also in cytochalasin D-treated individuals) along with a shortened distance between the internal cytomembrane and the outer continuous microtubule layer, was probably caused by the condensation and contraction of the cross-linking protein complexes that anchor the microtubules to the internal cytomembrane. Localisation of these complexes corresponded to the filamentous structures associated with microtubules in longitudinal sections. To our best knowledge, there is no data indicating that JAS and cytochalasin D influence the polymerisation of other proteins than actin. Hence we conclude that protein complexes observed in our study could be of actin nature. Although this observation requires further analysis, it could support the idea that the actin filaments might be localised in this area. Recent studies documented the microtubule-associated F-actin in *Plasmodium* gametocytes [64]. As this actin cytoskeleton was found in non-motile gametocytes [64], it is likely that F-actin plays a rather structural role, thereby providing a template for microtubule positioning. In such cases, it must be stable rather than dynamic. Similarly to our results in *S. nematoides*, the treatment with cytochalasin D did not disassemble the microtubule-associated F-actin in *Plasmodium* gametocytes [64]. Another study performed on *Arabidopsis* also suggested the possibility of crosstalk between the F-actin and cortical microtubules, as JAS treatment affected the orientation and parallel ordering of microtubules and stabilised actin filaments were found to align with and move along microtubules [65]. Similarly, disruption of the actin filaments using cytochalasin B affected microtubule organisation in developing *Zinnia elegans* [66]. Altogether, these apparently highly-stabilised filamentous structures in *S. nematoide*s might represent novel F-actin cytoskeleton supporting the layers of numerous subpellicular microtubules.

Subpellicular microtubules

The regularly arranged subpellicular microtubules in *S. nematoides* exhibit a characteristic longitudinal organisation and are nucleated from the apical polar ring, a microtubule-organising center (MTOC) unique to the Apicomplexa [2]. The helical arrangement of microtubules in apicomplexan zoites [2] and *S. nematoides* follow their serpentine body shape. The arrangement of subpellicular microtubules varies among Apicomplexa, but their number, length, and organisation are particular for the developmental stage of a species. The high number of *S. nematoides* subpellicular microtubules concurs with a positive correlation between the species dimensions and the number of subpellicular microtubules. In contrast to apicomplexan zoites with subpellicular microtubules usually ending in the region below the nucleus (2/3 of the cell length) [2], in *S. nematoides*, the microtubules extend along the entire length of the cell. Higher accumulation of α-tubulin in blastogregarine caudal region, accompanied by the lack of an increased number of microtubules in this area, is indicative of unpolymerised form of accumulated tubulin.

Drug-treated apicomplexans lacking subpellicular microtubules are generally non-motile and nonpolar [2]. Probes disrupting microtubules are usually effective only in certain taxonomic groups. Oryzalin is known to inhibit growth of protists but not to disrupt the vertebrate microtubules. For example, in *T. gondii* it binds to α-tubulin and prevents the formation of new microtubules in daughter cells, while the effect on existing stable microtubules in the mother cell is rather moderate [67, 68]; after prolonged treatment (40 h) in 2.5 μM oryzalin, all tubulin is unpolymerised and dispersed [69]. In contrast, colchicine binds to β-tubulin and effectively blocks microtubule assembly in animal cells [70]. For Chromista, corresponding to *S. nematoides*, the minimal effective concentration of colchicine is 10 mM [70]. Drugs disrupting dynamic microtubules are expected to be completely ineffective against the subpellicular microtubules of extracellular apicomplexans, thus indicating that these microtubules are not

dynamic [68]. In *S. nematoides*, however, prolonged incubation in high doses of oryzalin and colchicine led to a gradual vanishing of subpellicular microtubules. The motility of drug-treated blastogregarines attached to the host tissue was often limited to their apical region, equipped with numerous layers of subpellicular microtubules, and persisted for the longest incubation period. The effect of colchicine in extremely high doses (100 mM) applied for a shorter time was considerably more effective than oryzalin. While in colchicine-treated parasites the microtubules completely disappeared in some regions, in those treated with oryzalin, they rather gradually faded away. Experiments performed on archigregarine *S. fallax*, using 0.1–2% colchicine diluted in seawater, showed similar results; i.e. the movement ceased in 19–360 min depending on drug concentration, while the motility of the cilia of the host's epithelium was not affected [41]. Interestingly, the pellicular folding of treated archigregarines was considerably less pronounced or non-existent, suggesting that subpellicular microtubules are important in the formation and the maintenance of the longitudinal bulges. On the other hand, the presence of the second and third row of more precisely arranged microtubules on the inner curvature of bent parasites indicates the role of microtubules in archigregarine motility [41]. Accordingly, archigregarines lacking subpellicular microtubules were shown to be non-motile, although their longitudinal bulges were supported by arrays of fibrils reminiscent of circular myonemes [39]. Our ultrastructural data on drug-treated individuals of *S. nematoides* suggest that continuity of the outermost layer of subpellicular microtubules is essential for normal movement. According to the doses, the motility of drug-treated individuals stopped at a specific time on a regular basis, despite obvious differences in the number of preserved microtubules in ultrathin sections. This indicates that the changes must first occur along the length of microtubules; in longitudinal sections they appeared wavy (data not shown) and, despite their presence, non-functional. Further support can be found in the observations on a differential susceptibility of *T. gondii* subpellicular and spindle microtubules to drugs, which could be either influenced by associated proteins specifically interacting with some of the microtubule population, or, more likely, by the length that is required to become functional [68].

The cross-linking protein complexes in *S. nematoides* that likely anchor the subpellicular microtubules to the cytoplasmic face of IMC, might correspond to proteins, such as microtubule-associated proteins (MAPs), which are important in controlling the local interactions of microtubules with other structures. In general, MAPs are thought to control the spacing of microtubules within the cell via microtubules interconnecting with other parts of the cytoskeleton or the plasma membrane. It is likely that heavy decoration of subpellicular microtubules in Apicomplexa may account for their unusual stability. Observations, when tubulin-specific antibodies do not label the full length of microtubules, suggest that tubulin epitopes were occluded by MAPs [71]. The MAPs, such as dyneins or kinesins, are known to be responsible for sliding between adjacent microtubules [72]. A mechanism similar to that shown in ciliary axoneme, with the microtubules sliding against one another, could account for the undulating motility of archigregarines [42, 72] and blastogregarines. MAP-based mechanism has been already proposed to explain the undulating and bending movements in *Selenidium* representatives [40–42, 72]. The sliding might be localised during the bending movements and occurred uniformly during overall contractions of a trophozoite [41]. Numerous peripheral mitochondria detected in *Selenidium* archigregarines and *S. nematoides* seem to play an important role in the rapid and continuous generation of ATP needed to support the highly dynamic cell plasticity ([40, 58, 72], this study), and might provide the chemical energy necessary for MAP activity [72]. Accordingly, actively moving *Selenidium* species possess more subpellicular microtubules and ectoplasmic mitochondria than less active ones. In *Selenidium*, the microtubules in deeper layers appear to be orientated obliquely to the longitudinal cell axis [58].

Although numerous ultrathin sections of *S. nematoides* did not allow us to unequivocally assess the orientation of deeper microtubules, in longitudinal sections they appeared to be more undulated and arranged loosely when compared to those organised in the outermost layer. In addition, single microtubules or their small clusters oriented obliquely or perpendicularly to the longitudinal cell axis were detected in few sections.

Finally, the organisation of subpellicular microtubules along with their placement within the electron-lucent hexagonal chambers (= sheaths) in *S. nematoides* corresponds to the cortex organisation in archigregarines of the family Selenidiidae [35, 37, 39–41, 58, 72]. The function of these chambers remains to be elucidated, but they could play an important role in microtubule sliding.

Pellicle

In *Selenidium* trophozoites, the multi-layered pellicle, usually with broad longitudinal bulges separated by grooves [37, 58], might act as a stiff skeletal component, while the subpellicular microtubules function in cell motility [73]. It has been proposed that together they represent a unicellular analogue to the musculocuticular system of nematodes, in which longitudinal muscles function antagonistically against an elastic cuticle [41, 58]. Despite the striking similarity in motility mode and mechanism with *Selenidium*, however, the surface of *S. nematoides* is smooth.

The Kp of the plasma membrane in *S. nematoides* is significantly higher than in other apicomplexans analysed to date (Table 2), indicating that more proteins must be anchored to its protoplasmic face (the cortical supra-alveolar space). It is necessary to highlight that the widely varied sizes of IMPs in *S. nematoides* pellicle membranes (Table 1) had a significant impact on statistics, compared to studies, where only particles in the range from 6 to 14 nm were included in the statistical calculations ([17, 49, 50], Table 2 in this study). The IMC refers to single-membrane flattened, cortical alveoli, which underlie the plasma membrane and are coupled to a supporting cytoskeletal network of intermediate filaments [54]. Suture lines can be observed at the edges where the alveoli contact each other [74]. In the IMC of *S. nematoides*, no sutures were observed, so we assume that the IMC is formed from a single fused alveolus as also described in *Plasmodium* life stages (except for gametocytes) [75]. The values of Kp in cortical membranes of *S. nematoides* are higher than in eugregarines, but lower than in *Eimeria* or *Plasmodium* (Table 2). In apicomplexans with gliding motility, the IMC outer leaflet anchors the actomyosin motor; whereas the cytoplasmic face is intimately associated with the subpellicular microtubules and alveolins generating cell rigidity [54]. The PF of the internal cytomembrane in highly motile apicomplexan zoites shows longitudinal rows of 9 nm IMPs that likely anchor the cytoskeleton to the IMC, while the non-motile stages apparently lack them [74]. Similar subpellicular network intimately associated with the pellicle cytoplasmic face extends along the cell in *T. gondii* [76] and forms a resilient membrane skeleton that stabilises the alveoli [75]. Furthermore, a double linear array of IMPs might overlay the microtubules. As the helical path of some zoites during gliding corresponds to their helically coiled microtubules and linear IMPs arrays, these IMPs may function as anchorage points for an axial motor system [77]. In contrast, no regularly organised, linear IMP arrays were detected in the fractured planes of *S. nematoides* cortical cytomembranes. Interestingly, despite a lack of longitudinal IMP arrays in the IMC, the cytoplasmic face of the IMC exhibited imprints rather than IMP alignments matching the localisation of subpellicular microtubules (Fig 4D).

Micropores and pores

Apicomplexan micropores are defined as organelles formed by the pellicle and composed of two concentric rings (in transverse section), the inner of which corresponds to invagination of

the plasma membrane. They are generally assumed to possess a feeding function, e.g. endocytosis of the host cell cytoplasm during the vegetative phase of parasite development. In contrast to other pores, micropores are usually less numerous and widely scattered [74]. Although the presence of typical micropores (= cytostomes) has been confirmed in various apicomplexans, including extracellular gregarines [3, 18, 49, 74], no identical structures were seen in *S. nematoides*. Nevertheless, the pellicle of *S. nematoides* bears numerous pores of three different sizes; the majority of them are organised in four laterally located, longitudinal rows. Although pores were easily detected in cortical membranes by freeze-etching method, they do not seem to interrupt the plasma membrane. In *S. nematoides* ultrathin sections, the plasma membrane in the region of pores appears straight and not invaginated. Thus, these pores, observed only in some SEM preparations, were most likely visualised due to a specific fixative osmolarity. In eugregarines, the micropores are often located at the base of the grooves between the epicytic folds, while the smaller pores are randomly distributed on the base or on the lateral side of the folds [3, 17, 18, 78]. The diameter sizes of pores in *S. nematoides* correspond to those in *Gregarina* spp. [3]. In *S. nematoides*, the function of pores arranged in lateral rows remains to be elucidated. It is possible that they represent an alternate route to transport motor proteins between the parasite cytoplasm and the cortical supra-alveolar space, independent of the route through the apical complex, as it was described in *Plasmodium* ookinetes [74]. The largest pores in *S. nematoides*, connected to a vesicle containing lamellar structure, resemble the ectoplasmic structures observed in the bottom of the grooves in *Selenidium* representatives [37, 40, 58], which are assumed to serve for pinocytosis [58]. Based on comparable sizes and the putative absence of typical micropores in *S. nematoides*, the largest pores detected in this blastogregarine could possess similar function to the apicomplexan micropores.

Glycocalyx

A thick cell coat, the glycocalyx, covers the cell surface of *S. nematoides*. The thickness of the glycocalyx layer significantly increased towards parasites' apical end, hereby, suggesting that it is produced by some of the apical organelles; e.g. micronemes. Similar reinforcing of glycocalyx in the parasite's apical region was documented in *Selenidium* archigregarines ([79], personal unpublished data). The often highly decorated glycocalyx of unicellular parasites allows them to interact with and respond to their environment, and is often essential for their virulence [80].

Conclusions

Similar to archigregarines of the genus *Selenidium*, investigated blastogregarine *S. nematoides* infects the intestines of marine invertebrates and exhibits ecological, morphological, and motility traits inferred to reflect the early evolutionary history of apicomplexans. Despite the presence of key glideosome components such as three-layered apicomplexan pellicle, actin (including its filamentous form), myosin restricted to the cell cortex, subpellicular microtubules, numerous micronemes and prominent glycocalyx layer (where adhesins might be located), the motility mechanism of *S. nematoides* most likely differs from the glideosome machinery. Parasites move independently on a solid substrate and show no signs of gliding motility. We pointed to a possible role of the polymerised form of actin and tubulin in *S. nematoides* motility, which could be described as a combination of pendular, twisting, undulation, and sometimes spasmodic movements. Similar movements were described in *Selenidium* archigregarines. As already proposed for motility mechanism in *Selenidium* spp., our observations suggest that the subpellicular microtubules organised in several layers are the real leading motor structures. The majority of *S. nematoides* actin is stabilised in a polymerised form and

appears to be located beneath the IMC. The filamentous structures (i.e. cross-linking protein complexes) associated with subpellicular microtubules reacted to the JAS and cytochalasin D treatment, resulting in changes in spacing of microtubules, hereby indicating that they could be of actin origin. If the axoneme-like sliding mechanism of microtubules is applicable for *S. nematoides* motility, it is possible that this putative actin cytoskeleton associates lengthwise with subpellicular microtubules to position them within the cytoplasm just beneath the pellicle. Otherwise, the actin filaments may force the synchronised bending of microtubules in some cell regions and this way generate the typical undulating motility of *S. nematoides*.

Supporting information

S1 Video. The motility of *Siedleckia nematoides* individuals attached to the host intestine during incubation in seawater.
(MP4)

S2 Video. The motility of detached *Siedleckia nematoides* individuals during incubation in seawater.
(MP4)

S3 Video. The modified motility of detached *Siedleckia nematoides* individuals incubated with 30 μM oryzalin for 20 minutes. Note: one cell demonstrates oscillating movement, while another cell–decreased bending motility.
(MP4)

S4 Video. The slightly limited motility of attached and detached *Siedleckia nematoides* individuals incubated with 10 μM oryzalin for 30 minutes.
(MP4)

S5 Video. The limited motility of attached *Siedleckia nematoides* individuals incubated with 100 mM colchicine for 15 minutes.
(MP4)

S6 Video. The increased motility of attached *Siedleckia nematoides* individuals incubated with 30 μM jasplakinolide for 5 minutes.
(MP4)

S7 Video. The decreased motility of attached *Siedleckia nematoides* individuals incubated with 10 μM jasplakinolide for 3 hours.
(MP4)

S8 Video. The slightly increased and modified motility of attached and detached *Siedleckia nematoides* individuals incubated with 30 μM cytochalasin D for 25 minutes.
(MP4)

S9 Video. The decreased and limited motility of detached *Siedleckia nematoides* individuals incubated with 30 μM cytochalasin D for 6 hours.
(MP4)

Acknowledgments

Author Contributions

Conceptualization: AV.

Formal analysis: AV NV AD.

Investigation: AV MK NV AD GGP TGS.

Methodology: AV MK NV AD GGP TGS.

Resources: AV NV GGP AD MK TGS.

Validation: AV MK NV.

Writing – original draft: AV.

Writing – review & editing: AV NV GGP MK AD TGS.

References

1. Adl SM, Simpson AG, Lane CE, Lukeš J, Bass D, Bowser SS, et al. The revised classification of eukaryotes. J Eukaryot Microbiol. 2012; 59:429–493. https://doi.org/10.1111/j.1550-7408.2012.00644.x PMID: 23020233

2. Morrissette NS, Sibley LD. Cytoskeleton of apicomplexan parasites. Microbiol Mol Biol R. 2002; 66:21–38.

3. Valigurová A, Vaškovicová N, Musilová N, Schrével J. The enigma of eugregarine epicytic folds: Where gliding motility originates? Front Zool. 2013; 10:57. https://doi.org/10.1186/1742-9994-10-57 PMID: 24053424

4. Heintzelman MB, Mateer MJ. GpMyoF, a WD40 repeat-containing myosin associated with the myonemes of *Gregarina polymorpha*. J Parasitol. 2008; 94:158–168. https://doi.org/10.1645/GE-1339.1 PMID: 18372636

5. Kuhni-Boghenbor K, Ma M, Lemgruber L, Cyrklaff M, Frischknecht F, Gaschen V, et al. Actin-mediated plasma membrane plasticity of the intracellular parasite *Theileria annulata*. Cell Microbiol. 2012; 14:1867–1879. https://doi.org/10.1111/cmi.12006 PMID: 22891986

6. Frénal K, Polonais V, Marq JB, Stratmann R, Limenitakis J, Soldati-Favre D. Functional dissection of the apicomplexan glideosome molecular architecture. Cell Host Microbe. 2010; 8:343–357. https://doi.org/10.1016/j.chom.2010.09.002 PMID: 20951968

7. Daher W, Soldati-Favre D. Mechanisms controlling glideosome function in apicomplexans. Curr Opin Microbiol. 2009; 12:408–414. https://doi.org/10.1016/j.mib.2009.06.008 PMID: 19577950

8. Bullen HE, Tonkin CJ, O'Donnell RA, Tham WH, Papenfuss AT, Gould S, et al. A novel family of apicomplexan glideosome-associated proteins with an inner membrane-anchoring role. J Biol Chem. 2009; 284:25353–25363. https://doi.org/10.1074/jbc.M109.036772 PMID: 19561073

9. Santos JM, Lebrun M, Daher W, Soldati D, Dubremetz JF. Apicomplexan cytoskeleton and motors: Key regulators in morphogenesis, cell division, transport and motility. Int J Parasitol. 2009; 39:153–162. https://doi.org/10.1016/j.ijpara.2008.10.007 PMID: 19028497

10. Boucher LE, Bosch J. The apicomplexan glideosome and adhesins–Structures and function. J Struct Biol. 2015; 190:93–114. https://doi.org/10.1016/j.jsb.2015.02.008 PMID: 25764948

11. Tardieux I, Baum J. Reassessing the mechanics of parasite motility and host-cell invasion. J Cell Biol. 2016; 214:507–515. https://doi.org/10.1083/jcb.201605100 PMID: 27573462

12. Heintzelman MB. Actin and myosin in *Gregarina polymorpha*. Cell Motil Cytoskel. 2004; 58:83–95.

13. Mackenzie C, Walker MH. Substrate contact, mucus, and eugregarine gliding. J Protozool. 1983; 30:3–8.

14. Chen WJ, Fan-Chiang MH. Directed migration of *Ascogregarina taiwanensis* (Apicomplexa: Lecudinidae) in its natural host *Aedes albopictus* (Diptera: Culicidae). J Eukaryot Microbiol. 2001; 48:537–541. https://doi.org/10.1111/j.1550-7408.2001.tb00189.x PMID: 11596918

15. Ghazali M, Schrével J. Myosin-like protein (M_r 175,000) in *Gregarina blaberae*. J Eukaryot Microbiol. 1993; 40:345–354. PMID: 8508173

16. Ghazali M, Philippe M, Deguercy A, Gounon P, Gallo JM, Schrével J. Actin and spectrin-like ($M_r = 260–240\,000$) proteins in gregarines. Biol Cell. 1989; 67:173–184.

17. Schrével J, Caigneaux E, Gros D, Philippe M. The three cortical membranes of the gregarines. I. Ultrastructural organization of *Gregarina blaberae*. J Cell Sci. 1983; 61:151–174. PMID: 6411745

18. Walker MH, Lane NJ, Lee WM. Freeze-fracture studies on the pellicle of the eugregarine, *Gregarina garnhami* (Eugregarinida, Protozoa). J Ultrastruct Res. 1984; 88:66–76.

19. Schewiakoff W. Über die Ürsache der fortschreitenden Bewegung der Gregarinen. Z Wis Zool. 1894; 58:340–354.

20. Richter IE. Bewegungsphysiologische Untersuchungen an polycystiden Gregarinen unter Anwendung des Mikrozeitrafferfilmes. Protoplasma. 1959; 51:197–241.

21. Baines I, King CA. Demonstration of actin in the protozoan *Gregarina*. Cell Biol Int Rep. 1989; 13:679–686. PMID: 2509082

22. King CA. Cell surface interaction of the protozoan *Gregarina* with concanavalin A beads—Implications for models of gregarine gliding. Cell Biol Int Rep. 1981; 5:297–305. PMID: 6783325

23. King CA, Lee K. Effect of trifluoperazine and calcium ions on gregarine gliding. Experientia. 1982; 38:1051–1052.

24. Crawley H. The movements of gregarines. P Acad Nat Sci Philadelphia. 1905; 57:89–99.

25. Hildebrand HF. Electron-microscopic investigation on evolution stages of trophozoite of *Didymophyes gigantea* (Sporozoa, Gregarinida). III. The fine structure of the epicyte with emphasis on the contractile elements. Z Parasitenkd. 1980; 64:29–46. PMID: 6784366

26. Diakin A, Paskerova GG, Simdyanov TG, Aleoshin VV, Valigurová A. Morphology and molecular phylogeny of coelomic gregarines (Apicomplexa) with different types of motility: *Urospora ovalis* and *U. travisiae* from the polychaete *Travisia forbesii*. Protist. 2016; 167:279–301. https://doi.org/10.1016/j.protis.2016.05.001 PMID: 27239726

27. Desportes I, Schrével J. Treatise on zoology—Anatomy, taxonomy, biology. The gregarines (2 vols): The early branching Apicomplexa: Brill; 2013.

28. MacMillan WG. Conformational changes in the cortical region during peristaltic movements of a gregarine trophozoite. J Protozool. 1973; 20:267–274.

29. Leander BS, Lloyd SAJ, Marshall W, Landers SC. Phylogeny of marine gregarines (Apicomplexa)—*Pterospora*, *Lithocystis* and *Lankesteria*—and the origin(s) of coelomic parasitism. Protist. 2006; 157:45–60. https://doi.org/10.1016/j.protis.2005.10.002 PMID: 16352468

30. Warner FD. The fine structure of *Rhynchocystis pilosa* (Sporozoa, Eugregarinida). J Protozool. 1968; 15:59–73.

31. Miles HB. The fine structure of the epicyte of the acephaline gregarines *Monocystis lumbriciolidi*, and *Nematocystis magna*: Observations by electron microscope. Rev Iber Parasitol. 1968; 28:455–465.

32. Miles HB. The contractile system of the acephaline gregarine *Nematocystis magna*: Observations by electron microscope. Rev Iber Parasitol. 1966; 26:361–368.

33. Landers SC. *Pterospora floridiensis*, a new species of acephaline gregarine (Apicomplexa) from the maldanid polychaete *Axiothella mucosa* in St. Andrew Bay, Florida. Syst Parasitol. 2001; 48:55–59. PMID: 11213204

34. Fowell RR. The fibrillar structures of protozoa, with special reference to schizogregarines of the genus *Selenidium*. J R Micr Soc. 1936; 56:12–28.

35. Vivier E, Schrével J. Etude au microscope électronique d'une grégarine du genre *Selenidium* parasite de *Sabellaria alveolata* L. J Microsc. 1964; 3:651–670.

36. Schrével J. Observations biologiques et ultrastructurales sur les Selenidiidae et leurs conséquences sur la systématique des Grégarinomorphes. J Protozool. 1971; 18:448–470.

37. Schrével J, Valigurová A, Prensier G, Chambouvet A, Florent I, Guillou L. Ultrastructure of *Selenidium pendula*, the type species of archigregarines, and phylogenetic relations to other marine Apicomplexa. Protist. 2016; 167:339–368. https://doi.org/10.1016/j.protis.2016.06.001 PMID: 27423403

38. Schrével J, Buissonnet S, Métais M. Action de l'urée sur la motilité et les microtubules sous-pelliculaires du Protozoaire *Selenidium hollandei*. C R Acad Sci. 1974; 278:2201–2204.

39. Wakeman KC, Heintzelman MB, Leander BS. Comparative ultrastructure and molecular phylogeny of *Selenidium melongena* n. sp. and *S. terebellae* Ray 1930 demonstrate niche partitioning in marine gregarine parasites (Apicomplexa). Protist. 2014; 165:493–511. https://doi.org/10.1016/j.protis.2014.05.007 PMID: 24998785

40. Schrével J. Contribution a l'étude des Seleniidae parasites d'annélides polychètes. II. Ultrastructure de quelques trophozoïtes. Protistologica. 1971; 7:101–130.

41. Stebbings H, Boe GS, Garlick PR. Microtubules and movement in the archigregarine, *Selenidium fallax*. Cell Tissue Res. 1974; 148:331–345. PMID: 4208850

42. Mellor JS, Stebbings H. Microtubules and the propagation of bending waves by the archigregarine, *Selenidium fallax*. J Exp Biol. 1980; 87:149–161. PMID: 7420012

43. Gunderson J, Small EB. *Selenidium vivax* n. sp. (Protozoa, Apicomplexa) from the sipunculid *Phascolosoma agassizii* Keferstein, 1867. J Parasitol. 1986; 72:107–110.

44. Chatton E, Villeneuve F. La sexualité et le cycle évolutif des *Siedleckia* d'après l'étude de *S. caulleryi*, n. sp. hologrégarines et blastogrégarines. Sporozoaires hologamétogènes et blastogamétogènes. C R Acad Sci. 1936; 203:505–508.

45. Hayat M. Principles and techniques of electron microscopy: Biological applications. 4th Edn. Cambridge: Cambridge University Press; 2000.

46. Valigurová A. Sophisticated adaptations of *Gregarina cuneata* (Apicomplexa) feeding stages for epicellular parasitism. PLoS ONE. 2012; 7(8):e42606. https://doi.org/10.1371/journal.pone.0042606 PMID: 22900033

47. Valigurová A, Michalková V, Koudela B. Eugregarine trophozoite detachment from the host epithelium via epimerite retraction: Fiction or fact? Int J Parasitol. 2009; 39:1235–1242. https://doi.org/10.1016/j.ijpara.2009.04.009 PMID: 19460380

48. Branton D, Bullivant S, Gilula NB, Karnovsky MJ, Moor H, Muhlethaler K, et al. Freeze etching nomenclature. Science. 1975; 190:54–56. PMID: 1166299

49. Dubremetz JF, Torpier G. Freeze fracture study of the pellicle of an eimerian sporozoite (Protozoa, Coccidia). J Ultrastruct Res. 1978; 62:94–109. PMID: 418187

50. McLaren DJ, Bannister LH, Trigg PI, Butcher GA. Freeze fracture studies on the interaction between the malaria parasite and the host erythrocyte in *Plasmodium knowlesi* infections. Parasitology. 1979; 79:125–139. PMID: 120521

51. Chatton F, Dehorne L. Sporozoaires du genre *Siedleckia*, *S. dogieli* n.sp. et *S. mesnili* n.sp. Bull Zool Soc Fr. 1929; 54:28–33.

52. Chatton E, Dehorne L. Observations sur les Sporozoaires du genre *Siedleckia*, *S. dogieli* n.sp. et *S. mesnili* n.sp. Arch Anat Microsc. 1929; 25:530–543.

53. Schüler H, Matuschewski K. Regulation of apicomplexan microfilament dynamics by a minimal set of actin-binding proteins. Traffic. 2006; 7:1433–1439. https://doi.org/10.1111/j.1600-0854.2006.00484.x PMID: 17010119

54. Gould SB, Tham WH, Cowman AF, McFadden GI, Waller RF. Alveolins, a new family of cortical proteins that define the protist infrakingdom Alveolata. Mol Biol Evol. 2008; 25:1219–1230. https://doi.org/10.1093/molbev/msn070 PMID: 18359944

55. Kumpula EP, Kursula I. Towards a molecular understanding of the apicomplexan actin motor: on a road to novel targets for malaria remedies? Acta Crystallogr F Struct Biol Commun. 2015; 71:500–513. https://doi.org/10.1107/S2053230X1500391X PMID: 25945702

56. Egarter S, Andenmatten N, Jackson AJ, Whitelaw JA, Pall G, Black JA, et al. The *Toxoplasma* Acto-MyoA motor complex is important but not essential for gliding motility and host cell invasion. PLoS ONE. 2014; 9(3):e91819. https://doi.org/10.1371/journal.pone.0091819 PMID: 24632839

57. Whitelaw JA, Latorre-Barragan F, Gras S, Pall GS, Leung JM, Heaslip A, et al. Surface attachment, promoted by the actomyosin system of *Toxoplasma gondii* is important for efficient gliding motility and invasion. BMC Biol. 2017; 15(1):1. https://doi.org/10.1186/s12915-016-0343-5 PMID: 28100223

58. Leander BS. Molecular phylogeny and ultrastructure of *Selenidium serpulae* (Apicomplexa, Archigregarinia) from the calcareous tubeworm *Serpula vermicularis* (Annelida, Polychaeta, Sabellida). Zool Scripta. 2007; 36:213–227.

59. Caullery M, Mesnil F. Sur un Sporozoaire aberrant (*Siedleckia* n. g.). C R Soc Biol. 1898; 5:1093–1095.

60. Hakansson S, Morisaki H, Heuser J, Sibley LD. Time-lapse video microscopy of gliding motility in *Toxoplasma gondii* reveals a novel, biphasic mechanism of cell locomotion. Mol Biol Cell. 1999; 10:3539–3547. PMID: 10564254

61. Vanderberg JP. Studies on the motility of *Plasmodium* sporozoites. J Protozool. 1974; 21:527–537. PMID: 4138523

62. Valigurová A, Paskerova GG, Diakin A, Kováčiková M, Simdyanov TG. Protococcidian *Eleutheroschizon duboscqi*, an unusual apicomplexan interconnecting gregarines and cryptosporidia. PLoS ONE. 2015; 10:e0125063. https://doi.org/10.1371/journal.pone.0125063 PMID: 25915503

63. Beams HW, Tahmisian TN, Devine RL, Anderson E. Studies on the fine structure of a gregarine parasitic in the gut of the grasshopper, *Melanoplus differentialis*. J Protozool. 1959; 6:136–146.

64. Hliscs M, Millet C, Dixon MW, Siden-Kiamos I, McMillan P, Tilley L. Organization and function of an actin cytoskeleton in *Plasmodium falciparum* gametocytes. Cell Microbiol. 2015; 17:207–225. https://doi.org/10.1111/cmi.12359 PMID: 25224798

65. Sampathkumar A, Lindeboom JJ, Debolt S, Gutierrez R, Ehrhardt DW, Ketelaar T, et al. Live cell imaging reveals structural associations between the actin and microtubule cytoskeleton in *Arabidopsis*. Plant Cell. 2011; 23:2302–2313. https://doi.org/10.1105/tpc.111.087940 PMID: 21693695

66. Kobayashi H, Fukuda H, Shibaoka H. Interrelation between the spatial disposition of actin filaments and microtubules during the differentiation of tracheary elements in cultured *Zinnia* cells. Protoplasma. 1988; 143:29–37.

67. Morrissette NS, Mitra A, Sept D, Sibley LD. Dinitroanilines bind α-tubulin to disrupt microtubules. Mol Biol Cell. 2004; 15:1960–1968. https://doi.org/10.1091/mbc.E03-07-0530 PMID: 14742718

68. Morrissette NS, Sibley LD. Disruption of microtubules uncouples budding and nuclear division in *Toxoplasma gondii*. J Cell Sci. 2002; 115:1017–1025. PMID: 11870220

69. Beck JR, Rodriguez-Fernandez IA, Cruz de Leon J, Huynh M-H, Carruthers VB, Morrissette NS, et al. A novel family of *Toxoplasma* IMC proteins displays a hierarchical organization and functions in coordinating prasite division. PLoS Pathog. 2010; 6(9):e1001094. https://doi.org/10.1371/journal.ppat.1001094 PMID: 20844581

70. Dostál V, Libusová L. Microtubule drugs: action, selectivity, and resistance across the kingdoms of life. Protoplasma. 2014; 251:991–1005. https://doi.org/10.1007/s00709-014-0633-0 PMID: 24652407

71. Tran JQ, Li C, Chyan A, Chung L, Morrissette NS. SPM1 Stabilizes subpellicular microtubules in *Toxoplasma gondii*. Eukaryot Cell. 2012; 11:206–216. https://doi.org/10.1128/EC.05161-11 PMID: 22021240

72. Leander BS. Ultrastructure of the archigregarine *Selenidium vivax* (Apicomplexa)—A dynamic parasite of sipunculid worms (host: *Phascolosoma agassizii*). Mar Biol Res. 2006; 2:178–190.

73. Macgregor HC, Thomasson PA. The fine structure of two archigregarines, *Selenidium fallax* and *Ditrypanocystis cirratuli*. J Protozool. 1965; 12:438–443.

74. Raibaud A, Lupetti P, Paul RE, Mercati D, Brey PT, Sinden RE, et al. Cryofracture electron microscopy of the ookinete pellicle of *Plasmodium gallinaceum* reveals the existence of novel pores in the alveolar membranes. J Struct Biol. 2001; 135:47–57. https://doi.org/10.1006/jsbi.2001.4396 PMID: 11562165

75. Harding CR, Meissner M. The inner membrane complex through development of *Toxoplasma gondii* and *Plasmodium*. Cellular Microbiol. 2014; 16:632–641.

76. Mann T, Beckers C. Characterization of the subpellicular network, a filamentous membrane skeletal component in the parasite *Toxoplasma gondii*. Mol Biochem Parasitol. 2001; 115:257–268. PMID: 11420112

77. Menard R. Gliding motility and cell invasion by Apicomplexa: insights from the *Plasmodium* sporozoite. Cell Microbiol. 2001; 3:63–73. PMID: 11207621

78. Dallai R, Talluri MV. Freeze-fracture study of the gregarine trophozoite: I. The top of the epicyte folds. Ital J Zool. 1983; 50:235–244.

79. Simdyanov TG, Kuvardina ON. Fine structure and putative feeding mechanism of the archigregarine *Selenidium orientale* (Apicomplexa: Gregarinomorpha). Eur J Protistol. 2007; 43:17–25. https://doi.org/10.1016/j.ejop.2006.09.003 PMID: 17126539

80. Guha-Niyogi A, Sullivan DR, Turco SJ. Glycoconjugate structures of parasitic protozoa. Glycobiology. 2001; 11:45R–59R. PMID: 11358874

7.12

Melicherová J., Hofmannová L., **Valigurová A.**

2018

**Response of cell lines to actual and simulated inoculation
with *Cryptosporidium proliferans***

Response of cell lines to actual and simulated inoculation with *Cryptosporidium proliferans*

Janka Melicherová[a], Lada Hofmannová[b], Andrea Valigurová[a,*]

[a]*Department of Botany and Zoology, Faculty of Science, Masaryk University, Kotlářská 2, 611 37 Brno, Czech Republic*
[b]*Department of Pathological Morphology and Parasitology, University of Veterinary and Pharmaceutical Sciences, Palackého tř. 1946/1, 612 42 Brno, Czech Republic*

Abstract

The need for an effective treatment against cryptosporidiosis has triggered studies in the search for a working in vitro model. The peculiar niche of cryptosporidia at the brush border of host epithelial cells has been the subject of extensive debates. Despite extensive research on the invasion process, it remains enigmatic whether cryptosporidian host-parasite interactions result from an active invasion process or through encapsulation. We used HCT-8 and HT-29 cell lines for in vitro cultivation of the gastric parasite *Cryptosporidium proliferans* strain TS03. Using electron and confocal laser scanning microscopy, observations were carried out 24, 48 and 72 h after inoculation with a mixture of *C. proliferans* oocysts and sporozoites. Free sporozoites and putative merozoites were observed apparently searching for an appropriate infection site. Advanced stages, corresponding to trophozoites and meronts/gamonts enveloped by parasitophorous sac, and emptied sacs were detected. As our observations showed that even unexcysted oocysts became enveloped by cultured cell projections, using polystyrene microspheres, we evaluated the response of cell lines to simulated inoculation with cryptosporidian oocysts to verify innate and parasite-induced behaviour. We found that cultured cell encapsulation of oocysts is induced by parasite antigens, independent of any active invasion/motility.
© 2017 Published by Elsevier GmbH.

Keywords: Antigen; Apicomplexa; *Cryptosporidium muris*; *Cryptosporidium proliferans*; Encapsulation; Invasion

Introduction

The genus *Cryptosporidium* (Tyzzer, 1907) is an economically significant and zoonotic pathogen of the gastrointestinal tract, mainly threatening cattle/livestock and humans. In healthy hosts, cryptosporidiosis is usually a self-limiting disease; however, it produces a chronic and debilitating condition in immunocompromised hosts, with no effective treatment (Evering and Weiss 2006). One factor limiting the development of a functioning anti-cryptosporidial drug is the lack of any long-term in vitro cultivation system, although significant progress in long-term cultivation of *C. parvum* was recently reported (Morada et al. 2016). Furthermore, gaps remain in our understanding of cryptosporidian invasion mechanisms and formations of host-parasite interactions.

Using molecular markers (SSU rDNA, actin, HSP70 and COWP1 genes), two sister/related cryptosporidian groups have been distinguished (Xiao et al. 1999a,b) that differ in their localisation within the host's body, i.e. a gastric group, of which the most studied species are *C. andersoni*, *C. muris*, *C. galli*, *C. serpentis*, *C. proliferans*, and *C. fragile*, and an intestinal group, of which the best known species are *C. parvum*, *C. baileyi*, *C. pestis*, *C. hominis*, *C. canis* and *C. felis*. The cryptosporidian life cycle, both within the host organism and in vitro culture systems, shows distinct variation between these two groups as well as species. While the life cycle of the intestinal species *C. parvum* has been investigated in numerous in vivo and in vitro studies (Arrowood 2002; Fayer and Ungar 1986; Hijjawi et al. 2001; King et al. 2011; Upton et al. 1994, 1995), the life cycle of gastric species has only been studied occasionally (Aydin and Ozkul 1996; Melicherová et al. 2014; Taylor et al. 1999; Uni et al. 1987; Valigurová et al. 2007, 2008). Cryptosporidian species infecting intestinal sites are distinguished considerably by their response to the host environment or other biological factors when compared to gastric species. For example, *C. parvum*, an intestinal species, exhibits a shorter prepatent period and a more rapid occurrence of mature oocysts in host faeces than *C. proliferans* (Melicherová et al. 2014; Tzipori 1983). Many studies have described the successful in vitro cultivation of *C. parvum* and complete development of its asexual and sexual stages for a range of cell lines (Kato et al. 2001; King et al. 2011; Rosales et al. 1993; Yu et al. 2000). Gastric species, however, which develop in the more inhospitable environment of the host's stomach, appear to depend on more specific factors influencing parasite survival (Choi et al. 2004). Hence, long-term maintenance of gastric species has yet to be achieved in cell culture and the yield of newly formed oocysts still tends to be less than the initial inoculum (Hijjawi et al. 2002).

While some refer to cryptosporidia as intracellular though extracytoplasmic parasites, the others prefer the term "epicellular" to describe the peculiar localisation of cryptosporidian developmental stages (Barta and Thompson 2006; Bartošová-Sojková et al. 2015; Borowski et al. 2010; Cavalier-Smith 2014; Clode et al. 2015; Dumenil 2011; Ryan et al. 2016; Valigurová et al. 2008). Following attachment of the sporozoites to the surface of the host cell, the parasite apical plasma membrane interacts with the host's microvilli and the parasite gradually gets enveloped by a host-derived parasitophorous sac. The sac serves as a protective coat against the hostile conditions found in the host's gastrointestinal tract and reinforces attachment of the parasite to the host's epithelium (Valigurová et al. 2008). Interestingly, cryptosporidian extracellular stages have been reported in cell-free cultures (Aldeyarbi and Karanis 2015; Boxell et al. 2008; Hijjawi et al. 2004, 2010; Koh et al. 2013, 2014; Rosales et al. 2005; Ryan et al. 2016), though other studies have failed to repeat these results (Girouard et al. 2006).

This study focuses on the formation of host-parasite interactions in gastric pathogen *Cryptosporidium proliferans* cultivated in vitro. Our original intent was to establish a work-ing in vitro system for gastric cryptosporidia using protocols from previously published studies (Upton et al. 1994, 1995; Woods et al. 1995); however, repeated observations of an unusual cell line reaction to the parasite oocysts prompted us to design further experiments to investigate the reaction of cell lines to presence of foreign objects. Cell lines were inoculated with either cryptosporidia or polystyrene microspheres in order to compare their innate and parasite-induced behaviour. A combined microscopic approach using scanning electron and confocal laser scanning microscopy was used to evaluate modifications to the inoculated cultures.

Material and Methods

Specification of cell lines and cultivation conditions

Human ileocecal adenocarcinoma cell lines (HCT-8; ATCC® CCL244) and human colorectal carcinoma cell lines (HT-29; ATCC® HTB-38 TM) were cultured in RPMI 1640 medium with L-glutamine (Sigma–Aldrich, Prague, Czech Republic), supplemented with 10% foetal bovine serum (FBS), sodium bicarbonate (2 g/l), penicillin G (100 U/ml), streptomycin (100 μg/ml) and amphotericin B (250 μg/ml) (BioTech, Prague, Czech Republic). Our choice of HCT-8 and HT-29 cell lines was based on published data reporting high achievement in cultivating the intestinal species *C. parvum* and *C. hominis* (Arrowood 2002; Flanigan et al. 1991; Hashim et al. 2006) and the complete development of gastric *C. andersoni* in the HCT-8 cell line (Hijjawi et al. 2002).

The cells lines were maintained in 25-cm² tissue culture flasks in a 5% CO_2 atmosphere at 37 °C and 100% humidity and passaged every 2–3 days. A confluent monolayer of cells was lifted from the flask's surface by using a solution consisting of 0.25% (wt/vol) trypsin and 0.53 mM ethylenediaminetetraacetic acid (EDTA) in phosphate buffered saline (PBS). The cell suspension was centrifuged for 3 min at 216.3*g* in 15 ml falcon tubes. The resultant pellet was then re-suspended in maintenance medium and split between new flasks or well plates.

Preparation of cell culture for inoculation

For the experimental inoculations, confluent monolayers were washed with PBS, trypsinised and then centrifuged. The resultant pellets from two flasks (2 × 25 cm²) were re-suspended in fresh medium and split between 12-well test plates (3.2 cm² per well), each containing a 15 mm diameter cover glass on the bottom. The concentrated cell suspension was applied to each well and topped-up with RMPI 1640 (100 ml) with L-glutamine enriched with sodium bicarbonate (0.3 g/ml), bovine bile (0.02 g/ml), glucose (0.1 g/ml), folic acid (25 mg/ml), 4-aminobenzoic acid (100 mg/ml), calcium pantothenate (50 mg/ml), ascorbic acid (875 mg/ml), antibi-

otics (100 U/ml penicillin and 100 μg/ml streptomycin), antimycotics (250 μg/ml amphotericin B) and 5% FBS (BioTech, Prague, Czech Republic). This 'supplemented medium' was used for all experimental inoculations in our study as it produced better physiological conditions for keeping the culture and appeared to support the parasite invasion process. After two days, cells adhering to the cover glasses had created a 70–80% confluent monolayer.

Characterisation of parasites

The gastric species used in this and some of our published studies (Melicherová et al., 2014, 2016) was previously characterised as *Cryptosporidium muris* strain TS03, originating from an East African mole rat (*Tachyoryctes splendens*) (Feng et al. 2011; Kváč et al. 2008). A recent study of Kváč et al. (2016), however, concluded that this strain differs genetically from *C. muris* and other known cryptosporidia, and proposed a new species name for it, *C. proliferans*.

Microscopic identification of *C. proliferans* developmental stages was based on their description and measurements given in previous studies (Melicherová et al. 2014; Kváč et al. 2016).

Preparation of parasites

Oocysts of *C. proliferans* (strain TS03), originating from the Institute of Parasitology Biology Centre at the Academy of Sciences of the Czech Republic (České Budějovice), were passaged in experimentally inoculated southern multimammate mice (*Mastomys coucha*) kept at the Department of Pathological Morphology and Parasitology at the University of Veterinary and Pharmaceutical Sciences in Brno (UPVS) in agreement with Czech legislation (Act No 246/1992 Coll., on the Protection of Animals Against Cruelty). All housing, feeding and experimental procedures were conducted under Protocol 31-2014 approved by the UPVS and the Central Commission for Animal Welfare, Czech Republic.

Faeces were collected in morning each day and stored with aqueous potassium dichromate (2.5% w/v, final concentration) at 4 °C. Oocysts were purified using Sheather's sugar flotation method (Arrowood and Sterling 1987) and modified caesium chloride gradient centrifugation (Kilani and Sekla 1987) then stored in PBS at 4 °C for a maximum of four weeks. Viability of the *C. proliferans* oocysts was assessed using the fluorescein diacetate/propidium iodide staining protocol (Jones and Senft 1985). Based on the protocol standardized in our previous study (Melicherová et al. 2016), oocysts of *C. proliferans* were excysted in a 37 °C water bath using RPMI 1640 medium with 5% bovine serum albumin (BSA) for 30–60 min, until the percentage of oocyst excystation reached 40–50%. Then the suspension was centrifuged for 3 min at 100g and resultant pellet was re-suspended in supplemented medium. Prior to inoculation of cell cultures, activity/motility of excysted sporozoites was monitored using

the Olympus IX70 research inverted tissue culture microscope.

Inoculation of cell cultures with cryptosporidian oocysts or with foreign non-living objects

The 70–80% confluent cell line monolayer was washed with 0.1 M PBS and a mixture of 1×10^4 unexcysted/excysted oocysts and sporozoites of *C. proliferans* was placed into each of 12-well plates topped-up with 1 ml of fresh supplemented medium. Using the light microscope Olympus IX70, behaviour of parasites (such as estimation of the ratio between the excysted and intact oocysts, monitoring of the sporozoites' viability) inoculated into the cell culture was continuously controlled during the entire experiment and prior to each fixation for subsequent procedures. Cover glasses with inoculated culture were analysed 24-, 48- and 72-h post inoculation (HPI) using confocal laser scanning microscopy (CLSM) and scanning electron microscopy (SEM).

Simulated inoculation of HCT-8 and HT-29 cell lines with non-living foreign objects (polystyrene microspheres; specified more precisely in following sections) was undertaken in order to verify whether the embracing of *C. proliferans* oocysts by cell lines was provoked by the parasite itself or whether it represents an innate reaction of the culture to foreign objects in general. The same supplemented medium was used for cultures inoculated with either the parasite or the foreign objects.

Preparation of parasite antigen-coated polybead microspheres

Suspensions of *C. proliferans* oocysts were partially excysted (30 min) in sterile PBS, sonicated by placing the material on ice, centrifuged at 10,314g to remove undisrupted remnants and resulting supernatant was used as *C. proliferans* antigen. A model 150 V/T ultrasonic homogeniser (230 V/50 Hz, power 0–150 W, timer 0–15 min; Biologics Inc., Manassas, Virginia, USA) fitted with a 5/32″ diameter stepped titanium micro tip (300 μl–15 ml processing volume, very high intensity) was used to obtain *C. proliferans* protein homogenate. The *C. proliferans* antigen-coated polystyrene microspheres were prepared according to protocols of Valigurová et al. (2014). The coated polystyrene microspheres were re-suspended in RPMI 1640 medium supplemented with vitamins and glucose, and split between each well with a total volume of approximately 1000 microspheres/200 μl.

Scanning electron microscopy

HCT-8 and HT-29 cell lines were inoculated with either excysted oocysts of *C. proliferans* or polystyrene microspheres, i.e. 6 μm Polybead® Polystyrene Red Dyed Micro-
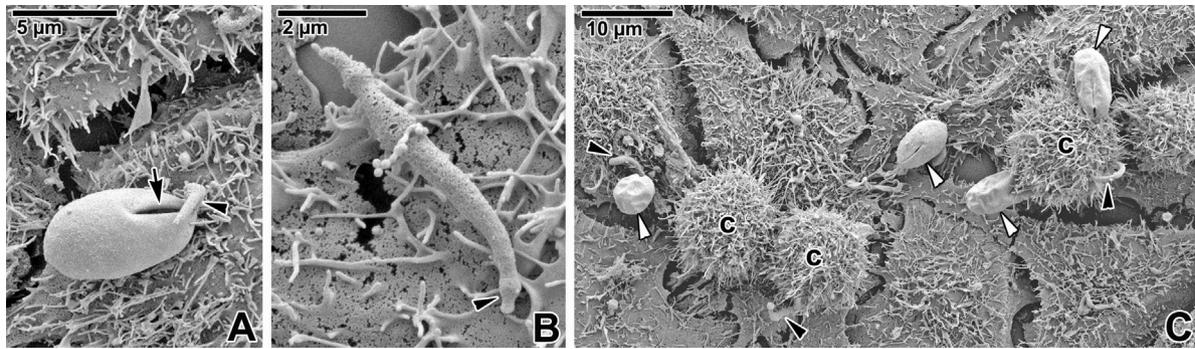
Fig. 1. Scanning electron micrographs of HCT-8 cell lines inoculated with *Cryptosporidium proliferans* at 24 HPI. (A) Excysting *C. proliferans* oocyst releasing a sporozoite (black arrowhead); suture (black arrow). (B) Free sporozoite with typically prolonged apical end (black arrowhead). (C) A general view of the HCT-8 monolayer inoculated with *C. proliferans*; newly formed round cultured cells (c), oocysts (white arrowheads) and invading sporozoites (black arrowheads).

spheres (CAT#15714) and 10 μm Polybead® Microspheres (CAT#17136; Polysciences Europe GmbH, Hirschberg an der Bergstrasse, Germany) coated with protein homogenate obtained from *C. proliferans* oocysts. Samples on cover glasses were fixed in 2.5% glutaraldehyde in pH 7.2 phosphate buffer at 24-, 48- and 72-HPI. Negative controls were evaluated in a similar manner. The specimens were then examined under a JEOL JSM-6300 scanning electron microscope (JEOL, Peabody, MA, USA).

Confocal laser scanning microscopy

Cell lines were grown in RPMI 1640 supplemented with vitamins and glucose on cover slides placed in 12-well plates (15 mm). Following inoculation with either *C. proliferans*, or pure/*C. proliferans* antigen-coated polystyrene microbeads (10 μm Fluoresbrite® YG Microspheres, CAT#18140 or 10 μm Polybead® Microspheres, CAT#17136; Polysciences Europe GmbH, Hirschberg an der Bergstrasse, Germany), samples were fixed in freshly prepared 4% paraformaldehyde (v/v) in 0.2 M PBS, washed in 0.1 M PBS and permeabilised in 0.3% Triton X-100. Thereafter, the specimens were washed with antibody diluent (containing 0.1 M PBS, 0.1% Triton X-100, 0.1% bovine serum albumin and 0.1% sodium azide at pH 7.4), incubated with TRITC-phalloidin (Sigma–Aldrich, Prague, Czech Republic), washed with antibody diluent and counterstained with Hoechst 33342 (Life Technologies, Prague, Czech Republic). Preparations were mounted in anti-fade based on 2.5% DABCO (Sigma–Aldrich, Prague, Czech Republic) mixed with glycerol and 0.1 M PBS or VECTASHIELD® (Vector Laboratories, Burlingame, CA, USA) and viewed under an Olympus IX80 microscope equipped with a laser scanning FluoView 500 confocal unit (Olympus FluoView 4.3 software), using the tetramethylrhodamine isothiocyanate (TRITC-phalloidin), UV (Hoechst) and fluorescein isothiocyanate (Fluoresbrite® YG Microspheres with excitation and emission spectra similar to FITC) filter sets (Olympus Czech Group, Prague, Czech Republic).

Results

Experimental inoculation of HCT-8 and HT-29 cell lines with *Cryptosporidium proliferans* strain TS03

In both cell lines (HCT-8 and HT-29), a 70–80% confluence provided an appropriate environment for culture inoculation and parasite development. Furthermore, the conditions used (see Section 'Material and methods') clearly inhibited the formation of cell multilayers, thus preventing unwanted overgrowth of parasites with cultured cells. Oocyst excysted continuously within the well plates with supplemented medium, while free motile sporozoites occurred repeatedly throughout the experiment.

The first interaction between the parasite developmental stages (unexcysted/excysted oocysts) and the cell line monolayer was noted at 24 HPI. Of the two cell lines examined, the reaction of the HCT-8 cell line to the parasite invasion process was more intense, as shown by formation of clearly elongated microvilli around the excysting oocysts and sporozoites. As expected, excystation of unexcysted oocysts continued during cell line incubation (Fig. 1A). Released sporozoites probed the cultured cell membrane with their prolonged apical end and attempted to invade the cultured cells (Fig. 1B). Developmental stages of *C. proliferans* were frequently found near dividing or newly formed round cells, with oocysts even observed stuck to the surface of the young cells (Fig. 1C). Slightly elongated cultured cell microvilli were observed surrounding some of the attached sporozoites. At 48 HPI, numerous viable sporozoites were observed searching for an appropriate invasion/attachment site within the HCT-8 cell culture (Fig. 2A–F). Invading sporozoites were partially embedded in cultured cells with obviously altered microvilli (Fig. 2A–D). Remarkably, some sporozoites had already been embraced by the cultured cell membrane (Fig. 2E, F). Early developmental stages corresponding with their size and shape to trophozoites (Fig. 2G–I), as well as more advanced stages resembling meronts or gamonts (Fig. 2J), were found. The
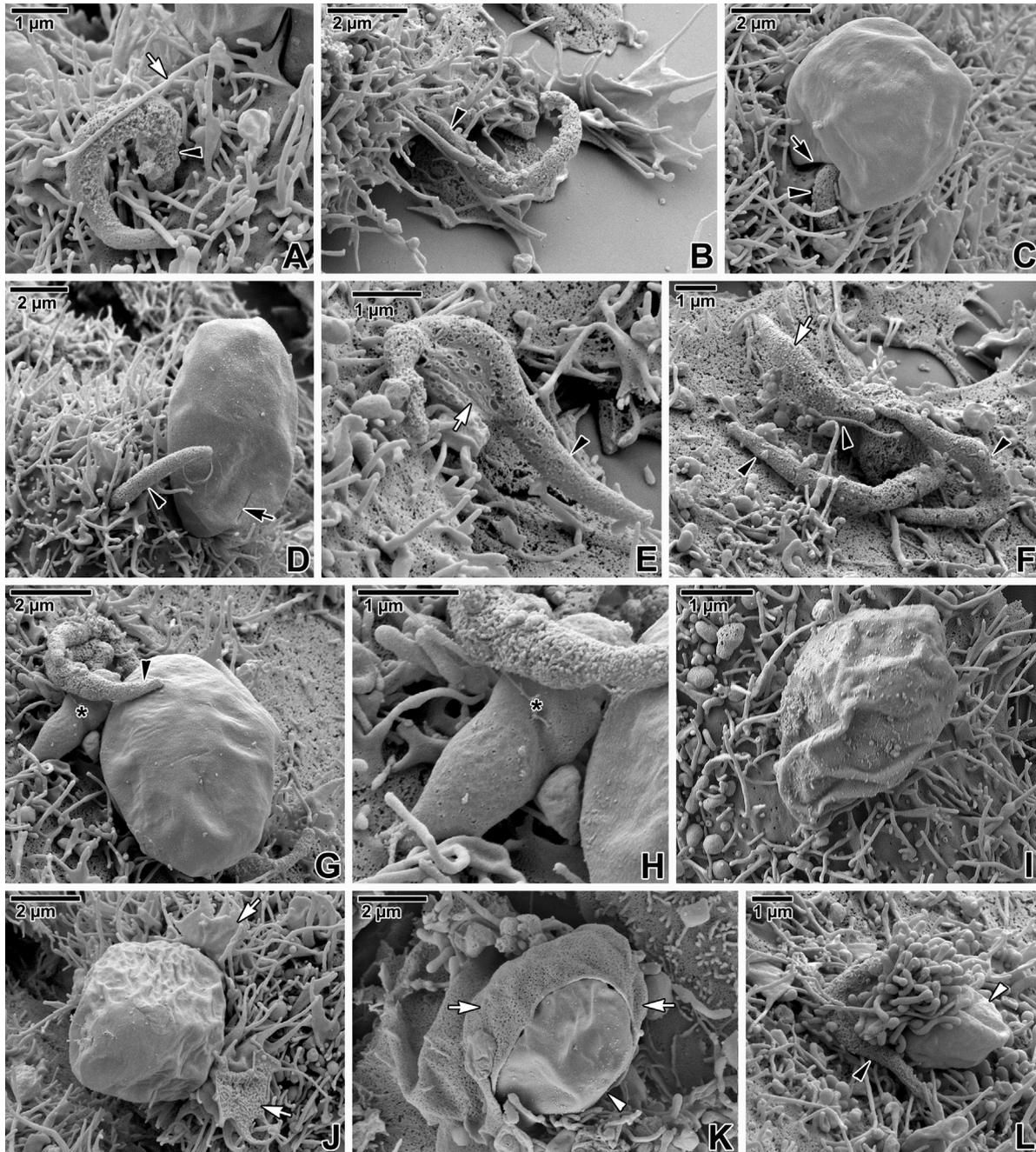
Fig. 2. Scanning electron micrographs of HCT-8 cell lines inoculated with *Cryptosporidium proliferans* at 48 HPI. (A, B) Invading sporozoite (black arrowhead); elongated microvilli of cultured cell (white arrow). (C) Excysting oocyst with opened suture (black arrow) releasing a sporozoite (black arrowhead). Note that the sporozoite immediately invades the cultured cell. (D) Oocyst with suture (black arrow) embedded into a newly formed, round cell and an invading sporozoite (black arrowhead). (E) Sporozoite (black arrowhead) partially covered by membrane fold (white arrow) formed by the cultured cell. (F) Free sporozoites (black arrowheads), one of which is already covered by a cultured cell membrane fold (white arrow). (G) Oocyst with a free sporozoite (black arrowhead) and an early trophozoite (asterisk). (H) Detail of the early trophozoite (asterisk) shown in G. (I) A more mature trophozoite stage of *C. proliferans*. (J) A newly-formed round cell with attached meront-/gamont-like stage within the parasitophorous sac. Note the elongated microvilli and membrane fold fragments (white arrows) of cultured cell. (K) Oocyst (white arrowhead) partially embraced by plasma membrane fold of a single cultured cell (white arrows). (L) Oocyst (white arrowhead) enveloped by cultured cell projection and a single free sporozoite (black arrowhead).

microscopic identification was based on description and measurements of particular developmental stages reported in our previous study (Melicherová et al. 2014). Though the stages

enveloped by parasitophorous sacs were hardly distinguishable from each other under SEM, there were some differences that allowed us to distinguish the trophozoites from more
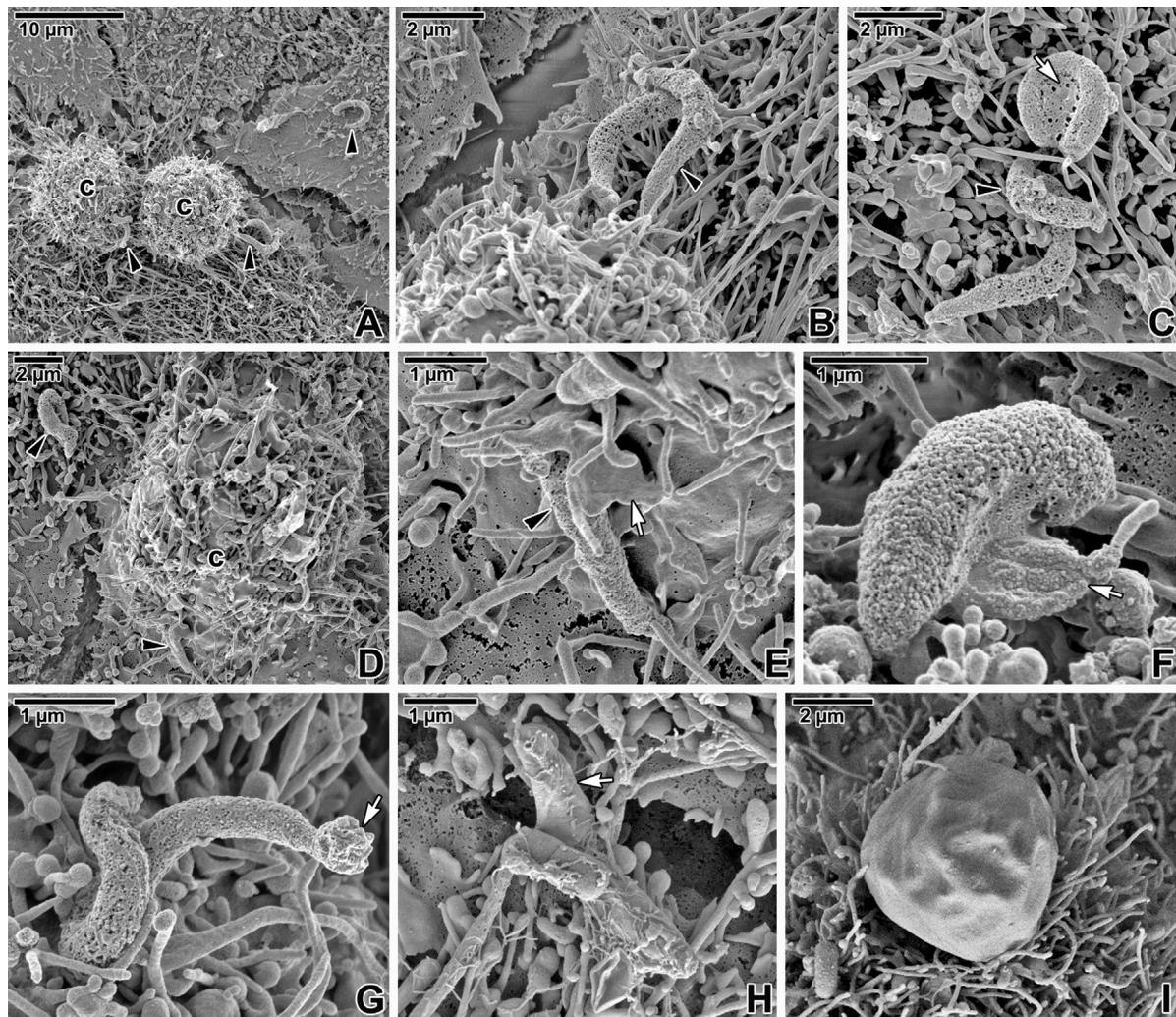
Fig. 3. Scanning electron micrographs of HCT-8 cell lines inoculated with *Cryptosporidium proliferans* at 72 HPI. (A) Free sporozoites (black arrowheads) attracted by the newly formed round cells (c). (B) Two sporozoites (black arrowhead) apparently checking the target site on the cultured cell's surface. (C) Three free sporozoites (black arrowhead), one of which is already covered by the cultured plasma membrane fold (white arrow). (D) Newly formed cultured cell (c) invaded by a sporozoite (black arrowhead) and one free sporozoite (black arrowhead on the left). (E) Detail of the invading sporozoite (black arrowhead) shown in D, partially embraced by a projection of the cultured cell (white arrow). (F) Putative merozoite partially covered by the fold of the cultured cell's plasma membrane (white arrow). (G) Sporozoite torn from the monolayer. Note the apical end with remnants of the cultured cell plasma membrane (white arrow). (H) Detached zoite transforming into a trophozoite stage, completely enveloped by a parasitophorous sac (white arrow). (I) More advanced developmental stage (meront or gamont) located within the parasitophorous sac and surrounded by elongated microvilli.

mature stages; i.e. trophozoites were more elongated in shape and significantly smaller in size. Nevertheless, it was almost impossible to distinguish the meronts stages from gamonts or zygotes. Excysting (Fig. 2C, D, G) or unexcysted *C. proliferans* oocysts were still observable on the surface of the cell lines, often completely or partially enveloped by cultured cell projections/plasma membrane fold (Fig. 2K, L). At 72 HPI, despite the increasingly obvious depleting effect of parasites, 40–50% of the previous cell culture monolayer was still preserved and new young round cells were observed (Fig. 3A, D). By 72 HPI, the quantity of sporozoites trying to invade culture cells had increased (Fig. 3A–E), with invading sporozoites inducing a cell culture response resulting in the

gradual formation of a parasitophorous sac from the cultured cell's plasma membrane (Fig. 3C–E). There was evidence that some sporozoites had been torn from the monolayer, with the remains of the invaded cell at their apical end (Fig. 3G). Zoites, with their size and shape corresponding to merozoites, lying on the surface of cell culture establishing another layer, were partially covered by cultured cell membrane folds (Fig. 3F), while others were completely enveloped by parasitophorous sacs (Fig. 3H). Few stages, completely enveloped by parasitophorous sac and corresponding to meronts or gamonts were detected (Fig. 3I).

HT-29 cell lines, incubated under the same conditions as HCT-8 and inoculated with an equal number of
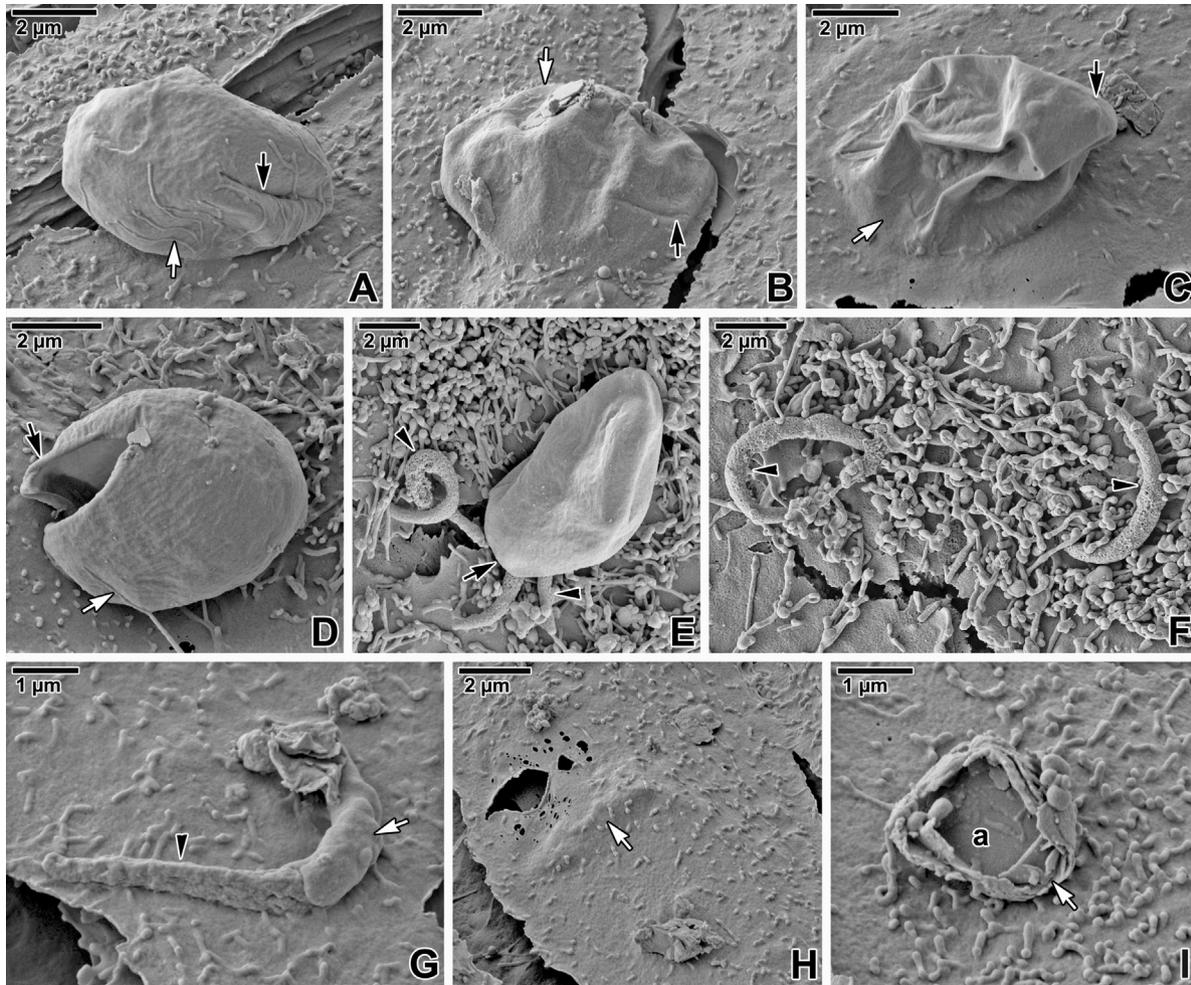
Fig. 4. Scanning electron micrographs of HT-29 cell lines inoculated with *Cryptosporidium proliferans* at 24 HPI. (A) Unexcysted oocyst with closed suture (black arrow) at the cell culture surface. Note the elongated microvilli (white arrow) adhering to the oocyst's surface. (B, C) Oocyst with closed suture (black arrow) embedded to the cultured cell, partially (C) or almost completely (B) encapsulated by its plasma membrane (white arrow). (D) Excysted oocyst with opened suture (black arrow) lying on the monolayer surface. The response of the cultured cell is demonstrated by the elongated microvilli (white arrow). (E) Excysting oocyst releasing three sporozoites (black arrowheads); suture (black arrow). (F) Two sporozoites (black arrowheads) apparently checking the cultured cell's surface. (G) Free sporozoite (black arrowhead) partially covered by the cultured cell's membrane fold (white arrow). (H) Zoite completely overlapped by a cultured cell (white arrow). (I) Modified area (a) following previous interaction with parasite, characterised by the remnants of raised and altered plasma membrane of cultured cell (white arrow).

excysted/unexcysted oocysts, showed a different reaction to inoculation with *C. proliferans*. In contrast to HCT-8, far more unexcysted oocysts with obviously closed sutures were observed on the HT-29 cell line surface at 24 HPI (Fig. 4A). Both unexcysted and empty oocysts were partially or completely encapsulated by the plasma membrane of cultured cells (Fig. 4B, C). Empty oocysts with opened sutures were observed in contact with elongated HT-29 cell microvilli (Fig. 4D). Oocysts continued to excyst and viable sporozoites were released (Fig. 4E, F). Free sporozoites were often noticed partially covered by cultured cell folds (Fig. 4G). Some zoites were completely overlapped by a new layer of HT-29 cells (Fig. 4H). Previous sites of parasites' interaction with the cell monolayer surface were clearly observable due to preservation of raised cultured cell plasma membrane

folds (Fig. 4I). At 48 HPI, free sporozoites continued to invade cultured cells (Fig. 5A). Numerous empty or unexcysted oocysts were observed on the HT-29 cell line surface, with some being embraced by cultured cells (Fig. 5A–C). Developmental stages, corresponding to meronts or gamonts (Fig. 5D, E) and sporadic individuals with their shape resembling oocysts (Fig. 5F), were detected developing within parasitophorous sacs on the cell line surface. At 72 HPI, a number of empty and unexcysted oocysts were observed being encapsulated by the cultured cells to a greater or lesser degree (Fig. 6A–C). The imprints from previous parasites' occurrence and modified sites of cultured cells with raised plasma membrane folds were often noticed (Fig. 6D–F). No free sporozoites or merozoites were observed at 72 HPI.
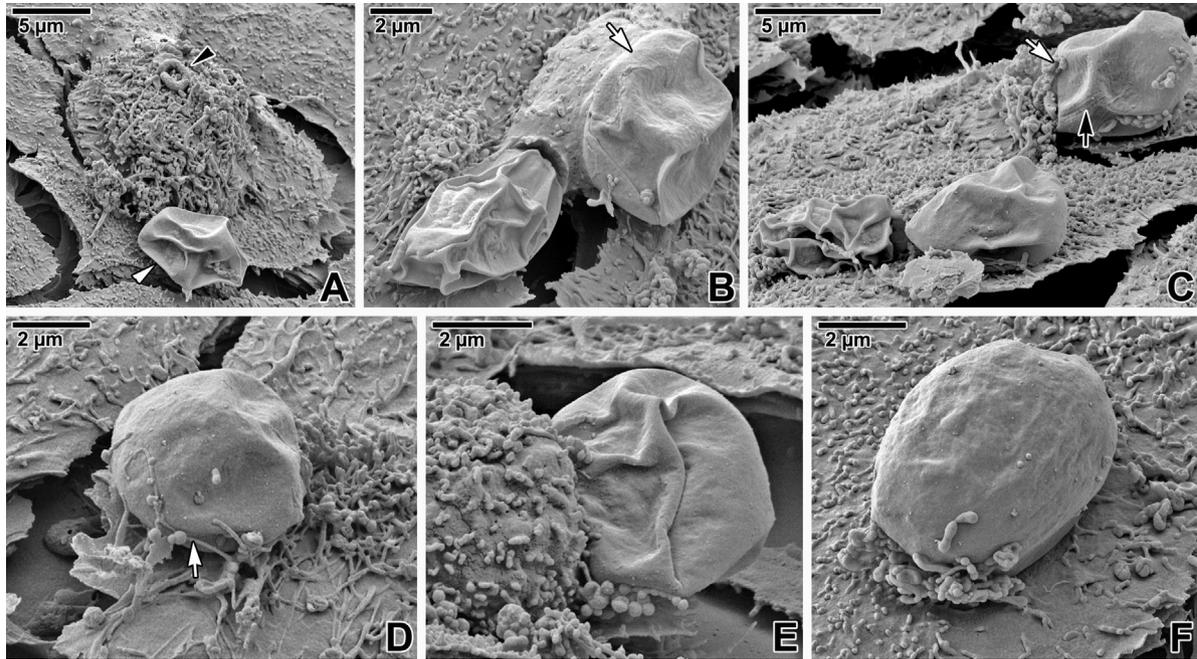
Fig. 5. Scanning electron micrographs of HT-29 cell lines inoculated with *Cryptosporidium proliferans* at 48 HPI. (A) Excysted oocyst (white arrowhead) and a sporozoite (black arrowhead) invading young HT-29 cell. (B) Two oocysts stuck into cultured cells, one of which is partially covered by a cultured cell's membrane fold (white arrow). (C) Three oocysts adhering to the surface of the cultured cells; biological debris adhering to the oocyst surface (white arrow), suture (black arrow). (D, E) More advanced developmental stage (meront or gamont) within parasitophorous sac; elongated microvilli (white arrow). (F) Mature developmental stage resembling oocyst within parasitophorous sac.
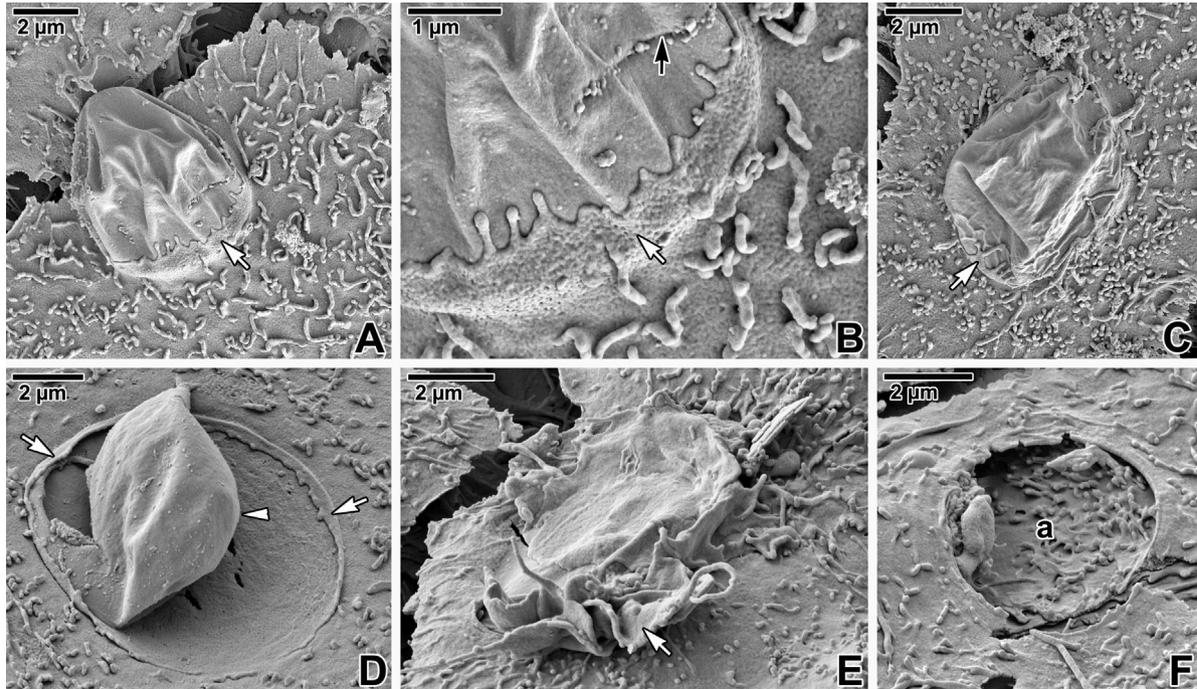

Fig. 6. Scanning electron micrographs of HT-29 cell lines inoculated with *Cryptosporidium proliferans* at 72 HPI. (A) Unexcysted oocyst gradually being enveloped by the cultured cell's plasma membrane (white arrow). (B) Detailed view of the plasma membrane fold (white arrow) raising along the oocyst shown in A; suture (black arrow). (C) Empty oocyst immersed into and partially embraced by the cultured cell (white arrow). (D) Circular imprint (white arrows) left after oocyst (white arrowhead) torn away from the cultured cell. (E) Remnants of raised plasma membrane (white arrow) of cultured cell left after previous parasitisation by *C. proliferans*. (F) Deep imprint of the parasite visible on the surface of the cultured cell (a).
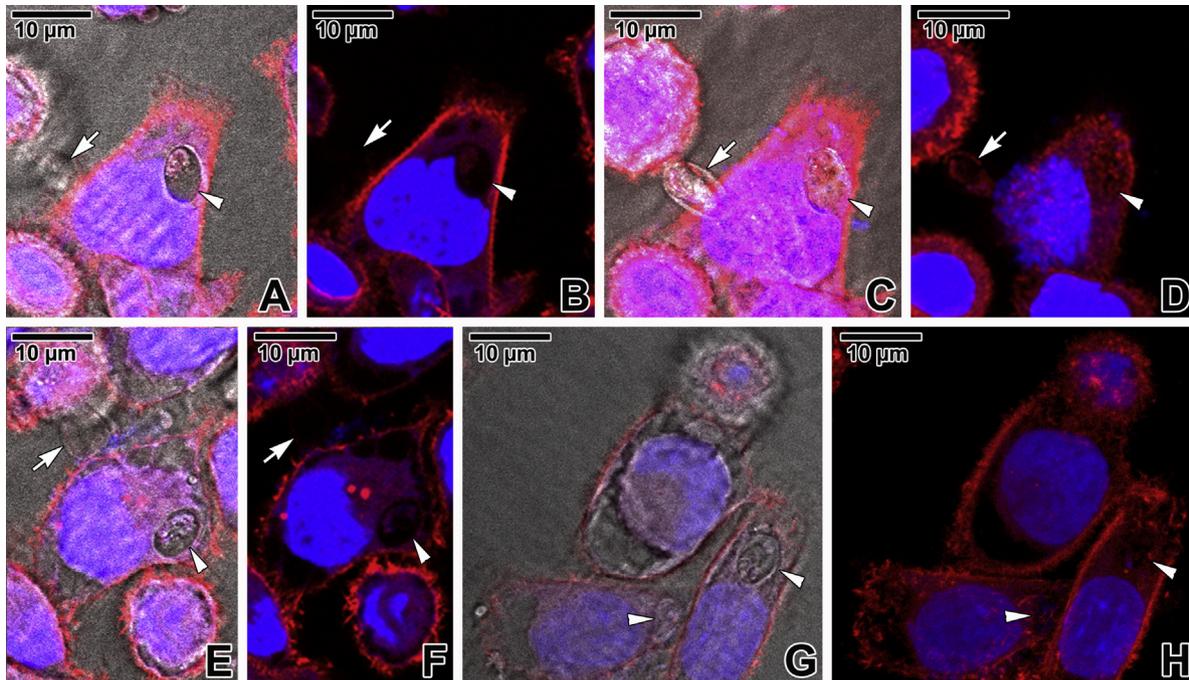
Fig. 7. Fluorescence visualisation of F-actin in HCT-8 cell lines inoculated with *Cryptosporidium proliferans* at 24, 48 and 72 HPI. (A–D) HCT-8 cells with *C. proliferans* oocysts at 24 HPI. One oocyst is partially immersed (white arrow), while the second is completely enveloped by the cultured cell (white arrowhead). CLSM with transmitted light (A, C) and CLSM (B, D). C–D represent different optical planes confirming that oocysts is completely embedded in the cultured cell. (E, F) Cultured cells at 48 HPI with one *C. proliferans* oocyst stuck to their surface (white arrow) and one embedded (white arrowhead). CLSM with transmitted light (E) and CLSM (F). (G, H) Two oocysts embedded in cultured cells (white arrowheads) at 72 HPI. CLSM with transmitted light (G) and CLSM (H). All micrographs are composite views created by flattening a series of optical sections using the TRITC (F-actin stained with phalloidin) and UV (nuclei stained with Hoechst) filter sets.

The same experiments, run under identical conditions, were also evaluated using phalloidin staining of filamentous actin (F-actin) for confocal laser scanning microscopy (CLSM). Different optical sections of the culture revealed the actual localisation of oocysts as well as their interactions with cultured cells. At 24 HPI, *C. proliferans* oocysts in both HCT-8 and HT-29 cell lines were predominantly located in gaps in the discontinuous monolayer and usually stuck to the lateral side of the cultured cells (Figs. 7A–D and 8A, B). At 48 HPI, when the monolayer was more continuous, oocysts occurred mainly on the free surface of cell culture, more or less embedded in individual cells. While fluorescently visualised cultured cell actin filaments started to envelope the oocysts in HT-29, a similar reaction was not observed in HCT-8 (Figs. 7E, F and 8C, D). At 72 HPI, oocysts were deeply embedded within the monolayer, with increased accumulation of F-actin surrounding the oocysts in the HT-29 cell lines (Fig. 8E, F), but negligible reorganisation of F-actin in the HCT-8 cell lines (Fig. 7G, H).

Experimental inoculation of HCT-8 and HT-29 cell lines with polystyrene microspheres

At 24 HPI, polystyrene microspheres were recorded lying on the surface of both the HCT-8 and HT-29 cell lines, with no significant response from individual cultured cells (Figs. 9A, B and 10A, B) and only biological debris adhering to the microspheres (Fig. 9C). Nevertheless, tiny elongated cultured cell microvilli were attached to the microspheres (Fig. 9D). At 48 HPI, the microspheres appeared to be clustering in gaps in the HCT-8 monolayer (Fig. 9E), while others were adhered to the culture's surface (Figs. 9F, G and 10C). At 72 HPI, similar results were observed, with no real interaction between microspheres and cells recorded (Figs. 9H–J and 10D–F). It is necessary to mention that daily washing and changing of the medium considerably reduced the total number of polystyrene microspheres adhering to the cell culture over time.

Fluorescence observations on HCT-8 and HT-29 cell lines inoculated with polystyrene microspheres were performed at the same time as those above. At 24 HPI, distribution of actin filaments within the cultured cells of both cell lines indicated no response to the polystyrene microspheres (Fig. 11A, B) or only shallow imprints of the cultured cell cytoskeleton (Fig. 12A–C). Evaluation of cultures at 48 HPI showed similar results, i.e. cultured cell actin filaments had not enveloped the microspheres (Fig. 12D–F); at most, microsphere imprints were seen on cell surfaces (Fig. 11C, D). Even at 72 HPI, no change in F-actin organisation was noticed (Fig. 11E, F).
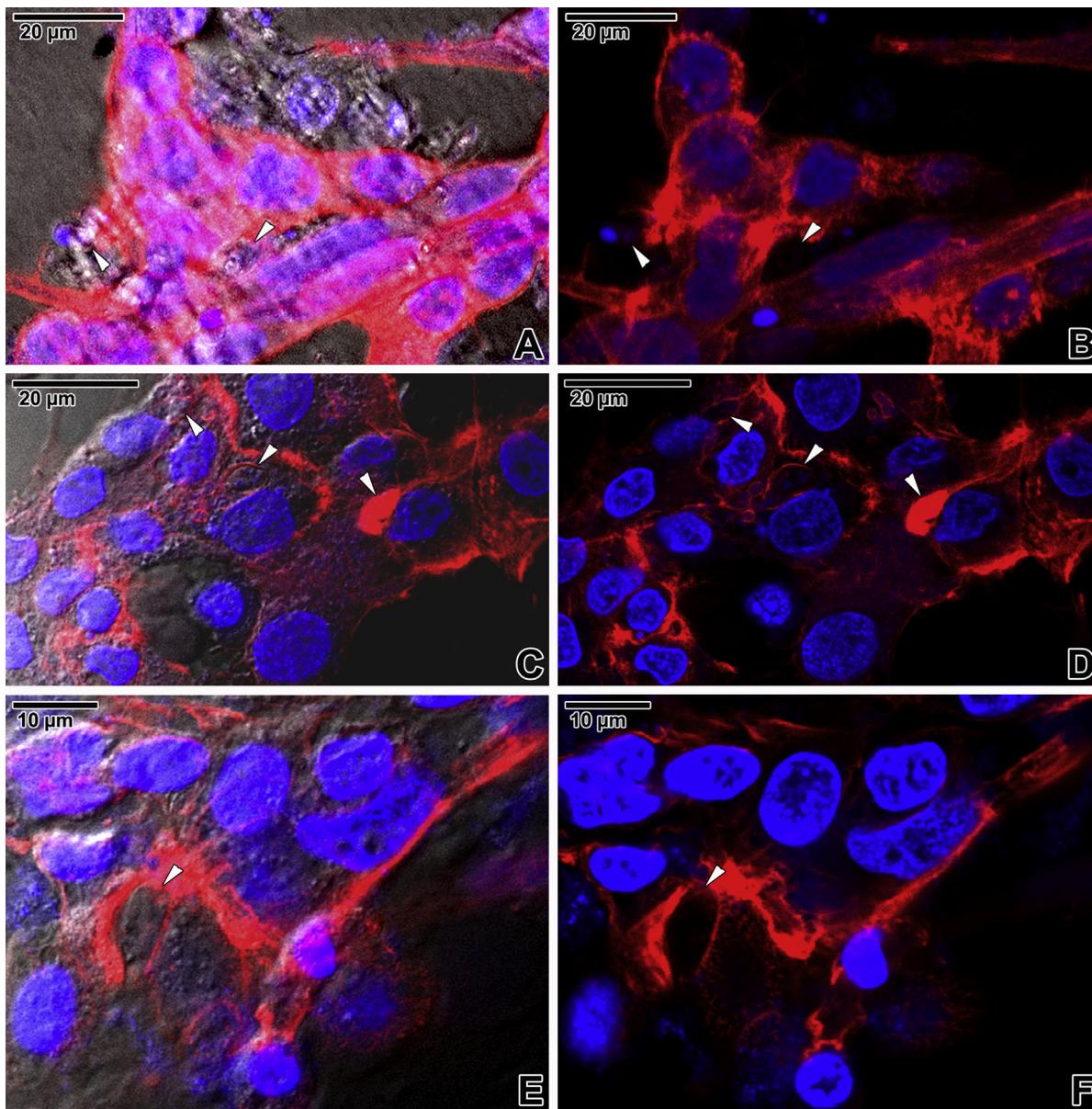
Fig. 8. Fluorescence visualisation of F-actin in HT-29 cell lines inoculated with *Cryptosporidium proliferans* at 24, 48 and 72 HPI. (A, B) HT-29 cells with *C. proliferans* oocysts (white arrowheads) at 24 HPI. CLSM with transmitted light (A) and CLSM (B). (C, D) Deeply immersed oocysts (white arrowheads), obviously enveloped by cultured cell F-actin at 48 HPI. CLSM with transmitted light (C) and CLSM (D). (E, F) Increased accumulation of F-actin surrounding the *C. proliferans* oocysts (white arrowheads) at 72 HPI. CLSM with transmitted light (E) and CLSM (F). All micrographs are composite views created by flattening a series of optical sections using the TRITC (F-actin stained with phalloidin) and UV (nuclei stained with Hoechst) filter sets.

Simulated parasitisation of HCT-8 and HT-29 cell lines with *C. proliferans* antigen-coated polystyrene microspheres

On the basis of data obtained during the previous two experiments, further trials were designed in which HCT-8 and HT-29 cell lines were inoculated with polystyrene microspheres coated with *C. proliferans* antigens (obtained from oocyst/sporozoite homogenate).

At 24 HPI, HCT-8 cell lines displayed elongated filamentous microvilli of cultured cells embracing the foreign object (Fig. 13A–C). At 48 HPI, the cell lines were showing an increased response to the antigen-coated microspheres (Fig. 13D, E), with microspheres now covered with cultured cell plasma membrane folds (Fig. 13F). At 72 HPI, we documented the gradual formation of cultured cell 'shelters', covering the microspheres in a manner similar to parasitophorous sacs (Fig. 13G–I). Formation of these shelters
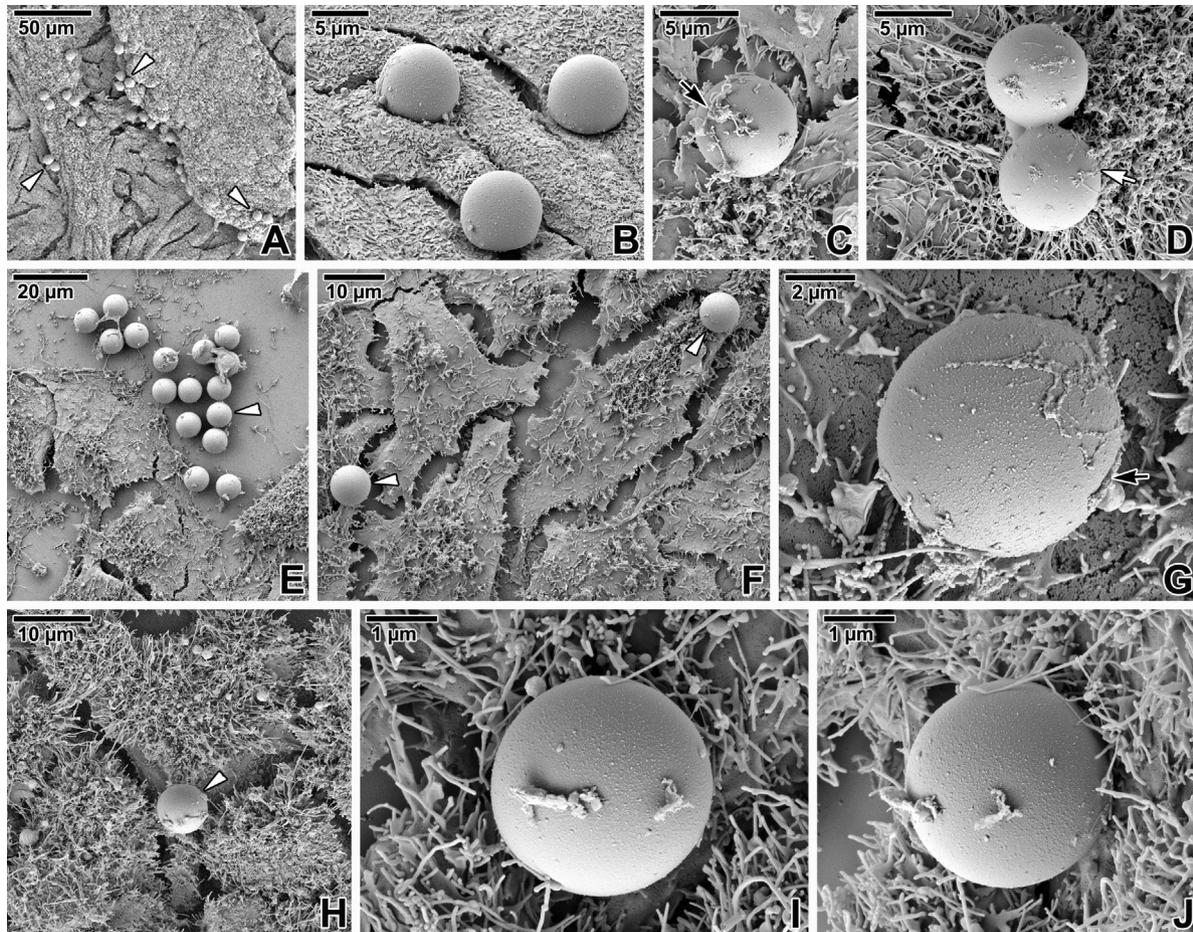
Fig. 9. Scanning electron micrographs of HCT-8 cell lines inoculated with polystyrene microspheres at 24, 48 and 72 HPI. (A) HCT-8 monolayer with polystyrene microspheres (white arrowheads) on its surface at 24 HPI. (B) Lateral view at 24 HPI of three polystyrene microspheres laying on the surface of cultured cells that show no reaction to the foreign objects. (C) A polystyrene microsphere at 24 HPI covered with biological debris (black arrow). (D) Polystyrene microspheres at 24 HPI with adhering microvilli of surrounding cells (white arrow). (E) Polystyrene microspheres (white arrowhead) located mostly within monolayer gaps at 48 HPI. (F) Polystyrene microspheres (white arrowheads) laying on the surface of the HCT-8 monolayer at 48 HPI. (G) A polystyrene microsphere with debris (black arrow) on its surface at 48 HPI. (H) The surface of HCT-8 multilayer with a polystyrene microsphere (white arrowhead) at 72 HPI. (I, J) Detailed view of the top (I) and lateral side (J) of the same polystyrene microsphere at 72 HPI. Cultured cells show no reaction to the foreign objects.

often included both mechanisms; i.e. encapsulation as well as overgrowth by cultured cells.

The inoculation of HT-29 cell lines with *C. proliferans* antigen-coated microspheres showed similar results. Compared to HCT-8 cells, HT-29 cells typically had shorter filamentous microvilli; hence, interactions between cultured cells and the microspheres were more obvious. At 24 HPI, the microspheres were apparently immersed in the cells and accumulating into small groups (Fig. 14A–C). At 48 HPI, the antigen-coated microspheres had been partially enveloped by cultured cell plasma membranes (Fig. 14D–F), and had been completely covered by the cell culture by 72 HPI (Fig. 14G–I).

Simulated parasitisation with *C. proliferans* antigen-coated fluoresbrite polystyrene microspheres also showed both cell lines reacting to the presence of foreign objects.

Distribution of F-actin in cell lines at 24 HPI indicated that many microspheres were either deeply imprinted into individual cultured cells or were already overgrown by a newly formed layer of cells, and that microspheres had apparently been surrounded by elongated cultured cell microvilli (Figs. 15A, B and 16A–C). Observations at 48 HPI revealed further changes in the distribution of F-actin, with numerous holes in the cell lines apparent. The microspheres had been partially enveloped by cultured cell actin filaments (Fig. 16D–F), indicating the raising of plasma membrane folds (Fig. 15C). Prolonged incubation to 72 HPI resulted in encapsulation of the microspheres by cultured cells (Figs. 15D, E and 16G–K). Similar to cultures inoculated with parasites, the HT-29 showed more obvious changes in F-actin organisation in cultures inoculated with parasite antigen-coated microspheres when compared to the HCT-8 cell lines.
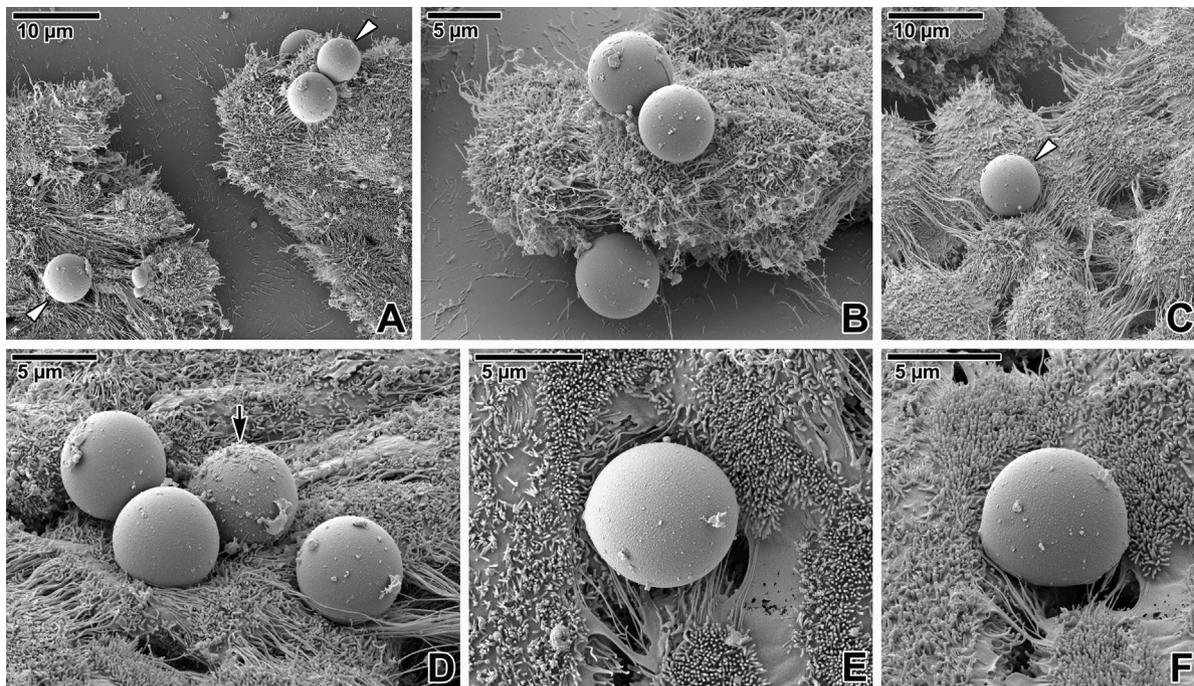
Fig. 10. Scanning electron micrographs of HT-29 cell lines inoculated with polystyrene microspheres at 24, 48 and 72 HPI. (A) HT-29 monolayer with polystyrene microspheres (white arrowheads) on its surface at 24 HPI. (B) Newly formed, round cells with polystyrene microspheres on their surface at 24 HPI. (C) HCT-8 multilayer surface with a polystyrene microsphere at 48 HPI. (D) Polystyrene microspheres covered with biological debris (black arrow) at 72 HPI. (E, F) Detailed view of the top (E) and lateral side (F) of the same polystyrene microsphere at 72 HPI. Cultured cells show no reaction to the foreign objects.

Discussion

In vitro systems have the benefit of allowing investigations into host-parasite interactions that cannot be observed within the host's own body, and thus the establishment of a successful in vitro culture system of *Cryptosporidium* spp. has been a challenge for many researchers. Since achievement of the first in vitro cultivation of cryptosporidian asexual developmental stages in 1983 (Woodmansee and Pohlenz 1983), only little progress has been made. While a further study reported the successful cultivation of human *Cryptosporidium* isolates, including both asexual and sexual stages in several cell lines (Current and Haynes 1984), anecdotal reports suggest that attempts to replicate these results have been disappointing (Arrowood 2002). Although later protocols appear suitable for developing cryptosporidian stages, long-term maintenance in culture systems has proven unsuccessful as the infection tends to peak and decline at around 48–72 HPI (Borowski et al. 2010; Gut et al. 1991; McDonald et al. 1990; Rosales et al. 1993; Upton et al. 1994; Wu et al. 2009).

In this study, *C. proliferans* strain TS03 (previously *C. muris*) was cultivated on the HCT-8 and HT-29 cell lines used in previous studies reporting completion of *Cryptosporidium* sp. life cycle in vitro (Alcantara Warren et al. 2008; Flanigan et al. 1991; Hijjawi et al. 2001, 2002; Upton et al. 1995). Based on suggestions in the studies mentioned above, the RPMI 1640 cultivation medium used in our study was supplemented with antibiotics/antimycotics, FBS, L-glutamine

and sodium bicarbonate and enriched with vitamins and glucose. In contrast to protocols using 10% FBS (Choi et al. 2004; Flanigan et al. 1991; McDonald et al. 1990) or 1% FBS (Borowski et al. 2010; Hijjawi et al. 2001, 2002), however, the concentration of FBS in our study was set at 5% based on observations on sporozoite motility using *C. proliferans* strain TS03 (Melicherová et al. 2016). Although there is some indication that components of FBS could inhibit parasite growth (Woods and Upton 2007), another study has shown that FBS can enhance the motility of sporozoites (Upton et al. 1995), consistent with our study. In general, appropriate concentrations of serum proteins (FBS, FCS, and BSA) appear to have a positive influence on parasite motility (Hijjawi et al. 2002; Melicherová et al. 2016; Upton et al. 1995). In addition, four vitamins (folic acid, 4-aminobenzoic acid, calcium pantothenate and ascorbic acid) were added to the medium as they have been shown to support interaction between the parasite (*C. parvum*) and host cells (Hijjawi et al. 2001; Upton et al. 1995). While investigating the optimal cultivation conditions for *C. muris* in human stomach adenocarcinoma cell lines, further study failed to notice any positive or negative effect of vitamins on parasite growth; though they do appear beneficial for the maintenance of cell cultures inoculated with pathogens (Choi et al. 2004). The positive impact of glucose on parasite growth has previously been described (Upton et al. 1995). Based on the results of previous studies, standardised in vitro cultivation conditions (i.e. 37 °C, 5% CO_2, 95% O_2) were adjusted as a reduc-
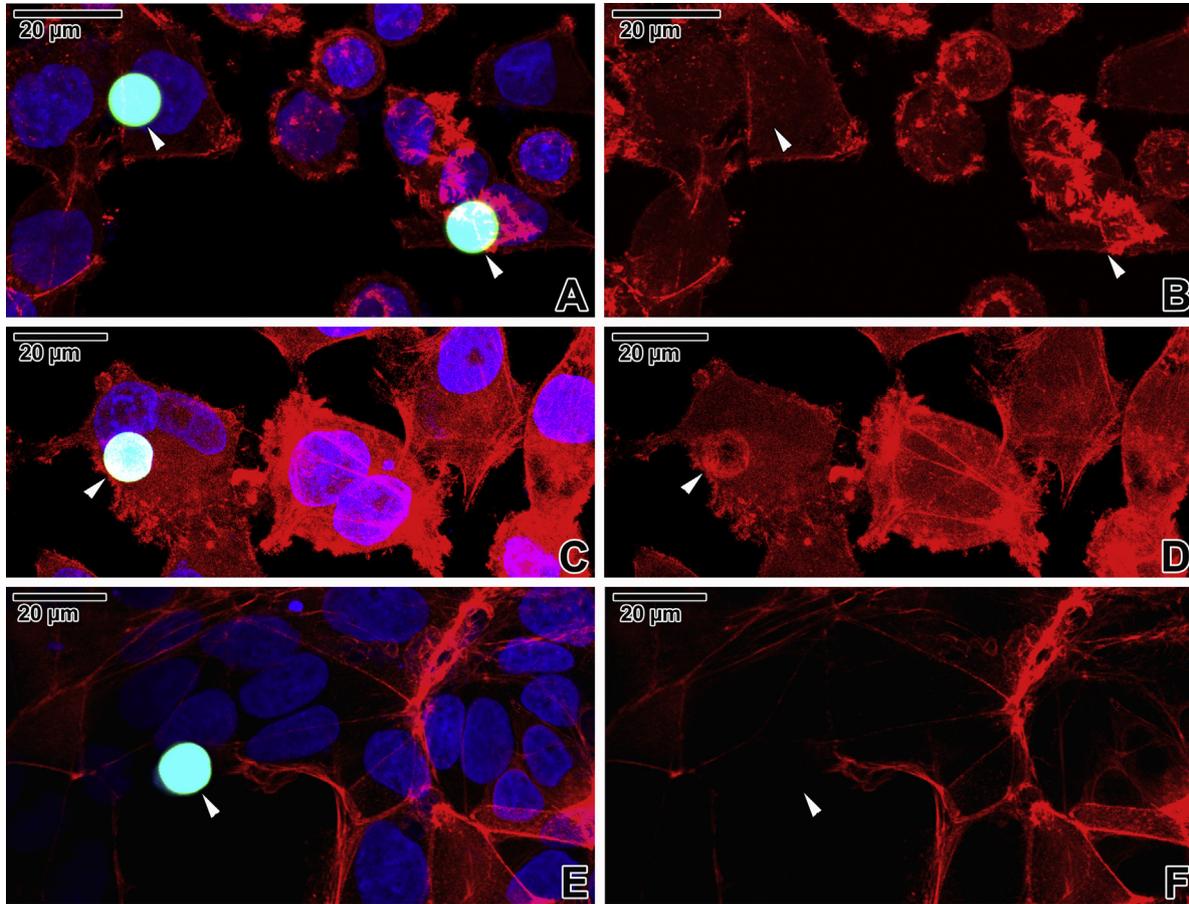
Fig. 11. Fluorescence visualisation of F-actin in HCT-8 cell lines inoculated with polystyrene microspheres at 24, 48 and 72 HPI. (A, B) HCT-8 cells inoculated with fluorescent microspheres (white arrowheads), showing no response to foreign objects at 24 HPI. CLSM. (C, D) HCT-8 cell lines at 48 HPI, showing a deep imprint only below the fluorescent microsphere (white arrowhead). CLSM. (E, F) HCT-8 cells with fluorescent microsphere (white arrowhead), showing no response to inoculation with foreign objects at 72 HPI. CLSM. A, C and E are composite views created by flattening a series of optical sections using the TRITC (F-actin stained with phalloidin), FITC (fluorescent microspheres) and UV (nuclei stained with Hoechst, fluorescent microspheres) filter sets. B, D and F are views created by flattening a series of optical sections using only the TRITC (F-actin stained with phalloidin) filter set.

tion in the level of O_2 in the atmosphere has been seen to have a stimulating effect on host cell penetration and subsequent parasite development (Borowski et al. 2010; Hijjawi et al. 2001; Upton et al. 1995). In our experiments, while the effect of O_2 reduction on parasite development was not significant it did have a positive effect on the cell lines, i.e. cultured cell mortality was reduced and culture viability was prolonged. Our preliminary (non-published) data indicated that the multilayers formed by older cultures hindered detection of attached cryptosporidia. Hence, we used 48-h 70–80% confluent monolayers exclusively for experimental inoculation with *C. proliferans*. While evaluating freshly confluent (48-h) and aged (up to six-days) HCT-8 cell monolayers for their ability to support *C. parvum* infection, another study showed that it was possible to use cell monolayers up to three weeks old as they developed the same number of parasite infection clusters as freshly confluent samples (Sifuentes and Di Giovanni 2007). In this study, majority of *C. proliferans* developmental stages were found near dividing or newly

formed round cells, hereby supporting the hypothesis that cryptosporidia prefer dividing cultured cells (Widmer et al. 2006).

In contrast to study documenting early trophozoites of *C. parvum* after six hours (Borowski et al. 2010), the first early trophozoites of *C. proliferans* were detected at 48 h. Here we should highlight that, while numerous cryptosporidian sporozoites were observed inspecting potential host cells with their prolonged apical ends, they often left without invasion. In accordance with Borowski et al. (2010), the thin and prolonged apical end is a typical feature for sporozoites that appear to be making host cell contact, while the sporozoites isolated from supernatant do not exhibit this apical prolongation. Moreover, our data (only few attached and successfully developing parasites observed throughout the entire experiment) suggest that the HCT-8 and HT-29 cell lines are appropriate for cultivation of both intestinal (e.g. *C. parvum* and *C. hominis*) and gastric (e.g. *C. andersoni*) pathogens that infect humans (Arrowood 2002; Hashim et al. 2006;
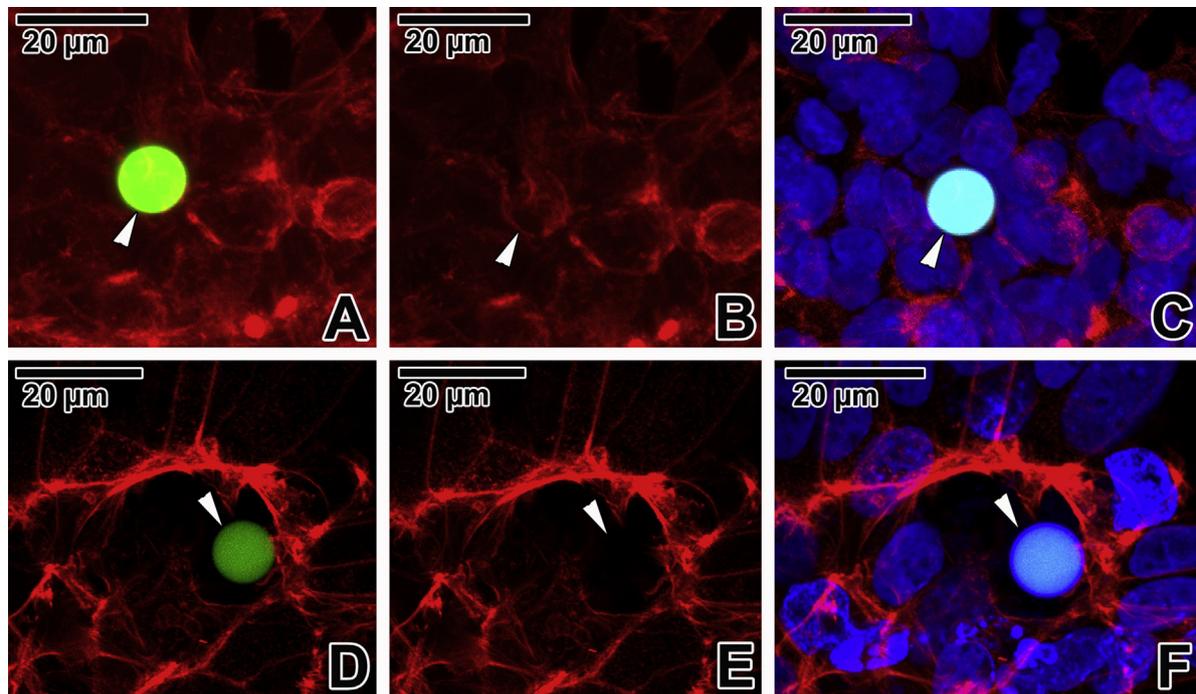
Fig. 12. Fluorescence visualisation of F-actin in HT-29 cell lines inoculated with polystyrene microspheres at 24 and 48 HPI. (A–C) HT-29 cells with fluorescent microsphere (white arrowhead), showing no reaction to foreign objects at 24 HPI. CLSM. (D–F) HT-29 cells with deeply immersed fluorescent microsphere (white arrowhead), showing no reaction to foreign objects at 48 HPI. CLSM. A and D are composite views created by flattening a series of optical sections using the TRITC (F-actin stained with phalloidin) and FITC (fluorescent microspheres) filter sets. B and E are views created by flattening a series of optical sections using the TRITC (F-actin stained with phalloidin) filter set only. C and F are composite views created by flattening a series of optical sections using the TRITC (F-actin stained with phalloidin), FITC (microspheres) and UV (nuclei stained with Hoechst, fluorescent microspheres) filter sets.

Jiang et al. 2014; Morada et al. 2016; Perez Cordon et al. 2007; Upton et al. 1994, 1995), but not the gastric pathogen *C. proliferans*, which mostly occurs in rodents.

Detailed electron microscopic studies showed that invading zoites of *Cryptosporidium* spp. became partially enveloped by the host cell membrane, resulting in formation of parasitophorous sac enclosing the entire parasite (e.g. Lumb et al. 1988; Valigurová et al. 2007, 2008). Unexpectedly, our in vitro system showed that embracing of parasites by the cultured cell membrane was not only induced by sporozoites but also unexcysted or empty oocysts, which were routinely observed encapsulated by the membrane. Analysis of oocyst adherence to hosts cells has revealed that the presence of molecules containing *N*-acetyl-galactosamine on oocysts may help them attach (Stein et al. 2006). The lectin-enhanced attachment to host cells could increase the efficiency of the infection process by bringing sporozoites into close proximity with host cells. Moreover, the excystation does not change the lectin binding sites on the oocyst (Stein et al. 2006). We speculate, the strong adhesion of oocysts to the cell line surface in our in vitro study could be explained by an excess of such molecules, the levels of which could be reduced in vivo while passing through the host's digestive system. Numerous unexcysted oocysts with sutures obviously closed were still present in the cell lines, even at 48 and 72 HPI. Hence, the question arises as to whether the oocysts described in other studies (e.g. Choi et al. 2004; Hijjawi et al. 2001; Rosales et al. 1993) were actually newly-formed oocysts or were simply oocysts from the original inoculation that had not been washed away during culture rinsing. Curiously, sutures visible on the unexcysted oocysts in our study were usually orientated toward the cultured cell's surface. Furthermore, sutures were often embedded in the cell culture and thus were difficult to distinguish from attached cryptosporidia. This positioning could be the result of sporozoites' movement inside the oocyst (in addition to oocyst balance and the pull of gravity), with such behaviour helping to shorten the distance between released sporozoites and the cell surface. Importantly, these oocysts were almost indistinguishable from advanced developmental stages such as meronts or gamonts enveloped by parasitophorous sacs, which could be responsible for the potential incorrect determination of developmental stages in studies based exclusively on light and scanning electron microscopy. In this study, we routinely used tilting and rotation of samples within the scanning electron microscope in order to confirm the shape of the cryptosporidian developmental stage and avoid misidentification as much as possible.

The numerous reported failures to replicate successful in vitro cultivation of cryptosporidia suggests that completion of their life cycle on cell lines may be attributable to either rare coincidence or the flexibility of specific cryptosporid-
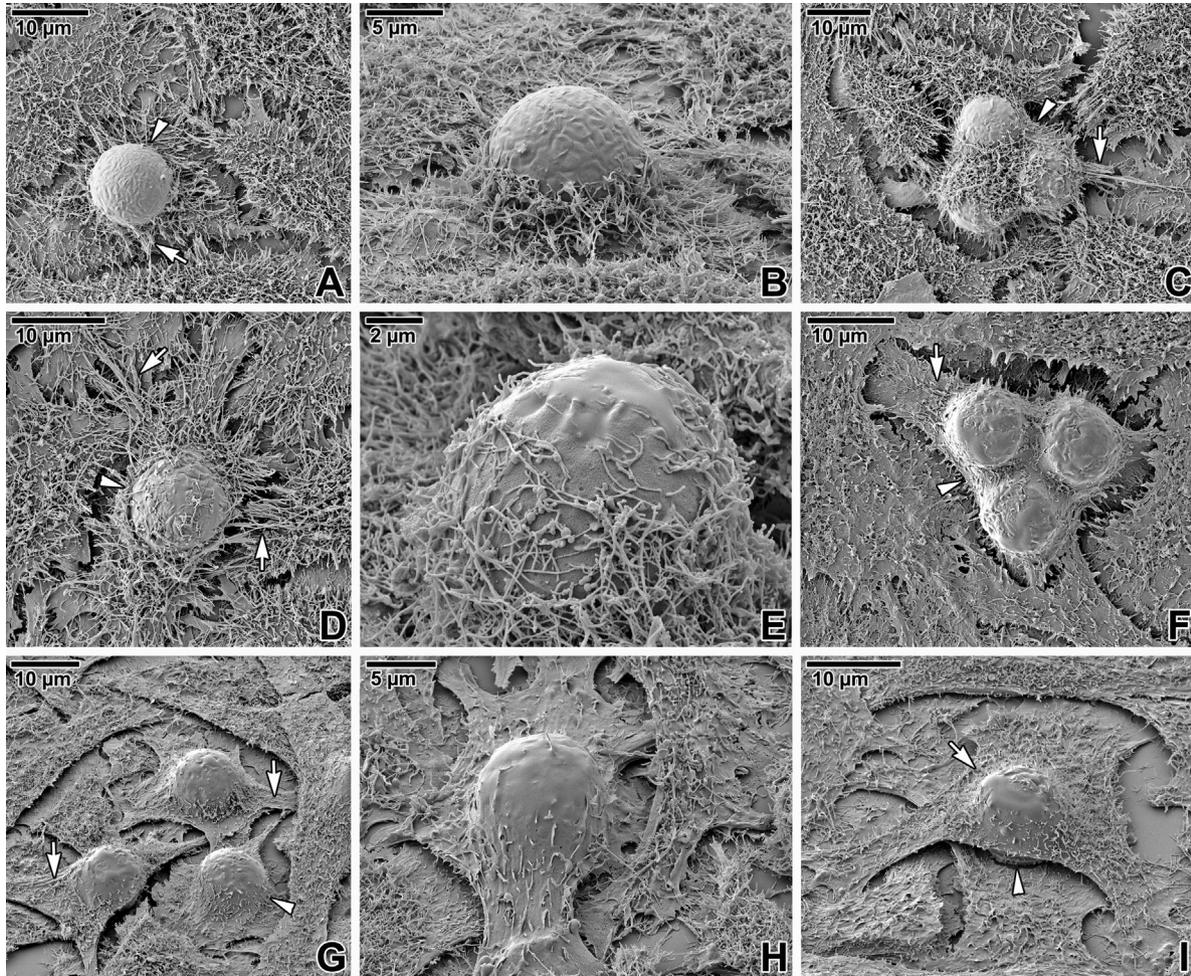
Fig. 13. Scanning electron micrographs of HCT-8 cell lines inoculated with *Cryptosporidium proliferans* antigen-coated polystyrene microspheres at 24, 48 and 72 HPI. (A) HCT-8 monolayer with an antigen-coated microsphere (white arrowhead) at 24 HPI. Note the slight elongation of surrounding microvilli (white arrow). (B) A more detailed, lateral view of the microsphere shown in A. (C) Three antigen-coated microspheres (white arrowhead) embraced by HCT-8 projections with elongated microvilli (white arrow) at 24 HPI. (D) HCT-8 cells with microsphere (white arrowhead) at 48 HPI. Note the more intensive reaction, characterised by the presence of numerous elongated microvilli (white arrows) enveloping the microsphere. (E) A detailed lateral view of the microsphere shown in D. (F) Three antigen-coated microspheres (white arrowhead) completely covered with HCT-8 cell plasma membrane (white arrow) at 48 HPI. (G) An HCT-8 multilayer at 72 HPI, with three microspheres (white arrowhead) completely covered with cultured cells (white arrows). (H, I) A detailed top (H) and lateral (I) view of an antigen-coated microsphere (white arrowhead) enveloped by HCT-8 cell (white arrow) at 72 HPI.

ian isolates to develop under unusual conditions. Between 48 and 72 HPI, many previous studies have recorded a peak in cryptosporidian development along with the presence of both asexual and sexual stages, with subsequent decrease in the parasite number (Aji et al. 1991; Flanigan et al. 1991; McDonald et al. 1990; Rochelle et al. 2001; Wu et al. 2009). Despite following the protocols and conditions specified in previous studies (Choi et al. 2004; Hijjawi et al. 2001; King et al. 2011; Rosales et al. 1993), we were only able to record the initial phase of the *C. proliferans* life cycle, up to the appearance of trophozoites and meront-/gamont-like stages, and these were only present in extremely low numbers. We detected few stages resembling oocysts enveloped by parasitophorous sac, however, their sporadic occurrence and

location not suitable for SEM tilting/rotation did not allow a reliable determination.

We used phalloidin staining and confocal laser scanning microscopy in our study in order to reveal changes in actin filaments distribution in parasitised cells or cultured cells with oocysts attached. It is well known that epithelial cells respond to the presence of cryptosporidia with cytoskeletal modulations such as actin polymerisation and villin aggregation (Elliott and Clark 2000). Previous studies described reorganisation of host F-actin into a plaque-like structure at the host-parasite interface during parasite invasion, the structure persisting during parasite development. Similar accumulation of polymerised actin was also documented at the base and within parasitophorous sacs surrounding another epicellular apicomplexan, protococcidian *Eleutheroschizon duboscqi*
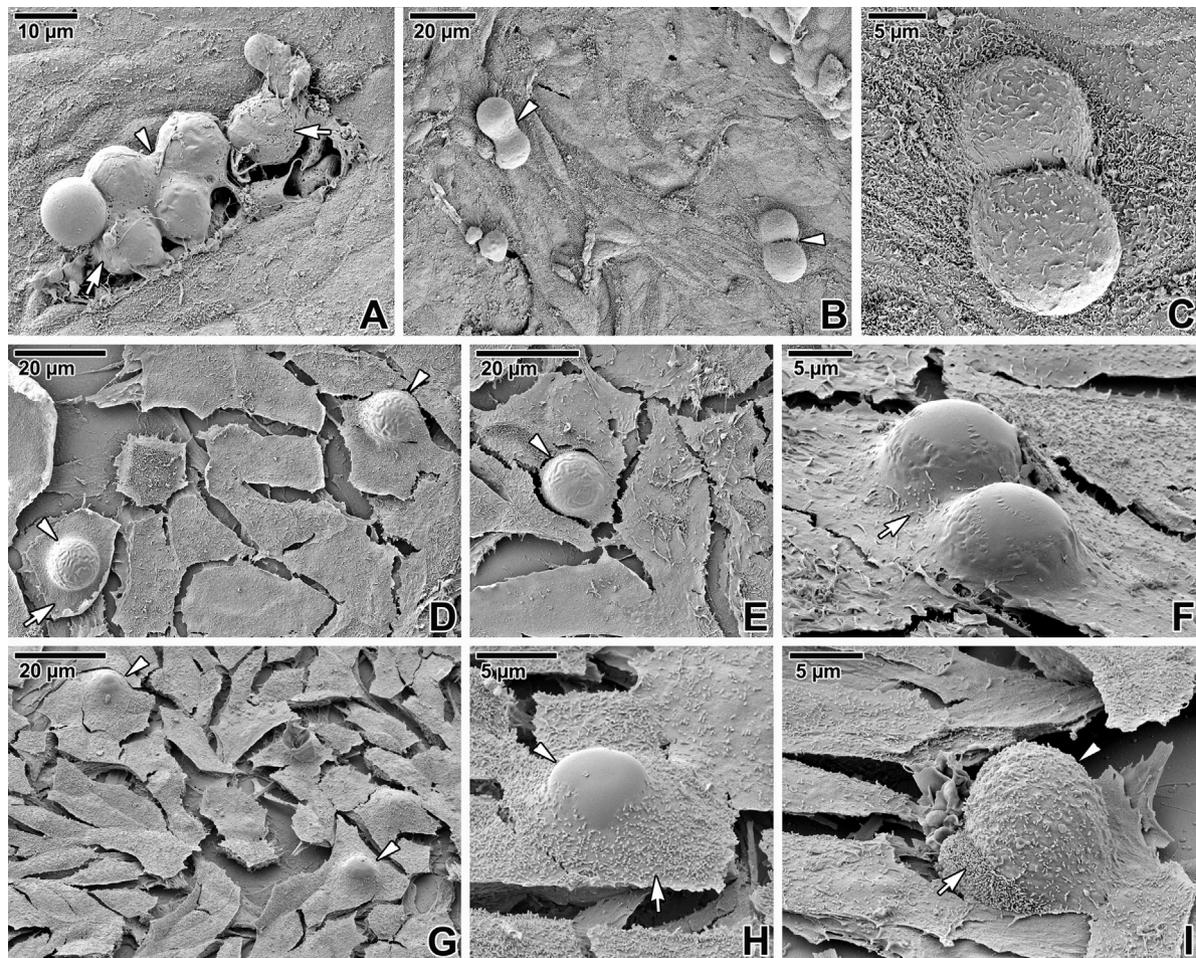
Fig. 14. Scanning electron micrographs of HT-29 cell lines inoculated with *Cryptosporidium proliferans* antigen-coated microspheres at 24, 48 and 72 HPI. (A) An HT-29 cell line with a group of antigen-coated microspheres (white arrowhead), showing signs of reaction (white arrows) to the foreign objects at 24 HPI. (B) Microspheres (white arrowheads) completely embraced by HT-29 cells at 24 HPI. (C) A detailed top view of the two microspheres shown in B. (D, E) HT-29 cell line with microspheres (white arrowheads) at 48 HPI. Note the intensive interaction of the HT-29 plasma membrane (white arrow) with the surface of the microspheres. (F) A detailed lateral view of two microspheres enveloped by HT-29 cell plasma membrane (white arrow) at 48 HPI. (G) Microspheres completely overlain by HT-29 cells at 72 HPI (white arrowheads). (H) A more detailed view of the microsphere (white arrowhead) shown in G. Note the HT-29 plasma membrane (white arrow) covering the microsphere. (I) Another view of a microsphere (white arrowhead) completely covered with HT-29 cells (white arrow) at 72 HPI.

(Valigurová et al. 2015). Cryptosporidia, in contrast, showed only low amounts of F-actin within their parasitophorous sacs (Bonnin et al. 1999). Interestingly, this study revealed that even contact with unexcysted oocysts or microspheres coated with cryptosporidian antigens induces the F-actin reorganisation in cultured cells, resulting in the formation of F-actin network surrounding the foreign object. This reaction was more evident in HT-29 cell lines with visibly shorter microvilli.

A further topic of this study was to evaluate whether the unusual enveloping of *C. proliferans* oocysts by cultured cell projections was provoked by the parasite itself or represents an innate reaction of cell lines to foreign objects in general. For this purpose, we designed a test that simulated parasitisation of cell lines using an experimental inoculation of polystyrene microspheres. Pure microspheres failed to induce an obvious reaction in both types of cell culture (HCT-8 and HT-29); however, those covered with cryptosporidian antigens were regularly enveloped by cultured cell plasma membrane folds. Hence, we conclude that this behaviour of cell culture is provoked by the parasite and is not innate.

It is usually assumed that a parasite actively manipulates the target cells before and during invasion (Borowski et al. 2008; Lumb et al. 1988). While motility of apicomplexan zoites is considered the main mechanism facilitating host cell invasion, our observations show that motility of *C. proliferans* sporozoites was limited and featureless (Melicherová et al. 2016). This concurs with the study stating that, in contrast to other apicomplexan zoites (e.g. *Plasmodium* spp., *Toxoplasma gondii*), *Cryptosporidium* invasion is a passive process that does not require actomyosin motility machinery (Forney et al. 1998). Aggregation of Gal-GalNAc glycoproteins in the plasma membrane of invaded cells at the sporozoite attachment site initiates a signalling cascade
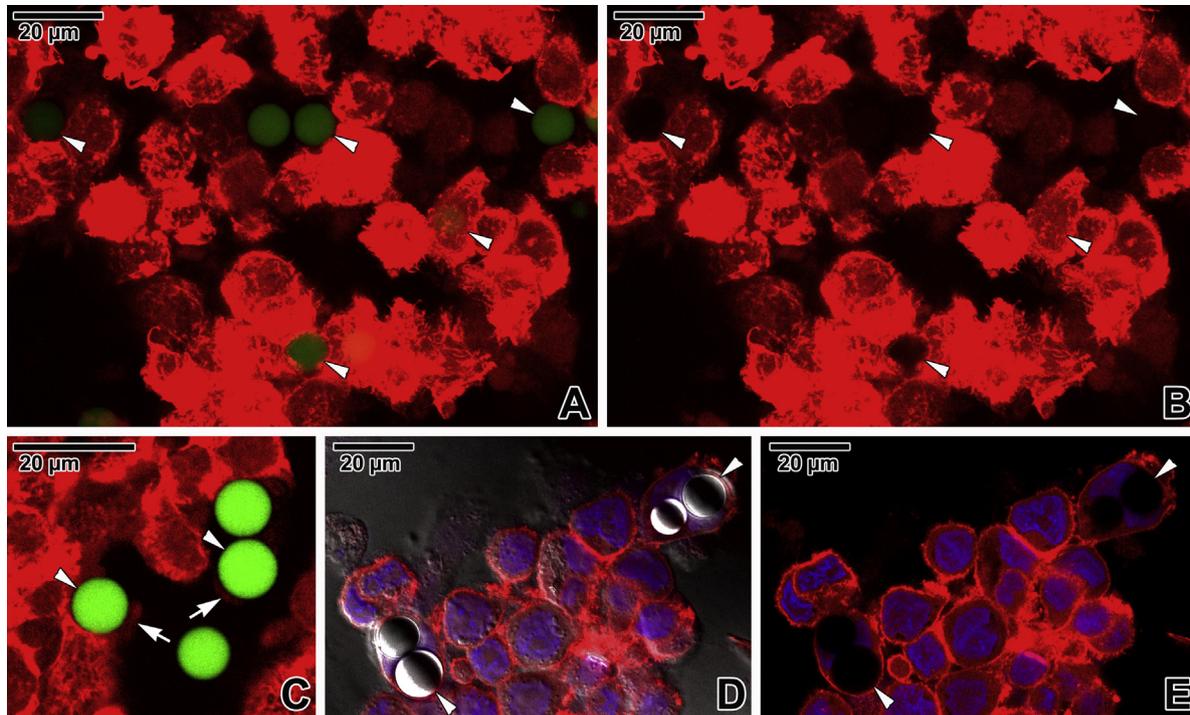
Fig. 15. Fluorescence visualisation of F-actin in HCT-8 cell lines inoculated with *Cryptosporidium proliferans* antigen-coated polystyrene microspheres at 24, 48 and 72 HPI. (A, B) HCT-8 cells with their projections gradually enveloping the antigen-coated fluorescent microspheres (white arrowheads) at 24 HPI. CSLM. (C) HCT-8 cells with fluorescent microspheres (white arrowheads) at 48 HPI. Note the cultured cell membrane folds (white arrows) containing actin filaments that embrace the microspheres. CLSM. (D, E) HCT-8 cells with four deeply embedded non-fluorescent microspheres (white arrowheads) at 72 HPI. CLSM with transmitted light (D) and CLSM (E). A and C are composite views created by flattening a series of optical sections using the TRITC (F-actin stained with phalloidin) and FITC (fluorescent microspheres) filter sets. B is a view created by flattening a series of optical sections using the TRITC (F-actin stained with phalloidin) filter set only. D and E are composite views created by flattening a series of optical sections using the TRITC (F-actin stained with phalloidin) and UV (nuclei stained with Hoechst) filter sets.

resulting in actin-dependent membrane protrusion and encapsulation of the sporozoite in a parasitophorous sac (Nelson et al. 2006). Earlier studies have confirmed the presence of specific surface lectins on cryptosporidian sporozoites that may facilitate the attachment of sporozoites to the host cell. In a study focusing on *C. parvum* invasion/attachment proteins, for example, 61 proteins including 27 previously reported, were identified (Singh et al. 2015). Of these, two have been widely studied. The first is p30 (30 kDA Gal/GalNAc-specific lectin), which associates with the mucin-like microneme glycoprotein gp900, localises on the apical region of *C. parvum* and *C. hominis* sporozoites, binds to epithelial cells and mediates sporozoite attachment to these cells. The second is the apical complex glycoprotein CSL (1300-kDa) of *C. parvum* sporozoites/merozoites with properties consistent with being a sporozoite ligand for intestinal epithelial cells (Bhat et al. 2007; Joe et al. 1994, 1998; Langer and Riggs 1999). Other data, however, suggest that pre-treatment of parasites with Gal/GalNAc inhibits the entry of *C. parvum* into HCT-8 cells and primary bovine cells but has no effect on entry of either *C. parvum* or *C. hominis* into primary human cells or *C. hominis* into HCT-8 cells (Hashim et al. 2006). These results confirm that success of in vitro cul-

tivation depends on the choice of the appropriate cell line preferred by specific cryptosporidian species. Another work, comparing the influence of FBS-enriched medium with and without Gal/GalNAc oligosaccharides and medium without FBS on trophozoite development, revealed that sporozoites were positively affected by the presence of Gal/GalNAc in FBS-medium, accelerating their transformation into trophozoites (Edwinson et al. 2016).

The outer layer of cryptosporidian oocysts is also covered by a carbohydrate matrix. This surface coat, the glycocalyx, plays an important role in modulation of resistance to proteolysis, antibody binding and adhesion to host cells (Nanduri et al. 1999). Our experiments revealed that, in addition to polybeads coated with an antigen 'cocktail' (obtained from oocysts with sporozoites), intact (unexcysted) or even empty oocysts were able to induce cultured cell plasma membrane modification and potentially complete envelopment within a cultured cell membrane-derived sac. Hence, oocyst surface antigens might not only serve for cell adhesion (Yao et al. 2007) but also represent a likely passive means of host cell manipulation at the oocyst stage. Furthermore, our data indicate that the enclosing of oocysts by HT-29 and HCT-8 cells was induced by the parasite antigens, and that this encapsu-
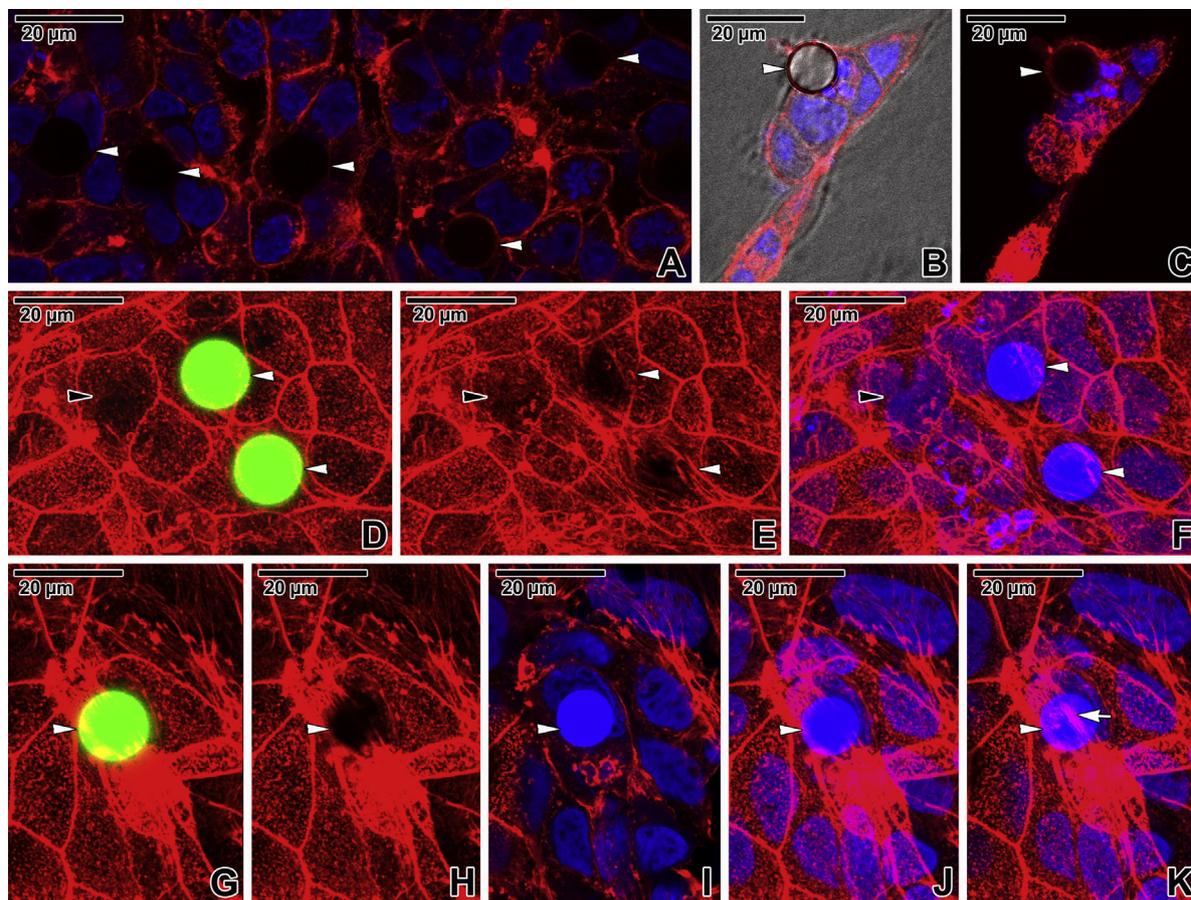
Fig. 16. Fluorescence visualisation of F-actin in HT-29 cell lines inoculated with *Cryptosporidium proliferans* antigen-coated polystyrene microspheres at 24, 48 and 72 HPI. (A–C) HT-29 cells with partially immersed antigen-coated non-fluorescent microspheres (white arrowheads) at 24 HPI. CLSM (A, C) and CLSM with transmitted light (B). (D–F) HT-29 cells with deeply immersed fluorescent microspheres that were partially enveloped by cultured cell actin filaments (white arrowheads) at 48 HPI. Note the crater (black arrowhead) from previously immersed microsphere that was probably washed away. CLSM. (G–K) The reaction of HT-29 cells to antigen-coated fluorescent microsphere (white arrowhead) at 72 HPI. The microsphere was completely encapsulated by the cultured cell (white arrow). CLSM. A-C, F and I-K are composite views created by flattening a series of optical sections using the TRITC (F-actin stained with phalloidin) and UV (nuclei stained with Hoechst, fluorescent microspheres) filter sets. D and G are composite views created by flattening a series of optical sections using the TRITC (F-actin stained with phalloidin) and FITC (fluorescent microspheres) filter sets. E and H are views created by flattening a series of optical sections using the TRITC (F-actin stained with phalloidin) filter set only.

lation of the parasite occurred independently of any active invasion by motile stages.

Several previous studies reported the occurrence of extracellular stages of cryptosporidia in cell-free cultures (Aldeyarbi and Karanis 2015; Boxell et al. 2008; Hijjawi et al. 2004; Yang et al. 2015). Moreover, some authors claim that even unexcysted cryptosporidian sporozoites (within oocysts) can continue to develop in cell-free culture systems and transform into their next stages (Hijjawi et al. 2010). These authors also observed morphologically distinct stages and considered them to be newly formed stages of *Cryptosporidium* spp. occurring exclusively in cell-free medium. Simultaneously, they conceded that the use of light microscopy only made it almost impossible to identify the exact developmental stage of cryptosporidia dispersed in medium. Nevertheless, it is important to mention that other studies have failed to propagate cryptosporidia in cell-free

culture and confirmed that some of the previously reported extracellular cryptosporidia-like objects could, in fact, be bacteria or debris (Girouard et al. 2006; Woods and Upton 2007). A study using molecular approaches has reported the proliferation of *C. parvum* in cell-free culture with a measurable, though limited, increase in the concentration of parasite DNA (Zhang et al. 2009). The latest study published on cell-free cultivation of cryptosporidia documented asexual stages only detected under a transmission electron microscope (Aldeyarbi and Karanis 2015). While a cell-free culture system would be very helpful for research focused on *Cryptosporidium* drug development, our data on the gastric pathogen *C. proliferans* indicates that individual cryptosporidian strains are variously susceptible to in vitro conditions. Moreover, during our in vivo (Melicherová et al. 2014) and in vitro studies (this study) of *C. proliferans*, we did not observe objects resembling the extracellular stages of

cryptosporidia. Nevertheless, it must be mentioned that light microscopic observation of the medium within well plates with inoculated cultures (performed in this study) might not be sufficient to reach unequivocal conclusion about non-existence of extracellular stages in *C. proliferans* cultivated in vitro.

Conclusions

In this study, we evaluated the development of the gastric parasite *Cryptosporidium proliferans* strain TS03 using in vitro culture systems HCT-8 and HT29. We documented free zoites apparently searching for an appropriate infection site and the presence of advanced stages enveloped by parasitophorous sac as well as already emptied sacs. Moreover, we recorded a curious reaction of cultured cells to the presence of the parasite, when even the unexcysted oocysts became enveloped by cultured cell projections. Therefore, we designed an experiment using polystyrene microspheres to evaluate the response of cell lines to simulated inoculation with cryptosporidian oocysts to verify their innate and parasite-induced behaviour. These observations revealed that cultured cell encapsulation of oocysts is induced by parasite antigens, independent of any active invasion or motility.

Acknowledgements

References

Aji, T., Flanigan, T., Marshall, R., Kaetzel, C., Aikawa, M., 1991. Ultrastructural study of asexual development of *Cryptosporidium parvum* in a human intestinal cell line. J. Protozool. 38, 82S–84S.

Alcantara Warren, C., Destura, R.V., Sevilleja, J.E., Barroso, L.F., Carvalho, H., Barrett, L.J., O'Brien, A.D., Guerrant, R.L., 2008. Detection of epithelial-cell injury, and quantification of infec-tion, in the HCT-8 organoid model of cryptosporidiosis. J. Infect. Dis. 198, 143–149.

Aldeyarbi, H.M., Karanis, P., 2015. Electron microscopic obser-vation of the early stages of *Cryptosporidium parvum* asexual multiplication and development in in vitro axenic culture. Eur. J. Protistol. 52, 36–44.

Arrowood, M.J., Sterling, C.R., 1987. Isolation of *Cryptosporid-ium* oocysts and sporozoites using discontinuous sucrose and isopycnic Percoll gradients. J. Parasitol. 73, 314–319.

Arrowood, M.J., 2002. In vitro cultivation of *Cryptosporidium* species. Clin. Microbiol. Rev. 15, 390–400.

Aydin, Y., Ozkul, I.A., 1996. Infectivity of *Cryptosporidium muris* directly isolated from the murine stomach for various laboratory animals. Vet. Parasitol. 66, 257–262.

Barta, J.R., Thompson, R.C.A., 2006. What is *Cryptosporidium*? Reappraising its biology and phylogenetic affinities. Trends Par-asitol. 22, 463–468.

Bartošová-Sojková, P., Oppenheim, R.D., Soldati-Favre, D., Lukeš, J., 2015. Epicellular apicomplexans: parasites on the way in. PLoS Pathog. 11, e1005080.

Bhat, N., Joe, A., PereiraPerrin, M., Ward, H.D., 2007. *Cryp-tosporidium* p30, a galactose/*N*-acetylgalactosamine-specific lectin, mediates infection in vitro. J. Biol. Chem. 282, 34877–34887.

Bonnin, A., Lapillonne, A., Petrella, T., Lopez, J., Chaponnier, C., Gabbiani, G., Robine, S., Dubremetz, J.F., 1999. Immunodetec-tion of the microvillous cytoskeleton molecules villin and ezrin in the parasitophorous vacuole wall of *Cryptosporidium parvum* (Protozoa: Apicomplexa). Eur. J. Cell Biol. 78, 794–801.

Borowski, H., Clode, P.L., Thompson, R.C.A., 2008. Active inva-sion and/or encapsulation? A reappraisal of host-cell parasitism by *Cryptosporidium*. Trends Parasitol. 24, 509–516.

Borowski, H., Thompson, R.C., Armstrong, T., Clode, P.L., 2010. Morphological characterization of *Cryptosporidium parvum* life-cycle stages in an in vitro model system. Parasitology 137, 13–26.

Boxell, A., Hijjawi, N., Monis, P., Ryan, U., 2008. Comparison of various staining methods for the detection of *Cryptosporidium* in cell-free culture. Exp. Parasitol. 120, 67–72.

Cavalier-Smith, T., 2014. Gregarine site-heterogeneous 18S rDNA trees, revision of gregarine higher classification, and the evo-lutionary diversification of Sporozoa. Eur. J. Protistol. 50, 472–495.

Choi, M.H., Hong, S.T., Chai, J.Y., Park, W.Y., Yu, J.R., 2004. In vitro culture of *Cryptosporidium muris* in a human stomach adenocarcinoma cell line. Korean J. Parasitol. 42, 27–34.

Clode, P.L., Koh, W.H., Thompson, R.C.A., 2015. Life without a host cell: what is *Cryptosporidium*? Trends Parasitol. 31, 614–624.

Current, W.L., Haynes, T.B., 1984. Complete development of *Cryp-tosporidium* in cell culture. Science 224, 603–605.

Dumenil, G., 2011. Revisiting the extracellular lifestyle. Cell. Microbiol. 13, 1114–1121.

Edwinson, A., Widmer, G., McEvoy, J., 2016. Glycoproteins and Gal-GalNAc cause *Cryptosporidium* to switch from an inva-sive sporozoite to a replicative trophozoite. Int. J. Parasitol. 46, 67–74.

Elliott, D.A., Clark, D.P., 2000. *Cryptosporidium parvum* induces host cell actin accumulation at the host–parasite interface. Infect. Immun. 68, 2315–2322.

Evering, T., Weiss, L.M., 2006. The immunology of parasite infections in immunocompromised hosts. Parasite Immunol. 28, 549–565.

Fayer, R., Ungar, B.L., 1986. *Cryptosporidium* spp. and cryptosporidiosis. Microbiol. Rev. 50, 458–483.

Feng, Y., Yang, W., Ryan, U., Zhang, L., Kváč, M., Koudela, B., Modrý, D., Li, N., Fayer, R., Xiao, L., 2011. Development of a multilocus sequence tool for typing *Cryptosporidium muris* and *Cryptosporidium andersoni*. J. Clin. Microbiol. 49, 34–41.

Flanigan, T.P., Aji, T., Marshall, R., Soave, R., Aikawa, M., Kaetzel, C., 1991. Asexual development of *Cryptosporidium parvum* within a differentiated human enterocyte cell line. Infect. Immun. 59, 234–239.

Forney, J.R., Vaughan, D.K., Yang, S.G., Healey, M.C., 1998. Actin-dependent motility in *Cryptosporidium parvum* sporozoites. J. Parasitol. 84, 908–913.

Girouard, D., Gallant, J., Akiyoshi, D.E., Nunnari, J., Tzipori, S., 2006. Failure to propagate *Cryptosporidium* spp. in cell-free culture. J. Parasitol. 92, 399–400.

Gut, J., Petersen, C., Nelson, R., Leech, J., 1991. *Cryptosporidium parvum*: in vitro cultivation in Madin-Darby canine kidney cells. J. Protozool. 38, 72S–73S.

Hashim, A., Mulcahy, G., Bourke, B., Clyne, M., 2006. Interaction of *Cryptosporidium hominis* and *Cryptosporidium parvum* with primary human and bovine intestinal cells. Infect. Immun. 74, 99–107.

Hijjawi, N.S., Meloni, B.P., Morgan, U.M., Thompson, R.C., 2001. Complete development and long-term maintenance of *Cryptosporidium parvum* human and cattle genotypes in cell culture. Int. J. Parasitol. 31, 1048–1055.

Hijjawi, N.S., Meloni, B.P., Ryan, U.M., Olson, M.E., Thompson, R.C., 2002. Successful in vitro cultivation of *Cryptosporidium andersoni*: evidence for the existence of novel extracellular stages in the life cycle and implications for the classification of *Cryptosporidium*. Int. J. Parasitol. 32, 1719–1726.

Hijjawi, N.S., Meloni, B.P., Ng'anzo, M., Ryan, U.M., Olson, M.E., Cox, P.T., Monis, P.T., Thompson, R.C., 2004. Complete development of *Cryptosporidium parvum* in host cell-free culture. Int. J. Parasitol. 34, 769–777.

Hijjawi, N., Estcourt, A., Yang, R., Monis, P., Ryan, U., 2010. Complete development and multiplication of *Cryptosporidium hominis* in cell-free culture. Vet. Parasitol. 169, 29–36.

Jiang, Y., Ren, J., Yuan, Z., Liu, A., Zhao, H., Liu, H., Chu, L., Pan, W., Cao, J., Lin, Y., Shen, Y., 2014. *Cryptosporidium andersoni* as a novel predominant *Cryptosporidium* species in outpatients with diarrhea in Jiangsu Province, China. BMC Infect. Dis. 14, 1–6.

Joe, A., Hamer, D.H., Kelley, M.A., Pereira, M.E., Keusch, G.T., Tzipori, S., Ward, H.D., 1994. Role of a Gal/GalNAc-specific sporozoite surface lectin in *Cryptosporidium parvum*–host cell interaction. J. Eukaryot. Microbiol. 41, 44S.

Joe, A., Verdon, R., Tzipori, S., Keusch, G.T., Ward, H.D., 1998. Attachment of *Cryptosporidium parvum* sporozoites to human intestinal epithelial cells. Infect. Immun. 66, 3429–3432.

Jones, K.H., Senft, J.A., 1985. An improved method to determine cell viability by simultaneous staining with fluorescein diacetate-propidium iodide. J. Histochem. Cytochem. 33, 77–79.

Kato, S., Jenkins, M.B., Ghiorse, W.C., Bowman, D.D., 2001. Chemical and physical factors affecting the excystation of *Cryptosporidium parvum* oocysts. J. Parasitol. 87, 575–581.

Kilani, R.T., Sekla, L., 1987. Purification of *Cryptosporidium* oocysts and sporozoites by cesium chloride and Percoll gradients. Am. J. Trop. Med. Hyg. 36, 505–508.

King, B.J., Keegan, A.R., Robinson, B.S., Monis, P.T., 2011. *Cryptosporidium* cell culture infectivity assay design. Parasitology 138, 671–681.

Koh, W., Clode, P.L., Monis, P., Thompson, R.C., 2013. Multiplication of the waterborne pathogen *Cryptosporidium parvum* in an aquatic biofilm system. Parasit. Vectors 6, 270.

Koh, W., Thompson, A., Edwards, H., Monis, P., Clode, P.L., 2014. Extracellular excystation and development of *Cryptosporidium*: tracing the fate of oocysts within *Pseudomonas* aquatic biofilm systems. BMC Microbiol. 14, 281.

Kváč, M., Sak, B., Květoňová, D., Ditrich, O., Hofmannová, L., Modrý, D., Vítovec, J., Xiao, L., 2008. Infectivity, pathogenicity, and genetic characteristics of mammalian gastric *Cryptosporidium* spp. in domestic ruminants. Vet. Parasitol. 153, 363–367.

Kváč, M., Havrdová, N., Hlásková, L., Daňková, T., Kanděra, J., Ježková, J., Vítovec, J., Sak, B., Ortega, Y., Xiao, L., Modrý, D., Chelladurai, J.R., Prantlová, V., McEvoy, J., 2016. *Cryptosporidium proliferans* n. sp. (Apicomplexa: Cryptosporidiidae): molecular and biological evidence of cryptic species within gastric *Cryptosporidium* of mammals. PLoS ONE 11, e0147090.

Langer, R.C., Riggs, M.W., 1999. *Cryptosporidium parvum* apical complex glycoprotein CSL contains a sporozoite ligand for intestinal epithelial cells. Infect. Immun. 67, 5282–5291.

Lumb, R., Smith, K., Odonoghue, P.J., Lanser, J.A., 1988. Ultrastructure of the attachment of *Cryptosporidium* sporozoites to tissue-culture cells. Parasitol. Res. 74, 531–536.

McDonald, V., Stables, R., Warhurst, D.C., Barer, M.R., Blewett, D.A., Chapman, H.D., Connolly, G.M., Chiodini, P.L., McAdam, K.P., 1990. In vitro cultivation of *Cryptosporidium parvum* and screening for anticryptosporidial drugs. Antimicrob. Agents Chemother. 34, 1498–1500.

Melicherová, J., Ilgová, J., Kváč, M., Sak, B., Koudela, B., Valigurová, A., 2014. Life cycle of *Cryptosporidium muris* in two rodents with different responses to parasitization. Parasitology 141, 287–303.

Melicherová, J., Mazourová, V., Valigurová, A., 2016. In vitro excystation of *Cryptosporidium muris* oocysts and viability of released sporozoites in different incubation media. Parasitol. Res. 115, 1113–1121.

Morada, M., Lee, S., Gunther-Cummins, L., Weiss, L.M., Widmer, G., Tzipori, S., Yarlett, N., 2016. Continuous culture of *Cryptosporidium parvum* using hollow fiber technology. Int. J. Parasitol. 46, 21–29.

Nanduri, J., Williams, S., Aji, T., Flanigan, T.P., 1999. Characterization of an immunogenic glycocalyx on the surfaces of *Cryptosporidium parvum* oocysts and sporozoites. Infect. Immun. 67, 2022–2024.

Nelson, J.B., O'Hara, S.P., Small, A.J., Tietz, P.S., Choudhury, A.K., Pagano, R.E., Chen, X.M., LaRusso, N.F., 2006. *Cryptosporidium parvum* infects human cholangiocytes via sphingolipid-enriched membrane microdomains. Cell. Microbiol. 8, 1932–1945.

Perez Cordon, G., Marin, C., Romero, D., Rosales, C., Sanchez Moreno, M., Rosales, M.J., 2007. More productive in vitro culture of *Cryptosporidium parvum* for better study of the

intra- and extracellular phases. Mem. Inst. Oswaldo Cruz 102, 567–571.

Rochelle, P.A., Ferguson, D.M., Johnson, A.M., De Leon, R., 2001. Quantitation of *Cryptosporidium parvum* infection in cell culture using a colorimetric in situ hybridization assay. J. Eukaryot. Microbiol. 48, 565–574.

Rosales, M.J., Mascaro, C., Osuna, A., 1993. Ultrastructural study of *Cryptosporidium* development in Madin-Darby canine kidney cells. Vet. Parasitol. 45, 267–273.

Rosales, M.J., Cordón, G.P., Moreno, M.S., Sánchez, C.M., Mascaró, C., 2005. Extracellular like-gregarine stages of *Cryptosporidium parvum*. Acta Trop. 95, 74–78.

Ryan, U., Paparini, A., Monis, P., Hijjawi, N., 2016. It's official—*Cryptosporidium* is a gregarine: what are the implications for the water industry? Water Res. 105, 305–313.

Sifuentes, L.Y., Di Giovanni, G.D., 2007. Aged HCT-8 cell monolayers support *Cryptosporidium parvum* infection. Appl. Environ. Microbiol. 73, 7548–7551.

Singh, P., Mirdha, B.R., Srinivasan, A., Rukmangadachar, L.A., Singh, S., Sharma, P., Gururao, H., Luthra, K., 2015. Identification of invasion proteins of *Cryptosporidium parvum*. World J. Microbiol. Biotechnol. 31, 1923–1934.

Stein, B., Stover, L., Gillem, A., Winters, K., Leet, J.H., Chauret, C., 2006. The effect of lectins on *Cryptosporidium parvum* oocyst in vitro attachment to host cells. J. Parasitol. 92, 1–9.

Taylor, M.A., Marshall, R.N., Green, J.A., Catchpole, J., 1999. The pathogenesis of experimental infections of *Cryptosporidium muris* (strain RN 66) in outbred nude mice. Vet. Parasitol. 86, 41–48.

Tzipori, S., 1983. Cryptosporidiosis in animals and humans. Microbiol. Rev. 47, 84–96.

Uni, S., Iseki, M., Maekawa, T., Moriya, K., Takada, S., 1987. Ultrastructure of *Cryptosporidium muris* (strain RN 66) parasitizing the murine stomach. Parasitol. Res. 74, 123–132.

Upton, S.J., Tilley, M., Brillhart, D.B., 1994. Comparative development of *Cryptosporidium parvum* (Apicomplexa) in 11 continuous host cell lines. FEMS Microbiol. Lett. 118, 233–236.

Upton, S.J., Tilley, M., Brillhart, D.B., 1995. Effects of select medium supplements on in vitro development of *Cryptosporidium parvum* in HCT-8 cells. J. Clin. Microbiol. 33, 371–375.

Valigurová, A., Hofmannová, L., Koudela, B., Vávra, J., 2007. An ultrastructural comparison of the attachment sites between *Gregarina steini* and *Cryptosporidium muris*. J. Eukaryot. Microbiol. 54, 495–510.

Valigurová, A., Jirků, M., Koudela, B., Gelnar, M., Modrý, D., Šlapeta, J., 2008. Cryptosporidia: epicellular parasites embraced by the host cell membrane. Int. J. Parasitol. 38, 913–922.

Valigurová, A., Michalková, V., Koník, P., Dindo, M.L., Gelnar, M., Vaňhara, J., 2014. Penetration and encapsulation of the larval endoparasitoid *Exorista larvarum* (Diptera: Tachinidae) in the factitious host *Galleria mellonella* (Lepidoptera: Pyralidae). Bull. Entomol. Res. 104, 203–212.

Valigurová, A., Paskerova, G.G., Diakin, A., Kováčiková, M., Simdyanov, T.G., 2015. Protococcidian *Eleutheroschizon duboscqi*, an unusual apicomplexan interconnecting gregarines and cryptosporidia. PLoS One 10, e0125063.

Widmer, G., Yang, Y.L., Bonilla, R., Tanriverdi, S., Ciociola, K.M., 2006. Preferential infection of dividing cells by *Cryptosporidium parvum*. Parasitology 133, 131–138.

Woodmansee, D.B., Pohlenz, J.F.L., 1983. Development of *Cryptosporidium* sp. in a human rectal tumor cell line. In: Proceedings of the Fourth International Symposium on Neonatal Diarrhea, Veterinary Infectious Disease Organization, University of Saskatchewan, Saskatoon, Canada, pp. 306–319.

Woods, K.M., Upton, S.J., 2007. In vitro development of *Cryptosporidium parvum* in serum-free media. Lett. Appl. Microbiol. 44, 520–523.

Woods, K.M., Nesterenko, M.V., Upton, S.J., 1995. Development of a microtitre ELISA to quantify development of *Cryptosporidium parvum* in vitro. FEMS Microbiol. Lett. 128, 89–94.

Wu, L., Chen, S.X., Jiang, X.G., Shen, Y.J., Lu, Z.X., Tu, G.H., Fu, X.L., Cao, J.P., 2009. Effect of select medium supplements on in vitro development of *Cryptosporidium andersoni* in HCT-8 cells. Parasitol. Res. 105, 1419–1424.

Xiao, L., Escalante, L., Yang, C., Sulaiman, I., Escalante, A.A., Montali, R.J., Fayer, R., Lal, A.A., 1999a. Phylogenetic analysis of *Cryptosporidium* parasites based on the small-subunit rRNA gene locus. Appl. Environ. Microbiol. 65, 1578–1583.

Xiao, L., Morgan, U.M., Limor, J., Escalante, A., Arrowood, M., Shulaw, W., Thompson, R.C., Fayer, R., Lal, A.A., 1999b. Genetic diversity within *Cryptosporidium parvum* and related *Cryptosporidium* species. Appl. Environ. Microbiol. 65, 3386–3391.

Yang, R., Elankumaran, Y., Hijjawi, N., Ryan, U., 2015. Validation of cell-free culture using scanning electron microscopy (SEM) and gene expression studies. Exp. Parasitol. 153, 55–62.

Yao, L., Yin, J., Zhang, X., Liu, Q., Li, J., Chen, L., Zhao, Y., Gong, P., Liu, C., 2007. *Cryptosporidium parvum*: identification of a new surface adhesion protein on sporozoite and oocyst by screening of a phage-display cDNA library. Exp. Parasitol. 115, 333–338.

Yu, J.R., Choi, S.D., Kim, Y.W., 2000. In vitro infection of *Cryptosporidium parvum* to four different cell lines. Korean J. Parasitol. 38, 59–64.

Zhang, L., Sheoran, A.S., Widmer, G., 2009. *Cryptosporidium parvum* DNA replication in cell-free culture. J. Parasitol. 95, 1239–1242.

7.13

Valigurová A., Pecková R., Doležal K., Sak B., Květoňová D., Kváč M.,
Nurcahyo W., Foitová I.

2018

**Limitations in the screening of potentially anti-cryptosporidial
agents using laboratory rodents with gastric cryptosporidiosis**

Folia Parasitologica 65, 010

Folia Parasitologica

Research Article

OPEN ACCESS

Limitations in the screening of potentially anti-cryptosporidial agents using laboratory rodents with gastric cryptosporidiosis

Andrea Valigurová[1], **Radka Pecková**[1], **Karel Doležal**[2], **Bohumil Sak**[3], **Dana Květoňová**[3], **Martin Kváč**[3,4], **Wisnu Nurcahyo**[5], **Ivona Foitová**[1,5]

[1] Department of Botany and Zoology, Faculty of Science, Masaryk University, Brno, Czech Republic;

[2] Department of Chemical Biology and Genetics & Laboratory of Growth Regulators, Centre of the Region Haná for Biotechnological and Agricultural Research, Faculty of Science, Palacký University, and Institute of Experimental Botany, Academy of Sciences of Czech Republic, Olomouc-Holice, Czech Republic;

[3] Institute of Parasitology, Biology Centre of the Czech Academy of Sciences, České Budějovice, Czech Republic;

[4] Department of Animal Husbandry Sciences, Faculty of Agriculture, University of South Bohemia in České Budějovice, Czech Republic;

[5] Department of Parasitology, Faculty of Veterinary Medicine, Gadjah Mada University, Yogyakarta, Indonesia

Abstract: The emergence of cryptosporidiosis, a zoonotic disease of the gastrointestinal and respiratory tract caused by *Cryptosporidium* Tyzzer, 1907, triggered numerous screening studies of various compounds for potential anti-cryptosporidial activity, the majority of which proved ineffective. Extracts of Indonesian plants, *Piper betle* and *Diospyros sumatrana*, were tested for potential anti-cryptosporidial activity using *Mastomys coucha* (Smith), experimentally inoculated with *Cryptosporidium proliferans* Kváč, Havrdová, Hlásková, Daňková, Kanděra, Ježková, Vítovec, Sak, Ortega, Xiao, Modrý, Chelladurai, Prantlová et McEvoy, 2016. None of the plant extracts tested showed significant activity against cryptosporidia; however, the results indicate that the following issues should be addressed in similar experimental studies. The monitoring of oocyst shedding during the entire experimental trial, supplemented with histological examination of affected gastric tissue at the time of treatment termination, revealed that similar studies are generally unreliable if evaluations of drug efficacy are based exclusively on oocyst shedding. Moreover, the reduction of oocyst shedding did not guarantee the eradication of cryptosporidia in treated individuals. For treatment trials performed on experimentally inoculated laboratory rodents, only animals in the advanced phase of cryptosporidiosis should be used for the correct interpretation of pathological alterations observed in affected tissue. All the solvents used (methanol, methanol-tetrahydrofuran and dimethylsulfoxid) were shown to be suitable for these studies, i.e. they did not exhibit negative effects on the subjects. The halofuginone lactate, routinely administered in intestinal cryptosporidiosis in calves, was shown to be ineffective against gastric cryptosporidiosis in mice caused by *C. proliferans*. In contrast, the control application of extract *Arabidopsis thaliana*, from which we had expected a neutral effect, turned out to have some positive impact on affected gastric tissue.

Keywords: *Cryptosporidium*, gastric, oocyst, pathology, treatment

The phylum Apicomplexa comprises exclusively parasitic protists infecting invertebrates and vertebrates, including humans. One of the most significant and widespread pathogens are coccidia of the genus *Cryptosporidium* Tyzzer, 1907, causative agents of zoonotic disease (cryptosporidiosis) of the gastrointestinal and respiratory tracts. In healthy hosts, cryptosporidiosis is self-limiting; nevertheless, in immunocompromised hosts, it represents a chronic and debilitating condition (Chen et al. 2002).

Although gastric cryptosporidia have been reported in fish, reptiles, amphibians, birds and mammals (Jirků et al. 2008, Ryan 2010, Nakamura and Meireles 2015), there is a dearth of useful studies dealing with the treatment of gastric cryptosporidiosis. In contrast to intestinal species, the

course of gastric cryptosporidiosis in both immunocompetent and immunodeficient animals is an asymptomatic and chronic infection (Kváč et al. 2008, 2011). In humans, gastric involvement is reported to be very common in patients with cryptosporidiosis when combined with severe immunodepression (Rivasi et al. 1999).

The recently described species *Cryptosporidium proliferans* Kváč, Havrdová, Hlásková, Daňková, Kanděra, Ježková, Vítovec, Sak, Ortega, Xiao, Modrý, Chelladurai, Prantlová et McEvoy, 2016 (previously known as strain TS03 of *Cryptosporidium muris* Tyzzer, 1907), used in this study, develops exclusively in the glandular part of the stomach, similar to *C. muris* and *Cryptosporidium andersoni* Lindsay, Upton, Owens, Morgan, Mead et Blagburn,

2000, with a life cycle corresponding to that of *C. muris* (see Tyzzer 1910, Melicherová et al. 2014, Kváč et al. 2016). Though *C. proliferans* had been considered identical with *C. muris* in previous years, their clinical courses of parasitisation in *Mastomys coucha* (Smith) differ considerably (Kváč et al. 2016). Compared to *C. muris*, rodents shed oocysts of *C. proliferans* for a much longer period and at a greater intensity, and only *C. proliferans* induces significant clinical and pathological changes, such as weight loss and massive proliferation of the gastric mucosa associated with a considerable increase in stomach weight (Kváč et al. 2016). The change in the ratio of glandular to non-glandular surfaces from 55 : 45 to 80 : 20, detected in *M. coucha* infected with *C. proliferans*, was not observed in *C. muris* infection (Kváč et al. 2016).

Cryptosporidiosis is recognised as a major medical concern as there is no effective treatment for either intestinal or gastric cryptosporidiosis (Fayer et al. 2000, Thompson et al. 2005). Numerous compounds have been screened *in vitro* and *in vivo* for potential anti-cryptosporidial activity, but the majority turned out to be ineffective and only a few agents have shown promise. The most commonly used drugs used against cryptosporidiosis include antibiotics (e.g. paromomycin or azithromycin) and halofuginone, which are partially effective. In contrast to chemotherapeutics, often with considerable side effects and a certain level of toxicity, the use of natural products or dietary supplements with anti-cryptosporidial activity could represent a new and safe approach to the effective pharmacological control of cryptosporidiosis. For example, L-arginine was shown to have a protective role during infection with *Cryptosporidium parvum* Tyzzer, 1912 in undernourished mice (Castro et al. 2012). Several studies have found probiotics to be effective against cryptosporidiosis in humans and animals, reporting prompt clinical improvement and resolution of the infection following treatment (Rotkiewicz et al. 2001, Pickerd and Tuthill 2004). *Lactobacillus* spp. significantly reduced the viability of oocysts of *C. parvum* (see Foster et al. 2003). Administration of exogenous agmatine seems to alter the metabolism of *C. parvum* enough to interfere with its ability to colonise the mammalian intestine (Moore et al. 2001). Mangiferin, widely distributed in higher plants and one of the constituents of folk medicines (Yoshimi et al. 2001), has significant anti-cryptosporidial activity comparable to the same dose (100 mg/kg/day) of paromomycin (Tarantino et al. 2004, Perrucci et al. 2006). Curcumin, which is active against a variety of diseases, was found to be effective against *C. parvum* in cell cultures (Shahiduzzaman et al. 2009).

Garlic (*Allium sativum*) appears to be a prophylactic and a promising therapeutic agent, as it successfully eradicated cryptosporidial oocysts from the faeces and intestines of infected immunocompetent mice that had received garlic two days before the experimental infection and continued for two weeks (Gaafar 2012). The administration of garlic to human HIV patients with chronic diarrhoea and confirmed cryptosporidiosis resulted in complete or partial remission (Fareed et al. 1996). Onion (*Allium cepa*) and cinnamon (*Cinnamomum zeylanicum*) oils also turned out

to be effective against the infection with *C. parvum* in mice (Abu El Ezz et al. 2011). In contrast, an *in vitro* study using HCT-8 cells inoculated with *C. andersoni* did not confirm the significant inhibition of parasite growth when exposed to garlicin (antifungal component extracted from garlic) (Wu et al. 2011). The authors concluded that garlicin inhibits the growth of cryptosporidia *in vivo* by enhancing macrophage activity, rather than by exerting direct effects on the parasite. This study also showed anti-cryptosporidial activity of ginkgolic acids extracted from maidenhair tree (*Ginkgo biloba*) sarcotesta. With the exception of the prophylactic effect of garlic, however, none of these natural products were able to completely eradicate cryptosporidiosis.

As humans and orang-utans exhibit phylogenetic similarities (Grehan and Schwartz 2009), we focused on orang-utans' feeding behaviour with an emphasis on specific plants consumed that would lead to a reduction in parasite infections. Recently we documented a secondary self-medication (the external application of a medicinal substance) in Bornean orang-utans (Morrogh-Bernard at al. 2017). These findings validate the anti-inflammatory properties of *Dracaena cantleyi* and its application to muscles and joints by orang-utans, and may serve as the first evidence for the deliberate external application of substances with bioactive potential for self-medication in great apes.

We selected few plants including *Piper betle* and *Diospyros sumatrana* with promising antiparasitic activity on the basis of behavioural data and decreases in parasite load (Foitová et al. 2010). Our analyses show a positive correlation between the prevalence of these plant species in orang-utan diets and the presence of parasites (based on the Jaccard index of known frequency in nature) that cannot be explained by their prevalence in the environment. The betel, *P. betle*, has been used as a medicinal plant in traditional medicine throughout South and South East Asia since ancient times. Experimental studies have revealed its wide and diverse biological and pharmacological effects (Pecková et al. 2018). *Diospyros sumatrana* has not yet been studied for pharmacological potential, but our study shows its possible potential.

This study aimed to test extracts of Indonesian plants selected by orang-utans for self-medication for potential anti-cryptosporidial activity, using a rodent host that had been experimentally inoculated with *C. proliferans*. The extract of *Arabidopsis thaliana* (the Eurasian plant routinely used as a model in research laboratories) was used as a control with an expected neutral effect. Halofuginone lactate (Halocur), an oral solution used for the treatment of cryptosporidiosis in calves, was tested for its potentially positive effect.

MATERIALS AND METHODS

Preparation of plant extracts

The dried leaves obtained from *Piper betle* (akar sirih), *Diospyros sumatrana* (kayu hitam) and *Arabidopsis thaliana* (thale cress) were homogenised to a fine powder in liquid nitrogen. Portions of the ground material (0.33 g) were then extracted sep-

arately in 10 ml of water, methanol (methanol) or methanol-tet-rahydrofurane (methanol-THF, 1 : 1). After 16 hours of extraction (overnight) at -20 °C, the resulting homogenates were centrifuged (26,000 *g*, 4 °C, 20 min); the sediments were then re-extracted for one hour in the same way and centrifuged. Afterward, these two supernatants were pooled and dried in a vacuum at 35 °C, and then dissolved in 100 μl of pure Dimethylsulfoxid (DMSO), except for samples dissolved in sterile water, which were further diluted in sterile water.

The parasite used in this study

The gastric species *Cryptosporidium proliferans* used in this study and our previous studies (Kváč et al. 2008, 2011, 2016 Melicherová et al. 2014, 2016) originated from a naturally infected East African mole rat *Tachyoryctes splendens* (Rüppell) and was kept in severe combined immunodeficiency (SCID) mice and southern multimammate mice (*Mastomys coucha*) under laboratory conditions.

Laboratory animals and experimental inoculations with oocysts of *Cryptosporidium proliferans*.

Eight-week old *M. coucha* mice (Biology Centre, CAS, České Budějovice) were used for this study. To prevent environmental contamination with oocysts, each group of mice was housed in plastic cages with sterile wood-chip bedding and supplied with sterilised food and water *ad libitum*. The rearing of animals was regulated by Czech legislation (Act No. 246/1992 Coll., on protection of animals against cruelty); these documents are consistent with legislation by the European Commission. All housing, feeding, and experimental procedures were conducted under protocols approved by the Institute of Parasitology, Biology Centre, CAS and Institute and National Committees (Protocols No. 52/2014).

For the experimental inoculation of mice, oocysts collected from faeces were purified using Sheather's sugar flotation method (Arrowood and Sterling 1987) and modified caesium chloride gradient centrifugation (Kilani and Sekla 1987). Each mouse was inoculated orally by an oesophagus tube with a dose of 106 viable oocysts of *C. proliferans*. Afterwards, fresh mouse faeces were collected daily in the morning and examined microscopically for the presence of oocysts using staining according to Miláček and Vítovec (1985). The intensity of oocyst excretion was assessed as the number of oocysts per gram of faeces (OPG) as previously described Kváč et al. (2007). In addition, faecal consistency, faecal colour and general health status were examined daily.

The treatment of parasitised animals using plant extracts

The potential antiparasitic effect of Indonesian plants (*P. betle* and *D. sumatrana*), was compared with the expected null effect of *A. thaliana*, as well as with the potentially positive effect of the Halocur oral solution (Intervet Production S.A., Rue de Lyons, France). Mice infected with *C. proliferans* two or three months before treatment with plant extracts were divided into groups (three animals per group) and treated with the following treatment doses administered *per os*. Treated non-infected and untreated infected and non-infected control groups were included in all experiments. The effect of administered extracts/drugs/diluents on the course of parasitisation was evaluated as change in the parasitisation intensity expressed by OPG in comparison to

parasitisation intensity of infected mice administered with only distilled water. The coefficient of determination (r^2) was calculated for each linear regression. All computation was carried out with the SigmaPlot 13.0 (Systat Software Inc., San Jose, CA). The histopathological changes of parasitised gastric mucosa were evaluated *post mortem*.

Trial 1. Groups of mice were treated daily for 14 days, beginning two months post inoculation with *C. proliferans*, with 12.5 mg per 100 g of body mass (BM) of either *P. betle*, *D. sumatrana* or *A. thaliana* extracted in methanol, dissolved in DMSO, and diluted with sterile water to obtain a final concentration of 0.5% DMSO. The effect of the Halocur (100 μg/kg BM) and the diluent (0.5% DMSO in sterile water) was evaluated in infected control mice.

Trial 2. A second trial was conducted after the completion of the first trial. The treatments began three months post inoculation with *C. proliferans*. Three extraction media were used: methanol, methanol-THF and sterile water. Extracted material was dissolved in DMSO (except for that dissolved in sterile water) and diluted with sterile water to obtain a final concentration of 0.5% DMSO. A dose of 40 mg of per 100 g BM of either *P. betle*, *D. sumatrana* or *A. thaliana* extract was administered twice a day for 21 days. Additionally, the effect of the Halocur (100 μg/kg BM) and the diluent (0.5% DMSO in sterile water) was evaluated in infected control mice.

Parasitological dissection and tissue processing for microscopic evaluation

After either 14 (Trial 1) or 21 (Trial 2) days of treatment, control and treated animals were euthanised by cervical dislocation and dissected according to protocols described by Melicherová et al. (2014). For histological sectioning, gastric tissue was fixed in AFA (Alcohol-Formalin-Acetic Acid) solution and processed according to Valigurová et al. 2008. The blocks were cut using a Zeiss Hyrax M 300 rotary microtome and the 7 μm thick sections were stained with haematoxylin-eosin. Preparations were viewed using an Olympus BX61 microscope.

For scanning electron microscopy, samples of gastric tissue were fixed overnight at 4 °C in freshly prepared 2.5% glutaraldehyde (v/v) in cacodylate buffer (0.1 M; pH 7.4), washed 3 × 15 min in the buffer, postfixed in 2% OsO_4 in cacodylate buffer for two hour at room temperature, and washed again 3 × 15 min in buffer. After dehydration in a graded acetone series, specimens were critical point-dried using CO_2, coated with gold, and examined using a JEOL JSM-7401F – Field Emission Scanning Microscope. Abbreviations used in Figs. 1–9: LM – light microscopy; SEM – scanning electron microscopy

RESULTS

Histopathological observations of the gastric tissue of uninfected and infected rodents

In the stomach of healthy (control) *Mastomys coucha* individuals, the surface of the gastric mucosa was smooth with a brain-like ornamentation (Fig. 1A). In histological sections stained with haematoxylin-eosin, the gastric mucosa, along with a thin layer of muscularis mucosae and subjacent submucosa, appeared homogeneously pink with well-demarcated blue nuclei (Fig. 1B). It was
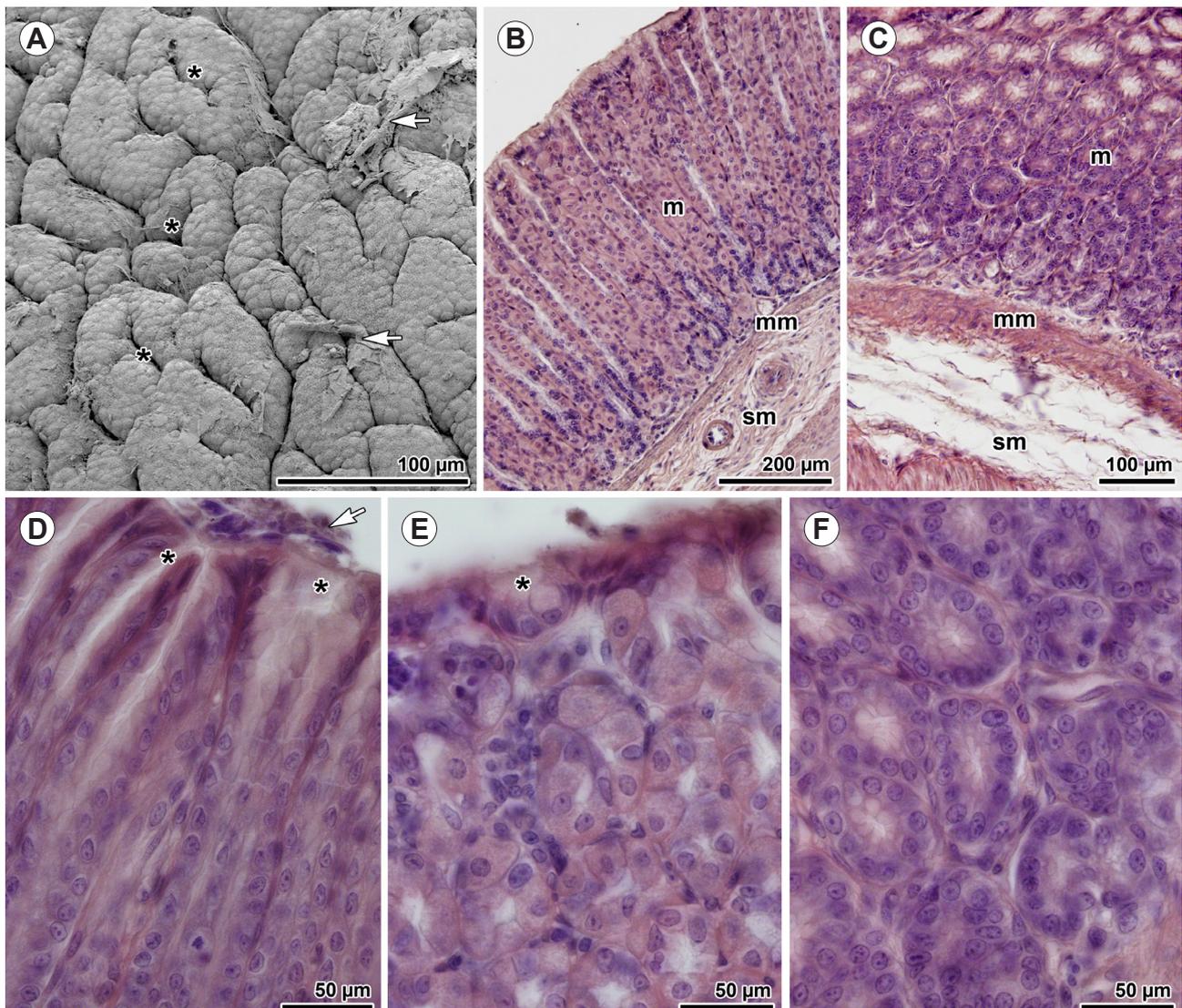
Fig. 1. Healthy gastric mucosa of *Mastomys coucha* (Smith). **A** – general view of surface of the gastric mucosa exhibiting constricted gastric pits; note the remnants of mucus not washed away during rinsing (SEM); **B** – general view of gastric mucosa showing the longitudinally sectioned pits and glands (LM); **C** – general view of mucosa with cross-sectioned gastric glands (LM, histology); **D** – detailed view of constricted gastric pits in longitudinal section (LM, histology); **E** – detailed view of constricted pits in cross section (LM, histology); **F** – detailed view of constricted glands in cross sections (LM, histology); asterisk – gastric pit; m – mucosa; mm – muscularis mucosae; sm – submucosa; white arrow – mucus with cell debris.

possible to distinguish quite easily the tubular glands and necks ended by pits invaginating the luminal surface of mucosa (Fig. 1B,C). The gastric pits and glands were obviously constricted and contained within a thin *lamina propria* (Fig. 1A–F). A tall simple columnar epithelium lined the mucosal surface and gastric pits (Fig. 1B). Surface mucous cells lining the pits as well as mucous neck cells demarcating the necks of gastric glands appeared pale (Fig. 1B), while the cells forming the base of glands were stained darker with prominent, intensively stained nuclei (Fig. 1C,F).

In mice infected with *Cryptosporidium proliferans*, parasite endogenous stages were restricted to the epithelial cells in the glandular part of the gastric mucosa. This species primarily parasitises epithelial cells lining the gastric pits and glands, though some parasites could be found attached to cells lining the luminal surface of the gastric epi-

thelium, especially as parasitisation progressed (most likely due to the increased space requirements). The duration of the prepatent period (18–21 days) and the chronology of pathological changes correspond to previously published data (Melicherová et al. 2014).

In the first trial, the use of mice in a relatively early stage of cryptosporidiosis (two months post inoculation with *C. proliferans*) was shown to be unsuitable for the microscopic evaluation of treatment effects, as affected gastric mucosa exhibited only mild to moderate pathological changes. The gastric tissue was also irregularly affected by cryptosporidia in an island-like manner, where individual parasitised gastric pits were surrounded by regions of healthy epithelium. The affected gastric tissue showed no obvious alterations and the pits appeared almost fully constricted when evaluated under SEM (Fig. 2A). Despite the mild character of pathological alterations visible by SEM,
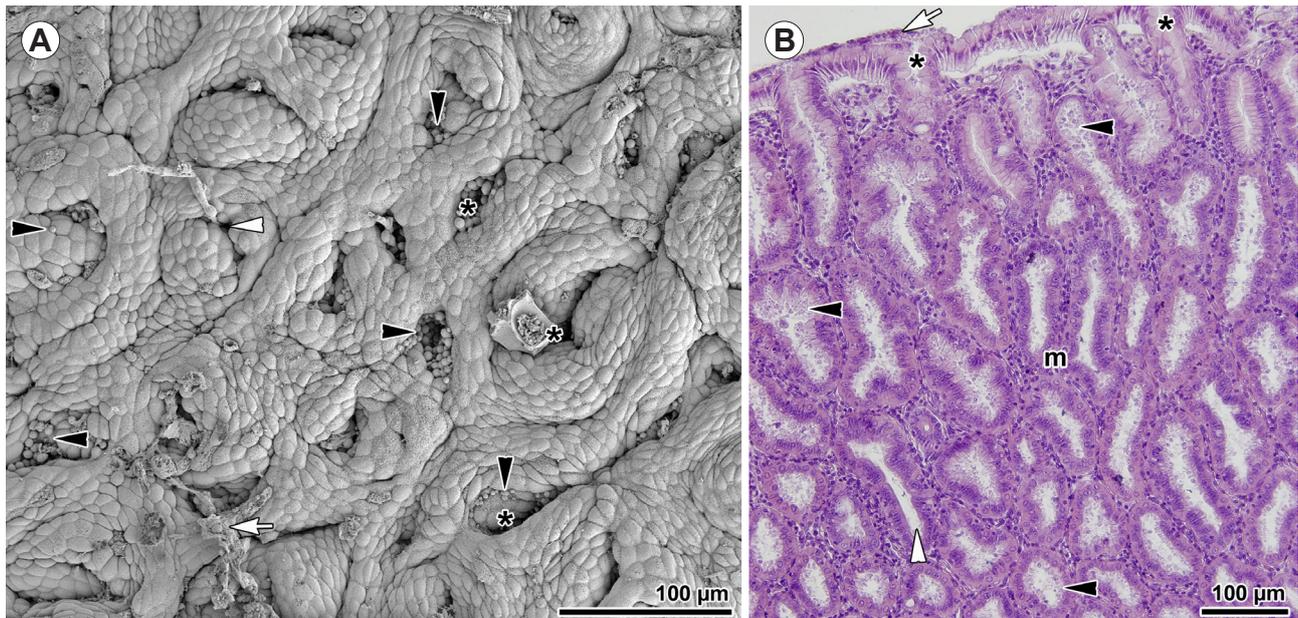
Fig. 2. Pathological alterations to gastric mucosa induced by *Cryptosporidium proliferans* Kváč, Havrdová, Hlásková, Daňková, Kanděra, Ježková, Vítovec, Sak, Ortega, Xiao, Modrý, Chelladurai, Prantlová et McEvoy, 2016 in control *Mastomys coucha* (Smith) from Trial 1. **A** – superficial view of surface of the gastric mucosa exhibiting slightly enlarged gastric pits (SEM); **B** – general view of the gastric mucosa with longitudinally sectioned pits. The gastric pits and glands exhibit moderate dilation when viewed in tangential and cross sections (LM, histology); asterisk – gastric pit, black arrowhead – cryptosporidia, m – mucosa, white arrow – mucus with cell debris, white arrowhead – cryptosporidia-free pit/gland.

histological sectioning revealed the moderate dilatation of gastric glands due to the presence of numerous cryptosporidia (Fig. 2B).

Pathological changes in affected gastric tissue became more prominent three months post inoculation with *C. proliferans*, when the parasitisation entered a chronic phase (Fig. 3A–I). Such mice, used in Trial 2, had the surface of their gastric glandular epithelium markedly deformed due to intense pathological changes. At the macroscopic level, the gastric mucosa was typified by a cauliflower-like appearance. The epithelium proliferated into the luminal space, so that the stomach exhibited extensive folding that was especially visible under SEM (Fig. 3A,C,D). This was the result of an increase in the volume of the *lamina propria*, which then increased the distance between individual gastric glands and caused the longitudinal folds to become twisted and obviously deformed. The progress of parasitisation caused a distinctive form of diffuse mucosal hypertrophy typified by the presence of enlarged/giant gastric folds and intensive epithelial hyperplasia.

The gastric glands, packed with various developmental stages of *C. proliferans* and necrotic material, were markedly dilated and hypertrophied (Fig. 3B,E–I). In addition, numerous cryptosporidia developed attached to the luminal surface of the gastric mucosa outside the dilated pits (Fig. 3D). The affected glands, lined with many undifferentiated cells, lost their normal architecture; the atrophic epithelial cells of the affected glands exhibited cuboidal or squamous metaplasia (Fig. 3G–I). Besides the more intense staining of affected tissue in histological sections, another feature typical of advanced cryptosporidiosis was the thickening of muscularis mucosae (Fig. 3B). Parasitised tissue ex-

hibited various degrees of oedema and the infiltration of the *lamina propria* and submucosa with neutrophils (Fig. 3B,E). Stomach weight (due to proliferating mucosa) and epithelial height were considerably greater than in non-infected animals. Interestingly, despite the chronicity of infection, no clinical signs were observed in infected rodents.

Treatment with plant extracts and Halocur

Trial 1 served as the primary screening of experimental protocols and the selected treatment doses based on related literature and empirical data on other unicellular parasites used in our research (Pecková et al. 2018). On the basis of the results obtained with daily doses of 12.5 mg/100 g BM applied for 14 consecutive days, we decided to increase the treatment doses to 40 mg per 100 g BM administered twice daily for 21 consecutive days in Trial 2. Furthermore, in Trial 2, we tested and compared the efficacy of selected plant extracts obtained using various solvent media – methanol, methanol-THF, and sterile water. In both trials, an oral administration containing 100 µg/kg BM halofuginone lactate (Halocur), a salt whose antiprotozoal properties and efficacy against *Cryptosporidium parvum* have been demonstrated under *in vitro* and *in vivo* conditions (Giadinis et al. 2008, Petermann et al. 2014), was used as a control treatment.

One of the parameters used to evaluate parasitisation intensity was the monitoring of the number of shed oocysts detected in faeces. Generally, the variations in oocyst shedding were comparable in all experimental groups treated with either plant extracts or Halocur. A decline in oocyst number in Trial 1 can be observed in groups treated for 14 days with *Diospyros sumatrana* extracted by metha-
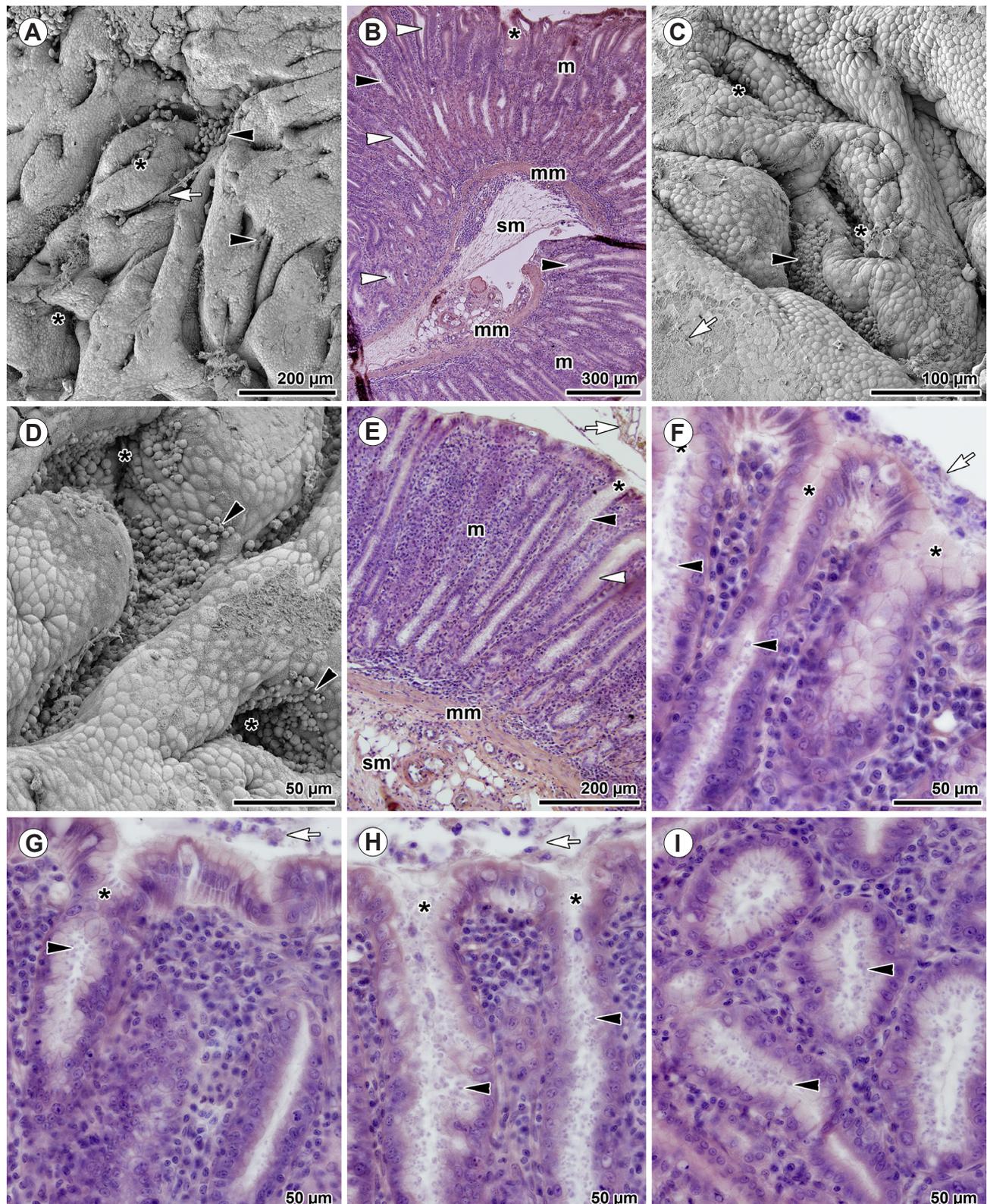
Fig. 3. Pathological alterations to gastric mucosa induced by *Cryptosporidium proliferans* Kváč, Havrdová, Hlásková, Daňková, Kanděra, Ježková, Vítovec, Sak, Ortega, Xiao, Modrý, Chelladurai, Prantlová et McEvoy, 2016 in control *Mastomys coucha* (Smith) from Trial 2. **A** – superficial view of the gastric mucosa exhibiting extensive folding and intense parasitisation (SEM); **B** – general view of the gastric mucosa and submucosa in longitudinal section (LM, histology); **C, D** – detailed view of dilated pits filled with numerous parasites (SEM); **E** – gastric mucosa showing the longitudinally sectioned pits and glands (LM, histology); **F–H** – detailed view of parasitised pits and glands in longitudinal section (LM, histology); **I** – detailed view of cross-sectioned gastric glands filled with parasites (LM, histology); asterisk – gastric pit; black arrowhead – cryptosporidia; m – mucosa; mm – muscularis mucosae; sm – submucosa; white arrow – mucus with cell debris; white arrowhead – cryptosporidia-free pit/gland.
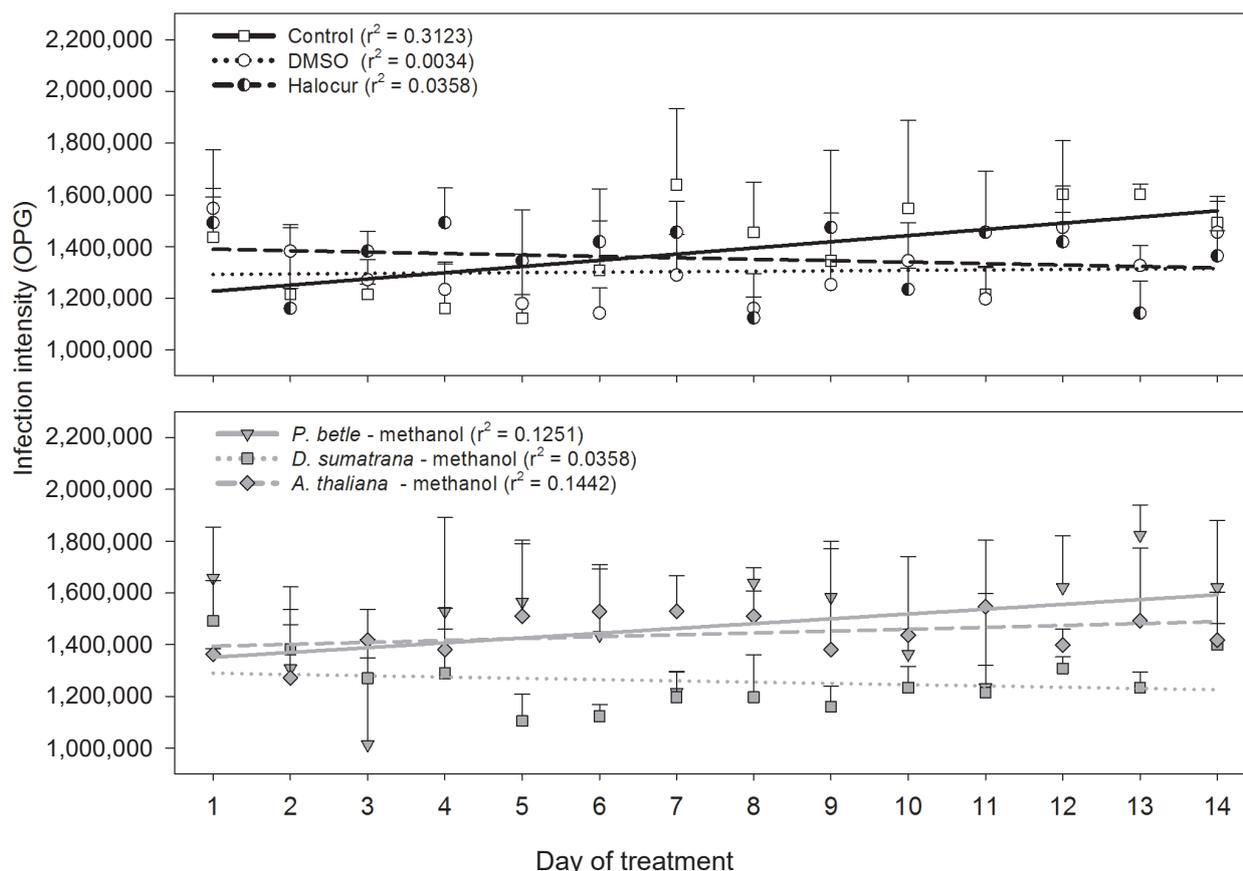
**Fig. 4.** Infection dynamics of *Cryptosporidium proliferans* Kváč, Havrdová, Hlásková, Daňková, Kanděra, Ježková, Vítovec, Sak, Ortega, Xiao, Modrý, Chelladurai, Prantlová et McEvoy, 2016 in Trial 1. Groups of eight-week-old *Mastomys coucha* (Smith) inoculated with a dose of 106 oocysts two months before treatment and subsequently treated daily for 14 days with 12.5 mg per 100 g of body mass of either *Piper betle*, *Diospyros sumatrana* or *Arabidopsis thaliana* extracted in methanol. The linear regression including regression coefficient is included for each experimental group.

nol and Halocur (Fig. 4). In contrast, non-treated controls, controls treated with pure DMSO and animals treated with *Piper betle* and *Arabidopsis thaliana* extracted by methanol exhibited an increase in oocyst shedding (Fig. 4). In Trial 2, a decline in oocyst shedding occurred in groups treated for 21 days with *A. thaliana* by methanol-THF, *D. sumatrana* by methanol-THF and Halocur (Fig. 5). An increase occurred in non-treated controls and animals treated with pure DMSO, *P. betle* extracted by methanol, *P. betle* by methanol-THF, *P. betle* by sterile water, *A. thaliana* by methanol *A. thaliana* by sterile water, *D. sumatrana* by methanol, and *D. sumatrana* by sterile water (Fig. 5). The coefficient of determination, however, was low in all experimental groups, with the exception of non-treated controls and controls treated with pure DMSO in Trial 2 (Fig. 5).

Despite an obvious decrease in oocyst shedding in some animals, *post mortem* histological examinations at the end of both trials revealed heavy cryptosporidiosis in all non-treated (Figs. 1–3) and treated animals (Figs. 6–9). Only histological sections from animals treated for 21 days (Trial 2) are shown to demonstrate the status of parasitised gastric tissue at the end of the trial. Histopathological data show that, independently of the solvent medium used, extracts from *P. betle* (Fig. 6A–I) and *D. sumatrana* (Fig.

7A–I) neither helped to eradicate the parasites nor cured the pathological changes induced by *C. proliferans*. When compared to non-treated controls (Fig. 3A–I), no significant difference was observed in parasitisation intensity or in associated pathological alterations to the gastric mucosa in treated animals examined in SEM or histological preparations.

Surprisingly, the application of a control with no expected effect, the extract of *A. thaliana* (Fig. 8A–I), seemed to have a positive impact on parasitised gastric mucosa, especially when dissolved in methanol-THF (Fig. 8G–I). This was obvious especially in SEM preparations, where the pathological folding of parasitised gastric tissue appeared less intense (Fig. 8G) when compared to those in non-treated animals (Fig. 3A,C,D) and the effects of other treatments (Figs. 7A,D,G, and 8A,D). Some degree of this effect of *A. thaliana* on parasitised gastric mucosa was also visible in histological sections; i.e. the architecture of the gastric glands was closer to the normal state and the epithelial cells lining the gastric glands were slightly less atrophic (Fig. 8I).

Although it slightly decreased oocyst excretion, even prolonged treatment with Halocur was insufficiently effective in treating gastric cryptosporidiosis (Fig. 9A–C). The
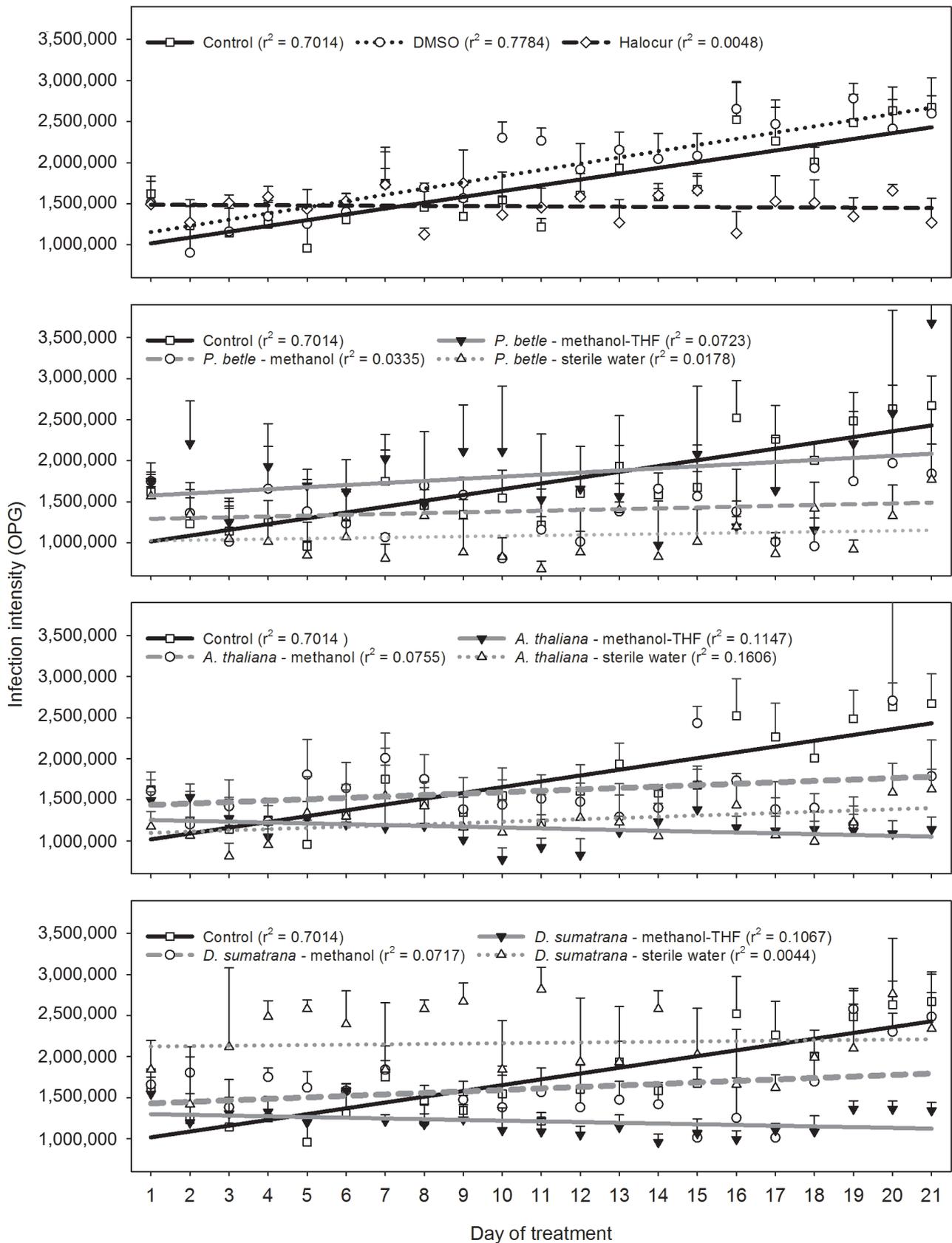
Fig. 5. Infection dynamics of *Cryptosporidium proliferans* Kváč, Havrdová, Hlásková, Daňková, Kanděra, Ježková, Vítovec, Sak, Ortega, Xiao, Modrý, Chelladurai, Prantlová et McEvoy, 2016 in Trial 2. Groups of eight-week-old *Mastomys coucha* (Smith) inoculated with a dose of 106 oocysts three months previously were treated twice a day for 21 days with a dose of 40.0 mg per 100 g of body mass of either *Piper betle*, *Diospyros sumatrana* or *Arabidopsis thaliana* extracted in methanol, ethanol-tetrahydrofuran (methanol-THF) or sterile water. The linear regression including regression coefficient is included for each experimental group.
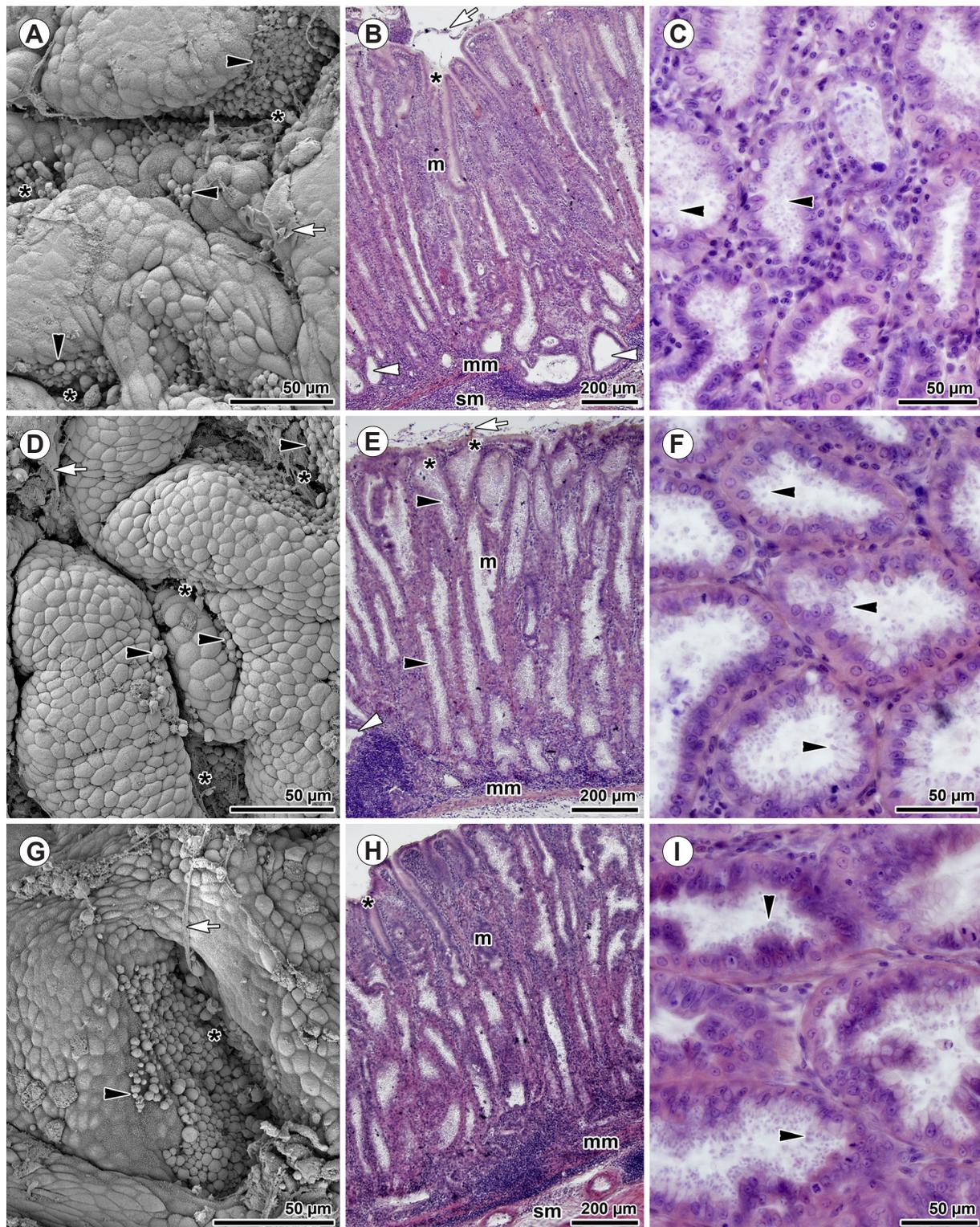
**Fig. 6.** The effect of *Piper betle* extract on *Mastomys coucha* (Smith) gastric mucosa parasitised with *Cryptosporidium proliferans* Kváč, Havrdová, Hlásková, Daňková, Kanděra, Ježková, Vítovec, Sak, Ortega, Xiao, Modrý, Chelladurai, Prantlová et McEvoy, 2016 in Trial 2. **A–C** – *P. betle* in sterile water: **A** – superficial view of the gastric mucosa (SEM); **B** – general view of the gastric mucosa in longitudinal section (LM, histology); **C** – detailed view of cross-sectioned glands filled with parasites (LM, histology); **D–F** – *P. betle* in methanol: **D** – superficial view of the gastric mucosa (SEM); **E** – general view of the gastric mucosa in longitudinal section (LM, histology); **F** – detailed view of cross-sectioned glands filled with parasites (LM, histology); **G–I** – *P. betle* in methanol-THF: **G** – superficial view of the gastric mucosa (SEM); **H** – general view of the gastric mucosa and submucosa in longitudinal section (LM, histology); **I** – detailed view of cross-sectioned glands filled with parasites (LM, histology); asterisk – gastric pit; black arrowhead – cryptosporidia; m – mucosa; mm – muscularis mucosae; sm – submucosa; white arrow – mucus with cell debris; white arrowhead – cryptosporidia-free pit/gland.
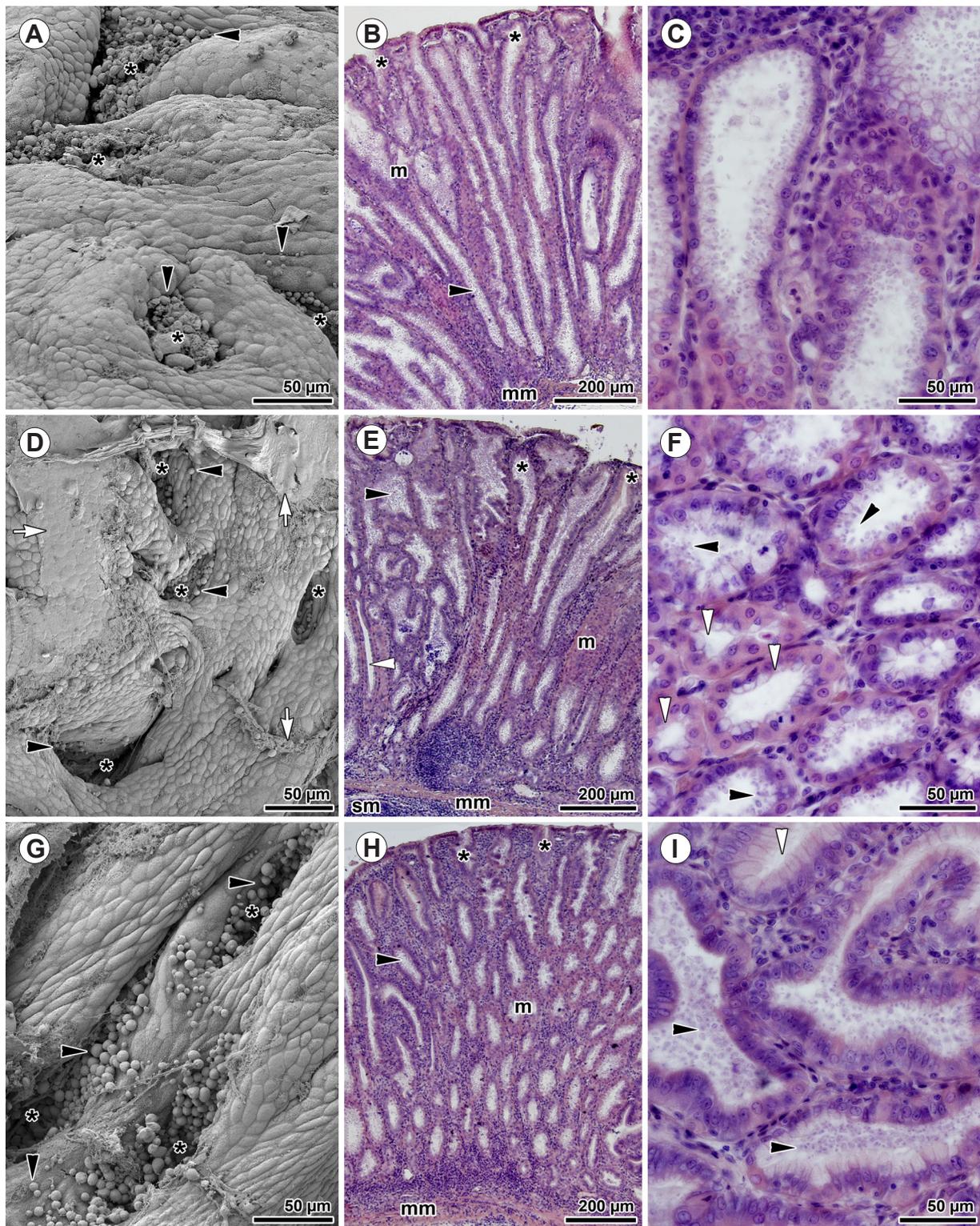
Fig. 7. The effect of *Diospyros sumatrana* extract on *Mastomys coucha* (Smith) gastric mucosa parasitised with *Cryptosporidium proliferans* Kváč, Havrdová, Hlásková, Daňková, Kanděra, Ježková, Vítovec, Sak, Ortega, Xiao, Modrý, Chelladurai, Prantlová et McEvoy, 2016 in Trial 2. **A–C** – *D. sumatrana* in sterile water: **A** – superficial view of the gastric mucosa (SEM); **B** – general view of the gastric mucosa in longitudinal section (LM, histology); **C** – detailed view of tangentially-sectioned glands filled with parasites (LM, histology); **D–F** – *D. sumatrana* in methanol: **D** – superficial view of the gastric mucosa (SEM); **E** – general view of the gastric mucosa in longitudinal section (LM, histology); **F** – detailed view of cross-sectioned glands filled with parasites and neighbouring empty glands (LM, histology); **G–I** – *D. sumatrana* in methanol-THF: **G** – superficial view of the gastric mucosa (SEM); **H** – general view of the gastric mucosa in longitudinal section (LM, histology); **I** – detailed view of tangentially-sectioned glands filled with parasites (LM, histology); asterisk – gastric pit, black arrowhead – cryptosporidia; m – mucosa; mm – muscularis mucosae; sm – submucosa; white arrow – mucus with cell debris; white arrowhead – cryptosporidia-free pit/gland.
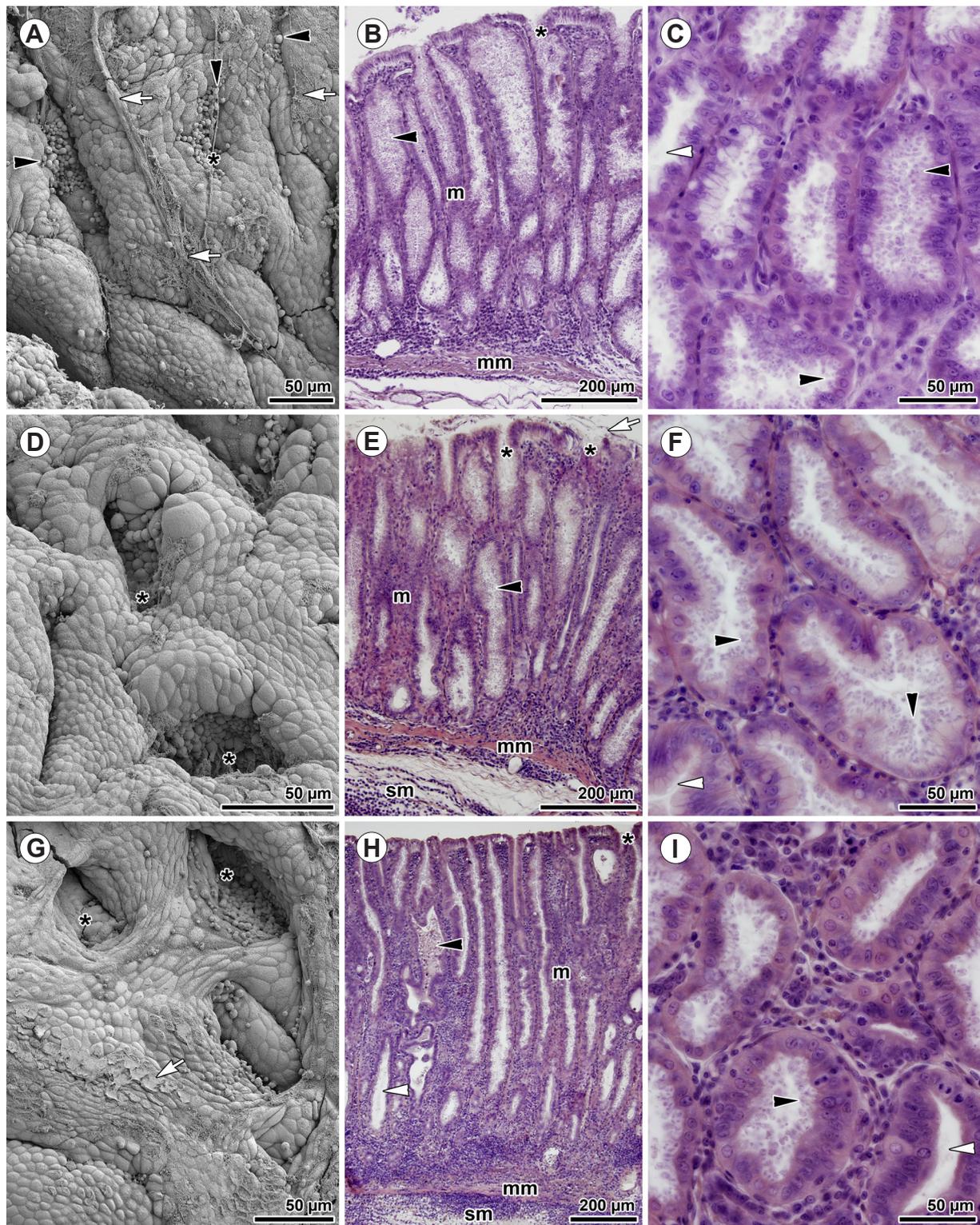
Fig. 8. The effect of *Arabidopsis thaliana* extract on *Mastomys coucha* (Smith) gastric mucosa parasitised with *Cryptosporidium proliferans* Kváč, Havrdová, Hlásková, Daňková, Kanděra, Ježková, Vítovec, Sak, Ortega, Xiao, Modrý, Chelladurai, Prantlová et McEvoy, 2016 in Trial 2. **A–C** – *A. thaliana* in sterile water: **A** – superficial view of the gastric mucosa (SEM); **B** – general view of the gastric mucosa in longitudinal section (LM, histology); **C** – detailed view of cross-sectioned glands filled with parasites (LM, histology); **D–F** – *A. thaliana* in methanol: **D** – superficial view of the gastric mucosa (SEM); **E** – general view of the gastric mucosa in longitudinal section (LM, histology); **F** – detailed view of cross-sectioned glands filled with parasites (LM, histology); **G–I** – *A. thaliana* in methanol-THF: **G** – superficial view of the gastric mucosa (SEM); **H** – general view of the gastric mucosa in longitudinal section (LM, histology); **I** – detailed view of cross-sectioned glands filled with parasites (LM, histology); asterisk – gastric pit; black arrowhead – cryptosporidia; m – mucosa; mm – muscularis mucosae; sm – submucosa; white arrow – mucus with cell debris; white arrowhead – cryptosporidia-free pit/gland.
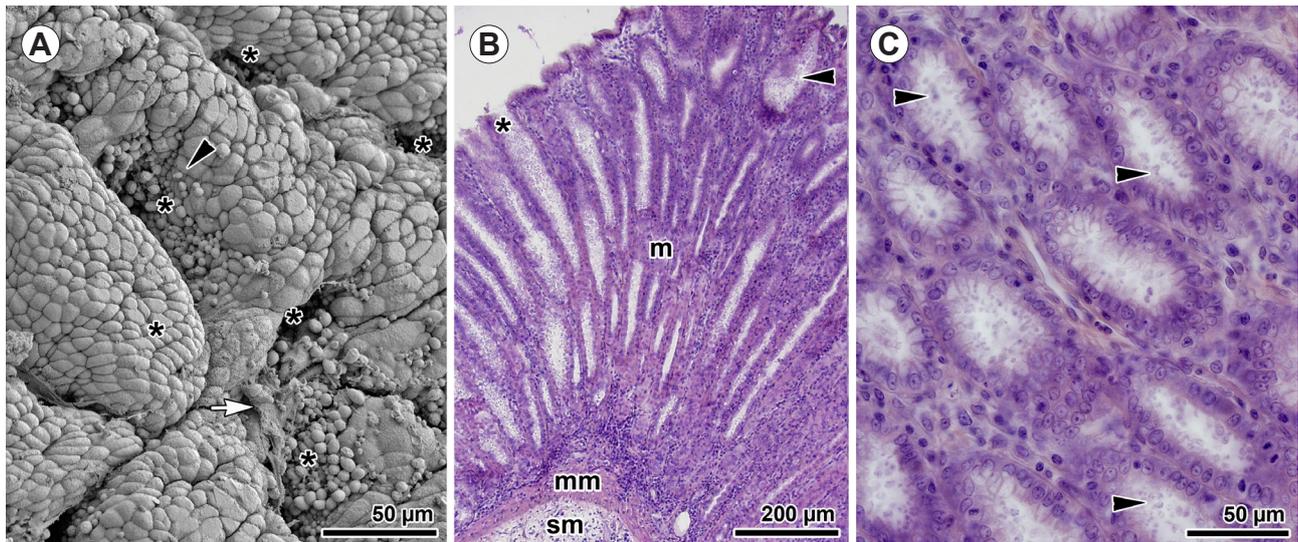
Fig. 9. The effect of Halocur on *Mastomys coucha* (Smith) gastric mucosa parasitised with *Cryptosporidium proliferans* Kváč, Havrdová, Hlásková, Daňková, Kanděra, Ježková, Vítovec, Sak, Ortega, Xiao, Modrý, Chelladurai, Prantlová et McEvoy, 2016 in Trial 2. **A** – superficial view of the gastric mucosa, halocur in PBS (SEM); **B** – general view of the gastric mucosa in longitudinal section, halocur in PBS (LM, histology); **C** – detailed view of cross-sectioned glands filled with parasites, halocur in PBS (LM, histology); asterisk – gastric pit, black arrowhead – cryptosporidia, m – mucosa, mm – muscularis mucosae, sm – submucosa, white arrow – mucus with cell debris, white arrowhead – cryptosporidia-free pit/gland.

generally recommended dose for intestinal cryptosporidiosis, corresponding to 100 µg/kg BM of halofuginone administered for seven consecutive days, was reported to be effective in the past (Giadinis et al. 2008, Petermann et al. 2014). In our study, the period of Halocur administration was extended to 14 (Trial 1) and 21 days (Trial 2). Treated animals showed no symptoms of toxicity (no clinical signs of overdosing). However, SEM observations of the intensively folded surface of the gastric mucosa, with the presence of various developmental stages of *C. proliferans*, confirmed heavy infection (Fig. 9A). Histopathological changes (Fig. 9A–C) were very similar to those found in untreated individuals (Fig. 3A–I). The only difference, noticeable at higher magnification, was the better preservation of epithelial cells lining the glands (Fig. 9C). These cells appeared less atrophic with more preserved nuclei compared to non-treated animals or those treated with *P. betle* and *D. sumatrana*.

DISCUSSION

Histopathological changes related to gastric cryptosporidiosis

Studies on animal gastric cryptosporidiosis usually report only mild histopathological changes represented by the dilatation and epithelial metaplasia of gastric glands. These are generally reported without obvious alterations to host health status, and with no or only insignificant inflammatory responses in the *lamina propria*, although inflammatory infiltrates are occasionally seen (e.g. Taylor et al. 1999, Masuno et al. 2006, Kváč et al. 2008). Nevertheless, there are obvious differences in histopathological changes induced by different gastric species, load of parasite inoculum or immunological status of their host.

In addition, other pathogens might escalate the impact of cryptosporidiosis on host tissue. For example, in mice simultaneously infected with *Cryptosporidium muris* and *Helicobacter felis*, the gastric glands were more severely parasitised by cryptosporidia, and their stomachs showed more severe cellular infiltrates (Tatar et al. 1995). The fundus glands of nude mice inoculated with strain RN 66 of *C. muris* showed dilatation with mild epithelial changes (Taylor et al. 1999), and only mice receiving an inoculum of 1,000,000 oocysts showed an inflammatory reaction.

A study using SCID mice reported only mild gastric cryptosporidiosis without gross pathologic findings (Jalovecká et al. 2010). The maximum peak of parasitisation intensity was 21 DPI, whereas the highest numbers of immune cells occurred in the gastric epithelium at 28 DPI, a period when the majority of mice had already been cured of the infection. Immunocompetent mice inoculated with either *C. muris* CB03 or *Cryptosporidium proliferans* developed T cell responses leading to a clearance of the primary infection and complete resistance to re-infection with the same strain (Jalovecká et al. 2010, Kváč et al. 2011). In contrast, the intensity of infection with *C. proliferans* in experimentally infected *Mastomys coucha* continued to increase throughout experiments with maximum oocysts' shedding at 126 DPI and animals developed lifelong (chronic) infection (Melicherová et al. 2014, Kváč et al. 2016).

Despite the considerable gross pathology of gastric epithelium documented in this and previous studies (Melicherová et al. 2014, Kváč et al. 2016), neither clinical signs of cryptosporidiosis, nor weight lost were observed in southern multimammate mice. In contrast to previous studies (Melicherová et al. 2014, Kváč et al. 2016), we observed the inflammatory infiltration of muscularis mucosae

and submucosa with neutrophils. Great variations in oocyst shedding accompanied by heavy cryptosporidiosis revealed in histological sections of southern multimammate mice stomach in this study are also rather inconsistent with the recent study by Kváč et al. (2016), in which high numbers of cryptosporidian developmental stages were typically associated with high oocyst shedding.

In cattle parasitised by *Cryptosporidium andersoni*, despite the lack of apparent clinical signs, severe infection was observed in the abomasum with prominent hyperplasia of mucosa, along with a moderate degree of inflammatory infiltration of *lamina propria* (Masuno et al. 2006). The number and length of gastric pits increased considerably because of the increasing number of epithelial cells. Thickening and granulation of abomasal mucosa were often reported (Anderson 1998). The epithelium of the stomach antrum in an immunocompetent human patient with isolated gastric cryptosporidiosis was shown to be disorganised, fragile, and infiltrated by neutrophils (Ramsay et al. 2007). Gastric involvement in AIDS patients is usually considered to be secondary to retrograde spread from the small intestine (Val-Bernal et al. 2013). Related to *Cryptosporidium* gastropathy, patients suffer from vomiting and epigastric pain. The gastric wall might exhibit a lack of distensibility, stiffness, thickening, distortion or erosions of the mucosal folds involving the antrum region (Val-Bernal et al. 2013). Regularly in the same biopsy, areas with cryptosporidia were contiguous to negative ones. Various degrees of mucosal alterations were observed, even in the same individual. Besides hyperplastic reactive changes, high intensity of infection correlates with erosions and acute inflammation. Commonly, individuals with gastric cryptosporidiosis show no significant endoscopic alteration to the gastric mucosa, even though histological features are highly modified. In this and previous studies (Melicherová et al. 2014), we also observed a patchy (island-like) distribution of *C. proliferans*. Similarly to the course of cryptosporidiosis in other homoiotherm vertebrates, the rodents in our study did not show any clinical signs of cryptosporidiosis.

Trends in drug development and screening studies testing potentially anti- cryptosporidial compounds

Cryptosporidium spp. represent a highly problematic target for drug development. One of the self-protective strategies of cryptosporidia against the harsh conditions of the host's gastrointestinal tract is their unique epicellular localisation within a parasitophorous sac of host cell origin (Valigurová et al. 2007, 2008). The oocysts of cryptosporidia sporulate inside the host and infective oocysts are transmitted by the faecal-oral route. Besides the most commonly used antibiotics and halofuginone, numerous compounds have been screened for potential anti-cryptosporidial activity, but the majority were ineffective. Although some drugs have shown promise in calves and lambs, they are too expensive (paramomycin) or highly toxic at effective doses (halfuginone lactate and lasalocid) (Tzipori 1998). Therefore, along with antibiotics administered to control secondary bacterial infections, it has

been recommended to treat intestinal cryptosporidiosis in calves with fluid therapy and the correction of acid-base disturbances (Tzipori 1998). Colostrum containing anti-*Cryptosporidium* antibodies also appears to be beneficial (O'Donoghue 1995).

More recent studies have reported halofuginone (Halocur) administration at the recommended dose of 100 µg/kg for 7–10 consecutive days as very effective in stopping diarrhoea and preventing deaths without side effects (Giadinis et al. 2008, Petermann et al. 2014). At this dose, it appears to inhibit the reproduction of cryptosporidia within the host and encourages the development of immunity in lambs (Causapé et al. 1999). Nitazoxanide, though not effective in immunocompromised patients, significantly shortens the duration of diarrhoea and decreases mortality in adults and malnourished children (Gargala 2008).

Similarly, newly synthesised nitro- or non nitro- thiazolide compounds, derived from nitazoxanide, have been shown to be effective against *Cryptosporidium parvum* (see Gargala 2008). Furthermore, compounds active against protein disulphide isomerases (PDI2 and PDI4), the epidermal growth factor (EGF) receptor, pp60v-src, and pp110gag-fes, as well as new isoflavone derivatives, seem to represent promising targets (Ortega-Pierres et al. 2009). SCID mice orally administered with the chicken egg yolk antibody against *C. parvum* infection demonstrated partial reduction in oocyst shedding (Kobayashi et al. 2004).

Whilst the majority of these studies have been performed on intestinal cryptosporidia, usually *C. parvum*, there is still a lack of experimental work dealing with the treatment of gastric cryptosporidiosis and most of the few published works deal with the treatment of AIDS patients. One of these papers has shown a positive effect of paramomycin on reducing inflammation of the gastric mucosa and mild relief from pain and diarrhoea, despite parasite persistence in mucosa (Ventura et al. 1997). Another study reported the eradication of AIDS-related gastric cryptosporidiosis with azithromycin and suggested long-term treatment (Díaz Peromingo et al. 1999).

In our study, none of the Indonesian plant extracts were shown to be effective against gastric cryptosporidiosis, despite their proven activity against other protists parasitising the small intestine (Pecková et al. 2018). For the first trial, the dosage was calculated based on behavioural observation of self-medication of wild animals (e.g. the number of plant leaves consumed), but the dosage for the second trial was increased to 40 mg to increase the potential antiparasitic effect. This dosage was calculated based on maximum concentrations of extracts reported in the literature (e.g. Bin-Hafeez et al. 2003, Squires et al. 2011). Although additional assays with different doses in a wide scale would be of interest, such an extensive experiment would be too demanding of time and material, especially in the number of laboratory rodents required. Hence, respecting the rules for breeding animals, regulated by Czech legislation and the legislation of the European Commission on protection of animals against cruelty, we have designed our experiments so that we do not use too many laboratory rodents unnecessarily, as do most of the world's laboratories.

The oral administration of Halocur – even for a prolonged period – was not sufficiently effective either, though it slightly decreased the degree of oocyst shedding and seemed to facilitate the regeneration of epithelial cells lining the gastric pits. Nevertheless, in contrast to previous reports, it did not seem to inhibit the reproduction of cryptosporidia, although some slight decrease might be observed in the trendline showing oocyst excretion (Figs. 4, 5). Similarly, halofuginone treatment did not produce a satisfactory therapeutic outcome for infection with *Cryptosporidium serpentis* Levine, 1980 affecting the gastric mucosa of snakes (Graczyk et al. 1996), suggesting its ineffectiveness against gastric cryptosporidiosis.

Of special interest, however, was the positive impact of *Arabidopsis thaliana* on the gastric mucosa pathologically altered by chronic cryptosporidiosis. *Arabidopsis thaliana* is a small Eurasian annual flowering plant routinely used as an important model plant in molecular biology research and is reported to be edible (Lindh et al. 2008, Hansson et al. 2016). The extract from the green parts (leaves) of this plant was used as a control and we expected it to have a neutral effect on animal health and its parasitised gastric tissue, as we found only a few studies reporting the positive effect of *A. thaliana* seed extract.

The use of plant-derived products as antimicrobial agents has been investigated in depth. Isothiocyanates (ITCs) are bioactive products resulting from enzymatic hydrolysis of glucosinolates (GLs), the most abundant secondary metabolites in the plant order Brassicales. Although the antimicrobial activity of ITCs against foodborne and plant pathogens has been well documented, little is known about their antimicrobial properties against human pathogens (Romeo et al. 2018). Concurrently, during the trial finalisation in this study, an unexpected positive effect of *A. thaliana* plant extract on the reduction of spores of microsporidian *Encephalitozoon cuniculi* Levaditi, Nicolau et Schoen, 1923 in the tissues of experimentally inoculated BALB/c mice was documented (Mynářová 2015). Different genetic programs, activated upon pathogen recognition and leading to the production of inducible antimicrobial compounds, have been identified in this plant (Tierens et al. 2001). Using the fungus *Neurospora crassa* as a test organism, Tierens et al. (2001) analysed the antimicrobial compounds from aqueous extracts of leaves of *Arabidopsis* and suggested their role in the plant's protection against some pathogens. The treatment of mice with Alloxan-induced diabetes with *A. thaliana* at a dose of 200 mg/kg BM led to a significant reduction in blood glucose levels and an improvement in insulin resistance (Rashid et al. 2013, 2014; Taha et al. 2014). The consumption of *A. thaliana* reversed most of the histological changes in the liver of the diabetic mice, stimulated protein synthesis by increasing the number of ribosomes and significantly reduced oxidative stress in diabetes (= antioxidant effect) (Rashid et al. 2014). Moreover, as *A. thaliana* plants have a close relationship with species of Brassica eaten by humans it is of particular interest with respect to further investigations.

Methods used for treatment efficacy evaluation: limitations in the screening of anti-cryptosporidial drugs.

During the course of our experiments, we found a number of unexpected difficulties and limitations. One of these is the need for sufficient (preferably more than estimated) stocks of tested plant extracts for individual trials, which can be a problem in screening studies using exotic plants where their availability and quantity might be strictly limited (such as those used in our study). Primary screening of experimental protocols, therapeutic doses and the effectiveness of selected plant extracts in various solvent media consumes a lot of material before starting the animal experiments. Therefore, for pilot screening of the antiparasitic effect, it is preferable to use an *in vitro* system, at least for parasites where cultivation is possible (e.g. *C. parvum*). *In vitro* studies require smaller volumes of plant extracts and this approach helps to minimise the number of animals used and to reduce their distress during experiments.

Another issue was the variability of the course of infection in tested animals inoculated at the same doses, resulting in variations in oocyst shedding. Similarly to Sréter et al. (1995) relatively small numbers of animals are required for the estimation of the length of the prepatent period, but large numbers of animals are needed for the estimation of the mean of oocyst excretion. Additionally, histological observations of treatment effects during early stage cryptosporidiosis can be misleading, due to mild histopathological changes and the patchy occurrence of the parasite.

Promising reports from studies focusing on anti-cryptosporidial drug development are usually based on a reduction in oocyst shedding. The results of this study, however, indicate that the evaluation of parasitisation intensity based exclusively on the number of oocysts shed in faeces can be misleading. For example, despite a decline in oocyst shedding in some treatment groups (including those administered with Halocur), all known developmental stages of *C. proliferans*, from early stages invading epithelial cells, or freshly attached to the epithelium surface to oocysts enveloped by a parasitophorous sac, were observed in corresponding SEM and histological preparations. This means that despite the fact that fewer oocysts were excreted in host faeces, their development did not stop. Recently, it has been shown that rats infected with *Cryptosporidium occultus* Kváč, Vlnatá, Ježková, Horčičková, Konečný, Hlásková, McEvoy et Sak, 2018 shed fewer oocysts than would be predicted from the massive infection of the colonic epithelium (Kváč et al. 2018). This could be explained by the presence of two types of oocysts, i.e. thick- and thin-walled, in life cycle of *C. proliferans* and other species/genotypes (Current and Reese 1986, Uni et al. 1987, Melicherová et al. 2014). It is likely that the treatment simply induces increased production of thin-walled oocysts, which excyst once they separate from host epithelium, are not usually excreted in faeces and appear to be responsible for autoinfection. The multiplication of cryptosporidia inside the same host via autoinfective oocysts (= sexual stage) appears to be beneficial for increasing parasite genetic variability, and thereby fitness and infectivity (Melicherová et

al. 2014). Alternatively, the drug-affected parasite could begin investing in asexual multiplication and undergo multiple rounds of merogony I to produce high numbers of invasive merozoites. Autoinfection and the recycling of type I merogony provide an explanation for persistent chronic infections (Bouzid et al. 2013).

A further problem in similar studies is the correct choice of microscopic techniques for screening for parasite presence and morphopathological changes of the parasitised tissue. The surface topology detectable by SEM is insufficient for gastric cryptosporidia if not supplemented by histological sectioning as the mucus, a thick substance naturally produced by surface cells and cells of the gland necks to prevent self-digestion of the gastric mucosa, might hamper the view inside the gastric gland. This relatively thick layer, forming a non-transparent film after chemical fixation, is usually almost impossible to wash away, despite the careful and repetitive rinsing of stomach tissue (Melicherová et al. 2014). In addition, SEM analyses did not prove helpful in evaluating parasitisation intensity of gastric tissue, as it did not enable close examination of constricted or only slightly dilated pits. Transmission electron microscopy represents a powerful tool for evaluating pathological aspects along with the presence of parasites, but it is too expensive and time consuming for studies not focusing on ultrastructural aspects. Hence, to more accurately assess anti-cryptosporidial treatment efficacy in laboratory-housed animals, the most reliable and economic approach seems to be the monitoring of oocyst shedding accompanied by histological (gastric tissue) or SEM analysis (applicable for intestinal tissue) of the parasitised epithelium *post mortem*. Although such an approach is not applicable for medical purposes or for studies dealing with livestock, experimental studies on small laboratory animals based on the most accurate evaluation would provide important information on the actual effect of the drug tested.

REFERENCES

Abu El Ezz N.M.T., Khalil F.A.M., Shaapan R.M. 2011: Therapeutic effect of onion (*Allium cepa*) and cinnamon (*Cinnamomum zeylanicum*) oils on cryptosporidiosis in experimentally infected mice. Glob. Vet. 7: 179–183.

Anderson B.C. 1998: Cryptosporidiosis in bovine and human health. J. Dairy Sci. 81: 3036–3041.

Arrowood M.J., Sterling C.R. 1987: Isolation of *Cryptosporidium* oocysts and sporozoites using discontinuous sucrose and isopycnic Percoll gradients. J. Parasitol. 73: 314–319.

Bin-Hafeez B., Haque R., Parvez S., Pandey S., Sayeed I., Raisuddin S. 2003: Immunomodulatory effects of fenugreek (*Trigonella foenum graecum* L.) extract in mice. Int. Immunopharmacol. 3: 257–265.

Bouzid M., Hunter P.R., Chalmers R.M., Tyler K.M. 2013: *Cryptosporidium* pathogenicity and virulence. Clin. Microbiol. Rev. 26: 115–134.

Castro I.C., Oliveira B.B., Slowikowski J.J., Coutinho B.P., Siqueira F.J.W., Costa L.B., Sevilleja J.E., Almeid C.A., Lima A.A., Warren C.A., others. 2012: Arginine decreases *Cryptosporidium parvum* infection in undernourished suckling mice involving nitric oxide synthase and arginase. Nutrition 28: 678–685.

Causapé A.C., Sanchez-Acedo C., Quilez J., Del Cacho E., Viu M. 1999: Efficacy of halofuginone lactate against natural *Cryptosporidium parvum* infections in lambs. Res. Rev. Parasitol. 59: 41–46.

Chen X-M., Keithly J.S., Paya C.V., LaRusso N.F. 2002: Cryptosporidiosis. N. Engl. J. Med. 346: 1723–1731.

Current W.L., Reese N.C. 1986: A comparison of endogenous development of three isolates of *Cryptosporidium* in suckling mice. J. Protozool. 33: 98–108.

Díaz Peromingo J.A., Callejo A.M., Rodríguez J.G., González C.G., Lago M.A., Alvariño J.C., Sánchez P.S. 1999: Eradication of AIDS-related gastric cryptosporidiosis with azithromycin. Eur. J. Intern. Med. 10: 220–222.

Fareed G., Scolaro M., Jordan W., Sanders N., Chesson C., Seattery M., Long D., Castro C. 1996: The use of a high-dose garlic preparation for the treatment of *Cryptosporidium parvum* diarrhea. In: Proceedings of the XI International Conference on AIDS in Vancouver, Canada, July 7–12, 1996, 11: 288

Fayer R., Morgan U., Upton S.J. 2000: Epidemiology of *Cryptosporidium*: transmission, detection and identification. Int. J. Parasitol. 30: 1305–1322.

Foitová I., Huffman M.A., Dušek L., Jarkovský J., Klapka R., Olšanský M. 2010: Parasites species diversity and infection intensity of orangutan - Ecology factors with an emphasis on food items in their diets. In: Proceedings of the XXIII Congress of the International Primatological Society in Kyoto University, Kyoto, Japan, September 12–18, 2010, 26: 146

Foster J.C., Glass M.D., Courtney P.D., Ward L.A. 2003: Effect of *Lactobacillus* and *Bifidobacterium* on *Cryptosporidium parvum* oocyst viability. Food Microbiol. 20: 351–357.

Gaafar M.R. 2012: Efficacy of *Allium sativum* (garlic) against experimental cryptosporidiosis. Alexandria J. Med. 48: 59–66.

Gargala G. 2008: Drug treatment and novel drug target against *Cryptosporidium*. Parasite 15: 275–281.

Giadinis N.D., Papadopoulos E., Lafi S.Q., Panousis N.K., Papazahariadou M., Karatzias H. 2008: Efficacy of halofuginone lactate for the treatment and prevention of cryptosporidiosis in goat kids: an extensive field trial. Small Ruminant Res. 76: 195–200.

Graczyk T.K., Cranfield M.R., Hill S.L. 1996: Therapeutic efficacy of halofuginone and spiramycin treatment against *Cryptosporidium serpentis* (Apicomplexa: Cryptosporidiidae) infections in captive snakes. Parasitol. Res. 82: 143–148.

Grehan J.R., Schwartz J.H. 2009: Evolution of the second orangutan: phylogeny and biogeography of hominid origins. J. Biogeogr. 36: 1823–1844.

Hansson C., Schön K., Kalbina I., Strid Äke, Andersson S., Bokarewa M.I., Lycke N.Y. 2016: Feeding transgenic

plants that express a tolerogenic fusion protein effectively protects against arthritis. Plant Biotechnol. J. 14: 1106–1115.

Jalovecká M., Sak B., Kváč M., Květoňová D., Kučerová Z., Salát J. 2010: Activation of protective cell-mediated immune response in gastric mucosa during *Cryptosporidium muris* infection and re-infection in immunocompetent mice. Parasitol. Res. 106: 1159–1166.

Jirků M., Valigurová A., Koudela B., Křížek J., Modrý D., Šlapeta J. 2008: New species of *Cryptosporidium* Tyzzer, 1907 (Apicomplexa) from amphibian host: morphology, biology and phylogeny. Folia Parasitol. 55: 81–94.

Kilani R.T., Sekla L. 1987: Purification of *Cryptosporidium* oocysts and sporozoites by cesium chloride and Percoll gradients. Am. J. Trop. Med. Hyg. 36: 505–508.

Kobayashi C., Yokoyama H., Van Nguyen S., Kodama Y., Kimata T., Izeki M. 2004: Effect of egg yolk antibody on experimental *Cryptosporidium parvum* infection in SCID mice. Vaccine 23: 232–235.

Kváč M., Havrdová N., Hlásková L., Daňková T., Kanděra J., Ježková J., Vítovec J., Sak B., Ortega Y., Xiao L., Modrý D., Chelladurai J.R., Prantlová V., McEvoy J. 2016: *Cryptosporidium proliferans* n. sp. (Apicomplexa: Cryptosporidiidae): molecular and biological evidence of cryptic species within gastric *Cryptosporidium* of mammals. PloS ONE 11: e0147090.

Kváč M., Kodádková A., Sak B., Květoňová D., Jalovecká M., Rost M., Salát J. 2011: Activated CD8+ T cells contribute to clearance of gastric *Cryptosporidium muris* infections. Parasite Immunol. 33: 210–216.

Kváč M., Ondráčková Z., Květoňová D., Sak B., Vítovec J. 2007: Infectivity and pathogenicity of *Cryptosporidium andersoni* to a novel host, southern multimammate mouse (*Mastomys coucha*). Vet. Parasitol. 143: 229–233.

Kváč M., Sak B., Květoňová D., Ditrich O., Hofmannová L., Modrý D., Vítovec J., Xiao L. 2008: Infectivity, pathogenicity, and genetic characteristics of mammalian gastric *Cryptosporidium* spp. in domestic ruminants. Vet. Parasitol. 153: 363–367.

Kváč M., Vlnatá G., Ježková J., Horčičková M., Konečný R., Hlásková L., McEvoy J., Sak B. 2018: *Cryptosporidium occultus* sp. n. (Apicomplexa: Cryptosporidiidae) in rats. Eur. J. Protistol. 63: 96–104.

Lindh I., Kalbina I., Thulin S., Scherbak N., Sävenstrand H., Bråve A., Hinkula J., Strid Å., Andersson S. 2008: Feeding of mice with *Arabidopsis thaliana* expressing the HIV-1 subtype C p24 antigen gives rise to systemic immune responses. APMIS 116: 985–994.

Masuno K., Yanai T., Hirata A., Yonemaru K., Sakai H., Satoh M., Masegi T., Nakai Y. 2006: Morphological and immunohistochemical features of *Cryptosporidium andersoni* in cattle. Vet. Pathol. 43: 202–207.

Melicherová J., Ilgova J., Kváč M., Sak B., Koudela B., Valigurová A. 2014: Life cycle of *Cryptosporidium muris* in two rodents with different responses to parasitisation. Parasitology 141: 287–303.

Melicherová J., Mazourová V., Valigurová A. 2016: *In vitro* excystation of *Cryptosporidium muris* oocysts and viability of released sporozoites in different incubation media. Parasitol. Res. 115: 1113–1121.

Miláček P., Vítovec J. 1985: Differential staining of cryptosporidia by aniline-carbol-methyl violet and tartrazine in smears from faeces and scrapings of intestinal mucosa. Folia Parasitol. 32: 50.

Moore D., Waters W.R., Wannemuehler M.J., Harp J.A. 2001: Treatment with agmatine inhibits *Cryptosporidium parvum* infection in infant mice. J. Parasitol. 87: 211–213.

Morrogh-Bernard H., Foitová I., Yeen Z., Wilkin P., De Martin R., Rárová L., Doležal K., Nurcahyo W., Olšanský M. 2017: Self-medication by orang-utans (*Pongo pygmaeus*) using bioactive properties of *Dracaena cantleyi*. Sci. Rep. 7: 16653.

Mynářová A. 2015: The prevalence and diversity of *Cryptosporidium*, *Giardia* and microsporidia in orangutans (*Pongo* spp.) and the effect of selected plant extracts on the course of experimental infection with *Encephalitozoon cuniculi* in BALB/c mice. University of South Bohemia in České Budějovice, 106 pp, Master's thesis. (In Czech)

Nakamura A.A., Meireles M.V. 2015: *Cryptosporidium* infections in birds – a review. Rev. Bras. Parasitol. Vet. 24: 253–267.

O'Donoghue P.J. 1995: *Cryptosporidium* and cryptosporidiosis in man and animals. Int. J. Parasitol. 25: 139–195.

Ortega-Pierres G., Cacciò S., Fayer R., Mank T.G., Smith H.V., Thompson R.C.A. (Eds.) 2009: *Giardia* and *Cryptosporidium*: From Molecules to Disease. CABI, Wallingford, 520 pp.

Pecková R., Doležal K., Sak B., Květoňová D., Kváč M., Nurcahyo W., Foitová I. 2018: Effect of *Piper betle* on *Giardia intestinalis* infection *in vivo*. Exp. Parasitol. 184: 39–45.

Perrucci S., Fichi G., Buggiani C., Rossi G., Flamini G. 2006: Efficacy of mangiferin against *Cryptosporidium parvum* in a neonatal mouse model. Parasitol. Res. 99: 184–188.

Petermann J., Paraud C., Pors I., Chartier C. 2014: Efficacy of halofuginone lactate against experimental cryptosporidiosis in goat neonates. Vet. Parasitol. 202: 326–329.

Pickerd N., Tuthill D. 2004: Resolution of cryptosporidiosis with probiotic treatment. Postgrad. Med. J. 80: 112–113.

Ramsay D.B., Long S.E., Ali M.A., Entwisle C., Orenstein J.M., Rossi C., Borum M.L. 2007: Isolated gastric cryptosporidiosis in an immunocompetent patient. Dig. Dis. Sci. 52: 1364–1366.

Rashid K.I., Aljibouri A.M., Zayer A.J., Khalid L.B., Abdul-Munaem A. 2013: Study the effect of *Arabidopsis thaliana* extract on reducing blood glucose level in diabetic white albino mice. Iraqi J. Pharm. Sci. 22: 115–119.

Rashid K.I., Kamel A.M., Bakir T.Y. 2014: Preventative effects of *Arabidopsis thaliana* extract on liver damage of diabetic mice induced by Alloxan. J. Pharm. Res. 4: 82–86.

Rivasi F., Rossi P., Righi E., Pozio E. 1999: Gastric cryptosporidiosis: correlation between intensity of infection and histological alterations. Histopathology 34: 405–409.

Romeo L., Iori R., Rollin P., Bramanti P., Mazzon E. 2018: Isothiocyanates: an overview of their antimicrobial activity against human infections. Molecules 23: 624.

Rotkiewicz T., Rotkiewicz Z., Depta A., Kander M. 2001: Effect of *Lactobacillus acidophilus* and *Bifidobacterium* sp. on the course of *Cryptosporidium parvum* invasion in new-born piglets. Bull. Vet. Inst. Pulawy 45: 187–196.

Ryan U. 2010: *Cryptosporidium* in birds, fish and amphibians. Exp. Parasitol. 124: 113–120.

Shahiduzzaman M., Dyachenko V., Khalafalla R.E., Desouky A.Y., Daugschies A. 2009: Effects of curcumin on *Cryptosporidium parvum* in vitro. Parasitol. Res. 105: 1155–1161.

Squires J.M., Ferreira J.F., Lindsay D.S., Zajac A.M. 2011: Effects of artemisinin and *Artemisia* extracts on *Haemonchus contortus* in gerbils (*Meriones unguiculatus*). Vet. Parasitol. 175: 103–108.

Sréter T., Varga I., Békési L. 1995: Age-dependent resistance to *Cryptosporidium baileyi* infection in chickens. J. Parasitol. 81: 827–829.

Taha M.A., Ahmed S.J., Rashid K.I. 2014: Histological study on the effect of *Arabidopsis thaliana* extraction on Alloxan-induced diabetic infertility mice. Int. J. Drug. Discov. 6: 207–212.

Tarantino C., Flamini G., Perrucci S. 2004: Anticryptosporidial activity of some extracts of *Santolina ligustica* and *Centaurea horrida* and of Mangiferin. Parassitologia 46: 130–131.

Tatar G., Haziroğlu R., Hascelik G. 1995: *Helicobacter felis* as a cofactor alone or together with stress in cryptosporidial activation in mice. J. Int. Med. Res. 23: 473–479.

Taylor M.A., Marshall R.N., Green J.A., Catchpole J. 1999: The pathogenesis of experimental infections of *Cryptosporidium muris* (strain RN 66) in outbred nude mice. Vet. Parasitol. 86: 41–48.

THOMPSON R.C.A., OLSON M.E., ZHU G., ENOMOTO S., ABRA-
    HAMSEN M.S., HIJJAWI N.S. 2005: *Cryptosporidium* and cryp-
    tosporidiosis. Adv. Parasitol. 59: 77–158.
TIERENS K.F., THOMMA B.P., BROUWER M., SCHMIDT J., KIST-
    NER K., PORZEL A., MAUCH-MANI B., CAMMUE B.P., BROE-
    KAERT W.F. 2001: Study of the role of antimicrobial glucosino-
    late-derived isothiocyanates in resistance of *Arabidopsi*s to
    microbial pathogens. Plant Physiol. 125: 1688–1699.
TYZZER E.E. 1910: An extracellular coccidium, *Cryptosporidi-
    um muris* (gen. et sp. nov.) of the gastric glands of the common
    mouse. J. Med. Res. 23: 487–510.
TZIPORI S. 1998: Cryptosporidiosis: laboratory investigations and
    chemotherapy. Adv. Parasitol. 40: 187–221.
UNI S., ISEKI M., MAEKAWA T., MORIYA K., TAKADA S. 1987:
    Ultrastructure of *Cryptosporidium muris* (strain RN 66) parasit-
    ising the murine stomach. Parasitol. Res. 74: 123–132.
VAL-BERNAL J.F., MAYORGA M., AZUETA A., CABEZAS J., LOZA-
    NO J.L., FERNÁNDEZ F. 2013: AIDS-related gastric cryptospo-
    ridiosis simulating malignancy. Rev. Esp. Patol. 46: 247–251.

VALIGUROVÁ A., HOFMANNOVÁ L., KOUDELA B., VÁVRA J. 2007:
    An ultrastructural comparison of the attachment sites between
    Gregarina steini and *Cryptosporidium muris*. J. Eukaryot. Mi-
    crobiol. 54: 495–510.
VALIGUROVÁ A., JIRKŮ M., KOUDELA B., GELNAR M., MODRÝ
    D., ŠLAPETA J. 2008: Cryptosporidia: epicellular parasites em-
    braced by the host cell membrane. Int. J. Parasitol. 38: 913–922.
VENTURA G., CAUDA R., LAROCCA L.M., RICCIONI M.E., TUM-
    BARELLO M., LUCIA M.B. 1997: Gastric cryptosporidiosis com-
    plicating HIV infection: case report and review of the literature.
    Eur. J. Gastroenterol. Hepatol. 9: 307–310.
WU L., JIANG X., SHEN Y., LU Z., TU G., FU X., CHEN S., CAO
    J. 2011: Efficacy of ginkgolic acids against *Cryptosporidium an-
    dersoni* in cell culture. Parasitol. Res. 109: 1475.
YOSHIMI N., MATSUNAGA K., KATAYAMA M., YAMADA Y.,
    KUNO T., QIAO Z., HARA A., YAMAHARA J., MORI H. 2001:
    The inhibitory effects of mangiferin, a naturally occurring glu-
    cosylxanthone, in bowel carcinogenesis of male F344 rats. Can-
    cer Lett. 163: 163–170.

Cite this article as: Valigurová A., Pecková R., Doležal K., Sak B., Květoňová D., Kváč M., Nurcahyo W., Foitová I. 2018: Lim-
itations in the screening of potentially anti-cryptosporidial agents using laboratory rodents with gastric cryptosporidiosis. Folia
Parasitol. 65: 010

7.14

Kováčiková M., Vaškovicová N., Nebesářová J.,

Valigurová A.

2018

**Effect of jasplakinolide and cytochalasin D on cortical elements
involved in the gliding motility of the eugregarine
Gregarina garnhami (Apicomplexa)**

Effect of jasplakinolide and cytochalasin D on cortical elements involved in the gliding motility of the eugregarine *Gregarina garnhami* (Apicomplexa)

Magdaléna Kováčiková[a],[*], Naděžda Vaškovicová[b], Jana Nebesářová[c], Andrea Valigurová[a]

[a] *Department of Botany and Zoology, Faculty of Science, Masaryk University, Kotlářská 2, 611 37 Brno, Czech Republic*
[b] *The Czech Academy of Sciences, Institute of Scientific Instruments, Královopolská 147, 612 64 Brno, Czech Republic*
[c] *University of South Bohemia, Faculty of Science and Biology Centre of the ASCR, Institute of Parasitology, České Budějovice, Czech Republic*

Abstract

Since apicomplexans represent exclusively parasitic unicellular organisms with medical and economic impacts, the principles of their motility have been studied intensively. By contrast, the movement in apicomplexan basal groups, such as gregarines, remains to be elucidated. The present study focuses on *Gregarina garnhami* parasitising the digestive tract of the locust *Schistocerca gregaria*, and investigates the involvement of cytoskeletal elements (the ectoplasmic network and myonemes) and the secretion of mucosubstances during eugregarine gliding motility. Combined microscopic analyses were used to verify the role of actin filaments and membranes' organisation in *G. garnhami* motility. A freeze-etching analysis of membranes revealed the size, density, and arrangement of intramembranous particles along with the distribution and size of pores and ducts. Experimental assays using actin-modifying drugs (jasplakinolide, cytochalasin D) confirmed that actin most likely plays a role in cell motility, principally in its filamentous form (=F-actin). Myonemes, localised in the border between the ectoplasm and endoplasm, correspond to the concentric bundles of F-actin. Microscopic analyses confirmed that changes in gamonts motility corresponding to the changes in the organisation and density of myonemes and the ectoplasmic network in drug-treated cells, suggesting that these structures might serve as contractile elements facilitating gliding motility in *G. garnhami*.

Introduction

Gregarines are a highly diversified, basal lineage of eukaryotic unicellular organisms belonging to the parasitic group Apicomplexa. Eugregarines are widespread in marine, freshwater, and terrestrial hosts and their development is traditionally considered to be restricted to invertebrate hosts (Schrével and Desportes 2015).

The gregarine pellicle comprises a plasma membrane beneath which an inner membrane complex (IMC), consisting of two closely apposed cortical cytomembranes, is located. The pellicle covering the surface of intestinal

---

*Corresponding author.
E-mail address:* kovacikova@sci.muni.cz (M. Kováčiková).

eugregarines creates numerous epicytic folds arranged in longitudinal lines separated by grooves (Schrével and Desportes 2015). The organisation of these folds shows an undulating pattern in some species (Valigurová and Koudela 2008; Valigurová et al. 2013; Vávra and Small 1969; Vivier 1968). The usually dilated tips of the epicytic folds comprise 12 nm filaments and ripple dense structures, thought to have a supportive scaffolding function or possibly representing a component of the motility motor (Kováčiková et al. 2017; Schrével et al. 1983; Valigurová et al. 2013; Walker et al. 1984).

In comparison to apicomplexan invasive stages (zoites), in which gliding motility is defined as substrate-dependent and facilitated by an actomyosin motor associated with their pellicle (Heintzelman 2015; Kappe et al. 2004; Keeley and Soldati 2004; Matuschewski and Schüler 2008; Sibley et al. 1998), the exact mechanism of motility in gregarines still remains to be elucidated (Valigurová et al. 2013). Intestinal eugregarines are usually capable of unidirectional progressive gliding with or without obvious changes of cell shape (King 1981, 1988; Kováčiková et al. 2017). The extrusion of a mucous material left to trail behind the gliding gregarines suggests this material to be a part of the gliding machinery (Mackenzie and Walker 1983; Valigurová et al. 2013; Walker et al. 1979). Ultrastructural analysis revealed diverse cortical filamentous structures (e.g. myonemes, ectoplasmic network), assumed to be involved in the motility and cell contraction (Beams et al. 1959; Hildebrand 1980; Valigurová et al. 2013; Walker et al. 1979). A more recent study on *Gregarina* representatives, comprising biochemical analysis, showed these ectoplasmic myonemes to be actin and myosin rich (Heintzelman 2004). Both proteins were also found in the gregarines' cortex (cell envelope comprising the three layered pellicle and associate cytoskeletal structures), following the pattern of longitudinally arranged epicytic folds (Ghazali et al. 1989; Ghazali and Schrével 1993; Heintzelman 2004; Valigurová et al. 2013). Nevertheless, only a few experimental studies have been performed to verify the role of actin filaments in eugregarine gliding motility, using cytoskeletal drugs such as jasplakinolide (inducing actin polymerisation) and cytochalasins (blocking the association or eventual dissociation of actin subunits) (King 1988; Valigurová et al. 2013; Walker et al. 1979).

The present study provides a complex microscopic analysis of the cell cortex in the eugregarine *Gregarina garnhami* (Gregarinidae Labbé, 1899) parasitising the intestine of the desert locust *Schistocerca gregaria* (Forskål, 1775) (Orthoptera, Acrididae). Using the combined approaches of light, electron and confocal microscopy, supplemented by experimental motility assays, we focused on structures that appear to be responsible for gliding motility in *G. garnhami*. A gliding force derived from the putative actomyosin system was already proposed by King (1988); however, the exact mechanism involved in eugregarine motility is still poorly characterised (Heintzelman 2004; Schrével and Desportes 2015; Valigurová et al. 2013). The main purpose of this study

was to perform experimental analyses comparable to those published on other apicomplexan species, to evaluate newly acquired data using different microscopic techniques and to link these data with already known fragmentary information about motility and related structures in *G. garnhami*. We have chosen this species for experimental purposes because it represents a model parasite from a widely available laboratory insect. Data obtained on this species is therefore verifiable and suitable for comparison with data published on other *Gregarina* spp. (e.g. Heintzelman 2004; Valigurová et al. 2013). For the first time, gamonts of *G. garnhami* were experimentally treated with jasplakinolide and cytochalasin D to observe their effect on eugregarine survival, motility and changes in cortical filaments of actin nature (myonemes and ectoplasmic network). Phalloidin, in comparison to actin antibodies, specifically binds to F-actin and provides the proof of drug-induced changes in organisation of actin filaments. This study also deals with a drug-induced changes of epicytic folds, the undulating pattern of which remains preserved, and with the role of mucus in gregarine gliding. Detailed FE analysis of gregarine cortex facilitated the visualisation and identification of structures that are difficult to observe under TEM (e.g. ectoplasmic network) and allowed us to distinguish between the types of pores. Additionally, complex statistical analysis of size/distribution of IMPs and pores' diameters was performed and compared with other *Gregarina* representatives (personal non-published data obtained during previous studies).

Material and Methods

Gamonts of *G. garnhami* were collected from the midgut and caeca of *S. gregaria* (Insecta, Orthoptera). After narcosis, decapitation, and dissection of the host, parasites were isolated from the host intestine using Ringer's saline solution (0.75% [w/v] NaCl, 0.035% [w/v] KCl, 0.021% [w/v] CaCl₂; pH = 7.2). Gregarine gamonts were then transferred to embryo dishes and carefully washed with Ringer's solution. The manipulation and observation of parasites were performed using an Olympus SZX7 stereomicroscope (Olympus).

For experimental assays, gregarines were divided among four embryo dishes with a 30 mm cavity. Afterwards, the parasites were treated with commercial membrane-permeable drugs influencing the polymerisation of actin: jasplakinolide (JAS, Invitrogen, Czech Republic) and cytochalasin D (CYT D, Invitrogen, Czech Republic). Both drugs were reconstituted in dimethyl sulfoxide (DMSO, Sigma-Aldrich, Czech Republic) to prepare a 1 mM stock solution and, prior to each experimental assay, diluted in Ringer's saline to prepare a working solution with a final concentration of 30 μM. For controls and each experimental assay with cytoskeletal drug, approximately 200 individuals of *G. garnhami* were used. The monitoring of parasite motility was performed hourly using a stereomicroscope. After 7 h of each experi-

mental assay, a portion of the gregarines (around 50 gamonts) was separated for the observation of mucus shedding, while the remaining portion was divided into thirds and fixed for electron (SEM and TEM) and confocal microscopic analyses.

Mucus shedding was observed on living drug-treated and control gregarines put on microscopic slides covered by a thin layer of microbiological LB agar (LB Broth with agar, Lennox; Sigma-Aldrich, Czech Republic) and slightly moistened with Ringer's solution. Observations were performed using an Olympus BX51 microscope (Olympus) equipped with phase contrast and an ND 25 filter.

For transmission electron microscopy (TEM), specimens were fixed in an ice bath in 2.5% (v/v) glutaraldehyde in phosphate buffered saline (PBS). Fixed samples were washed $3\times$ for 20 min and post-fixed in 2% (w/v) OsO_4 for 2 h in the same buffer. After rinsing $3\times$ for 20 min in PBS, samples were dehydrated in acetone series and embedded in Epon (Polybed 812). Ultrathin sections were cut with diamond knives using a Leica EM UC6 ultramicrotome (Leica Microsystems) and stained with uranyl acetate and lead citrate. Observations were made using a TEM-1010 (JEOL).

For scanning electron microscopy (SEM), specimens were fixed in 2.5% (v/v) glutaraldehyde in PBS, washed $3\times$ for 15 min and post-fixed in 2% (w/v) OsO_4 for 2 h, and finally washed $3\times$ for 15 min in the same buffer. After dehydration in an acetone series, parasites were critical point-dried with CO_2, coated with gold, and observed using a JSM-7401F (JEOL).

For freeze fracture, the cell suspension was fixed overnight in 2.77% (v/v) glutaraldehyde in 0.2 M cacodylate buffer (pH = 7.4). Afterwards, specimens were washed for 1 h in PBS and saturated with 20% glycerol (w) overnight in a refrigerator for cryprotection. Prior to further processing, the suspension was concentrated on a clock glass and the dense pellet was placed on a gold carrier using tweezers. Agar was used to ensure the better adhesion of the pellet to the gold carrier. Pellet was frozen in liquid nitrogen, mounted on a gold holder, and then processed in a BAF 060 freeze-etching system (BAL-TEC). The temperature for manipulation of the samples was set to $-100\,^{\circ}C$ and the pressure inside the chamber was 10^{-5} Pa. Subsequently, samples were fractured with a microtome knife and etched for 5 min. The surfaces of the fractured structures were coated with layers of platinum (2.4 nm at an angle 45°) and carbon (22.4 nm at an angle 90°). Afterwards, samples were removed from the BAF 060 device and melted at room temperature. Replicas were cleaned with 5% sodium hypochlorite and 70% sulfuric acid, then washed in distilled water and transferred to copper grids for examination using a Morgagni 268 D (FEI) transmission electron microscope. Statistical evaluation of intramembranous particles (IMP) per unit area (1 μm^2) was performed in ImageJ software; histograms illustrating the IMP size distribution were prepared in Microsoft Excel. The nomenclature follows that proposed in Branton et al. (1975) and used in Schrével et al. (1983) and Valigurová et al. (2013, 2017). Statistical data on gregarines from mealworms shown in Tables 2 and 4 were obtained from replicas used for study of Valigurová et al. (2013) and were not shown previously.

For confocal laser scanning microscopy (CLSM), specimens were fixed for 1 h in freshly prepared 4% paraformaldehyde in 0.1 M PBS at room temperature and washed $3\times$ for 15 min in 0.1 M PBS before further processing. Afterwards, the parasites were permeabilised in 0.5% Triton X-100 (Sigma-Aldrich, Czech Republic) for 1 h. For the direct fluorescent staining of F-actin, samples were incubated overnight at room temperature with phalloidin-tetramethylrhodamine B isothiocyanate (phalloidin-TRITC; Sigma-Aldrich, Czech Republic) and then washed $3\times$ for 10 min in 0.1 M PBS. Controls were incubated using the same protocol but without phalloidin. Preparations were mounted in VECTASHIELD Hard Set Mounting Medium (Vector laboratories, USA). Samples were examined under an Olympus IX81 FVBF-2 microscope equipped with a laser-scanning Fluo View 500 confocal unit (Fluo View 3.4 software; Olympus) and DP70 digital camera. Fluorescence was visualised using the TRITC (phalloidin, anti-myosin/544 nm) laser set.

Results

Cell motility in control and drug-treated gregarines

Gamonts of *G. garnhami* exhibited continuous progressive gliding motility without obvious abrupt changes in movement direction or speed (see Supplementary Video S1 for a video example in the online version at DOI: 10.1016/j.ejop.2018.08.006). The average of their gliding rate was 12.2 $\mu m/s$. After the application of 30 μM jasplakinolide (JAS) the gamonts were able to glide until the end of experiment (7 h) without obvious cell deformations or gliding deceleration (see Supplementary Video S2 for a video example in the online version at DOI: 10.1016/j.ejop.2018.08.006). The speed of movement of JAS-treated gamonts in the first half of the experiment (up to 4 h after drug application) was even slightly higher than in controls (15.5 $\mu m/s$ in average) and gradually decreased to a normal gliding rate (12.4 $\mu m/s$ in average). After washing the drug out and replacing it with Ringer's saline solution, gregarines still exhibited active forward gliding. In contrast, gregarines treated with 30 μM cytochalasin D stopped moving almost immediately after drug application (see Supplementary Video S3 for a video example in the online version at DOI: 10.1016/j.ejop.2018.08.006). At the end of the experiment (7 h after drug application) and after the careful washing out of cytochalasin D, their motility recovered, confirming that the gregarines were alive, but had suffered complete immobility (see Supplementary Video S4 for a video example in the online version at

Table 1. The treatment of living gamonts of *Gregarina garnhami* with actin-modifying drugs.

Changes/time after drug application	Drug (concentration)				
	Jasplakinolide (30 μM)	Cytochalasin D (30 μM)	Cytochalasin D (10 μM)	Cytochalasin D (5 μM)	Control in DMSO (30 μM)
Initial increase of gliding speed	≥10 min (100)	–	–	–	–
Decrease of gliding speed to a normal, regular movement	≥240 min (95)	–	–	–	–
Deceleration of gliding motility	–	–	–	≤60 min (100)	–
Complete stoppage of gliding	–	≥5 min (98)	≥5 min (95)	≥100 min (90)	–
Full recovery of gliding motility in majority of gregarines after washing in Ringer	gregarines exhibited gliding motility during entire experiment (95)	≥20 min (80)	≥20 min (80)	≥20 min (90)	gregarines exhibited active gliding motility during entire experiment (95)

The symbol '–' indicates no obvious changes; ≥changes appeared after the noted time period; ≤changes appeared only during the noted time period. The numbers in parenthesis represent the percentage of gamonts exhibiting the described motility changes.
NOTE: In control gregarines incubated with Ringer's saline solution the movement was regular with a constant gliding speed during the entire experiment duration.

Table 2. Summary of diameters of pores in *Gregarina garnhami* and three different *Gregarina* species.

Species	TEM			SEM			Replicas		
	SP	MP	LP	SP	MP	LP	SP	MP	LP
	Mean ± SE	Mean ± SE	Mean ± SE	Mean ± SE	Mean ± SE	Mean ± SE	Mean ± SE	Mean ± SE	Mean ± SE
Gregarina garnhami	–	39.8 ± 1.8	129.8 ± 6.3	–	–	41.9 ± 6.2	20.1 ± 0.6	47.8 ± 0.4	141.5 ± 1.9
Gregarina cuneata	–	24.5 ± 8.0	48.6 ± 3.2	13.4 ± 0.4	30.2 ± 1.0	48.6 ± 3.2	–	41.8 ± 1.2	120.0 ± 6.1
Gregarina polymorpha	–	–	42.8 ± 3.7	–	–	–	15.2 ± 2.7	40.5 ± 0.6	132.8 ± 4.1
Gregarina steini	–	39.6 ± 2.8	56.5 ± 3.3	14.1 ± 0.9	34.4 ± 2.2	87.5 ± 4.7	–	44.5 ± 1.1	128.9 ± 2.5

The mean diameter (nm) was calculated from measurements taken at the plasma membrane and cortical cytomembranes.
SP — small pore; MP — medium pore; LP — large pore/micropore.
SE — standard error.
− The character of the specimen did not allow the pore diameter to be reliably measured.

DOI: 10.1016/j.ejop.2018.08.006). In both cases (incubation with JAS and cytochalasin D), the monitoring of gliding in recovered cells for the next one hour showed that the majority of gregarines had survived the experiment and retained the ability to glide after the drugs had been washed out (Table 1).

The surface topology and ultrastructural organisation in control and drug-treated gregarines

Gamonts were divided into an anterior protomerite and posteriorly situated deutomerite, separated by a septum (Fig. 1a, c, e). The cell surface of *G. garnhami* gamonts was covered by a pellicle arranged into numerous, longitudinal epicytic folds (Figs. 1 a–f, 2 a–d, 3 a–f, 4 b, d, f, 6 a, b, e, f, 7 d–i). Individual folds clustering on several projections distributed regularly throughout the gregarine periphery created the so-called superfolds (Figs. 1 b, 2 a, b, d). Superficial SEM analysis revealed the presence of mucus drops on the apical and lateral parts of the epicytic folds, and deeper within the grooves (Figs. 1 a, b, 2 b, c). In addition, the site of the gregarine pellicle where the superfolds grouped together exhibited a denser secretion and accumulation of mucus, suggesting this part to be the gliding site (Fig. 1a, b; see Supplementary Fig. S1 for an example in the online version at DOI: 10.1016/j.ejop.2018.08.006). Either the epicytic folds of gregarines treated with JAS (Fig. 1c, d) or cytochalasin D (Fig. 1e, f) showed any significant changes in their arrangement under SEM when compared to control gregarines. Mucus drops were present on the surface of individuals in both drug-treated groups (Fig. 1d, f).

The pellicle was composed of three membranes: the plasma membrane and the underlying inner membrane complex (IMC; membrane system formed by a flattened alveolus) (Figs. 2 e, g, 6 a, b). In control samples, bundles of filamentous
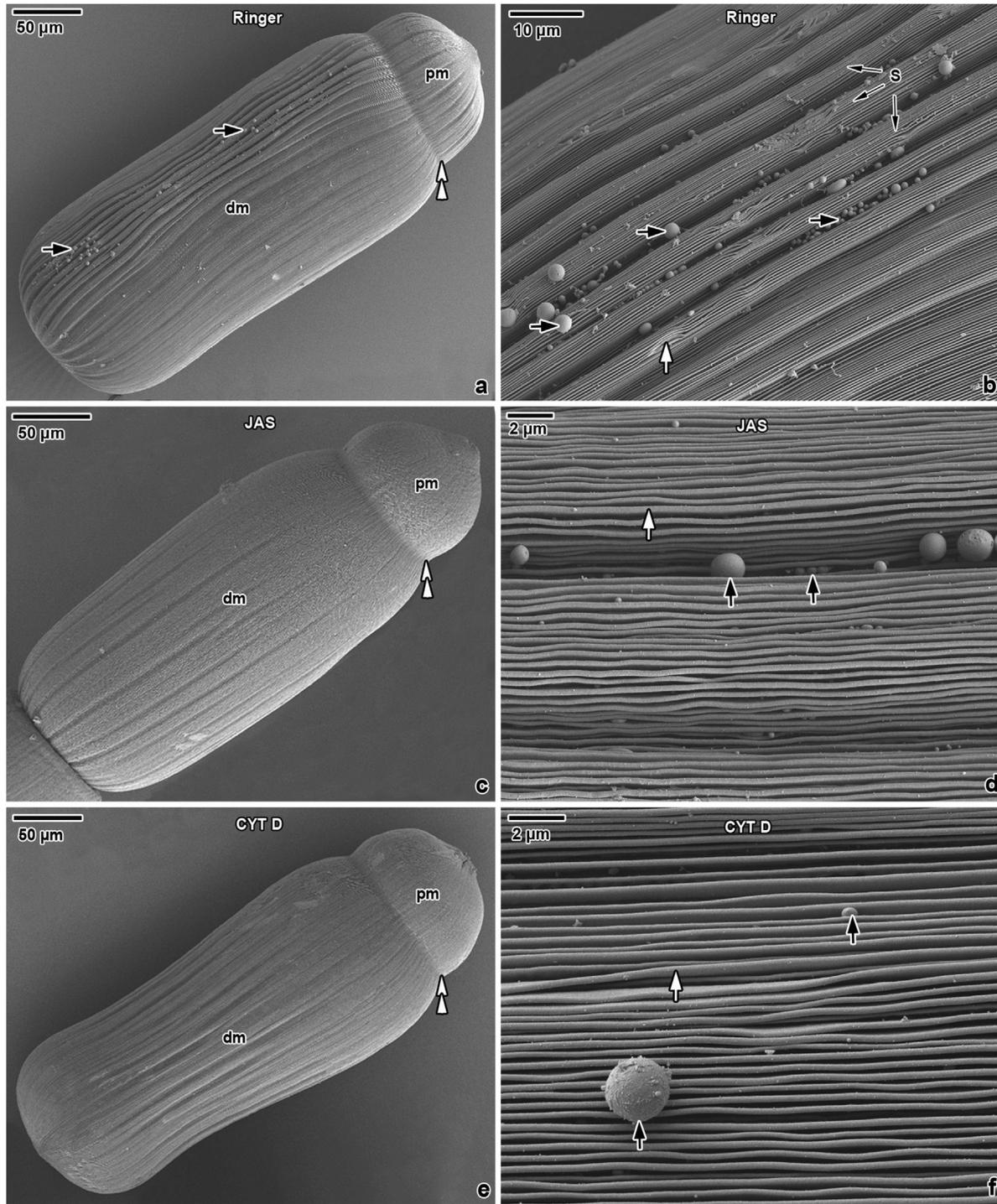
Fig. 1. General morphology of control and drug-treated *Gregarina garnhami* gamonts.
(a–b) The general (a) and detailed (b) view of epicytic folds and superfolds in control gregarines. Note epicytic folds grouped markedly at one side, with the increased secretion of a dense mucosubstance in this region. SEM. **(c–d)** General (c) and detailed (d) view of epicytic folds in an individuals incubated with 30 μm JAS for 7 h. SEM. **(e–f)** General (e) and detailed (f) view of epicytic folds in an individuals incubated with 30 μm cytochalasin D for 7 h. SEM.
black arrow — mucus drops, *dm* — deutomerite, *double white arrowhead* — constriction in the area of septum separating the protomerite from the deutomerite, *pm* — protomerite, *s* — superfolds, *white arrow* — epicytic folds.
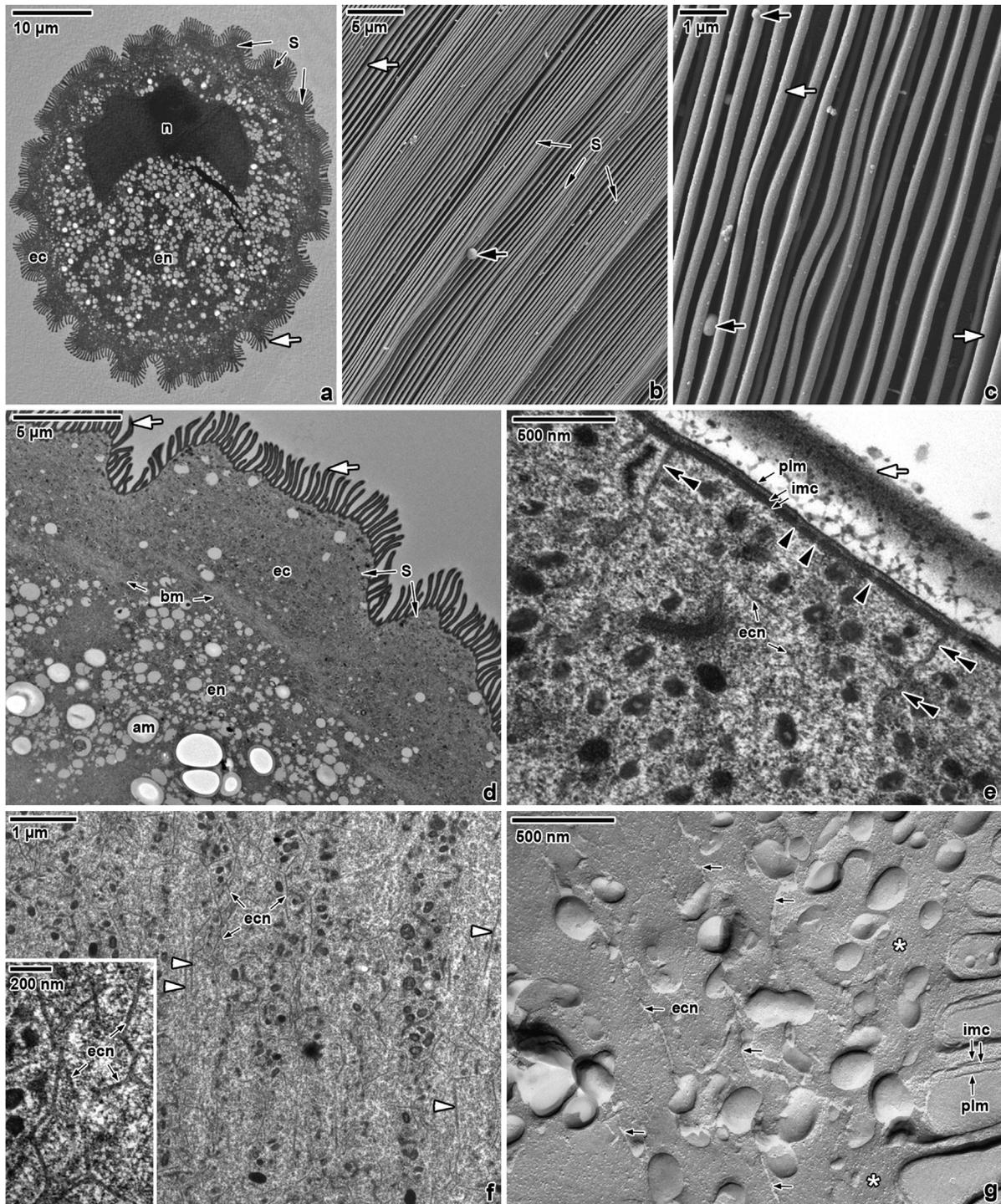
Fig. 2. Ultrastructure and morphology of *Gregarina garnhami* gamonts.
(a) Transversal section of deutomerite comprising the prominent nucleus, showing the organisation of superfolds. TEM. **(b–c)** Superficial view of longitudinal epicytic folds clustering together and forming the superfolds (b) and detail on their organisation at higher magnification (c) SEM. **(d)** Detail of superfolds and cytoplasm comprising the bundles of myonemes. TEM. **(e)** The three-layered pellicle and duct-like structures. TEM. **(f)** Superficial section of ectoplasm revealing the ectoplasmic filaments forming an anastomosing network. Inset shows the network in detail. TEM. **(g)** Organisation of the ectoplasm, comprising the filaments corresponding to the ectoplasmic network. FE TEM.
am — amylopectin*, black arrow* — mucus drops, *black arrowhead* — medium-sized pores, *bm* — bundles of myonemes, *double black arrowhead* — duct-like structure, *ec* — ectoplasm, *ecn* — ectoplasmic network, *en* — endoplasm, *imc* — inner membrane complex, *n* — nucleus, *plm* — plasma membrane, *s* — superfolds, *white arrow* — epicytic folds, *white arrowhead* — myonemes, *white asterisk* — cytoplasm.
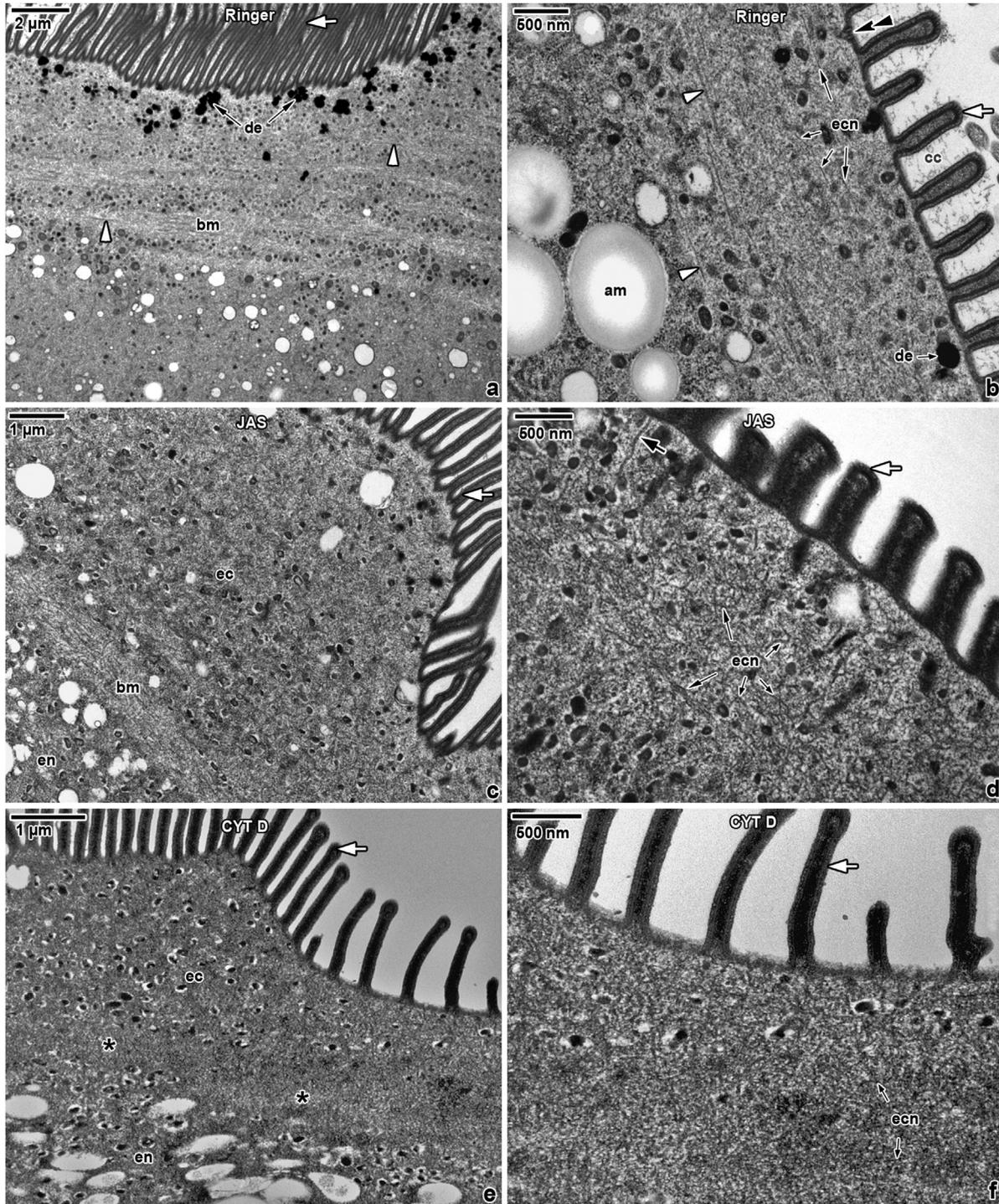
Fig. 3. Ultrastructure of cell cortex in control and drug-treated *Gregarina garnhami* gamonts.
(a–b) Cross section of cell cortex showing the ectoplasmic network and annular myonemes in control gamonts. TEM. **(c–d)** Cell cortex in gamonts incubated with 30 μm JAS for 7 h. TEM. **(e–f)** Cell cortex in gamonts incubated with 30 μm cytochalasin D for 7 h. Note the absence of annular myonemes and the fading ectoplasmic network. TEM.
am — amylopectin, *black arrow* — duct-like structure, *black asterisk* — area of usual occurrence of myonemes bundles in control gamonts, *bm* — bundles of myonemes, *cc* — cell coat, *de* — dense material, *double black arrowhead* — micropore, *ec* — ectoplasm, *ecn* — ectoplasmic network, *en* — endoplasm, *white arrow* — epicytic folds, *white arrowhead* — myonemes.
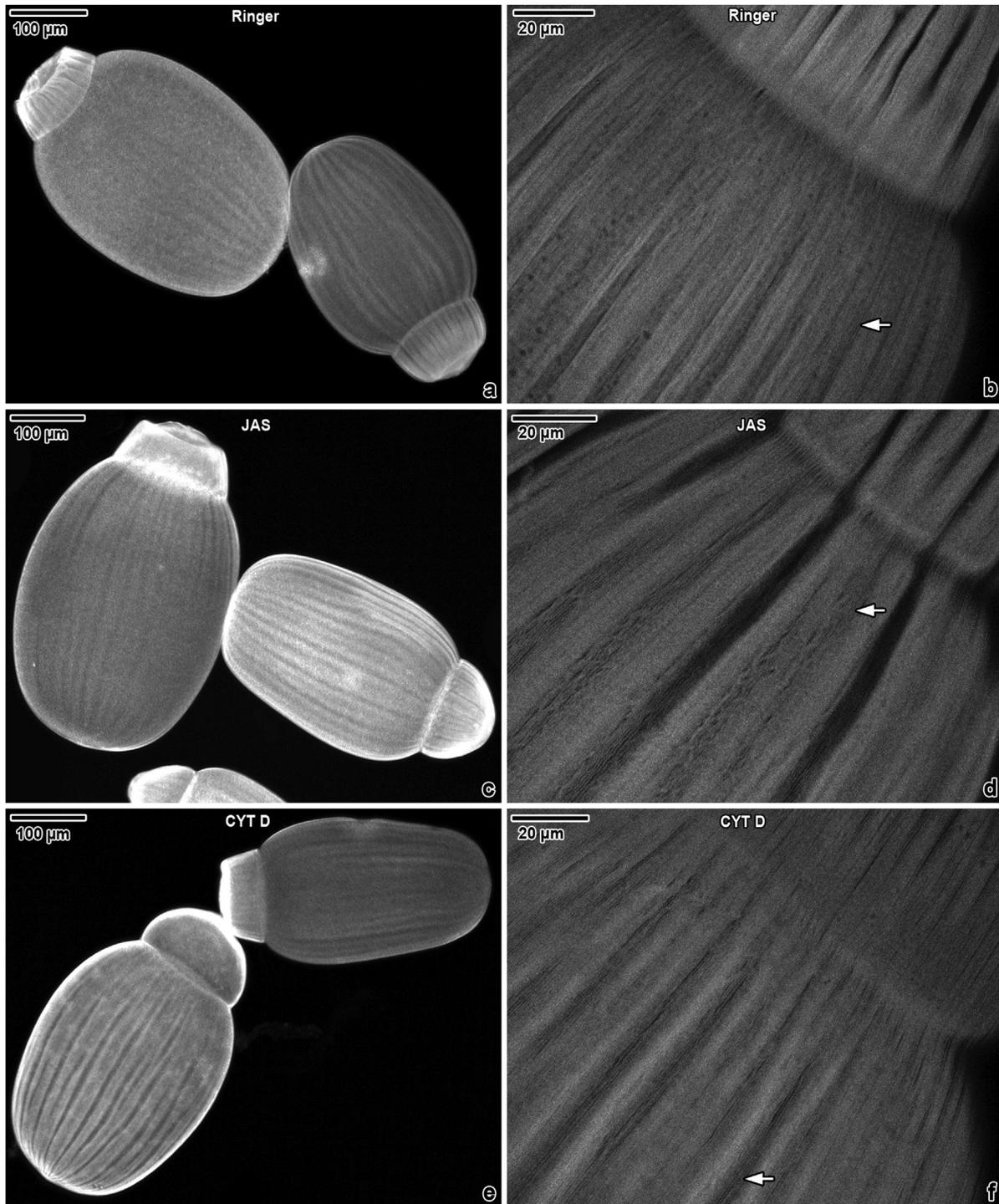
Fig. 4. Phalloidin staining of epicytic folds in control and drug-treated gamonts of *Gregarina garnhami*.
(a–b) Control gamonts incubated with Ringer's saline solution. **(c–d)** Gamonts treated for 7 h with 30 μm JAS. **(e–f)** Gamonts treated for 7 h with 30 μm cytochalasin D. a, c, e — overviews; b, d, f — composite views created by flattening a series of optical sections. CLSM, phalloidin-TRITC.
white arrow — epicytic folds.

annular myonemes (21 ± 1 nm thick) were located beneath the pellicle at the interface between the ectoplasm and endoplasm, and running perpendicular to the longitudinal cell axis (Figs. 2 d, f, 3 a, b). The ectoplasmic network was situated between the myonemes and the IMC (Fig. 2e) and was formed by anastomosing filaments, visible in superficial ultrathin sections (Fig. 2f). These correspond to the filamentous structures occupying the cytoplasm beneath the epicytic folds in replicas (Fig. 2g). Cytoskeletal structures showed differences in drug-treated gamonts. Under the pellicle of JAS-treated
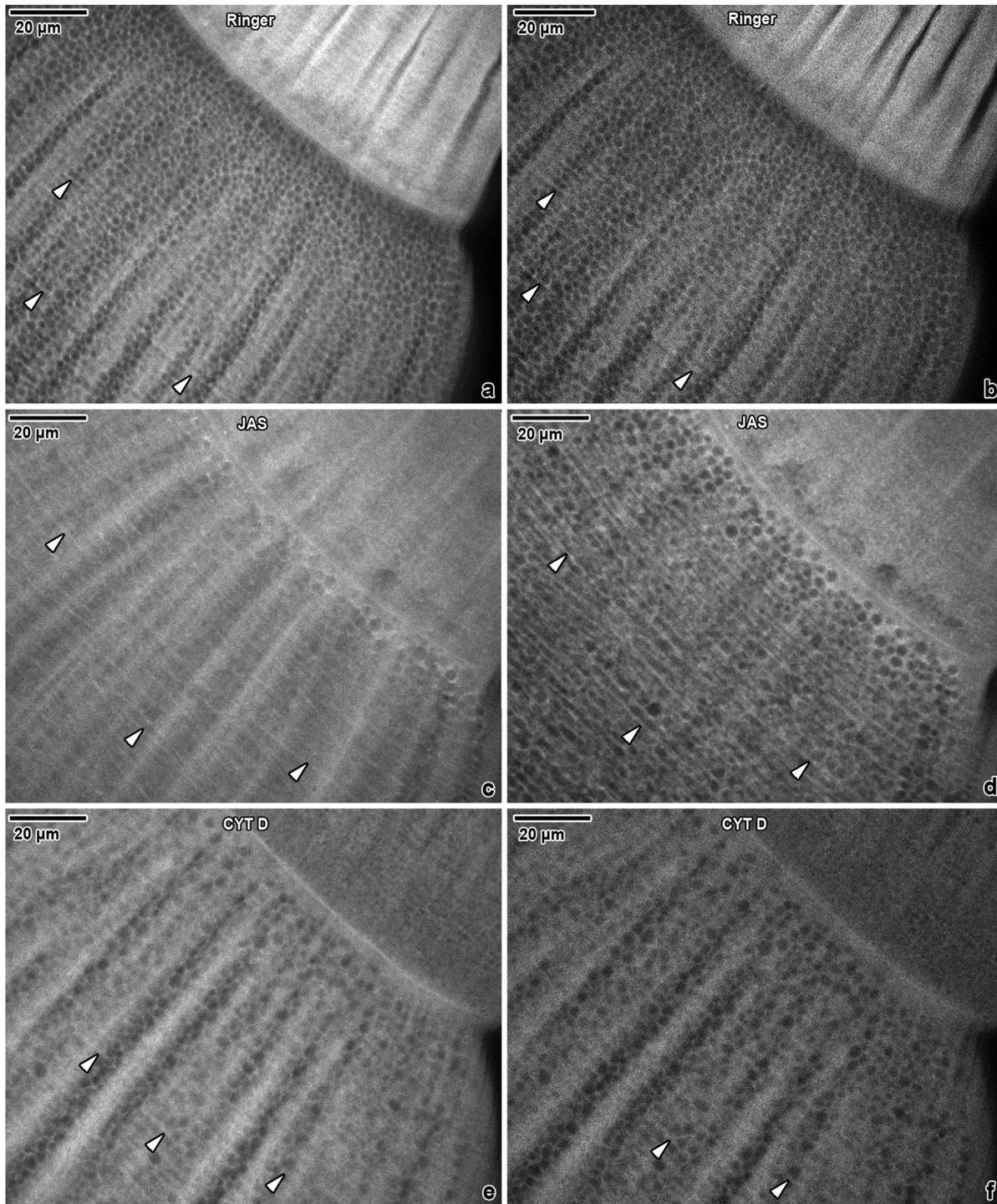
Fig. 5. Phalloidin staining of myonemes in control and drug-treated gamonts of *Gregarina garnhami.*
(a–b) Control gamonts incubated with Ringer's saline solution. **(c–d)** Gamonts treated for 7 h with 30 μm JAS. **(e–f)** Gamonts treated for 7 h with 30 μm cytochalasin D. a, c, e — composite views created by flattening all optical sections in the region of the myonemes; b, d, f — composite views created by flattening a series of optical sections. CLSM, phalloidin-TRITC.
white arrowhead — myonemes.

gregarines, the dense ectoplasmic network occurred in the form of filaments running in different angles to annular myonemes (Fig. 3c, d). The density of these structures was only slightly higher than in non-treated control parasites. In contrast, the gregarines incubated with cytochalasin D exhibited a different density of subpellicular structures (myonemes and ectoplasmic network), whose occurrence was less evident and they seemed to vanish (Fig. 3e, f).
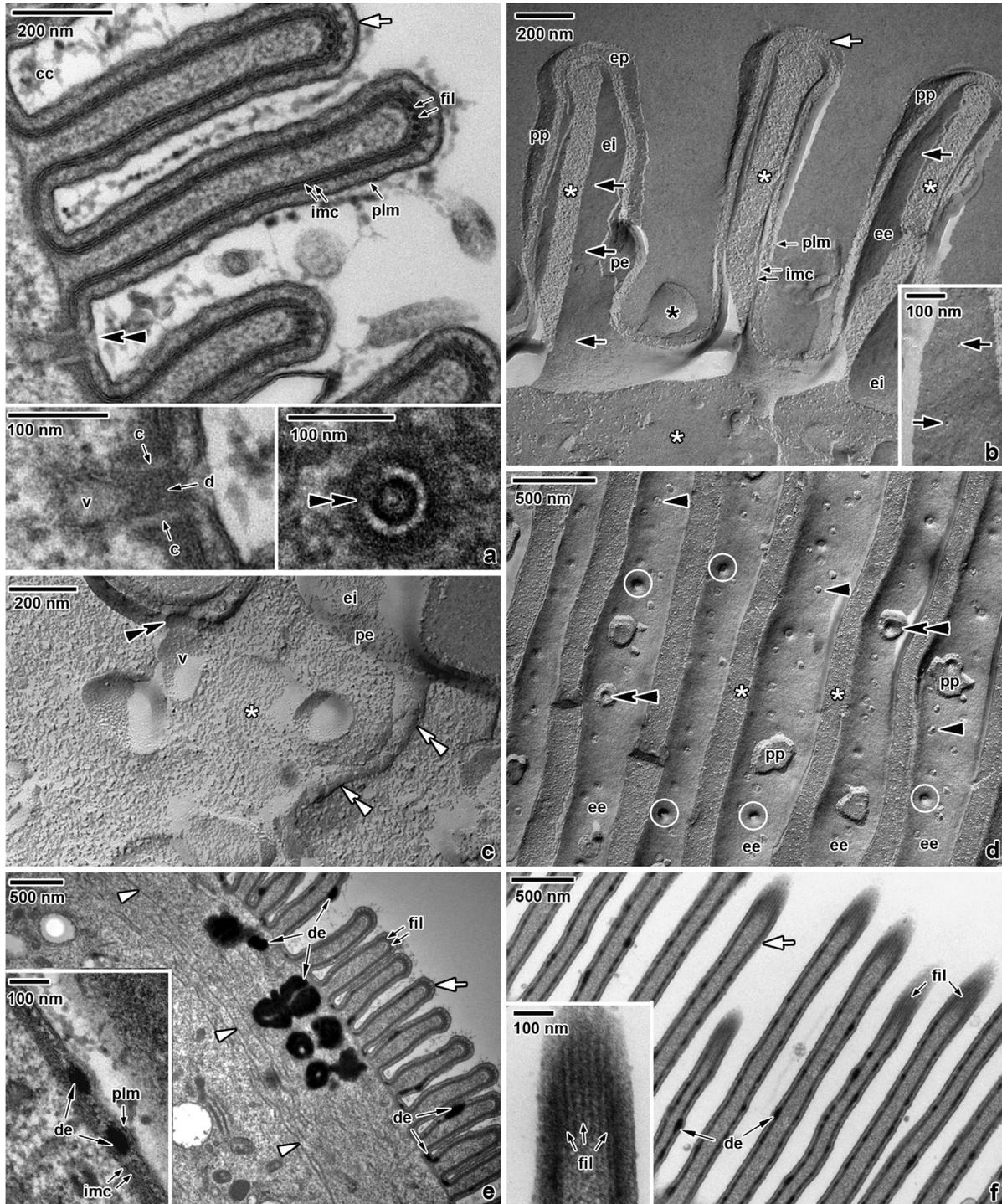
Fig. 6. Architecture of epicytic folds, pores and ducts in *Gregarina garnhami.*
(a) Longitudinally-sectioned micropore and cross-sectioned epicytic folds. Insets show the micropores in different sections in detail. TEM.
(b) Small-sized pores occurring in cytomembranes covering the lateral sides of epicytic folds. Inset shows the small-sized pores in detail. FE TEM. **(c)** Replica showing the duct and micropore. FE TEM. **(d)** Fracture face of IMC showing bases of the grooves between epicytic folds. Note the presence of ducts, micropores and medium-sized pores. FE TEM. **(e)** Cross section of epicytic folds comprising dense material on their lateral sides and clusters of dense material in ectoplasm. Inset shows position of dense material between the plasma membrane and IMC. TEM. **(f)** Tangential section of epicytic folds with apically situated 12 nm filaments and a dense material on their lateral sides. Inset shows apical filaments in detail. TEM.

The direct fluorescent labelling of F-actin with phalloidin for CLSM revealed the presence of F-actin located superficially, in longitudinal arrangement copying the pattern of epicytic folds (Fig. 4a–f). No significant changes were monitored between the control (incubated with Ringer's saline solution) and drug-treated gregarines (Fig. 4b, d, f). Second structures visualised after phalloidin labelling were the filaments running in circles, perpendicularly to the longitudinal cell axis. These annular structures, localised between the parasite pellicle (under the epicytic folds) and endoplasm, correspond to the myonemes (Fig. 5a–f). Detailed analysis of myonemes revealed differences in the fluorescent signals exhibited by control and drug-treated gamonts. In JAS-treated individuals, the prominent layer of annular myonemes, organised in a dense network of filaments running close to each other and linked lengthwise, exhibited very intense staining (Fig. 5c, d). A different situation occurred in gregarines treated with cytochalasin D. While traces of myonemes lying in the plane between the gregarine ectoplasm and endoplasm were still obvious, their density decreased and they seemed to be less distinct (Fig. 5e, f).

Epicytic folds, pores and ducts in *G. garnhami*

Electron microscopic analyses revealed three types of pores at the bottom of the grooves and on the lateral sides of the epicytic folds: micropores, medium-sized pores and small-sized pores (Fig. 6a–d). Typical apicomplexan micropores were situated between two adjacent epicytic folds (Figs. 3 b, 6 a, c, d). The central duct of each micropore, interrupting the pellicle, was circumscribed by a prominent collar and connected to a vacuolar structure located within the cell ectoplasm (Fig. 6a, c). The irregularly distributed micropores and medium-sized pores were clearly visible on freeze-fractured pellicle membranes (Fig. 6d). Medium-sized pores together with the small-sized pores were also present in both cytomembranes on the lateral sides of the epicytic folds, but did not reach the plasma membrane (Fig. 6b). In ultrathin sections, the medium-sized pores were noticeable as interruptions of the IMC (Figs. 2 e, 7 d). Measurements of the pore diameters in *G. garnhami* and another three *Gregarina* species (taken from our specimens) using several microscopic techniques are shown in Table 2.

Duct-like structures of wavy appearance and terminating at the bottom of the grooves between adjacent folds were detected in the ectoplasm (Figs. 2 e, 6 c). The openings of these ducts in the external cytomembrane formed

Table 3. The sizes of IMP in individual fracture faces of pellicle membranes in *Gregarina garnhami*.

Membrane	Face	Size of IMP (nm)					
		Mean	Median	SD	SE	Min	Max
Plasma	PF	4.5	3.9	2.7	0.1	0.5	15.2
membrane	EF	4.0	3.7	2.1	0.1	0.5	15.0
External	PF	4.4	4.0	2.3	0.1	0.5	16.1
cytomembrane	EF	3.6	3.2	1.8	0.1	0.5	12.8
Internal	PF	4.9	4.1	3.0	0.1	0.5	17.4
cytomembrane	EF	2.8	2.6	1.4	0.1	0.5	9.1

SD — standard deviation; SE — standard error.

extensive depressions (Fig. 6d). The cross-fractured termination of these duct-like structures in exoplasmic fracture face (EF) of the external cytomembrane measured 43.4 ± 1.4 nm in diameter, while in longitudinally fractured ducts it was 54.9 ± 2.5 nm in diameter. The interconnection of the ductus with the internal cortical cytomembrane measured 78.3 ± 2.4 nm in diameter (measured in replicas). In several ultrathin sections it seemed that the duct-like structures crossed the pellicle and opened to the external environment. Ducts were connected with vesicles located in the ectoplasm. In addition, clusters of a dense material in gregarine ectoplasm and filling the space between the plasma membrane and IMC on the lateral part of the epicytic folds and between two adjacent folds were observed (Figs. 3 a, b, 6 e, f).

In the apical part of the epicytic folds, linear IMP arrays were observed in EF of both cortical cytomembranes corresponding with their localisation to the 12 nm filaments observed under TEM (Fig. 6a, e, f). Analysis of the supramolecular organisation of the plasma membrane in *G. garnhami* showed similar sizes of intramembranous particle(s) (IMPs) in the protoplasmic (PF) and in the exoplasmic (EF) fracture faces. The size of IMPs varied from 0.5 to 17.4 nm, depending on the membrane type and its fractured face (Table 3, see Supplementary Fig. S2 for an example in the online version at DOI: 10.1016/j.ejop.2018.08.006). Unlike the plasma membrane, in cortical cytomembranes the density of IMPs was higher in the EF than in the PF of fractured faces (Table 4). Only particles ranging from 6 to 14 nm were used for statistical calculations of Kp (partition coefficient) in order to obtain data comparable with those so far published on other apicomplexans (Table 5). The statistical values differed considerably when including all visible IMPs. Therefore, the values listed in Table 3 include the total number of IMPs in the

---

black arrow — small-sized pores, *black arrowhead* — medium-sized pores, *black asterisk* — mucosubstance, *c* — micropore collar, *cc* — cell coat, *d* — micropore duct, *de* — dense material, *double black arrowhead* — micropore, *double white arrowhead* — duct-like structure, *ee* — EF of the external cytomembrane, *ei* — EF of the internal cytomembrane, *ep* — EF of the plasma membrane, *fil* — 12 nm apical filaments, *imc* — inner membrane complex, *pe* — PF of the external cytomembrane, *plm* — plasma membrane, *pp* − PF of the plasma membrane, *v* − vesicle, *white arrow* — epicytic folds, *white arrowhead* — myonemes, *white asterisk* — cytoplasm, *white circle* — termination of duct-like structure.
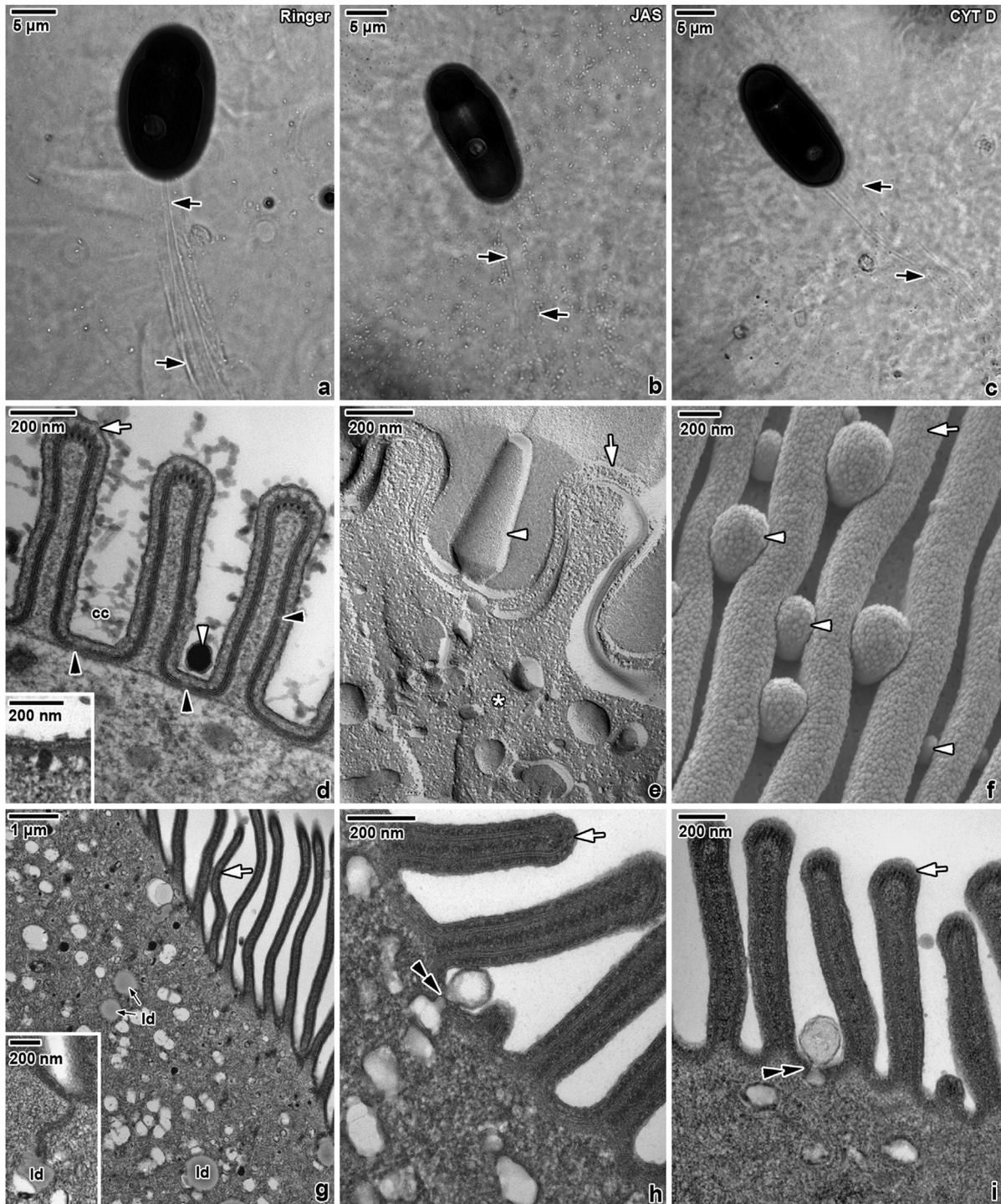
Fig. 7. Secretion in control and drug-treated gamonts of *Gregarina garnhami*.
(a–c) Mucous trail left behind gliding gregarine. a − Ringer's saline solution, b − 30 μm JAS, c − 30 μm cytochalasin D. LM, phase contrast. **(d)** Dense material observed between the epicytic folds. Note the medium-sized pores and a prominent layer of cell coat on the gregarine surface. Inset shows a dense material passing through the IMC. TEM. **(e)** Secretion of mucous material. FE TEM. **(f)** Mucus drops observed between the epicytic folds. SEM. **(g)** A view of ectoplasm and epicytic folds in a gregarine treated with 30 μm cytochalasin D. Note the presence of lipid-like droplets in ectoplasm. Inset shows the duct connecting to the lipid-like droplet. TEM. **(h-i)** Putative secretion of electron-lucent vesicles throughout the pore-like structures. h — 30 μm DMSO, i — 30 μm JAS. TEM.
black arrow — mucus trail, *black arrowhead* — medium-sized pores, *cc* — cell coat, *double black arrowhead* — termination of pore-like structure, *ld — lipid-like droplets*, *white arrow* — epicytic folds, *white arrowhead* — mucus, *white asterisk* — cytoplasm.

Table 4. Summary of density (particles/μm^2) and sizes of IMP (nm) in *Gregarina garnhami* and three other *Gregarina* species.

Species	Plasma membrane				External cytomembrane				Internal cytomembrane			
	EF		PF		PF		EF		EF		PF	
	Density of IMP	Size of IMP	Density of IMP	Size of IMP	Density of IMP	Size of IMP	Density of IMP	Size of IMP	Density of IMP	Size of IMP	Density of IMP	Size of IMP
	Mean ± SE	Min–Max	Mean ± SE	Min–Max	Mean ± SE	Min–Max	Mean ± SE	Min–Max	Mean ± SE	Min–Max	Mean ± SE	Min–Max
Gregarina garnhami	6115 ± 666	0.5–15	7138 ± 851	0.5–15.2	6741 ± 543	0.5–16.1	9832 ± 909	0.5–12.8	9273 ± 607	0.5–9.1	7365 ± 439	0.5–17.4
Gregarina cuneata	2950 ± 156	3.3–27.0	3621 ± 274	3.7–20.6	2633 ± 99	1.1–17.4	2681 ± 85	2.2–16.4	8297 ± 490	1.5–12.9	5991 ± 447	3.7–19.1
Gregarina polymorpha	3278 ± 42	3.2–11.7	5294 ± 225	2.98–11.6	1731 ± 158	3.7–13.7	3477 ± 347	2.1–10.5	1884 ± 99	2.7–9.7	2652 ± 86	2.7–12.7
Gregarina steini	2485 ± 99	2.1–15.1	2531 ± 127	2.1–14.1	3268 ± 202	2.2–14.2	4170 ± 37	2.1–14.4	3368 ± 230	1.7–13.3	3033 ± 95	2.1–9.8

The total number of all sizes of IMP in a membrane fracture was used for calculation.
SE — standard error.

fracture face of individual pellicle membranes as well as the maximum and minimum size of IMPs in specimens that were used in our previous studies. The actual IMP size distribution in each fractured membrane is shown in histograms (see Supplementary Fig. S2 for an example in the online version at DOI: 10.1016/j.ejop.2018.08.006).

Mucus secretion in control and drug-treated gregarines

Following treatment with cytoskeletal drugs, the gliding of gregarines on agar was examined to confirm the presence of secreted mucus trails. Clearly evident long and regular mucous paths were left behind gliding gamonts in all experimental groups (Fig. 7a–c); however, the paths of drug-treated gregarines were less noticeable (Fig. 7b, c).

Ultrastructural observations showed differences in cytoplasm organisation between the drug-treated and control gregarines. Control gregarines incubated with Ringer's saline solution exhibited a higher accumulation of dense granules in ectoplasm (Figs. 2 e, 3 a, b, 6 e). This dense material seemed to pass throughout both cortical cytomembranes to the space between the plasma membrane and IMC and reach the external environment via exocytosis (Figs. 6 e, f, 7 d). Presumably, the content of the abovementioned dense granules is secreted on the gregarine surface and forms the cell coat (Figs. 6 a, 7 d). Secreted globular or conical structures, situated in-between and on the top of the epicytic folds, and observed in our SEM and EF TEM preparations, correspond to mucus drops (Figs. 1a, b, d, f, 2 b, c, 7 e, f). In contrast, the ectoplasm of gregarines incubated with chemicals (pure DMSO, JAS, and cytochalasin D, the latter two both diluted in DMSO) exhibited a less pronounced concentration of dense granules, while the more prominent presence of lipid-like droplets was observed (Fig. 7g). Ducts were observed to connect cytoplasmic vesicles containing this lipid-like substance; some vesicles were already partially empty (Fig. 7g inset). The putative secretion of vesicles comprising an electron-lucent material was observed throughout the pore-like structures (similar to micropores but lacking a collar; 35–50 nm in diameter) located between two adjacent epicytic folds (Fig. 7h, i). While a prominent filamentous cell coat was observed in control gregarines, the drug-treated cells showed only an inconspicuous glycocalyx layer (Figs. 3 b, 6 a, 7 d vs. 3 c–f, 7 g–i).

Discussion

The supramolecular organisation of the pellicle in *Gregarina* representatives

Gamonts of *G. garnhami* analysed in this and a previous study (Valigurová and Koudela 2008) exhibited a pellicle of typical eugregarine organisation, consisting of the

Table 5. Density of IMP (particles/μm^2) in different apicomplexan species.

Species	Plasma membrane			External cytomembrane			Internal cytomembrane		
	EF	PF	Kp	PF	EF	Kp	EF	PF	Kp
Gregarina garnhami	3095 ± 242	4219 ± 249	1.4	3468 ± 213	1572 ± 247	2.2	2106 ± 212	3822 ± 241	1.8
Gregarina blaberae[a]	977 ± 235	1469 ± 233	1.5	285 ± 39	133 ± 34	2.1	158 ± 72	297 ± 33	1.9
Gregarina cuneata	2770 ± 96	2244 ± 283	0.8	1420 ± 190	1260 ± 211	1.1	1502 ± 273	1993 ± 253	1.3
Gregarina polymorpha	2473 ± 147	1446 ± 158	0.6	602 ± 265	863 ± 202	0.7	814 ± 246	1276 ± 200	1.6
Gregarina steini	1783 ± 233	2265 ± 154	1.3	2588 ± 189	3820 ± 211	0.7	1886 ± 274	2339 ± 132	1.2
Eimeria nieschulzi[b]	218 ± 21	648 ± 73	3.0	2360 ± 133	29 ± 7	81.4	146 ± 31	1780 ± 97	12.2
Plasmodium knowlesi[c]	185 ± 25	2198 ± 528	11.9	1751 ± 228	38 ± 15	46.1	48 ± 28	574 ± 200	12.0
Siedleckia nematoides[d]	183 ± 8	2926 ± 135	16.0	2745 ± 220	458 ± 15	6.0	797 ± 60	3342 ± 128	4.2

The size of IMP is in range 6–14 nm.

Kp partition coefficient defined as number of particles per μm^2 in the PF face/number of particles per μm^2 in the EF face.

[a] Values taken from Schrével et al. (1983).

[b] Values taken from Dubremetz and Torpier (1978).

[c] Values taken from McLaren et al. (1979).

[d] Values taken from Valigurová et al. (2017).

plasma membrane and IMC, folded into numerous, longitudinal epicytic folds (Desportes and Schrével 2013; Schrével et al. 1983; Valigurová et al. 2013; Vávra and Small 1969; Walker et al. 1984). The values of Kp coefficient (represents an objective comparative factor characterising the membranes skeleton) in the plasma membrane and both cortical cytomembranes of *G. garnhami* were comparable with those of all investigated species of the genus *Gregarina* Dufour, 1828 (Schrével et al. 1983; Valigurová et al. 2013). Nevertheless, it needs to be emphasized that the IMP density is apparently highest in *G. garnhami* compared to other apicomplexans investigated thus far (Table 5). Variability of IMPs (mostly the presence of small particles in all membranes) in *G. garnhami* significantly differs from other *Gregarina* representatives (Valigurová et al. 2013). Because the nature of documented IMPs remains unknown, we cannot speculate about their potential involvement in gregarine gliding motility.

Pores, ducts and mucus secretion in *Gregarina* representatives

In agreement with previous studies (Valigurová and Koudela 2008; Walker et al. 1984), we observed typical micropores consisting of a central duct lined by a dense collar. In general, the apicomplexan micropores (also called "cytostomes") were thought to have a role in the feeding of zoites by ingesting host cell cytoplasm via the formation of pinocytic vesicles (Aikawa 1966; Nichols et al. 1994; Scholtyseck and Mehlhorn 1970). A nutritive function has also been attributed to micropores in gregarines detached from host tissue (Desportes and Schrével 2013; Warner 1968). In addition, the freeze-fractured IMC in eugregarines showed the presence of medium-sized pores situated in both cortical cytomembranes on the lateral sides of epicytic folds and in the grooves between the folds (Walker et al. 1984;

this study). Moreover, this study revealed the presence of small-sized pores (with diameters more than 50% smaller compared to medium-sized pores; Table 2) occupying the lateral sides of epicytic folds, which were not described in freeze-etching study performed by Walker et al. (1984). To compare the sizes of micropores and different pores in several apicomplexan species (Valigurová et al. 2013, 2017), measurements were taken using different microscopic techniques (Table 2).

Duct-like structures of wavy appearance detected under the pellicle were seen to originate between two adjacent folds and pass inside the cytoplasm. Ectoplasmic ducts or channel-like structures previously observed in gregarines from mealworms and in *G. garnhami* (Valigurová et al. 2013; Walker et al. 1984) were postulated to pass to the exterior between the folds and to have a role in mucus secretion (Walker et al. 1984). In *G. cuneata*, some of the ducts were connected to the pore-like structures in the IMC (Valigurová 2012). In the present study, ultrathin sections did not reveal secretion of mucus on the gregarine surface throughout the duct-like structures, but the ducts were connected to cytoplasmic vesicles. In drug-treated gregarines, these cytoplasmic vesicles were filled with lipid-like content, suggesting their role in metabolic processes. In general, lipid droplets in apicomplexans play roles in lipid metabolism, cell signalling, and intracellular vesicle trafficking (Sonda and Hehl 2006).

Ultrathin sectioning also revealed the presence of unknown pore-like structures (similar to micropores but without a collar). The drug-treated gregarines exhibited an intensive secretion of vesicles comprising electron-lucent material throughout these pores, pointing to their role in the excretion of waste products or toxic material out of the cell. We also hypothesize their possible involvement in the transportation of material necessary for the restoration of natural conditions in the environment surrounding the gregarine.

The presence of mucus drops on the top of, and between the epicytic folds of *G. garnhami* was confirmed by SEM analysis

(Valigurová and Koudela 2008; this study). In eugregarines, the mucus trail left behind gliding gamonts was previously investigated as a potential lubricant for gliding locomotion (Schwiakoff 1894; Valigurová et al. 2013; Walker et al. 1979). Although mucus flow accompanies the gliding, there is no evidence to show whether it is the cause or a consequence of gliding movement (Mackenzie and Walker 1983). In our research, the presence of mucus trails left behind gliding gamonts in control and both experimentally affected groups was monitored. Importantly, the mucus trails in drug-treated gamonts indicate this substance to have a supportive function, maintaining an environment suitable for gregarine movement on a solid surface. It can be expected that the cell coat covering the entire surface of the gregarine is continuously reformed by the secretion of its components from the cell. In *G. garnhami*, a dense material occupying the space between the plasma membrane and IMC on the lateral sides of epicytic folds and in-between the epicytic folds, appears to be transported from gregarine cytoplasm to the intramembranous space through the cytomembranes. We hypothesize that this dense matter is subsequently secreted by exocytosis to the cell surface and represents the core component for the formation of the cell coat. Similarly, dense inclusions localised mainly in the ectoplasm of *G. blaberae* (Schrével 1972) were suggested to be associated with the dense filamentous cell coat rich in glycoconjugates and covering the plasma membrane (Philippe et al. 1979; Schrével 1972; Schrével et al. 1983).

Cytoskeletal organisation in *Gregarina* representatives

The actomyosin motor in apicomplexan zoites (considered to be the key component of the parasites' motor responsible for gliding and host invasion) is assumed to be embedded between the plasma membrane and the IMC and connected to transmembrane adhesin complexes contacting the substrate (Opitz and Soldati 2002). In gregarines, the actomyosin system was proposed as one of the potential mediators causing lateral undulations of epicytic folds and, in this way, contributing to the gliding movement (Desportes and Schrével 2013). In our SEM analysis of drug-treated gamonts with ceased motility, however, the reorganisation (undulation or striking of epicytic folds) was not substantiated. The rows of IMPs in both cytomembranes occurring in the apical parts of epicytic folds correspond to the position of the 12-nm filaments. Potential connections between IMPs anchoring these 12 nm filaments to the IMC at the tips of epicytic folds were detected in *G. garnhami* previously (Walker et al. 1984). The interaction between these structures might facilitate gregarine gliding (Dallai and Talluri 1983; Walker et al. 1984), nevertheless, their real functions is still poorly understood. It has been shown that the number of 12-nm filaments, exhibiting the properties of intermediate filaments, does not influence the gregarine gliding speed, but rather seems to control the direction of movement (Valigurová et al. 2013). However, while the number of detected 12-nm

filaments was the same in *G. garnhami* and in *G. cuneata* (=7), the gliding of gamonts in latter one was characterised by multiple and prolonged stops and changes of direction, i.e. linear vs. semi-circular gliding path (Valigurová et al. 2013). The frequent changes of gliding path in *G. cuneata* appear to be additionally influenced by the bending movements of its protomerite (Valigurová et al. 2013). Majority of eugregarines investigated in our long-term research (Kováčiková et al. 2017; Valigurová et al. 2013, and personal nonpublished data) exhibited more or less discontinuous gliding and we cannot provide any explanation of the occurrence in the stops in *G. cuneata* gliding. Considering the fact that all these observations were performed using parasites isolated from their host, it could simply represent a reaction of various intensity (differing among species) to *in vitro* conditions, or different sensitivity of gregarine species to the quality of the substrate and barriers in their gliding path.

For a deeper understanding of the actomyosin system in *Gregarina* spp., several biochemical and molecular investigations were performed (Baines and King 1989; Ghazali et al. 1989; Ghazali and Schrével 1993; Heintzelman 2004; Heintzelman and Mateer 2008; Philippe et al. 1982; Valigurová 2012; Valigurová et al. 2013). As observed in other terrestrial eugregarines, the cytoplasm of *G. garnhami* is divided into inner finely granular endoplasm and outer ectoplasm (Canning 1956), the latter lying under the pellicle and possessing cytoskeletal filamentous structures. Crawley (1905) described a layer of fibrils encircling the gregarine and joined together by connectives forming a network, which he called the myocyte. The myocyte is supposed to be formed by contractile elements that are responsible for gregarine motility and bending. In more recent publications (Beams et al. 1959; Hildebrand 1980; Valigurová and Koudela 2008; Valigurová et al. 2013; Walker et al. 1979) these filaments in eugregarines were divided into two types depending on their thickness and position relative to the gregarine axis. The ectoplasmic network underlies the inner cytomembrane, while deeper in the edge of the ectoplasm and endoplasm, annular rib-like myonemes are localised. In *Gregarina* representatives, the myonemes and ectoplasmic network were suggested to be the major contractile elements providing the driving force for cell locomotion and/or protomerite bending (Beams et al. 1959; Valigurová et al. 2013). The staining of actin for indirect immunofluorescence showed it to be confined to the cortical region, lacking a fibrillar pattern (Baines and King 1989; Valigurová et al. 2013). Surprisingly, contradicting the observations on *G. cuneata* (Valigurová et al. 2013), the presence of actin stained with antibody was not observed in ghosts (=cell cortex) of *G. garnhami* (Mackenzie 1980). A study, in which actin was specifically labelled with antibody generated to *G. polymorpha* actin, revealed its bilaminar staining pattern (Heintzelman 2004). The outer layer of actin was organised into longitudinal lines, copying the arrangement of epicytic folds, while the inner layer corresponded to rib-like myonemes oriented perpendicular to the longitudinal cell axis (Heintzelman 2004).

In *G. garnhami*, a dense layer of annular myonemes running perpendicular to the cell axis along with a network of ectoplasmic filaments were also observed under electron and confocal microscopy. Although Walker et al. (1979) described in *G. garnhami* circularly arranged microtubules in the transition area between the ectoplasm and endoplasm, these structures most likely correspond to the myonemes observed in the present study, since the presence of microtubules in *G. garnhami* by the negative staining of α-tubulin for immunofluorescent microscopy was not monitored (data not shown). The study on *Gregarina* species from mealworms came to the same conclusion (Valigurová et al. 2013). Though several biochemical analyses of *Gregarina* representatives confirmed the actin nature of myonemes, the form of present actin (monomeric vs. polymerised into filaments) was not determined. In gregarines from mealworms, the F-actin accumulated in the apical end of the protomerite and in the area of the membrane fusion site (i.e. osmiophilic ring); in addition, it was restricted to the cell cortex, fibrillar septum, and nucleus; however, the recognition of individual annular myonemes was not possible (Valigurová et al. 2009, 2013). In our study, labelling of F-actin with fluorescent phalloidin, revealed numerous subpellicular actin filaments running perpendicularly to the cell axis, which correspond in their organisation and localisation to myonemes detected in ultrathin sections. According to these observations, myonemes are most likely formed by the bundles of actin filaments and our experiments showed them to be essential in *G. garnhami* gliding motility. The association of actin filaments with different types of myosins (A, B and F) appears to be likely, because these myosins were immunofluorescently detected in other *Gregarina* spp. in similar localisation (restricted to the epicytic folds and annular myonemes) and organisation pattern (Heintzelman 2004; Heintzelman and Mateer 2008) as F-actin in *G. garnhami*. Actomyosin motor was proposed to participate in gliding motility, as well as myonemes-mediated bending of *G. polymorpha* (Heintzelman 2004; Heintzelman and Mateer 2008).

Effect of actin-modifying drugs on motility and cytoskeleton of *Gregarina* representatives

Experimental studies dealing with drugs influencing the actin polymerisation, namely jasplakinolide and cytochalasins, demonstrated their significant impact on eugregarine motility (King 1988; Valigurová et al. 2013; Walker et al. 1979). Jasplakinolide (JAS) is known to stabilise actin filaments and induce the polymerisation of monomeric actin (Bubb 2000). Concentrations of JAS ranging from 5 μM to 30 μM were used in motility experiments on eugregarines from mealworms (Valigurová et al. 2013). These eugregarines were able actively to glide for up to 150 min after the beginning of their incubation with JAS, and their movement recovered fully after the drug was washed out (Valigurová et al. 2013). Experiments with *G. garnhami* showed even greater tolerance of individuals to high concentrations of this

drug. After 7 h (420 min) of incubation with 30 μM JAS, gamonts were still able to glide and no superficial changes or abnormalities in their motility were noticed. We attribute the weak effect of JAS on *G. garnhami* gamonts to the assumption that the majority of actin in this species is already present in its polymerised form (even before incubation with JAS as an actin stabilising drug). This hypothesis is further supported by our CLSM data. The presence and density of myonemes in ultrathin sections after treatment with JAS was concordat with CLSM analysis.

An opposite effect on motility was documented in gregarines treated with cytochalasin D. Cytochalasins are fungal metabolites binding to actin filaments, which inhibit the association and dissociation of subunits at the barbed end (Cooper 1987). A previous study performed on *G. garnhami* described the irreversible cessation of gliding motility induced by 0.1% cytochalasin B, with no recovery after completion of the experiment (Walker et al. 1979). However, it is important to note that cytochalasin B binds to both actin filaments and glucose transporters. In contrast, cytochalasin D has a high affinity to actin filaments and specifically binds to them only, thereby reducing the probability that motility could be blocked by another mechanism (Cooper 1987). Our experiments on *G. garnhami* resulted in the rapid cessation of motility almost immediately after the application of 30 μM cytochalasin D. Subsequent microscopic analyses demonstrated less dense arrangements of ectoplasmic network and myonemes with fading connections. The gregarines were treated for 7 h, during which they showed no sign of gliding; however, after washing with Ringer's saline solution, the recovery of gliding motility was achieved in the majority of individuals. Lower cytochalasin D concentrations of 5 and 10 μM were also applied in order to compare the effects of various drug concentrations on *G. garnhami* motility, but no significant differences were observed (Table 1). In eugregarines from mealworms, the highest applied concentration of cytochalasin D (30 μM) blocked their motility from 10 to 75 min after beginning of experiment, and full recovery was observed 10 min after washing in Ringer's saline solution (Valigurová et al. 2013). It can be assumed that cytochalasin D did not lead to the mortality of gregarines (a fact demonstrated by their recovery), despite the fact that their motility was completely blocked. Further investigation is needed to specify the exact mechanism of this drug on actin filaments and their role in gregarine motility.

Conclusions

The present study revealed that the wavy pattern of epicytic folds in *G. garnhami* is similar in treated and non-treated gregarines, even in gregarines incubated with cytochalasin D, where the gliding motility was completely blocked for a long period (Figs. 1 a, b, 2 b, c vs. Fig. 1c–f). This observation contradicts the expectation that the lateral undulation of epicytic folds provides the force behind gregarine glid-

ing, an idea previously proposed by other authors (Schrével and Philippe 1993; Vávra and Small 1969; Vivier 1968). In addition, our results on drug-treated gamonts demonstrate the importance of subpellicular structures such as the ectoplasmic network and myonemes in *G. garnhami* motility. Changes in gliding motility, i.e. cessation of movement in cytochalasin D-treated gamonts, were accompanied with partial degradation of myonemes and their fading in CLSM micrographs. After the treatment with JAS, the changes in gliding motility were inconspicuous despite denser network of myonemes was observed after phalloidin labelling. Based on microscopic observations we conclude that annular myonemes, occurring at the border between the ectoplasm and endoplasm, consist of bundles of actin filaments and that the majority of actin is present in polymerised form. The organisation of myonemes and ectoplasmic network changed during the experiments with actin-modifying drugs in accordance with gamonts gliding activity. The actin filaments most likely represent contractile elements facilitating gliding motility in *G. garnhami* gamonts, while mucus secretion has only supportive function. In addition, our results suggest that the dynamic process of actin polymerisation and subsequent rapid depolymerisation, proposed for apicomplexan zoites using the so-called "glideosome" system to move over surfaces (Opitz and Soldati 2002), is not essential for gliding motility in studied eugregarines. In contrast, only the polymerised form of actin seems to be the main leading motor structure responsible for gliding movement in gamonts of *G. garnhami* and other *Gregarina* representatives. This conclusion is supported by the fact that the incubation with JAS, inducing further stabilisation of F-actin already present in treated gamonts, did not significantly change their motility. In contrast, treatment with cytochalasin D almost immediately blocked eugregarines motility due to depolymerisation of existing actin filaments.

Acknowledgements

References

Aikawa, M., 1966. The fine structure of the erythrocytic stages of three avian malarial parasites, *Plasmodium fallax, P. lophurae, and P. cathemerium*. Am. J. Trop. Med. Hyg. 15 (4), 449–471.

Baines, I., King, C.A., 1989. Demonstration of actin in the protozoon — *Gregarina*. Cell Biol. Int. Rep. 13 (8), 679–686.

Beams, H.W., Tahmisian, T.N., Devine, R.L., Anderson, E., 1959. Studies on the fine structure of a gregarine parasitic in the gut of the grasshopper, *Melanoplus differentialis*. J. Protozool. 6 (2), 136–146.

Branton, D., Bullivant, S., Gilula, N.B., Karnovsky, M.J., Moor, H., Muhlethaler, K., et al., 1975. Freeze etching nomenclature. Science 190 (4209), 54–56.

Bubb, M.R., 2000. Effects of jasplakinolide on the kinetics of actin polymerization. An explanation for certain in vivo observations. J. Biol. Chem. 275 (7), 5163–5170, http://dx.doi.org/10.1074/jbc.275.7.5163.

Canning, E.U., 1956. A new eugregarine of locusts, *Gregarina garnhami* n. sp., parasitic in *Schistocerca gregaria* Forsk. J. Protozool. 3, 50–63.

Cooper, J.A., 1987. Effects of cytochalasin and phalloidin on actin. J. Cell Biol. 105 (4), 1473–1478.

Crawley, H., 1905. The movements of gregarines. Proc. Acad. Nat. Sci. Phila. 57, 89–99.

Dallai, R., Talluri, M.V., 1983. Freeze-fracture study of the Gregarine trophozoite: I the top of the epicyte folds. Boll. Zool. 5, 235–244, http://dx.doi.org/10.1080/11250008309439448.

Desportes, I., Schrével, J., 2013. Gregarines, the Early Branching Apicomplexa (2 vols). Treatise on Zoology — Anatomy, Taxonomy, Biology. BRILL, Leiden, The Netherlands, p. 781.

Dubremetz, J.F., Torpier, G., 1978. Freeze fracture study of the pellicle of an eimerian sporozoite (Protozoa, Coccidia). J. Ultrasruct. Res. 62 (2), 94–109, http://dx.doi.org/10.1016/S0022-5320(78)90012-6.

Ghazali, M., Philippe, M., Deguercy, A., Gounon, P., Gallo, J.M., Schrével, J., 1989. Actin and spectrin-like (Mr = 260-240 000) proteins in gregarines. Biol. Cell 67 (2), 173–184.

Ghazali, M., Schrével, J., 1993. Myosin-like protein (Mr 175,000) in *Gregarina blaberae*. J. Eukaryot. Microbiol. 40, 345–354, http://dx.doi.org/10.1111/j.1550-7408.1993. tb04927.x.

Heintzelman, M.B., Mateer, M.J., 2008. GpMyoF, a WD40 repeat-containing myosin associated with the myonemes of *Gregarina polymorpha*. J. Parasitol. 94 (1), 158–168, http://dx.doi.org/10.1645/GE-1339.1.

Heintzelman, M.B., 2004. Actin and myosin in *Gregarina Polymorpha*. Cell Motil. Cytoskeleton 58 (2), 83–95, http://dx.doi.org/10.1002/cm.10178.

Heintzelman, M.B., 2015. Gliding motility in apicomplexan parasites. Semin. Cell Dev. Biol. 46, 135–142, http://dx.doi.org/10.1016/j.semcdb.2015.09.020.

Hildebrand, H.F., 1980. Elektronenmikroskopische Untersuchungen an den Entwicklungsstadien des Trophozoiten von *Didymophyes gigantea* (Sporozoa, Gregarinida). III. Die Feinstruktur des Epizyten mit besonderer Berücksichtigung der kontraktilen Elemente. Z. Parasitenkd. 64, 29–46.

Kappe, S.H., Buscaglia, C.A., Bergman, L.W., Coppens, I., Nussenzweig, V., 2004. Apicomplexan gliding motility and host cell invasion: overhauling the motor model. Trends Parasitol. 20 (1), 13–16, http://dx.doi.org/10.1016/j.pt.2003.10.011.

Keeley, A., Soldati, D., 2004. The glideosome: a molecular machine powering motility and host-cell invasion by apicomplexa. Trends Cell Biol. 14, 528–532, http://dx.doi.org/10.1016/j.tcb.2004.08.002.

King, C.A., 1981. Cell surface interaction of the protozoan gregarina with concanavalin a beads — implications for models

of gregarine gliding. Cell Biol. Int. Rep. 5 (3), 297–305, http://dx.doi.org/10.1016/0309-1651(81)90228-9.

King, C.A., 1988. Cell motility of sporozoan protozoa. Parasitol. Today 4 (11), 315–319, http://dx.doi.org/10.1016/0169-4758(88)90113-5.

Kováčiková, M., Simdyanov, T.G., Diakin, A., Valigurová, A., 2017. Structures related to attachment and motility in the marine eugregarine *Cephaloidophora* cf. *communis* (Apicomplexa). Eur. J. Protistol. 59, 1–13, http://dx.doi.org/10.1016/j.ejop.2017.02.006.

Mackenzie, C., 1980. Gliding in *Gregarina garnhami* — movement without actin? Cell Biol. Int. Rep. 4 (8), 769.

Mackenzie, C., Walker, M.H., 1983. Substrate contact, mucus, and eugregarine gliding. J. Protozool. 30 (1), 3–8, http://dx.doi.org/10.1111/j.1550-7408.1983. tb01024.x.

Matuschewski, K., Schüler, H., 2008. Actin/myosin-based gliding motility in apicomplexan parasites. In: Burleigh, B.A., Soldati-Favre, D. (Eds.), Molecular mechanisms of parasite invasion. Subcell. Biochem., 47, pp. 110–120.

McLaren, D.J., Bannister, L.H., Trigg, P.I., Butcher, G.A., 1979. Freeze fracture studies on the interaction between the malaria parasite and the host erythrocyte in *Plasmodium knowlesi* infections. Parasitology 79 (1), 125–139, http://dx.doi.org/10.1017/S0031182000052021.

Nichols, B.A., Chiappino, M.L., Pavesio, C.E., 1994. Endocytosis at the micropore of *Toxoplasma gondii*. Parasitol. Res. 80 (2), 91–98.

Opitz, C., Soldati, D., 2002. 'The glideosome': a dynamic complex powering gliding motion and host cell invasion by *Toxoplasma Gondii*. Mol. Microbiol. 45 (3), 597–604, http://dx.doi.org/10.1046/j.1365-2958.2002.03056.

Philippe, M., Fournet, B., Caigneaux, E., Schrével, J., 1979. Les polysaccharides associés à la surface cellulaire d'une Grégarine (Protozoaire parasite). II. Caractérisation cytochimique et analyses biochimiques des Ghosts. Biol. Cell 35, 165–174.

Philippe, M., Vinckier, D., Dubremetz, J.F., Schrével, J., 1982. The three cortical membranes of the gregarines (parasitic protozoa). III. Comparative studies of the membrane proteins among different sporozoan species during their vegetative phase. J. Protozool. 29 (3), 424–430.

Scholtyseck, E., Mehlhorn, H., 1970. Ultrastructural study of characteristic organelles (paired organelles, micronemes, micropores) of sporozoa and related organisms. Z. Parasitenkd. 34 (2), 97–127.

Schrével, J., 1972. Les polysaccharides associés à la surface cellulaire des Grégarines (Protozoaires parasites). I. Ultrastructure et cytochimie. J. Microsc. 15, 21–40.

Schrével, J., Caigneaux, E., Gros, D., Philippe, M., 1983. The three cortical membranes of the gregarines. I. Ultrastructural organization of *Gregarina blaberae*. J. Cell Sci. 61, 151–174.

Schrével, J., Desportes, I., 2015. Gregarines. In: Mehlhorn, H. (Ed.), Encyclopedia of Parasitology. Springer-Verlag, Berlin, Heidelberg, http://dx.doi.org/10.1007/978-3-540-48996-2, p. 47.

Schrével, J., Philippe, M., 1993. The Gregarines. In: Kreier, J.P., Baker, J.R. (Eds.), Parasitic Protozoa, 4, 2nd ed. Academic Press, pp. 133–245.

Schwiakoff, W., 1894. Über die Ursache der fortschreitenden Bewegung der Gregarinen. Z. Wiss. Zool. 58, 340–354.

Sibley, L.D., Hâkansson, S., Carruthers, V.B., 1998. Gliding motility: an efficient mechanism for cell penetration. Curr. Biol. 8 (1), R12–R14, http://dx.doi.org/10.1016/S0960-9822(98)70008-9.

Sonda, S., Hehl, A.B., 2006. Lipid biology of Apicomplexa: perspectives for new drug targets, particularly for *Toxoplasma gondii*. Trends Parasitol. 22 (1), 41–47, http://dx.doi.org/10.1016/j.pt.2005.11.001.

Valigurová, A., 2012. Sophisticated adaptations of *Gregarina cuneata* (Apicomplexa) feeding stages for epicellular parasitism. PloS One 7 (8), e42606, http://dx.doi.org/10.1371/journal.pone.0042606.

Valigurová, A., Koudela, B., 2008. Morphological analysis of the cellular interactions between the eugregarine *Gregarina garnhami* (Apicomplexa) and the epithelium of its host, the desert locust *Schistocerca gregaria*. Eur. J. Protistol. 44 (3), 197–207, http://dx.doi.org/10.1016/j.ejop.2007.11.006.

Valigurová, A., Michalková, V., Koudela, B., 2009. Eugregarine trophozoite detachment from the host epithelium via epimerite retraction: fiction or fact? Int. J. Parasitol. 39 (11), 1235–1242, http://dx.doi.org/10.1016/j.ijpara.2009.04.009.

Valigurová, A., Vaškovicová, N., Diakin, A., Paskerova, G.G., Simdyanov, T.G., Kováčiková, M., 2017. Motility in blastogregarines (Apicomplexa): native and drug-induced organisation of *Siedleckia nematoides* cytoskeletal elements. PLoS One 12 (6), e0179709, http://dx.doi.org/10.1371/journal.pone.0179709.

Valigurová, A., Vaškovicová, N., Musilová, N., Schrével, J., 2013. The Enigma of eugregarine epicytic folds: where gliding motility originates? Front. Zool. 10 (1), 57, http://dx.doi.org/10.1186/1742-9994-10-57.

Vávra, J., Small, B.E., 1969. Scanning electron microscopy of gregarines (Protozoa, Sporozoa) and its contribution to the theory of gregarine movement. J. Protozool. 42 (5), 1041–1057.

Vivier, E., 1968. L'organisation ultrastructurale corticale de la grégarine *Lecudina pellucida*; ses rapports avec l'alimentation et la locomotion. J. Protozool. 15, 230–246.

Walker, M.H., Lane, N.J., Lee, W.M., 1984. Freeze-fracture studies on the pellicle of the eugregarine, *Gregarina garnhami* (Eugregarinida, Protozoa). J. Ultrastruct. Res. 88, 66–76, http://dx.doi.org/10.1016/S0022-5320(84)90182-5.

Walker, M.H., Mackenzie, C., Bainbridge, S.P., Orme, C., 1979. A study of the structure and gliding movement of *Gregarina garnhami*. J. Protozool. 26 (4), 566–574.

Warner, F.D., 1968. The fine structure of *Rhynchocistys pilosa* (Sporozoa, Eugregarinidae). J. Protozool. 15, 59–73.

Simdyanov T.G., Paskerova G.G., **Valigurová A.**, Diakin A.,

Kováčiková M., Schrével J., Guillou L., Dobrovolskij A.A., Aleoshin V.V.

2018

First ultrastructural and molecular phylogenetic evidence from the blastogregarines, an early branching lineage of plesiomorphic Apicomplexa

Protist

ORIGINAL PAPER

First Ultrastructural and Molecular Phylogenetic Evidence from the Blastogregarines, an Early Branching Lineage of Plesiomorphic Apicomplexa

Timur G. Simdyanov[a,1], Gita G. Paskerova[b], Andrea Valigurová[c], Andrei Diakin[c], Magdaléna Kováčiková[c], Joseph Schrével[d,e], Laure Guillou[f], Andrej A. Dobrovolskij[b], and Vladimir V. Aleoshin[g,h]

[a]Faculty of Biology, Lomonosov Moscow State University, Leninskiye Gory 1-12, 119 234 Moscow, Russian Federation
[b]Department of Invertebrate Zoology, Faculty of Biology, Saint Petersburg State University, Universitetskaya emb. 7/9, 199 034 St. Petersburg, Russian Federation
[c]Department of Botany and Zoology, Faculty of Science, Masaryk University, Kotlářská 2, 611 37 Brno, Czech Republic
[d]CNRS 7245, Molécules de Communication et Adaptation Moléculaire (MCAM), CP 52, rue Cuvier, 75005 Paris, France
[e]Sorbonne Universités, Muséum National d'Histoire Naturelle (MNHN), UMR 7245, CP 52, rue Cuvier, 75005 Paris, France
[f]Sorbonne Université, Université Pierre et Marie Curie—Paris 6, CNRS, UMR 7144, Station Biologique de Roscoff, Place Georges Teissier, CS90074, 29688 Roscoff Cedex, France
[g]Belozersky Institute of Physico-Chemical Biology, Lomonosov Moscow State University, Leninskiye Gory 1-40, 119 234 Moscow, Russian Federation
[h]Institute for Information Transmission Problems, Russian Academy of Sciences, Bolshoy Karetny per. 19-1, 127 051 Moscow, Russian Federation

Blastogregarines are poorly studied parasites of polychaetes superficially resembling gregarines, but lacking syzygy and gametocyst stages in the life cycle. Furthermore, their permanent multinuclearity and gametogenesis by means of budding considerably distinguish them from other parasitic Apicomplexa such as coccidians and hematozoans. The affiliation of blastogregarines has been uncertain: different authors considered them highly modified gregarines, an intermediate apicomplexan lineage between gregarines and coccidians, or an isolated group of eukaryotes altogether. Here, we report the ultrastructure of two blastogregarine species, *Siedleckia nematoides* and *Chattonaria mesnili,* and provide the first molecular data on their phylogeny based on SSU, 5.8S, and LSU rDNA sequences.

---

[1]Corresponding author;
e-mail simdyanov@mail.bio.msu.ru (T.G. Simdyanov).

Morphological analysis reveals that blastogregarines possess both gregarine and coccidian features. Several traits shared with archigregarines likely represent the ancestral states of the corresponding cell structures for parasitic apicomplexans: a distinctive tegument structure and myzocytotic feeding with a well-developed apical complex. Unlike gregarines but similar to coccidians however, the nuclei of male blastogregarine gametes are associated with two kinetosomes. Molecular phylogenetic analyses reveal that blastogregarines are an independent, early diverging lineage of apicomplexans. Overall, the morphological and molecular evidence congruently suggests that blastogregarines represent a separate class of Apicomplexa.

Introduction

The name Apicomplexa was first introduced by Levine (Levine 1970) in order to unite "genuine" Sporozoa (gregarines, coccidians, and haemosporidians) and Piroplasmida relying on ultrastructural characters because the life cycles of the latter were poorly studied at that time and any molecular phylogenetic evidence was absent. Through the years, the composition of the group changed: in 1980, Levine moved piroplasms into Sporozoa, but simultaneously expanded the taxon (phylum) Apicomplexa, which comprised two subphyla that time: Perkinsezoa (with *Perkinsus*) and Sporozoa. Later, Perkinsezoa were consistently removed from Apicomplexa (e.g., Perkins et al. 2000), especially when *Perkinsus* was revealed to be an earliest branch of Dinozoa (Goggin and Barker 1993; Kuvardina et al. 2002), so that "Apicomplexa" was eventually reduced to "Sporozoa" and successively substituted this name, despite the fact that it was conventional during many decades before (e.g., Grassé 1953a,b). Thus, recently Apicomplexa is a junior synonym of Sporozoa in terms of the International Code of Zoological Nomenclature and consequently should be abolished. However, we support the original approach of Levine to combine Sporozoa and their closest relatives in a single taxon, and therefore, also following some recent viewpoints (e.g., Cavalier-Smith 2014; Votýpka et al. 2016), we consider Apicomplexa in this paper as a large phylogenetic clade comprising Chrompodellida (or Apicomonada in Cavalier-Smith's terminology) and Sporozoa (or Sporozoasida in Levine's terminology). Chrompodellids include free-living predatory flagellates (colpodellids) and symbiotic photosynthetic organisms (chromerids) closely related to each other (Janouškovec et al. 2015), whereas sporozoans are obligate parasites: many of them

are pathogens of humans and domestic animals causing serious diseases (Perkins et al. 2000). The major sporozoan groups of high practical importance are coccidians (e.g., *Toxoplasma* and *Eimeria*), cryptosporidians, haemosporidians (e.g., *Plasmodium* causing malaria), and piroplasms (e.g., *Babesia)*, therefore these organisms are popular subjects of scientific research while gregarines and other early branching invertebrate parasites remain understudied.

Phylogenetic relationships and evolutionary history of sporozoans within Apicomplexa are still an open question. The primary divergence of sporozoans occurred most likely in marine invertebrates (Cox 1994; Leander 2008; Théodoridès 1984), which are the hosts of early branching gregarines and coccidians, as well as of some sporozoans incertae sedis that could be a source of important evidence for reconstructing the ancestral states for the Apicomplexa as a whole.

One of such unusual and poorly studied organisms are the blastogregarines – a tiny group of uncertain taxonomic affiliation encompassing intestinal parasites of marine polychaetes of the family Orbiniidae. This group comprises four species formally belonging to the single genus *Siedleckia*: *S. nematoides* Caullery and Mesnil, 1898, *S. mesnili* Chatton and Dehorne, 1929, *S. caulleryi* Chatton and Villeneuve, 1936, and *S. dogieli* Chatton and Dehorne, 1929. The type species *S. nematoides* was described from the intestine of the polychaete *Scoloplos armiger* (Caullery and Mesnil 1898). Typical features of blastogregarines are epicellular parasitism like gregarines, persistent multinuclearity in trophozoites (unlike gregarines, which are uninuclear), bending motility like archigregarines – the most plesiomorphic gregarine group (Schrével and Desportes 2015; Schrével et al. 2013), and the capacity to produce globular buds, putative stages of game-

togenesis, from their posterior end (Chatton and Dehorne 1929; Chatton and Villeneuve 1936a). This latter feature is unknown from other sporozoans and led to the name "blastogregarines" (i.e., "budding gregarines") (Chatton and Villeneuve 1936a). The life cycle of blastogregarines (Fig. 1) was proposed by Chatton and co-authors relying on evidence from studies on *S. mesnili* and *S. caulleryi* (Chatton and Dehorne 1929; Chatton and Villeneuve 1936a). Although the sexual process was studied incompletely (gamete formation, especially microgametogenesis, and the development of zygote, i.e., sporogony, were not traced), Chatton and Villeneuve suggested that blastogregarines are more similar to coccidians than to gregarines due to the absence of the syzygy and gametocyst (characteristic for gregarines) and their extremely pronounced anisogamy (a coccidian feature) (Chatton and Villeneuve 1936b).

The persistent multinuclearity unusual for sporozoans and the peculiar life cycle (absence of so-called Leuckart's triade: a cyclic sequence of merogony, gamogony, and sporogony, which is characteristic for many sporozoans, e.g., coccidians, haemosporidians, and a part of gregarines (Perkins et al. 2000)) gave rise to discrepant and changeable interpretations of the taxonomic position of blastogregarines following their initial discovery. Different authors considered them as aberrant gregarines (Dogiel 1910), a group incertae sedis within sporozoans (Léger 1909; Léger and Duboscq 1910) or a protistean lineage unrelated to sporozoans at all (Caullery and Mesnil 1899). After more detailed studies on the life cycles of blastogregarines (see above), Chatton and Villeneuve (1936a,b) concluded that the permanent gametogenesis distinguished them from both gregarines and coccidians and suggested considering them as an independent group of the same rank (the order) within Sporozoa (Telosporidia). Grassé (1953a) supposed that blastogregarines should be included in the class Gregarinomorpha. Krylov and Dobrovolskij challenged the assignment of the blastogregarines to the phylum Sporozoa altogether and considered them only as an addendum to that (Krylov and Dobrovolskij 1980). Conversely, de Puytorac et al. (1987) adopted and developed the standpoint of Chatton and co-authors and assigned the blastogregarines as the separate sporozoan class Blastogregarinea along with the classes of gregarines, coccidians, and haemosporidians (de Puytorac et al. 1987). Finally, despite the absence of syzygy, Levine and his followers (Levine 1985; Perkins et al. 2000) assigned the blastogregarines to the order Eugregarinorida
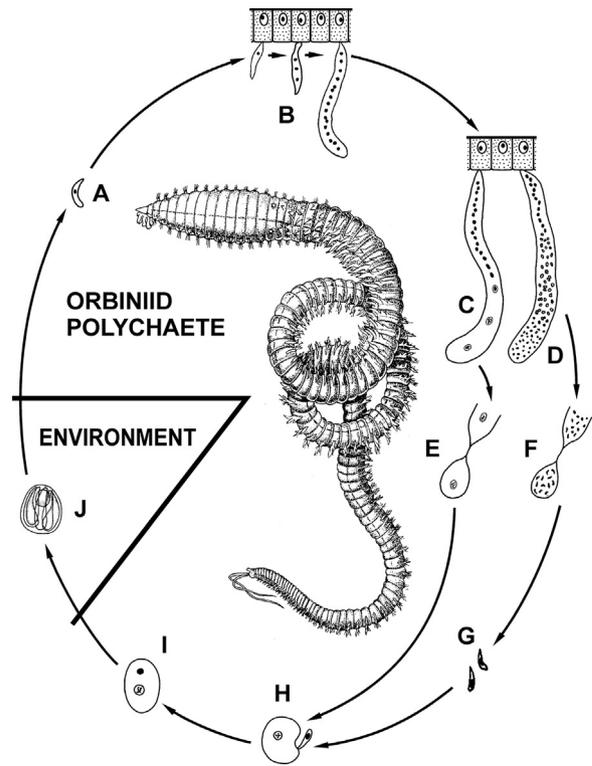

Figure 1. Diagram of the life cycle of blastogregarines according to Chatton and co-authors (Chatton and Dehorne 1929; Chatton and Villeneuve 1936a). (**A**) Young mononuclear vermicular individual similar to sporozoites of coccidians and gregarines. (**B**) Non-differentiated trophozoites attached to the intestinal epithelium of the host; the number of the nuclei increases during trophozoite growth. (**C**, **D**) The epicellular trophozoites develop into the gamonts of two types: macrogamonts (**C**) and microgamonts (**D**); the macrogamonts (female gamonts) have the nuclei arranged in a single row; the size of the nuclei increases towards the rear end of the cell; the microgamonts (male gamonts) have a similar arrangement and size of the nuclei in the anterior third of the cell, after that the distribution of the nuclei, which perform multiple divisions, becomes random and they decrease in size towards the rear end of the cell. (**E–H**) The gamonts attached to the intestinal epithelium produce either numerous uninuclear (**E**) or multinuclear (**F**) globular buds from their posterior ends. Chatton and Villeneuve (1936a) considered this process as gamogony giving rise to macrogametes (**E**, **H**) or multinuclear microgametocytes (**F**), which presumably release small microgametes (**G**). Chatton and colleagues detected stages in the hindgut content that were interpreted as gamete copulation (**H**) and zygotes (**I**). (**J**) Oocysts, found in the feces of the hosts, contain 10-16 free banana-shaped sporozoites (without sporocyst envelopes), and a residual body shifted to one of the oocyst poles. Adapted from (Caullery and Mesnil 1898) (**A**), and (Chatton and Villeneuve 1936a) (**B–J**).
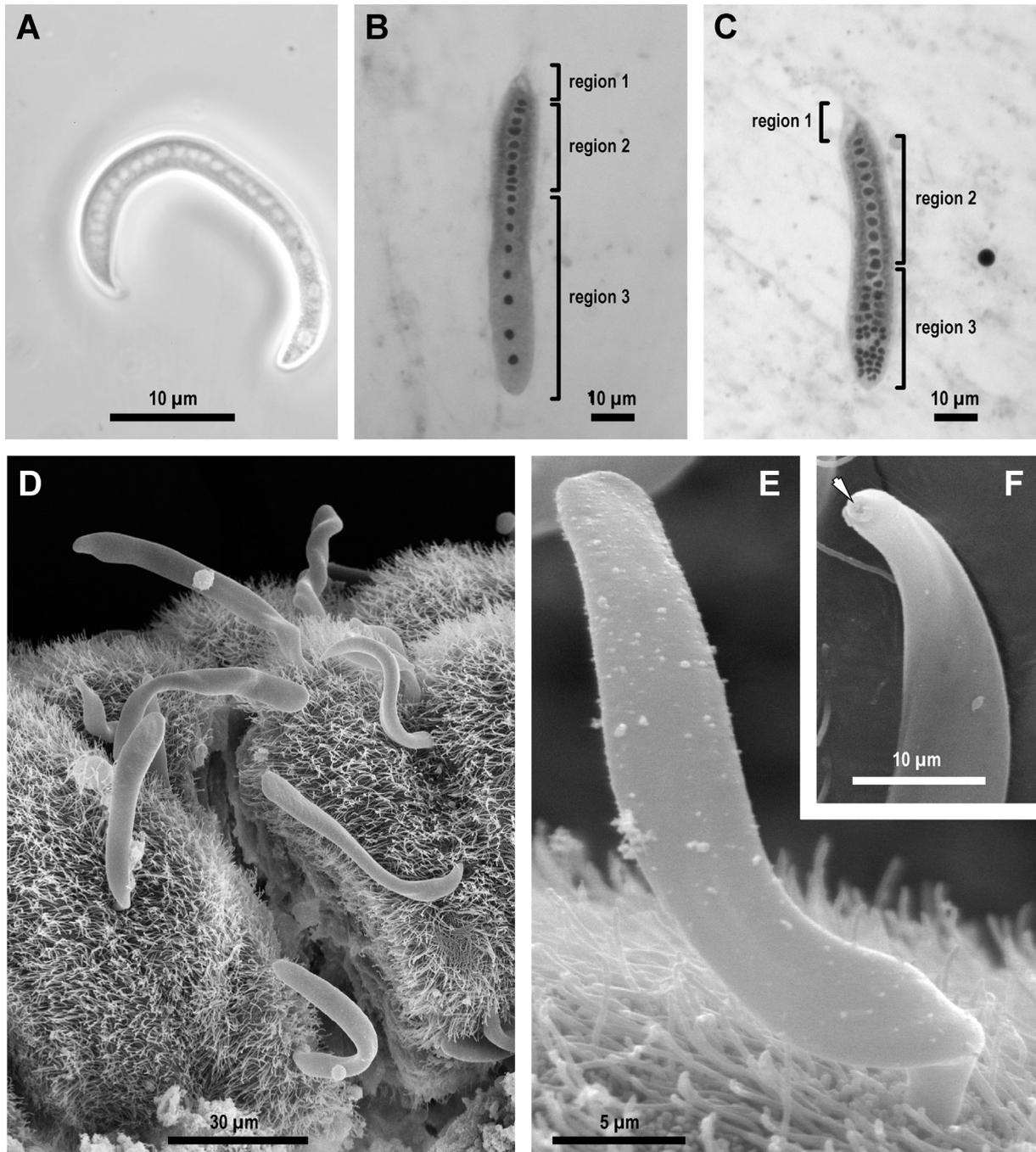
Figure 2. General morphology of the blastogregarine *Siedleckia* cf. *nematoides* ((**A–C**), LM, phase contrast or bright field; (**D–F**), SEM). (**A**) A living macrogamont individual. (**B**) and (**C**) The fixed young macrogamont and microgamont, respectively, stained by Böhmer's hematoxylin, flat views; three regions of the cell are conspicuous: #1 (mucron), #2 ("asexual"), and #3 ("sexual") – see next figure (Fig. 3) and Discussion for further explanations. (**D**) Individuals attached to the intestinal epithelium of the host. (**E**) An individual attached to the intestinal epithelium (under higher magnification) shows the smooth surface of the cell. (**F**) The mucron (arrow) of an individual dislodged from the gut epithelium.
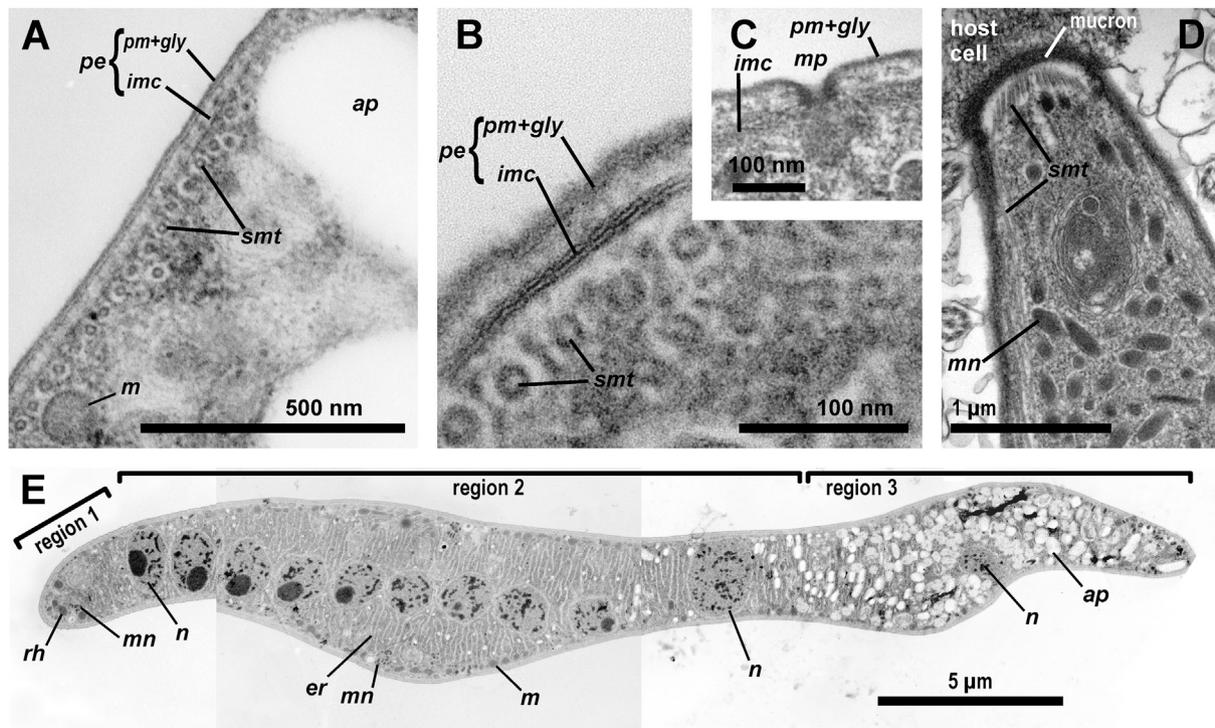
Figure 3. General ultrastructure of the blastogregarine *Siedleckia* cf. *nematoides* (TEM). (**A**, **B**) Cross sections through the cortical region of the cell showing the trimembrane pellicle (*pe*) consisting of the plasma membrane (*pm*) covered by the cell coat (glycocalyx, *gly*) and inner membrane complex (*imc*), longitudinal subpellicular microtubules (*smt*) chiefly arranged in a layer beneath the pellicle; mitochondria (*m*) and the granules of amylopectin (*ap*) are present in the cytoplasm. (**C**) Micropore (*mp*). (**D**) The longitudinal section through a parietal part of the anterior end (region 1–see below) of an individual attached to the host cell showing longitudinal subpellicular microtubules (*smt*) and numerous putative micronemes (*mn*). (**E**) two combined micrographs of the neighbored longitudinal sections of the anterior half of a macrogamont cell showing the subdivision of the cell into three regions: (1) mucronal region with rhoptries (*rh*) and putative micronemes (*mn*), (2) region of the linear arrangement of nuclei (*n*), which is rich in channels of endoplasmic reticulum (*er*), putative micronemes (*mn*), and mitochondria (*m*), and (3) posterior part of the cell (the section covered only its anterior part) rich in amylopectin granules (*ap*); see Figures 4–6 for details.

that was formally explained only by the absence of merogony in their life cycle. This taxonomic scheme has recently been accepted in the WoRMS and NCBI databases. The more recent reviews (e.g., Adl et al. 2012) largely ignored this group likely because of the absence of ultrastructural and molecular phylogenetic evidence that makes their phylogenetic relationships and taxonomic position actually obscure. It should be emphasized that the structure and biology of blastogregarines were not addressed since 1936 (Chatton and Villeneuve 1936a). Thus, the uncertain affiliation of these unusual organisms required efforts to be clarified with the use of modern methods. This work presents the first ultrastructural and molecular phylogenetic evidence from two blastogregarine species, *Siedleckia nematoides* and *Chattonaria mesnili* (formerly *S. mesnili*) gen. n., comb. n., which

lead us to redefine the phylogenetic and taxonomic position of the group.

Results

Morphology and Ultrastructure

***Siedleckia* cf. *nematoides* Caullery et Mesnil, 1898.** Although the morphology of these blastogregarines collected by us matched the first description of *Siedleckia nematoides* (Caullery and Mesnil 1898) and excellent drawings in a later paper about it (Caullery and Mesnil 1899), we use "cf." (Lat. *confer* – compare with) in the species name because the sampling was performed quite far from the type locality (Gulf of Wimereux, the English Chan-
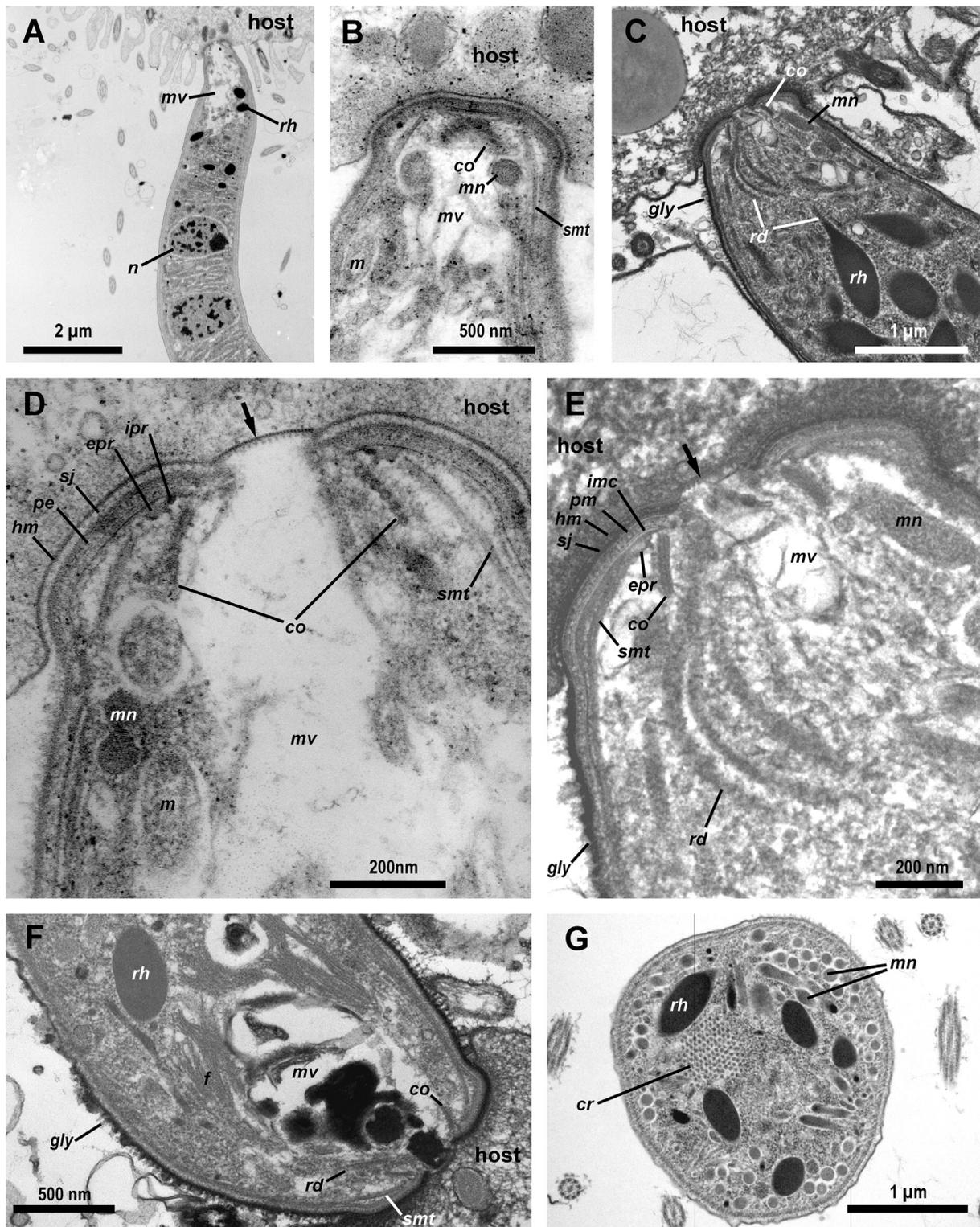
Figure 4. Ultrastructure of the attachment apparatus of the blastogregarine *Siedleckia* cf. *nematoides* (TEM). (**A**) Longitudinal section through the anterior part of a blastogregarine attached to the host intestinal epithelium showing the large mucronal vacuole (*mv*), rhoptries (*rh*), and nuclei (*n*). (**B–F**) Longitudinal sections of the mucron showing the details of its organization: the conoid (*co*), the mucronal vacuole (*mv*), the rhoptries (*rh*) with the ducts (*rd*), external and internal parts of the polar ring (*epr* and *ipr*,

nel, France) and, additionally, due to the possibly existence of cryptic species within this morphospecies (see below). Individuals of *S.* cf. *nematoides* were isolated from the intestine of the polychaete worm *Scoloplos* cf. *armiger* (O.F. Müller, 1776) from two localities in the White Sea, Russia: near Marine Biological Station of Saint Petersburg State University (MBS) and near White Sea Biological Station of Moscow State University (WSBS). All dissected worms (more than 200 individuals) from both localities were infected. The parasites were observed in the midgut (the area behind the stomach) among epithelial cells bearing microvilli and cilia. The intensity of the infection varied from few parasites per host up to 20 cells per 0.01 mm^2 in some loci of the host intestinal epithelium (SEM data on 30 samples). Neither light nor electron microscopy revealed any appreciable differences between individuals of *S.* cf. *nematoides* from the both sampling localities. The cells of *S.* cf. *nematoides* were elongated and flattened with pointed anterior and rounded posterior ends; their smooth surface lacked any grooves and folds (Fig. 2A–E). The cell size varied broadly among individuals: length 5–200 µm (av. 70 µm; mode 60 µm; n = 139), width 3–17 µm (av. 9 µm; mode 8 µm; n = 139) across flattened side, and 1–3 µm (n = 139) across narrow side. Living blastogregarines attached or dislodged from the intestinal epithelium were continuously motile with active bending, twisting, and squirming movements (for details, see: Valigurová et al. 2017).

In female gamonts (=macrogamonts), nuclei were arranged in a row along the cell's length (Fig. 2A, B). They were located closer to each other in the anterior half of the body and appeared compressed and ranged in size from 0.5 × 1.3 up to 0.7 × 2.2 µm (av. 0.9 × 1.3 µm, n = 60 nuclei in 10 individuals). The distance between the nuclei increased and they became a little larger towards the posterior end (from 0.5 × 1.6 up to 1.0 × 2.9 µm; av. 1.1 × 1.7, n = 32, the same 10 individuals). The nuclei in the male gamonts (=microgamonts) were much more numerous (Fig. 2C) with a linear arrangement only in the anterior part of the

cell. Like the nuclei of macrogamonts in this region, they were slightly compressed and ranged in size from 0.5 × 1.1 up to 1.8 × 2.2 µm (av. 1.1 × 1.5 µm, n = 56, 10 individuals). In the posterior part of microgamonts, the nuclei were distributed randomly; their shape became irregular and the size decreased (0.5 × 0.7 up to 1.1 × 1.4 µm; av. 0.7 × 0.9, n = 58, the same 10 individuals). The border between these patterns of distribution lay nearly in the middle of the body in smaller (younger) individuals (Fig. 2C) or moved to the anterior third of the body in larger (elder) ones (not shown, see: Caullery and Mesnil 1899). Compared with younger gamonts, the nuclei were more numerous in elder ones, both female and male.

Individuals of *S.* cf. *nematoides* embedded their apical end (mucron) into the brush border of enterocytes bearing microcilia and microvilli (Fig. 2D, E). When dislodged after fixation, some of them, with an intact attachment site, exhibited a small apical pit in its center (Fig. 2F). No additional structures providing attachment, e.g., hooks or other projections, were found.

The tegument of *S.* cf. *nematoides* cells (Fig. 3A, B) was represented by a trimembrane pellicle, 32 nm thick. It consisted of the plasma membrane with a well-developed glycocalyx, and two closely adjacent cytomembranes forming the inner membrane complex, IMC. The internal lamina, an electron-dense layer just beneath the IMC, which is characteristic for gregarines (Schrével et al. 2013) was not detected. A single layer of numerous regularly arranged longitudinal subpellicular microtubules arose from the anterior end and passed along the whole cell (Fig. 3D); each microtubule appeared to be surrounded by an electron-translucent area (Fig. 3A, B). Few additional microtubules were located just beneath this layer (Fig. 3A). Micropores (Fig. 3C) were detected rarely, in the anterior part of the cell. The cell of *S.* cf. *nematoides* is highly polarized and the ultrastructure allowed to define three regions (Fig. 3D, E): (1) the mucron (attachment and feeding apparatus) containing organelles of the apical complex and lacking nuclei, (2) the region of linear arrange-

---

respectively), longitudinal subpellicular microtubules (*smt*) arising from *epr*, putative micronemes (*mn*), and mitochondria (*m*); the mucron is covered by the pellicle (*pe*) forming a septate cell junction (*sj*) with the host cell; *hm*, plasma membrane of the host cell, *pm*, plasma membrane of the parasite cell, *imc*, inner membrane complex, *gly,* glycocalyx; *arrows* mark the modified part of the host cell surface facing parasite cytostome. Image (**F**) also shows longitudinal thick fibrils (*f*) around the posterior part of the mucronal vacuole. (**G**) Cross section through the anterior part of a blastogregarine cell behind the mucronal vacuole showing a crystalloid structure (*cr*). (**C**, **E**, **F**) fixed in the presence of ruthenium red (see "Methods").

ment of nuclei rich in endoplasmic reticulum (ER), and (3) the posterior half of the body (in full-sized individuals) with significant differences between the macro- and microgamonts in the structure, number, and arrangement of nuclei that will be detailed below.

TEM studies revealed that the attachment apparatus of *S.* cf. *nematoides* is a mucron. It was embedded in the host enterocyte between the microvilli (Fig. 4A) and contained the mucronal vacuole, the conoid, two (internal and external) polar rings, and numerous rhoptries (Fig. 4B–E). The conoid (Fig. 4B–E) had upper and basal diameters of nearly 290 and 400 nm, respectively, and its height was about 130 nm. It was built of coiled microtubules: six microtubules were visible on longitudinal sections (Fig. 4B, D); the anterior three of them were closely adjacent to each other, while the rear three were spaced 6–7 nm apart (Fig. 4D). The polar ring, located slightly higher than the upper opening of the conoid (Fig. 4D, E), gave rise to the longitudinal subpellicular microtubules, i.e., it is their MTOC (the microtubule organization center). The polar ring appeared to be subdivided into two parts of different electron density: external and internal. The external part having moderate electron density was about 40 nm thick with the external diameter about 450 nm. The internal part (Fig. 4D) of high electron density is thinner (~20 nm thick) and narrower (ext. diam ~360 nm, int. diam. ~340 nm) than the external one. The majority of longitudinal sections showed a voluminous mucronal vacuole with a loose fibrous material and a wide duct passing through the conoid and opening outside, i.e. into the space between the parasite and host cells (Fig. 4A–F). Several large rhoptries were distributed around and behind the mucronal vacuole; they formed ducts passing through the conoid and, apparently, opened outside the cell (Fig. 4C, E). Few putative micronemes and mitochondria were detected in the parietal area of the anterior region of the mucron (Fig. 4B–E). The number of the putative micronemes increased in the region behind the mucronal vacuole where they had a regular distribution on the periphery of cytoplasm (Figs 3D, 4G). The mucron was covered by the trimembrane pellicle excepting the region against the conoid with the wide inlet opening (diam. ~130 nm) of the mucronal vacuole: we consider it to be a cytostome-cytopharyngeal complex performing myzocytosis (Fig. 4D, E). The cytostome was opened into a gap (~20 nm) between the parasite and host cell plasma membranes, which had the appearance of the septate cell junction; the "septa" were putatively formed by both parasite and host cell coats (Fig. 4D, E). The region of host plasma membrane facing the parasite cytostome was of higher electron density than the rest of the membrane and had uniformly spaced electron-dense structures appeared as bold dots on the external surface of the host cell (Fig. 4D, E); it might be a perforated or modified host cell coat. No other significant modifications of the host cell were detected. Some additional structures were observed in the mucron and the region just behind it: thick fibrils around the posterior part of the mucronal vacuole, and a crystalloid structure (Fig. 4G).

The main feature of the anterior half of the cell behind the mucron (region 2) is the linear arrangement of nuclei (Fig. 3E). Another conspicuous characteristic is the abundance of the channels or cisterns of the endoplasmic reticulum (ER), arranged uniformly in the cytoplasm, chiefly perpendicularly to the longitudinal cell axis (Fig. 5). Occasionally, they were connected to the nuclear envelopes (Fig. 5A). In the subcortical layer of the cytoplasm, mitochondria and putative micronemes were numerous (Figs 3E, 5); the latter were concentrated in the lateral areas (Fig. 5A). Golgi apparatus, few small granules of amylopectin (the storage carbohydrate), and multimembrane structures were also observed in this cell region (Fig. 5).

In the macrogamont cells, the number and size of the amylopectin granules dramatically increased from the middle of the cell (region 2) towards its rear end (region 3) (Fig. 3E). In the region 3 of the cell, the ER was displaced with these granules (Figs 3E, 6A). In addition, rare large electron-dense globules (not observed in the anterior half of the cell) were present here (Fig. 6A). All nuclei in the macrogamont cells had similar structure: they contained small clods of heterochromatin and a single nucleolus, however, the nuclei in the posterior region were slightly larger than those in the region 2 of the cell: about 1-2 × 2 μm and 1.2 × 1.7 μm, respectively (Figs 3E, 6A).

Unlike macrogamonts, the structure of nuclei in the microgamont cells changed from the anterior to the posterior end of the body, with a gradual increase in chromatin condensation (Fig. 6B, C). In the middle of the cell (region 2), the nuclei were completely filled by highly condensed chromatin (Fig. 6B). Raikov called such nuclei "of spermal type" in his classification of protist nuclei (Raikov 1982). From the border between regions 2 and 3 and further towards the rear, the linear arrangement of the nuclei became disordered and the dividing nuclei were repeatedly observed; some of them were equipped with kinetosomes (Fig. 6C–E).
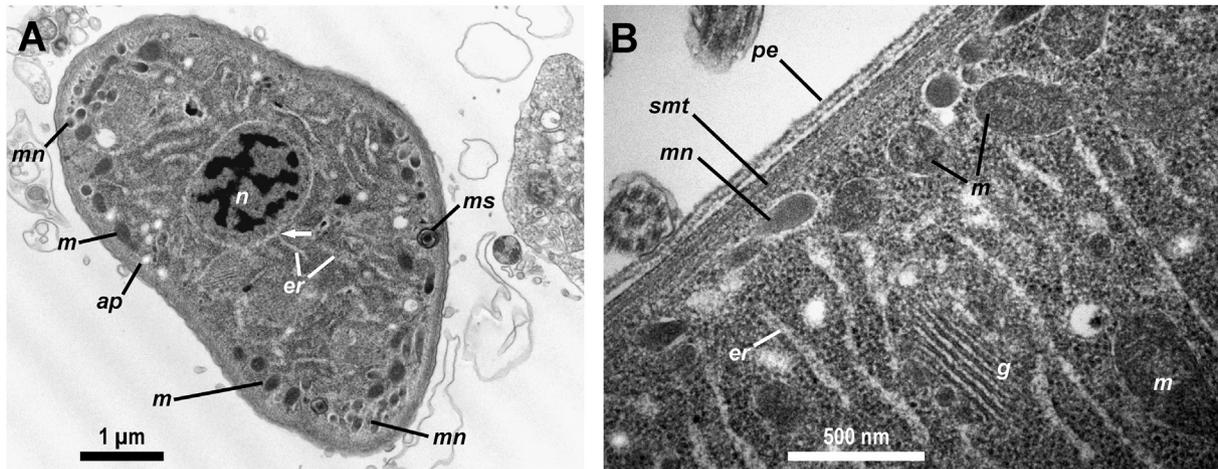
Figure 5. Cytoplasmic organelles of the blastogregarine *Siedleckia* cf. *nematoides* (TEM). (**A**) Cross section through the region 2 of the cell (linearly arranged nuclei) showing putative micronemes (*mn*) in the lateral regions of the cell and a connection of the endoplasmic reticulum (*er*) with the nuclear envelope (arrow). (**B**) Fragment of the longitudinal section of the same region as in (A) showing Golgi apparatus (*g*), abundant channels of the endoplasmic reticulum (*er*), numerous mitochondria (*m*), and putative micronemes (*mn*). Other abbreviations: *ms*, the multimembrane structure; *n*, nucleus; *pe*, pellicle; *ap*, amylopectin granules; *smt*, longitudinal subpellicular microtubules.

Electron-translucent areas within the dividing nuclei contained microtubules, probably the elements of a mitotic spindle (Fig. 6D, E). The connection of these microtubules with the kinetosome or any other possible MTOC was not observed. The nuclear divisions in the region 3 of the microgamont cells obviously correspond to progamic mitoses resulting in the production of microgametes based on the the appearance of two adjacent kinetosomes (Fig. 6D, E). The cytoplasm of the posterior region in the microgamont cells had a completely different structure than that of the macrogamont cells due to the presence of the ER channels and only few small amylopectin granules (Fig. 6D, E).

***Chattonaria* (*Syn. Siedleckia*) *mesnili* (*Chatton et Dehorne*, 1929) gen. n., comb. n.** Individuals of *Chattonaria mesnili* were isolated from the intestine of the polychaete worms *Orbinia* (Syn. Aricia) *latreillii* (Audouin et H. Milne Edwards, 1833) (Orbiniidae) collected on littoral zone of English Channel, France (see "Methods" for details). We managed to sample only 12 individuals of the host species *Orbinia latreillii*, four of them were free of parasites and eight were infected. The parasites were found in the stomach – the dilated part of the intestine situated immediately after the esophagus and covered by glandular cells lacking cilia. The intensity of infection varied from few to tens of parasites (30–40) per host (the latter was observed only in two worms). As a direct conse-

quence of difficulties to sample hosts with a high prevalence of the blastogregarine parasites, the number of *C. mesnili* cells analyzed under SEM, and TEM was significantly lower than in *S.* cf. *nematoides*. LM studies were not performed especially as the collected cells fully fit the first description of *Siedleckia mesnili* and its drawings of excellent quality (Chatton and Dehorne 1929). The collected cells were elongated (48.8 × 7.6 to 220 × 13 μm; av. 97.4 × 9.1 μm; n = 8) and cylindric with a roundly pointed posterior end. Their tegument formed longitudinal folds (Fig. 7A–E). These originated behind the mucron, where pairs of adjacent folds shared a common origin (Fig. 7D), and ran towards the posterior end of the cell, where they merged into a smooth terminal region (Fig. 7E). The number of the folds was 28 and 34 on the cross-sections of two different individuals. The anterior ends of the parasites were embedded in the cells of the host stomach (Fig. 7A). One of the individuals, artificially dislodged during mounting of the SEM preparation, exhibited the anterior end covered with a remnant of the host tissue, therefore we were not able to observe the superficial structure and the shape of the attachment apparatus (Fig. 7B, D), however, the first description suggested it equipped with hooks. In contrast to *S.* cf. *nematoides*, the living individuals of *C. mesnili* observed under a stereomicroscope immediately after the host dissection showed only weak motility by slow and intermittent bending movements.
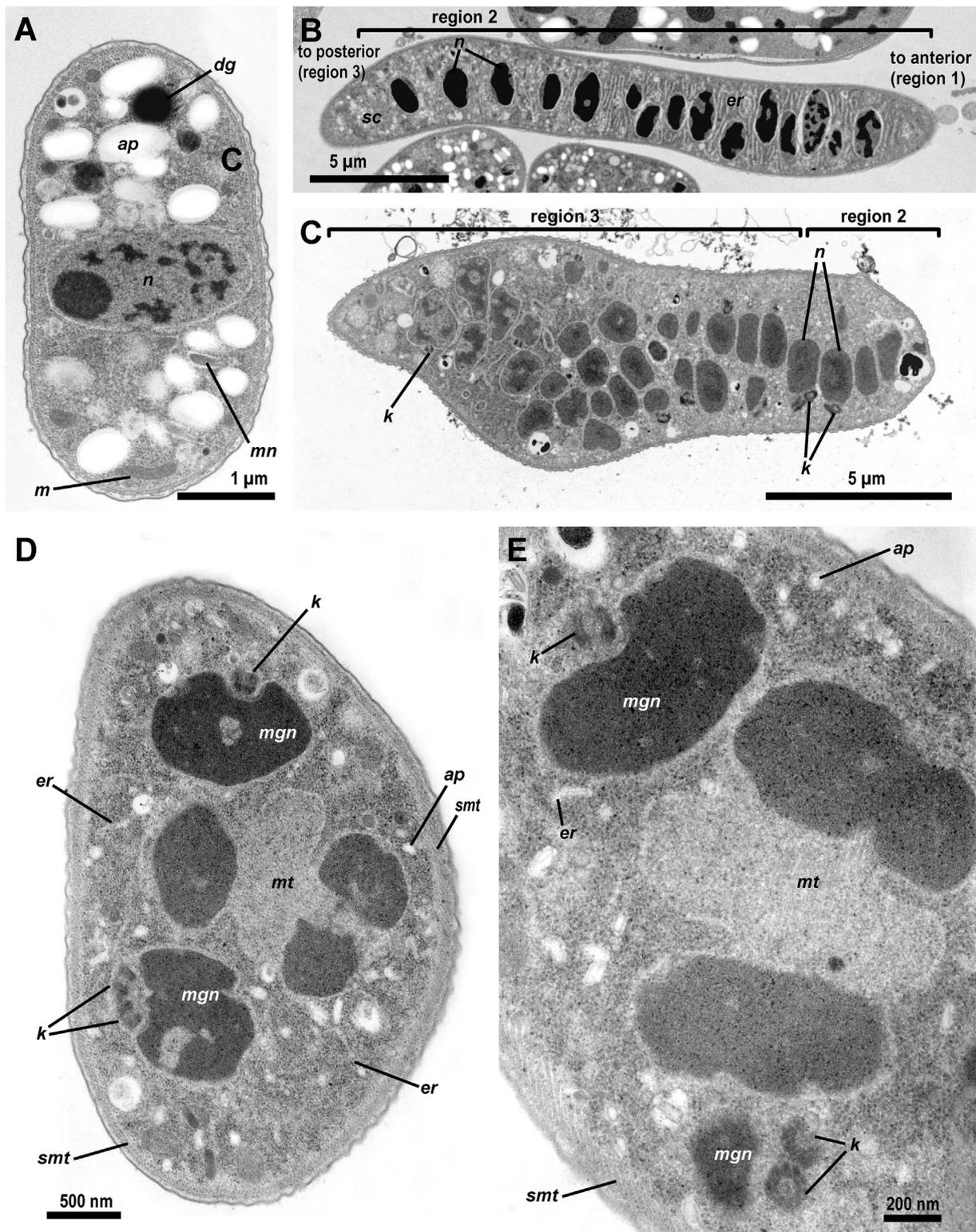
Figure 6. Nuclear apparatus of the blastogregarine *Siedleckia* cf. *nematoides* (TEM). (**A**) The cross section through the rear part (region 3) of a macrogamont cell showing the abundance of amylopectin granules of large size (*ap*), a mitochondrion (*m*), putative micronemes (*mn*), an electron-dense globule (*dg*), and a nucleus (*n*) containing heterochromatin and a nucleolus. (**B**) The longitudinal section of a microgamont cell in the

The cells of *C. mesnili* were covered by the trimembrane pellicle about 50 nm thick and organized in longitudinal folds with flattened tops (Fig. 7F, G). The size of the folds was about 1.1 μm high and 0.9 μm wide at their bases. The height was more and the width was less in the anterior part of the cell: about 2 and 0.3 μm at the bases, respectively, so the shape varied depending on the section site (compare Fig. 7F and G). Just beneath the pellicle, numerous longitudinal subpellicular microtubules were observed, with a regular distribution and arrangement: two layers in the tops of the folds and a single layer on their lateral sides and between them (Fig. 7G). Although no typical micropores were observed, micropore-like structures interrupting the IMC and the layer of subpellicular microtubules and connected to multimembrane vesicles were present (Fig. 7G, compare with Fig. 5A). Similarly to *S.* cf. *nematoides*, the cell of *C. mesnili* can be subdivided into three regions: (1) the mucronal region, (2) the region of the linearly arranged nuclei, and (3) the posterior region with developing gametic nuclei.

TEM studies revealed that the attachment apparatus of *C. mesnili* is a strongly modified mucron lacking the conoid and anchored in the host cell with peripheral bulges (several or the only circular one) formed by large alveoli between the cytomembranes of the IMC (Figs 7B, E; 8A–D, G). One observation suggested that a hook-like cytoplasmic projection jutted into the alveolus (Fig. 8A, C). The flat top of the mucron was covered by the pellicle of varying thickness (~14 to 27 nm) with a loose layer of fibrils just beneath it. In this region, the middle and inner membranes of the IMC terminated around an external opening (cytostome) of the mucronal vacuole. The diameter of the cytostome was about 110 nm (Fig. 8E). Similarly to *S.* cf. *nematoides*, a gap of varying width (~20 to 45 nm) was present between the parasite pellicle and the host cell membrane, but that was not a septate cell junction because of the absence of "septa". The host plasma membrane had an increased electron density in front of the cytostome (Fig. 8D–F). The frontal region of the mucron cytoplasm was free of organelles, with an exception of the mucronal vacuole connected to the cytostome by a wide duct (Fig. 8D, E). Near the IMC terminus, a structure similar to an apical polar ring was observed (Fig. 8E, F). This putative polar ring (~27 nm thick, ext. diam. ~240 nm) was not subdivided into any parts, as it was observed in *S.* cf. *nematoides*, and no microtubule contacting with it were detected, even though they were abundant within the mucron. The microtubules arose immediately from the fibrillar matter lying beneath the pellicle in the frontal region of the mucron. Numerous longitudinal microtubules were located in the cytoplasm behind the mucronal vacuole (Fig. 8D, E). Microneme-like bodies were detected in the parietal region of the mucron (Fig. 8D), but no obvious rhoptries or rhoptry ducts were observed. However, large electron-dense globules (~300 nm in diameter) without ducts were present in the region behind the mucron and around the first nucleus (Figs 8A, B; 9A).

The first non-differentiated nuclei of both macro- and microgamonts cells were slightly ellipsoid in shape (up to ~1.5 × 1 μm) and contained 1 nucleolus (Figs 8A–B; 9A–B). The channels of the ER, dense bodies (likely micronemes), and putative mitochondria were also present.

The region of linearly arranged nuclei (region 2) was studied only in the macrogamonts. The nuclei (up to ~2 × 1.5 μm) contained one nucleolus and heterochromatin that tended to congregate in a single lump (Fig. 9C). Other observed organelles include the small microneme-like bodies (Fig. 9C, D), few small amylopectin granules, putative mitochondria, and well developed ER; however, unlike *S.* cf. *nematoides*, the ER did not exhibit the regular arrangement (Fig. 9C).

The posterior end (region 3) of the macrogamont cells showed nuclei (up to ~1.7 × 1.2 μm) with the circular arrangement of the heterochromatin and excentric nucleolus. The cytoplasm appeared vacuolated and contained numerous

middle of the body (posterior part of region 2) and (**C**) the diagonal section of a microgamont cell through the border between regions 2 and 3: abundant nuclei (*n*) with the highly condensed chromatin are arranged in the raw in region 2; they acquire kinetosomes (*k*) near the border between regions 2 and 3 and then become arranged randomly; (**C**) fixation in the presence of ruthenium red. (**D, E**) Cross sections through the rear part of a microgamont cell (region 3) showing the channels of endoplasmic reticulum (*er*), the small and rare granules of amylopectin (*ap*), a putative progamic mitosis, and the nuclei of future microgametes (*mgn*) associated with the kinetosomes (*k*). Note microtubules, probably of the mitotic spindle: (*mt*) and compare with the subpellicular microtubules (*smt*).
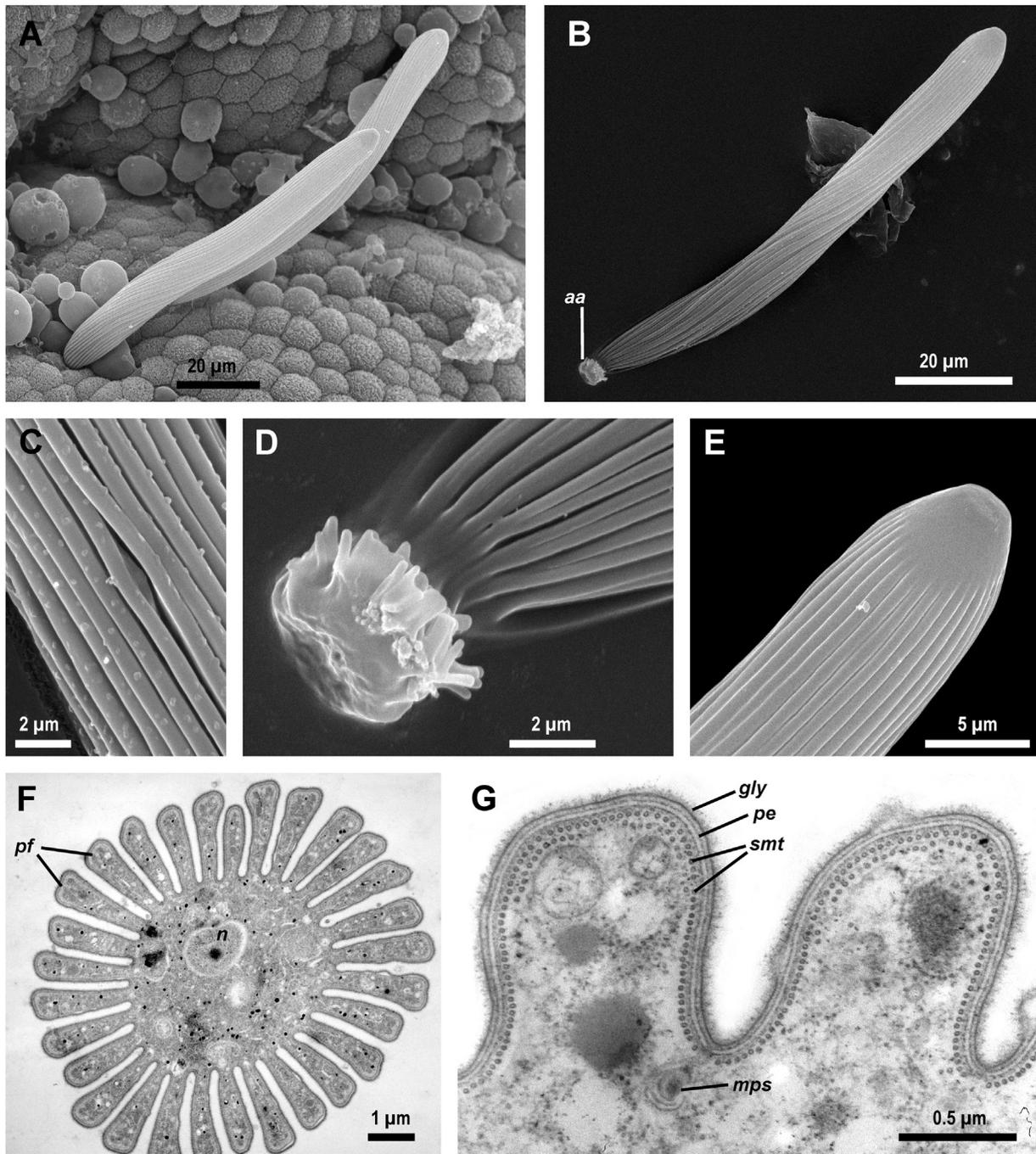
Figure 7. General morphology and cortex organization of the blastogregarine *Chattonaria mesnili* ((**A–E**) SEM; (**F**, **G**) TEM, cross sections). (**A**) Two individuals attached to the stomach epithelium of the host. (**B**) An individual artificially dislodged from the epithelium during mounting of the SEM preparation exhibiting the attachment apparatus (*aa*) embedded in the fragment of the intestinal lining. (**C–E**) Details of (**B**) under higher magnifications: surface with longitudinal pellicular folds (**C**), the attachment apparatus (*aa*) covered by the remnant of the host tissue (**D**), and the smooth posterior end (**E**). (**F**) Cross section of an individual through anterior region of the cell showing transversally cut longitudinal pellicular folds (*pf*) and a nucleus (*n*) with a single nucleolus. (**G**) A fragment of another cross section under higher magnification showing trimembrane pellicle (*pe*) coated by glycocalyx (*gly*), longitudinal subpellicular microtubules (*smt*) located just beneath it, and a micropore-like structure (*mps*).
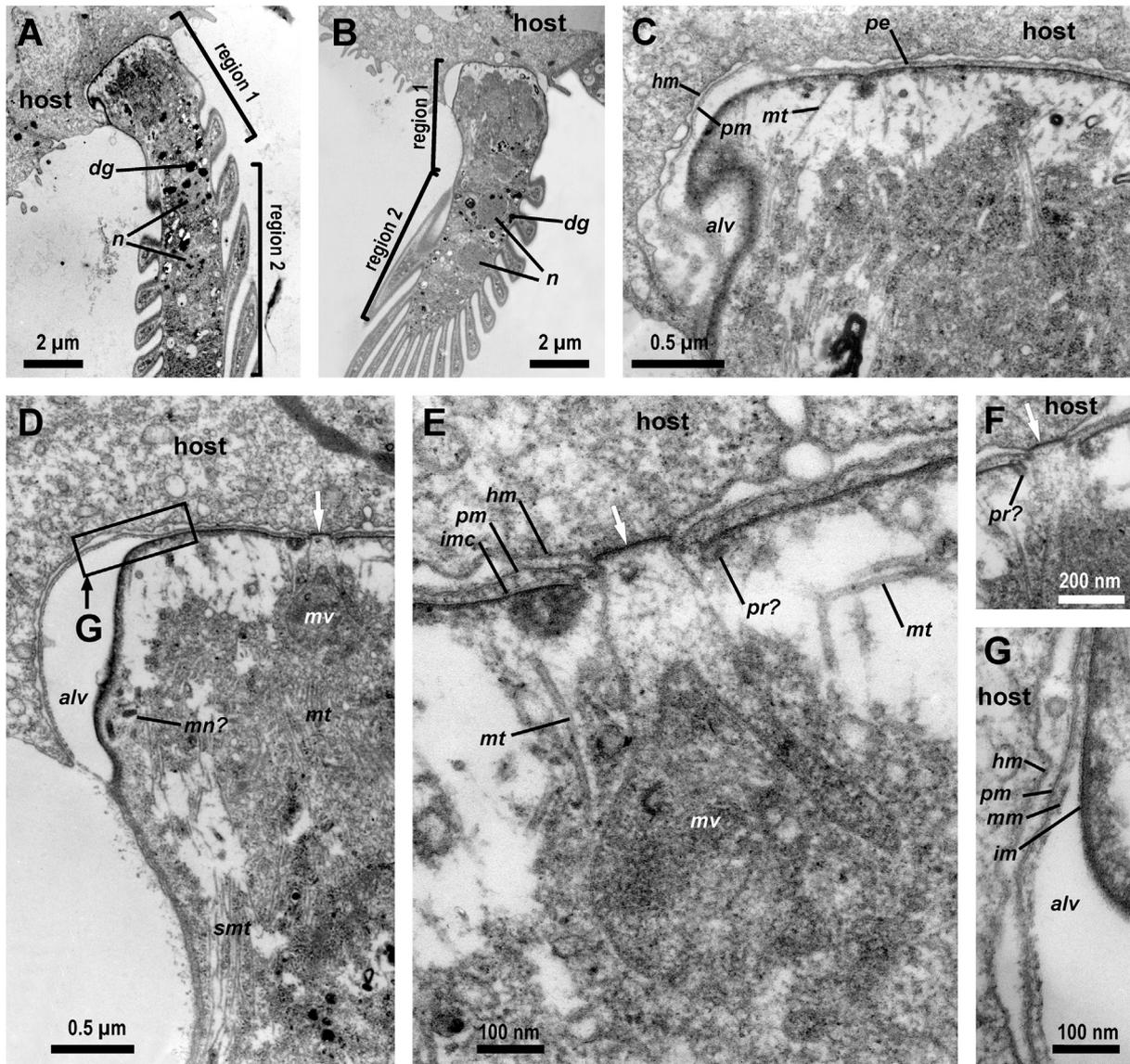
Figure 8. Attachment apparatus (mucron) of the blastogregarine *Chattonaria mesnili* (TEM). (**A–B**) Longitudinal sections of anterior parts of two individuals attached to the host cells: a microgamont (**A**) and a macrogamont (**B**) showing nuclei (*n*) and dense globules (*dg*) in the cytoplasm; two marked regions are corresponding those of *S.* cf. *nematoides* (see Fig. 3). (**C**) Longitudinal section of the same individual that in (A) showing a large alveolus (*alv*) with a protrusion of the cytoplasm and microtubules (*mt*) arising from the pellicle (*pe*) of the mucron; *hm* and *pm* are host and parasite plasma membranes, respectively. (**D–F**) Longitudinal sections of the mucron and its parts of the same individual as in (B) showing myzocytosis through the cytostome facing the electron-dense region of the host cell plasma membrane (white arrow), mucronal vacuole (*mv*), putative polar ring (*pr?*) closely adjacent to endings of the IMC (*imc*), subpellicular microtubules (*smt*) without any visible MTOC, microtubules (*mt*) arising from the frontal zone of the mucron, microneme-like bodies (*mn?*), the cell junction, which is a non-septate gap between parasite and host plasma membranes (*pm* and *hm*, respectively). (**G**) A detail of (D) showing the structure of the large alveolus (*alv*) formed as space between the middle (*mm*) and inner (*im*) membranes of the pellicle; *hm* and *pm* are the plasma membranes of the host and parasite cells, respectively.
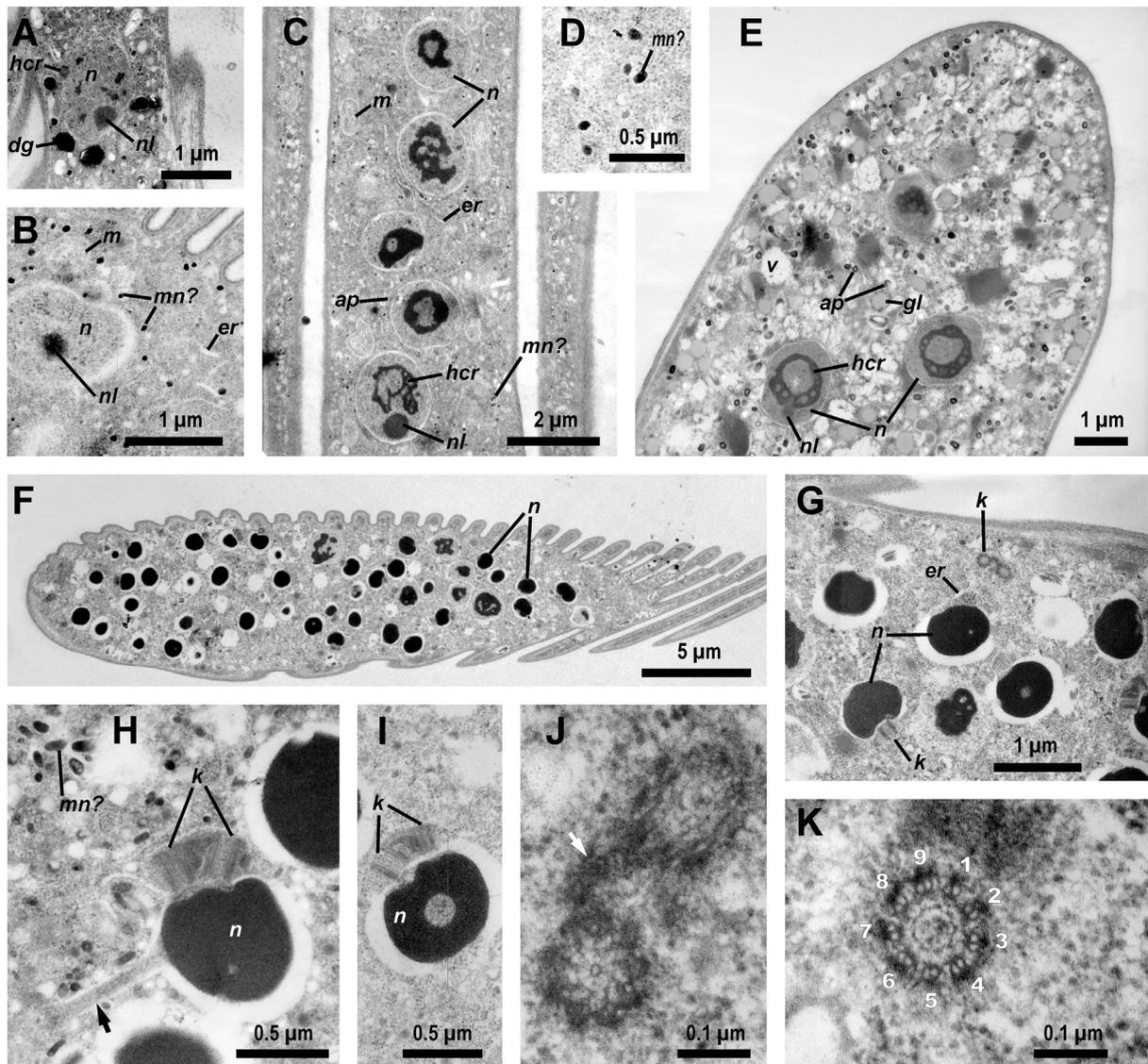
Figure 9. Nuclear apparatus and cytoplasm of the blastogregarine *Chattonaria mesnili* (TEM). (**A**) The first nucleus of a microgamont (the same cell as in Fig. 8A) containing heterochromatin (*hcr*) and a single nucleolus (*nl*) and surrounded by large dense globules (*dg*). (**B**) Fragment of a cross section through the anterior part of a macrogamont (the same cell as in Fig. 7F) showing a nucleus with a single nucleolus (*nl*), but lacking heterochromatin; the channels of the endoplasmic reticulum (*er*), microneme-like bodies (*mn?*), and a putative mitochondrion (*m*) are visible. (**C**) Longitudinal section of the middle part of a macrogamont cell (region 2, corresponding that of *S.* cf. *nematoides*) showing nuclei with the large lumps of the heterochromatin (*hcr*) and a single nucleolus (*nl*, visible in the lowest nucleus), the channels of the endoplasmic reticulum (*er*), putative mitochondria (*m*), rare small granules of the amylopectin (*ap*), and microneme-like bodies (*mn?*). (**D**) Fragment of the cytoplasm (the same region as in (C)) showing microneme-like bodies (*mn?*) under a higher magnification. (**E**) Longitudinal section of the posterior end of a macrogamont (region 3, corresponding to that of *S.* cf. *nematoides*) showing nuclei with the large lumps of the heterochromatin (*hcr*) and weakly developed nucleoli (*nl*, visible in the left lower nucleus); the cytoplasm is vacuolated (*v*, vacuoles) and contains numerous globules (*gl*), putatively of protein, and grains of amylopectin (*ap*). (**F–I**) Diagonal sections of the posterior parts of microgamonts (region 3) under different magnifications showing numerous randomly distributed male gametes' nuclei (*n*) associated with two kinetosomes (*k*) and connected to the main cytoplasm with a stalk (black arrow); the cytoplasm contains numerous microneme-like bodies (*mn?*, in (H)). (**J**) cross-section through two kinetosomes connected with an electron-dense link (white arrow). (**K**) cross section of the top of a kinetosome (the transitive zone to the future flagellum) showing 9 groups (doublets) of microtubules.

globules (putatively proteins), and amylopectin granules not abundant in this region (Fig. 9E). The posterior end of the microgamont cells contained numerous spherical ($\sim$0.6 μm in diameter) nuclei of "spermal" type according to the classification by Raikov (1982) with highly condensed chromatin in the whole volume (Fig. 9F − I). Each nucleus was encircled by an electron-translucent zone; some with a stalk connected them to the main cytoplasm (Fig. 9H). Most nuclei were associated with two kinetosomes containing nine peripheral groups of microtubules, apparently triplets or doublets depending on the kinetosome region; the kinetosomes were connected to each other by an electron-dense link (Fig. 9J, K). The cytoplasm appeared vacuolated, with abundant microneme-like bodies (Fig. 9H); the amylopectin granules and putative protein globules were not detected. No mitochondria were observed in the posterior regions of both macrogamont and microgamont cells.

Molecular Phylogenetic Analyses

For *S.* cf. *nematoides*, the contiguous sequence of the near-completed ribosomal operon (SSU rDNA + ITS1 + 5.8S rDNA + ITS2 + LSU rDNA) was obtained from the WSBS sample, whereas only a partial sequence of SSU rDNA was obtained from the MBS sample. For the sample of *C. mesnili*, the obtained contiguous sequence covered near-complete gene of SSU rRNA, ITS1, 5.8S rDNA, ITS2, and a large part ($\sim$2,000 bp) of LSU rDNA (Table 1). All these sequences were involved in phylogenetic analyses with the use of Bayesian inference (BI) and Maximum likelihood (ML) methods (see "Methods" for details).

Analyses of 18S (SSU) rDNA. Both Bayesian inference and Maximum likelihood (ML) analyses resulted in almost identical tree topologies with some differences in the branching within the coccidia + hematozoa clade (not shown). The Bayesian tree appeared more accurate than the ML one: in the ML tree *Plasmodium* spp. grouped not with piroplasms, but with adeleid coccidians, although with low support (BP = 38%), i.e. hematozoans were split up. We consider this an artifact, which is absent in the Bayesian tree. This point does not affect the position of blastogregarines and neighboring branches. The higher accuracy of Bayesian inference than ML bootstrap analysis was also revealed previously (Alfaro et al. 2003). Overall the newly obtained phylogenies matched molecular phylogenetic evidence from alveolates and apicomplexans published recently (e.g., Cavalier-Smith 2014; Janouškovec et al., 2015; Lepelletier et al. 2014; Rueckert and Horák 2017; Schrével et al. 2016). The Bayesian tree inferred from the dataset of 110 taxa and 1,550 sites (Fig. 10) showed the monophyly of major alveolate groups, although with moderate or low statistical support. The backbone of the apicomplexan region in the newly obtained tree was poorly resolved by both Bayesian and ML analyses. The three obtained blastogregarine sequences together with environmental sequence D3P05D06 formed a clade with full PP (posterior probabilities in Bayesian analysis) and high BP (bootstrap percentage in ML analysis) supports (1.0 and 90%, respectively). This robust blastogregarine clade was located between two archigregarine lineages, but all node supports in this region of the tree backbone were extremely low (Fig. 10). The archigregarine split had been already recovered before, also with very weak supports (Rueckert et al. 2015; Rueckert and Horák 2017; Schrével et al. 2016; Wakeman et al. 2014; Wakeman and Horiguchi 2017; Wakeman and Leander 2013), i.e. this is not an effect of the addition of blastogregarines to the taxon sampling. SSU rDNA identities between the two *S.* cf. *nematoides* samples and the environmental sequence D3P05D06 were at about 90% (MBS vs. D3P05D06 = 90%, WSBS vs. D3P05D06 = 92.1%, WSBS vs. MBS = 93.7%), whereas those between *C. mesnili* and *S.* cf. *nematoides* were lower, at 82.8%–83.9% (see Supplementary Material Table S1 for details).

Analyses of 28S (LSU) rDNA and the ribosomal DNA operon. All phylogenies based on these phylogenetic markers resulted in identical topologies both in the Bayesian (Fig. 11) and ML (not shown) analyses. Overall, they recovered the major alveolate clades that agreed the phylogenies inferred from SSU rDNA – both already published (see above) and newly obtained – but with the higher resolution of all-alveolate and myzozoan deep branching than in SSU rDNA trees.

In the LSU rDNA-alone-based phylogeny (Fig. 11A), the monophyletic apicomplexan clade comprised the moderately supported chrompodellid lineage and sporozoans; the latter were subdivided into the clades of firmly supported coccidiomorphs (coccidians + hematozoans) and moderately supported by BP cryptosporidians + gregarines. All presented (available) gregarine sequences formed a monophyletic clade, although the BP support was only moderate (PP = 1.0, BP = 84%). Similar val-

ues of BP supports were also obtained for other nodes in the backbone of this clade. The monophyly of eugregarines was broken due to the archigregarine *Selenidium* sp. In contrast to the SSU rDNA phylogenies, the blastogregarine LSU rDNA sequences showed no affinity to gregarines, but formed a sister branch to the coccidiomorph clade, although with rather low PP and BP supports (0.67 and 52%, respectively).

Compared with the LSU rDNA, phylogenies using the near complete ribosomal DNA operons (concatenated SSU, 5.8S, and LSU rDNAs) showed higher BP supports for the dinozoans and for the sporozoans (Fig. 11B). In contrast, BP supports for the cryptosporidians + gregarines clade and its internal branching decreased. The sistership of the blastogregarines and coccidiomorphs was also recovered, although with lower support (PP = 0.50, BP = 37%).

Testing alternative topologies. The alternative topologies of phylogenetic trees were analyzed with the use of the set of six widespread tests (see "Methods" for details). Among 12 alternative SSU rDNA phylogenies (Supplementary Material Fig. S1), six were found to reject by no test (Fig. 12A); four of them represented the blastogregarines as a member of the clade cryptosporidians + gregarines and two as a sister group either to this clade or to the sporozoans as a whole. However, approximately unbiased test and majority of others did not reject any alternative topology including the direct association of the blastogregarines with the coccidiomorph clade (see Supplementary Material Table S2 and Fig. S1, topologies #7 and 10). However, the boostrap probability rejected this location (topologies #7 and 10 in the Supplementary Material Fig. S1), even though it was the best in the LSU rDNA and the ribosomal operon phylogenies (Fig. 11, the reference topologies #0 and alternative topologies #1 in Fig. 12B and C). In contrast, among LSU rDNA and ribosomal operon phylogenies, all tests rejected any position of the blastogregarines within the cryptosporidian + gregarine clade, as chiefly preferred in SSU rDNA phylogenies (Supplementary Material Table S2; Fig. 12B, C). However, no test rejected the blastogregarines as the sister group to all other sporozoans. In summary, the blastogregarines as the earliest branch of the sporozoans was the only case permitted by all tests in all three genetic markers examined (i.e., SSU rDNA, LSU rDNA, and ribosomal operon phylogenies).

Discussion

The general morphology and ultrastructure of blastogregarines represent a fanciful combination of the features characteristic to different far-related taxa of sporozoans (Fig. 13). This is congruent with the uncertain position of blastogregarines within the sporozoans provided by the conflicting SSU rDNA and LSU rDNA ribosomal operon molecular phylogenies. On the one hand, blastogregarines share many ultrastructural features with archigregarines, the most plesiomorphic group of the sporozoans known to date (Schrével 1971b; Schrével and Desportes 2015; Schrével et al. 2013) – that agrees with SSU rDNA-based phylogenies placing these organisms in the close neighborhood to each other, although with low supports. First, both blastogregarines and archigregarines possess longitudinally folded or smooth pellicle – in archigregarines, the latter is rare, but sometimes exists (Simdyanov 1992) – and longitudinal subpellicular microtubules arranged in layer(s) just beneath it (Schrével 1971a,b; Simdyanov and Kuvardina 2007). Second, the mucron and apical complex in both these groups does not disappear in the early developmental stages as in majority of sporozoans, but persists over a long period of time: during the larger part of their life cycle indeed. The trophic stages of both blastogregarines and archigregarines attach to host cells with the mucron that contains the mucronal vacuole and well-developed components of the apical complex (at least in *S.* cf. *nematoides* among blastogregarines) and performs myzocytotic feeding (Schrével 1968, 1971b; Simdyanov and Kuvardina 2007). In blastogregarines, this mucronal complex (the apical complex and mucronal vacuole) remains active (myzocytosis) during the trophozoite lifespan. Unlike blastogregarines, archigregarines have non-feeding mature gamonts (syzygy stage), but the conoid and rhoptries persist in them until starting progamic mitoses at least (Schrével et al. 2013; Simdyanov and Kuvardina 2007). Despite generally plesiomorphic body plan, the studied blastogregarines exhibit modifications of the cortex and mucron, which can be considered autapomorphies, and they show a mosaic distribution. Thus, the folded pellicle characteristic for both *C. mesnili* and many *Selenidium* spp. appears to be a plesiomorphic trait, but the major modification of its mucron (loss of conoid and rhoptries) is a distinct apomorphy. On the contrary, *S.* cf. *nematoides*, has a plesiomorphic mucron with the complete apical complex; however, its smooth pellicle appears rather an apomorphy. The more

Table 1. The main characteristics of the obtained blastogregarine sequences: the source and total length of assembled contiguous sequences, the length of overlapping PCR-amplified fragments used for their creation, and PCR primers used for the amplification of the fragments.

Sources and total lengths of assembled sequences	Amplified fragments[a]	Fragment length	PCR primers: forward (F) and reverse (R); annealing temperature used in the PCRs
Siedleckia cf. *nematoides* from MBS (1,645 bp) MH061197	SSU rDNA (part)	1,645 bp	(F) 5′-GTATCTGGTTGAT CCTGCCAGT-3′ (R) 5′-GCGACGGGCGGTGTGTAC-3′ t° = 48 °C
Siedleckia cf. *nematoides* from WSBS (5,617 bp) MH061198	(I) SSU rDNA (part)	1,765 bp	(F) 5′-GTATCTGGTTGAT CCTGCCAGT-3′ (R) 5′-GAATGATCCWTC MGCAGGTTCACCTAC-3′ t° = 48 °C
	(II) SSU rDNA (part), ITS1, 5.8S rDNA, ITS2, LSU rDNA (part)	2,004 bp	(F) 5′-GCATGGCCGTTCT TAGTTGGTGG-3′ (R) 5′-CCTTGGTCCGTGTTTCAAGAC-3′ t° = 48 °C
	(III) LSU rDNA (part)	1,021 bp	(F) 5′-ACCCGCTGAAYTT AAGCATAT-3′ (R) 5′-GCTATCCTGAGGG AAACTTCGG-3′ t° = 53 °C
	(IV) LSU rDNA (part)	1,549 bp	(F) 5′-GTCTTGAAACACG GACCAAGG-3′ (R) 5′-CAGAGCAGTGGGC AGAAATC-3′ t° = 53 °C

Table 1 (*Continued*)

Sources and total lengths of assembled sequences	Amplified fragments[a]	Fragment length	PCR primers: forward (F) and reverse (R); annealing temperature used in the PCRs
	(V) LSU rDNA (part)	1,001 bp	(F) 5′-GTAACTTCGGGAW AAGGATTGG CT-3′ (R) 5′-GTCTAAACCCAGC TCACGTTCC CT-3′ t° = 53 °C
Chattonaria mesnili (4,560 bp) MH061199	(VI) SSU rDNA (part)	1,782 bp	(F) 5′-GTATCTGGTTGAT CCTGCCAGT-3′ (R) 5′-GATCCTTCTGCAG GTTCACCTAC-3′ t° = 48 °C
	(VII) SSU rDNA (part), ITS1, 5.8S rDNA, ITS2, LSU rDNA (part)	∼1,600 bp	(F) 5′-GTCCCTGCCCTTT GTACACACCGCCCG-3′ (R) 5′-CCTTGGTCCGTGT TTCAA GAC-3′ t° = 53 °C
	(VIII) LSU rDNA (part)	∼2,000 bp	(F) 5′-ACCCGCTGAAYTT AAGCATAT-3′ (R) 5′-AGCCAATCCTTWTCCCGAAG TTAC-3′ t° = 53 °C

[a]The sequence overlap between fragments I and II is about 480 bp, II and III—about 720 bp, III and IV—about 280 bp, IV and V—about 230 bp. The overlap between fragments VI and VII is about 180 bp, between VII and VIII—about 750 bp.
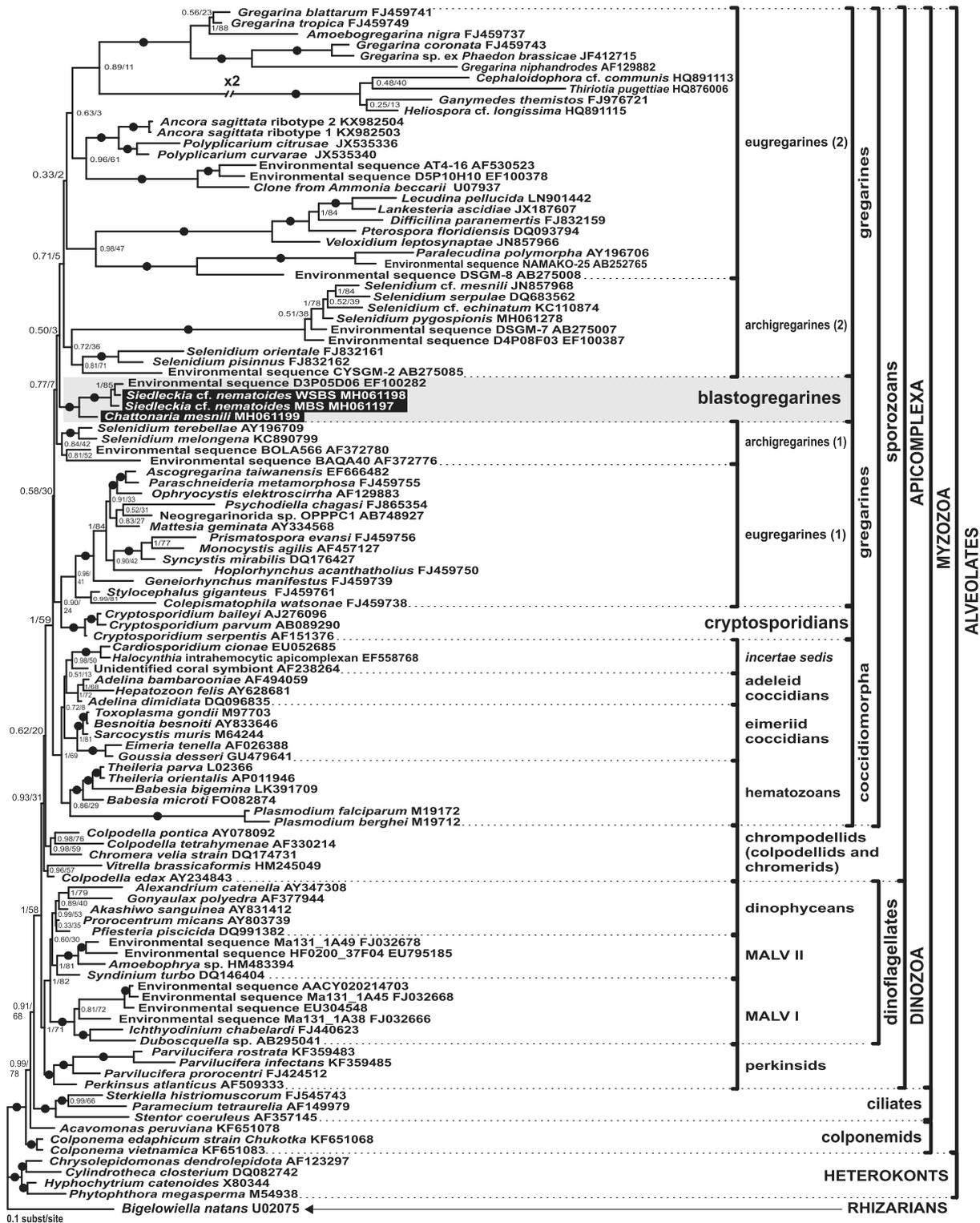
Figure 10. Bayesian inference tree of alveolates obtained by using the GTR + Γ + I model from the dataset of 110 SSU rDNA sequences (1,550 sites). Numbers at the nodes indicate Bayesian posterior probabilities (numerator) and ML bootstrap percentage (denominator). Black dots on the branches indicate Bayesian posterior probabilities and bootstrap percentages of 0.95 and 90%, respectively, and higher. The blastogregarine clade is highlighted by gray. The newly obtained sequences of blastogregarines (*Siedleckia nematoides* and *Chattonaria mesnili*) are given on black background.

Figure 11. Bayesian inference trees of alveolates obtained by using the GTR + Γ + I model from two rDNA datasets of the same 54-taxon sampling. (**A**) LSU rDNA dataset (2,912 sites); (**B**) Ribosomal operon dataset (4,618 sites). Numbers at the nodes indicate Bayesian posterior probabilities (numerator) and ML bootstrap
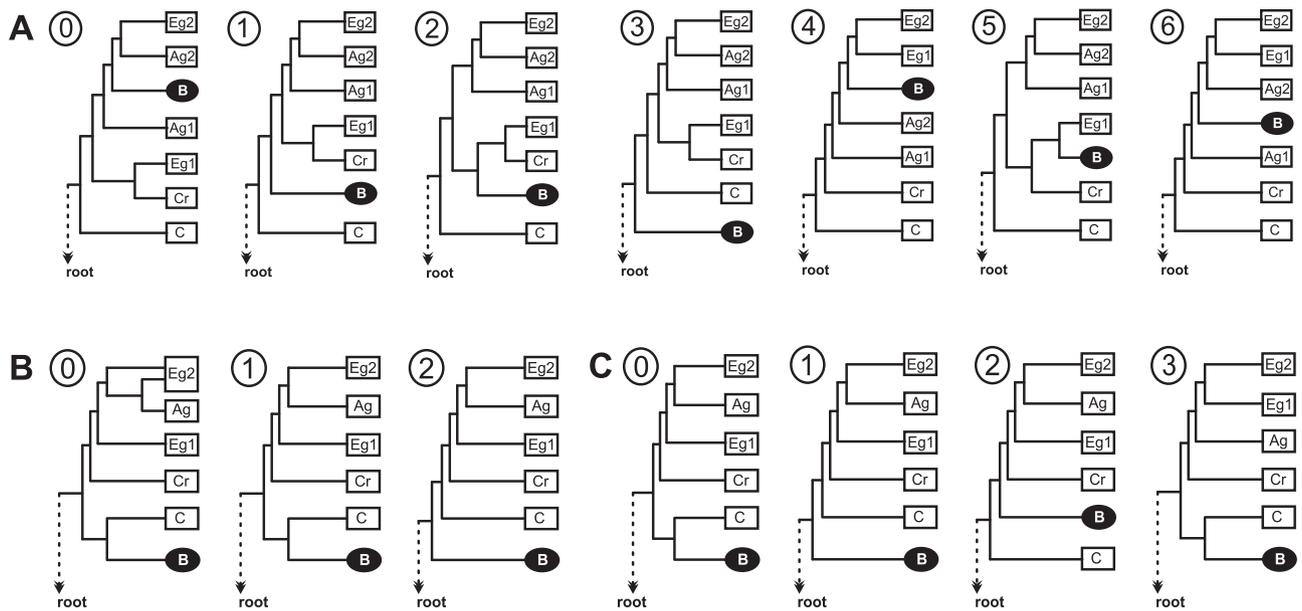
Figure 12. Diagrams of the reference ("best") phylogenies and alternative topologies rejected by none test: (**A**) SSU rDNA (110-taxon dataset); (**B**) LSU rDNA (54-taxon dataset); (**C**) ribosomal operon (54-taxon dataset). Only tree regions comprising parasitic apicomplexans are shown, the major clades correspond to those in the phylogenies obtained by the phylogenetic analyses (Figs 10 and 11) and are shown schematically. The reference trees are designated as (0). The alternative topologies are arranged from (1) and further on the decrease of the test values (see Table S3): the phylogenies having number (1) are the most likely of all alternative topologies in each category (A, B, C) and the last tree topologies are the least likely. Abbreviations: B, blastogregarines; Ag1 and 2, archigregarine clades (see Fig. 10); Eg1 and 2, eugregarine clades (see Figs 10 and 11); Cr, cryptosporidians; C, coccidiomorphs (coccidians + hematozoans). In the reference LSU rDNA phylogeny (B0) the archigregarine *Selenidium pygospionis* is grouped with the eugregarine *Ancora sagittata* belonging to the clade Eg2 in the phylogenies inferred from SSU rDNA and ribosomal operon (compare Figs 10 and 11), where they are separated; however, no one test did rejected they separation in the LSU rDNA phylogeny too (topology B1; the P-value of the AU test is even higher than for (0), see Supplementary Material Table S3).

primitive morphology of the mucron in this species could be the result of something like the paedomorphosis, i.e. the retention of "juvenile" features in an adult individual. The third common feature is shared by blastogregarines not only with archigregarines, but with all other gregarines too: their sporozoites lie in the oocysts freely (Chatton and Villeneuve 1936a), without additional internal cysts (sporocysts) characteristic for core coccidians, both eimeriids and adeleids; however, in some divergent blood-parasitic coccidians (e.g., *Lanketerella*) as well as in the majority of haemosporidians the sporocysts are absent too.

Apart from obvious similarities, there is a conspicuous difference between blastogregarine and archigregarine ultrastructure: the extensive development of the ER in the anterior half of the blastogregarine cell vs. secondary food vacuoles in the medullary part of the cytoplasm in the archigregarine cell (Schrével 1968, 1971b; Schrével et al. 2013; Simdyanov and Kuvardina 2007). One possible explanation for this is that the numerous nuclei in blastogregarines obstruct the traffic of food vacuoles along the axial microtubules from the mucron along the cell towards its rear. Such feeding mechanism was previously suggested for the archi-

percentage (denominator). Black dots on the branches indicate Bayesian posterior probabilities and bootstrap percentages of 0.95 and 90%, respectively, and higher. The blastogregarine clade is highlighted by gray. The newly obtained sequences of blastogregarines (*Siedleckia nematoides* and *Chattonaria mesnili*) are given on the black background. Accession numbers in (B) are arranged in following order: SSU rDNA, 5.8S (if exists), LSU rDNA.
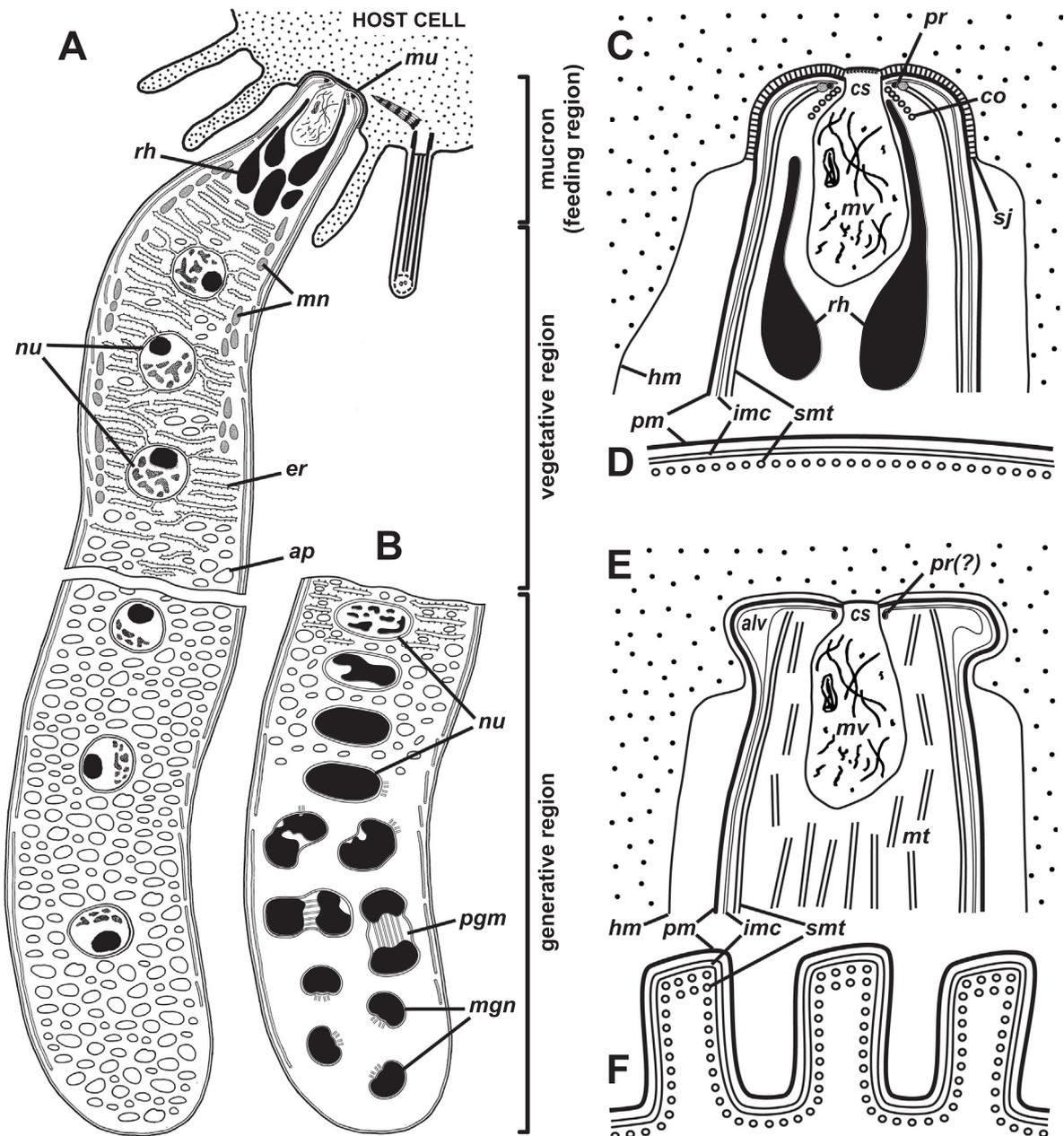
Figure 13. Key features of the organization of the blastogregarines. (**A**, **B**) Scheme of the general ultrastructure of a macrogamont cell and the egenerative region of a microgamont cell, respectively. (**C**, **D**) *Siedleckia nematoides*: the schemes of the longitudinal and cross sections of the mucron and tegument, respectively. (**E, F**) *Chattonaria mesnili*: the schemes of the longitudinal and cross sections of the mucron and tegument, respectively. Abbreviations: *alv*, alveoles between the cytomembranes of the IMC; *ap*, amylopectin granules; *co*, conoid; *cs*, cytostome; *er*, endoplasmic reticulum; *hm*, plasma membrane of the host cell; *imc*, inner membrane complex of pellicle; *pm*, plasma membrane; *mgn*, microgamete nuclei; *mt*, microtubules; *mv*, mucronal vacuole; *mu*, mucron; *nu*, nuclei; *pgm*, progamic mitoses in the microgamont; *pm*, plasma membrane of the parasite; *pr*, polar ring (gives rise to the longitudinal subpellicular microtubules (*smt*) in *Siedleckia*); *rh*, rhoptries; *sj*, septate cell junction between the parasite and host cells.

gregarine *Selenidium orientale* (Simdyanov and Kuvardina 2007). In the absence of that system, the ER may substitute the function of nutrient distribution. One more possible explanation is that the "overdeveloped" ER provides membranes necessary for blastogregarine budding.

On the other hand, the blastogregarines share some features with the coccidiomorphs that agrees with the topologies of the LSU rDNA and ribosomal operon phylogenies (although the blastogregarine position is also weakly supported there). First, like eimeriid coccidians and hematozoans, they lack one of the most characteristic features of the gregarine life-cycle: the stage of syzygy followed by the formation of the gametocyst (Grassé 1953a; Levine 1971; Perkins et al. 2000; Schrével and Desportes 2015; Schrével et al. 2013) – at least it was never reported in the literature and also did not detected by us throughout more than 10 years of observations. It should be noted here that the syzygy is characteristic not only for the gregarines, but for the adeleid coccidians too, but the gametocyst is still absent in them (Grassé 1953b; Perkins et al. 2000). Thus, the absent of the gametocyst is a common feature of the blastogregarines and coccidiomorphs. Second, judging by the two kinetosomes associated with the spermal nuclei, the male gametes (=microgametes) of blastogregarines must bear two flagella as in the majority of coccidians (Grassé 1953b; Perkins et al. 2000), whereas gregarine male gametes are chiefly uniflagellated or, sometimes (in Monocystidae), lack flagella at all (Grassé 1953a; Martinucci et al. 1981; Perkins et al. 2000; Schrével et al. 2013). Third, blastogregarines exhibit an extremely pronounced difference in size between male (micro-) and female (macro-) gametes (oogamy; Fig. 1H) that is a characteristic feature of all coccidians and haemosporidians (Chatton and Villeneuve 1936a). Thus, the atypical life cycle of blastogregarines is more similar to coccidians – as it was noted by Chatton and Villeneuve (1936b). For example, the multiple rounds of mitosis without immediate cytokinesis, that leads to multinuclearity (Fig. 1B–D), is characteristic not only for blastogregarines (Caullery and Mesnil 1899; Chatton and Dehorne 1929; Chatton and Villeneuve 1936a), but for the growing meronts of eucoccidians and haemosporidians too, e.g., in *Eimeria*, *Adelea*, and *Plasmodium* (Grassé 1953b; Perkins et al. 2000), although the multinuclearity is temporary in them. The only difference here is seemingly that these "merogonic" mitoses in blastogregarines do not result in the formation of merozoites (Chatton and Villeneuve 1936b).

The microgametogenesis of blastogregarines has not been traced, but the budding-off of already multinucleate spherical cells from microgamonts (Fig. 1E–F) has been previously reported for all examined blastogregarine species: *S.* cf. *nematoides*, *S. caullery*, and *S. mesnili* (Caullery and Mesnil 1899; Chatton and Dehorne 1929; Chatton and Villeneuve 1936a). These "buds" are supposed by Chatton and Dehorne (1929) to produce microgametes and, if so, they may be considered as microgametocytes or microgametoblasts – the latter is a peculiarity known in Protococcidia (e.g., *Myriospora*), which lack merogony (Grassé 1953b; Perkins et al. 2000). The formation of the microgametoblasts in blastogregarines and, probably, in the aforementioned protococcidians, may be considered as the deferred merogonic divisions of the cell. In blastogregarine macrogamonts, the suggested "deferred merogony" results in budding-off uninucleate putative macrogametocytes supposed to mature into macrogametes directly, i.e. without nuclear and cell divisions (again a coccidian feature) (Chatton and Dehorne 1929; Chatton and Villeneuve 1936a). To corroborate or dismiss these putative homologies in the blastogregarine and coccidian life cycles, the "asexual" nuclear divisions (not leading directly to the gamete formation) in the anterior part of the cell should be studied in details and the fate of these nuclei should be revealed: whether their "merogonic" divisions stop with the gamogony starting or they may continue within the lifespan of an individual. Another question is: whether the female nuclei really descend directly from the "asexual" (vegetative) nuclei of region 2 or there are additional progamic mitoses on the border between regions 2 and 3 as in microgamonts. The fate of the individuals after gametogenesis is also uncertain: whether they disintegrate totally during the gamete formation or the gametogenesis stops at some point and "merogonic" mitoses start again? Anyway, the merogonic (asexual) nuclear divisions and the formation of gamete nuclei appear to run in blastogregarines within the same cell, although in its different places – in region 2 and in region 3, respectively – therefore we introduce the name "merogamont" for blastogregarine individuals. The merogamont cell is differentiated into three regions specialized on different functions: mucron or feeding region (#1), merogonic or vegetative region (#2) where vegetative nuclei proliferate, and gamogonic or generative region (#3) where sexual (gametic, generative) nuclei arise and develop (Figs 2B, C; 3C, and 13).

Although the peculiarities of the nuclear apparatus and life cycle create a certain affinity between the blastogregarines and coccidians, the former also retain a set of plesiomorphic morphological characteristics shared with the archigregarines (see above), which should be therefore considered as common ancestral features of the sporozoans. Thus, we have two plesiomorphic groups of the Sporozoa with a quite similar organization, but one of them possesses the gregarine life cycle (archigregarines) while the other (blastogregarines) – the coccidia-like one. Summing up the morphological and molecular phylogenetic data, the blastogregarines should be considered as a relatively isolated group of plesiomorphic sporozoans. This conclusion appear to correlate with the results of the alternative topology testing that revealed the most basal position of blastogregarines within sporozoans as the only possible consensus between conflicting SSUrDNA and LSU rDNA ribosomal operon phylogenies. The mismatch of the "best" topologies might be referred to the twice less taxon sampling of LSU rDNA (54 vs. 110 taxa), but the comparison with the SSU rDNA trees computed on the reduced 54-taxon dataset (see Supplementary Material Fig. S2) showed the same features as in 110-taxon sampling SSU rDNA phylogeny: the split of gregarines and the affiliation blastogregarines to them. On the other hand, these reduced SSUrDNA phylogenies were considerably worse resolved and less consistent in the region of the apicomplexan backbone than both the LSU rDNA/operon-based trees (Fig. 11) and the SSU rDNA phylogenies inferred from the 110-taxon sampling (Fig. 10). This point rather corroborates the previously published opinion that SSU rDNA is likely not the most eligible marker for the study of apicomplexan deep branching (Simdyanov et al. 2015, 2017). The expanded taxon sampling of LSU rDNA and multigene analyses may resolve this ambiguity in the future.

Molecular phylogenetic analyses have failed to assign blastogregarines firmly to either gregarines or coccidiomorphs, but unequivocally indicate them as a robust clade affiliated to sporozoans that is in full agreement with the ultrastructural evidence. Apart from that, putative cryptic species within the morphospecies *S.* cf. *nematoides* were revealed by means of the molecular approach that may be inferred from significant differences between the sequences obtained from WSBS and MBS samples. The single available environmental blastogregarine-like sequence, D3P05D06 from oxygen-depleted sediment from littoral of Greenland (Stoeck et al. 2007), is also closely related to both sequences of *S.* cf. *nematoides*. To indicate these putative cryptic species more firmly, the molecular datasets must cover highly variable regions of the genome such as the internal transcribed spacers of the ribosomal operon, ITS1 and ITS2 (Müller et al. 2007). The hosts of the cryptic species might be cryptic species revealed within the *Scoloplos armiger* (Bleidorn et al. 2006) and the polychaetes closely related to it.

Conclusion

From all diversity of the contradicting to each other opinions reviewed in the Introduction, the results of this study corroborate the viewpoint on the taxonomic position of the blastogregarines of Chatton and co-authors and their pioneering interpretation of the blastogregarine life cycle (Chatton and Dehorne 1929; Chatton and Villeneuve 1936a,b) and dismiss the more recent and widespread taxonomic scheme of Levine and his followers, which consider blastogregarines a part of eugregarines (Levine 1985; Perkins et al. 2000; WoRMS). First, our ultrastructural data confirm the formation of microgamete nuclei in the formerly hypothetical microgamonts. Second, both molecular phylogenies and morphological data indicate that the blastogregarines definitely belong to the Apicomplexa and, more exactly, to the sporozoans. Third, molecular phylogenetic analyses fail to assign blastogregarines firmly either to the gregarines or coccidiomorphs (combined coccidians and hematozoans): these "best" SSU and LSU rDNA phylogenies conflict with each other and, additionally, are weakly supported in both cases; the morphological data reveal a plesiomorphic status blastogregarines as the relatively isolated group with the mixed features of coccidians and plesiomorphic gregarines. Proceeding from the aforesaid we classify the blastogregarines as a separate class Blastogregarinea (also see: de Puytorac et al. 1987) within the phylum Apicomplexa, subphylum Sporozoa. This class includes a single order Sidleckiida comprising two families, which separation from each other is based on the conspicuous differences in the structure of the attachment apparatus in *S.* cf. *nematoides* and *C. mesnili* manifested in the loss of the apical complex, change of the cell junction type, and development of additional attachment devices (alveolar bulge(s)) in the latter species. These differences are comparable with those between archi-

and eugregarines possessing mucron or epimerite, respectively, and this is in use as a relevant taxonomic criterion for the separation of the afore-mentioned orders within the genuine gregarines (Schrével and Desportes 2013a,b, 2015; Schrével et al. 2013; Simdyanov et al. 2017). Applying this morphological approach to the blastogre-garines, however in the "limited mode" because of the sparsity of the group, we establish the new genus *Chattonaria* for *Siedleckia mesnili* (in honour of Édouard Chatton, who described this species and contributed significantly to the field of blastogregarine research), as well as the new family Chattonariidae, which, together with the family Siedleckiidae, compose the order Blastogre-garinida, single in the class. We expect future increasing the species composition of the fam-ily Chattonariidae due to the addition of other named blastogregarine species as, e.g., *Siedleckia caulleryi* and the poorly described *S. dogieli*. Presumably, these organisms with longitudinal stri-ations and complex attachment apparatus (as far as it may be inferred from light-microscopic data) can be members of the same genus *Chattonaria*. The composition of the family Siedleckiidae is expected to increase rather due to future rec-ognizing cryptic species in the morphotype *S. nematoides* (see above). The consequent formal taxonomical actions are stated in the summary below.

Taxonomic Summary

Fixing the taxonomic position of the blastogre-garines we leave the taxonomic ranks of Api-complexa (phylum) and Sporozoa (subphylum) as originally established by Levine (Levine 1970, 1985; Levine et al. 1980) and update their diagnoses tak-ing into consideration recent evidence.

Phylum APICOMPLEXA Levine, 1970

Diagnosis. The apical complex initially fulfill-ing myzocytosis and giving rise to longitudinal subpellicular microtubules arranged in layer(s); micropores.

Subphylum Sporozoa Leuckart, 1879 (Syn. Sporo-zoasida Levine, 1985)

Diagnosis. Parasitic Apicomplexa largely with the complex life cycle (Leuckart's triade) resulting in the oocysts performing sporogony and finally contain-ing sporozoites; reduced plastid (apicoplast).

Class Blastogregarinea Chatton et Villeneuve, 1936, emend.

Diagnosis. Sporozoa. Epicellular parasites with permanent multinuclearity and gametogenesis: nuclear divisions of merogony and gamogony pro-ceed within the same individual (merogamont) throughout its lifespan. The merogamonts with plesiomorphic ultrastructure: the well-developed apical (mucronal) complex performing myzocytotic feeding, regularly arranged longitudinal subpellic-ular microtubules arising from the mucron. The merogamonts are motile (bending), and sexually differentiated: in female individuals, the nuclei lie in a row along the cell axis, in male individuals they lie linearly only in the anterior part, but are scattered randomly in the posterior part of the cell. Oogamy is characteristic: female gamogony is realized by continuous budding of mononuclear macrogame-tocytes or macrogametes from the posterior part of female merogamonts, while male gamogony is real-ized by budding of multinuclear microgametocytes or microgametoblasts apparently followed by their dissociation into small putatively biflagellated male gametes with spermal nuclei. According to Chatton and co-workers (1929, 1936a) oocysts with many (10–16) free sporozoites (no sporocysts). Intestinal parasites of the polychaetes Orbiniidae.

Order Siedleckiida nom. nov.

With the characteristics of the class.

Family Siedleckiidae Chatton et Villeneuve, 1936, emend.

Diagnosis. With the characteristics of the order. Merogamonts with smooth surface lacking any grooves or folds. Mucron contains all components of the apical complex and performs myzocytotic feeding; apical ring(s) is likely MTOC of subpellicu-lar microtubules. Monotypic.

Type genus. *Siedleckia* Caullery et Mesnil, 1898, emend.

Diagnosis. With the characteristics of the family. Merogamonts elongate and flattened with pointed anterior and rounded posterior ends. Monotypic, although the complex of cryptic species is sug-gested (molecular-phylogenetic data).

Type species. *Siedleckia nematoides* Caullery et Mesnil, 1898

Family Chattonariidae, fam. nov.

Diagnosis. With the caracteristics of the order. The mucron is modified: it performs myzocytotic feed-ing, but the apical complex is significantly reduced:

it retains only mucronal vacuole and, probably, polar ring, which is not connected with microtubules; no conoid and rhoptries. Monotypic.

Type genus. *Chattonaria*, gen. nov.

Diagnosis. With the characteristics of the family. Merogamonts elongate, cylindric, with roundly pointed posterior end; the surface with large longitudinal folds; mucron bearing voluminous alveoli with protuberances of the cytoplasm.

Type species. *Chattonaria mesnili* (Chatton et Dehorne, 1929), comb. nov. for *Siedleckia mesnili* Chatton et Dehorne, 1929

Etymology. Named in honour of Édouard Chatton, the eminent protistologist.

Note. *Siedleckia caulleryi* Chatton et Villeneuve, 1936 and *Siedleckia dogieli* Chatton et Dehorne, 1929 likely belong to the family Chattonariidae and to the genus *Chattonaria*, judging by their general morphology studied with LM. Ultrastructural and molecular-phylogenetic studies are required for a more precise conclusion. The species *S. dogieli* was established relying solely on a draft drawing by Dogiel with the indication of the host (Chatton and Dehorne 1929), i.e. it does not have a valid description and should be considered a nomen nudum.

Methods

Sampling: The hosts of *S.* cf. *nematoides* were collected from two littoral sites located in the Kandalaksha Gulf of the White Sea, Russia: on Bolshoy Gorely Island (66°18′46″N, 33°37′40″E) near Marine Biological Station of Saint Petersburg State University (MBS) and from the coast of Velikaya Salma Straight (66°33′11″N, 33°06′33″E) near White Sea Biological Station of Moscow State University (WSBS). The hosts of *Chattonaria mesnili* were collected on the lowest littoral zone of a sandy beach (48°41′23″N, 4°04′17″W) near Moguériec, coastal zone of English Channel, France.

The blastogregarine individuals were isolated by tearing apart the intestine of the hosts with fine tip needles under a stereomicroscope (MBS-1 or MBS-10 (LOMO, Russia) for *S.* cf. *nematoides*, or Olympus SZ40 (Olympus, Japan) for *C. mesnili*). The released parasites and small fragments of the host gut with the attached individuals were rinsed three times in filtered seawater using fine glass pipettes and then prepared for light microscopy (*S.* cf. *nematoides* only), scanning electron microscopy, transmission electron microscopy, and further DNA extraction.

Light microscopy: After rinsing in seawater, the living parasites were examined under light microscopes Leica DM2500, and Leica DM5000B (Leica Microsystems, Germany). Digital images of the living *S.* cf. *nematoides* were acquired under an MBR-1 microscope (LOMO, Russia) in phase-contrast mode with a Canon EOS 300D camera (Canon, Japan). Also wet smears of small pieces of the host intestine content were fixed by Bouin's fluid, stained by Böhmer's hematoxylin, and examined under a light microscope Zeiss AxioImager A1 with a digital camera AxioCam MRc5 (Carl Zeiss, Germany).

Electron microscopy: For SEM study, individual blastogregarines and small fragments of the host gut with attached blastogregarines were fixed with 2.5% (v/v) glutaraldehyde in 0.05 M cacodylate buffer (pH = 7.4) containing NaCl 1.28% (w/v) (for White Sea samples) or 2.3% (w/v) (for English Channel samples): two replacements of the fixative for 1 h each, in the ice bath in the dark, then rinsed three times (20 min each) with filtered seawater, and post-fixed with 2% (w/v) OsO_4 in the same buffer (room temperature, 2 h). Fragments of dissected gut containing the parasites were dehydrated in a graded series of ethanol up to 96% (v/v), transferred to a 96% ethanol/pure acetone mixture (1:1, v/v), rinsed three times with pure acetone, and critical point dried with CO_2. Alternatively, after 96% ethanol, the samples were rinsed three times with 100% ethanol and then critical point dried with CO_2. The samples were mounted on stubs, sputter coated with gold/palladium, and examined under a LEO-420 scanning electron microscope (Carl Zeiss, Germany) or a JSM-6380LA scanning electron microscope (JEOL, Japan).

The same fixation protocol as for SEM was used for the majority of TEM samples. To visualize the cell coat, some specimens of *S.* cf. *nematoides* were fixed with the mixture of glutaraldehyde and ruthenium red (3% (v/v) and 0.05% (w/v), respectively) in 0.2 M cacodylate buffer (pH = 7.4) and post-fixed with the mixture of OsO_4 and ruthenium red (1% (v/v) and 0.05% (w/v), respectively) in the same buffer – all under the same conditions as described above (Luft 1971a,b). After dehydration through ascending series of ethanol, the fixed samples were transferred into embedding mediums (Epon (Sigma-Aldrich, USA) or Spurr (Ted Pella, USA)) according to manufacturer's protocols, using acetone or isopropanol as intermediate dehydrating reagents for Epon and Spurr, respectively. Ultrathin sections (40 to 50 nm) were obtained using an LKB-III (LKB, Sweden), Reichert-Jung Ultracut E (C. Reichert, Austria) or Leica EM UC6 (Leica Microsystems, Germany) ultramicrotomes and then contrasted with uranyl acetate and lead citrate (Reynolds 1963) and examined under a JEM-100B, JEM-1010 or JEM-1011 electron microscopes (JEOL, Japan).

DNA isolation, PCR, cloning, and sequencing: After rinsing in seawater, blastogregarine individuals were collected into 1.5-ml microcentrifuge tubes: ~10 individuals of *S.* cf. *nematoides* from MBS (2003), ~100 individuals of *S.* cf. *nematoides* from WSBS (2004), and ~25 individuals *C. mesnili* (2010). For *S.* cf. *nematoides*, the material was lysed by an alkaline procedure (Floyd et al. 2002), and directly used for PCR amplification. For *C. mesnili*, the material was preserved in the "RNAlater" reagent (Life Technologies, USA), then stored at −20 °C until DNA extraction. The DNA extraction was performed using the "Diatom DNA Prep 200" kit (Isogen Laboratory, Russia). The resulting ribosomal DNA (rDNA) sequences were deduced from a combination of shorter fragments individually amplified using different pairs of primers (Table 1) and represented 18S or small subunit (SSU), 5.8S, 28S or large subunit (LSU) rDNAs, and internal transcribed spacers 1 and 2 (ITS 1 and ITS 2, respectively). All fragments were PCR amplified with an Encyclo PCR kit (Evrogen, Russia) in 25 μL of the reaction mixture prepared according to the manufacturer's protocol and contained 1 μL of the DNA extract using a DNA Engine Dyad thermocycler (Bio-Rad Laboratories, USA) and the following protocol: initial denatu-

ration at 95 °C for 3 min, 40 cycles of 95 °C for 30 s, 48 °C or 53 °C (see Table 1) for 30 s, and 72 °C for 1.5 min, and a final extension at 72 °C for 10 min. The PCR products of the expected size were cut from the gel and extracted by using a Cytokine DNA isolation kit (Cytokine, Russia). The PCR products were directly sequenced for fragments obtained from C. mesnili and S. cf. *nematoides* from MBS. The fragments obtained from S. cf. *nematoides* from WSBS were heterogeneous and therefore were cloned by using InsTAclone PCR Cloning Kit (Fermentas, Lithuania). Sequencing was performed using an ABI PRISM BigDye Terminator v. 3.1 reagent kit on an automatic sequencer Applied Biosystems 3730 DNA Analyzer (Applied Biosystems, USA). All sequences were tested with BLAST in order to detect the matches for apicomplexans and retain them for further analyses. For the sample of S. cf. *nematoides* from WSBS, the contiguous sequence of the near-completed ribosomal operon (SSU rDNA + ITS1 + 5.8S rDNA + ITS2 + LSU rDNA) was assembled from 5 overlapping PCR-amplified and cloned fragments, whereas only partial sequence of SSU rDNA alone was obtained from the sample of S. cf. *nematoides* from MBS. For the sample of C. mesnili, the assembled contiguous sequence (from 3 overlapped PCR-amplified fragments) covered near-complete gene of SSU rRNA, ITS1, 5.8S rDNA, ITS2, and a large part (∼2,000 bp) of LSU rDNA (Table 1). The contiguous sequences were built with the use of BioEdit 7.0.9.0 (Hall 1999). The overlapped regions (180–750 sites, see Table 1) revealed 100% of matches. All obtained sequences were deposited in NCBI GenBank (accession numbers: MH061197-9).

Phylogenetic analyses: Three alignments were prepared for phylogenetic analyses: SSU rDNA (110 sequences, 1,550 sites), LSU rDNA (54 sequences, 2,913 sites), and the ribosomal operon (concatenated SSU, 5.8S, and LSU rDNAs: 54 sequencess, 4,618 sites). The alignments were generated in MUSCLE 3.6 (Edgar 2004) under default parameters and then manually adjusted with BioEdit 7.0.9.0 (Hall 1999); columns containing few nucleotides and hypervariable regions were removed. The taxon sampling of SSU rDNA alignment was designed in order to maximize the phylogenetic diversity and completeness of sequences in alignments, by preferentially selecting taxa having their SSU and LSU rDNA both sequenced. Representatives of heterokonts and rhizarians were used as outgroups.

The final alignment of SSU rDNA included 110 representative sequences (1,550 sites). To assess similarities among the SSU rDNA sequences within the blastogregarine clade, we calculated the percentage of identities as it is implemented in NCBI BLAST: the ratio of the matching sites to the total amount of unambiguous sites in the overlapping regions of each pair of aligned sequences: $b/a \times 100\%$, where a = total number of the aligned unambiguous sites, b = number of matches between them.

For the LSU rDNA and ribosomal operon (concatenated SSU, 5.8S and LSU rDNA sequences) analyses, the taxon sampling of only 54 sequences was used due to the limited availability of data for LSU rDNA, and, especially, 5.8S rDNA. Therefore, the 5.8S rDNA (155 sites in the alignment) was not represented in the analysis of concatenated rDNA genes for seven sequences (Chromera velia, Colponema vietnamica, Goussia desseri, Stentor coeruleus, and 3 environmental sequences: Ma131 1A38, Ma131 1A45, and Ma131 1A49): the corresponding positions were replaced with "N" in the alignment. The resulting multiple alignments contained 54 sequences (2,913 sites) for the LSU rDNA, and the same 54 sequences (4,618 sites) for the concatenated rDNAs (ribosomal operon). Thus, both taxon sampling comprised an identical set

of species, all of which were also represented in the alignment of the 110 SSU rDNA sequences.

Maximum-likelihood (ML) analyses were performed with the RAxML 8.2.9 program (Stamatakis 2006) under the GTR + Γ model and CAT approximation (25 rate categories per site). The procedure included 100 alternative runs of the ML analysis and 1,000 replicates of multiparametric bootstrap. Bayesian inference (BI) analyses were conducted using MrBayes 3.2.6 program (Ronquist et al. 2012) under GTR + Γ + I model with 8 discrete categories of gamma distribution. The program was set to operate using the following parameters: nst = 6, ngammacat = 8, rates = invgamma, covarion = yes; parameters of Metropolis Coupling Markov Chains Monte Carlo (mcmc): nchains = 4, nruns = 4, temp = 0.2, ngen = 7,000,000, samplefreq = 1,000, burninfrac = 0.5 (first 50% of 7,000 sampled trees, i.e. first 3,500 generations were discarded in each run). The following average standard deviations of split frequencies were reached at the end of calculations: 0.009432 for the SSU rDNA analysis, 0.002976 for the LSU rDNA analysis, and 0.001371 for the ribosomal operon analysis.

Alternative tree topologies were manually created and edited using TreeView 1.6.6 program (Page 1996). The reference tree topology of SSU rDNA phylogeny (110-taxon dataset) was copied from the Bayesian tree (Fig. 10) that appeared more accurate in point of branching order within coccidiomorphs' clade (coccidians and hematozoans), but was identical with the corresponding ML tree in other respects. The reference topologies of LSU rDNA and ribosomal operons (54-taxon datasets) were copied from the trees showed in Figure 11; their ML and Bayesian phylogenies were identical. Alternative topologies were constructed by positioning the blastogregarines as a sister group successively to the major sporozoan clades, which were picked out as either high-resolved (high statistical supports) molecular phylogenetic lineages in the reference trees and published phylogenies or, in respect of low-resolved gregarines in SSU rDNA phylogenies, additionally relying on relevant morphological evidence (Simdyanov et al. 2017). As a result, we examined the relations of the blastogregarines to coccidiomorphs, cryptosporidians, different gegarine lineages, combined gregarine-cryptosporidian clade and sporozoa as a whole. Topology tests were performed with TREE-PUZZLE 5.3.rc16 and CONSEL 0.1j programs (Schmidt et al. 2002; Shimodaira and Hasegawa 2001). The following tests were used: Bootstrap Probability (Felsenstein 1985), Expected-Likelihood Weights (Strimmer and Rambaut 2002), Kishino-Hasegawa test (Kishino and Hasegawa 1989), Shimodaira-Hasegawa test (Shimodaira and Hasegawa 1999), Weighted Shimodaira-Hasegawa test (Shimodaira and Hasegawa 1999), and approximately unbiased test (Shimodaira 2002).

Acknowledgements

Appendix A. Supplementary Data

Supplementary data associated with this article can be found, in the online version, at https://doi.org/10.1016/j.protis.2018.04.006.

References

Adl SM, Simpson AG, Lane CE, Lukeš J, Bass D, Bowser SS, Brown M, Burki F, Dunthorn M, Hampl V, Heiss A, Hoppenrath M, Lara E, leGall L, Lynn DH, McManus H, Mitchell EAD, Mozley-Stanridge SE, Parfrey LW, Pawlowski J, Rueckert S, Shadwick L, Schoch C, Smirnov A, Spiegel FW (2012) The revised classification of eukaryotes. J Eukaryot Microbiol **59**:429–514

Alfaro ME, Zoller S, Lutzoni F (2003) Bayes or bootstrap? A simulation study comparing the performance of Bayesian Markov Chain Monte Carlo sampling and bootstrapping in assessing phylogenetic confidence. Mol Biol Evol **20**:255–266

Bleidorn C, Kruse I, Albrecht S, Bartolomaeus T (2006) Mitochondrial sequence data expose the putative cosmopolitan polychaete *Scoloplos armiger* (Annelida, Orbiniidae) as a species complex. BMC Evol Biol **6**:47

Caullery M, Mesnil F (1898) Sur un Sporozoaire aberrant (*Siedleckia* n. g.). CR Soc Biol **5**:1093–1095

Caullery M, Mesnil F (1899) Sur quelques parasites internes des Annelides. Trav Stat Zool Wimereux **7**:80–99

Cavalier-Smith T (2014) Gregarine site-heterogeneous 18S rDNA trees, revision of gregarine higher classification, and the evolutionary diversification of Sporozoa. Europ J Protistol **50**:472–495

Chatton E, Dehorne L (1929) Observations sur les Sporozoaires du genre *Siedleckia*. *S. dogieli*, n. sp. et *S. mesnili* n. sp. Arch Anat Microsc **25**:530–543

Chatton E, Villeneuve F (1936a) La sexualite et le cycle évolutif des Siedleckia d'apres l'étude de *S. caulleryi*, n. sp. Hologrégarines et Blastogrégarines. Sporozoaires Hologamétogènes et Blastogamétogènes. CR Acad Sci D Nat **203**:505–508

Chatton E, Villeneuve F (1936b) Le cycle évolutif de l' *Eleutheroschizon duboscqui* Brasil. Prevue expérimentale de l'absence de schizogonie chez la *Siedleckia caulleryi* Ch et Vill. CR Acad Sci D Nat **203**:834–837

Cox FEG (1994) The evolutionary expansion of the Sporozoa. Int J Parasitol **24**:1301–1316

Dogiel V (1910) Catenata. Organization of the genus *Haplozoon* and some forms similar to it. St Petersburg (In Russian)

Edgar RC (2004) MUSCLE: multiple sequence alignment with high accuracy and high throughput. Nucleic Acids Res **35**:1792–1797

Felsenstein J (1985) Confidence limits on phylogenies: an approach using the bootstrap. Evolution **39**:783–791

Floyd RM, Abebe E, Papert A, Blaxter ML (2002) Molecular barcodes for soil nematode identification. Mol Ecol **11**:839–850

Goggin CL, Barker SC (1993) Phylogenetic position of the genus *Perkinsus* (Protista, Apicomplexa) based on small subunit ribosomal RNA. Mol Biochem Parasitol **60**:65–70

Grassé P-P (1953a) Classe des Grégarinomorphes. In Grassé P-P (ed) Traité de Zoologie. Masson Paris, pp 550–690

Grassé P-P (1953b) Classe des Coccidiomorphes. In Grassé P-P (ed) Traité de Zoologie. Masson Paris, pp 691–797

Hall TA (1999) BioEdit: a user-friendly biological sequence alignment editor and analysis program for Windows 95/98/NT. Nucleic Acids Symp Ser **41**:95–98

Janouškovec J, Tikhonenkov DV, Burki F, Howe AT, Kolísko M, Mylnikov AP, Keeling PJ (2015) Factors mediating plastid dependency and the origins of parasitism in apicomplexans and their close relatives. Proc Natl Acad Sci USA **112**:10200–10207

Kishino H, Hasegawa M (1989) Evaluation of the maximum likelihood estimate of the evolutionary tree topologies from DNA sequence data, and the branching order in hominoidea. J Mol Evol **29**:170–179

Krylov MV, Dobrovolskij AA (1980) Macrosystem and phylogeny of the Sporozoa. In Krylov MV, Starobogatov YI (eds) Principles of the construction of the macrosystem of the unicellular animals. Academy of Sciences of the USSR Press, Leningrad, pp 62–74 (in Russian with English summary)

Kuvardina ON, Leander BS, Aleshin VV, Myl'nikov AP, Keeling PJ, Simdyanov TG (2002) The phylogeny of Colpodellids (Alveolata) using small subunit rRNA gene sequences suggests they are the free-living sister group to Apicomplexans. J Eukaryot Microbiol **49**:498–504

Leander BS (2008) Marine gregarines: evolutionary prelude to the apicomplexan radiation? Trends Parasitol **24**:60–67

Léger L (1909) Les Schizogregarines des Tracheates. II. Le genre *Schizocystis*. Arch Protistenkd **18**:5–15

Léger L, Duboscq O (1910) *Selenococcidium intermedium* Lég. et Dub. et la systématique des Sporozoaires. Arch Zool Exp Gen Ser **5**:187–238

Levine ND (1970) Taxonomy of the Sporozoa. J Parasit **56**:208–209

Levine ND (1971) Uniform terminology for the protozoan subphylum Apicomplexa. J Protozool **18**:352–355

Levine ND (1985) Phylum 2. Apicomplexa Levine, 1970. In Lee JJ, Hutner SH, Bovee EC (eds) An Illustrated Guide To The Protozoa. Society of Protozoologists, Kansas, pp 322–374

Levine ND, Corliss JO, Cox FEG, Deroux G, Grain J, Honigberg BM, Leedale GF, Loeblich AR, Lom J, Lynn D, Merinfeld EG, Page FC, Poljansky G, Sprague V, Vavra J, Wallace FG (1980) A newly revised classification of the Protozoa. J Protozool **27**:37–58

Lepelletier F, Karpov SA, Le Panse S, Bigeard E, Skovgaard A, Jeanthon C, Guillou L (2014) *Parvilucifera rostrata* sp. nov. (Perkinsozoa), a novel parasitoid that infects planktonic dinoflagellates. Protist **165**:31–49

Luft JH (1971a) Ruthenium red and violet. I. Chemistry, purification, methods of use for electron microscopy and mechanism of action. Anat Rec **171**:347–368

Luft JH (1971b) Ruthenium red and violet. II. Fine structural localization in animal tissues. Anat Rec **171**:369–415

Martinucci GB, Crespi P, Ferragosti E (1981) Contributions to the study of monocystid gregarines parasites of *Octolasium transpadanum*. III. Ultrastructural features of *Apolocystis* sp. gamonts, gametes and zygotes. Bolletino Zool **48**:243–253

Miller MA, Pfeiffer W, Schwartz T (2010) Creating the CIPRES Science Gateway for inference of large phylogenetic trees. Gateway Computing Environments Workshop (GCE), New Orleans, LA, pp 1–8

Müller T, Philippi N, Dandekar T, Schultz J, Wolf M (2007) Distinguishing species. RNA **13**:1469–1472

NCBI: National Center for Biotechnology Information. Available via https://www.ncbi.nlm.nih.gov.

Page RDM (1996) TREEVIEW: An application to display phylogenetic trees on personal computers. Comp Appl Biosci **12**:357–358

Perkins FO, Barta JR, Clopton RE, Peirce MA, Upton SJ (2000) Phylum Apicomplexa. In Lee JJ, Leedale GF, Bradbury P (eds) An Illustrated Guide to the Protozoa. Society of Protozoologists, Lawrence, KS (USA), pp 190–370

de Puytorac P, Grain J, Mignot J-P (1987) Précis de Protistologie. Societe Nouvelle des Editions Boubée, Paris, 581 p

Raikov IB (1982) The protozoan nucleus. Morphology and evolution. Springer, Vienna, New York, 474 p

Reynolds ES (1963) The use of lead citrate at high pH as an electron opaque stain in electron microscopy. J Cell Biol **17**:208–212

Rueckert S, Wakeman KC, Jenke-Kodama H, Leander BS (2015) Molecular systematics of marine gregarine apicomplexans from Pacific tunicates, with descriptions of five novel species of *Lankesteria*. Int J Syst Evol Microbiol **65**:2598–2614

Rueckert S, Horák A (2017) Archigregarines of the English Channel revisited: New molecular data on *Selenidium* species including early described and new species and the uncertainties of phylogenetic relationships. PLoS ONE **12**:e0187430

Ronquist F, Teslenko M, van der Mark P, Ayres DL, Darling A, Höhna S, Larget B, Liu L, Suchard MA, Huelsenbeck JP (2012) MrBayes 3. 2: Efficient Bayesian phylogenetic inference and model choice across a large model space. Syst Biol **61**:539–542

Schmidt HA, Strimmer K, Vingron M, von Haeseler A (2002) TREE-PUZZLE: maximum likelihood phylogenetic analysis using quartets and parallel computing. Bioinformatics **18**:502–504

Schrével J (1968) L'ultrastructure de la région antérieure de la Grégarine Selenidium et son interêt pour l'étude de la nutrition chez les Sporozoaires. J Microsc Paris **7**:391–410

Schrével J (1971a) Contribution à l'étude des Selenidiidae parasites d'Annélides Polychètes. II. Ultrastructure des quelques trophozoïtes. Protistologica **7**:101–130

Schrével J (1971b) Observations biologiques et ultrastructurales sur les Selenidiidae et leurs conséquences sur la systématique des Grégarinomorphes. J Protozool **18**:448–479

Schrével J, Desportes I (2013a) Introduction: Gregarines among Apicomplexa. In Desportes I, Schrével J (eds) Treatise on Zoology—Anatomy, Taxonomy, Biology. The Gregarines. Brill, Leiden, pp 7–24

Schrével J, Desportes I (2013b) Marine Gregarines. In Desportes I, Schrével J (eds) Treatise on Zoology—Anatomy, Taxonomy, Biology. The Gregarines. Brill, Leiden, pp 197–354

Schrével J, Desportes I (2015) Gregarines. In Mehlhorn H (ed) Encyclopedia of Parasitology. 4th edn Springer, Berlin, Heidelberg, pp 1–47

Schrével J, Desportes I, Goldstein S, Kuriyama R, Prensier G, Vávra J (2013) Biology of Gregarines and their Host-parasite Interactions. In Desportes I, Schrével J (eds) Treatise on Zoology—Anatomy, Taxonomy, Biology. The Gregarines. Brill, Leiden, pp 25–195

Schrével J, Valigurová A, Prensier G, Chambouvet A, Florent I, Guillou L (2016) Ultrastructure of *Selenidium pendula*, the type species of archigregarines, and phylogenetic relations to other marine Apicomplexa. Protist **167**:339–368

Shimodaira H (2002) An approximately unbiased test of phylogenetic tree selection. Syst Biol **51**:492–508

Shimodaira H, Hasegawa M (1999) Multiple comparisons of log-likelihoods with applications to phylogenetic inference. Mol Biol Evol **16**:1114–1116

Shimodaira H, Hasegawa M (2001) CONSEL: for assessing the confidence of phylogenetic tree selection. Bioinformatics **17**:1246–1247

Simdyanov TG (1992) *Selenidium pennatum* sp. n.—a new species of archigregarines from *Flabelligera affinis* (Polychaeta: Flabelligeridae). Parazitologiya **26**:344–347 (in Russian with English summary)

Simdyanov TG, Kuvardina ON (2007) Fine structure and putative feeding mechanism of the archigregarine *Selenidium orientale* (Apicomplexa: Gregarinomorpha). Europ J Protistol **43**:17–25

Simdyanov TG, Diakin AY, Aleoshin VV (2015) Ultrastructure and 28S rDNA phylogeny of two gregarines: *Cephaloidophora* cf. *communis* and *Heliospora* cf. *longissima* with remarks on gregarine morphology and phylogenetic analysis. Acta Protozool **54**:241–263

Simdyanov TG, Guillou L, Diakin AY, Mikhailov KV, Schrével J, Aleoshin VV (2017) A new view on the morphology and phylogeny of eugregarines suggested by the evidence from the gregarine *Ancora sagittata* (Leuckart, 1860) Labbé, 1899 (Apicomplexa: Eugregarinida). PeerJ **5**:e3354

Stamatakis A (2006) RAxML-VI-HPC: maximum likelihood-based phylogenetic analyses with thousands of taxa and mixed models. Bioinformatics **22**:2688–2690

Stoeck T, Kasper J, Bunge J, Leslin C, Ilyin V, Epstein S (2007) Protistan diversity in the Arctic: a case of paleoclimate shaping modern biodiversity? PLoS ONE **2**:e728

Strimmer K, Rambaut A (2002) Inferring confidence sets of possibly misspecified gene trees. Proc Roy Soc Lond B **269**:137–142

Théodoridès J (1984) The phylogeny of the Gregarinia (Sporozoa). Orig Life Evol Biosph **13**:339–342

Valigurová A, Vaškovicová N, Diakin A, Paskerova GG, Simdyanov TG, Kováčiková M (2017) Motility in blastogregarines (Apicomplexa): native and drug-induced organisation of *Siedleckia nematoides* cytoskeletal elements. PLoS ONE **12**:e0179709

Votýpka J, Modrý D, Oborník M, Šlapeta J, Lukeš J (2016) Apicomplexa. In Archibald J, Simpson A, Slamovits C (eds) Handbook of the Protists. Springer, Cham, pp 567–624

Wakeman KC, Horiguchi T (2017) Morphology and molecular phylogeny of the marine gregarine parasite *Selenidium oshoroense* n. sp. (Gregarina, Apicomplexa) isolated from a Northwest Pacific *Hydroides ezoensis* Okuda 1934 (Serpulidae, Polychaeta). Mar Biodivers, http://dx.doi.org/10.1007/s12526-017-0643-1

Wakeman KC, Leander BS (2013) Molecular phylogeny of marine gregarine parasites (Apicomplexa) from tube-forming polychaetes (Sabellariidae, Cirratulidae, and Serpulidae), including descriptions of two new species of *Selenidium*. J Eukaryot Microbiol **60**:514–525

Wakeman KC, Heintzelman MB, Leander BS (2014) Comparative ultrastructure and molecular phylogeny of *Selenidium melongena* n. sp. and *S. terebellae* Ray 1930 demonstrate niche partitioning in marine gregarine parasites (Apicomplexa). Protist **165**:493–511

WoRMS: World register of marine species. Available via https://www.marinespecies.org.

7.16

Paskerova G.G., Miroliubova T.S., Diakin A., Kováčiková M.,

Valigurová A., Guillou L., Aleoshin V.V., Simdyanov T.G.

2018

Fine structure and molecular phylogenetic position of two marine gregarines, *Selenidium pygospionis* sp. n. and *S. pherusae* sp. n., with notes on the phylogeny of Archigregarinida (Apicomplexa)

Protist

ORIGINAL PAPER

Fine structure and Molecular Phylogenetic Position of Two Marine Gregarines, *Selenidium pygospionis* sp. n. and *S. pherusae* sp. n., with Notes on the Phylogeny of Archigregarinida (Apicomplexa)

Gita G. Paskerova[a,1], Tatiana S. Miroliubova[a], Andrei Diakin[b],
Magdaléna Kováčiková[b], Andrea Valigurová[b], Laure Guillou[c],
Vladimir V. Aleoshin[d], and Timur G. Simdyanov[e]

[a]Department of Invertebrate Zoology, Faculty of Biology, Saint Petersburg State University, Universitetskaya emb. 7/9, St Petersburg 199 034, Russian Federation
[b]Department of Botany and Zoology, Faculty of Science, Masaryk University, Kotlářská 2, 611 37 Brno, Czech Republic
[c]Sorbonne Université, Université Pierre et Marie Curie – Paris 6, CNRS, UMR 7144, Station Biologique de Roscoff, Place Georges Teissier, CS90074, 29688 Roscoff Cedex, France
[d]Belozersky Institute for Physico-Chemical Biology, Lomonosov Moscow State University, Leninskie Gory, Moscow 119 234, Russian Federation
[e]Department of Invertebrate Zoology, Faculty of Biology, Lomonosov Moscow State University, Leninskie Gory, Moscow 119 234, Russian Federation

Archigregarines are a key group for understanding the early evolution of Apicomplexa. Here we report morphological, ultrastructural, and molecular phylogenetic evidence from two archigregarine species: *Selenidium pygospionis* sp. n. and *S. pherusae* sp. n. They exhibited typical features of archigregarines. Additionally, an axial row of vacuoles of a presumably nutrient distribution system was revealed in *S. pygospionis*. Intracellular stages of *S. pygospionis* found in the host intestinal epithelium may point to the initial intracellular localization in the course of parasite development. Available archigregarine SSU (18S) rDNA sequences formed four major lineages fitting the taxonomical affiliations of their hosts, but not the morphological or biological features used for the taxonomical revision by Levine (1971). Consequently, the genus *Selenidioides* Levine, 1971 should be abolished. The branching order of these lineages was unresolved; topology tests rejected neither para- nor monophyly of archigregarines. We provided phylogenies based on LSU (28S) rDNA and near-complete ribosomal operon

---

[1]Corresponding author; fax +7 812 3289703
e-mail gitapasker@yahoo.com, g.paskerova@spbu.ru (G.G. Paskerova).

(concatenated SSU, 5.8S, LSU rDNAs) sequences including *S. pygospionis* sequences. Although being preliminary, they nevertheless revealed the monophyly of gregarines previously challenged by many molecular phylogenetic studies. Despite their molecular-phylogenetic heterogeneity, archigregarines exhibit an extremely conservative plesiomorphic structure; their ultrastructural key features appear to be symplesiomorphies rather than synapomorphies.

Introduction

Apicomplexa is a large group of unicellular parasites infecting a wide range of invertebrate and vertebrate hosts. Some apicomplexans, such as the human pathogens *Plasmodium*, *Toxoplasma*, and *Cryptosporidium*, are well studied. At the same time, basal apicomplexans, archigregarines, agamococcidia, blastogregarines, and protococcidia inhabiting exclusively marine invertebrate hosts and being crucial for our understanding of the evolution of parasitism and evolutionary paths of apicomplexans in general, are still poorly investigated.

Archigregarines (Archigregarinida Grassé, 1953, Apicomplexa Levine, 1970) are unicellular parasites inhabiting marine invertebrates, mostly polychaetes. They are thought to have retained a number of plesiomorphic characteristics from the most recent ancestor of all apicomplexans (Cavalier-Smith and Chao 2004; Cox 1994; Desportes and Schrével 2013; Grassé 1953; Leander 2008a; Leander and Keeling 2003). The most often encountered stage of their life cycle is a trophozoite. It is a relatively large cell usually attached to the host cell by the mucron, an attachment apparatus with organelles of the apical complex typical of the invasive stages (zoites). The mucron participates in myzocytosis, feeding by sucking out the cytoplasmic contents of the host cell into food vacuoles (Cavalier-Smith and Chao 2004; Desportes and Schrével 2013; Schrével 1968; Schrével et al. 2016; Simdyanov and Kuvardina 2007; Wakeman and Horiguchi 2018; Wakeman et al. 2014). The pellicle of archigregarines is organized as a three-layered membrane complex. It is supported by microtubules arranged in one or more subpellicular layers (Desportes and Schrével 2013).

The life cycle of archigregarines, a sequence of gamogony (gamete production) and sporogony (zygote fission for producing sporozoites), is often thought to include asexual cell multiplication in the trophozoite stage – merogony (Adl et al. 2012; Desportes and Schrével 2013; Grassé 1953). Levine (1971) and his followers placed great importance on the presence/absence of merogony in the life cycle for the classification of archigregarines, transferring species without merogony to eugregarines (Levine 1971, 1985; Perkins et al. 2000). On the contrary, Schrével with coauthors considered merogony to be non-important for the high-level classification of archigregarines (Desportes and Schrével 2013; Schrével 1970, 1971a,b; Schrével et al. 2016). This point of view was shared by several contemporaneous authors (Kuvardina and Simdyanov 2002; Leander 2006, 2007; Rueckert and Leander 2009; Rueckert and Horák 2017; Simdyanov and Kuvardina 2007). It should be noted that the absence of merogony is difficult to prove. In this context, taxa delineation should be based on the presence of the easiest observable stage (trophozoites) and morphological characteristics. At present, taxonomy and determination of basic taxonomic characters are routinely determined by electron microscopy and molecular phylogenies.

SSU rDNA-based phylogenetic trees obtained recently are in good accordance with the interpretation that archigregarines are a paraphyletic stem group from which other gregarine lineages evolved (Cavalier-Smith 2014; Cavalier-Smith and Chao 2004; Grassé 1953; Rueckert and Leander 2009; Rueckert and Horák 2017; Schrével et al. 2016; Wakeman and Horiguchi 2018; Wakeman and Leander 2012, 2013; Wakeman et al. 2014). To date, there are more than 70 species of archigregarines. Most of them belong to the genus *Selenidium* (Desportes and Schrével 2013; Levine 1971; Rueckert and Horák 2017; Rueckert and Leander 2009; Wakeman and Horiguchi 2018; Wakeman and Leander 2012, 2013; Wakeman et al. 2014; WoRMS 2018).

Despite their significant molecular-phylogenetic heterogeneity, species of *Selenidium* possess a similar and extremely conservative morphology. It is represented by the morphostasis, a set of characters typical of the invasive stages (zoites)
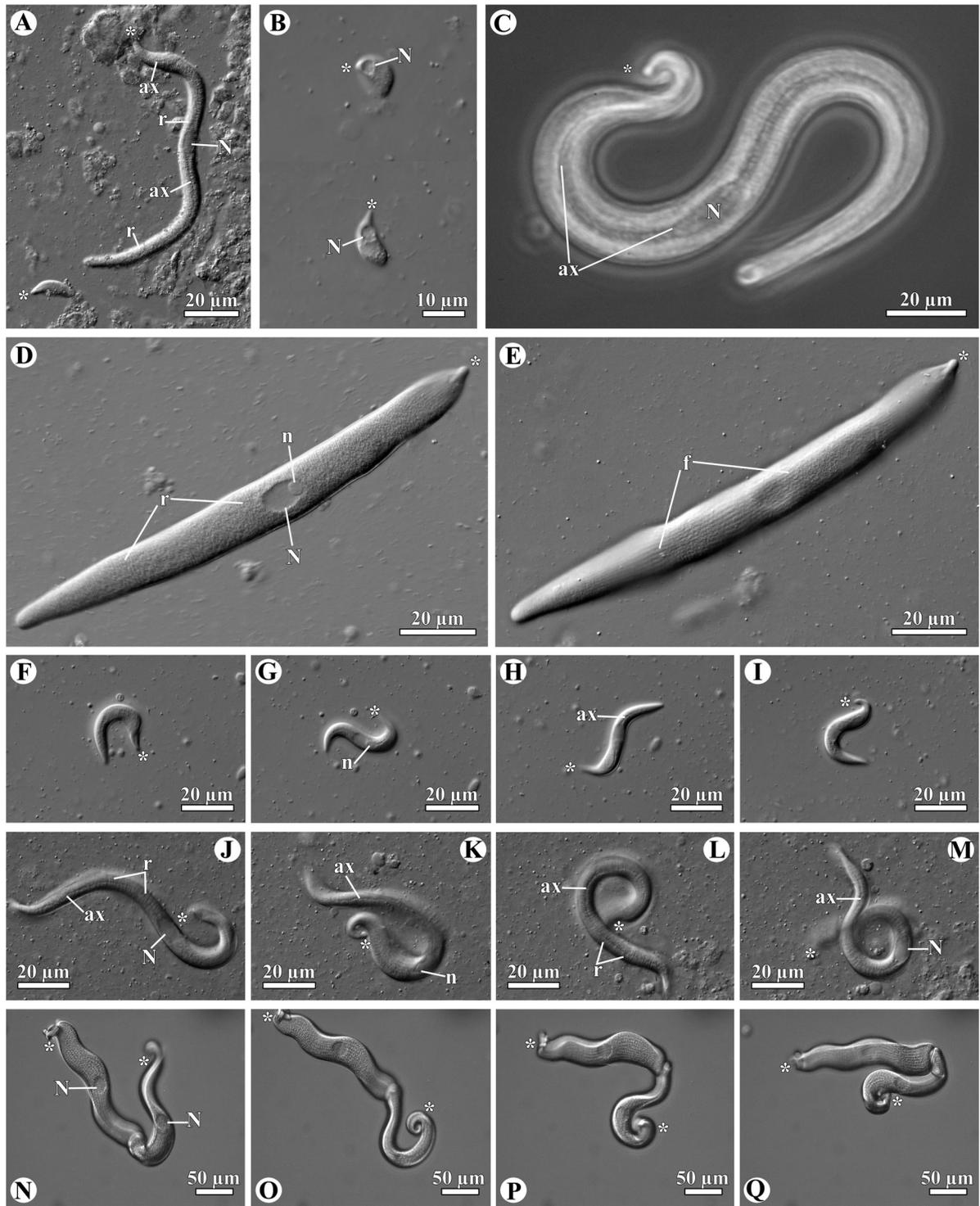
Figure 1. General morphology and motility of S*elenidium pygospionis* sp. n. Differential interference contrast (DIC) and phase-contrast (PH) light micrographs. **A**. Attached large and detached small trophozoites. In the large trophozoite, note the axial streak along the longitudinal cell axis and radial threads running from the axial streak towards the cell periphery. DIC. **B**. Young trophozoite showing bending motility; the composition of two micrographs of the same cell. DIC. **C**. Large trophozoite lying on one of the narrow sides and slightly pressed with the coverslip. Note the axial streak. PH. **D–E**. Large trophozoite lying on one of the flattened sides and pressed with the coverslip; D and E—different optical sections of the same cell. The axial streak is not visible. DIC. **F–I**. Medium-sized trophozoite lying on one of the narrow sides;

of parasitic apicomplexans (Leander and Keeling, 2003). Additionally, molecular phylogenetic studies have repeatedly demonstrated a host-parasite coevolution when closely related archigregarines parasitize closely related hosts (Desportes and Schrével 2013; Rueckert and Horák 2017; Schrével et al. 2016; Wakeman and Leander 2013). Whether these two observations are linked is unknown.

In this study, we report the discovery of two new archigregarine species, *Selenidium pygospionis* sp. n. isolated from spionid polychaetes *Pygospio elegans* and *Polydora glycymerica*, and *S. pherusae* sp. n. isolated from flabelligerid polychaetes *Pherusa plumosa.* We examined the new species using light and electron microscopy, conducted phylogenetic analyses based on the SSU rDNA and obtained the first LSU rDNA sequences of archigregarines.

Results

Selenidium pygospionis sp. n.

Occurrence

The gregarine *Selenidium pygospionis* sp. n. was found in the intestine of the polychaete *Pygospio elegans* (Spionidae) collected at the silty-sand intertidal zone of the White Sea. There were 109 infected polychaetes out of the 302 dissected. The intensity of infection usually varied from 1 to 50 (mode = 1, average = 9.8) gregarines per host; in two cases, the number of parasites reached 100 and 150 cells per host. Both attached and non-attached trophozoites of different sizes were found in the host intestine (Fig. 1A). Syzygies were extremely rare (a few in all dissected polychaetes). In squash preparations (see Methods) of more than 100 examined polychaetes, no other stages of the life cycle (gametocysts or stages of merogony) were observed.

We also found very similar parasites in the intestine of the shell-boring polychaete *Polydora glycymerica* (Spionidae) inhabiting the bivalve *Glycymeris yessoensis* from the Sea of Japan. The intensity of infection was about 30 parasites per host.

Parasites isolated from polychaetes of both species were identical in their morphology, fine structure, and DNA sequences. Therefore, we considered them to belong to the same species. Further description of *S. pygospionis* was predominantly based on the evidence obtained from the White Sea samples as the most representative ones.

General Morphology

As shown with light microscopy (LM) and scanning electron microscopy (SEM), trophozoites *S. pygospionis* were anchored in the host tissue with their anterior end (Figs 1 A, 2 A, B). The parasites were easy to dislodge from the intestinal epithelium during the dissection of the hosts.

The smallest trophozoites, presumably young trophozoites not long after their transformation from zoites (most likely, sporozoites), were observed occasionally. They were spindle-shaped with a pointed anterior end and a rounded posterior end. Their length varied from 15 to 23 μm (n = 2), and their width, from 6 to 7 μm (n = 2) in the middle part of the cell. A single rounded nucleus was located in the anterior half of the cell. The parasites could bend slightly in one plane but never glided (Fig. 1B).

Well-developed trophozoites were elongated, vermiform and slightly flattened (Figs 1 C–M, 2 C, D). Their length varied from 34 to 288 μm (average 144 μm, mode 146 μm, n = 79); their maximum width (4–25 μm, average 12 μm, mode 11 μm, n = 76) was in the middle of the cell where an oval nucleus [6–22 μm (av. 17 μm, n = 40) × 5–11 μm (av. 8.4 μm, n = 26)] was located. The nucleus was elongated along the longitudinal axis of the cell (Fig. 1A, C, D). A single spherical nucleolus (3.1–6.3 μm, n = 6) was commonly situated at the anterior pole of the nucleus (Fig. 1D). The anterior end of the parasites was usually hook-like, bent in the median plane (the plane perpendicular to the flattened sides) towards one of the flattened sides of the cell (Figs 1 C–E, 2 C, D). The mucron was dome-shaped with a smooth surface. In some individuals, it had a small pit in the center (Fig. 2C). The posterior end was rounded (Fig. 2D). The entire surface bore 22–30 (n = 12), usually 28, broad and low folds separated by grooves (Figs 1 E, 2 B–E).

a series of micrographs illustrating bending motility (1–2 bends along the cell). DIC. **J–M**. Large trophozoite lying on one of the narrow sides; a series of micrographs illustrating bending motility (2–3 bends along the cell). Note the coiling of the anterior end (K). DIC. **N–Q**. Syzygy; a series of micrographs illustrating bending motility (up to 4 bends along the cell) and the coiling of the anterior end. The axial streak is not visible. DIC. *, anterior end; ax, axial streak; f, folds; N, nucleus; n, nucleolus; r, radial threads.
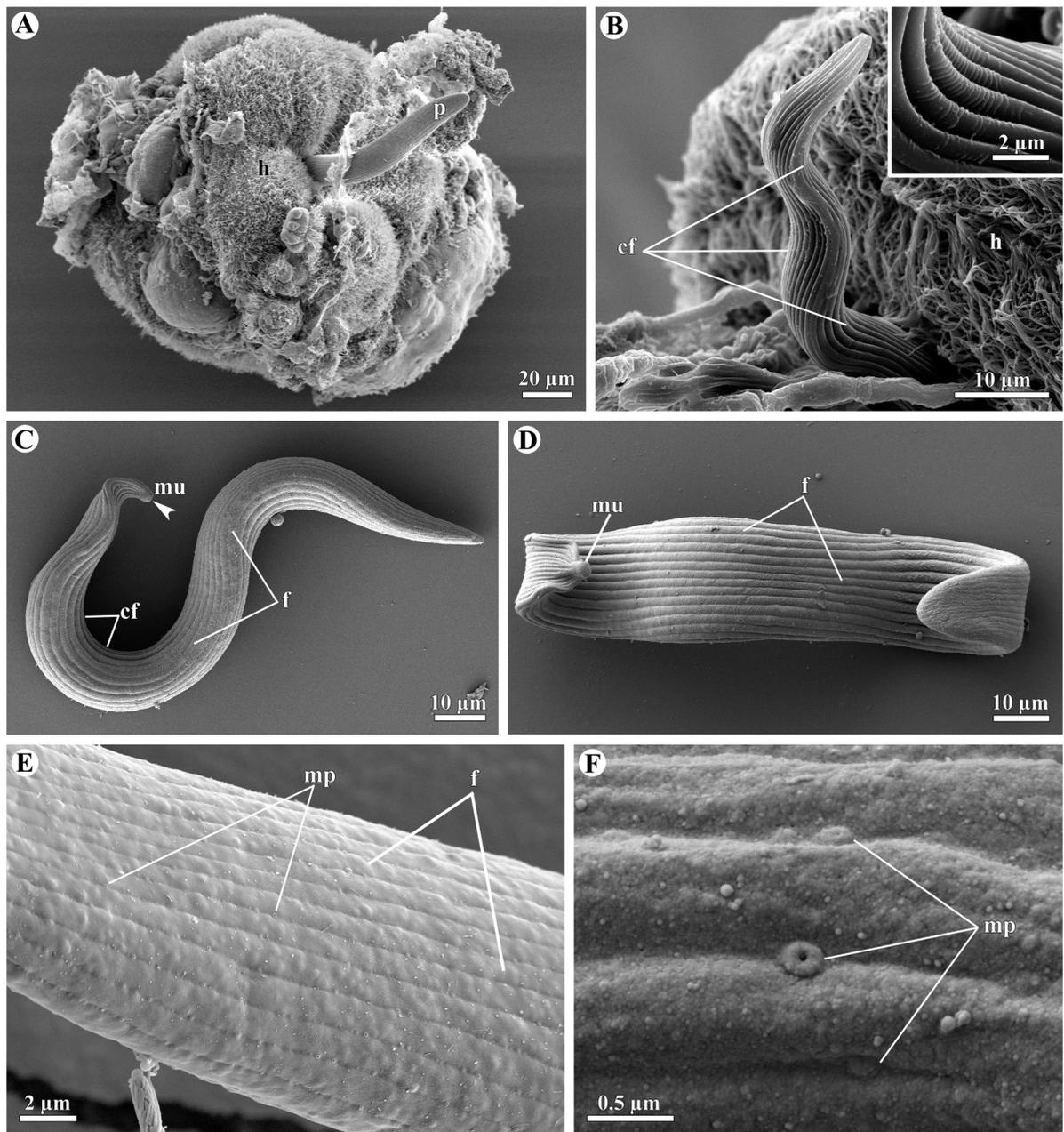
Figure 2. Surface morphology of S*elenidium pygospionis* sp. n. Scanning electron micrographs. **A**. Trophozoite attached to a fragment of the host intestinal epithelium by its anterior end. **B**. Attached trophozoite with three bends of its cell. Note small transversal compression folds of the parasite's pellicle at the inner surface of each bend. **Inset**. Transversal compression folds at high magnification. **C–D**. Detached trophozoites lying on one of the narrow sides (C) and one of the wide sides (D) of their cells. Note a hook-bent anterior end with a smooth, dome-shaped mucron, and folds at the cell surface. The arrowhead points to the pit at the center of the mucron in C. **E**. Micrograph of the trophozoite surface showing the number and location of micropores (mp). **F**. Micropore at high magnification. cf, transversal compression folds; f, folds; h, host intestinal epithelial tissue; mu, mucron; mp, micropores; p, parasite.

The width of the folds varied from 0.5 to 1.5 μm (av. 0.9, n = 21) in archigregarines fixed according to different protocols (Fig. 2D, E). Numerous micropores (10–20 per 50 μm^2, n = 2) were observed at the bottom of the grooves; their edges were slightly raised above the cell surface (Fig. 2E, F). The outer and the inner diameter of the micropores was 134–287 and 38.5–74.6 nm (n = 6), respectively.

LM studies showed that well-developed trophozoites had an intracellular axial streak of optically distinct cytoplasm extending from the anterior end to the posterior end and forming an expansion around the nucleus. Numerous radial threads ran from the axial streak towards the cell periphery. The axial streak was easy to observe in trophozoites lying on one of the narrow sides (Fig. 1A, C, H, J–M).

Both attached and non-attached cells performed very active bending movements in the median plane (Fig. 1A, C, F–M, and Supplementary Material Video S1). Non-attached archigregarines usually moved non-progressively on one of their narrow sides along the substrate. Medium-sized trophozoites usually formed 1–2 bending sections along the cell, while large-sized ones combined 2–4 bends with coiling of their anterior end (Fig. 1F–I vs J–Q). Bending and coiling of the cell always started at the hook-like anterior end. Fixed archigregarines usually retained the bends of their body resulting from their motility (Fig. 2A–D). There were small transversal compression folds of the pellicle at the inner surface of each bend (Fig. 2B, C). In addition, the trophozoites of *S. pygospionis* never shortened along their anterior-posterior axis.

Syzygies were caudal when two gamonts coupled with their posterior ends. The syzygy partners moved asynchronously (Fig. 1N–Q, Supplementary Material Video S2).

Fine Structure

Transmission electron microscopic (TEM) studies showed that the trophozoite tegument was represented by a trimembrane pellicle [the plasma membrane and the inner membrane complex (IMC)] (Fig. 3 A). The IMC consisted of the external and the internal cortical cytomembrane separated from each other by an electron-transparent space (8–10 nm thick), while the plasma membrane was separated from the IMC by a space of higher electron density (12–14 nm thick). The thickness of the pellicle varied from 36 to 40 nm. The cell coat (glycocalyx) covering the parasite surface was poorly visible. The pellicle was underlain by longitudinally oriented subpellicular microtubules (Fig. 3A–D).

They were arranged in a single layer, the continuity of which was interrupted under the grooves where micropores were usually located. Additionally, groups of irregularly arranged microtubules were present under the main layer. Each microtubule was surrounded by an electron-transparent sheath of the cell cytoplasm (Fig. 3A). Micropores were present as invaginations of the plasma membrane. Each invagination was surrounded with a thick cylindrical structure, formed by the cytomembranes of the IMC, and some electron-dense substance (Fig. 3A, inset). Numerous vesicles with some multi-membranous whorls or dense material inside were incorporated in the microtubule layer and the inner membrane complex of the pellicle; they were connected with the plasma membrane (Fig. 3C, D).

It could be seen in ultrathin sections of trophozoite-infected intestines that the anterior end of *S. pygospionis* was inserted between folds of the host intestinal epithelium (Fig. 3E, F). There was no direct contact between the host cell and the attached parasite in any of the examined cases. Several rhoptries and numerous groups of putative micronemes were present in the cytoplasm of the anterior end (Fig. 3E). The basal part of the conoid, several ducts of rhoptries within the conoid, and a large mucronal vacuole containing some loose fibrillar material could be seen in some tangential sections through the mucron (Fig. 3F).

The cytoplasm of the trophozoites was indistinctly differentiated into two areas: the ectoplasm and the endoplasm. The former was a narrow cortical region containing subpellicular microtubules, numerous mitochondria arranged at the peripheral layer and vesicles with some multi-membranous whorls or dense material under grooves. The endoplasm, the rest of the cytoplasm, contained a large nucleus, numerous amylopectin granules, lipid droplets, some small electron-dense bodies, and a few mitochondria (Fig. 3G, H). The distribution of organelles and inclusions in the endoplasm was irregular. Narrow, electron-light spaces without any visible organelles could be seen around the nucleus, along the cell axis and perpendicular to it (Figs 3 G–I, 4 B, C). In addition, a series of differently-sized vacuoles was arranged along the cell axis in front and behind the nucleus in the endoplasm. Some of them were linked to each other by membrane tunnels. The content of these vacuoles was mainly electron-transparent with a small amount of some loose filamentous material (Fig. 4 A–C). Small vacuoles of similar appearance also surrounded the nucleus alongside with an electron-transparent area of the cytoplasm (Fig. 4B, inset).
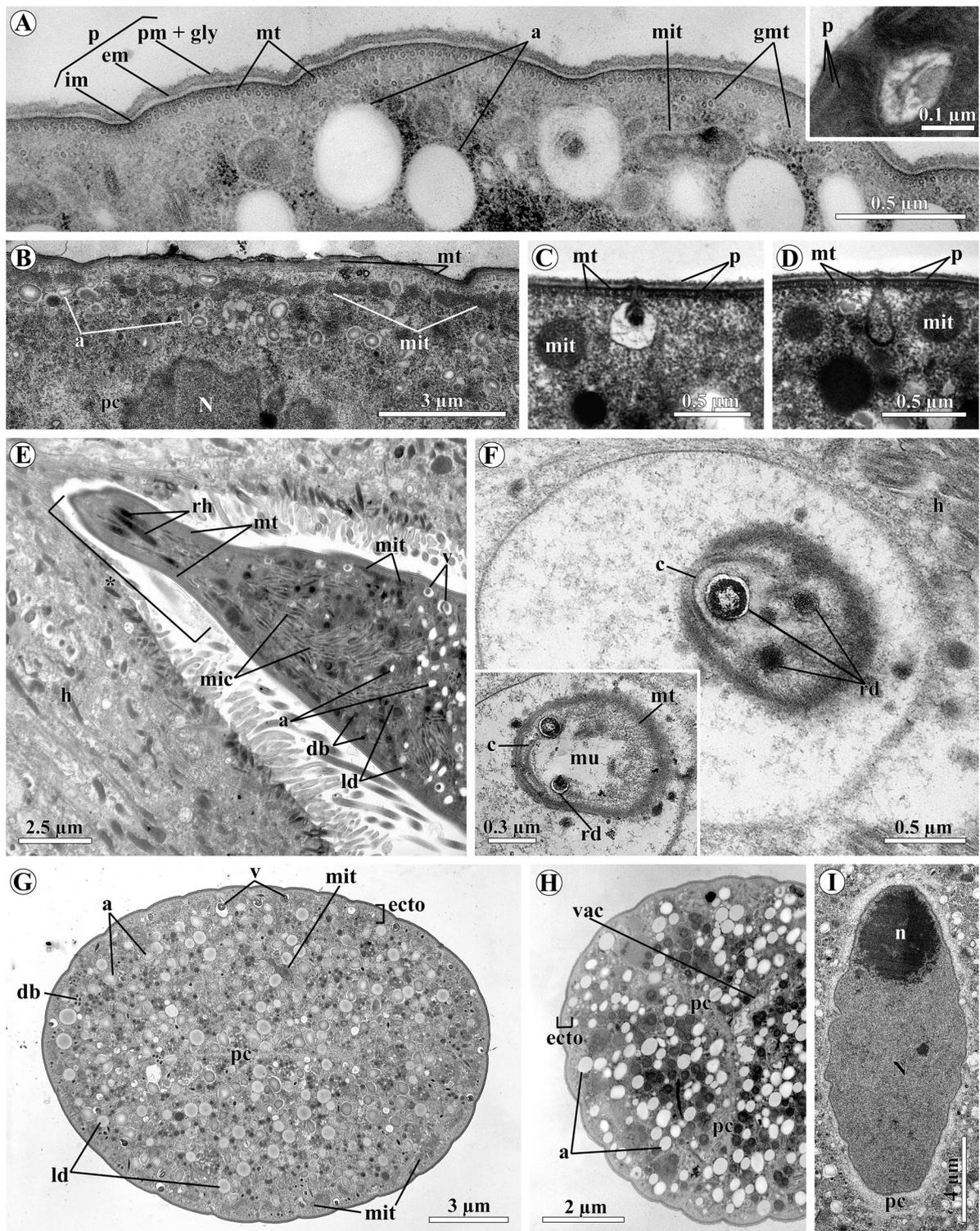
Figure 3. Fine structure of *Selenidium pygospionis* sp. n. Transmission electron micrographs. **A**. Transverse section showing details of the cortex organization. **Inset**. Micropore at high magnification. **B**. Superficial longitudinal section of a trophozoite showing the layer of longitudinal microtubules and the layer of mitochondria under the pellicle. **C–D**. Transversal sections of the pellicle showing vesicles inserted in the microtubule layer and the inner membrane complex. **E**. Superficial longitudinal section of the anterior end of a trophozoite inserted

As shown in a SEM study of de-paraffinized histological sections of *P. elegans*, some gregarines were deeply embedded in the intestinal epithelium almost reaching the basal lamina (Fig. 4D–E).

TEM observations of ultrathin sections revealed that some small single trophozoites (up to 40 μm in length) were localized intracellularly within parasitophorous vacuoles (Fig. 4F–G). The organization of these individuals was generally identical to that of well-developed trophozoites (Fig. 4F, G). The internal space of the parasitophorous vacuole was electron-transparent and filled with filamentous material and electron-dense granules. The density of their arrangement increased towards the periphery. In some sections, there were agglomerations of the electron-dense granules near the parasitophorous vacuole membrane (Fig. 4G, inset). Parasitophorous vacuoles were surrounded on the outside by electron-dense fibrillar material, membranes of endoplasmic reticulum, numerous mitochondria, and cytoplasmic vesicles with multilaminar inclusions, whereas the rest of the host cytoplasm was electron-transparent with rare organelles and vesicles (Fig. 4F–G).

Selenidium pherusae sp. n.

Occurrence

Five polychaetes *Pherusa plumosa* collected at the sublittoral zone of the Sea of Japan were dissected. All of them were infected with *S. pherusae* sp. n. Trophozoites were all localized in the host midgut. Up to several tens of trophozoites per host were found in four of the worms, while the fifth harbored more than 100 trophozoites. No other stages were observed.

General Morphology

S. pherusae trophozoites were attached to the host intestinal epithelium by their anterior end, but were easy to dislodge during the dissection of the hosts.

The trophozoites were elongated, vermiform, 38–269 μm (n = 6) in length and 10–18 μm (n = 4) in maximum width. The anterior end was narrowed and slightly truncated (Fig. 5A, B), while the posterior one was usually rounded in large individuals (Fig. 5A, B) or pointed in small trophozoites (Fig. 5C, D). A spherical nucleus (11–12 μm, in two large trophozoites of 215 and 269 μm in length) was located in the posterior half of the trophozoite, in the widest part of the cell. It contained one nucleolus, 3–5 μm (Fig. 5A, B). Trophozoites had neither longitudinal pellicular folds at the surface nor the axial streak in the cytoplasm (Fig. 5A–C).

Both attached and non-attached gregarines showed a bending motility of the entire cell, usually one bend along the cell at a time. During bending, transient transverse folds formed on the inner surface of the bent part of the cell (Fig. 5A, B). Some fixed gregarines were slightly helically twisted along the longitudinal cell axis (Fig. 5D).

Fine Structure

The tegument of *S. pherusae* had almost the same structure as that of *S. pygospionis*, but the pellicle seemed smooth, without any grooves or folds (Figs 5, 6). Its thickness varied from 33 to 44 nm. The plasma membrane and both cortical cytomembranes were separated from each other by electron-transparent spaces of a similar thickness (7–11 nm). The cell coat was poorly visible (Fig. 6A, C–E). Though the trophozoite surface seemed to be smooth (Fig. 5C, D), micropores were sometimes observed in transverse sections (Fig. 6D, E). They were also similar in structure and size, about 80 μm wide at the surface and 150 μm deep (Fig. 6E). Although the subpellicular microtubules were usually poorly preserved in the ultrathin sections because of fixation artefacts, it could be seen in some sections that they were organized in an uninterrupted layer under the pellicle (Fig. 6C).

between the folds of the host intestinal epithelium. **F**. Oblique-transverse section of the mucron of a trophozoite inserted between the folds of the host intestinal epithelium. **Inset**. Another section of the cell shown in F. **G–H**. Transverse sections of the pre-nuclear (G) and post-nuclear (H) parts of trophozoites showing an indistinct division of the cytoplasm into the ectoplasm at the periphery and the endoplasm occupying the remaining cell volume. Note an electron-light space of the cytoplasm (pc) not containing any visible organelles. Total number of folds in G is 25. **I**. Longitudinal section showing the nucleus. Note an electron-light area of the cytoplasm around the nucleus. *, anterior end; a, amylopectin granules; c, conoid; db, dense bodies; ecto, ectocyte; em, external cytomembrane; gmt, group of microtubules; gly, glycocalyx; h, host tissue; im, inner cytomembrane; ld, lipid droplets; mic, micronemes; mit, mitochondria; mt, microtubules; mu, mucronal vacuole; N, nucleus; n, nucleolus; p, pellicle; pc, electron-light area of the cytoplasm; pm, plasma membrane; rd, ducts of rhoptries; rh, rhoptries; vac, vacuole; v, vesicles with multi-membrane whorls or dense material.
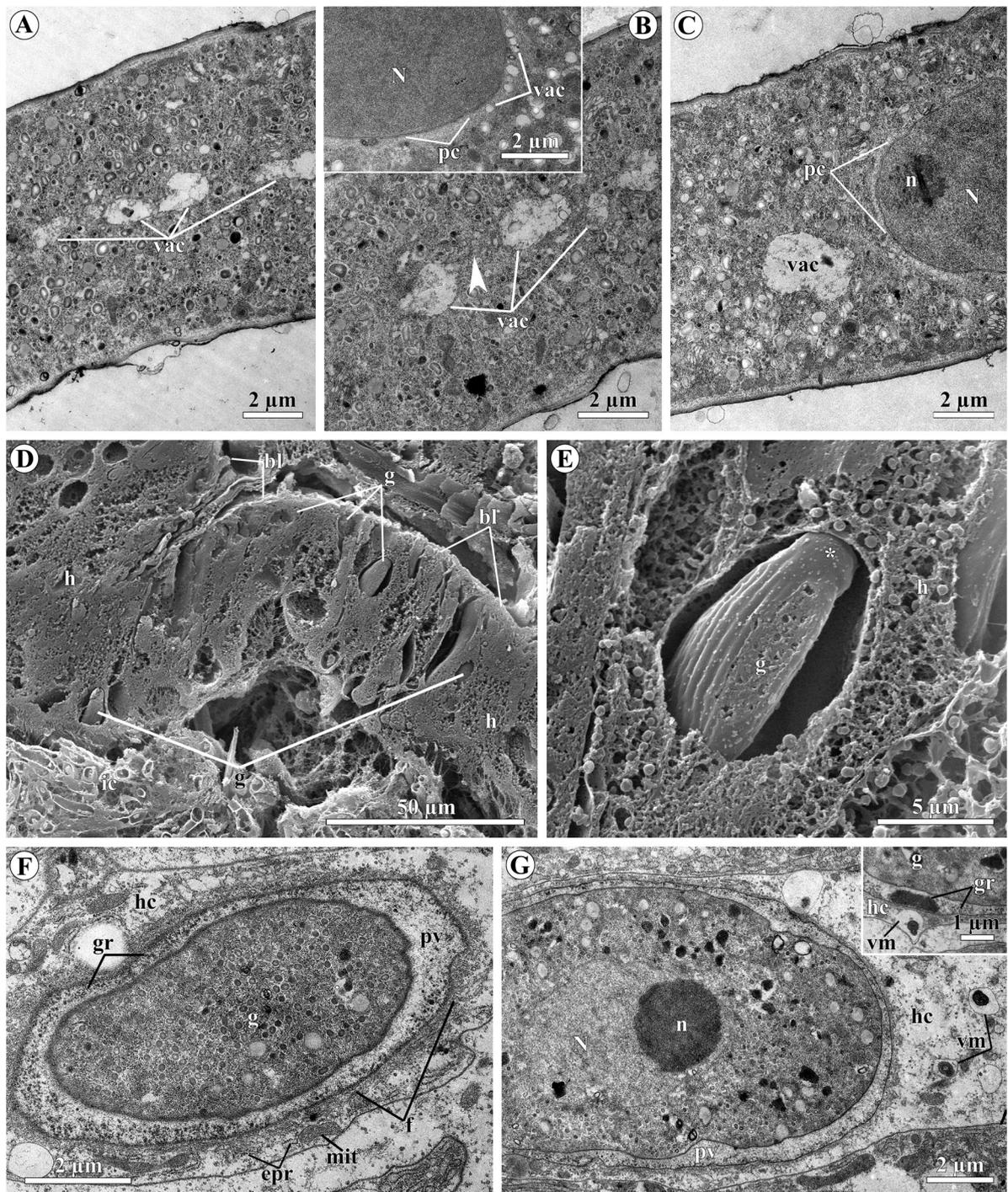
Figure 4. *Selenidium pygospionis* sp. n.: organization of the cytoplasm, localization in the host epithelium, intracellular stage. Transmission (TEM) and scanning (SEM) electron micrographs. **A–C**. Longitudinal thin sections of the trophozoites in the regions where the nucleus is localized showing a series of connected vacuoles along the cell axis. TEM. **Inset in B**. Electron-light area of the cytoplasm around the nucleus with small vacuoles. TEM. **D**. Sagittal histological section of an infected host showing well-developed trophozoites and the degree of their embedding in the host intestinal epithelium. SEM. **E.** Fragment of D at higher magnification. SEM. **F–G**. Superficial oblique thin section (F) and nearly longitudinal thin section (G, inset) showing intracellular stages of the trophozoite development. TEM. **Inset in G**. Agglomeration of electron-dense granules in the parasitophorous vacuole and a vesicle with myelin-like structures in the
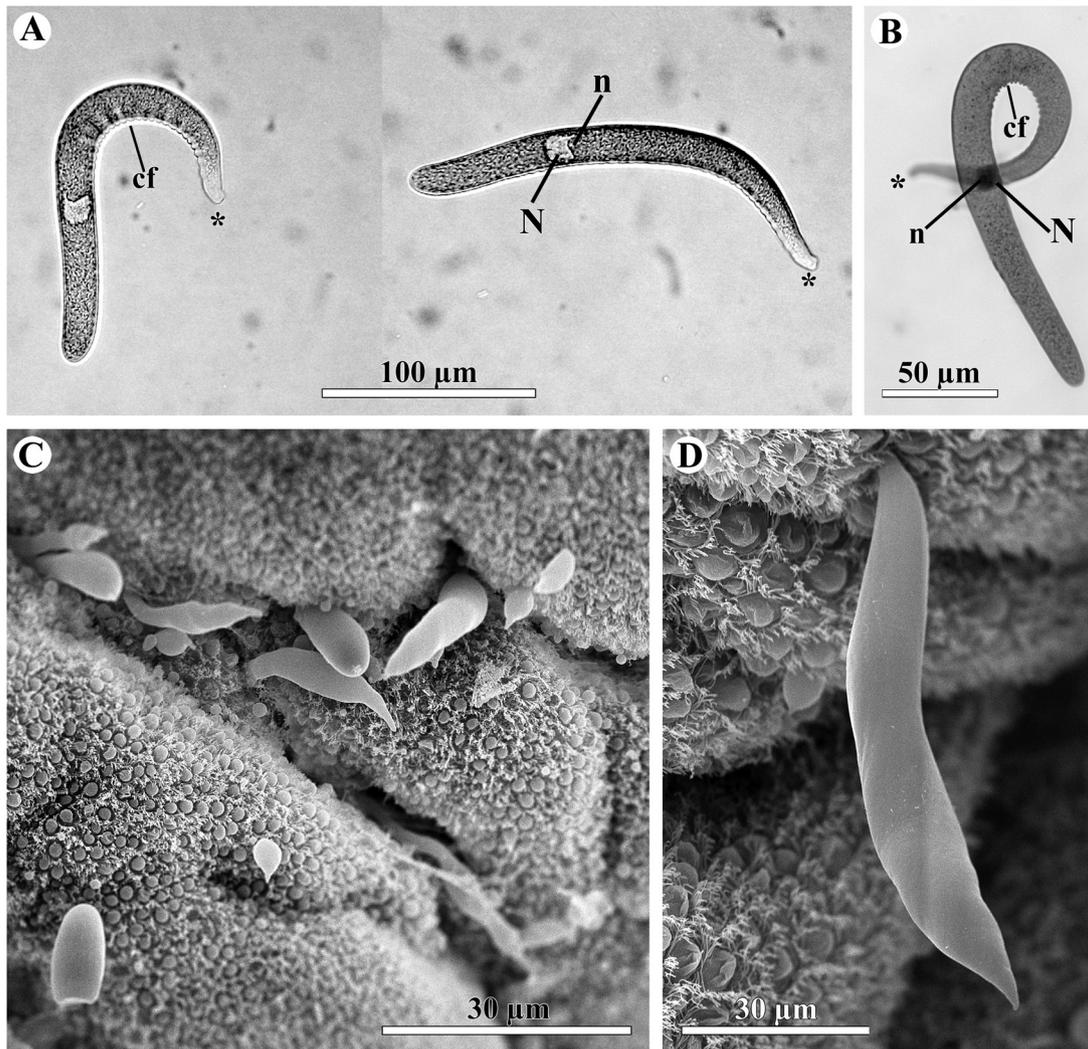
Figure 5. General morphology and motility of S*elenidium pherusae* sp. n. Light microscopic (LM) and scanning electron (SEM) micrographs. **A**. Detached trophozoite showing bending motility; a composition of two micrographs of the same cell. LM. **B**. Detached trophozoite fixed and stained with Carazzi's hematoxylin. LM. **C–D**. Differently sized trophozoites attached to the host intestinal epithelium. SEM. *, anterior end; cf, transversal compression folds; N, nucleus; n, nucleolus.

A truncated and asymmetrical mucron of the parasites formed an extended (up to 4 µm long) zone of cell junction with the host cell (Fig. 6A, C). This junction was represented by a gap 10–30 nm wide. The polar ring, the conoid, several rhoptries and micronemes were observed (Fig. 6A, B). The conoid was a truncated hollow cone consisting of 6–7 spirally arranged microtubules. It measured about 200 nm in height, 286 nm in apical diameter, and 514 nm in basal diameter. The IMC terminated near the apical end of the conoid, where there was a polar ring, adjacently located to the IMC. Sub-

host cell cytoplasm near the membrane of the parasitophorous vacuole. TEM. *, anterior end; arrowhead, membrane tunnel between two vacuoles; bl, basal lamina of the host intestinal epithelium; epr, membranes of the rough endoplasmic reticulum in the host cell; g, archigregarine; gr, electron-dense granules; h, host intestinal epithelium; hc, host cell; ic, intestinal contents; N, nucleus; n, nucleolus; mit, host cell mitochondria; f, fibrils in the host cell; pc, electron-light area of the cytoplasm; pv, parasitophorous vacuole; vac, vacuoles; vm, vesicles with multilaminar inclusions.
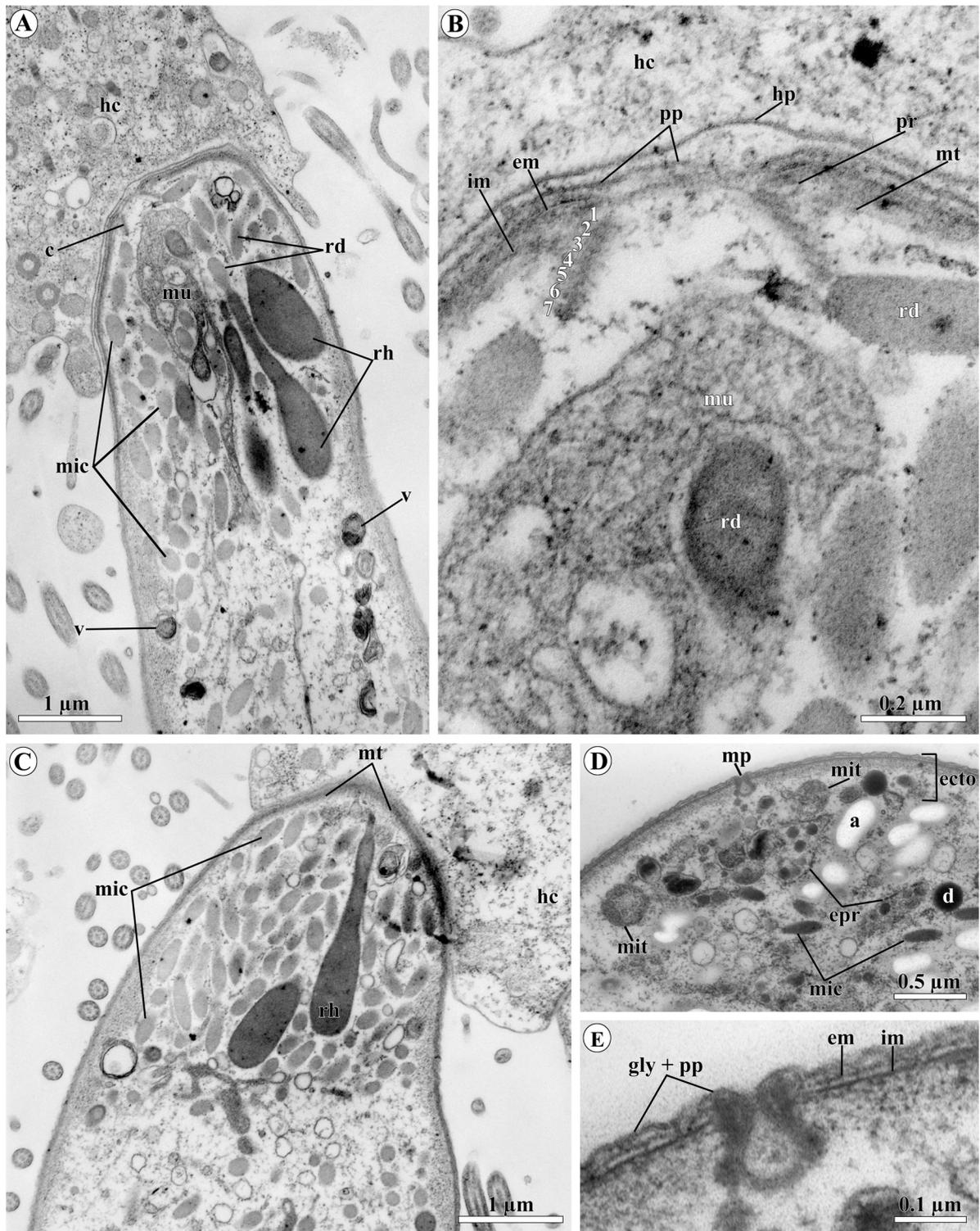
Figure 6. Fine structure of *Selenidium pherusae* sp. n. Transmission electron micrographs. **A**. Longitudinal section of the anterior end of a trophozoite. **B**. Detail of A showing the mucron structure. Numerals indicate the ordering numbers of the conoid microtubules. **C**. Superficial longitudinal section of the anterior end of another trophozoite. **D**. Transversal section of the anterior third of the trophozoite showing its cytoplasmic organization. **E**. Detail of D showing the micropore and pellicle structure. a, amylopectin granules; c, conoid; d,

pellicular microtubules arose from the polar ring and ran along the cell (Fig. 6B, C). A voluminous mucronal vacuole of irregular shape was present in the basal part of the conoid (Fig. 6A). It contained unidentified heterogeneous material and a few vesicles with electron-translucent content. The mucronal vacuole was surrounded by numerous rhoptries and micronemes. The ducts of the rhoptries extended to the apical pole of the parasite and closely adjoined the mucronal vacuole. The content of the ducts was less electron-dense than that of the rhoptries (Fig. 6A–C).

Numerous putative micronemes and several vesicles with an electron-dense material within multi-membranous whorls were present in the cytoplasm of the anterior third of the parasite (Fig. 6A). Similarly to *S. pygospionis*, the entire cytoplasm of *S. pherusae* trophozoites was indistinctly differentiated into the ectoplasm and the endoplasm, which had a similar content (Fig. 6D). In contrast to *S. pygospionis*, only a few mitochondria were observed near the pellicle, under subpellicular microtubules (Fig. 6D).

Molecular Phylogeny

Characteristics of DNA sequences: The contiguous sequence of *S. pygospionis* from *Pygospio elegans* (White Sea) was generated from four overlapping fragments and comprised SSU (small subunit or 18S), 5.8S, LSU (large subunit or 28S) rDNAs, and the internal transcribed spacers ITS 1 and 2 (4,910 bp totally). For *S. pygospionis* from *Polydora glycymerica* (Sea of Japan), only the near complete SSU rDNA sequence (1,610 bp) was obtained; it was nearly identical with that from the White Sea sample (only 2 substitutions). The contiguous sequence of *S. pherusae* (2,551 bp) was generated from two overlapping fragments and comprised SSU, 5.8S, the first ∼600 nucleotides of the LSU rDNA, and the internal transcribed spacers ITS 1 and ITS 2 (Table 1 and Supplementary Material Fig. S1).

Phylogenies inferred from SSU rDNA: Both Bayesian inference (BI) and Maximum likelihood (ML) analyses resulted in similar tree topologies differing from each other by the position of platyproteids ("squirmids"): they were the earliest branch of

Myzozoa in the Bayesian tree (Fig. 7), but the sister group of Apicomplexa in the ML tree (data not shown). Overall, the newly obtained phylogenies matched recent molecular phylogenetic evidence from alveolates and apicomplexans (e.g., Cavalier-Smith 2014; Janouškovec et al., 2015; Lepelletier et al. 2014; Rueckert and Horák 2017; Schrével et al. 2016). The resulting Bayesian tree inferred from the dataset of 128 taxa and 1,550 sites (Fig. 7) showed the monophyly of major alveolate groups, although chiefly with moderate or low support, especially in the ML analysis. The backbone of the apicomplexan region in the obtained trees was poorly resolved by both BI and ML analyses. Within the sporozoans (parasitic apicomplexans), the cryptosporidians were consistently located as the sister group of the "short-branching" eugregarine clade Eg1 (Actinocephaloidea and Stylocephaloidea) in both analyses, although with moderate Bayesian posterior probabilities (PP) and low ML bootstrap percentage (BP) supports. The top of the phylogenetic tree was formed by several long branches of eugregarines grouping into the loose clade Eg2 (Fig. 7); thus, eugregarines and, consequently, gregarines in general were not monophyletic, but polyphyletic.

Archigregarines branched after the cryptosporidians + Eg1 clade; they were not monophyletic either, being split into four firmly supported major lineages of greatly variable lengths (Ag1–Ag4), which arose successively from the backbone of the phylogenetic tree (Fig. 7). The earliest lineage Ag4 (PP = 0.99, BP = 40%) encompassed a robust clade comprising four parasites from polychaetes of the family Terebellidae and its sister group (PP = 99, BP = 62%) consisting of two environmental sequences. In contrast to the results obtained by Rueckert and Horák (2017), the archigregarine *Selenidium fallax* from the cirratulid polychaete *Cirriformia tentaculata* represented the isolated lineage Ag3 located not as sister to the cryptosporidia + gregarines clade but between the archigregarine clades Ag4 and Ag2 + Ag1 in the resulting phylogenies from both BI and ML analyses, though its nodal support was weak (Fig. 7). The robust lineages Ag2 and Ag1 formed a common clade, although weakly supported. This clade was located as a sister to the very weakly supported eugregarine clade Eg2

electron-dense droplet; ecto, ectocyte; em, external cytomembrane; epr, membranes of the rough endoplasmic reticulum; gly, glycocalyx; hc, host cell; hp, host cell plasmalemma; im, inner cytomembrane; mic, micronemes; mit, mitochondria; mp, micropore; mt, microtubules; mu, mucronal vacuole; pp, parasite plasmalemma; pr, polar ring; rd, ducts of rhoptries; rh, rhoptries; v, vesicles with multi-membrane whorls or dense material.

Table 1. Main characteristics of the archigregarine sequences obtained in this study.

Sample name, length of resulting sequence and its accession number	Amplified fragment	Length	Primers: forward (F) and reverse (R); annealing temperature used in the PCRs
Selenidium pygospionis from *Pygospio elegans* (White Sea) 4,910 bp MH061278	(I) SSU rDNA (part)	~1,640 bp	(F)[a] 5′-GTATCTGGTTGATCCTGCCAGT-3′ (R) 5′-GGAAACCTTGTTACGACTTCTC-3′ t° = 45 °C
	(II) SSU rDNA (part), ITS1, 5.8S rDNA, ITS2, LSU rDNA (part)	~1,110 bp	(F) 5′-CCGTTCTTAGTTGGTGG-3′ (R)[b] 5′-CRGTACTTGTBBDCTATCG-3′ t° = 45 °C
	(III) LSU rDNA (part)	~1,770 bp	(F)[b] 5′-ACCCGCTGAAYTTAAGCATAT-3′ (R)[b] 5′-GCCAATCCTTATCCCGAAGTTAC-3′ t° = 50 °C
	(IV) LSU rDNA (part)	~1,740 bp	(F)[b] 5′-TCCGCTAAGGAGTGTGTAACAAC-3′ (R)[b] 5′-TTCTGACTTAGAGGCGTTCAG-3′ t° = 50 °C
Selenidium pygospionis from *Polydora glycymerica* (Sea of Japan) 1,610 bp MH061279	(V) SSU rDNA (part)	~1,610 bp	(F)[a] 5′-GTATCTGGTTGATCCTGCCAGT-3′ (R) 5′-GGAAACCTTGTTACGACTTCTC-3′ t° = 45 °C
Selenidium pherusae 2,551 bp MH061280	(VI) SSU rDNA (part)	~1,600 bp	(F)[a] 5′-GTATCTGGTTGATCCTGCCAGT-3′ (R) 5′-GGAAACCTTGTTACGACTTCTC-3′ t° = 45 °C
	(VII) SSU rDNA (part), ITS1, 5.8S rDNA, ITS2, LSU rDNA (part)	~1,040 bp	(F)[b] 5′-TCCGCTAAGGAGTGTGTAACAAC-3′ (R)[b] 5′-CCTTGGTCCGTGTTTCAAGAC-3′ t° = 50 °C

[a]The primer sequence was based on Medlin et al., 1988.
[b]The primer sequences were based on Van der Auwera et al., 1994.

(see above), i.e. archigregarines were paraphyletic in the resulting SSU rDNA-based phylogenies; however, the nodal support of this grouping was low (Fig. 7). The archigregarine paraphyly has been repeatedly reported before but always with weak support (Rueckert and Horák 2017; Rueckert et al. 2011; Schrével et al. 2016; Wakeman et al. 2014; Wakeman and Horiguchi 2018; Wakeman and Leander 2013). Thus, the deep branching of archigregarine lineages had remained unresolved. Therefore, we tested alternative phylogenies (see below). The lineage Ag2 comprised two parasites of sipunculids and one environmental sequence.

The lineage Ag1 was the largest and comprised parasites of polychaetes from the families Cirratulidae, Flabelligeridae, Opheliidae, Sabellidae, Sabellariidae, Serpulidae, and Spionidae, including the newly obtained archigregarine sequences, and a number of environmental sequences, only two of which were involved in the final phylogenetic analyses. This was the longest archigregarine branch, which had full support in both BI and ML analyses. Number "1" was assigned to this clade because *Selenidium pendula*, the type species of the genus *Selenidium*, belonged to it (Fig. 7). Within the clade, the parasites of Serpulidae and Sabellariidae formed robust subclades, whilst the subclade of the parasites of Spionidae had full BP and moderate BP support. The two available sequences of the parasites of Sabellidae did not form a subclade, although they occupied neighbouring positions in the tree with moderate or low nodal supports; this indicates that their positions are actually unresolved. Both sequences of *S. pygospionis* (from *Pygospio elegans* and *Polydora glycymerica*) grouped with the sequences of *S. boccardiellae* and *S. pendula* within the subclade of parasites of spionid polychaetes (see above). The sequence of *S. pherusae* branched earlier, after *S. opheliae* from the polychaete *Ophelia roscoffensis* (Opheliidae); both these branches had moderate or low nodal supports.

Analyses of LSU rDNA and the ribosomal operon: All phylogenies based on these phylogenetic markers resulted in identical topologies both in the BI (Fig. 8) and the ML (not shown) analysis. Overall, they recovered the major alveolate clades that agreed with the phylogenies inferred from SSU rDNA, both already published (see above) and newly obtained, but with a higher resolution of all-alveolate and myzozoan deep branching.

Unlike SSU rDNA-based phylogenies, all analyses of the LSU rDNA dataset (53 sequences, 2,913 sites) resulted in the well-supported monophyly of

gregarines (PP = 1.0, BP = 91). The only archigregarine sequence (*S. pygospionis* from *P. elegans*) formed a long branch (PP = 1.0, BP = 70) immediately after the clade Eg1 containing sequences of the "short-branching" gregarines *Ascogregarina taiwanensis* and Neogregarinida sp. OPPPC1 AB748927 and before the clade Eg2 including sequences of the "long-branching" eugregarines. Therefore, it broke down the monophyly of eugregarines (Fig. 8A).

The resulting phylogenetic trees inferred from the ribosomal operon dataset (alignment of 53 sequences, 4,618 sites) showed the same topology as the LSU rDNA-based phylogenetic tree with increased support for several branches (Fig. 8B). Within the sporozoan clade, all the studied gregarines were monophyletic, and the support was almost the same as in the LSU rDNA phylogenies. However, the BP support for the position of *S. pygospionis*, splitting eugregarine monophyly, was somewhat lower (BP = 64% vs 70% in the LSU rDNA tree).

Testing alternative phylogenies: Alternative topologies of phylogenetic trees were analyzed together with the topologies of the resulting tree yielded by the phylogenetic analyses (the reference tree, Fig. 7) with the use of the set of six widespread tests (see Methods). The results are presented in Figure 9 and Supplementary Material Table S1. For SSU rDNA phylogenies based on 128 sequences, the hypotheses on the monophyly of archigregarines and various positions of this combined lineage (Ag1 + Ag2 + Ag3 + Ag4) within the cryptosporidian-gregarine clade and sisterly to it were tested under the assumptions of monophyly or polyphyly of eugregarines (Fig. 9A). In addition to the resulting phylogenetic trees exhibiting the archigregarine paraphyly (see above), two of the four alternative SSU rDNA phylogenies containing monophyletic archigregarines were found not to be rejected by any test; this contradicts the results obtained by Rueckert and Horák (2017). Both these phylogenies included monophyletic eugregarines: (i) monophyletic archigregarines as a sister group either to monophyletic eugregarines (which means the monophyly of the gregarines as a whole) or (ii) to the clade comprising cryptosporidians and monophyletic eugregarines. All the tests rejected simultaneous monophyly of archigregarines and polyphyly of eugregarines (Fig. 9A and Supplementary Material Table S1).

For the LSU rDNA- and ribosomal operon-based phylogenies, the phylogenetic position of the only available archigregarine sequence, *S. pygospionis*
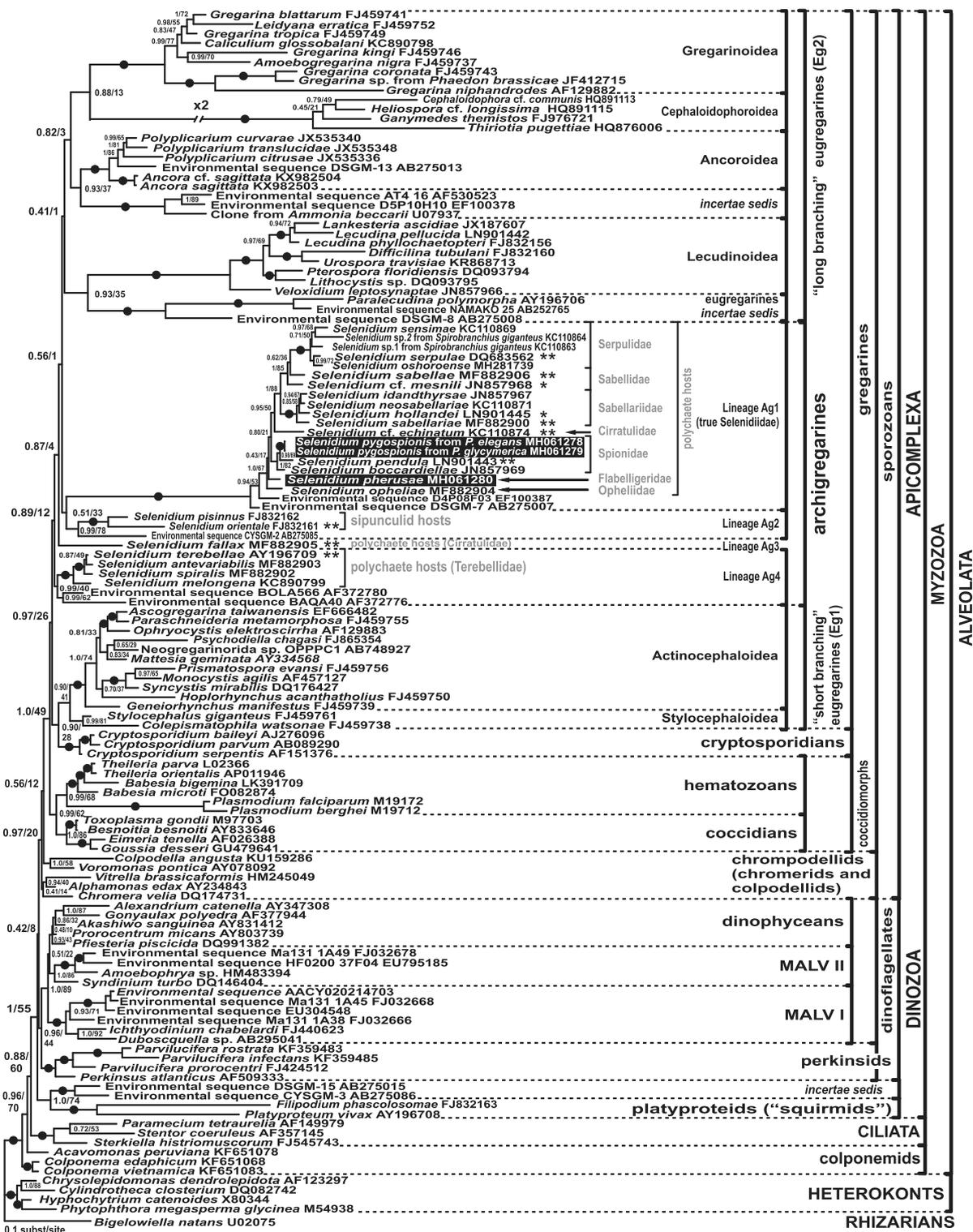
Figure 7. Bayesian inference tree of alveolates inferred from the dataset of 128 SSU rDNA sequences and 1,550 sites under the GTR + Γ + I model. Numbers at the nodes indicate Bayesian posterior probabilities (numerator) and ML bootstrap percentage (denominator). Black dots on the branches indicate Bayesian posterior probabilities and bootstrap percentages of 0.95 and 90% or more, respectively. The newly obtained sequences

from *P. elegans*, was examined, and the same set of topologies was used (Fig. 9B and C, and Supplementary Material Table S1). Congruently to SSU rDNA-based phylogenies, the hypothesis of its sister position to monophyletic eugregarines was not rejected by any test among the phylogenies based both on LSU rDNA (Fig. 9B) and on the ribosomal operon (Fig. 9C). All the other topologies were rejected by all tests among LSU rDNA-based phylogenies but among operon-based phylogenies the polyphyly of eugregarines was not rejected in the case when the archigregarine was a sister lineage to the eugregarine clade Eg2 and cryptosporidians were a sister group to the clade Eg1, i.e. as in the SSU rDNA reference tree.

Summing up, the monophyletic archigregarines as a sister group to the monophyletic eugregarines was the only possible alternative topology (permitted by all the tests) shared by the phylogenies based on all the three genetic markers used (SSU rDNA, LSU rDNA, and ribosomal operon phylogenies). However, the number of sequences in the LSU rDNA/ribosomal operon database is significantly lower than in the SSU rDNA database and is still insufficient to make valid comparisons and meaningful conclusions.

Discussion

Justification of Newly Described Species

Selenidium pygospionis sp. n.

There are currently eleven species of archigregarines inhabiting polychaetes of the family Spionidae (Dibb 1938; de Faria et al. 1917; Fowell 1936a,b; Ganapati 1946; Giard 1884; Levine 1971; Ray 1930; Reichenow 1932; Wakeman and Leander 2012). They are described in varying degree of detail; in particular, only three species have been examined by electron microscopy: *Selenidium pendula*, *S. boccardiellae*, and *S. pygospionis sp. n.* (Rueckert and Horák 2017; Schrével et al. 2016; Wakeman and Leander 2012; this study). Most of these archigregarines belong to the genus *Selenidium*, one archigregarine belongs to the genus *Selenocystis* (*S. foliata*). However, *Selenidium foliatum* Ray, 1930 is suggested to be a synonym of *S. foliata* Dibb, 1938 (Desportes

and Schrével 2013; Dibb 1938; Schrével 1970). We also suspect that *Selenidium intraepitheliale* Reichenow, 1932 may be a synonym of *S. spionis* (Kolliker, 1945) Ray, 1930 as these archigregarines parasitizing the same host are identical (Levine 1971; Ray 1930; Reichenow 1932; Schrével 1970). The resulting combinations of archigregarines from spionid polychaetes are presented in Supplementary Material Table S2. Additionally, three *Selenidium* species were reported from the spionid polychaetes *Dipolydora coeca* (Caullery and Mesnil 1899), *Spio filicornis* (Caullery and Mesnil 1901), and *Pygospio elegans* (Caullery and Mesnil 1899; Reichenow 1932) without species descriptions.

The archigregarines from spionids are usually characterized by a high frequency and a middle intensity of parasite infection (Douglass and Jones 1991). Merogony was reliably shown only in *S. axiferens* (Fowell 1936b). At the same time, the presence of numerous individuals of an archigregarine in a spionid polychaete was considered as an indirect evidence of the presence of merogony in their life cycle (Schrével et al. 2016). They usually have a vermiform, more or less flattened cell, with a knob-shaped (dome-shaped) mucron. Some of them, including the type species *S. pendula*, have an optically distinct cytoplasm arranged along the cell axis, around the nucleus and in the radials running to the cell periphery (Desportes and Schrével 2013; Fowell 1936a,b; Ray 1930; Rueckert and Horák 2017).

Trophozoites of *Selenidium pygospionis* sp. n. isolated from *Pygospio elegans* polychaetes in this study were somewhat similar with *S. spionis*, *S. intraepitheliale*, *S. martinensis*, parasitizing in various hosts, in cell size, cell shape, and in the number of longitudinal folds (Levine 1971; Ray 1930; Reichenow 1932; Supplementary Material Table S2). However, the trophozoites of *S. pygospionis* were easy to distinguish from other species of *Selenidium* by their hook-like anterior end. Therefore, we established a new species for these archigregarines using host-specific and morphological characteristics as well as molecular-phylogenetic markers.

The molecular-phylogenetic analyses revealed an almost full identity (two substitutions per 1,610 bp) of sequences from archigregarines isolated from the polychaetes *P. elegans* of the

---

of *Selenidium* spp. are highlighted by black. Single asterisks indicate "*Selenidioides*" spp. and double asterisks – "*Selenidium*" spp. as proposed in the revision by Levine (1971). The information about the host taxonomical affiliations is given in gray.
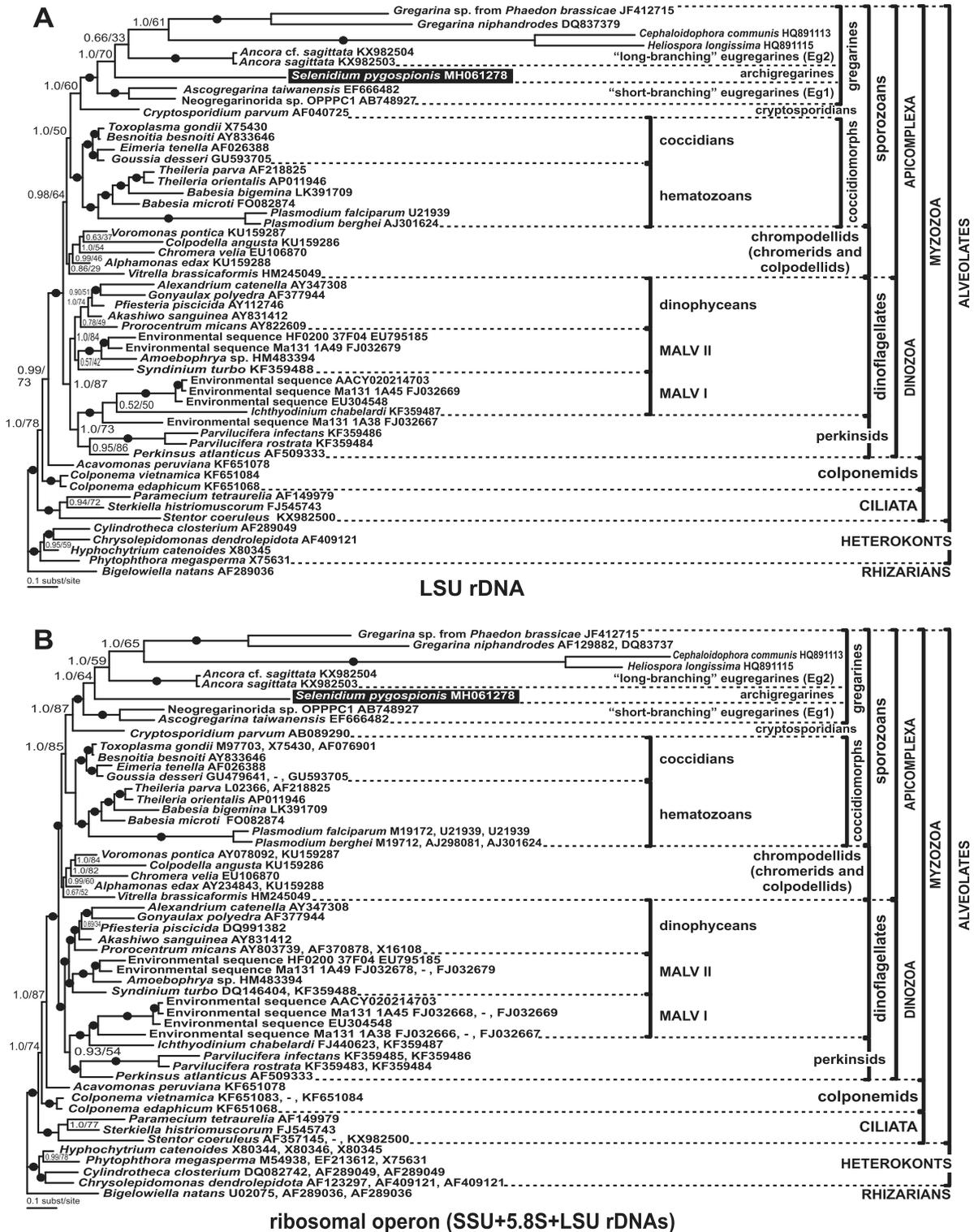
Figure 8. Bayesian inference trees of alveolates inferred from the datasets of 53 taxa under GTR + Γ + I model for, **A**, LSU rDNA (2,913-sites dataset); **B**, ribosomal operon (4,618-sites dataset). Numbers at the nodes indicate Bayesian posterior probabilities (numerator) and ML bootstrap percentage (denominator). Black dots on the branches indicate Bayesian posterior probabilities and bootstrap percentages of 0.95 and 90% or more,
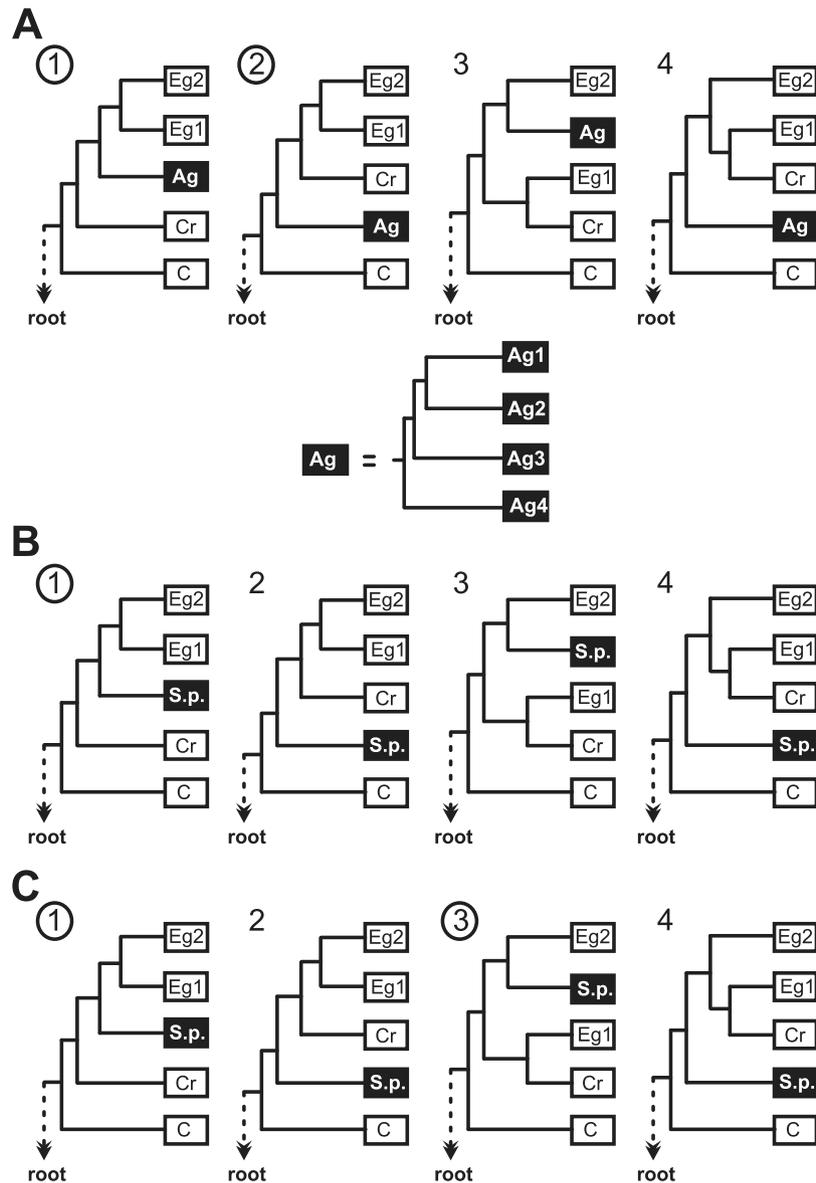
Figure 9. Tested alternative topologies of phylogenetic trees. **A**, testing archigregarine monophyly on alternative topologies for the SSU rDNA phylogenies (the dataset of 128 taxa and 1,550 sites). The scheme below the raw of the alternative topologies shows the structure of the artificially composed monophyletic archigregarine clade. **B** and **C**, testing phylogenetic position of the archigregarine *Selenidium pygospionis* from *Pygospio elegans* on alternative topologies for the (**B**) LSU rDNA phylogenies (the dataset of 53 taxa and 2,913 sites) and (**C**) ribosomal operon phylogenies (the dataset of 53 taxa and 4,618 sites). Permissible topologies (not discarded by all tests) are marked by numbers within circles. Abbreviations: **Ag1**, archigregarines (the subclade numbers in the scheme correspond those in Fig. 8); **Eg1** and **2**, eugregarine clades (short- and long-branching, respectively; see Figs 8 and 9); **Cr**, cryptosporidia; **C**, coccidiomorphs (Coccidia and Hematozoa); **S.p.**, the sequences of *S. pygospionis*.

respectively. The newly obtained sequences of the archigregarine *Selenidium pygospionis* is highlighted by black. Accession numbers in the tree **B** are arranged in following order: SSU rDNA, 5.8S (if not available then "–"), LSU rDNA.

White Sea and *Polydora glycymerica* of the Sea of Japan. This means that these archigregarines, though isolated from hosts from geographically distinct regions, belong to the same species, *S. pygospionis*. We also suspect that *Selenidium* sp. from *P. elegans* (former *P. seticornis*) collected near Plymouth, the English Channel (Caullery and Mesnil 1899; Reichenow 1932), is *S. pygospionis* described in the present study. These data indicate that the biogeographic distribution of archigregarines may be extensive and that the systematic principle "new host – new species", sometimes used for gregarines (Levine 1971), should be applied to archigregarines with caution.

We believe that the archigregarine recently found to harbor the microsporidium *Metchnikovella dogieli* (Paskerova et al. 2016) is likely to be *S. pygospionis* since it had been sampled at the same site where samples for the present study were taken. Metchnikovellidean microsporidia, inhabiting both archigregarines and eugregarines (Desportes and Schrével 2013; Mikhailov et al. 2017; Rotari et al. 2015; Sokolova et al. 2013, 2014), appear to possess a universal complex of adaptations (mechanisms of invasion, life cycles, metabolic strategies, etc.) allowing them to parasitize in structurally different gregarines.

Selenidium pherusae sp. n.

Only four archigregarine species have been known to parasitize polychaetes of the family Flabelligeridae (Bogolepova 1953; Castellon and Gracia 1988; Kuvardina and Simdyanov 2002; Simdyanov 1992; Tuzet and Ormières 1958; Tuzet and Ormières 1965). The resulting combinations of archigregarines from flabelligerid polychaetes are presented in Supplementary Material Table S3. All of them belong to the genus *Selenidium*, and almost all have a longitudinally folded cortex, except *S. pennatum* which has two lateral vanes or ridges (Simdyanov 1992). Only one archigregarine species has been described from the polychaete *Pherusa plumosa*, *S. curvicollum* (Bogolepova 1953). Its trophozoites have 13–15 cortical grooves per side and a large, curved proboscis-like anterior end. The archigregarine described in the present study parasitizes the intestine of the polychaete *Ph. plumosa*; however, it lacks any folds at the surface and has a small, slightly truncated mucron. Hence, we consider it as a new species, *Selenidium pherusae* sp. n.

Nutrition of Archigregarines

Myzocytotic feeding (myzocytosis), i.e. sucking the host cell cytoplasm via a well-developed apical complex, was found in *S. hollandei*, *S. pendula* and *S. orientale* (Schrével 1968, 1971b; Schrével et al. 2016; Simdyanov and Kuvardina 2007). It is thought that myzocytosis is common in archigregarines (Desportes and Schrével 2013; Schrével et al. 2016; Simdyanov and Kuvardina 2007; Wakeman and Horiguchi 2018; Wakeman et al. 2014). In the mucron of *S. pygospionis* and *S. pherusae*, we observed the organelles of the apical complex such as the conoid, the mucronal vacuole, rhoptries, and micronemes. Additionally, a series of connected vacuoles arranged along the cell axis and around the nucleus was present in *S. pygospionis*. We suggest that the axial streak of *S. pygospionis*, well visible in living archigregarines under a light microscope, is a system of the observed (presumably digestive) vacuoles originating in the mucron during the myzocytosis and transporting nutrients from the anterior to the posterior end along the cell axis. To note, numerous vacuoles around the nucleus have also been found in the cytoplasm of *S. pendula* (Schrével 1970, 1971a). These vacuoles may be a component of a similar system of digestive vacuoles.

Different cytoplasmic vesicles containing some multi-membranous whorls or dense material and located in the ectoplasm near the pellicle or inserted in the inner membrane complex were previously observed in several *Selenidium* spp. (Schrével 1971a; Schrével et al. 2016; Wakeman and Horiguchi 2018). It was suggested that these structures might be involved in a surface-mediated nutrition present alongside with the nutrition via the typically organized micropores (Wakeman and Horiguchi 2018).

The heterogeneity of the organelles' distribution (narrow electron-translucent spaces lacking any visible organelles) observed in the cytoplasm of *S. pygospionis* may point to the presence of microfilaments similar to those demonstrated around the nucleus in *S. pendula* and *S. hollandei* (Schrével 1971a). Putative digestive vacuoles and coexisting microfilaments may play a role in the transport of nutrients from the anterior to posterior end during myzocytotic feeding.

Motility of Archigregarines

In general, archigregarines show different types of movement such as bending, twisting, coiling, rolling, and pendular motility. Some of them can also contract their cell. These movements were often likened to those of nematode worms (Fowell 1936a,b; Gunderson and Small 1986; Leander 2007, 2008b; Mellor and Stebbings 1980; Schrével 1971a,b; Schrével et al. 1974, 2016; Stebbings et al. 1974; Wakeman et al. 2014). Both archigregarines described in the present study can move by forming 1–4 (in *S. pygospionis*) or only one (in *S. pherusae*) bending sections along the cell but never contract. Additionally, as it can be easily seen in flattened trophozoites of *S. pygospionis*, their bending motility is generated only in one cell plane. We propose to refer to this type of motility as a nematode-like bending, where the alternate sides (flattened sides in *S. pygospionis* or body halves in *S. pherusae*) act antagonistically in the bending sections forming in a single plane of the cell. It is similar to the pendular motility of *S. pendula*, where one bend is generated in the anterior part of the cell and runs to the posterior one, but considerably different from the bending motility of other *Selenidium* spp. (e.g. *S. hollandei*, *S. sabellariae*), where bends, generated in different cell planes, can combine with contraction and twisting of the cell in different cell sections (Desportes and Schrével 2013; Rueckert and Horák 2017; Schrével 1967, 1970). The character of archigregarine motility may reflect the dynamics and architecture of the cytoskeleton.

Nematode-like bending is an evidence in favour of the general hypothesis about motility of *Selenidium* spp. postulating that the three-membrane pellicle and the longitudinal microtubules are skeletal and motile units representing together a unicellular analogue of the musculocuticular system of nematodes (Leander 2007, 2008b; Stebbings et al. 1974). A similar motility mechanism was also demonstrated in the blastogregarine *Siedleckia nematoides.* It performs pendular, twisting, undulating movements and possesses the longitudinal microtubules organized in a layer or layers under the trimembrane pellicle (Valigurová et al. 2017). To note, the axial streak together with putative microfilaments may also be involved in the cell motility as an additional skeletal element helping to reverse movement and maintenance of the cell shape in bends as suggested by the concept of the statomotor system (Fowell 1936b).

According to the previous authors, the dynamic motility of archigregarines and blastogregarines is correlated with the number of mitochondria located directly beneath the subpellicular microtubules (Desportes and Schrével 2013; Leander 2006, 2007; Mellor and Stebbings 1980; Schrével 1971b; Stebbings et al. 1974; Valigurová et al. 2017). Our observations of the ultrastructure of both studied archigregarines may lend further support to this idea. An actively bending (up to 4 bends at a time) *S. pygospionis* has numerous mitochondria arranged in a layer beneath the subpellicular microtubules, while a less pronouncedly bending (only one bend at a time) *S. pherusae* has fewer mitochondria.

Intracellular Development in *Selenidium pygospionis* sp. n.

We observed small cells of putative *S. pygospionis* localized within the parasitophorous vacuoles in the host enterocytes. Intracellular young trophozoites were also found in other archigregarines such as *Selenidium spionis*, *S. mesnili*, *S. foliatum*, and *S. cauleryi* (Ray 1930). An intracellular localization may be an initial stage of the trophozoite development in some archigregarines. As trophozoites grow, the host cells are destroyed, and the location of the parasites becomes extracellular. In the case of *S. pygospionis*, well-developed and extracellularly localized trophozoites are anchored between the host intestinal epithelium folds by their hook-like anterior end. We do not know whether they form any attachment site with the host cell at some period of their development. Intra-tissue stages mentioned in the description of *S. spionis* and *S. foliatum* (Caullery and Mesnil 1899, 1901; Ray 1930) as a few full-grown individuals embedded in the intestine wall tissue under the epithelial layer and lying parallel to the host longitudinal axis can be regarded as an abnormal and occasional development of trophozoites.

Notes on the Taxonomy and Phylogeny of Archigregarines

Levine (1971) proposed to divide the genus *Selenidium* into two genera based on the presence/absence of merogony in the life cycle. He established a new genus, *Selenidioides*, for gregarines with merogony and assigned it to the archigregarines. The species without merogony (or in which merogony was unknown) were transferred to the eugregarines within the genus *Selenidium*.

In his opinion (Levine 1971), the data on ultra-structure and life cycles of archi- and eugregarines available at that time (MacGregor and Thomasson 1965; Schrével 1966, 1970, 1971a,b; Vávra 1969; Vivier and Schrével 1964, 1966; Vivier et al. 1970; etc.) were insufficient for the separation of these two groups. Levine's classification has become popular and has been applied in some revisions on pro-tists and taxonomic databases (Perkins et al. 2000; WoRMS).

Available molecular phylogenetic evidence (Rueckert and Horák 2017; Rueckert and Leander 2009; Schrével et al. 2016; Wakeman and Horiguchi 2018; Wakeman and Leander 2012, 2013; Wakeman et al. 2014) and the results of this study show that the archigregarines are separated into several phylogenetic lineages. However, this separation does not correspond to the taxonomical action proposed by Levine. On one hand, the type species of the genus *Selenidium*, *S. pendula*, belong to the clade Ag1 ("true Selenidiidae" as proposed by Schrével et al. (2016)) together with representatives of the "*Selenidioides*" group, *S. mesnili* and *S. hollandei*. On the other hand, some gregarines of the "*Selenidium*" group, *S. terebellae*, *S. fallax*, and *S. orientale*, belong to the clades Ag2, Ag3, and Ag4 respectively, not to the clade Ag1 (Fig. 7). Thus, the taxonomical approach proposed by Levine (1971) for archigregarines should be abolished together with the genus *Selenidioides* Levine, 1971 as has already been suggested by different authors (Rueckert and Horák 2017; Rueckert and Leander 2009; Schrével et al. 2016; Wakeman and Leander 2012).

Overall, the molecular phylogeny of the archigregarines based on the available DNA sequences is largely congruent with the taxonomical affiliations of their hosts (Schrével et al. 2016; this study). Indeed, archigregarines of the lineage Ag4 inhabit poly-chaetes of the family Terebellidae, archigregarines of the lineage Ag2 occur in sipunculid hosts, while most *Selenidium* spp. of the lineage Ag1 parasitize in different sedentary polychaetes (Fig. 7), how-ever, their grouping in subclades within this clade also agrees well with the taxonomical affiliations (families) of hosts. We consider that this reflects in various degrees some aspects of host-parasite co-evolution, which may become an important subject of research in the future.

The macrosystem of archigregarines is ques-tionable because of the issue of their monophyly, unresolved both in terms of the molecular phy-logeny and the classic cladistic approach based on morphology. The morphology-based hypothesis about the monophyly of *Selenium*-like archigre-garines is difficult to substantiate in terms of cladistics, as all their ultrastructural key features (the ultrastructure of the cortex and mucron) appear to be symplesiomorphies (the aforemen-tioned morphostasis) rather than synapomorphies. Apart from *Selenidium* spp., morphologically differ-ent representatives of the genera *Ditrypanocystis*, *Exoschizon*, *Merogregarina*, *Meroselenidium*, and *Selenocystis* have also been affiliated to archigre-garines (Desportes and Schrével 2013; Perkins et al. 2000). They are intestinal parasites of poly-chaetes and sipunculids as well as of colonial ascidians and oligochaetes. No molecular phylo-genetic evidence from these parasites is currently available (Desportes and Schrével 2013) and electron-microscopic data are extremely scanty (Butaeva et al. 2006). Some of these organisms may be neither archigregarines nor even gre-garines. A demonstrative example is the case of *Platyproteum* (formerly *Selenidium*) *vivax* and *Fil-ipodium fascolosomae*, gregarine-like organisms, which have been shown to be an indepen-dent lineage of Myzozoa, so-called "squirmids" (Cavalier-Smith 2014; Rueckert and Leander 2009). Both parasites are capable of very dynamic cellular deformations referred to as the peristaltic motility (metaboly) (Gunderson and Small 1986; Leander 2006; Rueckert and Leander 2009). Since this is dissimilar to the real squirming, we prefer to call this lineage "platyproteids" (Fig. 7) instead of "squirmids" proposed by Cavalier-Smith (2014).

The SSU rDNA-based phylogenies (Cavalier-Smith 2014; Cavalier-Smith and Chao 2004; Grassé 1953; Rueckert and Leander 2009; Rueckert and Horák 2017; Schrével et al. 2016; Wakeman and Horiguchi 2018; Wakeman and Leander 2012, 2013; Wakeman et al. 2014; this study) reveal archigregarines as a paraphyletic group, although their deep branching is actu-ally unresolved and shows weak nodal supports. The test of alternative topologies, provided in this study, did not reject archigregarine monophyly, but only within the framework of the hypothesis that eugregarines were monophyletic too (Fig. 9A). Thus, the phylogenetic analyses of the SSU rDNA yield ambiguous results. As explained previously (Simdyanov et al. 2017), SSU rDNA-based phylo-genies appear to be of little use for resolving the deep branching order of gregarines and apicom-plexans altogether. This is likely a consequence of an explosive evolutionary radiation of gre-garines and/or rapid evolution of their SSU rDNA sequences. The LSU rDNA and near-complete rDNA operon provide an increased phylogenetic resolution over SSU rDNA and could be useful in

advancing the phylogeny and taxonomy of archigregarines and gregarines in general (Simdyanov et al. 2015, 2017). Unfortunately, only one archigregarine LSU rDNA sequence is now available (this study), and it even forms a long branch, so that its position in the obtained phylogenies might be affected by the long branch attraction artifact. An enhanced taxon sampling of archigregarine LSU rDNA sequences is necessary for more substantial conclusions, with special attention to short-branching species, representatives of the lineages Ag2, Ag3, and Ag4. Multigenic phylogenies including a broad representative sampling of archigregarines could provide the ultimate test of the hypotheses about the evolution within Apicomplexa.

Taxonomic Summary

Phylum Apicomplexa Levine, 1970

Subphylum Sporozoa Leuckart, 1879

Class Gregarinomorpha Grassé, 1953, emend. Simdyanov et al., 2017

Order Archigregarinida Grassé, 1953

Family Selenidiidae Brasil, 1907

Genus *Selenidium* Giard, 1884

Selenidium pygospionis sp. n.

Diagnosis. Trophozoites aseptate, elongated and slightly flattened with narrowed ends, embedded in the host intestinal epithelium (extracellular or intracellular location) or freely localized in the intestinal lumen. Anterior end usually hook-like, bent towards one of the wide sides. Mucron naked, dome-shaped. Trophozoites measuring 34 to 288 µm (average 144 µm, mode 146 µm, n = 79) in length, 4 to 25 µm (average 12 µm, mode 11 µm, n = 76) in width. Cell surface with 22–30 (usually 28, n = 12) broad and low folds separated by grooves. 10–12 grooves per flattened side and 1–3 grooves per narrow side. Nucleus oval, 6–22 µm (av. 17 µm, n = 40) × 5–11 µm (av. 8.4 µm, n = 26), located in the widest part and expanding along the longitudinal axis of the cell. Single nucleolus situated in nucleus part facing anterior end. Intracellular axial streak of optically distinct cytoplasm expanding from anterior to posterior end and forming expansion around nucleus and numerous radial threads toward cell periphery. Syzygy caudo-caudal. Attached or non-attached trophozoites and syzygy partners moving by nematode-like bending (formation of bends in a single plane of cell).

DNA sequences. SSU, ITS1, 5.8 S, ITS2, and LSU rDNA sequences for individuals, isolated from the polychaetes *Pygospio elegans* (White Sea) (GenBank MH061278) and SSU rDNA – from the polychaetes *Polydora glycymerica* (Sea of Japan) (GenBank MH061279).

Type material (syntypes). Resin blocks and fixed slides containing archigregarines and pieces of infected host intestine deposited in the collection of Department of Invertebrate Zoology, St Petersburg State University; Figures 1–4 (this publication) show some of the syntypes.

Hosts and localities. Polychaetes *Pygospio elegans* Claparède, 1863 (Spionidae, Polychaeta); Bolshoy Goreliy Island, Keret' Archipelago, Chupa Inlet, Kandalaksha Bay, White Sea, 66°18.770′N; 33°37.715′E; Velikaja Salma, Kandalaksha Bay, White Sea, 66°33.200′N, 33°6.283′E. Polychaetes *Polydora glycymerica* Radashevsky, 1993 (Spionidae, Polychaeta); Peter the Great Bay, Sea of Japan, 42°53′29″N, 132°44′07″E.

Location within host. Intestine (midgut and hindgut).

Etymology. Species name, *pygospionis*, refers to the genus name of one of the hosts.

Selenidium pherusae sp. n.

Diagnosis. Trophozoites aseptate, vermiform. Anterior end narrowed, slightly truncated; posterior end pointed in young or rounded in mature individuals. Cell surface smooth, without well-developed folds or grooves. Trophozoites measuring 38–269 µm (n = 6) in length, 10–18 µm (n = 4) in width. Nucleus spherical (11–12 µm, n = 2), located in the widest part of the posterior half of the cell, with the single nucleolus. Attached and detached trophozoites exhibiting bending motility.

DNA sequences. SSU rDNA sequences (GenBank MH061278).

Type material (syntypes). Resin blocks and fixed slides containing archigregarines and pieces of infected host intestine deposited in the collection of the author TGS, Department of Invertebrate Zoology, Lomonosov Moscow State University; Figures 5–6 (this publication) show some of the syntypes.

Host and locality. Polychaetes *Pherusa plumosa* (Müller, 1776) (Flabelligeridae, Polychaeta); Peter the Great Bay, Sea of Japan, 42°53′29″N, 132°44′07″E.

Location within host. Midgut.

Etymology. The species name, *pherusae*, refers to the genus name of the host.

Methods

Collection of polychaete hosts and isolation of gregarines: Polychaetes *Pygospio elegans* Claparède, 1863 (Spionidae, Polychaeta) were collected at two sites of the littoral zone near the Marine Biological Station of St Petersburg State University (Bolshoy Goreliy Island, Keret' Archipelago, Chupa Inlet, Kandalaksha Bay, White Sea, 66°18.770′N; 33°37.715′E) and the White Sea Biological Station of Lomonosov Moscow State University (Velikaja Salma, Kandalaksha Bay, White Sea, 66°33.200′N, 33°6.283′E) during the summers of 2002–2015 years.

Polychaetes *Polydora glycymerica* Radashevsky, 1993 (Spionidae, Polychaeta) boring shell walls of the living bivalves *Glycymeris yessoensis* (G. B. Sowerby III, 1889) and polychaetes *Pherusa plumosa* (Müller, 1776) (Flabelligeridae, Polychaeta) inhabiting druses of the Far East mussels *Crenomytilus grayanus* (Dunker, 1853) were collected by SCUBA divers in 2007 near Vostok biological station, National Scientific Center of Marine Biology, Russian Academy of Sciences (Peter the Great Bay, Sea of Japan, near Nakhodka, 42°53′29″N, 132°44′07″E).

Prior to dissection, the examined animals were stored in small containers (about 50 worms per 250 ml container) at +10 °C with periodically changed seawater. The polychaetes were cultured up to a month. Dissection of polychaetes and isolation of parasites were performed with the help of fine needles and hand-drawn glass pipettes under a stereomicroscope (MBS-10, Russia). The released parasites or small fragments of the host intestine with attached gregarines were rinsed thrice with seawater filtered through Millipore (0.22 μm), then prepared for light microscopy or fixed for electron microscopy. Individual cells were also subjected to DNA extraction.

Light microscopy: More than 100 polychaetes of *P. elegans* were investigated in squash preparations [compressing of a polychaete specimen between the object and cover slides before microscopic analysis] (Fig. 1A–B, D–M). Separate archigregarines isolated from the intestines of *P. elegans* (Fig. 1C, N–Q), *P. glycymerica* (data not shown) and *Ph. plumosa* (Fig. 5A) were also investigated in living preparations. All preparations were investigated with the use of a series of light microscopes equipped with different digital cameras: a MBR-1 microscope (LOMO, Russia) equipped with phase contrast and connected to a Canon EOS 300D digital camera; a Zeiss microscope (Carl Zeiss, Germany) connected to a Nikon Coolpix 7900 camera; a Zeiss Axio Imager.A1 connected to an AxioCam MRc5 digital camera (Carl Zeiss, Germany); a Leica DM 2500 microscope equipped with DIC optics and Plan-Apo objective lenses and connected to a DFC 295 digital camera (Leica, Germany).

Several individuals of *S. pherusae* from polychaetes *Ph. plumosa* were fixed with 3% formaldehyde in seawater, stained with Carazzi's hematoxylin and examined under a Zeiss microscope connected to a Nikon Coolpix 7900 camera (Fig. 5B).

Electron microscopy: Small pieces of the polychaete intestine with attached archigregarines or free archigregarines released from the host gut lumen were fixed in 2.5% glutaraldehyde in 0.2 M cacodylate buffer with/without 0.05% MgCl2 (pH 7.4, final osmolarity 720 mOsm) for 1–4 h, washed in filtered seawater and postfixed in 1–2% osmium tetroxide in the same buffer for 1–2 h. The entire procedure of fixation was performed at +4 °C. Fixed samples were dehydrated in an ascending ethanol series. Some of them were additionally transferred to an ethanol/acetone mixture and rinsed in pure acetone before the following procedure. For SEM, the fixed and dehydrated samples were critical point dried in liquid CO_2 and then coated with gold or platinum. The samples were investigated with a Tescan MIRA3 LMU scanning electron microscope (TESCAN Brno, Czech Republic), JSM-7401F (JEOL, Japan), FEI Quanta 250 (Thermo Fisher Scientific, Netherlands) and Hitachi S-405A scanning electron microscope (Hitachi, Japan) (Figs 2, 5C, D). For TEM, fixed and dehydrated samples were embedded in Epon-Araldite or Epon blocks. They were sectioned with ultramicrotomes Leica EM UC6 and Leica EM UC7 (Leica, Germany). Ultra-thin sections were stained according to standard protocols (Reynolds, 1963) and examined using a JEM 2100 (JEOL, Japan), TEM–1010 (JEOL, Japan), and LEO 910 (Carl Zeiss, Germany) electron microscopes equipped with a digital or film cameras. In total, more than 20 gregarines from *P. elegans* (Figs 3, 4A–C, F, G), about five gregarines from *P. glycymerica* (data not shown) and five gregarines from *Ph. plumosa* (Fig. 6) were sectioned and examined by TEM.

Ten entire worms of *P. elegans* were fixed in Bouin's solution. The material was dehydrated in a graded alcohol series, infiltrated in a graded series of chloroform-Histomix and finally embedded in Histomix paraffin wax (BioVitrum, Russian Federation). Serial sagittal or coronal sections were prepared on a Microm HM 360 rotary microtome (0.1–1 mm in thick). Sections were mounted on the object slides. The preparations were deparaffinized in xylol and then washed in acetone. After critical point drying in liquid CO_2 and coating with gold, they were observed under a Tescan MIRA3 LMU scanning electron microscope (TESCAN Brno, Czech Republic) (Fig. 4D, E).

DNA isolation, PCR and sequencing: Trophozoites of the gregarine *Selenidium pygospionis*, about 100 cells isolated from the polychaete *P. elegans* (Bolshoy Goreliy Island, Kandalaksha Bay, White Sea, 2009), were fixed and stored in RNAlater stabilization solution (Life Technologies, USA). DNA extraction of this sample was performed with the Diatom DNA Prep 200 kit (Isogen, Russia). About ten trophozoites and one syzygy of *S. pygospionis* isolated from polychaetes *P. glycymerica* (Peter the Great Bay, Sea of Japan, 2007) were rinsed with seawater, deposited into 1.5-ml microcentrifuge tubes and then were lyzed by the alkaline procedure (Floyd et al. 2002). In a similar manner, 25 trophozoites of the gregarine *S. pherusae* isolated from polychaete *Ph. plumosa* (Peter the Great Bay, Sea of Japan, 2007) were lysed. The lysates obtained in two last cases were directly used in PCR.

The nucleotide sequences of *S. pygospionis* from *P. elegans* and *S. pherusae* were amplified in several PCRs with different pairs of primers (Table 1 and Supplementary Material Fig. S1). A set of overlapping fragments (I–IV and VI–VII, respectively; see Supplementary Material Fig. S1) encompassing SSU rDNA, ITS 1 and 2, 5.8S rDNA, and LSU rDNA was obtained. For *S. pygospionis* from *P. glycymerica*, only one fragment (V) containing the near complete SSU rDNA was PCR-amplified (Table 1 and Supplementary Material Fig. S1). All PCRs were performed with an Encyclo PCR kit (Evrogen, Russia) in a total

volume of 25 μl using a DNA Engine Dyad thermocycler (Bio-Rad) and the following protocol: initial denaturation at 95 °C for 3 min; 40 cycles of 95 °C for 30 sec, annealing at 45 °C (fragments I, II, V, and VI) or 50 °C (fragments III, IV, and VII) for 30 sec, and extension at 72 °C for 1.5 min; and final extension at 72 °C for 10 min. PCR products of the expected size were gel-isolated by a Cytokine DNA isolation kit (Cytokine, Russia). For fragments I, II, and IV–VII, the PCR products were sequenced directly. Fragment III was cloned by using an InsTAclone PCR Cloning Kit (Fermentas, Lithuania) because the corresponding PCR product was heterogeneous. Sequences were obtained by using an ABI PRISM BigDye Terminator v. 3.1 reagent kit and an Applied Biosystems 3730 DNA Analyzer for automatic sequencing. After assembling the read fragments with the use of the BioEdit 7.0.9.0 program (Hall 1999), the resulting contiguous sequences were deposited in GenBank (accession numbers: MH061278–80).

Molecular phylogenetic analysis: Four nucleotide alignments were prepared for phylogenetic analyses: SSU (18S) rDNA (128 and 53 sequences), LSU (28S) rDNA, and ribosome operon (concatenated SSU, 5.8S, and LSU rDNA sequences). The alignments were generated in the MUSCLE 3.6 program (Edgar 2004) and manually adjusted with the use of the BioEdit 7.0.9.0 program (Hall 1999): gaps, columns containing few nucleotides and hypervariable regions were removed. The final length of the alignments was 1,550 bp. The taxon sampling of 128 sequences alignment was designed as to maximize the phylogenetic diversity and the completeness of sequences in the alignments. Representatives of heterokonts and rhizarians were used as outgroups. The "reduced" SSU rDNA alignment (53 sequences, 1,550 sites) was used as a constituent part of the concatenated ribosomal operon dataset and, consequently, covered the same taxon sampling.

For the LSU rDNA and ribosomal operon (concatenated SSU, 5.8S, and LSU rDNAs) analyses, taxon sampling of only 53 sequences were used due to the limited availability of data for LSU rDNA and, especially, 5.8S rDNA. Therefore, the 5.8S rDNA (155 sites in the alignment) was rejected from the analysis of concatenated rDNA genes for seven sequences (*Chromera velia*, *Colponema vietnamica*, *Goussia desseri*, *Stentor coeruleus*, and 3 environmental sequences: Ma131 1A38, Ma131 1A45, and Ma131 1A49): the corresponding 155 positions were replaced with "N" in the final ribosomal operon dataset. The resulting datasets contained 53 sequences (2,913 sites) for the LSU rDNA and the concatenated rDNA sequences (4,618 sites) of the same 53 taxa for the ribosomal operon. Thus, both taxon samplings comprised an identical set of species, all of which were also represented in the alignment of the 128 SSU rDNA sequences.

Maximum-likelihood (ML) analyses were performed with the RAxML 7.2.8 program (Stamatakis 2006) under the GTR + Γ model and CAT approximation (25 rate categories per site). The procedure included 100 independent runs of the ML analysis and 1,000 replicates of multiparametric bootstrap. Bayesian inference (BI) analyses were conducted with the MrBayes 3.2.6 program (Ronquist and Huelsenbeck 2003) under GTR + Γ + I model with eight categories of discrete gamma distribution. The program was set to operate under the following parameters: nst = 6, ngammacat = 6, rates = invgamma; the parameters of Metropolis Coupling Marcov Chains Monte Carlo (mcmc): nchains = 4, nruns = 4, temp = 0.2, ngen = 10,000,000, samplefreq = 1,000, burninfrac = 0.5 (the first 50% of the 20,000 sampled trees, i.e., the first 5,000, were discarded in each run). The following averages and standard deviations of split frequencies were obtained: 0.014059 for the SSU rDNA analysis, 0.001084 for the LSU rDNA analysis, and 0.001113 for

the ribosomal operon concatenated analysis. The calculations of bootstrap support for the resulting Bayesian trees were performed with the use of the RAxML 7.2.8 program under the same parameters as for the ML analyses (see above).

Alternative tree topologies were manually created and edited with the use the TreeView 1.6.6 program (Page 1996). The reference trees topologies of SSU rDNA (128-taxon dataset), LSU rDNA, and ribosomal operons (53-taxon datasets each) were copied from the trees showed in Figures 7 and 8. Alternative topologies of SSU rDNA phylogenies were constructed by combining all *Selenidium*-like archigregarines in a single clade (see Fig. 9A) followed by positioning this clade within the sporozoans clade successively as a sister group to the cryptosporidians and eugregarine clades Eg1 and Eg2 under assumptions of either their monophyly or polyphyly, or as a sister group to the combined clade cryptosporidians + eugregarines (monophyletic or polyphyletic variants). The eugregarine clades Eg1 and Eg2 were picked out as repeatedly recovered in the reference trees and published phylogenies. Alternative topologies of LSU rDNA and ribosomal operon phylogenies were constructed in the same way, but with the use of the only archigregarine sequence (*S. pygospionis* from *P. elegans*) available to date. Topology tests were performed in Moscow State University with TREE-PUZZLE 5.3.rc16 and CONSEL 0.1j programs (Schmidt et al. 2002; Shimodaira and Hasegawa 2001). The following tests were used: bootstrap probability (Felsenstein 1985); expected-likelihood weights (Strimmer and Rambaut 2002); Kishino–Hasegawa test (Kishino and Hasegawa 1989); Shimodaira–Hasegawa test (Shimodaira and Hasegawa 1999); weighted Shimodaira–Hasegawa Test (Shimodaira and Hasegawa 1999); approximately unbiased test (Shimodaira 2002).

Acknowledgements

Appendix A. Supplementary Data

Supplementary data associated with this article can be found, in the online version, at https://doi.org/10.1016/j.protis.2018.06.004.

References

Adl SM, Simpson AG, Lane CE, Lukeš J, Bass D, Bowser SS, Brown M, Burki F, Dunthorn M, Hampl V, Heiss A, Hoppenrath M, Lara E, Gall LL, Lynn DH, McManus H, Mitchell EAD, Mozley-Stanridge SE, Parfrey LW, Pawlowski J, Rueckert S, Shadwick L, Schoch C, Smirnov A, Spiegel FW (2012) The revised classification of eukaryotes. J Eukaryot Microbiol **59**:429–514

Bogolepova II (1953) Gregarines of Peter the Great Bay. Trav Inst Zool Acad Sci URSS **13**:38–56 (in Russian)

Butaeva F, Paskerova G, Entzeroth R (2006) *Ditrypanocystis sp.* (Apicomplexa, Gregarinia, Selenidiidae): the mode of survival in the gut of *Enchytraeus albidus* (Annelida, Oligochaeta, Enchytraeidae) is close to that of the coccidian genus *Cryptosporidium*. Tsytologiya **48**:695–704

Castellon C, Gracia MP (1988) *Lecudina capensis* sp. n. parasitic gregarine of *Pherusa laevis* (Stimpson, 1856) (polychaete annelid). Acta Protozool **27**:291–296

Caullery M, Mesnil F (1899) Sur quelques parasites internes des Annélides. Trav Sta Zool Wimereux **7**:80–99

Caullery M, Mesnil F (1901) Le parasitisme intracellulaire et la multiplication asexuée des grégarines. C R Hebd Séanc Mém Soc Biol Paris **53**:84–87

Cavalier-Smith T (2014) Gregarine site-heterogeneous 18S rDNA trees, revision of gregarine higher classification, and the evolutionary diversification of Sporozoa. Europ J Protistol **50**:472–495

Cavalier-Smith T, Chao EE (2004) Protalveolate phylogeny and systematics and the origins of Sporozoa and dinoflagellates (phylum Myzozoa nom. nov.). Europ J Protistol **40**:185–212

Cox FEG (1994) The evolutionary expansion of the Sporozoa. Int J Parasitol **24**:1301–1316

de Faria G, da Cunha AB, da Fonseca OR (1917) Sobre es protozoarios parasitos da *Polydora socialis*. Brazil Med **31**:243

Desportes I, Schrével J (eds) Treatise on Zoology—Anatomy, Taxonomy, Biology. The Gregarines (2 vols). The early branching Apicomplexa. Brill Leiden, Boston, 781 p

Dibb MJ (1938) *Selenocystis foliata* (Ray) from *Scolelepis fuliginosa* Clpde. and its identity with *Haplozoon* sp. Parasitology **30**:296–308

Douglass TG, Jones I (1991) Parasites of California spionid polychaetes. Bull Mar Sci **48**:308–317

Edgar RC (2004) MUSCLE: multiple sequence alignment with high accuracy and high throughput. Nucleic Acids Res **35**:1792–1797

Felsenstein J (1985) Confidence limits on phylogenies: an approach using the bootstrap. Evolution **39**:783–791

Floyd RM, Abebe E, Papert A, Blaxter ML (2002) Molecular barcodes for soil nematode identification. Mol Ecol **11**:839–850

Fowell (1936a) Observations on the Sporozoa inhabiting the gut of the polychaete worm *Polydora flava* Claparède. J Parasitol **28**:414–430

Fowell (1936b) The fibrillar structures of protozoa, with special reference to schizogregarines of the genus *Selenidium*. J Roy Microsc Soc **56**:12–28

Ganapati PN (1946) Notes on some gregarines from polychaetes of the Madras coast. Proc Ind Acad Sci Sect B **23**:228–248

Giard A (1884) Note sur un nouveau groupe de protozaires parasites des annélides, et sur quelques points de l'histoire des grégarines (*Selenidium pendula*). Association française pour l'avancement des sciences. Congres de Blois, 1884. Première partie. Documents officiels, procès-verbaux **1**:192

Grassé PP (1953) Classe des Grégarinomorphes. In Grassé PP (ed) Traité de Zoologie. Masson, Paris, pp 550–690

Gunderson J, Small EB (1986) *Selenidium vivax* n. sp. (Protozoa, Apicomplexa) from the sipunculid *Phascolosoma agassizii* Keferstein, 1867. J Parasitol **72**:107–110

Hall TA (1999) BioEdit: a user-friendly biological sequence alignment editor and analysis program for Windows 95/98/NT. Nucleic Acids Symp Ser **41**:95–98

Janouškovec J, Tikhonenkov DV, Burki F, Howe AT, Kolísko M, Mylnikov AP, Keeling PJ (2015) Factors mediating plastid dependency and the origins of parasitism in apicomplexans and their close relatives. Proc Natl Acad Sci USA **112**:10200–10207

Kishino H, Hasegawa M (1989) Evaluation of the maximum likelihood estimate of the evolutionary tree topologies from DNA sequence data, and the branching order in hominoidea. J Mol Evol **29**:170–179

Kuvardina ON, Simdyanov TG (2002) Fine structure of syzygy in *Selenidium pennatum* (Sporozoa, Archigregarinida). Protistology **2**:169–177

Leander BS (2006) Ultrastructure of the archigregarine *Selenidium vivax* (Apicomplexa)—A dynamic parasite of sipunculid worms (host: *Phascolosoma agassizii*). Mar Biol Res **2**:178–190

Leander BS (2007) Molecular phylogeny and ultrastructure of *Selenidium serpulae* (Apicomplexa, Archigregarinia) from the calcareous tubeworm *Serpula vermicularis* (Annelida, Polychaeta, Sabellida). Zool Scr **36**:213–227

Leander BS (2008a) Marine gregarines: evolutionary prelude to the apicomplexan radiation? Trends Parasitol **24**:60–67

Leander BS (2008b) A hierarchical view of convergent evolution in microbial eukaryotes. J Eukaryot Microbiol **55**:59–68

Leander BS, Keeling PJ (2003) Morphostasis in alveolate evolution. Trends Ecol Evol **18**:395–402

Lepelletier F, Karpov SA, Le Panse S, Bigeard E, Skovgaard A, Jeanthon C, Guillou L (2014) *Parvilucifera rostrata* sp. nov. (Perkinsozoa), a novel parasitoid that infects planktonic dinoflagellates. Protist **165**:31–49

Levine ND (1971) Taxonomy of the Archigregarinorida and Selenidiidae (Protozoa, Apicomplexa). J Protozool **18**:704–717

Levine ND (1985) Phylum 2. Apicomplexa Levine, 1970. In Lee JJ, Hutner SH, Bovee EC (eds) An Illustrated Guide to the Protozoa. Society of Protozoologists, Kansas, pp 322–374

MacGregor HC, Thomasson PA (1965) The fine structure of two archigregarines, *Selenidium fallax* and *Ditrypanocystis cirratuli*. J Protozool **12**:438–443

Mellor JS, Stebbings H (1980) Microtubules and the propagation of bending waves by the archigregarine, *Selenidium fallax*. J Exp Biol **87**:149–161

Mikhailov KV, Simdyanov TG, Aleoshin VV (2017) Genomic survey of a hyperparasitic microsporidian *Amphiamblys* sp. (Metchnikovellidae). Genome Biol Evol **9**:454–467

Miller MA, Pfeiffer W, Schwartz T (2010) In Creating the CIPRES Science Gateway for inference of large phylogenetic trees. Gateway Computing Environments Workshop (GCE) : pp 1–8

Page RDM (1996) TREEVIEW: An application to display phylogenetic trees on personal computers. Comp Appl Biosci **12**:357–358

Paskerova GG, Frolova EV, Kováčiková M, Panfilkina TS, Mesentsev ES, Smirnov AV, Nassonova ES (2016) *Metchnikovella dogieli* sp. n (Microsporidia: Metchnikovellida), a parasite of archigregarines *Selenidium* sp. from polychaetes *Pygospio elegans*. Protistology **10**:148–157

Perkins FO, Barta JR, Clopton RE, Peirce MA, Upton SJ (2000) Phylum Apicomplexa Levine, 1070. In Lee JJ, Leedale GF, Bradbury P (eds) An Illustrated Guide to the Protozoa **Vol 1**, 2nd edn Society of Protozoologists, Lawrence, Kansas, USA, pp 190–370

Ray HN (1930) Studies on some Sporozoa in polychaete worms. I. Gregarines of the genus *Selenidium*. J Parasitol **22**:370–398

Reichenow E (1932) Sporozoa. In Grimpe G, Wagler E (eds) Die Tierwelt der Nord und Ostsee. Leipzig, Lief 21 (Teil II), pp 1–88

Ronquist F, Huelsenbeck JP (2003) MrBayes 3: Bayesian phylogenetic inference under mixed models. Bioinformatics **19**:1572–1574

Rotari YM, Paskerova GG, Sokolova YY (2015) Diversity of metchnikovellids (Metchnikovellidae, Rudimicrosporea), hyperparasites of bristle worms (Annelida, Polychaeta) from the White Sea. Protistology **9**:50–59

Rueckert S, Horák A (2017) Archigregarines of the English Channel revisited: New molecular data on *Selenidium* species including early described and new species and the uncertainties of phylogenetic relationships. PLoS ONE **12**:e0187430

Rueckert S, Leander BS (2009) Molecular phylogeny and surface morphology of marine archigregarines (Apicomplexa), *Selenidium* spp. , *Filipodium phascolosomae* n. sp. and *Platyproteum* n. g. and comb. from North-Eastern Pacific peanut worms (Sipuncula). J Eukaryot Microbiol **56**:428–439

Rueckert S, Simdyanov TG, Aleoshin VV, Leander BS (2011) Identification of a divergent environmental DNA sequence clade using the phylogeny of gregarine parasites (Apicomplexa) from crustacean hosts. PLoS ONE **6**:e18163

Schmidt HA, Strimmer K, Vingron M, von Haeseler A (2002) TREE-PUZZLE: maximum likelihood phylogenetic analysis using quartets and parallel computing. Bioinformatics **18**:502–504

Schrével J (1966) Cycle de *Selenidium pendula* Giard, 1884, gregarine parasite de *Nerine cirratulus* delle Chiaje (annelide polychete). Protistologica **2**:31–34

Schrével J (1967) Mouvements chez les grégarines. SFRS-CERIMES. www.canal-u.tv/video/cerimes/mouvements_chezle sgregarines.13331

Schrével J (1968) L'ultrastructure de la region aterieure de la Gregarine *Selenidium* et son interet pour l'etude de la nutrition chez les Sporozoaires. J Microsc **7**:391–410

Schrével J (1970) Contribution à l'étude des Selenidiidae parasites d'annélides polychètes. 1.—Cycle biologiques. Protistologica **6**:389–426

Schrével J (1971a) Contribution à l'étude des Selenidiidae parasites d'annélides polychètes. II. Ultrastructure de quelques trophozoites. Protistologica **7**:101–130

Schrével J (1971b) Observations biologiques et ultrastructurales sur les Selenidiidae et leurs conséquences sur la systématique des Grégarinomorphes. J Protozool **18**:448–479

Schrével JS, Buissonnet S, Metais MM (1974) Action de l'uree sur la motilite et les microtubules sous-pelliculaires de Protozoaire *Selenidium hollandei*. C R Acad Sc Paris **278**:2201–2204

Schrével J, Valigurová A, Prensier G, Chambouvet A, Florent I, Guillou L (2016) Ultrastructure of *Selenidium pendula*, the type species of archigregarines, and phylogenetic relations to other marine Apicomplexa. Protist **167**:339–368

Shimodaira H (2002) An approximately unbiased test of phylogenetic tree selection. Syst Biol **51**:492–508

Shimodaira H, Hasegawa M (1999) Multiple comparisons of log-likelihoods with applications to phylogenetic inference. Mol Biol Evol **16**:1114–1116

Shimodaira H, Hasegawa M (2001) CONSEL: for assessing the confidence of phylogenetic tree selection. Bioinformatics **17**:1246–1247

Simdyanov TG (1992) *Selenidium pennatum* sp. n., a new species of archigregarines from *Flabelligera affinis* (Polychaete: Flbelligeridae). Parazitologiya **4**:344–347 (in Russian with English summary)

Simdyanov TG, Kuvardina ON (2007) Fine structure and putative feeding mechanism of the archigregarine *Selenidium orientale* (Apicomplexa: Gregarinomorpha). Europ J Protistol **43**:17–25

Simdyanov TG, Diakin AY, Aleoshin VV (2015) Ultrastructure and 28S rDNA phylogeny of two gregarines: *Cephaloidophora cf. communis* and *Heliospora cf. longissima* with remarks on gregarine morphology and phylogenetic analysis. Acta Protozool **54**:241–262

Simdyanov TG, Guillou L, Diakin AY, Mikhailov KV, Schrével J, Aleoshin VV (2017) A new view on the morphology and phylogeny of eugregarines suggested by the evidence from the gregarine *Ancora sagittata* (Leuckart, 1860) Labbé, 1899 (Apicomplexa: Eugregarinida). PeerJ **5**:e3354 https://peerj.com/articles/3354/

Sokolova YY, Paskerova GG, Rotari YM, Nasonova ES, Smirnov AV (2013) Fine structure of *Metchnikovella incurvata* Caullery and Mesnil 1914 (microsporidia), a hyperparasite of gregarines *Polyrhabdina sp.* from the polychaete *Pygospio elegans*. Parasitology **140**:855–867

Sokolova YY, Paskerova GG, Rotari YM, Nassonova ES, Smirnov AV (2014) Description of *Metchnikovella spiralis* sp. n (Microsporidia: Metchnikovellidae), with notes on the ultrastructure of metchnikovellids. Parasitology **141**:1108–1122

Stamatakis A (2006) RAxML-VI-HPC: maximum likelihood-based phylogenetic analyses with thousands of taxa and mixed models. Bioinformatics **22**:2688–2690

Stebbings H, Boe GS, Garlick PR (1974) Microtubules and movement in the archigregarine, *Selenidium fallax*. Cell Tissue Res **148**:331–345

Strimmer K, Rambaut A (2002) Inferring confidence sets of possibly misspecified gene trees. Proc R Soc Lond B **269**:137–142

Tuzet O, Ormières R (1958) *Selenidium flabelligerae* n. sp. parasite de *Flabelligera diplochaitos* Otto (Annélide sédentaire). Ann Sci Nat Zool Ser **11(20)**:71–76

Tuzet O, Ormières R (1965) *Selenidium productum* nom. nov. pour *Selenidium flabelligerae* Tuz. et Orm., 1958, préémployé. Vie et Milieu **15**:801–802

Valigurová A, Vaškovicová N, Diakin A, Paskerova GG, Simdyanov TG, Kováčiková M (2017) Motility in blastogregarines (Apicomplexa): native and drug-induced organisation of *Siedleckia nematoides* cytoskeletal elements. PLoS ONE **12(6)**:e0179709

Vávra J (1969) *Lankesteria barretti* n. sp. (Eugregarinida, Diplocystidae), a parasite of the mosquito *Aedes triseriatus* (Say) and a review of the genus *Lankesteria* Mingazzini. J Protozool **16**:546–570

Vivier E, Schrével J (1964) Etude au microscope electronique de une gregarine du genre *Selenidium*, parasite de *Sabellaria alveolata* L. J Microscopie Paris **3**:651–670

Vivier E, Schrével J (1966) Les ultrastructures cytoplasmiques de *Selenidium hollandei*, n. sp., Grégarine parasite de *Sabellaria alveolata* L. J Microscopie Paris **5**:213–228

Vivier E, Devauchelle G, Petitprez A, Porchet-Henneré E, Prensier G, Schrével J, Vinckier D (1970) Observations de cytologie comparée chez les sporozoaires. I.—Les structures superficielles chez les formes végétatives. Protistologica **6**:127–150

Wakeman KC, Horiguchi T (2018) Morphology and molecular phylogeny of the marine gregarine parasite *Selenidium oshoroense* n. sp. (Gregarina, Apicomplexa) isolated from a Northwest Pacific *Hydroides ezoensis* Okuda 1934 (Serpulidae, Polychaeta). Mar Biodiv **48**:1489–1498 https://doi.org/10.1007/s12526-017-0643-1

Wakeman KC, Leander BS (2012) Molecular phylogeny of pacific archigregarines (Apicomplexa), including descriptions of *Veloxidium leptosynaptae* n. gen., n. sp., from the sea cucumber *Leptosynapta clarki* (Echinodermata), and two new species of *Selenidium*. J Eukaryot Microbiol **59**:232–245

Wakeman KC, Leander BS (2013) Molecular phylogeny of marine gregarine parasites (Apicomplexa) from tube-forming polychaetes (Sabellariidae, Cirratulidae, and Serpulidae), including descriptions of two new species of *Selenidium*. J Eukaryot Microbiol **60**:514–525

Wakeman KC, Heintzelman MB, Leander BS (2014) Comparative ultrastructure and molecular phylogeny of *Selenidium melongena* n. sp. and *S. terebellae* Ray 1930 demonstrate niche partitioning in marine gregarine parasites (Apicomplexa). Protist **165**:493–511

WoRMS (2018) *Selenidium* Giard, 1884. Accessed through: World Register of Marine Species at http://www.marinespecies.org/aphia.php?p=taxdetails&id=562744 on 2018-03-03